Springer Series in Materials Science 216

Vladimir E. Fortov

Extreme States of Matter

High Energy Density Physics

Second Edition

Springer

Springer Series in Materials Science

Volume 216

Series Editors

Robert Hull, Charlottesville, USA
Chennupati Jagadish, Canberra, Australia
Richard M. Osgood, New York, USA
Jürgen Parisi, Oldenburg, Germany
Tae-Yeon Seong, Seoul, Korea, Republic of (South Korea)
Shin-ichi Uchida, Tokyo, Japan
Zhiming M. Wang, Chengdu, China

The Springer Series in Materials Science covers the complete spectrum of materials physics, including fundamental principles, physical properties, materials theory and design. Recognizing the increasing importance of materials science in future device technologies, the book titles in this series reflect the state-of-the-art in understanding and controlling the structure and properties of all important classes of materials.

More information about this series at http://www.springer.com/series/856

Vladimir E. Fortov

Extreme States of Matter

High Energy Density Physics

Second Edition

Springer

Prof. Vladimir E. Fortov
President of the Russian Academy of Sciences
Joint Institute for High Temperatures
Moscow, Russia

Translated by Prof. Eugene N. Ragozin
Desk editor Dr. Valery G. Sultanov
Managing editor Dr. Maria S. Aksenteva

Based on updated and integrated translations of "Ekstremal'nye sostoyaniya veshchestva" (Fizmatlit, Moscow 2009), [English translation: Extreme States of Matter (Springer, Berlin-Heidelberg 2011)] and "Fizika Vysokikh Plotnostei Energii" (High Energy Density Physics) (Fizmatlit, Moscow 2012)

ISSN 0933-033X ISSN 2196-2812 (electronic)
Springer Series in Materials Science
ISBN 978-3-319-18952-9 ISBN 978-3-319-18953-6 (eBook)
DOI 10.1007/978-3-319-18953-6

Library of Congress Control Number: 2015959700

Springer Cham Heidelberg New York Dordrecht London
© Springer-Verlag Berlin Heidelberg 2011
© Springer International Publishing Switzerland 2016
This work is subject to copyright. All rights are reserved by the Publisher, whether the whole or part of the material is concerned, specifically the rights of translation, reprinting, reuse of illustrations, recitation, broadcasting, reproduction on microfilms or in any other physical way, and transmission or information storage and retrieval, electronic adaptation, computer software, or by similar or dissimilar methodology now known or hereafter developed.
The use of general descriptive names, registered names, trademarks, service marks, etc. in this publication does not imply, even in the absence of a specific statement, that such names are exempt from the relevant protective laws and regulations and therefore free for general use.
The publisher, the authors and the editors are safe to assume that the advice and information in this book are believed to be true and accurate at the date of publication. Neither the publisher nor the authors or the editors give a warranty, express or implied, with respect to the material contained herein or for any errors or omissions that may have been made.

Printed on acid-free paper

Springer International Publishing AG Switzerland is part of Springer Science+Business Media (www.springer.com)

...but thou hast ordered all things in measure and number and weight
The Wisdom of Solomon 11:20

Preface to the First Edition

This book is concerned with the physical properties of matter and the diverse processes that occur in nature at ultrahigh energy densities, which correspond to extreme pressures and temperatures. It is based on the lecture course I hold at the Moscow Institute of Physics and Technology, as well as reviews and invited papers written for scientific conferences and symposia.

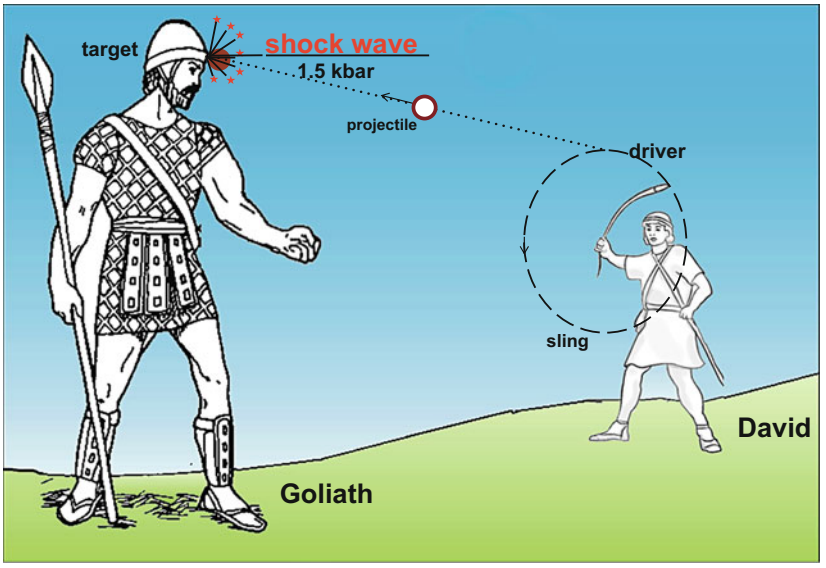

Fig. 1 The battle between David and Goliath [1]

Interest in the physics of extreme states has always been strong, owing to the natural desire of humans to achieve more and to operate with record parameters, as well as owing to the wealth of applications to astrophysics, energy production, and defense. It was indeed military application that fostered the first successful

experiment involving extreme states, which was conducted more than 3000 years ago – during the battle between David and Goliath (Fig. 1). According to the Old Testament [1], the high-velocity impact of a stone, which was shot from David's sling, on Goliath's head killed him. It gave rise to a shock wave in Goliath's head with an amplitude pressure of $\approx$1.5 kbar, which was more than twice the strength of Goliath's frontal bone and determined the outcome of the duel, to the great joy of the army and people of Israel. Discovered to be successful at that time, this scheme of action serves as the basis for all subsequent experiments in the area of dynamic high-energy-density physics.

The application of more powerful and highly sophisticated energy cumulation systems – chemical and nuclear explosives, powder, light-gas, and electrodynamic "guns", charged-particle fluxes, laser and X-ray radiation – has enabled the velocity of "thrown" projectiles to be raised by three or four orders of magnitude, since the time of David, and the pressure in the shock wave by six to eight orders of magnitude, thereby reaching the megabar-gigabar pressure range and "nuclear" energy densities in substances.

In the 20th century, mainstream high-energy-density physics was closely related to the arrival of the atomic and space era in our civilization. In nuclear charges, the high energy densities generated by intense shock waves serve to initiate chain nuclear reactions in compressed nuclear fuel. In thermonuclear charges and microtargets for controlled fusion, high-energy states are the main instrument for compressing and heating the thermonuclear fuel and initiating thermonuclear reactions in it.

Recently, interest in the science of extreme states has been rekindled as a result of the emergence of new experimental techniques for the generation of high-energy states in terrestrial conditions as well as intriguing new observational astrophysical data obtained by modern-generation ground-based and space telescopes operating at different wavelengths and by unmanned space stations.

Although the limiting pressures in laboratory plasmas so far differ from the maximum astrophysical values by 20–30 orders of magnitude, this gap is rapidly shrinking. The physical processes in a laboratory and in space quite frequently exhibit an amazing diversity and, at the same time, striking similarities, thereby testifying, at the least, to the uniformity of the physical principles of the behavior of matter over an extremely broad range of pressures (42 orders of magnitude) and temperatures (up to 10^{13} K).

However, as pointed out by Voltaire, "... in nature this phenomenon is perfectly natural and commonplace. The domains of some rulers in Germany and Italy, which can be circled in about a half hour, when compared with the empires of Turkey, Moscow, or China, give only a faint idea of the remarkable contrasts that are hidden in all of nature" (Voltaire, *Le Micromégas*, Paris 1752) [3].

It is significant that the range of technical problems related to the physics of extreme states is progressively broadening along with the range of the fundamental ones. These states of matter underlie the operation of pulsed thermonuclear reactors with inertial confinement of the hot plasma, high-power explosive-driven magnetic generators, power installations and rocket propulsors with gas-phase nuclear

reactors, plasmachemical and microwave reactors, plasmatrons, and high-power sources of optical radiation and X-rays. In the energy installations of the future, strongly compressed and heated plasmas will be employed as the working medium, like water vapor in modern thermal power stations.

Extreme states emerge when a substance is subjected to intense shock, detonation, or electroexplosion waves, concentrated laser radiation, electron and ion beams, in powerful chemical and nuclear explosions, in the pulsed vaporization of liners in pinches and magnetic cumulation generators, in the hypersonic motion of bodies in dense planetary atmospheres, in high-velocity impacts, and in many other situations characterized by ultrahigh pressures and temperatures. The physics of near-electrode, contact, and electroexplosion processes in vacuum breakdown is intimately related to the high-energy plasma that defines the operation of high-power pulsed accelerators, microwave radiation generators, and plasma switches.

High energy densities determine the behavior of matter in a vast domain of the phase diagram that occupies the range from a solid and a fluid to a neutral gas, covers the phase boundaries of melting and boiling, and also the metal-dielectric transition domain. The metal–dielectric transition problem has been much explored in experiments involving the multiple (quasi-isentropic) shock-wave compression of dielectrics, their metallization, and the recently discovered plasma phase transitions in the megabar pressure range, as well as dielectrization of strongly compressed simple metals.

Scientific interest in high-energy plasmas has also been rekindled along with pragmatic interest, because the great bulk of matter in the universe is in precisely this exotic state. For about 95% of the mass (neglecting dark matter), according to modern estimates, is the plasma of ordinary and neutron stars, pulsars, black holes, and giant planets of the solar system, as well as the recently discovered hundreds of planets beyond the solar system.

Prior to becoming a star, the matter of the universe experiences the most diverse physical transformations: from quarks and elementary particles to complex molecules and again to atoms and particles; from relativistic energies to absolute zero and again to the state of high-energy-density plasma; from enormous densities to ultrahigh vacuum and again to the densities of atomic nuclei and quarks. And so our fundamental knowledge of the structure, evolution, and history of the universe is directly dependent on our understanding of the behavior of matter in all of its transformations up to ultrahigh energy densities, which forms not only specific physical models, but also the world-outlook of modern natural science because, by steadily increasing the high energy densities attainable by investigations on Earth and in space, we delve into the past, using a "time machine", looking for the singular conditions of the Big Bang – the instant of the universe's inception $\approx$1.5 billion years ago.

Today we can clearly see that the study of matter in extreme states is one of the "hottest" and most rapidly developing basic scientific disciplines, situated at the interface between plasma physics, nonlinear optics, condensed-matter physics, nuclear, atomic and molecular physics, relativistic and magnetic hydrodynamics, involving a wealth of compression- and heating-stimulated physical effects and a

constantly widening variety of objects and states in which the plasma nonideality is critically important. Despite the extraordinary diversity of the objects and experimental and astrophysical situations, they all share the common property that high energy densities play a decisive role in their physical behavior.

These circumstances are a permanent steadfast incentive for intensive theoretical and experimental investigations, which have recently resulted in a great body of new and, most important, reliable information about the thermodynamic, structural, gasdynamic, optical, electrophysical, and transport properties of matter under extreme conditions. These specific data are contained in a massive flow of original publications, some of which are not easily accessible to Russian scientists, especially young ones.

This book attempts to systematize, generalize, and set forth from a unified viewpoint the theoretical and experimental material related to this new realm of science, and to show, following Titus Lucretius Carus, "Thus from the mixture of the elements there emerge infinite multitudes of creatures, which are Strange and highly diversified in appearance" (Titus Lucretius Carus) [2]. In it I endeavor to discuss the maximally broad range of problems related to high-energy-density physics. That is why many interesting astrophysical, laser, and nuclear-physical problems as well as technical applications are briefly outlined and the reader is referred to original papers and monographs. In doing this, I did not aim to include everything known about extreme states to date. Emphasis was placed on the issues which appeared to be most interesting to me and which I happened to work on directly. Realizing that the material touched upon in this book will steadily broaden, become defined more precisely, and inevitably become obsolete owing to the extremely rapid development of high-energy-density physics, I would be thankful to readers who send me critical remarks and suggestions.

It is hoped that this book will be beneficial to a wide readership of scientists, postgraduates, and students in the natural sciences by offering them access to original papers and being a helpful guide through the exciting problems of modern Extreme State Physics.

In the preparation of the manuscript I benefited from the assistance, stimulating discussions, and advice of Yu.Yu. Balega, N.E. Andreev, A.Ya. Faenov, S.I. Blinnikov, M.B. Kozintsova, A.N. Starostin, V.S. Imshennik, I.L. Iosilevskii, N.S. Kardashev, V.G. Sultanov, A.N. Sissiakian, B.Yu. Sharkov, and V.A. Yakovleva, to whom I express my sincere gratitude.

Abramtsevo, Russia Vladimir Fortov
May 2009

References

1. Bible. Old Testament, 1 Samuel, 17: 34, 40, 43, 48–51
2. Lucretius: The Nature of Things. Penguin, London (2007)
3. Voltaire: Micromégas and Other Short Fiction. Penguin, London (2002)

Preface to the Second Edition

Dear reader!

The monograph before you is concerned with the diverse physical phenomena occurring in matter in which there is an extremely high energy density, generating in turn ultrahigh pressures and temperatures.

This second edition results from a thorough revision of the first edition [1], which was published in English in 2011, together with the addition of material from another monograph [2], published in Russian in 2012. All the material included herein has been substantially updated and the subject matter of the book considerably expanded by including recent experimental results as well as new theoretical approaches and models. This is also reflected in the new subtitle, which corresponds to the contents more adequately.

This book will hopefully arouse readers' curiosity and be helpful to scientists, post-graduates, and students interested in this fascinating realm of modern physics, and especially to those who have decided to make this field the subject of their future research activities.

Abramtsevo, Moscow — Vladimir E. Fortov
April 2015

References

1. Fortov, V.E.: Ekstremal'nye sostoyaniya veshchestva (Extreme States of Matter). Fizmatlit, Moscow (2009) [Translated into English: Extreme States of Matter. Series: The Frontiers Collection. Springer, Berlin/Heidelberg (2011)]
2. Fortov, V.E.: Fizika Vysokikh Plotnostei Energii (High Energy Density Physics). Fizmatlit, Moscow (2012)

Contents

Chapter 1
Introduction

We already know the laws that govern the behavior of matter under all but the most extreme conditions

S. Hawking. A Brief History of Time (p. 168).

The states of matter at extremely high temperatures and densities, and hence with extraordinarily high energy densities, have always attracted researchers, owing to the possibility of reaching record parameters, advancing to new domains of the phase diagram, and producing in the laboratory the exotic states that gave birth to our universe through the Big Bang and which now account for the great bulk (90–95 %) of the mass of baryon (visible) matter—in stellar and interstellar objects, planets, and exoplanets [9, 12, 15–17, 22, 29, 35, 36]. That is why the study of these states of matter—so exotic for us in terrestrial conditions and yet so typical for the rest of the universe—is of great cognitive importance, forming our modern notions of the surrounding world. Furthermore, a constant pragmatic incentive for such investigations is the application of high-energy-density states in nuclear, thermonuclear, and impulse power engineering, high-voltage and high-power electrophysics, for the synthesis of superhard materials, for strengthening and welding materials, for the impact protection of space vehicles, and, of course, in defense. For the nuclear devices with controllable (inertial confinement fusion, ICF) and quasi-controllable (atomic and hydrogen bombs) energy release rely on the initiation of nuclear reactions in a strongly compressed and heated nuclear fuel.

The revolutionary discoveries in astronomy of recent decades [9, 16, 17, 22, 29, 35, 36] (neutron stars, pulsars, black holes, wormholes, γ-ray bursts, exoplanets) furnish new examples of extreme states, which call for investigation in order to solve the most fundamental problems of modern astrophysics.

Beginning in the mid-1950s in the framework of nuclear defense projects, high-energy-density research has made considerable progress owing to the advent of new devices for the generation of high energy densities, such as lasers, charged-particle beams, high-current Z-pinches, explosion and electric explosion generators of intense shock waves, multistage light-gas guns and diamond anvils. These complicated and expensive technical devices have made it possible to substantially advance along the scale of energy density attainable in a physical experiment and to obtain in laboratory or quasi-laboratory conditions the states that range into

© Springer International Publishing Switzerland 2016

V.E. Fortov, *Extreme States of Matter*, Springer Series in Materials Science 216,
DOI 10.1007/978-3-319-18953-6_1

the megabar–gigabar pressure domain, which is unattainable with the traditional techniques of experimental physics. The use of new generators for the cumulation of high energy densities leads to a variety of fascinating physical effects, such as a radical restructuring of the energy spectrum and composition of a compressed and heated material [12, 13, 15, 22, 29], new cooperative effects and diverse instabilities in the interaction of directed energy fluxes with a dense plasma, its transient motion under the conditions of substantial radiative energy transfer, and relativistic, gravitational, and nuclear phenomena as well as a number of other exotic effects, which may be predicted, if at all, only in the most general form [16, 17, 29].

By now high-energy-density physics has turned into an extensive and rapidly developing branch of modern science that makes use of the most sophisticated means of generation, diagnostic techniques, and numerical simulations with high-power supercomputers.

It is no accident that half of the 30 problems of "the physics minimum at the beginning of the XXIst century" proposed by Academician V.L. Ginzburg [17] are to a greater or lesser degree dedicated to high-energy-density physics.

The term "high" is conventionally [9, 12, 15, 22, 29] used to refer to in-substance energy densities exceeding $\approx 10^4$–10^5 J/cm^3, which corresponds to the binding energy of condensed media (for instance, high explosives (HEs), H_2, or metals) and the pressure level of millions of atmospheres. For comparison: the pressure at the center of the Earth is equal to $\approx$3.6 Mbar, of Jupiter to $\approx$40 Mbar, and at the center of the Sun to $\approx$200 Gbar. We mention that the term "substance" is considered to mean a lengthy continuous medium of macroscopic size. The "ultra-extreme" states inside the atomic nucleus and the conditions occurring in microscopic volumes in the individual collisions of the nuclei speeded up in accelerators to subluminal velocities, which are the subject of relativistic nuclear physics [31], are therefore beyond the scope of detailed consideration.

As a rule, a substance under high-energy-density conditions is in the plasma state—an ionized state arising from thermal- and/or pressure-induced ionization. In astrophysical objects, such compression and heating is effected by gravitational forces and nuclear reactions, and in laboratory conditions by intense shock waves, which are excited by a wide variety of "drivers", ranging from two-stage gas guns [30] to lasers [2, 19] and high-current Z-pinches [18, 24] with powers of hundreds of terawatts.[1] However, while the lifetime of extreme states in astrophysical objects ranges from milliseconds to billions of years, making it possible to conduct detailed observations and measurements of them with the help of space probes and orbital and ground-based telescopes of different wavelengths, in terrestrial conditions we have to do with the microsecond–femtosecond duration range [2, 12, 15], which calls for the application of ultrafast specific diagnostic techniques.

At present, every large-scale physical facility that generates extremely high pressures and temperatures is engaged in work programs (not infrequently interna-

[1] The total power of terrestrial electric power plants amounts to about 3.5 TW.

tional) on the basic physics of high energy density, in addition to having practical, applied tasks in impulse energetics or defense. It is significant that the experimental capabilities of these devices are extending rapidly. In particular, modern short-pulse laser systems (NIKE; OMEGA; TRIDENT, LULI-200, the first module of the National Ignition Facility (NIF), USA; Laser Mégajoule (LMJ), France; GEKKO-XII, Japan; VULKAN, Great Britain; Iskra-6, Russia; etc. (see Tables 2.1 and 3.1)) are capable of releasing 1–1.8 MJ in a volume of the order of 1 mm^3 in several nanoseconds to produce pressures of tens to hundreds of megabars.

Furthermore, the Z-pinch technology is now exhibiting considerable progress: at the Sandia facility, USA, ≈1.8 MJ soft X-ray radiation was obtained in the collapse of plasma liners during 5–15 ns in a region measuring about 1 cm^3 [8, 33, 34]. Supplemented by experiments with diamond anvils, explosion and electric explosion devices, and light-gas guns in the megabar pressure range, these data at record parameters are now the source of new and sometimes unexpected information about the behavior of extreme-parameter plasmas [15].

Interestingly, when conducting experiments on extreme-state laboratory plasma, even today it is possible to partly reproduce on a small scale many parameters, effects, and processes occurring in astrophysical objects, information on which has become accessible by use of ground- and space-based means of observation. These are the data on hydrodynamic mixing and instabilities, shock-wave phenomena, strongly radiating and relativistic streams and jets, solitons, relativistic phenomena, equations of state, and the composition and spectra of nonideal plasmas, as well as the characteristics of interstellar cosmic plasma, dust, and a number of other effects.

The physics of high-energy densities is intimately related to several branches of science, for example plasma physics and condensed-matter physics, relativistic physics, the physics of lasers and charged-particle beams, nuclear, atomic, and molecular physics, radiative, gas and magnetic hydrodynamics, and astrophysics. In this case, the distinguishing features of high-energy-density physics are an extreme complexity and strong nonlinearity of the plasma processes occurring in it, the significance of collective interparticle interaction, and relativity. This makes the study of phenomena occurring in this area a fascinating and absorbing task, which attracts a constantly increasing number of researchers.

For all these reasons, the National Research Council of the USA National Academies of Science formulated a large-scale national program of research [29] in the area of high-energy-density physics and gave it high priority. In our subsequent discussions we shall orient ourselves with respect to this document in several aspects [29]. Similar work programs are being vigorously pursued in many developed countries capable of making the requisite experimental devices and having qualified personnel in sufficient number.

The aim of this book is to discuss the current state-of-the-art in high-energy-density physics and its trends, the advantages and limitations of different experimental techniques for generating and diagnosing dense plasmas, and to briefly analyze the results achieved. Because of the vastness and dissimilarity of the material, in several cases the presentation will be abstract-like in form, referring the reader

to the corresponding reviews and monographs [1, 3–7, 9–12, 14–17, 20–23, 25–29, 32, 35, 36].

In the second chapter of the monograph we classify the states of substance under high energy densities and discuss the general form of the phase diagram, dimensionless parameters, and the physical conditions corresponding to terrestrial and astrophysical objects.

The means for generating extreme states available to experimenters are outlined in the third chapter. Considered separately in the fourth chapter are the extreme states of a nuclear explosion—from the excitation of chain reactions and fusion reactions to the damaging action.

The use of lasers and relativistic heavy ion beams for the production and diagnostics of high energy density states will be considered in the fifth chapter of the monograph.

The sixth chapter is concerned with the problems of high energy density physics in the collision of heavy ions accelerated to subluminal velocities, which is attended with the formation of superdense nuclear matter—quark-gluon plasma (QGP).

Numerous technical applications of high energy density physics are briefly outlined in the seventh chapter.

In the eighth chapter we discuss the problems of the physics of ultrahigh energy density, which gives rise to nuclear matter transformations.

The monograph is concluded with a discussion of the most characteristic astrophysical objects and phenomena associated with the realization of extreme energy densities.

The author endeavored to introduce the reader to the rather broad scope of diverse problems of high-energy-density physics, and therefore many topics are discussed by no means in sufficient detail, for the aim of this book is to help readers orient themselves in the vast sea of information accumulated to date, see the trend, and to help young scientists choose the directions of future investigations rather than provide answers to all steadily arising questions.

High energy density physics is a rapidly developing realm of modern science and technology, so that the material set forth in the monograph will be permanently supplemented and improved by new measurements, observations, and models. The author will be thankful to the readers for their additions and criticism of the material presented here.

References

1. Al'tshuler, L.V., Krupnikov, K.K., Fortov, V.E., Funtikov, A.I.: Origins of megabar pressure physics. Herald Russ. Acad. Sci. **74**(6), 613 (2004)
2. Anisimov, S.I., Prokhorov, A.M., Fortov, V.E.: Application of high-power lasers to study matter at ultrahigh pressures. Sov. Phys. – Usp. **27**(3), 181–205 (1984)
3. Ashkroft, N.A.: Condensed matter at higher densities. In: Chiarotti, G.L., Hemley, R.J., Bernasconi, M., Ulivi, L. (eds.) High Pressure Phenomena, Proceedings of the International School of Physics "Enrico Fermi" Course CXLVII, p. 151. IOS Press, Amsterdam (2002)

4. Atzeni, S., Meyer-ter-Vehn, J.: The Physics of Inertial Fusion. Oxford University Press, Oxford (2004)
5. Avrorin, E.N., Vodolaga, B.K., Simonenko, V.A., Fortov, V.E.: Intense shock waves and extreme states of matter. Phys. Usp. **36**(5), 337–364 (1993)
6. Calderola, P., Knopfel, H. (eds.): Physics of High Energy Density. Academic, New York (1971)
7. Chen, F.F.: Introduction to Plasma Physics and Controlled Fusion, vol. 1, 2nd edn. Springer, New York (1984)
8. Cuneo, M.E., Vesey, R.A., Bennett, G.R., et al.: Progress in symmetric ICF capsule implosions and wire-array Z-pinch source physics for double-pinch-driven hohlraums. Plasma Phys. Controlled Fusion **48**(2), R1–R35 (2006)
9. Drake, R.P.: High-Energy-Density Physics. Springer, Berlin/Heidelberg (2006)
10. Fortov, V.E. (ed.): Entsiklopediya nizkotemperaturnoi plazmy (Encyclopedia of Low-Temperature Plasma). Nauka, Moscow (2000)
11. Fortov, V.E.: Intense Shock Waves and Extreme States of Matter. Bukos, Moscow (2005)
12. Fortov, V.E.: Intense shock waves and extreme states of matter. Phys. Usp. **50**(4), 333 (2007)
13. Fortov, V.E., Ternovoi, V.Y., Zhernokletov, M.V., et al.: Pressure-produced ionization of nonideal plasma in a megabar range of dynamic pressures. J. Exp. Theor. Phys. **97**(2), 259–278 (2003)
14. Fortov, V.E., Al'tshuler, L.V., Trunin, R.F., Funtikov, A.I.: High-Pressure Shock Compression of Solids VII: Shock Waves and Extreme States of Matter. Springer, New York (2004)
15. Fortov, V., Iakubov, I., Khrapak, A.: Physics of Strongly Coupled Plasma. Oxford University Press, Oxford (2006)
16. Ginzburg, V.L.: The Physics of a Lifetime: Reflections on the Problems and Personalities of 20th Century Physics. Springer, Berlin/Heidelberg (2001)
17. Ginzburg, V.L.: On superconductivity and superfluidity (what I have and have not managed to do), as well as on the "physical minimum" at the beginning of the XXI century (December 8, 2003). Phys. Usp. **47**(11), 1155 (2004)
18. Grabovskii, E.V., Vorob'ev, O.Y., Dyabilin, K.S., et al.: Excitation of intense shock waves by soft x radiation from a Z-pinch plasma. JETP Lett. **60**(1), 1 (1994)
19. Hammel, B.A., National Ignition Campaign Team: the NIF ignition program: progress and planning. Plasma Phys. Controlled Fusion **48**(12B), B497–B506 (2006)
20. Hemley, R.J., Mao, H.K.: Overview of static high pressure science. In: Hemley, R.J., Chiarotti, G.L., Bernasconi, M., Ulivi, L. (eds.) High Pressure Phenomena, Proceedings of the International School of Physics "Enrico Fermi" Course CXLVII, p. 3. IOS Press, Amsterdam (2002)
21. Hogan, W.J. (ed.): Energy from Inertial Fusion. IAEA, Vienna (1995)
22. Kirzhnits, D.A.: Extremal states of matter (ultrahigh pressures and temperatures). Sov. Phys. – Usp. **14**(4), 512–523 (1972)
23. Kirzhnits, D.A., Lozovik, Y.E., Shpatakovskaya, G.V.: Statistical model of matter. Sov. Phys. – Usp. **18**(9), 649–672 (1975)
24. Knudson, M.D., Hanson, D.L., Bailey, J.E., et al.: Equation of state measurements in liquid deuterium to 70 GPa. Phys. Rev. Lett. **87**(22), 225501 (2001)
25. Kruer, W.L.: The Physics of Laser Plasma Interactions. Addison-Wesley, Reading, MA (1988)
26. Lindl, J.D.: Inertial Confinement Fusion. Springer, New York (1998)
27. Maksimov, E.G., Magnitskaya, M.V., Fortov, V.E.: Non-simple behavior of simple metals at high pressure. Phys. Usp. **48**(8), 761 (2005)
28. Mourou, G.A., Tajima, T., Bulanov, S.V.: Optics in the relativistic regime. Rev. Mod. Phys. **78**(2), 1804–1816 (2006)
29. National Research Council: Frontiers in High Energy Density Physics. National Academies Press, Washington, DC (2003)
30. Nellis, W.J.: Dynamic compression of materials: metallization of fluid hydrogen at high pressures. Rep. Prog. Phys. **69**(5), 1479–1580 (2006)
31. Okun', L.B.: Leptony i kvarki, 2nd edn. Nauka, Moscow (1990) [English Transl.: Leptons and Quarks. North-Holland, Amsterdam (1982)]

32. Pukhov, A.: Strong field interaction of laser radiation. Rep. Prog. Phys. **66**(1), 47–101 (2003)
33. Quintenz, J., Sandia's Pulsed Power Team: pulsed power team. In: Proceedings of 13th International Conference on High Power Particle Beams, Nagaoka (2000)
34. Spielman, R.B., Deeney, C., Chandler, G.A., et al.: Tungsten wire-array Z-pinch experiments at 200 TW and 2 MJ. Phys. Plasmas **5**(5), 2105–2111 (1998)
35. Vacca, J.R. (ed.): The World's 20 Greatest Unsolved Problems. Prentice Hall PTR, Englewood Cliffs, NJ (2004)
36. Zasov, A.V., Postnov, K.A.: Obshchaya astrofizika (General Astrophysics). Vek 2, Fryazino (2006)

Chapter 2
Matter Under Extreme Conditions: Classification of States

Figures 2.1 and 2.2 show the diagrams for the extreme conditions that are realized in a number of natural physical objects and in laboratory experiments. Of course, the parameters given are no better than an estimate and provide only the most general impression of the order of magnitude of the quantities under discussion.

The emergence of extreme states in nature is caused by the forces of gravity, which are inherently long range and unscreened, unlike Coulomb forces (in plasmas). These forces compress and heat the substance either directly or by stimulating exothermic nuclear reactions in massive astrophysical objects and during the early stages of the evolution of the universe [27, 28, 34].

The scale of extreme states realized in nature defies the most vivid imagination, see Figs. 2.3, 2.4 and 2.5. At the bottom of the Mariana Trough in the Pacific Ocean (11 km) the water pressure amounts to 1.2 kbar (1 kbar = 100 MPa), at the Earth's center the pressure is 3.6 Mbar, the temperature[1] $T \approx 0.5$ eV, and the density $\rho \approx$ 10–20 g/cm^3; at the center of Jupiter $P \approx$ 40–60 Mbar, $\rho \approx 30$ g/cm^3, $T \approx 2 \times 10^4$ K; at the center of the Sun $P \approx 240$ Gbar, $T \approx 1.6 \times 10^3$ eV, $\rho \approx 150$ g/cm^3; in the cooling-down stars—white dwarfs—$P \approx 10^{10}$–10^{16} Mbar, $\rho \approx 10^6$–10^9 g/cm^3, and $T \approx 1.6 \times 10^3$ eV. In the targets for controlled fusion with inertial plasma confinement $P \approx 200$ Gbar, $\rho \approx$ 150–200 g/cm^3, and $T \approx 10^8$ eV. Neutron stars, which are elements of pulsars, black holes, γ-ray bursts and magnetars, have what are thought to be the record parameters $P \approx 10^{19}$ Mbar, $\rho \approx 10^{11}$ g/cm^3, $T \approx 10^4$ eV for the mantle and for the core $P \approx 10^{23}$ Mbar, $\rho \approx 10^{14}$ g/cm^3, $T \approx 10^4$ eV for a great magnetic field of 10^{11}–10^{16} Gs (1 Gs = 10^{-4} T).

In the collisions of heavy nuclei accelerated to relativistic velocities in modern accelerators there emerge supercompressed quark-gluon plasma states with ultraextreme parameters $P \approx 10^{30}$ bar, $\rho \approx 10^{15}$–10^{16} g/cm^3, $T \approx 10^{14}$ K, which exceed those realized in extreme astrophysical objects.

[1] In certain fields, such as plasma physics, the electronvolt is used as a unit of temperature. The conversion to kelvins is defined using k, the Boltzmann constant: 1 eV/$k \approx 11.6$ kK (kilokelvin).

© Springer International Publishing Switzerland 2016

V.E. Fortov, *Extreme States of Matter*, Springer Series in Materials Science 216,
DOI 10.1007/978-3-319-18953-6_2

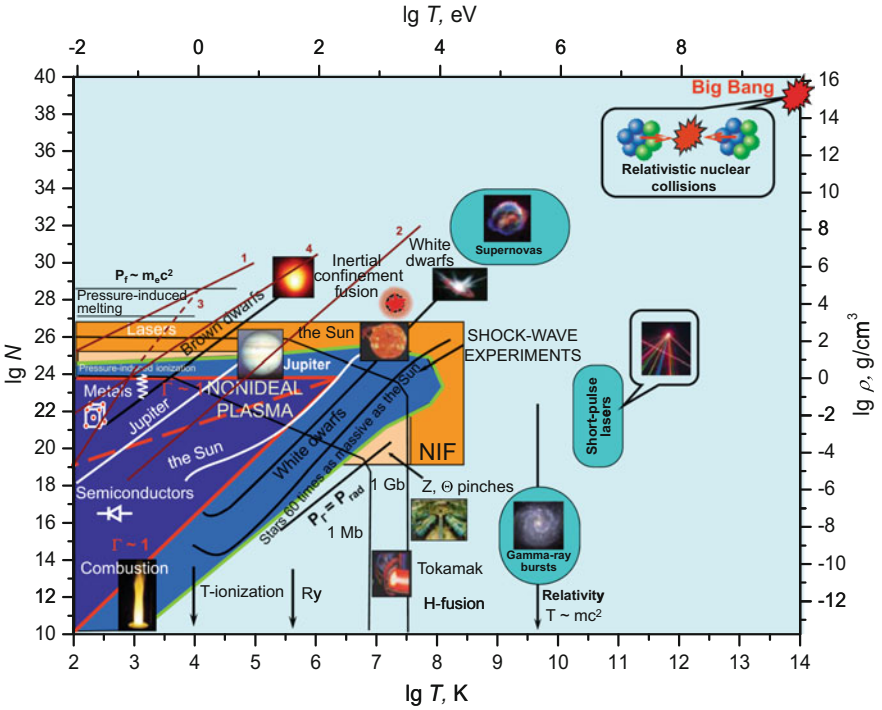

Fig. 2.1 Matter phase diagram [20, 48]. Curves *1–4* denote the states of nuclear-matter component (neon) [34] on the lg ρ scale: *1*—boundary of nuclei degeneracy region; *2*—boundary of ideality region; *3*—melting curve; *4*—boundary of the region in which the lattice may be treated as classical

Amazing is not only the width of the range of parameters realized in nature, but also the huge difference in the characteristic times and dimensions. The dimensions of the visible part of the Universe amount to 1.3×10^{19} cm. The impression produced by this figure becomes even stronger when it is compared with the time of 10^{-24} s taken by light to traverse a distance equal to about the proton size (10^{-13} cm). And the theory of relativity and other modern physical models do operate throughout this tremendous range.

As noted above, by the lower bound of "high energy densities" we mean an energy density comparable to the binding energy of condensed matter, 10^4–10^5 J/cm^3, which corresponds to the valence electron binding energy (of several electron volts) and to pressures of ca. 100 kbar–1 Mbar. These pressures far exceed the ultimate mechanical strength of materials and call for the inclusion of their compressibility and hence hydrodynamic motion under pulsed energy liberation.

In the domain of low pressures and temperatures, matter exhibits the exceptional diversity of properties and structures that we encounter under normal conditions day after day [34].

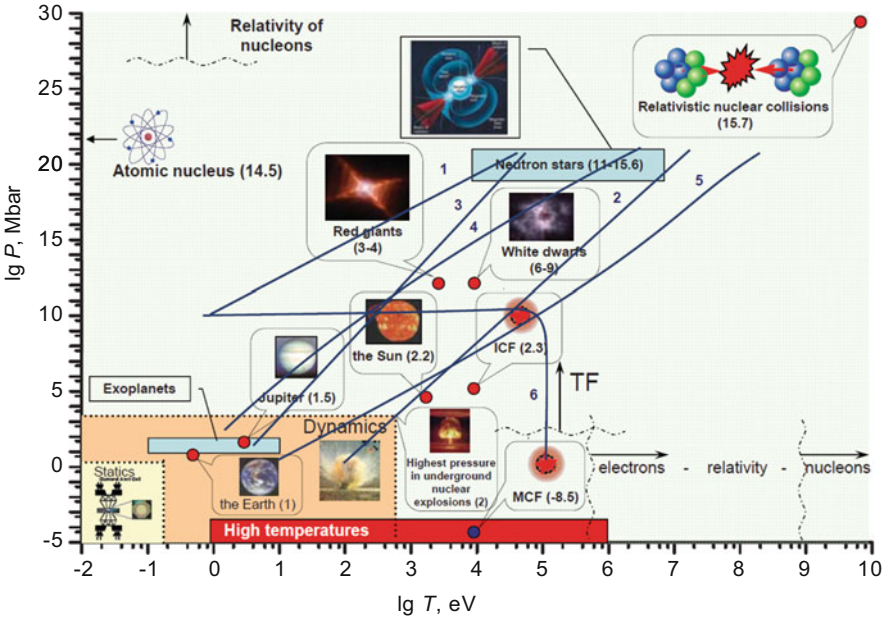

Fig. 2.2 Extreme states [34] in nature and in the laboratory. The *figures in parentheses* indicate the logarithm of density (in g/cm^3). The "statics" domain corresponds to static techniques for high-pressure production, the "dynamics" domain to the dynamic ones, and "high temperatures" to high-temperature experiments. The curves denote the state of the electron component of carbon substance [34]: *1*—boundary of the domain of nuclei degeneracy; *2*—boundary of ideality domain; *3*—melting curve; *4*—boundary of the domain wherein the lattice may be treated as being classical; *5*—boundary of the domain of electron degeneracy; *6*—boundary of the domain of electron relativism

The physical, chemical, structural, and biological properties of substances are sharp nonmonotonic functions of composition. The classification of these "low-energy" states is complicated and cumbersome. They are defined by the position, properties, and occupation features of the electron levels of atoms, ions, and molecules and ultimately underlie the amazing wealth of the forms and manifestations of organic and inorganic nature on Earth.

Laser and evaporative cooling techniques (Fig. 2.6) enable ultralow (10^{-9} K) ion temperatures to be reached and interesting quantum phenomena such as Bose–Einstein condensation, Rydberg matter, and Coulomb condensation to be studied.

With increasing energy density (P and T), substances acquire an increasingly universal structure [34, 35, 61]. The distinctions between the neighboring elements of the periodic system smooth out and the properties of a substance become progressively smoother functions of its composition. Owing to an increase in energy density there occurs an obvious "universalization" or simplification of the substance properties. The growth of pressure and temperature ruptures molecular complexes to form atomic states, which next lose outer-shell electrons, which are responsible for

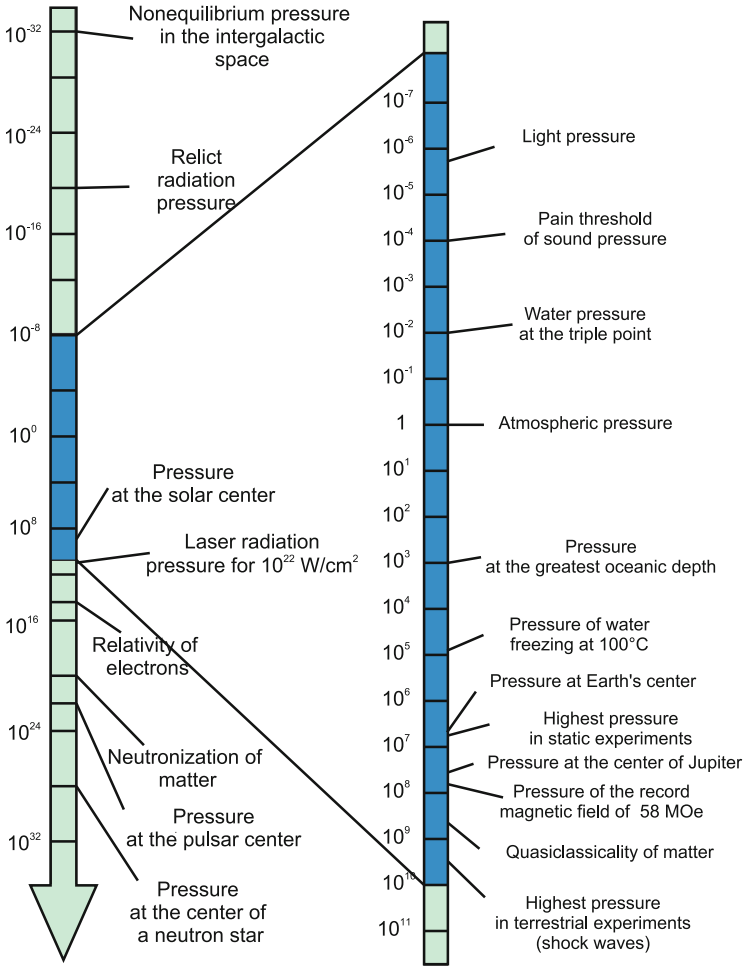

Fig. 2.3 The pressure scale (1 atm $\approx$ 10^5 Pa) in nature encompasses $\approx$64 orders of magnitude. The right-hand scale relates to experimentally attainable conditions [4]

the chemical individuality of the substance, due to thermal and/or pressure-induced ionization. Atomic and ion electron shells restructure to acquire an increasingly regular level occupation, and a crystal lattice after a number of polymorphic transformations (this ordinarily takes place for $P < 0.5$ Mbar) transforms to a close-packed body-centered cubic arrangement common to all substances.

These substance "simplification" processes take place at energy densities comparable to the characteristic energies of the aforementioned "universalization" processes. When the characteristic energy density is of the order of the valence shell energies, $e^2/a_0^4 \approx 3 \times 10^{14}\,\mathrm{erg/cm^3}$ ($a_0 = \hbar/(mc^2) = 5.2 \times 10^{-9}$ cm is the Bohr radius, 1 erg $= 1^{-7}$ J), the order of magnitude of the lower substance

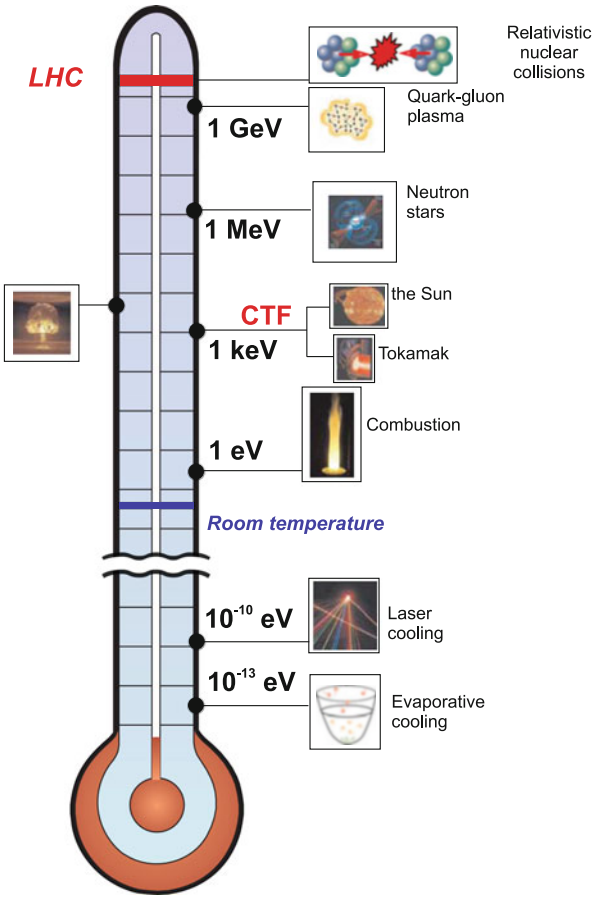

Fig. 2.4 Experimentally attainable temperatures

"universalizing" bound $T \approx 10\,\text{eV}$, $P \approx 300\,\text{Mbar}$, is reached. The exact quantitative determination of these bounds is an important task of the experimental physics of high energy densities (see Chap. 7), especially as theory [35, 61] also predicts a highly varied behavior of substances in the ultramegabar pressure range (shell effects [35, 61], electron and plasma phase transitions [1, 2, 7, 14, 16–18, 22, 23, 32, 41, 64], etc.).

The upper bound of the domain of extreme states is defined by the contemporary level of knowledge in high-energy physics [27, 50, 63] and observational astrophysical data, and is expected to be limited only by our imagination. The ultraextreme matter parameters accessible using modern physical concepts are defined by the so-called Planck quantities [27, 50], which are combinations of the fundamental constants Planck's constant $\hbar$, the velocity of light c, the gravitational constant G,

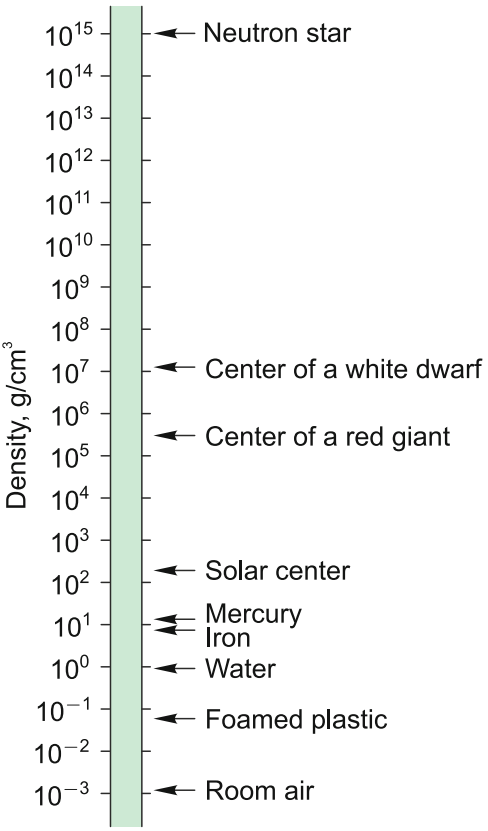

Fig. 2.5 Substance densities on Earth and in the cosmos

and the Boltzmann constant k:

– the length $l_\mathrm{p} = \sqrt{\dfrac{\hbar G}{c^3}} = \dfrac{\hbar}{m_\mathrm{p} c} \approx 1.62 \times 10^{-33}$ cm;

– the mass (the so-called "maximon" mass) $m_\mathrm{p} = \sqrt{\dfrac{\hbar c}{G}} = 2.18 \times 10^{-5}$ g;

– the time $t_\mathrm{p} = \dfrac{l_\mathrm{p}}{c} = \dfrac{\hbar}{m_\mathrm{p} c^2} = \sqrt{\dfrac{\hbar G}{c^5}} = 5.39 \times 10^{-44}$ s;

– the temperature $T_\mathrm{p} = \dfrac{m_\mathrm{p} c^2}{k} = \sqrt{\dfrac{\hbar c^5}{G k^2}} = 1.42 \times 10^{32}$ K;

– the energy $W_\mathrm{p} = m_\mathrm{p} c^2 = \dfrac{\hbar}{t_\mathrm{p}} = \sqrt{\dfrac{\hbar c^5}{G}} = 1.96 \times 10^{9}$ J;

– the density $\rho_\mathrm{p} = \dfrac{m_\mathrm{p}}{l_\mathrm{p}^3} = \dfrac{\hbar t_\mathrm{p}}{l_\mathrm{p}^5} = \dfrac{c^5}{\hbar G^2} = 5.16 \times 10^{93}$ g/cm^3;

– the force $F_\mathrm{p} = \dfrac{W_\mathrm{p}}{l_\mathrm{p}} = \dfrac{\hbar}{l_\mathrm{p} t_\mathrm{p}} = \dfrac{c^4}{G} = 1.21 \times 10^{44}$ N;

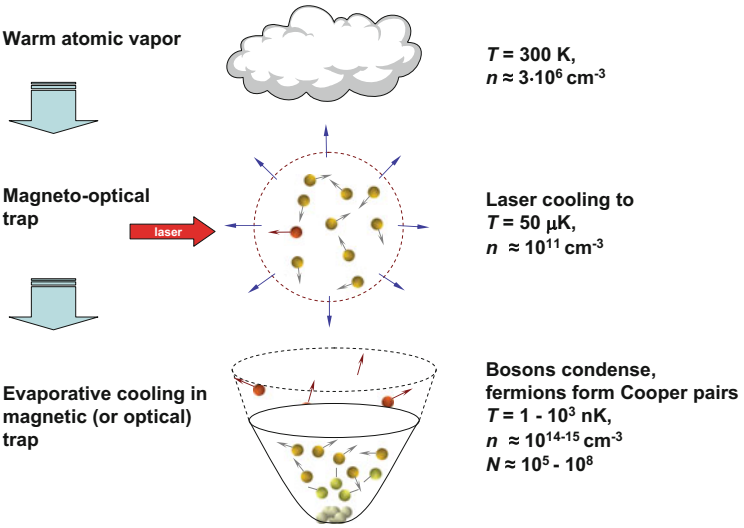

Fig. 2.6 Methods of obtaining extremely low temperatures

- the pressure $p_\mathrm{p} = \dfrac{F_\mathrm{p}}{l_\mathrm{p}^2} = \dfrac{\hbar}{l_\mathrm{p}^3 t_\mathrm{p}} = \dfrac{c^7}{\hbar G^2} = 4.63 \times 10^{113}$ Pa;
- the charge $q_\mathrm{p} = \sqrt{\hbar c 4\pi\varepsilon_0} = 1.78 \times 10^{-18}$ C;
- the power $P_\mathrm{p} = \dfrac{W_\mathrm{p}}{t_\mathrm{p}} = \dfrac{\hbar}{t_\mathrm{p}^2} = \dfrac{c^5}{G} = 3.63 \times 10^{52}$ W;
- the circular frequency $\omega_\mathrm{p} = \sqrt{\dfrac{c^5}{\hbar G}} \approx 1.85 \times 10^{43}\ \mathrm{s}^{-1}$;
- the electric current $I_\mathrm{p} = \dfrac{q_\mathrm{p}}{t_\mathrm{p}} = \sqrt{\dfrac{c^6 4\pi\varepsilon_0}{G}} = 3.48 \times 10^{25}$ A;
- the voltage $V_\mathrm{p} = \dfrac{W_\mathrm{p}}{q_\mathrm{p}} = \dfrac{\hbar}{t_\mathrm{p}} = \sqrt{\dfrac{c^4}{G 4\pi\varepsilon_0}} = 1.05 \times 10^{27}$ V;
- the impedance $Z_\mathrm{p} = \dfrac{V_\mathrm{p}}{I_\mathrm{p}} = \dfrac{\hbar}{q_\mathrm{p}^2} = \dfrac{1}{4\pi\varepsilon_0 c} = \dfrac{Z_0}{4\pi} = 29.98$ Ohm;
- the electric field intensity $E_\mathrm{p} = \dfrac{V_\mathrm{p}}{l_\mathrm{p}} = \dfrac{1}{G}\sqrt{\dfrac{c^7}{4\pi\varepsilon_0\hbar}} = 6.4 \times 10^{59}$ V/cm;
- the magnetic field intensity

$$H_\mathrm{p} = \frac{1}{G}\sqrt{\frac{c^9 4\pi\varepsilon_0}{\hbar}} = 2.19 \times 10^{60}\ \mathrm{A/m} = 2.75 \times 10^{58}\ \mathrm{Oe}.$$

These superextreme matter parameters, at which the known physical laws are thought to be no longer valid, might have been realized early in the Big Bang or at the singularity in the collapse of black holes. In the former case, according to an expanding model of the Universe (A. Friedman, J. Lemaitre [27, 48, 54]) the Universe originated from a domain of Planckian size of the order of 10^{-33} cm with ultrahigh Planckian physical parameters and expanded to the modern size of the order of 10^{28} cm in about 13.7–14.5 billion years. Here, owing to the gravitational compression of stars to the stage of black holes there again emerge singularities—ultrahigh parameters of Planckian scale. In this field physical models are discussed that assume that our space has more than three dimensions and that ordinary matter is in a three-dimensional manifold—the "3-brane world" [54]—embedded in this many-dimensional space. For the present, the capabilities of modern experiments in the area of high-energy-density physics are far from these "Planck" values and allow the properties of elementary particles to be elucidated up to energies on the order of 0.1–10 TeV and down to distances $\approx 10^{-16}$ cm. The launch of the proton–proton collider at CERN with a proton collision energy of 7×7 TeV is an important milestone, opening up the teraelectronvolt energy range.

Considering (following Kirzhnits [34]) the energy range $mc^2 \approx 1$ GeV, which is amenable to a more substantial analysis and is nonrelativistic for nucleons, we obtain a boundary temperature of 10^9 eV, an energy density of 10^{37} erg/cm^2, and a pressure of $\approx 10^{25}$ Mbar, although it is not unlikely that even more extreme states of matter are realized in the cores of massive pulsars and could be found early in the evolution of the universe.

Although our experimental capabilities are progressing rapidly, of course they are only partly able to enter the province of ultraextreme astrophysical states. Material strengths abruptly limit the use of static techniques for investigating high energy densities, because the overwhelming majority of constructional materials are unable to withstand the pressures of interest to us. An exception is diamond—the record holder in hardness ($\sigma_n \approx 500$ kbar); its use in diamond anvils enables a pressure of 3–5 Mbar to be reached in static experiments [31, 32, 41].

Currently superior are dynamic techniques [1, 2, 20, 21, 24, 49, 64], which rely on the pulsed cumulation of high energy densities in substances. The lifetime of such high-energy states is defined by the time of inertial plasma expansion, typically in the range 10^{-10}–10^{-6} s, which calls for the application of sophisticated fast diagnostic techniques. Table 2.1 gives the physical conditions corresponding to the lower bound of the states of interest [9, 24, 48]. One can see that the production of high energy densities in plasmas imposes high demands on the means of generation, necessitating efficient spatial and temporal power compression.

At present, the palm of supremacy is borne by dynamic techniques [1, 2, 20, 21, 24, 49, 64], which are based on the pulsed cumulation of high energy densities in a substance. The lifetime of these high-energy states is defined by the time of inertial plasma expansion, typically in the range 10^{-10}–10^{-6} s, which calls for the

Table 2.1 Physical conditions corresponding to high energy densities of 10^4–10^5 J/cm^3 [48]

Physical conditions	Values of physical parameters
Energy density	$\approx 10^4$–10^5 J/cm^3
Pressure	≈0.1–1 Mbar
Condensed explosives	$W \approx 10^4$ J/cm^3
Pressure	≈400 kbar
Temperature	≈4000 K
Density	≈2.7 g/cm^3
Velocity of detonation	$\approx 9 \times 10^5$ cm/s
Impact of aluminum plate on aluminum, velocity	5–13.2×10^5 cm/s
Impact of molybdenum plate on molybdenum, velocity	3–7.5×10^5 cm/s
Electromagnetic radiation	
Laser, intensity q ($W \sim q$)	2.6×10^{15}–3×10^{15} W/cm^2
Blackbody temperature T ($p \sim T^4$)	2×10^2–4×10^2 eV
Electric intensity E ($W \sim E^2$)	0.5×10^9–1.5×10^9 V/cm
Magnetic induction B ($W \sim B^2$)	1.6×10^2–5×10^2 T
Plasma density for a temperature $T = 1$ keV ($p = nkT$)	6×10^{19}–6×10^{20} cm^{-3}
Laser radiation intensity q, for $\lambda = 1\,\mu$m, $W \sim q^{2/3}$	0.86×10^{12}–4×10^{12} W/cm^2
Blackbody temperature T ($p \sim T^{3.5}$)	66–75 eV

application of sophisticated fast diagnostic techniques. Table 2.1 gives the physical conditions corresponding to the lower bound of the states of interest [9, 24, 48]. One can see that the production of high energy densities in plasmas imposes high demands on the means of generation, necessitating efficient spatial and temporal power compression.

The matter phase diagram corresponding to high energy densities is depicted in Fig. 2.1 [20, 21, 24, 48], which indicates the conditions existing in astrophysical objects as well as in technical and laboratory experimental devices. Being the most widespread state of matter in nature (95 % of the mass of the universe, neglecting dark matter), plasma occupies virtually all the domains of the phase diagram as seen in Fig. 2.1. In this case, special difficulties in the physical description of such a medium are presented by the nonideal plasma domain, where the Coulomb interparticle interaction energy $e^2 n^{1/3}$ is comparable to or higher than the kinetic energy E_k of particle motion. In this domain, $\Gamma = e^2 n^{1/3}/E_k > 1$, plasma nonideality effects cannot be described by perturbation theory [24, 34], while the application of computer parameter-free Monte-Carlo or molecular dynamics methods [18, 41] is fraught with the difficulties of selection of adequate pseudopotentials and correct inclusion of quantum effects.

The effects of electron relativity in the equation of state and transport plasma properties, when $m_e c^2 \approx kT$, correspond to $T \approx 0.5\,\text{MeV} \approx 6 \times 10^6$ K. Above this temperature, the matter becomes unstable with respect to spontaneous electron–positron pair production.

Quantum effects are defined by the degeneracy parameter $n\lambda^3$ ($\sqrt{\hbar^2/2mkT}$ is the thermal de Broglie wavelength). For a degenerate plasma, $n\lambda^3 \gg 1$, the kinetic

energy scale is the Fermi energy $E_F \sim \hbar^2 n^{2/3}/2m$, which increases with plasma density, making the plasma more and more ideal as it contracts, $n \to \infty$; $\Gamma = me^2/(\hbar^2 n^{1/3}) \to 0$. The relativity condition, which corresponds to the condition $m_e c^2 \sim E_F \approx 0.5$ MeV, yields a density of $\approx 10^6$ g/cm^3.

Similar asymptotes are also found in the other limiting case $T \to 0$ of a classical ($n\lambda\!\!\!^{-3} \ll 1$) plasma, where $E_k \approx kT$ and the plasma becomes increasingly ideal, $\Gamma \approx e^2 n^{1/3}/(kT)$, under heating. One can see that the periphery of the matter phase diagram is occupied by ideal ($\Gamma \ll 1$), Boltzmann ($n\lambda\!\!\!^{-3} \ll 1$), or degenerate ($n\lambda\!\!\!^{-3} \gg 1$) plasmas, which are adequately described by currently available physical models [7, 16–18, 20, 23, 24, 34].

The electron plasma in metals and semiconductors corresponds to the degenerate case with an interaction energy $E_{\text{int}} \sim e^2/r_0$, $r_0 \sim \hbar/k_f$, $E_k \sim k_f^2/m$; $\Gamma \sim e^2/\hbar v_f \approx$ 1–5, where $v_f \approx 10^{-2}$–10^{-3} s and the subscript f indicates parameters at the Fermi limit.

For a quark–gluon plasma $E_{\text{int}} \sim g^2/r_0$, $r_0 \sim 1/T$, $E_k \sim T$; Γ up to 300–400. For an ultracold plasma in a trap $\Gamma \sim (n/10^9)^{1/3}/T_k$. The most significant challenge to the theory is presented by the vast domain of nonideal plasmas $\Gamma \geqslant 1$ occupied by numerous technical applications (semiconductor and metal plasma, impulse energetics, explosions, arcs, electric discharges, etc.), where theory predicts qualitatively new physical effects (metallization, "cool" ionization, dielectrization, plasma phase transitions, etc. [19, 20, 24]). Their study requires substantial experimental and theoretical efforts.

Of special interest are plasma phase transitions in strongly nonideal Coulomb systems: the crystallization of dust plasmas (Fig. 2.7) [22, 23] and ions in electrostatic traps [14] and cyclotrons [57, 58], electrolytes [51, 55] and colloidal systems [47], two-dimensional electron systems on the surface of liquid helium [60], exciton condensation in semiconductors [16], etc. Special mention should be made of the recently discovered phase transition in thermal deuterium

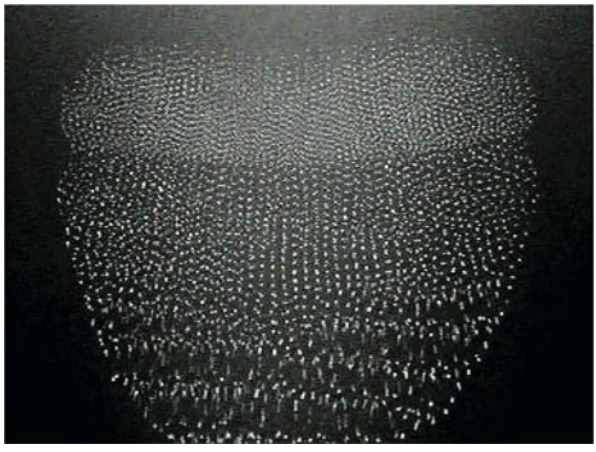

Fig. 2.7 Dust plasma crystal and plasma liquid

plasma [7, 16, 17, 25] quasi-adiabatically compressed to megabar pressures by a series of reverberating shock waves.

The quest for qualitatively new effects of this kind in the nonideal parameter domain is a powerful and permanent incentive to investigate substances at high energy densities [20, 24, 48].

Another characteristic property of a high-energy-density plasma is the collective nature of its behavior and the strong nonlinearity of its response to external energy actions such as shock and electromagnetic waves, solitons, laser radiation, and fast particle fluxes. In particular, the propagation of electromagnetic waves in plasma excites several parametric instabilities (Raman, Thomson, and Brillouin radiation scattering) and is accompanied by the self-focusing and filamentation of radiation, the development of inherently relativistic instabilities, the production of fast particles and jets, and—at higher intensities—the "boiling" of the vacuum with electron–positron pair production [3, 5, 8, 11, 19, 37, 38, 40, 42, 43, 46, 48, 52, 56].

Of special interest in the exposure to extreme energy actions are transient hydrodynamic phenomena such as the instabilities of shock waves and laminar flows [37], transition to the turbulent mode [15], turbulent mixing, and jet and soliton dynamics [13, 15].

Figure 2.8, which is taken from [48], shows the domains of the dimensionless parameters Reynolds number $Re \sim Ul/\nu$ and Mach number $M = v/c$ (where

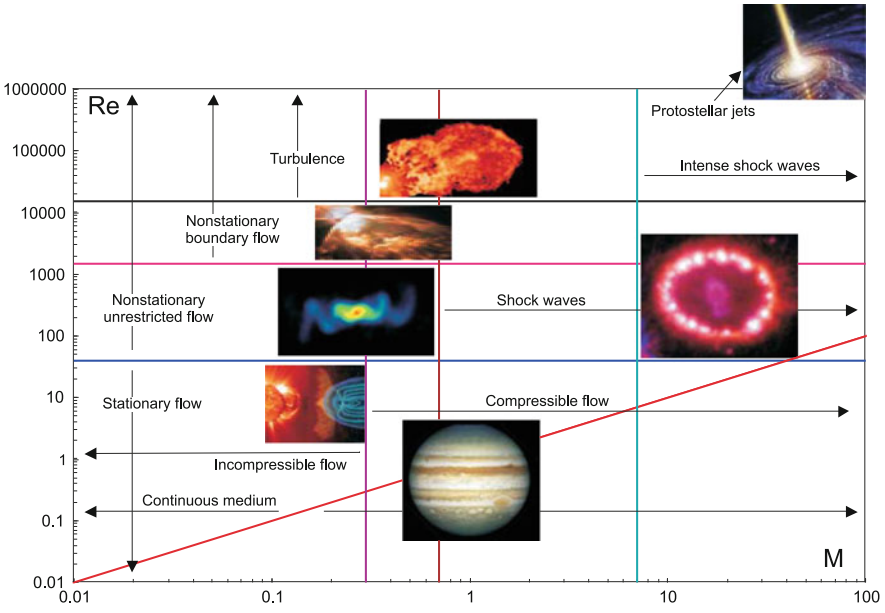

Fig. 2.8 Hydrodynamic modes related to high-energy-density physics [48]. In the explosion of a type Ia supernova, the Mach number ranges from 0.01 in the region of thermonuclear combustion to 100 in the shock wave of its surface explosion. In the majority of astrophysical phenomena $Re > 10^6$ [48]

c is the velocity of sound, l is the characteristic dimension, and ν is the kinematic viscosity) in which the different hydrodynamic phenomena related to high-energy-density physics occur. To astrophysical applications there correspond the flow modes, where $Re > 10^4$ and $M > 0.5$.

All these fascinating and inherently nonlinear phenomena manifest themselves in both astrophysical and laboratory plasmas and, despite the enormous difference in spatial scale, have much in common and make up the subject of "laboratory astrophysics" [13, 56].

Laboratory astrophysics [13, 56] permits the states of matter and processes with high energy densities characteristic for astrophysical objects to be reproduced in microscopic volumes. These are the effects of instability and hydrodynamic mixing; ordinary and magnetohydrodynamic turbulence; the dynamics of intense radiative, soliton, and shock waves; expansion waves; magnetically compressed and fast relativistic jets; and strongly radiating flows.

Of considerable interest is information about the equation of state, composition, optical and transport properties, emission and absorption spectra, cross sections of elementary processes, radiative thermal conductivity coefficients, and properties of relativistic plasma. This makes it possible to study and model the physical conditions, stationary and pulsed processes in astrophysical objects and phenomena such as giant planets and exoplanets, stellar evolution and supernova explosions, gamma-ray burst structure, substance accretion dynamics in black holes, processes in binary and neutron stars as well as in the radiative motion of molecular interplanetary clouds, collisionless shock wave dynamics, and charged-particle acceleration to ultrahigh energies.

Nonlinear optical effects in the interaction of high-power short laser pulses with plasmas enable a major advance in the scales of energy density, specific power, pressure, and temperature by generating extreme-parameter relativistic plasmas in laboratory conditions and attaining record electric and magnetic intensities in terrestrial conditions, which lead, in particular, to the production of high-energy electron and ion flows [46, 52]. These investigations have already provided a wealth of new information for plasma physics, controlled fusion, and astrophysics, as well as technological and defense applications. The progress of this research may result in radically new strong-gradient electron accelerators (see Sect. 7.4), new sources of high-frequency radiation and light (Sect. 7.5), diagnostic techniques, and novel thermonuclear fusion schemes (Sects. 7.2 and 7.3).

Short-pulse electron beams with a density exceeding the plasma density may generate intense plasma waves, which, in combination with ponderomotive forces [46, 52], expel electrons from a plasma channel and produce plasma lenses for the energy transport to the center of compressed fusion targets. Furthermore, relativistic electron beams of tremendous peak power emerge inside the plasma under the action of intense intraplasma fields. In particular, with the help of lasers with a petawatt peak power it has been possible to obtain incredibly high electron and ion currents, which exceed the Alfvén limit by several orders of magnitude, and charged-particle flows of the megavolt energy range [11, 42, 43, 46, 52].

The interaction of intense electron beams with high-power short laser pulses in turn furnishes the possibility of conducting laboratory experiments in the area of quantum electrodynamics, leading to electron–positron pair production and giving rise to Compton X-ray radiation [6, 8, 46, 52]. This opens up interesting practical opportunities for the development of new-generation compact X-ray sources with record radiation brightness for materials science and medicine (see Sect. 7.4).

The generation of high-intensity relativistic electron beams is attractive also from the standpoint of using them as an active medium for free-electron lasers (see Sect. 7.5). The case in point is "fourth-generation" X-ray sources with a record power and tunable wavelength, which is highly important for molecular, biological, and material science research.

Considerable progress has been recently achieved in the technology of high-current Z-pinches [30, 36, 39] produced by magnetodynamic compression of multiple-wire ($\varnothing \approx 6\,\mu$m) and gas liners by passing current pulses (100 ns, ≈20 MA) through them. These experiments enabled the radiative magnetic hydrodynamics of a dense plasma to be studied and produce, in the axial plasma compression, a 5–15 ns soft X-ray pulse with an energy of 1.8 MJ [12, 53, 62].

At the same facility, a current pulse with a megaampere amplitude was employed for the time-programmable electrodynamic acceleration of a metallic liner to a velocity of 12 km/s for the purpose of generating intense shock and adiabatic compression waves. These waves were used to study the equations of substance states in the magabar pressure range [36].

In experiments at the high-current ANGARA facility, soft (with $T \approx 100$ eV) X-ray radiation was used for the highly symmetrical generation of intense shock and radiative waves, as well as for Propelling metallic liners with velocities up to 10 km/s [30]. At the MAGPIE electrophysical facility [44] supersonic plasma jets with characteristics close to the astrophysical ones were obtained.

Experiments on high-energy plasmas yield valuable information about the spectral properties and radiative energy transfer in compressed plasmas. Of special interest are the findings in the strongly nonideal parameter domain [20, 24], where the interparticle interaction effects are responsible for a radical distortion of atomic and ion spectra, partial "transparentization" of compressed plasma, and substantial shifts and broadening of spectral lines (more details are given by Ryutov et al. [56]).

Pulsed energy cumulation in plasma gives rise to diverse hydrodynamic effects, which are comprehensively studied in the corresponding laboratory experiments [13, 48]. These are the Rayleigh–Taylor, Richtmyer–Meshkov, and other instabilities in nonlinear regimes; high-velocity ($M \approx$ 15–20) shock, magnetohydrodynamic, and radiative (thermal) waves; and turbulence and turbulent mixing in compressible emitting media [13].

The application of shock waves generated by sources of locally high energy densities makes it possible to greatly extend the range of experimentally attainable pressures and temperatures and penetrate the parameter domain intermediate between the parameters of chemical HEs and the unique conditions in underground nuclear explosions. Even in the first experiments involving laser-, beam-, and electrodynamically driven shock waves it was possible to obtain interesting

experimental data about the equations of state of hydrogen, deuterium, copper, iron, carbon, and water, and to employ them in the structure analysis of the giant planets of the Solar system and exoplanets [3, 19–21, 24, 30, 36, 49].

Finally, research in the area of high-energy-density physics provides the necessary scientific basis for inertial confinement fusion research [5, 33, 38, 40, 59]. The objective of this work is to ignite the thermonuclear fusion reaction in deuterium–tritium microtargets under high-intensity laser irradiation (the NIF, USA [24, 45], and LMJ, France [10, 29], facilities), under exposure to the soft X-ray radiation of high-current Z-pinches (Zeta, USA) [12, 53, 62] or relativistic heavy-ion beams [26, 59].

We now turn to a more detailed description of the laboratory (Chaps. 3, 5 and 6) and quasilaboratory (Chap. 4) techniques of generating high energy densities in substance developed to date.

References

1. Al'tshuler, L.V.: Use of shock waves in high-pressure physics. Sov. Phys. Usp. **8**(1), 52–91 (1965)
2. Al'tshuler, L.V., Trunin, R.F., Urlin, V.D., et al.: Development of dynamic high-pressure techniques in Russia. Phys. Usp. **42**(3), 261 (1999)
3. Anisimov, S.I., Prokhorov, A.M., Fortov, V.E.: Application of high-power lasers to study matter at ultrahigh pressures. Sov. Phys. Usp. **27**(3), 181–205 (1984)
4. Ashkroft, N.A.: Condensed matter at higher densities. In: Chiarotti, G.L., Hemley, R.J., Bernasconi, M., Ulivi, L. (eds.) High Pressure Phenomena, Proceedings of the International School of Physics "Enrico Fermi" Course CXLVII, p. 151. IOS Press, Amsterdam (2002)
5. Atzeni, S., Meyer-ter-Vehn, J.: The Physics of Inertial Fusion. Oxford University Press, Oxford (2004)
6. Bamber, C., Boege, S.J., Koffas, T., et al.: Studies of nonlinear QED in collisions of 46.6 GeV electrons with intense laser pulses. Phys. Rev. D **60**(9), 092004 (1999)
7. Bezkrovniy, V., Filinov, V.S., Kremp, D., et al.: Monte Carlo results for the hydrogen Hugoniot. Phys. Rev. E **70**(5), 057401 (2004)
8. Burke, D.L., Field, R.C., Horton-Smith, G., et al.: Positron production in multiphoton light-by-light scattering. Phys. Rev. Lett. **79**(9), 1626–1629 (1997)
9. Calderola, P., Knopfel, H. (eds.): Physics of High Energy Density. Academic, New York (1971)
10. Cavailler, C.: Inertial fusion with the LMJ. Plasma Phys. Controlled Fusion **47**(12B), B389–B403 (2005)
11. Clark, E.L., Krushelnick, K., Davies, J.R., et al.: Measurements of energetic proton transport through magnetized plasma from intense laser interactions with solids. Phys. Rev. Lett. **84**(4), 670–673 (2000)
12. Cuneo, M.E., Vesey, R.A., Bennett, G.R., et al.: Progress in symmetric ICF capsule implosions and wire-array Z-pinch source physics for double-pinch-driven hohlraums. Plasma Phys. Controlled Fusion **48**(2), R1–R35 (2006)
13. Drake, R.P.: High-Energy-Density Physics. Springer, Berlin, Heidelberg (2006)
14. Dubin, D.H.E., O'Nail, T.M.: Trapped nonneutral plasmas, liquids and crystals (the thermal equilibrium states). Rev. Mod. Phys. **71**, 87 (1999)
15. Faber, T.E.: Fluid Dynamics for Physicists. Cambridge University Press, Cambridge (1977)
16. Filinov, V.S., Bonitz, M., Levashov, P., et al.: Plasma phase transition in dense hydrogen and electron–hole plasmas. J. Phys. A **36**(22), 6069–6076 (2003)

17. Filinov, V.S., Levashov, P.R., Bonitz, M., Fortov, V.E.: Calculation of the shock Hugoniot of deuterium at pressures above 1 Mbar by the path-integral Monte Carlo method. Plasma Phys. Rep. **31**(8), 700–704 (2005)
18. Fortov, V.E. (ed.): Entsiklopediya nizkotemperaturnoi plazmy (Encyclopedia of Low-Temperature Plasma). Nauka, Moscow (2000)
19. Fortov, V.E.: Intense Shock Waves and Extreme States of Matter. Bukos, Moscow (2005)
20. Fortov, V.E.: Intense shock waves and extreme states of matter. Phys. Usp. **50**(4), 333 (2007)
21. Fortov, V.E., Ternovoi, V.Y., Zhernokletov, M.V., et al.: Pressure-produced ionization of nonideal plasma in a megabar range of dynamic pressures. J. Exp. Theor. Phys. **97**(2), 259–278 (2003)
22. Fortov, V.E., Khrapak, A.G., Khrapak, S.A., et al.: Dusty plasmas. Phys. Usp. **47**(5), 447 (2004)
23. Fortov, V.E., Ivlev, A.V., Khrapak, S.A., et al.: Complex (dusty) plasma: current status, open issues, perspectives. Phys. Rep. **421**(1), 1–103 (2005)
24. Fortov, V., Iakubov, I., Khrapak, A.: Physics of Strongly Coupled Plasma. Oxford University Press, Oxford (2006)
25. Fortov, V.E., Ilkaev, R.I., Arinin, V.A., et al.: Phase transition in a strongly nonideal deuterium plasma generated by quasi-isentropical compression at megabar pressures. Phys. Rev. Lett. **99**(18), 185001 (2007)
26. Fortov, V.E., Hoffmann, D.H.H., Sharkov, B.Y.: Intense ion beams for generating extreme states of matter. Phys. Usp. **51**(2), 109 (2008)
27. Ginzburg, V.L.: The Physics of a Lifetime: Reflections on the Problems and Personalities of 20th Century Physics. Springer, Berlin, Heidelberg (2001)
28. Ginzburg, V.L.: On superconductivity and superfluidity (what I have and have not managed to do), as well as on the "physical minimum" at the beginning of the XXI century (December 8, 2003). Phys. Usp. **47**(11), 1155 (2004)
29. Giorla, J., Bastian, J., Bayer, C., et al.: Target design for ignition experiments on the laser Mégajoule facility. Plasma Phys. Controlled Fusion **48**(12B), B75–B82 (2006)
30. Grabovskii, E.V., Vorob'ev, O.Y., Dyabilin, K.S., et al.: Excitation of intense shock waves by soft x radiation from a Z-pinch plasma. JETP Lett. **60**(1), 1 (1994)
31. Hemley, R.J., Ashcroft, N.W.: The revealing role of pressure in the condensed matter sciences. Phys. Today **51**(8), 26–32 (1998)
32. Hemley, R.J., Mao, H.K.: Overview of static high pressure science. In: Hemley, R.J., Chiarotti, G.L., Bernasconi, M., Ulivi, L. (eds.) High Pressure Phenomena, Proceedings of the International School of Physics "Enrico Fermi" Course CXLVII, p. 3. IOS Press, Amsterdam (2002)
33. Hogan, W.J. (ed.): Energy from Inertial Fusion. IAEA, Vienna (1995)
34. Kirzhnits, D.A.: Extremal states of matter (ultrahigh pressures and temperatures). Sov. Phys. Usp. **14**(4), 512–523 (1972)
35. Kirzhnits, D.A., Lozovik, Y.E., Shpatakovskaya, G.V.: Statistical model of matter. Sov. Phys. Usp. **18**(9), 649–672 (1975)
36. Knudson, M.D., Hanson, D.L., Bailey, J.E., et al.: Equation of state measurements in liquid deuterium to 70 GPa. Phys. Rev. Lett. **87**(22), 225501 (2001)
37. Konyukhov, A.V., Likhachev, A.P., Oparin, A.M., et al.: Numerical modeling of shock-wave instability in thermodynamically nonideal media. J. Exp. Theor. Phys. **98**(4), 811–819 (2004)
38. Kruer, W.L.: The Physics of Laser Plasma Interactions. Addison-Wesley, Reading (1988)
39. Lebedev, S.V., Ciardi, A., Ampleford, D.J., et al.: Magnetic tower outflows from a radial wire array Z-pinch. Mon. Not. R. Astronom. Soc. **361**(1), 97–108 (2005)
40. Lindl, J.D.: Inertial Confinement Fusion. Springer, New York (1998)
41. Loubeyre, P., Occelli, F., Le Toulec, R.: Optical studies of solid hydrogen to 320 GPa and evidence for black hydrogen. Nature **416**(6881), 613–617 (2002)
42. Mackinnon, A.J., Borghesi, M., Hatchett, S., et al.: Effect of plasma scale length on multi-MeV proton production by intense laser pulses. Phys. Rev. Lett. **86**(9), 1769–1772 (2001)

43. Maksimchuk, A., Gu, S., Flippo, K., et al.: Forward ion acceleration in thin films driven by a high-intensity laser. Phys. Rev. Lett. **84**(18), 4108–4111 (2000)
44. Mitchell I.H., Bayley J.M., Chittenden J.P. et al.: A high impedance mega-ampere generator for fiber z-pinch experiments. Rev. Sci. Instrum. **67**, 1533 (1996)
45. Moses, E.I., Bonanno, R.E., Haynam, C.A., et al.: The National Ignition Facility: path to ignition in the laboratory. Eur. Phys. J. D **44**(2), 215–218 (2006)
46. Mourou, G.A., Tajima, T., Bulanov, S.V.: Optics in the relativistic regime. Rev. Mod. Phys. **78**(2), 1804–1816 (2006)
47. Murray, C.A., Wenk, R.A.: Observation of order–disorder transitions and particle trajectories in a model one-component plasma: time resolved microscopy of colloidal spheres. In: Van Horn, H.M., Ichimaru, S. (eds.) Strongly Coupled Plasma Physics, p. 367. University of Rochester Press, Rochester (1993)
48. National Research Council: Frontiers in High Energy Density Physics. National Academies Press, Washington (2003)
49. Nellis, W.J.: Dynamic compression of materials: metallization of fluid hydrogen at high pressures. Rep. Prog. Phys. **69**(5), 1479–1580 (2006)
50. Okun', L.B.: Leptony i kvarki, 2nd edn. Nauka, Moscow (1990). [English Transl.: Leptons and Quarks. North-Holland, Amsterdam (1982)]
51. Pieranski, P.: Colloidal crystals. Contemp. Phys. **24**(1), 25–73 (1983)
52. Pukhov, A.: Strong field interaction of laser radiation. Rep. Prog. Phys. **66**(1), 47–101 (2003)
53. Quintenz, J., Sandia's Pulsed Power Team: Pulsed power team. In: Proc. 13th Int. Conf. on High Power Particle Beams. Nagaoka, Japan (2000)
54. Rubakov, V.A.: Large and infinite extra dimensions. Phys. Usp. **44**(9), 871 (2001)
55. Russel, W.B., Saville, D.A., Schowalter, W.R.: Colloidal Dispersions. Cambridge University Press, Cambridge (1989)
56. Ryutov, D.D., Remington, B.A., Robey, H.F., Drake, R.P.: Magnetodynamic scaling: from astrophysics to the laboratory. Phys. Plasmas **8**(5), 1804–1816 (2001)
57. Schatz, T., Schramm, U., Habs, D.: Crystalline ion beams. Nature **412**(6848), 717–720 (2001)
58. Schramm, U., Schatz, T., Bussmann, M., Habs, D.: Cooling and heating of crystalline ion beams. J. Phys. B **36**(3), 561–571 (2003)
59. Sharkov, B.Y. (ed.): Yadernyi sintez s inertsionnym uderzhaniem (Inertial Confinement Nuclear Fusion). Fizmatlit, Moscow (2005)
60. Shashkin, A.A.: Metal–insulator transitions and the effects of electron–electron interactions in two-dimensional electron systems. Phys. Usp. **48**(2), 129 (2005)
61. Shpatakovskaya, G.: Kvaziklassicheskii metod v zadachakh kvantovoi fiziki (Quasiclassical Method in Problems of Quantum Physics). LAP LAMBERT Academic Publishing, Moscow (2012)
62. Spielman, R.B., Deeney, C., Chandler, G.A., et al.: Tungsten wire-array Z-pinch experiments at 200 TW and 2 MJ. Phys. Plasmas **5**(5), 2105–2111 (1998)
63. Vacca, J.R. (ed.): The World's 20 Greatest Unsolved Problems. Prentice Hall PTR, Englewood Cliffs (2004)
64. Zel'dovich, Y.B., Raizer, Y.P.: Fizika udarnykh voln i vysokotemperaturnykh gidrodinamicheskikh yavlenii, 2nd edn. Nauka, Moscow (1966). [English Transl.: Physics of Shock Waves and High-Temperature Hydrodynamic Phenomena. Dover, Mineola (2002)]

Chapter 3
High Energy Densities in Laboratories

3.1 Main Lines of Research

The ultimate objective of experiments in high-energy-density physics consists in the generation of extreme material parameters, whose values are at the boundaries of modern experimental capabilities (Table 3.1). Already, plasma states with peak pressures of hundreds or thousands of megabars, temperatures up to 10 billion degrees, and energy densities of 10^9 J/cm^3, which is comparable to the energy density of nuclear matter, have become the subject of laboratory investigations [14, 15, 63, 73, 192]. According to the ideas developed to date [13, 100, 115, 122], to implement a controlled thermonuclear reaction with inertial plasma confinement requires an energy of several megajoules to be delivered to a spherical target in 10^{-9} s to generate at its center a deuterium–tritium plasma with extremely high parameters $T \approx (1\text{–}2) \times 10^8$ K, $\rho \approx 200$ g/cm^3, $P \approx 150\text{–}200$ Gbar, which is close to the conditions at the center of the Sun. The corresponding output laser power should exceed the total power of all terrestrial electric power plants by several orders of magnitude.

These conditions, which are required for the ignition of a controlled thermonuclear reaction, are quite extraordinary by terrestrial standards, but are quite typical for the great bulk of the universe's matter compressed by gravitational forces in the interior of stars and other astrophysical objects. In this case, in the physics of high energy densities there arise several absorbing problems, the progress in this and allied fields of knowledge depending on their solution [138].

The ignition of thermonuclear reactions with inertial plasma confinement under controlled conditions is the principal pragmatic objective of research in high-energy-density physics. Here, lasers are in the lead [7, 13, 19, 32, 37, 37, 81, 82, 94, 108, 115, 122, 135, 161], although electrodynamic techniques (Z-pinches [49, 82, 102, 153, 177, 182] and heavy-ion schemes [75, 99, 171]) are making rapid strides. The operation of such targets is basically close to supernovae explosions,

© Springer International Publishing Switzerland 2016

V.E. Fortov, *Extreme States of Matter*, Springer Series in Materials Science 216,
DOI 10.1007/978-3-319-18953-6_3

Table 3.1 Energy sources and experimental devices employed in high-energy-density physics [73]

Primary energy source	Final form of the energy source	Energy density (MJ/cm^3)	Temperature (eV)	Pressure (10^5 Pa)	Total energy (MJ)	Duration (s)	Power (W)
Chemical HEs	Chemical HEs	10^{-2}	0.5	5×10^5	10^2	10^{-7}	10^{10}
	Metallic plates	0.3	60	10^7	3	10^{-6}	10^{10}
	1 MOe magnetic field	4×10^{-3}	0.3	5×10^4	5	10^{-6}	5×10^{12}
	25 MOe magnetic field	2.5	200	2.5×10^7	1	10^{-7}	10^{13}
	Explosion plasma generators	10^{-2}	60	10^5	30	10^{-6}	10^{12}
Nuclear explosives	Nuclear explosives	10^4	10^7	10^{10}	10^{11}	10^{-6}	10^{22}
	Neutron-induced heating	10	50	2×10^7	10^3	10^{-6}	10^{15}
	Shock waves in solids	5	50	5×10^7	10^4	3×10^{-6}	10^{15}
	Shock waves in gases	0.3	40	2×10^5	10^7	10^{-5}	10^{18}
Compressed gas	Adiabatic compression	2×10^{-5}	0.3	150	10^3	6×10^{-3}	10^5
	Pneumatic shock tubes	10^{-4}	1	250	10^{-2}	10^{-4}	3×10^8
	Combustion-driven shock tube	10^{-6}	2	10	2×10^{-2}	3×10^{-4}	10^8
Compressed gas	Shock tubes, electric discharges	10^{-7}	2	1	10^{-2}	10^4	10^8

Capacitor	–	10^{-8}	–	–	40	10^{-5}	10^{12}
Rotor energy-storage device	–	10^{-3}	–	–	100	10^{-4}	10^{12}
Inductive storage device	–	10^{-4}	–	–	100	10^{-4}	10^{12}
Storage battery	–	5×10^{-4}	–	–	1000	10^{-3}	10^{12}
	Fast wire explosion	5×10^{-2}	4	10^{5}	10^{-3}	10^{-6}	10^{9}
	Slow wire explosion	2×10^{-2}	0.5	5×10^{2}	10^{-3}	10^{-4}	10^{7}
	Pulsed discharges	10^{-3}	10	10^{4}	10^{-4}	10^{-3}	10^{9}
	Plasma focus	10^{-2}	10^{3}	10	10^{-4}	10^{-5}	10^{10}
	High-pressure arcs	10^{-5}	2	10^{4}	10^{-4}	∞	10^{4}
	Experiments involving furnaces	10^{-3}	0.3	5×10^{3}	10^{-3}	∞	10^{3}
Laser	–	10^{-6}	–	–	0.5×10^{-3}		10^{14}
	Target	10^{4}	10^{6}	10^{8}	0.5	10^{-10}	5×10^{14}
Electron beam	–	10^{-6}	–	–	1	10^{-8}	10^{13}
	Target	5×10	5×10^{3}	10^{7}	0.1	10^{-8}	10^{13}

allowing the vast wealth of experimental results and sophisticated computer codes for the calculation of fusion microtargets to be employed in astrophysics.

Of fundamental significance is the study of the equation of state of matter and plasma composition in a broad domain of the phase diagram, including the conditions inherent in giant planets, exoplanets, dwarfs, giants, and neutron stars, and the determination of quasi-classicality bounds (the Thomas–Fermi model [106, 107]) in thermodynamics. Of considerable interest are the properties of degenerate compressed plasmas, their thermodynamics, equilibrium, kinetic, and transport properties in the region of strong nonideality and in the presence of intense magnetic fields, as well as the properties of a quark–gluon plasma, and the existence and properties of its hypothetical phase transition.

The construction and verification of the structural and evolutional models of planets and exoplanets calls for the derivation of reliable experimental data in laboratory conditions. For Jupiter and other planets it is vital to ascertain or disprove the existence of a hard core and determine the dimensions of the domain occupied by metallic hydrogen and the metallization bound for H_2 and H_2+He. Of fundamental importance is the analysis of Jupiter's energetics with the inclusion of phase layering of the mixtures He–H, C–O, etc., as well as the study of the origin and dynamics of its magnetic field. Similar problems are also encountered in studies of giant planets and exoplanets. In this case, a large part is played by shock-wave experiments, which enable the metallization bounds to be determined and the occurrence of a plasma phase transition to be ascertained.

The intriguing question of a phase transition of the first kind in a strongly nonideal plasma has remained open for almost 80 years (see the first data on the observation of this transition in deuterium [74]).

The more distant future will see studies of the conditions for pycnonuclear reactions ("cold" fusion) and the conditions of strong Coulomb screening, which speeds up thermonuclear reactions in the interior of massive stars, as well as the production of relativistic degenerate matter with the Fermi energy $E_F > m_e c^2$ and the investigation of its equation of state.

The methods of laboratory energy cumulation now being developed will make it possible to obtain [55, 138] relativistic jets and intense collisional, collisionless, and magnetohydrodynamic shock waves, much like those observed in astrophysical objects.

Under discussion are projects involving the production of radiation-dominated hot plasmas, like the conditions in black holes and accretion disks of neutron stars, as well as the stability of these regimes (see the experiments involving nuclear explosions [14, 15, 192], lasers [55, 136, 152], and Z-pinches [49, 86, 153, 182]). Interesting suggestions have been put forward concerning the generation of radiatively collapsing magnetohydrodynamic and collisionless shocks, fast particles, relativistic jets, and their focusing [55, 136, 138, 152].

The high-energy-density techniques under development open up the possibility of generating ultrahigh ($B > 1$ GGs) magnetic fields and investigating their effect on the physical properties of matter. Already the fields obtained in laser-produced plasmas range into hundreds of megagauss.

Ultrahigh laser power levels may bring closer the prerequisites for the observation of relativistic gravitational effects.

The list may be easily lengthened and is perhaps limited only by our imagination. At present it is hard to tell, even to within decades, which of these fascinating problems of high-energy-density physics will be solved, if at all, at the existing and projected laboratory facilities. However, according to the favorite advice of academician P.L. Kapitsa, "When going fishing there is good reason to take the rod with the largest fish hook in the hope of the largest fish".

3.2 Generators of High Energy Densities

The spectrum of experimental devices for generating high energy densities is highly diversified. It includes diamond anvils for static material compression, gunpowder and light-gas launching devices ("guns"), explosion generators of intense shock waves, electroexplosion devices, magnetic cumulation generators, lasers, high-current generators of high-power electric current pulses, charged-particle accelerators, and possible combinations of these devices. The characteristics of these ways of generation are collected in Table 3.1, which shows typical (not necessarily the highest) parameters of the plasma states generated.

Table 3.2 [138] compares the parameters of the highest-power facilities either in service today or under construction: lasers, pulsed electrical devices, Z-pinches, and charged-particle accelerators [142, 154]. Developed for carrying out plasma research in the interests of defense and high-energy physics, they are presently employed to advantage for research in basic plasma physics of high energy densities. Tables 3.3 and 5.2 and Figs. 3.1 and 3.2 give the parameters of laser devices being constructed or designed, whose commissioning would greatly enhance the capabilities of experiments in laser plasma physics. The foremost among those currently working is the OMEGA (Fig. 3.3) American laser facility (Rochester University) [19, 32], which consists of 60 laser beams with a total energy of 30 kJ at a wavelength of 0.35 μm. A broad spectrum of investigations on laser fusion is conducted at the facility with direct and soft–X-ray conversion ignition schemes, on the generation of intense shock waves, the equation of state and optical properties of dense plasmas, hydrodynamic instabilities, the generation of intense X-ray radiation, etc. [20, 38, 60, 85, 161, 185].

Table 3.2 Facilities for generating high energy densities [138]

	Laser facilities			Z-pinch					
				Sandia		C-300		Angara V	
	NIF	LMJ	Petawatt laser	Current	X-rays	Current	X-rays	Current	X-rays
Energy per particle	3.6 eV	3.6 eV	1.5 eV	20 MA	50–250 eV	1.5–4 MA	70 eV	2–5 MA	100 eV
Pulse duration	1–20 ns	≈10 ns	0.5 ps	100 ns(rise time)	5–15 ns	80 ns	12 ns	90 ns	6 ns
Spot size	0.3 mm	0.3 mm	5 μm	–	1 mm(cylinder)	–	2 mm	–	2 mm
Pulse energy	1.8 MJ	2 MJ	0.5–5 kJ	16 MJ	1.8 MJ	400 kJ	50 kJ	600 kJ	120 kJ
Intensity (W/cm^2)	2×10^{15}	$\approx10^{15}$	10^{22}	–	10^{14}	–	$(2–3)\times10^{12}$	–	$(6–10)\times10^{12}$
	Accelerators								
	Electron accelerator (SLAC)		LHC accelerator	SIS 18		SIS 100		TWAC	
				Today	Design				
Energy per particle	50 GeV		7 TeV	1 GeV	1 GeV	4 GeV		700 MeV	
Pulse duration	5 ns		0.25 ns	200 ns	50 ns	20 ns		100 ns	
Spot size	3 mm		16 mm	1 mm	1 mm	1 mm		1 mm	
Pulse energy	150 J		334 MJ	≈1 kJ	30 kJ	300 kJ		100 kJ	
Intensity (W/cm^2)	10^{20}		10^{19}	5×10^{11}	6×10^{13}	10^{15}		10^{14}	

Table 3.3 Parameters of laser facilities for high-energy-density physics

Laser facility	Parameters	Year of commissioning	Comment
Great Britain			
VULCAN CLF, Rutherford	2.6 kJ, several nanoseconds, 100 TW, 0.5–1 ps, 10^{21} W/cm^2	1999	The largest European Center, which runs high-power ns and fs lasers simultaneously.
VULCAN-PW CLF, Rutherford	1 PW, 0.5–1 ps	2002	Two-beam laser with a 100–1000 times higher repetition rate, 10 times higher intensity at target
ASTRA TA1, TA 2 CLF, Rutherford	Site 1: 10 fs, 10–1000 Hz, 1 TW Site 2: 40 fs, 10 Hz, 12 TW, 10^{19} W/cm^2	2005	
ASTRA-GEMINI CLF, Rutherford	15 J, 30 fs, 1 shot per minute, 0.5 PW in either of the 2 beams	2007	Ultrahigh-intensity ultrashort-pulse laser with a wavelength tunable from the infrared to vacuum UV, combined with a synchrotron as a diagnostic complex. Radiation shielding of the interaction chamber provided
VULCAN-OPCPA CLF, Rutherford	10 PW 0.5–1 ps, 10^{23} W/cm^2.	2011	Ultrahigh-intensity ultrashort-pulse laser. Using optical parametric approaches will make it possible to obtain a very high intensity contrast ratio at the target
Orion Atomic Weapons Establishment	500 J, 1 ns, 3 ω_0, 10 beams + 2 beams 500 J, 500 fs, 1 PW, 10^{21} W/cm^2		
European Project			
HiPER Future European Facility	40 beams with a total energy of 200 kJ + 24 beams with a total energy of 70 kJ and a $\approx$10 ps pulse duration for target ignition	Early in 2010	The feasibility of future operation in a pulse-periodic mode is under consideration

(continued)

Table 3.3 (continued)

Laser facility	Parameters	Year of commissioning	Comment
France			
LMJ CESTA, Bordeaux	2 MJ, 0.35 μm, ≈10 ns, 550 TW, 240 beams	2010–2012	The nuclear fusion energy yield is expected to amount to 25 MJ with 1.4 MJ absorbed laser energy
LIL CESTA, Bordeaux	≈40 kJ, 0.35 μm, 9 ns, 8 beams	2006	The first beam launched in 2003
PETAL Region Aquitaine, Bordeaux	3.5 kJ 0.5–5 ps	2007–2008	Ultrahigh-intensity laser, will operate in combination with 8 beams of the LIL (CESTA) laser, which is a prototype of LMJ
LOA Laboratoire d'Optique Appliquée	30 J, 30 fs, 100 TW, 1–10 Hz	2004	Electrons were accelerated to 200 MeV and monochromatic collimated high-current electron beams obtained
LULI Laboratoire pour l'Utilisation des Lasers Intenses	Several ns, 2 beams, ≈1 kJ each + 30 J, 300 fs, 100 TW with upgrade into the PW range	2000 2007	
USA			
NIF LLNL, Livermore	4.2 MJ, 192 beams, 5–25 ns, 1 ω_0	2010	Attainment of radiative temperature of 300 eV is expected in 2010 for a 1 MJ laser energy. The laser-to-target energy conversion ratio is expected to amount 14–16%
OMEGA LLE Rochester	30 kJ, several ns, 60 TW, 60 beams, 3 ω_0	1995	A record number (10^{14}) of neutrons was obtained
OMEGA EP LLE Rochester	6.5 kJ, 3 ω_0, 4 beams, there will be 2 beams (High-Energy Petawatt laser, HEPW) with 2.6 kJ, 10 ps in 1 ω_0	2007	Capability of conducting cryogenic experiments

Japan			
FIREX I project Laser LFEX Institute of Laser Engineering, Osaka	3.6 kJ/beam, 10 ps, 4 beams, 14.4 kJ total energy	2007–2008	Objective: to demonstrate that a target can be heated up to 5–10 keV
FIREX II project Institute of Laser Engineering, Osaka	100 kJ, 1 Hz laser for heating and 100 kJ, 1 Hz laser for ignition	> 2010	The thermonuclear reaction power is expected to amount to 10 MW and the energy gain to 50. 40% of the energy will be converted to electric energy. 2 MW of this electric energy with 10% efficiency will be used for laser operation
China			
SG-II	6 kJ in 1 ω_0, 1 ns, 3 kJ in 3 ω_0, 8 beams 8 TW power in ω_0 for 100 ps	2005	
SG-IIU	3 ns, 18 kJ in 3 ω_0, + PW laser with a ps pulse duration and 1–2 kJ energy + 3 ns, 4.5 kJ laser for X-ray backlighting	2007	
SG-III	3 ns, 150 kJ in 3 ω_0, 64 beams	2010	
Russia			
VNIIEF+IAP RAS	1 PW (100 J, 100 fs)	2006	10^{22} W/cm^2 on-target laser intensity achieved
Iskra-5 VNIIEF+IAP RAS	120 TW, 0.3 ns, iodine laser, 12 beams, $1\omega_0 = 1.315$ μm, $2\omega_0$	2002	A temperature $T_e \approx 180$ eV obtained
Iskra-6 VNIIEF+IAP RAS	300 kJ, 1–3 ns, 128 beams		
IHED, JIHT RAS	10 TW, 40 fs, 10^{19}W/cm^2	2006	

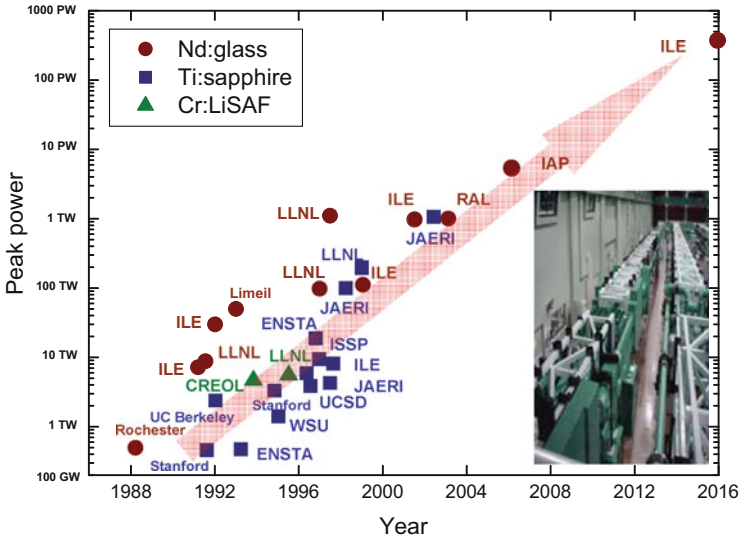

Fig. 3.1 Peak power of laser facilities

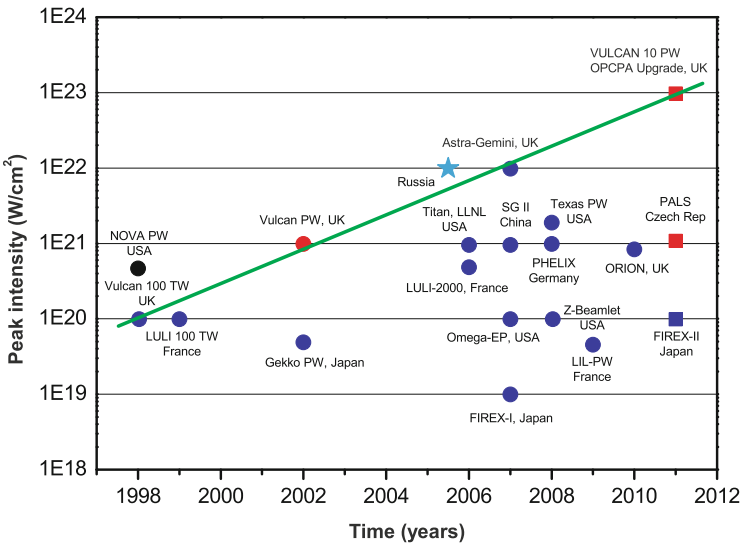

Fig. 3.2 Development of the world's petawatt laser facilities (http://www.scitech.ac.uk/). *Blue circles* indicate the presently funded laser facilities and the *blue squares* those projected for funding. *Red symbols* correspond to single-beam laser facilities and the *blue ones* to ultrahigh-intensity laser facilities with additional capabilities. The *black circle* stands for the petawatt laser system that operated at the Livermore Laboratory. The *green line* shows the development trend of the Rutherford Laser Laboratory. The *sky-blue star* denotes the VNIIEF+IAP RAS laser facility

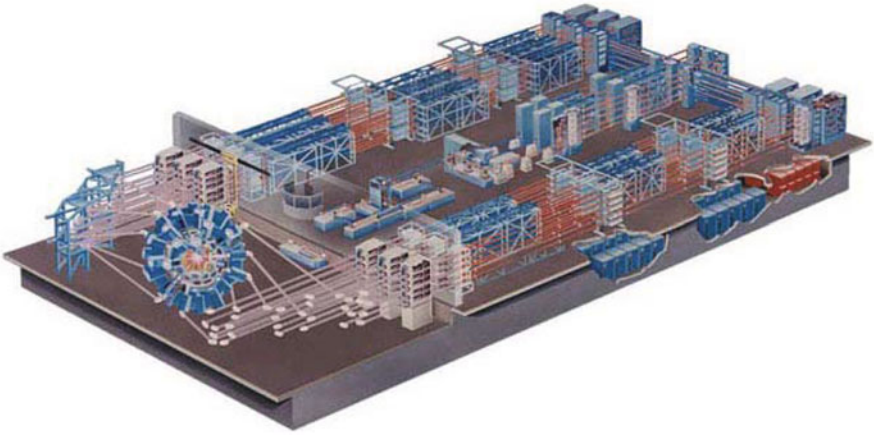

Fig. 3.3 OMEGA laser complex

The subsequent presentation in this section primarily follows [114]. About 20 facilities with a peak output laser power above 100 TW and a pulse length below 1 ps are operated in the world's leading laboratories. At least ten facilities of the same level are under construction or upgrading. These are the biggest complexes for laser thermonuclear fusion: National Ignition Facility (NIF) (USA), Laser MegaJoule/PETawatt Aquitaine Laser (LMJ/PETAL) (France), and the High Power laser Energy Research (HiPER) project (Great Britain). In these facilities use is made or planned of nanosecond laser pulses of tens of radiation channels with a total power of hundreds of TW. Planned for achieving fast ignition (see Sect. 7.2.3) is the construction of picosecond multipetawatt laser channels.

Apart from the presently operating or nearly completed facilities presented in the table, of special interest are next-generation projects which aspire to reach multipetawatt output powers and are in the preparatory stage or at the early stage of implementation. Among these projects are two European infrastructure megaprojects: Extreme Light Infrastructure (ELI) and HiPER, as well as the Vulcan-10PW at the Rutherford Appleton Laboratory (RAL) (Great Britain), the ILE-Apollon project at the Institut de la Lumiere Extreme (ILE) (France), and the PEtawatt pARametric Laser (PEARL-10) project at the Institute of Applied Physics of the Russian Academy of Sciences (IAP RAS).

The ELI European megaproject involves [114] the making of a unique research infrastructure open to scientists who study laser–matter interactions at the highest attainable power level and to developers of the corresponding applications. Four main application lines have been defined: the physics of vacuum in the presence of extremely high light fields, attosecond physics, production of the secondary sources of accelerated charged particles and hard photons, and nuclear processes under superhigh laser fields.

The ELI project lasers will reach a peak power of 0.2 Exawatts ($0.2 \cdot 10^{18}$ W). ELI will reach this power by concentrating a relatively moderate energy (about 3–4 kJ) in ultrashort time intervals (about 15 fs). Owing to the ultrashort pulse duration, ELI will exceed in peak power the world's highest-power existing lasers by several hundred times. Planned in the framework of the ELI project, along with an exawatt laser, is the construction of three other unique laser complexes with a peak power of 10–20 PW.

It is expected [114] the ELI laser complexes will advance the frontiers of science and technology in the realms indicated above and make possible investigations in plasma physics, astrophysics, nuclear physics, and high-energy physics under previously unattainable conditions. These laser complexes will permit making unique sources of hard photons and high-energy charged particles with previously unattainable brightness and spatio-temporal concentration of electromagnetic energy on nanometer spatial and attosecond time scales. ELI's ultrabright beams of protons and X-rays may promote significant progress in the diagnostics and therapy of cancer as well as in structural biology in their application in proton/ion therapy, phase-contrast X-ray radiography, and diffraction X-ray radiography of separate biological molecules and nanoobjects. High-brightness attosecond X-ray beams will in turn [114] make it possible to obtain four-dimensional images with subatomic resolution, i.e. to detect dynamic images of microscopic substance structure with picometer resolution in space and attosecond resolution in time.

In the framework of the ILE project it is planned to make the 10 PW laser—ILE-Apollon laser using a CPA technology with the final Ti:Sa crystal amplification stage 20 cm in diameter. Developed in the MPQ was the basic technology for amplifying ultimately short pulses down to 5 fs in duration using optical parametric chirped-pulse amplification (OPCPA) with nonlinear BBO crystals; the same technology is employed in the RAL in the construction of the Vulcan-10PW laser with final wide-aperture DKDP crystals.

The total cost of the project, which will be funded by the EC infrastructure for 5–6 years, will supposedly [114] amount to 740 million Euros; more than 600 scientists are directly participating in the project implementation.

The international HiPER project [114], which aims at constructing the first prototype of an industrial energy-producing inertial fusion reactor, will play the role similar to the role of the International Experimental Thermonuclear Reactor (ITER) in implementing controlled magnetic fusion (see Chap. 7). Its further development and passage to the demonstration stage depend heavily on the nearest results of operation of the American NIF and the French LMJ facility.

In the case of success to achieve the conditions of and demonstrate the fusion effect in inertially confined laser plasmas on the NIF and/or LMJ, the HiPER project will pass into the practical stage, which includes the construction, during the next decade, of a laser complex for initiating the fusion reaction with a repetition rate of 5–10 Hz, a laser target factory, a radiation–target chamber, and the outer shell for

the continuous conversion of fusion reaction products to thermal energy. The laser complex must have about 50 channels each with a pulse energy of 10 kJ, a pulse duration of several nanoseconds, and a pulse repetition rate of 5–10 Hz. Separate channels of multipetawatt power with a picosecond pulse duration mast be made for initiating fusion in the fast ignition or shock wave modes.

The main stage of project development is planned for the 2020s.

The Vulcan-10PW laser complex (RAL, Great Britain) is intended to make a source of 30 fs long laser pulses with an energy of 300 J, and intensity of up to 10^{23} W/cm^2, and a repetition rate of two pulses per hour using parametric chirped-pulse amplification. The Vulcan-10PW laser will employ kilojoule pulses delivered from the amplifier stages of the Vulcan laser for pumping the parametric amplifiers. In this case it is planned that two final OPCPA stages will use wide-aperture (40 × 40 cm) DKDP crystals.

The ILE-Apollon project (Extreme Light Institute, France) aims [114] at making a laser with a peak power of 10 PW, a peak intensity of 10^{24} W/cm^2, a single pulse energy of 150 J, a duration of 15 fs, and a repetition rate of one pulse per minute. The final amplifying stages will be made of active Ti:Sa crystals 20 cm in diameter. So far crystals of requisite optical quality of this size do not exist, but several manufacturers of laser crystals are working in this direction. Another important technology that needs development is the making of kilojoule pump lasers operating at a repetition frequency of one shot per minute. A serious problem may be posed by the absence of adaptive mirrors—wavefront correctors—required for focusing high-energy pulses to a spot of about 1 μm, which would permit reaching the above intensity value.

It is noteworthy [114] that the ILE-Apollon project is assigned a special part in the activities in the framework of ELI. First, it is planned that the Apollon laser scheme will underlie the Czech and Romanian ELI complexes. Second, most likely the Extreme Light Institute will play the leading role in the construction of the fourth ELI complex in France after 2012, which is intended for studying the properties of vacuum under superhigh fields. In this case it is evident that Apollon will be the prototype of a separate channel of the exawatt laser.

The PEARL-10 project is underway in the Institute of Applied Physics of the RAS [114]. Commissioned in the IAP RAS in 2007 was the PEARL laser with a pulsed power 0.56 PW, a pulse duration of 45 fs, and an energy of 25 J, which now is among the world's ten highest-power lasers. PEARL-10 makes use of parametric amplification in a DKDP crystal with an aperture of 10 × 10 cm grown in the IAP RAS by a special technology of fast oriented growth. Today the Institute has mastered the production of crystals with an aperture of 40 × 40 cm, which opens unrivaled possibilities to further advance OPCPA. The PEARL-10 project relies on the results obtained in the Institute earlier and is aimed at making a source of laser pulses with an energy above 200 J, duration of 20 fs, a peak at-focus intensity of

over 10^{23} W/cm^2, and a repetition rate of one shot per minute. The complex will involve parametric amplification in DKDP crystals, with the final stage apertures of 20×20 cm.

The PEARL-10 research program comprises [114]:

- production of coherent and incoherent ultrashort ultrabright radiation sources in the hard X-ray and gamma-ray ranges based on the synchrotron radiation of ultrarelativistic charged particles in superhigh laser fields; the use of these sources for diagnosing processes and structures with picometer spatial and subfemtosecond time resolutions;
- production of compact 10–1000 MeV ion accelerators and development of their applications, including those for beam therapy; production of 1–10 GeV electron accelerators and execution of high-energy physics research, including prototyping accelerators for the International Linear Collider (ILC) project;
- production and investigation of extreme states of substance emerging under the laser fields of ultrarelativistic intensity; laboratory modeling of astrophysical and early cosmological phenomena; investigation into the nonlinear properties of vacuum in the presence of ultrahigh laser fields as well as the generation of electron-positron pairs and particle showers.

The National Ignition Facility (NIF), which was projected for implementing the controlled fusion reaction in inertial confinement mode [94, 134, 135] (Fig. 3.4), bears the palm in the development of laser complexes with extreme pulse energetics.

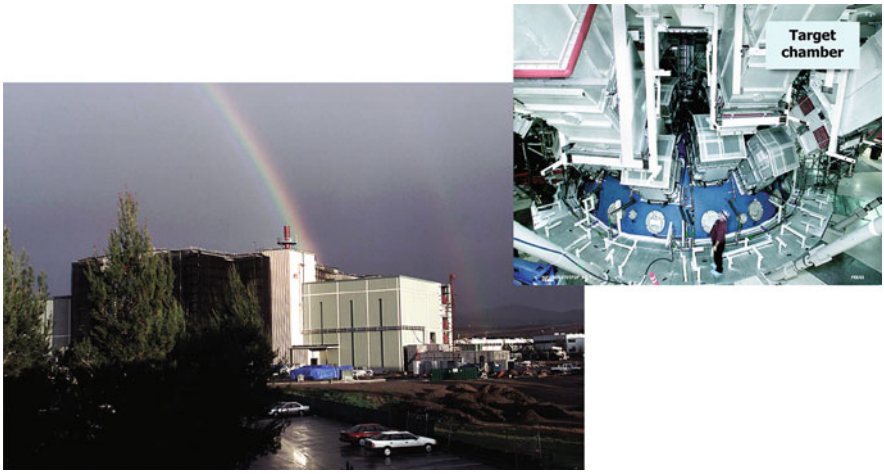

Fig. 3.4 NIF laser complex (USA) intended for controlled thermonuclear fusion with inertial plasma confinement

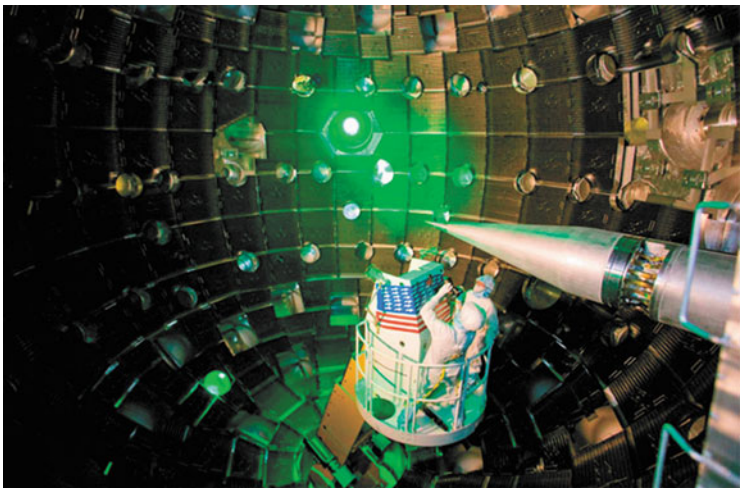

Fig. 3.5 NIF target chamber (USA): a 10 m diameter sphere of 10 cm thick aluminum coated with a 40 cm thick neutron shield. The chamber weighs about 500 tons. At the *right*: the beam injection system [134]

The NIF comprises 192 laser beams with a total energy of 4.2 MJ. Focusing this energy onto a microtarget must result in its thermonuclear explosion with an energy gain of ≈10–30. The corresponding experiments will be considered in Sect. 7.2.1.

This world's largest laser facility occupies an area of ≈350,000 m^2. Each of the 192 beams employs an optical system of 36–38 precision large-aperture optical elements and hundreds of smaller-scale optical elements with a surface of ≈3600 m^2 and a radiation aperture of ≈22 m^2. For comparison: one of world's biggest optical reflecting telescopes Keck (Hawaii) has an optical surface of ≈152 m^2, which amounts to 4 % of the NIF figure.

A 10-m target chamber (Fig. 3.5 [134]) provides input for 192 laser beams and about 100 inputs for diagnostic instrumentation (35 different diagnostic means). The 192 laser beams are focused with a high precision onto a fusion target 2.5 mm in diameter (Fig. 7.17, Chap. 7). Each of these beams with energies of 19 kJ may operate at the fundamental frequency of 1053 nm, the 2nd or 3rd harmonics and for experiments in high energy density physics [134].

The master fiber-optical laser feeds the radiation to a system of fiber-optical elements, which form the desired temporal and frequency pulse shapes. The pulse is then branched into 48 channels and each of them is then amplified in preamplifiers, after which is divided into four beams. Each beam depicted in Fig. 3.6 [134] is amplified in a four-pass amplifier controlled by a wide-aperture Pockels cell [134].

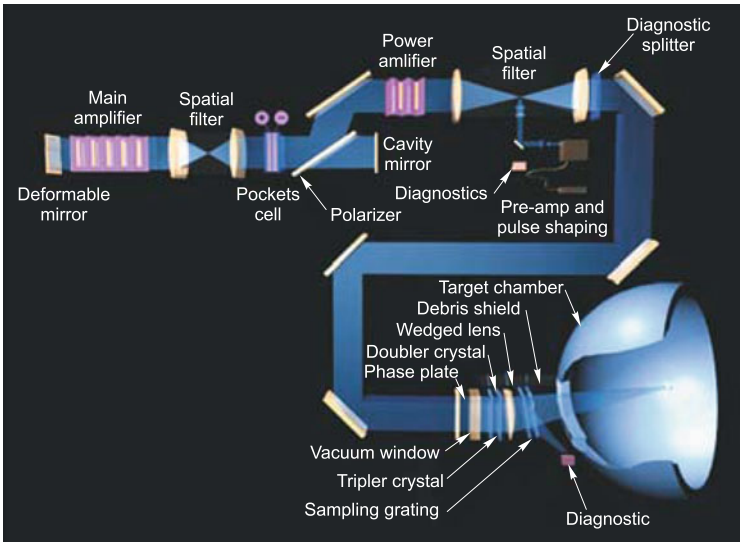

Fig. 3.6 Optical diagram of one of 192 laser channels [134]

The amplified radiation passes through polarization rotation devices, adaptive mirrors, the target debris shield and is injected into the target chamber. In the construction of the NIF, advantage was taken of the latest achievements of laser technology like high-performance optical glasses, high-performance KDP crystals, and many other achievements (see [134] and references therein).

The French LMJ system [7, 37, 81] will radiate an energy of 1.8–2 MJ (in the third harmonic) in 240 beams to furnish the condition for thermonuclear microtarget ignition and will permit modeling different effects of a nuclear explosion. These facilities will make it possible to carry out experiments with shock waves of the gigabar pressure range, thereby advancing to the domain of quasiclassical substance description [107], and to study plasma flows under the conditions of developed radiation effects.

In the VNIIEF (Russia, Sarov) an "Iskra-5" iodine photodissociation facility (Fig. 3.7) [77] was made, which consists of 12 laser channels with a total output of 30–40 kJ for a pulse duration of $\approx$0.36 ns. A capacitive energy storage complex with a total stored energy of $\approx$65 MJ was made to pump flashlamps and electric discharge sources.

The target chamber of the "Iskra-5" facility is equipped with 12 three-component catadioptric lenses. The main 12-channel irradiation experiments were performed with an output energy of 9–10 kJ for a pulse length of 0.3–0.4 ns. At present the facility has been changed to operate at the second harmonic [77] and provides

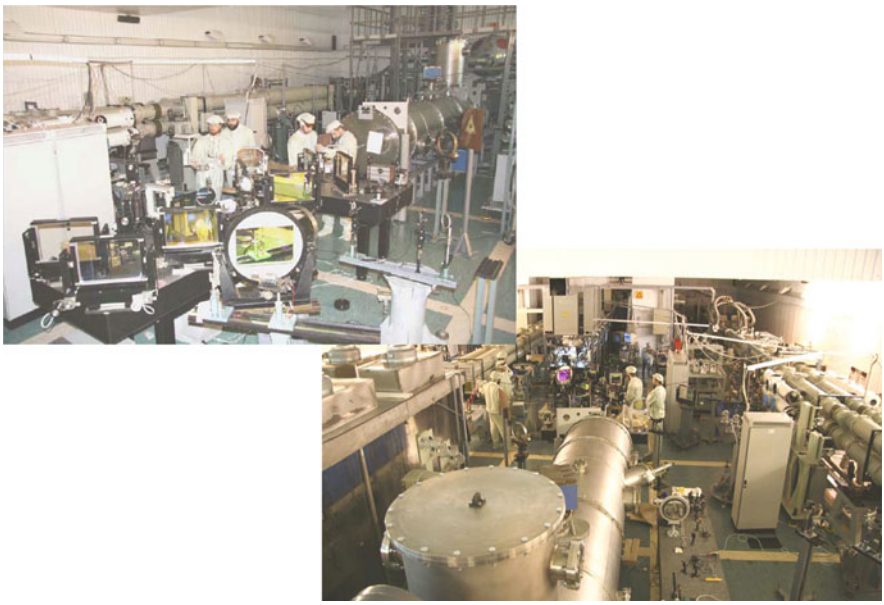

Fig. 3.7 Petawatt laser complex in VNIIEF

injection of 2.4–3 kJ of laser energy into the interaction chamber for a pulse duration of 0.5–0.6 ns. This facility was used to carry out experiments on controlled laser fusion and high energy density physics. The next stage—"Iskra-6" facility—will be ten times higher in power [77].

To summarize, it is safe to say that pulsed laser sources with a peak power of up to 10 PW and a radiation intensity of up to 10^{23} W/cm^2 would be expected to emerge in several countries within several years. In this connection it is instructive to discuss what new possibilities for the physics of extreme light–matter interactions will be provided by these laser complexes.

The action of laser radiation of nanosecond duration at up to 10^{18} W/cm^2 intensities has been adequately studied and described in the literature [9, 13, 36, 39, 115, 136, 152]. The laser energy is released primarily in the vicinity of the critical density, $n_c \approx 10^{21}/\pi m/(e\lambda)^2\,\mathrm{cm}^{-3}$ (where n_c is the critical density and λ the wavelength), located in the expanding plasma corona and is transferred to the target interior by means of electron thermal conduction. The plasma corona heated by the laser radiation moves towards the laser beam and generates an intense shock wave traveling into the target interior. The shock either compresses the target to pressures of hundreds of megabars or accelerates the outer target shell

to velocities of hundreds of kilometers per second, which in turn compresses and heats the thermonuclear fuel or the substance under investigation. This scheme is the earliest of the thermonuclear schemes and is referred to as the "direct" drive scheme [13, 115, 122].

An alternative "indirect" drive scheme (see Sect. 7.2.1) [13, 115, 122] relies on the conversion of laser radiation to X-ray radiation (with a brightness temperature ranging into hundreds of electronvolts), which effects the highly symmetric compression of the spherical target, as does the ablative pressure in the "direct"-drive compression scheme.

The second class of laser systems, which are less costly and therefore more easily accessible for the physics of high energy densities, corresponds to lower pulse energies and durations, but higher intensities at the target $\approx 10^{16}$–10^{22} W/cm^2. Their action relies on the chirping effect discovered in the early 1980s, where the laser radiation of the master oscillator is stretched in time by diffraction systems, amplified in amplifier stages, and then compressed to a femtosecond duration [183, 184]. Since such tera- to petawatt-power laser systems have become accessible to university laboratories, the work front in the plasma physics of high energy densities has broadened greatly: from relativistic plasma studies to the generation of accelerated electron, ion, and soft X-ray radiation (for lithography, medicine, and thermonuclear fusion) fluxes and electron–positron pairs, the implementation of nuclear reactions, and many other tasks.

Future progress in this direction will involve the advance of laser power to the zettawatt (10^{21} W) power level (see Fig. 5.2). These fantastic power levels can be reached both by shortening the laser pulse duration to tens of attoseconds (1 as = 10^{-18} s) and by raising the energies of laser beams (increasing the diameter and number of laser beams in femtosecond facilities). The feasibility of generating an isolated single-cycle 130 as long pulse has already been demonstrated [162].

Among the multitude of interesting physical experiments with such systems we mention the interaction of ultrashort laser pulses with clusters [54], in which their multiple nonequilibrium ionization knocks out electrons from a cluster and stimulates a "Coulomb explosion" with the production of kiloelectronvolt ions, laser-induced shock waves, and even thermonuclear reactions.

Since the shortest femto- and attosecond laser pulses are comparable to light cycles in duration, they are a unique instrument of extremely fast action on a substance for studying the kinetics of ultrafast atomic and molecular processes, the kinetics of chemical reactions, and many other fascinating phenomena.

3.3 Static Methods Using Diamond Anvils

Substantial progress in the area of static pressures was made in the early 1980s with the advent of the experimental technique of diamond anvils (Fig. 3.8) [97, 124]. In these facilities, two diamonds cut in a special way compress thin (10–100 μm)

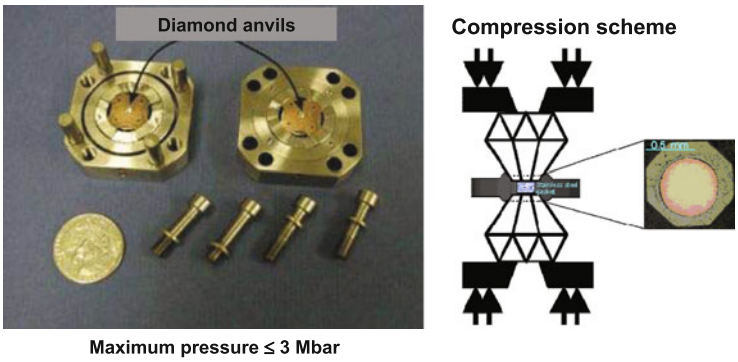

Fig. 3.8 Facility for the static compression of substances in diamond anvils [96, 97]

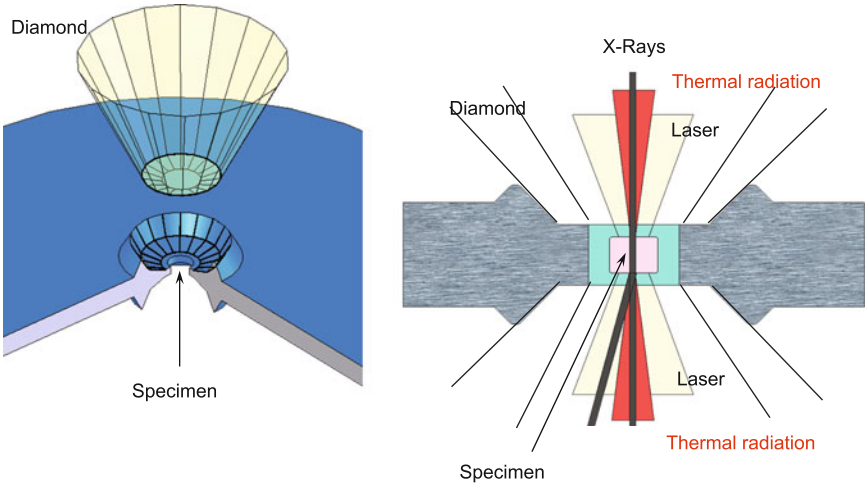

Fig. 3.9 Schematic representation of a static experiment on the compression of a substance in a diamond anvil involving laser heating [23]

plane layers of the substance under investigation to the highest attainable pressures of the megabar range, their upper limit being defined by the ultimate strength of diamond of ≈ 0.5–1.0 Mbar. In a number of experiments, the compressed substance is heated by laser radiation (Fig. 3.9) [22, 23] or the material compressed in diamond anvils is the target for its subsequent compression by laser-driven shock waves (Fig. 3.10) [125].

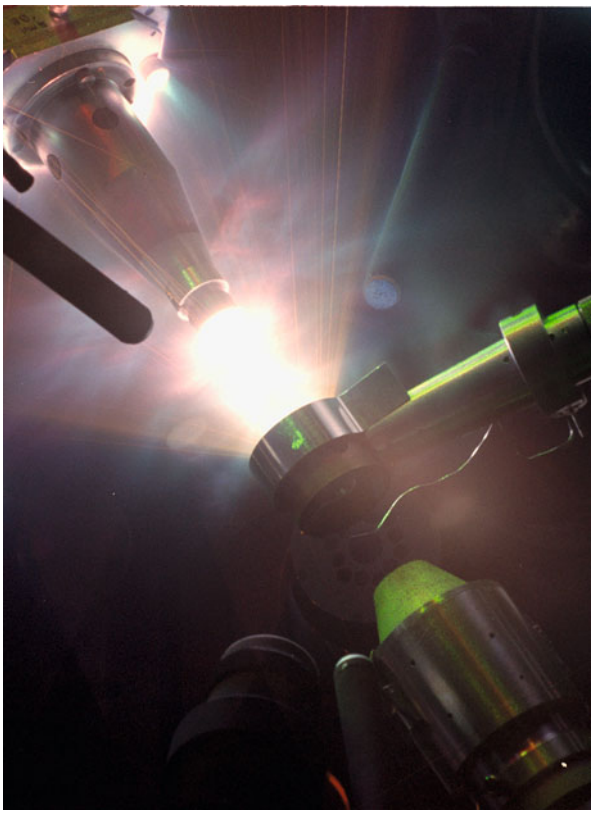

Fig. 3.10 Laser-driven shock-wave compression of a substance precompressed in a diamond anvil at the OMEGA facility [125]

The unlimited time of static compression permits a wide spectrum of diagnostic tools to be employed, including different kinds of spectroscopy, and also X-ray structure analysis to be performed with the use of kiloelectronvolt X-ray and synchrotron radiation. Experiments of this kind have yielded a wealth of useful information about the mechanical properties, thermodynamics, and phase transformations in geophysical objects (Fig. 3.11) in the parameter range $P \approx 0.1$–$3.6\,\mathrm{Mbar}$, $T \approx 10^3$–$6 \times 10^3\,\mathrm{K}$, which is extreme for terrestrial conditions.

The capabilities of diamond anvil techniques are limited by the strength of diamond (the strongest known terrestrial material) and will hardly go beyond the megabar pressure range.

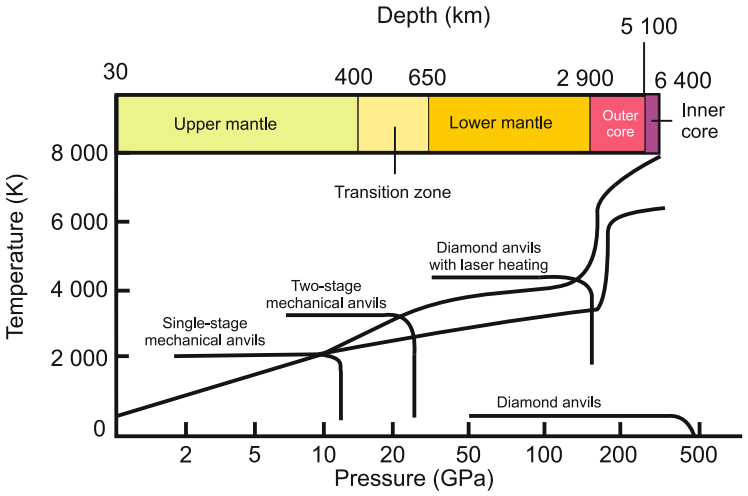

Fig. 3.11 Comparison of the parameters [96, 97] attainable under static conditions and the physical conditions in the Earth's interior

3.4 Dynamic Methods

Further advancement towards higher energy densities is related to the transition to dynamic methods of investigation [1, 4, 5, 14, 15, 63, 65, 71, 73, 139, 192, 197, 199], which rely on pulsed energy cumulation in the substance under investigation by means of intense shock waves or by means of electromagnetic radiation or particle beams of different types. The plasma temperatures and pressures occurring in this case are far greater than the thermal and mechanical strength of the structural materials of the facilities, resulting in limitations on the characteristic plasma lifetime in dynamic experiments, which is defined by the target expansion dynamics and is equal to $\approx 10^{-10}$–10^{-5} s. In the dynamic approach there are no fundamental limitations on the magnitudes of the maximum energy density and pressure: they are limited only by the power of the energy source, the "driver".

The routine tool for producing high energy densities is intense shock waves [1, 4, 63, 197], which emerge due to nonlinear hydrodynamic effects in a substance as a result of motion caused by pulsed energy liberation. In this case, a major part is played by the shock wave, a viscous compression shock, in which the kinetic energy of the oncoming flow is converted to thermal energy of the compressed and irreversibly heated plasma (Fig. 3.12).

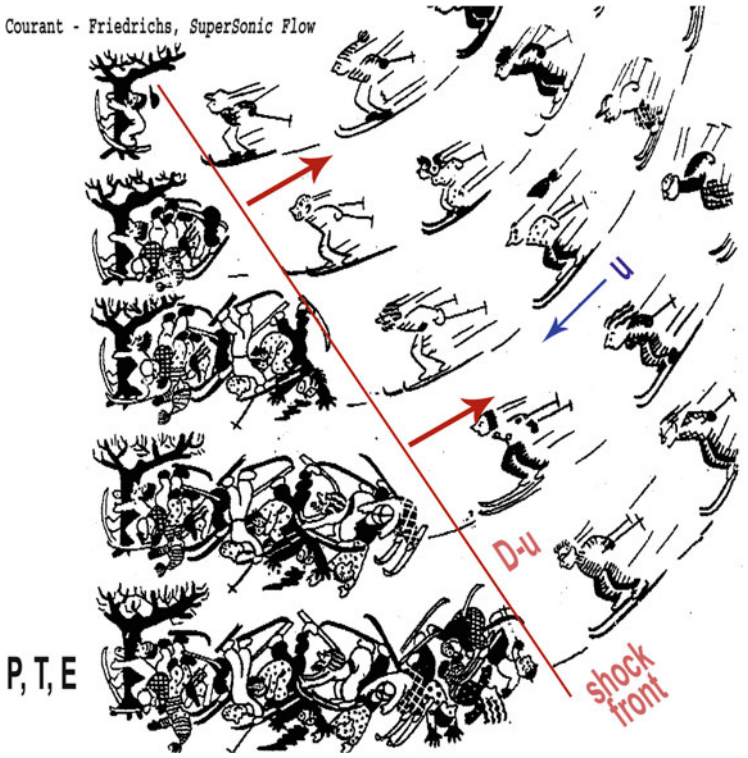

Fig. 3.12 Shock-wave compression and heating of substance [47]

Shock-wave techniques play a leading role in high-energy-density physics today, making it possible to produce amplitude pressures of the megabar and gigabar range for many chemical elements and compounds. This range of peak dynamic pressures is six orders of magnitude higher than the pressures occurring upon the impact of a bullet and three orders of magnitude higher than the pressure at the center of the Earth, and is close [14, 15, 192] to the pressure in the central layers of the Sun and inertial thermonuclear fusion targets. These exotic states of matter were realized during the birth of our universe, within several seconds after the Big Bang [80, 138, 196]. In a sense, we can say that by progressively increasing the pressure and temperature in dynamic experiments it is as if we are traveling backwards on the time axis to approach the instant of creation of the universe—the Big Bang (see Chap. 10, Fig. 10.55).

Not only do the shock waves compress the substance, they also heat it to high temperatures, which is of particular importance for the production of plasma, the ionized state of matter. A number of dynamic techniques are presently employed in experimental studies of strongly nonideal plasmas [1, 4, 17, 63, 65, 71, 73, 199], see Fig. 3.13.

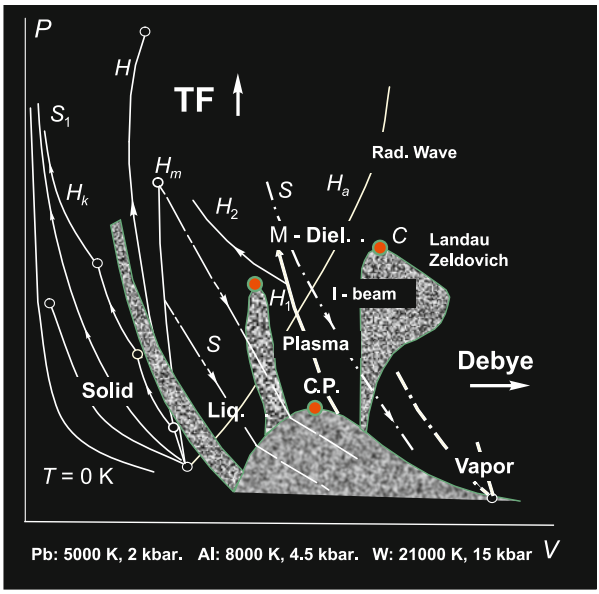

Fig. 3.13 Thermodynamic trajectories for dynamic substance investigation techniques [73]. The critical point parameters of several metals are given at the *bottom*

The shock compression of an initially solid or liquid substance enables states of nonideal degenerate (Fermi statistics) and classical (Boltzmann statistics) plasmas to be produced behind the shock front, compressed to peak pressures of $\approx$4 Gbar and heated to temperatures of $\approx 10^7$ K [14, 15, 192]. At these parameters, the density of the internal plasma energy is comparable to the nuclear energy density and the temperatures approach the conditions at which the energy and pressure of equilibrium radiation begin to play a significant role in the total thermodynamics of these high-energy states.

To reduce the irreversible heating effects, it is expedient to compress a material by a sequence of incident and reflected H_k shock waves [63, 70, 74, 139]. As a result, this multistage compression becomes closer to the "softer" isentropic compression, making it possible to obtain substantially higher compression ratios (10–50 times) and lower temperatures ($\approx$10 times) in comparison with a single-stage shock-wave compression. Multiple shock compression has been used validly for the experimental study of pressure-induced plasma ionization [63, 70, 74, 139] and substance dielectrization [126] at megabar pressures. Quasi-adiabatic compression has also been realized in the highly symmetric cylindrical explosive compression of hydrogen and rare gases (Fig. 3.14) [63, 70, 74]. The highest plasma parameters were attained using spherical explosive compression [129] (Fig. 3.15). The experiment was carried out employing an X-ray complex of three betatrons and a multichannel optoelectronic system for recording the X-ray images of spherical deuterium compression. In experiments involving "soft" adiabatic plasma

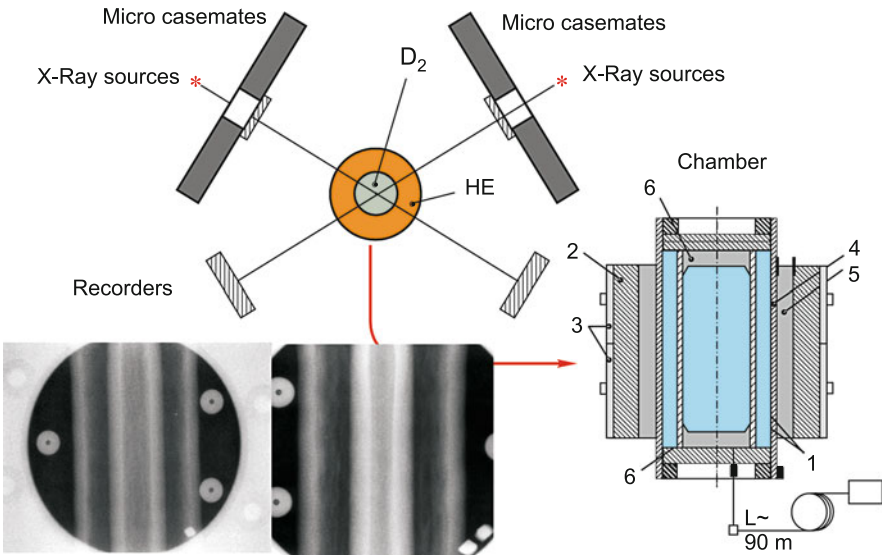

Fig. 3.14 Cylindrical explosion devices for quasi-adiabatic plasma compression [69, 72, 74, 173]: 1—cylindrical specimen; 2—HE charge; 3, 4—outer and inner metal liners; 5—X-ray radiation source; 6—X-ray recorders

compression, advantage was taken of the explosive compression of samples by megagauss magnetic fields [95, 146].

In another limiting case, when a high-temperature plasma is required, it is expedient to effect the shock compression of lower (in comparison with solid) density targets, for example, porous metals H_m [1, 4, 5, 65, 71, 92, 197] or aerogels H_a [93]. This provides a way to sharply strengthen the irreversibility effects of shock compression and thereby increase the entropy and temperature of the compressed state.

Figure 3.16 shows experimental data on the thermodynamics of high-energy states in the range of solid-state densities and high temperatures obtained by shock compression of porous nickel samples [92]. This parameter range is unconventional for plasma physics. Interestingly, these experimental data [92] correspond to the metal–dielectric transition region (Fig. 3.17), where pressure-induced and temperature ionization effects are significant for the description of plasma thermodynamics [61, 73, 92].

The shock compression of rare gases and saturated alkali metal vapor by incident and reflected shock waves allows the plasma to be studied in the domain with developed thermal ionization, where the electrons obey Boltzmann statistics [5, 63, 65, 70, 73] (Fig. 3.18).

A characteristic feature of the shock technique is that it permits high pressures and temperatures to be obtained in compressed media, while the low-density domain (including the boiling curve and the neighborhood of the critical point) turns out to

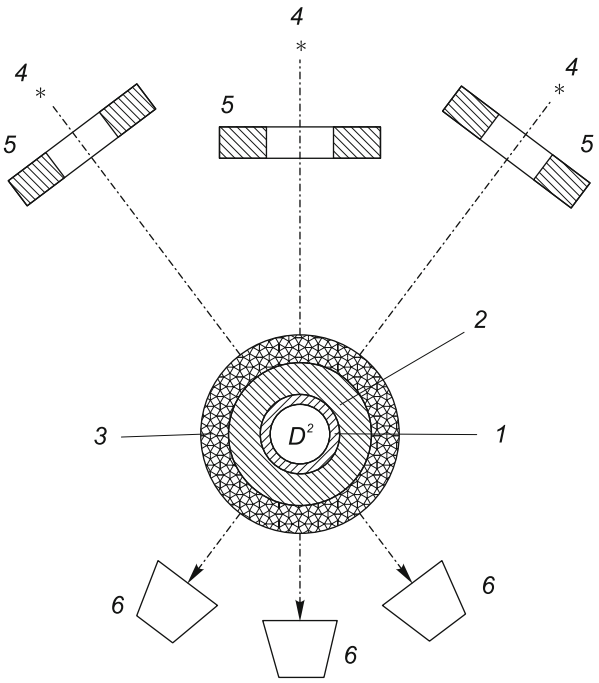

Fig. 3.15 Schematic of the experiment: *1*—spherical chamber; *2*—spacer (polyethylene); *3*—HE block; *4*—radiation sources; *5*—protective device; *6*—streak cameras [129]

be inaccessible to it [63, 65, 73]. Investigation of the plasma states intermediate between a solid and a gas is made by the isentropic expansion technique. This technique involves the generation of plasma in the adiabatic expansion S of a condensed substance precompressed and irreversibly preheated at the front of an intense shock wave [63, 65, 73]. It was precisely this technique that was first employed for the experimental investigation of the high-temperature portions of the boiling curves, the transcritical states, and the metal–dielectric transition domains for a large number of metals (for more details, see [65, 73, 198]). By way of example, Fig. 3.19 shows the domain of high-temperature vaporization of uranium [63, 67, 198], which was obtained using its adiabatic expansion data as the basis.

We see that dynamic techniques in their different combinations permit a broad spectrum of plasma states with a variety of strong interparticle interactions to be realized experimentally and investigated. In this case, not only is the actual realization of high energy density conditions possible, but so is sufficiently thorough diagnostics of these high-energy states, because shock and adiabatic waves are not merely a means of production, but also a specific tool for the diagnostics of extreme states of matter with a high energy density [1, 4, 65, 73, 197]. Measurements of the mechanical parameters of the motion of shock waves and contact discontinuities make it possible to determine the thermodynamic plasma properties and, with the use of modern high-speed diagnostic techniques, many physical characteristics of extreme parameter plasmas.

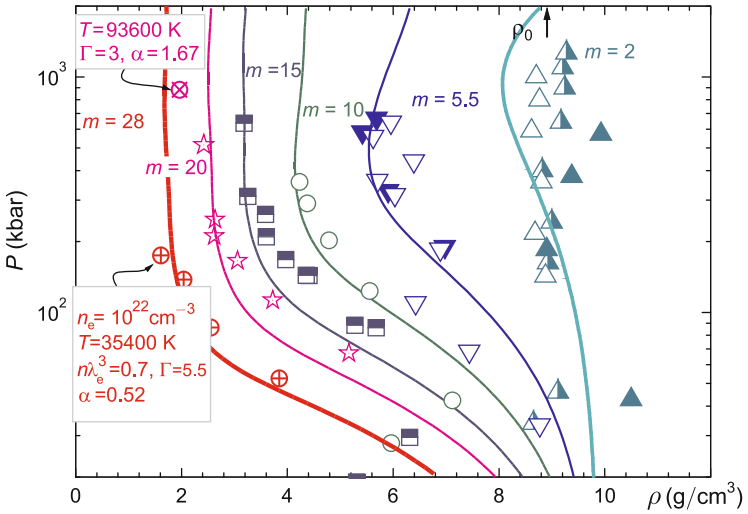

Fig. 3.16 Thermodynamics of nonideal nickel plasma [92]. *Symbols*: the results of shock compression of porous ($m = \rho_0/\rho_{00}$) specimens; α: the degree of ionization

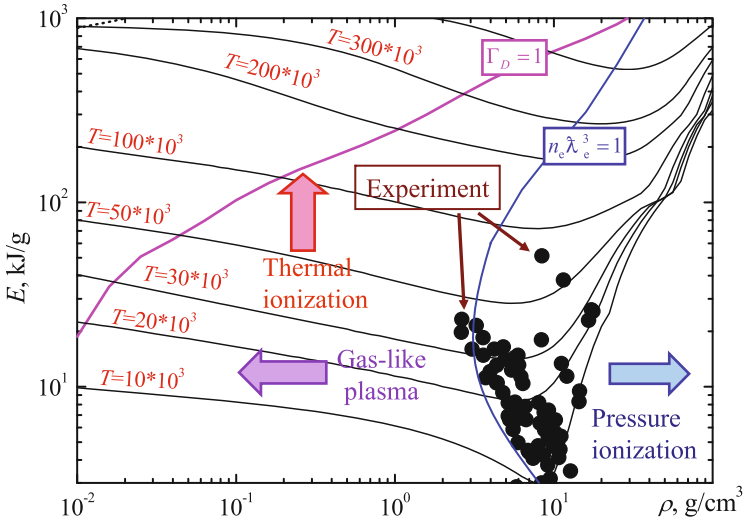

Fig. 3.17 Energy density of shock-compressed nickel plasma [92]

At present, use is made of a substantial number of dynamic cumulation sources of high energy density in dense media (Fig. 3.20).

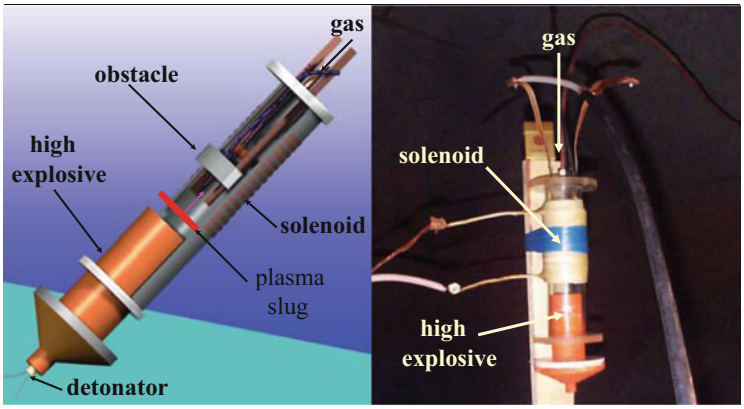

Fig. 3.18 Explosion shock tubes for measuring the low-frequency and Hall conductivities as well as the equation of state of shock-compressed plasma [70, 73]

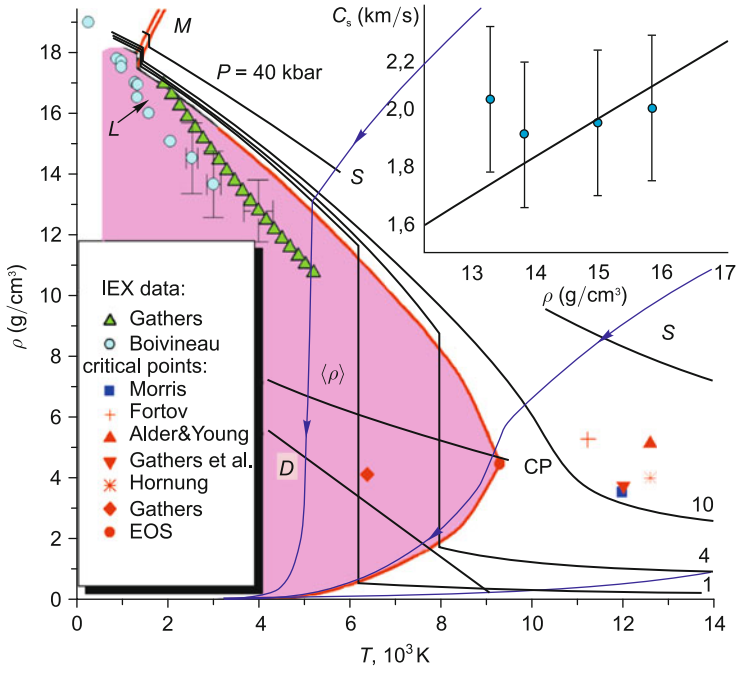

Fig. 3.19 High-temperature evaporation of uranium in the transcritical domain. The data were obtained employing the adiabatic expansion technique [67, 198]

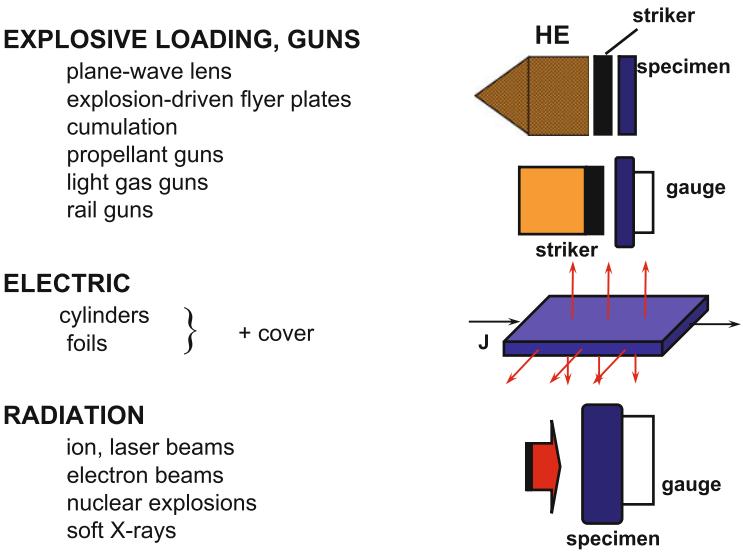

Fig. 3.20 Schemes for intense shock generation

3.5 Light-Gas Guns and Chemical Explosions

Today the technique of intense shock waves generated by the impact of metal liners (strikers) accelerated to velocities of several kilometers per second on a target of the substance under investigation is the main source of physical information about the plasma behavior at pressures up to 10–15 Mbar. Here we shall not describe in great depth the liner acceleration technique and the means of diagnostics—they are dealt with in comprehensive reviews and monographs [1, 3–5, 14, 55, 63, 65, 70, 71, 73, 139, 186]. We only note that in shock-wave experiments of this kind it is possible to carry out sufficiently ample measurements of the physical plasma properties. The equation of state is determined by electrocontact and optical recording of the time intervals in the motion of shock-wave discontinuities and contact surfaces. Pyrometric, spectroscopic, protonographic, X-ray diffraction, and adsorption measurements are performed; use is made of pulsed X-ray and synchrotron radiation sources; laser interferometric measurements are made, as are low- and high-frequency Hall conductivity measurements and the detection of piezo- and magnetoelectric effects. Unique information was gained in the study of mechanical properties of shock-compressed media: elastoplastic properties, splitting off, polymorphism, viscosity, fracture, and fragmentation [103]. Many unexpected results were also obtained in the study of chemical reactions and the kinetics of physicochemical transformations in shock and detonation waves [103].

In the USA, gunpowder and light-gas launching devices—"guns" (Fig. 3.21) [139]—were most often used, while in the USSR preference was given to explosion launching devices [3].

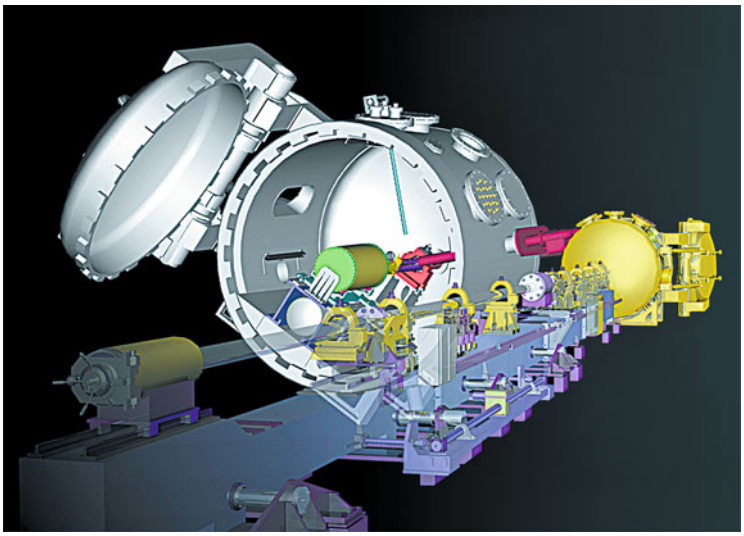

Fig. 3.21 Schematic of a light-gas gun, Livermore, USA [139]

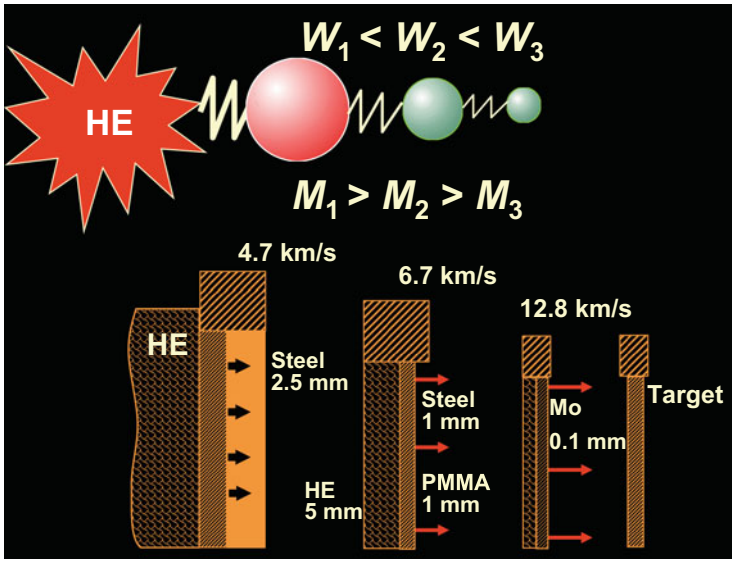

Fig. 3.22 Principle of "gradient" cumulation [195] and three-stage "layer cake" explosion [1, 4]

To increase the velocity of launching and hence the shock-compressed plasma pressure, advantage is taken of highly sophisticated gas-dynamic techniques. The technique of "gradient" cumulation (Fig. 3.22 [92, 195]) relies on a successive increase of the velocity of strikers in alternating heavy and light material planar layers. This technique is not related to the effects of geometrical energy focusing and

therefore possesses a higher stability of acceleration and compression in comparison with the spherical one. The thus-obtained three-stage "layer cake" explosion [3, 92] accelerated a 100 μm striker to velocities of 5–14 km/s. The impact of such a striker excites in the target plasma a plane shock wave or a series of reverberating shock waves with a pressure amplitude ranging into the megabar region. The geometrical parameters of these experimental devices are selected in such a way as to eliminate the distorting effect of side and rear unloading waves to ensure the one-dimensionality and stationarity of gas dynamic flow in the region of recording.

Interestingly, the kinetic energy of a metal striker moving at a speed of 10 km/s is close [139] to the kinetic energy of a proton beam in the Fermilab cyclotron accelerator. The high kinetic energy in shock-wave experiments produces a strongly compressed high-temperature plasma just as a relativistic ion collision produces a quark–gluon plasma with enormous energy densities.

To increase the parameters of shock compression, in several experiments use was made of explosion generators of counter-propagating shock waves (Fig. 3.23), where the material under investigation was loaded on both sides by the synchronous impact of steel strikers symmetrically accelerated by explosive charges [68, 137].

Very-high-precision spherical explosion generators of intense shock waves (Fig. 3.24) were made in the USSR [1, 3–5, 91] for the study of thermodynamic material properties at pressures ranging up to 10 Mbar. Using the geometrical cumulation effects in the centripetal motion (implosion) of detonation products and hemispherical shells, in devices weighing 100 kg with an energy release of 300 MJ it was possible to accelerate metal strikers to velocities of 23 km/s.

Today the use of the experimental technique of high-power shock waves for studying extreme states of matter [12, 66, 138] is the main source of information about the behavior of strongly nonideal heavy-compressed plasmas in the domain of record-high temperatures and pressures of megabar and gigabar ranges [24, 25, 27, 46, 50, 57, 70, 74, 87, 88, 91, 98, 111, 112, 139, 188, 193]. Being exotic for terrestrial conditions, these ultraextreme states are quite characteristic of the majority of

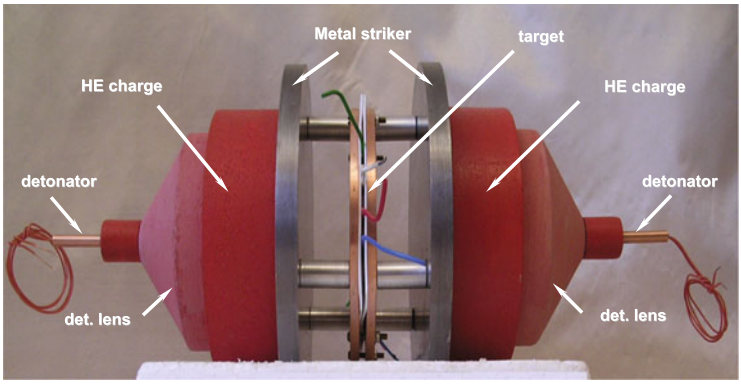

Fig. 3.23 Explosion generator of counter-propagating shock waves [68, 137]

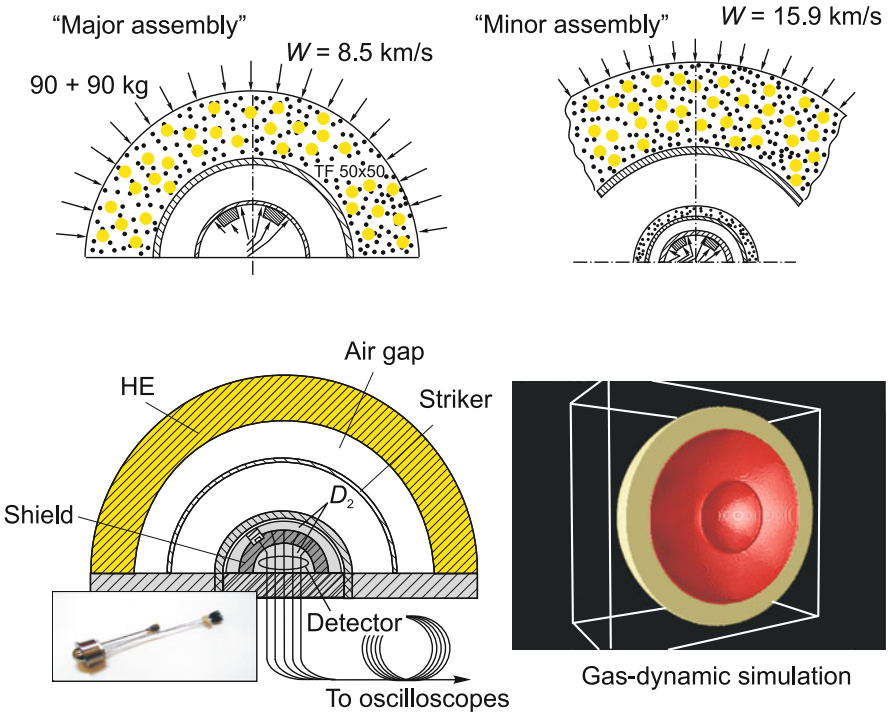

Fig. 3.24 Explosion generators of spherically converging intense shock waves [3, 5, 71]

astrophysical objects and define the structure, evolution, and luminosity of stars, the planets of the Solar system, as well as of more than 100 recently discovered exoplanets [66, 138].

Furthermore, promising energy projects on controlled fusion with inertial plasma confinement [66, 138] and the realization of high-temperature states in compressed hydrogen [12] are associated with plasmas of ultramegabar range. These circumstances are a permanent factor which lends impetus to experimental studies into the properties of heavily compressed nonideal plasmas of hydrogen, deuterium, and rare gases by high-power shock waves, which are excited by light-gas [139] and plane or hemispherical devices [24, 70, 91, 188, 193], high-power lasers, and electrodynamic accelerators [111, 112].

Significantly higher pressures, which exceed by nearly an order of magnitude the pressures under single-stage shock-wave compression and involve a significant lowering of irreversible heating effects, are realized in the quasi-entropic substance heating by a sequence of incident and reflected shock waves in devices of plane, cylindrical, and spherical geometry [25, 27, 74, 87, 88, 139]. Using this experimental technique it has been possible to obtain a density of compressed hydrogen of ≈ 2 g/cm^3 in the pressure range of up to 800 GPa [87, 88].

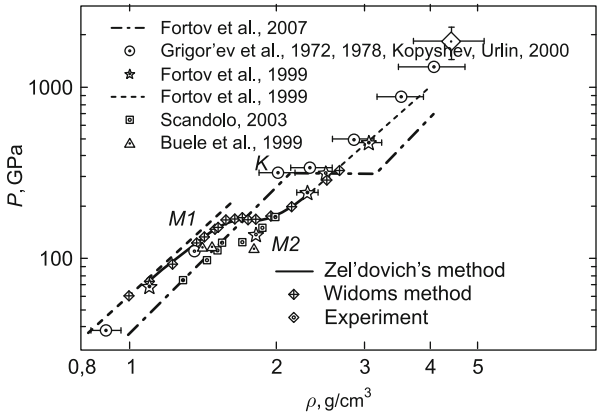

Fig. 3.25 Quasi-entropic compression of deuterium gas in the pressure range of up to 1800 GPa [129]. The experimental density from [87, 88, 113] is doubled in going from hydrogen to deuterium. The step in density is referred to the plasma phase transition

Record deuterium plasma parameters were obtained in [129]. For an initial deuterium gas pressure $p_0 = 267\,\text{atm}$ and $T_0 = 10.5°$, the density of shock-compressed deuterium plasma was measured at $\rho = (4.3 \pm 0.7)\,\text{g/cm}^3$ for a pressure $P = 1830\,\text{GPa}$. Under these conditions the plasma is strongly nonideal ($\Gamma \approx 4.5 \cdot 10^2$) with a degenerate ($n\lambda_e^3 \approx 2.8 \cdot 10^2$) electron component of density $\approx 2.8 \cdot 10^{23}\,\text{cm}^{-3}$ (Fig. 3.25).

In [130] the kinematic and thermodynamic parameters of the shock compression of liquid nitrogen were measured behind the front of a plane shock wave with the use of plane-wave and hemispherical shock-wave generators. High compression parameters were achieved in the experiments: a shock-compressed liquid nitrogen density $\rho \approx 3.25\,\text{g/cm}^3$ and a temperature $T \approx 56{,}000\,\text{K}$ at a pressure $P \approx 265\,\text{GPa}$. Measurements were made of the density, pressure, temperature, and electrical conduction of the nonideal plasma of shock-compressed liquid nitrogen. A close-to-isochoric behavior of the shock adiabat of nitrogen was observed in the $P = 100$–$300\,\text{GPa}$ pressure range. The experimental data are interpreted as the detection of the boundary for the shock-compressed nitrogen transition from a polymer phase to a strongly nonideal dense plasma state for $P \approx 100\,\text{GPa}$, $\rho \approx 3.4\,\text{g/cm}^3$.

The experimental data on the thermodynamic properties of nonideal deuterium plasma obtained under cylindrical and spherical shock-wave compression are shown in Figs. 3.25 and 3.26, where they are compared with the data of laser (Fig. 3.4) [18] and electrodynamic (Fig. 6.8) experiments [110]. Dedicated estimates show that the shock-compressed plasma in these experiments is strongly nonideal (Debye coupling parameter $\Gamma > 1$) with developed ionization $n_e/n_\text{D} \approx 1$ (where n_e and n_D are the electron and Debye densities, respectively) and partial degeneracy $n_e\lambda_e^3 \approx 3$, where λ_e is the thermal de Broglie wavelength. One can see (Fig. 3.26) that the

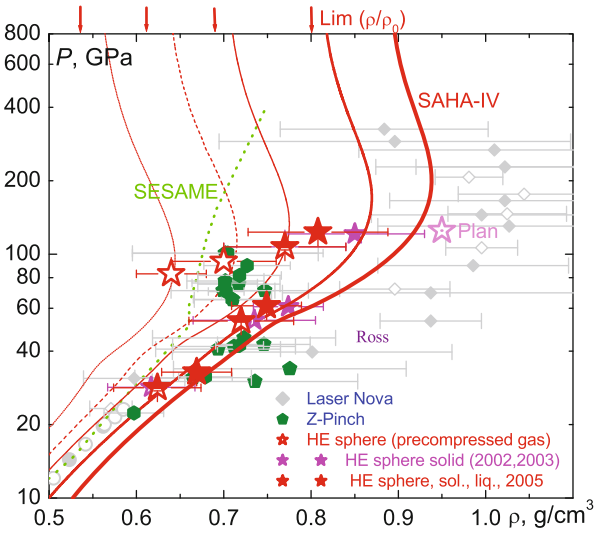

Fig. 3.26 Shock-wave compression of deuterium plasma [18, 24, 50, 110]

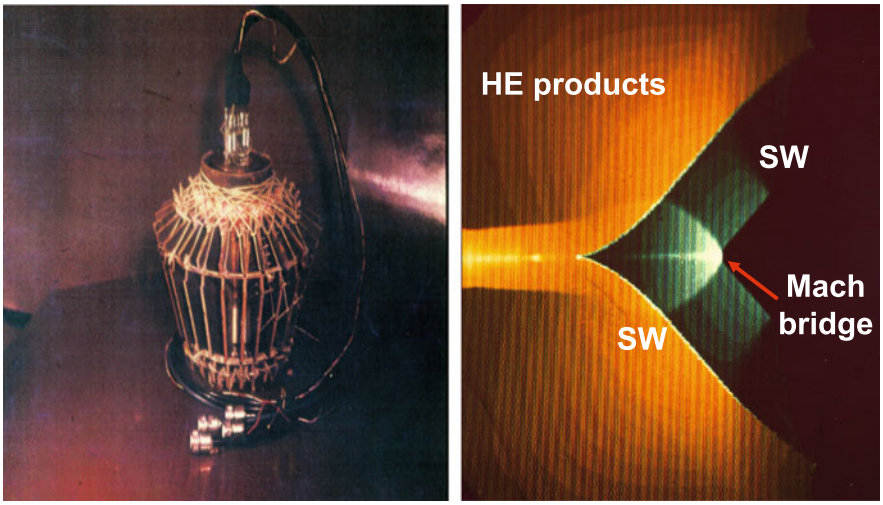

Fig. 3.27 Explosion conic generators of "Mach" shock waves [17]. Shown at the *right* are the results of a two-dimensional hydrodynamic simulation

models of nonideal plasmas [1, 4, 71, 197] provide a reasonable description of the data from explosion and electrodynamic experiments.

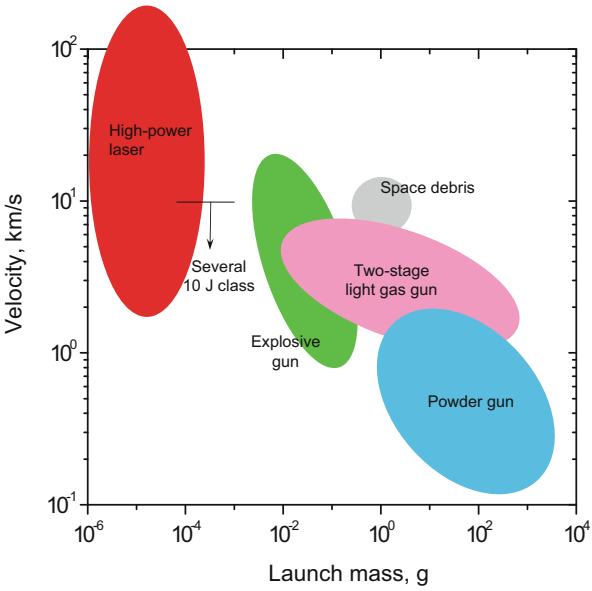

Fig. 3.28 Capabilities of different high-velocity launching techniques

In higher-stability conical explosion generators, use was made of cumulation effects in the irregular ("Mach") convergence of cylindrical shock waves (Fig. 3.27). The combination of irregular cylindrical and "gradient" cumulation effects enabled excitation in copper of a shock wave with an amplitude of ≈20 Mbar, which is comparable with pressures in the near zone of a nuclear explosion.

The capabilities of different launching techniques are compared in Fig. 3.28.

3.6 Underground Nuclear Explosions and Quasi-Classical Model of a Substance

Specific plasma energy densities that were records for terrestrial conditions were obtained in the near-source zone of a nuclear explosion. Several physical experiments of this kind are schematized in Figs. 3.29 and 3.30 [3, 14, 15, 71, 186, 187, 192]. The collection of experimental data on shock-compressed aluminum plasma is represented in Fig. 3.31, where the highest points correspond to record parameters in terrestrial conditions [192]. The density of the internal energy of this plasma is $E \approx 10^9\,\mathrm{J/cm^3}$, which is close to the energy density of nuclear matter, and the pressure $P \approx 4\,\mathrm{Gbar}$ is close to the pressure in internal layers of the Sun. The plasma under these conditions ($n_e \approx 4 \times 10^{24}\,\mathrm{cm^3}$, $T \approx 8 \times 10^6\,\mathrm{K}$) is nondegenerate, $n\lambda\!\!\!^{-3} \approx 0.07$, it is 12 times ionized, and the nonideality parameter is small ($\Gamma \approx 0.1$), which is an experimental illustration of the thesis of Chap. 2 about simplification of the physical plasma properties in the limit of ultrahigh

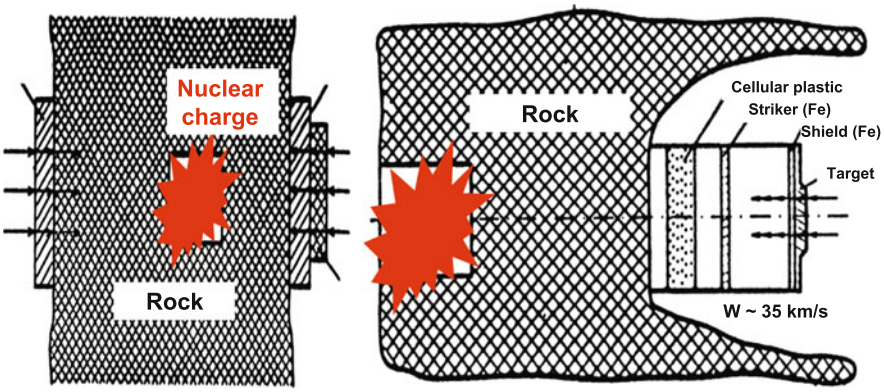

Fig. 3.29 Scheme of experiments on the generation of intense shock waves in the immediate vicinity of a nuclear explosion [14, 15, 186, 187]

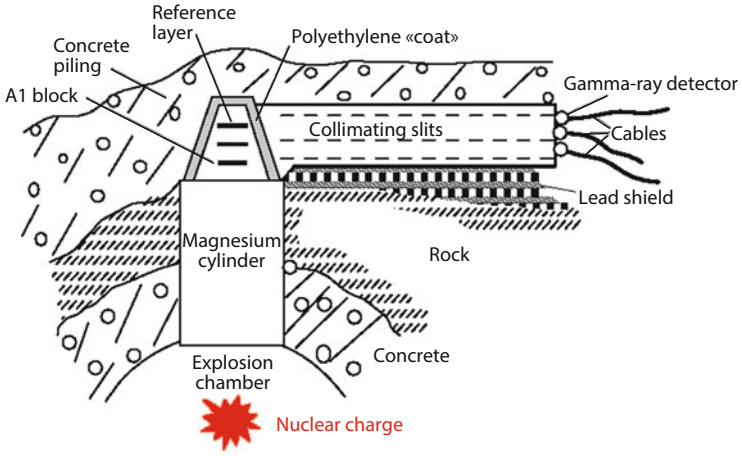

Fig. 3.30 Schematic representation of experiments with an underground nuclear explosion using a gamma-active reference layer. Reprinted, with permission, from [15]

energy density. Interestingly, the parameter range investigated is adjacent to the domain where the energy and pressure of equilibrium radiation make an appreciable contribution to the thermodynamics of the system:

$$E_{\mathrm{R}} = 4\sigma T^4/c; \qquad P_{\mathrm{R}} = E_{\mathrm{R}}/3 = \frac{4}{3}\sigma T^4/c.$$

Therefore the plasma dynamics regime is realized close to the radiative gas-dynamic one [55].

The pressures realized by means of nuclear explosions [3, 5, 14, 15, 71, 186, 192] (Fig. 3.31) belong to the multimegabar domain and are close to the characteristic

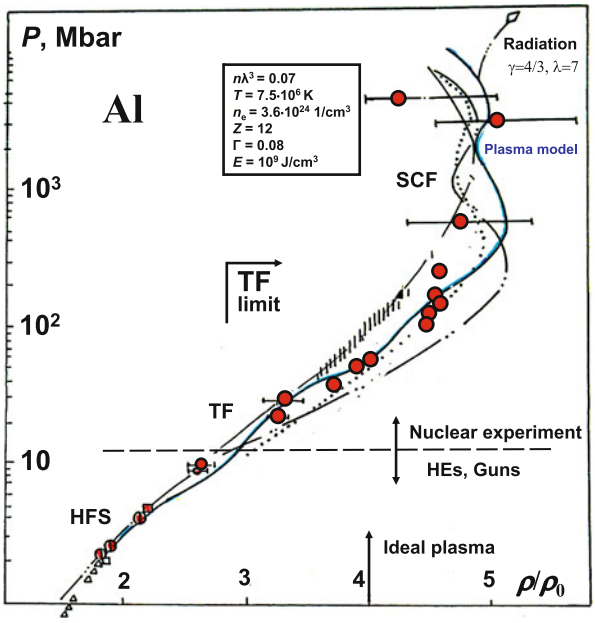

Fig. 3.31 Shock-wave compression of aluminum to gigabar pressures [14, 15, 192]

"physical" pressure, which may be found from dimensionality considerations $P \approx e^2/a_B^4 \approx 300\,\text{Mbar}$ ($a_B = \hbar^2/(me^2)$ is the Bohr electron radius). Beginning with these pressures, the Thomas–Fermi model [106, 107] applies, which implies a simplified quantum-statistical description of a strongly compressed substance and the "self-similarity" of its physical properties. This model [107], which relies on the quasi-classical approximation to the self-consistent field method, is a substantial simplification of the many-particle quantum-mechanical problem and therefore enjoys wide use in the solution of astrophysical and special problems.

As discussed in Chap. 2, the description of bound electron states in the high-density domain, $\rho \leq \rho_0$, is radically simplified at extremely high pressures $P \gg e^2/a_B^4$ or temperatures $T \leqslant 1\,\text{Ry} \approx 10^5\,\text{K}$, when electron shells are "crushed" and their properties are described by the quasi-classical approximation to self-consistent field theory—the Thomas–Fermi theory. In this model, the description of a system in terms of wave functions and energy eigenvalues is replaced by a simplified statistical representation in terms of the average electron density $\rho(x)$, which obeys the relationships of a quasi-uniform degenerate electron gas (in the subsequent discussion we use the atomic system of units):

$$n(x) = \frac{1}{\sqrt{2}\pi}\, T^{3/2} f_{1/2}\left(\frac{p_F^2(x)}{2T}\right) \underset{T\to 0}{\to} \frac{p_F^2(x)}{3\pi^2},$$

where $f_{1/2}(\alpha)$ is the Fermi function and μ is the chemical potential.

To simplify calculations, in the quasi-classical model a substance is divided into electroneutral spherical Wigner–Seitz cells of radius R, which contain a nucleus and

Z electrons surrounding it, making it possible to go over from the multicentered problem to a one-centered spherically symmetric problem. The electrons are in the self-consistent potential $U(r)$ which satisfies the Poisson equation:

$$-\nabla^2 U = 4\pi n,$$

$$\left(U(r) \underset{r\to 0}{\sim} \frac{1}{r}, \qquad U(r) \underset{r\to R}{\sim} (r-R)^2 \right),$$

where the cell radius R is defined by the electroneutrality condition $\int n(x)\,dx = Z$. Numerical integration of this equation enables one to determine the electron density $\rho(x)$, which underlies the determination of all thermodynamic functions of the electron gas of the atomic cell. To obtain the net thermodynamic characteristics of the substance, account must be taken, along with the electronic terms, of the nuclear motion, which is commonly described in either the ideal-gas or quasi-harmonic approximation. The equations of the Thomas–Fermi model are inherently self-similar with respect to the nuclear charge: upon introduction of the variables ZV, $Z^{-4/3}T$, $Z^{-10/3}P$, $Z^{-7/3}E$ they do not contain Z explicitly and their solution applies to any element, which simplifies the practical employment of this model.

The Thomas–Fermi model is the quasi-classical limit with respect to the Hartree equations of the self-consistent field, and therefore modifications of this model involve taking correlation, quantum-mechanical, and relativistic effects into account in more detail [107]. Correlation corrections exist because the self-consistent Hartree field is different from the true field inside an atomic cell. These corrections arise from the antisymmetry of electron wave functions and are interpreted as exchange-correlation effects. In addition, owing to inexactness of the picture of independent particles accepted in the model, there emerge force correlation effects.

Quantum-mechanical corrections stem from the use of a quasi-classical formalism and are divided into the regular (in $\hbar^2$) part (termed quantal), which reflects the nonlocality of the relation between $n(x)$ and $U(x)$ due to the uncertainty principle, and the nonregular correction, which reflects the nonmonotonicity of physical quantities arising from discreteness of the energy spectrum [107]. It is significant that the introduction of the oscillatory correction characterizes the most up-to-date versions of the Thomas–Fermi model [107], while the inclusion of exchange, correlation, and quantum corrections is conventional practice for high-energy-density physics.

The relative magnitude of correlation and quantum effects is determined by the dimensionless parameters [107]

$$\delta_{\text{corr}} \sim \delta_0^{\nu} \quad \text{and} \quad \delta_{\text{quant}} \sim \delta_{\text{exch}} \sim n/p_{\text{F}}^4.$$

In the degeneracy domain ($n^{2/3} \gg T$, $p_{\text{F}} \sim n^{1/3}$, $\delta_0 \sim n^{-1/3}$, $\nu = 2$) these parameters are

$$\delta_{\text{corr}} \sim n^{-2/3}, \qquad \delta_{\text{exch}} \sim n^{-1/3},$$

and in the classical domain ($n^{2/3} \ll T$, $p_F \sim T^{1/2}$, $\delta_0 \sim n^{1/3}/T$, $\nu = 3/2$)

$$\delta_{corr} \sim n^{1/2}/T^{3/2}, \qquad \delta_{exch} \sim n/T^2.$$

A drawback of the Thomas–Fermi model is an incorrect description of the electron density at the cell periphery and near the nucleus due to violation of the quasi-classicality condition there. Kirzhnits et al. [107] came up with a method for removing this drawback by employing the method of successive approximations in the solution of the Thomas–Fermi equations with quantum corrections without expanding in a series in a small parameter. This approach forms the basis of the quantum-statistical model, in which the solution rapidly converges near the nucleus and exhibits a qualitatively correct quantum-mechanical behavior away from the nucleus. However, the resultant formulae are no longer self-similar with respect to Z. Numerical calculations have to be carried out anew for each element, and the equations themselves are much more arduous for numerical calculations.

Several other modifications [107, 174] to the quasi-classical model in the vicinity of the nucleus were also proposed, which differ in the way the corrections are introduced. However, in the thermodynamic description the difference between these models and the Thomas–Fermi model with corrections is noticeable only outside of the domain of their formal applicability, which underlies the preference for the simpler Thomas–Fermi model to carry out specific calculations.

When use is made of the quasi-classical method of description, it is well to bear in mind the specific inaccuracies introduced by the cell model itself. All electron correlations in this model are automatically limited to the dimensions of the atomic cell and therefore cannot exceed the average internuclear distance, and nucleus–nucleus correlation effects are absent. These circumstances obviously limit the applicability of the Thomas–Fermi model for the description of plasma in conditions typical for this state of matter, when the screening sphere contains a substantial number of nuclei, whose correlations make the main contribution to the Debye correction [94]. That is why this model does not encompass the Debye limit in the plasma domain and, furthermore, its extrapolation properties become worse as the plasma becomes more tenuous (see [73]), because the model does not describe the stepwise nature of thermodynamic functions in gas plasmas owing to ionization effects (Fig. 3.32).

The divergence between the calculations made in the framework of the Thomas–Fermi model and more exact quantum-mechanical calculations by the Hartree–Fock–Slater model in the parameter range characteristic for the plasma state is considered in [71, 73].

Nuclear correlation effects may also be significant in the condensed phase, since the cell model ignores the deviation of the real cell volume from the average one due to nuclear motion, which is valid only for ordered systems. For nonideality parameter values $\Gamma \approx 100$ typical for the condensed state and dense plasmas, in the equation of state it is necessary to take into account the motion of nuclei, which also leads to atomic volume fluctuations. For the Thomas–Fermi model an estimate

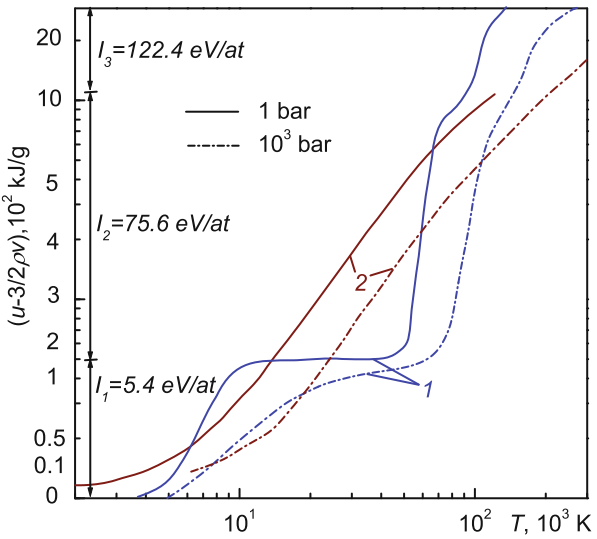

Fig. 3.32 Equation of state of lithium plasma [101]. Calculation: *1* chemical model, *2* Thomas–Fermi model with quantum and exchange corrections. I_1, I_2, I_3 sequential ionization potentials

of this effect using the example of SiO_2 showed [133] that the inclusion of nuclear motion in the range $1 < \Gamma < 100$ increases the pressure by ≈15 %.

The physical conditions for the validity of the quasi-classical model, as noted above, correspond to extremely high pressures $P \gg 300$ Mbar and temperatures $T \gg 10^5$ K, which are realized in different astrophysical objects but are hard to attain by experimental techniques in terrestrial conditions. The presently attainable highest-pressure and highest-temperature states are realized, as is evident from the foregoing, with the help of dynamic methods that make use of the techniques of intense shock waves. Although the majority of shock-wave experimental data do not correspond exactly to quantum-statistical conditions, they permit the properties of the quasi-classical models to be extrapolated beyond the limits of their formal applicability defined [107, 174] by the smallness of the corresponding literal criteria. These constructions suggest that the introduction of quantum, exchange, and correlation corrections (oscillation corrections were not included) improves extrapolation, which becomes possible in this case, in the view of Al'tshuler et al. [2], to pressures $P \geqslant 300$ Mbar for zero temperature and to ≈50 Mbar for $T \geqslant 10^4$ K. At the same time, the data of comparative measurements made in underground nuclear explosions allow ambiguous interpretations and do not provide an unequivocal answer to the question about the superiority of one or other version of the quasi-classical model, and are at variance with the data of absolute measurements [15].

It is also noteworthy that experiments on the shock compression of high-porosity copper performed for pressures of 10–20 Mbar and temperatures up to 2×10^6 K (see [14, 63, 65]) and of solid materials for pressures up to 160 Mbar [2, 14, 63, 65, 163, 164, 187] are indicative of significant shell effects in the domain that was previously described by tradition by the standard Thomas–Fermi model.

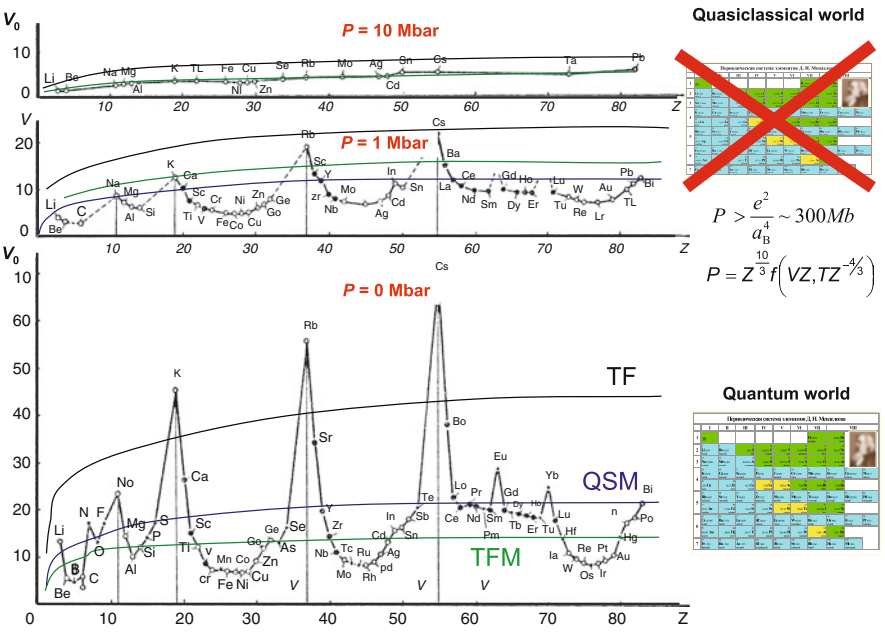

Fig. 3.33 Variation of elemental atomic volumes with increasing pressure [1, 4]

On the strength of initial simplifications, the quasi-classical model with quantum and exchange corrections is inapplicable at low pressures, but it provides [1, 4] (Fig. 3.33) a reasonable averaging of elemental atomic volumes over the periodic system. We emphasize that the Thomas–Fermi model itself, due to the absence of cohesion forces in it, for a zero pressure leads to an infinite radius of an atomic cell and therefore to an incorrect—zero—substance density, and that the finite substance density is not obtained until the corrections are introduced. As noted in [1, 4], with increasing pressure the oscillations of atomic volume decrease and approach the calculations by modified Thomas–Fermi models. However, this is partly attributable to the fact that the comparison at high pressures was made with the results of extrapolation of experimental data to quasi-classical calculations themselves.

In reality the tendency for substance properties to become simpler is violated at higher pressures due to the existence of inner atomic shells in atoms. As determined in [107], shell effects may be qualitatively described in the framework of the quasi-classical approximation by including the correction irregular in $\hbar^2$ that corresponds to the oscillatory part of the electron density, which was previously disregarded by mistake. In this case it is significant that the shell effects are described even in the lowest quasi-classical approximation for the wave function and should therefore be taken into account along with the regular corrections considered above. The shell effects reflect the irregularities of substance characteristics arising from the

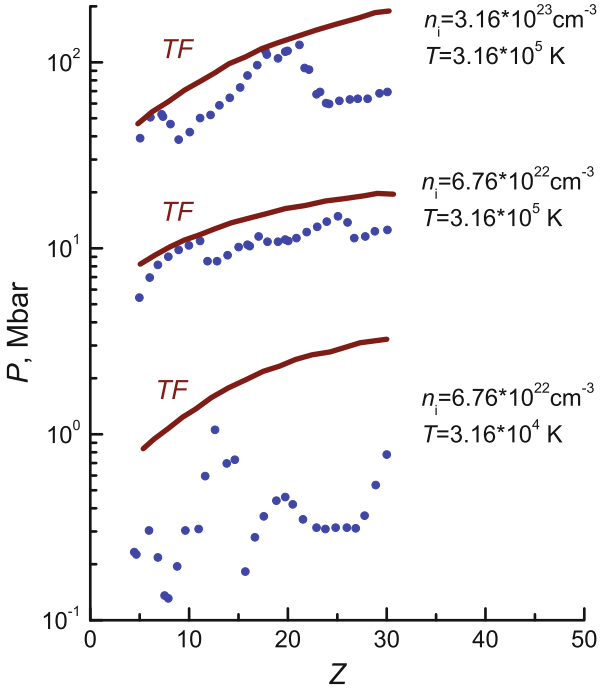

Fig. 3.34 Pressure as a function of atomic number for fixed densities and temperatures [118]. The *solid lines* represent calculations by the Thomas–Fermi model and the points correspond to the inclusion of shell effects in the central field approximation

discrete energy spectrum and emerge in the quasi-classical model as a result of the interference of de Broglie waves [107].

Therefore, the quasi-classical model in its most up-to-date version [107] is much more substantive than considered before. It turns out that this model not only describes the averaged behavior of electrons in heavy and strongly compressed atoms, but it also qualitatively reproduces the atomic inner-shell structure and in many cases yields results that are close to the data calculated by more accurate quantum-mechanical models, being profitably different from them in simplicity and obviousness.

The inclusion of shell effects appreciably changes the equation of state of substances, giving rise to discontinuities in the atomic volume curve $V(Z)$ in the high-pressure domain (where this approximation is justified) [73, 107]. In this case, in the equation of state there emerge characteristic nonmonotonic features caused by electron phase transitions, when the energy levels are expelled from the discrete spectrum into the continuum. One might expect these features to smooth out with increasing temperature under the influence of resonance electrons, however, the data calculated in the central-field approximation [118] testify (Fig. 3.34) to a significant influence of the shell structure even for a strongly heated substance. The significance of the contribution from the shell effects at hyper-megabar pressures also follows from the data of quantum-mechanical calculations in the more exact Hartree–Fock–Slater approximation [178, 179] and by the augmented plane wave method [128].

These effects are predicted for a broad parameter range and should vanish for $n \gg Z^4$ in the homogeneity domain [106], when all atomic energy levels pass into the continuum. In this connection we note that the question of the asymptotic behavior of the quasi-classical model is not trivial, for it has been shown [121] that this model corresponds to the exact solution of the Schrödinger equation only for $Z \to \infty$, but not in the high-density limit.

Therefore, the question of the limits of validity of the quasi-classical model is still, to a large extent, open, and the behavior of substances in the $P > 300$ Mbar domain turns out to be more varied than assumed on the basis of earlier simplified ideas [107]. Experimental verification of the predictions of the quasi-classical shell model is presently the most interesting problem of ultrahigh-pressure physics; solving this problem is thought to call for new experimental techniques relying on intense directional energy fluxes (see the following sections).

For the time being, only the underground nuclear explosion techniques [3, 14, 15, 71, 192] furnish the opportunity to approach the multimegabar pressure domain, making no more than an estimate of the lower bounds of validity of the quasi-classical model possible (Fig. 3.35). It was determined [1, 4] that this model applies beginning from pressures of about 100 Mbar in the Hugoniot curve, whereas its validity range becomes substantially narrower with increasing temperature (the Hugoniot curves of a porous material).

The thermodynamics of superdense plasmas in the ultramegabar dynamic pressure range invites further investigation. Figure 3.36 shows the pressures thus far

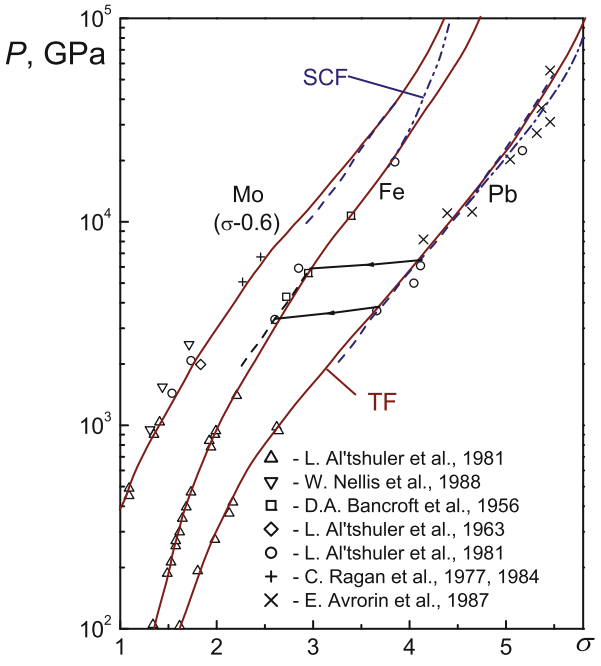

Fig. 3.35 Extrapolation properties of the quasi-classical (Thomas–Fermi) model [1, 4]; $\sigma = \rho/\rho_0$; SCF, self-consistent field

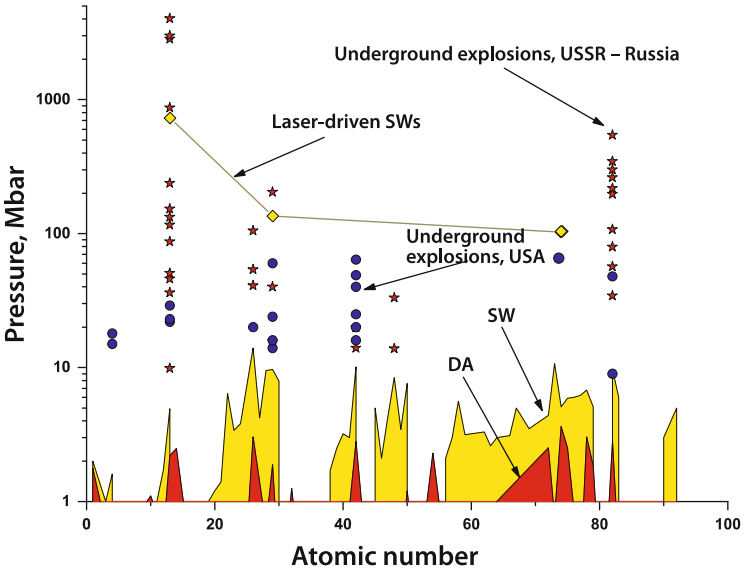

Fig. 3.36 Characteristic pressures realized in terrestrial experiments. DA—static technique involving diamond anvils, SW—shock waves driven by light-gas guns and chemical explosives

attained under controllable conditions with the help of shock waves and diamond anvils. One can see that going to pressures above 10 Mbar calls for the application of unconventional techniques of shock wave generation (Sect. 3.8), primarily laser-based techniques (Chap. 5).

The reader interested in ultrahigh-pressure problems is referred to [3, 14, 15, 63, 186, 192].

3.7 High Magnetic Fields

The highest magnetic fields that are possible to obtain in macroscopic volumes on the Earth are produced using magnetic explosion (magnetic cumulation) generators [28, 62, 90]. Today these explosive assemblies hold the records for magnetic intensity (28 MGs) and the magnitude of pulsed electric current ($\approx$300 MA), which corresponds to an extremely high electromagnetic energy density $H^2/8\pi \approx 3\,\mathrm{MJ/cm^3}$. Magnetic explosion generators are the highest-power energy devices today. Their power ranges up to $\approx$100 GW.

A schematic diagram of the first explosion magnetic generators proposed by academician A.D. Sakharov is shown in Fig. 3.37. In a radial generator (field generator) the initial magnetic flux of induction B_0 is radially compressed by a metal cylinder, which is driven to the center by the detonation of condensed explosive.

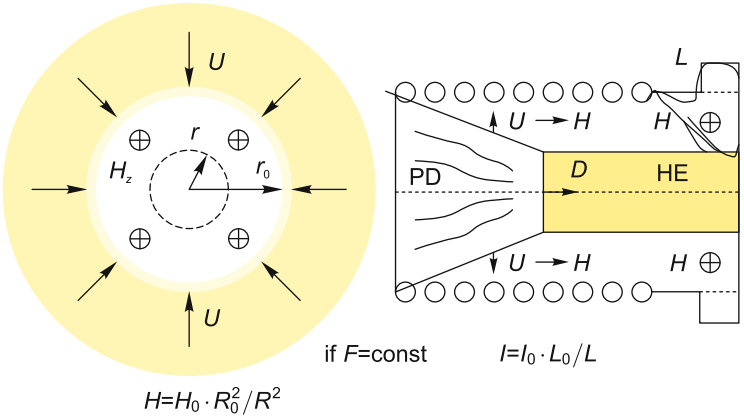

Fig. 3.37 Disk explosion magnetic generator [90]

With retention of magnetic flux $S = H_0\pi R_0^2 = H\pi R^2$ the magnetic intensity $H = H_0\left(\frac{R_0}{R}\right)^2$ inside the cylinder is of many megagauss.

In a spiral generator (energy generator) the condition of magnetic flux retention leads to a growth in current with a lowering in coil inductance, which is driven by the detonation of high explosive (HE) placed in a metal cartridge on the coil axis. The energy gain coefficient achieved in this case is at a level of 1000.

In what follows we adhere to review [90], which points to the existence of two main limitations imposed on the rate of magnetic flux compression. First, this compression must be rapid enough so as to satisfy the condition $dL/dt \gg R$ and prevent the load damage by the action of ponderomotive forces. Second, since a fast variation of the flux Φ gives rise to a high electric voltage $U = -Ldl/dt$, reliable electric insulation should by provided to guard against electrical breakdown.

A disk explosion magnetic generator (DEMG) is shown schematically in Fig. 3.38. When the magnetic flux in the generator reaches a prescribed magnitude, the generator circuit closes, thereby trapping the introduced magnetic flux. At the same point in time the HE charges are synchronously detonated. Under the action of explosion products the conducting plates collapse to compress the magnetic flux simultaneously in all cavities and force it out from the compression cavities into a load via a transmission line. The shape of conducting plates is so selected that the compression obeys an exponential law.

In experiment [90], for an initial magnetic flux of ≈1 Wb introduced into the circuit of the device with the help of a capacitor bank, an initial current pulse with an amplitude of 6.5 MA was formed, which was then amplified by a DEMG up to 90 MA. A high coefficient of magnetic flux retention was obtained: $\eta \approx 0.6$. An energy of ≈10 MJ was stored in the DEMG.

In an experiment [90] with a ten-module DEMG 400 mm in diameter, for a final DEMG inductance of 4.7 nH the energy of magnetic field amounted to 25 MJ, with 15 MJ of them in the load.

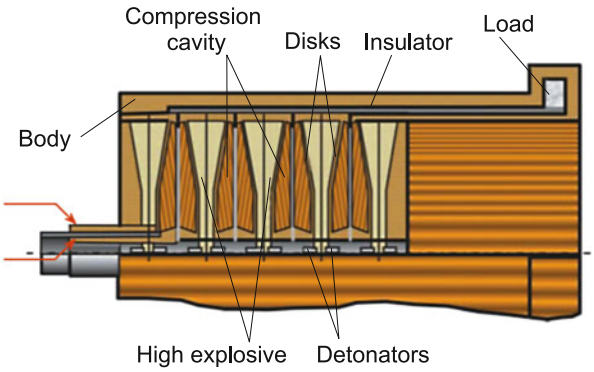

Fig. 3.38 Disk magnetic explosion generator [90]

To date, a family of DEMGs has been made with HE charges ranging from 240 to 1000 mm in diameter. The following parameters were attained in experiments with DEMGs [11, 41–43, 52, 53, 76, 131, 144, 148, 168, 172]: an energy gain coefficient of 10–30; a characteristic time of 3–10 μs; a specific energy of 600 J/cm^3; and an output energy of 200 MJ. These generators are employed to accelerate metal liners for the purpose of generating shock waves. A velocity of 50 km/s was achieved for a liner of mass 1 g [33], and a velocity of 15 km/s for a liner of mass 0.25 kg [89]. Furthermore, the feasibility of quasispherical liner implosion under the action of axially symmetric magnetic field was experimentally confirmed.

Spiral explosive magnetic generators (SEMGs) [90], which have a substantially higher inductance and rate of its reduction in comparison with those in other types of explosive magnetic generators, can efficiently operate on loads over a wide range of inductances and resistances (Fig. 3.39). The key SEMG elements are a cylindrical solenoid and a metal tube with an HE charge, which are coaxially arranged and connected via a load. The magnetic flux produced in the generator volume by an external energy source is compressed by the central tube. When the HE charge is initiated at the end face opposite to the load, under the action of detonation products this tube expands in the form of a cone, which travels with the detonation velocity along the device axis [159, 160]. The central tube is made of soft copper or soft aluminum alloys.

One of the highest-power SEMGs developed in the VNIIEF is the generator with a 240-mm internal diameter of turns [90]. For an initial energy of ≈40 kJ, in 50–120 nH loads it provides a current of up to 15 MA and a magnetic energy of ≈8 MJ. The generator characteristics outperforms the world level by a factor of 2–3 in specific energy, by a factor of 10–20 in energy gain coefficient, and by a about factor of 2 in specific speed.

Explosive magnetic generators permit obtaining high electromagnetic energy densities and are employed in many large-scale experimental systems. In the next section we consider experiments performed in the framework of the

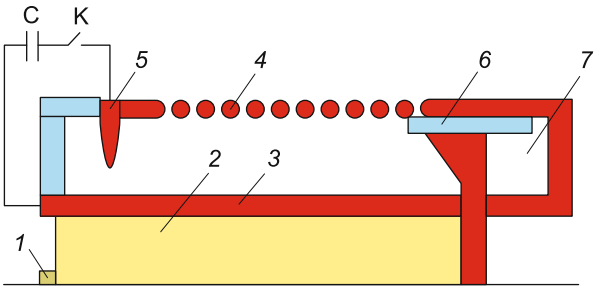

Fig. 3.39 Spiral explosive magnetic generator: *1*—electric detonator; *2*—HE charge; *3*—liner; *4*—solenoid (stator); *5*—crowbar; *6*—insulator; *7*—load; C— capacitor, K—gap [90]

MAGO ("MAGnitnoe Obzhatie", or, in English, magnetic compression) fusion program [90].

An explosive magnetic pulsed neutron source was made on the basis of a high-inductance SEMG with a stator 80 mm in diameter and a chamber with a plasma focus [51]. For a current of ≈1 MA, the generator produced about 10^{12} neutrons per pulse with a high temporal and amplitude stability.

An SEMG 200 mm in diameter [90], which produced a current higher than 5 MA with a rise time of 400 ns was employed for powering a Z-pinch. Recorded in this case was the generation of a soft X-ray pulse with an energy of ≈180 kJ and a half-amplitude duration of 20 ns [169]. In the VNIIEF, SEMGs were first employed for powering microwave generators [31].

SEMGs found use for accelerating solid liners to high velocities. Best known is the series of seven experiments *R-Damage* executed jointly by the VNIIEF and the Los-Alamos National Laboratory (LANL) to study dynamic fracture in convergent geometry using an explosive magnetic device as the driver of a cylindrical aluminum liner, which produced an axially symmetric impact action on the target under investigation [190]. The experiments were intended to investigate the features of initiation and development of spall fracture as well as of damage compacting in extruded aluminum.

In the powering of high-impedance loads with current, brought to the forefront is the problem of high energy generation in the final EMG circuit and energy transfer to the load with step-up transformers [90]. One of the tasks solved with the aid of EMGs in this scheme was the pumping of neodymium and photodissociation lasers [149, 150]. The energy of laser radiation was equal to about 100 kJ.

A spiral-coaxial EMG 160 mm in diameter with a cable-type transformer provided an energy of up to 2 MJ in a 12–15 μH load. The highest output voltage ranged up to ≈200 kV.

The possibility of making fully independent SEMGs permits their use for testing the lightning proofness of important industrial objects. In experiments involving reproduction of a lightning current pulse in a protective grounding, for the first time it was possible to record the production and development of high-power spark

channels up to 30 m in length along the ground surface. In these experiments, for a current of ≈70 kA the active resistance of the earth electrode lowered by more than an order of magnitude [166].

A medium-class DEMG (with a HE charge diameter of 400 mm) was validly used in a series of joint VNIIEF–LANL RHSR (Russian High Strain Rate) experiments [10] involving investigations of the dynamic materials strength by perturbation growth technique for deformation rates $d\varepsilon/dt = 10^5$–$10^6\ s^{-1}$ in the mode of shock-free loading [90]. The three-layer cylindrical liner consisted of current-carrying aluminum, polyethylene or water, and the material under investigation (copper) (Al–H_2O (polyethylene)–Cu). Axially symmetric sinusoidal perturbations with wavelengths $\lambda = 2$ and 4 mm were exited on two sequential segments of the outer surface of copper.

The series of RHSR experiments yielded data on the dynamic strength of polyethylene (2–3 kbar, greater than the static one by a factor of 20) and confirmed the data on dynamic strength of copper. The stable operation of the DEMG-based pulsed power system underlay the success of this series of experiments: the inaccuracy of current pulse reproduction was ≤3 %.

One of the lines of inertial confinement fusion research involves production of high-power soft-X-ray SXR) pulses with an energy of up to ≈10 MJ in a time of ≈10 ns and compression of the thermonuclear fusion target by this radiation [56, 165, 181]. To generate SXR radiation in the Emir Project [165], use was made of one- and two-stage liners of tungsten ≈0.01-mm diameter wires powered by an EMG. At the initial stage of research, advantage was taken of spiral 100- and 200-mm diameter EMGs with explosive current interrupters (ECIs). In these experiments, the current pulses had an amplitude of 2.5–5.5 MA and a pulse rise time of 300–400 ns. An SRX yield of up to ≈180 kJ was recorded; the duration of SXR radiation was ≈20 ns and its temperature was ≈50 eV [167]. With the use of a 10-element DEMG with 240-mm diameter HE charges and an electric ECI, in liners it was possible to obtain currents at a level of 14 MA with a characteristic rise time of 1.1 μs. The energy of the SXR radiation was ≈0.8 MJ [169]. This is the highest-power SXR radiation source in Russia. Envisaged for the future is the use of DEMGs with 480-mm diameter HE charges, 5-to-15 elements, and ECIs. Currents in the liner are expected to range up to ≈50 MA and have a rise time of ≈0.5 μs. According to calculations, the SXR energy will exceed 10 MJ for these current parameters.

Now let us consider, following [28], the physical experiments which employ explosive magnetic generators.

To this end, a family of radial explosive magnetic generators was made (Fig. 3.40), which permitted obtaining megagauss magnetic fields with a high

reproducibility. In doing this, substantial difficulties were overcome [28]:

- Designers began to make generator shells of variable-conductivity materials. In the initial state such a material is nonconducting or conducts current in only one direction. At the desired point in time a shock wave from an HE is transmitted through the material and it becomes conducting in all directions.
- Special initial-magnetic-field solenoids were made in the form of a cylinder of a composite material. The wires in its inner layer form a multiple-entry (≈500 wire entries) multilayer (7–13 winding layers) solenoid. This permitted obtaining high initial magnetic fluxes and employing the solenoid as a liner compressing magnetic field: after the passage of a HE-driven shock wave through the composite, its wires close to form a continuous conducting cylinder, which captures and compresses the magnetic flux.

As a result, as family of radial explosive magnetic generators was made, which permitted obtaining magnetic fields on the 10-megagauss range in laboratory conditions. The generator shown in Fig. 3.40 possesses the following characteristics [35, 145]. Initial generator parameters: an initial inner shell diameter of 139 mm, a HE mass of 16 kg, initial magnetic field of up to 250 kGs. The second and third generator cascades, with respective inner and outer diameters of 28 and 35 mm and 12 and 17 mm, may be made of a wire composite or a composite based on a finely dispersed metal powder and a binding polymer [28].

In a generator three times larger in size (the HE mass was increased eight-fold), ≈20 MGs magnetic field were obtained and ≈28 MGs in one of the experiments [28].

The behavior of high-temperature superconductors in megagauss magnetic fields generated by explosive magnetic generators was studied in [34, 147].

Experiments showed that the critical field in $YBa_2Cu_3O_{7-x}$ at a temperature of 4.2 K exceeds 200 T [147]. For a field above 210 T only a small fraction of vortexes remains in the pinning state (there is an imaginary part in the conductivity), the sample is primarily in the mode of viscous flow motion. To the disappearance of the imaginary part there corresponds the second critical field $B_{c2}(8 \pm 3\,\mathrm{K}) = 340 \pm 40\,\mathrm{T}$.

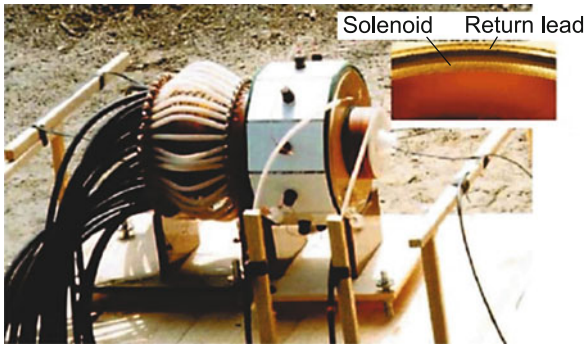

Fig. 3.40 External view of a cascade generator prepared for an explosive experiment. The *inset* shows a fragment of the cross section of the solenoid shell of the generator [28]

Investigation of semiconductors in superhigh magnetic fields permits studying energy band structure, investigate materials with a low carrier mobility or with a density of defects or impurities. In these experiments it has been possible to determine the effective electron mass in the conduction band, the Luttinger parameters for the valence band, and the g-factor for electrons and holes. All these quantities are functions of the electron energy which may be determined only in superhigh magnetic fields. Three resonance peaks were discovered in 90, 270, and 410 T fields, which permitted determining the effective masses and dispersion of electronic states [151].

The fundamental cyclotron resonance of holes and interband magnetoabsorption were studied in InGaAs/GfAs with quantum wells [28]. In the measurement of transmittance at a wavelength of $\lambda = 0.87\,\mu$m, which precisely corresponds to the band gap in GaAs (the photon energy of 1.425 eV), the sample became transparent only in the 50-T field. For the same reason, for $\lambda = 0.82\,\mu$m the sample becomes transparent for a field of 150 T [79]. Observed in higher fields are absorption bands in a range from 230 to 350 T. They arise from transitions from the two upper spin-split Landau levels in the first hole subband to the two lower Landau levels in the first electron subband.

Spin reorientation in superhigh magnetic fields was the main object of research in magnetics. The step magnetization curve of the multi-sublattice magnetic $Ho_{0.7}Y_{2.3}Fe_5O_{12}$, spin flip and spin flop transitions in MnF_2, $KMnF_3$, and $FeBO_3$ antiferromagnetics, were investigated [200]. Magnetic field may distort the electronic structure of the ground state, which results in induced band magnetism.

The effect of level crossing in the paramagnetic $YbPO_4$, $TmPO_4$, $ErVO_4$, and $PrVO_4$ zircons was investigated at a temperature of 4.2 K by induction technique in the fields of up to 400 T [104, 105].

Superhigh magnetic fields may induce a change of valence in some compounds containing Ce, Sm, Eu, Tm, and Yb rare-earth ions [28].

Induced in $EuNi_2(Si_{1-x}Ge_x)_2$ compounds is a valence transition from the state of primarily trivalent ions to the state of primarily bivalent ions, which is attended with a jump of magnetic moment. For these compounds, the fields of magnetoinduced valence transitions were experimentally determined for the Ge density range up to $x = 0.5$. In the entire density range the critical field B_c increases linearly with decreasing density [120].

Investigations into the Faraday effect in terbium gallate-garnet $Tb_3Ga_5O_{12}$ (the energy spectrum of its magnetic subsystem has been adequately studied in static fields) in an experiment with superhigh magnetic fields, whose buildup rate in a radial generator amounts to 10^7–10^8 T/s, permitted determining the magnitude of methodically important magnetocaloric effect. The temperature in the adiabatic magnetization in a 75-T field amounts to 35 K [120].

Megagauss magnetic fields are a unique tool for the adiabatic compression of substance at low temperatures and megabar pressures [28]. This experiment is schematized in Fig. 3.41. According to [28], located coaxially under the squeezing tube are a reference sample and the sample under investigation (at the center). A cryogenic device, which contains a vessel for keeping liquid helium and an

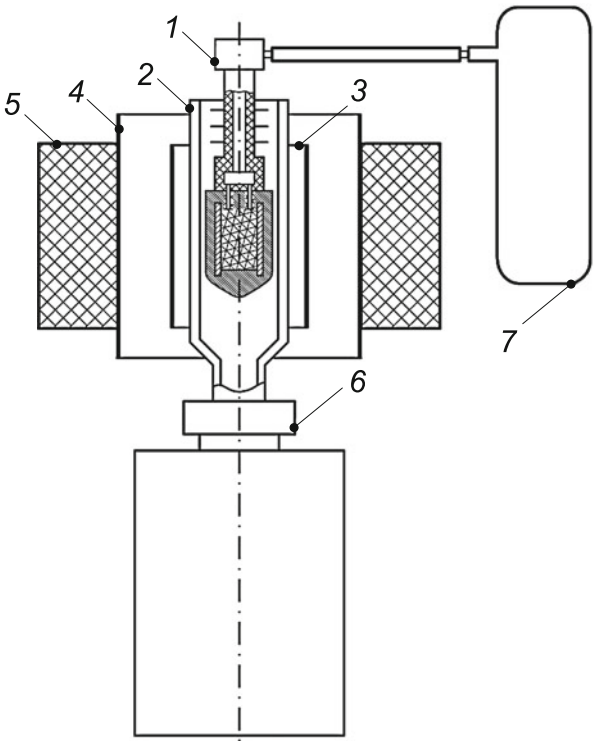

Fig. 3.41 Diagram of compression device: 1—cryocontainer with compression chamber filled with the substance under investigation; 2—cryoconductor; 3—second stage of the generator; 4—solenoid of initial generator field (the first stage); 5—annular explosive charge; 6—vessel for storing liquid helium; 7—container with the gas under investigation

evacuated cryogenic conductor of cold, is intended to preliminary cool the gas under investigation to a solid state ($T_0 \approx 5$ K). Under the excess pressure produced in the cryogenic vessel, the coolant rises along the cryogenic conductor of cold to gradually cool the compression chamber and its contents. During the discharge of a powerful capacitor bank onto the generator solenoid, an initial magnetic flux is produced in the gap between the solenoid and the squeezing tube. During the operation of a radial magnetic cumulation generator, the magnetic field in the gap rises to megagauss values and exerts a uniform magnetic pressure $B^2/8\pi$ on the outer surface of compression chamber. As a result, the camera tube collapses without shock wave production and compresses (during $\approx 15\,\mu$s) the substances inside of it to megabar pressures.

The method of determining the density ρ and pressure P of compressed substance is as follows. In the execution of experiment the central part of the experimental device is X-rayed by a bremsstrahlung pulse of the BIM-234 betatron and the transmission image is recorded on an X-ray film [116, 143]. The X-raying is performed at the moment the pressure in the compression chamber becomes ultrahigh. Processing of the X-ray image obtained in the experiment yields the size and, hence, the compression ratio of the reference and studied samples. From the known values of compression ratio and initial density ρ_0 of the sample it is easy to determine its density at the instant of X-raying. From the density of the reference

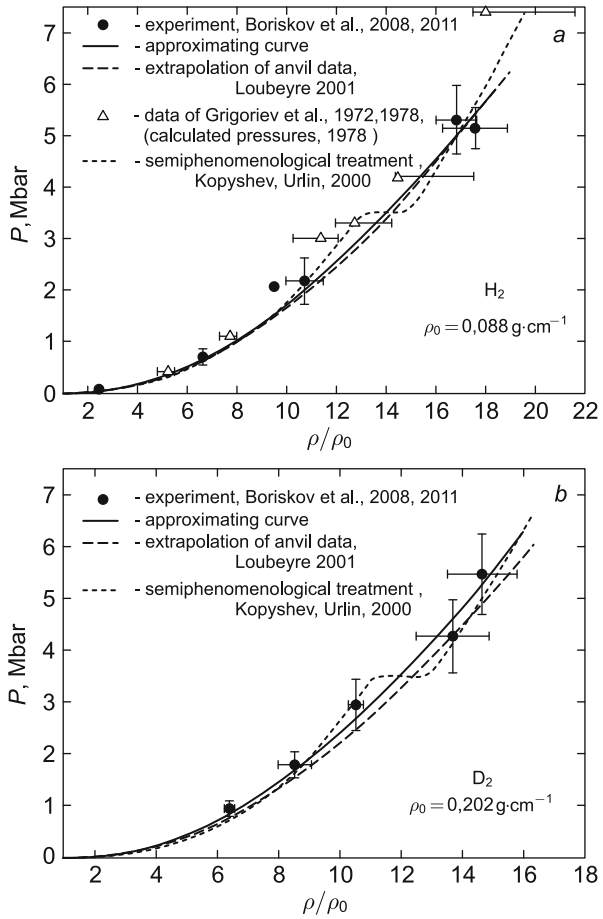

Fig. 3.42 Pressure–compression diagrams for protium (**a**) and deuterium (**b**) [28]

and its known isentrope it is possible to determine its pressure and, after including small computational corrections, in the studied substance as well. Therefore, on executing the experiment with X-raying we obtain a point in the $P \div \rho$ plane for the substance under investigation.

Series of experiments [26, 29] were performed using this compression device and the measurement technique, zero isotherms were constructed for protium and deuterium in the 1–5 Mbar pressure range [28]. The experimental points (in $P \div \rho/\rho_0$ coordinates) obtained for H_2 and D_2 are plotted in Fig. 3.42. The solid line represents the curve which approximates the experimental data. The dashed line shows an extrapolation of the zero isoterm, which was constructed in diamond anvil experiments, to the megabar range [123]. Also given is a similar curve (the dotted line) proposed for the molecular and atomic phases of protium and deuterium in [113].

3.8 Devices of High-Current Impulse Energetics

Devices of high-current (10^5–10^7 A) impulse energetics are employed to produce high-energy-density plasmas in various kinds of experimental facilities. Electric energy may effect the direct pulsed Joule heating (electroexplosion) of conductors or the magnetohydrodynamic compression and heating of plasma objects. The stored energy may be used to produce intense bursts of soft X-ray radiation (with a radiation temperature of 200–300 eV) with the subsequent generation of intense shock or radiative thermal waves by this radiation, or for the electrodynamic generation of shock waves, as well as for the electrodynamic acceleration of metallic liners. The energy capabilities of electrodynamic devices of this kind are, as a rule (with the exception of the NIF and MJL), several orders of magnitude higher than for lasers, making it possible to conduct experiments with thicker targets, raise the accuracy of measurements, and relax the time-resolution requirements (10^5–10^7 s) on the means of diagnostics.

The electroexplosion of conductors and metal foils by a pulsed current of ≈50–200 kA is the traditional direction of research into the thermophysical properties of refractory materials in the domain of condensed matter [117] for characteristic energy densities of ≈10 kJ/cm^3 (Fig. 3.43). This range was recently extended to 20–30 kJ/cm^3 with the attainment of strongly supercritical metal states, which permits, in particular, the "metal–dielectric" transition to be studied in the continuous supercritical expansion of metal plasmas.

The highest plasma parameters have been obtained in high-power Z-pinches of the terawatt power range, in which the electric energy of capacitors, after the corresponding peaking, effects the electrodynamic plasma acceleration followed by the focusing of its kinetic energy on the cylinder axis [21, 45, 48, 58, 59, 78, 102, 109, 119, 127, 140, 155, 156, 175, 176, 180, 189]. In this way an approximately 10 ns long burst of soft X-ray 150–200 eV radiation with an energy of ≈1.8 MJ and a power of ≈230 TW [48, 49, 109, 119, 140, 153, 155, 176, 180, 182, 191] was produced in the Z-pinch facility at the Sandia National Laboratories, USA [49, 153, 182]. In these experiments a cylindrical plasma shell was produced by the electric explosion of hundreds of thin (6–50 μm) tungsten conductors by a 20 MA current with a rise time of ≈100 ns. A tungsten plasma with an ion density of ≈10^{20} cm^{-3} and a degree of ionization higher than 50 was obtained in the implosion on the axis.

The second interesting application of this facility (Fig. 6.8) involves the electrodynamic generation of intense shock waves [110]. To this end, a high-power electric current pulse effected the electrodynamic acceleration of a metal liner to velocities of ≈20 km/s and the generation of megabar-range shock-wave pressures at its impact on a target. In this case there is the possibility of controlling the current parameters and realizing a shock-free ("soft") compression of the target to a pressure of ≈3 Mbar. Laser-assisted recording of the parameters of the quasi-isentropic compression was used, and it was possible to observe compressed states with lower temperatures and entropies than for shock-wave heating.

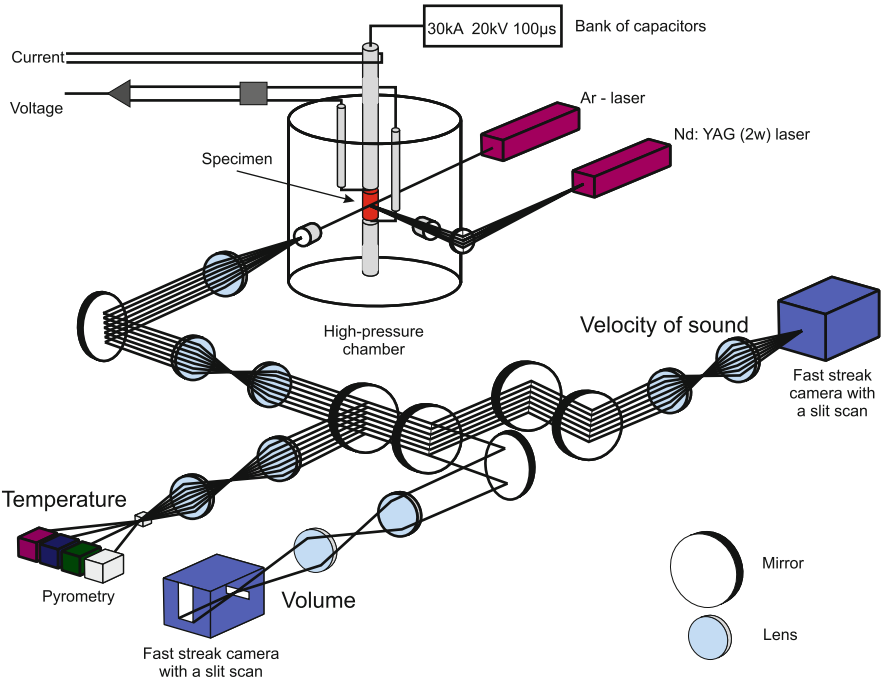

Fig. 3.43 Schematic representation of an exploding-wire experiment [117]

In experiments in the Angara facility [86] (Fig. 3.44), a pulsed current of ≈4 MA accelerated a xenon liner to a velocity of ≈500 km/s. The highly symmetric impact of this liner on the surface of a cylindrical highly porous target excited in it a thermal radiative wave, which emitted soft X-ray radiation with a temperature of ≈100 eV. This high-intensity X-ray radiation from the cylindrical cavity was employed for highly symmetric production of plane shock waves with a pressure amplitude of ≈5 Mbar, for the excitation of thermal radiative waves with a propagation velocity of 100 km/s, as well as for the acceleration of metallic liners to velocities of ≈10–12 km/s.

Interesting plasma parameters were obtained in Z-pinches with an initially gaseous shell [78, 140, 189] of centimeter size, which is ionized by 100–200 ns long megampere current and implodes to a millimeter-sized column, increasing the plasma density by factors of 20–50 (to 10^{20} cm^{-3}) for an electron temperature of several electronvolts.

A high-energy plasma is generated in the X-pinch geometry produced by crossing two current-carrying wires [6, 44, 83, 102]. Devices of this kind hold considerable promise as X-ray radiation sources for microlithography and other applications.

According to [6], an X-pinch is a load for high-current generators, which consists of two or more crossed wires. The singularity of this configuration defines its

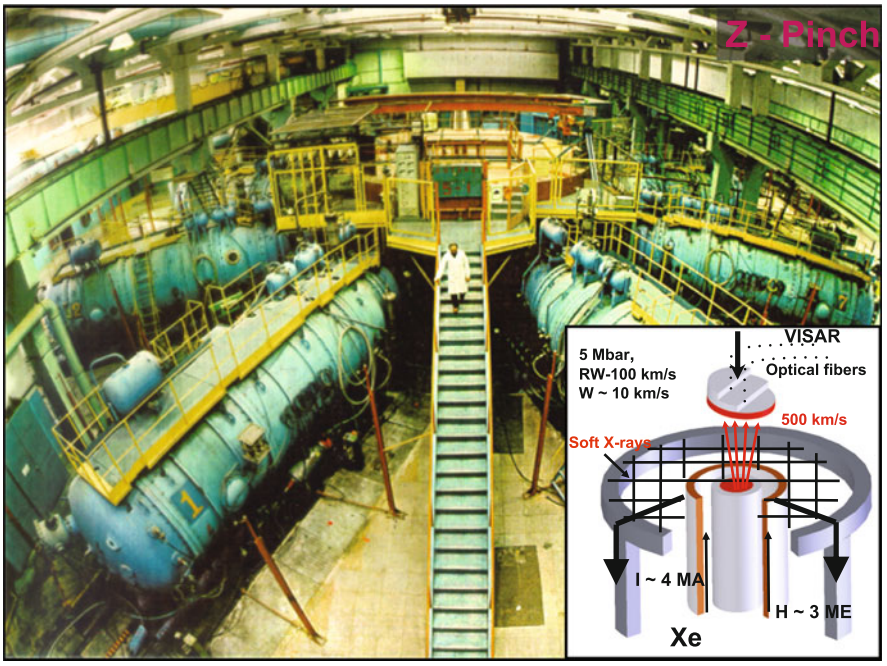

Fig. 3.44 Pulsed Angara-5 generator, TRINITI, Russia, intended for controlled thermonuclear fusion and experiments on high-energy-density plasmas and shock and thermal waves [86]

unique properties, specifically: in a wide range of the initial parameters (the number and material of the wires, their diameter, their crossing angle, the diode gap, the discharge current and its buildup rate) there forms a hot plasma in the crossing region, which radiates in the ultraviolet and X-ray wavelength ranges. The radiating plasma structure may be quite complicated, but its extreme parameters are attained in special plasma regions termed hot spots. Numerous previous experiments showed that a high spot must possess the following parameters:

- the image size in the photon energy range of about several kiloelectronvolts is less than 10 μm;
- the lifetime, which is measured from the emission duration in the same photon energy range, is shorter than 100 ps;
- the electron plasma density is higher than 10^{22} cm^{-3};
- the electron plasma temperature is ≈0.5–2 keV;
- the emission spectrum during the first 10 ps is close to the blackbody radiation spectrum.

Therefore, the hot spots of an X-ray pinch are a unique point source of pulsed soft X-ray radiation (up to 10 keV) with a record brightness, which permits using it for the radiography of short-lived objects. Best suited to this purpose is an X-ray pinch

in which there forms primarily one hot point of minimal size and highest brightness for a shortest duration of its radiation pulse [6].

Considered in [157] was a nontrivial mode of pulsed action of electromagnetic field on conductors: the mode of Coulomb explosion. The effect consists in the electric explosion of a positively charged crystal in the fast removal of conduction electrons from the metal volume without a significant heating of the lattice itself. In the case of a low-frequency field (when its frequency is lower than the electron collision frequency) it is possible to realize the conditions for the Coulomb explosion of a metal when the field pulse duration is shorter than the electron energy relaxation time due to elastic collisions and the electron temperature is much higher than the Fermi energy and the work function. In the opposite case of a high-frequency field, for instance under a high-power pulse of ultraviolet laser radiation, the Coulomb explosion occurs when the field intensity is much higher than the intraatomic field, i.e. for a laser intensity $\geq 10^{19}\,\mathrm{W/cm^2}$.

In the operation of modern high-current pinches, in the course of production of high energy densities there occur developed magnetohydrodynamic flows in which a crucial role is played by radiation [48, 59, 102, 127, 155, 158, 175], which is of significance in its own right in radiative gas-dynamic simulations of astrophysical objects.

Promise may be held by the line of research in the generation of high-energy-density plasmas reliant on the quasi-adiabatic cylindrical compression of plasma structures [8, 21, 102, 109, 127, 176, 180, 194] that initially contain preformed closed magnetic configurations—so-called "inverse" magnetic field structures [44]. Additional compression and heating of this plasma is effected by an external metallic liner electrodynamically heated by a megampere current. Estimates show [138] that the 30 MA current of the ATLAS facility is capable of producing a several-centimeter-long plasma column 1 cm in diameter with a plasma pressure of $\approx$1 Mbar, an ion density of $10^{19}\,\mathrm{cm^{-3}}$, and a temperature of $\approx$10 keV.

In the MAGO project (Fig. 3.45) [132], a pulsed current of 7 MA delivered by an explosion magnetic generator [30, 64] compresses and heats the preliminarily prepared magnetized plasma to parameters close to thermonuclear conditions, $\rho \approx 20\,\mathrm{g/cm^3}$, $T \approx$ 3–4 keV, which furnished a deuterium–tritium (DT) reaction neutron yield of $(3\text{–}5)\times10^{13}$. In this case, an energy density of $\approx10^7\,\mathrm{J/cm^3}$ was realized in the plasma-compressing metallic liner.

One can see in Fig. 3.45 that the operation of the MAGO chamber [90], which comprises two compartments connected by a Laval nozzle and filled with a deuterium-tritium mixture, necessitates two SEMGs. The first of them performs a preliminary powering of the chamber; engaged on its completion is the source of fast powering, which consists of an SEMG and a current sharpener. In the first chamber compartment there emerges a gas discharge, with the result that the magnetic field is frozen into the plasma. Under the action of magnetic field the resultant plasma flows through the nozzle from the first compartment into the second one. For a fast buildup of magnetic field the plasma flow becomes supersonic at the nozzle output and a shock wave is formed in the second compartment, in which the plasma

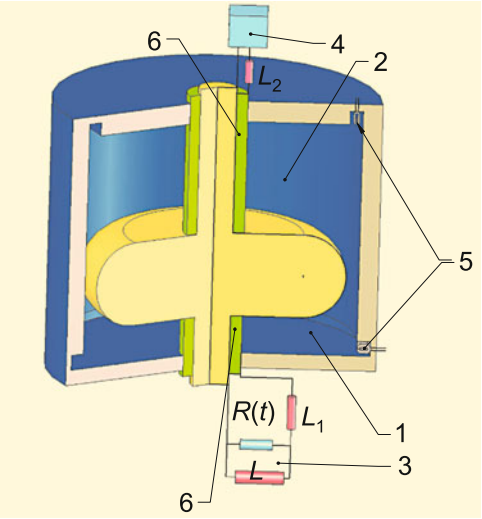

Fig. 3.45 Schematic diagram of the MAGO plasma generator [132]. 1, 2—plasma chamber; 3, 4—power sources, explosion magnetic generators; 5—sensors; 6—insulators

decelerates and heats up [40]. Obtained in the chamber were $5 \cdot 10^{13}$ neutrons per pulse.

The devices of high-current impulse energetics considered above show good promise as regards improving the main parameters and developing the elements and schemes of power compression.

The Baikal facility [16, 84] projected in Russia should become a source of soft X-ray radiation with an output energy of ≈10 MJ intended for experiments with indirect-drive thermonuclear targets and other problems of high-energy-density physics (Fig. 3.46). In this Project, 4 GJ of electric energy is stored in inductive energy storage devices and, after the corresponding power peaking, will feed a fast liner system with a power up to 500–1000 TW.

It is planned to develop the success achieved on the Z facility at Sandia, USA, employing the X-1 facility, which feeds two pinch units, each generating 7 MJ of soft X-ray radiation with a power of ≈1000 TW. This X-ray power will be delivered to a thermonuclear target 4 mm in diameter exposed to X-ray radiation with a temperature of more than 225 eV for 10 ns. The thermonuclear energy yield of the X-1 facility is anticipated to be 200–1000 MJ.

A development of the Z generator at Sandia, USA, is the IFE-Z Project [141], which is substantially no less than a prototype of a pulsed thermonuclear reactor (Fig. 3.47). Use will be made of a double Z-pinch, each pinch generating 8 MJ of X-ray radiation under a 66 MA current pulse. In this case, the planned thermonuclear energy yield is 3 GJ and the gain coefficient ≈ 83.

Figure 3.48 shows the employed scaling of the X-ray energy yield with the pinch current.

The use of chemical explosives for generating intense pulsed currents and magnetic fields relies [95] on the explosive compression of the initial magnetic

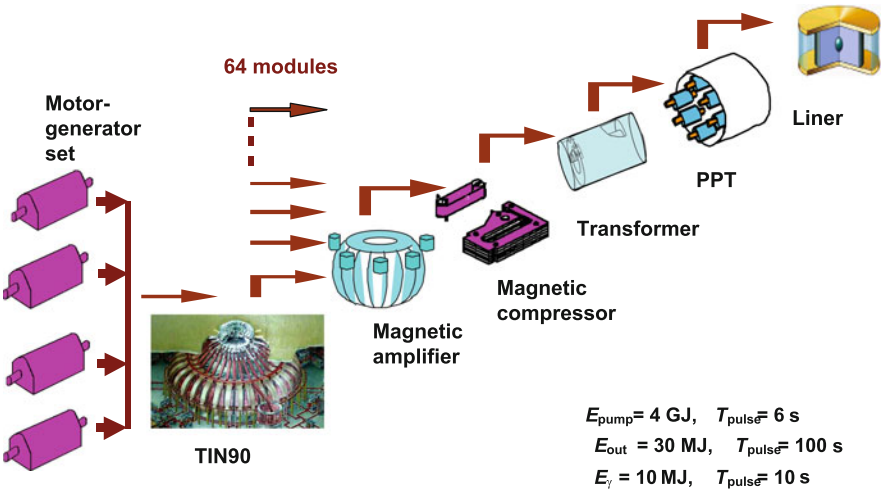

Fig. 3.46 Schematic representation of the Baikal facility [16]

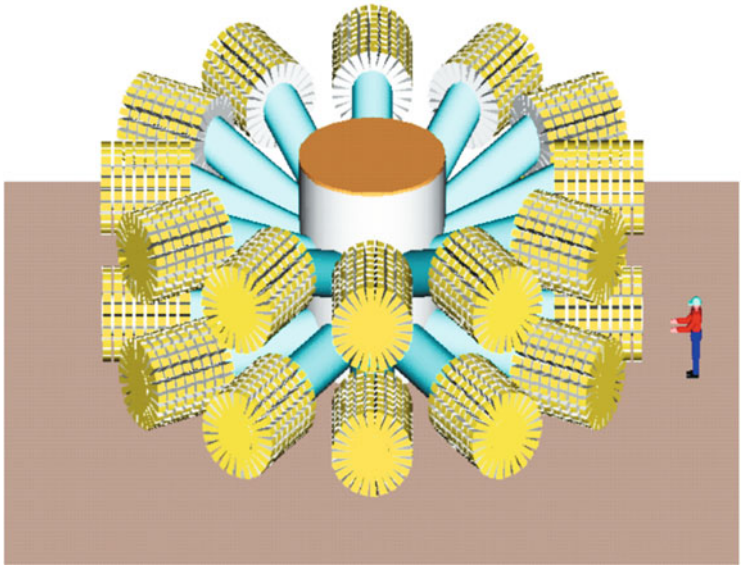

Fig. 3.47 Schematic drawing of the IFE-Z facility [141]

flux by conducting metallic liners [64, 95, 146] accelerated to velocities of several kilometers per second by the detonation products of condensed explosives. This is precisely how it has been possible to achieve values of electric current of ≈300 MA and magnetic induction of ≈29 MGs, which are the record values achieved under terrestrial conditions [30]. In the latter case, the magnetic field

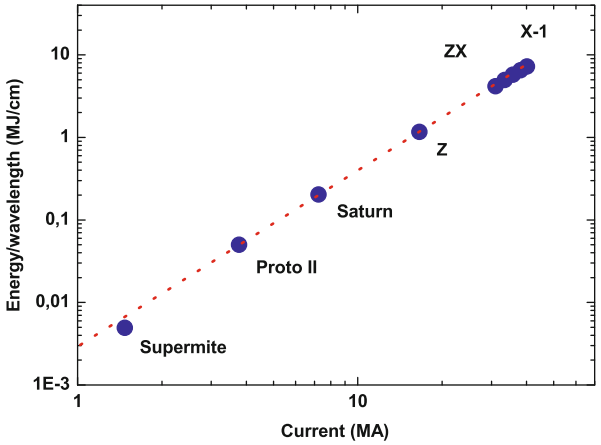

Fig. 3.48 Soft X-ray radiation yield as a function of Z-pinch current

energy density was equal to 3×10^6 J/cm^3, making it possible to carry out interesting physical experiments in megagauss magnetic fields: the quasi-isentropic compression of substances [95, 146], the study of magnetoresistance, magnetooptical effects, Shubnikov–de Haas effect, and many other phenomena at high energy densities [170].

References

1. Al'tshuler, L.V.: Use of shock waves in high-pressure physics. Sov. Phys. – Usp. **8**(1), 52–91 (1965)
2. Al'tshuler, L.V., Kalitkin, N.N., Kuz'mina, L.V., Chekin, B.S.: Shock adiabats for ultrahigh pressures. J. Exp. Theor. Phys. **45**, 167 (1977)
3. Al'tshuler, L.V., Trunin, R.F., Krupnikov, K.K., Panov, N.V.: Explosive laboratory devices for shock wave compression studies. Phys. Usp. **39**(5), 539 (1996)
4. Al'tshuler, L.V., Trunin, R.F., Urlin, V.D., et al.: Development of dynamic high-pressure techniques in Russia. Phys. Usp. **42**(3), 261 (1999)
5. Al'tshuler, L.V., Krupnikov, K.K., Fortov, V.E., Funtikov, A.I.: Origins of megabar pressure physics. Herald Russ. Acad. Sci. **74**(6), 613 (2004)
6. Anan'ev, S., Bakshaev, Y., Blinov, P., et al.: Investigations of the mega-ampere multiwire X pinch. JETP Lett. **87**(7), 364–370 (2008)
7. Andre, M.: Conceptual design of the French LMJ laser. In: First SPIE International Conference on Solid State Lasers for Application to ICF, Monterey, CA, p. 39 (1999)
8. Andreev, V.F., Karaev, J.A., Umrihin, N.M., et al. (eds.): Uslovija generacii impul'snogo nejtronnogo izluchenija pri vzryvnom obzhatii termojadernoj plazmy. IAE-5519/7 (Conditions of Generation of Pulse Neutron Radiation by Explosive Compression of Thermonuclear Plasma). IAE, Moscow (1992)
9. Anisimov, S.I., Prokhorov, A.M., Fortov, V.E.: Application of high-power lasers to study matter at ultrahigh pressures. Sov. Phys. – Usp. **27**(3), 181–205 (1984)

10. Arinin, V.A., Buyko, A.M., Burenkov, O.M., et al.: A series of joint VNIIEF/LANL Explosive Magnetic Experiments RHSR-0,1,2 on Radiographic Study of Perturbations growth at a Copper Liner Boundary with Polyethylene or Water. In: von Ortenberg, M. (ed.) Megagauss-X: Proceedings of the Tenth International Conference on Megagauss Magnetic Field Generation and Related Topics, Berlin, pp. 348–354 (2005)
11. Aryutkin, M.Y., et al.: In: The 13th International Conference on Megagauss Magnetic Field Generation and Related Topics, Suzhou (2010)
12. Ashkroft, N.A.: Condensed matter at higher densities. In: Chiarotti, G.L., Hemley, R.J., Bernasconi, M., Ulivi, L. (eds.) High Pressure Phenomena, Proceedings of the International School of Physics "Enrico Fermi" Course CXLVII, p. 151. IOS Press, Amsterdam (2002)
13. Atzeni, S., Meyer-ter-Vehn, J.: The Physics of Inertial Fusion. Oxford University Press, Oxford (2004)
14. Avrorin, E.N., Vodolaga, B.K., Simonenko, V.A., Fortov, V.E.: Intense shock waves and extreme states of matter. Phys. Usp. **36**(5), 337–364 (1993)
15. Avrorin, E.N., Simonenko, V.A., Shibarshov, L.I.: Physics research during nuclear explosions. Phys. Usp. **49**(4), 432 (2006)
16. Azizov, E.A., Alexandrov, V.V., Alikhanov, S.G., et al.: Pulse power system development for megajoule X-ray facility BAIKAL. AIP Conf. Proc. **651**(1), 29–32 (2002)
17. Bazanov, O.V., Bespalov, V.E., Zharkov, A.P., et al.: Irregular reflection of conically converging shock waves in plexiglas and copper. High Temp. **23**(5), 781 (1986)
18. Belov, S.I., Boriskov, G.V., Bykov, A.I., et al.: Shock compression of solid deuterium. JETP Lett. **76**(7), 433–435 (2002)
19. Betti, R., Anderson, K., Boehly, T.R., et al.: Progress in hydrodynamics theory and experiments for direct-drive and fast ignition inertial confinement fusion. Plasma Phys. Control. Fusion **48**(12B), B153–B163 (2006)
20. Betti, R., Chang, P.Y., Spears, B.K., et al.: Thermonuclear ignition in inertial confinement fusion and comparison with magnetic confinement. Phys. Plasmas **17**(5), 058102 (2010)
21. Bland, S.N., Lebedev, S.V., Chittenden, J.P., et al.: Implosion and stagnation of wire array Z pinches. Phys. Plasmas **14**(5), 056315 (2007)
22. Boehler, R.: Temperatures in the Earth's core from melting-point measurements of iron at high static pressures. Nature **363**(6429), 534–536 (1993)
23. Boehler, R., Forzandonea, D.: The laser heated diamond cell: high P–T phase diagrams. In: Chiarotti, G.L., Hemley, R.J., Bernasconi, M., Ulivi, L. (eds.) High Pressure Phenomena, pp. 55–66. IOS Press, Amsterdam (2002)
24. Boriskov, G.V., Bykov, A.I., Il'kaev, R.I., et al.: Shock compression of liquid deuterium up to 109 GPa. Phys. Rev. B **71**(9), 092104 (2005)
25. Boriskov, G.V., Bykov, A.I., Egorov, N.I., et al.: In: Garanin, S.G. (ed.) Xth Khariton's Topical Scientific Readings (in Russian), p. 281. RFYaTs-VNIIEF (2006)
26. Boriskov, G.V., Bykov, A.I., Egorov, N.I., et al.: Building zero isotherm of hydrogen isotopes taking into account experimental results of isentropic compression up to pressures of several megabar. J. Phys.: Conf. Ser. **121**(8), 072001 (2008)
27. Boriskov, G.V., Bykov, A.I., Egorov, N.I., et al.: In: Mikhailov, A.S. (ed.) XIth Khariton's Topical Scientific Readings (in Russian), p. 771. RFYaTs-VNIIEF (2009)
28. Boriskov, G.V., Bykov, A.I., Dolotenko, M.I., et al.: Research in ultrahigh magnetic field physics. Phys. Usp. **54**(4), 421–427 (2011)
29. Boriskov, G.V., Bykov, A.I., Egorov, N.I., et al.: Isentropic compression of substances using ultra-high magnetic field: zero isotherms of protium and deuterium in pressure range up to $\sim$ 5 Mbar. Contrib. Plasma Phys. **51**(4), 339–348 (2011)
30. Boyko, B., Bykov, A., et al.: More than 20 MG magnetic field generation in the cascade magnetocumulative MC-1 generator. In: Schneider-Muntau, H. (ed.) Proceedings VIIIth International Conference Megagauss Magnetic Field Generation and Related Topics, FL, 18–23 Oct 1998, p. 61. World Sci, Tallahassee (2004)
31. Brodskii, A.Y., et al.: Sov. Phys. Dokl. **35**, 876 (1990)

32. Bunkenberg, J., Boles, J., Brown, D., et al.: The omega high-power phosphate-glass system: design and performance. IEEE J. Quantum Electron. **17**(9), 1620–1628 (1981)
33. Buyko, A.M., et al.: In: Titov, V.M., Shvetsov, G.A. (eds.) Megagauss Fields and Pulsed Power Systems, p. 743. Nova Science Publishers, Commack, NY (1990)
34. Bykov, A.I., et al.: Sverkhprovodimost'. Fiz. Khim. Tekh. **8**(1), 37 (1995)
35. Bykov, A.I., Dolotenko, M.I., Kolokol'chikov, N.P., et al.: The cascade magnetocumulative generator of ultrahigh magnetic fields — a reliable tool for megagauss physics. Physica B: Condens. Matter **216**(3–4), 215–217 (1996)
36. Calderola, P., Knopfel, H. (eds.): Physics of High Energy Density. Academic, New York (1971)
37. Cavailler, C.: Inertial fusion with the LMJ. Plasma Phys. Control. Fusion **47**(12B), B389–B403 (2005)
38. Chang, P., Betti, R., Spears, B.K., et al.: Generalized measurable ignition criterion for inertial confinement fusion. Phys. Rev. Lett. **104**, 135002 (2010)
39. Chen, F.F.: Introduction to Plasma Physics and Controlled Fusion, vol. 1, 2nd edn. Springer, New York (1984)
40. Chernyshev, V.K., et al.: Vopr. At. Nauki Tekh. Metod. Prog. Chisl. Resh. Zadach Mat. Fiz. **3**(14), 30 (1983)
41. Chernyshev, V.K., Protasov, M.S., Shevtsov, V.A.: In: Titov, V.M., Shvetsov, G.A. (eds.) Sverkhsil'nye magnitnye polya. Fizika. Tekhnika. Primenenie (Ultrahigh Magnetic Fields: Physics, Techniques, Application): Trudy VII Mezhdunarodnoi Konferentsii po Generatsii Megagaussnykh Magnitnykh Polei i Rodstvennym Eksperimentam (Proceedings of VII International Conference on Megagauss Magnetic Field Generation and Related Experiments), p. 23. Nauka, Moscow (1984)
42. Chernyshev, V.K., et al.: In: Titov, V.M., Shvetsov, G.A. (eds.) Megagauss Fields and Pulsed Power Systems, p. 347. Nova Science Publishers, Commack, NY (1990)
43. Chernyshev, V.K., et al.: Vopr. At. Nauki Tekh. Mat. Model. Fiz. Protsessov **4**, 33 (1992)
44. Chittenden, J.P., Ciardi, A., Jennings, C.A., et al.: Structural evolution and formation of high-pressure plasmas in X-pinches. Phys. Rev. Lett. **98**(2), 025003 (2007)
45. Chuvatin, A.S., Kantsyrev, V.L., Rudakov, L.I., et al.: Operation of a load current multiplier on a nanosecond mega-ampere pulse forming line generator. Phys. Rev. ST Accel. Beams **13**, 010401 (2010)
46. Collins, G.W., Da Silva, L.B., Celliers, P., et al.: Measurements of the equation of state of deuterium at the fluid insulator-metal transition. Science **281**(5380), 1178–1181 (1998)
47. Courant, R., Friedrichs, K.O.: Supersonic Flow and Shock Waves. Interscience, New York (1948)
48. Coverdale, C., Jones, B., Ampleford, D., et al.: K-shell X-ray sources at the Z accelerator. High Energy Density Phys. **6**(2), 143–152 (2010)
49. Cuneo, M.E., Vesey, R.A., Bennett, G.R., et al.: Progress in symmetric ICF capsule implosions and wire-array Z-pinch source physics for double-pinch-driven hohlraums. Plasma Phys. Control. Fusion **48**(2), R1–R35 (2006)
50. Da Silva, L.B., Celliers, P., Collins, G.W., et al.: Absolute equation of state measurements on shocked liquid deuterium up to 200 GPa (2 Mbar). Phys. Rev. Lett. **78**(3), 483–486 (1997)
51. Demidov, V.A., Kazakov, S.A.: Helical magneto-cumulative generators for plasma focus powering. IEEE Trans. Plasma Sci. **38**(8), 1758–1761 (2010)
52. Demidov, V.A., Selemir, V.D.: Explosive pulsed power for controlled fusion. In: Kiuttu, G.F., Reinovsky, R.E., Turchi, P.J. (eds.) Megagauss Magnetic Fields and High Energy Liner Technology: Proceedings of the 2006 International Conference on Megagauss Magnetic Field Generation and Related Topics and International Workshop on High Energy Liners & High Energy Density Applications, pp. 245–254 (2006)
53. Demidov, V.A., et al.: In: Titov, V.M., Shvetsov, G.A. (eds.) Megagauss Fields and Pulsed Power Systems, p. 351. Nova Science Publishers, Commack, NY (1990)
54. Ditmire, T., Springate, E., Tisch, J.W., et al.: Explosion of atomic clusters heated by high-intensity femtosecond laser pulses. Phys. Rev. A **57**(1), 369–382 (1998)

55. Drake, R.P.: High-Energy-Density Physics. Springer, Berlin/Heidelberg (2006)
56. Dyabilin, K.S., et al.: An investigation of the thermal-properties of materials under the effect of a powerful pulse of soft X-radiation of Z-pinch plasma. High Temp. **34**(3), 473 (1996)
57. Eggert, J., Brygoo, S., Loubeyre, P., et al.: Hugoniot data for helium in the ionization regime. Phys. Rev. Lett. **100**, 124503 (2008)
58. Fan, Y., Zheng-Hong, L., Yi, Q., et al.: Spatially-resolved spectroscopic diagnosing of aluminum wire array z-pinch plasmas on qiangguang-i facility. Chin. Phys. B **19**(7), 075204 (2010)
59. Faussurier, G., Blancard, C., Cossé, P., Renaudin, P.: Equation of state, transport coefficients, and stopping power of dense plasmas from the average-atom model self-consistent approach for astrophysical and laboratory plasmas. Phys. Plasmas **17**(5), 052707 (2010)
60. Florido, R., Mancini, R., Nagayama, T., et al.: Argon K-shell and bound-free emission from OMEGA direct-drive implosion cores. High Energy Density Phys. **6**(1), 70–75 (2010)
61. Fortov, V.E. (ed.): Entsiklopediya nizkotemperaturnoi plazmy (Encyclopedia of Low-Temperature Plasma). Nauka, Moscow (2000)
62. Fortov, V.E. (ed.): Vzryvnye generatory moshchnykh impul'sov elektricheskogo toka (Explosion Generators of High-Power Pulses of Electric Current). Nauka, Moscow (2002)
63. Fortov, V.E.: Intense Shock Waves and Extreme States of Matter. Bukos, Moscow (2005)
64. Fortov, V.E. (ed.): Explosive-Driven Generators of Powerful Electrical Current Pulses. Cambridge International Science, Cambridge (2007)
65. Fortov, V.E.: Intense shock waves and extreme states of matter. Phys. Usp. **50**(4), 333 (2007)
66. Fortov, V.E.: Ekstremal'nye sostoyaniya veshchestva (Extreme States of Matter). Fizmatlit, Moscow (2009) [Translated into English: Extreme States of Matter. Series: The Frontiers Collection. Springer, Berlin/Heidelberg (2011)]
67. Fortov, V.E., Lomonosov, I.V.: Thermodynamics of extreme states of matter. Pure Appl. Chem. **69**(4), 893–904 (1997)
68. Fortov, V.E., Yakushev, V.V., Kagan, K.L., et al.: Anomalous electric conductivity of lithium under quasi-isentropic compression to 60 GPa (0.6 Mbar). Transition into a molecular phase? JETP Lett. **70**(9), 628–632 (1999)
69. Fortov, V.E., Gryaznov, V.K., Mintsev, V.B., et al.: Thermophysical properties of shock compressed argon and xenon. Contrib. Plasma Phys. **41**(2–3), 215–218 (2001)
70. Fortov, V.E., Ternovoi, V.Y., Zhernokletov, M.V., et al.: Pressure-produced ionization of nonideal plasma in a megabar range of dynamic pressures. J. Exp. Theor. Phys. **97**(2), 259–278 (2003)
71. Fortov, V.E., Al'tshuler, L.V., Trunin, R.F., Funtikov, A.I.: High-Pressure Shock Compression of Solids VII: Shock Waves and Extreme States of Matter. Springer, New York (2004)
72. Fortov, V.E., Mintsev, V.B., Ternovoi, V.Y., et al.: Conductivity of nonideal plasma. High Temp. Mater. Processes **8**(3), 447–459 (2004)
73. Fortov, V., Iakubov, I., Khrapak, A.: Physics of Strongly Coupled Plasma. Oxford University Press, Oxford (2006)
74. Fortov, V.E., Ilkaev, R.I., Arinin, V.A., et al.: Phase transition in a strongly nonideal deuterium plasma generated by quasi-isentropical compression at megabar pressures. Phys. Rev. Lett. **99**(18), 185001 (2007)
75. Fortov, V.E., Hoffmann, D.H.H., Sharkov, B.Y.: Intense ion beams for generating extreme states of matter. Phys. Usp. **51**(2), 109 (2008)
76. Fowler, C.M., et al.: In: Titov, V., Shvetsov, G. (eds.) Megagauss Fields and Pulsed Power Systems, p. 337. Nova Science Publishers, Commack, NY (1990)
77. Garanin, S.G.: High-power lasers and their applications in high-energy-density physics studies. Phys. Usp. **54**(4), 415–421 (2011)
78. Gasilov, V.A., Zakharov, S.V., Smirnov, V.P.: Generation of intense radiation fluxes and megabar pressures in liner systems. JETP Lett. **53**(2), 85 (1991)
79. Gavrilenko, V.I.: In: Proceedings of the 14th International Symposium "Nanostructures: Physics and Technology", St. Petersburg, p. 166 (2006)

80. Ginzburg, V.L.: The Physics of a Lifetime: Reflections on the Problems and Personalities of 20th Century Physics. Springer, Berlin/Heidelberg (2001)
81. Giorla, J., Bastian, J., Bayer, C., et al.: Target design for ignition experiments on the laser Mégajoule facility. Plasma Phys. Control. Fusion **48**(12B), B75–B82 (2006)
82. Glenzer, S.H., MacGowan, B.J., Meezan, N.B., et al.: Demonstration of ignition radiation temperatures in indirect-drive inertial confinement fusion hohlraums. Phys. Rev. Lett. **106**, 085004 (2011)
83. Glidden, S.C., Richter, M., Hammer, D.A., Kalantar, D.H.: 1 kW X-pinch soft X-ray source powered by a 500 kA, 100 ns, 40 pps pulser. In: 9th IEEE International Pulsed Power Conference, 1993. Digest of Technical Papers, vol. 1, p. 459 (1993)
84. Glushkin, V., Velikhov, E., et al.: Perspective of kiloterawatt soft x-ray source based on slow inductive storage with energy 1 gigajoule. In: Van Horn, H., Ichimaru, S. (eds.) Proceedings 12^{th} International Conference on High-Power Particle Beams, June 7–12, 1998, Haifa, p. 71 (1998)
85. Goncharov, V.N., Sangster, T.C., Boehly, T.R., et al.: Demonstration of the highest deuterium-tritium areal density using multiple-picket cryogenic designs on OMEGA. Phys. Rev. Lett. **104**, 165001 (2010)
86. Grabovskii, E.V., Vorob'ev, O.Y., Dyabilin, K.S., et al.: Excitation of intense shock waves by soft x radiation from a Z-pinch plasma. JETP Lett. **60**(1), 1 (1994)
87. Grigor'ev, F.V., Kormer, S.B., Mikhailova, O.L., et al.: Experimental determination of the compressibility of hydrogen at densities 0.5–2 g/cm3. Metallization of hydrogen. JETP Lett. **16**(5), 201 (1972)
88. Grigor'ev, F.V., Kormer, S.B., Mikhailova, O.L., et al.: Equation of state of molecular hydrogen. Phase transition into the metallic state. J. Exp. Theor. Phys. **48**(5), 847 (1978)
89. Grinevich, B.E., et al.: In: Chernyshev, V.K., Selemir, V.D., Plyashkevich, L.N. (eds.) Megagauss and Megaampere Pulsed Technology and Applications. Proceeding of the 7th International Conference on Megagauss Magnetic Field Generation and Related Topics, p. 677. RFYaTs-VNIIEF, Sarov (1997)
90. Grinevich, B.E., Demidov, V.A., Ivanovsky, A.V., Selemir, V.D.: Explosive magnetic generators and their application in scientific experiments. Phys. Usp. **54**(4), 403–408 (2011)
91. Grishechkin, S.K., Gruzdev, S.K., Gryaznov, V.K., et al.: Experimental measurements of the compressibility, temperature, and light absorption in dense shock-compressed gaseous deuterium. JETP Lett. **80**(6), 398–404 (2004)
92. Gryaznov, V.K., Fortov, V.E., Zhernokletov, M.V., et al.: Shock compression and thermodynamics of highly nonideal metallic plasma. J. Exp. Theor. Phys. **87**(4), 678–690 (1998)
93. Gryaznov, V.K., Nikolaev, D.N., Ternovoi, V.Y., et al.: Generation of a nonideal plasma by shock compression of a highly porous SiO_2 aerogel. Chem. Phys. Rep. **17**(1–2), 239–245 (1998)
94. Hammel, B.A., National Ignition Campaign Team: The NIF ignition program: progress and planning. Plasma Phys. Control. Fusion **48**(12B), B497–B506 (2006)
95. Hawke, P.S., Burgess, T.J., Duerre, D.E., et al.: Observation of electrical conductivity of isentropically compressed hydrogen at megabar pressures. Phys. Rev. Lett. **41**(14), 994–997 (1978)
96. Hemley, R.J., Ashcroft, N.W.: The revealing role of pressure in the condensed matter sciences. Phys. Today **51**(8), 26–32 (1998)
97. Hemley, R.J., Mao, H.K.: Overview of static high pressure science. In: Hemley, R.J., Chiarotti, G.L., Bernasconi, M., Ulivi, L. (eds.) High Pressure Phenomena, Proceedings of the International School of Physics "Enrico Fermi" Course CXLVII, p. 3. IOS Press, Amsterdam (2002)
98. Hicks, D.G., Boehly, T.R., Celliers, P.M., et al.: Laser-driven single shock compression of fluid deuterium from 45 to 220 gpa. Phys. Rev. B **79**, 014112 (2009)
99. Hoffmann, D., Tahir, N., Udrea, S., et al.: High energy density physics with heavy ion beams and related interaction phenomena. Contrib. Plasma Phys. **50**(1), 7–15 (2010)
100. Hogan, W.J. (ed.): Energy from Inertial Fusion. IAEA, Vienna (1995)

101. Iosilevskii, I.L., Griaznov, V.K.: Comparative accuracy of thermodynamic description of properties of a gas plasma in the Thomas–Fermi and Saha approximations. High Temp. **19**(6), 799–803 (1982)
102. Jones, B., Ampleford, D.J., Vesey, R.A., et al.: Planar wire-array *Z*-pinch implosion dynamics and X-ray scaling at multiple-MA drive currents for a compact multisource hohlraum configuration. Phys. Rev. Lett. **104**, 125001 (2010)
103. Kanel, G.I., Rasorenov, S.V., Fortov, V.E.: Shock-Wave Phenomena and the Properties of Condensed Matter. Springer, New York (2004)
104. Kazei, Z.A., Kirste, A., von Ortenberg, M., et al.: Are the crossover effects observable in $ErBa_2Cu_3O_{7-\delta}$ and $ErVO_4$ in pulsed magnetic fields. Physica B: Condens. Matter **346–347**(0), 241–245 (2004)
105. Kirste, A., von Ortenberg, M., Demidov, A.A., et al.: Crossover in the van vleck paramagnet $tmpo_4$. Physica B: Condens. Matter **336**(3–4), 335–343 (2003)
106. Kirzhnits, D.A.: Extremal states of matter (ultrahigh pressures and temperatures). Sov. Phys. – Usp. **14**(4), 512–523 (1972)
107. Kirzhnits, D.A., Lozovik, Y.E., Shpatakovskaya, G.V.: Statistical model of matter. Sov. Phys. – Usp. **18**(9), 649–672 (1975)
108. Kline, J.L., Glenzer, S.H., Olson, R.E., et al.: Observation of high soft X-ray drive in large-scale hohlraums at the national ignition facility. Phys. Rev. Lett. **106**, 085003 (2011)
109. Klir, D., Kravarik, J., Kubes, P., et al.: Neutron emission generated during wire array Z-pinch implosion onto deuterated fiber. Phys. Plasmas **15**(3), 032701 (2008)
110. Knudson, M.D., Hanson, D.L., Bailey, J.E., et al.: Equation of state measurements in liquid deuterium to 70 GPa. Phys. Rev. Lett. **87**(22), 225501 (2001)
111. Knudson, M.D., Hanson, D.L., Bailey, J.E., et al.: Use of a wave reverberation technique to infer the density compression of shocked liquid deuterium to 75 gpa. Phys. Rev. Lett. **90**, 035505 (2003)
112. Knudson, M.D., Hanson, D.L., Bailey, J.E., et al.: Principal Hugoniot, reverberating wave, and mechanical reshock measurements of liquid deuterium to 400 GPa using plate impact techniques. Phys. Rev. B **69**, 144209 (2004)
113. Kopyshev, V.P., Urlin, V.D.: Izentropicheskaya szhimaemost' i uravnenie sostoyaniya vodoroda do davleniya 1 TPa (Isentropic compressibility and equation of state of hydrogen up to a pressure of 1 TPa). In: Fortov, V.E., Altshuler, L.V., Trunin, R.F., Funtikov, A.I. (eds.) Udarnye Volny i Ekstremal'nye Sostoyaniya Veshchestva (Shock Waves and Extreme States of Matter), Chap. 5, pp. 297–314. Nauka, Moscow (2000)
114. Korzhimanov, A.V., Gonoskov, A.A., Khazanov, E.A., Sergeev, A.M.: Horizons of petawatt laser technology. Phys. Usp. **54**(1), 9–28 (2011)
115. Kruer, W.L.: The Physics of Laser Plasma Interactions. Addison-Wesley, Reading, MA (1988)
116. Kuropatkin, Y., Mironenko, V., Suvorov, V., et al.: Uncored betatron bim-m a source of bremsstrahlung for flash radiography. In: Cooperstein, G., Vitkovitsky, I. (eds.) 1997 11th IEEE International Pulsed Power Conference, 1997. Digest of Technical Papers, vol. 2, pp. 1669–1673 (1997)
117. Lebedev, S.V., Savvatimskii, A.I.: Metals during rapid heating by dense currents. Sov. Phys. – Usp. **27**(10), 749–771 (1984)
118. Lee, C.M., Thorsos, E.I.: Properties of matter at high pressures and temperatures. Phys. Rev. A **17**(6), 2073–2076 (1978)
119. Lemke, R.W., Sinars, D.B., Waisman, E.M., et al.: Effects of mass ablation on the scaling of X-ray power with current in wire-array *Z* pinches. Phys. Rev. Lett. **102**, 025005 (2009)
120. Levitin, R.Z., Zvezdin, A.K., Ortenberg, M., et al.: Faraday effect in $Tb_3Ga_5O_{12}$ in a rapidly increasing ultrastrong magnetic field. Phys. Solid State **44**, 2107–2111 (2002)
121. Lieb, E.H., Simon, B.: Thomas–Fermi theory revisited. Phys. Rev. Lett. **31**(11), 681–683 (1973)
122. Lindl, J.D.: Inertial Confinement Fusion. Springer, New York (1998)
123. Loubeyre, P., LeToullec, R., Hausermann, D., et al.: X-ray diffraction and equation of state of hydrogen at megabar pressures. Nature **383**(6602), 702–704 (1996)

124. Loubeyre, P., Occelli, F., Le Toulec, R.: Optical studies of solid hydrogen to 320 GPa and evidence for black hydrogen. Nature **416**(6881), 613–617 (2002)
125. Loubeyre, P., Celliers, P.M., Hicks, D.G., et al.: Coupling static and dynamic compressions: first measurements in dense hydrogen. High Pressure Res. **24**(1), 25–31 (2004)
126. Maksimov, E.G., Magnitskaya, M.V., Fortov, V.E.: Non-simple behavior of simple metals at high pressure. Phys. Usp. **48**(8), 761 (2005)
127. McBride, R.D., Shelkovenko, T.A., Pikuz, S.A., et al.: Implosion dynamics and radiation characteristics of wire-array Z pinches on the Cornell Beam Research Accelerator. Phys. Plasmas **16**(1), 012706 (2009)
128. McMahan, A.K., Ross, M.: In: Timmerhaus, K.D., Barber, M.S. (eds.) High Pressure Science and Technology, p. 920. Plenum, New York (1979)
129. Mochalov, M.A., Il'kaev, R.I., Fortov, V.E., et al.: Measurement of the compressibility of a deuterium plasma at a pressure of 1800 GPa. JETP Lett. **92**(5), 300–304 (2010)
130. Mochalov, M.A., Zhernokletov, M.V., Il'kaev, R.I., et al.: Measurement of density, temperature, and electrical conductivity of a shock-compressed nonideal nitrogen plasma in the megabar pressure range. J. Exp. Theor. Phys. **110**(1), 67 (2010)
131. Mokhov, V.N.: Sov. Phys. Dokl. **24**, 557 (1979)
132. Mokhov, V.N.: Formation of the thermonuclear fusion ideas. In: Selemir, V.D., Plyashkevichu, L.N. (eds.) Megagauss-IX, p. 665. VNIIEF, Sarov (2004)
133. More, R.M., Skupsky, S.: Nuclear-motion corrections to the Thomas–Fermi equation of state for high-density matter. Phys. Rev. A **14**(1), 474–479 (1976)
134. Moses, E.I.: The National Ignition Facility and the National Ignition Campaign. IEEE Trans. Plasma Sci. **38**(4, Part 2, SI), 684–689 (2010). 36th IEEE International Conference on Plasma Science, San Diego, CA, May 31–Jun 05, 2009
135. Moses, E.I., Bonanno, R.E., Haynam, C.A., et al.: The National Ignition Facility: path to ignition in the laboratory. Eur. Phys. J. D **44**(2), 215–218 (2006)
136. Mourou, G.A., Tajima, T., Bulanov, S.V.: Optics in the relativistic regime. Rev. Mod. Phys. **78**(2), 1804–1816 (2006)
137. Nabatov, S.S., Dremin, A.M., Postnov, V.I., Yakushev, V.V.: Measurement of the electrical conductivity of sulfur under superhigh dynamic pressures. JETP Lett. **29**(7), 369 (1979)
138. National Research Council: Frontiers in High Energy Density Physics. National Academies Press, Washington, DC (2003)
139. Nellis, W.J.: Dynamic compression of materials: metallization of fluid hydrogen at high pressures. Rep. Prog. Phys. **69**(5), 1479–1580 (2006)
140. Notake, T., Saito, T., Tatematsu, Y., et al.: Development of a novel high power sub-THz second harmonic gyrotron. Phys. Rev. Lett. **103**, 225002 (2009)
141. Oslon, C., Rochau, G., et al.: Development path for Z-pinch IFE. Fusion Sci. Technol. **47**(3), 633–640 (2005)
142. Parsons, W., Ballard, E., Bartsch, R., et al.: The Atlas project – a new pulsed power facility for high energy density physics experiments. IEEE Trans. Plasma Sci. **25**(2), 205–211 (1997)
143. Pavlovskii, A.I., et al.: Sov. Phys. Dokl. **10**, 30 (1965)
144. Pavlovskii, A.I., et al.: In: Titov, V.M., Shvetsov, G.A. (eds.) Sverkhsil'nye magnitnye polya. Fizika. Tekhnika. Primenenie (Ultrahigh Magnetic Fields: Physics, Techniques, Application): Trudy VII Mezhdunarodnoi Konferentsii po Generatsii Megagaussnykh Magnitnykh Polei i Rodstvennym Eksperimentam (Proceedings of VII International Conference on Megagauss Magnetic Field Generation and Related Experiments), p. 347. Nauka, Moscow (1984)
145. Pavlovskii, A.I., et al.: In: Titov, V.M., Shvetsov, G.A. (eds.) Sverkhsil'nye magnitnye polya. Fizika. Tekhnika. Primenenie (Ultrahigh Magnetic Fields: Physics, Techniques, Application): Trudy VII Mezhdunarodnoi Konferentsii po Generatsii Megagaussnykh Magnitnykh Polei i Rodstvennym Eksperimentam (Proceedings of VII International Conference on Megagauss Magnetic Field Generation and Related Experiments), p. 19. Nauka, Moscow (1984)
146. Pavlovski, A., Boriskov, G., et al.: Isentropic solid hydrogen compression by ultrahigh magnetic field pressure in megabar range. In: Fowler, C., Caird, R., Erickson, D. (eds.) Megagauss Technology and Pulsed Power Applications, p. 255. Plenum Press, New York/London (1987)

147. Pavlovskii, A.I., Kolokolchikov, N.P., Platonov, V.V., et al.: Destruction of superconductivity in $YBa_2Cu_3O_{7-x}$ ceramics by ultrahigh magnetic field. Physica C: Superconductivity **162–164, Part 2**(0), 1659–1660 (1989)
148. Pavlovskii, A.I., Lyudaev, R.Z., Kravchenko, A.S., et al.: In: Titov, V.M., Shvetsov, G.A. (eds.) Megagauss Fields and Pulsed Power Systems, p. 331. Nova Science Publishers, Commack, NY (1990)
149. Pavlovskii, A.I., Ludaev, R.Z., Plyashkevich, V.N., et al.: MGG applications for powered channeling neodim laser. In: Cowan, V., Spielman, R.B. (eds.) Megagauss Magnetic Field Generation and Pulsed Power Applications, pp. 969–976. Nova Science Publishers, Commack, NY (1994)
150. Pavlovskii, A.I., et al.: In: Cowan, V., Spielman, R.B. (eds.) Megagauss Magnetic Field Generation and Pulsed Power Applications, p. 977. Nova Science Publishers, Commack, NY (1994)
151. Puhlmann, N., Tatsenko, O.M., Stolpe, I., et al.: Cyclotron resonance on galliumnitride in fields up to 700 t generated by explosive driven flux compression. Physica B: Condens. Matter **294–295**(0), 447–452 (2001)
152. Pukhov, A.: Strong field interaction of laser radiation. Rep. Prog. Phys. **66**(1), 47–101 (2003)
153. Quintenz, J., Sandia's Pulsed Power Team: Pulsed power team. In: Proceedings of 13th International Conference on High Power Particle Beams, Nagaoka (2000)
154. Reinovsky, R.E., Anderson, W.E., Atchison, W.L., et al.: Shock-wave and material properties experiments using the Los Alamos Atlas pulsed power system. AIP Conf. Proc. **706**(1), 1191–1194 (2004)
155. Rochau, G.A., Bailey, J.E., Maron, Y., et al.: Radiating shock measurements in the *Z*-pinch dynamic hohlraum. Phys. Rev. Lett. **100**, 125004 (2008)
156. Rochau, G.A., Bailey, J.E., Maron, Y.: Applied spectroscopy in pulsed power plasmas. Phys. Plasmas **17**(5), 055501 (2010)
157. Rukhadze, A.A., Yusupaliev, U.: On the feasibility of the Coulomb explosion of a metal. Tech. Phys. **49**(7), 933 (2004)
158. Ryutov, D.D., Derzon, M.S., Matzen, M.K.: The physics of fast Z-pinches. Rev. Mod. Phys. **72**(1), 167–223 (2000)
159. Sakharov, A.D.: Magnetoimplosive generators. Phys. Usp. **9**(2), 294–299 (1966)
160. Sakharov, A.D., et al.: Sov. Phys. Dokl. **10**, 1045 (1966)
161. Sangster, T.C., Goncharov, V.N., Betti, R., et al.: Shock-tuned cryogenic-deuterium-tritium implosion performance on Omega. Phys. Plasmas **17**(5), 056312 (2010)
162. Sansone, G., Benedetti, E., Calegari, F., et al.: Isolated single-cycle attosecond pulses. Science **314**(5798), 443–446 (2006)
163. Schatz, T., Schramm, U., Habs, D.: Crystalline ion beams. Nature **412**(6848), 717–720 (2001)
164. Schramm, U., Schatz, T., Bussmann, M., Habs, D.: Cooling and heating of crystalline ion beams. J. Phys. B **36**(3), 561–571 (2003)
165. Selemir, V.D., Demidov, V.A., Ivanovskii, A.V., et al.: Explosion complex for the generation of pulsed soft X radiation. Plasma Phys. Rep. **25**(12), 1000 (1999)
166. Selemir, V.D., Terekhin, V.A., Kravchenko, A.S., et al.: Investigation of spark discharge in the ground on reproduction a lightning current pulse by means of EMG. In: Maenchen, J., Schamiloglu, E. (eds.) Pulsed Power Conference, 2005, pp. 541–544. IEEE (2005)
167. Selemir, V.D., Demidov, V.A., Ermolovich, V.F., et al.: Generation of soft X-ray emission by Z-pinches powered from helical explosive magnetocumulative generators. Plasma Phys. Rep. **33**, 381–390 (2007)
168. Selemir, V.D., Demidov, V.A., Boriskin, A.S., et al.: Disk magnetocumulative generator of 480-mm diameter for explosive EMIR facility. IEEE Trans. Plasma Sci. **38**(8), 1762–1767 (2010)
169. Selemir, V.D., Demidov, V.A., Repin, P.B.: Explosive electrophysical complex EMIR: current state and perspectives. IEEE Trans. Plasma Sci. **38**(8), 1754–1757 (2010)

170. Selimir, V., Tatsenko, O., et al.: Investigations in solid state physics in ultra-high magnetic fields — experimental results of kapitsa series. In: von Ortenberg, M. (ed.) Megagauss-X, Berlin, p. 219 (2005)
171. Sharkov, B.Y. (ed.): Yadernyi sintez s inertsionnym uderzhaniem (Inertial Confinement Nuclear Fusion). Fizmatlit, Moscow (2005)
172. Shevtsov, V.A., et al.: In: Chernyshev, V.K., Selemir, V.D., Plyashkevich, L.N. (eds.) Megagauss and Megaampere Pulsed Technology and Applications. Proceeding of the 7th International Conference on Megagauss Magnetic Field Generation and Related Topics, p. 282. RFYaTs-VNIIEF, Sarov (1997)
173. Shilkin, N.S., Dudin, S.V., Gryaznov, V.K., et al.: Measurements of the electron concentration and conductivity of a partially ionized inert gas plasma. J. Exp. Theor. Phys. **97**(5), 922–931 (2003)
174. Shpatakovskaya, G.: Kvaziklassicheskii metod v zadachakh kvantovoi fiziki (Quasiclassical Method in Problems of Quantum Physics). LAP LAMBERT Academic Publishing, Moscow (2012)
175. Shrestha, I., Kantsyrev, V., Safronova, A., et al.: Investigation of characteristics of hard X-rays produced during implosions of wire array loads on 1.6 MA Zebra generator. High Energy Density Phys. **6**(1), 113–120 (2010)
176. Sinars, D.B., Cuneo, M.E., Yu, E.P., et al.: Measurements and simulations of the ablation stage of wire arrays with different initial wire sizes. Phys. Plasmas **13**(4), 042704 (2006)
177. Sinars, D.B., Slutz, S.A., Herrmann, M.C., et al.: Measurements of magneto-Rayleigh–Taylor instability growth during the implosion of initially solid metal liners. Phys. Plasmas **18**(5), 056301 (2011)
178. Sinko, G.V.: Calculation of thermodynamic functions of simple substances on the basis of the equations of the self-coordinated field (in Russian). Chis. Met. Meh. Spl. Sred. **10**(1), 124 (1979)
179. Sinko, G.V.: Some results of calculations of thermodynamic functions of aluminum, copper, cadmium and lead. A method of the self-coordinated field (in Russian). Chis. Met. Meh. Spl. Sred. **12**(1), 121 (1981)
180. Slutz, S.A., Herrmann, M.C., Vesey, R.A., et al.: Pulsed-power-driven cylindrical liner implosions of laser preheated fuel magnetized with an axial field. Phys. Plasmas **17**(5), 056303 (2010)
181. Spielman, R.B., Long, F., Martin, T.H., et al.: PBFA II-Z: A 20-MA driver for Z-pinch experiments. In: Baker, W., Cooperstein, G. (eds.) Tenth IEEE International Pulsed Power Conference, 1995. Digest of Technical Papers, vol. 1, pp. 396–404 (1995)
182. Spielman, R.B., Deeney, C., Chandler, G.A., et al.: Tungsten wire-array Z-pinch experiments at 200 TW and 2 MJ. Phys. Plasmas **5**(5), 2105–2111 (1998)
183. Strickland, D., Mourou, G.: Compression of amplified chirped optical pulses. Opt. Commun. **56**(3), 219–221 (1985)
184. Strickland, D., Mourou, G.: Compression of amplified chirped optical pulses. Opt. Commun. **55**(6), 447–449 (1985)
185. Theobald, W., Anderson, K.S., Betti, R., et al.: Advanced-ignition-concept exploration on OMEGA. Plasma Phys. Control. Fusion **51**(12), 124052 (2009)
186. Trunin, R.F.: Shock compressibility of condensed materials in strong shock waves generated by underground nuclear explosions. Phys. Usp. **37**(11), 1123 (1994)
187. Trunin, R.F., Podurets, M.A., Simakov, G.V., et al.: An experimental verification of the Thomas–Fermi model for metals under high pressure. Sov. Phys. – JETP **35**, 550 (1972)
188. Trunin, R.F., Urlin, V.D., Medvedev, A.B.: Dynamic compression of hydrogen isotopes at megabar pressures. Phys. Usp. **53**(6), 577–593 (2010)
189. Turchi, P.J., Baker, W.L.: Generation of high-energy plasmas by electromagnetic implosion. J. Appl. Phys. **44**(11), 4936–4945 (1973)
190. Vasyukov, V.A., et al.: In: The 13th International Conference on Megagauss Magnetic Field Generation and Related Topics, Suzhou (2010)

191. Vesey, R.A., Herrmann, M.C., Lemke, R.W., et al.: Target design for high fusion yield with the double Z-pinch-driven hohlraum. Phys. Plasmas **14**(5), 056302 (2007)
192. Vladimirov, A.S., Voloshin, N.P., Nogin, V.N., et al.: Shock compressibility of aluminum at p > 1 Gbar. JETP Lett. **39**(2), 82 (1984)
193. Weir, S.T., Mitchell, A.C., Nellis, W.J.: Metallization of fluid molecular hydrogen at 140 gpa (1.4 mbar). Phys. Rev. Lett. **76**, 1860–1863 (1996)
194. Winterberg, F.: The magnetic booster target inertial confinement fusion driver. Z. Naturforsch. A **39A**, 325 (1984)
195. Zababahin, E.I., Zababahin, I.E.: Yavleniya neogranichennoj kumulyacii (The Phenomena of Unlimited Cumulating). Nauka, Moscow (1988)
196. Zasov, A.V., Postnov, K.A.: Obshchaya astrofizika (General Astrophysics). Vek 2, Fryazino (2006)
197. Zel'dovich, Y.B., Raizer, Y.P.: Fizika udarnykh voln i vysokotemperaturnykh gidrodinamicheskikh yavlenii, 2nd edn. Nauka, Moscow (1966) [English Transl.: Physics of Shock Waves and High-Temperature Hydrodynamic Phenomena. Dover, Mineola, NY (2002)]
198. Zhernokletov, M.V.: Shock compression and isentropic expansion of natural uranium. High Temp. **36**(2), 214–221 (1998)
199. Zhernokletov, M.V., Zubarev, V.N., Trunin, R.F., Fortov, V.E.: Eksperimental'nye dannye po udarnoi szhimaemosti i adiabaticheskomu rasshireniju kondensirovannyh vewestv pri vysokih plotnostjah energii (Experimental Data on Shock Compressibility and Adiabatic Expansion of Condensed Matter at High Energy Density). IHF RAN, Chernogolovka (1996)
200. Zvezdin, A.K., Lubashevsky, I.A., Levitin, R.Z., et al.: Spin-flop and metamagnetic transitions in itinerant ferrimagnets. In: Wagner, D., Brauneck, W., Solontsov, A. (eds.) Proceedings of the NATO Advanced Research Workshop on Itinerant Electron Magnetism: Fluctuation Effects & Critical Phenomena, NATO Science Partnership, vol. 55, p. 285. Kluwer Academic Publishers, Moscow (1998)

Chapter 4
Extreme States in a Nuclear Explosion

People have always attributed the quest for and mastering of new energy sources to high-priority lines of basic and applied research [114]. The first third of the twentieth century has seen vigorous investigations into the structure of atoms and atomic nuclei. Leaning upon the achievements in this area made by several world's leading physicists, E. Fermi, L. Scillard, F. Joliot-Curie, Ya.B. Zel'dovich, Yu.B. Khariton, et al. even in 1939 substantiated the feasibility of a nuclear fission chain reaction in uranium and therefore the prospect of practical use of a radically new—nuclear—energy source, millions of times more powerful than traditional chemical reactions. A short time later, conditions [122] for the realization of a chain nuclear reaction of explosive type (previously discovered by academician N.N. Semenov for chemical reactions) attended with the liberation of an unprecedented amount of energy. This signified that scientists were on the verge of creating weapons of extraordinary destructive power [107].

To implement the practical use of nuclear energy, scientists had to solve a wealth of complicated scientific and technical problems. Their effort resulted in the advent of a new science—the physics of high energy densities, whose basic elements have been set forth in a large number of publications and generalized in a review [58] and the materials of the Session of the Physical Sciences Division of the Russian Academy of Sciences [9].

In the 1940s, in the USA and USSR the first steps were made towards the solution of the problem of implementing an explosive-type nuclear reaction and developing nuclear weapons. The scientific and technological achievements in this area still remain the military and state secrets of the countries possessing nuclear weaponry. International treaties strictly regulate the publication of technologies relating to the production of nuclear weapons and prohibit their transfer to other countries.

However, a nuclear explosion is also a unique physical phenomenon, whose study is of interest to scientists in various realms of knowledge, including scientists in high energy density physics.

© Springer International Publishing Switzerland 2016

V.E. Fortov, *Extreme States of Matter*, Springer Series in Materials Science 216,
DOI 10.1007/978-3-319-18953-6_4

It is well known [36, 37] that the study and large-scale practical use of extreme states of matter are inseparably linked with the entry of our civilization to the atomic era, with the first step in this direction—the development of nuclear and thermonuclear weapons [4, 5, 11, 15, 49, 88, 94–97]. The pressures of tens-hundreds of megabars generated in nuclear charges by powerful spherical shock waves produce a several-fold compression of the nuclear fuel to initial chain nuclear reaction with pulsed energy liberation. This nuclear energy liberation in its turn is the main instrument for compressing and heating thermonuclear fuel to billions of atmospheres and tens of millions of degrees with the aim of initiating in it the thermonuclear fusion of a deuterium-tritium mixture [4, 5, 11, 15, 49, 52, 88, 94–97, 115].

A nuclear explosion, in the broad sense, begins with providing conditions for the implementation of an explosive chain nuclear fission reaction in a small volume of uranium or plutonium in a time of the order of tens of nanoseconds and ends with the many years lasting decay of radioactive explosion products dispersed over the atmosphere and terrestrial surface. The nuclear explosion itself, if this term is meant to imply the primary energy liberation, develops in a time no longer than several microseconds—initially in the chain reaction of uranium or plutonium fission and then (in the case of a thermonuclear explosive device) in a certain sequence of tritium-deuterium nuclear fusion reactions [9, 58, 107, 114, 122]. While on the subject of a nuclear explosion, implied most often is the outward appearance (Fig. 4.1 [107, 114])—the emergence of a luminous domain, the arrival of a shock wave to the point of observation, the ascent of explosion cloud, etc. To state it different terms, the notion of a "nuclear explosion" is commonly associated with the formation and development of the physical processes which are traditionally termed the destructive factors of a nuclear explosion [114].

In the first and second sections of this chapter we consider the first stage—the initiation. The last section of this chapter is concerned with experiments in the generation and study of extreme states of matter with the help of powerful shock waves driven by the nuclear explosion.

4.1 Exothermal Nuclear Reactions

The key finding that marked the entry of humanity into the nuclear era was E. Rutherford's introduction of the planetary atomic model in 1911 [93] (Fig. 4.2). Unlike the previously existing J. Thomson's model, in which an atom was uniformly filled with electrons and ions, Rutherford's model assumed a tiny nucleus at the center of the atom surrounded by electrons moving at a long ($\approx 10^{-8}$ cm) distance from the nucleus. To compensate the Coulomb repulsion of positive charges in the nucleus, nuclear binding forces had to be introduced, whose energy was millions of times higher than that of Coulomb repulsion.

Fig. 4.1 General view of a nuclear explosion [114]

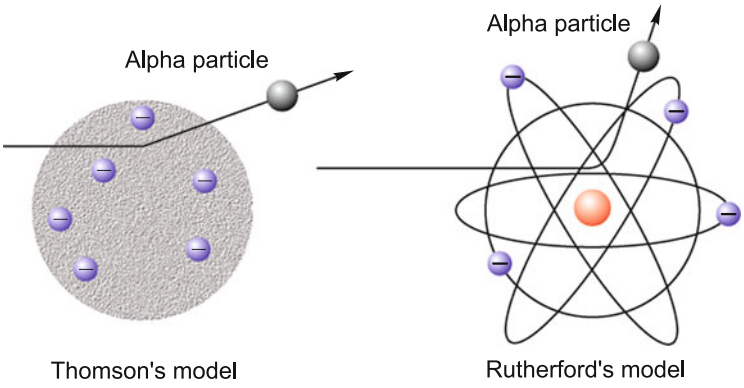

Fig. 4.2 Model of atomic structure

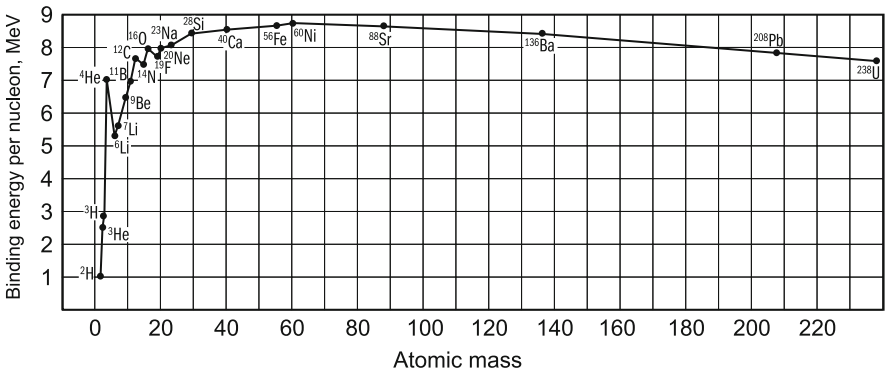

Fig. 4.3 Binding energy per nucleon for atomic nuclei [108]

Following [19], in the formation of a nucleus of mass m made up of Z protons of mass m_p and $(A - Z)$ neutrons of mass m_n the mass defect is written as $\Delta m = Zm_p + (A - Z)m_n - m$.

For a stable nucleus the mass defect $\Delta m > 0$ and the binding energy $B = \Delta mc^2$.

The energy liberation in a nuclear reaction corresponds to the energy difference between the reacting nuclei and reaction products:

$$Q = \sum_f B_f - \sum_i B_i.$$

The average binding energy per nucleon (Fig. 4.3) shows a slow growth in B/A with increase in nuclear mass A to attain a maximum of $\approx$8.7 MeV for $A_0 = 57$. Exothermal reactions are possible when the reaction products have a higher B/A, value, and therefore, according to Fig. 4.3, nuclear fission (for $A > A_0$) into lighter fragments will be exothermal and fusion reactions (for $A < A_0$) will proceed with energy liberation in the production of heavier nuclei.

Hence it also follows that the production of light (lighter than Fe) elements in nature occurs in thermonuclear fusion reactions and of heavier ones in the neutron or proton capture and in fission.

4.1.1 Thermonuclear Fusion

For a fusion reaction to occur, two positively charged nuclei of mass A_1 and A_2 have to overcome Coulomb repulsion and come within a distance of $\approx 1.44 \cdot 10^{-13}(A_1^{1/3} + A_2^{1/3})$ cm—the range of nuclear attraction forces (Fig. 4.4) with a potential $U_0 \approx$ 30–40 MeV. The magnitude of this potential at a maximum is equal to several MeV. Putting $Z = 90$, and $r \approx 10^{-12}$ cm, we obtain $U_b \approx 26$ MeV. In classical dynamics, an outgoing particle must possess this energy to overcome this potential.

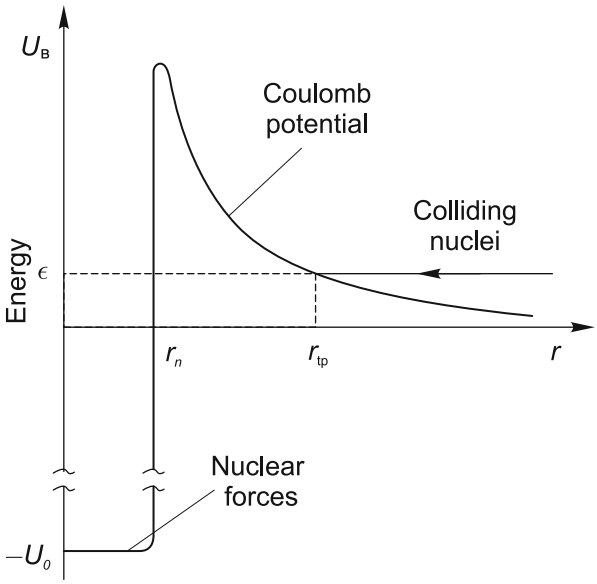

Fig. 4.4 Potential energy as a function of the distance between two charged nuclei. Borrowed from [19]

In quantum mechanics, a particle is a wave packet of size on the order of a thermal de Broglie wavelength $\lambda \sim \sqrt{\hbar^2/(2mkT)}$.

When this wavelength is comparable to the thickness of the peak in Fig. 4.4, the particle may execute a tunnel transition even though its energy may be lower than the peak of potential U_b in Fig. 4.4.

Following [19], we represent the fusion reaction cross section as

$$\sigma \sim \sigma_{\text{geom}} \cdot \Upsilon \cdot \Re,$$

where $\sigma_{\text{geom}} \sim \hbar^2$ is the geometrical cross section, Υ is the penetration factor for the barrier in Fig. 4.4, $\Re$ is the probability that the nuclei enter into a reaction, $\Upsilon \sim \Upsilon_\Gamma = \exp\left(-\sqrt{\frac{\epsilon_\Gamma}{\epsilon}}\right)$ is the Gamow factor, where $\epsilon_\Gamma = \left(\pi\alpha_f Z_1 Z_2\right)^2 2m_r c^2 \approx 986.1 Z_1^2 Z_2^2 A_r$ keV, $A_r = m_r/m_p$, and $\alpha_f = e^2/\hbar c = 1/137.04$ is the fine structure constant.

This relation shows that the likelihood of entering into a reaction in the case of a tunnel transition decreases rapidly with increase in atomic nuclear mass.

As for the $\Re$ parameter, it is determined by the nature of the nuclear reaction. It is large for strong nuclear interaction, orders of magnitude smaller for electromagnetic interaction, and 20 orders of magnitude smaller for weak nuclear interaction. In this case, the variation of $\Re$ is, as a rule, smaller than the strong variation of the Gamow factor.

Quite often [19] used is the representation

$$\sigma(\epsilon) = \frac{S(\epsilon)}{\epsilon} \exp\left(-\sqrt{\frac{\epsilon_\Gamma}{\epsilon}}\right),$$

Table 4.1 Fusion reactions: reaction cross section for a center-of-mass energy of 10 keV and 100 keV, maximum reaction cross section σ_{max}, and the maximum location ϵ_{max}

Reaction	σ(10 keV) [barn]	σ(100 keV) [barn]	σ_{max} [barn]	ϵ_{max} [keV]
$D + T \rightarrow \alpha + n$	$2.72 \cdot 10^{-2}$	3.43	5.0	64
$D + D \rightarrow T + p$	$2.81 \cdot 10^{-4}$	$3.3 \cdot 10^{-2}$	0.096	1250
$D + D \rightarrow {}^3He + n$	$2.78 \cdot 10^{-4}$	$3.7 \cdot 10^{-2}$	0.11	1750
$T + T \rightarrow \alpha + 2n$	$7.90 \cdot 10^{-4}$	$3.4 \cdot 10^{-2}$	0.16	1000
$D + {}^3He \rightarrow \alpha + p$	$2.2 \cdot 10^{-7}$	0.1	0.9	250
$p + {}^6Li \rightarrow \alpha + {}^3He$	$6 \cdot 10^{-10}$	$7 \cdot 10^{-3}$	0.22	1500
$p + {}^{11}B \rightarrow 3\alpha$	$(4.6 \cdot 10^{-17})$	$3 \cdot 10^{-4}$	1.2	550
$p + p \rightarrow D + e^+ + \nu$	$(3.6 \cdot 10^{-26})$	$(4.4 \cdot 10^{-25})$		
$p + {}^{12}C \rightarrow {}^{13}N + \gamma$	$(1.9 \cdot 10^{-26})$	$2.0 \cdot 10^{-10}$	$1.0 \cdot 10^{-4}$	400
${}^{12}C + {}^{12}C$ (all branches)		$(5.0 \cdot 10^{-102})$		

Theoretically estimated quantities are enclosed in parentheses, the remaining data were experimentally obtained

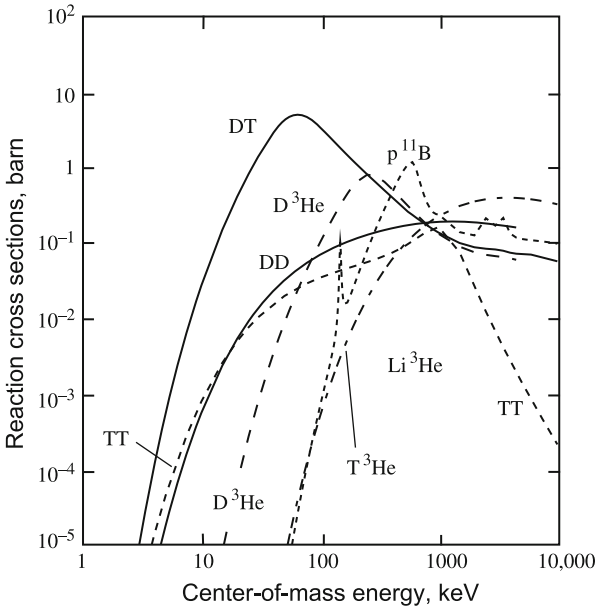

Fig. 4.5 Reaction cross sections as functions of the center-of-mass energy, which are of interest for controlled thermonuclear fusion. The DD curve is the sum of different reaction cross sections. Borrowed from [19]

where $S(\epsilon)$ is the so-called astrophysical S factor—a weakly varying energy function.

The cross sections and parameters for several reactions of interest for thermonuclear applications are given in Table 4.1 and Fig. 4.5 [19].

One can see from Fig. 4.5 that the deuterium-tritium fusion reaction

$$D + T \rightarrow \alpha(3.5\,\text{MeV}) + n(14.1\,\text{MeV}) \tag{4.1}$$

has the greatest cross section of ≈5 barn for a relatively modest energy of ≈64 keV. The energy liberation of this reaction is high, ≈17.6 MeV. Furthermore, this reaction has a broad resonance for the formation of ^{5}He for ≈64 keV.

An analysis shows that reactions of the type

$$\mathrm{D} + \mathrm{D} \rightarrow \mathrm{T}\,(1.01\,\mathrm{MeV}) + \mathrm{p}\,(3.03\,\mathrm{MeV}),$$

$$\mathrm{D} + \mathrm{D} \rightarrow {}^3\mathrm{He}\,(0.82\,\mathrm{MeV}) + \mathrm{n}\,(2.45\,\mathrm{MeV})$$

have a 100 times smaller cross section for 10–100 keV, and the reaction D (d, γ)^{4}He has a cross section even 4 orders of magnitude smaller than the D + D reaction.

The reaction

$$\mathrm{p} + {}^{11}\mathrm{B} \rightarrow 3\alpha + 8.6\,\mathrm{MeV}$$

is interesting in that it is not associated with radioactive products and does not yield neutrons.

Not discussing other possible reactions here, we emphasize that it is precisely the DT reaction (4.1) which is presently associated with the main practical applications of controlled and quasicontrolled thermonuclear fusion. Other reactions are of major significance for astrophysics [19].

First and foremost, these are proton-proton cycle reactions, whose scheme is considered in detail below. Here we note that the pp and pD reactions have the lowest Gamow energies ϵ_G, but their cross sections are also low. The pp cycle is related to the low-probability beta decay, so that the S factor for these reactions is 25 orders of magnitude lower than for the DT reaction. The pD reaction involves electromagnetic transitions, which are much more probable than the pp processes, but their cross section is nevertheless significantly smaller than for deuterium and tritium reactions, which are due to strong nuclear interaction.

For our Sun (a yellow dwarf, which belongs to the system of 10^{11} stars that make up our Galaxy) we give here the two most important energy cycles: the helium cycle (Fig. 4.6) and the carbon-nitrogen one (Fig. 4.7) [67].

According to the proton-proton scheme in Fig. 4.6, produced in the collision of two protons is the nucleus of heavy hydrogen (of deuterium) D, which consists of a proton and a neutron:

$$\mathrm{p} + \mathrm{p} \rightarrow {}^2_1\mathrm{D} + e^+ + \nu.$$

This reaction produces a neutrino ν, which freely escapes from the star, and a positron e^+, which collides with one of numerous electrons immediately after production, and both particles annihilate to turn into several photons: $e^+ + e^- \rightarrow \gamma + \gamma$. The newly born deuterium nucleus collides and fuses with a proton to make up the nucleus of the light helium isotope:

$${}^2_1\mathrm{D} + \mathrm{p} \rightarrow {}^3_2\mathrm{He}.$$

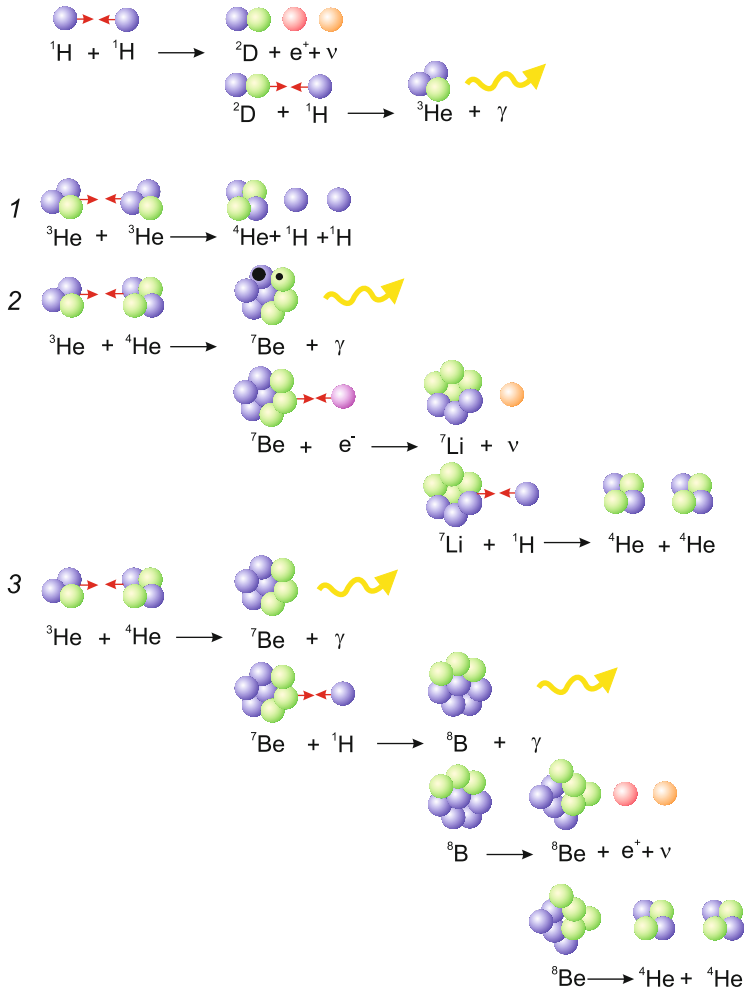

Fig. 4.6 Proton-proton cycle [67]

Then, produced in the collision of two $^3_2$He nuclei is the unstable nucleus of beryllium $^6_4$Be, which almost instantly decays into two protons and the nucleus of "ordinary" helium of atomic mass 4:

$$^3_2\text{He} + ^3_2\text{He} \rightarrow ^4_2\text{He} + 2\text{p}.$$

If we omit the intermediate products of this proton-proton reaction chain, it boils down to the transformation of four hydrogen nuclei to the nucleus of helium-4. The luminosity of a main-sequence star increases rapidly with mass. The luminosity of a star of mass $10M_\odot$, for instance, exceeds the solar one by almost a factor of

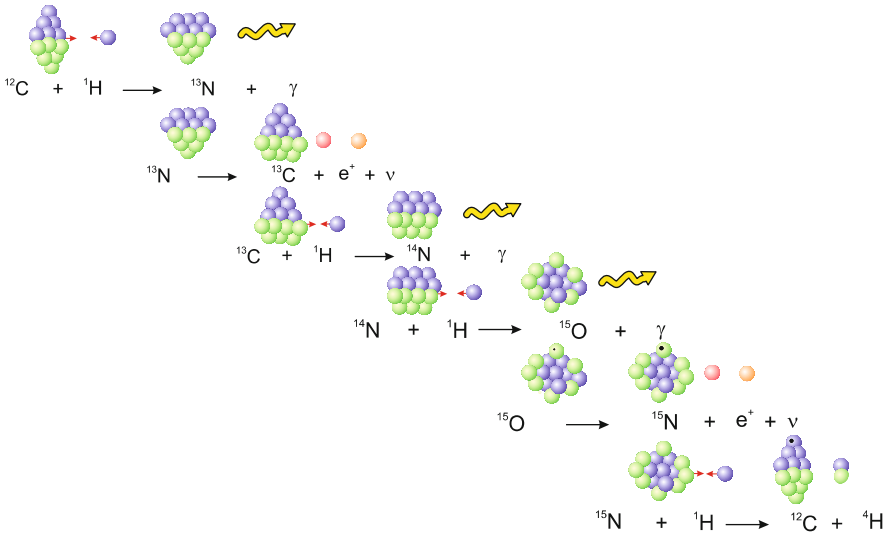

Fig. 4.7 Carbon-nitrogen cycle [67]

10^4. Consequently, thermonuclear reactions in the interior of massive stars proceed much more rapidly. And since the rate of these reactions depends primarily on the temperature, the greater is the mass of a main-sequence star, the higher is its central temperature. This is borne out by simulations of the stars with the solar chemical composition: the temperature at the center of the stars of mass 0.1, 1, and $10M_{\odot}$ is equal to 5, 14, and 30 million degrees. The central density of such stars, by contrast, decreases with their mass: at the solar center it is close to 150 t/m^3, while for a star of mass $10M_{\odot}$ it is approximately ten times lower.

The ultimate result of the helium cycle: four protons transform to the nucleus of helium-4. Produced in this case are two neutrinos and γ-ray photons as well as two positrons, which subsequently combine with electrons to also produce γ-ray radiation. The production of one nucleus of ^{4}He out of four protons is attended with the liberation of an energy of 26.7 MeV equal to the difference between the energy of four protons and the resultant nucleus energy. The carbon-nitrogen cycle shown in Fig. 4.7 is of major significance, because the amount of carbon is almost 10^7 times greater than the amount of its sequents—lithium, beryllium and boron. Calculations suggest that a reaction chain referred to as the CNO cycle, named after the names of its participating elements, is possible at a temperature above 10 million K.

In accordance with [108], the nuclei $^{13}_{7}$N, $^{14}_{7}$N, and $^{15}_{8}$O play the role of intermediate links in the CNO cycle, so that the ultimate result of these reactions, like in the pp chain, is the fusion of four protons with the production of a helium nucleus. Also produced are two neutrinos, which escape from the star, and two positrons, which immediately annihilate.

Carbon in the CNO cycle plays the part of a catalyst: a $^{12}_{6}$C nucleus, which is required to initiate the process, reappears in the last reaction of the cycle. The abundance of this element nevertheless decreases by a factor of several hundred during the lifetime of a main-sequence star, and the reason is as follows. Calculations suggest that the $^{14}_{7}\mathrm{N} + \mathrm{p} \rightarrow ^{15}_{8}\mathrm{O}$ reaction is the slowest of the six reactions that make up the CNO cycle. This has the effect that the fusion of $^{14}_{7}$N nitrogen nuclei proceeds much faster than their transformation to oxygen nuclei. And so, immediately after the cycle onset the amount of nitrogen nuclei in the zone of nuclear reactions begins to accumulate at the expense of the corresponding decrease of the amount of carbon nuclei. However, for the star as a whole the rate of lowering of the total number of nitrogen nuclei depends not only on the rate of the fourth reaction of the cycle, but also on the number of these reactions, and it will grow with increase in the number of nitrogen nuclei in the zone where these reactions take place. At some point in time the amount of nitrogen nuclei will be so large that equal amounts of the $^{14}_{7}$N nuclei will vanish and be synthesized—kinetic equilibrium will set in. The fifth and sixth reactions of the CNO cycle proceed much faster than the fourth one, and so it is valid to say that the cycle rapidly comes to an end after the disappearance of the $^{14}_{7}$N nucleus and the $^{12}_{5}$C nucleus (along with the $^{4}_{2}$He nucleus, of course) is produced—the cycle closes. The newly emerging carbon nuclei initiate a new round of the cycle, and this process is repeated until all hydrogen transforms to helium. After the kinetic equilibrium sets in, the relative abundance of nitrogen and carbon no longer changes with time, but in this case is radically different from the initial one—almost all carbon has transformed to nitrogen. The time in which the kinetic equilibrium is reached in the star is much shorter than the hydrogen burnup time. That is why in the stars which leave the main sequence the content of nitrogen in the central region is hundreds of times higher than in the stellar shell.

In the solar interior the CNO cycle provides only several percent of the liberated energy, but in the stars with $M > 2M_{\odot}$ this cycle accounts for virtually all of the energy liberation. In reactions with participation of protons and carbon nuclei $Z_1Z_2 = 6$, and in the collisions of protons with nitrogen nuclei $Z_1Z_2 = 7$. Consequently, the gas temperature in the interior of the stars in the upper part of the main sequence is high enough for the reaction $^{4}_{2}\mathrm{He} + ^{4}_{2}\mathrm{He} \rightarrow ^{4}_{2}\mathrm{Be}$ to also proceed, for which $Z_1Z_2 = 4$. However, the beryllium nucleus $^{4}_{2}$Be is unstable: on living for only 10^{-16} s it decays into two α-particles, and therefore in the main-sequence stars helium does not "burn away", but merely accumulates [108].

The nuclear reactions considered above give rise to γ-ray photons, which propagate through the solar substance. In their path they interact with ions, electrons, and atoms of the medium. The mean free path is equal to 1 cm, while the solar radius is equal to $7 \cdot 10^7$ cm. Several hundred thousand years pass until the "distant relatives" of the γ-ray photons produced in the solar interior manage to get out and become detectable to an external observer, making life on the Earth possible. According to modern notions, hydrogen in the solar interior burns primarily via

the proton-proton cycle and only 1.6 % of hydrogen burns in the carbon-nitrogen reaction cycle.

The CNO cycle reactions are of importance for energetics and production of hydrogen in stars. And though their S factor is not low, the Gamow energy $\epsilon_G \approx 40$ MeV, so that the total cross section turns out to be much smaller than for the pp cycle. That is why the CNO cycle prevails over the pp cycle at temperatures above $\approx$1.5 keV.

Reactions with ^{12}C participation are important for the evolution of white dwarfs. Owing to a very high Coulomb barrier the S factor is quite large in this case. These reactions come to the fore at extreme densities of $\approx 10^9$ g/cm^3 due to the screening of Coulomb potential in dense plasmas.

The reaction probability per unit time per unit target density is of the form [19]

$$\langle \sigma v \rangle = \int_0^\infty \sigma(v) v f(v) dv. \tag{4.2}$$

For the Maxwellian distribution function

$$f_j(v_j) = \left(\frac{m_j}{2\pi kT}\right)^{3/2} \exp\left(-\frac{m_j v_j^2}{2kT}\right), \tag{4.3}$$

it follows [19] that

$$\langle \sigma v \rangle = \frac{4\pi}{(2\pi m_r)^{1/2}} \frac{1}{(kT)^{3/2}} \int_0^\infty \sigma(\epsilon) \epsilon \exp\left(-\frac{\epsilon}{kT}\right) dv,$$

Upon simplifications this leads to an approximate dependence—the Gamow formula [19]:

$$\langle \sigma v \rangle = \frac{6.4 \cdot 10^{-18}}{A_r Z_1 Z_2} S \xi^2 \exp(-3\xi)\ \mathrm{cm}^3/\mathrm{s},$$

where $\xi = 6.2696 (Z_1 Z_2)^{2/3} A_r^{1/3} T^{-1/3}$ and the temperature is in keV.

The results of direct integration of the cross sections for nuclear fusion reactions over the Maxwellian distribution function (4.3) are depicted in Fig. 4.8. One can see that the cross section for the DT reaction is 100 times higher than for other reactions in the 10–20 keV temperature range and 10 times higher for $T < 25$ keV. This reaction has competitors only at extremely high temperatures $T > 10^2$–10^3 K. Semiempirical formulas describing the dependences of Fig. 4.8 are given in [19]:

$$\langle \sigma v \rangle_{\mathrm{DT}} = 9.10 \cdot 10^{16} \exp\left(-0.572 \left| \ln \frac{T}{64.2} \right|^{2.13}\right) \mathrm{cm}^3/\mathrm{s}.$$

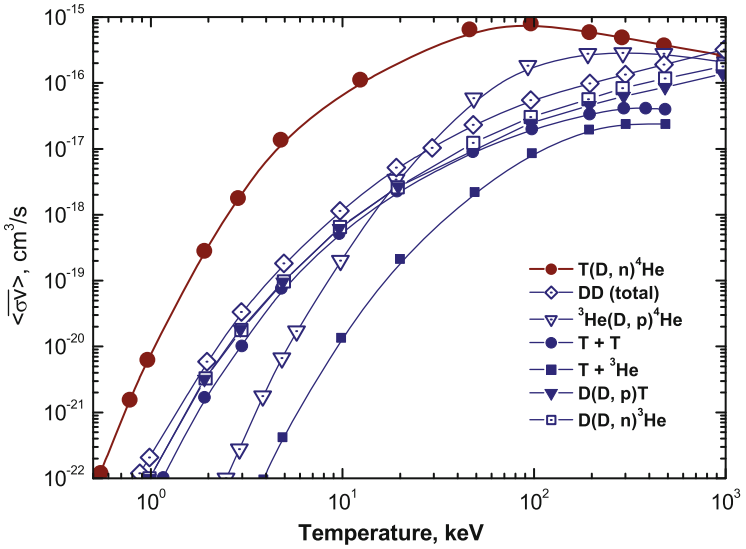

Fig. 4.8 Temperature dependences of thermonuclear reaction rates [55]. It is evident that the deuterium-tritium fusion reaction has the largest cross section and is therefore the easiest to implement in practice

This expression is accurate to within ≈10 % for 3–100 keV and to 20 % for 0.3–3 keV [54]. At temperatures of 8–25 keV, the DT reaction rate is [19]

$$\langle \sigma v \rangle_{\mathrm{DT}} = 1.1 \cdot 10^{-18} T^2 \,\mathrm{cm}^3/\mathrm{s}.$$

The rates of the two DD reaction branches, correct to ≈10 % for 3–100 keV, are [53]

$$\langle \sigma v \rangle_{\mathrm{DD_p}} = 2 \cdot 10^{-14} \frac{1 + 0.00577 T^{0.949}}{T^{2/3}} \exp\left(-\frac{19.31}{T^{1/3}}\right) \mathrm{cm}^3/\mathrm{s}$$

and

$$\langle \sigma v \rangle_{\mathrm{DD_n}} = 2.72 \cdot 10^{-14} \frac{1 + 0.00539 T^{0.917}}{T^{2/3}} \exp\left(-\frac{19.80}{T^{1/3}}\right) \mathrm{cm}^3/\mathrm{s}.$$

For the pp reaction [16]:

$$\langle \sigma v \rangle_{\mathrm{pp}} = 1.56 \cdot 10^{-37} T^{-2/3} \exp\left(-\frac{14.94}{T^{1/3}}\right) \times$$
$$\times \left(1 + 0.044 T + 2.03 \cdot 10^{-4} T^2 + 5 \cdot 10^{-7} T^3\right) \mathrm{cm}^3/\mathrm{s}.$$

It turns out that this central solar reaction is 24–25 orders of magnitude slower than the DT reaction. It is amazing that nuclear energy liberation at the solar center is quite low, ≈0.018 W/kt, which amounts to only 1/50 of the power of a human heart [19].

With increase in plasma density the interparticle interaction $V(r) \sim e^2/a$ becomes comparable to the kinetic particle energy, so that the nonideality parameter $\Gamma \sim e^2/(akT)$ will approach unity. This increases the rates of thermonuclear reactions [57, 99]:

$$\langle \sigma v \rangle_{\text{es}} \sim \left(1 + \sqrt{3}\Gamma^{3/2}\right) \langle \sigma v \rangle.$$

Under solar conditions for $\rho \approx 130\,\text{g/cm}^3$ and $T \approx 1.5\,\text{keV}$, this effect is moderate and amounts to 1.5 % for $\langle \sigma v \rangle$. Nor is it strong for laser fusion: for $\rho \approx 100\,\text{g/cm}^3$ and $T \approx 5\,\text{keV}$ it is within 0.2 %.

As the nonideality Γ increases, the correction for screening becomes $\sim \exp(\Gamma_i)$, but nevertheless remains small for thermonuclear temperatures and is neglected, as a rule. In the case of a strongly nonideal plasma ($\Gamma > 170$), its ions "freeze" to make up a crystal lattice and execute vibrations about their equilibrium positions at a frequency ω [36].

In this case, ions may enter into thermonuclear reactions with their neighboring ions. As this takes place, the Gamow barrier penetration factor is proportional to $\exp(-\rho^{1/6})$ and is independent of the temperature. Detailed calculations for the carbon-carbon reaction for $\Gamma_i > 170$ yield [57, 100]

$$\langle \sigma v \rangle_{\text{CC}} = 10^7 \left(\frac{\rho}{10^8}\right)^{-0.6} \exp\left(-258 \left(\frac{\rho}{10^8}\right)^{-1/6}\right).$$

This pyknonuclear regime was invoked to provide an explanation for a sharp energy liberation in a dense and relatively cool white dwarf with a carbon nucleus [19]. In this model, the carbon nucleus compression to $10^9\,\text{g/cm}^3$ sharply increases the thermonuclear reaction rate $\langle \sigma v \rangle_{\text{CC}}$ and thus raises the temperature and pressure to give rise to fusion burn.

The spin polarization of nuclei may exert a strong effect on the rate of thermonuclear reactions. In particular, the DT collision of nuclei with an even spin and an angular momentum $J = 3/2$ (in units of $\hbar$) has a reaction probability higher by two orders of magnitude than in other cases. This circumstance makes attractive the idea [69, 70, 76], which as yet remains to be practically implemented.

The idea of muonic catalysis [26, 80] relies on the replacement of an atomic electron with a heavier muon of mass $m_\mu = 208 m_e$. Replacing electrons with muons will lead to the formation of muonic atoms, which are 208 time smaller, will bring closer the nuclei in D_2 and T_2 molecules and will raise the probability of thermonuclear reactions even at room temperature. This results in a 50-fold increase in the tunneling of the fusion reaction in comparison with an ordinary molecule. For the DT reaction in a $D_\mu T$ pseudomolecule, calculations give $\tau_f \approx 7 \cdot 10^{-13}\,\text{s}$ and

$\tau_f \approx 1.5 \cdot 10^{-9}$ s for the DD reaction in a $D_\mu D$ molecule. After the reaction, muons may enter in other similar reactions, playing the role of a peculiar catalyst.

For the energy balance in the muon catalysis to be positive, the energy liberated in this cycle should exceed the energy expended to produce a muon itself, ≈ 5 GeV (in the decay of a pion). If one muon participates in N fusion reactions, each with an energy liberation of 17.6 MeV, and the energy-to-electricity conversion efficiency is equal to 40 %, then N must exceed 700; for practical applications it is desirable that $N > 3000$. To date, the attained number of muon catalysis events is ≈ 200 [26, 80].

One more possibility for fusion reactions deserves notice [19]. The deuterium-tritium fusion reaction (4.1) at collision energies of 25–300 keV has a cross section of 1–5 barn and an energy liberation of 17.6 MeV. The idea of implementing this reaction by way of direct collisions of D and T ions in the one-dimensional electrostatic acceleration of deuterium and tritium ions is referred to as beam fusion. However, this method shows little promise for power engineering, because the Coulomb interaction cross sections are far greater than the nuclear fusion cross sections for D and T ions. And so a D or T beam will primarily heat the target rather than excite nuclear fusion reactions.

A positive energy yield may be achieved when the reacting D and T agents are in a high-temperature plasma state [19] with high kinetic velocities sufficient to overcome interparticle repulsion (Fig. 4.4). In thermodynamic equilibrium, Coulomb collisions merely redistribute the kinetic energy between the plasma particles, which enter into fusion reactions in their interactions. For the energy yield to be greater than unity, the plasma should have a sufficiently high temperature and density and long lifetime. This method of obtaining fusion energy is the main one today and is called the thermonuclear fusion. This is precisely the energy source for stars, bombs, and in the near future for terrestrial electric power stations.

In the subsequent discussion we follow [19] and consider the energy balance of thermonuclear plasmas. The ignition and stationary plasma burn conditions reduce to the equality of fusion energy liberation and energy loss. The main energy loss channel for fully ionized thermonuclear plasmas is thermonuclear radiation [19]:

$$W_b = G_b n_e^2 T^{1/2} = 5.34 \cdot 10^{-24} n_e^2 T^{1/2} \,\mathrm{erg\,s^{-1}\,cm^{-3}}. \tag{4.4}$$

The power of thermonuclear energy liberation for the DT fuel [19]

$$W_{\mathrm{fus}} = \frac{1}{4} n^2 \langle \sigma v \rangle Q = 7.04 \cdot 10^{-6} n^2 \langle \sigma v \rangle Q \,\mathrm{erg\,s^{-1}\,cm^{-3}}. \tag{4.5}$$

Neutrons with an energy of 14.1 MeV, which as a rule escape from the reaction zone, account for 80 % of this power; 20 % of the power is accounted for by α-particles, which are absorbed in the plasma and heat it, maintaining fusion burn.

These temperature dependences are plotted in Fig. 4.9. The equality between the fusion energy liberation and the radiative energy loss defines the ignition temperature $T_{id} = 4.3$ keV. Since the fusion reactions and the bremsstrahlung arise

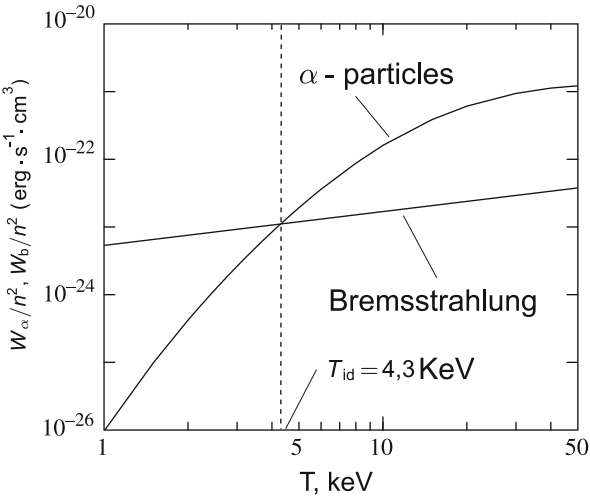

Fig. 4.9 Power of thermonuclear plasma heating by α-particles and thermal loss power due to bremsstrahlung. Borrowed from [19]

Table 4.2 Main fuels for controlled thermonuclear fusion [19]

	T_{id} (keV)	H_B^{min} (g/cm^2)	T (H_B^{min}) (keV)	Yield (GJ/mg)
DT	4.3	7.3	40	0.337
DD	35	52	500	0.0885
DD (full catalysis)	25	35	500	0.350
D^{3}He	28	51	38	0.0357
p^{11}B	–	73	250	0.0697

from binary collisions [19], the magnitude of T_{id} is independent of the plasma density.

This is true, of course, for optically thin plasmas. Otherwise, reabsorption locks up the radiation and, in accordance with the Teller–Ulam idea, improves the ignition conditions [19]. The idea of employing radiation for fuel compression and facilitating fuel ignition also belongs to them. The ignition conditions for other thermonuclear fuels are considerably worse than for DT—Table 4.2 [19]. Initially, the pure deuterium reaction does not contain tritium—it and ^{3}He appear due to the succeeding reaction. This process is termed the catalytic thermonuclear burn of deuterium. A D^{3}He reaction is interesting in that it contains only charged particles. However, for a fuel it requires a very rare ^{3}He. A p^{11}B reaction attracts attention because it produces only charged particles and does not give radioactive substances and neutrons.

Owing to the extremely high temperatures required to implement controlled thermonuclear reactions, the plasma confinement problem is extremely difficult [19]. Academicians A.D. Sakharov and I.E. Tamm proposed a scheme for plasma confinement by magnetic field. This device—a tokamak—is diagrammed in Fig. 7.10. The kinetic plasma pressure $p = (n_e + n_i)kT$ in these systems should not exceed

the magnetic field pressure B^2 by 10–15 %: for $B \approx 100$ kGs and $T \approx 10^4$ keV we obtain $n_i \approx 10^{14}$ cm^{-3}. The confinement time in such a device is unlimited.

Inertial—alternative to magnetic—confinement does not make use of external magnetic field and implies the realization of fusion during a short (≈1–10 ns) time defined by inertial plasma expansion. To ensure the burn of sufficient amount of fuel in so short a time requires a high reaction rate and therefore a high target compression.

The thermonuclear fuel is compressed and heated by either gravitation (Chap. 9), or the radiation of a nuclear explosion (Chap. 4), or high-power laser radiation (Chap. 7), depending on the situation.

Using expressions for the power of fusion energy liberation (4.4) and the loss power (4.5) it is possible to obtain [19]:

$$n\tau_{\mathrm{E}} = \frac{3kT}{\frac{1}{4}\left[(1/Q) + (1/5)\right]Q_{\mathrm{DT}}\langle\sigma v\rangle - C_b T^{1/2}},$$

where $C_b = 5.34 \cdot 10^{-24}$ erg cm^3 s^{-1} keV$^{-1/2}$, $Q_{\mathrm{DT}} = 2.86 \cdot 10^{-5}$ erg.

This parameter depends only on T and is termed the Lawson criterion; it defines the fusion ignition conditions. The ignition curve has a vertical asymptotics for $T = T_{id}$ and a minimum $n\tau_{\mathrm{E}} \approx 2 \cdot 10^{14}$ cm^{-3} s for $T \approx 20$ keV. Apart from the Lawson criterion, use is quite often made of the parameter $n\tau_{\mathrm{E}}T$, which has a value of $3.3 \cdot 10^{15}$ cm^{-3} s keV for ignition conditions. We will apply this parameter in Chap. 7, bearing in mind that $n\tau_{\mathrm{E}}T \sim p\tau_{\mathrm{E}}$.

For spherical targets for controlled laser fusion the Lawson criterion is easily represented in the form ρR, which requires a magnitude of several units to ignite the DT reaction (Fig. 4.10). In a more elegant scheme of inertial fusion [19] the reaction ignition is effected not uniformly over the whole target, but in a small part of its central region—the "hot spot". Next the fusion burn wave propagates from this hot spot nonuniformly throughout the target to cause its microexplosion (see Fig. 7.12).

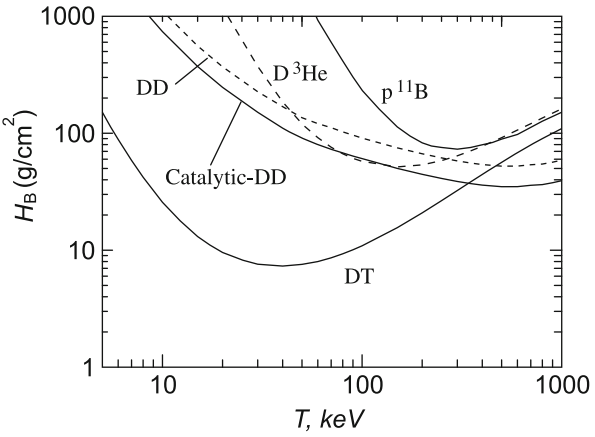

Fig. 4.10 Ignition parameter as a function of temperature for equimolar DT, DD, catalytic D, D^{3}He and p^{11}B mixtures. Borrowed from [19]

This scheme is more efficient and requires smaller ρR values. The requirement that the α-particles produced in DT reactions should transfer their energy to the fusion fuel leads to close ρR value.

More sophisticated multilayer target schemes for inertial fusion are briefly discussed in Chap. 7.

The thermonuclear fusion reactions discussed in the foregoing are of fundamental significance to humanity, because they explain the energetics of our Sun and the stars. And therefore explain the energetics of our entire civilization [39]. For the primary source of the overwhelming majority of renewable organic, hydraulic, biological, wind and other energy sources on the Earth employed by mankind is the thermonuclear fusion energy of a tremendous fusion reactor—the Sun.

This exceptional role of thermonuclear reactions as the energy source of cosmic objects was determined by Wigner, a Nobel Laureate, in the 1920s of the past century. With the exception of hydrogen bombs, in the path to ignition and practical use of thermonuclear reactions under controllable terrestrial conditions, humanity has faced enormous technical problems, which have not been solved despite the application of tremendous intellectual effort and a lot of material expenses.

4.1.2 Fission Reaction

The exothermal fission reactions of heavy elements (uranium and plutonium isotopes) located in the right part of the mass defect curve turned out to be realizable much earlier (Fig. 4.3).

"We can do more than we know"—these words of Enrico Fermi about the degree of comprehension of the essence of nuclear fission, which date back to the late 1930s, hold true even today. Specifically, the several next years saw the development of atomic bombs and reactors, whose operation relies on precisely the nuclear fission reaction, while its theoretical comprehension based on adequate experiments began much later—approximately in the mid-50s.

And this comes as no surprise. Nuclear fission became essentially the first-known really complicated nuclear transformation, which was attended with cardinal restructuring of the nucleus and a total change of not only quantitative but also qualitative characteristics of the system as a whole. Perhaps, in this instance the use was bound to get ahead of the comprehension, which did happen. Concerning nuclear fission, however, even today we are a long way still from embodying the famous maxim of academician Yu.B. Khariton: "We must know ten times more than we need today". That is why physicists control not the physical process in modern devices, but some of its consequences. Were it not so, the safety of nuclear technologies, which is so topical today, would be stated quite differently.

The discovery of atomic nuclear fission is one of the most fundamental discoveries that enjoyed numerous practical applications. Nuclear fission research is considered to have its origin in brilliant E. Fermi's works of 1934 on neutron irradiation of heavy atomic nuclei aimed at obtaining heavier elements—transuranium

ones. The absence of electric charge in neutrons ruled out the Coulomb nuclear repulsion, facilitating their arrival at the atomic nucleus.

The isotopes considered were ^{238}U, ^{235}U and ^{234}U. The most abundant uranium isotope is ^{238}U. The abundance of the rest is low: ^{235}U accounts for $\frac{1}{140}$ and ^{234}U for $\frac{1}{17{,}000}$ fraction of all uranium. Several elements were obtained with new extraordinary halflives. In 1939 the German chemists O. Hahn, L. Meitner and F. Strassmann discovered elements from the middle of the periodic system (barium, lanthanum, etc.) when investigating the reaction products in the neutron irradiation of uranium and thorium.

The nature of these amazing phenomena was understood by L. Meitner and her nephew O. Frisch in mid-January 1939. They hypothesized that the excited nucleus of uranium or thorium produced after neutron capture split into two smaller parts of approximately equal mass, which were called fragments. The radioactive isotopes discovered by Curie and Savitch, Hahn and Strassmann, which lay in the middle of the periodic table, were precisely the fragments of uranium and thorium nuclei. Since the relative neutron fraction in nuclei rises with their mass, these fragments resulting from heavy nuclei are overloaded with neutrons. That is why in the fragment nuclei there occur neutron transformations to protons by way of electron emission. The same also occurs in the daughter nuclei resulting from these transformations. This accounts for the chains of successive β^--transformations observed even by Fermi. One would expect—and this was confirmed by subsequent research—that the nucleus may split not only into two, but also into three and higher number of fragments. However, such fission events are by far less frequent than the splitting into two fragments.

The hypothesis of Meitner and Frisch was promptly borne out by Frisch's experiments with recoil atoms, in which it was possible to observe the explosive character of nuclear fission. One can see from Fig. 4.3 that the average nucleon binding energy in heavy nuclei is lower than in the nuclei from the middle of the periodic table of the elements. Let us assume that a ^{235}U nucleus splits into two similar fragments upon capturing a neutron. Referring to Fig. 4.3, the average nucleon binding energy in the uranium nucleus is equal to 7.6 MeV, while in each of the fragments it is equal to 8.5 MeV. Therefore, the fission of the uranium nucleus is attended with an energy release of 8.5–7.6 = 0.9 MeV per nucleon. Since the total number of nucleons remains invariable in the fission, the total energy released in one uranium fission event is $0.9 \cdot 236 \approx 210$ MeV. This huge energy manifests itself primarily in the form of kinetic energy of the resultant fragments.

This simple estimate is supplemented by significantly more recent sophisticated theoretical models, which we do not set out here.

Experiment suggests that a nucleus splits most often into two fragments. But the mass ratio of these fragments may be different. In the fission induced by thermal neutrons, fragments of equal or close mass are scarcely observed. Most probable is the splitting into fragments one of which is approximately half as heavy again as the other one. This is illustrated in Fig. 4.11, which shows the percentage of

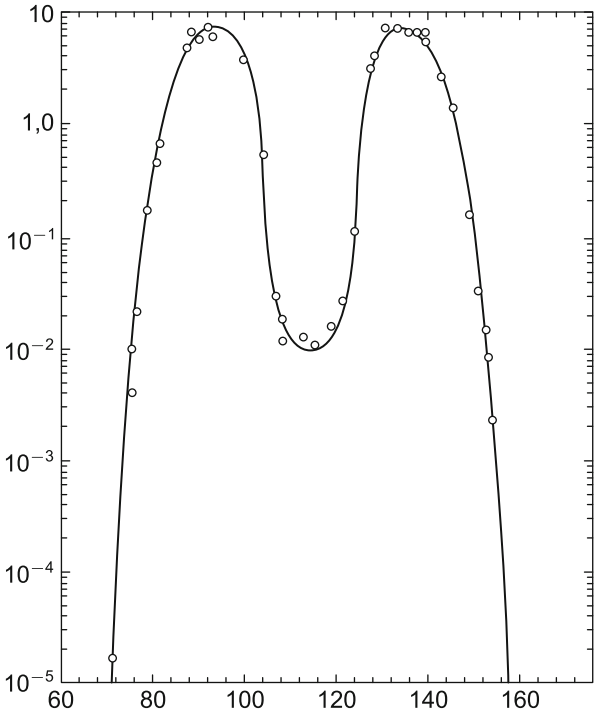

Fig. 4.11 Percentage of the fragments of different mass number in the fission of ^{235}U by thermal neutrons. Borrowed from [106]

the fragments of different mass number in the fission of ^{235}U induced by thermal neutrons. It is believed that this fission asymmetry is attributable to the influence of nuclear neutron shells: the nucleus splitting is energy-expedient when the number of neutrons in each of the fragments is close to one of the magic numbers—50 or 82.

Nuclear fission is accompanied with the ejection of secondary neutrons [106]. This is to be expected from the following simple considerations. The ratio between the number N of neutrons and that of protons Z in the nucleus is shown in Fig. 4.12. One can see that the larger and heavier is the nucleus, the more neutrons it contains.

Now let us assume that a heavy nucleus splits into two fragments. If the total number of neutrons in the system were invariable, the N/Z ratios in both fragments would either be equal to this ratio in the initial heavy nucleus, or it would be greater in one of them and smaller in the other fragment. So, at least one of the fragments would be neutron-excessive and would have to get rid of excess neutrons.

The dynamics of nuclear fission may be conventionally represented as follows: the fissile nucleus undergoes three stages corresponding to the increase in eccentricity parameter (growth of the degree of deformation of the initial nucleus up to its disintegration).

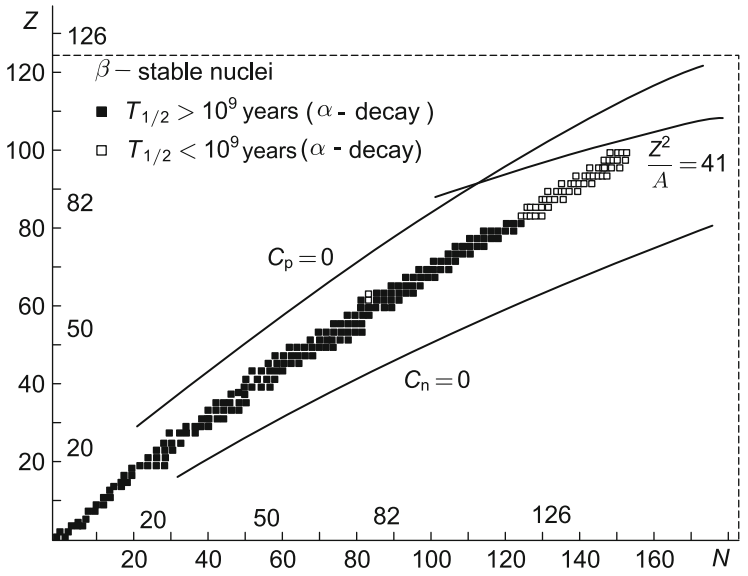

Fig. 4.12 Neutron-to-proton number ratio N, Z for stable nuclei. Borrowed from [106]

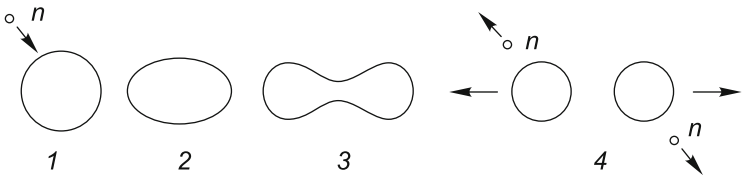

Fig. 4.13 Neutron-induced nuclear fission according to the liquid drop model of a nucleus. Borrowed from [106]

These stages are:

- attainment of the saddle point and its transit;
- system's descent from the saddle point to the pre-disintegration state;
- break of the waist between the fragments.

The emergence of secondary neutrons may be understood also from the standpoint of the liquid drop model of a nucleus. At the waist of the dumbbell-shaped nucleus (position *3* in Fig. 4.13) there are hardly any protons: due to Coulomb repulsion they concentrate primarily in the remote—ball-shaped—parts of the nucleus. That is why only neutrons may be ejected from the neck in its rupture in the course of fission, this occurring on the nuclear time scale (10^{-22}–10^{-23} s), i.e. virtually instantly. Such secondary neutrons are termed prompt.

Lastly, according to modern views, in the immediate vicinity of the break point there forms a charge distribution of the fission fragments, which defines their independent yields.

Table 4.3 Retarded neutrons [106]

Halflife	Yield, % relative to the total number of secondary neutrons	Kinetic energy of retarded neutrons (MeV)
55.7	0.021	0.25
22.7	0.140	0.56
6.2	0.125	0.43
2.3	0.253	0.62
0.6	0.074	0.42
0.2	0.027	–
–	–	–
8.97 on average	0.64	0.508

Along with prompt neutrons, in the fission of nuclei there also emerge retarded secondary neutrons. The matter is that nuclear fission fragments are radioactive. Their β-decay may give rise to neutron-excessive nuclei in strongly excited states. The excitation of such nuclei is removed by the competing emissions of neutrons and γ-ray photons. Both events occur almost instantly. The former process produces retarded neutrons. The retardation is understood in the sense of the time delay of the instant of neutron escape relative to the instant of emission of prompt neutrons (which emerge directly in nuclear fission). It is defined by the halflife of the parent isotope, whose β-decay produced the excited nucleus which later emitted the neutron.

Retarded neutrons are classified into several groups, which differ in time delay and energy. Table 4.3 shows the characteristics of the retarded neutrons emerging in the fission of uranium-235 nuclei.

Over 99 % of all neutrons released in the neutron fission are instantaneously liberated. Retarded neutrons account for about 0.75 % of the neutron yield. Despite this, retarded neutrons play an important role in nuclear power engineering: they permit making controllable the nuclear reactions occurring in the fission in nuclear reactors.

From the outset it was clear that only three of the actinide nuclei (the number of known actinide nuclei progressively increased from the early 1950s) are capable of playing this role: ^{235}U (a halflife of 710 million years), ^{239}Pu (24,100 years), and ^{233}U (160 thousand years). At the same time, the practically important statuses of these actinides are significantly different.

Uranium-235 holds a unique position among them: it alone exists in nature. And since the production of the other two in industrial amounts is possible only using reactor technologies, it is precisely the uranium-235 that "underlies everything". Were it not in existence in nature, atomic technology and nuclear power engineering would not have been possible in their present form.

Historically and essentially, plutonium-239 is second in this ranking. The reason lies with its production technology: the capture of a reactor neutron by the nucleus

of the most abundant natural uranium isotope (uranium-238) followed by two subsequent β^- decays, with subsequent radiochemical reprocessing of the irradiated fuel. A special feature of the implementation of this method is that no preenrichment of uranium in uranium-235 is required when use in the reactor is made of one of the two moderators (heavy water, graphite). This has been precisely the way of plutonium-239 production for equipping nuclear charges. The exceptional nuclear physical properties of plutonium make it an indispensable material of any modern nuclear charge—for this purpose it has virtually no alternative today [49, 94–96].

We set forth the approximate distribution of fission energy between its different liberation channels in the fission of ^{235}U by thermal neutrons [106]:

Kinetic energy of fragments	166.2 ± 1.3 MeV
Energy of fission neutrons	4.8 ± 0.1 MeV
Energy of prompt γ-ray photons	8.0 ± 0.8 MeV
Energy of β-particles from fission products	7.0 ± 0.3 MeV
Energy of γ-radiation from fission products	7.2 ± 1.1 MeV
Energy of antineutrinos from fission products	9.6 ± 0.5 MeV
Total	202.8 ± 0.4 MeV

We see that the fission of heavy nuclei is attended with the liberation of energy equal on average to about 200 MeV per every fissionable nucleus. This figure is hundreds of millions and billion times higher than the energy released in a single event of a chemical reaction. The latter quantity amounts to several electronvolts at most, but ordinarily tenths and even hundredths of an electronvolt. This underlines the unique promise on nuclear fuel for civil and especially military energetics.

Only one nuclear fuel occurs in nature under natural conditions—uranium. Natural uranium contains about 0.7 % of the ^{235}U isotope. Strictly speaking, the ^{235}U isotope is the nuclear fuel which maintains the reaction of nuclear fission. In natural uranium the isotope ^{238}U accounts for almost 99.3 %. ^{238}U as well as ^{232}Th are the raw materials for the artificial production of fissile isotopes ^{239}Pu and ^{233}U, which also are nuclear fuels. But these isotopes are not fount in nature under ordinary conditions. Plutonium-239 is produced in the reaction:

$$ {}^{1}_{0}\mathrm{n} + {}^{238}_{92}\mathrm{U} \rightarrow {}^{239}_{92}\mathrm{U} \xrightarrow{\beta^-} {}^{239}_{94}\mathrm{Np} \xrightarrow{\beta^-} {}^{239}_{94}\mathrm{Pu} \xrightarrow[2.4\cdot 10^4 \text{ years}]{\alpha}, $$

and uranium-233 in the reaction:

$$ {}^{232}_{90}\mathrm{Th}(\mathrm{n},\gamma) \xrightarrow[22.4\,\mathrm{min}]{\beta^-} {}^{233}_{91}\mathrm{Pa} \xrightarrow[27.4\text{ days}]{\beta^-} {}^{233}_{92}\mathrm{U} \xrightarrow[1.6\cdot 10^5 \text{ years}]{\alpha}. $$

The highest transuranium elements—americium, curium, berkelium, californium—cannot be used for the release of large amounts of nuclear energy due to the difficulty and high cost of their production.

The leading role in nuclear energetics is played by the $^{235}_{92}$U, $^{238}_{94}$Pu, and $^{233}_{92}$U isotope nuclei containing odd numbers of neutrons, because they are fissionable by neutrons of any energy, including thermal ones. The term "thermal" is used in reference to neutrons whose energy is of the order of kT. At room temperature (300 K, $kT \approx 4.14 \cdot 10^{-14}$ erg ≈ 0.025 eV. At these low energies the fission cross section is proportional to $1/v$, where v is the neutron velocity. Neutrons with energies ≥ 1 MeV are termed "fast". The nuclei of ^{238}U and ^{232}Th are not fissionable by slow neutrons and are fissionable only by fast neutrons.

The most important quantity which characterizes a fissionable nucleus is the average number ν of secondary neutrons emerging in the fission of one nucleus. Another quantity η characterizes an infinite uniform medium of the same nuclei. This is the average number of secondary neutrons per unit event of neutron capture by a nucleus. The numbers ν and η do not coincide: neutrons in the medium are responsible not only for the fission of nuclei, but they are also captured by the nuclei to emit γ-ray photons without causing fission, i.e. they enter the radiative capture reaction (n, γ). Let σ_{nf} be the fission cross section and $\sigma_{\mathrm{n}\gamma}$ the cross section for the radiative capture. Then the average fraction of the nuclei which are capable of undergoing fission and which do experience fission is $\sigma_{\mathrm{nf}}/(\sigma_{\mathrm{nf}} + \sigma_{\mathrm{n}\gamma})$. The average number of emitted secondary neutrons per one event of neutron capture by a fissionable nucleus is

$$\eta = \nu \frac{\sigma_{\mathrm{nf}}}{\sigma_{\mathrm{nf}} + \sigma_{\mathrm{n}}\gamma}.$$

The values of ν and η for nuclei fissionable by thermal and fast neutrons are collected in Table 4.4. In the domain of not-too-high a nucleus excitation energy (<10MeV), the number ν increases by about 0.11 with increasing excitation energy by 1 MeV.

One can see from Table 4.4 that $\eta > 1$ is the necessary (but not sufficient) condition for the implementation of a chain reaction of the fission of atomic nuclei. By a chain reaction is meant a process whereby one of the initial reactants is reproduced—in larger amount—and enters the same reaction again. As a result, this reacting substance is reproduced again in a still larger amount.

Reproduced in a chain nuclear fission reaction are neutrons, which then enter new nuclear reactions. Let a body of sufficiently large size consist of pure uranium-235. Let us assume that a neutron emerges in the body due to spontaneous fission or under the action of cosmic rays. For simplicity we assume that every neutron is

Table 4.4 Values of ν and η for nuclei fissionable by thermal and fast neutrons [106]

Nucleus		$^{233}_{92}$U	$^{235}_{92}$U	$^{239}_{94}$Pu
Thermal neutrons (0.025 eV)	ν	2.48	2.42	2.86
	η	2.28	2.07	2.11
Fast neutrons (1 MeV)	ν	2.59	2.52	2.98
	η	2.45	2.3	2.7

sooner or later captured by one of ^{235}U nuclei to cause its fission with the emergence of two new neutrons, which will be called the first-generation neutrons. These two neutrons will, in turn, cause the fission of two nuclei, resulting in the emergence of four second-generation neutrons. The four second-generation neutrons will be replaced by $2^3 = 8$ third-generation neutrons etc. The number of nth-generation neutrons will exponentially rise with time.

The average lifetime of one generation of neutrons in uranium-235 is of the order of 10^{-7}–10^{-8} s [106]. We take, as an example, the value 10^{-7} s. Then, even in a time of 10^{-5} s after the onset of the reaction there emerge hundredth-generation neutrons numbering $n_{100} = 2^{100} = 1.27 \cdot 10^{30}$. This period of time will see $1 + 2 + 2^2 + \ldots + 2^{100} \approx 2^{101} \approx 2.54 \cdot 10^{30}$ nuclear fission events with the liberation of an energy of $200 \cdot 2.54 \cdot 10^{30} \approx 5 \cdot 10^{32}$ MeV$\approx 8 \cdot 10^{26}$ erg. This will result in a tremendous explosion with an average power of about $8 \cdot 10^{31}$ erg/s. For comparison we note that the total power of solar radiation amounts to $3.8 \cdot 10^{33}$ erg/s. The mass of all uranium-235 nuclei which undergo fission during the period under consideration amounts to 10^3 t.

The chain reaction is practically implemented using the so-called enriched uranium, which contains, along with ^{238}U, the ^{235}U fraction increased from 0.7 to 2–5 %. The natural uranium ^{238}U is enriched by way of isotope separation—by way of gas and thermal diffusion, centrifugal separation, and electromagnetic method. The ^{238}U isotope, which is added to natural uranium, may be replaced by plutonium-239 or uranium-233, whose properties are similar to those of uranium-235 as regards the fission reaction [4, 5, 49, 115].

When the active zone is filled with an isotope mixture, the coefficient η introduced above retains its meaning as the average number of secondary fission neutrons per one neutron absorbed by the mixture. When only one isotope in the mixture is fissionable, then

$$\eta = \frac{\nu \sigma_{\mathrm{nf}}}{\sigma_{\mathrm{nt}}},$$

where σ_{nf} is the fission cross section and σ_{nt} is the total cross section for neutron capture by all components of the mixture. Specifically, the cross section for uranium-235 fission by thermal neutrons $\sigma_{\mathrm{nf}}^{235} = 582$ barn, the radiative capture cross sections $\sigma_{\mathrm{n}\gamma}^{235} = 100$ barn, $\sigma_{\mathrm{n}\gamma}^{238} = 2.73$ barn [106]. In natural uranium, one uranium-235 atom falls on 140 uranium-238 atoms, and so the total cross section for thermal neutrons and natural uranium is

$$\sigma_{\mathrm{nt}} = \sigma_{\mathrm{nf}}^{235} + \sigma_{\mathrm{n}\gamma}^{238} + 140 \cdot \sigma_{\mathrm{n}\gamma}^{238} \approx 1064 \text{ barn}.$$

For thermal neutrons $\nu = 2.42$ (see Table 4.4). And therefore for natural uranium and thermal neutrons

$$\eta = \frac{\nu \sigma_{\mathrm{nf}}^{235}}{\sigma_{\mathrm{nt}}} = 1.32.$$

The most important quantity which characterizes the active reactor zone is the neutron multiplication factor k. This is the ratio between the total number of neutrons in some generation and the total number of their parent previous-generation neutrons.

For $k = 1$ the fission reaction is stationary—there is no neutron multiplication. The corresponding reactor state is called critical. For $k > 1$ the number N_n increases with n—this state is termed supercritical. For $k < 1$ the number N_n decreases with increasing n—this state is termed subcritical. In the limiting ideal case, when the reactor consists of the active zone alone and this zone is infinitely large, the neutron multiplication factor is supplemented with a subscript ∞, i.e. is denoted as k_∞.

High values of parameter σ_{nf}/σ_{nt} in the neutron energy range up to 1 MeV underlie the uniqueness of nuclear physical properties of plutonium-239. Its critical mass in the "bare ball" configuration amounts to 15 kg, while for uranium-235 the figure is 50 kg. Furthermore, plutonium possesses favorable mechanical properties: unlike hard and brittle uranium, it is easily compressible. From the standpoint of weapons design, this permits realizing an efficient method of reaching the critical mass—implosion [4, 5, 15, 115, 122] (the passage to the supercritical state for an invariable mass by increasing the density and lowering the effective surface). The use of this method permits making modern nuclear ammunition with very high performance characteristics.

However, plutonium-239 has deserved the title of the "nuclear fuel of the future" not in the least due to its "military merits". It is precisely its use as the nuclear fuel for nuclear power engineering that enables extending its resource potential by several thousand years.

If the active zone consisted of only one fissionable isotope (for instance, uranium-235), then $k_\infty = \eta$. This is not so in the case of a real reactor. For concreteness, let us consider a natural or slightly enriched uranium reactor. The major part of secondary neutrons emerges in the fission of uranium-235 nuclei by thermal neutrons. However, produced in the fission are primarily fast neutrons. To make them more efficient, use is made of different moderators, whose nuclei scatter the neutrons and moderate them to thermal velocities. Such a reactor is called a thermal neutron reactor [106].

Figure 4.14 depicts the approximate spectrum of the neutrons produced in the fission of ^{235}U [106]. As may be seen in Fig. 4.14, produced in this case are mostly fast neutrons. The nuclei of uranium-238 are fissionable only by fast neutrons with energies of $\approx$1 MeV. But the effective cross section for this fission is very small—about 0.3 barn. By contrast, the nuclei of uranium-235 are fissionable by neutrons of arbitrary energy, the effective fission cross section rapidly increasing with decreasing energy. For thermal neutrons it is as high as 582 barn. That is why it would be expedient to moderate neutrons to thermal energies.

Of course, neutrons are moderated in elastic collisions with the nuclei of uranium-238 and uranium-235; however, this process is very slow owing to the large mass of uranium nuclei. But the main impediment to the moderation of neutrons in

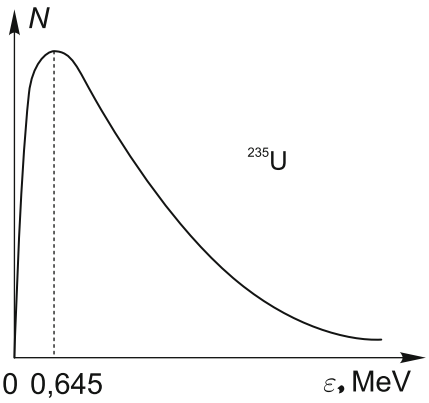

Fig. 4.14 Approximate neutron spectrum in the fission of ^{235}U. Borrowed from [106]

natural uranium is the radiative neutron capture by uranium-238 nuclei [106]. The radiative capture is especially efficient in the resonance energy range. In the course of moderation the neutrons have to pass through the resonance range, where they are absorbed and therefore do not reach the thermal energy range. Furthermore, a certain neutron fraction escapes from the active zone. To maximize the neutron fraction moderated to thermal velocities, use is made of a moderator, i.e. a substance containing light nuclei with a small cross section for neutron capture. Graphite is often used as a moderator. Also employed are heavy and ordinary water, beryllium and its oxide, as well as some organic substance.

When the active zone of a nuclear reactor contains a neutron moderator, the bulk of nuclear fission events are induced by thermal neutrons.

When there is no moderator in the active zone, the bulk of nuclear fissions are induced by fast neutrons with energies > 1 MeV [106]. Also possible are intermediate nuclear reactors with neutron energies of 1–1000 keV.

In the course of moderation, a neutron may be absorbed by ^{238}U nuclei, moderator nuclei, and the nuclei of other structural reactor elements. It is clear that the multiplication factor is proportional to the probability that the neutron is not absorbed by these nuclei. Of course, some uranium-238 nuclei will undergo fission due to collisions with the fast neutrons that have not had time to moderate. This circumstance is taken into account by introducing a factor ε—the fast neutron multiplication factor. The fast neutron multiplication factor is the ratio of the number of neutrons emerged in the fission by fast and thermal neutrons to the number of neutrons emerged in the fission by only thermal neutrons. We also introduce a thermal utilization factor f—the probability that the moderated neutron will be absorbed by the nuclei of uranium isotopes rather than the nuclei of the moderator and other structural reactor materials. Then

$$k_\infty = \eta p f \varepsilon.$$

Since the active zone dimensions are finite, a part of the neutrons will leave to the outside. We can therefore put

$$k_\infty = k_\infty P,$$

where P is the probability that a neutron does not escape from the active zone. This formula holds good for reactors of any type, irrespective of the specific expression for k_∞. It also retains significance for an atomic bomb, whose active zone consists of pure uranium-235 or plutonium-239. The magnitude of P depends on the composition, dimensions, and shape of the active zone as well as on the medium surrounding the active zone. If this medium reflects neutrons back into the active zone, it increases P. In this case, it is called a "reflector"; it consists of light atoms which have low neutron absorption (graphite, beryllium).

As discussed above, the reactor operation requires that $k \equiv k_\infty P \geq 1$. In the limit when $k_\infty P = 1$, the chain reaction occurring in the reactor is self-sustaining, stationary. The dimensions and mass of the active reactor zone as well as the probability P for which the self-sustained chain reaction becomes possible, i.e. when

$$P = P_{\text{crit}} = 1/k_\infty,$$

are called critical [106]. These quantities, of course, depend on the composition and shape of the active zone as well as on the reactor structure.

To reduce the neutron escape, the active zone is given a spherical or near-spherical shape, for instance the shape of a cylinder with a height of about its diameter or the shape of a cube, because the surface-to-volume ratio is minimal or close to minimal for bodies of such shape. The critical mass is equal to approximately 0.8 kg for pure ^{235}U, to 0.5 kg for ^{239}Pu and to 10 g for ^{251}Cf [106].

When the mass of the active zone is substantially greater than the critical one, the chain reaction acquires the character of an explosion. This principle underlies the action of an atomic bomb, which is discussed below.

It is well known that the parameters of the processes occurring in a reactor are reflected in the fate of neutrons produced as a result of the fission chain reaction. A part of them goes to sustain the reaction itself, another part escapes from the active zone, a part is captured by reactor controls and structural elements. Of interest in the context under discussion is the last-mentioned part of the neutrons captured by uranium-238 nuclei, which are present in the reactor fuel, with the subsequent accumulation of plutonium-239, as discussed in the foregoing. However, plutonium-239 is not only the "bomb" material. In an appropriate embodiment it is also an efficient nuclear fuel.

The basic question of fuel resource provision for atomic power engineering becomes clear: What is the ratio between the accumulation rate of the thus produced plutonium-239 and the burn rate of the primary fuel (uranium-235 or plutonium-239 itself)? If this ratio is smaller than unity, atomic energetics will persist as long as uranium-235 exists in nature, because for obvious reasons plutonium-239 does not exist in it. This is precisely the case with the overwhelming majority of present-day

thermal neutron reactors: this ratio (the conversion coefficient) is always smaller than unity, 0.8 at the most. In this case, the fraction of uranium-238 involved in energy liberation is very small (several percent), and the resource lifetime of this atomic power engineering is limited to 100–150 years.

Physically, the problem is that the amount of neutrons is insufficient for capture by uranium-238 nuclei in a thermal neutron reactor which utilizes uranium-235 or plutonium-239 fuels: attempts to raise the capture intensity have the result that the reactor lacks neutrons for sustaining the chain reaction and the reactor shuts down. However, the situation is radically different in a fast neutron reactor (there is no moderator) utilizing a plutonium-based fuel. Under the hard (unmoderated) spectrum of prompt fission neutrons the effective multiplication factor for plutonium-239 is very large owing to the anomalously high (in comparison with uranium isotopes) value of parameter α and high ν, which increases the fraction of "excess" neutrons (relative to those required for sustaining the chain reaction). With the appropriate embodiment of the reactor itself (the existence, apart from the active zone, of a special reproduction zone accommodating uranium-238), these "excess" neutrons may be directed to the production of plutonium-239. In this case, it is possible to obtain greater-than-unity values of the accumulation-to-burn rate ratio (breeding ratio) mentioned above, i.e. the reactor produces more new fuel than it burns the primary one. It is clear that this nuclear power engineering will not "settle down" until it burns down not only uranium-235, which accounts for only 0.71 % in the primary uranium, but also uranium-238 (all the rest), and the resource lifetime transforms from one hundred to thousands of years.

Perhaps, the time of uranium-233 will also come. Although it is an excellent nuclear fuel by itself (in the "bare ball" configuration its critical mass, like that of plutonium, is close to 15 kg [4, 5, 15, 106, 115, 122]), its production is associated with major technical difficulties, because natural thorium does not contain a high-fissility isotope (similar to uranium-235 in natural uranium). Meanwhile, adequate studies have been made of the nuclear fuel cycle whereby uranium-233 is produced in the reproduction zone, which accommodates natural thorium-232. The production of uranium-233 is similar to that of plutonium-239 described above (the capture of a neutron by a thorium-232 nucleus with the formation of thorium-233 followed by two β^- decays).

India, which has very modest resources of natural uranium and vast resources of thorium, has embarked on the implementation of this fuel cycles [106]. It is significant that this nuclear fuel cycle may be realized with a breeding ratio of somewhat greater than unity in thermal neutron reactors: the nuclear constant ratios for uranium-233 are technically favorable for this purpose at precisely the low energies. For unmoderated neutrons (in the fast reactor spectrum), uranium-233 is much inferior to plutonium-239. Perhaps, the practical implementation of thorium-based nuclear fuel cycles will commence in the 1930s of our century. And it is not unlikely that this will call for a wide use of new reactor types—like, for instance, high-temperature reactors with gas (helium) cooling.

4.2 High Energy Densities for Explosive Nuclear Reactions

It is amazing how quickly humanity learned to harness quasi-controlled nuclear and thermonuclear energy. The first nuclear explosion was carried out only six and a half year after the discovery of nuclear fission reactions.

In 1938–1939, realizing E. Fermi's idea of synthesizing superheavy elements by neutron irradiation of uranium, O. Hahn and F. Strassmann much to their surprise discovered not superheavy but lighter elements, which were fragments of the targets under study.

- In 1942 a start was made on the Manhattan Project in the USA. That same year E. Fermi put into operation the first stationary nuclear fission reactor.
- One and a half months later, on 28 September 1942, the USSR resumed research on uranium, which had been interrupted by the War.
- The Los Alamos Research Laboratory was set up in 1943.
- The first successful nuclear explosion was carried out in the USA in July 1945.
- In August 1945 the atomic weapon was used against Japan.
- In December 1946 academician I.V. Kurchatov put into operation a fission reactor, the first in Europe.
- In August 1949, the USSR set off its first atomic bomb made within 4 years after launching the large-scale stage of the Soviet Atomic Project.
- In the USA a start was made to develop thermonuclear weapons—a superbomb.
- In 1952 the USA detonated an untransportable nuclear device and in 1954 a deliverable hydrogen bomb.
- The USSR tested the first deliverable hydrogen bomb (a "layer cake") [97] in August 1953 and 2 years later a fully fledged deliverable charge ("3rd idea" of A.D. Sakharov) [97].

In the opinion of the scientific supervisor of the Russian Nuclear Center Arzamas-16 (presently the RFYaTs—VNIIEF) academician Yu.B. Khariton [63], "the rapid advance and the ultimate success was possible because the scientists of both countries, being people of high skills and education, leaned in their activity upon the excellent European physical science school. The USA and USSR scientists did everything in their power to ensure victory over Germany".

Furthermore, as E. Fermi would speak about the work on the nuclear project, "This is an interesting physics after all".

The development of nuclear and thermonuclear weapons was not only an outstanding scientific and technical achievement of mankind, but it also provided the geopolitical stability and peace on the Earth for 75 years. With the exception of the centennial period (1815–1914) after the Congress of Vienna, which finished Napoleonic wars, the mankind has never lived for so long without large-scale battles.

In the subsequent discussion we will touch on the issues of generation and use of extreme states in nuclear explosions using only open publications [1–8, 11, 13–15, 27, 29, 30, 33, 43–52, 56, 60, 63–65, 88, 91, 94–97, 102, 109, 115].

The majority of these materials were declassified [1–3, 94–96] and became publicly available during the work of an expert group of the Ministry of Atomic Energy of the Russian Federation on the collection "Atomic Project of the USSR" (edited by L.D. Ryabov), which was published by the Ministry. These materials became publicly available in accordance with the Decree No. 160 issued by the President of the Russian Federation B.N. Yeltsin on 17 February 1995 "On the Preparation and Publication of an Official Collection of Archival Documents on the History of Nuclear Weapons Development in the USSR". A part of these documents have already published in the volumes [94–96] of this Collection, others are under preparation for publication. Not only does this chapter give references to these sources, but it also reproduces text fragments of some of the documents.

4.2.1 Explosive Fission Reactions

In the paper "Kinetics of chain uranium fission" published in 1940, Ya.B. Zel'dovich and Yu.B. Khariton described the conditions required for implementing a nuclear explosion in the following way: "The explosive use of chain fission requires special devices for effecting a very fast and deep transition to the supercritical domain and decreasing the natural thermal transfer". They hypothesized that the realization of one or other type of measures will make it possible "to produce conditions for the chain fission of uranium by way of branching chains, whereby an arbitrarily weak neutron irradiation will result in an intensive progress of the chain reaction and macroscopic effects". They emphasized the high exponential growth rate of neutron density in such a system for a high supercriticality (an increase by e times in 10^{-7} s) and the difficulties associated, in their opinion, with this circumstance: "For so rapid a growth of the chain fission we no longer have no right to digress from considering the production of the supercriticality conditions themselves only whereby the chain fission is possible. It will hardly be possible to make the time taken to effect the transition to supercriticality, for instance the time required for bringing together two uranium masses each of which is subcritical as regards the chain reaction, at all comparable with the reaction buildup time". Ya.B. Zel'dovich and Yu.B. Khariton underlined "the decisive role of the kinetics of chain fission development when judging about one or other way of practical, power-producing, or explosive use of uranium fission" [49]. It is significant that even at that time the necessity was recognized of employing and therefore studying the states of matter with extremely high energy densities [49, 94–96].

On 20 March 1943, within a month odd after his appointment as scientific supervisor of research on uranium, I.V. Kurchatov addressed a letter to M.G. Pervukhin, which read [94, 95]: "Early in the uranium bomb explosion, the bulk of substance which has not managed to participate in the reaction will be in the special state of almost complete ionization of all its atoms; the subsequent development of the process and the destructive effect of the bomb will depend on the state of this substance.

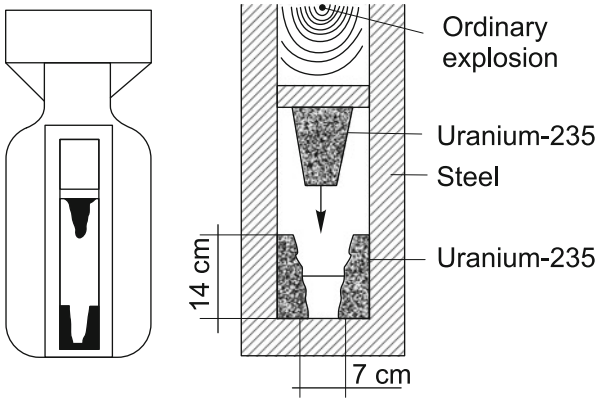

Fig. 4.15 Schematic of the "Little Boy" atomic bomb dropped on the city of Hiroshima. The function of nuclear explosive was fulfilled by uranium-235 divided into two parts of lower-than-critical mass each. The critical mass of uranium-235 required for detonation was produced by joining both parts by the "gun method" with the aid of ordinary explosive [4, 5]

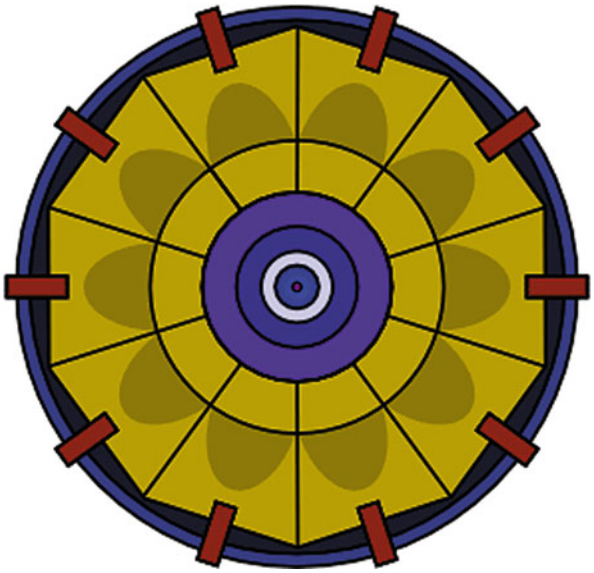

Fig. 4.16 Schematic of an implosion nuclear charge [4]

In experiments, even on a very low scale, nothing similar to this state of substance has been observed and may not be observed prior to the implementation of the bomb. This substance state is hypothesized to rexist only in stars. Theoretically it seems possible to consider in outline the course of explosion at this stage".

At the initial stage of nuclear weapon development in the USA, two nuclear charge schemes were realized [49, 88, 94–96]—the "gun", or "ballistic" scheme (Fig. 4.15) and the "implosive" one (Fig. 4.16). Academician I.V. Kurchatov's memo

"Structure of atomic bombs with uranium-235 and plutonium-239" [49, 94–96] reads: "The atomic bomb may be actuated in two ways:

- by the fast approach of the two halves of a uranium-235 or plutonium-239 charge spaced at 0.5–1 m prior to approach,
- by densifying uranium-235 or plutonium-239 charges with a powerful explosion of a trotyl charge surrounding these substances."

In the memo dated 18 May 1944, I.V. Kurchatov gave the scheme of an atomic bomb of the gun-approach type and provided the following description of its structure and operation [49]: "An atomic aviation bomb consists of a cylindrical shell at the ends of which is the atomic explosive – uranium-235 or plutonium-239. The bomb is actuated by detonating the powder charges laid under the active substance. The atomic bomb explosion occurs at the instant of the joining of halves (a) and (b) of uranium-235 or plutonium-239.

According to simulations, to implement a bomb equivalent in its action to 1000 tons of toluene requires 2–5 kg of uranium-235 or plutonium-239.

At present there are still no perfectly reliable data showing that the thus constructed bomb will be operative; however, the more experiments are carried out, the higher is the confidence in the correctness of the scheme.

The main difficulty in implementing the atomic bomb consists in the production of uranium-235 or plutonium-239."

The gun scheme applied in the city of Hiroshima is shown in Fig. 4.15.

The pressures emerging at the instant of collision of the two uranium halves of mass ≈ 0.7 of the critical one [35] range up to a relatively modest value $P = \rho W^2 \approx$ 100 bar, which is insufficient for an appreciable compression of the nuclear fuel.

The "implosion" scheme (an alternative to the "gun" scheme), which was used in the bombing of the city of Nagasaki ("Fat Man"), is schematized in Fig. 4.16.

For a fuel, use was made of plutonium ^{239}Pu—an artificial element not found on the Earth, which is produced in stationary nuclear reactors by neutron irradiation of natural uranium ^{238}U. Plutonium in the form of a bare ball has a critical mass of $\approx$10 kg, while uranium-235 that of 50 kg [35]. In comparison with uranium-235 its production is five times more expensive [35]. Since the critical fuel mass sharply (quadratically) decreases with compression, this scheme permits using smaller quantities of expensive nuclear fuel (hundreds of grams) [2, 4–7, 11, 13, 15, 27, 29, 35, 43–52, 56, 63, 88, 91, 94–97, 102, 109, 115] and improving the charge "fission efficiency" [35, 49, 94–96].

The operability of this scheme and its main characteristics depend critically on the physical properties of the materials and substances in use under extreme conditions: on the shack-wave compressibility of the nuclear fuel in the pressure range up to tens of Mbar, on the thermodynamic properties of the detonation products of the condensed explosives which drive the explosive compression and generate intense spherical shock waves in the nuclear charge, on the thermophysical properties of the structural materials and on many other characteristics of charge elements in the course of initiation and explosive nuclear energy liberation [2, 4–7, 11, 13, 15, 27, 29, 43–52, 56, 63, 88, 91, 94–97, 102, 109, 115].

At the early stages of the work there was significant uncertainty and a poor understanding of substance behavior under the exotic conditions of a nuclear explosion. For instance, according to [88] several scientists believed that metals were incompressible under these conditions, and the high uncertainty concerning the equations of state of the explosion products of condensed explosives cast doubt on the very fact of "device" operability [11, 49, 97], with all the ensuing "organizational consequences" for the Soviet scientists [11, 49].

To acquire the requisite data about the physical properties and gas-dynamic features of substance behavior under the extreme conditions of a nuclear explosion, a start was made on a complex of experimental and theoretical research programs, which gave birth to a new science—the physics of high energy densities [5, 10, 36, 37, 110, 122] and the dynamic physics of high pressures (Chap. 3).

The diagrams and photographs of the nuclear devices made at that time are given in Figs. 4.17, 4.18, and 4.19 [8]. Their designs fully embody the derived fundamental data on the physical properties of the substances and structural materials at superhigh pressures and temperatures as well as a wealth of original ideas and approaches.

We give several characteristics of the American implosion atomic bomb [4, 5, 15]. The bomb was a pear-shaped shell with a maximal diameter of 127 cm, a length (including stabilizer) of 325 cm and a mass of about 4500 kg.

The neutron initiator was a polonium-beryllium system 10 mm in radius. To total amount of polonium was equal to 50 Ci.

The fissionable bomb material was the δ phase of plutonium with a density of 15.8 g/cm^3. The external diameter of the plutonium ball was equal to 80–90 mm.

The plutonium core was accommodated inside a hollow sphere of metallic uranium with an external diameter of 230 mm [4, 5, 15].

The uranium sphere was accommodated inside an aluminum shell, which was a hollow sphere with an external diameter of 460 mm [4, 5].

Fig. 4.17 American atomic bombs "Little Boy" (of gun type, with a blast equivalent of 15 kt of TNT, based on uranium-235) and "Fat Man" (of implosion type, based on plutonium-239, with a blast equivalent of 21 kt of TNT) dropped on the cities of Hiroshima and Nagasaki [8]

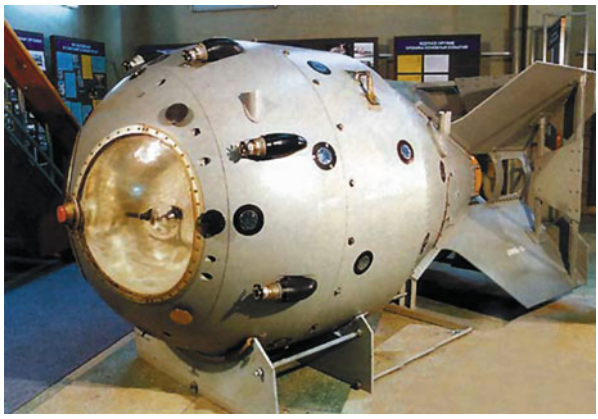

Fig. 4.18 RSD-1 nuclear charge, which was first tested in the Semipalatinsk proving ground on 29 August 1949. The TNT equivalent is below 20 kt. The RFYaTs-VNIIEF museum, the city of Sarov [4]

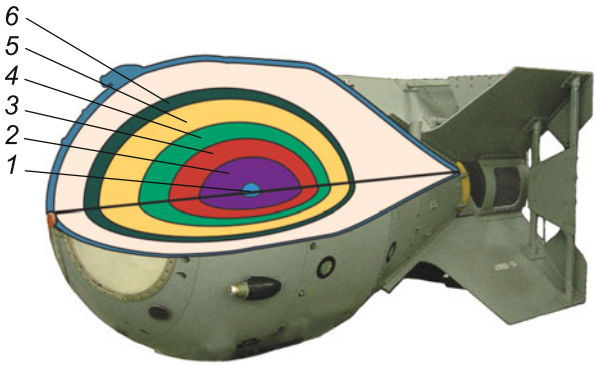

Fig. 4.19 Schematic diagram of the first Soviet implosion atomic bomb, which is an analogue of the American "Fat Man" bomb [8]

Above the aluminum layer was a layer of explosive with a focusing lens system of 32 specially shaped blocks. The total mass of the explosive amounted to about 2 t [4, 5].

During the work on a uniform charge, the research team of Prof. L.V. Alt'shuler arrived at a better design, which combined "gun" and "implosion" ideas (the "shell-nucleus design") [11, 49, 94–96]. In this case, the detonation of the explosive does not directly compresses the uniform spherical charge; instead, it accelerates a spherical shell of a fissionable material, which strikes against a sphere of smaller size [35, 49, 94–96, 110]. The density is several times higher in this case [110]. This made it possible to improve the device efficiency by a factor of two for a substantial lowering of its size and weight.

Along with this, use was made of external neutron initiation systems for the controllable triggering of the chain reaction, which were more elaborate than the polonium-beryllium ones. The response time of this bomb's "power plant" [115] is defined by highly sophisticated gas-dynamic simulations, which involve the equations of state of substances at extremely high energy densities. These ideas were amply borne out by the tests carried out in 1954 [115].

According to [27, 35], another way to achieve automatic timing is as follows. A small amount of deuterium-containing substance is accommodated at the charge center. The shock wave driven by the chemical explosive charge gives rise to the nuclear deuterium–deuterium reaction with the emission of neutrons, which stimulate the chain reaction [35].

Before long, the subsequent development of nuclear weapons revealed the limitations (tens of kilotons) of purely fission explosion schemes arising from the rapid expansion of the nuclear fuel in the course of the fission reaction and—as a consequence—the limitations on its efficiency (20 % of 6.2 kg of the plutonium charge fissioning in the "Fat Man" device and 1.4 % of 64 kg enriched uranium fissioning in the "Small Boy" device).

The further prospects for advancement were related to thermonuclear fusion reactions, which, according to academician A.D. Sakharov's statement [97], "are the energy source of the Sun and stars, the source of life on the Earth, and the possible cause of its death".

4.2.2 Pulsed Thermonuclear Fusion

The role of nuclear energy sources for powering the stars was evident even in the beginning of the twentieth century. In 1920, A. Eddington spoke to the meeting of the British Association for the Promotion of Science [47]:

> A star is a shell pulled over a huge energy reservoir by unknown means. This reservoir is unlikely to be anything but intraatomic energy, which is known to be inherent in any substance... This store of energy is nearly inexhaustible if it is at all amenable to measurement... If the intraatomic energy in the stars is indeed used on a large scale to maintain the huge hearth, which is a star, this seems to bring us much closer to the realization of our dream of controlling this hidden energy for the benefit of mankind or its self-destruction.

The discovery of the leading role of precisely the thermonuclear reactions as the stellar energy source is due to H. Bethe, a 1926 Nobel Laureate; later he became leader of the Los Alamos Research Laboratory, where the nuclear and thermonuclear weapons were made (USA). Although the corresponding thermonuclear reaction schemes and the requisite reaction cross sections were well known by the mid-1940s [2, 4–7, 11, 13, 15, 27, 29, 43–52, 56, 63, 88, 91, 94–97, 102, 109, 115], the practical implementation of explosive thermonuclear reaction in terrestrial conditions ran into serious difficulties arising from the necessity of producing in the thermonuclear fuel an ultrahigh pressure and a temperature ranging up to tens of millions of degrees.

Enormous efforts in quest for acceptable physical schemes and technical tricks for making a thermonuclear "superbomb" have been detailed in several publications [1–3, 6–8, 11, 14, 29, 30, 33, 35, 46, 49–52, 60, 64, 65, 88, 97, 109], which reflect the breathtaking history of the thermonuclear project full of drama, despair, and brilliant flashes of inspiration.

According to [14], "the main concern was to heat and ignite, employing the energy released in the atomic bomb explosion, the mixture of heavy hydrogen isotopes – deuterium and tritium – i.e. to produce with energy release the fusion reactions

$$\mathrm{D} + \mathrm{D} = \mathrm{H} + \mathrm{T} + 4\,\mathrm{MeV},$$

$$\mathrm{D} + \mathrm{D} = \mathrm{n} + {}^{3}\mathrm{He} + 3.3\,\mathrm{MeV}$$

thereby capable to be self-sustainable. To increase the fraction of "burnt" deuterium, A.D. Sakharov came up with the idea of enclosing deuterium in a heavy envelope of ordinary natural uranium, which was to moderate expansion and substantially increase the deuterium density [4, 5, 14, 15, 97].

The progress of the DD reaction results in the production of tritium in appreciable amounts, which immediately participates in the thermonuclear reaction

$$\mathrm{D} + \mathrm{T} = \mathrm{n} + {}^{4}\mathrm{He} + 17.6\,\mathrm{MeV}$$

with deuterium, its cross section being 100 times greater and its energy liberation being five time higher than that those of the DD-reaction. Furthermore, the nuclei of uranium envelope undergo fission under irradiation by the fast neutrons produced by the DD-reaction and substantially increase the explosion power. It is precisely this circumstance that selecting uranium as the envelope substance and not another heavy material.

The power of thermonuclear process in deuterium could be substantially increased if a part of the deuterium were replaced by tritium from the very outset.

Indeed, making a thermonuclear charge in the form of deuteride-tritide and lithium-6 deuteride resulted in a radical increase of the thermonuclear process power and an energy liberation from the uranium shell, which was several times higher than the thermonuclear energy liberation.

Such are the physical ideas underlying the first version of our thermonuclear weapon".

The temperature dependence of thermonuclear reaction rates (Fig. 4.8) makes preferable the deuterium-tritium fusion reaction, whose efficient progress requires temperatures of ≈2–10 keV. For a thermonuclear plasma expansion velocity of 10^8 cm/s this leads to a characteristic time of the order of 10^{-8} for a spherical target with a radius of about 1 cm. The energy balance condition for such a thermonuclear reaction (the Lawson criterion [55]) is of the form

$$n\tau \sim \rho r/4c_s m_i \approx 2 \cdot 10^{14}\,\mathrm{c/cm^3},$$

which corresponds to $\rho r \approx 0.1$–$3\,\mathrm{g/cm^2}$ and requires compressing the thermonuclear fuel to a density of tens of grams per $\mathrm{cm^3}$. For a temperature of 10 keV this corresponds to v immense pressures of several Gbar [35].

A high thermonuclear plasma density is also required to enhance the reaction progress and shorten the range of thermonuclear alpha particles: they are stuck [35–37] in a dense target and produce a thermonuclear burn wave, which propagates from the microsphere center to its periphery (see Fig. 7.12 in Sect. 7.2.1).

4.2.3 Hydrodynamic Thermonuclear Fusion

The hopes to produce the requisite superextreme thermonuclear fuel conditions with the aid of chemical explosives (like in a nuclear fission charge) were not realized [82] owing to the insufficient power of explosives and the development of several instabilities, in particular the Rayleigh–Taylor instability, under high degrees of compression. Despite a significant effort in "hydrodynamic" ignition, to date this approach permitted obtaining a thermonuclear neutron yield of $\approx 5 \cdot 10^{13}$ [17, 82, 119].

The VNIIEF scientific supervisor academician R.I. Il'kaev views this problem as one of important unsolved problems of explosion nuclear energetics [58]: "It seemed highly attractive to "set on fire" the thermonuclear fuel by cumulating in it the energy of explosive's detonation. Since then over a hundred major experiments have been carried out, but the problem remains unsolved and its solution supposedly is still a long way off. Under these conditions the degrees of compression of the central metallic shells range up to ≥ 50 and the thermonuclear fuel density exceeds 10^2 g/cm^3. Perhaps, here we are dealing with the fundamental development of instabilities whose suppression is still beyond our practical capabilities".

In the discussion of this line of thermonuclear research we shall follow a review [82].

The work on hydrodynamic thermonuclear fusion (HDTF) supposedly was first undertaken in Germany during the Second World War in connection with the German Atomic Project [61, 119]. In elaboration of the principle of a cumulative charge (panzerfaust), which was first proposed also in Germany, there emerged an idea of implementing thermonuclear fusion at the focus of a spherical charge with an embedded shell [83]. This research was favored by the construction of the theory, which became classical, of a converging spherical shock wave by Guderlay.

At that time these works were not known in the USSR. It was not until 1945 that L.D. Landau and K.P. Stanyukovich proved, independently of each other, the fact of pressure increase, i.e. the cumulation at the front of a converging shock wave in a continuous medium [71].

In the USSR the work on HDTF was pioneered by A.S. Kozyrev's idea (1945) that the pressures and temperatures sufficiently high for the progress of thermonuclear reactions in heavy hydrogen isotopes may be attained at the focus of a spherical charge of a chemical explosive [68]. Furthermore, proceeding from this idea Kozyrev proposed the design of an explosion thermonuclear reactor.

According to the subsequently made estimates, to attain the high (≈ 2 keV) temperatures required to excite a self-sustained thermonuclear reaction (ignition)

with an explosive charge of ≈50 cm requires a spherically symmetric shell "convergence" down to a radius of several tenths of a millimeter. In this case, it would be possible to excite a thermonuclear burst in a DT-mixture of mass $\approx 10^{-3}$ g [81].

The subsequent intensive experimental efforts (see review [82]) were aimed at finding optimal spherical cumulation schemes, studying the instabilities which impeded deep implosion, finding suitable highly uniform explosives, and studying other complex gas-dynamic processes.

The most advanced of the HDTF charges developed consists [82] of alternating layers of light and heavy materials, which efficiently extract energy from the explosive.

Advantage was taken of a liquid explosion, which made it possible to get rid of explosive density variations emerging from the nonuniformity of explosive composition and eliminate technological joints and gaps between structural elements.

A change-over to a highly symmetrical multipoint initiation system with the highest possible position uniformity of 1000 initiation points on the external spherical charge surface with the symmetry of a regular dodecahedron permitted attaining a high precision of focusing, which was different from the expected geometry by no more than 0.1 mm [81, 82]. In this case, it was possible to bring the accuracy of manufacturing of this cumulative system down to a level of ≈0.03 mm for external layers of the system and to ≈0.003 mm for its internal elements [18].

A maximum yield of $5 \cdot 10^{13}$ neutrons, which is currently record high for suchlike advanced systems, was recorded on 10 December 1982 from the center of a target containing DT-gas with an initial radius $r_0 \approx 1$ mm and an initial density $\rho_0 \approx 0.1$ g/cm^3. According to estimates [82], a temperature $T \approx 0.65$ keV and a highest density $\rho \approx 80$ g/cm^{-3} were achieved. A value $\rho r \approx 0.8$ g/cm^2 is presently record high for inertial thermonuclear fusion and sufficient for the ignition of the DT gas if the temperature is raised by about a factor of 3–4. However, in this experiment the neutron yield turned out to be lower than the calculated one by 2–3 orders of magnitude [18, 82].

To explain this disparity, a hypothesis was introduced about the existence of a systematic vertical asymmetry constituent in the liquid explosive charge, which was probably due to the effect of gravity on the density of the liquid explosive, and tolerance-related fluctuations, which are random in amplitude and appear from experiment to experiment (these fluctuations give rise to a neutron yield instability of several tens of percent). This hypothesis was partly confirmed by dedicated experiments [82].

The discordance between the idealized simulational and experimental values of the neutron yield in HDTF systems is attributable [82] to the effects of asymmetry and mixing at the interfaces between different-density substances, which are neglected in simulations. The degree to which these effects are taken into account by contemporary simulation techniques does not permit making an adequate description of the available experimental data.

Scientists have recently begun to computationally take into account the inflow of jets of the heavy substance of the compressing shell to the central gas. The jet formation takes place due to the growth of small-scale perturbations, which

originate from the structural features of the materials of the central shells and their surfaces. The simulations that include this mechanism of gas pollution and the consequential lowering of its peak temperature reveal a substantially greater effect than the calculations by the existing theories of developed turbulence.

The simulations made to date to include jet mixing yield promising results both as regards explaining the experimentally observed neutron yield and lowering this effect (and therefore increasing the neutron yield) with the corresponding structural and technological improvements of the HDTF systems.

The Rayleigh–Taylor instability and turbulent mixing emerge on the light-material side for a tangential discontinuity of velocities at the interface between different-density media when the interface is accelerated (in particular, in the deceleration of the compressing heavy shell by the central light gas, as well as in the deceleration and acceleration of the heavy shells of a layered structure by its light layers) [25, 28, 73, 89]. An instability of the interface between two different-density media also emerges after the passage of a shock wave front through this interface—the Richtmyer–Meshkov instability [73, 101]. Also worthy of mention is the strong dependence of the instability and turbulent mixing on the physical viscosity and strength of materials, which particularly important for the outer domains of the HDTF systems. The positive effect of high strength and refractoriness of the materials in use has been experimentally proved [82].

Another possible sources of small-scale perturbations are related to substance mesostructure [62]. External layers, in which the substance has not yet melted, are partially deformed. according to modern notions, the plastic flow of continuous medium proceeds not as the deformation of continuum but as the motion of plasticity sites at the meso-scale level of 1–100 μm. These sites are likely to be inherently vertical. The velocity dispersion for a free boundary at the instant of arrival of a shock wave was experimentally recorded and measured. That is, the nonuniformity of plastic flow at the meso-scale level may be a source of small-scale velocity perturbations. This flow may be figuratively compared with the motion of a freezing river, when needle ice is flowing. It is therefore necessary to employ and develop elastoplastic flow models. In doing this it is possible to lean upon the vast materials of theoretical and experimental research in this field [62].

The plastic flow of molten inner shells located at low radii may also be a source of such perturbations. A cumulative flow converging to the center is always attended with a shear, which in turn is a source of small-scale turbulence.

The conditions for the ignition of thermonuclear reactions may be attained by suppressing the adverse effect of mixing and improving symmetry (by compensating or removing the regular constituent of asymmetry, etc.) [82]. With retention of the achieved level of asymmetry and mixing, it is possible to approach the fulfillment of ignition conditions by increasing the charge size.

The difference of HDTF from other kinds of inertial thermonuclear fusion consists in the degree of energy cumulation, which was estimated from the temperature ratio [82]: $k = T_{\text{eff}}/T_{\text{BB}}$, where $T_{\text{eff}} = 2\,\text{keV}$ is the effective DT-mixture ignition temperature and $T_{\text{BB}} \approx 1\,\text{eV}$ is the temperature of explosive detonation products. Hence we obtain $k \approx 10^3$ for the HDTF. For laser- and ion-beam thermonuclear

fusion projects, the temperature of the vaporized part of the shell is $\approx$100 eV, i.e. $k \approx 10$. This difference underlies the main difficulties associated with the feasibility of HDTF implementation. That is why it is unlikely that any information obtained in laser fusion research can be directly extended to the HDTF. Quite the reverse: the data of HDTF research as obtained under more severe conditions may be employed for other kinds of inertial thermonuclear fusion.

The method of moderately precompressed (to a density of the order of several tens of grams per 1 cm^3) gas ignition by a focusing shock wave may turn out to be more promising, because in this case the effects of Rayleigh–Taylor instability and mixing are not so strong for the peak shell-driven gas compression required for the ignition. True, the question remains of how to achieve the moderate cool precompression of the gas with its subsequent compression and heating by a sufficiently symmetric ignitor shock wave. Suchlike experimental investigations of not only the HDTF systems but also, for instance, laser targets exposed to a double pulse, which produces precompression and the formation of an intense focusing shock wave capable of igniting the target, are unfortunately absent so far.

A different HDTF scheme is depicted in Fig. 4.20 [17]. In this scheme, a metal liner accelerated by the detonation products of a condensed explosive effected a quasi-spherical compression of deuterium and its mixture with xenon at the end of a conical target. The use of a plane "layer cake" version for raising the liner velocity to 6 km/s and a small admixture (1–3 %) of xenon for increasing the deuterium plasma temperature made it possible to record a neutron yield of about 10^6 thermonuclear neutrons per explosion in these experiments.

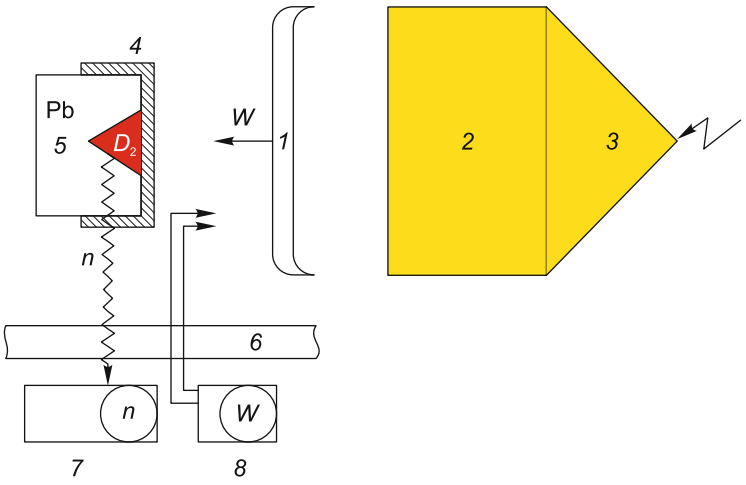

Fig. 4.20 Schematic representation of the facility for dynamic thermonuclear plasma compression in conditions of acute-angled geometry: *1*—liner; *2*—explosive charge; *3*—detonation lens; *4*—target lid; *5*—target; *6*—protective steel housing; *7*—neutron detection unit; *8*—liner velocity measurement unit [17]

A series of numerical simulations of deuterium plasma compression under laser irradiation were performed for analyzing the processes in targets and optimizing experimental parameters. The simulations were made in the framework of the simplest model of a spherically symmetric two-temperature plasma with the inclusion transfer processes, radiative loss, and thermonuclear reactions. This model had been employed earlier to describe the dynamics of conical targets in laser experiments. The simulations suggest that there are two compression stages. At first a series of waves, which experience successive reflections from the liner and the center, heat and ionize the gas to produce radially quasi-uniform profiles of hydrodynamic parameters. Next there occurs an adiabatic aftercompression of the plasma with an entropy determined by the irreversible processes of the first stage. Estimates suggest the effect of nonsphericity of the liner is negligible. The shock waves that emerge in lead at the instant of liner–target collision have no effect on the process of compression either. The initial stage of real compression is therefore described adequately by the one-dimensional model. Appreciable non-one-dimensionality effects may be expected at the final stage, when the cone deformation and thermal conductivity become significant. Until this moment the compression stage may be considered to be adiabatic, and the limiting parameters required for calculating the neutron yield may be estimated knowing the specific plasma entropy and using the semiempirical equation of state of lead. The calculations give the following values: $P \approx$ 50–100 Mbar, $T \approx$ 0.3–0.5 keV, $\rho/\rho_0 \approx 10^3$, which corresponds to a neutron yield in the 10^4–10^8 range.

In conclusion of the section devoted to HDTF we note that experiments in explosive compression offer an instructive approach to the study and optimization of targets for pulsed thermonuclear fusion. Apart from a significant broadening of the energy range, the explosive method permits studying the hydrodynamics of compression in pure form, without considering the complicated processes of the interaction between corpuscular beams or light with plasmas.

4.2.4 Explosive Thermonuclear Fusion

A nuclear explosion provides a million times higher power than a chemical one, which makes it a more attractive way of initiating explosive thermonuclear reactions [49, 88, 94–97].

Considered at the first stage in 1952–1954 in the framework of the Soviet Atomic Project [72] was the hydrodynamic problem of a thermonuclear explosion in a normal-density liquid deuterium ball (Fig. 4.21). The main conclusion was that the explosion shock wave in deuterium is strongly attenuated due to radiative energy loss and the nonlocality of fast neutron energy liberation. At that time this negative result in essence signified that the direct way of making a hydrogen bomb led to a deadlock. Detailed numerical simulations performed independently 60 years later bore out this “historical” result and revealed the special physical features of the resultant attenuation. Most pernicious is the radiative energy loss, which is made up

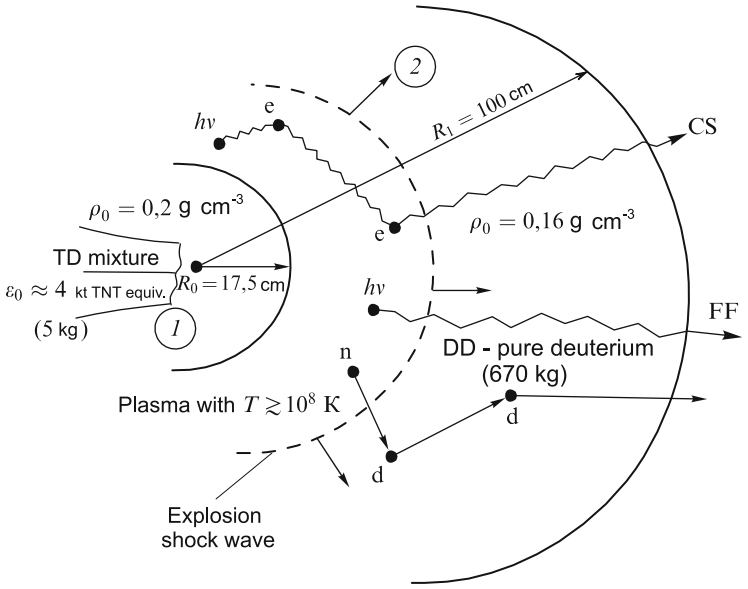

Fig. 4.21 Schematic of the thermonuclear explosion of a deuterium sphere (for details see [72])

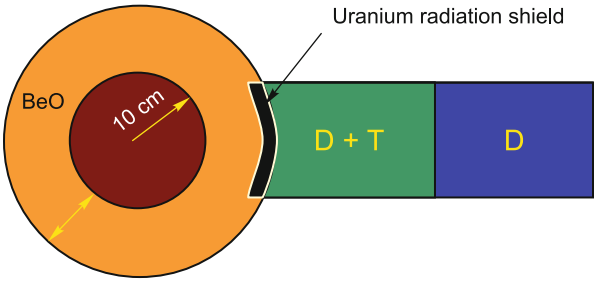

Fig. 4.22 Diagram of the "Classical Superbomb" from Fuchs's material [47]

of bremsstrahlung and the effect of inverse Compton scattering of the generated photons from hot electrons. The role of energy transfer by fast neutrons is less significant, and it was adequately taken into account.

The "Classical Superbomb" version, which is due to E. Fermi, intended for the ignition of thermonuclear reactions with a fissioning charge is schematized in Fig. 4.22 [47].

This thermonuclear reaction ignition scheme, which is referred to as the "Tube", was under active development in the USSR and the USA in the early 1950s [17, 49, 88, 94–97]. The device under consideration comprises a tube filled with a deuterium–tritium mixture; at the end of the tube is a nuclear detonator charge, which is intended to excite a thermonuclear detonation wave in the tube. The propagation conditions for this thermonuclear detonation are determined by the tube

diameter, which the lateral radiative plasma cooling depends strongly on. Unlike the well-known "critical diameter" theory for Yu.B. Khariton's "chemical" detonation, in this problem there emerge two critical diameters, which are numerically close to each other and eventually do not permit implementing this thermonuclear charge scheme (for more details, see [34, 35, 97]).

According to [34], the foundation of thermonuclear detonation treatment is Yu.B. Khariton's theorem [121] that any exothermal substance is capable of detonation when its characteristic dimension exceeds some minimal ("critical") diameter. The thermonuclear reaction rate is a strong function of the temperature. Along with energy liberation there is energy loss due to the heat transfer through the side surface. The equality of volume energy release and surface loss defines the typical temperature $T_{\max}$ and therefore the burn time. On the other hand, the plasma lifetime, which is defined by its hydrodynamic expansion, by the order of magnitude is

$$t_\rho = \frac{r}{c_s} \cong \frac{r}{\sqrt{T_{\max}}}.$$

Comparing these two times gives the critical dimension [34]. Since the burn rate is proportional to the substance density ρ, in different systems the similarity is constructed in the "optical thickness" parameter ρr. This signifies that dimensionless quantities, like the burnup depth, are functions of ρr. In particular, the critical dimension $r \sim 1/\rho$, and therefore the mass capable of burning, is $M \sim 1/\rho^2$ for a sphere and $M \sim 1/\rho$ for a cylinder.

At the same time, researchers encountered another difficulty when studying the thermonuclear detonation in deuterium: an upper limitation on the tube radius [34, 97]. This limitation did not emerge in the detonation of chemical substances. The physical reason was as follows. It is well known that a photon loses a part of its energy in the scattering by an immobile electron. But when the electron is energetic and the photon, on the contrary, is soft, the collision leads to an increase in photon energy. These processes—direct (the Compton effect) and inverse (Comptonization)—eventually result in the thermal equilibrium between the plasma and the radiation (radiation "Planckovization") [34].

Since the main photon source in a hydrogen medium is a very soft bremsstrahlung, in a hot plasma there occurs a parasitic flow of energy from matter to the radiation. To somehow decrease this flow, the tube dimension has to be reduced so as the photons escape to the outside before they gain appreciable energy from the electrons. This signifies that the tube radius may not significantly exceed the Compton photon range [34] ($l = 5/\rho$, $\rho = 0.14\,\mathrm{g/cm^3}$ for liquid helium). According to all calculations, the lower bound for the radius nearly overlapped with the upper one, and the system turned out to be highly sensitive to the details of the process [34]. For instance, the thickness and material of the wall confining liquid hydrogen had a significant effect on the general picture [34].

The combination of two factors—the lowest hydrogen charge ($Z = 1$) and a strong D + T reaction—had the consequence that the radiation did not manage to

become Planckian during burning. As a result, the effective radiation temperature remained low and the energy liberation was transferred to the temperature of the material medium.

It has been possible to experimentally observe this effect [34]. From the Doppler energy broadening of 14 MeV neutrons, the DT burn products, an extremely high temperature exceeding 1 billion degrees was recorded directly in an explosion experiment.

Chemical and thermonuclear detonations have much in common. On the other hand, there is a significant difference apart from the simplest one—the difference in caloricity. Usually considered in nuclear fusion is only the DT reaction as the fastest one. It is precisely the use of a deuterium-tritium mixture that makes it possible to minimize the size of the detonation cylinder. This is the only realistic way to pass from the military use of thermonuclear detonation to the peaceful one with any acceptable initiation energy expenditures in conditions of a "laboratory" experiment.

In this case it turns out that a self-sustaining reaction takes place for $\rho r \geq 0.35\,\mathrm{g/cm^2}$ [31]. A hot plasma with a temperature of $\approx 10\,\mathrm{keV}$ exhibits a multitude of energy transfer mechanisms: hydrodynamic detonation, electron thermal conduction, energy transfer by charged α particles and neutrons, and radiative phenomena [34, 35]. Different processes prevail under different conditions: for instance, the energy transfer by 14 MeV neutrons, which carry 80 % of the energy of the $\mathrm{D} + \mathrm{T} \rightarrow \alpha + \mathrm{n}$ reaction, may turn out to be dominant in an infinite medium. For a cylinder of extremely small size, on the contrary, the role of neutrons in "forward" energy transfer is minor, because the medium is transparent for them (the neutron path $l_\mathrm{n} = 5/\rho$ is tens of times longer than the radius). In pure hydrogen substance, as mentioned above, radiative transfer is also insignificant. The energy transfer by α particles is considerably less significant than the electron thermal conduction owing to their short path. In essence, two processes compete: the Jouguet–Zel'dovich hydrodynamic detonation and the high velocity (heat-conductive) burning [34].

For a chemical detonation, the lateral thermal loss, as a rule, is of little significance, while in the thermonuclear detonation there is no way of neglecting the energy loss in the cases of greatest interest. For instance, under some conditions the energy removal by α particles, and not the expansion, defines the critical cylinder radius. Several thermonuclear wave problems were considered in [31, 77].

Therefore, because of radiation loss (the inverse Compton effect) the scheme (Fig. 4.22) turned out to be inoperative [47] and its development had to be abandoned.

A real breakthrough in the initiation of thermonuclear reactions was achieved by academician A.D. Sakharov, who came up with the idea of a thermonuclear "Sloika" (a "Layered Pastry Cake") [49, 88, 94–97].

According to Yu.A. Romanov, one of the key developers of thermonuclear weapons [91]: A.D. Sakharov proposed a novel design: a heterogeneous structure of alternating layers of light (deuterium, tritium, and their chemical compounds) and heavy (^{238}U) substances, which he named "Sloika".

A.D. Sakharov characterized his proposed scheme as follows [98]:

1) "In a "Sloika" there is local temperature equilibrium between substance and radiation. The question of whether this detonation regime exists does not arise (it undoubtedly exists)... The zone of detonation wave is not very wide.
2) Thermal reactions in D give rise to fast neutrons capable of inducing the fission of ^{238}U nuclei, which substantially raises the caloricity.
3) The low photon transmittance of uranium ensures a moderate width of the zone of the shock wave traveling ahead of the burn zone.
4) ... The temperature in the neighboring phases is equalized by radiation transfer, and so from the equality of pressures in the neighboring phases there follows the equality of the number of particles in unit volumes of U and D; ionized uranium "swells" and compresses D by its electron pressure..."

A.D. Sakharov's central idea consisted, first and foremost, in going over to the ignition of compressed thermonuclear fuel by a shock wave in detonation mode and then by a process which received the name "Sakharization" [59].

It turns out that the like considerations were expressed by Taylor in 1946 (the "Alarm Clock" scheme [47]), but American developments took a different path, which was found to be less efficient.

According to [58], the device was a system of alternating layers of fusion material (lithium deuteride-tritide and lithium deuteride) and uranium with different densities of the ^{235}U isotope, providing their gas-dynamic implosion.

Firstly, the initial heating of the fusion material was provided by the nuclear explosion of the central core of ^{235}U. In this case, the ignition of the fusion material requires that it should also undergo implosion. Secondly, when the isothermal regime between the fusion material and the surrounding uranium set in, there occurred additional compression of the fusion material due to pressure equalization (known as "Sakharization"). Thirdly, the fusion material burn took place in the mode of radiation–substance thermodynamic equilibrium. Fourthly, the uranium fission by "thermonuclear" neutrons provided an additional temperature increase of the medium and speeded up fusion reaction, then the additional fission of uranium etc.

During the device development, great importance was attached to the precision of gas-dynamic implosion, and experiment bore out the absence of an appreciable effect of gas-dynamic instabilities on the thermonuclear burn.

The problem of energy liberation scaling was solved [58] along the path of radiation implosion. In 1954, when the capabilities of this approach were recognized, a prototype of a thermonuclear module was made, which was the central part of RDS-6s. Now, under the new conditions of a manifold stronger implosion, the fusion unit exhibited a substantially greater energy liberation (for a fusion material advantage was taken of lithium deuteride). This approach was implemented on 22 November 1955 in the RDS-37 test. It is significant that the influence of hydrodynamic instabilities on fusion burn did not manifest itself in going over to this new type of implosion, either.

The "Sloika" version offers the following advantages [49, 88, 94–97]. First, it provides the possibility to realize the "fission–fusion–fission" principle required to

increase the energy of explosion. The DT-reaction neutrons with energies above the fission threshold of ^{238}U split it to give rise to additional energy liberation. But, what is more important, owing to the low thermal conduction of uranium the heat removal from the bomb substance is greatly reduced. Lastly, being in direct contact with uranium, the light substance turns out to be several-fold compressed and heated to a temperature of tens of millions of degrees. In the circles of nuclear weapons developers this effect received the name "Sakharization" [5, 49, 91, 97]. The physical cause of "Sakharization" is extremely simple: under superhigh temperatures, when the substance is almost completely ionized, the pressure balance between a heavy substance and a light one corresponds to equal electrons densities in them.

This signifies that the light substance must be in a strongly compressed state, which is required for increasing the fusion reaction rate. Should lithium be incorporated into the "Sloika", under neutron irradiation it will transform to tritium, which highly efficiently participates in the fusion reaction, as discussed above [4, 5, 49, 88, 94–97].

The idea of employing the ^{6}Li isotope in the "Sloika" belongs to V.L. Ginzburg. He amiably called lithium deuteride (^{6}LiD) "Lidochka". The fundamental features of the "Sloika" permit varying over wide limits its structural features and constituent materials. The first such suggestion was made shortly after A.D. Sakharov formulated the basic ideas. This is how he wrote about it: "Before long my suggestion was essentially contributed by V.L. Ginzburg, who came up with the "second idea" [97]. On 3 March 1949, in a report "Use of ^{6}LiD in the "Sloika"" V.L. Ginzburg noted: "Emphasized are the advantages associated with the use of $^{6}_{3}$LiD as a deuterium-bearing substance in the "Sloika". In this case, reaction $^{6}_{3}\mathrm{Li} + ^{1}_{0}\mathrm{n} \rightarrow ^{4}_{2}\mathrm{He} + ^{3}_{1}\mathrm{H}$ results in the production of tritium $^{3}_{1}\mathrm{H} \equiv \mathrm{T}$, which gives uranium-splitting neutrons via reactions $\mathrm{D} + \mathrm{T} \rightarrow ^{4}_{2}\mathrm{He} + \mathrm{n}$ and $\mathrm{T} + \mathrm{T} \rightarrow ^{4}_{2}\mathrm{He} + 2\mathrm{n}$ [42]."".

I.V. Kurchatov duly recognized the promise of using ^{6}Li and promptly organized its production. As a result, the Soviet Union was the first to employ it in 1953 hydrogen weapon tests.

Academician R.I. Il'kaev wrote [59]: "The device operation was divided into several stages. The first stage involved the device implosion by a spherically symmetric converging explosion of a HE and ended with the actuation of neutron initiator similar to the initiator in the first atomic bomb RDS-1.

The second stage begins with the onset of a chain reaction in the fissile substance and is a nuclear explosion intended to excite thermonuclear reactions.

The third stage involves an increase in the temperature of the inner fusion fuel and attainment of the level sufficient for thermonuclear burning. This process drives the burn of uranium nuclei and the ignition of the next fusion fuel layer. Of major importance at this stage is the "Sakharization" process".

Unlike the untransportable American installation "Mike" (Fig. 4.23) of mass 62 t, Sakharov's "Sloika" was a transportable device and was dropped from a plane. It was then that a start was made on the development of a rocket carrier for it in S.P. Korolev's design engineering bureau. Subsequently thermonuclear devices became substantially lighter, and Korolev's rocket carrier fulfilled the function of launching the first satellite and the first man in space [49].

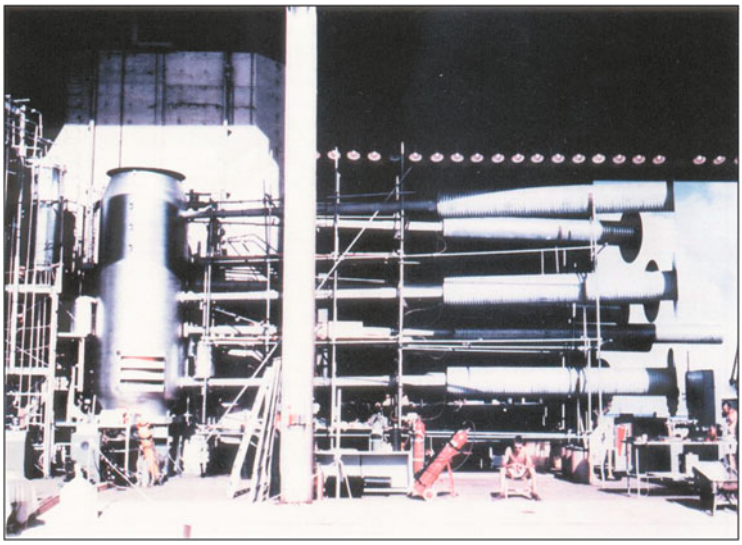

Fig. 4.23 Full-scale two-stage device of Teller–Ulam configuration named "Ivy Mike" was detonated at Eniwetok Atoll in the Marshall Islands on 1 November 1952. The explosion was rated at 10.4 megatons. The installation of overall mass 62 tons comprised a cryogenic vessel, which contained a liquid deuterium–tritium mixture, and an ordinary nuclear charge (the primary) on top of it. Located on the axis of the cryogenic vessel was a plutonium rod, which served as a "spark plug" for the fusion reaction. Both charge units were housed in a common shell of uranium of mass 4.5 tons filled with polyethylene foam, which played the role of a conductor for X- and gamma-ray radiation from the primary to the secondary

The first ideas of thermonuclear weapon were discussed in private by E. Teller in the early 1940s. At the same time Ya.B. Zel'dovich and his colleagues forwarded the corresponding suggestion to the Soviet Government. The basic "thermonuclear" idea, which defines the structure of modern nuclear weapons, was formulated by Teller and Ulam in the February of 1951 [47] and by A.D. Sakharov and his colleagues (the "third idea") [97] in the spring of 1954.

According to [59], at issue was replacement of the hydrodynamic "Sloika" implosion by the compression driven by an atomic explosion. In this case, it was decided to take the "layered" system of spherical configuration as the basis for the physical system of the secondary unit. Since then the compression driven by an atomic explosion has acquired its canonical form, whereby X-ray radiation is considered as the energy carrier from the primary (charge) to the thermonuclear unit. To form directional energy transfer, on A.D. Sakharov's suggestion the primary and the secondary were enclosed in a common shell, which had the capacity to reflect X-ray radiation, and inside of it measures were taken to favor the transfer of X-ray radiation in the desired direction.

The successful test of a hydrogen bomb dropped from a plane on 22 November 1955 marked the completion of the development stage of the basis of Soviet

thermonuclear weapon. Earlier, the corresponding tests "Mike" (1952) and "Bravo" (1954) confirmed the ideas of Teller and Ulam.

Therefore, proceeding along different paths, after failures and successes, the USA and the USSR arrived at the modern design of thermonuclear weapon at about the same time [27]. Its further development followed the paths of refinement and specialization.

In the opinion of academician A.D. Sakharov, the advent of the "third" idea [43–45, 47–49, 88, 94–97] and passage to superextreme plasma states turned out to be a "paradise" for theorists.

A.D. Sakharov reminisced [97]: "By purely theoretical methods, using relatively simple calculations it was possible to describe with confidence what may at temperatures of tens of millions of degrees, i.e. at temperatures like those which exist at stellar centers". For instance, while the equation of state at moderate pressures and temperatures cannot be calculated by a theoretical approach that is anywhere near simple (so far such calculations are impossible even with computers), here it is expressed by a simple formula:

$$P = a\rho T + bT^4$$

(P is the pressure, ρ is the density, T is the absolute temperature, a and b are easily calculable coefficients). The first term is the pressure of completely ionized ideal gas and the second one is the radiation pressure. Lebedev once measured the pressure of light in experiments extremely delicate for his time—here it was immense and determinative. Calculation of the pressure of substance is also simplified at this tremendous temperature: its ionization is complete and the interparticle interaction may be neglected!. Equally simple are formulas for the thermonuclear reaction rate: the number of reaction events per unit time is (for instance, for the $\mathrm{D}+\mathrm{T} \rightarrow \mathrm{n}+{}^4\mathrm{He}$ reaction)

$$N = (\sigma v)_{\mathrm{DT}} \mathrm{n_D n_\tau}$$

(D is a deuteron, T is a triton, n is a 14 MeV neutron, $\mathrm{n_D}$ and $\mathrm{n_T}$ are the densities of deuterium and tritium nuclei), where $(\sigma v)_{\mathrm{DT}}$ is the average value of the product of effective reaction cross section and the relative velocity of the nuclei. The magnitude of $((\sigma v)_{\mathrm{DT}})$ is easily calculated by elementary integration if the reaction cross section σ is known from experiment as a function of colliding particle energy E (Fig. 4.8).

Figure 4.24 shows a sketch of the two-stage device suggested by academicians Ya.B. Zel'dovich and A.D. Sakharov [43–45, 47–49].

According to [47], the charge considered in the memo was large in size and weight (26–30 tons). It comprised two units: a primary atomic bomb and a separate secondary thermonuclear unit, which were enclosed in a massive housing. Initially it was assumed that the compression of the thermonuclear unit would be effected by the pressure of gases flowing to the thermonuclear unit accommodation zone after the detonation of the primary bomb. The description of the physical processes

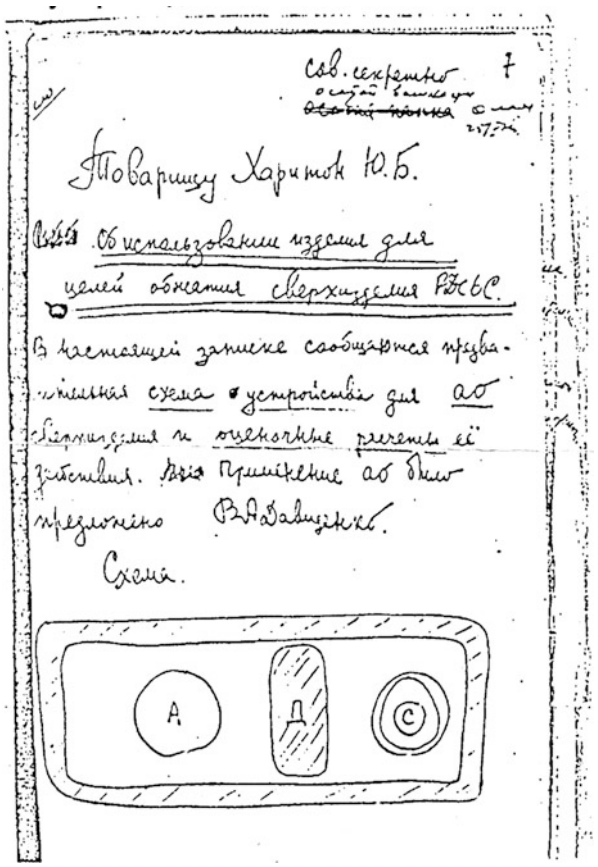
Сов. секретно
Товарищу Харитон Ю.Б.
Об использовании излучения для
целей обжатия сверхсжатия РДС6С
В настоящей записке сообщается предва-
рительная схема устройства для об
сверхсжатия и оценочные расчеты ее
действия. Все приближение об было
предложено Я.Б.Зельдовичем.
Схема.
A
Д
C

Fig. 4.24 First page of Ya.B. Zel'dovich–A.D. Sakharov's memo of 14 January 1954 showing the schematic of a two-stage thermonuclear charge [47]

in the detonation of the charge read as follows [47, 94–96]: "The first stage – the energy propagation through device A (by device A is meant the primary atomic bomb) – is not discussed: during this stage the energy by more than a half is the radiation energy and propagates by radiative heat transfer; however, by the end of this stage there forms a shock wave, whose velocity becomes higher than that of radiation diffusion". Subsequently [47] the radiative mechanism was assumed to be the principal one.

The operation of the thermonuclear "Mike" charge, which implements Teller–Ulam's idea of "photon-driven" compression, is schematized in Figs. 4.25 and 4.26 [5, 27].

In Mike's test (blast yield equivalent to 10 Mt) use was made of a two-stage scheme with liquid deuterium as the thermonuclear fuel. It employed a nuclear detonator and the idea of radiation implosion [5, 13, 27, 43–45, 47–49, 56, 91, 94–96].

The device detonated in the "Mike" experiment and nicknamed "sausage" was a bomb of the megaton class designed according to Teller–Ulam's scheme [5, 13,

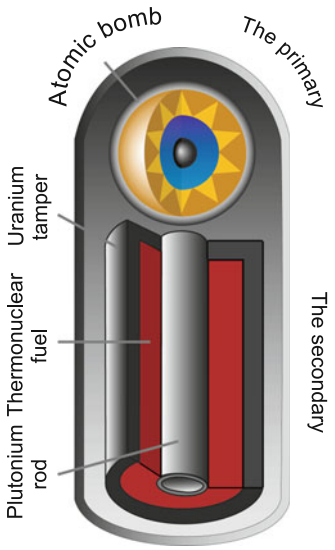

Fig. 4.25 Teller–Ulam's scheme [5, 27]

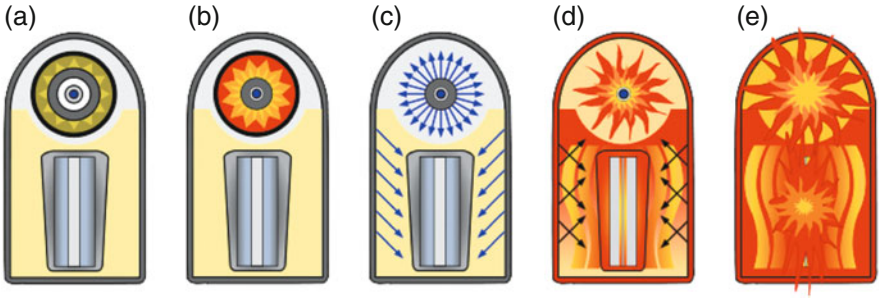

Fig. 4.26 (**a**) Warhead prior to explosion; the primary stage is *above*, the secondary is *below*; (**b**) chemical explosive detonates the primary, compressing the plutonium core to a supercritical state to initiate the fission chain reaction; (**c**) during fission, the primary generates an X-ray radiation pulse, which propagates along the shell interior, penetrating through foam polystyrene filler; (**d**) the secondary compresses due to ablation under X-ray irradiation, and the plutonium rod located inside the secondary passes to a supercritical state and initiates the chain reaction to release a huge amount of heat; (**e**) a fusion reaction proceeds in compressed and heated lithium-6 deuteride, the emitted neutron flux induces the fission of tamper [5, 27]

27, 43–45, 47–49, 56, 91, 94–96]. It was a two-stage charge utilizing a TX-5 atomic bomb at the first stage; the second stage was liquid deuterium stored in a Dewar vessel (Fig. 4.23). Running down the center of the vessel was a plutonium rod, which fulfilled the function of igniting the fusion reaction (Fig. 4.26) . The vessel was enclosed in a housing of natural uranium over 5 tons in mass. The assembly as a whole was accommodated in a huge steel shell two meters in diameter and 6.1 m in

height, with walls 25–30 cm thick (at the left of Fig. 4.23). The inner side of the shell was layered with lead and polyethylene, which formed a channel for conducting thermal radiation from the primary stage to the secondary one. The entire "sausage" weighted 82 tons.

The fission of uranium housing of the charge provided 77 % (8 megatons) of the energy yield. The fusion reaction accounted for only the remaining 2.4 megatons. The isle where the facility was sited was completely destroyed by the explosion; the crater measured 2 km in diameter and 52 m in depth.

A modern thermonuclear warhead is schematically shown in Fig. 4.27 and in [5, 27]. According to [5, 27], in these devices the fissile charge is surrounded by special substances, in which nuclear fusion reactions are initiated under certain conditions.

At the initial stage the detonation of ordinary explosive in the primary charge compresses plutonium irradiated by neutrons from a special triggering "generator". There occurs plutonium nuclear fission attended with energy liberation. This energy in the form of X-ray radiation is directed to the secondary charge, which contains elements capable of thermonuclear fusion. This reaction proceeds between hydrogen isotopes (deuterium and tritium) in a lithium deuteride charge. This self-sustaining reaction results in the formation of a thermonuclear fireball.

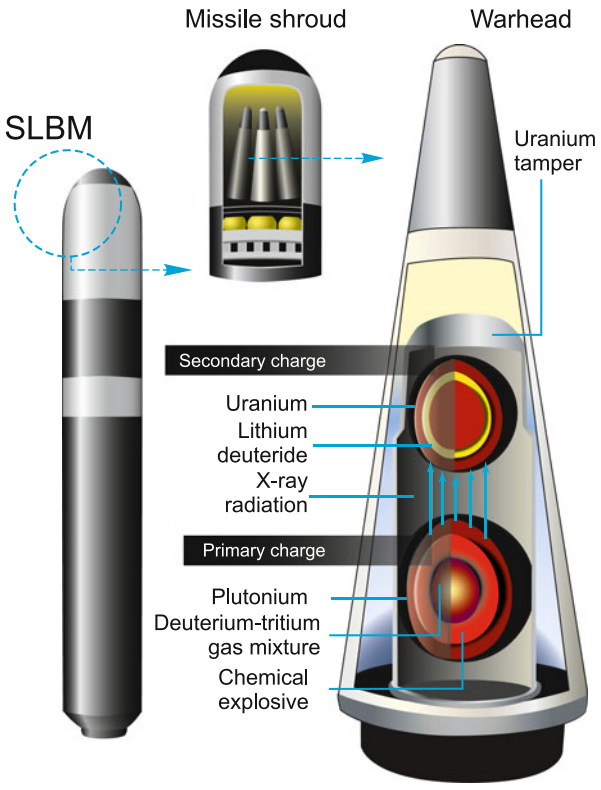

Fig. 4.27 Modern warheads—thermonuclear fusion charges [27]

According to Yu.A. Romanov [97]: "A feature of this bomb is that the energy of its explosion is largely determined by the amount of designed-in thermonuclear fuel and may range into the megatons, while the explosion energy of a fission atomic bomb is limited by a variety of reasons, including the necessity of using large amounts of expensive fissile substance. The matter is that the separation and production of deuterium is much simpler and cheaper than uranium isotope separation and extraction of plutonium".

The development of the high-performance devices of this kind led to the emergence of an important line of basic research—radiative gas dynamics (hydrodynamics) [58]. Review [58] reads:

"This line of basic research is first and foremost related to the problems of thermonuclear charge development. Basic to this development is the principle of radiation implosion, which implies:

- release of a significant fraction of energy in the explosion of a nuclear charge (of the primary unit) in the form of X-ray radiation;
- transportation of X-ray radiation energy to a thermonuclear unit;
- implosion of the thermonuclear unit with the energy of the delivered X-ray radiation.

The implementation of each of the three constituents of this principle relies on radiative gas dynamics.

The nuclear charge explosion, in which the bulk of energy is released in neutron-nuclear reaction in the fissile substance, is attended with transformation of this energy to X-ray radiation energy and the thermal energy of the substance, which are in local thermodynamic equilibrium (as well as to the kinetic energy of the medium). The X-ray radiation is transferred through the substance, emanates from the surface of the fissioning material, and next propagates through the outer regions of the primary unit.

Clearly this mechanism depends heavily on the basic characteristics—X-ray photon path lengths, in which the photon–substance interaction occurs. For substances like uranium, photoabsorption and bound-bound transitions are of first importance...

Investigations into the processes of radiative gas dynamics permitted controlling the transfer of X-ray radiation inside the primary unit and improving greatly the quality of the units as energy sources for radiation implosion, which was of paramount practical importance.

The second part of the principle of radiation implosion is primarily related to research, in the framework of radiative gas dynamics models, into the reflection and passage of X-ray radiation through layered configurations of different materials, which often are multi-element geometrical figures with a complex dynamics. While the main requirement at the first stage was to maximize the X-ray energy yield from the primary unit, at the second stage the main requirement was to minimize the energy loss.

The third part of the principle of radiation implosion is associated with the investigation of X-ray energy transformation to the pressure field which compresses the thermonuclear unit. This field, which is the complex result of radiation propagation through different materials, is axisymmetric in structure. To obtain acceptable compression of the thermonuclear unit requires transforming the axisymmetric boundary conditions in order to achieve symmetric implosion. The solution of this problem calls for the control of radiation fluxes and the gas-dynamic fluxes of high-temperature and low-temperature high-density plasmas, which is realized in the framework of 2D radiative gas-dynamic models.

It is pertinent to note that the features of the "boundary conditions" are such that the thermonuclear unit implosion may be relatively stable or unstable. There are important practical applications in which the processes are inherently three-dimensional; in view of this, 3D radiative gas-dynamic models have also been developed. It is noteworthy that the pressures of radiation implosion which determine the compression of thermonuclear units amount to several hundred TPa and that the implosion is attended with compressions whereby the density of the substances in use exceeds the initial one by several tens of times.

In the solution of these problems the leading part is played by physicomathematical simulation techniques, which is due to the characteristic properties of the information obtained in the tests of thermonuclear charges as well as due to the absence of such possibilities at the present time. The major experimental result involved determination of "stability zones" for the radiation implosion in thermonuclear units as well as determination of the physical factors that push implosion out of these zones.

I emphasize that radiative gas dynamics is a remarkable example of how a basic scientific discipline has made possible the design of devices with an interplay of complicated physical processes, the experimental data on their key parameters being quite scarce".

It is noteworthy that somewhat similar processes take place in the microtargets of controlled inertial fusion, which we discuss in Chap. 7.

The long-term vigorous research has resulted in the development of a variety of witty and elegant schemes of thermonuclear charges for a wide range of applications (including peaceful ones), from minicharges to the most powerful bomb with an energy liberation of 50 megatons. Part of them are shown in Fig. 4.28.

At the present time, intensive efforts are underway to improve the reliability and safety of nuclear charges and efforts to achieve nonproliferation of nuclear weapons. Despite this, the club of nuclear weapon states is gradually expanding (presently numbering nine members) and the number of military nuclear charges is approaching 25 thousand (Fig. 4.29). The Moscow Strategic Offensive Reductions Treaty (SORT) limits the numbers of operationally deployed Russian and US nuclear warheads to 2200 by the year of 2012.

Fortunately, this arsenal is used only as a deterrent and no thermonuclear devices have been used against people.

Fig. 4.28 Arzamas-16. Museum of nuclear weapons

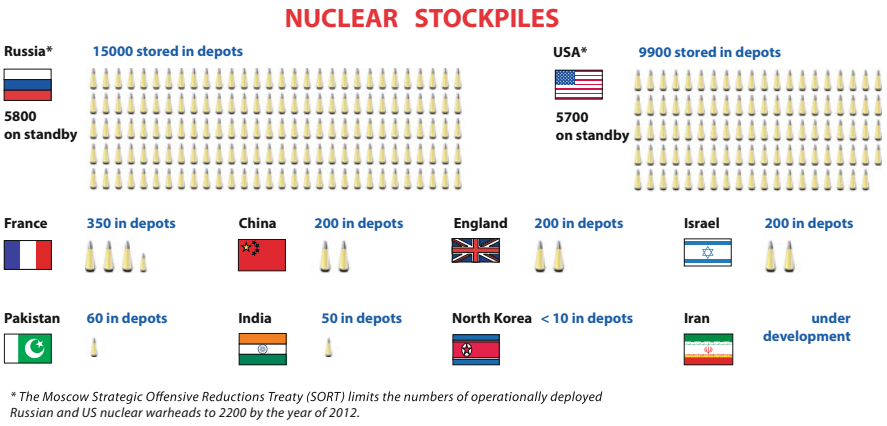

Fig. 4.29 Worldwide numbers of nuclear warheads

4.3 Nuclear Explosions for Studying Extreme States of Matter

The advent of nuclear weapon gave experimenters a source of unprecedented energy density for generating high-power shock waves in condensed media [22, 110]. That is why, along with the measurements of integral characteristics of nuclear explosions, even in the first experiments a start was made on studying the physical properties of substances under extreme pressures and temperatures.

Physicists, and developers of nuclear weapons in the first place, immediately and fully recognized the potentialities of nuclear explosions as an instrument for

generating superhigh-power shock and radiation waves and studying ultraextreme substance states with their aid [10, 22, 36, 37, 110].

Comparative possibilities offered by nuclear explosions for generating high energy densities were considered in Sect. 3.6. Here we discuss these issues in greater detail.

Apart from the possibility of producing ultrahigh energy densities, these experiments possess a number of other unique features. These are a very broad range of pressure variation in experiments, one-dimensionality, and a good symmetry in the pursuance of measurements with the use of large samples, which exceed the laboratory ones in size by orders of magnitude. As a result, a large body of invaluable experimental information was obtained in the ultrahigh-pressure area, whose lower bound is now approached using high-power laser technology [110] (see Chaps. 3 and 5).

The plasma energy densities that are record-high for terrestrial conditions were obtained in precisely the near zone of a nuclear explosion. The physical formulation and main physical results of these experiments are described in a comprehensive review [110], which we will follow in the subsequent discussion.

In the first works on shock waves, measurements were made of the relative compressibility of substances by means of reflection [10, 110] (Figs. 3.29 and 4.30).

This method relies [10, 110] on velocity measurements of a shock wave which successively passes through the layers of substances under investigation; one of these substances is treated as a reference one and its equation of state is assumed to be known. Its Hugoniot adiabat is defined by interpolation between the experimental region and the computation domain which lends itself to description by appropriate theoretical models. The parameters of the initial states of the reference substance are found from the shock velocity in the reference, and the sought characteristics in the

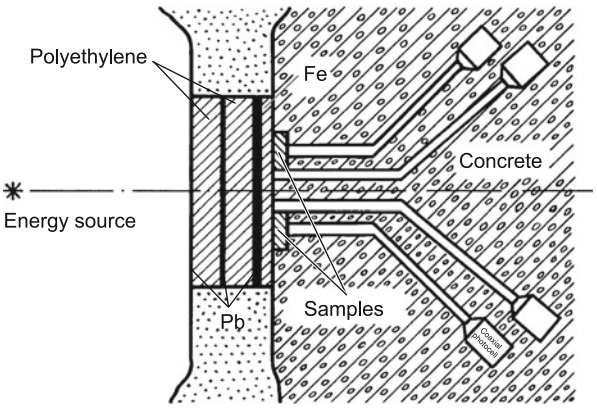

Fig. 4.30 Formulation of experiments to investigate the relative compressibility in the system Fe(screen)–Pb–Cu–Ti [110]

samples under investigation are determined by constructions in the pressure–mass velocity diagram [10, 123].

The first experiments using this technique were performed, according to [110], at the end of 1965 and published somewhat later [10, 12]. At that time the 1 TPa threshold was overcome in a Fe–Pb–U system (3.8 TPa in Fe and 4.0 TPa in U).

Next obtained were data on the comparative compressibility of water (for more details, see [22, 110]) at a pressure of 1.4 TPa, of quartz with initial densities of 1.75 and 1.35 g/cm^{-3} at pressures of 2.0 and 1.8 TPa, of plexiglass $(C_5H_8O_2)n$ at 0.6 TPa, of graphite, rutile (TiO_2), rock salt, aluminum, several rocks (graphite, shale, dolomite) as well as several continuous and porous substances at pressures ranging up to 1 TPa.

The comparative compressibility of metals in a Pb–Cu–Cd system was investigated at a pressure of 1.5 TPa [111] in 1968 and more recently at 5 TPa [112]. In [112], a pressure of 5.2–5.8 TPa was produced for a Fe–Pb system [113, 124] and compressibility measurements were made for porous metals (copper, iron, tungsten [110, 113, 124]) and several other elements at terapascal pressures.

Since the energy of nuclear charges under test was not limited at that time, it was possible [110] to carry out measurements of shock parameters at pressures of several terapascals at a relatively long (up to 10 m) distance from the explosion center. This simplified interpretation of the data and made measurements with attenuation more reliable, because at these distances the shock wave has a good symmetry and relatively low beyond-horizon pressures.

The 10 TPa milestone was passed in [20] and then moved to a level of 700 TPa [21, 116].

The world record of pressure, at which measurements were made of the parameters of the equation of state of a strongly compressed and multiply ionized plasma, is $P \approx 4$ billion atmospheres, which was obtained in the near zone of a nuclear explosion [24, 104, 116].

The Los Alamos data on the absolute compressibility obtained in conditions of underground nuclear explosions are contained in [84–87], and those of the Livermore Laboratory (USA) in [74]. Chinese scientists made themselves known in this capacity in 1990 [41].

Experiments to measure the relative compressibility of substances contain an uncertainty arising from uncertainties in the equation of state and the reference. This uncertainty increases with the pressure range under investigation.

The technique of "absolute" measurements of the shock compressibility of materials is devoid of this drawback, Fig. 4.31 [22, 110]. In this scheme, an iron liner is accelerated by a nuclear device to a velocity W and strikes an iron target. The approach velocity W and the in-target shock velocity D_{Fe} are measured in these experiments. From symmetry considerations the mass substance velocity in the shock wave $U_{Re} = W/2$, which gives the pressure $P_{Fe} = g_0 D_{Fe} U_{Fe}$ and the energy $E_{Fe} = U_{Fe}^2/2$.

The data obtained using this technique are independent of "reference" properties, but several conditions must be fulfilled: the initial conditions ρ_0, P_0, T_0 of the liner and the target should be well known (the heating by the radiation of a nuclear

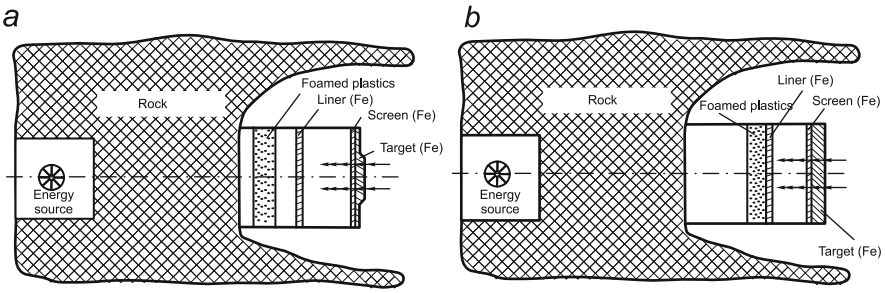

Fig. 4.31 Two versions of an accelerating device for determining the shock compressibility of iron using deceleration technique [110]

Table 4.5 The parameters of the experiments [110]

Experiment scheme	W_1 (km/s)	W_2 (km/s)	W_{cp} (km/s)	D (km/s)	U (km/s)	P (TPa)	ρ (g/cm^3)	$\sigma = \rho/\rho_0$
11a	36.5	36.5	36.5 ± 1.0	28.85 ± 0.7	18.25	4.13	21.34	2.72
11b	42.7	42.7	42.7 ± 1.2	32.4 ± 0.8	21.35	5.42	22.99	2.93
11c	48.6	58.8	60.8 ± 2.54	43.5 ± 1.0	30.60	10.50	26.50	3.37

explosion should be low), the velocity of liner approach must be constant ($W = const$) and well known at the instant of collision, the in-flight symmetry of the liner and the symmetry of the shock wave in the target should be good. The rigorous equality $U = W/2$ may be achieved only for a smooth heating-free acceleration of the liner with retention of its integrity. In reality, departures from this equality are due to the shock-wave heating of the liner and its backing by the vaporized material. According to [110], in the scheme of Fig. 4.31a the liner acquires 80 % of its velocity W on traversing 20 % of its path to the target. The parameters of the experiments of Fig. 4.31 a, b are collected in Table 4.5 [110].

The subsequent development of dynamic methods in the high-pressure range is related to the use of penetrating physical fields [22, 36, 37, 110].

American researchers [87] came up with a scheme for measuring the mass velocity in the high-pressure range, which is based on the shift of the resonances of neutron interaction with the nuclei of moving substance relative to their position for the nuclei at rest (Doppler shift). To obtain high pressures, use is made of the energy of uranium nuclear fission by the neutrons produced in a nuclear explosion.

According to [84], the sample of a material under investigation abuts on a plane uranium layer. The velocity of the shock front is determined from the instant of the occurrence of light flashes on the check surfaces of the sample. To measure the mass velocity, use is made of neutrons with energies in the 10–10^3 eV range, in which resonances are usually located. Of interest are substances with pronounced nuclear resonances, which provides appreciable attenuation of the neutron flux transmitted through the sample and recorded in experiments. When the resonance in a sample is observed for a neutron energy ε_n (or for a neutron velocity v_n) and a part of the

sample's substance is moving in the direction of observation with a velocity u, there will additionally occur attenuation of the flux of neutrons with velocity $v_n' = v_n + u$. In the spectrum of the neutron flux transmitted through the sample there will be two minima due to the specified resonance. Experimentally the problem consists in recording the spectrum of the neutron flux. If the neutron source may be treated as an instantaneous one, measurements of the neutron spectrum are made from the neutron time of flight through a known distance L. In this case, the time resolution of the resonances will be defined by the difference of at-detector arrival times for the neutrons with velocities v_n and v_n'. The ratio $u/v_n \ll 1$, so that $t \sim u$.

For a resonance at an energy $\varepsilon_n = 10^3\,\text{eV}$ and a shock wave intensity $u \geq 10\,\text{km/s}$, the values $t = 1\,\mu\text{s}$ are obtained for $L \approx 20\,\text{m}$. The neutrons will traverse the distance in a time $t \approx 5 \cdot 10^3\,\mu\text{s}$. According to paper [87], the neutron source duration is equal to 0.5–0.8 μs. The sample thickness is so selected that a significant part of the sample becomes involved in motion during the source operation.

The neutron spectral flux density in the resonance range $\varepsilon_n = 10\text{–}10^3\,\text{eV}$ is essential to the experimental implementation of the method. The number of such neutrons in the fission spectrum is quite small. To increase it, in [87] a thin layer of a hydrogen-bearing substance (plexiglass) was placed between uranium and the sample (Fig. 4.32). This trick permits increasing the neutron flux at the boundary by about an order of magnitude.

The method under discussion for measuring the mass velocity is not universal. For substances under investigation, the resonance cross sections should provide a well-detectable attenuation of the neutron flux both by immobile and by moving substances over a thickness comparable to the measuring base. These properties are inherent in molybdenum, iron, copper, etc. Furthermore, there are elements whose nuclei possess anomalously large resonance cross sections (tungsten, gold, cobalt). Placing thin layers of these elements in the sample under investigation may also be employed for mass velocity measurements. Furthermore, in some cases the energy broadening of individual resonances may be used for estimating the substance temperature before and after the shock front.

The resonances are most pronounced for molybdenum, which was investigated in [87]. A pressure $P \approx 90\,\text{Mbar}$ was realized in uranium; recorded in molybdenum were $D = 18.7\,\text{km/s}$ (±5 %) and $u = 10.2\,\text{km/s}$ (±5 %). The accuracy achieved in the measurements hinders the use of the resultant experimental point for calibrating the equations of state of molybdenum (Fig. 4.33). The main sources of measurement uncertainties arise from the uncertainty in neutron source duration and different resonance spreading mechanisms.

However, the contributions of many of these factors become smaller with increase in mass velocity, so that for $u \approx 100\,\text{km/s}$ there is a possibility in principle to attain an accuracy $\Delta u/u \approx 1\,\%$. This gives impetus to attempts to further improve the method.

The authors of [117] proposed a method for the simultaneous measurement of D and u with the aid of gamma-active reference layers introduced into the substance under investigation. In the course of gas-dynamic motion the reference layers

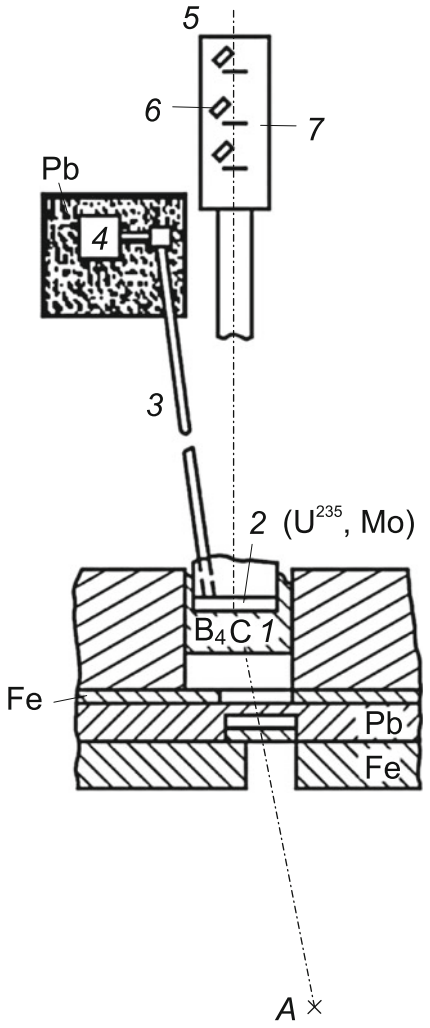

Fig. 4.32 Schematic of experiments on the generation of intense shock waves by an underground nuclear explosion [87], *A*—nuclear device; *1*—neutron absorber B_4C; *2*—experimental assembly of uranium-235 and molybdenum; *3*—12-m long waveguides; *4*—optical radiation detectors; *5*—time-of-flight neutron spectrometer; *6*—solid-state detectors; *7*—lithium and plutonium foils

are entrained by the moving substance. A system of collimating slits (Figs. 4.33 and 3.30) is employed to detect the moments the layers pass the check positions.

The "plane" geometry of a shock front, reference layers, and collimating slits, whereby the planes of the corresponding surfaces are parallel to each other, is easiest to realize in experiments (Figs. 4.33 and 3.30). To this end, placed in the path of the shock wave is a cylindrical channel made of a substance (magnesium, organic matter, etc.) with a density that is lower than the density of the material in which the experimental facility is accommodated. As follows from the data of two-dimensional gas-dynamic simulations, placement of this channel has the effect that the shock front passes ahead of the shock front in the surrounding medium and the wave front is plane in the central part of the cylinder, its diameter being

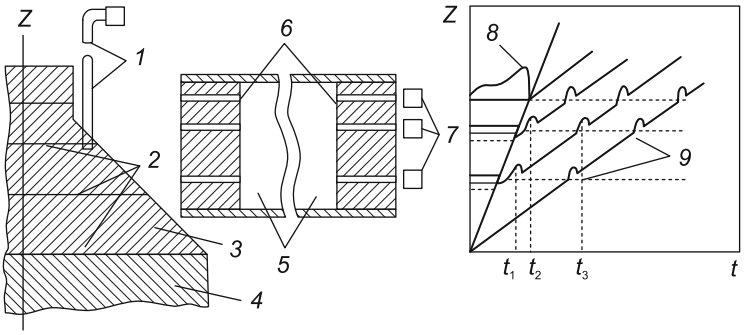

Fig. 4.33 Layout of the experiment for measuring the absolute compressibility of aluminum: *1*—optical channel; *2*—reference layers; *3*—substance under investigation; *4*—channel of shock formation; *5*—collimating system; *6*—collimating slits; *7*—γ-ray detectors; *8*,*9*—radiation signals from immobile and moving references [23, 117]

equal to $\approx 2/3$ of the external diameter. The measuring unit is placed at the end of the cylinder. The collimating system is protected by placing dense material layers (lead, steal) in the path of the shock wave to rule out damage to the system prior to completion of recording the moments the reference layers pass the check positions.

To measure the mass velocity u it is sufficient to record the instants of time at which one reference layer passes the planes of two collimating slits; then, $u = d/(t_3 - t_1)$, where d is the interplane distance (see Figs. 4.33 and 3.30). Placing two reference layers by two collimating slits permits determining D by comparing the instants of the onset of their motion, $D = d/(t_2 - t_1)$. In this case, the shock compression δ at the shock wave front is determined from the measurements of only the time intervals: $\delta = (t_3 - t_1)/(t_3 - t_2)$. The number of reference layers and collimating slits in experimental facilities usually exceeds the specified minimum. This makes it possible to obtain information about the nonstationarity of the shock-wave phenomenon under study as well as about neutron- and gamma-ray-induced effects.

The key element in the proposed simple scheme, which enables time measurements, is a reference layer. Its radiation must pass through the peripheral layers of the substance under investigation, in which the gas-dynamic motion is much different from the "plane" shock-wave flow implied. That is why hard gamma-ray radiation sources are used in the reference layer. Because of the nonstationarity and high velocity of the processes, the radiation intensity of the layer must provide the possibility of recording the moments it traverses the plane of the collimating slits with the use of detectors like a PM or a coaxial photocell in an analog mode.

That is why in [24, 117] use was made of pulsed sources which existed at the preferred stage of the gas-dynamic process. In particular, a high-intensity gamma-ray source was obtained in the neutron irradiation of a substance whose nuclear possess a radiative capture cross section which exceeds the corresponding cross section of aluminum by a factor of $\approx 10^3$. Existing pulsed sources normally produce

fast neutrons ($E_n \approx 1$ MeV). Radiative capture reactions are effective at lower E_n. The neutron pulse must therefore pass ahead of the recorded gas-dynamic motion by a time interval required to moderate neutrons in the substance under investigation to optimal energies. In some cases, in reference layers use can be made of europium, for which the (n, γ) reaction cross section is $\sigma = 220 \pm 80$ barn for $E_n = 10$–100 eV.

As seen from the foregoing, aluminum is widely used as a reference material in the applications of reflection technique. In the 5–150 Mbar range there are significant ambiguities in the equation of state of this substance. This underlies the interest in aluminum in the application of this technique [24, 117]. Of course, other reference/sample substance combinations are possible. In individual cases, it is supposedly possible to use pulsed neutron sources (converters) in reference layers.

During moderation of neutrons, their density is hardly affected by diffusion and absorption. The relation between the requisite gamma-ray reference intensity Γ (s^{-1}), on the one hand, and the fast neutron flux Φ (cm^{-2}) and the reference mass M, on the other, was estimated in [117]:

$$\Gamma \sim \Phi \sigma N v M / \ell \sim 0.2 \cdot 10^7 \Phi M.$$

Here σ is the (n, γ) reaction cross section for the nuclei of the reference material; N is the number of these nuclei per unit reference mass; ϑ is the moderated neutron velocity; ℓ is the path of external flux neutrons in the substance under investigation. The numerical value is given in [24] for aluminum and the reference material—europium oxide EU_2O_3 compacted to a density of 2.7 g/cm^3. For europium, σ increases with neutron deceleration faster than v^{-1}, and therefore Γ will increase until the rate of neutron inflow to the aluminum reference layer becomes equal to the rate of its absorption by europium. On further neutron moderation the magnitude of Γ will decrease due to neutron depletion of the aluminum domains surrounding the reference layer. If the layer thickness is ~ 5 cm, its highest radiation intensity is attained for $\sigma \approx 200$ barn, which corresponds to a neutron energy $E_n \approx 10$–100 eV. The characteristic time of neutron moderation to the specified E_n is equal to 10–15 μs.

The neutron moderation in the sample heats the substance under investigation, which affects its shock compressibility. For simplicity of experimental data interpretation it is required that this effect should be weak. This sets an upper bound on the flux Φ. In the study of aluminum, acceptable values are $\Phi < 10^{17}$ cm^{-2} [24, 117]. The lower bound on the flux stems from the necessity of increasing the dimensions of the measuring unit.

The reference layers are nonuniformities in the material under investigation, which are taken into account in the interpretation of experimental data with the use of gas-dynamic calculations. To lower the uncertainties arising from the introduction of computed corrections, the reference layer thickness may not exceed 10 % of the measuring base length. The instrumentation employed in the experiments permits obtaining acceptable accuracy of measurements of the time intervals ($\Delta t/t \approx 1$ %) for their length of ≈ 2 μs. In the study of the shock compressibility of aluminum at

a pressure of ~ 10 Mbar ($D \sim 25$ km/s) the base is therefore selected at ≈ 5 cm and the reference layer thickness is $\Delta \leq 0.5$ cm.

The measuring unit (Figs. 4.33 and 3.30) was made in the form of a set of AD-1 (99 % Al, $\rho_0 = 2.7\,\mathrm{g/cm^3}$) aluminum plates, in which reference layers were introduced in the form of tablets. This layer shape is consistent with the cylindrical geometry of the shock formation channel and permits, if need be, accommodating additional collimating systems. To maximize the recorded radiation flux, in the detector direction the thickness of the substance under study should be as small as possible, not distorting the motion of the front and the substance behind it in the region of reference location. That is why the side surface of the unit on the side of the collimating system was made in the form of a plane oriented at an angle of 45° to the direction of front propagation. The shape was checked using three optical channels located at the apexes of an equilateral triangle on a circle of diameter 150 mm (one channel is shown in Fig. 4.33). Measurements were made of the instants of light flashes occurring when the shock wave reached the reference surface perpendicular to the axis of the unit.

The procedure of measurements is complicated by appreciable background phenomena. The main background sources are the primary source neutrons as well as the gamma-ray photons produced in (n, γ) reactions in the sample, in the structural elements of the experimental facility and in the ambient medium. Neutron shielding is achieved by moving detectors away from the substance under investigation. Protection from capture gamma rays was provided by a collimating system. Its lead partitions in fact completely suppress the gamma-ray flux emanating from the measuring unit and its environment. Only the radiation passing through the collimating slits remains unattenuated. When use is made of coaxial photocell detectors, a collimating system length $L \approx 2$ m is sufficient. In the experiments of [117], use was made of ≈ 0.4 cm thick reference tablets ≈ 9 cm in diameter.

The collimating system was made in the form of a set of coaxial lead disks rigidly connected with each other, which had slits of cross section 3×90 cm. The slit width is determined by the characteristic thickness of a shock-compressed reference tablet (≈ 1 mm) and the possibility of aligning the collimating system. The separation between the slit planes are the measuring bases. The uncertainty of determining these base lengths is due to the inaccuracy of system fabrication as well as the nonparallelism of the slit planes, reference layer, and shock front surfaces. The slit planes and the reference layer planes were set parallel to within $\pm 0.2°$. The uncertainty in determining the base length which arises from this nonparallelism is negligible in comparison with the inaccuracy of system fabrication, which amounts to ≈ 2 % for a base length of 50 mm. Checking the shape of the shock front enables, if need be, taking into account the correction to the base length arising from the nonparallelism of the front and reference layer planes.

When determining D, in order to lower the gamma-ray background recorded by detectors prior to the shock arrival, the second and third reference layers (the reference layers and collimated slits are numbered in the direction of shock propagation) were deepened by 1 mm relative to the corresponding slit planes (see Fig. 4.33). The fourth reference layer was located at the center of the slit,

Table 4.6 Results of absolute measurements in aluminum [10, 117]

Experiment	D (km/s)	U (km/s)	P (TPa)	$\sigma = \rho/\rho_0$
1	24.2 ± 0.7	15.1 ± 0.4	0.99 ± 0.03	2.65 ± 0.1
2	23.4 ± 0.6	14.5 ± 0.3	0.93 ± 0.02	2.63 ± 0.7
3	40.0 ± 5.0	30.0 ± 2.0	3.20 ± 0.5	3.90 ± 1.2
4	30.5 ± 0.7	21.0 ± 0.6	1.73 ± 0.07	3.21 ± 0.2

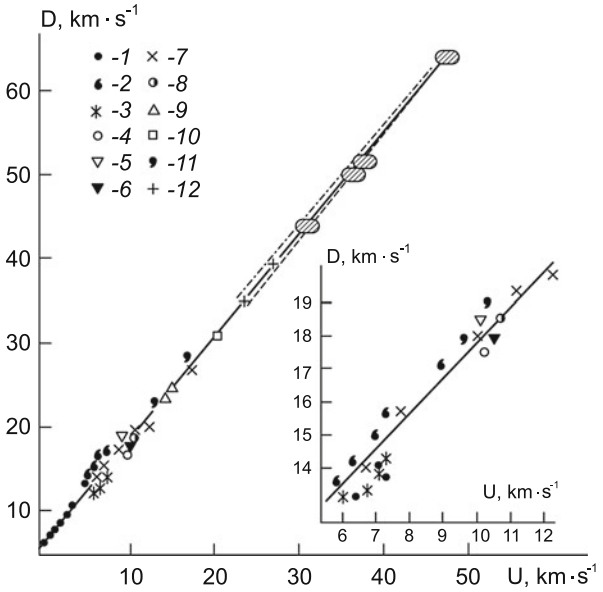

Fig. 4.34 $D \div U$ diagram for aluminum according to the data of laboratory measurements and underground explosions: 7–10—absolute measurements; 11, 12—relative measurements. The ellipses representing different processing versions of the experimental data of [117] are hatched. The *dash-dotted line* shows the interpolation according to [75] and the *dashed line* stands for the calculation using the Thomas–Fermi–Kopyshev (TFK) model

which permitted obtaining experimental information about neutron and gamma-ray processes .

The introduction of high-intensity sources into the sample entails substance heating by radiation. By the instant of shock arrival, the aluminum–reference interface shifts and the state of the sample and reference layer substances changes. This has an appreciable effect on the interpretation of experimental data, and the corresponding processes must therefore be taken into account using gas-dynamic calculations.

The results of measurements processed with the inclusion of the latest methodical achievements in the oscilloscopic treatment, nonstationarity of motion, and reference layers are outlined in [23, 110, 117]. Here we restrict ourselves to a summary table (Table 4.6) and Fig. 4.34, which gives the Hugoniot adiabat of aluminum [110]

with the resultant experimental data. One can see that the Hugoniot adiabat provides, on average, a reasonable description of the experimental data; however, some points deviate by more than the ordinary 1–1.5 % in velocity uncertainty. The possible underlying reasons are considered in [110].

The high-intensity gamma-ray radiation of the reference layers increases the internal energy of aluminum up to ≈1.5 kJ/g [116, 117]. The pressure emerging in this case results in a lowering of aluminum density to ≈2.55 g/cm^3 and compression of the porous reference material, i.e. the wave enters the sample characterized by the initial state $\rho_0 = 2.71$ g/cm^3, $E_0 = 1.5$ kJ/g. The experimental points in the shock adiabat that emanates from this initial state are collected in lines 1 and 3 of Table 4.6. Given in lines 2 and 4 of Table 4.6 are the data converted to the shock adiabat with $\rho_0 = 2.71$ g/cm^3; $E_0 = 0$, at constant pressure. The result of this recalculation depends only slightly on model considerations.

In the third experiment, measurements were carried out near the lower pressure bound for the manifestation of shell effects.

The experience acquired in the use of the reference technique to measure the shock compressibility suggests [117] that there is still large room for its improvement when employing different reference combinations as well as different organization of experiments.

For high energy densities in a substance, which are typical, for instance, for several processes in stellar interior, of major significance is the energy transfer by electromagnetic radiation [10, 36, 37, 123]. To correctly describe these processes requires knowing the optical properties of the substance at different substance densities ρ and temperatures T. There is a vast class of phenomena for which the conditions of local thermodynamic equilibrium between the radiation and the substance are fulfilled [123]. In these cases, to describe the radiative energy transfer it is sufficient to know the Rosseland opacity coefficient $\varkappa$, which is a function of ρ and T [123]. In the general case, the dependence $\varkappa(\rho, T)$ is nonlinear and the energy transfer by electromagnetic radiation is a nonlinear thermal conduction in character.

The presently available theoretical information about the radiative energy transfer coefficients in substances was obtained using calculations based on different theoretical substance models. The methods for calculating opacity coefficients include the Compton scattering, the inverse bremsstrahlung due to free electrons, and the photoabsorption in the lines arising from bound electron transitions. The main difficulties are encountered in the calculation of absorption in spectral lines. They are due to the necessity of including the plethora of electron configurations and all possible transitions between them as well as different mechanisms of spectral line broadening and splitting: the Stark effect, the Doppler effect, etc.

The calculation of $\varkappa$ in a substance with given ρ, T is preceded by the determination of ionic wave functions, the occupation numbers of electron states, the self-consistent potential, energy levels, oscillator strengths, etc. The difficulties encountered in the construction of the theory of a substance which takes a sufficiently full account of the real properties of polyatomic systems in the density and temperature ranges under consideration are discussed in Chap. 8. The simplifications used by the authors of different models exert effect on the

thermophysical characteristics and, in particular, on opacity coefficients, which is quite hard to estimate.

The experimental investigation of the optical properties of substances at high energy densities is an intricate task as regards providing well-controllable conditions of the process and recording the parameters which carry the desired information. One possibility of obtaining experimental data about opacity coefficients involves measurements of the radiation flux through the sample of a substance under investigation, whose thickness is selected proceeding from the applicability condition for the radiative thermal conduction approximation. Another possibility to study the opacity of substances consists in comparing the calculated and experimental transit times of the radiative thermal conduction wave through the samples. When a sufficiently high temperature is produced on the inner boundary of the experimental assembly, initially the energy transfer in the sample proceeds in the regime of a thermal wave (see, for instance, [123]). After a distance the thermal wave front is overtaken by the shock-wave discontinuity. At this stage the substance flow may be treated as a self-similar one [123]. The wave transit time through the sample depends on its thickness and density, the opacity coefficient, the equation of state and the temperature at the sample's boundary. To determine the ratios between the opacity coefficients in different substances it will suffice to employ the same temperature source in the measurements [123] (the dependence on the uncertainty in the initial temperature T vanishes). The relative measurements of $\varkappa$ in a pure substance and in the same substance with a small admixture of an impurity substance which does not change the equation of state of the sample.

The absolute measurements of opacity coefficients are realized in systems with the known temperature distribution between their elements. For instance, it is possible to use a specifically configured channel made of the material under investigation, in which the temperature distribution is controlled by the heat exchange of the walls in accordance with [32].

The results of investigations for aluminum and iron in the form of ratios $\varkappa_{\text{exp}}/\varkappa_{\text{calc}} < \varkappa_{\text{calc}}$ calculated by the method of [32] are given in Table 4.7. The uncertainty is $\pm 15\,\%$.

The data of Table 4.7 and the data of [32] are compared in Fig. 4.35.

These experiments employed the same technology of measurements and recording as in the investigation of the shock compressibility of substances [104, 116]. To calculate the wave arrival at the reference surface, use was made of the equations of state calibrated in the investigations of [104, 116]. The results of opacity coefficient measurements are best described by the calculation in which all requisite quantities are calculated by the Hartree–Fock–Slater model and not the Thomas–Fermi model.

Table 4.7 The results of investigations for aluminum and iron calculated by the method of [32]

	T (eV)			
Substance	0.5	0.75	1.0	1.25
Aluminum	1.26	1.44	1.41	1.32
Iron	1.31	1.0	0.85	0.81

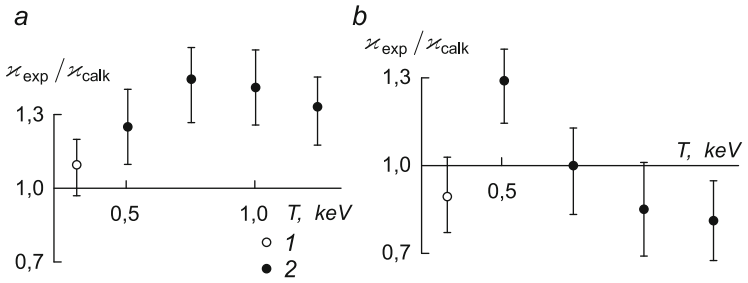

Fig. 4.35 Opacity coefficient ratio: in the calculations of $\varkappa_{calc}$, use was made of the TF model [66, 78]: *a*—aluminum; *b*—iron; *1*—experiment[32]; *2*—experiment[78]

As discussed above (Chap. 2) [104, 116], no thermodynamic theory has been constructed to date capable of describing the entire phase diagram of a substance. Owing to the fundamental difficulties encountered in the implementation of a consistent theoretical approach, it has been possible to obtain the main results only in the framework of the models based on simplifying notions regarding the structure, the energy spectrum and the nature of interparticle interactions. Of course, the applicability domain of this kind of models is limited by the nature of the assumptions made, and experimental materials are required to estimate their quality.

In particular, one of the fundamental problems of the physics of extreme states is the role of "hell" effects and their induced possible phase transitions under ultraextreme pressures [24, 36, 37, 66].

In Sect. 3.6 we analyzed the limits of applicability of quantum-statistical substance models by comparing them with the thermodynamic data obtained in underground nuclear explosions.

We dwell briefly only on the shell effects emerging in the quasiclassical substance description [66]. According to the most advanced versions of this model [36, 38, 66, 103], in the high-pressure domain the averaged smooth behavior of thermodynamic functions will be replaced by oscillations caused by the transition of bound states into the continuum (an analogue of "pressure-induced ionization"). In some cases these oscillations might result in phase transitions of the first kind.

The point is that the philosophy of statistical description implies the possibility of using the quasiclassical approach and the averaged description of the system of electrons in an atom, which disregards the particular specificity of the filling of electron shells and its related nonmonotony of the thermodynamic functions under compression of the system. It is pertinent to note that the role of shell effects, which are quite natural for plasma models [38, 40], has come under the scrutiny of theorists and experimenters during the last decades. A subtle analysis of quantum-mechanical effects [38, 66] shows that a quantum-statistical model embraces oscillation effects, which have been successfully taken into account for final temperatures [118].

A more consistent account of the shell effects calls for going beyond the framework of the quasiclassical model and invites recourse to quantum-mechanical self-consistent field methods. In [79] the electron band theory with several simpli-

fying assumptions was used to calculate the compression of elementary substances at close-to-zero temperatures. It was found that portions of the zero isotherms of several elements showed anomalous behavior. However, quantitatively the results deviated widely from experimental data, which is supposedly attributable to the significant effect of simplifying assumptions (sphericity of atomic cells, Hartree approximation, neglect of correlation effects, etc.) on the magnitudes of the calculated quantities.

More recently there appeared papers (see [66] and references therein) in which attempts were made to take into account the effect of shell structure in the traditional domain of application of the Thomas–Fermi model. These calculations revealed a wavy or even step-wise behavior of thermodynamic quantities, the positions and amplitudes of the oscillations differing markedly from one model to another.

Despite certain progress reliant on the quasiclassical method of estimating shell effects, their more rigorous inclusion is possible on the basis of the Hartree–Fock model (HF) in which exchange interaction is taken into account in the Slater approximation (HFS). In the model of [79], the parameters of the Slater exchange potential were determined from the condition of minimizing the free energy and an expression was obtained for the exchange potential in terms of the electron density and temperature. This circumstance is embodied in the name of the model—the modified Hartree–Fock–Slater model (MHFS). MHFS equations were derived by density functional method. At the heart of the method is not the calculation of the multiparticle electron wave function and the subsequent finding of the electron density distribution function but some density functional, whose form is determined by the accepted approximation. The value of the density functional, which coincides with the thermodynamic Gibbs potential, is minimal for the equilibrium electron density, which makes the MHFS model thermodynamically consistent. In this model (like in the band one) the electron energy bands are obtained with the aid of boundary Bloch conditions. A thorough elaboration of numerical algorithms resulted in decreasing greatly the computational labor and permitted calculating extensive tables of thermodynamic functions for lithium, aluminum, and iron.

The decrease in computational labor arising from the inclusion of the contribution of highly excited electrons in the quasi-classical approximation somewhat lowers the physical accuracy of the model. The boundary of the quasiclassical domain is determined individually for each substance.

Another self-consistent field model, SCF, which is an elaboration of the model of [92], was constructed in [105]. Its equations were derived by the density functional method. The lattice cell is spherical as before. A pseudoband approximation is employed instead of the true band, which is obtained with the boundary Bloch conditions.

The simplifying assumptions made in the development of self-consistent field models, SCF and MHFS (modified Hartree–Fock–Slater model) are as follows:

- adiabatic approximation (splitting of thermodynamic functions into the electron and nuclear components);
- cell electroneutrality (the intercell correlations are disregarded);

- cell sphericity (there is no way of describing uncompressed substance);
- replacement, after Slater, of exchange interaction with "local exchange";
- the existence of energy bands in the vaporized substance, in which not only the long-range order is absent, but also the short-range one;
- transition from the multiparticle problem to a single-electron approximation.

The mere enumeration of the simplifying assumptions shows that these models evidently call for experimental verification. The applicability domain of the models, which stems from their intrinsic properties, has not been reliably determined. The effect of some of the model simplifications on the thermodynamic functions is hard to comprehend, but their engendered deviations are comparable to the total effect of the shell structure.

This is confirmed by the example of the shock adiabats of aluminum in Fig. 4.36. One can see that the shell structure exerts an appreciable effect even in the domain where the TF approximation has been thought of as being applicable; the greatest departures of the oscillating shock adiabats from each other and from a smooth dependence are observed at pressures of 100 Mbar. Also shown in Fig. 4.36 are the shock adiabats plotted according to the ACTEX [90] and INFERNO [120] models, which take account of the shell atomic structure. ACTEX [90] is based on the ionized equilibrium plasma model, which employs the effective electron potential determined from experimental spectroscopic data; also included is the strong ion-

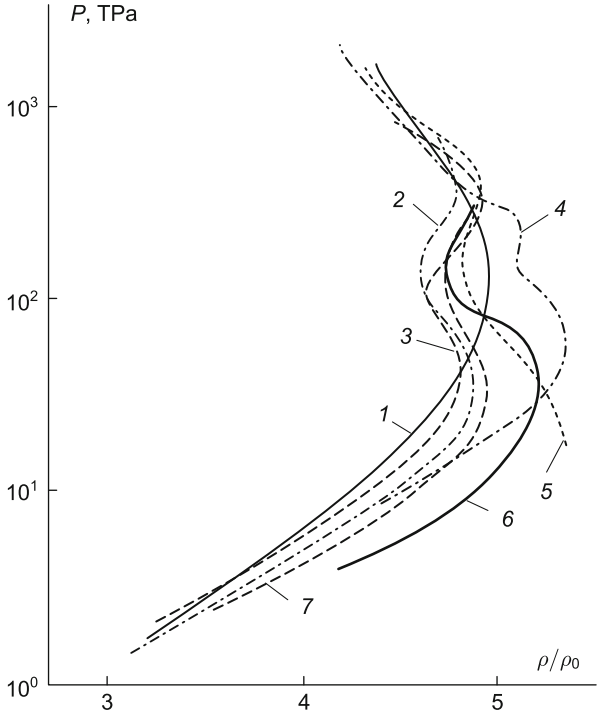

Fig. 4.36 Aluminum compression diagram according to different models [23, 24, 110]: *1*—TFK; *2*, *3*, *6*—MHFS; *4*—INFERNO [120]; *5*—ACTEX [90]; *7*—SCF [105]

ion interaction. The calculated ACTEX data in the applicability domain of the model lie between the data given by the solution of the Saha equations with and without the Debye–Huckel correction. In the *L*-shell ionization domain in the chock adiabat of aluminum the electron-ion interaction becomes comparable to the kinetic energy, i.e. the lower oscillation halfwave is beyond the domain of model applicability. This accounts for the marked difference of the ACTEX adiabat from the remaining ones in this region. A good agreement is observed at higher pressures (temperatures).

Several approximations used in MHFS and SCF coincide with the approximations used in the development of INFERNO [120]. In [120], however, there is no band splitting, which affects the behavior of the lower portion of the adiabat: according to INFERNO the onset of shell structure manifestation is shifted to the domain of higher pressures and is stronger pronounced in comparison with the splitting case. Furthermore, in INFERNO the thermodynamic quantities are related by different (three possibilities are reported) model relationships, unlike their strict correspondence in the SCF and MHFS models. At present it is difficult to explain the difference in phase between the INFERNO shock adiabat and the others at pressures above 1000 Mbar without complete information about the model.

Figure 4.37 shows the data on the shock compressibility of Al and Pb obtained by reflection method in the pressure ranges 25–240 Mbar and 80–550 Mbar, respectively [40]. A significant departure from quantum-statistical (QS) models has thus been revealed, which counts in favor of the manifestation of "shell" effects in the thermodynamics of shock-compressed plasmas.

The complete model of the modern quantum-mechanical equation of state comprises three components: equations describing the behavior of electrons; equations for nuclei; boundary conditions at the boundary of an atomic cell, which take into account the effect of electrons and nuclei of the neighboring cells. These components should be self-consistent. In the majority of modern models this is not the case (the exception is provided by the TF and QS models [38]). The effect of inconsistent thermodynamics on the behavior of shock adiabats has not been completely elucidated. However, the possibility that the disagreement in amplitude and phase is partly attributable to this circumstance must not be ruled out.

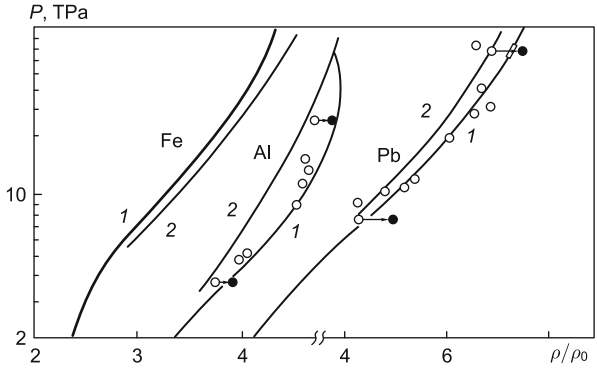

Fig. 4.37 Shock adiabats of aluminum and lead at ultrahigh pressures [40]. The *arrows* indicate the shift of experimental data in the transition of the iron reference adiabat from curve 1 to curve 2

The set of experimental data on the shock-compressed aluminum plasma is given in Fig. 3.31, where the highest points correspond to record parameters—the most extreme ones obtained in terrestrial conditions [24, 104, 116]. The internal energy density of such plasma is $E \approx 10^9\,\mathrm{J/cm^3}$, which is close to the energy density of nuclear matter, and the pressure $P \approx 4\,\mathrm{Gbar}$ is close to the pressure in the inner layers of the Sun. Under these conditions ($n \approx 4.10^{24}\,\mathrm{cm^{-3}}$, $T \approx 8.10^6$ [104, 116]) is not degenerate, $n\lambda^3 \approx 0.07$, 12-fold ionized, and the nonideality parameter is not high, $\Gamma \approx 0.1$. This is an experimental illustration of academician A.D. Sakharov's statement [97] about the "paradise" for theorists in the analysis of ultraextreme states and the simplification of physical plasma properties in the limit of ultrahigh energy densities. One can see that the investigated parameter range is adjacent to the domain in which the energy and pressure of equilibrium optical radiation make an appreciable contribution to the thermodynamics of the system:

$$E_n \sim \frac{4\sigma T^4}{c}, \quad P_R \sim \frac{E_R}{3},$$

i.e. the mode realized is the substance dynamics mode required for the implementation of the "third" idea [97].

In conclusion of this chapter we cite academician Yu.B. Khariton—the chief designer of the Arzamas-16 nuclear center, presently the RFYzTs–VNIIEF: "I am surprised at and admire what was accomplished by our people in 1946–1949... Later on it was not easy, either. But that period defies description as regards effort, flight of creativity, and dedication. Within four years of the completion of the mortal combat with fascism, my country broke the United States' atomic bomb monopoly. In eight years after the War it made and tested the world's first hydrogen bomb, in 12 years launched the first Earth satellite, and four years later it opened the way to space for mankind... You can see that these are landmarks of eternal significance in the history of civilization...

The development of nuclear-missile weapons required enormous strain of human intellect and strength. Perhaps its justification is that the unprecedented destructive power of nuclear weapons, whose use imperils life on the Earth, for nearly fifty years has kept the world powers from war, from the irretrievable step leading to a universal catastrophe. The central paradox of our time apparently consists in that the most sophisticated weapon of mass destruction serves to maintain peace on the Earth, being a powerful deterrent..." [49, 63–65].

References

1. Archive of the President of the Russian Federation (AP RF). Fund 93, File 265/52
2. Archive of the President of the Russian Federation (AP RF). Fund 93, File 3/45
3. Archive of the President of the Russian Federation (AP RF). Fund 93, File 3/46
4. Nuclear weapon. Wikipedia
5. Thermonuclear weapon. Wikipedia

6. US Congress Joint Committee on Atomic Energy, Policy and Progress in the H-Bomb Program: A Chronology of Leading Events. US Govt. Printing Office, Washington, DC (1953)
7. U istokov sovetskogo atomnogo proekta: rol' razvedki 1941–1946 (At the Origin of the Soviet Atomic Project: the Role of Intelligence1941–1946). Voprosy Istorii Estestvoznaniya i Tekhniki (3), 97–134 (1992)
8. 60 let mira. K shestidesyatiletiyu ispytaniya pervoi sovetskoi atomnoi bomby (60 Years of Peace. On the Sixtieth Anniversary of the Testing of the First Soviet Atomic Bomb). RFYaTs-VNIIEF, Sarov (2009)
9. Celebrating the 65th Anniversary of the Russian Federal Nuclear Center—All-Russian Research Institute of Experimental Physics (Scientific session of the Physical Sciences Division of the Russian Academy of Sciences, 6 October 2010). Phys. Usp. **54**(4), 387–427 (2011)
10. Al'tshuler, L.V.: Progress in high-pressure physics. Phys. Usp. **13**(2), 301–303 (1970)
11. Al'tshuler, B.L., Fortov, V.E. (eds.): Ekstremal'nye sostoyaniya L'va Al'tshulera (Extreme States of Lev Al'tshuler). Fizmatlit, Moscow (2011)
12. Al'tshuller, L.V., Moiseev, B.N., Popov, L.V., et al.: Relative compressibility of iron and lead at pressures of 31 to 34 Mbar. J. Exp. Theor. Phys. **27**(3), 420 (1968)
13. Al'tshuler, L., Brish, A., Smirnov, Y.: Na puti k pervomy sovetskomy yadernomy ispytanitu (On the way to the first Soviet atomic test). In: Istoriya sovetskogo atomnogo proekta: dokumenty, vospominaniya, issledovaniya (The History of the Soviet Atomic Project: Documents, Memoirs, Investigations), pp. 9–48. Izd. RKhGI (2002)
14. Andryushin, I.A., Chernyshev, A.K., Yudin, Y.A.: Ukroshchenie yadra. Stranitsy istorii yadernogo oruzhiya i yadernoi infrastructury SSSR (Mastering the Nucleus. Pages of the History of Nuclear Weapons and Nuclear Infrastructure of the USSR). Krasnyi Oktyabr', Sarov, Saransk (2003)
15. Andryushin, I.A., Ilkaev, R.I., Chernyshev, A.K.: Reshayushchii shag k miru. Vodorodnaya bomba s atomnym obzhatiem RDS–37 (The Decisive Step Towards Peace. The Hydrogen Bomb with an Atomic Compression RDS–37). RFYaTs-VNIIEF, Sarov (2010)
16. Angulo, C., Arnould, M., Rayet, M., et al.: A compilation of charged-particle induced thermonuclear reaction rates. Nucl. Phys. A **656**(1), 3–183 (1999)
17. Anisimov, S.I., Bespalov, V.E., Vovchenko, V.I., et al.: Generation of neutrons as a result of explosive initiation of the DD reactions in conical targets. JETP Lett. **31**(1), 61 (1980)
18. Anisimov, A.N., et al.: Khim. Fiz. **14**, 749 (1993)
19. Atzeni, S., Meyer-ter Vehn, J.: The Physics of Inertial Fusion: Beam Plasma Interaction, Hydrodynamics, Hot Dense Matter. International Series of Monographs on Physics. Oxford University Press, New York (2004)
20. Avrorin, E.N., Vodolaga, B.K., Volkov, L.P., et al.: Shock compressibility of lead, quartzite, aluminum, and water at a pressure of 100 Mbar. JETP Lett. **31**(12), 685 (1980)
21. Avrorin, E.N., Vodolaga, B.K., Voloshin, N.P., et al.: Experimental study of the influence of electron shell structure on shock adiabats of condensed materials. J. Exp. Theor. Phys. **66**(2), 347 (1987)
22. Avrorin, E.N., Vodolaga, B.K., Simonenko, V.A., Fortov, V.E.: Intense shock waves and extreme states of matter. Phys. Usp. **36**(5), 337–364 (1993)
23. Avrorin, E.N., Vodolaga, B.K., Simonenko, V.A., Fortov, V.E.: Intense shock waves and extreme states of matter. Phys. Usp. **36**(5), 337–364 (1993)
24. Avrorin, E.N., Simonenko, V.A., Shibarshov, L.I.: Physics research during nuclear explosions. Phys. Usp. **49**(4), 432 (2006)
25. Belen'kii, S.Z., Fradkin, E.S.: Teoriya turbulentnogo peremeshivaniya (Theory of turbulent mixing). In: Trudy FIAN, vol. 29. FIAN (1965)
26. Bertin, A., Vitale, A.: Experimental frontiers in muon-catalyzed fusion. In: Salvetti, C., Ricci, R.A., Sindoni, E. (eds.) Status and Perspectives of Nuclear Energy: Fission and Fusion, Proceedings of the International School of Physics 'Enrico Fermi', Course CXVI, pp. 449–468. North-Holland, Amsterdam (1992)

27. Biello, D.: Nuzhny li novye boegolovki? (A need for new warheads?). V Mire Nauki (2), 32 (2008) [Sci. Am., November 1 (2007)]
28. Birkhoff, G.: Hydrodynamics. Princeton University Press, Princeton (1960)
29. Bondarev, N.D., Keda, A.A., Selezneva, N.V.: Osobaya papka iz arkhiva I.V. Kurchatova (Special file from I.V. Kurchatov's archive). Voprosy Istorii Estestvoznaniya i Tekhniki (2), 114–122 (1994)
30. Chitaikin, V.I.: O rabotakh Fiziko-energeticheskogo instituta po termoyadernomu oruzhiyu (On the works of the Institute of Physics and Power Engineering on thermonuclear weapon). In: Nauka i obshchestvo: istoriya sovetskogo atomnogo proekta (40–50 gody) (Science and Society: The History of the Soviet Atomic Project (the 40s–50s)). Trudy Mezhdunarodnogo Simposiuma ISAP-96, Moscow, vol. 2, pp. 471–475 (1999)
31. Chu, M.S.: Thermonuclear reaction waves at high densities. Phys. Fluids **15**(3), 413–422 (1972)
32. Eliseev, G.V., Model', I.S., et al.: Dokl. Akad. Nauk SSSR **289**, 850 (1966)
33. Feoktistov, L.D.: Vodorodnaya bomba: kto zhe vydal ee sekret (The hydrogen bomb: who betrayed its secret). In: Nauka i obshchestvo: istoriya sovetskogo atomnogo proekta (40–50 gody) (Science and Society: The History of the Soviet Atomic Project (the 40s–50s)). Trudy Mezhdunarodnogo Simposiuma ISAP-96, Moscow, vol. 1, pp. 223–230 (1997)
34. Feoktistov, L.P.: Thermonuclear detonation. Phys. Usp. **41**(11), 1139–1147 (1998)
35. Feoktistov, L.P.: Lev i Atom (Lev and the Atom). Tvortsy yadernogo veka (The Makers of the Nuclear Age). Voskresen'e (2003)
36. Fortov, V.E.: Ekstremal'nye sostoyaniya veshchestva (Extreme States of Matter). Fizmatlit, Moscow (2009) [Translated into English: Extreme States of Matter. Series: The Frontiers Collection. Springer, Berlin/Heidelberg (2011)]
37. Fortov, V.E.: Extreme states of matter on earth and in space. Phys. Usp. **52**(6), 615–647 (2009)
38. Fortov, V.E.: Uravneniya sostoyaniya veshchestva (Equations of State of Matter). Fizmatlit, Moscow (2013)
39. Fortov, V.E., Popel', O.S.: Energetika v Sovremennom Mire (Energetics in the Modern World). Intellekt, Moscow (2011)
40. Fortov, V., Iakubov, I., Khrapak, A.: Physics of Strongly Coupled Plasma. Oxford University Press, Oxford (2006)
41. Fuqian, J.: Shock wave physics research in China. In: Schmidt, S.C., Johnson, I.N., Davison, L.W. (eds.) Proc Shock Compression of Condensed Matter - 1989, p. 133. Elsevier Science, Amsterdam (1990)
42. Ginzburg, V.L.: 1. Ispol'zovanie Li-6D v "sloike". 2. Vliyanie vzaimodeistviya mezhdu yadrami urana v "sloike" (1. The use of Li-6D in the "layer cake". 2. Effect of the interaction between uranium nuclei in the "layer cake"). In: Andryushin, I.A., Il'kaev, R.I., Chernyshev, A.K. (eds.) "Sloika" Sakharova. Put' geniya (Sakharov's "Layer Cake". The Path of a Genius), p. 144. FGUP "RFYaTs-VNIIEF", Sarov (2011)
43. Goncharov, G.A.: Thermonuclear milestones. Phys. Today **49**(11), 44–61 (1996)
44. Goncharov, G.A.: Khronologiya osnovnykh sobytii istorii sozdaniya vodorodnoi bomby v SSSR i SShA (Chronology of major events in the history of the hydrogen bomb in the USSR and the USA). In: Nauka i obshchestvo: istoriya sovetskogo atomnogo proekta (40–50 gody) (Science and Society: the History of the Soviet Atomic Project (the 40s–50s)). Trudy Mezhdunarodnogo Simposiuma ISAP-96, Moscow, vol. 1, pp. 231–255 (1997)
45. Goncharov, G.A.: On the history of creation of the Soviet hydrogen bomb. Phys. Usp. **40**(8), 859–867 (1997)
46. Goncharov, G.A.: The 50th anniversary of the beginning of research in the USSR on the potentialcreation of a nuclear fusion reactor. Phys. Usp. **44**(8), 851–858 (2001)
47. Goncharov, G.: Termoyadernyi proekt SSSR: predystoriya i desyat' let puti k vodorodnoi bombe (Thermonuclear project of the USSR: background and ten years on the road to the

hydrogen bomb). In: Istoriya sovetskogo atomnogo proekta: dokumenty, vospominaniya, issledovaniya (The History of the Soviet Atomic Project: Documents, Memoirs, Investigations), pp. 49–146. Izd. RKhGI (2002)
48. Goncharov, G.A.: K istorii sozdaniya yaderno-oruzheinoi programmy SSSR (On the history of the nuclear weapons program of the USSR). In: Istoriya atomnykh proektov (The History of Atomic Projects). Trudy Mezhdunarodnogo Simposiuma ISAP-99, Moscow, vol. 1 (2004)
49. Goncharov, G.A., Ryabev, L.D.: The development of the first Soviet atomic bomb. Phys. Usp. **44**(1), 71–93 (2001)
50. Gosling, F.G.: The Manhatten Project: Making the Atomic Bomb. United Station Department of Energy, Washington, DC (1994)
51. Gurevich, I.I., Zeldovich, Y.B., Pomeranchuk, I.Y., Khariton, Y.B.: Utilization of the nuclear energy of the light elements. Phys. Usp. **34**(5), 445–446 (1991)
52. Hansen, C.: US Nuclear Weapons: The Secret History. Orion Books, New York (1988)
53. Hively, L.M.: Convenient computational forms for Maxwellian reactivities. Nucl. Fusion **17**(4), 873 (1977)
54. Hively, L.M.: A simple computational form for Maxwellian reactivities. Nucl. Technol./Fusion **3**(2), 199–200 (1983)
55. Hogan, W.J. (ed.): Energy from Inertial Fusion. IAEA, Vienna (1995)
56. Holloway, D.J.: Stalin and the Bomb: The Soviet Union and Atomic Energy, 1939–1956. Yale University Press, New Haven (1994)
57. Ichimaru, S.: Statistical Plasma Physics, Volume II: Condensed Plasmas (Frontiers in Physics). Addison-Wesley Publishing Company, Reading, MA (1994)
58. Ilkaev, R.I.: Fundamental physics research at the all-Russian research institute of experimental physics. Phys. Usp. **54**(4), 387–392 (2011)
59. Il'kaev, R.I.: Sakharov at KB-11. The path of a genius. Phys. Usp. **55**(2), 183–189 (2012)
60. Ioffe, B.L.: "Truba", pochemu ona ne poshla. Tyazelovodorodnye reaktory v ITEF ("The Tube", why it did not work. Heavy-hydrogen reactors in ITEP). In: Nauka i obshchestvo: istoriya sovetskogo atomnogo proekta (40–50 gody) (Science and Society: The History of the Soviet Atomic Project (the 40s–50s)). Trudy Mezhdunarodnogo Simposiuma ISAP-96, Moscow, vol. 2, pp. 207–244 (1999)
61. Irving, D.: The German Atomic Bomb: The History of Nuclear Research in Nazi Germany. Da Capo Press, New York (1983)
62. Kanel, G.I., Fortov, V.E., Razorenov, S.V.: Shock waves in condensed-state physics. Phys. Usp. **50**(8), 771–791 (2007)
63. Khariton, Y.B.: Speech at the presentation of an Oppenheimus Award
64. Khariton, Y.B., Adamskii, V.B., Smirnov, Y.N.: On the making of the Soviet hydrogen (thermonuclear) bomb. Phys. Usp. **39**(2), 185–189 (1996)
65. Khariton, Y.B., Adamskii, V.B., Smirnov, Y.N.: O sozdanii sovetskoi vodorodnoi (termoyadernoi) bomby (On the making of the Soviet hydrogen (thermonuclear) bomb). In: Nauka i obshchestvo: istoriya sovetskogo atomnogo proekta (40–50 gody) (Science and Society: The History of the Soviet Atomic Project (the 40s–50s)). Trudy Mezhdunarodnogo Simposiuma ISAP-96, Moscow, vol. 1, pp. 200–213 (1997)
66. Kirzhnits, D.A., Lozovik, Y.E., Shpatakovskaya, G.V.: Statistical model of matter. Phys. Usp. **18**(9), 649–672 (1975)
67. Kocharov, G.E.: Termojadernyj kotel v nedrah solnca i problema solnechnyh nejtrino (Thermonuclear copper in the center of the sun and the problem of solar neutrinos). In: Soifer, V.N. (ed.) Sovremennoe Estestvoznanie. Entsiklopediya (Modern Natural Science. Encyclopedia), vol. 4, p. 28. Magistr-Press, Moscow (2000)
68. Kozyrev, A.S.: Gazodinamicheskii termoyadernyi sintez (Gas-dynamic thermonuclear fusion). In: Vysokie plotnosti energii (High Energy Densities), p. 493. RFYaTs-VNIIEF, Sarov (1997)
69. Kulsrud, R.M., Furth, H.P., Valeo, E.J., Goldhaber, M.: Fusion reactor plasmas with polarized nuclei. Phys. Rev. Lett. **49**, 1248–1251 (1982)

70. Kulsrud, R., Valeo, E., Cowley, S.: Physics of spin-polarized plasmas. Nucl. Fusion **26**(11), 1443 (1986)
71. Landau, L.D., Stanyukovich, K.P.: Dokl. Akad. Nauk SSSR **46**(9), 399 (1943)
72. Marchuk, G.I., Imshennik, V.S., Basko, M.M.: The physics of a thermonuclear explosion of a normal-density liquefied deuterium sphere (on the impossibility of a spherically symmetric thermonuclear explosion in liquid deuterium at normal density). Phys. Usp. **52**(3), 267–273 (2009)
73. Meshkov, E.E., Nikiforov, V.V.: Vysokie plotnosti energii (High Energy Densities), p. 188. RFYaTs-VNIIEF, Sarov (1997)
74. Mitchel, A.C., Nellis, N.C.: Shock impedance match experiments in aluminum between 0,1–2,5 TPa (1–25 Mbar). In: Asay, I.R., Graham, R.A., Straub, G.R. (eds.) Shock Waves in Condensed Matter. Amsterdam: Elsevier Sciens Publ. (1983)
75. Model', I.S., Narozhnyi, A.T., Kharchenko, A.I., et al.: Equations of state for graphite, aluminum, titanium, and iron at pressures > 13 Mbar. JETP Lett. **41**(6), 332 (1985)
76. More, R.M.: Nuclear spin-polarized fuel in inertial fusion. Phys. Rev. Lett. **51**, 396–399 (1983)
77. Nepomnyashchii, A., Shevchenko, L.: Atomnaya Energiya (32), 451 (1972)
78. Nikiforov, A.F., Uvarov, V.E.: Dokl. Akad. Nauk SSSR **191**, 47 (1970)
79. Nikiforov, A., Novikov, V., Uvarov, V.: Voprosy Atomnoi Nauki i Tekhniki **4**(16), 16 (1979)
80. Ponomarev, L.I.: Muon catalysed fusion. Contemp. Phys. **31**(4), 219–245 (1990)
81. Popov, N.A.: Vysokie plotnosti energii (High Energy Densities), p. 493. RFYaTs-VNIIEF, Sarov (1997)
82. Popov, N.A., Shcherbakov, V.A., Mineev, V.N., et al.: Thermonuclear fusion in the explosion of a spherical charge (the problem of a gas-dynamic thermonuclear fusion). Phys. Usp. **51**(10), 1047–1053 (2008)
83. Rainer, K.: Hitlers Bombe. Deutsche Verlags-Anstalt, Munchen (2005)
84. Ragan, C.E.: Ultrahigh-pressure shock-wave experiments. Phys. Rev. A **21**(2), 458–463 (1980)
85. Ragan, C.E.: Shock compression measurements at 1 to 7 TPa. Phys. Rev. A **25**(6), 3360–3375 (1982)
86. Ragan, C.E.: Shock-wave experiments at threefold compression. Phys. Rev. A **29**(3), 1391–1402 (1984)
87. Ragan III, C.E., Silbert, M.G., Diven, B.C.: Shock compression of molybdenum to 2.0 TPa by means of a nuclear explosion. J. Appl. Phys. **48**(7), 2860–2870 (1977)
88. Rhodes, R.: Dark Sun; The Making of the Hydrogen Bomb. Simon and Schuster, New York (1995)
89. Richtmyer, R.D.: Taylor instability in shock acceleration of compressible fluids. Commun. Pure Appl. Math. **13**(2), 297–319 (1960)
90. Rogers, F.J.: Equation of state of dense, partially degenerate, reacting plasmas. Phys. Rev. A **24**(3), 1531–1543 (1981)
91. Romanov, Y.A.: Otets sovetskoi vodorodnoi bomby (The father of the Soviet hydrogen bomb). Priroda (8), 21 (1990)
92. Rozsnyai, B.F.: Relativistic Hartree-Fock-Slater calculations for arbitrary temperature and matter density. Phys. Rev. A **5**(3), 1137–1149 (1972)
93. Rutherford, E.: The scattering of α and β particles by matter and the structure of the atom. Philos. Mag., Ser. 6 **21**, 669–688 (1911)
94. Ryabev, L.D. (ed.): Atomnyi proekt SSSR. Dokumenty i materialy (Atomic Project of the USSR. Documents and Materials). Vol. 1. 1938–1945. Part 1. Fizmatlit, Moscow (1998)
95. Ryabev, L.D. (ed.): Atomnyi proekt SSSR. Dokumenty i materialy (Atomic Project of the USSR. Documents and Materials). Vol. 2. Atomnaya bomba (Atomic Bomb). 1945–1954. Book 1. Fizmatlit, Moscow (1999)
96. Ryabev, L.D. (ed.): Atomnyi proekt SSSR. Dokumenty i materialy (Atomic Project of the USSR. Documents and Materials). Vol. 2. Atomnaya bomba (Atomic Bomb). 1945–1954. Book 2. Fizmatlit, Moscow (2000)

97. Sakharov, A.D.: Nauchnye trudy (Scientific Works). OTF FIAN–TsentrKom, Moscow (1995)
98. Sakharov, A.D.: Statsionarnaya detonatsionnaya volna v geterogennoi sisteme A-9 + "180" (Stationary detonation wave in the heterogeneous system A-9 + "180"). In: Andryushin, I.A., Il'kaev, R.I., Chernyshev, A.K. (eds.) "Sloika" Sakharova. Put' geniya (Sakharov's "Layer Cake". The Path of a Genius), p. 144. FGUP "RFYaTs-VNIIEF", Sarov (2011)
99. Salpeter, E.E.: Electron screening and thermonuclear reactions. Aust. J. Phys. **7**, 373–388 (1954)
100. Salpeter, E.E., Van Horn, H.M.: Nuclear reaction rates at high densities. Astrophys. J. **155**, 183–202 (1969)
101. Seshkov, E.E.: Izv. Akad. Nauk SSSR. Ser. Mekhanika Zhidkosti i Gaza (5), 151 (1969)
102. Shafranov, V.D.: The initial period in the history of nuclear fusion research at the Kurchatov Institute. Phys. Usp. **44**(8), 835–843 (2001)
103. Shpatakovskaya, G.: Kvaziklassicheskii metod v zadachakh kvantovoi fiziki (Quasiclassical Method in Problems of Quantum Physics). LAP LAMBERT Academic Publishing, Moscow (2012)
104. Simonenko, V.A., Voloshin, N.P., Vladimirov, A.S., et al.: Absolute measurements of shock compressibility of aluminum at pressures $P > 1$ TPa. J. Exp. Theor. Phys. **61**(4), 869 (1985)
105. Sin'ko, G.V.: Chislennye Metody Mekhaniki Sploshnykh Sred (10), 124 (1979)
106. Sivukhin, D.V.: Obshhij kurs fiziki (The General Course of Physics) Vol. 5 Atomnaya i Yadernaya Fizika (Atomic and Nuclear Physics). Fizmatlit, Moscow (2002)
107. Smyth, H.D.: Atomnaya energiya dlya voennykh tselei (Atomic Energy for Military Purposes). Transzheldorizdat, Moscow (1946)
108. Surdin, V.G. (ed.): Zvezdy (The Stars), 2nd edn. Astronomiya i astrofizika (Astronomy and Astrophysics). Fizmatlit, Moscow (2009)
109. Teller, E.: The Work of Many People. Science **121**(3139), 267–275 (1955)
110. Trunin, R.F.: Shock compressibility of condensed materials in strong shock waves generated by underground nuclear explosions. Phys. Usp. **37**(11), 1123–1145 (1994)
111. Trunin, R.F., Podurets, M.A., Moiseev, B.N., et al.: Relative compressibility of copper, cadmium, and lead at high pressures. J. Exp. Theor. Phys. **29**(4), 630 (1969)
112. Trunin, R.F., Podurets, M.A., Simakov, G.V., et al.: An experimental verification of the Thomas-Fermi model for metals under high pressure. J. Exp. Theor. Phys. **35**(3), 550 (1972)
113. Trunin, R.F., Medvedev, A.B., Funtikov, A.I., et al.: Shock compression of porous iron, copper, and tungsten, and their equation of state in the terapascal pressure range. J. Exp. Theor. Phys. **68**(2), 356 (1989)
114. Verkhovtsev, V.N., Fortov, V.E. (eds.): Fizika yadernogo vzryva (The Physics of a Nuclear Explosion), vol. 1. Ministerstvo Oborony RF, LEM, Fizmatlit (2009)
115. Vizgin, V.P. (ed.): Istoriya Sovetskogo atomnogo proekta (The History of the Soviet Atomic Project). Izd. RKhGU, St. Petersburg (2002)
116. Vladimirov, A.S., Voloshin, N.P., Nogin, V.N., et al.: Shock compressibility of aluminum at p > 1 Gbar. JETP Lett. **39**(2), 82 (1984)
117. Volkov, A.P., Voloshin, N.P., Vladimirov, A.S., et al.: Shock compressibility of aluminum at a pressure of 10 Mbar. JETP Lett. **31**(11), 588 (1980)
118. Voropinov, A.I., Gandel'man, G.M., Podval'nyi, V.G.: Electronic energy spectra and the equation of state of solids at high pressures and temperatures. Phys. Usp. **13**(1), 56–72 (1970)
119. Winterberg, F. : Atomkernenerg. Kerntech **41**(1), 1 (1982)
120. Young, D.A., Wolford, J.K., Rogers, F.J., Holian, K.S.: Theory of the aluminum shock equation of state to 10^4 Mbar. Phys. Lett. A **108**(3), 157–160 (1985)
121. Zel'dovich, Y.B.: Izbrannye trudy. Khimicheskaya fizika i gidrodinamika (Selected Works. Chemical Physics and Hydrodynamics). Nauka, Moscow (1984)
122. Zel'dovich, Y.B., Khariton, Y.B.: Zh. Eksp. Teor. Fiz. **10**, 477 (1940)

123. Zel'dovich, Y.B., Raizer, Y.P.: Fizika udarnykh voln i vysokotemperaturnykh gidrodinamicheskikh yavlenii, 2nd edn. Nauka, Moscow (1966) [English Transl.: Physics of Shock Waves and High-Temperature Hydrodynamic Phenomena. Dover, Mineola, NY (2002)]
124. Zubarev, V.N., Podurets, M.A., Popov, L.V., et al.: Udarnaya szhimaemost' i uravnenie sostoyaniya medi v oblasti vysokikh davlenii (Shock compressibility and equation of state of copper at high pressures). In: Dokl. Vsesoyuzn. simp. po impul'snym davleniyam (Reports of the All-Union Symposium on Pulsed Pressures), vol. 1, p. 61 (1974)

Chapter 5
High-Power Lasers in High-Energy-Density Physics

The rapid progress of laser technology has opened up the possibility of generating ultrashort laser pulses of the nano–pico–femto[1]–atto-second range and of bringing (see Tables 3.2 and 3.3; Fig. 3.2) the existing and projected laser complexes into the petawatt–zettawatt power range (Figs. 5.1 and 5.2), making it possible to span a wide range of power densities up to the highest values achievable today, $q \approx 10^{22}$–10^{23} W/cm^2 [41, 71, 272, 273, 392], which will undoubtedly rise with time.

The action of these enormous intensities on targets leads to diverse new physical effects in hot plasmas [42, 71, 273], such as multiphoton ionization, self-focusing and filamentation of different types, the generation of superintense electric and magnetic fields, electron and ion acceleration to relativistic velocities, nuclear reactions caused by these fast particles, relativistic plasma "transparentization", nonlinear modulation and multiple generation of harmonics, ponderomotive effects in hydrodynamics, and many other effects, which are the subject of vigorous research today (see reviews [273, 304] and references therein). Some of these effects will be briefly considered in this chapter.

5.1 Growth of Laser Radiation Intensity

The further growth of power density will be accompanied by qualitatively new phenomena [271, 283], such as spontaneous electron–positron pair production (the "boiling" of the vacuum and the loss of its transparency [19, 36, 42, 46, 75, 76, 134, 137, 174, 218, 224, 241, 273, 283, 304, 308, 322, 339]), the emergence of microscopic quantities of relativistic matter, the generation of relativistic plasma streams and shock waves, solitons, jets, and γ-bursts similar to the astrophysical

[1] For comparison, the ratio between 10 fs and 1 min is equal to the ratio between 1 min and the age of the universe.

© Springer International Publishing Switzerland 2016

V.E. Fortov, *Extreme States of Matter*, Springer Series in Materials Science 216,
DOI 10.1007/978-3-319-18953-6_5

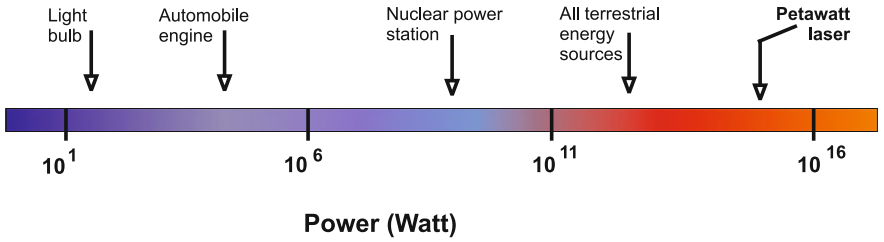

Fig. 5.1 Power scale

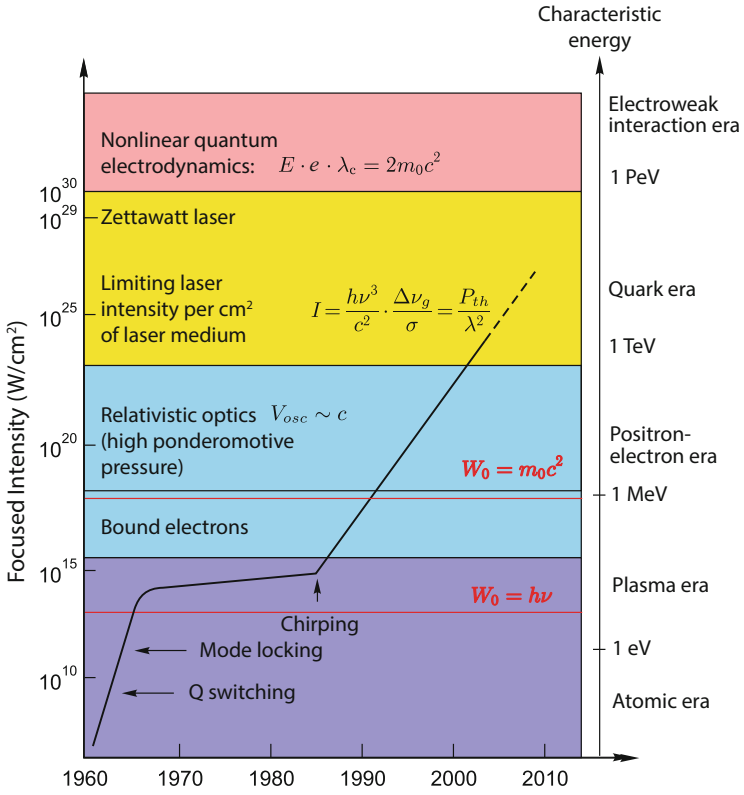

Fig. 5.2 Growth of laser radiation intensity with time [273, 283]. The rapid increase of radiation intensity in the 1960s resulted in the discovery of numerous nonlinear effects induced by bound electrons (characteristic energies on the order of an electronvolt). Contemporary swift intensity growth permits processes at relativistic electron energies ($W \sim m_ec^2 \approx 0.5\,\mathrm{MeV}$) to be studied

ones, and—in the distant future—the realization of quantum gravitation conditions [83, 335, 371]. This new intensity level may see the advent of new schemes of controlled thermonuclear fusion (Sect. 7.2), a new way of producing short-lived isotopes, as well as extraordinary schemes of high-efficiency compact accelerators (Sect. 7.4).

Figure 5.2 shows the progress in increasing the irradiation intensity and the possibilities that open up for studying the processes in high-energy density physics [271, 273, 283].

With the invention of lasers it became possible to record numerous nonlinear optical effects [46, 75, 76, 134, 174, 253, 308, 339], such as the deformation of intraatomic and molecular fields by laser radiation; stimulated Raman, Brillouin, and Thomson scattering; multiphoton ionization; and several other nonlinear effects related to bound electrons.

Since the advent of the first laser, raising the peak power of laser radiation has been and still is one of the principal goals of quantum electronics. The very notion of high peak power is permanently changing, and today means a power of no less than 1 PW (10^{15} W). The rapid progress of output laser power in the 1960s and 1970s was based on the principles of Q-switching and mode locking, which enabled the laser pulse duration to be reduced from microseconds to picoseconds over 40 years [273]. Further advancement in this direction was limited by the large dimensions and cost of lasers and the need to operate at the limit of radiation resistance of the optical elements.

The present-day "renaissance" in laser physics is related to the invention of the chirped optical pulse technique (Fig. 5.2) in 1985 [346], which opened up the way for multiterawatt, petawatt, and even exawatt laser systems [219, 271] to raise the intensities on target to $q \approx 10^{22}$ W/cm^2, with the theoretical limit equal to $\approx 3 \times 10^{23}$ W/cm^2. In this technique [78, 247, 248, 346, 347], an initially short laser pulse is stretched in time (Fig. 5.3, [214]) on passing through dispersion elements (for

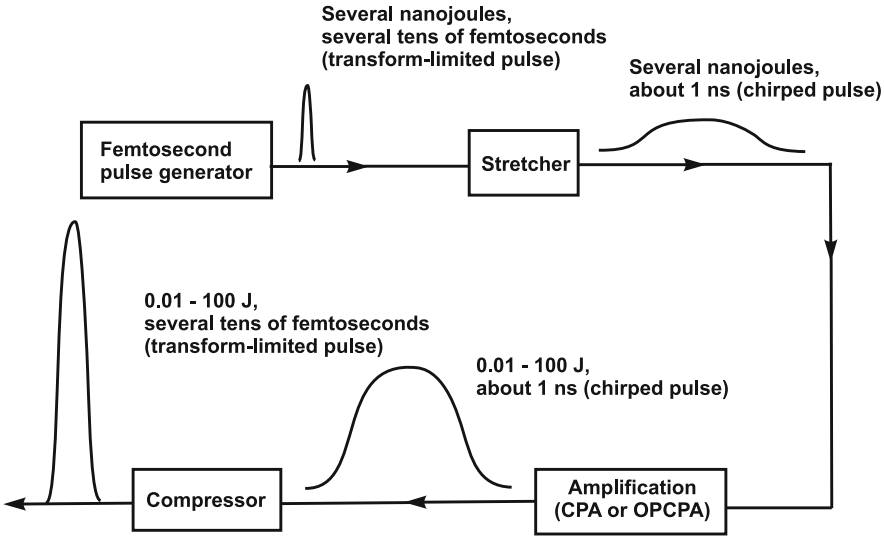

Fig. 5.3 General schematic of a femtosecond laser (*CPA* chirped pulse amplification, *OPCPA* optical parametric chirped pulse amplification). Reprinted, with permission, from [214]

instance, diffraction gratings). The pulse is decomposed into spectral components, each of which traces a slightly different path, depending on its wavelength, and the pulse stretches in time. Spectral clipping ("chirping") also occurs—the frequency continuously varies from the beginning to the end of the pulse. The stretched pulse possesses a lower intensity and is amplified in the ordinary way by the laser-active medium and arrives at the other nonlinear element for optical compression in the compressor. While conventional techniques enable the radiation to be focused by lenses in two mutually perpendicular directions, the new technique does this simultaneously in three dimensions and sharply increases the resultant intensity at the target.

Chirping is employed without exception in all lasers of power 1 TW and above [214]. The chirp principle has made it possible to raise the attainable intensity of laser radiation by 5–6 orders of magnitude and to radically lower the cost and dimensions of lasers, which have become "table-top" devices affordable by university laboratories. Furthermore, these lasers combine well with big facilities for controlled laser fusion ("fast" ignition, see Sect. 7.2.3) and charged-particle accelerators (Sect. 7.4, Fig. 6.10) and have provided a way of recording nonlinear quantum-electrodynamic effects such as pair production in vacuum [42, 46, 70, 75, 76, 79, 339] as well as intense radiation for studying photon–photon collisions [358].

Developed simultaneously with the development of the chirp technique was a new method of obtaining superhigh-power pulses, which relied on the parametric light amplification in nonlinear optical crystals—Optical Parametric Chirped Pulse Amplification (OPCPA) [299]. An advantage of the parametric amplification is an unrivaled high chirped-pulse gain: an energy gain of up to 3–4 orders of magnitude in one pass through the crystal. Another valuable aspect is that the technology of growing wide-aperture crystals of the KDP family (potassium dihydrophosphate) has been thoroughly elaborated, making it possible to increase the generated pulse energy by scaling the amplifier stages. At present, three classes of amplifiers are at about the same frontier of laser power of 1 PW: CPA in titanium-sapphire crystals, CPA in neodymium glass, and OPCPA in KDP crystals and potassium dideuterophosphate (DKDP) crystals.

The existing and projected petawatt lasers are divided into three types according to the amplifying medium: (1) neodymium glass, (2) sapphire, and (3) KDP and DKDP parametric crystal amplifiers (see Table 5.1 in [214]). In all three laser types the energy (in the form of population inversion) is stored in neodymium ions in glass. In the first case this energy is directly converted to the energy of a chirped pulse, which subsequently undergoes compression. In the second and third cases the stored energy is converted to the energy of a narrow-band nanosecond pulse, which is converted to the second harmonic to serve a pump for the amplifiers of chirped pulses. This pump either produces population inversion in a sapphire crystal or decays parametrically into two chirped pulses in a nonlinear crystal.

The peak power is defined by the duration of compressed pulses and their energy. The highest energy is achieved in neodymium glass lasers, because the energy stored in the form of population inversion is directly converted to a chirped pulse. However, the narrow spectral amplification band in neodymium laser glasses limits

Table 5.1 Comparison of petawatt laser concepts

Amplifying medium	Nd:glass		Ti:sapphire		DKDP		Cr:YAG ceramics	
Energy source	Nd:glass		Nd:glass		Nd:glass		Nd:glass	
Pump		(+)	2 ω Nd[a]	(−)	2 ω Nd	(−)	1 ω Nd[b]	(0)
Pump duration, ns		(+)	>10	(0)	1	(−)	>10	(0)
Amplifier aperture, cm	40	(0)	8	(−)	40	(0)	>50	(+)
Minimal duration, fs	250	(−)	25	(+)	25	(+)	25	(+)
Efficiency (1 ω Nd → fs), %	80	(+)	15	(0)	10	(−)	25	(0)
Number of petawatts out of 1 kJ 1 ω Nd	3.2(3)[c]		6(1.5)[d]		4		10	
Power attained, PW	1.36		1.1		1.0		—	

Symbols "+", "−" and "0" are indicative of above-average, below-average, and average characteristics, respectively [214]

[a]Second harmonic of a neodymium laser

[b]Fundamental harmonic of a neodymium laser

[c]From the pulse of the fundamental harmonic of a neodymium laser to a femtosecond pulse

[d]The radiation resistance of diffraction gratings and sapphire crystals limits the peak power at levels of 3 and 1.5 PW, respectively

the compressed pulse duration at a level of several hundred femtoseconds. As a result, the radiation resistance of diffraction gratings limits advancement to the multipetawatt range.

Unlike neodymium glass lasers, sapphire lasers provide broadband amplification, which permits compressing pulses down to 10–20 fs. At the same time, the aperture of sapphire crystals does not exceed 10 cm for the existing crystal growth technology. In an attempt to cross the petawatt threshold, this small aperture will limit the chirped-pulse energy due to optical breakdown and self-focusing.

Today, tens of petawatt lasers are either in operation in the world (see Fig. 3.2 and Tables 3.3, 5.2 from [219]) or will be commissioned before long; present-day leading-edge technologies give hope that ultrahigh intensities of the order of 10^{28} W/cm^2 will be obtained in the future [271, 273, 304]. Table 5.2 of [219] gives the characteristics of suchlike systems with indication of projected experiments.

The HERCULES laser system [176] is capable of generating ≈300 TW laser pulses once in 10 s. This laser now holds record for the at-target radiation intensity of $\approx 2 \cdot 10^{22}$ W/cm^2 obtained by focusing pulses to a 1-μm sized focal spot.

The neodymium glass German PHELIX laser [296] permits obtaining >500 TW laser pulses with an energy of up to 1 kJ. The laser is operated in two modes: a long mode (0.7–20 ns, 0.3–1 kJ, 10^{16} W/cm^2) and a short one (0.5–20 ps, 120 J, 10^{20} W/cm^2).

Let us consider several other high-power laser projects [214]. First of all we mention the Russian project [48] executed in the Russian Federal Nuclear Center (Sarov) with participation of the IAP RAS. One of the channels of the "Luch" facility (2-ns second-harmonic pulse of energy 1 kJ) is employed as a pump. A special master oscillator was developed for the "Luch" facility channel to time the pump both to a femtosecond laser and to the pump laser of the previous

Table 5.2 Operating facilities with a peak output power >100 TW and a pulse duration ≤ 1 ps

Country Laser name Research center	Laser type	Peak power	Pulse energy (J)	Shortest duration (fs)	Peak intensity (W/cm^2)	Repetition rate	Main lines of research
Russia							
Femta-Luch Russian Federal Nuclear Center "All-Russian Research Institute of Experimental Physics" (RFYaTs–VNIIEF)	DKDP	1 PW	70	70		Several times per day	The physics of laser thermonuclear fusion (LTF), extreme states of matter, laser-driven particle acceleration
PEARL Institute of Applied Physics, Russian Academy of Sciences (IAP RAS)	DKDP	560 TW	24	43		Several times per day	Electron acceleration, biomedical applications
USA							
NIF Lawrence Livermore National Laboratory (LLNL)	Nd:Glass	$1.8 \cdot 10^6$	$3 \cdot 10^3$			Several times per day	Laser thermonuclear fusion
Callisto LLNL	Ti:Sa	300 TW	18	60	$5 \cdot 10^{20}$		Electron acceleration

USA							
Trident Los Alamos National Laboratory (LANL)	Nd:Glass	200 TW	100	500	$5 \cdot 10^{20}$		Ion acceleration, laboratory astrophysics
OMEGA EP Laboratory of Laser Energetics (LLE), University of Rochester	DKDP	1 PW	1000	1000	$>10^{20}$		New ignition schemes for LTF, experiments in high energy density
Hercules Center for Ultrafast Optical Science (CUOS), University of Michigan	Ti:Sa	300 TW	17	50	$2 \cdot 10^{22}$	0.1 Hz	Relativistic laser plasma, particle acceleration, generation of X-ray radiation (XR)
Texas Petawatt Laser University of Texas at Austin (UT Austin))	Nd:Glass	1.1 PW	186	165		Several times per hour	Particle acceleration, biomedical applications
BELLA Lawrence Berkeley National Laboratory (LBNL)	Ti:Sa	1.1 PW	43	40		1 Hz	
Titan Lawrence Livermore National Laboratory (LLNL)	Nd:Glass	500 TW	200	400			

(continued)

Table 5.2 (continued)

Country Laser name Research center	Laser type	Peak power	Pulse energy (J)	Shortest duration (fs)	Peak intensity (W/cm^2)	Repetition rate	Main lines of research
USA							
Diocles University of Nebraska, Lincoln (UNL)	Ti:Sa	700 TW	20	30			
Great Britain							
Vulcan Rutherford Appleton Laboratory (RAL)	DKDP	1 PW	500	500	10^{21}	Several times per hour	LTF physics, extreme states of matter, laser-driven particle acceleration, laboratory astrophysics
Astra Gemini RAL	Ti:Sa	2 × 0.5 PW	2 × 20	40	10^{22}	1/20 Hz	Particle acceleration, coherent XR sources, laboratory astrophysics
Orion Atomic Weapon Establishment (AWE)	Nd:glass	2 × 0.8 PW	2 × 500	600			
France							
PETAL Atomic Energy and Alternative Energies Commission (CEA)	Nd:Glass	2 PW	3000	500			

Germany							
PHELIX GSI Helmholtz Center for Heavy-Ion Research	Nd:Glass	1 PW	500	500			Interaction of laser radiation with heavy-ion beams
PEnELOPE Helmholtz Center Dresden-Rossendorf	Ti:Sa	1.3 PW	200	150			
Japan							
Institute of Laser Engineering (ILE), Osaka University	DKDP	1 PW	500	500	10^{20}	3–4 times a day	LTF, high energy density physics
Advanced Photon Research Center (APRC), Japan Atomic Energy Agency (JAEA)	Ti:Sa	850 TW	29	33		10 Hz	Relativistic optics
Canada							
ALLS Advanced Laser Light Source (ALLS), Institut National de la Recherche Scientifique (INRS)	Ti:Sa	200 TW	5	25		10 Hz	Interactions with matter in the range from X-ray to infrared radiation

(continued)

Table 5.2 (continued)

Country Laser name Research center	Laser type	Peak power	Pulse energy (J)	Shortest duration (fs)	Peak intensity (W/cm^2)	Repetition rate	Main lines of research
Korea							
Advanced Photonics Research Institute (APRI), GIST, Gwangju	Ti:Sa	100 TW 1 PW	3 30	30 30		10 Hz 0.1 Hz	Relativistic Thomson scattering, hard XR generation, electron acceleration
China							
Shanghai Institute of Optics and Fine Mechanics (SIOFM)	Ti:Sa	890 TW		29		10 Hz	Relativistic laser plasma, particle acceleration, XR generation
Shengan-IIU Changchun Institute of Optics, Fine Mechanics and Physics, Chinese Academy of Sciences	Ti:Sa	1.1 PW	32	28		1 Hz	

parametric amplifier channels. Today the highest energy of chirped pulses after the final amplifier stage is equal to about 100 J. The four-grating compressor efficiency is equal to 68 %. An output power of about 2 PW will be achieved upon completion of the work on pulse compression.

It is planned to upgrade the existing 1-PW Vulcan OPCPA laser facility (Rutherford-Appleton Lab., UK) to a power of 10 PW by 2014 [82]. Two channels of the Vulcan neodymium glass laser, each of energy 600 J, are used to pump two final amplifiers. Advantage is taken of a superbroadband phase matching in a DKDP crystal at the wavelength of chirped pulses near 910 nm. A special feature of this project is a very long (3 ns) chirped pulse.

Recently a start was made on two major pan-European laser projects: HiPER (High Power laser Energy Research) [179] and ELI (Extreme Light Infrastructure) [121]. The HiPER project is aimed at controlled laser fusion research for a relatively modest energy of the radiation that compresses the laser target: less than 0.4 MJ in the second harmonic in comparison with 1.8 MJ in the third harmonic on the National Ignition Facility (NIF). This energy "saving" is achieved by using, along with nanosecond pulses, shorter (about 1 ps) 150 to 2000 PW power pulses to ignite fusion targets (Fast Ignition). The objective of ELI project is to set up a network of three research centers with an ultrahigh-power (10–30 PW) femtosecond laser constructed in each of them to carry out unique research in the area of high energy density physics. In these pan-European projects the femtosecond laser architecture (parametric amplification of chirped laser pulses centered at a wavelength of 910 nm in DKDP crystals) is assumed to be optimal for further scaling up.

The OPCPA scheme is not the only presently discussed scheme intended for constructing multipetawatt and exawatt lasers in the future. Quite possible is the emergence of sapphire crystals 30–40 cm in diameter and the use of several neodymium glass types to broaden the amplification band. Of special interest is the concept related to laser ceramics—a new optical material, which combines the virtues of glasses and monocrystals. Laser ceramics has already introduced major improvements into lasers with a high average output power. This line of laser technology is vigorously developing, and even now there is a wealth of publications on femtosecond low-power ceramic lasers. So far ceramics has not been used in high-power lasers, but ceramics-based lasers may well go into competition with neodymium glass, sapphire, and OPCPA lasers in the future.

In particular, a new concept of superhigh-power femtosecond Cr:YAG ceramic lasers has been introduced [214], which combines both traditional principles (energy source—nanosecond pulses of a neodymium glass laser, CPA) and new possibilities that open up due to the use of laser ceramics. As is evident from Table 5.1, a Cr:YAG ceramics possesses three key properties simultaneously: a broad amplification band, which permits amplifying pulses down to 20 fs in duration; a large aperture, which permits amplifying chirped multikilojoule pulses; and a high conversion efficiency for the narrow-band radiation of neodymium glass lasers. These properties open up the door to the construction of a unique laser with a peak power of 100 PW for

pump energy of 10 kJ. We note that, although Cr:YAG ceramic elements have not been employed as active elements, they enjoy wide use as passive Q switches.

Apart from a large aperture, a critically important advantage of ceramics is the possibility of making active media that cannot be grown in the form of a monocrystal. An example is provided by neodymium- and ytterbium-doped oxides of rare-earth elements: Nd:Y_2O_3, Nd:Lu_2O_3, (Nd, Yb):Sc_2O_3,, Yb:Yb_2O_3, etc. One more version of multipetawatt laser scheme has been proposed: CPA in a flashlamp-pumped wide-aperture (Nd, Yb):Lu_2O_3 or (Nd, Yb):Sc_2O_3 ceramics by analogy with neodymium glass lasers, whose pulses are much longer. The excitation of neodymium ions is transferred to ytterbium ions, which provide a broad band (direct pumping of ytterbium is possible only with diode lasers, which hinders the possibility of scaling up). An even broader band may be obtained by simultaneous use of several oxide crystals (Sc_2O_3, Y_2O_3, Lu_2O_3, etc.) similarly to the use of several neodymium glass types or several garnets with chromium ions. Therefore, the near future may see the emergence of new petawatt and multipetawatt projects reliant on CPA in laser ceramics.

Petawatt lasers, which are constructed throughout the world, will shortly become a tool for mastering a new realm of knowledge in high energy density physics—the physics of extreme light fields. In the future, petawatt lasers may be used as charged particle accelerators in basic research, defense technology, and medical applications. Among the last-named ones, mention should be made of an isotope factory for positron emission tomography as well as of a compact inexpensive ion source for hadron therapy.

These and other potential applications as well as significant progress in the area of petawatt lasers generate interest among commercial companies towards mastering the petawatt range, which lends additional impetus to the development of laser technologies. All this gives hope that within 5–10 years petawatt lasers (including OPCPA lasers) will not be exotics and will become available to many laboratories throughout the world.

The passage to shorter (attosecond) durations of laser pulses opens new interesting possibilities in high energy density physics, chemistry, biology and medicine [219]. The first attosecond pulse sources were supposedly the sources involving the generation of high-order harmonics in the interaction of laser radiation with a gas jet. Owing to the nonlinear radiation action on an atom in its ionization, high-order harmonics emerge even for 10^{13} W/cm^2. The use of ultrashort-pulse (1–2 optical cycles) laser radiation permitted obtaining $\approx$100-as pulses with jets, which is of interest in the of atomic and molecular processes on the ultrashort time scale.

More efficient is the generation of ultrashort-pulse radiation in the interaction of lasers with solid targets [219]. The Doppler effect is considered [219] as one of the mechanisms of generation of this radiation.

The next significant step in the study of the mechanism of high-order harmonic generation at the surface of a solid-state plasma was made in [40]. Its authors gave consideration to the fact that the radiation of electrons in the ultrarelativistic case is synchrotronic in nature and takes place for a short period, with the result that the cutoff frequency of the generated spectrum is defined not by the square of the

electron relativistic factor but by its cube. This theoretical result was experimentally confirmed on the Vulcan facility in the RAL [114–116].

One of the most intriguing purposes of converting optical radiation to attosecond pulses is the solution of the problem of generating ultrahigh intensities for the observation of nonlinear vacuum effects. In particular, according to the results of recent calculations and estimates [134], to observe the avalanches of electron-positron pair production in vacuum requires an intensity of about 10^{26} W/cm^2. This is three orders of magnitude higher than the intensity which international projects plan to reach in the near future [121]. An obvious way to increase the intensity is to shorten the wavelength, which will permit decreasing the volume in which the energy is concentrated under ultimate focusing limited by the diffraction limit. Apart from the focusing scheme of attosecond pulses generated at a spherical plasma surface [163], they came up with the idea of focusing the counterpropagating laser pulse reflected from a relativistic electron mirror, which is produced in the breaking of a wake wave [73] or in the ponderomotive expulsion of electrons from thin films [226]. In practice this mechanism is strongly limited by a relatively low efficiency and poor spatial coherence of the generated radiation.

The mode of high-power attosecond pulse production in the oblique irradiation of the surface of a supercritical plasma appears to be highly attractive from the standpoint of improving energy conversion efficiency [13, 65]. The ponderomotive force exerted on electrons by an electromagnetic wave incident on the layer shifts the electrons into the plasma interior. Unlike the normal-incidence case, in the case of oblique incidence the existence of a plasma flow in the moving frame of reference gives rise to magnetic field produced by the stripped ions on displacement of the electrons into the plasma interior [219]. This in turn underlies the difference in the ponderomotive wave action on the electrons during two halfcycles of the field.

The emergence of internal fields in the plasma and the accelerated motion of a part of the plasma electrons have the effect that the plasma accumulates the energy of the incident wave at this stage. In the case of linear polarization the force of light pressure oscillates during the field cycle, and therefore at some point in time a nanodimensional beam formed of displaced electrons under the charge separation force breaks away and travels towards the incident wave to become the source of an attosecond burst. In this case the energy accumulated at the first stage is radiated in a period of the order of several tens of attoseconds. Owing to similarity with the scenario of energy accumulation by a mechanical spring, this three-stage process description has come to be known as the model of a relativistic electron spring [162].

According to particle-in-cell simulations, with the use of a 10-PW laser pulse it is possible to reach an intensity of $1.8 \cdot 10^{26}$ W/cm^2 in a domain of size several nanometers.

Another promising mechanism [219] of high-order harmonic generation is a so-called wake radiation [306], which consists in the following. In the interaction of laser radiation with the surface of a solid target there occurs generation of electron bunches traveling into the plasma interior [67]. In the presence of a density gradient these bunches are capable [219] of exciting plasma oscillations whose frequency is a multiple of the bunch repetition rate. The latter in turn is defined by the frequency

of the laser pulse. These plasma oscillations are executed for some density gradient, and therefore they are capable of radiating electromagnetic waves of the same frequency. In this way there occurs harmonic generation up to harmonics of the plasma frequency corresponding to the highest electron density in the target.

The generation of coherent wake radiation was observed in several experiments. In a 2004 experiment [360], in the irradiation of thin carbon and aluminum foils by laser radiation for an intensity of about 10^{18} W/cm^2 it was possible to observe harmonics from the rear side of the target under irradiation. Harmonics up to the 18th were observed under irradiation by a laser pulse with an intensity of only $2 \cdot 10^{16}$ W/cm^2.

To summarize, we see that multiterawatt laser sources permitting to reach radiation intensities of the order of 10^{23} W/cm^2 would be expected to emerge. Today work is underway to develop laser facilities with a rated peak power of 10 PW simultaneously in several countries in the world. These are Vulcan-10PW in the UK, ILE-Apollon in France, and PEARL-10 in Russia. Constructed in the framework of ELI European megaproject are three superhigh-power laser complexes in the Czech Republic, Hungary, and Romania, which will be employed to execute research into the basic physics in superhigh fields, the problem of attosecond pulse generation, and photonuclear processes. Anticipated are the production of monoenergetic electron beams with energies of several GeV, ion beams with an energy at a level of 1 GeV, ultrabright gamma-ray radiation with photon energies of the order of several GeV, ultrashort pulses of subattosecond duration, as well as attainment of record radiation intensities at a level of 10^{26} W/cm^2 with the use of attosecond pulses [219].

5.2 Physical Effects Under High-Intensity Laser Irradiation

The advent of this laser technology of high energy density made it possible to substantially advance along the intensity scale and go from atomic and solid-state processes in laboratory research to hot plasma studies, laser nuclear physics, high energy physics, relativism, and even cosmology beyond the Standard model [158, 273, 292].

The action of high-power laser radiation leads to new and strongly nonlinear physical phenomena in relativistic plasmas with pressures up to gigabars, with electric fields of teravolts per centimeter, and gigagauss magnetic fields [227, 273, 282, 304, 311] (Fig. 5.2).

In addition to the well-known effects of self-focusing, stimulated scattering, and front steeping there emerge new effects: light filamentation, relativistic and ponderomotive effects in hydrodynamics, as well as fully developed generation of nonthermal gigavolt electrons and multimegavolt ions in laser plasmas, which result in nuclear reactions [74, 84, 147, 150, 175, 273, 283, 304, 384, 385, 391, 411]. Here, we are dealing with extremely short—femtosecond—durations of a laser pulse, during which the electromagnetic wave executes only a few cycles.

When analyzing the physical effects that emerge with increase in irradiation power, we will ascend the curve of laser intensities (Fig. 5.2). Beginning with $q > 10^{14}\,\mathrm{W/cm^2}$ (for $\lambda = 1\,\mu\mathrm{m}$), the amplitude pressures of laser-driven shock waves pass into the megabar range [19, 36, 118, 224, 239, 244, 273, 285, 304, 327, 328], in accordance with the scaling law

$$P\,(\mathrm{TPa}) = 0.87\left[q(\mathrm{W/cm^2})\right]^{2/3} \cdot \left[\lambda(\mu\mathrm{m})\right]^{-2/3}.$$

Beginning with $q > 3.4 \times 10^{18}\,\mathrm{W/cm^2}$, the electric intensity $E = \sqrt{4\pi q/c}$ in the laser wave is comparable with the intensity of the electric field of the nucleus $E_a = e/a_\mathrm{B}^2 \approx 5 \times 10^9\,\mathrm{V/cm}$ in the first Bohr orbit of hydrogen. To ionize the energy level U_i [eV] requires an intensity

$$q\,\left[\mathrm{W/cm^2}\right] = \frac{4 \times 10^9\, U_i^4\ [\mathrm{eV}]}{Z^2}.$$

Under these conditions, laser radiation ionizes the medium, which turns into a heated plasma. Interesting experiments in the generation of intense shock waves by laser radiation [19, 51, 244, 285] (Fig. 5.4) and in the production of fast charged particles in laser plasmas [42, 125, 250, 304, 305] (Fig. 5.5) can be conducted in this parameter domain.

It is significant that it has been possible to apply the method of fast Thomson scattering in experiments to apply laser-driven shock waves for constructing the equations of state of shock-compressed high-density plasmas [223]. This substan-

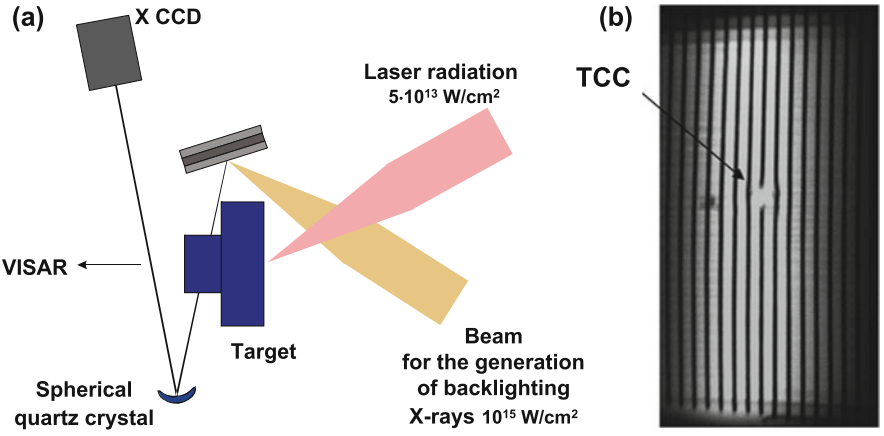

Fig. 5.4 Experiment (**a**) with laser-driven shock waves [51] involving the measurement (**b**) of the density of shock-compressed plasma from the absorption of 5 keV X-ray radiation (*VISAR* velocity interferometry system for any reflector, *CCD* charge-coupled device, *TCC* target chamber center)

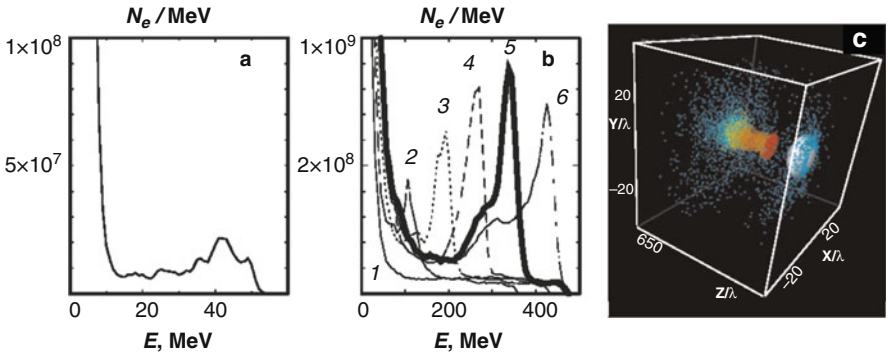

Fig. 5.5 Energy spectrum of electrons [304, 305] accelerated by laser radiation: (**a**) 20 mJ, 6.6 fs. (**b**) 12 J, 33 fs. Temporal evolution of the spectrum: (*1–6*) $ct/\lambda = 350, 450, 550, 650, 750, 850$, respectively. (**c**) Propagation of the laser pulse 12 J, 33 fs, $z/\lambda = 690$ through a plasma with a density of $10^{19}\,\mathrm{cm}^{-3}$. Three-dimensional picture of nonthermal electron energy distribution for $q \approx 10^{19}\,\mathrm{W/cm^2}$. The electrons that differ by 10 keV above 10 MeV are indicated by different colors

tially broadens the information value of shock-wave experiments in comparison with the ordinary technique of high-power shock waves [138, 139].

Beginning with roughly the same intensities $q > 10^{17}\,\mathrm{W/cm^2}$, an appreciable number of nonthermal electrons and ions of the multimegaelectronvolt range are generated in the absorption region [68, 74, 77, 84, 109, 125, 147, 150, 175, 220, 235, 250, 252, 255, 263, 290, 291, 293, 317, 384, 391, 411]. Beginning with $10^{18}\,\mathrm{W/cm^2}$, the ponderomotive light pressure is comparable with the hydrodynamic plasma pressure [36, 224, 273, 283, 304].

Relativistic effects become significant when the kinetic energy of an electron accelerated in the laser wave field is of the order of its rest energy $m_e c^2$, which leads to the condition

$$q_{pe}\lambda^2 \approx 1.37 \times 10^{18}\,\frac{\mathrm{W}\,\mu\mathrm{m}^2}{\mathrm{cm}^2}.$$

For $\lambda = 1\,\mu\mathrm{m}$ this gives $10^{18}\,\mathrm{W/cm^2}$.

Therefore, for the first time it has been possible to obtain microscopic quantities of matter with relativistic energies in terrestrial conditions [36, 273, 304], with relativistic electron mass on the order of 100 times the mass of the rest energy.

The proton motion will become relativistic at intensities

$$q_{pp} = \left(\frac{M_p}{m_e}\right)^2 q_{pe} \approx 5 \times 10^{24}\,\mathrm{W/cm^2},$$

which will hopefully be realized in experiments soon.

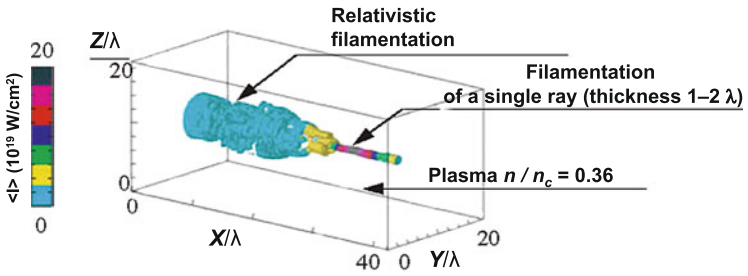

Fig. 5.6 Self-focusing of a laser pulse [304]

The transition to "relativistic" intensities of laser radiation [273] has already brought several interesting physical results [272]. The case in point is the generation of X-ray [145, 181, 216, 334, 395] and gamma-ray [159, 171, 213, 242] radiation, of betatron radiation [10, 363], relativistic self-focusing in plasmas (Fig. 5.6) [95, 182, 227, 280, 329] and in the atmosphere [53, 119, 120, 243, 310, 320, 332, 350, 408], high-order harmonic generation [30, 208, 286, 340, 341, 348, 361, 407], acceleration of electrons [42, 68, 109, 125, 220, 250, 255, 257, 263, 290, 293, 304], protons and ions [74, 77, 126, 150, 175, 235, 252, 291, 317, 385, 391, 411], neutron [105, 178, 238] and positron [46, 84, 147, 384] generation, electron vortex and soliton generation [109, 273, 304, 311], multimegagauss magnetic field generation [237, 265, 282, 311], as well as the manifestations of quantum electrodynamics [36, 42, 75, 76, 79, 134].

Under high-intensity irradiation there occurs relativistic plasma "transparentization" [273, 283, 304], which is related to the relativistic growth of the electron mass and the corresponding lowering of the critical plasma frequency $\omega_p = \sqrt{4\pi e^2 n_e/\gamma m}$ (where γ is the relativistic Lorentz factor and n_e the number density of electrons), the plasma density modification by ponderomotive forces, as well as the frequency transformation of a laser pulse itself [208, 271, 298].

Along with the effect of relativistic plasma "transparentization", of considerable interest is the effect of relativistic self-focusing of laser radiation [273] caused by plasma permittivity variation due to the relativistic growth of the electron mass in the transverse direction relative to the beam propagation direction and the spatial plasma density redistribution under the action of ponderomotive forces. The critical power for self-focusing was derived by Sarkisov et al. [329]:

$$W_{cr} = \frac{m_e c^5 \omega^2}{e^2 \omega_{pe}^2} \approx 17 \left(\frac{\omega}{\omega_{pe}}\right)^2 \text{ GW}.$$

Experiments carried out to observe this effect are reported in [53, 95, 182, 227, 280]. Particle-in-cell simulations [304] of laser beam filamentation are presented in Fig. 5.7. This multiray structure of the laser pulse occurs due to the filamentation instability and the buildup of transverse beam nonuniformity, which resembles the

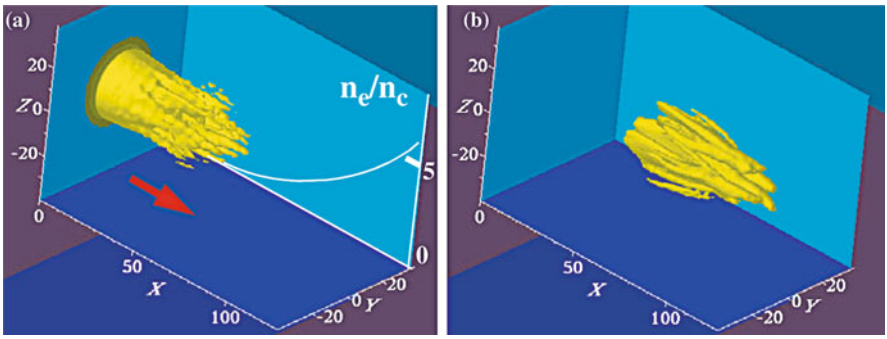

Fig. 5.7 Multiple filamentation of a wide laser beam of petawatt power [304]. There emerge several channels, which propagate quasi-independently due to their plasma screening

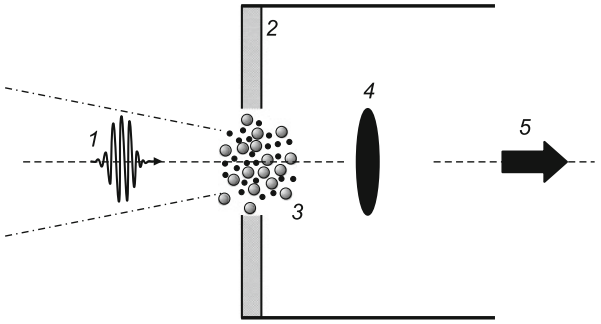

Fig. 5.8 Schematic of the generator under investigation [104]: *1*—laser pulse; *2*—target; *3*—plasma; *4*—virtual cathode; *5*—generated radiation

effect of self-focusing. The self-focusing and filamentation of laser radiation in plasma result in the formation of electron vortices [331], high-intensity compensative currents, and the generation of high magnetic fields. The problem of mega- and gigagauss magnetic fields in laser plasmas is considered in Sect. 5.8.

In [104] a study was made of the feasibility of generating terahertz radiation ($\approx$0.6 THz) in the irradiation of $\approx$0.1-ns laser pulses of high intensity $I \approx 10^{18}$–10^{19} W/cm^2. This investigation was performed by numerical simulations using a relativistic electromagnetic PIC code. In the interaction of such a pulse with the target there forms a plasma at the target (Fig. 5.8). The electrons escaping from the plasma form a virtual cathode, whose oscillations are defined not only by their own field but also by the field of plasma ions. The generation proceeds in the terahertz frequency range, the generation efficiency being three times higher than without ions, i.e. than with the traditional reditron generation mechanism, and amounts to $\approx$10 % of the electron beam power.

The state of things and prospects of laser generation of terahertz megavolt pulses were analyzed in [153].

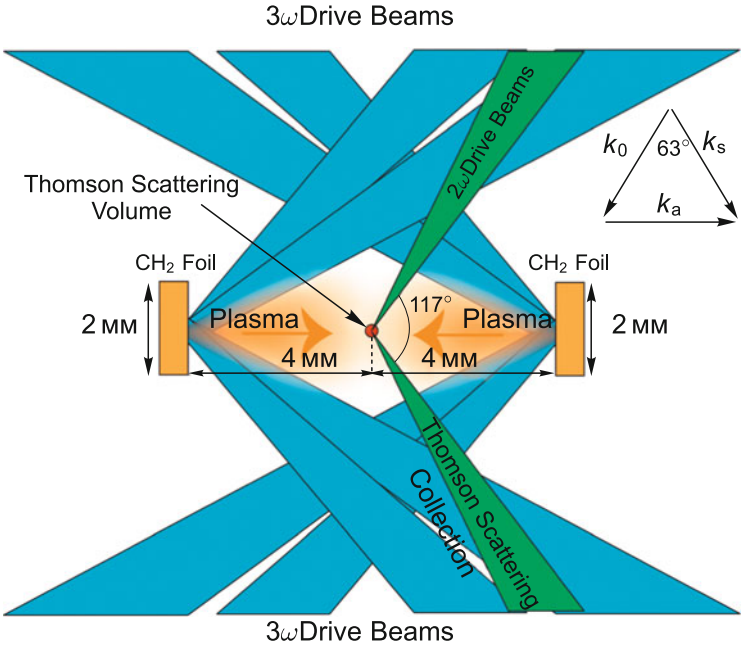

Fig. 5.9 Setup of the experiment on the laser generation of collisionless shock waves [316]. Each foil is irradiated by ten laser beams with a wavelength of ≈351 nm (3ω), a pulse duration of 1 ns, and a focal spot size of ≈250 μm

Experiments [316] in the frontal collision of laser plasma flows for the purpose of generating collisionless shock waves are shown in Fig. 5.9. CH_2 foils were irradiated by laser fluxes of intensity $\approx 10^{16}$ W/cm^2 on the OMEGA laser facility. Using Thomson scattering techniques it was shown that the ablated plasma possessed an electron temperature of ≈110 eV and a density of $\approx 10^{18}$ cm^{-3} for an expansion velocity of ≈2000 km/s. The frontal collision of such flows results in the generation of collisionless shock waves, which frequently occur in astrophysical plasmas [325] (Chap. 10).

The development of Kelvin–Helmholtz turbulence associated with collisionless shock waves was described in [228], where optical interferometric and proton radiographic techniques were used to study the dynamics of shock waves, contact discontinuities, and flows as a whole.

Similar interesting effects of relativistic nature [36, 304] are related to strongly nonlinear plasma waves, which form vacuum channels and "bubbles" (Fig. 5.10 [304]) in the plasma, produce plasma lenses for charged particles, and give rise to intense electromagnetic radiation in the frequency range from terahertz to X-rays [208, 271, 298], as well as excite collisionless shock waves [273].

The propagation of two collinear laser beams of relativistic intensity through a plasma [71] leads to the generation of intense electromagnetic wake waves. These

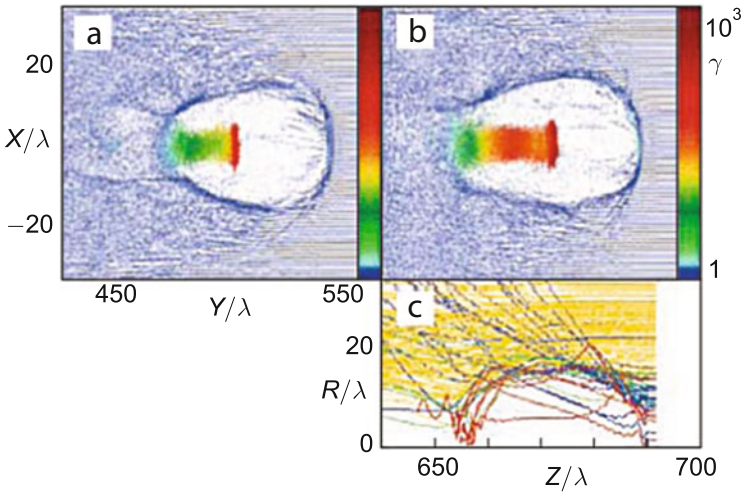

Fig. 5.10 Soliton "bubbles" in plasma under the irradiation of a 33-fs laser pulse with an energy of 12 J: (**a**) $ct/\lambda = 500$; (**b**) $ct/\lambda = 700$. (**c**) Electron trajectories in the frame of reference co-moving with the laser pulse. The trajectories of electrons initially located at different distances from the axis are indicated in color [304]

wake waves enable electrons to be accelerated (Fig. 5.5) with acceleration rates up to 100 MV/cm, which is thousands of times greater than ordinary acceleration gradients of ≈5 kV/cm (see Sect. 7.4). Gigantic longitudinal electric fields are generated in this case [42]: for an intensity $q \approx 10^{18}$ W/cm^2 the electric intensity is equal to ≈2 TV/m, for 10^{23} W/cm^2 it amounts to ≈0.1 PV/m. These acceleration rates imply that the laser version of the ordinary 50 GeV SLAC accelerator would be only 100 μm long [42]. Successful experiments have been carried out on laser-driven acceleration of electrons to energies of 10–170 MeV at laser radiation intensities of 10^{18}–10^{19} W/cm^2 [167, 236, 249]. There are reasons to believe that the advent of multipetawatt and exawatt lasers in the future would lead to the implementation of acceleration rates of the order of a teravolt per centimeter for a total kinetic energy ranging into the gigavolts—for more details, see Sect. 7.4.

In the interaction of laser radiation of moderate intensity $W \approx 5 \cdot 10^{17}$ W/cm^2 with frozen nanotargets it was possible to obtain a flux of protons with energies of 5.5–7.5 MeV [411].

Among other interesting manifestations of nonlinearities in laser plasma, we mention the nonlinear steepening of the optical front (similar to the formation of a shock wave in hydrodynamics [72]), plasma jet formation [207, 217], and high-order harmonic generation [30, 208, 286, 298, 340, 341, 348, 361, 407], which is of practical interest for lithography, holography, medicine, etc.

Under the action of a circularly polarized electric field, the plasma electrons are set in motion to generate synchrotron radiation [145, 157, 216, 273, 334], relativistic effects being significant in its description at high intensities. For $\lambda = 1$ μm this

radiation-dominant regime is realized, beginning at intensities $q \approx 3 \times 10^{23}\,\mathrm{W/cm^2}$, when a substantial fraction of laser energy is radiated in the form of hard X-rays.

Quantum optical effects come into play at $q \approx 1.4 \times 10^{26}\,\mathrm{W/cm^2}$ [42], the kinetic electron energy being equal to ≈50 TeV in this case. For $q \approx 10^{21}\,\mathrm{W/cm^2}$, the light pressure is equal to ≈300 Gbar, which is close to the pressure at the center of the Sun and is much higher than the pressure in the near-source zone of a nuclear explosion [38, 39, 369, 381]—see Chap. 4.

High-intensity lasers make it possible to achieve superstrong acceleration $a_\mathrm{e} = a_0\omega \cdot c \approx 10^{30}\mathrm{g}$ (for a dimensionless radiation amplitude $a_0 = eA/m_\mathrm{e}c \approx 10^5$), which is close to the accelerations in the vicinity of the Schwarzschild radius of a black hole [209, 396]—see Sect. 9.3. This permits the conditions in the neighborhood of black holes and wormholes to be modeled, and therefore the predictions of general relativity theory to be verified.

In particular, for $q \approx 10^{26}\,\mathrm{W/cm^2}$ the electron acceleration amounts to $a = 10^{27}g$, which is close to the conditions of the black-hole event horizon [158, 283, 374, 396]. If such acceleration is realized, an opportunity is expected to open up to study the specific electromagnetic Unruh radiation [83, 335, 371], which is similar to the Hawking radiation caused by gravitational effects. In this case, additional (in comparison with calculations by Maxwell's equations) electromagnetic radiation with an effective temperature $kT = \hbar a/c$ is bound to occur. The ratio between the power of this radiation and the synchrotron radiation power is equal to 10^{-6} at an intensity $q \approx 10^{18}\,\mathrm{W/cm^2}$ and increases proportionally with intensity, which raises expectations that it would be possible to observe it at high intensities of laser radiation.

At higher laser radiation intensities $q \approx 3 \times 10^{29}\,\mathrm{W/cm^2}$ there is a good chance to verify the predictions of modern quantum gravity theories [29, 156, 158, 318, 319] about the change of space–time dimensionality at short distances. According to Arkani-Hamed et al. [29], this distance $r_n \approx 10^{32/n-17}$ cm, where n is the number of dimensions greater than 4. In this case, the electron wave function will be reflective of a different law of gravitation for n up to 3 at distances less than 10^{-6} cm.

The effects of quantum electrodynamics, polarization, breakdown of vacuum, and spontaneous electron–positron pair production [46, 75, 76], and then of the emergence of quark–gluon plasma become significant at high optical radiation intensities $q \approx 3 \times 10^{29}\,\mathrm{W/cm^2}$.

The problem of spontaneous electron–positron pair production in vacuum touches upon many interesting situations, such as the collisions of heavy nuclei (with $Z_1 + Z_2 > 135$) [397], evaporation of black holes [170], and particle production in the universe [294]. The characteristic electric field scale [283] for the manifestation of the breakdown effect in quantum electrodynamics is the Schwinger intensity

$$E_\mathrm{S} = \frac{m^2c^3}{e\hbar} \approx 10^{16}\,\mathrm{W/cm},$$

which is sufficient to accelerate an electron to relativistic velocities over the Compton wavelength $\lambda_C = 2\pi\hbar/(mc)$ and corresponds to ultrahigh intensities of laser radiation

$$q_{QED} = q_{pe}\frac{\lambda^2}{\lambda_C^2} \approx 8.1 \times 10^{30}\ \mathrm{W/cm^2}.$$

To realize these ultraextreme conditions, the focusing of $\lambda \approx 1\ \mu$m laser radiation in a 1 mm^3 volume requires the release of ≈1 MJ of energy! This intensity threshold for electron–positron pair production is substantially lowered (to 10^{22} W/cm^2) in the case of scattering by nuclei [76, 240].

The composition of two counterpropagating laser beams yields a critical intensity of $\approx 10^{26}$ W/cm^2 for pair production, which is two orders of magnitude below the limit for a single beam [281].

Thoma [362] analyzed the feasibility of producing an ultrarelativistic $kT \gg m_e c^2$ electron–positron plasma with a temperature of ≈10 MeV by way of double-sided irradiation of a gold foil by 330-fs long laser pulses at an intensity of $\approx 7\times 10^{21}$ W/cm^2. He took advantage of quantum electrodynamics (QED) techniques and analogies with quark–gluon plasma.

The high energy densities supplied to laser plasmas turn out to be sufficient not only for diverse electronic processes, but also for nuclear transformations such as activation, fission and fusion, and transmutation [42, 96, 147, 151, 233, 246, 291, 336, 337, 370]. Apart from low-energy nuclear reactions caused by gamma-ray, electron, and proton radiation fluxes, which are generated by plasma fields, more sophisticated mechanisms of nuclear transformations are also possible. For instance, at intensities $\approx 10^{17} Z^6$ W/cm^2 there occurs a Z-fold ionization of atoms, which destabilizes nuclei of charge Z. Thus knocking out inner-shell electrons leads to disintegration of heavy elements [206, 337].

One of the directions in this research [96, 151, 159, 171, 233, 242] involves harnessing laser-accelerated electrons with energies above 200 MeV that decelerate in heavy targets to generate multimegavolt gamma-ray bremsstrahlung, which gives rise to photonuclear reactions. The photonuclear fission of uranium was successfully demonstrated and theoretically substantiated in [233, 336, 370]. Recently Magill et al. [246] realized (as a result of the (γ, n)-reaction) the laser-induced transmutation of ^{129}I—the main radioactive waste component with a half-life of 15.7 million years—into ^{128}I with a half-life of 25 min. Of considerable importance in experiments of this kind is the mechanism of the reactions of electron–positron pair production in the Coulomb field of heavy nuclei, the cross sections for these reactions being substantially (two orders of magnitude) greater than the cross section for the photonuclear reactions of $^{238}U(\gamma, f)$.

Among the possible uses of laser-induced photonuclear reactions, mention should be made [151] of the production of radioactive isotopes for medicine, the transmutation of long-lived isotopes, determination of nuclear constants, and radioactive material detection for antiterrorist purposes.

Owing to a high (≈12 % [233]) efficiency of laser radiation energy transformation to high-energy protons they may be used for the development of pulsed neutron sources by means of the nuclear reactions (p, xn) and (p, f). In any case their intensity may [151] far exceed the intensity (10^5 neutrons per joule) of Coulomb explosions of deuterium clusters. In the experiments reported in [258, 394], about 1.2×10^9 bismuth atoms were recorded, which requires via the (p, xn)-reaction more than 2×10^9 neutrons arising from the (p, xn) reaction. In this case, the neutron yield per joule of laser energy is equal to $\approx 5 \times 10^6$. Estimates for the conditions of the Vulcan laser system made in [284] predict a neutron yield of 2×10^9 for the Zn(p, xn) reaction and of order 10^8–10^{10} for the Li(p, n) reaction. The like scheme was implemented on the Titan laser facility (LLNL); it permits achieving a neutron yield of $1.8 \cdot 10^9$ [178]. We emphasize that the currently available compact neutron generators or spontaneous fission sources exhibit characteristic intensities on the order of 10^8–10^{10} neutron/s and 10^{10} neutron/(s cm^2), respectively, while stationary and pulsed reactors possess intensities of 10^7–10^{13} neutron/s and 10^{14} neutron/(s cm^2).

As noted in the foregoing, in the field of high-intensity laser radiation there occurs production of positrons, which annihilate with target electrons to emit two photons with an energy of ≈0.511 MeV. An analysis of the spectra of this radiation yields valuable information about the electronic properties of the target. Therefore positron sources are presently employed in annihilation positron spectroscopy in materials science, in positron spectroscopy in basic research, etc. Low-energy positrons find use in electron–positron plasma research, atomic and molecular physics, antihydrogen production, simulations of astrophysical phenomena, and materials science.

Estimates and experiments in positron production in laser plasmas made to date [151] suggest that the number of positrons per plasma electron may amount to 10^{-4}–10^{-2} for a total number on the order of 10^8 positrons per laser pulse. For comparison, a linear electron accelerator yields on the order of 10^9 positrons per second, which in turn is 1000 times the yield of a radioisotope source. Laser sources of positrons therefore turn out to be comparable to the traditional ones when the pulse repetition rate is increased to 10 Hz or higher.

Electrons and ions accelerated in laser plasmas may be employed to produce isotopes by means of (γ, n) and (p, n) nuclear reactions. Such devices are more compact than the existing cyclotrons and are located directly in clinics, for instance, for positron-emission tomography [84, 88, 144, 146, 147, 234]. In particular, in the Lawrence Berkeley National Laboratory a laser-plasma electron accelerator on the basis of a 10-TW solid-state laser was employed to produce the ^{62}Cu and ^{61}Cu isotopes in the (γ, n) reaction of ^{63}Cu. Considerable recent attention in the USA, Europe, and Japan has been paid to the idea of developing laser-plasma accelerators of protons with energies on the order of 200 MeV for different medical applications [271].

Proton tomography shows considerable promise for the diagnostics of fast processes in shock-wave physics and defense engineering, making it possible to obtain high-contrast pictures with a high temporal resolution [52, 244, 317, 327, 330,

382, 388]. Along with proton beams, the high-intensity 20–100 keV X-ray radiation of laser plasmas has been validly used for the X-ray diagnostics of pulsed plasma processes (Fig. 5.4) [51]. An important step in this area was made by French and Russian scientists [51, 52, 244], who accomplished a direct X-ray measurement of the density of a shock-compressed plasma in experiments involving intense laser-driven shock waves (Fig. 5.4).

Electron–positron pair production under laser irradiation was reported in [42, 76, 96, 240], where observations were made of other interesting effects as well, such as multiphoton interference and polarization of the vacuum. Nonlinear Compton scattering and pair production were recorded in the interaction of 46.6- and 49.1-GeV electrons accelerated by SLAC accelerators with laser radiation, $q \approx 5 \times 10^{18}$ W/cm^2 [283].

Tajima [353] proposed employing a high-energy (8 GeV) electron accelerator (SPring-8) and high-power lasers for experiments in QED by generating high-intensity γ-ray radiation for photonuclear reactions. In this case, a study can be made of the interplay of strong and weak interactions. Combining accelerators with lasers may hold much promise for the development of new-generation optical sources, such as femtosecond synchrotrons and coherent X-ray radiation sources [148, 171, 174, 283, 339].

Further advancement along the laser intensity scale (Fig. 5.2) is hard to predict, for it is limited by our knowledge of the structure of matter in the immediate spatiotemporal neighborhood of the Big Bang at ultrahigh energy densities.

5.3 Laser-Induced Shock Waves

High-power pulsed lasers, which were developed for controlled thermonuclear fusion and nuclear substance simulation, provide a unique possibility of generating light pulses with energies ranging into the megajoules and powers of several hundred terawatts. Irradiating a condensed medium by such pulses produces record local energy densities, which no other method is able to provide in laboratory conditions. This circumstance makes high-power laser systems a highly promising tool for investigating substance in a plasma state with extremely high energy densities.

Measuring the parameters of compressed substance is a special problem. This is partly due to the small spatial size, strong nonuniformity, and short lifetime of the substance in a strongly compressed and heated state. This difficulty may in principle be overcome by increasing the laser energy. However, it is easily seen that the requisite energy is proportional to the cube of the characteristic size (or, which is the same, to the cube of inertial confinement time), and therefore the practical feasibility of increasing the scale of the experiments is severely limited. Another difficulty of diagnosing the compressed and heated substance is due to the spherical laser experiment geometry itself, whereby the compressed inner target layers are "screened" by the hot and relatively tenuous expanding plasma of the corona.

The diagnostics is substantially simplified on going over to planar compression geometry: in this case, to determine the parameters of compressed substance it is possible to use the mass, momentum, and energy conservation laws, which assume the simplest form of a system of algebraic equations in the case one-dimensional quasistationary flow (see Sects. 3.4–3.6). The approach based on the application of the conservation laws to a stationary shock discontinuity is central to dynamic high-pressure physics [138]. It was validly employed for studying the thermodynamic and kinetic substance properties in the megabar pressure range. In this case, chemical explosives or light-gas launching devices were used to generate shock waves.

The employment of high-power lasers for the generation of shock waves makes it possible to substantially broaden the attainable pressure range. It is evident that in laser experiments, too, the classical approach reliant on the use of plane quasistationary shock waves holds the greatest promise for executing quantitative measurements. To date, the majority of experiments in the laser generation of intense shock waves have been carried out in precisely this traditional formulation, which imposes certain restrictions on the target and laser pulse parameters. In this formulation it is presently possible to generate in metals the laser-driven shock waves with behind-front pressures of tens of megabars and even gigabars. These values are several times higher than those attainable with the conventional technique of condensed explosives and light-gas "guns"; they are comparable only to the pressures achieved in the near zone of underground nuclear explosions (see Chap. 4).

Immediately after the advent of lasers their unique properties were employed to advantage for generating intense shock waves and obtaining extreme substance states with their aid [19]. The first experiments are schematized in Fig. 5.11.

Long-term irradiation of a target (Fig. 5.11) produces an evaporated substance cloud above its surface. For a moderate laser intensity this is a vapor of neutral molecules and atoms, which is normally transparent to the radiation [16]. Then, the energy is absorbed in the near-surface layer of condensed substance. This layer

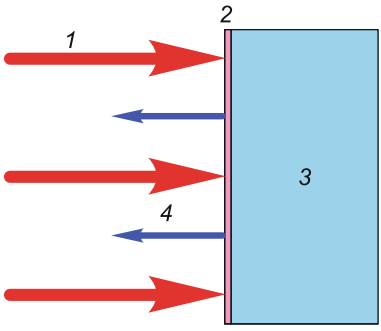

Fig. 5.11 Schematic representation of the first laser target irradiation experiments. Vapor expands along *arrows 4* in opposition to the laser beam shown by *arrows 1*. If the vapor is transparent to radiation, its absorption takes place in the surface layer *2*. This layer separates the target and the vapor. The vapor pressure sets in motion the target material *3*

heats up, melts, and vaporizes. The vapor flows in the opposite direction to the laser beam [16]. This flow exerts pressure, which makes the vapor expand towards the laser beam.

At high intensities I the substance removed from the condensed target surface ionizes to form a plasma cloud or a plume. This cloud is also referred to as the laser plasma corona. The issues of corona dynamics have been thoroughly studied for many years in connection with the problem of inertial laser fusion (see, for instance, [18, 19, 303]). The plasma is normally opaque to the radiation: its absorption takes place inside the corona (with its density decreasing away from the target) in the vicinity of the critical surface. This surface is so named because the electron density at this surface is equal to the critical value, whereby the plasma frequency, which lowers away from the surface, is equal to laser radiation frequency. This density is $\approx$10–100 times (depending on the hardness of a laser photon) lower than the solid-state density, with which the plasma is delivered to the corona.

The heat absorbed at the critical surface *2* in Figs. 5.12 and 5.13 is transported by electron thermal conduction to the target surface. The heat transfer by thermal conduction is shown by arrow *3* in Fig. 5.12. The corresponding thermal wave profile is shown in Fig. 5.13. Ablation front *4* forms the target boundary. The solid-density substance begins to heat up at this front, its density lowers, and a new portion of the substance is delivered to the flow from the target to the corona. The velocity of this portion of the substance is shown by the left arrow u in Fig. 5.12. This portion reaches the critical surface *2*, crosses it, and continues its expansion in vacuum.

The target surface is termed the ablation front. To the right of front *4* is the relatively cold target substance of solid-state density. The flow is subsonic in the

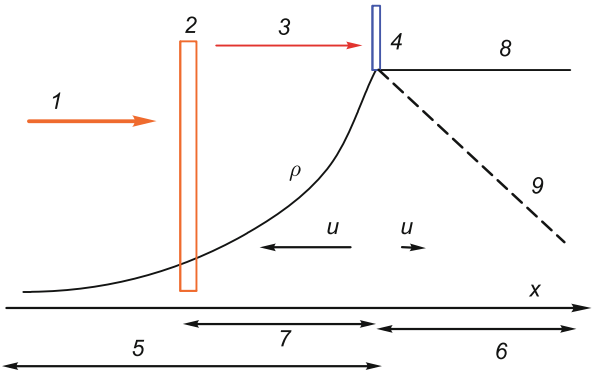

Fig. 5.12 Structure of laser plasma corona near the target: *1*—laser beam; *2*—neighborhood of critical density surface, where the laser energy is absorbed; ρ–density profile in the target *6* and the corona *5*; profiles *8* and *9* refer to the cases of thick and thin targets, respectively; *4*—ablation front, which separates in the drawing the cold dense substance to the right of the front and the hot low-density plasma to the left. *Arrow 3* indicates the heat flux from the critical surface *2* to the ablation front *4*. The *left arrow u* denotes the plasma outflow from the ablation front. The hot plasma pressure in subsonic "pillow" *7* moves the dense target substance in the direction of the *right arrow u*. In this sense the corona acts as a piston which pushes the target substance

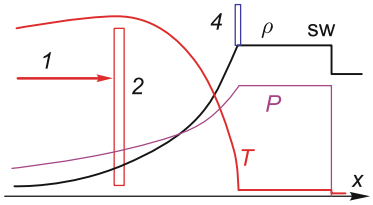

Fig. 5.13 Density ρ, pressure p, and temperature T profiles produced under irradiation by a long pulse of sufficiently high power. This case is of interest for laser fusion problems; *1*—laser beam reaching the critical density surface *2*; *4*—ablation front. It is the thermal wave front behind which the temperature rises sharply. The corona pressure sustains the quasistationary propagation of a shock wave (SW) through the uniform target substance

space *7* between the critical density *2* and the ablation front *4*. The hot plasma pressure ahead of the ablation front is transferred to the solid-state density substance behind the ablation front. Like in the case of vapor, it is precisely the corona pressure that drives the flow in the target, which is indicated by the right arrow u in Fig. 5.12. The u arrows indicate the flow direction in the coordinate system related to the initially immobile target substance. In the case of a thick target the density profile ρ extends into the target along a straight line *8* in Fig. 5.12. In this case, the corona pressure sustains the shock wave traveling into the target interior. This shock wave is shown in Fig. 5.13.

By recording the parameters of this wave in experiments it is possible to gain information about the thermodynamics of the shock-compressed substance (see Sect. 5.5).

Recording the shape of the compression pulse as it exits the free surface yields ample information about the mechanical properties of the medium at high pressures, temperatures, and deformation rates.

In the case of a thin target, the pressure vanishes at the rear target side (the side reverse to the ablation front *4*). That is why the substance density and pressure decrease in the direction of curve *9* in Fig. 5.12. The pressure gradient in the dense substance on the right of the ablation front in Fig. 5.12 accelerates the target substance. This underlies the well-known principle of spherical shell acceleration.

The resultant flow may be represented as consisting of three portions: (1) a stationary shock wave followed by (2) a Chapman–Jouguet deflagration wave, where the light energy is absorbed, and the closing flow in the form of (3) a simple centered rarefaction wave (adiabatic or isothermal).

In this case, the highest attainable pressure is

$$p_{\max} = I^{2/3}\rho_c^{1/3},$$

where I is the intensity of laser radiation of frequency ω and ρ_c is the critical plasma density ($\omega_0 = \omega_p = \sqrt{4\pi e^2 n_e/m_e}$).

An analysis of this relation suggests that the pressures attainable under laser irradiation depend only slightly on the chemical target composition. Herein lies a significant difference between the laser methods of pressure generation and the classical methods of dynamic physics which use the impact of metallic plates or the detonation products of condensed explosives. It is instructive that high-frequency radiation offers considerable advantages from the standpoint of maximizing plasma pressures. However, the main advantage of short-wavelength radiation consists in a lowering of the effect of nonthermal electrons with increasing laser frequency.

It is well to bear in mind that the above qualitative estimate was obtained for the interval of laser pulse parameters in which the simplified interaction model mentioned above is purely schematic [19]. The matter is that the absorption of light is essentially nonlinear in character at radiation intensities of 10^{13}–10^{17} W/cm^2. In this case, a substantial fraction of light is reflected from the plasma, and the reflection coefficient also depends on the radiation intensity. As a result, the formula for the absorption coefficient used to estimate the screening time turns out to be oversimplified. For high laser intensities there arise a number of complications, which may be fully taken into account only in the framework of arduous numerical simulations. The results of these simulations are approximated by the relation:

$$p_{\max} = \alpha I^{\alpha} \lambda_0^{-\beta},$$

where $\alpha \approx$ 0.3–0.7 and $\beta \approx$ 0.3–2.0, depending on the model and the radiation intensity [19].

The requirements imposed on laser radiation and target size to obtain plane stationary shock discontinuities propagating through a relatively cold substance were formulated in [19]. This will permit using the dynamic diagnostic method based on the application of the conservation laws to the flow of shock-compressed plasmas. The limitations emerging in this case will define the highest pressure level attainable with the aid of contemporary lasers. With the inclusion of shock wave attenuation and curvature due to the rear and side unloading waves as well as considering the nonhydrodynamic target heating by nonthermal electrons, a conclusion was drawn that the energy E_{las} of laser radiation of wavelength λ_0 required for generating pressure p may be represented as [19]:

$$E_{\text{las}} \sim p^6 \lambda_0^{11}.$$

Therefore, the constructive way of advancing further along the pressure scale of laser-driven shock waves involves the use of shorter wavelengths and layered targets to suppress the role of electron heating. This is the reason why experimenters aspire to use the high-order harmonics of the fundamental radiation or laser-to-soft X-ray radiation conversion in “hohlraum” schemes in experiments with laser-induced shock waves (see Sect. 7.2.1).

In accordance with the general ideology of dynamic experiments[138], to investigate the equation of state requires measuring independently any two of the

five parameters which characterize the propagation of a plane stationary shock discontinuity (D, u, p, V, E), with the subsequent calculation of the remaining parameters from the general conservation laws at the shock front. This permits finding the equation of state of the substance under investigation in the caloric form $E = E(p, V)$. The phase velocity D of shock propagation is measured most easily and accurately in dynamic experiments by baselength electrocontact and optical techniques. For measuring baselengths of ≈20–50 μm typical for laser-induced shock waves and discontinuity propagation velocities of 20–50 km/s, the characteristic experiment time is of the order of 1 ns, making optical measurements the method of choice.

In opaque materials a shock wave may be recorded at the instant it reaches the free surface of a stepped target. In this case, it becomes visible on approaching the free surface to within several light paths l_r. For the optical range in metals $l_r \approx 10^{-5}$ cm; for a propagation velocity $D \approx 20$ km/s this will lead to a light signal rise time $\tau \sim l_r/D \approx 5$ ps, which determines the requisite time resolution of the streak cameras employed in these experiments.

Measurements of the second dynamic parameter run into significantly greater difficulties. In the dynamic experiments that use explosive equipment and light-has launching devices, in the determination of the mass velocity u of shock-compressed substance the widest acceptance has been gained by a method of "reflections", which is based on the application of general gas-dynamic laws, which are obeyed in the breaking of an arbitrary discontinuity. Specific measurements involve recording the phase velocities of shock propagation in the substance under investigation and a "reference" (the substance with the known shock adiabat), which permits finding the mass velocity of motion of the substance under investigation on the strength of the pressure and velocity continuity conditions at the contact boundary. The shock adiabat of the "reference" is independently determined by a "deceleration" method, in which measurements are made of the shock wave velocity in the reference and the flight velocity $w = 2u$ of the liner made of the "reference" material. The method of "reflections", which is central to the dynamic high pressure physics, has made it possible to determine the shock compressibility of many chemical elements and compounds. The characteristics of more than 300 substances investigated to date at pressures of up to ≈5 Mbar are collected in reference books [254, 376]. With strong underground explosions and nuclear charge detonation (see Sects. 3.6 and 4.3), shock pressures of tens of megabars were obtained, for which the problem of references is a challenge, since the "deceleration" method is hard to apply here. In this case. it has been possible to measure only the relative substance compressibilities from the reference adiabat extrapolated beyond the domain of direct measurements. Used as references in this case are elements with a high atomic number, for which quantum-statistical calculations are most reliable. It is significant that in doing so it is necessary to resort to distant (from 5 to 300 Mbar) extrapolations in the construction of reference shock adiabats.

The method of recording u proposed in [365] involves displacement measurements of the contrast interface between heavy and light substances using a side X-ray backlighting of a layered target and a fast-response X-ray detector [302].

According to estimates [365], this method of measuring u may yield an accuracy of about 6–8 %.

In next-generation laser experiments, apart from kinematic characteristics, measurements are made of a more complete set of physical parameters. For significant substance compressions in the shock waves of extreme intensity, measuring the wave and mass velocities of motion is not optimal from the standpoint of determining the equation of state. In this case, along with D it is desirable to directly measure the degree of plasma compression in the shock wave from either the absorption of X-rays, like was done in [52, 136] for a nonideal plasma, or the Stark broadening of spectral lines in the X-ray spectral range [37]. Quite helpful are temperature measurements (pyrometric or spectral Doppler) measurements: in view of shell structure manifestations at high pressures, it is precisely the temperature dependence which would be expected to exhibit significant nonmonotonicities.

Experiments with plane stationary shock waves are the simplest and easily interpretable type of experiments to study substance properties at high pressures and temperatures. however, the use of high-power lasers also opens other interesting possibilities in experimental high energy density physics. Irradiating thin (1–10 μm) metallic targets by laser radiation with $I\lambda_0^2 > 10^6$ W results in the heating of the opposite side of the target by nonthermal electrons [80, 98, 160, 367] and ions. By comparing the measured temperature with simulation data [251, 262] it is possible to improve the theoretical models relating to this phenomenon, which has not been adequately studied. At lower values of $I\lambda_0^2$ this is the way to investigate the special features of electron thermal conduction in laser-produced plasmas [251, 256, 390]. We note that nonthermal electrons are an efficient source of the rapid volume heating of condensed substances to temperatures of several electronvolts. The decay of such high-temperature states was used for generating intense shock waves in [161].

As is well known, under a single shock compression the density of compressed substance may not exceed some limiting density. That is why the extremely interesting domain of the phase diagram corresponding to supercompressed substance is unattainable in the simplest experiments with one stationary shock wave. Several approaches were proposed for reaching this domain; their common feature is a small increase in entropy in the compression. In experiments with high-power lasers it is possible to employ not a single pulse, but a sequence of several pulses optimized in amplitude and frequency, or one continuous pulse of specially tailored shape and growing intensity [15, 389]. Instead of programming the laser pulse shape it is possible to use a layered or shell target with a desired initial density profile. Some other possibilities are discussed in [47]. We emphasize that the task of measuring the parameters of compressed substance is quite intricate for all experiments with quasi-isentropic compression. In resembling experiments aimed at solving laser fusion problems advantage is taken of X-ray photography, spectroscopy of multiply charged ions, detection of fusion reaction products, and indirect techniques based on the measurement of corona parameters. Certain possibilities are offered by the method of recording shock waves at an appreciable distance from the place of laser radiation focusing. Using the theory of a point explosion [338] enables estimating the effective explosion energy [3].

Laser methods may by helpful not only in studying strongly compressed substances with above-solid densities. Using the expansion of a material heated by a laser-driven shock wave or nonthermal electrons [161] it is possible to obtain a broad spectrum of states in an isentropic unloading wave. These include the domain of strongly nonideal Boltzmann plasma, the neighborhood of the high0temperature boiling curve, and metal-dielectric transition domain [136, 164].

Even a brief enumeration of the possible and already executed experiments at very high local energy densities attainable with modern lasers shows that this technique offers enormous advantages over other methods of obtaining high pressures and enables obtaining new physical information about extreme states of substance. Naturally, such measurements are at the forefront of modern fast-response recording instruments and interpreting these experiments calls for new physical models and complex numerical simulations.

In conclusion we consider some experiments in laser production of shock waves in solids and discuss the effects associated with this method of shock production.

The first experiments in the excitation of shock waves in solid hydrogen and plexiglass were carried out with a modest-power neodymium laser [375] for an energy $E \approx 12\,\mathrm{J}$ and a pulse length $\tau = 5\,\mathrm{ns}$. Owing to the small ($\approx 40\,\mu\mathrm{m}$) size of the focal spot, the shock waves with the peak pressure of $\approx 2\,\mathrm{Mbar}$ rapidly became spherical and decayed. For a radiation intensity $I = 3.5 \cdot 10^{14}\,\mathrm{W/cm^2}$ a shock pressure of $\approx 1.7\,\mathrm{Mbar}$ was obtained in polyethylene [56], and the respective amplitude pressures obtained in hydrogen and plexiglass for $I = 2 \cdot 10^{14}\,\mathrm{W/cm^2}$ were equal to ≈ 2 and 4 Mbar [355]. Measurements of the energy of plasma corona ions and the target recoil momentum (integral methods) permitted estimating the pressure in the aluminum target for $I \approx 10^{14}\,\mathrm{W/cm^2}$ [166].

A higher-power neodymium-glass Janus laser system [231] with a pulse energy of up to 100 J and a pulse duration of 300 ps was employed for producing plane shock waves [351, 366, 377]. Radiation intensities I of up to $3 \cdot 10^{14}\,\mathrm{W/cm^2}$ were produced in focal spots 300–700 μm in diameter.

From the shock transit time through a stepped aluminum sample it was possible to estimate the shock discontinuity front velocity at 13 km/s (corresponding to a pressure of $\approx 2\,\mathrm{Mbar}$) and measure also the velocity of plasma corona expansion. Recording the temporal buildup of radiation intensity as the shock reached the free surface ($\Delta t \leq 50\,\mathrm{ps}$) permitted estimating the thickness of the shock discontinuity at $\lesssim 0.7\,\mu\mathrm{m}$. The shock pressures were increased by an order of magnitude. In [366] use was made of a small diameter target to lower, in the authors' opinion, the effect of surface currents [50, 307], and an agreement was obtained between theory [412] and experiment [366].

Plasma pressures $p \approx 35\,\mathrm{Mbar}$ were obtained [368] in the irradiation of a target consisting of a 22 μm thick aluminum layer and a 32 μm thick gold layer by ten overlapping beams of the Shiva neodymium laser facility with $\lambda_0 = 1.05\,\mu\mathrm{m}$ [232]. The peak intensity was equal to $2.9 \cdot 10^{15}\,\mathrm{W/cm^2}$ for a pulse duration of 625 ps. The velocity of the shock wave in gold was measured at 17.3 ± 0.3 km/s and was consistent with a two-dimensional hydrodynamic simulation [412], in which the absorbed energy fraction was equal to 30 % and the laser beam convergence

was taken into account [169]. Measurements of the X-ray emission spectrum in this experiment enabled estimating the heating of the rear target side by nonthermal electrons. It turned out to be under 500 °C, while the temperature of the shock-compressed plasma was about 5 eV.

A version of the "reflection" method was implemented in experiments [378] with a layered target, when a shock wave with an amplitude $p \approx 3$ Mbar transited from aluminum to gold ($p \approx 6$ Mbar) in low-attenuation conditions. Like in [377], the laser radiation ($E \approx$ 20–30 J, $\tau = 300$ ps) was nonuniformly distributed over the focal spot, its shape varying from circular (with a diameter of $\varnothing 100$ μm) to elliptical (with axes of 200 and 500 μm). In the authors' opinion, the latter circumstance was the main source of errors in these experiments ($\delta D = 15$ %, $\delta p = 30$ %).

Systematic investigations of the shock compressibility of aluminum and copper were carried out using comparative method on the Janus laser facility [183] in the intensity range $I \approx 5 \cdot 10^{13} - 4 \cdot 10^{14}$ W/cm^2 ($E \approx 30$ J, $\tau = 300$ ps). A thin gold layer in the target was employed to absorb nonthermal electrons and lengthen the duration of the shock wave (lowering, however, the peak pressure to an extent). The resultant data pertain to a 2–6 Mbar pressure range in aluminum and to 4–8 Mbar in copper and are in good agreement with the findings of dynamic experiments performed using high explosives and light-gas launching facilities [12, 267].

Along with the reflection technique, elaborated in laser experiments [52, 302] is the method of plasma velocity measurements by pulsed X-ray radiography. A 17 μm thick aluminum target was irradiated by a laser beam of the Shiva facility with an intensity $I = 6 \cdot 10^{14}$ W/cm^2 ($E = 110$ J, $\tau = 600$ ps). In this case, one of the beams of this facility irradiated a tantalum target, which gave rise to X-rays with a characteristic energy of 1.9 keV. The picture of motion in the field of X-ray radiation was recorded with a fast-response X-ray camera (an X-ray microscope [302]) with a temporal resolution of 15 ps and spatial resolution of 4.5 μm, which permitted measuring the plasma velocity at $8 \cdot 10^6$ cm/s.

We mention the experiments on the generation of shock waves by short-wavelength laser radiation performed in [368], because predictions are made for these modes about an increase in the peak pressures of shock-compressed plasmas due to an increase in absorbed laser energy fraction and nonthermal electron suppression. The laser radiation with $\lambda_0 = 0.35$ μm and an intensity of $(1–2) \cdot 10^{14}$ W/cm^2 ($\tau = 700$ ps) irradiated a 25 μm thick aluminum target to generate in it a shock wave with a pressure of 10–12 Mbar. In this case, the energy absorbed by the plasma amounted to ≈95 % of the incident flux. Irradiation by long-wavelength ($\lambda_0 = 1.06$ μm) radiation with $I = 3 \cdot 10^{14}$ W/cm^2 (the absorbed intensity was $1.2 \cdot 10^{14}$ W/cm^2) for the same formulation of the experiment produced a pressure of ≈6 Mbar.

Several other early papers on the laser-assisted production of intense shock waves may be found in [19, 138].

Experimental data on the shock-wave compression of hydrogen, deuterium, and rare gases in the megabar range are given in Sect. 3.4 and Chap. 10.

5.4 Mechanics of Ultrafast Deformations

High-power lasers are not only a modern physical instrument for producing high energy densities, but a unique means for implementing and studying ultrafast processes in condensed substance states.

The physics and mechanics of interactions depend strongly on the duration of a laser pulse. For a duration of ≈ 1 ns and above, the main mechanism is the evaporative one (Fig. 5.11), while the thermomechanical mechanism is basic to the femtosecond range. In both cases, ultrahigh deformation rates are dealt with.

5.4.1 Mechanical Properties in Ultrafast Deformations

The shock wave technique is a powerful tool for studying the properties of materials at extremely high deformation rates. The methodology of this scientific area relies on the relation between the experimentally recorded parameters of substance flow and the physical and chemical processes occurring therein. The progress of research into the high-speed deformation, disruption, and physicochemical transformations in shock waves is largely related to the development of modern techniques for measuring wave processes with high spatial and temporal resolution [209–211]. To date, a great body of experimental data has been gained about the elastoplastic and strength properties of technical metals and alloys, geological materials, ceramics, glasses, polymers and elastomers, plastic and brittle monocrystals in the microsecond and nanosecond ranges of action duration, and considerable progress has been reached in the development of methods for obtaining information about the kinetics of energy liberation in detonation and initiating shock waves. The experimental data underlie the phenomenological rheological models of deformation and disruption, and the macrokinetic models of physicochemical transformations, which are required for calculating explosions, high-speed impacts, and high-power pulsed radiation–substance interactions.

The use of high-power pulsed lasers for generating shock waves offers several advantages over the impact of plates, but it is also associated with some problems. Pulsed laser technology provides the possibility of advancing to the domain of ultrashort load duration, down to the picosecond range. In this case, the test sample survives for the subsequent microstructure analysis under minimal additional actions produced by the high kinetic energy of a striker. On the other hand, the radiation power distribution over the cross section of the laser beam is nonuniform, and additional precautions must be taken to generate plane shock waves with the one-dimensional motion of the substance behind them.

Among the objects of measurements and analysis are the shock compression wave, its following rarefaction wave, as well as the wave interactions in the reflection of the compression pulse from the free rear surface of the test sample. The structural transformation, plastic flow, and disruption processes are associated

with changes in substance compressibility and therefore manifest themselves in the structure of compression and rarefaction waves. The pulse of shock compression in a plane sample is usually generated by the impact of a plate accelerated in one or other way to a velocity ranging from several hundred m/s to several km/s, and to tens of km/s in record experiments. The diameter-to-thickness ratios for the striker and sample are taken to be high so as to ensure the one-dimensionality of the wave process throughout the measurement time. The experiments involve continuous measurements of the velocity profiles $u_{\mathrm{fs}}(t)$ of the free sample surface, for which purpose use is made of the laser Doppler velocity meters VISAR [43] or ORVIS [57] with nanosecond temporal resolution.

A typical measurement result is displayed in Fig. 5.14, which shows the velocity profile of the free surface of a 40Kh steel sample loaded by the impact of an aluminum plate with a velocity of 1.9 ± 0.05 km/s. In this experiment the shock compression pressure was equal to 19 GPa. The velocity profile exhibits the moments at which three compression waves sequentially reach the sample's surface. Owing to an increase in longitudinal compressibility on transiting from elastic to plastic deformation, the shock wave loses stability and splits into an elastic precursor and its following plastic compression wave. At a pressure of $\approx$13 GPa the material experiences a transition from the body-centered lattice to the face-centered close-packed lattice ($\alpha \rightarrow \varepsilon$) attended with a lowering of the specific volume, with the result that the plastic compression wave splits into two in this pressure domain. The pressure behind the front of the first plastic shock wave corresponds to the onset of the transformation, while its attenuation and compression rate in the second plastic wave are determined by the kinetics of the structural transformation. After the shock wave circulation in the striker there forms a rarefaction wave, which then propagated through the sample after the shock wave. The arrival of the rarefaction wave at the sample's surface results in a lowering of the surface velocity. The reflection of compression pulse from the free surface gives rise to tensile stress inside the sample. The material disruption (the splitting-off) under the tension is attended with stress relaxation and gives rise to a compression wave, which arrives at the surface in the form of a so-called split-off pulse to increase its velocity once again. Measurements

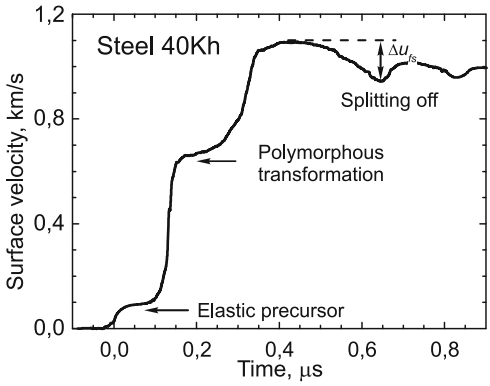

Fig. 5.14 Velocity profile of the free surface of a 4 mm thick 40Kh steel sample impacted by a 2 mm thick aluminum plate with a velocity of 1.9 ± 0.05 km/s

of the resistance to splitting-off provide information about the strength material properties under submicrosecond load durations.

The longitudinal stress at the front of the elastic precursor or the Hugoniot elastic limit (HEL)

$$\sigma_{\mathrm{HEL}} = 0.5 u_{\mathrm{fse}} \rho_0 c_{\mathrm{l}},$$

where u_{fse} is the free surface velocity jump in the precursor, ρ_0 is the initial material density, and c_{l} is the longitudinal sound velocity in the material; the stresses are assumed to be positive. The elastic limit under a one-dimensional deformation is related to the yield strength σ_{T}, in the ordinary sense of the word, by the equation

$$\sigma_{\mathrm{T}} = \frac{3}{2} \sigma_{\mathrm{HEL}} \left(1 - c_{\mathrm{b}}^2 / c_{\mathrm{l}}^2\right),$$

where $c_{\mathrm{b}} = \sqrt{K/\rho}$ is the "bulk" sound velocity and K is the compression modulus. Since the rate of plastic deformation of crystalline bodies is determined by the density of dislocations and their velocity, which are limited in magnitude, the stress of plastic flow increases with shortening the duration of load action. In shock wave experiments the dependence of the flow stress on the deformation rate manifests itself, in particular, in the attenuation of the elastic precursor with propagation and in the finite parameter growth times in the shock wave.

The split-off disruption in the reflection of the shock compression pulse from the free surface of a body takes place by way of initiation and growth of numerous cracks or pores. The rate of these processes and, accordingly, the stress relaxation rate in the disruption depend on the magnitude of the acting tension and may not be arbitrarily high. This is the reason why the higher is the rate of load application, the higher is the split-off (spall) strength. An analysis of the split-off effects in the compression pulse reflection from the free surface of a body makes it possible to determine the rupture tension (the split-off material strength) for submicrosecond load durations from the measured profile of the free surface velocity $u_{\mathrm{fs}}(t)$. The split-off strength σ_{sp} is determined from the velocity decrease $\Delta u_{\mathrm{fs}}(t)$ from the peak velocity to its value ahead of the front of the split-off pulse. In the linear (acoustic) approximation the simplified formula for determining the split-off strength is of the form

$$\sigma_{\mathrm{sp}} = \frac{1}{2} \rho_0 c_{\mathrm{b}} \left(\Delta u_{\mathrm{fs}} + \delta\right),$$

where δ is a correction for the velocity profile distortion due to the difference between the velocity (c_{l}) of the split-off pulse, which propagates through the tensile material, and the velocity of the plastic part of the incident unloading wave in front of it (c_{b}) [28, 212]. To take into account the nonlinearity of material compressibility, the magnitude of σ_{sp} is actually calculated using equation-of-state extrapolations to the negative-pressure domain.

To date a considerable body of measurements of the elastoplastic and strength properties of solids has been carried out with the use of laser-driven shock waves. At present, the use of laser-driven shock wave technique permits making measurements at tension levels comparable to the limiting, or "ideal", strength of condensed substances, which defines the upper bound for the possible resistance to rupture. It is well known that the elastic moduli of solids (and liquids) increase with compression and, accordingly, decrease under tension. For some value of tensile stress the bulk modulus must vanish: $dp/dV = 0$, which corresponds to the absolute loss of condensed state stability. It is these strain values that are meant by the term "ideal strength". The states with zero bulk modulus correspond to the spinodal of condensed substance [342] and, generally speaking, must be unattainable in real experiments. Apart from the limiting tensile strength there exists a limitation on the magnitude of shear stress in a solid. The ideal shear strength is defined as the shear stress τ whereby its derivative with respect to shear deformation γ vanishes: $d\tau/d\gamma = 0$. There also exist definitions of ideal shear strength as the stress required for the nucleation of dislocations and production of stacking faults in a perfect crystal without participation of thermal fluctuations or as the condition for the phonon instability of the crystal lattice.

Figure 5.15 shows the normalized values σ_{sp}/σ_{id} of the split-off strength σ_{sp} for metal monocrystals, amorphous polymers and liquids as functions of deformation rate [211, 212]. Although the measured the split-off strengths of these materials differ by more than two orders of magnitude, in the normalized coordinates the data scatter is smaller.

The data presented in Fig. 5.15 suggest that up to 30 % of the ideal strength of condensed substance is realized for nanosecond load durations. The fcc-structured ductile monocrystals of copper and aluminum exhibit a somewhat higher degree of realization of the ideal strength than iron and molybdenum, which possess a bcc crystal lattice. This is supposedly due to the possibility of higher stress densities in the neighborhood of microdefects for bcc-lattice metals with higher yield strengths. The degree of realization of the ideal split-off strength for amorphous polymers and liquids is at least no smaller than for metals. The difference in the degree

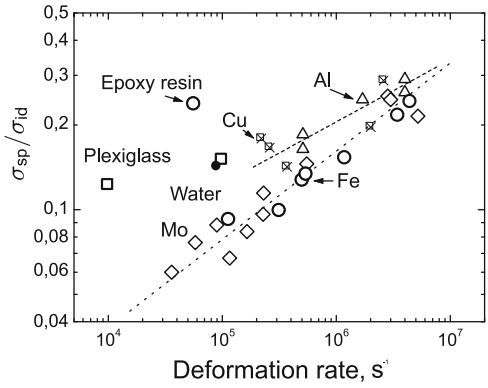

Fig. 5.15 Degree of realization of the ideal split-off (spall) strength σ_{id} of homogeneous materials (single crystals, amorphous polymers and liquids) as a function of deformation rate

of realization of the ideal strength becomes smaller as the load duration becomes shorter.

The temporal resolution of the laser Doppler velocity meters VISAR and ORVIS is limited by a value of about 10^{-9} s, which is defined by the interferometer delay line. In this case, the uncertainty of amplitude measurements is inversely proportional to the time delay. The duration of compression pulses generated by femtosecond laser pulses is determined, apart from the parameters of the laser pulse itself, by the temperature distribution in the surface target layer several hundred nanometers in thickness, which is formed in the course of temperatures equalization of the electrons and ions of the crystal lattice. The characteristic duration of the shock load under these conditions amounts to tens of picoseconds, making the use of VISAR or ORVIS impossible. The employment of femtosecond interference microscopy [6, 268, 359] permits attaining a time resolution of 10^{-12} s. This method makes it possible to measure, correct to 1 nm, the sample surface displacement with time in the course of arrival of the shock compression pulse at the surface. To obtain the surface velocity profile required for the analysis, these data must be differentiated in one or other way, which is associated with an additional uncertainty, which is not too high, by the way.

Femtosecond laser techniques are employed to investigate the shock-wave phenomena in metallic film ranging from hundreds of nanometers to several micrometers in thickness [9, 32, 33, 97, 387]. Suchlike thin films are insufficiently rigid, and therefore experiments are carried out on metallic samples deposited by evaporation on glass substrates.

Figure 5.16 shows the data of measurements [32, 33] of the shock wave velocity U_S and mass velocity u_p behind the shock front in submicrometer-thick aluminum samples in comparison with its shock adiabat measured on samples several millimeters in thickness. The reason for the disagreement of these data is that the dynamic elastic limit in submicrometer-thick aluminum samples amounts to 21 GPa, i.e. the measured values of U_S and u_p pertain to the shock adiabat of elastic compression. for comparison we note that the dynamic elastic limit of diamond lies in the 50–

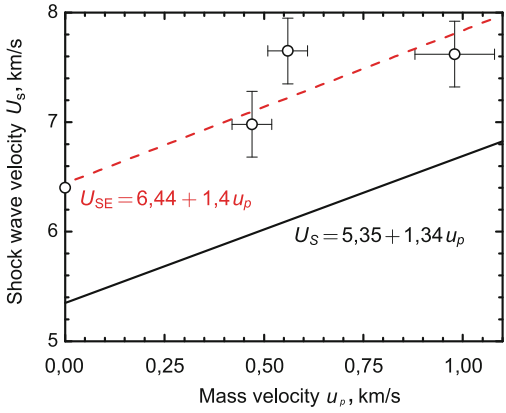

Fig. 5.16 Results of measurements of the shock wave velocity and mass velocity behind the shock front in submicrometer samples of aluminum in comparison with its shock adiabat

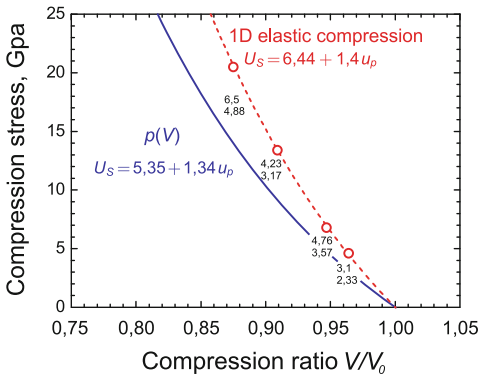

Fig. 5.17 Aluminum shock-compressed states realized in submicrometer film samples irradiated by femtosecond laser pulses

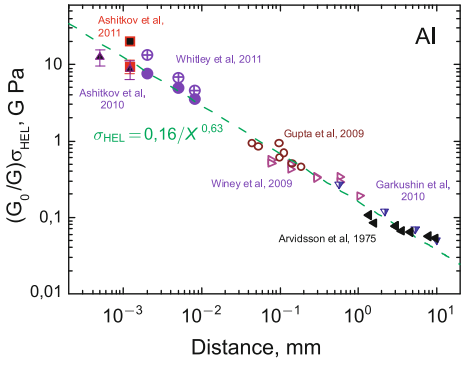

Fig. 5.18 Amplitude of elastic shock wave in aluminum as a function of traversed distance

100 GPa range [204, 261], i.e. in the picosecond load duration range the elastic limit of aluminum becomes comparable to the elastic limit of diamond. With reference to the data given in Fig. 5.17, the departure of the elastic shock-compressed state of aluminum realized in film samples from the three-dimensional compression shock adiabat amounts to 6.5 GPa. This corresponds to the highest shear stress of about 4.9 GPa, which exceeds the aluminum's ideal shear strength of 3.2–3.5 GPa predicted by ab initio calculations and molecular-kinetic simulations [90, 205]. On the other hand, the elastic modulus and, accordingly, the ideal shear strength of materials increase under compression.

The experimental data on the attenuation of the elastic precursor in aluminum are collected in Fig. 5.18. According to these measurements, the compression stress behind the precursor front, which is equal to the dynamic elastic limit (HEL) of aluminum, ranges from 50 MPa at a distance of 10 mm to 20.5 GPa at a distance of 1.2 μm. We note that an elastic compression of up to 20.5 GPa is also realized in a stationary plastic shock wave with the same propagation velocity $U_S = 7.8$ km/s for a final shock compression pressure of 38.7 GPa. So strong a compression results in a substantial increase in shear modulus. Full symbols in Fig. 5.18 show the normalized quantities $\sigma_{\mathrm{HEL}} G_0/G$ [33]. With this correction the entire set of experimental data

in Fig. 5.15 is described with a reasonable accuracy by an empirical relation

$$\sigma_{\mathrm{HEL}} = S(h/h_0)^{-\alpha},$$

where $h_0 = 1$ mm, $S = 0.16$ GPa, and the index $\alpha = 0.63$. The highest shear stress behind the precursor front is

$$\tau_{\mathrm{HEL}} = (3/4)\sigma_{\mathrm{HEL}}\left(1 - c_{\mathrm{b}}^2/c_{\mathrm{l}}^2\right) = \sigma_{\mathrm{HEL}}G/E',$$

where $E' = \rho_0 c_{\mathrm{l}}^2$ is the Young modulus. The attenuation of the elastic precursor of the shock compression wave, which arises from stress relaxation, is related to the rate of plastic deformation behind its front by the equation $\dot{\gamma}_p = (\dot{\varepsilon}_x^p - \dot{\varepsilon}_y^p)/2$ [31, 117]:

$$\left.\frac{d\sigma_x}{dh}\right|_{\mathrm{HEL}} = -\frac{4}{3}\frac{G\dot{\gamma}_p}{c_{\mathrm{l}}},$$

where h is the distance traversed by the wave, G is the shear modulus, and c_{l} is the precursor front propagation velocity, which is assumed to be equal to the longitudinal sound velocity under this approximation.

As a result the empirical dependences transform to the dependence of the initial plastic deformation rate on the shear stress:

$$\dot{\gamma}_p = \frac{4}{3}\left[\frac{\tau E'}{SG}\right]^{\frac{\alpha+1}{\alpha}}\frac{S\alpha c_{\mathrm{l}}}{h_0 G} = 9.1\cdot 10^7(\tau/\tau_0)^{2.59}s^{-1}, \tag{5.1}$$

where $\tau_0 = 1$ GPa. As is evident from Fig. 5.19, the initial rate of plastic deformation behind the elastic precursor during propagation front decreases from 10^9 s^{-1} at a distance of 1 μm to 10^3 s^{-1} at 5–10 mm, and subsequently the precursor attenuation strongly moderates.

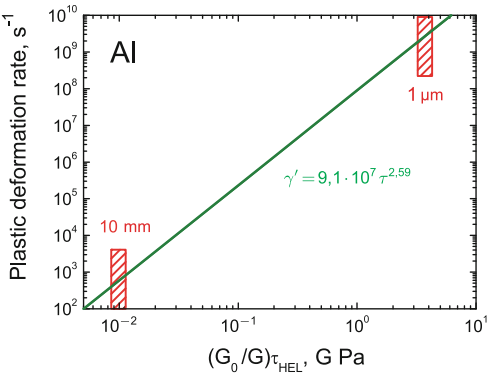

Fig. 5.19 Initial plastic deformation rate behind the elastic precursor front in aluminum in relation to shear stress in accordance with (5.1)

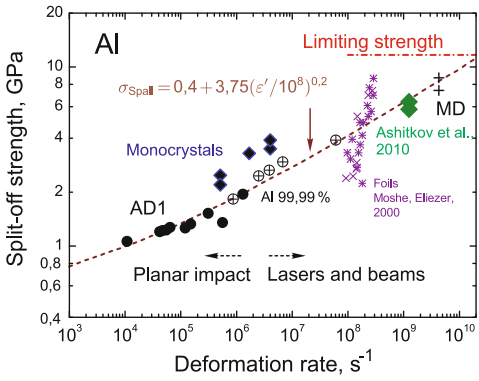

Fig. 5.20 Results of split-off strength measurements for aluminum of different purity in comparison with the data for monocrystalline aluminum, molecular-dynamic splitting-off simulation data, as well as ab initio calculations of ideal aluminum strength

The experimental data on the split-off strength of aluminum for shock-wave load durations ranging from tens of picoseconds to several microseconds are collected in Fig. 5.20 [32]. Also shown are the results of the atomistic simulation [402, 410] of a high-rate rupture and splitting-off and of the ab initio calculations [250] of aluminum's "ideal" strength. Resistance to split-off rupture for monocrystals is higher than for polycrystalline aluminum and aluminum alloys. Polycrystalline materials contain relatively large stress concentrators like intergranular boundaries, inclusions, etc. These defects lower the stress level required to trigger disruption. The high bulk strength of single crystals is evidently caused by their high homogeneity. The data of measurements of the split-off strength of aluminum are shown in relation to the deformation rate. Here, by the deformation rate is meant the rate of substance expansion in the unloading portion of the incident compression pulse: $\dot{V}/V_0 = \dot{u}_{fs}/2c$, where $\dot{u}_{fs}$ is the decrease rate in the unloading portion of the measured wave profile. The initial disruption rate was shown [28] to be equal to a few times this quantity. Extrapolation of the experimental data to higher deformation rates shows their agreement with molecular-dynamic calculations and predicts attainment of the "ideal" strength for a tension rate of about $2 \cdot 10^{10}\,s^{-1}$.

5.4.2 *Dynamic Strength of the Melts and Solid Phases of Metals*

Ultrashort laser pulses (see Sect. 5.5) provide a unique possibility of measuring the tensile strength of condensed media for extremely high tension rates $\dot{V}/V \approx 10^9\,s^{-1}$. These tremendous values of the parameter $\dot{V}/V \sim u/d_T$ are obtained due to the thinness d_T of the heated target layer. For instance, for a hydrodynamic expansion rate $u = 0.1$ km/s and $d_T \approx 100$ nm we obtain $\dot{V}/V \sim u/d_T \approx 10^{-3}\,ps^{-1} = 10^9\,s^{-1}$. In the calculations involving the methods of molecular dynamics, the $\dot{V}/V$ parameter is determined at precisely the point of nucleation

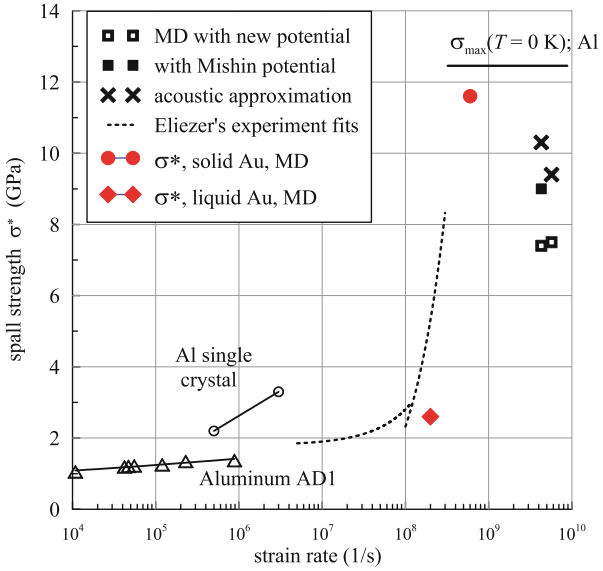

Fig. 5.21 Increase in tensile strength σ^* with increase in tension rate $\dot{V}/V$. The data for the highest rate were obtained by way of molecular-dynamic (MD) simulations. They are borne out by experiments with ultrashort laser pulses (USLPs). The data of Eliezer et al. ([122, 270], see also [44, 142]) for aluminum occupy an intermediate position between the data of MD simulation of USLP experiments, on the one hand, and the data of rather conventional experiments with the use of strikers, which pertain to microsecond times, on the other hand [210, 211]. The data calculated for gold are added to this drawing dedicated to the analysis of the situation for aluminum, see text

immediately prior to its onset [26, 27, 99, 100]. The dependence of strength on the logarithm of the parameter is significant. It is shown in Fig. 5.21.

Experimental data (aluminum) obtained with projectile strikers and lasers are collected in Fig. 5.21. One group of laser experiments was performed using sub-nanosecond and longer-duration pulses [44, 122, 142, 270]. The corresponding data are shown with two dashed curves [122]. Another set of data represent experiments with ultrashort laser pulses. We describe the data obtained in the experiments and calculations with ultrashort laser pulses. The crosses stand for the split-off strength of the solid phase of aluminum, which were obtained using an estimate based on linear acoustics. This estimate is applied to molecular-dynamic (MD) simulation data. The estimate is compared with the exact MD simulation data. They are represented by empty squares.

In this case, the MD simulations were performed with a new [27, 402] interatomic interaction potential (EAM potential, Embedded Atom Method). The symbols in the form of empty squares pertain to the simulations with the new potential. The new potential is constructed is accordance with the data calculated by the density functional method for high-deformation states. For comparison the full square shows the result of Mishin et al.[266], when the EAM potential is applied in our

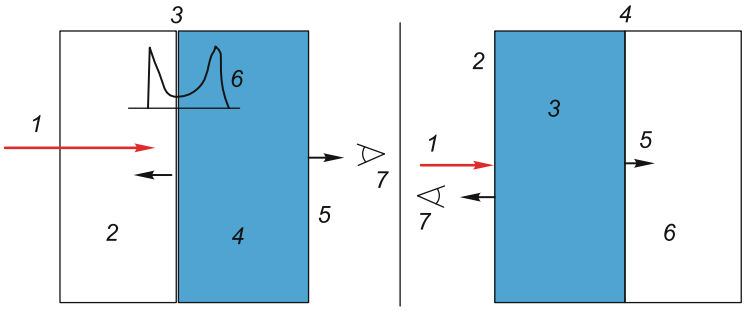

Fig. 5.22 Formulation of experiments to determine the split-off strength of the solid phase (*left panel*) and the melt strength (*right panel*). A dielectric plate (usually glass)is required to support a thin (normally 0.1–10 μm) metallic film. Experiments with free-standing metallic films have also been made, but we shall not enlarge on them. A pump-probe technique is employed for heating and measurements. The heating (pump) USLP *1* penetrates through the dielectric *2* and is absorbed at the dielectric–metal interface *3* (*left panel*). This generates a shock wave traveling into the dielectric *2* and a compression wave in the metal *4*. Shown is the corresponding pressure profile *6*. The compression wave in metal has time or does not have time to break with the formation of a shock wave. This depends on the wave amplitude and the metal thickness on the dielectric. The arrival of the shock or compression wave at the rear film boundary *5* gives rise to the splitting-off of solid metal provided the wave amplitude is high enough. Normally the metallic film *4* is thicker than the melt layer at the interface *3* in the *left panel*. That is why the splitting-off takes place in the solid phase. The *right panel* is described in the body of text

MD simulation. Substantial uncertainties are associated with this EAM potential for high deformations of the medium. As is evident, the calculation with Mishin's potential somewhat overestimates the strength of the solid phase of aluminum.

The diamond and full circle in Fig. 5.21 pertain to the MD simulation of gold ablation in vacuum and to the splitting-off in vacuum at the rear boundary of the film front side-irradiated by a heating ultrashort laser pulse. The schematics of these two experiments are explained in Fig. 5.22. The ablation takes place at the front side of the film, i.e. on the side exposed to the ultrashort laser pulses. The scheme of heating *1* and diagnostic data acquisition *7* is shown in the right panel of Fig. 5.22. Here we are dealing with an experiment with ablation towards vacuum, which permits determining the strength of the melt. In this case, by varying the absorbed energy F_{abs} it is possible to find the dependence of the dynamic strength σ^* on the temperature of the liquid phase.

The experiment to determine the strength of the solid phase is schematized in the left panel of Fig. 5.22. Heating of the front metal side *3* initiates a compression wave. The arrival of the compression wave of sufficient amplitude at the rear boundary *5* in the left panel of Fig. 5.22 results in the splitting-off of a layer near the boundary *5*. By analyzing the data on the velocity of the rear boundary it is possible to determine the strength σ^* of the solid phase. These data are collected by detector *7*. The film must be thicker than the metal melt layer at the front boundary *3* in the left panel of Fig. 5.22. This is required so as to determine the strength σ^* of precisely the solid. The melt thickness is ≈60–140 nm for

$F_{abs} \approx 100\,mJ/cm^2$. In the interval of F_{abs} values corresponding to the threshold of rear-side splitting-off, the amplitudes of compression or shock waves are such that the substance temperature in the compression wave changes only slightly. That is why to study the temperature dependence of the solid phase strength σ^* requires experiments and simulations with preheated films; the data given below correspond to the initial room temperature. Experiments with ultrashort laser pulses and heated films will correspond to experiments [211] with heated targets and for much higher deformation rates. Until now such experiments and simulations have not been performed.

As stated in the caption to Fig. 5.22, the heating is effected by an ultrashort laser pulse, which arrives at the front film boundary *4* in the left panel and the film boundary *3* in the right panel to generate a compression wave *6*, which travels through the film, arrives at its rear boundary *5* and sets it in motion. If the split-off threshold is exceeded, the near-surface layer at the rear boundary splits off (left panel in Fig. 5.22). The motion of the rear boundary in the left panel is monitored using a series of diagnostic ultrashort laser pulses, see [9]. The acceptance aperture for the diagnostic pulses reflected from the moving boundary is indicated by figure *7*. The rear boundary position is determined from the phase of reflected pulse.

An example of measurements with the help of a series of diagnostic ultrashort laser pulses is provided in Fig. 5.23. As a result, the trajectory $x_{rear}(t)$ of the rear boundary is found in the experiment shown in the left panel in Fig. 5.22. The velocity of the boundary is found from the trajectory: $u_{rear}(t) = dx_{rear}/dt$. A two-temperature hydrodynamic simulation is exemplified in Fig. 5.24.

In the processing of experiments, the velocity–time relationship is extracted from the dependence shown in Fig. 5.23 (see, for instance, [34]). Initially the velocity of the rear boundary rises sharply when the compression wave with a steep front arrives at the boundary, see an example in Fig. 5.24. Then the amplitude of the compression wave decreases, the boundary begins to decelerate and its velocity lowers under the resistance of condensed substance to tension. The deceleration next terminates. The strength is estimated from the velocity loss Δu in the segment of boundary deceleration by using the formula $\sigma^* \approx \rho c_s \Delta u$, which follows from linear acoustics.

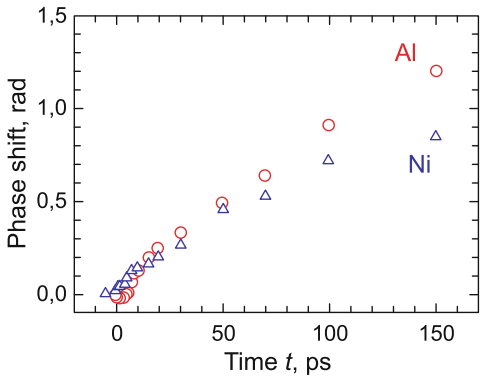

Fig. 5.23 Trajectory of the rear boundary according to pump-probe measurement data, see[34]. The origin corresponds to the moment the compression wave or the shock wave reaches the rear boundary. The boundary displacement $\Delta x_{rear}(t) = \lambda_{probe}\psi_{probe}/4\pi$ is judged by the phase ψ_{probe} of reflected diagnostic USLPs. This phase is plotted on the vertical axis

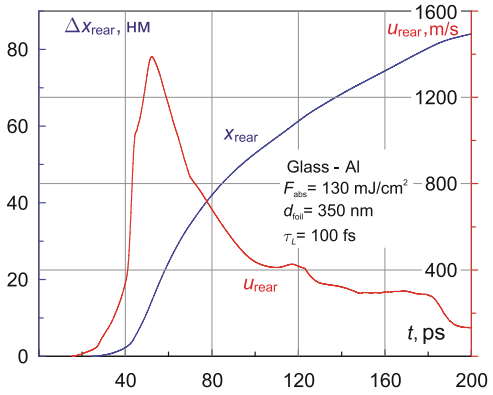

Fig. 5.24 Two-temperature hydrodynamic simulation of laser action in the formulation shown in the *left panel* of Fig. 5.22. The heating beam passes through the dielectric (glass) and is partly absorbed at the film boundary *3*. The film is thin ($d_{\text{foil}} = 350\,\text{nm}$), and therefore the compression wave breaking has not yet occurred, although the profile steepening near the inflection point is obvious

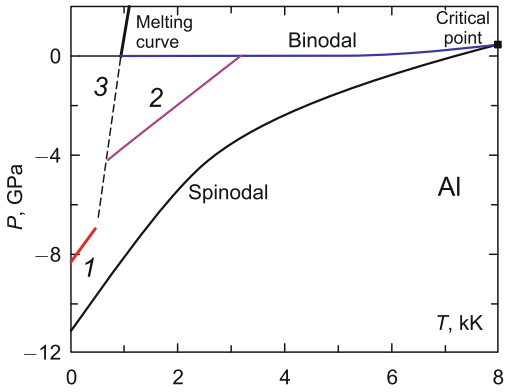

Fig. 5.25 Solid phase (curve 1) and melt (curve 2) strengths $\sigma^*(T)$ of aluminum as functions of temperature. The split-off data were obtained by molecular-dynamic simulations of USLP irradiation in the situation shown in the *left panel* of Fig. 5.22. The tension rate $\dot{V}/V$ amounts to $\approx 2 \cdot 10^9\,\text{s}^{-1}$ for the melt and to $\approx 4 \cdot 10^9\,\text{s}^{-1}$ for the crystal. The crystal tension was effected in the 110 direction

Corrections are added to amend this formula, see strength calculations reliant on ultrashort laser pulse experiments in [34]. These calculations are consistent with the data of hydrodynamic simulation outlined here.

The temperature dependences of the strengths of solid and liquid phases are plotted in Fig. 5.25. The function $\sigma^*(T)$ decreases with temperature, the data showing the existence of a stepwise decrease in strength on melting.

The data in Fig. 5.25 are indicative of a sharp decrease in strength $\sigma^*(T)$ in the vicinity of the continuation of the melting curve. Dashed curve *3* in Fig. 5.25

corresponds to the expected run of the melting curve in the nonequilibrium tension negative-pressure domain. It is hypothesized that curve *3* for aluminum at low temperatures $T \to 0$ passes above the spinodal [300, 301]. Aluminum is believed to differ in this respect from other metals, in which curve *3* intersects the spinodal for a finite value of the temperature [200]. Our simulations combine hydrodynamics and molecular dynamics (a combined approach). The calculated pressure and temperature values in curves *1* and *2* in Fig. 5.25 were obtained directly at the point of the future fragmentation in the splitting-off or nucleation in the cavitation in a melt. They are determined immediately before the very instant of fragmentation or cavitation. After this point in time, the amplitude of tension at this point begins to decrease rapidly. To determine the dependence $\sigma^*(T)$ in the solid phase calls for experiments involving ultrashort laser pulse irradiation of solid film targets.

Figure 5.25 shows the equilibrium curve between condensed phase and saturated vapor (the binodal). This curve terminates at the critical point. The bimodal consists of two portions: the sublimation curve and the boiling curve. In the sublimation curve the vapor pressure is negligible, and in the pressure–temperature plane this curve therefore merges with the zero-pressure axis on the linear pressure scale adopted in Fig. 5.25. Even at the critical point the vapor pressure is small in comparison with the amplitudes of tension at the threshold of ablation or splitting-off in experiments with ultrashort laser pulses, when these amplitudes are quite high. These amplitudes approach the maximal values $p_{\max}\big|_{\text{cold}}$ of the modulus of negative pressure in cold crystal curves. According to the calculations with our elaborated EAM interatomic interaction potential [402], the $p_{\max}\big|_{\text{cold}}$ and $V_{\max}\big|_{\text{cold}}/V_0$ values amount to 12.2 GPa and 1.5 in the crystal tension along the 100 direction, where V_0 is the equilibrium crystal volume at zero temperature.

Figure 5.25 pertains to aluminum. The data for gold are given in Fig. 5.21. The strength of cold gold is higher than that of aluminum, see Fig. 5.21. The modulus values in the cold curves are approximately 1.8–2 times higher for Au. This is supposedly why the split-off (spall) strength of solid-phase gold targets is higher in out calculations simulating the actions of USLPs, see Fig. 5.21. In this case, aluminum in the fragmentation, which marks the onset of splitting-off in the crystal, is closer to the point $p_{\max}\big|_{\text{cold}}$ than aluminum. For aluminum the threshold split-off tension amounts to about 70 % of the ideal strength $p_{\max}\big|_{\text{cold}}$; for gold the figure is 55 %. We also note a substantially greater strength reduction on melting for gold in comparison with aluminum: we compare the symbols corresponding to splitting-off (splitting-off in the solid phase) and ablation (cavitation in the melt) for gold in Fig. 5.21.

Furthermore, in experiments with ultrashort laser pulses the tension rate $\dot{V}/V$ for gold is much lower—by about an order of magnitude—than that in the case of aluminum [99, 100]. This is due to the fact that, first, the heated layer thickness d_T in gold is nearly two times greater because of the far lower electron-ion thermal exchange rate. The lower value of the rate coefficient is primarily due to the large mass of gold nuclei. Second, in gold the expansion rate at the threshold of ablation or splitting-off is several times lower owing to the high substance density.

5.5 Thermodynamics for Ultrashort Pulses

In the previous section we considered the case of laser irradiation whereby the pressure of hot vapor or plasma gives rise to a flow in a dense substance. In the case of ultrashort laser pulses (USLPs) the situation is entirely different.

A USLP heats the electron subsystem inside the skin layer δ_{skin} [17] of an initially solid target, see Fig. 5.26. Subsequently the skin-layer heat propagates supersonically through the electron subsystem into the target interior. The supersonic propagation of the electron thermal wave continues until there occurs temperature relaxation between the electron and ion subsystems [190, 198]. In the course of relaxation the electron energy is transferred to ions and their local temperatures T_{e} and T_{i} gradually converge.

The temperatures T_{e} and T_{i} equalize in a time period t_{eq} of the order of 2–10 ps, depending on the specific metal. An important point is that heated layer thickness d_T is considerable: the "sonic time" $t_s = d_T/c_s$ the sound takes to traverse the distance d_T exceeds the time t_{eq} of heated layer formation, where c_s is the sound velocity in the condensed target substance. For instance, for aluminum the heating thickness $d_T \approx 100\,\text{nm}$, $c_s \approx 5 - 6\,\text{km/s}$, $t_s \approx 20\,\text{ps}$, and $t_{\text{eq}} \approx 2\,\text{ps}$. Next, for $t > t_{\text{eq}}$ the electron thermal wave passes into the conventional mode of subsonic propagation.

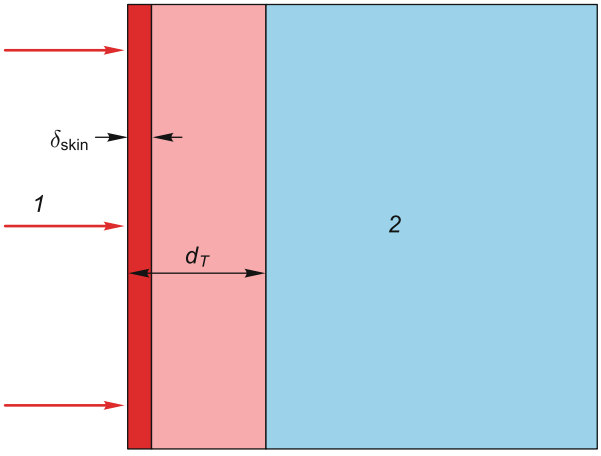

Fig. 5.26 USLP action is radically different from the action of a long laser pulse. During a short time τ_{L} an USLP strongly heats the electrons of the skin layer $\delta_{\text{skin}} \approx$ 10–20 nm. The typical temperatures $T_{\text{e}} \approx$ 1–5 eV. These temperatures are characteristic for the threshold of thermomechanical ablation. In this case, electron thermal conduction heats a layer of thickness $d_T \approx$ 50–150 nm. It is significant that the formation of the layer d_T proceeds in a time $t_{\text{eq}} \approx$ 2–10 ps, which is short in comparison with the sonic time $t_s = d_T/c_s \approx$ 15–50 ps. It is therefore valid to say that the high-pressure layer d_T is produced supersonically. All the subsequent hydrodynamic phenomena are related to precisely the hydrodynamic decay of the high-pressure solid-density layer d_T. Therein lies the difference from the long-pulse case, when the substance motion of the high-density part of the target is caused by the corona's pressure

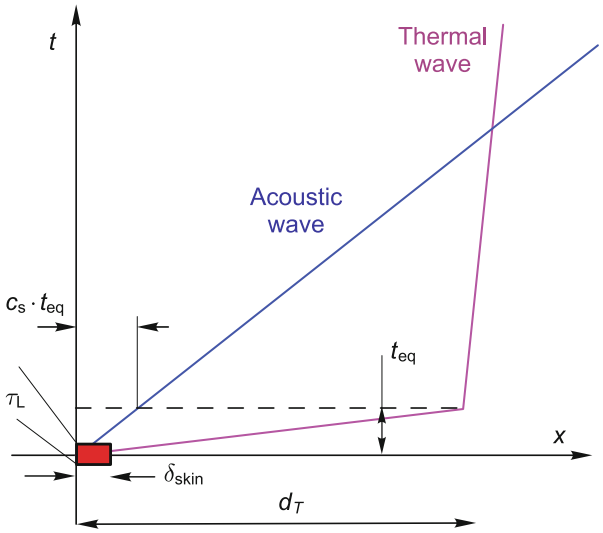

Fig. 5.27 (x; t) – diagram of the propagation of electron thermal wave (ETW) and sonic perturbation. The sonic perturbation starts from a point $x = 0$, $t = -\tau_L$. Prior to pulsed irradiation the target substance occupies the right half-space $x > 0$, the vacuum is on the left. A laser beam impinges on the target from the left. The rectangular at the origin shows the region heated by the laser beam in space (the skin layer thickness δ_{skin}) and in time (the pulse duration τ_L). The ETW trajectory consists of a steep (in the t-axis) supersonic portion and a gently sloping, strongly subsonic portion—compare with the slope of the sound wave. The supersonic ETW propagation continues for a time interval t_{eq}. During the time t_{eq} the sound wave traverses a distance $c_s t_{eq}$, which is short in comparison with the heated layer thickness d_T. During the sonic time $t_s = d_T/c_s$ the acoustic perturbation leaves the heated layer and the entire heated layer is entrained in hydrodynamic motion

That is why in a time t of the order of the sonic time the heated layer thickness d_T is little changed [27, 189, 190, 409]. The aforesaid is illustrated in Fig. 5.27.

5.5.1 *Hydrodynamics of Ultrashort Pulses*

As described above, the fast (supersonic) heating gives rise to a heated layer of thickness d_T. For an isochoric heating $\rho(x,t) \sim const = \rho_0$, $t < t_{eq} \ll t_s$, high temperatures are associated with high pressures. The heating time t_{eq} is shorter than the hydrodynamic decay time $t_s = d_T/c_s$ of the high-pressure layer. The description of the hydrodynamic stage accordingly reduces to the description of the problem of high-pressure layer decay. Two situations are possible. In the first one, a USLP pulse passes through a transparent dielectric (for instance, glass) and is absorbed in the metal at the dielectric–metal interface. In this situation, on the left in Fig. 5.27 is the dielectric and the metal is on the right. In this case, a shock wave travels into

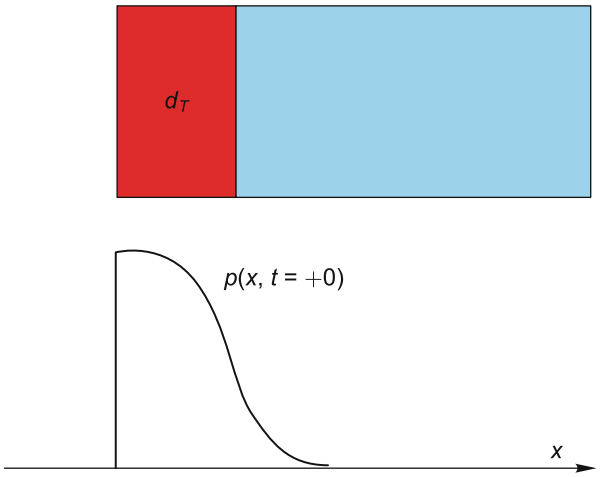

Fig. 5.28 Reduction of the problem on the hydrodynamic flow initiated by a USLP to an initial data problem. The initial data problem is required for explaining the fundamental points related to hydrodynamics. The flow during acoustic times and later is formed due to the decay of the high-pressure layer at the vacuum–metal interface. The vacuum is on the left, the high-pressure layer has an effective thickness d_T. In the target interior on the right the temperature approaches the room temperature and the pressure falls to zero

the dielectric interior (i.e. to the left in Fig. 5.27). Another compression wave travels into the metal. Here, we consider the case when a low (for instance, atmospheric) pressure gas or vacuum is at the left in Fig. 5.27.

The situation with the high-pressure layer at vacuum–metal interface is depicted in Fig. 5.28. If the formation time t_{eq} of the high-pressure layer of thickness d_T is neglected in comparison with the characteristic acoustic time scale $t_s = d_T/c_s$, we arrive at a problem with given initial conditions. At the point in time $t = 0$ we have a uniform density profile $\rho(x, t = 0) = \rho_0, x > 0$ and a nonuniform pressure profile, which is shown in Fig. 5.28.

The solution of the one-dimensional problem of the decay of a high-pressure layer inside a uniform medium is given by D'Alembert's formula with two receding compression waves, provided the pressure is low in comparison with the compression modulus K. The solution is shown in Fig. 5.29. It is of the form

$$p(x, t) = p_0(x + c_s t)/2 + p_0(x - c_s t)/2,$$

provided the medium was at rest prior to the decay. Here the function $p_0(x)$ defines the initial pressure distribution.

In our case of a USLP-produced high-pressure layer at the vacuum–metal interface (see Fig. 5.28), the D'Alambert solution for a time $t > 0$, $t < t_s$ is a combination of three waves [188]. specifically, there is a wave traveling to the right,

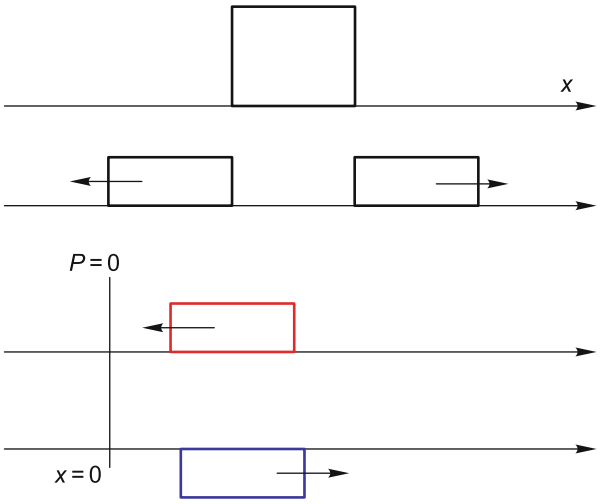

Fig. 5.29 Decay of the initial state with a high-pressure layer in a uniform medium (*upper panel*) into two receding half-amplitude waves (*second panel from top*). Wave reflection from the $x = 0$ boundary with vacuum $P = 0$. An important point is that the compression wave $P > 0$ transforms to a tensile wave $P < 0$ on reflection. Thus tensile stress is formed. For a sufficiently high amplitude of this tension there occurs a splitting-off: a layer near the boundary $x = 0$ detaches from the main part of the target. The thickness of the split-off layer is determined by the effective thickness of the compression wave and its shape. In the case of a strictly rectangular wave (like in the drawing) the split-off layer thickness is equal to half the thickness of the rectangular wave

plus a wave traveling to the left, and plus a reflected tensile wave:

$$p(x,t) = p_0(x + c_s t)/2 + p_0(x - c_s t)/2 - p_0(c_s t - x)/2.$$

This wave corresponds to the three lower panels in Fig. 5.29. In the linear approximation we neglect the displacement of the vacuum–metal interface. The sum of the first and third terms in the three-wave solution gives the zero value of the pressure at the vacuum interface for an arbitrary $p_0(x)$ function. In our case the initial pressure distribution is shown in Fig. 5.28.

For short times $t \ll t_s$ the flow near the boundary is determined by the summation of the leftward directed wave and the wave reflected from the boundary. In this case there occurs a half-space decay with a homogeneous nonzero pressure at the half-space–vacuum boundary, because for short times it is possible to neglect the pressure decrease with depth in the target, see Fig. 5.28, and consider the pressure distribution over the target to be uniform. Near the boundary there emerges a rarefaction wave, in which the substance expands in vacuum. The corresponding solution has been well studied in hydrodynamics [210, 229, 398]. The sound velocity in gas vanishes when the gas pressure turns to zero. In the case of condensed substance, the sound velocity and the density remain finite when the pressure

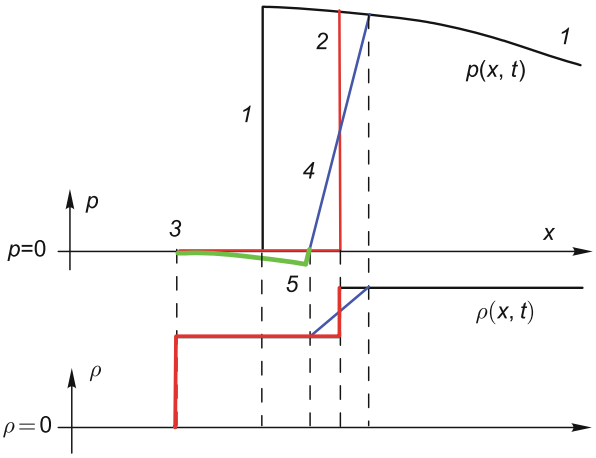

Fig. 5.30 Decay of the initial pressure profile for short times, when the rarefaction wave has traversed a short distance toward the target interior in comparison with the characteristic length d_T. Then the nonuniformity of the initial pressure distribution shown in the *lower panel* of Fig. 5.28 may be neglected: *1*—initial pressure distribution borrowed from Fig. 5.28; *2*—jump-like decrease in pressure to the pressure of expansion medium. In the case of vacuum, this pressure is equal to zero. Along with the pressure, a jump-like decrease is experienced by the density. The jump takes place in a linear acoustic approximation. On going beyond the scope of this approximation the jump *2* transforms to the slope of rarefaction wave *4*. An important point is that the rarefaction wave in a condensed medium has a flow region with constant parameters—a step or a plateau. The plateau terminates at the boundary *3* of the condensed substance. The cause for the emergence of region *5* with tensile stress $P < 0$ is discussed in the body of text

decreases to zero. Associated with these circumstances is the formation of a peculiar rarefaction wave shown in Fig. 5.30 (see [20, 87, 184]).

The density experiences a jump at the condensed phase boundary *3* (Fig. 5.30), which expands in vacuum. From the jump *3* to the slope *4* of the rarefaction wave the pressure is identically equal to zero in the expansion in a zero-pressure medium. In this case the density is constant. The constant-density layer forms a plateau in the density profile of the rarefaction wave, see [20, 184]. The plateau existence gives zest to the rarefaction wave. When the pressure in the target is everywhere uniform (of course, outside of the layer involved in motion), the rarefaction wave is self-similar with the self-similar variable x/t. Such a wave is referred to as the centered rarefaction wave, because its profile is covered by a fan of rectilinear characteristics diverging from the origin. At the zero point in time the origin is at the vacuum–metal interface. The nontrivial portion of the fan corresponds to the slope *4* in Fig. 5.30. The centered wave exemplifies a self-similar simple Riemann wave. The substance inside the plateau is in the equilibrium state belonging to the binodal (the curve of vapor–condensed phase coexistence). In this case, there is no tension beyond the binodal in the two-phase region, and accordingly there are no negative pressures[20, 184].

When account is taken of the nonuniformity of the initial pressure distribution in Fig. 5.28 there emerge negative pressures [187]. In our case the pressure falls off in the target volume. And so at the initial stage the boundary *3* in Fig. 5.30 moves with a velocity corresponding to the higher initial pressure at the boundary. Owing to the pressure decrease with depth, this velocity must decrease with time. As a result there appears tension of the plateau substance and there emerges a negative pressure region *5* in Fig. 5.30. The departure of pressure from the zero value in region *5* is caused by the departure of the initial pressure distribution from the peak value, which was located at the boundary at the point in time $t = 0$ (see Fig. 5.28).

For the moment we abandon the discussion of the growth of negative pressure, the attainment of strength limit, and the description of splitting-off phenomenon. Let us recall the comparison of USLPs with long pulses and the role of evaporation.

5.5.2 *Role of Evaporation*

We estimate the amount of vaporized substance for an energy deposition of the order of the threshold of thermomechanical ablation. As discussed in connection with Figs. 5.29 and 5.30, the reflection of compression wave gives rise to the field of time-dependent tension. When the peak tension exceeds the material strength at some point in time, a layer of thickness of about the heating layer depth d_T breaks away. Since this mechanical detachment leads to substance removal from the target surface under irradiation, this way of substance removal is also referred to as ablation (as mentioned in the foregoing, by ablation is meant the process of mass loss). The emergence of tension is associated with rapid heating, and therefore use is made of the term thermomechanical ablation. Furthermore, this term permits separating the evaporative ablation and the thermomechanical one.

Since the thermomechanical ablation is associated with the attainment of a fixed value—the material strength—this ablation is threshold in nature. For when the tensile stress only slightly lower than the strength there is no thermomechanical substance removal. Calculations for aluminum, gold, and nickel suggest that the absorbed laser energy at the threshold of thermomechanical ablation for metals is $F_{\text{abs}} \approx 0.1\,\text{J/cm}^2$. As this takes place the peak electron temperature $\approx$2 eV, the peak surface temperature on completion of two-temperature ($2T$) relaxation $\approx$2000–3000 K, and the peak pressure $\approx$10 GPa. When the threshold is exceeded, detached near the threshold is a layer of thickness 20 (Ni)–50 (Al)–90 (Au) nm, depending on the sort of metal.

We estimate the amount of vaporized substance according to the kinetic theory of gases. A crude estimate follows from the Hertz–Knudsen formula. In the vapor outflow in vacuum the highest flux and the layer thickness evaporated per pulse are limited by the values $\dot{m} \sim m_i n_{\text{sat}} c$ and $h_{\text{evap}} \sim \dot{m}\tau_{\text{cool}}/\rho_0$, where m_i is the atomic mass, $p_{\text{sat}}(T) = n_{\text{sat}}(T)k_B T$ is the saturation vapor pressure, $c(T)$ is the sound velocity in the vapor, $\tau_{\text{cool}} \approx$ 0.1–1 ns is the cooling time of the irradiation spot, and ρ_0 is the density of the condensed phase. In accordance with the Clapeyron–Clausius

formula, the saturation vapor pressure at temperatures below the critical one is a steep (exponential) function of the temperature.

For metals, temperatures of 2000–3000 K are comparable with metals' boiling temperatures. And so the saturation vapor pressure of a metal in the vicinity of the threshold of thermomechanical ablation is of the order of one atmosphere. The atomic number density of saturation vapor at this pressure is $\approx 3 \cdot 10^{18}\,\mathrm{cm}^{-3}$. This density is four orders of magnitude lower than the density of atoms in the condensed phase. The vaporized layer thickness is $h_{\mathrm{evap}} \sim 0.2\alpha = 0.6\,\mathrm{nm}$, where $\alpha \approx 0.3 \cdot 10^{-7}\,\mathrm{cm}$ is the interatomic distance. In this calculation we assumed the maximal parameter values: $\tau_{\mathrm{cool}} = 1\,\mathrm{ns}$, the sound velocity in the vapor $c = 1\,\mathrm{km/s}$. As is evident, the amount of substance removed from the target surface by mechanical detachment above the threshold of thermomechanical ablation is $\approx 10^2$ times greater than the upper estimate for the amount of substance removed by evaporation in vacuum.

5.5.3 *Shape of Acoustic Wave Traveling into the Target Interior*

For a time of the order of the acoustic time $t_s = d_T/c_s$, the hydrodynamic flow in the target is determined by the combined action of three waves (the right, left, and reflected waves), see the foregoing text. In a time $\sim t_s$ the left wave vanishes. Accordingly, subsequently in time the flow is the combination of the right and reflected waves, see Fig. 5.31. The right and reflected waves are separated by the "zero" characteristic *4*, which emanates from the origin at the onset of USLP irradiation, see Fig. 5.31.

The trajectory of target boundary is indicated by figures *8*, *9* in Fig. 5.31. The boundary is accelerated and acquires the peak velocity during the course of a USLP. Then the boundary decelerates in the course of reflection of the left wave. The portions of acceleration and deceleration are indicated by figure *8* in Fig. 5.31. The deceleration is caused by the fact that the left-wave amplitude decreases in the direction from the boundary to the target interior, see the lower panel in Fig. 5.28. After complete reflection of the left wave the bounder ceases to shift leftwards. The trajectory of the boundary upon stopping is shown by vertical straight line *9* in Fig. 5.31. Numerical simulation of the problem using two-temperature hydrodynamic codes and molecular dynamic techniques is the concern of the following papers: [7–9, 21–27, 34, 35, 86, 99–101, 185–187, 189–196, 198, 202, 295, 345, 372, 399–402].

A USLP sends into the target interior a characteristic wave with an advance compression bump followed by a tension well. This shape is depicted in the inset in Fig. 5.31. In linear acoustics the positive and negative pressure amplitudes are equal to half the amplitude of the initial pressure distribution profile in Fig. 5.28. For energy inputs of the order of the threshold one, initial pressures of $\approx 10\,\mathrm{GPa}$ constitute an appreciable fraction of the compression modulus $K \approx 100\,\mathrm{GPa}$. Nonlinear effects most strongly affect the shape of the reflected wave, whose

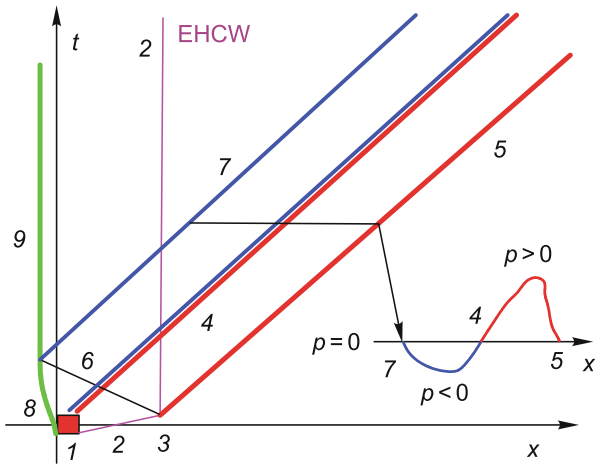

Fig. 5.31 Propagation of compression and rarefaction waves into a target: *1*—location of the region of heating due to USLP absorption. The absorption depth is of the order of the skin layer thickness of 10–20 nm, the heating time is defined by the USLP duration, usually ≈0.01–1 ps; *2*—the supersonic and subsonic portions of electron heat conduction wave (EHCW); *3*—transonic portion in which the thermal wave propagation mode changes. From this region the leading compression wave characteristics *4*, *5* (the right-traveling wave) begin their propagation into the target interior; *6*—trailing characteristics of the left-traveling wave. This wave, as we see, propagates towards the vacuum–target interface; *7*—trailing characteristics of the right-traveling reflected wave *4*–*7*. The reflected wave follows immediately after the compression wave *5*–*4*. As this takes place, the pressure profile, which forms as the sum of the right-traveling and reflected waves, assumes a "zigzag" shape shown in the *inset*

amplitude turns out to be appreciably smaller in magnitude than half the peak initial pressure.

The wave shape deforms with time due to nonlinearity, see Fig. 5.32. Beyond the heating layer the wave propagates through a uniform substance with a constant temperature. Inside the heating layer the wave propagation is affected, first, by the existence of a melt layer and, second, by the temperature profile in the heated region. Beyond the heated substance temperature profile of thickness $\sim d_T$, the inward directed wave is a simple Riemann wave. Well known are the effects of steepening (the growth of gradient's magnitude) of the compression wave in its leading portion and of wave profile lengthening in the region of pressure decrease. The profile of the tensile wave is also steepened and lengthened ($p < 0$). In the latter case, however, the steepening takes place in the trailing part of the tensile wave, where the pressure builds up [99, 100, 191, 402].

The arrows in the upper panel of Fig. 5.32 indicate the inflection points in the leading portion of the compression wave and in the trailing part of the tensile wave. The wave profile steepens owing to the convergence of Riemann wave characteristics. There is an instant of caustic formation, after which a part of the characteristics begin to intersect. These instants are different for the compressive

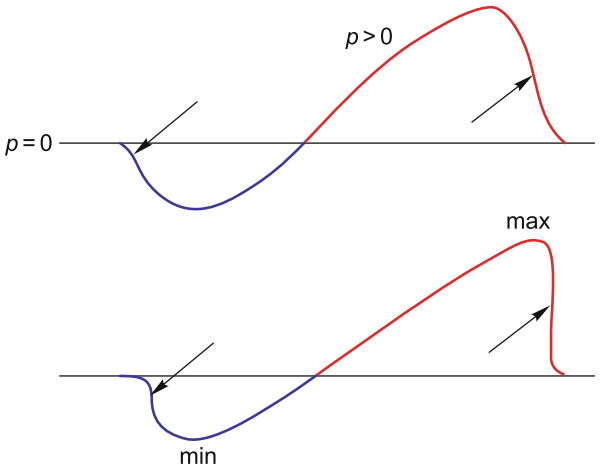

Fig. 5.32 Breaking of compressive and tensile waves. In the $((x, t))$ diagram in Fig. 5.31, bands *5–4* and *4–7* correspond to compressive and tensile waves, respectively

and tensile waves. The arrows in Fig. 5.32 indicate the positions of the shock waves formed after breaking.

The wave evolution proceeds in a peculiar way [26] for short times, the portion of the wave near the "zero" characteristic is steep, because this portion corresponds to the fan of characteristics at pressure decrease in the rarefaction wave. This is portion *4* in Fig. 5.30. It is the image of the portion of a sharp decay of the initial pressure at the vacuum–metal interface in Fig. 5.28. In this case, the extent of the leading part of the compression wave and the trailing part of the tensile wave is of the order of the initial profile thickness in Fig. 5.28. Then, the situation changes due to nonlinear processes. The zone near the zero characteristic expands and the pressure profile steepness decreases in this zone. The zones of pressure growth, conversely, become steeper. The maximum and minimum of the pressure propagate along the characteristics of their own. That is why the wave amplitudes at the maximum and minimum do not change with time, until the characteristic of the maximum finds itself in the leading shock wave and the characteristic of the minimum in the trailing shock. After this the maximum and minimum amplitudes begin to slowly vary with time [197, 199].

The evolution outlined above proceeds faster when the initial pressure is higher. Above the thermomechanical threshold, upon layer detachment, the profile of the tensile wave propagating into the target interior changes significantly. The well depth becomes smaller. The higher the initial pressure, the higher is the ratio between the maximum positive pressure and the magnitude of the maximum negative pressure in the wave combined of the right wave $p > 0$ and the negative wave $p < 0$: the initial pressure shown in Fig. 5.28 rises with increasing absorbed energy F_{abs}, while the magnitude of the negative pressure is limited by the tensile strength of the substance.

5.5.4 Melting and Nucleation

Calculations suggest the threshold of USLP-induced melting is two to four times lower than the thermomechanical ablation threshold. This is a highly significant circumstance. Then, for an energy of about the thermomechanical ablation threshold $F_{\text{abs}}\big|_{\text{abl}}$ the melting takes place within the electron–ion (T_e–T_i) temperature relaxation time interval $-\tau_L < t < t_{\text{eq}}$. The matter is that, for such excess over the melting temperature, even during this time interval the temperature t rises above the temperature T_i in the spinodal of the crystal–melt transition[189]. The temperature in the spinodal is $\approx$20 % higher than the melting temperature for a fixed density. The melt layer thickness is comparable with the heating layer thickness d_T.

The hydrodynamic decay of the high-pressure surface layer in Fig. 5.28 proceeds after the melt formation. And so the right, left, and reflected waves mentioned in the foregoing propagate through the melt. The growth of tensile stress in time (the onset of this process is shown in Fig. 5.30, downward deviation of the pressure, profile *5*) proceeds in the liquid substance. It turns out that the greatest tension in the metals investigated (Al [402]; Au [99, 100]; Ni [101]) is attained in a liquid. Consequently, the fragmentation of the initially continuous substance begins with bubble nucleation in the liquid phase upon attaining the strength limit of the melt.

The formation of vapor-filled bubbles in a liquid is termed cavitation. We emphasize that the effect of vapor pressure on the vapor-liquid mixture dynamics is negligible in the USLP-induced thermomechanical ablation problem under consideration. For, as noted above, in the 2000–3000 K temperature range characteristic for the ablation threshold the saturation vapor pressure is of the order of a few atmospheres, $\approx 10^{-4}$ GPa, while the dynamic melt strength amounts to a few GPa in the experiments under discussion.

We note that the attainment of highest tension and nucleation occur at the one-temperature stage $T_i = T_e = T$. The matter is that the attainment of highest tension takes a time of the order of the acoustic time $t_s = d_T/c_s$, and this time exceeds the temperature equilibration time t_{eq}. However, there are papers in which cavitation is considered inside of the two-temperature time interval, when the electron pressure plays a significant role in the expansion dynamics of a two-temperature heated substance [289]. We also note that the temperature profile has a significant effect on the depth at which nucleation sets in at the ablation threshold. This is so because the strength becomes higher with a decrease in temperature. There is competition between the growth of the amplitude of the highest instantaneous tension with propagation of the reflected wave into the target interior, on the one hand, and the temperature lowering with depth, on the other hand. Portion 5 of the pressure profile in Fig. 5.30 shows how the reflected wave amplitude grows with propagation distance.

The vapor pressure inside of the cavitation bubbles is insignificant. Surface tension is significant. The situation whereby the surface tension of the bubbles affects the deceleration of a split-off plate is unusual. This is a special feature of precisely the USLP with its extreme thinness of the heated layer: $d_T \approx 100$ nm—

only several skin layer depths. This effect is negligible in conventional experiments with splitting-off in a liquid, when the split-off layer has a thickness of about a fraction of a millimeter or more. In USLP experiments the inertia of the split-off plate is negligible owing to its superthinness. That is why surface tension comes into play, see[35, 400, 401].

The melt–vapor mixture passes three stages in the tension of the mixture. At the first stage there occurs nucleation with the formation of separate vapor phase nuclei of size comparable with the interatomic distance [45, 86, 201, 287, 372, 400, 402]. This is so because tension is high, of the order of several GPa, and the diameter of a viable nucleus is very small. In the nucleation the distances between the nuclei are far longer than the diameters of viable nuclei. That is, individual nuclei are formed independently. However, a short time after the nucleation of the first group of bubbles there emerges interaction between them. The amplitude of tension around a bubble decreases from the high nucleation value to a value which is only little higher than $2\sigma/r$. The quantity $2\sigma/r$ is defined by the current bubble radius and the surface tension coefficient. The tension amplitude decreases inside of the sonic sphere around the bubble. The radius of this sphere lengthens with the sound velocity A short time later the spheres of neighboring bubbles overlap, the tension lowers, and the nucleation of new nuclei terminates.

It is noteworthy that here we are dealing with a near-threshold situation. When the ablation threshold is substantially exceeded (for instance, by a factor of 2–3), after the formation of the first group of nucleation bubbles at a depth h_1 under the target surface the tensile stress lowers at first but then increases again [99, 100]. As a result, a new group of bubbles nucleates at a greater depth h_2.

At the second stage the resultant bubbles expand. As this takes place, the volume fraction $\zeta = V_{\text{vap}}/(V_{\text{vap}} + V_{\text{liq}})$ of the vapor phase in the liquid–vapor phase mixture increases. In the nucleation of the first nuclei this fraction is very small. At the second stage there occurs percolation of the liquid phase; the vapor is isolated in the bubbles and there is no vapor percolation. The second stage continues until the fraction ζ reaches a value of about 0.5. Next begins the third stage, during which the liquid-vapor mixture forms a foam with a rather low volume content of the melt [27, 402]. In this case, the vapor still remains isolated, like during the first and second stages. Liquid films prevent the vapor from flowing from one cavity to another. The resistance to mixture tension, and hence the split-off plate deceleration, continues due to the film surface tension in the foam.

So, initially the plate deceleration is associated with the tension of continuous melt to lower densities than the equilibrium density at low (zero, it may be said) pressure. This is the main contribution to deceleration. At the second stage the deceleration is caused by the bubble surface tension $2\sigma/r$. This stage may a substantial contribution to deceleration for superthin split-off plates and their small inertia. Lastly, a small and yet appreciable contribution to deceleration is associated with the third stage, when plate velocity lowers owing to the resistance of liquid foam films to their tension [27].

The third stage terminates when the liquid films become several interatomic distances thick. The films start breaking and the plate deceleration terminates[400,

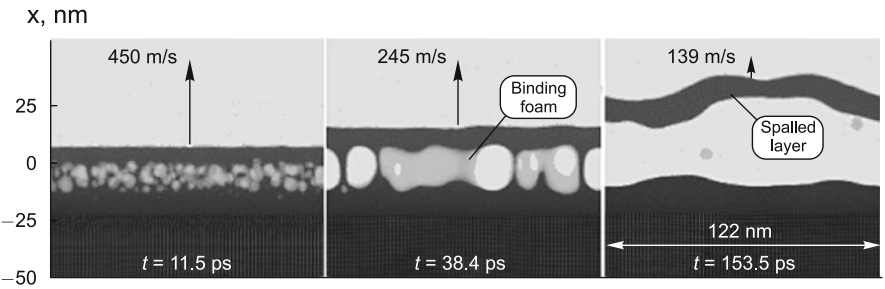

Fig. 5.33 Simulation of USLP action on a metal target by the example of aluminum. The quantity d_T is artificially decreased sixfold. This was done to model the foam formation up to its breaking for a limited computational capability [400, 401]. The input energy is slightly higher than the thermomechanical ablation threshold. The split-off (spalled) layer at the top is clearly seen. The *arrow* shows the layer velocity and its magnitude. One can see that this velocity continues to decrease significantly even after bubble nucleation. This situation is impossible for large thicknesses of the split-off plate and accordingly a large plate mass per unit area. The smooth shading distribution and the mesh structure at the bottom are separated by a melting front. The liquid phase (the region of smooth shading) is on top and the crystal lattice is at the bottom. The left and middle frames pertain to the second and third stages of the existence of the liquid-vapor mixture. In the right frame the films are broken, and a vapor-droplet cloud with a low volume liquid content is formed under the split-off plate. After foam breaking the plate retains its momentum in the subsequent flight

401]. The stage of film breaking continues for some time. During this period the melt percolation vanishes. Accordingly, in the case of metals the resistivity of the liquid–vapor mixture rises sharply. The mixture transforms from the foam state to the state of droplets in the vapor with a small volume content of the droplets. The quantity ζ monotonically tends to zero on further expansion of the mixture.

The second and third stages of bubble ensemble development are shown in Fig. 5.33.

5.5.5 *Newton Rings*

Interference Newton rings were the first experimental [345] indication of the decisive role of mechanical effects in USLP irradiation experiments. However, extensive theoretical work had to be done to recognize this [21–23, 184, 187, 399]. We describe briefly why there emerge interference rings. The reason lies with the detachment of the split-off layer and enhancement of laser radiation near the beam axis (Fig. 5.34).

Let the laser beam shown in Fig. 5.34 be normally incident on the target surface. Let the beam intensity distribution be symmetric about the beam axis. Then the irradiated region on the target surface in which the energy density F (the fluence) exceeds the thermomechanical ablation threshold $F\big|_{\text{abl}}$ forms a circle on the target

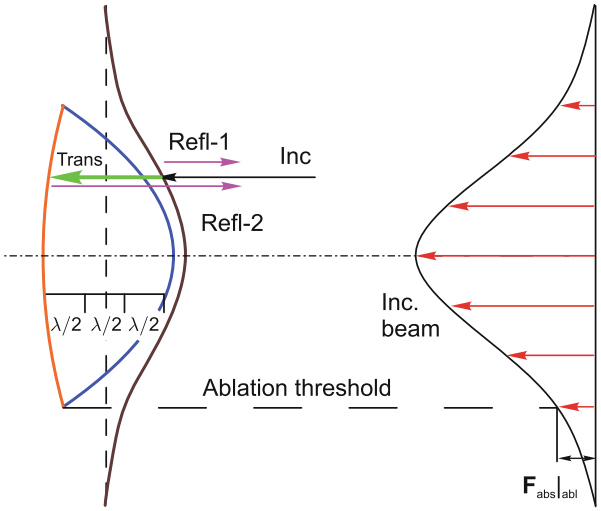

Fig. 5.34 Schematic explaining the formation of Newton rings. The beam of laser radiation is incident on the target surface. The lateral beam intensity distribution is shown on the *right*. The intensity is highest in the beam axis. The target is at the *left*. Prior to the arrival of a USLP the target boundary is a plane shown with a *vertical dashed line*. Initially the target substance is to the *left* of this plane. The USLP sets in motion the target substance. The transverse beam size $r_{\text{beam}} \approx$ 10–100 μm is far greater than the USLP-heated layer thickness $d_T \approx 100$ nm. Locally, to small plane portions in comparison with r_{beam}; it is therefore possible to apply an approach with a one-dimensional flow normal to the target surface. This picture is exemplified in Fig. 5.33 for a near-threshold portion of fluences F. An example with summation of five flows with different $F/F\big|_{\text{abl}}$ ratio values is shown in Fig. 5.35. See the body of text for the explanation concerning the number of half-waves and interference

surface. The threshold value is marked with an arrow in the intensity distribution in Fig. 5.34. Nucleation and the formation of a split-off plate begin above the ablation threshold. The velocity of this plate depends on the local value of absorbed energy: the higher is the energy, the higher is the velocity. That is why the split-off plate bends to take on the shape of a convex dome, see Fig. 5.34.

Under the plate there remains the bottom of the future crater. A gap is formed between the crater and the dome. The dome thickness decreases towards the center, because the plate thickness depends on the local fluence: the thickness decreases with increasing F. There is a fluence value at which the thickness turns to zero [7, 8, 187]. When the central fluence in the distribution plotted in Fig. 5.34 exceeds this value, a hole is produced in the dome, see Fig. 5.35. Of course, there are no Newton rings inside the hole. An example with experimental and simulation pictures is given in Fig. 5.36.

The split-off plate produced under USLP irradiation is very special in the sense that it is extremely thin. Its thickness is of the order of the skin layer thickness, which amounts to 10–20 nm. We are therefore dealing with a nanosplitting-off [187]. Although the existence of splitting-off has been well known, the split-off layers of

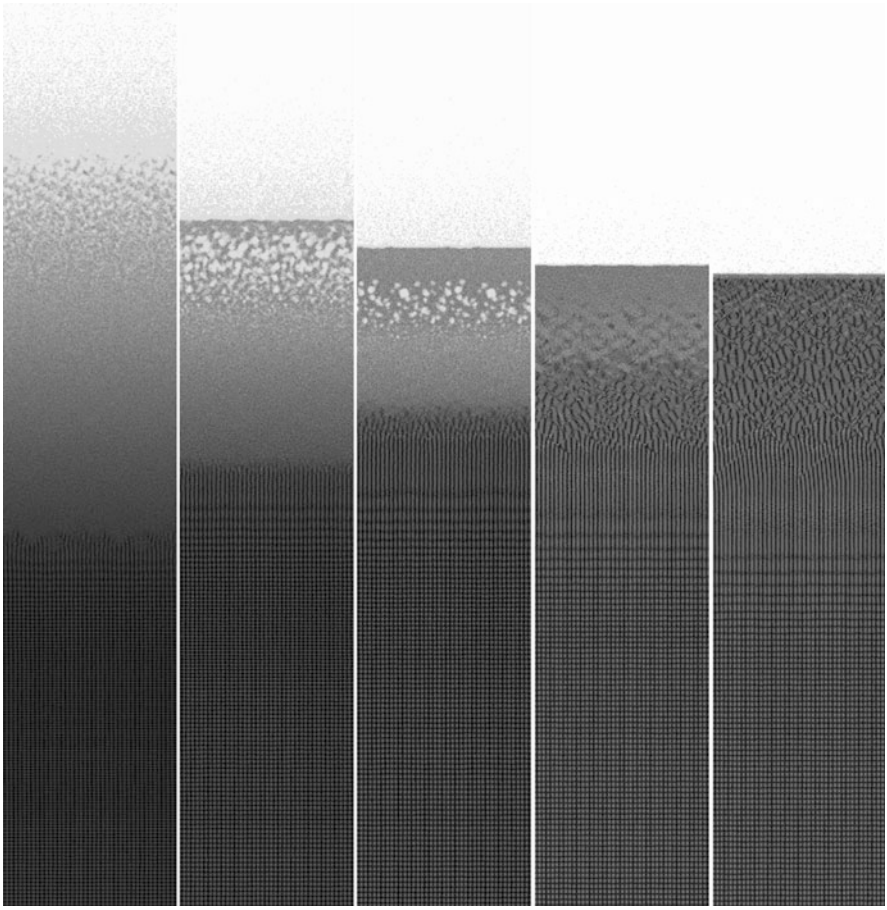

Fig. 5.35 Example of the composition of a two-dimensional flow with a dome. The flow is composed of five one-dimensional flows with a fluence ratio $F/F\big|_{\mathrm{abl}}$ increasing *from right to left* in each specific frame. One can see that, first, there is no nucleation, detachment, and split-off plate for two insufficiently high fluences at the *right*. Second, the plate thickness decreases with increasing fluence, compare the 2nd and 3rd frames at the *left*. In the *leftmost frame* the fluence ratio is such that the split-off plate vanishes

so small a thickness have never before been obtained. Owing to the thinness of the dome in Fig. 5.34, the light of probing laser pulses penetrates through the dome. In Fig. 5.34 the incident ray is marked with "Inc" and the transmitted ray with "Trans". The transmitted beam reflects from the crater bottom and emanated from under the dome as "Refl-2" to interfere with the "Refl-1" beam produced in the first reflection of the "Inc" beam from the dome. When the gap under the dome is equal to an integer number of the half-waves of laser radiation, there forms a Newton ring.

It is noteworthy that the dome shape is easy to control by changing the intensity distribution over the laser spot. We also note that the pattern with Newton rings

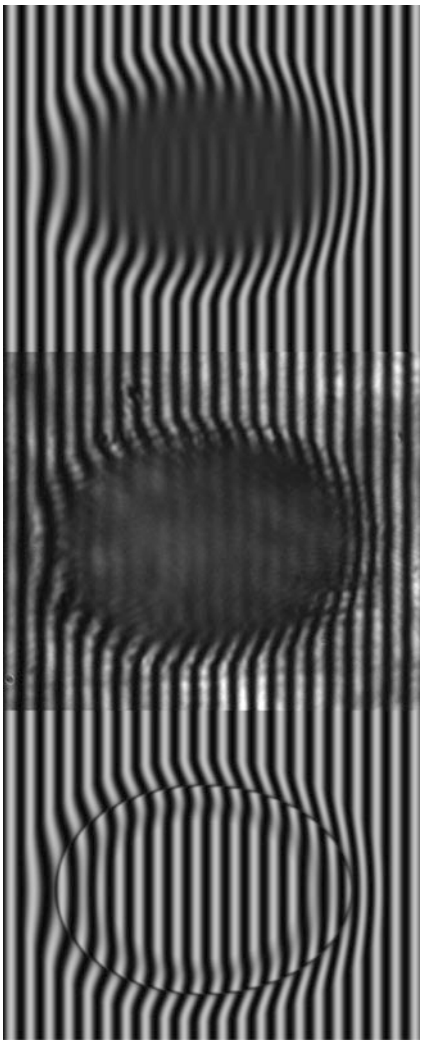

Fig. 5.36 Pattern with Newton rings obtained in the experiment on gold (*central frame*) and two versions of theoretical interference simulations [187]

in Fig. 5.36 varies with time, because the dome shown in Figs. 5.34 and 5.35 is in motion. The dome–crater bottom increases with time. Initially there are no rings in the image of irradiated spot. In order for the first ring to emerge, the gap under the central point of the dome must amount to one half-wave. This necessitates a certain period of time after the irradiation by a heating USLP. For instance, for a laser wavelength of 1 μm and a central velocity of 1 km/s this time is equal to 500 nm/1 [nm/ps] = 0.5 ns. The higher is the input energy, the shorter is this time. The second ring emerges when two half-waves fit into the gap under the dome. A new ring emerges at the center. In this case, the previous rings shift towards the edge of the circle in Fig. 5.34 at which the ablation threshold was reached.

5.6 Laser-Induced Explosion of Cluster Plasma

The interaction of an ultrahigh-power laser pulse of femtosecond duration with cluster targets permits obtaining plasmas with unique properties [221, 222]. On the one hand, at cluster locations there forms a plasma with a density far greater than the critical one, which consists of multiply charged ions and electrons with kiloelectronvolt energies. On the other hand, owing to the smallness of the average density of the medium and individual cluster size, the electromagnetic wave propagates freely and interacts with all atoms of the target, i.e. it freely penetrates the domains with above-critical electron density and is not reflected, unlike the case with solid-state targets. Furthermore, the heating of conduction electrons in the case of metallic clusters (or primary ionized electrons in the case of rare-gas atomic clusters), on the one hand, and the absence of the possibility of fast heat removal like in ordinary plasmas, on the other, permit attaining a substantially higher excitation of the electron subsystem in comparison with isolated atoms and molecules. As this takes place, atomic ions are hardly heated. After the rapid primary multiple ionization during the course of the main part of the laser pulse, the cluster ion substance is an ideal plasma consisting of electrons and multiply charged atomic ions.

Under a strong excitation the clusters transform to completely ionized plasma, which initially occupies the region occupied by the cluster and freely expands into the ambient space later on. To excite the cluster matter, the time of energy deposition must therefore be short in comparison with the plasma expansion time. For a characteristic cluster size of about 10 nm ($\approx 10^4$ atoms per cluster) and an ion expansion velocity of 10^7–10^8 cm/s, the ion flight time amounts to 10^{-13}–10^{-12} s, which calls for femtosecond excitation times of cluster excitation and plasma production.

Therefore, in a cluster target it is possible to attain a high specific absorption of laser energy and, accordingly, a higher specific substance excitation in comparison with other targets. The characteristic charge of the resultant plasma exceeds the average charge of the plasma produced in the interaction of laser radiation with solid or gaseous targets. The fraction of laser pulse energy converted to X-ray radiation with the use of a cluster target amounts to about 10–15 % and is nonthermal in nature. Moreover, since the absorption of laser radiation is substantially enhanced, this results in the high-efficiency generation of fast electrons and multiply charged ions with kinetic energies ranging from tens of keV to hundreds of MeV. Therefore, execution of investigations into the laser radiation–cluster interaction, on the one hand, permits obtaining new information about the fundamental properties of matter under extreme conditions [81, 108, 124, 135, 141, 180, 221, 222, 264, 321, 324, 352] and, on the other hand, provides a possibility for using new approaches to the solution of several applied problems like initiation of nuclear reactions [69, 107, 165, 177, 215, 230, 245], electron and heavy particle acceleration [106, 326, 354, 404], as well as production of a bright X-ray radiation source for medical, biological, and lithographic purposes [85, 89, 110, 173, 225, 260, 344, 403].

In this section we show that the simultaneous use of laser pulses with a high temporal contrast ratio of 10^8–10^{10} and submicrometer-sized clusters provides a high laser-cluster interaction efficiency and permits generating different high-intensity photon beams of soft and hard X-ray (up to gamma-ray) radiation as well as intense high-energy electron and ion fluxes. Also we will briefly consider examples of the application of such plasma femtosecond laser-cluster sources to radiography.

5.6.1 *Models of the Interaction of High-Power Laser Pulses with an Atomic Medium*

During the course of a laser pulse and for some time later, the parameters of the plasma produced in the cluster target and the nature of the processes occurring in it change greatly. The characteristic times of the processes are depicted in Fig. 5.37. At the first irradiation stage, atoms and ions are ionized, a part of the electrons escape from the cluster and are uniformly distributed over the whole space, so that the cluster acquires a positive charge; the remaining electrons are captured by the self-consistent potential of the cluster. There occurs cluster heating and production of a high-temperature high-density plasma in the regions of initial cluster positions. The duration of this stage is determined by the laser pulse duration and the cluster size. Normally it amounts to several tens or hundreds of femtoseconds.

At the second stage, under the action of the positive charge and the hydrodynamic pressure of the captured electrons the structure decays, all spatial gradients vanish, and there forms a spatially uniform plasma channel of diameter corresponding to the diameter of the laser spot. Simultaneously with the decay of heated clusters the kinetic energy of the electrons converts to X-ray radiation and kinetic ion energy. The duration of the second stage ranges from several tens to hundreds of picoseconds. It is noteworthy that the characteristic final energy of the ions exceeds that of the electrons.

At the third stage, the resultant spatially uniform plasma decays on a time scale of several nanoseconds.

The parameters of the plasma produced at the first stage depend heavily on the laser pulse contrast ratio and the cluster size, because the existence of a picosecond-long prepulse of sufficient intensity may result in the disruption of clusters even prior to the arrival of the main femtosecond pulse. The pulse contrast

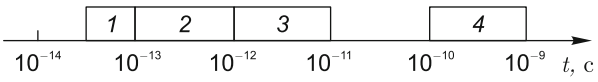

Fig. 5.37 Characteristic times of the processes occurring in the excitation of a cluster beam by an ultrahigh-power ultrashort laser pulse in accordance with [222]: *1*—laser pulse duration; *2*—cluster lifetime; *3*—time of uniform plasma production after cluster decay; *4*—time of uniform plasma decay

ration, i.e. the ratio of the peak intensity of the main laser pulse and the prepulse intensities is, as a rule, of the order of 10^4–10^6 or lower, unless special arrangements are made to suppress the prepulses. When the contrast ratio is so low and the main pulse is intense enough (and these experiments are usually carried out for intensities I_{las} ranging from 10^{17} to 10^{20} W/cm^2), the prepulse intensity will not be lower than 10^{13}–10^{14} W/cm^2. This would suffice to destroy the clusters even prior to the arrival of the main pulse. Evidently one of the possible solutions to this problem involves improving the laser contrast ratio to a level of 10^{10}–10^{12}. Another possibility involves the use of large clusters of size of the order of the laser wavelength containing 10^9–10^{11} atoms, which would only partly be destroyed by laser prepulses.

Following the theoretical approaches developed in [221, 222], in this section we consider the basics of the interaction of femtosecond laser radiation with cluster systems and show the main changes in this interaction when the cluster size is increased to the submicrometers [344].

The advent of new laser technologies that provide the generation of relativistic ultrashort pulses of electromagnetic energy endows a new quality to the radiation–medium interaction problem. Specifically, the characteristic magnitude of atomic electric field intensity, which is constructed with atomic units, is

$$F_0 = \frac{e}{a_0^2} = \frac{m_e^2 e^5}{\hbar^4} = 5.14 \cdot 10^9 \text{ V/cm},$$

and the electromagnetic wave intensity corresponding to this field is

$$I = \frac{cF_0^2}{8\pi} = 3.5 \cdot 10^{16} \text{ W/cm}^2.$$

Here, e is the electric charge, a_0 is the Bohr radius, m_e is the electron mass, $\hbar$ is Planck's constant, and c is the speed of light. The fields produced by the laser pulses of modern facilities exceed this figure by several orders of magnitude. The practice of experiments shows that the attainment of laser radiation intensities in the range $I = 10^{16}$–10^{19} W/cm^2, which corresponds to the peak electric intensity $F = (0.6\text{–}20)F_0$ in the electromagnetic wave, has become an ordinary event. In this case, the pulse duration amounts to 30–100 fs, or 15–50 electromagnetic wave oscillation cycles, and the electromagnetic wave frequency is usually much lower than the corresponding atomic quantity.

It was shown [222] that the Keldysh parameter, which defines the character of electromagnetic wave interaction with an atomic system, is small for the ionization of atoms by the electromagnetic wave field. This condition is fulfilled not only for atoms, but also for the atomic ions produced in the sequential ionization of the atoms. When the intensity of external laser field becomes comparable with the field produced by the atomic core, the atomic system is substantially restructured and the rate of nonresonance (multiphoton) processes becomes comparable with the rates of resonance transitions. On further increase in laser wave intensity, the above-barrier

ionization of valence electrons becomes possible. In this case, the above-barrier transition of the valence electrons to the spatial domains where the electron remains free on termination of the electromagnetic field (the Bethe mechanism) becomes one of the most efficient mechanisms of the absorption of a strong electromagnetic wave at the first stage of interaction with the atomic system. The characteristic amplitude of ionized electron oscillations in a laser field is estimated by the quantity

$$a = \frac{eF}{m_e \omega^2}$$

and turns out to be large in comparison with the atomic size a_0. For instance, for an electric intensity $F = 10^{18}$ V/cm of electromagnetic wave field and a wavelength $\lambda = 0.8\,\mu$m of a titanium-sapphire laser we obtain $a \approx 1500 a_0 = 82$ nm. This is the value of the radius of metallic cluster containing $\approx 10^8$ atoms.

We note that a gas consisting of separate atoms or molecules is not suited for an efficient laser target: for a low atomic number density, electrons execute free oscillations in only the electromagnetic laser field and their interaction with the atomic core is relatively weak. This results in a weak absorption of the laser-pulse energy in the medium. On the other hand, when the atomic number density is high, even after single ionization of the atoms the electron density may attain the critical value and the radiation will not be able to penetrate into the resultant plasma. Therefore, clusters or a macroscopic atomic system must be selected for a target for maximizing the plasma temperature.

5.6.2 *Cluster Ionization in the Field of an Intense Electromagnetic Wave*

One of the main processes which determine the cluster evolution is ionization, which may be subdivided into internal, i.e. the ionization of atoms and ions in the cluster, and external—the ionization of the cluster as a whole. The description of ionization in the framework of the Bethe approximation permits elucidating the nature of the processes taking place and the dependence of ionization parameters on the parameters of the electromagnetic wave.

It is commonly assumed that the electron released in the ionization of an atom by a laser field is in the Coulomb field of the atomic core and that the laser field does not change the ionization potential of the atomic particle. When use is made of the hydrogenic ionization potential $J = Z^2 J_0 / n^2$ (J_0 is the ionization potential of a hydrogen ion in the ground state and n is the principal quantum number), the maximal charge of the atomic ion produced by the field of intensity F may be estimated [222] as

$$Z = n^{3/4} \left(\frac{F}{F_0} \right)^{1/3}.$$

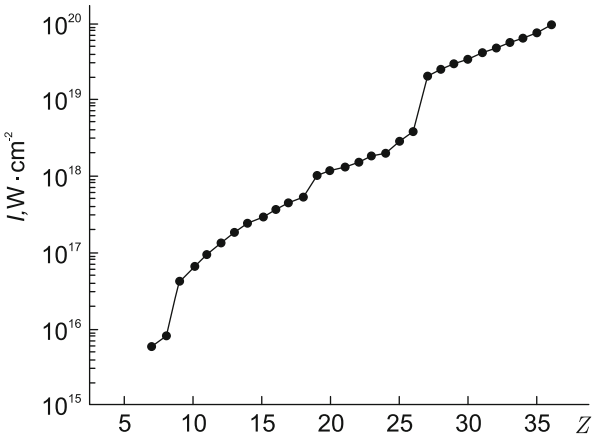

Fig. 5.38 Atomic ion charge Z in a xenon cluster plasma, which is produced by the excitation of a cluster beam by a laser pulse, as a function of laser pulse intensity [222]

An important factor which affects the ionization of a multielectron atom is the step dependence of the ionization potential on the ion charge. The steps of the ionization potential correspond to variations in the principal quantum number. A typical dependence of the atomic ion charge Z in a cluster plasma on the intensity of laser radiation is shown in Fig. 5.38 by the example of xenon cluster plasma. This dependence has plateau portions for charge values corresponding to a constant quantum number.

Internal ionization proceeds on an atomic time scale, i.e. instantly in our consideration, and therefore the highest degree of ionization is reached at the points in time when the harmonic electromagnetic wave field is at its maximum. An increase in wave intensity leads to an increase in resultant ion charge. The detachment of new electrons within the same electron shell proceeds monotonically for a relatively small variation of the field intensity, while the ionization of a new shell requires a substantially greater increase in intensity.

In the treatment of external ionization of a cluster as a whole under laser irradiation, advantage is commonly taken of the Bethe approximation as well. In this case, the cluster charge Q is evaluated by the formula [222]

$$Q = 4Fr_{\mathrm{w}}^2 N^{2/3},$$

where r_{w} is the Wigner–Seitz radius related to the cluster size by the formula $R = r_{\mathrm{w}} N^{1/3}$ and N is the number of atoms in the cluster. The electrons liberated in the ionization of the atoms and atomic ions of the cluster are partially trapped in the cluster by its self-consistent field and partially escape from the cluster. The fraction of electrons that escape from the cluster or the degree α of cluster ionization may be represented in the form [222]

$$\alpha = \left(\frac{8F}{F_0}\right)^{2/3} \frac{r_{\mathrm{w}}^2}{a_0^2 N^{1/3}}.$$

As follows from this formula, the degree of cluster ionization in a given electric field lowers with increase in cluster size. For a fixed cluster size it rises with increasing field intensity. Under laser irradiation with an intensity of 10^{16}–10^{18} W/cm^2 the degree of cluster ionization may range up to $\alpha = 0.01$–1.

It is pertinent to note that the ionization of atoms and ions in a cluster is caused not only by the action of external electric field, but also by the action of the self-consistent cluster field associated with the uncompensated charge of the atomic ions inside the cluster. The self-consistent field combines with the laser wave field to enhance the ionization. In particular, if the charge distribution in the cluster is assumed to be uniform, the self-consistent field intensity inside the cluster ($r \leq R$) is [222]

$$F_{\mathrm{cl}}(r) = \frac{dU_{\mathrm{cl}}}{dr} = \frac{Q}{R^3} r = 4F\frac{r}{R}.$$

This field is equal to zero at the cluster center and is nonzero at the cluster boundary. Accordingly, the atomic ion charge at the cluster boundary is higher than at its center. For instance, assuming that the ionization of a cluster as a whole proceeds similarly to the ionization of a hydrogen-like ion in the ground state, for the charge Z of an atomic ion in relation to its distance r from the cluster center we have

$$Z(r) = Z_0 \left(1 + 4\frac{r}{R}\right)^{1/3},$$

where Z_0 is the charge of the ions located at the cluster center. Hence it follows that the atomic ion charge at the cluster surface is $5^{1/3} \approx 1.7$ times higher that at the center.

The electrons captured by the self-consistent cluster field execute harmonic oscillations, thereby moving throughout the cluster volume. This oscillation frequency is comparable to the corresponding atomic quantity and is usually higher than the oscillation frequency of laser radiation. The electrons propagate swiftly in the cluster and so similar conditions are settled in different parts of the cluster.

5.6.3 Absorption of Laser Radiation by the Cluster Medium

For classical plasmas it is well known that an electromagnetic wave cannot penetrate into the plasma interior when the plasma oscillation frequency exceeds the wave frequency. If it is assumed that the plasma is uniform, the possibility of wave penetration into the plasma is determined by comparing the wave frequency ω with the plasma oscillation frequency ω_{p}. A weak electromagnetic signal penetrates a high-density cluster plasma to a depth of the order of the Debye–Huckel radius, which is quite short. For a plasma with an electron density $N_e = 10^{22}\,\mathrm{cm}^{-3}$ and an electron temperature $T_e = 100\,\mathrm{eV}$, the Debye–Huckel radius is equal to 0.5 nm.

For the strong electromagnetic field of ultrahigh-intensity laser radiation the situation is different. First, the displacement of boundary electrons resulting from the radiation–cluster interaction cannot induce the requisite screening field (which is induced in the weak radiation case), and therefore the electromagnetic field penetrates the plasma much deeper. Second, the electrons execute oscillations whose amplitude can be quite high in a strong field. This amplitude may be treated as the depth of electromagnetic wave penetration into the plasma. Therefore, the radius R of a cluster penetrated by a strong wave is comparable with the free-electron oscillation amplitude a in the electromagnetic wave field, $R \sim a$ [222]. For instance, for a laser field of intensity $I \approx 10^{19}\,\mathrm{W/cm^2}$ and the number $N \approx 4 \cdot 10^9$ of cluster atoms the field penetration depth is estimated at $a \approx 280\,\mathrm{nm}$, which is a very large figure.

Therefore, the ionization of atoms and atomic ions in a cluster due to the above-barrier transitions of valence electrons underlies the absorption of a strong electromagnetic wave by the cluster. The resultant-electron propagation into the cluster interior and their interaction with the collective degrees of freedom of the cluster plasma in the field of the electromagnetic wave leads to the energy transfer of the electromagnetic wave to the energy of the generated plasma. We also note that the rate of relaxation to the equilibrium electron energy distribution is determined by electron-electron collisions. Estimates of the characteristic electron Maxwellization time in the cluster plasma suggest that it is far longer than the laser pulse duration and the plasma expansion time. This is testimony to the nonequilibrium state of this plasma medium. The irradiation of clusters by high-power laser pulses of short duration permits inputting a high ($>1\,\mathrm{keV}$) specific energy into the electron subsystem, which gives rise to a specific hot plasma.

5.6.4 Cluster Production and Formulation of Experiments

The interaction of ultrashort laser pulses with a cluster target is a more intricate problem that the interaction with solid or gaseous targets. This is due to the fact that the initial target state itself is unknown, which may be spatially nonuniform. We note: while the number of works concerned with the evolution of clusters under laser irradiation amounts to many tens (see, for instance, [69, 81, 85, 89, 106–108, 110, 124, 135, 165, 173, 177, 180, 215, 221, 222, 225, 230, 245, 260, 264, 321, 324, 326, 344, 352, 354, 403, 404]), the very production of clusters and especially of submicrometer-sized clusters remained practically unexplored. At the initial stage of research, to estimate the cluster parameters in a jet advantage was taken of the multiparametric Hagena formula [168], which was derived by generalizing empirical data:

$$\Gamma = \mathrm{k}\left(\frac{d}{\tan\alpha}\right)^{0.85} \frac{p}{T_0^{2.29}}.$$

Here, d is the diameter of the critical section of a supersonic nozzle, μm, 2α is the nozzle apex angle, p is the pressure, Mbar, k is an empirical coefficient, which is different for different atoms (for instance, k = 2900 for krypton atoms and k = 180 for neon atoms), and T_0 is the initial gas temperature. Clusterization begins for Hagena parameters $\Gamma > 300$. For $\Gamma > 50{,}000$ clusters each contain more than 10,000 atoms.

However, the above formula permits estimating only the average values of cluster size and density, which pertain to the gas flow as a whole. Meanwhile, knowing the spatial and temporal dependences of cluster target parameters is absolutely necessary both for the correct numerical simulation of the heating by laser radiation and for the implementation of some important applications which require the uniformity of large-size plasma along one of the spatial directions, for instance, for making an X-ray laser.

It has been suggested [61–63] to obtain such data by simulating gas-dynamic processes with the inclusion of phase transitions occurring in a gas jet. In this case, to describe the formation of clusters advantage is taken of the model based on the so-called moments method; this model was developed and applied primarily to investigate the flows of humid water vapor in nozzles and turbine cascades. In this model the gas flow is considered at initial room temperature (experiments are usually executed under these conditions), i.e. the gas does not contain ions. Then, condensed-phase nuclei (only the liquid phase is considered in these simulations) are produced due to fluctuations in the supercooled gas (spontaneous condensation). Owing to surface effects, a small liquid droplet may be in equilibrium or vaporize even in the supercooled gas. Surface tension forms an additional potential barrier for a molecule that deposits on the droplet. Therefore, for specific gas parameters there exists a critical droplet radius r_{cr}. A droplet of critical radius is in equilibrium with the supercooled gas, the droplets of shorter radius vaporize and vanish, and only the droplets of greater-than-r_{cr} radius can grow. The following assumptions are made then to describe the formation of clusters: (1) the droplet velocities are equal to the gas velocity; (2) the droplet temperature is equal to the saturation temperature; (3) the effects of droplet fragmentation and merging, viscosity, thermal conduction, and turbulence are negligible; (4) the possibilities of droplet freezing and crystalline nucleation are neglected.

The elaborated model and the ensuing simulations made it possible to demonstrate for the first time that the use, for instance, of the well-known Laval nozzle for producing clusters has the effect that their density and size vary strongly across the nozzle [61] (the gas produced at the center of jet is a dryer gas with a lower cluster density than at the nozzle wall). Systematic simulations with different (Ar, Kr, Xe) gas media [63] also allowed the first prediction of the effect, which is significant from the standpoint of laser-cluster interaction, that only a small part (≈10–20 %) of the gas is normally clusterized, while the greater part remains in the gas stage. The use of this model also enabled designing a three-stage nozzle [62, 63], which opened up the possibility of investigating laser interactions with submicrometer-sized clusters (for more details, see Sect. 5.6.5) as well as with clusters produced in the expansion of different gas mixtures. All these results, which were obtained in the

expansion simulations of different gaseous media, were borne out by experimental data, which followed from the analysis of the Rayleigh scattering of laser radiation by cluster jets performed, for instance, in [111, 152].

Now we discuss the formulation of typical experiments on the interaction of high-power short laser pulses with clusters. The majority of experiments described in [221, 222] was carried out on the clusters of rare-gas atoms or simple diatomic molecules, the number of particles in these clusters ranging up to one million. The results outlined in Sect. 5.6.5 of this chapter were obtained for a substantially larger cluster size [54, 132, 133, 149, 172, 297]. The number of atoms in them amounted to a figure of 10^8–10^{10}, which was provided by the use of a special conical nozzle with input and output openings with respective diameters of 0.5 and 2.0 mm. A typical setup of this experiment is shown in Fig. 5.39 [404].

The cluster beam is formed in the expansion of gas in its supersonic flow through the nozzle in vacuum; the gas pressure at the input nozzle opening is equal to 70 atmospheres. The laser beam is focused to a spot $\approx 6\,\mu$m in diameter at a distance of 1 mm from the nozzle outlet. The Ar gas expands in the nozzle, and the outgoing clusters are irradiated by a 100-fs laser beam at a distance of 1 mm from the nozzle outlet. The size of laser–cluster interaction zone is monitored using Thomson scattering in the direction perpendicular to the direction of laser radiation propagation (in this case, from the chamber top). The electrons produced in the course of interaction are measured using an electron spectrometer in the direction of laser radiation propagation and are also visualized in the perpendicular direction. Different experiments additionally make use of soft- and hard-X-ray spectrometers as well as of various ion detectors (see the results outlined in Sect. 5.6.5). In conclusion of this section, there is good reason to emphasize once again the unique properties of cluster targets in comparison solid targets: (1) a very high

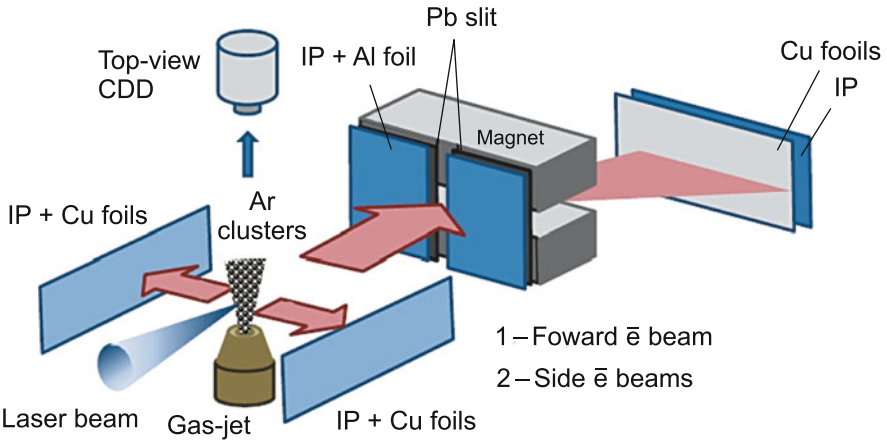

Fig. 5.39 Typical setup of experiments to investigate the interaction of ultrahigh-intensity laser pulses with cluster targets, which is considered by the example of experiments on the generation and recording of relativistic electron beams [404]

shot-to-shot stability of cluster target generation; (2) the ease of timing of cluster target generation to the heating laser radiation; (3) the absence of finely dispersed parasitic particles, which are normally produced in the interaction of laser radiation with solid targets; (4) the high, nearly 100 % absorption of laser radiation by the cluster target.

Until recently the use of radiographic and ionographic techniques of research necessitated the application of experimental facilities of huge size and cost: synchrotrons in the former case and heavy-ion accelerators in the latter. However, in many cases the synchrotron sources and heavy-ion accelerators may be replaced to advantage by compact femtosecond lasers, because sufficiently intense X-ray and VUV radiation fluxes as well as fast proton or ion beams are generated in the interaction of short laser pulses with matter. Given below is a review of the best recent results on the generation of quantum particles obtained in laser-cluster interactions.

5.6.5 Production of Ultrabright X-ray Radiation

Of major interest for several applications is soft X-ray radiography, while for other applications the use of hard X-ray photons is preferential. The variety of gases which lend themselves to submicrometer cluster production is wide and permits making ultrabright X-ray sources in different spectral regions. Specifically, for the soft X-ray region use can be made of clusters that contain light chemical elements like C, N, O. Medium-Z chemical elements like Ar, Kr and Xe may be employed for generating hard X-ray radiation.

5.6.5.1 Production of Soft X-ray Radiation

X-ray fluxes in the Ly_α and He_β spectral lines of oxygen ions were measured in the experiments to generate soft X-ray radiation with an energy of $\approx$0.7 keV performed on the JLITE-X facility (Kansai Photon Science Institute JAEA, JAPAN) using three types of cluster targets (CO_2 and N_2O gases, a 90 % He + 10 % CO_2 gas mixture) [132, 149]. The 36-fs long pulse of a Ti:Sa laser with an energy of 120 mJ was focused with a parabolic mirror to a spot 50 μm in diameter to provide a laser irradiation intensity of $4 \cdot 10^{17}$ W/cm^2 in the focal spot. The intensity of the oxygen lines was observed to be highest for gas pressures at which largest-size (up to 1 μm in diameter) clusters were produced. It is noteworthy that the number of photons with the use of clusters from the gas mixture (90 %He + 10 % CO_2) as the target was four to nine times greater than with the use of pure CO_2 or N_2O gases and was as high as 2.7 and $2.8 \cdot 10^{10}$ photons/sr per laser pulse for the Ly_α and He_β lines, respectively. The measured brightness of both lines was also higher for the gas mixture and was equal to $1.6 \cdot 10^{23}$ and $1.3 \cdot 10^{23}$ photons/s/ mm^2/mrad^2/0.1 % spectral line bandwidth), respectively.

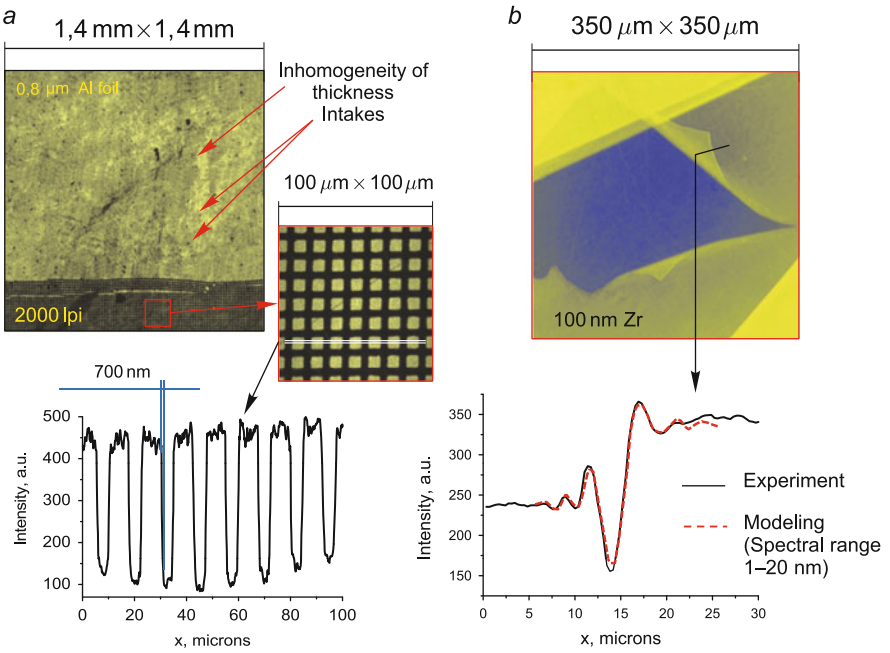

Fig. 5.40 Use of a laser cluster soft X-ray radiation source and a LiF crystal detector for the high-resolution high-contrast radiography of microobjects [132, 149]: (**a**) fluorescent images of aluminum foil of thickness 0.8 μm and a square mesh (2000 lines per inch) placed in contact with the LiF surface; (**b**) fluorescent image of a damaged segment of 100-nm thick zirconium foil obtained in the mode of phase contrast (the sample–detector surface spacing was equal to 3.8 mm). The effect of intensity increase at the foil edge is clearly seen and coincides with a simulation made assuming that the spatial coherence length is equal to ≈5 μm at a distance of 500 mm from the source

The developed source of soft X-ray radiation was used to obtain the contact soft X-ray radiographic images of different foils and biological nano- or micrometer-thick objects with a high (≈700 nm) spatial resolution, a large (several cm^2) field of view, and a large dynamic range (see Fig. 5.40a). The high efficiency of the radiographic method developed using a high-intensity point-like laser-cluster X-ray source and a high-contrast high-resolution LiF crystal detector is made evident by the image of a 0.8-μm thick Al foil (Fig. 5.40a). The fine features arising from the impurities and inhomogeneities of the Al foil less than 1 μm in size are clearly discernible throughout the image.

A major virtue of the developed source and detection system is not only the possibility of carrying out contact radiography, but also the capability of obtaining informative phase-contrast images. As is evident in Fig. 5.40b, in the resultant image there occurs an improvement of the contrast, making it possible not only to enhance the definition of foil edges, but also to resolve finer features in the film structure. The improvement of image contrast was achieved owing to the well-known effect which

has come to be known as the phase contrast technique [297]. This result allowed estimating the spatial coherence length of the laser-cluster X-ray radiation source at $\approx 5\,\mu$m.

5.6.5.2 Production of Hard X-ray Radiation

To obtain hard X-ray radiation in the 3–30 keV energy range, use was made of Ar, Kr, and Xe clusters.

Figure 5.41a shows a typical spectrum obtained in the experiments with Ar clusters executed on the Extreme Light-III laser facility (Institute of Physics, Chinese Academy of Sciences) for laser radiation intensities $I_{las} \approx 2.6 \cdot 10^{19}$ W/cm^2 and a high (10^{10}) contrast of a 100-fs laser pulse. Under the conditions of this experiment, the emission peak in the Ar K_α energy region is primarily due to the emission of different multiply charged ion lines, which lie between the He_α lines of Ar XVI and the K_α line of neutral Ar[133]. An investigation of the dependence of the X-ray yield on the gas pressure [403] showed (see Fig. 5.41b) that the X-ray yield is relatively low for low gas pressures. It monotonically increases with increasing gas pressure (due to an increase in size of the clusters, which amount to 0.3 μm in diameter for an Ar gas pressure of 70 bar) to attain a record figure of $\approx 2.5 \cdot 10^{11}$ photons/J. In this case, the laser-to-X-ray conversion efficiency was quite high ($\approx 1.2 \cdot 10^{-4}$), which permitted using the resultant source for the radiography of biological objects with a high spatial resolution in one laser shot [403].

To produce a high-intensity X-ray source in a harder ($\approx$13 keV) X-ray range, use was made of Kr gas, which has a higher atomic number. Figure 5.41c shows the observed X-ray spectrum [172] consisting of a continuous (bremsstrahlung) spectrum and peaks with energies of 12.7 and 2.7 keV, which correspond to the linear spectra in the region of Kr K_α and L_α lines recorded for a Ti:Sa laser radiation intensity of only $\approx 8 \cdot 10^{16}$ W/cm^2 [172]. The full width at half-maximum (FWHM) of the K_α peak is equal to 0.28 keV, which is in reasonable agreement

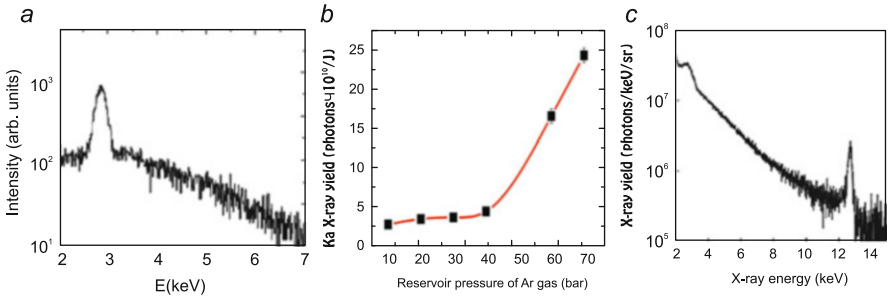

Fig. 5.41 (**a**) Typical spectrum of Ar cluster plasma in the 2–7 keV photon energy range; (**b**) photon flux in the Ar K_α spectral line as a function of gas pressure [403]; (**c**) typical Kr cluster plasma in the 2–15 keV photon energy range [172]

with the energy resolution of the X-ray CCD equal to 0.25 keV in these energy ranges. Another picture is observed for the 2.7 keV peak. the halfwidth of this peak amounts to 0.74 keV, which is approximately four times greater than the ideal energy resolution of the X-ray CCD (≈0.18 keV in this energy range). This large halfwidth of the peak is due to the fact that this energy range comprises not only the radiation of the L_α resonance line, but also the radiation from the L shell of multiply charges Kr ions.

Like in the case of experiments on Ar discussed above, the X-ray radiation yield shows a trend for a sharp rise with increasing gas pressure in the nozzle to reach values in the $(5.0–7.5) \cdot 10^7$ photons/sr range for energies of ≈2.7 keV and in the $(6.8 \pm 2.6) \cdot 10^5$ photons/sr range for energies of ≈13 keV. In this case, the brightness of the bremsstrahlung and the Kr K_α line corresponded to $2.5 \cdot 10^{13}$ and $1.8 \cdot 10^{14}$ photons/(s mrad^2 mm^2)/(0.1 % bandwidth), respectively, assuming an X-ray pulse duration of 1 ps. Also noteworthy is a high (≈20 %) stability of this X-ray source based on submicrometer-sized Kr clusters. Further increase in the X-ray yield with the use of submicrometer-sized Kr clusters and high-contrast Ti:Sa lasers was achieved in experiments on the higher-power Extreme Light-III laser facility (Institute of Physics, Chinese Academy of Sciences)[403]. Increasing the laser–Kr cluster interaction intensity to $2.6 \cdot 10^{19}$ W/cm^2 enabled reaching an X-ray radiation yield of $\approx 8 \cdot 10^8$ photons/J near the Kr K_α line, which corresponds to a conversion coefficient of $\approx 1.6 \cdot 10^{-6}$.

Harder X-ray radiation may be obtained with the use of Xe clusters with a nuclear charge $Z = 54$ [173]. These experiments were carried out using the J-KAREN Ti:Sa laser facility (Kansai Photon Science Institute, JAEA, Japan), in which the employment of an optical chirped pulse amplification scheme made it possible to reach a very high contrast, $\approx 10^{11}$, and have a prepulse laser intensity below $\approx 10^8$ W/cm^2. Despite the relatively small size of Xe clusters, this intensity was not high enough to destroy them prior to the arrival of the main laser pulse. The hard X-ray yield near the Xe K_α line (≈30 keV) for a laser irradiation intensity of $\approx 4 \cdot 10^{18}$ W/cm^2 was measured [173] at $\approx 3.1 \cdot 10^7$ photons/pulse and corresponds to a laser-to-X-ray radiation conversion efficiency of $\approx 1.5 \cdot 10^{-7}$ for a 40-fs laser pulse. The X-ray spectrum has a sharp peak in the 30-keV region with a halfwidth of ≈0.7 keV, which is considerably greater than the energy resolution of the X-ray CCD and is indication that several gas ionization stages ranging from Xe^{+30} to Xe^{+40} were reached in the experiments under discussion (see, for instance, [54] for a more detailed information about the ionization of Xe clusters by ultrahigh-intensity laser pulses). Furthermore, the action of high-energy electrons may directly remove the K-shell electrons of multiply charged ions; in this case, the emission from these ions is superimposed to increase the halfwidth of the energy spectrum in the vicinity of the Xe K_α line, which was observed in the experiment being discussed. We note that the observed spectrum is best described assuming a two-temperature plasma model. Specifically, while for a 40-fs long laser pulse the effective temperature was Maxwellian with $T_{el1} = 1.3$ and $T_{el2} = 5.4$ keV, for a 300-fs laser pulse it was equal to $T_{el1} = 1.6$ and $T_{el2} = 4.8$ keV. It was also determined that the X-ray radiation intensity in the neighborhood of the Xe K_α line for a laser pulse duration of 40 fs

was definitely higher than for a pulse duration of 300 fs. The efficiency of laser energy conversion to the X-ray line radiation corresponded to $\approx 1.3 \cdot 10^{-7}$ for the 40-fs pulses and to $2.4 \cdot 10^{-8}$ for the 300-fs pulses. This result contradicts the data obtained in [112, 203], in which a laser pulse duration of 200–300 fs was optimal for maximizing the hard X-ray Kr cluster radiation yield. The dependence measured for Xe may be attributed to the fact that the Xe K_α photon energy ($\approx$30 keV) is substantially higher than the Kr K_α photon energy ($\approx$13 keV). This signifies that the laser pulse has to accelerate electrons to higher energies, which are required for ionizing the inner shells of Xe (>35 keV in comparison with >15 keV required for ionizing the inner shells of Kr). This assumption was confirmed in [173] by way of particle-method simulations of the number of electrons with energies above 35 keV generated in the plasma under heating by 40- and 300-fs long laser pulses. In the former case the number of electrons with energies above 35 keV was an order of magnitude higher, which naturally led to an increase in X-ray radiation yield in the vicinity of the Xe K_α line.

5.6.6 Production of Fast Electrons in Cluster Plasma

The effect of the high contrast of femtosecond laser pulses on the interaction with a gaseous medium containing large argon clusters was investigated in [404]. These experiments were carried out on the Extreme Light-III Ti:Sa laser facility delivering 100-fs long pulses for a contrast ratio of 10^{10} and a laser irradiation intensity of $\approx 2.6 \cdot 10^{19}$ W/cm^2. The energy spectrum of electrons accelerated in the direction of laser radiation propagation (indicated by figure 1 in Fig. 5.39) was measured using a magnetic spectrometer. In order to realize the conditions for the efficient generation of electron beams, the nozzle position relative to the focal point of the laser beam and the gas pressure were optimized, which determined the cluster size and other characteristics of the gas-cluster target. When the argon pressure was varied from 1 to 6 MPa, no electron beam was produced in the direction of laser beam propagation (direction 1 in Fig. 5.39), irrespective of the nozzle position. Reliable generation of electrons was detected when the gas pressure reached 7 MPa, which initiated the production of clusters up to 0.28 μm in diameter for an ambient gas density of $\approx 5.5 \cdot 10^{19}$ cm^{-3}. The highest intensity of the electron beam in the energy range from 80 to 600 MeV was obtained when the laser pulses were focused at a distance of 1 mm from the nozzle outlet, approximately 0.5 mm off center in the direction of laser beam axis (see Fig. 5.42a, b). One can see from the drawing that the beam is rather well collimated in the vertical direction and its divergence does not exceed 1.4 mrad. Assuming a Maxwellian electron distribution above 80 MeV, the total electron charge was found to be no less than 50 pC. This efficient fast-electron production in the longitudinal direction corresponds to the conditions when the laser radiation absorption depth in the cluster target is equal to 3 mm; this was monitored in the visible spectral range from the shape and intensity of Thomson scattering, which was recorded from top of the interaction zone, as shown in Fig. 5.39.

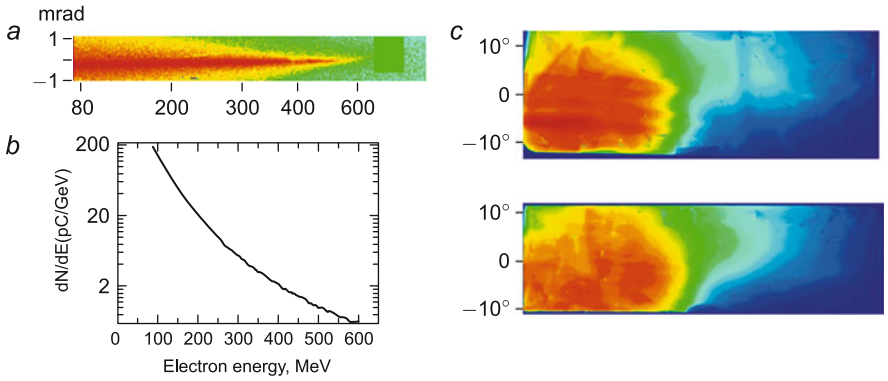

Fig. 5.42 (**a**) Electron-beam image obtained with an electron spectrometer in the energy range between 80 and 600 MeV in one laser shot (longitudinal direction 1) [404]]; (**b**) electron spectrum corresponding to the image in (**a**); (**c**) images of the electron beams generated perpendicular to the axis of laser radiation (directions 2)

A special feature of the use of gas clusters as targets manifested itself in the simultaneous observation of relativistic electron fluxes not only in the direction of laser radiation propagation, but also in perpendicular directions (directions 2 in Fig. 5.39). Side detectors (see Fig. 5.42c) recorded intense electron beam with energies >1 MeV and a charge greater than 3 nC. These electron beams, which carry large charges, may be of considerable practical interest, for instance, for electron injection in conventional accelerators or as THz radiation sources. As is evident from Fig. 5.42c, the beams also possess wide angular dimensions and may therefore be highly efficient in wide-field electron radiography.

5.6.7 Production of High-Energy Ions in Cluster Plasma

Among the important applications of ion sources is the radiography of different objects using the beams both of high-energy multiply charged ions and of high-energy protons (for brevity such radiography will be referred to as ionography and protonography). In particular, the radiography reliant on a laser-plasma proton source (see, for instance, [64, 356]) enjoys wide use for recording images with a high spatial (at a level of several micrometers) and temporal (several picoseconds) resolution without resorting to complicated charged-particle optics, which is required, as a rule, when use is made of conventional particle accelerators.

We note that an important requirement in ionography is to provide a wide field of view, which calls for the use of an ion source isotropic over a broad angular emission range. From general physical considerations it follows that this isotropic production of fast ions would be expected in precisely the employment of cluster targets. The contrast of an ionographic image will be highest when the free probe-ion path in

the substance under investigation is only slightly longer than the expected sample thickness. On lowering the energy of a femtosecond laser pulse to 0.1 J (for a flux density of about 10^{16} W/cm^2) the accelerated ion energy lowers to hundreds of keV. Therefore, going to lower-power laser facilities and decreasing the average probe-ion energy optimizes the conditions for investigating and imaging extremely thin samples, like micro- and nanofoils and membranes. Since the accelerated-ion absorption cross sections in the substance under investigation are inversely proportional to the squared ion charge, highly charged ions are a great advantage in the imaging of these object, while protons are most convenient in imaging the objects of considerable thickness [132].

The high efficiency of using cluster targets for the ionography of submicrometer-thin foils by exposing them to multiply charged ions with energies of several hundred keV was demonstrated in experiments on the JLITE-X facility. Measurements executed using the Thomson parabola and X-ray spectroscopy (see Fig. 5.43a, b) showed that the use of a 90 % He + 10 % CO_2 gas mixture as the cluster target resulted in a virtually isotropic acceleration of the H- and He-like ions of carbon $C^{V,VI}$ and oxygen $O^{VII,VIII}$ to energies of the order of 100–1000 keV in the resultant plasma source; in this case, accelerated helium ions were hardly present. The number of these energetic ions is greater than 10^8 per laser pulse in the 4π total solid angle. By way of example Fig. 5.43c shows an ionographic image obtained using a laser-cluster plasma source on the 90 % He +10 % CO_2 mixture, which demonstrates a high (much better than 100 nm) sensitivity of the ionographic visualization method to the thickness of material and a high (0.6–0.8 μm) spatial resolution. Considering that in this case the probe ion flux uniformly irradiates object areas measuring tens

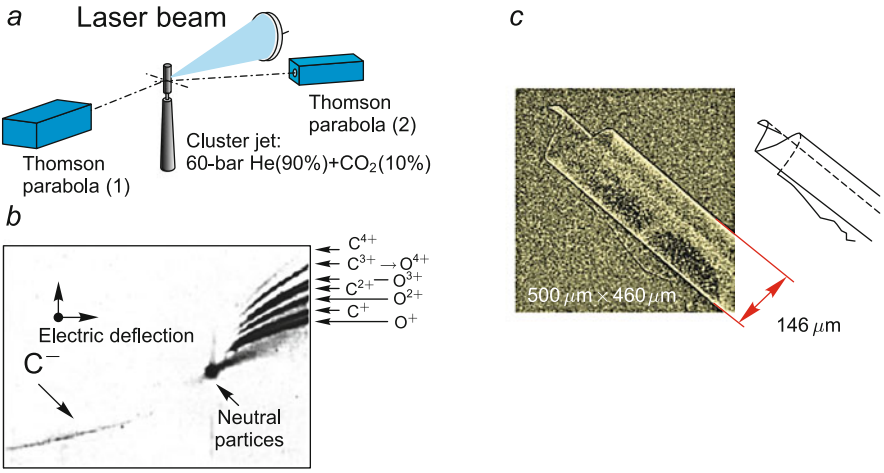

Fig. 5.43 (**a**) Setup for recording the ion spectra of a laser-plasma cluster source; (**b**) typical form of the spectrum of CO_2-cluster plasma ions obtained with the use of a Thomson parabola [64, 356]; (**c**) ion radiographic image obtained with a CR-39 detector—the tip of a 100-nm thick Zr foil rolled into a tube—and a graphic reconstruction of its shape [132]

of millimeters, we can reach a conclusion about the development of a unique means of constructing microscopic ion-radiographic images with a field-of-view/resolution ratio of the order of 10^5.

Another interesting application of a laser-cluster source is the possibility of accelerating negative ions to submegaelectronvolt energies. As is clear from the data given in Fig. 5.43b, negatively charged ion beams are also generated in the interaction of short laser pulses with large-size clusters [276, 277]. Specifically, the highest energy of C^{-1} negative ions recorded in this experiment was equal to about 0.6 MeV. To explain the production of high-energy negative ions, the authors of [276, 277] proposed the mechanism of a Coulomb implosion (directed into the cluster interior, unlike a conventional Coulomb explosion directed away from the cluster center), which leads to negative-ion acceleration. When a cluster is irradiated by a high-intensity laser pulse, electrons are "blown off" the cluster by the ponderomotive pressure of the laser light. Produced in this case is a large uncompensated charge of positive ions, which results in the Coulomb explosion of the cluster. The model under consideration supposes that negative ions may be accelerated in the same region where ordinary ions are accelerated. However, they are accelerated in the opposite direction, resulting in the back-reflection at the symmetry center and the production of high-energy negative ions. a similar mechanism of negative ion acceleration was earlier considered in [343] for multicomponent clusters. An in-depth simulation by the particle-in-cell method was carried out in [276, 277] and showed a rather good agreement with the experimental data shown in Fig. 5.43b.

The above ion acceleration mechanism based on the Coulomb cluster explosion does not permit accelerating ions to energies of tens of MeV, which is one of the currently central problems of relativistic laser physics. As shown above, this acceleration mechanism permits generating isotropic ion beams of not too high an energy. However, other, higher-efficiency mechanisms of high-energy ion acceleration are also possible in laser-cluster interactions. For instance, the possibility of producing multiply charged ions with energies of the order of 20 MeV/nucleon was demonstrated [150] in the irradiation of submicrometer-sized clusters by high-intensity femtosecond laser pulses. This is associated with the unique properties of cluster plasmas, which permit laser beams to efficiently self-focus [11], produce multimillimeter-long plasma channels, and generate intense electron beams with energies of tens and hundreds of MeV [404]. These properties of the cluster medium are highly important for efficient ion acceleration, because the resultant plasma waveguide favors the unimpeded transport of laser pulses over long distances and the large number of accelerated fast electrons produces high electric and magnetic fields.

Experiments on the generation of ion beams with MeV energies were carried out on the JLITE-X facility. For a target use was made of submicrometer-sized CO_2 clusters produced in the expansion of a 90 % He+10 % CO_2 gas mixture in vacuum. In these experiments the in-vacuum laser intensity was equal to $\approx 7 \cdot 10^{17}$ W/cm^2. However, in the propagation of the laser beam through the cluster target the intensity of laser radiation increased significantly, because the peak intensity of the main laser pulse far exceeded the critical power of relativistic self-focusing. The occurrence of

self-focusing and self-channeling of the laser radiation was experimentally borne out by way of recording the shadow images of the laser plasma channel for different time delays of the probing laser radiation. The recorded shadow images reveal the formation of a plasma channel approximately 5 mm in length, which is significantly greater than the nozzle diameter (2 mm) and the Rayleigh length ($\approx$900 μm) of the focusing lens employed in these experiments. High ion energies (10–20 MeV/nucleon) were measured with the help of nuclear track detectors (SSNTD) accommodated on the axis of laser beam propagation at 200 mm from the laser focal plane. The data obtained with the track detectors show that the ions with such high energies are well collimated and propagate within an angle of 3.4° in the direction of laser radiation propagation.

The fact of production of the ions with such high energies was confirmed using time-of-flight measurements with the use of a microchannel plate (MCP) detector placed at a distance of 930 mm in the direction of laser radiation propagation. Figure 5.44 shows the ion energy spectrum (under the assumption that it is due to carbon ions) measured with the TOF spectrometer in 285 sequential laser shots. The highest recorded ion energy was equal to $\approx$18.5 MeV/nucleon, which agrees nicely with the ion energies measured using CR-39 track detectors.

It is pertinent to note that increasing the laser prepulse energy (the laser contrast ratio was lowered from $\approx 10^6$ to $\approx 10^4$, which permitted destroying clusters with certainty prior to the arrival of the main femtosecond pulse) had the consequence that neither the long plasma channel produced by laser self-focusing nor the accelerated MeV ions were observed. To elucidate the mechanisms of ion acceleration, two-dimensional particle-in-cell simulations were undertaken in [150]. According to [278], ions are accelerated along the propagation axis of laser radiation, which induces high-intensity electromagnetic fields during this propagation. This process is largely similar to the ion acceleration in a plasma discharge column. Furthermore, the ions are accelerated perpendicular to the surface of the sheath formed by the field of nonuniform magnetic pressure, resulting in a rather low ($\approx$5°) divergence of the

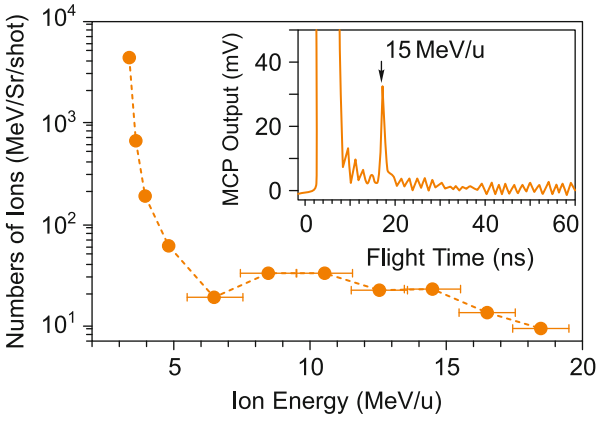

Fig. 5.44 Ion energy spectrum obtained by the time-of-flight method and integrated over a large number of pulses [150]. The *inset* shows the time-of-flight signal from a single shot, in which one can clearly see a prominent peak corresponding to an energy of 15 MeV/nucleon. The signal saturation in the time region $t = 5$ ns is due to the saturation caused by hard X-ray radiation

ion beam, which is in good agreement with the experimentally observed divergence of $\approx 3.4°$.

5.6.8 Conclusions

In this section it was shown that the interaction of high-power high-contrast (the time contrast ratio between the main pulse and the prepulse is no worse than 10^8–10^{10}) femtosecond laser pulses with gas clusters of large size permits producing bright X-ray radiation sources and high-intensity electron and ion beams.

The generated radiation wavelengths may lie in the soft and hard X-ray ranges, depending on the elemental composition of the cluster target. For instance, the clusters of carbon dioxide CO_2 are an efficient source of soft X-rays with a photon energy $h\nu \approx 0.7$ keV: a photon yield of $>2 \cdot 10^{10}$ photons/pulse was obtained in the Ly_α spectral lines of hydrogen-like ions and He_α lines of helium-like ions of oxygen.

For the argon K_α lines ($h\nu \approx 3$ keV), a flux of $\approx 2 \cdot 10^{10}$ photons/J was obtained for a uniquely high conversion coefficient of $\approx 1.2 \cdot 10^{-4}$, which permitted using this source for the radiography of low-absorbing objects. In the hard X-ray range ($h\nu \approx 12 - 30$ keV), with the use of Kr and Xe rare-gas clusters the K_α radiation intensity was equal to $0.7 \cdot 10^6$–$3 \cdot 10^7$ photons/pulse for a laser radiation intensity of $8 \cdot 10^{16}$–$4 \cdot 10^{18}$ W/cm^2.

The laser–cluster interaction was shown to produce, along with X-ray radiation, accelerated relativistic electron fluxes of, conventionally speaking, two types: high-energy (with an energy of tens and hundreds of MeV) low-divergence (several milliradians) fluxes propagating near the axis of laser radiation and wide-field fluxes with an energy of several MeV produced in the perpendicular direction to the laser radiation. In the irradiation of Ar clusters by 10-TW pulses, electrons with energies of up to 600-MeV were recorded in the forward direction; in this case, the total charge of the electrons with energies above 80 MeV amounted to ≈ 50 pC. Simultaneously, in the transverse direction the electron charge of the electrons with energies >1 MeV amounted to >3 nC in an angular field of $\approx 20°$.

The laser–cluster interaction was shown to be highly efficient as a virtually isotropic intensive source of ions with energies <1 MeV. Uniformly irradiated ion radiographic images of test samples were obtained with submicrometer spatial resolution over a wide field of view (tens of cm^2). Therefore, the cluster ion source is of considerable interest for the development of high-precision methods of measurement and quality monitoring of thin films and other low-contrast objects and submicrometer-scale structures.

Conditions were found in laser–cluster interactions, which permit implementing the mode of ion acceleration up to energies of 19 MeV/nucleon in the direction of laser radiation propagation. This result confirms the significant potentialities of laser systems for the development of compact high-repetition-rate ion sources for practical applications, including medical ones.

5.7 Spectra of Hollow Ions in Superdense Laser Plasma

Improvement of the time contrast ratio for laser radiation up to 10^{10} and over as well as commissioning of the first X-ray free-electron laser (LCLS in the Stanford National Laboratory, USA, and SACLA of the Institute of Physical and Chemical Research (RIKEN), Japan) open up new possibilities for the investigation of such exotic states of substance as "hollow ions" [380].

Even the first experiments carried out with a femtosecond laser characterized by an ultrahigh contrast (the pulse-to-prepulse intensity ratio) of the order of 10^{11} [128, 129, 373] permitted to record for the first time the spectra of a new type previously unobserved in this spectral domain (see Fig. 5.45c). The appearance of the new type of spectra was an unambiguous indication that the passage to ultrahigh laser contrast ratios is attended with a radical change in resultant plasma parameters and the emergence of its induced new physical effects.

The observed "extraordinary" spectra differ from the more usual ones by their complex quasicontinuous spectral structure, in which the main, resonance, lines are embedded. Theoretical spectra calculated in the framework of a coronal quasistationary kinetic plasma model [58] (see Fig. 5.45d) resemble the previously observed experimental emission spectra of the plasmas produced by nano-, pico-, and femtosecond laser pulses with a low contrast, but turned out to be absolutely unsuitable for describing the new type of spectra.

The physical reason for this dramatic spectral restructuring is naturally associated with the difference in plasma production mechanisms. The absence of preplasma underlay the direct interaction of an ultrashort laser pulse with a solid substance. This gave rise to a plasma with a substantially higher electron density, on the one hand, and tremendous spatial gradients of the density and temperature, on the other hand. Under these densities, a wealth of spectral lines which are hardly excited in uniform coronal plasmas come to dominate the emission plasma spectrum.

In [128, 129, 373] it was shown for the first time that the new type of observed spectra may be interpreted only with the inclusion of the radiation emitted by multiply charged hollow ions (i.e. by the ions with an empty K shell, see Fig. 5.46) in superdense plasmas. Transitions of this type (see Figs. 5.47 and 5.48) in neutral and quasineutral objects (hollow atoms) were observed in experiments on the interaction of ion beams (see, for instance, [66, 259, 323, 333]) or synchrotron radiation (see, for instance, [102, 103]) with a solid surface and have been under active investigation during the past two decades. Similar structures for multiply charged ions were first observed supposedly in the spectra from the near-surface regions of the plasma produced by the nanosecond pulse of the NIKE laser [5].

A strong incentive for the development of theoretical and experimental hollow-ion spectroscopy is that these spectra should be excited in warm dense matter and in nonideal plasmas [138, 143, 288, 315]. As is clear from Figs. 5.46 and 5.47, these spectra arise from electron transitions between deeply lying inner ion shells, and therefore the nonideality effects, which are hard to calculate quantitatively, will not have an appreciable effect on the spectra of hollow ions. This signifies that it will be

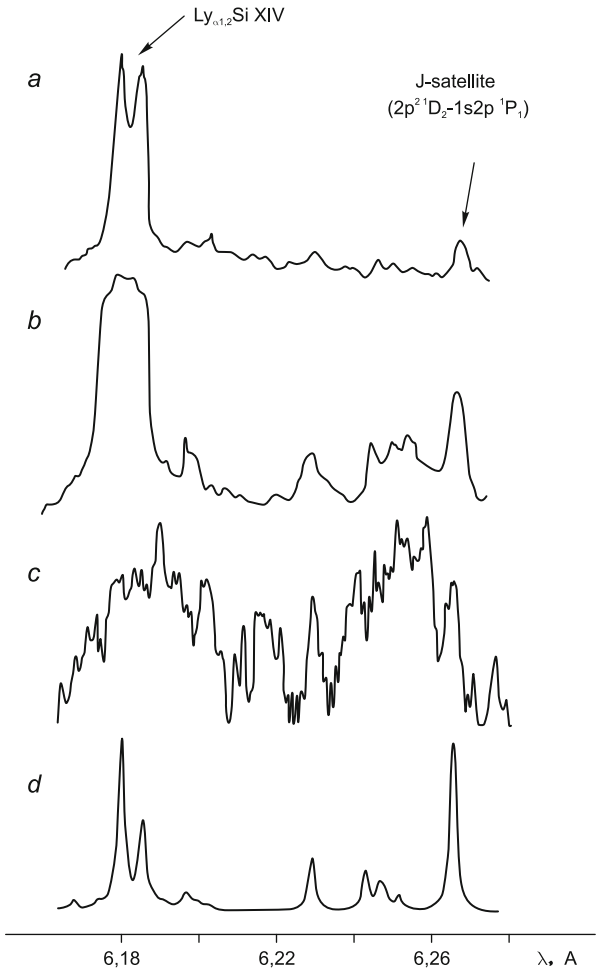

Fig. 5.45 Emission spectra of silicon plasmas heated by nanosecond (**a**) [58] as well as low-contrast (**b**) [127] and high-contrast (**c**) [128] subpicosecond laser pulses in the vicinity of the resonance Ly$_\alpha$ line of H-like ions Si XIV. Theoretical spectrum (**d**) corresponds to the coronal plasma model

possible to employ the hollow-ion spectra for the X-ray spectroscopic diagnostics of nonideal plasmas with hardly any modifications.

We emphasize: for a significant amount of hollow ions to be produced in a plasma, there must be a mechanism which efficiently removes inner-shell electrons without ionizing the outer shells. Strictly speaking, such a mechanism does not exist; however, we may endeavor to find processes whereby the probability of removing inner-shell electrons will not be too small in comparison with the ionization of the

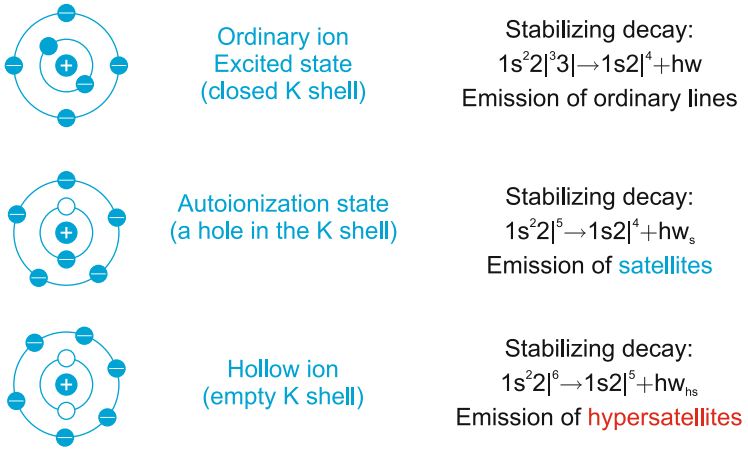

Fig. 5.46 Electron shell structure of excited, autoionization, and hollow ion states

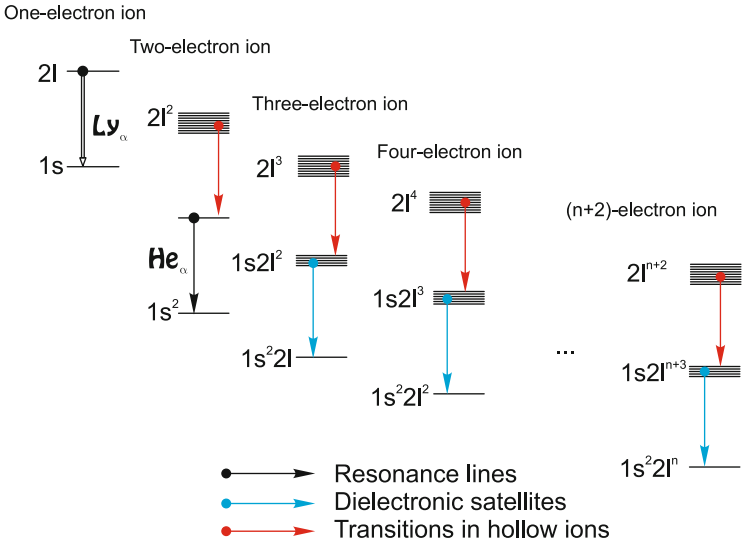

Fig. 5.47 Energy level diagram for ordinary, autoionization, and hollow ion states with valence *K*- and *L*-shells

outer-shell ones. Broadly speaking, the ionization in a plasma may occur in ion collisions with electrons, other ions, or photons.

Ion-ion collisions may result in the nonresonance ionization by the Coulomb field of the incident ion as well as in resonance charge exchange. The former process may be neglected in plasmas, because the cross sections for the ionization by ion impact are large only for superhigh ion energies achieved only in accelerators [139]. It is pertinent to note, however, that the first observations of the spectra of hollow atoms

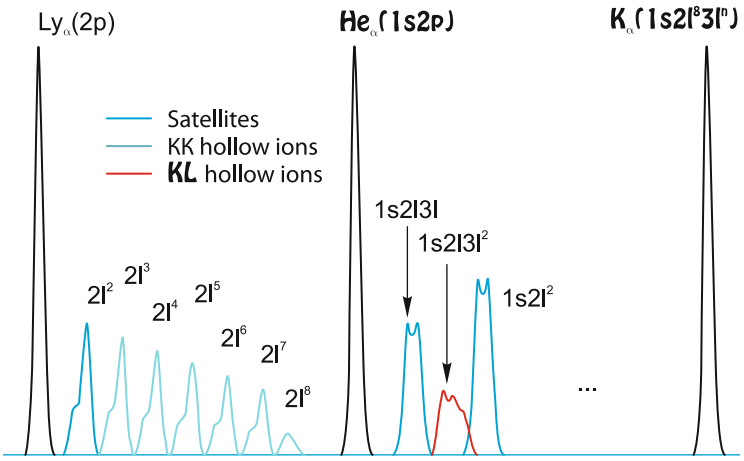

Fig. 5.48 Approximate positions of the Ly$_\alpha$ resonance line of an H-like ion, the He$_\alpha$ line of a He-like ion, the characteristic K$_\alpha$ line, dielectronic satellites ($2l^2$, $1s2l^2$, $1s2/3/$), and hypersatellites (the lines of hollow ions) in the ion emission spectrum. The configurations of the upper levels of spectral transitions are indicated for all lines. The location of the dielectronic satellites and hypersatellites with the number of electrons greater than three is marked with ellipsis

(a hollow atom is the special case of a hollow ion with a zero total charge) were made in precisely the accelerator experiment [66]. The latter mechanism (resonance charge exchange) may excite hollow ion states, for which purpose the interaction of ions of significantly different multiplicity is to occur.

Ionization events in a plasma occur most often due to electron impact. In this case, the electron energy must also be rather high in comparison with the inner-shell ionization energy, but nevertheless lower than in the case of ionization by ion impact. For ions with charges of about 10 it would suffice to have electrons with energies of several keV and, as is commonly known (see, for instance, [1, 2, 405]), in the plasma production by subpicosecond laser pulses at intensities above 10^{16} W/cm^2 such electrons are generated in sufficient quantities.

Hot electrons may produce hollow ions, but do this with not-too-high an efficiency. Specifically, the electron impact ionization rates are approximately proportional to n^3, where n is the principal quantum number of the electron being ionized. Hence it follows that a hot electron will ionize the L shell with a much higher (by nearly an order of magnitude) probability than the K shell (see Fig. 5.49). Therefore, in the collisions of ions with hot electrons the K^2 hollow ions will be produced, but in far lower numbers than ordinary ions. This conclusion is practically independent of whether the hot ions are monoenergetic (an ion beam) or thermal, as is evident from Fig. 5.49. Broadly speaking, hollow ions may be produced not only by way of inner-shell ion ionization, but also due to the excitation of an inner electron to an outer shell. However, the situation is hardly changed on including this process (see the dashed and dotted curves in Fig. 5.49).

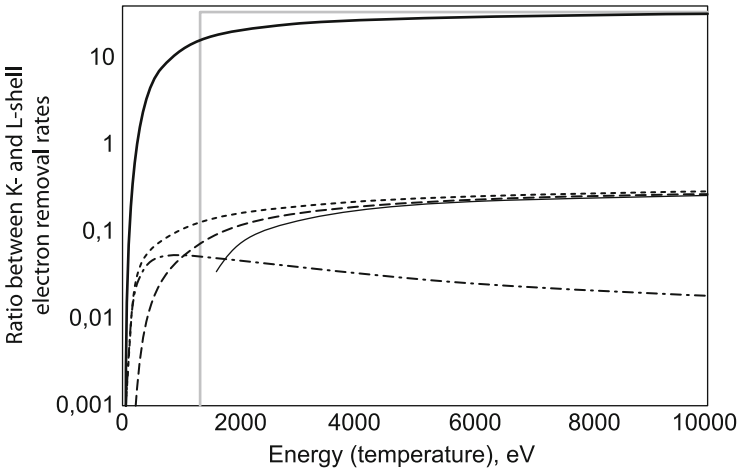

Fig. 5.49 Ratios between the probabilities of electron removal from the K and L shells of the ion with $Z = 10$ induced by photons (*grey and dark solid bold lines*) and electrons (the remaining curves) as functions of their energy or temperature [380]. The *grey bold line* stands for a monochromatic X-ray source, the *dark bold line* stands for blackbody radiation. The *thin solid curve* stands for a monochromatic electron beam, the *dashed curve* stands for ionization by Maxwellian electrons, the *dash-dot* stands for excitation by Maxwellian electrons, and the *dotted curve* is the net result of ionization and excitation by Maxwellian electrons

The case with $KL\,L^2\,LM$, and the like hollow ion production is somewhat better. In this case, the ratio between electron-impact ionization rates for neighboring shells is closer to unity and the amount of hollow ions may be quite significant. Therefore, even from simple estimates it follows that the presence of hot electrons in plasmas may result in the production of hollow ions, but usually the population of these states will not be high.

The case is quite different in the interaction of an ion with an X-ray photon. In this case, the electron removal cross section (the photoionization cross section) is approximately proportional to n^{-5}, i.e. the photon incident on the ion will remove electrons with overwhelmingly high probability from the innermost shell whose ionization energy does not exceed the photon energy. For example, Fig. 5.49 shows schematically the ratio between the probabilities of electron removal from the K and L-shells of the H-like ion with $Z = 10$ for the photoionization by monochromatic radiation (grey curve) and by blackbody radiation (dark bold curve). One can clearly see that it is precisely the K^2 hollow ion production which is the prevailing process in the photon energy (temperature) range exceeding the ionization potential (a quarter of the ionization potential) of the K-shell.

The intrinsic X-ray plasma radiation may be capable of producing hollow ions. This effect should be most pronounced when the plasma is strongly nonuniform and there are regions with substantially different temperatures [91, 92]. In this case, the

radiation generated in the hot region will produce hollow ions in the cold region, where the electron temperature is not high enough to ionize the outer ion shells.

It is believed that the energy transfer to the dense substance under irradiation is dominated by precisely the radiative mechanisms and that up to 30 % of the energy of the laser pulse is converted to X- and gamma-ray radiation when the intensity of laser radiation is higher than 10^{20} W/cm^2 [94, 279, 406].

At present the process of hollow ion production by X-ray radiation is becoming highly topical in connection with the advent of high-power X-ray lasers, both plasma-based and free-electron lasers [113, 274, 309, 379, 393]. In this case, the very energy input will be directly related to hollow ion production, unlike the case when laser radiation of the optical range interacts with matter. Recall that the major part of the energy of a substance-irradiating optical laser pulse initially goes to heat the emerging free electrons. And only later, in electron-ion collisions, does the energy go into internal ion energy (collisional ionization and production of multiply charged ions) and subsequently into the ion kinetic energy. By contrast, in the absorption of an X-ray photon the major part of energy may immediately go into the internal energy of emerging autoionization and hollow-ion states, and only then will a part of it be transferred to the free plasma electrons in the course of autoionization. In this case, the plasma production will depend heavily on the ratios between the X-ray laser photon energy and the ionization potentials of the various atomic shells of the target material. In this connection, mention should be made of a very interesting recent experiment [274] in the absorption of high-power X-ray radiation by aluminum foil.

The interaction of sufficiently intense monochromatic X-ray radiation with targets may give rise to target self-bleaching, whereby the target ceases to absorb the radiation and becomes almost transparent in the course of heating. In the simplest (and the least interesting) case this may be due simply to the complete ionization of target atoms to the state of bare nuclei, which is of course possible, but requires high fluences. However, owing to the production of hollow ions this effect may occur for substantially lower energy inputs. As noted above, the inner K-shell photoionization cross section far exceeds the photoionization cross section of the L shell (and all the more those of M-, N- ... shells). This signifies that, as soon as the K^2 hollow ions come to prevail in the plasma, the absorption of photons with energies above the K edge will decrease sharply, i.e. the target self-bleaching will occur. In this case, the degree of substance ionization will not be too high, low-charged ions may prevail in the target substance, and substantially lower energy inputs will therefore be required to produce such a state. Naturally, a similar effect may also be obtained for L^8 hollow ions, but it will be weaker pronounced, since the difference between the L- and M-shell photoionization cross sections is not so significant.

The effect of induced transparency is of major practical significance. The execution of X-ray structural investigations of microobjects, including medical and biological ones, calls for exposing these objects to rather high X-ray irradiation doses in order to obtain high-quality diffraction images. However, raising the irradiation dose increases, as a rule, the absorbed dose. The latter is undesirable, for it may cause damage to the object under study. We note that the typical damage

threshold amounts to 200 X-ray photons per square Angstrom. The self-bleaching effect permits raising the incident fluence with hardly any increase in absorbed fluence [393].

Highly interesting situations may be realized provided there is a possibility to continuously tune the frequency of monochromatic X-ray radiation, i.e. with the use of free-electron lasers [113, 274, 309, 379, 393]. Since the energy required for the excitation of the K^1 autoionization state is lower than the energy for the K^2 hollow ion excitation, it is possible to so select the X-ray photon energy that it suffices to generate the autoionization state and is insufficient for producing the hollow ion. It is then possible to obtain a plasma void of hollow ions, and the self-bleaching will take place at the stage of autoionization level excitation. An experiment of this kind was recently carried out in [274].

Similarly, by continuously tuning the free-electron laser frequency it is possible to select the photon energy so as to optimize the photopumping of K^2 hollow ions and thereby produce a solid-state substance consisting virtually of only such hollow ions. This experiment on the generation of hollow ions and the use of their radiation for the diagnostics of the resultant solid-state plasma was recently made in [379]. Furthermore, optimization of the parameters of the free-electron pump laser in [309] made it possible to make for the first time an X-ray laser with a photon energy of 849 eV on the transitions of Ne^{+1} hollow ions, which possessed a high monochromaticity, stability, and a unique brightness.

As already mentioned, in the production of hollow ions by X-ray radiation their abundance may be quite high. This follows not only from the simple estimates of photoionization cross sections given above, but also from detailed kinetic calculations. A kinetic model was constructed in [312, 313] to describe the plasma produced by the radiation of an ordinary laser of the optical range, which is additionally irradiated by an X-ray free-electron laser. The results of these works as well as of [94] clearly demonstrate: in the absence of X-ray pumping the K^2 hollow ions are hardly produced, while in the presence of the pumping the hollow state populations are practically the same as or even higher than the populations of the resonance levels.

Plasma exposure to an X-ray photon beam makes it possible not only to observe the spectra of hollow ions, but also to use them in diagnostic purposes. This is most topical when the state produced by optical laser radiation corresponds to a warm dense matter or a nonideal plasma [138, 140, 143]. As shown by the simulation data of [94, 312, 313], the spectra of hollow ions depend heavily on the temperature of the substance and therefore permit measuring it.

The production of hollow ions must play a highly important part in the course of ionization of a medium by the radiation of high-power X-ray lasers, the mechanism of ionization being strongly dependent on the X-ray photon energy. By way of example consider the ionization of a neon target exposed to X-ray photons of different wavelength, as was done in [393].

When the X-ray photon energy is below the neutral neon K-shell ionization threshold (which is equal to 870 eV), the incident X-ray radiation will photoionize the outer (valence) L-shell, with the result that we obtain a plasma containing the

He-like ions Ne IX. In this case, the only process leading to ionization of the medium is the photoionization of the valence shell.

If the photon energy is raised to exceed 993 eV, other ionization schemes will take place. Initially the photoionization of a K electron will occur with the formation of an autoionization state, and then two versions of the progress of events will be possible: either autoionization will occur with the filling of the K-shell vacancy and an L-electron detachment, or another K-electron photoionization with the formation of a hollow ion and the subsequent autoionization. This chain of events may terminate on the attainment of some ion multiplicity, depending on the photon energy, and subsequently only the photoionization of valence electrons will take place. The plasma of Ne IX ions will eventually result again.

When the photon energy exceeds 1360 eV, the chains of ionization events will proceed to the end to produce the plasma of bare nuclei Ne XI. It is significant that the photoionization–autoionization–photoionization... chains, which take place with participation of the inner ion shell, are a significantly faster process than simply the photoionization of the valence shell [393]. This signifies that the same degree of ionization of the substance in this case will be reached in a substantially shorter time.

Quite recently the ionization of a neon target exposed to the pulse of the LCLS (Linac Coherent Light Source, USA) X-ray laser was investigated experimentally [393]. The X-ray photon energy was equal to 800, 1050, or 2000 keV in different experiments for a maximum photon fluence of 10^5 photons/A^2. For an energy of 800 eV the highest ion charge was equal to $+6$, for 1050 eV it increased to $+8$ and for the highest energy to $+10$ (see Fig. 5.50). It is noteworthy that the self-beaching effect was also discovered in this work for an energy of 2000 eV.

Therefore, at present there are numerous observations of the spectra of exotic atomic objects like hollow ions (for more details, see review [380]). We see that such spectra are excited in the interaction of ultrashort laser pulses with condensed targets (solid targets, clusters) [93, 128, 129, 131, 373] and even dense gases (see, for instance, [314]). And although the spectra of hollow ions are exotic in this sense, they are a rather widespread physical object. The fact that their excitation is especially efficient in high-density plasmas, broadly speaking, permits developing X-ray spectral techniques for superdense plasma diagnostics. This is well illustrated by the recent Russian–British experiments carried out on the VULCAN petawatt femtosecond laser facility in the Rutherford Laboratory [94]. Figure 5.51 shows the spectra of an aluminum target heated by high-contrast ($>10^{10}$) laser radiation for an intensity higher than 10^{20} W/cm^2 at the target. One can see from the drawing that the time-integrated intensity of hollow-ion emission lines under certain conditions may exceed the intensity of resonance lines and of ordinary satellite lines.

It is highly significant that such spectra are bound to be excited in warm dense matter [138–140, 143, 288, 315] and in nonideal plasmas [143]. For instance, in [155] they were recorded in a plasma, which was nonideal in ion-ion interaction and weakly nonideal in electron-ion interaction. In this case it is highly significant that the nonideality effects will hardly tell on the spectra themselves even though the hollow-ion spectra may be emitted by a nonideal plasma, because they arise

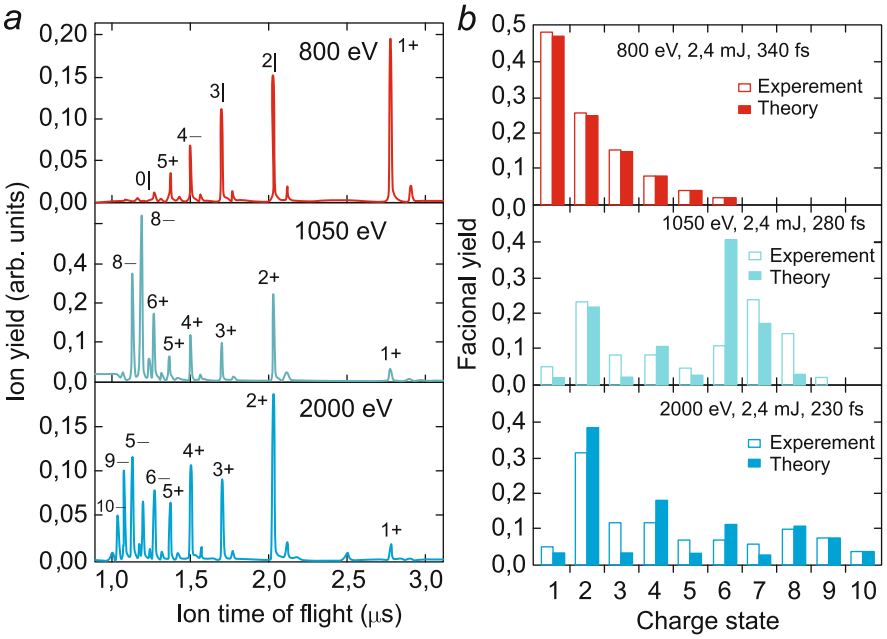

Fig. 5.50 Abundances of differently charged ions produced in a neon target under irradiation by an LCLS X-ray laser pulse: (**a**) time-of-flight measurement data; (**b**) comparison with simulations [393]

from transitions between deeply lying inner ion shells. This signifies that their based X-ray spectral techniques may be used to advantage for nonideal plasma diagnostics. By contrast, the use of methods reliant on the spectral transitions between outer ion shells invites reconsidering the existing collisional-radiative kinetic plasma models and, perhaps, even constructing a new theory of the spectra of a strongly nonideal plasma, which will undoubtedly take a considerable period of time.

The spectra of hollow ions will acquire even greater significance with the advancement of research in the area of development and use of plasma X-ray lasers and free-electron X-ray lasers (see, for instance, [55, 113, 130, 154, 274, 348, 364, 393]). And it is not so much the possibility of employing hollow ion states for producing lasing in the X-ray range (see, for instance, [269, 309]) as the fundamental features of the interaction of high power X-ray laser radiation with substance. For, irrespective of whether the X-ray laser radiation source is a plasma laser or a free-electron laser, in experiments of this kind the ionization of the inner shells of atoms and ions, which are responsible for the production of hollow ions, will be the main mechanisms of laser energy absorption. In this case, the resultant state of the medium will be characterized by solid-state density and moderate temperature, i.e. in many cases will be a nonideal plasma, only a few reliable techniques being suitable for determining its parameters, as mentioned in the foregoing.

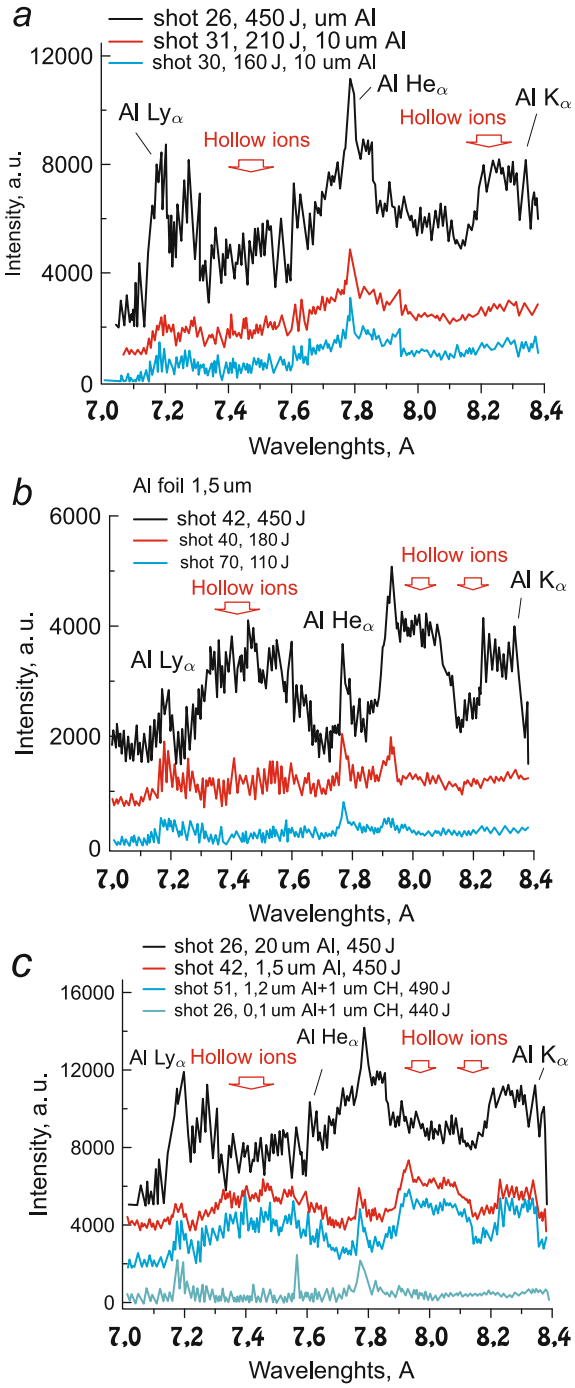

Fig. 5.51 X-ray spectra of Al targets in 7.0–8.4 Å spectral range (Ly_α–He_α–K_α lines) heated by the high-contrast ($>10^{10}$) radiation of the VULCAN petawatt laser facility for laser radiation intensities exceeding 10^{20} W/cm^2 [91] (*lower panel*). The *black* and *green curves* in the *lower panel* correspond to the spectra produced in the irradiation of a 1.5-μm Al foil by laser radiation with respective energies of 160 and 64 J. The blue spectrum (lowered fivefold) was obtained in the irradiation of a 20-μm Al foil by laser radiation with an energy of 160 J. The lower spectrum was obtained in [14] in the irradiation of an Al target by a 150-fs laser pulse with an energy of 80 mJ, a high contrast and an intensity of $5 \cdot 10^{17}$ W/cm^2. *Broken vertical lines* correspond to the Ly_α, He_α, and K_α lines of Al. The *upper panel* shows the results of numerical simulation of the spectra performed using the ATOMIC code with and without the inclusion of spectrum excitation by fast electron fluxes and high-intensity X-ray plasma radiation

In our view, to realize the potentialities of using hollow-ion spectra for diagnostic (as well as any other) purposes calls for the further development of the methods of calculating atomic structures with a large number of open electron shells. Only on attaining the spectroscopic calculation precision (a relative uncertainty of $\approx 10^{-4}$) will it be possible to confidently identify the spectra of hollow ions as regards their charge state as well as their origin to one or other configuration and, in special cases, to fine structure levels. The development of the methods of calculation in its turn calls even now for the experimental information about the spectra of such ions, which poses the problem of undertaking systematic experimental investigations in this area.

The situation is essentially similar to the one with satellite spectra, which formed in the second part of the past century [4, 58–60]. By the time the importance of such spectra for practical applications was recognized, the accuracy of calculating satellite structures was obviously insufficient. Within just one-two decades, however, different theoretical groups developed alternative approaches (relativistic perturbation theory, multiconfiguration Hartree–Fock methods with relativistic corrections, Dirac–Fock methods, semiempirical relativistic model-potential method), which permitted obtaining the necessary data with the accuracy required for experiments. This in turn fostered the development of X-ray spectral diagnostic techniques, which came into good use both for tenuous astrophysical plasmas and for dense laboratory plasmas. This step now is to be made as regards the spectra of hollow ions.

5.8 High Magnetic Fields

Production of ultrahigh magnetic field in laser-produced plasma is an interesting and vigorously developing line of research (see review [49], which we follow in the subsequent discussion).

Different mechanisms of magnetic field generation in the interaction of high-intensity laser radiation with solid targets give rise to magnetic fields with a magnetic induction of up to 1 GGs, which are produced in the interaction of high-intensity laser radiation with dense plasmas. These fields are localized near the critical surface, where there occurs the main absorption of laser energy. Several main mechanisms have been proposed responsible for the generation of quasistatic magnetic fields: (1) the difference in directions of the plasma temperature and density gradients; (2) the flux of fast electrons accelerated by ponderomotive forces along and across the laser pulse direction; (3) collisionless Weibel instability.

The generation of magnetic fields with an induction of about 1 GGs in relativistic dense plasmas was first predicted in [349]. According to the theory proposed in this work, the source of quasistationary magnetic field is the ponderomotive force acting on electrons. It generates radial electron current away from the axis of the laser beam towards its periphery until the beginning of a combined vibrational motion of ions and electrons caused by the requirement of electroneutrality.

The Weibel instability mechanism in the plasma arises from the anisotropy of electrons in their velocity directions. This anisotropy emerges in the course of ionization of atoms and atomic ions by superhigh laser field. The majority of electrons escapes along the direction of the electric intensity vector of a linearly polarized laser wave. The number of electrons escaping in the transverse directions is considerably smaller. Both the longitudinal and transverse velocities are defined by the energy–time uncertainty relations. Weibel [386] was the first to show that the presence of electron current anisotropy gives rise to instability in Maxwell equations relative to a spontaneous buildup of quasistatic magnetic field.

The thermoelectric mechanism [49], unlike the previous one, is realized in a collisional plasma in which there are gradients of the electron density and electron temperature directed at an angle to each other. The density gradient is directed along the radius of the electron beam. It is caused by the nonuniformity of laser radiation intensity across the focal spot. As a result, the number of electrons on the axis of the laser beam is far greater than at the beam periphery owing to a strong difference in the degree of ionization of the atoms of the medium. The temperature gradient is evidently directed along the normal to the target surface. The growth increment of spontaneous magnetic field is proportional both to the temperature gradient and the velocity gradient. In this case the magnetic field possesses toroidal symmetry: its circular lines of force embrace the laser beam.

In the passage of a laser pulse of relativistic intensity, the plasma electrons are accelerated along the direction of laser pulse propagation by the magnetic part of the Lorentz force. This gives rise to a magnetic field, which is also annular in character.

There also exist more sophisticated methods of magnetic field generation is a laser plasma, a part of which is considered in [49].

In [275] measurements were made of the magnetic field in a subcritical laser plasma. An azimuthal magnetic field with an induction of 2-to-8 MGs on a scale of 200 μm was shown to emerge for a duration of a linearly polarized laser pulse of 30 fs and an intensity of $4.2 \cdot 10^{18}$ W/cm^{-2}; for an intensity of $8 \cdot 10^{18}$ W/cm^{-2} the field amounted to 7 MGs. Both fields existed for several picoseconds. Their production is attributed to the fast electron fluxes produced in the laser plasma.

Measurements [357] permit determining the range of generated magnetic fields in the dense plasma at the critical surface, which is found to correspond to 340–460 MGs (Fig. 5.52). The magnetic pressure of such fields exceeds 10^9 atm.

Outlined in [383] were the results of experiments on the irradiation of solid targets by a laser pulse with an intensity of the order of 10^{20} W/cm^{-2}. By way of polarization measurements of radiation harmonic yields it was found that there emerged magnetic fields with an induction of about 700 MGs in the laser plasma. These magnetic fields also exist in the domains which far exceed the skin layer. This is attributable to the ultrarelativistic motion of electrons in so high a laser field as well as to the deep penetration of the high-order harmonics of laser radiation into the target substance.

In [123] the magnetic field induction in laser experiments was estimated at about 1 GGs.

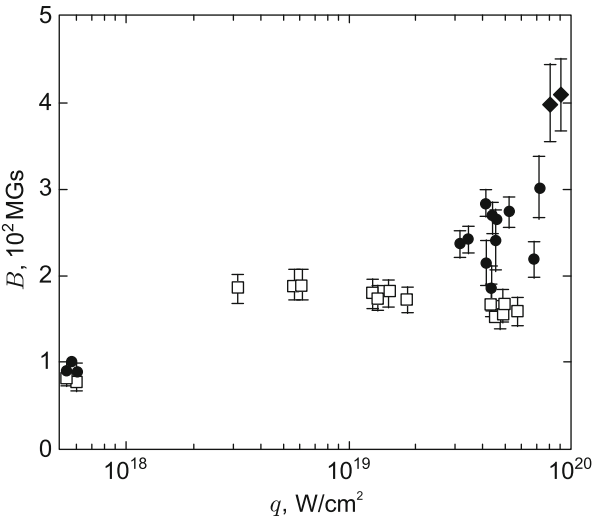

Fig. 5.52 Measured magnetic field induction as a function of laser radiation intensity [357] at 5ω (*filled diamond*), 4ω (*filled circle*), and 3ω (*open square*) harmonics

References

1. Abdallah, J., Faenov, A.Y., Skobelev, I.Y., et al.: Hot-electron influence on the x-ray emission spectra of Ar clusters heated by a high-intensity 60-fs laser pulse. Phys. Rev. A **63**, 032706 (2001)
2. Abdallah, J., Csanak, G., Fukuda, Y., et al.: Time-dependent Boltzmann kinetic model of X-rays produced by ultrashort-pulse laser irradiation of argon clusters. Phys. Rev. A **68**, 063201 (2003)
3. Afanas'ev, Y.V., Basov, N.G., et al.: Vzaimodeistvie moshchnogo lazernogo izlucheniya s plazmoi (Interaction of High-Power Laser Radiation with Plasma). In: Itogi nauki i tekhniki, vol. 17. VINITI, Moscow (1978)
4. Aglitskii, E.V., Safronova, U.I.: Spektroskopiya avtoionizatsionnykh sostoyanii atomnykh sistem (Spectroscopy of Autoionization States of Atomic Systems). Energoatomizdat, Moscow (1985)
5. Aglitskiy, Y., Lehecka, T., Deniz, A., et al.: X-ray emission from plasmas created by smoothed KrF laser irradiation. Phys. Plasmas **3**(9), 3438–3447 (1996)
6. Agranat, M.B., Andreev, N.E., Ashitkov, S.I., et al.: Determination of the transport and optical properties of a nonideal solid-density plasma produced by femtosecond laser pulses. JETP Lett. **85**(6), 271–276 (2007)
7. Agranat, M.B., Anisimov, S.I., Ashitkov, S.I., et al.: Dynamics of plume and crater formation after action of femtosecond laser pulse. Appl. Surf. Sci. **253**(15), 6276–6282 (2007)
8. Agranat, M.B., Anisimov, S.I., Ashitkov, S.I., et al.: Nanospallation induced by a femtosecond laser pulse. Proc. SPIE **6720**(39), 672002.1–672002.12 (2008)
9. Agranat, M.B., Anisimov, S.I., Ashitkov, S.I., et al.: Strength properties of an aluminum melt at extremely high tension rates under the action of femtosecond laser pulses. JETP Lett. **91**(9), 471–477 (2010)
10. Albert, F., Phuoc, K.T., Shah, R., et al.: Full characterization of a laser-produced keV X-ray betatron source. Plasma Phys. Controlled Fusion **50**(12), 124008 (2008)
11. Alexeev, I., Antonsen, T.M., Kim, K.Y., Milchberg, H.M.: Self-focusing of intense laser pulses in a clustered gas. Phys. Rev. Lett. **90**, 103402 (2003)

12. Al'tshuler L.V., Bakanova A.A., Dudoladov I.P. et al.: Shock adiabatic curves of metals. J. Appl. Mech. Tech. Phys. **22**(2), 145–169 (1981)
13. an der Brügge, D., Pukhov, A.: Enhanced relativistic harmonics by electron nanobunching. Phys. Plasmas **17**(3), 033110 (2010)
14. Andiel, U., Eidmann, K., Witte, K., et al.: Comparative study of time-resolved K-shell spectra from aluminum plasmas generated by ultrashort laser pulses at 395 and 790 nm. Appl. Phys. Lett. **80**(2), 198–200 (2002)
15. Anisimov, S.I.: Transition of hydrogen into the metallic state in a compression wave induced by a laser pulse. JETP Lett. **16**(10), 404 (1972)
16. Anisimov, S., Imas, Y.A., Romanov, G.S., Khodyko, Y.V.: Deistvie izlucheniya bol'shoi moshchnosti na metally (Action of High-Power Radiation on Metals). Nauka, Moscow (1970)
17. Anisimov, S.I., Kapeliovich, B.L., Perelman, T.P.: Electron emission from metal surfaces exposed to ultrashort laser pulses. J. Exp. Theor. Phys. **39**(2), 375 (1974)
18. Anisimov, S.I., Ivanov, M.F., Inogamov, N.A., et al.: Chislennoe modelirovanie lazernogo nagrevaniya i szhatiya prostykh obolochechnykh mishenei (Numerical simulation of laser-driven heating and compression of simple shell targets). Fiz. Plazmy **3**(4), 723–732 (1977)
19. Anisimov, S.I., Prokhorov, A.M., Fortov, V.E.: Application of high-power lasers to study matter at ultrahigh pressures. Sov. Phys. Usp. **27**(3), 181–205 (1984)
20. Anisimov, S., Inogamov, N., Oparin, A., et al.: Pulsed laser evaporation: equation-of-state effects. Appl. Phys. A **69**, 617–620 (1999)
21. Anisimov, S.I., Zhakhovskii, V.V., Inogamov, N.A., et al.: Destruction of a solid film under the action of ultrashort laser pulse. JETP Lett. **77**(11), 606–610 (2003)
22. Anisimov, S., Zhakhovskii, V., Inogamov, N., et al.: Ablated matter expansion and crater formation under the action of ultrashort laser pulse. J. Exp. Theor. Phys. **103**(2), 183–197 (2006)
23. Anisimov, S.I., Zhakhovskii, V.V., Inogamov, N.A., et al.: Formirovanie kratera i otkol'noi obolochki korotkim lazernym impul'som (Crater and split-off shell formation by a short laser pulse). Matem. Modelirovanie **18**(8), 111–122 (2006)
24. Anisimov, S., Inogamov, N., Petrov, Y., et al.: Numerical simulation of the expansion into vacuum of a crystal heated by an ultrashort laser pulse. In: Phipps, C. (ed.) Laser Ablation and Its Applications. Springer Series in Optical Sciences, vol. 129, pp. 1–16. Springer, Berlin (2007)
25. Anisimov, S., Zhakhovskii, V., Inogamov, N., et al.: Simulation of the expansion of a crystal heated by an ultrashort laser pulse. Appl. Surf. Sci. **253**(15), 6390–6393 (2007)
26. Anisimov, S.I., Inogamov, N.A., Petrov, Y.V., et al.: Interaction of short laser pulses with metals at moderate intensities. Appl. Phys. A **92**, 939–943 (2008)
27. Anisimov, S.I., Inogamov, N.A., Petrov, Y.V., et al.: Thresholds for front-side ablation and rear-side spallation of metal foil irradiated by femtosecond laser pulse. Appl. Phys. A **92**, 797–801 (2008)
28. Antoun, T., Seaman, L., Curran, D.R., et al.: Spall Fracture. Springer, New York (2003)
29. Arkani-Hamed, N., Dimopoulos, S., Dvali, G.: Phenomenology, astrophysics, and cosmology of theories with submillimeter dimensions and TeV scale quantum gravity. Phys. Rev. D **59**(8), 086004 (1999)
30. Arpin, P., Popmintchev, T., Wagner, N.L., et al.: Enhanced high harmonic generation from multiply ionized argon above 500 eV through laser pulse self-compression. Phys. Rev. Lett. **103**, 143901 (2009)
31. Asay, J.R., Fowles, G.R., Gupta, Y.: Determination of material relaxation properties from measurements on decaying elastic shock fronts. J. Appl. Phys. **43**(2), 744–746 (1972)
32. Ashitkov, S.I., Agranat, M.B., Kanel', G.I., et al.: Behavior of aluminum near an ultimate theoretical strength in experiments with femtosecond laser pulses. JETP Lett. **92**(8), 516–520 (2010)

33. Ashitkov, S.I., Agranat, M., Kanel, G.I., Fortov, V.E.: Approaching the ultimate shear and tensile strength of aluminum in experiments with femtosecond pulse laser. AIP Conf. Proc. **1426**(1), 1081–1084 (2012)
34. Ashitkov, S.I., Inogamov, N.A., Komarov, P.S., et al.: Strength of metals in liquid and solid states at extremely high tension produced by femtosecond laser heating. AIP Conf. Proc. **1464**(1), 120–125 (2012)
35. Ashitkov, S.I., Inogamov, N.A., Zhakhovskii, V.V., et al.: Formation of nanocavities in the surface layer of an aluminum target irradiated by a femtosecond laser pulse. JETP Lett. **95**(4), 176–181 (2012)
36. Atzeni, S., Meyer-ter-Vehn, J.: The Physics of Inertial Fusion. Oxford University Press, Oxford (2004)
37. Auerbach, J.M., Bailey, D., et al.: Lawrence Livermore Lab. Report UCRL-79636 (1977)
38. Avrorin, E.N., Vodolaga, B.K., Simonenko, V.A., Fortov, V.E.: Intense shock waves and extreme states of matter. Phys. Usp. **36**(5), 337–364 (1993)
39. Avrorin, E.N., Simonenko, V.A., Shibarshov, L.I.: Physics research during nuclear explosions. Phys. Usp. **49**(4), 432 (2006)
40. Baeva, T., Gordienko, S., Pukhov, A.: Theory of high-order harmonic generation in relativistic laser interaction with overdense plasma. Phys. Rev. E **74**, 046404 (2006)
41. Bahk, S.W., Rousseau, P., Planchon, T.A., et al.: Generation and characterization of the highest laser intensities (10^{22} W/cm^2). Opt. Lett. **29**(24), 2837–2839 (2004)
42. Bamber, C., Boege, S.J., Koffas, T., et al.: Studies of nonlinear QED in collisions of 46.6 GeV electrons with intense laser pulses. Phys. Rev. D **60**(9), 092004 (1999)
43. Barker, L.M., Hollenbach, R.E.: Shock wave study of the alpha$\rightleftarrows$epsilon phase transition in iron. J. Appl. Phys. **45**(11), 4872–4887 (1974)
44. Batani, D., Vovchenko, V.I., Kanel', G.I., et al.: Mekhanicheskie svoistva veshchestva pri bol'shikh skorostyakh deformirovaniya, vyzvannogo deistviem lazernoi udarnoi volny (Mechanical properties of a material at ultrahigh strain rates induced by a laser shock wave). Dokl. Phys. **48**(3), 123 (2003)
45. Bazhirov, T.T., Norman, G.E., Stegailov, V.V.: Cavitation in liquid metals under negative pressures. Molecular dynamics modeling and simulation. J. Phys. Condens. Matter **20**(11) (2008)
46. Bell, A.R., Kirk, J.G.: Possibility of prolific pair production with high-power lasers. Phys. Rev. Lett. **101**, 200403 (2008)
47. Belokon', V., Zabrodin, A.V., et al.: Preprint No. 39, IPM AN SSSR. Moscow (1978)
48. Belov, I.A., et al.: In: Int. conf. "X Kharitonov's thematic scientific readings", p. 145. RPhNZ-VNIIEPh, Sarov (2008)
49. Belyaev, V.S., Krainov, V.P., Lisitsa, V.S., Matafonov, A.P.: Generation of fast charged particles and superstrong magnetic fields in the interaction of ultrashort high-intensity laser pulses with solid targets. Phys. Usp. **51**(8), 793 (2008)
50. Benjamin, R.F., McCall, G.H., Ehler, A.W.: Measurement of return current in a laser-produced plasma. Phys. Rev. Lett. **42**, 890–893 (1979)
51. Benuzzi-Mounaix, A., Koenig, M., Ravasio, A., et al.: Laser-driven shock waves for the study of extreme matter states. Plasma Phys. Controlled Fusion **48**(12B), B347–B358 (2006)
52. Benuzzi-Mounaix, A., Loupias, B., Koenig, M., et al.: Density measurement of low-Z shocked material from monochromatic X-ray two-dimensional images. Phys. Rev. E **77**, 045402 (2008)
53. Berg, L., Skupin, S., Nuter, R., et al.: Ultrashort filaments of light in weakly ionized, optically transparent media. Rep. Prog. Phys. **70**(10), 1633 (2007)
54. Berkelbach, T.C., Colgan, J., Abdallah, J., et al.: Modeling energy dependence of the inner-shell X-ray emission produced by femtosecond-pulse laser irradiation of Xenon clusters. Phys. Rev. E **79**, 016407 (2009)
55. Berrill, M., Brizuela, F., Langdon, B., et al.: Warm photoionized plasmas created by soft-x-ray laser irradiation of solid targets. J. Opt. Soc. Am. B **25**(7), B32–B38 (2008)

56. Billon, D., Cognard, D., Launspach, J., et al.: Experimental study of plane and cylindrical laser driven, shock wave propagation. Opt. Commun. **15**(1), 108–111 (1975)
57. Bloomquist, D.D., Sheffield, S.A.: Optically recording interferometer for velocity measurements with subnanosecond resolution. J. Appl. Phys. **54**(4), 1717–1722 (1983)
58. Boiko, V.A., Vinogradov, A.V., Pikuz, S.A., et al.: Rentgenovskaya spektroskopiya lazernoi plazmy (X-Ray Spectroscopy of Laser-Produced Plasma). VINITI, Moscow (1980)
59. Boiko, V.A., Vinogradov, A.V., Pikuz, S.A., et al.: J. Sov. Laser Res. **6**, 85 (1985)
60. Boiko, V.A., Pikuz, S.A., Skobelev, I.Y., Faenov, A.Y.: Rentgenovskaya spektroskopiya mnogozaryadnykh ionov (X-Ray Spectroscopy of Multiply Charged Ions). Energoatomizdat, Moscow (1988)
61. Boldarev, A.S., Gasilov, V.A., Blasco, F., et al.: Modeling cluster jets as targets for high-power ultrashort laser pulses. J. Exp. Theor. Phys. Lett. **73**, 514–518 (2001)
62. Boldarev, A., Gasilov, V., Faenov, A.: On the generation of large clusters in forming gas-jet targets for lasers. Tech. Phys. **49**, 388–395 (2004)
63. Boldarev, A.S., Gasilov, V.A., Faenov, A.Y., et al.: Gas-cluster targets for femtosecond laser interaction: modeling and optimization. Rev. Sci. Instrum. **77**(8), 083112 (2006)
64. Borghesi, M., Audebert, P., Bulanov, S.V., et al.: High-intensity laser-plasma interaction studies employing laser-driven proton probes. Laser Part. Beams **23**(03), 291–295 (2005)
65. Boyd, T.J.M., Ondarza-Rovira, R.: Anomalies in universal intensity scaling in ultrarelativistic laser-plasma interactions. Phys. Rev. Lett. **101**, 125004 (2008)
66. Briand, J.P., de Billy, L., Charles, P., et al.: Production of hollow atoms by the excitation of highly charged ions in interaction with a metallic surface. Phys. Rev. Lett. **65**, 159–162 (1990)
67. Brunel, F.: Not-so-resonant, resonant absorption. Phys. Rev. Lett. **59**, 52–55 (1987)
68. Buck, A., Nicolai, M., Schmid, K., et al.: Real-time observation of laser-driven electron acceleration. Nat. Phys. **7**, 543–548 (2011)
69. Buersgens, F., Madison, K.W., Symes, D.R., et al.: Angular distribution of neutrons from deuterated cluster explosions driven by femtosecond laser pulses. Phys. Rev. E **74**, 016403 (2006)
70. Bula, C., McDonald, K.T., Prebys, E.J., et al.: Observation of nonlinear effects in Compton scattering. Phys. Rev. Lett. **76**(17), 3116–3119 (1996)
71. Bulanov, S.V.: New epoch in the charged particle acceleration by relativistically intense laser radiation. Plasma Phys. Controlled Fusion **48**(12B), B29–B37 (2006)
72. Bulanov, S.V., Inovenkov, I.N., Kirsanov, V.I., et al.: Nonlinear depletion of ultrashort and relativistically strong laser pulses in an underdense plasma. Phys. Fluids B **4**(7), 1935–1942 (1992)
73. Bulanov, S.V., Esirkepov, T., Tajima, T.: Light Intensification towards the Schwinger Limit. Phys. Rev. Lett. **91**, 085001 (2003)
74. Bulanov, S.S., Bychenkov, V.Y., Chvykov, V., et al.: Generation of GeV protons from 1 PW laser interaction with near critical density targets. Phys. Plasmas **17**(4), 043105 (2010)
75. Bulanov, S.S., Esirkepov, T.Z., Thomas, A.G.R., et al.: Schwinger limit attainability with extreme power lasers. Phys. Rev. Lett. **105**, 220407 (2010)
76. Bulanov, S.S., Mur, V.D., Narozhny, N.B., et al.: Multiple colliding electromagnetic pulses: a way to lower the threshold of e^+e^- pair production from vacuum. Phys. Rev. Lett. **104**, 220404 (2010)
77. Bulanov, S.V., Echkina, E.Y., Esirkepov, T.Z., et al.: Unlimited ion acceleration by radiation pressure. Phys. Rev. Lett. **104**, 135003 (2010)
78. Bunkenberg, J., Boles, J., Brown, D., et al.: The omega high-power phosphate-glass system: design and performance. IEEE J. Quantum Electron. **17**(9), 1620–1628 (1981)
79. Burke, D.L., Field, R.C., Horton-Smith, G., et al.: Positron production in multiphoton light-by-light scattering. Phys. Rev. Lett. **79**(9), 1626–1629 (1997)
80. Burnett, N.H., Josin, G., Ahlborn, B., Evans, R.: Generation of shock waves by hot electron explosions driven by a CO_2 laser. Appl. Phys. Lett. **38**(4), 226–228 (1981)
81. Bychenkov, V., Kovalev, V.: Relativistic coulomb explosion of spherical microplasma. JETP Lett. **94**, 97–100 (2011)

82. Checkhlov, O., Divall, E.J., Ertel, K., et al.: Development of petawatt laser amplification systems at the central laser facility. Proc. SPIE **6735**(1), 67350J (2007)
83. Chen, P., Tajima, T.: Testing Unruh radiation with ultraintense lasers. Phys. Rev. Lett. **83**(2), 256–259 (1999)
84. Chen, H., Wilks, S.C., Meyerhofer, D.D., et al.: Relativistic quasimonoenergetic positron jets from intense laser-solid interactions. Phys. Rev. Lett. **105**, 015003 (2010)
85. Chen, L.M., Liu, F., Wang, W.M., et al.: Intense high-contrast femtosecond K-shell x-ray source from laser-driven Ar clusters. Phys. Rev. Lett. **104**, 215004 (2010)
86. Cherednikov, Y., Inogamov, N.A., Urbassek, H.M.: Atomistic modeling of ultrashort-pulse ultraviolet laser ablation of a thin LiF film. J. Opt. Soc. Am. B **28**(8), 1817–1824 (2011)
87. Chimier, B., Tikhonchuk, V.T.: Liquid-vapor phase transition and droplet formation by subpicosecond laser heating. Phys. Rev. B **79**, 184107 (2009)
88. Chiu, C., Fomytskyi, M., Grigsby, F., et al.: Laser electron accelerators for radiation medicine: a feasibility study. Med. Phys. **31**(7), 2042–2052 (2004)
89. Chu, H.H., Tsai, H.E., Chou, M.C., et al.: Collisional excitation soft X-ray laser pumped by optical field ionization in a cluster jet. Phys. Rev. A **71**, 061804 (2005)
90. Clatterbuck, D.M., Krenn, C.R., Cohen, M.L., Morris, J.W.: Phonon instabilities and the ideal strength of aluminum. Phys. Rev. Lett. **91**, 135501 (2003)
91. Colgan, J., Abdallah, J. Jr., Faenov, A., et al.: MUTA calculations of a laser-produced Mg hollow atom spectrum. Phys. Scr. **78**(1), 015302 (2008)
92. Colgan, J. Jr., Abdallah, J., Fontes, C., et al.: Non-LTE and gradient effects in K-shell oxygen emission laser-produced plasma. High Energy Density Phys. **6**(3), 295–300 (2010)
93. Colgan, J. Jr., Abdallah, J., Faenov, A.Y., et al.: Observation and modeling of high resolution spectral features of the inner-shell X-ray emission produced by 10^{-10} contrast femtosecond-pulse laser irradiation of argon clusters. High Energy Density Phys. **7**(2), 77–83 (2011)
94. Colgan, J., Abdallah, J.J., Faenov, A.Y., et al.: Exotic dense matter states pumped by relativistic laser plasma in a radiation dominated regime. Phys. Rev. Lett. **110**, 125001 (2013)
95. Couairon, A., Mysyrowicz, A.: Femtosecond filamentation in transparent media. Phys. Rep. **441**(2–4), 47–189 (2007)
96. Cowan, T.E., Hunt, A.W., Phillips, T.W., et al.: Photonuclear fission from high energy electrons from ultraintense laser-solid interactions. Phys. Rev. Lett. **84**(5), 903–906 (2000)
97. Crowhurst, J.C., Armstrong, M.R., Knight, K.B., et al.: Invariance of the dissipative action at ultrahigh strain rates above the strong shock threshold. Phys. Rev. Lett. **107**, 144302 (2011)
98. Decoste, R., Kieffer, J.C., Pépin, H.: Spatial characteristics of continuum x-ray emission from lateral energy transport in CO_2-laser-produced plasmas. Phys. Rev. Lett. **47**, 35–38 (1981)
99. Demaske, B.J., Zhakhovsky, V.V., Inogamov, N.A., Oleynik, I.I.: Ablation and spallation of gold films irradiated by ultrashort laser pulses. Phys. Rev. B **82**, 064113 (2010)
100. Demaske, B.J., Zhakhovsky, V.V., Inogamov, N.A., Oleynik, I.I.: Molecular dynamics simulations of femtosecond laser ablation and spallation of gold. AIP Conf. Proc. **1278**(1), 121–130 (2010)
101. Demaske, B.J., Zhakhovsky, V.V., White, C.T., Oleynik, I.I.: Evolution of metastable elastic shockwaves in nickel. AIP Conf. Proc. **1426**(1), 1303–1306 (2012)
102. Diamant, R., Huotari, S., Hämäläinen, K., et al.: Evolution from threshold of a hollow atom's x-ray emission spectrum: the Cu $K^h\alpha_{1,2}$ hypersatellites. Phys. Rev. Lett. **84**, 3278–3281 (2000)
103. Diamant, R., Huotari, S., Hämäläinen, K., et al.: Diagram x-ray emission spectra of a hollow atom: the $K^h\alpha_{1,2}$ and $K^h\beta_{1,3}$ hypersatellites of Fe. Phys. Rev. Lett. **91**, 193001 (2003)
104. Didenko, A.N., Rashchikov, V.I., Fortov, V.E.: O vozmozhnosti generatsii moshchnogo izlucheniya teragertsovogo diapazona chastot pri vozdeistvii moshchnykh lazernykh impul'sov na mishen' (Mechanism of generation of high-intensity terahertz radiation under the action of high-power laser pulsed on a target). Tech. Phys. **56**(10), 1535 (2011)
105. Disdier, L., Garconnet, J.P., Malka, G., Miquel, J.L.: Fast neutron emission from a high-energy ion beam produced by a high-intensity subpicosecond laser pulse. Phys. Rev. Lett. **82**(7), 1454–1457 (1999)

106. Ditmire, T., Tisch, J., Springate, E., et al.: High-energy ions produced in explosions of superheated atomic clusters. Nature **386**(6620), 54–56 (1997)
107. Ditmire, T., Zweiback, J., Yanovsky, V.P., et al.: Nuclear fusion from explosions of femtosecond laser-heated deuterium clusters. Nature **398**(6727), 489–492 (1999)
108. Ditmire, T., Bless, S., Dyer, G., et al.: Overview of future directions in high energy-density and high-field science using ultra-intense lasers. Radiat. Phys. Chem. **70**(4–5), 535–552 (2004)
109. Dong, P., Reed, S.A., Yi, S.A., et al.: Formation of optical bullets in laser-driven plasma bubble accelerators. Phys. Rev. Lett. **104**, 134801 (2010)
110. Donnelly, T.D., Ditmire, T., Neuman, K., et al.: High-order harmonic generation in atom clusters. Phys. Rev. Lett. **76**, 2472–2475 (1996)
111. Dorchies, F., Blasco, F., Caillaud, T., et al.: Spatial distribution of cluster size and density in supersonic jets as targets for intense laser pulses. Phys. Rev. A **68**, 023201 (2003)
112. Dorchies, F., Blasco, F., Bonté, C., et al.: Observation of subpicosecond x-ray emission from laser-cluster interaction. Phys. Rev. Lett. **100**, 205002 (2008)
113. Doumy, G., Roedig, C., Son, S.K., et al.: Nonlinear atomic response to intense ultrashort x rays. Phys. Rev. Lett. **106**, 083002 (2011)
114. Dromey, B., Zepf, M., Gopal, A., et al.: High harmonic generation in the relativistic limit. Nat. Phys. **2**(7), 456–459 (2006)
115. Dromey, B., Kar, S., Bellei, C., et al.: Bright multi-keV harmonic generation from relativistically oscillating plasma surfaces. Phys. Rev. Lett. **99**(8) (2007)
116. Dromey, B., Adams, D., Hoerlein, R., et al.: Diffraction-limited performance and focusing of high harmonics from relativistic plasmas. Nat. Phys. **5**(2), 146–152 (2009)
117. Duvall, G.E.: Propagation of plane shock waves in a stress-relaxing medium. In: Kolsky, H., Prager, W. (eds.) Stress Waves in Anelastic Solids. Springer, Berlin (1964)
118. Eggert, J.H., Hicks, D.G., Celliers, P.M., et al.: Melting temperature of diamond at ultrahigh pressure. Nat. Phys. **6**(1), 40–43 (2010)
119. Eisenmann, S., Pukhov, A., Zigler, A.: Fine structure of a laser-plasma filament in air. Phys. Rev. Lett. **98**, 155002 (2007)
120. Eisenmann, S., Peñano, J., Sprangle, P., Zigler, A.: Effect of an energy reservoir on the atmospheric propagation of laser-plasma filaments. Phys. Rev. Lett. **100**, 155003 (2008)
121. ELI: The Extreme Light Infrastructure European Project: ELI homepage
122. Eliezer, S., Moshe, E., Eliezer, D.: Laser-induced tension to measure the ultimate strength of metals related to the equation of state. Laser Part. Beams **20**(01), 87–92 (2002)
123. Eliezer, S., Mendonca, J.T., Bingham, R., Norreys, P.: A new diagnostic for very high magnetic fields in expanding plasmas. Phys. Lett. A **336**(4–5), 390–395 (2005)
124. Erk, B., Hoffmann, K., Kandadai, N., et al.: Observation of shells in Coulomb explosions of rare-gas clusters. Phys. Rev. A **83**, 043201 (2011)
125. Esarey, E., Schroeder, C.B., Leemans, W.P.: Physics of laser-driven plasma-based electron accelerators. Rev. Mod. Phys. **81**, 1229–1285 (2009)
126. Esirkepov, T., Yamagiwa, M., Tajima, T.: Laser ion-acceleration scaling laws seen in multiparametric particle-in-cell simulations. Phys. Rev. Lett. **96**(10), 105001 (2006)
127. Faenov, A.Y., Skobelev, I.Y., Pikuz, S.A., et al.: High-resolution x-ray spectroscopy of a subpicosecond-laser-produced silicon plasma. Phys. Rev. A **51**, 3529–3533 (1995)
128. Faenov, A.Y., Joseph Abdallah, J., Clark, R.E.H., et al.: High-resolution X-ray spectroscopy of hollow atoms created in plasma heated by subpicosecond laser radiation, pp. 10–20. In: Proceedings of SPIE (1997)
129. Faenov, A.Y., Magunov, A.I., Pikuz, T.A., et al.: High-resolved x-ray spectra of hollow atoms in a femtosecond laser-produced solid plasma. Phys. Scr. **1999**(T80B), 536 (1999)
130. Faenov, A.Y., Inogamov, N.A., Zhakhovskii, V.V., et al.: Low-threshold ablation of dielectrics irradiated by picosecond soft X-ray laser pulses. Appl. Phys. Lett. **94**(23), 231107 (2009)
131. Faenov, A.Y., Pikuz, T.A., Skobelev, I.Y., et al.: Hollow ion spectra in warm dense laser-produced plasma: observation and modeling. J. Plasma Fusion Res. Ser. **8**, 1210–1213 (2009)

132. Faenov, A.Y., Fukuda, Y., Pikuz, T.A., et al.: Investigation of interaction of short laser pulses with large clusters and applications to imaging processes. J. Korean Phys. Soc. **56**(1), 279–286 (2010)
133. Faenov, A., Skobelev, I., Pikuz, T., et al.: Diagnostics of the early stage of the heating of clusters by a femtosecond laser pulse from the spectra of hollow ions. JETP Lett. **94**, 171–176 (2011)
134. Fedotov, A.M., Narozhny, N.B., Mourou, G., Korn, G.: Limitations on the attainable intensity of high power lasers. Phys. Rev. Lett. **105**, 080402 (2010)
135. Fennel, T., Meiwes-Broer, K.H., Tiggesbäumker, J., et al.: Laser-driven nonlinear cluster dynamics. Rev. Mod. Phys. **82**, 1793–1842 (2010)
136. Fortov, V.E.: Dynamic methods in plasma physics. Phys. Usp. **25**(11), 781–809 (1982)
137. Fortov, V.E.: Intense Shock Waves and Extreme States of Matter. Bukos, Moscow (2005)
138. Fortov, V.E.: Ekstremal'nye sostoyaniya veshchestva (Extreme States of Matter). Fizmatlit, Moscow (2009). [Translated into English: Extreme States of Matter. Series: The Frontiers Collection. Springer, Berlin, Heidelberg (2011)]
139. Fortov, V.E.: Extreme states of matter on earth and in space. Phys. Usp. **52**(6), 615–647 (2009)
140. Fortov, V.E.: Extreme States of Matter. Springer, Berlin (2010)
141. Fortov, V.E., Morfill, G.E.: Complex and Dusty Plasmas: From Laboratory to Space. CRC Press, Boca Raton (2010)
142. Fortov, V.E., Batani, D., Kilpio, A.V., et al.: The spall strength limit of matter at ultrahigh strain rates induced by laser shock waves. Laser Part. Beams **20**(02), 317–320 (2002)
143. Fortov, V., Iakubov, I., Khrapak, A.: Physics of Strongly Coupled Plasma. Oxford University Press, Oxford (2006)
144. Fortov, V.E., Hoffmann, D.H.H., Sharkov, B.Y.: Intense ion beams for generating extreme states of matter. Phys. Usp. **51**(2), 109 (2008)
145. Fuchs, M., Weingartner, R., Popp, A., Major, Z., Becker, S., Osterhoff, J., Cortrie, I., Zeitler, B., Horlein, R., Tsakiris, G.D., Schramm, U., Rowlands-Rees, T.P., Hooker, S.M., Habs, D., Krausz, F., Karsch, S., Grüner, F.: Laser-driven soft-X-ray undulator source. Nat. Phys. **5**(09), 826–829 (2009)
146. Fujimoto, M., Matsukado, K., Takahashi, H., et al.: Diagnosis of laser-induced relativistic plasma by positron imaging technique. Appl. Phys. Lett. **93**(25), 251101 (2008)
147. Fujimoto, M., Matsukado, K., Takahashi, H., et al.: Repetitive production of positron emitters using deuterons accelerated by multiterawatt laser pulses. Rev. Sci. Instrum. **80**(11), 113301 (2009)
148. Fujiwara, M., Kawase, K., Titov, A.T.: Parity non-conservation measurements with photons at SPring-8. AIP Conf. Proc. **802**(1), 246–249 (2005)
149. Fukuda, Y., Faenov, A.Y., Pikuz, T., et al.: Soft X-ray source for nanostructure imaging using femtosecond-laser-irradiated clusters. Appl. Phys. Lett. **92**(12), 121110 (2008)
150. Fukuda, Y., Faenov, A.Y., Tampo, M., et al.: Energy increase in multi-MeV ion acceleration in the interaction of a short pulse laser with a cluster-gas target. Phys. Rev. Lett. **103**, 165002 (2009)
151. Galy, J., Maucec, M., Hamilton, D.J., et al.: Bremsstrahlung production with high-intensity laser matter interactions and applications. New J. Phys. **9**(2), 23 (2007)
152. Gao, X., Wang, X., Shim, B., et al.: Characterization of cluster/monomer ratio in pulsed supersonic gas jets. Appl. Phys. Lett. **100**(6), 064101 (2012)
153. Garnov, S.V., Shcherbakov, I.A.: Laser methods for generating megavolt terahertz pulses. Phys. Usp. **54**(1), 91–96 (2011)
154. Gasparyan, P.D., Starikov, F.A., Starostin, A.N.: Angular divergence and spatial coherence of X-ray laser radiation. Phys. Usp. **41**(8), 761–792 (1998)
155. Gauthier, J.C., Geindre, J.P., Audebert, P., et al.: Observation of $KL \rightarrow LL$ x-ray satellites of aluminum in femtosecond laser-produced plasmas. Phys. Rev. E **52**, 2963–2968 (1995)
156. Giddings, S.B., Thomas, S.: High energy colliders as black hole factories: the end of short distance physics. Phys. Rev. D **65**(5), 056010 (2002)

157. Ginzburg, V.L.: Applications of Electrodynamics in Theoretical Physics and Astrophysics. Gordon and Breach, New York (1989)
158. Ginzburg, V.L.: The Physics of a Lifetime: Reflections on the Problems and Personalities of 20th Century Physics. Springer, Berlin, Heidelberg (2001)
159. Giulietti, A., Bourgeois, N., Ceccotti, T., et al.: Intense γ-ray source in the giant-dipole-resonance range driven by 10-TW laser pulses. Phys. Rev. Lett. **101**, 105002 (2008)
160. Giovanielli, D.V.: Wavelength effects in laser fusion. Bull. Am. Phys. Soc. **21**, 1047 (1976)
161. Goldstone, P.D., Benjamin, R.F., Schultz, R.B.: Shock-wave production and plasma motion in CO_2-laser-irradiated targets. Appl. Phys. Lett. **38**(4), 223–225 (1981)
162. Gonoskov, A.A., Korzhimanov, A.V., Kim, A.V., et al.: Ultrarelativistic nanoplasmonics as a route towards extreme-intensity attosecond pulses. Phys. Rev. E **84**, 046403 (2011)
163. Gordienko, S., Pukhov, A., Shorokhov, O., Baeva, T.: Coherent focusing of high harmonics: a new way towards the extreme intensities. Phys. Rev. Lett. **94**, 103903 (2005)
164. Graboske, H., Wong, L.: Lawrence Livermore Lab. Report UCRL-52323 (1977)
165. Grillon, G., Balcou, P., Chambaret, J.P., et al.: Deuterium-deuterium fusion dynamics in low-density molecular-cluster jets irradiated by intense ultrafast laser pulses. Phys. Rev. Lett. **89**, 065005 (2002)
166. Grun, J., Decoste, R., Ripin, B.H.: Naval Res. Lab. Memorandum Report 4410 (1981)
167. Hafz, N.A.M., Jeong, T.M., Choi, I.W., et al.: Stable generation of GeV-class electron beams from self-guided laser-plasma channels. Nat. Photonics **2**, 571–577 (2008)
168. Hagena, O.F.: Cluster ion sources (invited). Rev. Sci. Instrum. **63**(4), 2374–2379 (1992)
169. Harrach, R.J., Lee, Y.T., et al.: In: Nellis, W.J., Seaman, L., Graham, R.A. (eds.) Shock Waves in Condensed Matter-1981, p. 164. American Institute of Physics, New York (1982)
170. Hawking, S.W.: Particle creation by black holes. Commun. Math. Phys. **43**(3), 199–220 (1975)
171. Hayakawa, T., Ohgaki, H., Shizuma, T., et al.: Nondestructive detection of hidden chemical compounds with laser compton-scattering gamma rays. Rev. Sci. Instrum. **80**(4), 045110 (2009)
172. Hayashi, Y., Fukuda, Y., Faenov, A.Y., et al.: Intense and reproducible Kα emissions from micron-sized Kr cluster target irradiated with intense femtosecond laser pulses. Jpn. J. Appl. Phys. **49**(12), 126401 (2010)
173. Hayashi, Y., Pirozhkov, A.S., Kando, M., et al.: Efficient generation of Xe K-shell X-rays by high-contrast interaction with submicrometer clusters. Opt. Lett. **36**(9), 1614–1616 (2011)
174. Heinzl, T., Seipt, D., Kämpfer, B.: Beam-shape effects in nonlinear Compton and Thomson scattering. Phys. Rev. A **81**, 022125 (2010)
175. Henig, A., Steinke, S., Schnürer, M., et al.: Radiation-pressure acceleration of ion beams driven by circularly polarized laser pulses. Phys. Rev. Lett. **103**, 245003 (2009)
176. HERCULES, http://www.engin.umich.edu/research/cuos/researchgroups/hfs/experimentalfacilities/herculespetawattlaser.htm
177. Higginbotham, A.P., Semonin, O., Bruce, S., et al.: Generation of Mie size microdroplet aerosols with applications in laser-driven fusion experiments. Rev. Sci. Instrum. **80**(6), 063503 (2009)
178. Higginson, D.P., McNaney, J.M., Swift, D.C., et al.: Laser generated neutron source for neutron resonance spectroscopy. Phys. Plasmas **17**(10), 100701 (2010)
179. HiPER: High Power Laser Energy Research Project: HiPER homepage
180. Hoffmann, K., Murphy, B., Kandadai, N., et al.: Rare-gas-cluster explosions under irradiation by intense short XUV pulses. Phys. Rev. A **83**, 043203 (2011)
181. Hudson, L., Seely, J.: Laser-produced X-ray sources. Radiat. Phys. Chem. **79**(2), 132–138 (2010)
182. Huntington, C.M., Thomas, A.G.R., McGuffey, C., et al.: Current filamentation instability in laser wakefield accelerators. Phys. Rev. Lett. **106**, 105001 (2011)
183. Holmes, N.C., Trainor, R.J., Anderson, R.: In: Nellis, W.J., Seaman, L., Graham, R.A. (eds.) Shock Waves in Condensed Matter-1981, p. 160. American Institute of Physics, New York (1982)

184. Inogamov, N.A., Anisimov, S.I., Retfeld, B.: Rarefaction wave and gravitational equilibrium in a two-phase liquid-vapor medium. J. Exp. Theor. Phys. **88**(6), 1143 (1999)
185. Inogamov, N.A., Petrov, Y.V., Anisimov, S.I., et al.: Expansion of matter heated by an ultrashort laser pulse. JETP Lett. **69**(4), 310–316 (1999)
186. Inogamov, N.A., Anisimov, S.I., Petrov, Y.V., et al.: Theoretical and experimental study of hydrodynamics of metal target irradiated by ultrashort laser pulse. In: Proc. SPIE 7005, High-Power Laser Ablation VII, pp. 70052F–70052F–10 (2008)
187. Inogamov, N.A., Zhakhovskii, V.V., Ashitkov, S.I., et al.: Nanospallation induced by an ultrashort laser pulse. J. Exp. Theor. Phys. **107**(1), 1 (2008)
188. Inogamov, N.A., Faenov, A.Y., Khokhlov, V.A., et al.: Spallative ablation of metals and dielectrics. Contrib. Plasma Phys. **49**(7–8), 455–466 (2009)
189. Inogamov, N.A., Zhakhovskii, V.V., Ashitkov, S.I., et al.: Two-temperature relaxation and melting after absorption of femtosecond laser pulse. Appl. Surf. Sci. **255**(24), 9712–9716 (2009)
190. Inogamov, N., Ashitkov, S., Zhakhovsky, V., et al.: Acoustic probing of two-temperature relaxation initiated by action of ultrashort laser pulse. Appl. Phys. A **101**, 1–5 (2010)
191. Inogamov, N.A., Zhakhovsky, V.V., Ashitkov, S.I., et al.: Pump-probe method for measurement of thickness of molten layer produced by ultrashort laser pulse. AIP Conf. Proc. **1278**(1), 590–599 (2010)
192. Inogamov, N.A., Zhakhovsky, V.V., Faenov, A.Y., et al.: Spallative ablation of dielectrics by X-ray laser. Appl. Phys. A **101**, 87–96 (2010)
193. Inogamov, N.A., Anisimov, S.I., Zhakhovskii, V.V., et al.: Ablation of insulators under the action of short pulses of X-ray plasma lasers and free-electron lasers. J. Opt. Technol. **78**(8), 473 (2011)
194. Inogamov, N.A., Anisimov, S.I., Zhakhovsky, V.V., et al.: Ablation by short optical and X-ray laser pulses. Proc. SPIE Int. Soc. Opt. Eng. **7996** (2011)
195. Inogamov, N.A., Faenov, A.Y., Zhakhovskii, V.V., et al.: Interaction of short laser pulses in wavelength range from infrared to x-ray with metals, semiconductors, and dielectrics. Contrib. Plasma Phys. **51**(4), 361–366 (2011)
196. Inogamov, N.A., Faenov, A.Y., Zhakhovsky, V.V., et al.: Two-temperature warm dense matter produced by ultrashort extreme vacuum ultraviolet-free electron laser (EUV-FEL) pulse. Contrib. Plasma Phys. **51**(5), 419–426 (2011)
197. Inogamov, N.A., Zhakhovskii, V.V., Khokhlov, V.A., Shepelev, V.V.: Superelasticity and the propagation of shock waves in crystals. JETP Lett. **93**(4), 226–232 (2011)
198. Inogamov, N.A., Zhakhovsky, V.V., Ashitkov, S.I., et al.: Laser acoustic probing of two-temperature zone created by femtosecond pulse. Contrib. Plasma Phys. **51**(4), 367–374 (2011)
199. Inogamov, N., Khokhlov, V., Petrov, Y., et al.: Ultrashort elastic and plastic shockwaves in aluminum. AIP Conf. Proc. **1426**(1), 909–912 (2012)
200. Inogamov, N.A., Petrov, Y.V., Zhakhovsky, V.V., et al.: Two-temperature thermodynamic and kinetic properties of transition metals irradiated by femtosecond lasers. AIP Conf. Proc. **1464**(1), 593–608 (2012)
201. Insepov, Z., Hassanein, A., Bazhirov, T.T., et al.: Molecular dynamics simulations of bubble formation and cavitation in liquid metals. Fusion Sci. Technol. **52**(4), 885–889 (2007)
202. Ishino, M., Faenov, A.Y., Tanaka, M., et al.: Nanoscale surface modifications and formation of conical structures at aluminum surface induced by single shot exposure of soft X-ray laser pulse. J. Appl. Phys. **109**(1), 013504 (2011)
203. Issac, R.C., Vieux, G., Ersfeld, B., et al.: Ultra hard x rays from krypton clusters heated by intense laser fields. Phys. Plasmas **11**(7), 3491–3496 (2004)
204. Lang, J.M. Jr., Gupta, Y.M.: Strength and elastic deformation of natural and synthetic diamond crystals shock compressed along [100]. J. Appl. Phys. **107**(11), 113538 (2010)
205. Jahnátek, M., Hafner, J., Krajčí, M.: Shear deformation, ideal strength, and stacking fault formation of FCC metals: a density-functional study of Al and Cu. Phys. Rev. B **79**, 224103 (2009)

206. Jung, I.D., Kartner, F.X., Matuschek, N., et al.: Self-starting 6.5-fs pulses from a Ti:sapphire laser. Opt. Lett. **22**(13), 1009–1011 (1997)
207. Kando, M., Nakajima, K., Arinaga, M., et al.: Interaction of terawatt laser with plasma. J. Nucl. Mater. **248**(1), 405–407 (1997)
208. Kando, M., Pirozhkov, A.S., Kawase, K., et al.: Enhancement of photon number reflected by the relativistic flying mirror. Phys. Rev. Lett. **103**, 235003 (2009)
209. Kanel, G.I., Rasorenov, S.V., Fortov, V.E.: Shock-Wave Phenomena and the Properties of Condensed Matter. Springer, New York (2004)
210. Kanel, G.I., Razorenov, S.V., Fortov, V.E.: Shock-Wave Phenomena and the Properties of Condensed Matter. High Pressure Shock Compression of Condensed Matter. Springer (2004)
211. Kanel, G.I., Fortov, V.E., Razorenov, S.V.: Shock waves in condensed-state physics. Phys. Usp. **50**(8), 771–791 (2007)
212. Kanel, G.: Spall fracture: methodological aspects, mechanisms and governing factors. Int. J. Fract. **163**, 173–191 (2010)
213. Karagodsky, V., Schieber, D., Schächter, L.: Enhancing X-ray generation by electron-beam–laser interaction in an optical Bragg structure. Phys. Rev. Lett. **104**, 024801 (2010)
214. Khazanov, E.A., Sergeev, A.M.: Petawatt laser based on optical parametric amplifiers: their state and prospects. Phys. Usp. **51**(9), 969 (2008)
215. Kishimoto, Y., Masaki, T., Tajima, T.: High energy ions and nuclear fusion in laser–cluster interaction. Phys. Plasmas **9**(2), 589–601 (2002)
216. Kneip, S., McGuffey, C., Martins, J.L., et al.: Bright spatially coherent synchrotron X-rays from a table-top source. Nat. Phys. **6**(10), 980–983 (2010)
217. Kodama, R., Tanaka, K.A., Sentoku, Y., et al.: Observation of ultrahigh gradient electron acceleration by a self-modulated intense short laser pulse. Phys. Rev. Lett. **84**(4), 674–677 (2000)
218. Konyukhov, A.V., Likhachev, A.P., Oparin, A.M., et al.: Numerical modeling of shock-wave instability in thermodynamically nonideal media. J. Exp. Theor. Phys. **98**(4), 811–819 (2004)
219. Korzhimanov, A.V., Gonoskov, A.A., Khazanov, E.A., Sergeev, A.M.: Horizons of petawatt laser technology. Phys. Usp. **54**(1), 9–28 (2011)
220. Kotaki, H., Daito, I., Kando, M., et al.: Electron optical injection with head-on and countercrossing colliding laser pulses. Phys. Rev. Lett. **103**, 194803 (2009)
221. Krainov, V.P., Smirnov, M.B.: The evolution of large clusters under the action of ultrashort superintense laser pulses. Phys. Usp. **43**(9), 901–920 (2000)
222. Krainov, V.P., Smirnov, B.M., Smirnov, M.B.: Femtosecond excitation of cluster beams. Phys. Usp. **50**(9), 907–931 (2007)
223. Kritcher, A.L., Neumayer, P., Castor, J., et al.: Ultrafast X-ray Thomson scattering of shock-compressed matter. Science **322**(5898), 69–71 (2008)
224. Kruer, W.L.: The Physics of Laser Plasma Interactions. Addison-Wesley, Reading (1988)
225. Kugland, N.L., Constantin, C.G., Neumayer, P., et al.: High Kα X-ray conversion efficiency from extended source gas jet targets irradiated by ultra short laser pulses. Appl. Phys. Lett. **92**(24), 241504 (2008)
226. Kulagin, V.V., Cherepenin, V.A., Hur, M.S., Suk, H.: Theoretical investigation of controlled generation of a dense attosecond relativistic electron bunch from the interaction of an ultrashort laser pulse with a nanofilm. Phys. Rev. Lett. **99**, 124801 (2007)
227. Kuramitsu, Y., Sakawa, Y., Morita, T., et al.: Time evolution of collisionless shock in counterstreaming laser-produced plasmas. Phys. Rev. Lett. **106**, 175002 (2011)
228. Kuramitsu, Y., Sakawa, Y., Dono, S., et al.: Kelvin-Helmholtz turbulence associated with collisionless shocks in laser produced plasmas. Phys. Rev. Lett. **108**, 195004 (2012)
229. Landau, L.D., Lifshits, E.M.: Fluid Mechanics, 2nd edn. Pergamon Press, Oxford (1987)
230. Last, I., Ron, S., Jortner, J.: Aneutronic $H + {}^{11}B$ nuclear fusion driven by Coulomb explosion of hydrogen nanodroplets. Phys. Rev. A **83**, 043202 (2011)
231. Lawrence Livermore Lab. Laser Program Annual Report LCRL-ECC21-75, p. 64 (1976)
232. Lawrence Livermore Lab. Laser Program Annual Report UCRL-5C021-78, p. 21 (1979)

233. Ledingham, K.W.D., Spencer, I., McCanny, T., et al.: Photonuclear physics when a multiterawatt laser pulse interacts with solid targets. Phys. Rev. Lett. **84**(5), 899–902 (2000)
234. Ledingham, K.W.D., McKenna, P., Singhal, R.P.: Applications for nuclear phenomena generated by ultra-intense lasers. Science **300**(5622), 1107–1111 (2003)
235. Lee, K., Lee, J.Y., Park, S.H., et al.: Dominant front-side acceleration of energetic proton beams from plastic targets irradiated by an ultraintense laser pulse. Phys. Plasmas **18**(1), 013101 (2011)
236. Leemans, W.P., Nagler, B., Gonsalves, A.J., et al.: Gev electron beams from a centimetre-scale accelerator. Nat. Phys. **2**(10), 696–699 (2006)
237. Li, C.K., Séguin, F.H., Frenje, J.A., et al.: Observation of the decay dynamics and instabilities of megagauss field structures in laser-produced plasmas. Phys. Rev. Lett. **99**, 015001 (2007)
238. Li, H., Liu, J., Ni, G., et al.: Parameter optimization for fusion neutron yield from deuterium cluster explosion driven by intense femtosecond laser pulses. Phys. Rev. A **79**, 043204 (2009)
239. Li, Y., Lan, K., Lai, D., et al.: Radiation-temperature shock scaling of 1 ns laser-driven hohlraums. Phys. Plasmas **17**(4), 042704 (2010)
240. Liang, E.P., Wilks, S.C., Tabak, M.: Pair production by ultraintense lasers. Phys. Rev. Lett. **81**(22), 4887–4890 (1998)
241. Lindl, J.D.: Inertial Confinement Fusion. Springer, New York (1998)
242. Litz, M.S., Merkel, G., Pereira, N.R., et al.: Anomalous fluorescence line intensity in megavoltage bremsstrahlung. Phys. Plasmas **17**(4), 043302 (2010)
243. Liu, Y., Durand, M., Chen, S., et al.: Energy exchange between femtosecond laser filaments in air. Phys. Rev. Lett. **105**, 055003 (2010)
244. Loupias, B., Koenig, M., Falize, E., et al.: Supersonic-jet experiments using a high-energy laser. Phys. Rev. Lett. **99**, 265001 (2007)
245. Lu, H.Y., Liu, J.S., Wang, C., et al.: Efficient fusion neutron generation from heteronuclear clusters in intense femtosecond laser fields. Phys. Rev. A **80**, 051201 (2009)
246. Magill, J., Schwoerer, H., Ewald, F., et al.: Laser transmutation of iodine-129. Appl. Phys. B **77**(4), 387–390 (2003)
247. Maine, P., Mourou, G.: Amplification of 1-nsec pulses in Nd:glass followed by compression to 1 psec. Opt. Lett. **13**(3), 467–469 (1988)
248. Maine, P., Strickland, D., Bado, P., et al.: Generation of ultrahigh peak power pulses by chirped pulse amplification. IEEE J. Quantum Electron. **24**(2), 398–403 (1988)
249. Malka, V., Fritzler, S., Lefebvre, E., et al.: Electron acceleration by a wake field forced by an intense ultrashort laser pulse. Science **298**(5598), 1596–1600 (2002)
250. Malka, V., Faure, J., Gauduel, Y.A., et al.: Principles and applications of compact laser–plasma accelerators. Nat. Phys. **4**(06), 447–453 (2008)
251. Malone, R.C., McCrory, R.L., Morse, R.L.: Indications of strongly flux-limited electron thermal conduction in laser-target experiments. Phys. Rev. Lett. **34**, 721–724 (1975)
252. Mancic, A., Robiche, J., Antici, P., et al.: Isochoric heating of solids by laser-accelerated protons: experimental characterization and self-consistent hydrodynamic modeling. High Energy Density Phys. **6**(1), 21–28 (2010)
253. Manenkov, A.A.: Self-focusing of laser pulses: current state and future prospects. Phys. Usp. **54**(1), 100–104 (2011)
254. March, S.P. (ed.): Los Alamos Sci. Lab. Shock Wave Data. University of California Press, Berkeley (1980)
255. Martins, S.F., Fonseca, R.A., Lu, W., et al.: Exploring laser-wakefield-accelerator regimes for near-term lasers using particle-in-cell simulation in Lorentz-boosted frames. Nat. Phys. **6**(04), 311–316 (2010)
256. Mason, R.J.: Apparent and real thermal inhibition in laser-produced plasmas. Phys. Rev. Lett. **47**, 652–656 (1981)
257. McGuffey, C., Thomas, A.G.R., Schumaker, W., et al.: Ionization induced trapping in a laser wakefield accelerator. Phys. Rev. Lett. **104**, 025004 (2010)
258. McKenna, P., Ledingham, K.W., Shimizu, S., et al.: Broad energy spectrum of laser-accelerated protons for spallation-related physics. Phys. Rev. Lett. **94**(8), 084801 (2005)

259. McMahon, S.J., Kavanagh, A.P., Watanabe, H., et al.: Characterization and parametrization in terms of atomic number of X-ray emission from *K*-shell filling during ion-surface interactions. Phys. Rev. A **83**, 022901 (2011)
260. Mcpherson, A., Thompson, B.D., Borisov, A.B., et al.: Multiphoton-induced X-ray-emission at 4–5 keV from Xe atoms with multiple core vacancies. Nature **370**(6491), 631–634 (1994)
261. McWilliams, R.S., Eggert, J.H., Hicks, D.G., et al.: Strength effects in diamond under shock compression from 0.1 to 1 tpa. Phys. Rev. B **81**, 014111 (2010)
262. Mead, W.C., Haas, R.A., Kruer, W.L., et al.: Observation and simulation of effects on parylene disks irradiated at high intensities with a 1.06-μm laser. Phys. Rev. Lett. **37**, 489–492 (1976)
263. Meyer-ter Vehn, J.: From laser fusion to laser accelerators: basic studies into high power laser plasmas. Plasma Phys. Controlled Fusion **51**(12), 124001 (2009)
264. Milchberg, H.M., Kim, K.Y., Kumarappan, V., et al.: Clustered gases as a medium for efficient plasma waveguide generation. Philos. Trans. R. Soc. A Math. Phys. Eng. Sci. **364**(1840), 647–661 (2006)
265. Mima, K., Ohsuga, T., Takabe, H., et al.: Wakeless triple-soliton accelerator. Phys. Rev. Lett. **57**(12), 1421–1424 (1986)
266. Mishin, Y., Farkas, D., Mehl, M.J., Papaconstantopoulos, D.A.: Interatomic potentials for monoatomic metals from experimental data and *ab initio* calculations. Phys. Rev. B **59**, 3393–3407 (1999)
267. Mitchell, A.C., Nellis, W.J.: Shock compression of aluminum, copper, and tantalum. J. Appl. Phys. **52**(5), 3363–3374 (1981)
268. Moore, D.S., Gahagan, K.T., Reho, J.H., et al.: Ultrafast nonlinear optical method for generation of planar shocks. Appl. Phys Lett. **78**(1), 40–42 (2001)
269. Moribayashi, K., Sasaki, A., Tajima, T.: Ultrafast X-ray processes with hollow atoms. Phys. Rev. A **58**, 2007–2015 (1998)
270. Moshe, E., Dekel, E., Henis, Z., Eliezer, S.: Development of an optically recording velocity interferometer system for laser induced shock waves measurements. Appl. Phys. Lett. **69**(10), 1379–1381 (1996)
271. Mourou, G., Tajima, T.: More intense, shorter pulses. Science **331**(6013), 41–42 (2011)
272. Mourou, G.A., Barry, C.P.J., Perry, M.D.: Ultrahigh-intensity lasers: physics of the extreme on a tabletop. Phys. Today **51**(1), 22–28 (1998)
273. Mourou, G.A., Tajima, T., Bulanov, S.V.: Optics in the relativistic regime. Rev. Mod. Phys. **78**(2), 1804–1816 (2006)
274. Nagler, B., Zastrau, U., Faustlin, R.R., et al.: Turning solid aluminium transparent by intense soft X-ray photoionization. Nat. Phys. **5**(9), 693–696 (2009)
275. Najmudin, Z., Walton, B.R., Mangles, S.P.D., et al.: Measurements of magnetic fields generated in underdense plasmas by intense lasers. AIP Conf. Proc. **827**(1), 53–64 (2006)
276. Nakamura, T., Fukuda, Y., Yogo, A., et al.: Coulomb implosion mechanism of negative ion acceleration in laser plasmas. Phys. Lett. A **373**(30), 2584–2587 (2009)
277. Nakamura, T., Fukuda, Y., Yogo, A., et al.: High energy negative ion generation by Coulomb implosion mechanism. Phys. Plasmas **16**(11), 113106 (2009)
278. Nakamura, T., Bulanov, S.V., Esirkepov, T.Z., Kando, M.: High-energy ions from near-critical density plasmas via magnetic vortex acceleration. Phys. Rev. Lett. **105**, 135002 (2010)
279. Nakamura, T., Koga, J.K., Esirkepov, T.Z., et al.: High-power γ-ray flash generation in ultraintense laser-plasma interactions. Phys. Rev. Lett. **108**, 195001 (2012)
280. Nakatsutsumi, M., Marques, J.R., Antici, P., et al.: High-power laser delocalization in plasmas leading to long-range beam merging. Nat. Phys. **6**(10), 1010–1016 (2010)
281. Narozhny, N.B., Bulanov, S.S., Mur, V.D., Popov, V.S.: e^+e^- – pair production by a focused laser pulse in vacuum. Phys. Lett. A **330**(1–2), 1–6 (2004)
282. Naseri, N., Bychenkov, V.Y., Rozmus, W.: Axial magnetic field generation by intense circularly polarized laser pulses in underdense plasmas. Phys. Plasmas **17**(8), 083109 (2010)
283. National Research Council: Frontiers in High Energy Density Physics. National Academies Press, Washington, DC (2003)

284. Nellis, W.J.: Shock compression of hydrogen and other small molecules. In: Chiarotti, G.L., Hemley, R.J., Bernasconi, M., Ulivi, L. (eds.) High Pressure Phenomena, Proceedings of the International School of Physics "Enrico Fermi" Course CXLVII, p. 607. IOS Press, Amsterdam (2002)
285. Nilson, P.M., Mangles, S.P.D., Willingale, L., et al.: Generation of ultrahigh-velocity ionizing shocks with petawatt-class laser pulses. Phys. Rev. Lett. **103**, 255001 (2009)
286. Nomura, Y., Hörlein, R., Tzallas, P., et al.: Attosecond phase locking of harmonics emitted from laser-produced plasmas. Nat. Phys. **5**(02), 124–128 (2009)
287. Norman, G.E., Stegailov, V.V.: Homogeneous nucleation in a superheated crystal. Molecular-dynamic simulation. Dokl. Phys. **47**(9), 667 (2002)
288. Norman, G.E., Skobelev, I.Y., Stegailov, V.V.: Excited states of warm dense matter. Contrib. Plasma Phys. **51**(5), 411–418 (2011)
289. Norman, G.E., Starikov, S.V., Stegailov, V.V.: Atomistic simulation of laser ablation of gold: effect of pressure relaxation. J. Exp. Theor. Phys. **114**(5), 792 (2012)
290. Norreys, P.A.: Laser-driven particle acceleration. Nat. Photonics **3**(8), 423–425 (2009)
291. Ogura, K., Shizuma, T., Hayakawa, T., et al.: Proton-induced nuclear reactions using compact high-contrast high-intensity laser. Appl. Phys. Express **2**(6), 066001 (2009)
292. Okun', L.B.: Leptony i kvarki, 2nd edn. Nauka, Moscow (1990). [English Transl.: Leptons and Quarks. North-Holland, Amsterdam (1982)]
293. Pak, A., Marsh, K.A., Martins, S.F., et al.: Injection and trapping of tunnel-ionized electrons into laser-produced wakes. Phys. Rev. Lett. **104**, 025003 (2010)
294. Parker, L.: Quantized fields and particle creation in expanding universes. I. Phys. Rev. **183**(5), 1057–1068 (1969)
295. Petrov, Y.V., Zhakhovskii, V.V., Inogamov, N.A., et al.: Equation of state of matter irradiated by short laser pulse and geometry of spalled cupola. In: Proc. SPIE 7005, High-Power Laser Ablation VII, pp. 70051W–70051W–12 (2008)
296. PHELIX, http://www.gsi.de/forschung/pp/phelix/index_e.html
297. Pikuz, T.A., Faenov, A.Y., Gasilov, S.V., et al.: Propagation-based phase-contrast enhancement of nanostructure images using a debris-free femtosecond-laser-driven cluster-based plasma soft X-ray source and an LiF crystal detector. Appl. Opt. **48**(32), 6271–6276 (2009)
298. Pirozhkov, A.S., Kando, M., Esirkepov, T.Z., et al.: Soft-x-ray harmonic Comb from relativistic electron spikes. Phys. Rev. Lett. **108**, 135004 (2012)
299. Piskarskas, A., Stabinis, A., Yankauskas, A.: Phase phenomena in parametric amplifiers and generators of ultrashort light pulses. Phys. Usp. **29**(9), 869–879 (1986)
300. Povarnitsyn, M.E., Itina, T.E., Sentis, M., et al.: Material decomposition mechanisms in femtosecond laser interactions with metals. Phys. Rev. B **75**, 235414 (2007)
301. Povarnitsyn, M.E., Khishchenko, K.V., Levashov, P.R.: Phase transitions in femtosecond laser ablation. Appl. Surf. Sci. **255**(10), 5120–5124 (2009)
302. Price, R.H., Rosen, M.D., Banner, D.L.: In: Nellis, W.J. Seaman, L. Graham, R.A. (eds.) Shock Waves in Condensed Matter-1981, p. 155. American Institute of Physics, New York (1982)
303. Prokhorov, A.M., Anisimov, S.I., Pashinin, P.P.: Laser thermonuclear fusion. Phys. Usp. **19**(7), 547–560 (1976)
304. Pukhov, A.: Strong field interaction of laser radiation. Rep. Prog. Phys. **66**(1), 47–101 (2003)
305. Pukhov, A., Meyer-ter-Vehn, J.: Laser wake field acceleration: the highly non-linear broken-wave regime. Appl. Phys. B **74**(4–5), 355–361 (2002)
306. Quéré, F., Thaury, C., Monot, P., et al.: Coherent wake emission of high-order harmonics from overdense plasmas. Phys. Rev. Lett. **96**, 125004 (2006)
307. Raven, A., Willi, O., Rumsby, P.T.: Megagauss magnetic field profiles in laser-produced plasmas. Phys. Rev. Lett. **41**, 554–557 (1978)
308. Reiss, H.R.: Unsuitability of the Keldysh parameter for laser fields. Phys. Rev. A **82**, 023418 (2010)
309. Rohringer, N., Ryan, D., London, R.A., et al.: Atomic inner-shell X-ray laser at 1.46 nanometres pumped by an X-ray free-electron laser. Nature **481**, 488–491 (2012)

310. Rohwetter, P., Kasparian, J., Stelmaszczyk, K., et al.: Laser-induced water condensation in air. Nat. Photonics **4**(7), 451–456 (2010)
311. Romagnani, L., Bigongiari, A., Kar, S., et al.: Observation of magnetized soliton remnants in the wake of intense laser pulse propagation through plasmas. Phys. Rev. Lett. **105**, 175002 (2010)
312. Rosmej, F.: Exotic states of high density matter driven by intense XUV/X-ray free electron lasers. In: Varro, S. (ed.) Free Electron Laser, chap. 8, pp. 187–212. InTech (2012)
313. Rosmej, F.B., Lee, R.W.: Hollow ion emission driven by pulsed intense X-ray fields. Europhys. Lett. **77**(2), 24001 (2007)
314. Rosmej, F.B., Faenov, A.Y., Pikuz, T.A., et al.: Charge-exchange-induced formation of hollow atoms in high-intensity laser-produced plasmas. J. Phys. B Atomic Mol. Opt. Phys. **32**(5), L107 (1999)
315. Rosmej, F.B., Lee, R.W., Riley, D., et al.: Warm dense matter and strongly coupled plasmas created by intense heavy ion beams and XUV-free electron laser: an overview of spectroscopic methods. J. Phys. Conf. Ser. **72**(1), 012007 (2007)
316. Ross, J.S., Glenzer, S.H., Amendt, P., et al.: Characterizing counter-streaming interpenetrating plasmas relevant to astrophysical collisionless shocks. Phys. Plasmas **19**(5), 056501 (2012)
317. Roth, M., Alber, I., Bagnoud, V., et al.: Proton acceleration experiments and warm dense matter research using high power lasers. Plasma Phys. Controlled Fusion **51**(12), 124039 (2009)
318. Rubakov, V.A.: Multidimensional models of particle physics. Phys. Usp. **46**(2), 211 (2003)
319. Rubakov, V.A., Shaposhnikov, M.E.: Do we live inside a domain wall? Phys. Lett. B **125**(2–3), 136–138 (1983)
320. Rubenchik, A.M., Fedoruk, M.P., Turitsyn, S.K.: Laser beam self-focusing in the atmosphere. Phys. Rev. Lett. **102**, 233902 (2009)
321. Rusek, M., Lagadec, H., Blenski, T.: Cluster explosion in an intense laser pulse: Thomas-Fermi model. Phys. Rev. A **63**, 013203 (2000)
322. Ryutov, D.D., Remington, B.A., Robey, H.F., Drake, R.P.: Magnetodynamic scaling: from astrophysics to the laboratory. Phys. Plasmas **8**(5), 1804–1816 (2001)
323. Rzadkiewicz, J., Gojska, A., Rosmej, O., et al.: Interpretation of the Si $K\alpha$ x-ray spectra accompanying the stopping of swift Ca ions in low-density SiO_2 aerogel. Phys. Rev. A **82**, 012703 (2010)
324. Saalmann, U., Siedschlag, C., Rost, J.M.: Mechanisms of cluster ionization in strong laser pulses. J. Phys. B Atomic Mol. Opt. Phys. **39**(4) (2006)
325. Sagdeev, R.Z.: Cooperative phenomena and shock waves in collisionless plasmas (Collective processes in rarefied plasma, analyzing nonlinear undamped oscillations and shock waves). In: Leontovich, M.A. (ed.) Problems in Plasma Theory. Reviews of Plasma Physics, vol. 4, pp. 23–91. Consultants Bureau, New York (1966)
326. Sakabe, S., Shimizu, S., Hashida, M., et al.: Generation of high-energy protons from the coulomb explosion of hydrogen clusters by intense femtosecond laser pulses. Phys. Rev. A **69**, 023203 (2004)
327. Sangster, T.C., Goncharov, V.N., Betti, R., et al.: Shock-tuned cryogenic-deuterium-tritium implosion performance on Omega. Phys. Plasmas **17**(5), 056312 (2010)
328. Sano, T., Ozaki, N., Sakaiya, T., et al.: Laser-shock compression and Hugoniot measurements of liquid hydrogen to 55 GPa. Phys. Rev. B **83**, 054117 (2011)
329. Sarkisov, G.S., Bychenkov, V.Y., Novikov, V.N., et al.: Self-focusing, channel formation, and high-energy ion generation in interaction of an intense short laser pulse with a He jet. Phys. Rev. E **59**(6), 7042–7054 (1999)
330. Sarri, G., Cecchetti, C.A., Jung, R., et al.: Spatially resolved measurements of laser filamentation in long scale length underdense plasmas with and without beam smoothing. Phys. Rev. Lett. **106**, 095001 (2011)
331. Sarri, G., Kar, S., Romagnani, L., et al.: Observation of plasma density dependence of electromagnetic soliton excitation by an intense laser pulse. Phys. Plasmas **18**(8), 080704 (2011)

332. Sasaki, A., Kishimoto, Y., Takahashi, E., et al.: Percolation simulation of laser-guided electrical discharges. Phys. Rev. Lett. **105**, 075004 (2010)
333. Schenkel, T., Hamza, A., Barnes, A., Schneider, D.: Interaction of slow, very highly charged ions with surfaces. Prog. Surf. Sci. **61**(2–4), 23–84 (1999)
334. Schlenvoigt, H.P., Haupt, K., Debus, A., et al.: A compact synchrotron radiation source driven by a laser-plasma wakefield accelerator. Nat. Phys. **4**(2), 130–133 (2008)
335. Schutzhold, R., Schaller, G., Habs, D.: Signatures of the Unruh effect from electrons accelerated by ultrastrong laser fields. Phys. Rev. Lett. **97**(12), 121302 (2006)
336. Schwoerer, H., Ewald, F., Sauerbrey, R., et al.: Fission of actinides using a tabletop laser. Europhys. Lett. **91**(1), 47–52 (2003)
337. Schwoerer, H., Magill, J., Beleites, B. (eds.): Lasers and Nuclei: Applications of Ultrahigh Intensity Lasers in Nuclear Science. Lecture Notes in Physics, vol. 694. Springer, Berlin (2006)
338. Sedov, L.I.: Metody podobiya i razmernosti v mekhanike (Similarity and Dimensional Methods in Mechanics). Nauka, Moscow (1966). [Transl. of 4th Russ. ed. Academic Press, New York (1959)]
339. Seipt, D., Kämpfer, B.: Nonlinear Compton scattering of ultrashort intense laser pulses. Phys. Rev. A **83**, 022101 (2011)
340. Seres, J., Seres, E., Hochhaus, D., et al.: Laser-driven amplification of soft X-rays by parametric stimulated emission in neutral gases. Nat. Phys. **2**(06), 455–461 (2010)
341. Seres, J., Seres, E., Verhoef, A.J., et al.: Laser technology: source of coherent kiloelectronvolt X-rays. Nature **433**(02), 596 (2005)
342. Skripov, V.P.: Metastabil'naya zhidkost' (Metastable Fluid). Nauka, Moscow (1972)
343. Smirnov, B.M.: Negative Ions. McGraw-Hill, New York (1992)
344. Smirnov, M.B., Skobelev, I.Y., Magunov, A.I., et al.: Microdroplet evolution induced by a laser pulse. J. Exp. Theor. Phys. **98**(6), 1123 (2004)
345. Sokolowski-Tinten, K., Bialkowski, J., Cavalleri, A., et al.: Transient states of matter during short pulse laser ablation. Phys. Rev. Lett. **81**, 224–227 (1998)
346. Strickland, D., Mourou, G.: Compression of amplified chirped optical pulses. Opt. Commun. **56**(3), 219–221 (1985)
347. Strickland, D., Mourou, G.: Compression of amplified chirped optical pulses. Opt. Commun. **55**(6), 447–449 (1985)
348. Suckewer, S., Jaegle, P.: X-Ray laser: past, present, and future. Laser Phys. Lett. **6**(6), 411–436 (2009)
349. Sudan, R.N.: Mechanism for the generation of 10^9 G magnetic fields in the interaction of ultraintense short laser pulse with an overdense plasma target. Phys. Rev. Lett. **70**(20), 3075–3078 (1993)
350. Sugiyama, K., Fujii, T., Miki, M., et al.: Laser-filament-induced corona discharges and remote measurements of electric fields. Opt. Lett. **34**(19), 2964–2966 (2009)
351. Solem, L.C., Veeser, L.R.: Los Alamos Sci. Lab. Report LASL-LA-96 9667-MS (1977)
352. Taguchi, T., Antonsen, T.M., Palastro, J., et al.: Particle in cell analysis of a laser-cluster interaction including collision and ionization processes. Opt. Express **18**(3), 2389–2405 (2010)
353. Tajima, T.: Summary of Working Group 7 on "Exotic acceleration schemes". AIP Conf. Proc. **569**(1), 77–81 (2001)
354. Tajima, T., Kishimoto, Y., Downer, M.C.: Optical properties of cluster plasma. Phys. Plasmas **6**(10), 3759–3764 (1999)
355. Tan, K.O., James, D.J., Nilson, J.A., et al.: Compact 0.1 tw co_2 laser system. Rev. Sci. Instrum. **51**(6), 776–780 (1980)
356. Tanaka, K.A., Yabuuchi, T., Sato, T., et al.: Calibration of imaging plate for high energy electron spectrometer. Rev. Sci. Instrum. **76**(1), 013507 (2005)
357. Tatarakis, M., Gopal, A., Watts, I., et al.: Measurements of ultrastrong magnetic fields during relativistic laser–plasma interactions. Phys. Plasmas **9**(5), 2244–2250 (2002)

358. Telnov, V.: Photon collider at TESLA. Nucl. Instrum. Methods Phys. Res. A **472**(1–2), 43–60 (2001)
359. Temnov, V.V., Sokolowski-Tinten, K., Zhou, P., von der Linde, D.: Ultrafast imaging interferometry at femtosecond-laser-excited surfaces. J. Opt. Soc. Am. B **23**(9), 1954–1964 (2006)
360. Teubner, U., Eidmann, K., Wagner, U., et al.: Harmonic emission from the rear side of thin overdense foils irradiated with intense ultrashort laser pulses. Phys. Rev. Lett. **92**, 185001 (2004)
361. Teubner, U., Gibbon, P.: High-order harmonics from laser-irradiated plasma surfaces. Rev. Mod. Phys. **81**, 445–479 (2009)
362. Thoma M.H.: Field theoretic description of ultrarelativistic electron-positron plasmas. Rev. Mod. Phys. **81**, 959 (2009)
363. Thomas, A.G.R., Krushelnick, K.: Betatron X-ray generation from electrons accelerated in a plasma cavity in the presence of laser fields. Phys. Plasmas **16**(10), 103103 (2009)
364. Toleikis, S., Fäustlin, R., Cao, L., et al.: Soft X-ray scattering using FEL radiation for probing near-solid density plasmas at few electron volt temperatures. High Energy Density Phys. **6**(1), 15–20 (2010)
365. Trainor, R.J., Graboske, H.G., et al.: Lawrence Livermore Lab. Preprint UCRL-52562 (1978)
366. Trainor, R.J., Shaner, J.W., Auerbach, J.M., Holmes, N.C.: Ultrahigh-pressure laser-driven shock-wave experiments in aluminum. Phys. Rev. Lett. **42**, 1154–1157 (1979)
367. Trainor, R.J., Holmes, N.C., More, R.M.: Lawrence Livermore Lab. Report UCRL-82429 (1979)
368. Trainor, R.J., Holmes, N.C., Anderson, R.A.: In: Nellis, W.J. Seaman, L. Graham, R.A. (eds.) Shock Waves in Condensed Matter-1981, p. 145. American Institute of Physics, New York (1982)
369. Trunin, R.F.: Shock compressibility of condensed materials in strong shock waves generated by underground nuclear explosions. Phys. Usp. **37**(11), 1123 (1994)
370. Umstadter, D.: Photonuclear physics: laser light splits atom. Nature **404**(6775), 239 (2000)
371. Unruh, W.G.: Notes on black-hole evaporation. Phys. Rev. D **14**(4), 870–892 (1976)
372. Upadhyay, A.K., Inogamov, N.A., Rethfeld, B., Urbassek, H.M.: Ablation by ultrashort laser pulses: atomistic and thermodynamic analysis of the processes at the ablation threshold. Phys. Rev. B **78**, 045437 (2008)
373. Urnov, A.M., Dubau, J., Faenov, A.Y., et al.: X-ray spectra of multiply-charged hollow ions in the emission from a femtosecond laser plasma. JETP Lett. **67**(7), 489–494 (1998)
374. Vacca, J.R. (ed.): The World's 20 Greatest Unsolved Problems. Prentice Hall PTR, Englewood Cliffs (2004)
375. van Kessel, C.G.M., Sigel, R.: Observation of laser-driven shock waves in solid hydrogen. Phys. Rev. Lett. **33**, 1020–1023 (1974)
376. van Thiel, M. (ed.): Compendium of Shock Wave Data: Lawrence Livermore Lab. Report UCRL-50108 (1977)
377. Veeser, L.R., Solem, J.C.: Studies of laser-driven shock waves in aluminum. Phys. Rev. Lett. **40**, 1391–1394 (1978)
378. Veeser, L.R., Solem, J.C., Lieber, A.J.: Impedance-match experiments using laser-driven shock waves. Appl. Phys. Lett. **35**(10), 761–763 (1979)
379. Vinko, S.M., Ciricosta, O., Cho, B.I., et al.: Creation and diagnosis of a solid-density plasma with an X-ray free-electron laser. Nature **482**, 59–62 (2012)
380. Virovlyansky, A.L., Makarov, D.V., Prants, S.V.: Ray and wave chaos in underwater acoustic waveguides. Phys. Usp. **55**(1), 18–46 (2012)
381. Vladimirov, A.S., Voloshin, N.P., Nogin, V.N., et al.: Shock compressibility of aluminum at p > 1 Gbar. JETP Lett. **39**(2), 82 (1984)
382. Volpe, L., Batani, D., Vauzour, B., et al.: Proton radiography of laser-driven imploding target in cylindrical geometry. Phys. Plasmas **18**(1), 012704 (2011)

383. Wagner, U., Tatarakis, M., Gopal, A., et al.: Laboratory measurements of 0.7 *gg* magnetic fields generated during high-intensity laser interactions with dense plasmas. Phys. Rev. E **70**(2), 026401 (2004)
384. Wang, X., Ischebeck, R., Muggli, P., et al.: Positron injection and acceleration on the wake driven by an electron beam in a foil-and-gas plasma. Phys. Rev. Lett. **101**, 124801 (2008)
385. Wang, W.P., Shen, B.F., Zhang, X.M., et al.: Efficient acceleration of monoenergetic proton beam by sharp front laser pulse. Phys. Plasmas **18**(1), 013103 (2011)
386. Weibel, E.S.: Spontaneously growing transverse waves in a plasma due to an anisotropic velocity distribution. Phys. Rev. Lett. **2**(3), 83–84 (1959)
387. Whitley, V.H., McGrane, S.D., Eakins, D.E., et al.: The elastic-plastic response of aluminum films to ultrafast laser-generated shocks. J. Appl. Phys. **109**(1), 013505 (2011)
388. Willingale, L., Thomas, A.G.R., Nilson, P.M., et al.: Fast advection of magnetic fields by hot electrons. Phys. Rev. Lett. **105**, 095001 (2010)
389. Wood, L.L., Killer, R.N., Nuckolls, J.H.: Lawrence Livermore Lab. Report UCRL-79610 (1977)
390. Yaakobi, B., Bristow, T.C.: Measurement of reduced thermal conduction in (layered) laser-target experiments. Phys. Rev. Lett. **38**, 350–353 (1977)
391. Yan, X.Q., Wu, H.C., Sheng, Z.M., et al.: Self-organizing GeV, Nanocoulomb, collimated proton beam from laser foil interaction at 7×10^{21} W/cm^2. Phys. Rev. Lett. **103**, 135001 (2009)
392. Yanovsky, V., Chvykov, V., Kalinchenko, G., et al.: Ultra-high intensity- 300-TW laser at 0.1 Hz repetition rate. Opt. Express **16**(3), 2109–2114 (2008)
393. Young, L., Kanter, E.P., Krassig, B., et al.: Femtosecond electronic response of atoms to ultra-intense X-rays. Nature **466**(07), 56–61 (2010)
394. Zagar, T., Galy, J., Magill, J., Kellett, M.: Laser-generated nanosecond pulsed neutron sources: scaling from VULCAN to table-top. New J. Phys. **7**, 253 (2005)
395. Zamponi, F., Lübcke, A., Kämpfer, T., et al.: Directional bremsstrahlung from a Ti laser-produced x-ray source at relativistic intensities in the 3–12 keV range. Phys. Rev. Lett. **105**, 085001 (2010)
396. Zasov, A.V., Postnov, K.A.: Obshchaya astrofizika (General Astrophysics). Vek 2, Fryazino (2006)
397. Zeldovich, Y.B., Popov, V.S.: Electronic structure of superheavy atoms. Sov. Phys. Usp. **14**, 673 (1972)
398. Zel'dovich, Y.B., Raizer, Y.P.: Fizika udarnykh voln i vysokotemperaturnykh gidrodinamicheskikh yavlenii, 2nd edn. Nauka, Moscow (1966). [English Transl.: Physics of Shock Waves and High-Temperature Hydrodynamic Phenomena. Dover, Mineola (2002)]
399. Zhakhovskii, V.V., Nishihara, K., Anisimov, S.I., Inogamov, N.A.: Molecular-dynamics simulation of rarefaction waves in media that can undergo phase transitions. JETP Lett. **71**(4), 167–172 (2000)
400. Zhakhovskii, V., Inogamov, N., Nishihara, K.: Laser ablation and spallation of crystalline aluminum simulated by molecular dynamics. J. Phys. Conf. Ser. **112**(4), 042080 (2008)
401. Zhakhovskii, V.V., Inogamov, N.A., Nishihara, K.: New mechanism of the formation of the nanorelief on a surface irradiated by a femtosecond laser pulse. JETP Lett. **87**(8), 423–427 (2008)
402. Zhakhovskii, V.V., Inogamov, N.A., Petrov, Y.V., et al.: Molecular dynamics simulation of femtosecond ablation and spallation with different interatomic potentials. Appl. Surf. Sci. **255**(24), 9592–9596 (2009)
403. Zhang, L., Chen, L.M., Yuan, D.W., et al.: Enhanced Kα output of Ar and Kr using size optimized cluster target irradiated by high-contrast laser pulses. Opt. Express **19**(25), 25812–25822 (2011)
404. Zhang, L., Chen, L.M., Wang, W.M., et al.: Electron acceleration via high contrast laser interacting with submicron clusters. Appl. Phys. Lett. **100**(1), 014104 (2012)

405. Zhidkov, A.G., Sasaki, A., Fukumoto, I., et al.: Pulse duration effect on the distribution of energetic particles produced by intense femtosecond laser pulses irradiating solids. Phys. Plasmas **8**(8), 3718–3723 (2001)
406. Zhidkov, A., Koga, J., Sasaki, A., Uesaka, M.: Radiation damping effects on the interaction of ultraintense laser pulses with an overdense plasma. Phys. Rev. Lett. **88**, 185002 (2002)
407. Zhidkov, A., Esirkepov, T., Fujii, T., et al.: Characteristics of light reflected from a dense ionization wave with a tunable velocity. Phys. Rev. Lett. **103**, 215003 (2009)
408. Zhidkov, A.G., Pikuz, S.A., Faenov, A.Y., et al.: Generation of hard X-rays by femtosecond laser pulse interaction with solid targets in atmosphere. Opt. Lett. **37**(5), 884–886 (2012)
409. Zhigilei, L.V., Lin, Z., Ivanov, D.S.: Atomistic modeling of short pulse laser ablation of metals: connections between melting, spallation, and phase explosion†. J. Phys. Chem. C **113**(27), 11892–11906 (2009)
410. Zhilyaev, P.A., Kuksin, A.Y., Stegailov, V.V., Yanilkin, A.V.: Influence of plastic deformation on fracture of an aluminum single crystal under shock-wave loading. Phys. Solid State **52**(8), 1619 (2010)
411. Zigler, A., Palchan, T., Bruner, N., et al.: 5.5–7.5 MeV proton generation by a moderate-intensity ultrashort-pulse laser interaction with H_2O nanowire targets. Phys. Rev. Lett. **106**, 134801 (2011)
412. Zimmerman, G.B., Kruer, W.L.: Numerical simulation of laser-initiated fusion. Comm. Plasma Phys. Controlled Fusion **2**, 51 (1975)

Chapter 6
Relativistic Charged Particle Beams

The highest energy densities attainable under terrestrial conditions are generated in relativistic heavy-ion collisions. Accelerators [81] required for this purpose operate in several laboratories throughout the world and are well known as the principal experimental tool in nuclear physics, elementary particle physics, quantum chromodynamics, and superdense nuclear matter physics research [89, 119, 165, 169, 190], i.e. in the areas which have always been at the forefront of the natural sciences. There exists a demand for constant advancement into the domain of higher energies and higher phase densities of accelerated particle beams.

Investigations in the realm of high energy physics and relativistic nuclear physics permit determining that the main laws controlling the motion and interaction of elementary particles are highly unusual and quite simple. They are based on symmetry and the principle that everything not contradicting to the symmetry is allowed and so it may and must occur. This is fully realized in gravitational, electromagnetic, weak, and strong particle interactions.

Accelerator science and technology have come a long way from the first 1.2 MeV proton cyclotron invented by E. Lawrence in 1932 to the Large Hadron Collider (LHC) (Fig. 6.1), just beginning operation at CERN, with energies of 7,000,000 MeV in either of the counter-propagating beams, which is 7000 times the proton rest energy $m_{\mathrm{p}}c^2$. In the center-of-mass system this corresponds to a proton collision energy of $\approx$14 TeV.

During this period, the world has seen the construction of thousands of accelerators of different types, which are giant electrical facilities incorporating cutting-edge engineering ideas and exhibiting a high degree of reliability. Today they hold the record in high-energy-density physics.

It is planned to collide two proton beams with an energy of 7×7 TeV in the LHC accelerator complex, which is the largest man-made experimental installation, to reach the new domain of distances of 10^{-16} cm and energies on the 1 TeV scale, which is sufficient, in particular, for the production of the particles of dark matter (their mass $m_{\mathrm{DM}} \approx 10$ GeV–1 TeV), the Higgs boson, quark–gluon plasma, perhaps

© Springer International Publishing Switzerland 2016

V.E. Fortov, *Extreme States of Matter*, Springer Series in Materials Science 216,
DOI 10.1007/978-3-319-18953-6_6

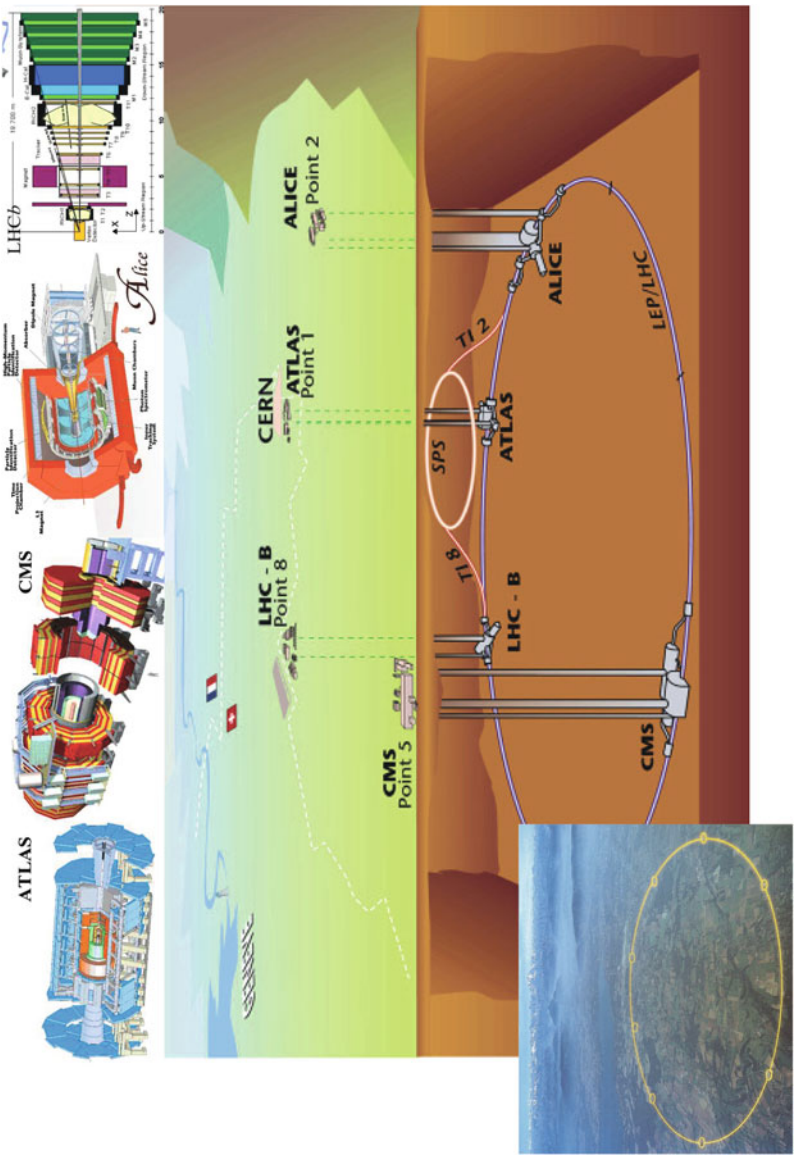

Fig. 6.1 Schematic of the large hadron collider (LHC) at the European Center for Nuclear Research (CERN). Its underground tunnel measures about 27 km in diameter. Shown at the *top* are the main detectors: ALICE, ATLAS, CMS, and LHC-B

for discovering new dimensions, and for the solution of other intriguing problems of high energy physics [189, 191]. The main purpose of the experiments at LHC is to check the so-called Standard Model of particle physics and to see if there is any new physics in the teraelectronvolt range of energies [135].

The main lines of research on the LHC are discussed in [64]:

- the search for the Higgs boson;
- the search for supersymmetry;
- the search for new physics outside the scope of the SM and MSSM (Minimal Supersymmetric Standard Model);
- B-physics;
- heavy-ion physics;
- top-quark physics; and
- standard physics (QCD and electroweak interactions).

In the LHC, protons will move in the form of 3000 bunches distributed over the entire 27 km circumference of the collider. Each bunch of up to 100 billion protons measures, at the points of collision, several centimeters in length and only 16 μm in diameter—like a thin human hair. A total of 2808 bunches of 100 billion protons each will collide in the zones where detectors are located to cause over 600 million proton collisions of particles per second (up to 20 collisions at intersection). These collisions will take place between the particles that constitute protons—quarks and gluons. At the maximum particle energy, the energy release will be equal to approximately one seventh of the energy contained in the initial neutrons, or about 2 TeV.

The detectors, which are impressive giant engineering structures—the biggest one having a volume half that of Notre Dame cathedral in Paris and the heaviest one containing more iron than the Eiffel Tower—will measure the parameters of the thousands of particles escaping at each collision event. Despite the huge size of the detectors, their individual elements should be mounted with a precision of 50 μm. Later on it will be possible to study the processes in the collision of highly ionized lead ions (Pb^{82+}) with energies of up to 155 GeV per nucleon. We discuss the LHC project at length in Sect. 6.6.

The Stanford Linear Accelerator at SLAC, Menlo Park, California, generates a 5 ps pulse of 10 electrons with a kinetic energy of 50 GeV, which is focused to a 3-μm-sized spot to provide a power density of 10^{20} W/cm^2.

The actively operating Relativistic Heavy Ion Collider (RHIC) (Fig. 6.2) of the Brookhaven National Laboratory (Long Island, NY, USA) affords an energy of up to 500 GeV per nucleon in the center-of-mass system for colliding gold ions, 39 TeV for Au+Au, and 13 TeV for Cu+Cu [187]. The new experimental data obtained on this accelerator are discussed in [97]. In Darmstadt (Germany), in November 2007 a start was made on the construction of the unique ion and antiproton accelerator facility FAIR (Facility for Antiproton and Ion Research) with an energy of 1.5–34 GeV per nucleon for $\approx 5 \times 10^{11}$ and $\approx 4 \times 10^{13}$ accelerated U^{92+} ions and antiprotons, respectively. The construction cost of each of these major ultrarelativistic hadron accelerator complexes amounts to several billion dollars and

Fig. 6.2 Relativistic Heavy Ion Collider (RHIC) of the Brookhaven National Laboratory (USA)

is close to the limit of the economic potentials of the world's wealthiest countries and even international communities such as the European Union.

The scientific programs at these complexes comprise experimental research into the basic problems of high energy physics in hadron collisions, which are accompanied by the production of superdense nuclear substance—quark–gluon plasma. According to contemporary notions, this was precisely the state of the universe's substance during the first microseconds after the Big Bang (Fig. 9.50), and this is precisely the state of the substance of astrophysical objects such as gamma-ray bursts, neutron stars, and black holes.

It is no coincidence that during the preparation of these experiments there emerged concerns about their safety because of the possibility that a black hole would emerge in laboratory conditions with the subsequent absorption of our civilization. However, calculations showed that the state of a mini black hole in accelerator experiments would exist for a very short time ($\approx 10^{-26}$ s), which is insufficient for catastrophic consequences. Furthermore, the absence of catastrophic events in the transit of superhigh-energy cosmic particles is supposedly an additional argument for the safety of the acceleration experiments in this energy density range.

Possible concerns about increasing the energy of collisional experiments were analyzed in [223] (Fig. 6.3). In the subsequent discussion we follow this work. The matter is that the collisions of energetic particles may, in principle, trigger a phase

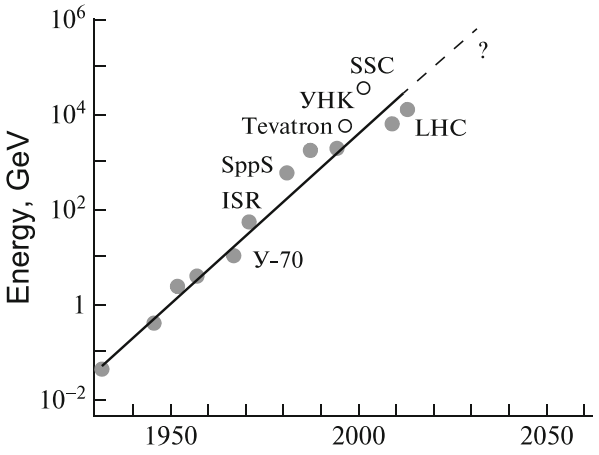

Fig. 6.3 Dependence of accelerators energy (in terms of center-of-mass energy) on the time of their construction. Drawing borrowed from [223]

transition of the first kind, whereby a decay of the false vacuum and a complete change of the physical properties of the Universe will take place. Experiment, including that with cosmic rays, shows that this will not happen for low energies. However, it is required to determine the safe level to which it is admissible to increase the energy. This level may be estimated with the knowledge of the highest energy of cosmic rays, $E_{\text{lab}} = 10^{20}$ eV. The equivalent center-of-mass energy on the collider is approximately 10^6 GeV. This is precisely the level to which the particle collision energy may be increased without concerns about consequences like phase transitions of the first kind.

Since the Planckian scale is 10^{19} GeV, the safe-for-investigations energy scale amounts to its fraction equal to 10^{-13}. Experiments performed below the safe energy limit may leave unanswered [223] a multitude of questions: the origin of elementary particle masses, the understanding of supersymmetry, the nature of hidden mass, the problems of neutrino physics, grand unification, superunification, multidimensionality, etc. There nevertheless exists the possibility that in the future we will able to study the entire energy scale without going beyond the safety limit.

If the idea of multidimensionality turns out to be true, then the Planckian energy scale, which characterizes quantum-gravitational effects, may be considerably lower. In the simplest versions of the theories which rely on the idea of additional dimensions with the geometry of a d-dimensional sphere of radius R, there holds the relation [223]

$$m_d = \left(\frac{m_4^2}{R^d}\right)^{\frac{1}{(d+2)}},$$

where $m_4 = 10^{19}$ GeV and m_d is the energy scale of $(d+4)$-dimensional space. The true ($(d+4)$-dimensional) Planckian scale may be much lower, depending on the scale R of compact measurements. Accordingly, all effects of the new physics must lie below it [223].

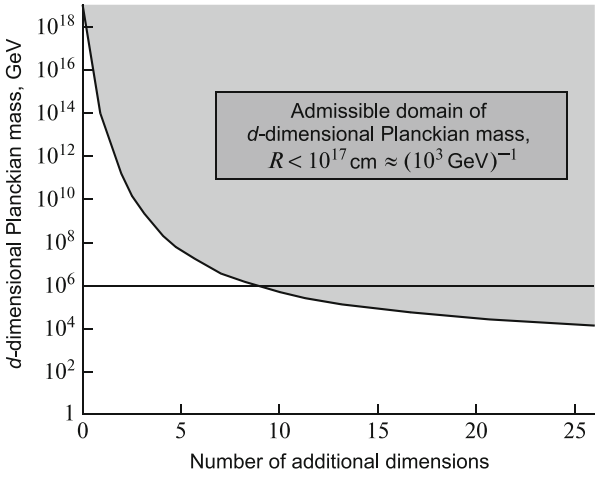

Fig. 6.4 Admissible domain of d-dimensional Planckian mass (*grey color*), $R < 10^{-17}$ cm $\approx (10^3\,\text{GeV})^{-1}$. Drawing borrowed from [223]

Possible R values are determined by modern experimental with the upper bound of the order of 10^{-17} cm in the case when all fields "feel" additional dimensions. The domain of possible values of d-dimensional Planckian mass is shown in grey in Fig. 6.4. The horizontal line indicates the "safety limit". On can see that the d-dimensional Planckian mass may turn out to be attainable on future colliders if the number of spatial dimensions is higher than 8 [223].

The problem of increasing the colliders energy makes topical the further experimental investigations to improve the accuracy of measurements without raising the particle energy. Examples are provided by measurements of the magnetic moments of electrons and muons, atomic energy shifts, mass mixing in K^0-, D^0-, and B^0 mesons, rare decays, etc. In particular, in the measurement of muon magnetic moment, the resultant departure from the SM was in the ninth decimal digit at a 3.2σ confidence level [223].

For our consideration it is significant that these acceleration experiments are aimed not only at the production of particle beams with ultrarelativistic energies and the investigation of individual hadron collision events (Fig. 9.51) [140], but also for macroscopic substance heating [81, 106, 204].

6.1 Production of Macroscopic Hot Plasma Volumes

The methods of gas-dynamic acceleration of condensed strikers as described in Sects. 3.4 and 3.5 have a fundamental disadvantage arising from the limited value of the velocity of sound c_s in the pusher gas, so that the acceleration efficiency decreases sharply (exponentially) when the striker reaches the velocity of sound. The techniques of high-energy-density generation relying on the use of high-intensity fluxes of charged particles—electrons, light or heavy ions—as well

as on electrodynamic acceleration techniques, where the velocity of light fulfills the role of the velocity of sound, are devoid of these limitations. An important positive feature of charged particle beams is the volume nature of their energy release [204]. This distinguishes them from laser irradiation, where the bulk of the energy for radiation of frequency ω_l is released in a narrow critical zone [22, 27, 137, 143] $\omega_l \sim \omega_p \sim \sqrt{4\pi e^2 n_e / m_e}$ and is then transferred to the target interior by electron thermal conduction [22, 27, 137, 143].

As a result of deceleration of the charged particles there emerges a layer of isochorically (at constant-volume) heated plasma, which subsequently broadens to generate a shock wave traveling into the target or a cylindrical shock diverging from the beam axis. Modern research in the area of high-energy-density physics takes advantage of both of these techniques—isochoric heating and compression by shocks generated by particle beams.

For particle beam generators use is made of either cyclotrons developed for high-energy and nuclear physics research [106], or high-current diode systems [34, 152]. Involved in the latter case are subnanosecond current pulses of the megampere range with kinetic particle energies of 1–20 MeV [177, 195].

Fortov et al. [77] employed relativistic MeV electron beams to excite shock waves in aluminum targets for the purpose of studying the features of electron absorption in a dense plasma and elucidating the effect of intrinsic magnetic fields of the beams on the stopping power of magnetized plasma (the magnetic "stopping" effect).

Owing to the substantially shorter paths of ions in comparison with electrons (Fig. 6.5), ion beams make it possible to obtain higher specific energy densities in plasmas (Fig. 6.6). In a series of investigations by Baumung et al. [34] performed on the pulsed high-current KALIF accelerator, the ≈2 MeV proton beam with a current

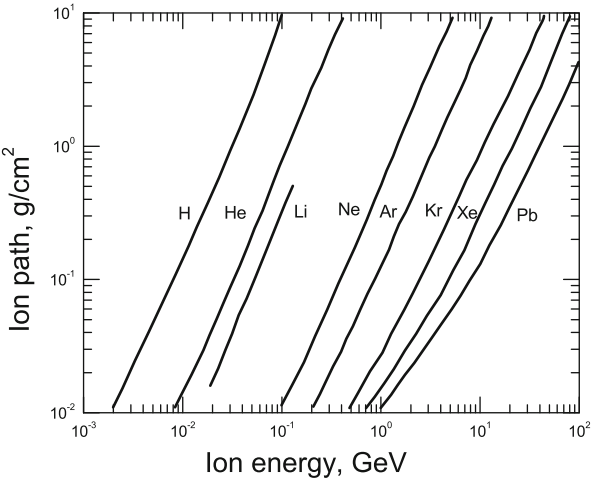

Fig. 6.5 Characteristic ion paths in a cold material [204]

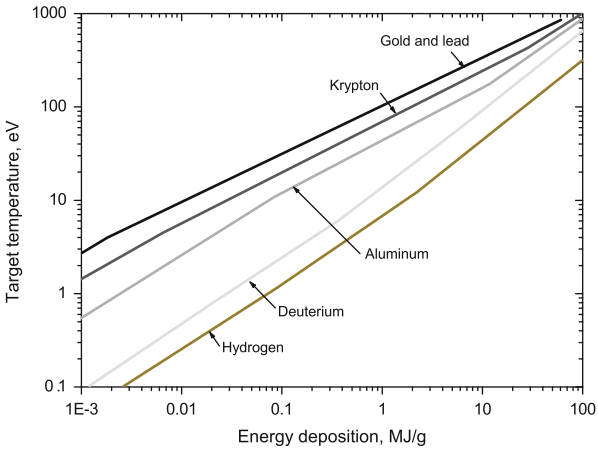

Fig. 6.6 Typical plasma temperature as a function of energy deposited by charged particle beams [204]

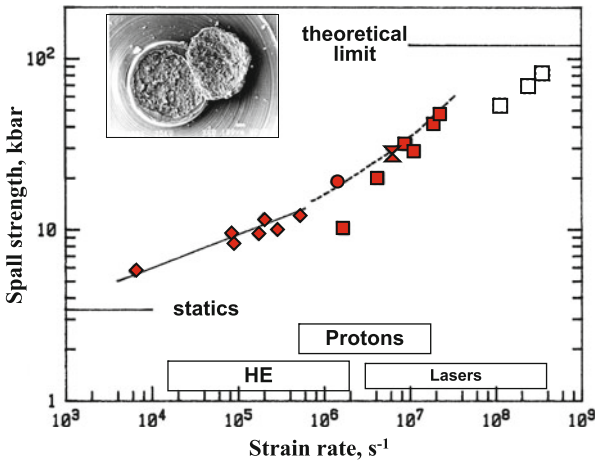

Fig. 6.7 Spalling strength of an aluminum-magnesium alloy for high strain rates (HE: high explosive)

of ≈400 kA produced a power density on the order of 10^{12} W/cm^2. This enabled thin (50–100 μm) flyers to be accelerated to velocities of 12–14 km/s and informative measurements of the dense-plasma stopping power to be performed for fast protons, the thermodynamic parameters and viscosity of the shock-compressed plasma to be recorded, and the spalling resistance of metals at ultrahigh rates of straining to be found. It turned out (Fig. 6.7) that the spalling resistance of metals significantly rises (by 1–2 orders of magnitude) with increasing rate of strain to approach its theoretical limit, which is related to the propagation kinetics of dislocations and cracks in a pulsed stress field [34, 116].

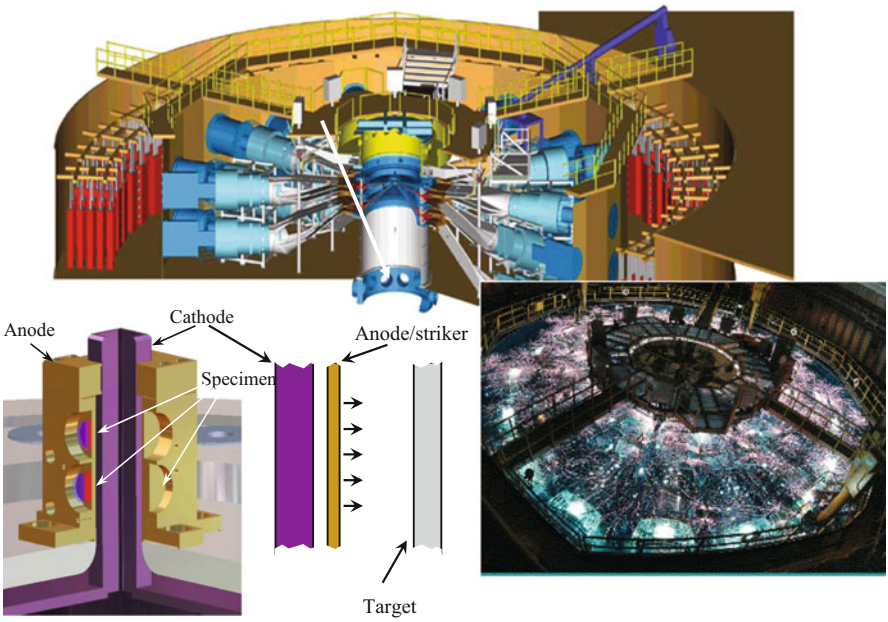

Fig. 6.8 Schematic of electrodynamic acceleration of metal liners at the Z-pinch facility of the Sandia National Laboratories, USA [124]

The pulsed high-current BPFA-II generator (Sandia National Laboratories, USA, Fig. 6.8) was earlier used to advantage for producing megavolt lithium ion beams with an intensity on the order of 10^{12} W/cm^2 for the inertial confinement fusion (ICF) program [57, 147]. At present this facility is employed in the high-current Z-pinch mode for the production of soft X-rays and electrodynamic generation of shocks and adiabatic compression waves [58, 124, 181, 217].

The relativistic heavy-ion accelerators constructed for high-energy physics experiments turned out to be candidates (Table 3.2) for controlled nuclear fusion with inertial plasma confinement and for experiments on the compression and heating of dense plasmas (Fig. 6.9) [81, 204].

The LHC (CERN) (Fig. 6.1), constructed to study the collisions of two proton beams with an energy of 7 TeV each, generates 2808 bunches, each 0.5 ns long, which contain 1.1×10^{11} protons each and are spaced at 25 ns, so that the total beam duration is 89 μs and the energy $\approx$ 350 MJ, which is sufficient to melt 500 kg of copper. The energy density in one beam is 10^{10} J/cm^3. The characteristic kinetic energy of one heavy relativistic ion is comparable to the kinetic energy of a metal liner accelerated by the high explosive (HE) detonation products of the launching system described in Sect. 3.5.

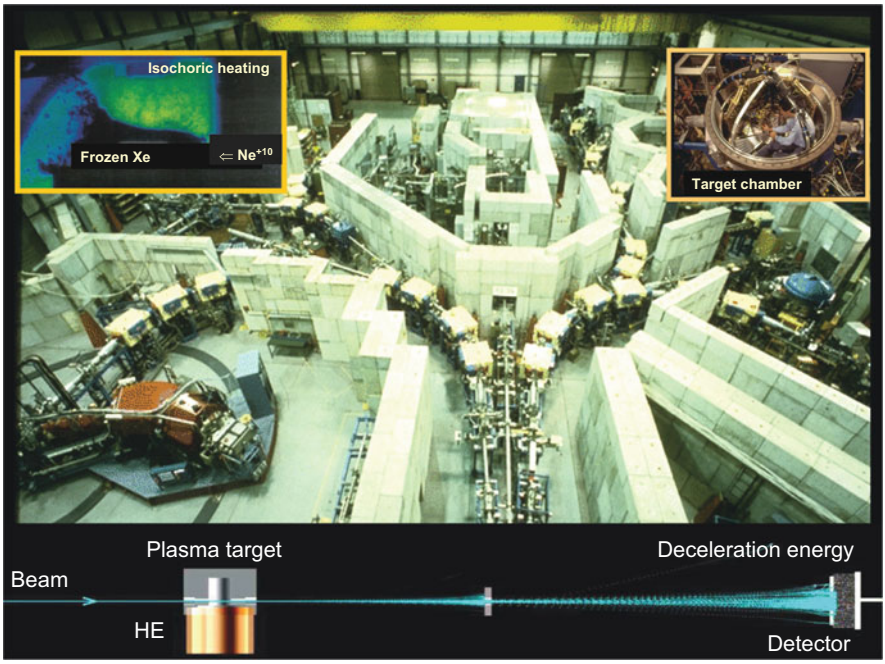

Fig. 6.9 Relativistic heavy-ion beam interaction experiments at the GSI accelerator (Darmstadt, Germany) [81, 106]

Heavy-ion beams with a kinetic energy of 3–300 MeV per nucleon were employed in experiments on the heating of condensed and porous targets, the measurement of plasma stopping power for ions, and the interaction of charged beams with shock-compressed plasma produced by miniexplosion-driven shock tubes [68, 81, 154, 188, 230].

Of special interest is the possibility of employing the GSI (Darmstadt, Germany) heavy-ion accelerator in combination with the high-power petawatt PHELIX laser system (Fig. 6.10), which would qualitatively enhance the experimental capabilities of this device.

The potential and application prospects of the acceleration complexes at the GSI heavy-ion center are depicted in Figs. 6.11 and 6.12. One can see that high-intensity relativistic heavy-ion beams are interesting candidates for the generation of high-energy-density plasmas as well as for pulsed nuclear fusion [81, 106] (see Sect. 7.3).

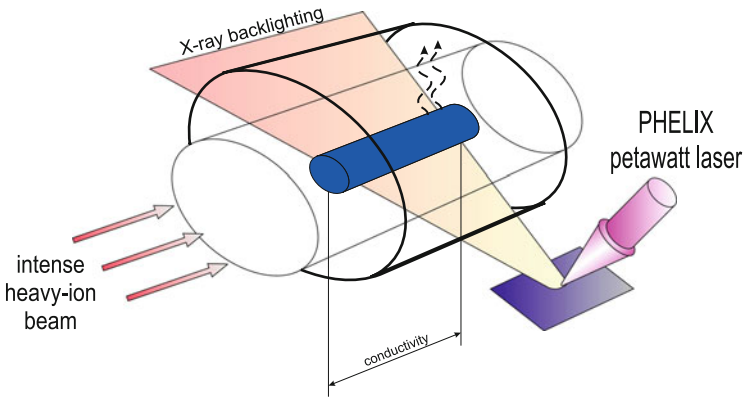

Fig. 6.10 Setup of the experiment using a relativistic heavy-ion beam and a petawatt laser [81, 106, 229, 230]

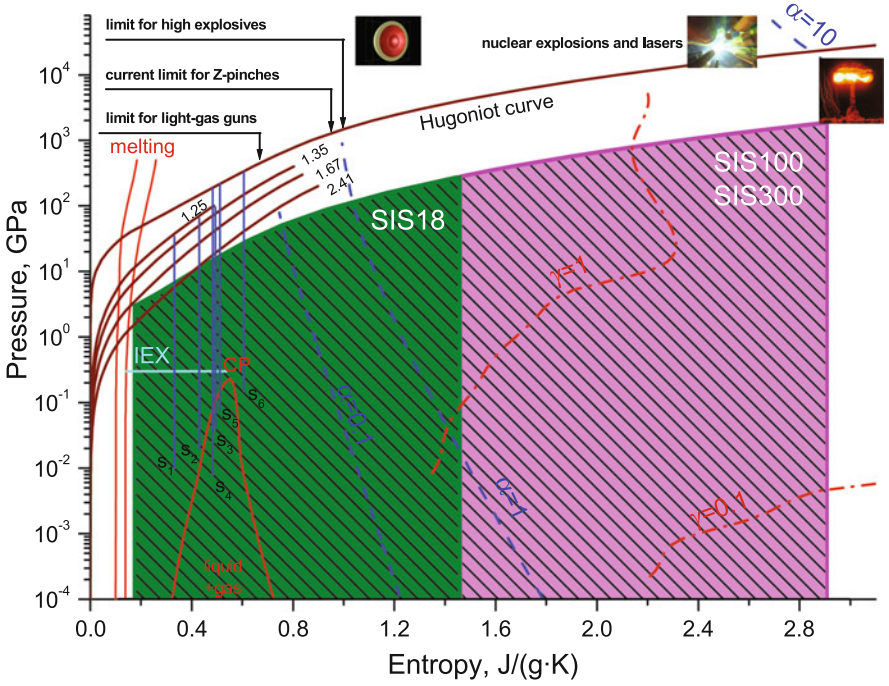

Fig. 6.11 Capabilities of the SIS 18, SIS 100, and SIS 300 heavy-ion accelerators (see Table 3.2) for producing high energy densities in lead [81, 106, 229, 230]

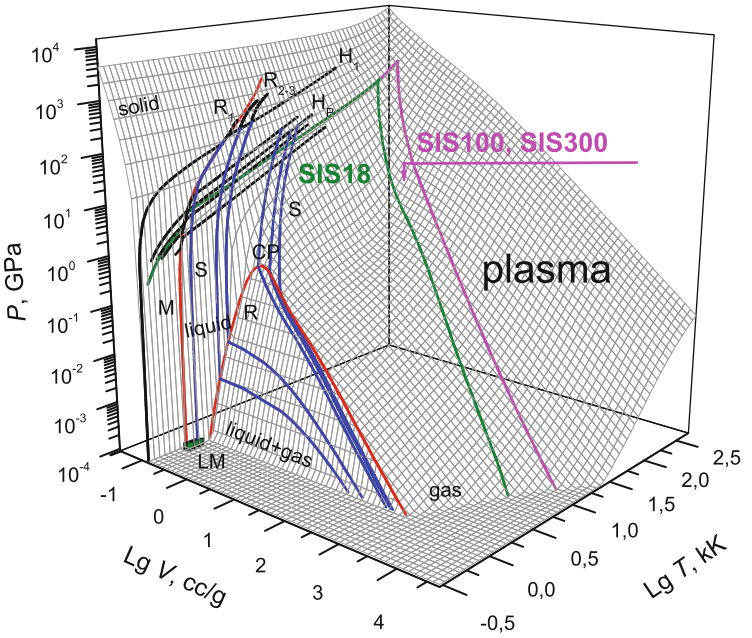

Fig. 6.12 Parts of the phase diagram of zinc attainable with heavy-ion generators [81, 106, 229, 230]

6.2 Relativistic Nuclear Collisions

As already noted, record high energy densities are now achieved in the head-on collisions of heavy ions (Figs. 6.13 and 6.14 [85]) accelerated to subluminal velocities in accelerators. These collision experiments are aimed at the quest for new particles (Fig. 6.15), at experimental investigations into the basic problems of high-energy physics, elementary particle and relativistic nuclear physics in hadron collisions, which are attended with the production of superdense nuclear substance—quark-gluon plasma (QGP) (Figs. 6.16 and 6.32). Specifically, unique experiments were executed on the CERN and Brookhaven accelerators to generate ultraextreme baryon substance in a superdense and heated state with a density of the order of 10^{15} g/cm^3, a pressure of 10^{30} bar, a temperature of about 200 MeV, and a specific energy density of $\approx$1 GeV/fm^3 (Figs. 2.1 and 2.2) in individual Cu–Cu and Au–Au nuclear collision events. Implemented in experiments on the RHIC were collisions of iron nuclei with a specific energy of 100 GeV/nucleon (the nucleon mass is equal to 1 GeV), resulting in a heat-up temperature of 300–600 MeV.

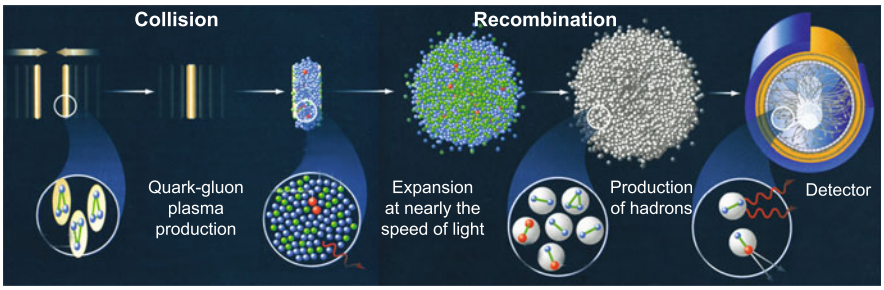

Fig. 6.13 Dynamics of relativistic heavy-nuclei collisions in accelerators [187]

The emergence of a domain with extremely high parameters in a laboratory ion collisions and its subsequent expansion are sometimes referred to as a "Micro Bang" (Fig. 6.15), whose analogy to the cosmological Big Bang is a subject for special analysis [65].

The internal structure and interaction of particles and nuclei are the main objects of studies on accelerators [65]. According to modern views, strong interactions are described by quantum chromodynamics, which considers quarks and gluons as the elementary objects (partons) responsible for the interactions. At low energies the partons are retained within strongly interacting particles (hadrons).

The matter produced in the interactions is undoubtedly different from that mentioned above. Strong internal fields and highly coherent partonic configurations become especially important. In the collision of two heavy nuclei at ultrarelativistic energies one would expect the emergence of a hot and dense internally colored medium. This medium must manifest some collective properties different from those observed under static conditions.

Figure 6.17 gives the characteristics of baryon matter attainable for different accelerators [146].

The study of substance properties in relativistic nuclear collisions will always be the most advanced field of natural science [90]. In the opinion of H.A. Bethe, in the twentieth century the mankind expended more intellectual effort on the study of nuclear forces and the corresponding processes than on the study of all the rest scientific disciplines taken together.

Following [64, 208, 209] we briefly discuss the main results obtained on accelerators.

World's leading scientific centers are involved in the research with accelerators:

- GSI, Germany, $E_{\text{lab}} \approx$ 1–2 AGeV, which corresponds to a nucleon-nucleon center-of-mass energy $\sqrt{s_{NN}} \approx$ 2– 2.5 GeV;
- CERN, SPS, Switzerland/France, $E_{\text{lab}} \approx$ 20–158 AGeV, $\sqrt{s_{NN}} \approx$ 6–17 GeV;
- BNL, RHIC, USA, $\sqrt{s_{NN}} \approx$ 20–200 GeV;
- JINR, Nuclotron, Russia, $E_{\text{lab}} \approx$ 1–6 AGeV, $\sqrt{s_{NN}} \approx$ 2.5–3 GeV.

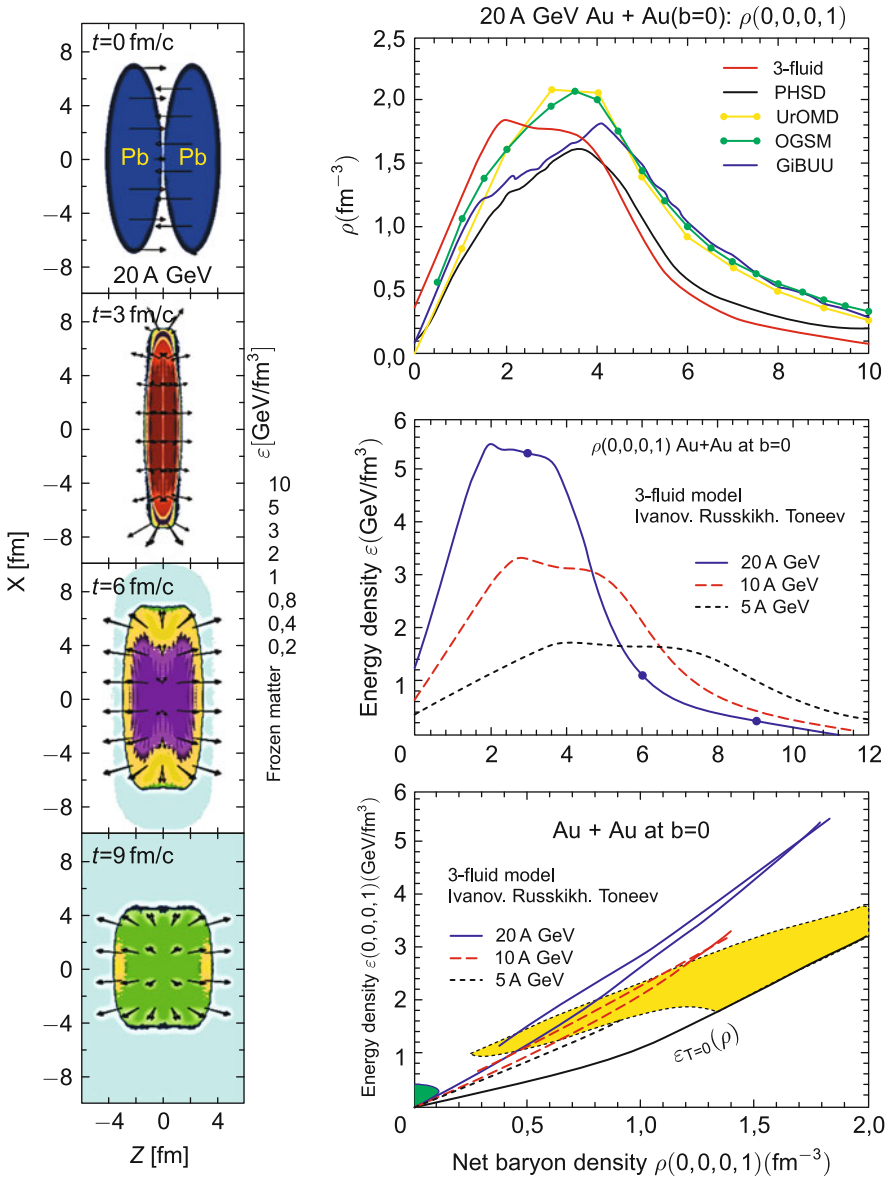

Fig. 6.14 Relativistic collision of gold nuclei. At the *left*: energy density, the domain of hadronization is *light-colored*. At the *right*: the time evolution of the total baryon energy density at the center and the trajectory of parameter variation. The domain of phase coexistence is marked in *yellow* and the domain of phase transition is shown in *green*. Figure borrowed from [85]

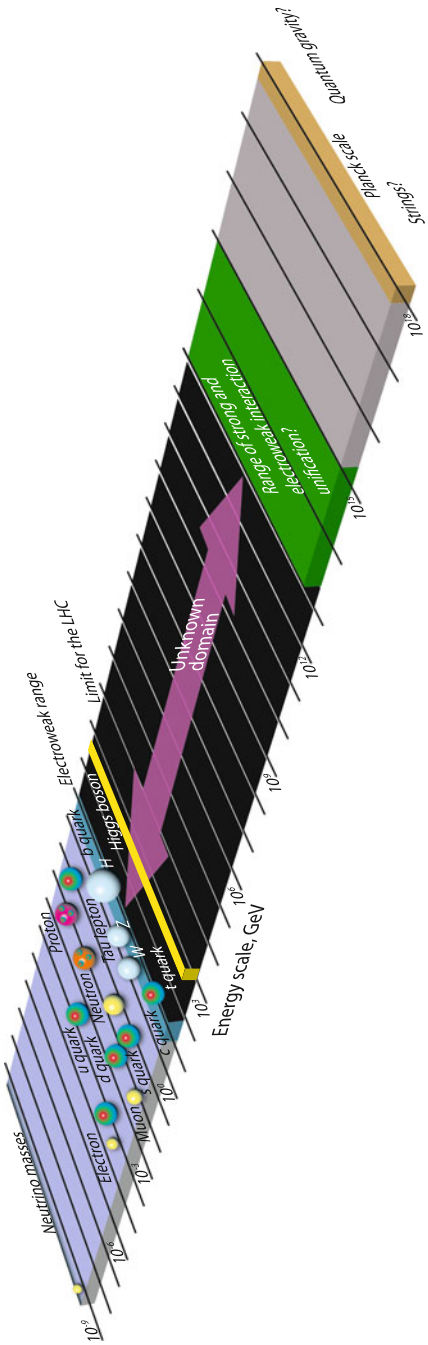

Fig. 6.15 Particle hierarchy problem [180]

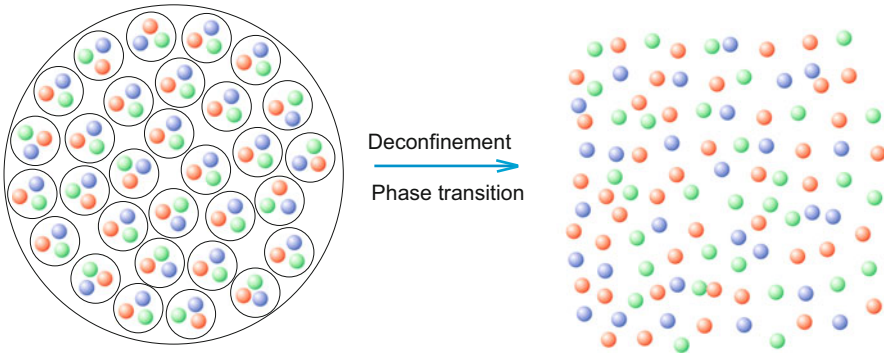

Fig. 6.16 Quark–gluon plasma production. Under ordinary conditions (at the *left*) quarks (*shaded balls*) are bound in hadrons. At high temperatures $T > T_c$ there occurs deconfinement of quarks and they cease to be bound in hadrons and form a QGP

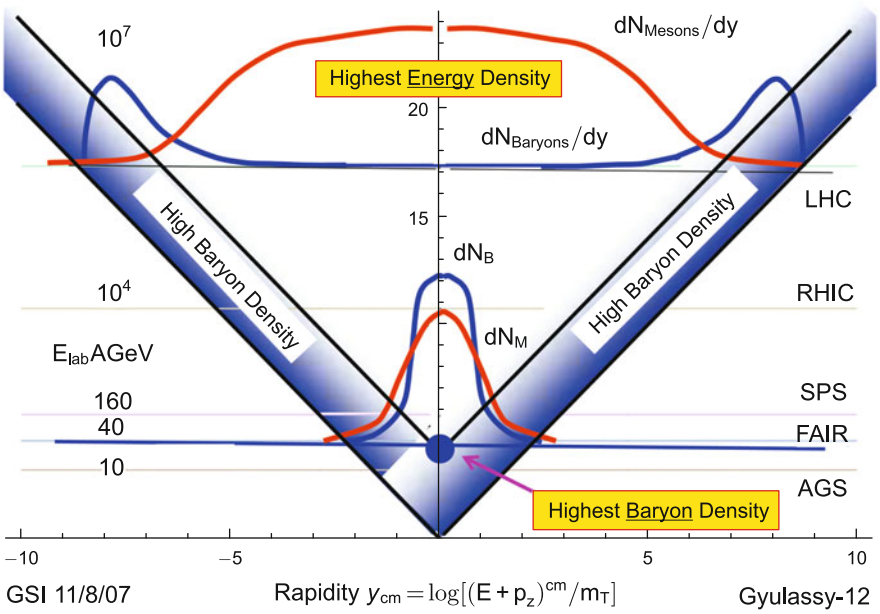

Fig. 6.17 Characteristics of baryon matter achievable for different accelerators [146]

The SPS accelerator in the CERN yielded a wealth of data about the total cross sections, elastic scattering amplitudes, diffraction processes, inclusive fissions, and other general characteristics of hadronic interactions for an energy of up to 450 GeV. Also recorded there were manifestations of collective effects, which became indications of a quark-gluon plasma. The SPS accelerator is now employed as a 450 GeV particle injector for the LHC and as a neutrino source, whose

flux penetrates the 730-km depth of rock to reach the underground Grand-Sasso laboratory in Italy.

The LHC accelerator was constructed in place of the Large Electron-Positron Collider (LEP), which was the site of the interaction of colliding beams of electrons and positrons with a total energy of up to 200 GeV. With the help of the LEP accelerator, quark and gluon jets were found for the first time, measurements were made of the QCD coupling constant α_s and its energy dependence (with the presently available accuracy $\alpha_s(\mathrm{M}_z) = 0.1176 \pm 0.002$), the W and Z bozons—the weak interaction carriers—were discovered and investigated, and the lower mass bound on the Higgs boson (114 GeV) was determined.

The Hadron-Electron Ring Accelerator (HERA) in Hamburg, which was recently decommissioned, was used to accelerate and collide the beams of electrons with an energy of up to 27.5 GeV and protons with an energy of up to 920 GeV. This enabled physicists to comprehensively study the so-called proton structure functions and thereby elucidate the quark-gluon composition of high-energy protons [64].

Tevatron at the Enrico Fermi Laboratory in Chicago is closest in energy and nature of colliding objects to the LHC. In the Tevatron, protons collide with antiprotons with a center-of-mass energy of almost 2 TeV. Therefore the particle collisions are the source of information about the $q\hat{q}$-, gg-, $\gamma\gamma$- and γ-Pomeron processes. Also highly intensive and successful were the mass and width investigations of W and Z bosons as well as of top quarks (their respective masses are equal to about 80.4, 91.2 and 172 GeV). The lower mass bound to the Higgs boson was also determined. Detailed investigations were made of quantum-chromodynamic (QCD) jets and processes with high transverse momenta. But even now the Tevatron continues to yield data which arouse keen interest. All these data will be studied on the LHC with an even higher accuracy. The statistics of such events (for instance, jets of the same energy) on the LHC will be approximately one thousand times greater than on the Tevatron for the same accumulation time [64].

Another accelerator, Relativistic Heavy Ion Collider (RHIC), operated in Brookhaven. The main objective of research on the RHIC consists [64] in the study of head-on ion beam collisions for a total energy of up to 200 GeV per nucleon and in the comparison of results with similar data about proton collisions. The RHIC experiments yielded ample information about the behavior of baryon substance. It was possible to obtain states with record high energy densities of $\approx 5\,\mathrm{GeV/fm^3}$ in lieu of the previously attained figure equal to $\approx 0.15\,\mathrm{GeV/fm^3}$. Quark-gluon plasma was obtained, which possessed, as it turned out, a high stopping power and the properties of a nonviscous liquid. The presence of clearly pronounced "collective" flows, rapid thermalization, a fast growth of pressure in the course of collisions, and several other fundamentally new effects were demonstrated. The properties of the nuclear substance produced in these collisions were thoroughly studied, which lent additional support to the ideas of quark-gluon plasma formation. These properties were found to be closer to the properties of a ideal liquid than to those of gases, as hypothesized earlier (for more details, see Sect. 6.4). Clearly observed were other collective effects as well: azimuthal asymmetry of particle fluxes and softening of the particle spectra in jets in the passage through this medium.

High beam intensities in KEK (Japan) and SLAC (Stanford Linear Acceleration Center, USA) B factories permitted carrying out accurate measurements of the γ-boson family properties as well as of other processes with b-quark production. This led to a clearer understanding both of the CP-invariance violation problem and of the emergence of differences between matter and antimatter as well as permitted investigating in greater detail rare particle decays and obtaining limitations on the masses of supersymmetric partners of our known particles.

We summarize the main results [209]:

- strong deceleration of colliding nuclei,
- collective fluxes of secondary particles,
- anomalously large broadening of momentum distributions,
- anomalous enhancement of multistage hyperon production,
- significant broadening of ρ-meson spectral maximum,
- strong modification of fast hadrons,
- suppression of jets in their motion through the nuclear medium.

A number of these observations may be related to the emergence of quark-gluon plasmas.

Also obtained was a wealth of other interesting results, which lay at the foundation of modern conceptions of high-energy physics.

In accordance with modern notions, strong interactions are described by quantum chromodynamics (QCD), which views quarks and gluons as elementary particles (partons) responsible for the interaction. At low energies the partons are confined inside strongly interacting particles (hadrons) and determine their static properties. At high densities we have a nonperturbative QCD mode, which describes strongly interacting matter under thermodynamic equilibrium at a finite temperature. The matter produced in collisions exhibits new interesting properties. Strong internal fields and highly coherent partonic configurations become highly significant. In the collision of two heavy nuclei at ultrarelativistic energies there emerges a hot dense color medium. Following [65] we note that this medium must manifest some collective properties different from those observed under static conditions. Low-momentum modes in nuclear wave functions may be described in terms of classical fields related to certain high-momentum static color sources. According to modern views [65] the collision process (evolution in energy for all modes) passes through several stages (Fig. 6.13). At the beginning of this chapter we discussed some of them. At one stage for a short time interval and in a finite volume, quarks and gluons may be deconfined and, according to modern theories, may form some ideal liquid—quark-gluon plasma. Collective properties of this plasma manifest themselves in its mechanical motion as a whole, which is described in the framework of hydrodynamics, as well as in its chromodynamic response to the propagation of partons in it, which is described by QCD in the medium [65].

For high transferred momenta the QCD coupling constant becomes small (asymptotic freedom) and a perturbative approach reliant on the perturbation theory becomes applicable. Experiments on high-energy particle collisions are required for studying processes with high transferred momenta, i.e. on progressively shorter

distances. Studied in this way are the quark-gluon structure of a particle, its scale dependence, and the properties of interaction range. Furthermore, hard processes in the medium may induce its collective coherent response. Nuclear-nuclear (AA) collisions were studied [65] in experiments on the SPS and RHIC heavy-ion accelerators. The primary problem under study: the difference of process properties in AA and proton-proton (pp) high-energy collisions. Observations and comparisons were made of various characteristics, which showed clearly that nuclear collisions may not be treated as the coherent superposition of nucleon-nucleon collisions. Explaining the differences requires taking into account the collective properties of the medium, some of their manifestations being attributable to the emergence of quark gluon plasma.

The theoretical and experimental effort to study the phase diagram of compressed baryon substance and the intensive search for new unusual phases of the strongly interacting substance at high energy densities have been mounted for about a quarter of a century [209]. These investigations will help understanding the behavior of hadrons in a hadronic medium, obtaining the equation of state of hadronic and nuclear substance, and recording the observable manifestations of quark deconfinement and chiral symmetry violation (Fig. 6.18 [85]).

The main trend in relativistic collision research is to advance upwards in relativistic particle energy scale. This increase in collision energy gives rise, of course, to fundamentally new high-energy effects; however, as we shall see below, this shortens the interaction time in nuclear collisions, making nonequilibrium processes in ultrarelativistic interactions more probable. This circumstance accounts for the opposite research trend: the interest in a lower energy range (in comparison with the record one) of 8–40 GeV in the domain of the phase boundaries of new hadronic phase formation [208, 209, 213].

According to modern physical notions, nuclear matter may undergo a series of phase transitions with increase in baryon temperature and/or density (see Figs. 6.19 and 6.20). One of them is a transition with chiral symmetry violation caused by the strong interaction. This interaction violates chiral symmetry at low temperatures

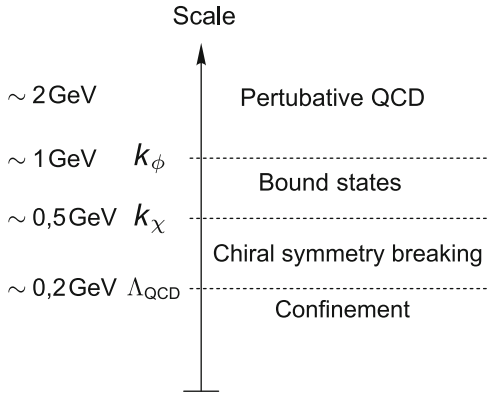

Fig. 6.18 Hierarchy of momenta (energies) and scale of nonperturbative effects. Figure borrowed from [85]

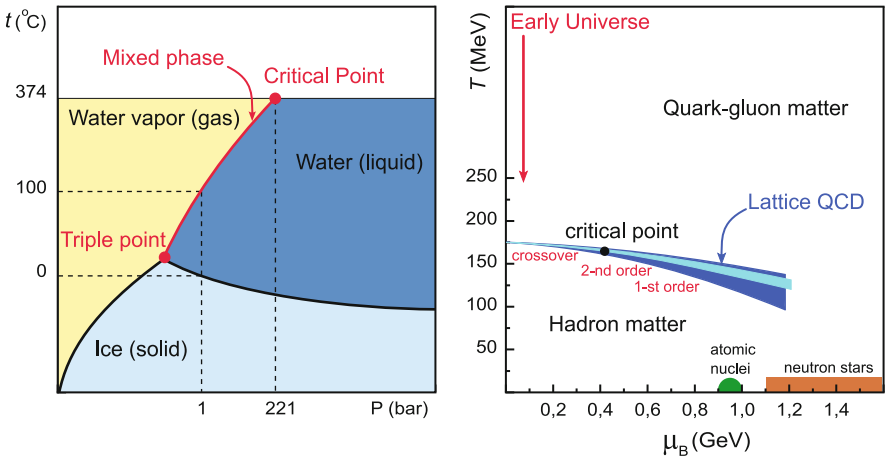

Fig. 6.19 At the *left*: water–vapor transition (a phase transition of the first kind with latent heat of vaporization) terminates at the critical point (of the second kind). There is no difference between vapor and water above the critical point. At the *right*: according to modern theoretical models, the structure of a quarks–hadrons phase transition is similar to the water–vapor transition, with the absence of differences between the phases above the critical point (μ_B is the baryon chemical potential related to the baryon density and T is the temperature)

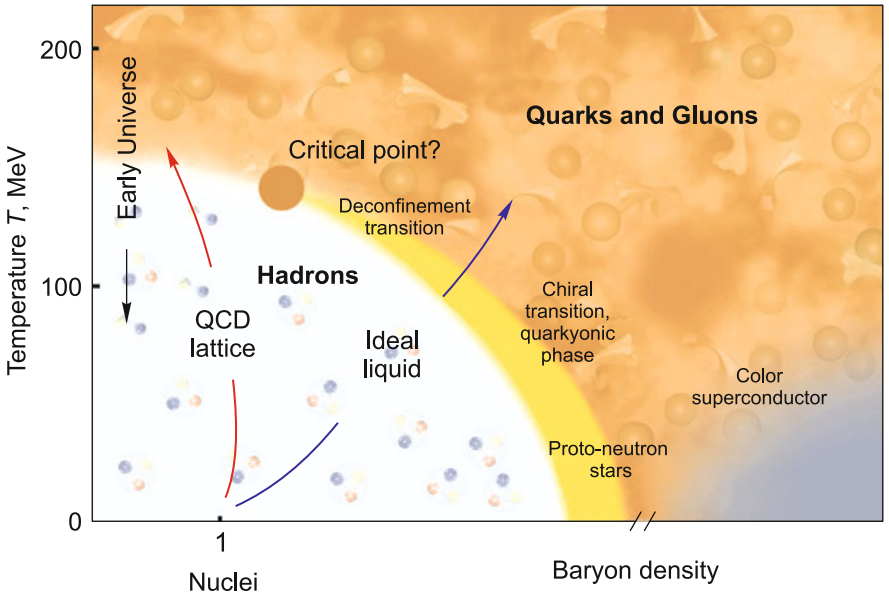

Fig. 6.20 Phase diagram of strongly interacting baryon matter. Posted on the NICA site [40, 163]

and/or low baryon densities, which recovers for high parameters. Possible in this case is the existence domain with violated and recovered symmetry phases, like

is the case in water vapor under subcritical conditions (see Fig. 6.19). Owing to the possibility of quark pairing, luminal supervisibility effects with crystallization of the system may take place. Another example of exotic phase transitions is a transition to quark-gluon plasma [184], which is considered at length below.

The existence of suchlike phase transitions brings about a qualitative change in the usual form of the phase diagram of baryon substance (Fig. 6.20) and results in new phase boundaries of chiral and quark-gluon transitions, which in turn may mutually overlap or even coincide [40, 208].

Color superconductivity may vanish at high hadronic densities and very low temperatures. This effect is intensively studied now by neutron star scientists. This effect may lead to the emergence of a new baryon phase named "quarkyonic".

We therefore see that investigations into the physical properties of strongly compressed baryon matter are of significant interest even in the moderate-energy range, providing the possibility of discovering new exotic states of matter. However, the aspiration for operating with the highest attainable collision energies remains the main line of work in high energy physics. Discussed in this case is the now-hypothetical possibility of reaching the short range and the Grand Unification domain [170]. At these distances the electromagnetic and weak interactions are unified even stronger in the sense that they will be described by a common interaction constant. Would the strong chromodynamic interaction be expected to join these two? In other words, that leptons and quarks at short range make up a unified group. The expectation to get a positive answer to this question relies on the fact that the three constants are not to much different from each other at a range of about 10^{-19} m show a trend for further convergence. There are theoretical models of this unification, in which these constants tend to a common value,

$$\alpha_{\mathrm{GU}} = g_{\mathrm{GU}}^2/4\pi \approx 1/40,$$

at a range of about 10^{-32} m. The characteristic Grand Unification energy (10^{16} GeV) is only three orders of magnitude than the Planck mass, whereby the gravitational interaction becomes stronger than the electroweak and strong ones. So that in this case there appear conditions for Supergrand Unification of all particles and interactions in the framework of supergravity [170].

To describe a chiral phase transition, the authors of [174] studied the melting of different crystal structures on heating under domination of pionic degrees of freedom.

6.3 Quark-Gluon Plasma

Among the wealth of interesting physical results obtained using accelerator facilities, here we discuss the production of QGP, which emerges in the deconfinement of quarks for energies ≥ 200 MeV [97, 157, 207]. The experiment scheme is as follows: in the collision of two nuclei (Fig. 6.13 [187]) their kinetic energy is

converted to the internal nucleons energy. In accordance with the predictions of quantum chromodynamics (QCD [157]) this gives rise to a so-called "color glass condensate" and subsequently, with thermalization, to a new state of matter—quark-gluon plasma—"a quark soup" [97, 157] (Fig. 6.16). Colliding in the RHIC are gold nuclei, which move at nearly the speed of light. Each collision (a miniexplosion) proceeds in several stages. Initially there emerges a short-lived expanding "fireball", which consists of gluons (green), quarks, and antiquarks, primarily of upper (top), lower (bottom), and strange (s-) (blue) quarks with a small amount of heavier charmed (c-) and beautiful (red) quarks. Eventually the fireball explodes to decay into hadrons (silvery), which are detected together with photons and other decay products. The physical properties of the quark-gluon plasma are determined from the properties of detected particles. In doing this it is assumed that the collision time suffices for substance thermalization, so that the kinetic energy has time (this is the subject of special consideration) to be converted to the internal energy of the resultant plasma.

The QGP emerging in such collisions consists of quarks, antiquarks, and gluons [91, 103, 165, 190, 235]. The masses of quarks and other fermions are shown in Fig. 6.21 [235]. This plasma is sometimes called the "oldest" form of matter, because it existed even in the first microseconds after the Big Bang (see Sect. 10.4); hadrons were formed in the course of expansion and cooling of this matter. QGP is highest in density, approximately $9–10\rho_0$ ($\rho_0 = 2.8 \cdot 10^{14}$ g/cm^3 is the nuclear density), and may emerge at the center of neutron stars, black holes, and in the collapse of ordinary stars (see Chap. 9). Undertaken for the quest for QGP were large-scale experimental programs on the collision of ultrarelativistic ions on the

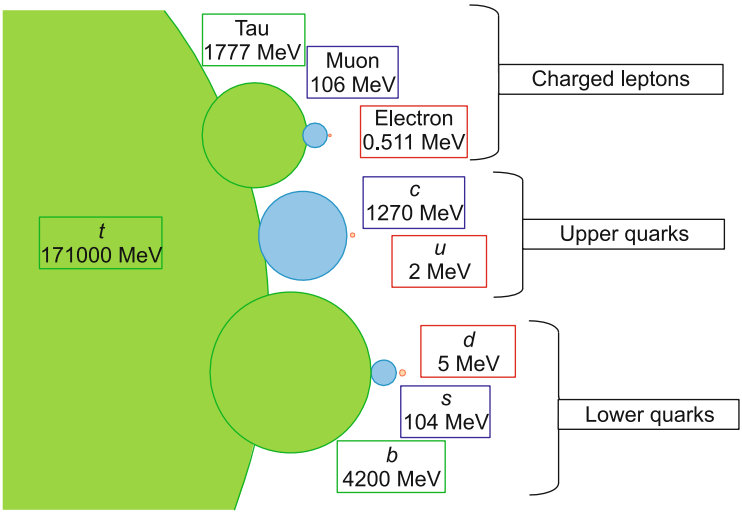

Fig. 6.21 Masses of charged SM fermions. The area of a circle is proportional to particle mass [235]

accelerators HERA, RHIC in Brookhaven, GSI in Darmstadt, and SPS, LHC in the CERN.

Even the first QGP experiments in Brookhaven (RHIC) and the CERN (SPS) revealed a greater diversity of QGP plasma behavior than assumed earlier (the gas of quarks and gluons). It was found that special attention should be paid to the energy domain $\sqrt{s_{NN}} \approx$ 2–10 GeV, where a strongly interacting (nonideal) QGP was expected to emerge. This domain will be studied in the framework of the CBM experiment of the FAIR project (for more details, see Sect. 6.7, where collisions with $E_{\text{lab}} \approx$ 5–35 AGeV and $\sqrt{s_{NN}} \approx$ 3–8.5 GeV) will be studied. Furthermore, BHL–RHIC plan to carry out experiments in a lower (down to $\sqrt{s_{NN}} \approx 5$ GeV) energy range in comparison with $\sqrt{s_{NN}} \approx 200$ GeV. Unfortunately, in this case the beam luminosity will be lower by several orders of magnitude.

In any case we are dealing with the collisions of heavy nuclei with per-nucleus-energies of the order of 100 GeV and higher in the center-of-mass system or with per-nucleus-energies of 20 TeV in the laboratory frame of reference. The conditions achievable on modern accelerators are shown in the phase diagram of nuclear matter. The domain of low temperatures and baryon densities is occupied by hadrons (nuclei and mesons) [91, 160, 165, 169, 190]. The limit of high densities (five to ten times higher than the nuclear density: $\rho_0 = 2.8 \cdot 10^{14}$ g/cm^3) and high ($T > 200$ MeV $\approx 10^{12}$ K) temperatures corresponds to quarks and gluons, which are not confined in hadrons in this case and form "quark-gluon plasma". The transition between these states may be either nonabrupt or abrupt, like a phase transition of the first kind with a critical point (Fig. 6.20). To describe the behavior of compressed baryon matter in the corresponding domain of the phase diagram, use is made of the methods of quantum chromodynamics, which itself is the object of experimental verification. The phase diagram with the inclusion of quantum-chromodynamic calculations is plotted in Fig. 6.22 [85].

QGP is a significant element of matter transformation after the origination of our Universe (see Sect. 10.4). During the first microseconds [165, 190] after the Big Bang, the temperature decreased as T[MeV] $\sim 1/t^{1/2}$, where t is time [s], so that a QGP with a temperature of several hundred MeV could exist during the first 5–10 μs after the Big Bang (for more details, see Fig. 6.23). At that time, the baryon density was not so high. As the universe expanded, the plasma became cooler, which resulted in the "hadronization" of matter and the subsequent production of pions. If a first-order transition occurred, "bubbles" of hadrons (neutrons, protons, and pions) would form inside the plasma.

QGP [113, 117, 205, 206] is a superhot and superdense form of nuclear matter with unbound quarks and gluons, which are bound inside hadrons at lower energies (Fig. 6.16).

Four types of interaction (gravitational, electromagnetic, weak, and strong) are schematically shown in Fig. 6.24; three of them enclosed in a frame are described by the Standard Model. Electromagnetic and weak interactions are unified in electroweak theory (Fig. 6.25).

We know that ordinary substances consist of atoms. An atom consists of an atomic nucleus and electrons. Atomic nuclei consist of protons and neutrons.

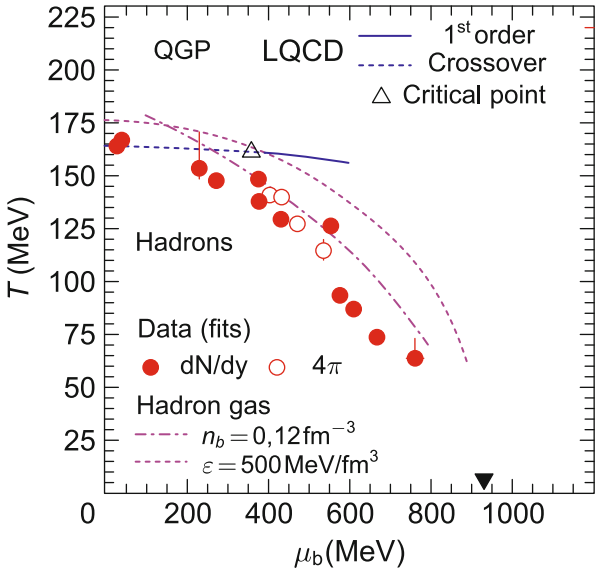

Fig. 6.22 Phase diagram of hadronic and quark-gluon matter. The *circles* stand for experiments and lattice QCD simulations. The *empty triangle* is the critical point and the full one is atomic nucleus [85]

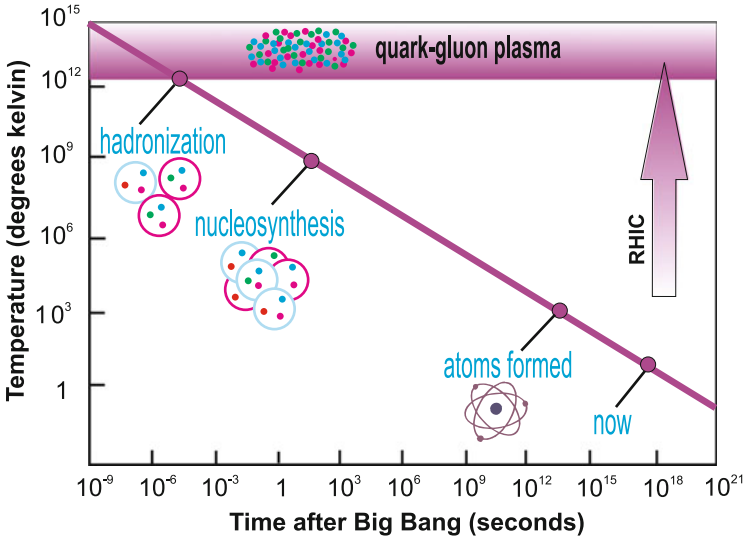

Fig. 6.23 Transformation of matter after the Big Bang. The *arrow* indicates the RHIC accelerator parameters

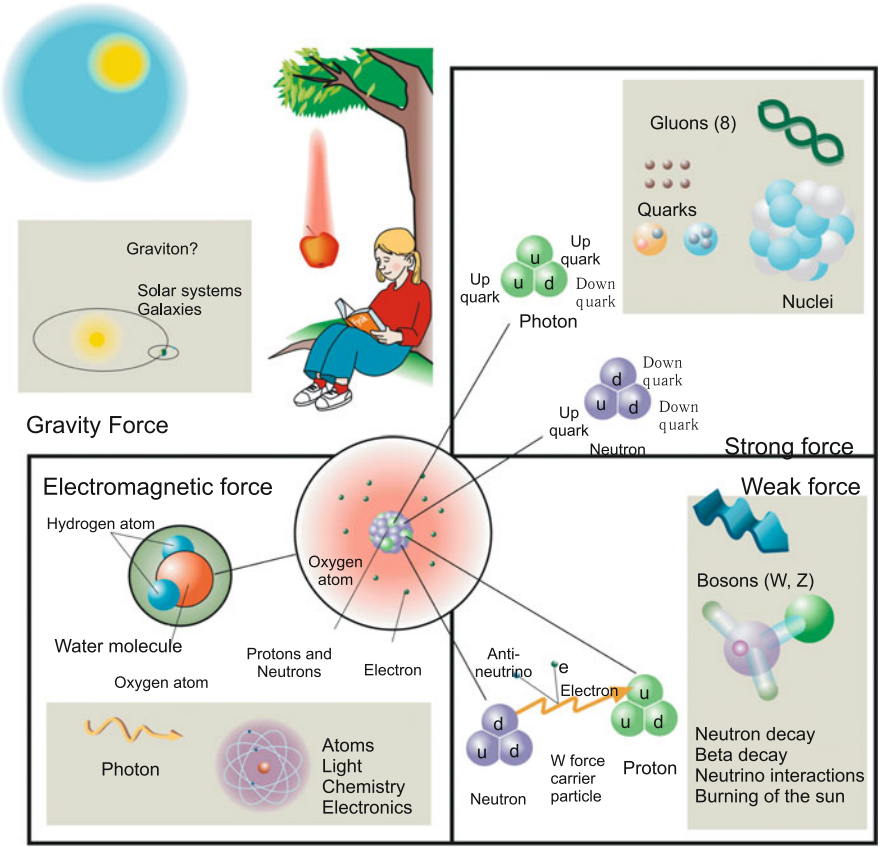

Fig. 6.24 Four types of interaction in nature and structure of matter. The domains of Standard Model operation are enclosed in *squares* [95]

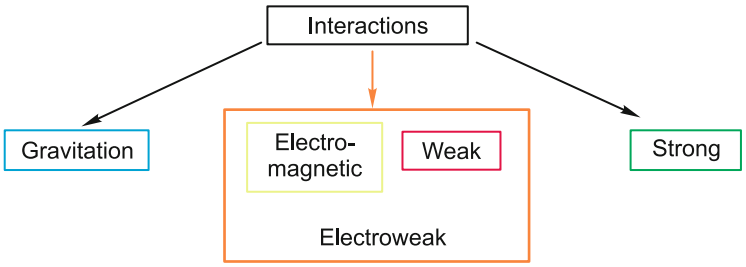

Fig. 6.25 Interaction of elementary particles [95]

Protons and neutrons in turn consist of quarks, u and d. And so the basic particles which make up ordinary substances are the electron and two types of quarks, u and d.

Quantum chromodynamics was constructed for describing strong interactions [65, 71, 207]. The basic QCD particles, unlike other particles of the Standard Model, may not be directly observed—these are quarks and gluons. Instead of them we see bound hadronic states.

One of the central ideas of chromodynamics is the principle of asymptotic freedom. At low energies the coupling constant is large; with increasing energy it becomes smaller (Fig. 6.26) and approaches zero. The large magnitude of the coupling constant at low energies does not permit changing the perturbation theory in this case. This theory works and yields good results in the high energy limit.

At low (below 1 GeV) energies, bound states and their interactions may be described by a nonperturbative lattice theory. In this case, the passage to the continuous spectrum is effected by decreasing the lattice parameter.

An important property of the principle of asymptotic freedom is that, with increasing energy (and hence the temperature), the main contribution is made not by bound hadronic states but by free quarks and gluons (the Stefan–Boltzmann limit). Therefore, there emerge two phases (hadronic and quark-gluon ones), with a phase transition between them, a critical temperature $T_c \approx 200$ MeV, and an energy density of $\approx 0.7\,\text{GeV/fm}^3$.

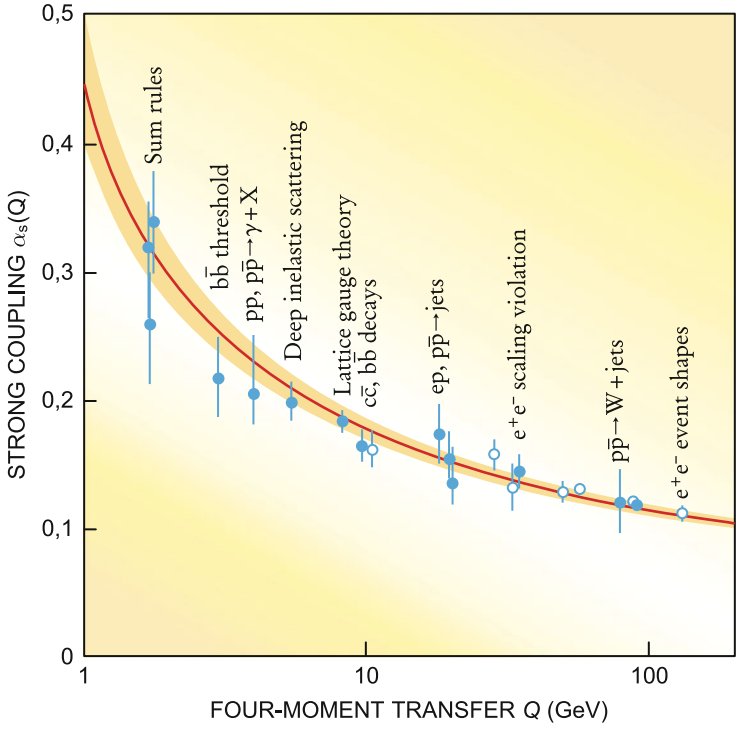

Fig. 6.26 Coupling constant as a function of energy [251]

The compression of nuclear matter leads to the same effect [65, 71, 207]. At high baryon densities the coupling constant is small, because the Fermi surface corresponds to high energies, which also results in quark deconfinement. The corresponding phase diagram of baryon matter is nontrivial in form (Figs. 6.19 and 6.20) and is the object of many papers [48, 49, 52, 55, 61, 63, 65, 71, 87, 96, 102, 118, 127, 139, 141, 142, 150, 207, 216, 220, 238, 246, 256], which describe not only the domain of the phase transition of the Ist kind, of the IInd kind, the thermodynamics and kinetics of hadronic and quark-gluon phase mixture, but also the analytical crossover under supercritical conditions.

We note (see Fig. 6.21 [235]) that, according to the principle of asymptotic freedom, fermions will weakly interact at a high density (chemical potential). Since quarks experience mutual attraction, they will make up Cooper pairs to give rise to color superconductivity [71] (see Fig. 6.20).

In the Standard Model (Figs. 6.27 and 6.28), which provides a complete description of the modern notions of particle physics, the number of quark types is equal to six. Additional quarks are denoted as s, c, b, and t. The reason why we do not discover them in ordinary substances is that these quarks are unstable under ordinary conditions. The matter is [235] that the effective coupling constant in quantum chromodynamics increases with a decrease in energy (see Fig. 6.26), with the result that the particles which experience strong interaction cannot exist in the free form and are present in bound states (hadrons). A physical explanation may consist in the screening of point sources by virtual pairs produced in a vacuum. When we approach a charge source, we penetrate its surrounding screening cloud. In this case, the effective charge becomes higher due to the absence of screening. This brings up an analogy with the passage through the electron cloud surrounding an atomic nucleus. The difference is that electrons are real particles on the mass surface. Electron screening is in essence a classical effect. An increase in renormalization group charge is associated with the lowest contribution of virtual particles and is a purely quantum effect. The binding forces responsible for quark confinement arise

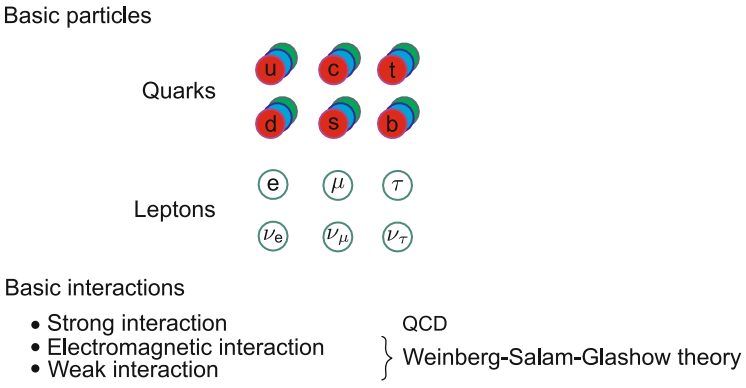

Fig. 6.27 Components of the Standard Model [125]

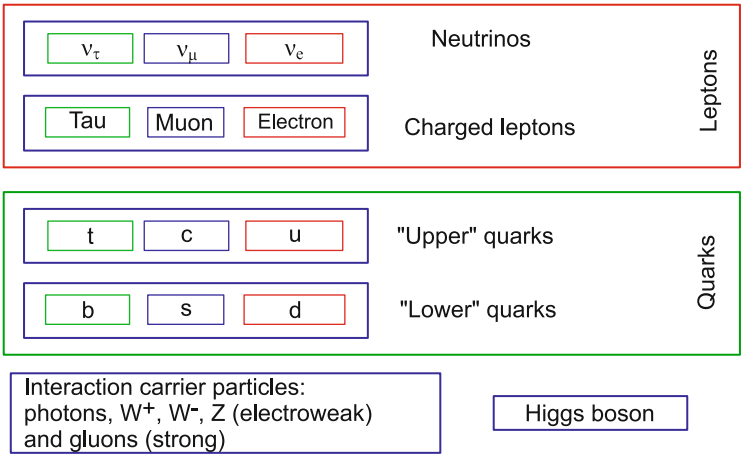

Fig. 6.28 Elementary particles described by the Standard Model [235]

Table 6.1 Problems of the Standard Model

	Problem
Matter structure	1. Quark-gluon matter
	2. Going beyond the framework of the Standard Model (Higgs boson)
	3. Supersymmetry, grand unification, additional dimensions
	4. Neutrino properties
Properties of the Universe	5. Baryon asymmetry
	6. Dark matter
	7. Nature of cosmic rays

due to exchange of rather soft gluons. Like quarks, the electron is a member of the family of six components called leptons. Among these leptons are three types of neutrinos.

Basic interactions are another important constituent of the Standard Model. Quarks and leptons experience three types of forces. Strong interactions are described by quantum chromodynamics, and electromagnetic and weak interactions by the Weinberg–Salam–Glashow theory. All three interaction types are described in the framework of special field theories, which are called gauge theories. Several problems associated with the Standard Model are indicated in Table 6.1.

The characteristics of quarks (which possess a fractional charge), which make up hadrons, are collected in Table 6.2. For instance:

$$\text{proton} = u + u + d$$

$$\text{neutron} = u + d + d$$

$$\pi^+ = u + \overline{d}, \text{ etc.}$$

Table 6.2 Quark characteristics

Designation	Type of quark and its flavor	Charge ($\|e\|$)	Mass (MeV)
u	*up*—up[a]	$-2/3$	5
d	*down*—down[a]	$-1/3$	10
s	*strange*—strange (strangeness, $S = -1$)	$-1/3$	150
c	*charm*—charmed (charm, $C = +1$)	$-2/3$	1300
b	*beauty*—beautiful (beauty, $B = +1$)	$-1/3$	4200
t	*top*—top[b], *truth*—truth	$-2/3$	175,000

[a] There is no quark flavor and the corresponding additive quantum number is not used
[b] There is no conventional flavor name

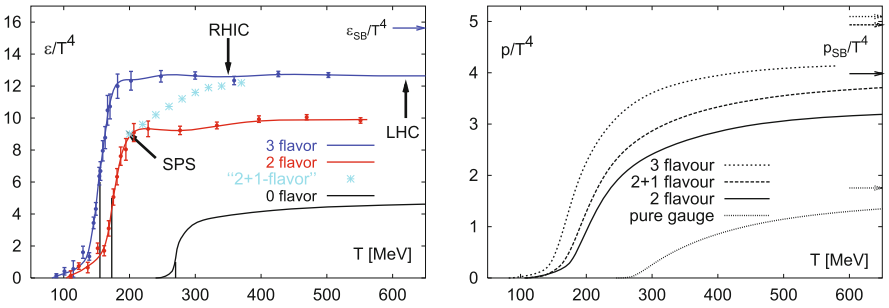

Fig. 6.29 QCD calculations of the temperature dependence of the energy density (*left*) and pressure (*right*) [97]. The most realistic case corresponds to flavor 2+1. (The subscript SB stands for Stefan–Boltzmann.)

The existence of QGP follows from the property of asymptotic freedom of QCD [36, 46, 53, 84], which yields a value of 1–10 GeV/fm for the corresponding transition energy density, which is close to the energy density inside a proton and exceeds the nuclear energy density by an order of magnitude. Detailed numerical simulations yield the critical conditions for the emergence of QGP: $T_c \approx$ 150–200 MeV $\approx$ (1.8–2.4) $\cdot$ 10^{12} K (Fig. 6.29)—100,000 times higher than the temperature at the solar center—and the critical energy density $e_{cr} \approx 0.7\,\text{GeV/fm}^3$.

The emergence of this plasma manifests itself as an increase in the number of degrees of freedom (Fig. 6.30 [110]): from 3 for hadrons to 8 for gluons multiplied by 2 spin ones, plus 2–3 for light flavors of quarks, which in turn have 2 spins and 3 colors. Therefore, according to quantum electrodynamics, quarks possess 24–26 degrees of freedom; excited in quark-gluon plasma for $T \approx (1\text{–}3)T_c$ are 40–50 degrees of freedom versus 3 for a pion gas at low temperatures, $T < T_c$. Since the energy density, pressure and entropy are roughly proportional to the excited degrees of freedom of a system, an abrupt change of these thermodynamic parameters in a narrow temperature range about T_c accounts for a large (several-fold) difference in energy (Fig. 6.29) between ordinary nuclear matter and QGP.

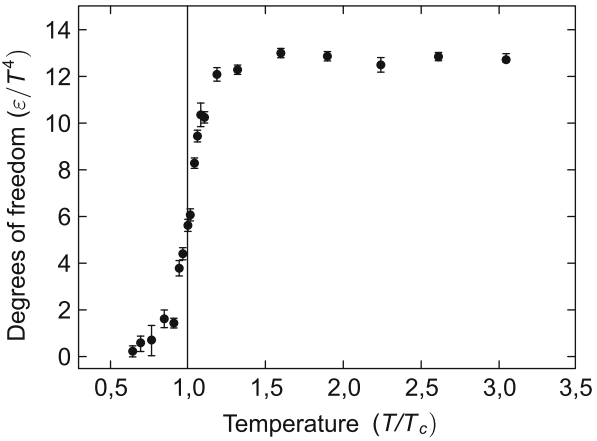

Fig. 6.30 Number of thermally active degrees of freedom of a system for a temperature T is proportional to its energy ε density divided by T^4. Depicted in the drawing is the expected temperature dependence ε/T^4 for extended hadronic matter calculated under a lattice approximation in the framework of quantum chromodynamics. The ε/T^4 ratio is given in natural units (The Planck and Boltzmann constants are equal to 1 in this case) and is dimensionless. Plotted on the abscissa is the ratio between the temperature T and the critical temperature T_c (roughly 170 MeV), whereby ε/T^4 rises most sharply, testifying to the transition from a hadronic gas to a quark-gluon plasma [110]

In view of the aforesaid, the equation of an ideal, $g \to 0$, QGP is of the form (Gyulassy, M.: Quark gluon plasmas: femto cosmology 2008)

$$P_{\mathrm{SB}}^{\mathrm{QCD}}(T) = (\underbrace{2_s \times 8_c}_{\text{gluons}} + \frac{7}{8} \times \underbrace{2_c \times 3_c \times 2_{q\bar{q}} \times n_f}_{\text{quarks}}) \frac{\pi^2 T^4}{90} - \underbrace{B}_{\text{vac}}.$$

For hadronic matter (Gyulassy, M.: Quark gluon plasmas: femto cosmology 2008)

$$P^{\mathrm{H}}(T) = (\underbrace{3_{\mathrm{ISO}}}_{\text{pions}} + \underbrace{O(e^{-M/T})}_{\rho,\omega,\ldots}) \frac{\pi^2 T^4}{90}.$$

A comparison of these expressions defines the critical QGP transition temperature T_{c}.

Like our customary "electromagnetic" plasma (EMP), the QGP may be ideal for $T \gg T_{\mathrm{c}}$ and nonideal for $T \approx (1\text{–}3)T_{\mathrm{c}}$. The corresponding nonideality parameter—the ratio between the interparticle interaction energy and the kinetic energy—in this case is of the form $\Gamma = 2Cg^2/4\pi aT = 1.5\text{–}5$, where C is the Casimir invariant ($C = 4/3$ for quarks and $C = 3$ for gluons), the interparticle distance $a \approx 1/T \approx 0.5\,\mathrm{fm}$, $T = 200\,\mathrm{eV}$, and the strong interaction constant $g \approx 2$. The factor 2 in the numerator takes into account magnetic interaction, which is of the same order of magnitude as the Coulomb interaction in the relativistic case.

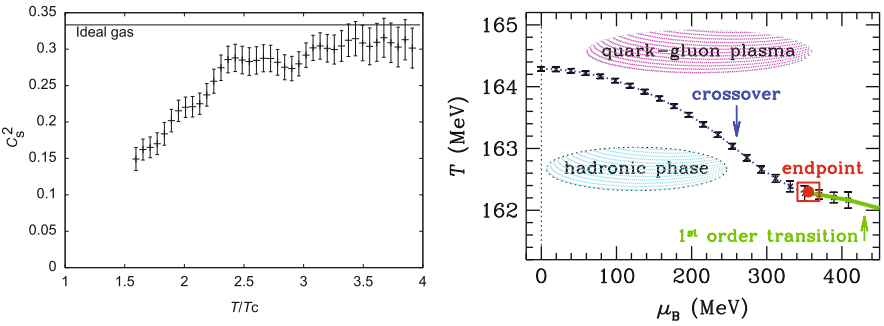

Fig. 6.31 Features of the equation of state of a QGP [97]. *Left*: Temperature dependence of the speed of sound. *Right*: Phase boundary and critical point according to [56, 71]

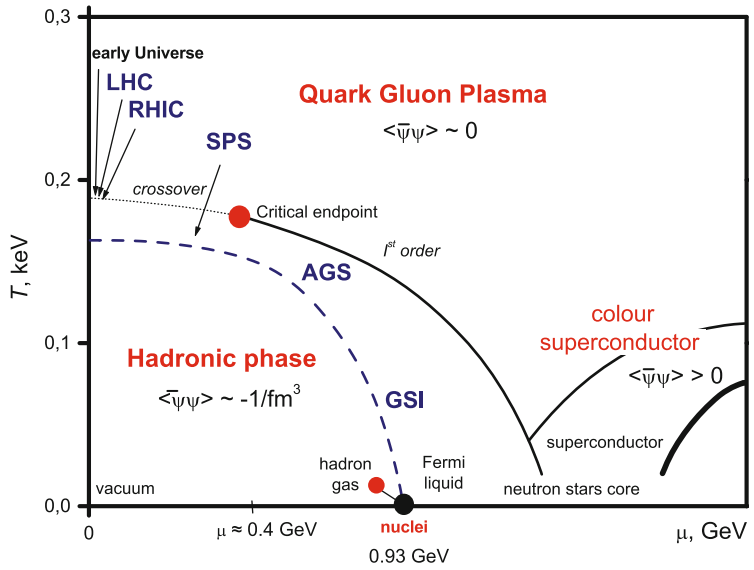

Fig. 6.32 Phase diagram of QGP [35] (Gyulassy, M.: Quark gluon plasmas: femto cosmology 2008)

At present it is hard to tell unambiguously whether the transition to a QGP is a true thermodynamic phase transition with an energy density jump or a sharp and yet continuous transition [97]. Conceivably (Fig. 6.31 [97]) for low baryon densities μ_B this might be a continuous transition and for high μ_B a phase transition of the first kind (Fig. 6.32). In any case, the theory [97] predicts a low value for the velocity of sound in the transition region (Figs. 6.31 and 6.29), which is reflected in the hydrodynamic anomalies accessible to observations in the relativistic collisions of heavy nuclei. The specified features of adiabatic compressibility of the QGP testify to a "softer" equation of state for $T \approx T_c$ and a "stiffer" one at high temperatures as well as for $T \leqslant T_c$. In the limit $T \ll T_c$, the equation of

state of hadronic matter becomes "softer", although in this case the uncertainty is quite high and the description of this matter by quantum electrodynamics (QED) techniques encounters serious problems. Proceeding from lattice simulations in [50] a conclusion is drawn about the emergence of magnetic vortices in a QGP.

A picture of a relativistic heavy nuclei collision is shown in Figs. 6.33, 6.34, and 6.35. In this case, hundreds and thousands of high energy particles (Figs. 6.34

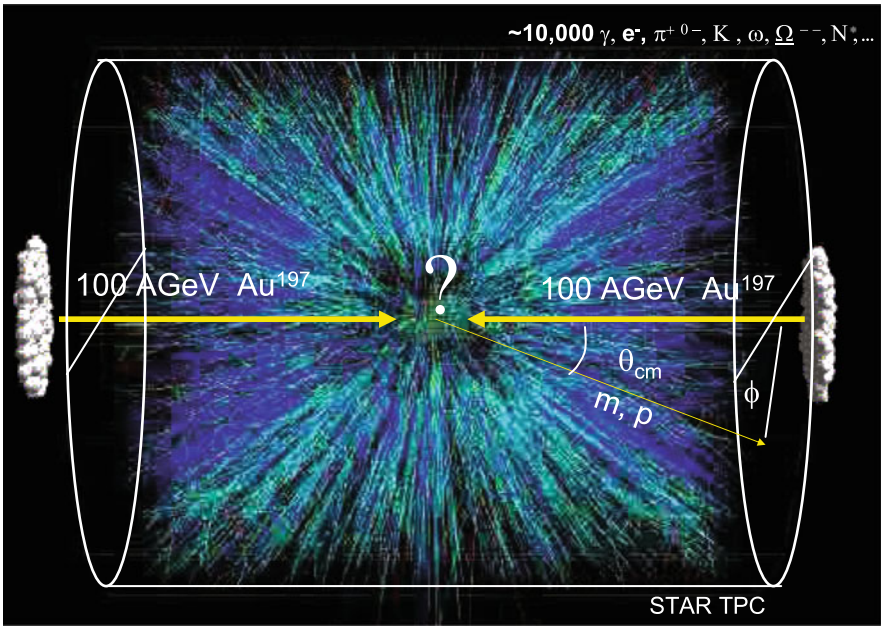

Fig. 6.33 A relativistic hadron collision: "burning of the vacuum" [140]

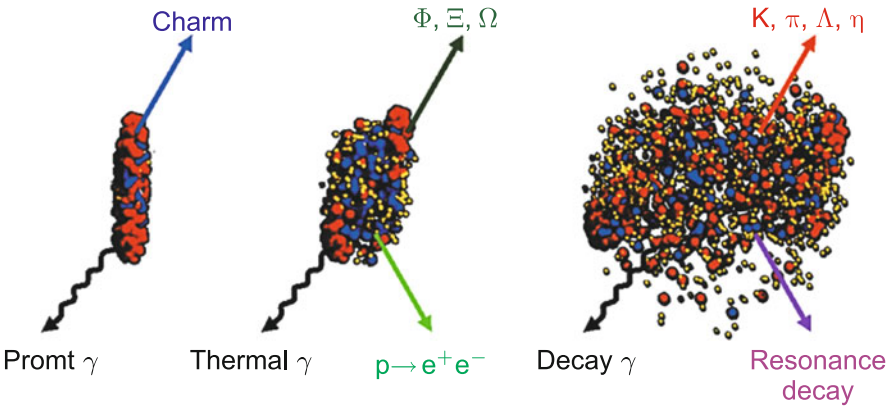

Fig. 6.34 Schematic representation of uranium nuclear collision for 25 AGeV (laboratory frame) at points in time: early in the collision, high-density phase, and expansion phase. As a result, about 1000 particles are ejected, most of them being pions [85]

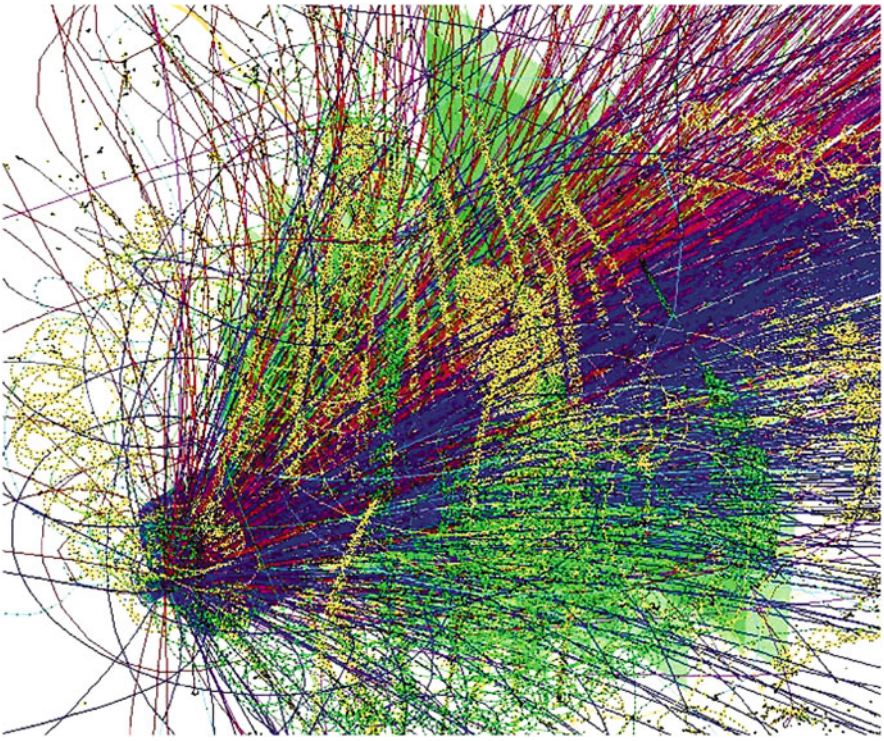

Fig. 6.35 Trajectories of the particles produced in the collision of gold nuclei with an energy of 25 AGeV [85]

and 6.35) are produced in every collision, most of them being mesons. The detectors' task is to select and analyze the requisite events.

Under the conditions of the RHIC experiment, the longitudinal Lorentzian compression of the size of colliding nuclei is on the order of 100. The characteristic volume of the U–U collision domain ($\approx$3000 fm^3) contains $\approx$10,000 quarks and gluons, while the characteristic collision time is $\tau_0 \approx 0.2$–$2\,\text{fm}/c \approx (5\text{–}50)\times 10^{-25}$ s. That is why some of high-energy processes supposedly take place in the expanding substance, when the nuclear bunches have already passed through each other.

These nonequilibrium effects become stronger with increase in ion collision velocity and are a limiting factor for studying compressed baryon matter (for more details, see Sects. 6.6–6.8). In particular, the characteristic atom-atom collision time, $\tau \sim 2R/\gamma$, is $\approx$1.5 fm/c for SPS accelerator and $\approx$0.14 fm/c for the RHIC.

Gyulassy and McLerran [97] called attention to the fact that the production of fast particles in the expanding plasma after nuclear collisions is similar to the production of new forms of matter after the Big Bang (Sect. 10.4). However, the difference is that the expansion in nuclear collisions is one-dimensional rather

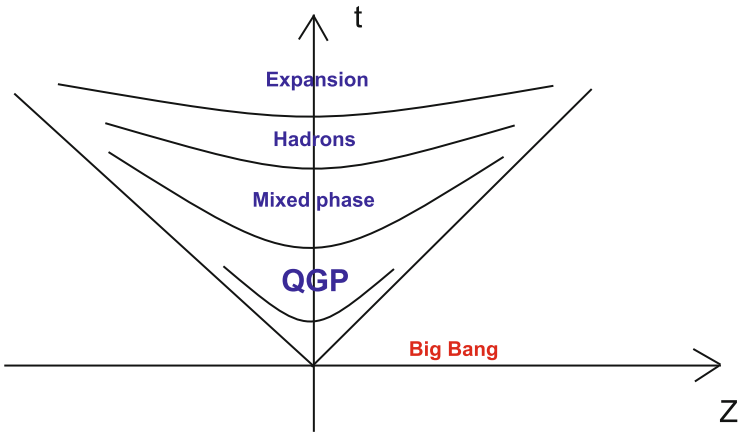

Fig. 6.36 Spatiotemporal matter evolution after a collision [157]

than three-dimensional as in cosmology. The spatiotemporal evolution of matter following a relativistic collision is shown in Fig. 6.36.

During the collision, as the nuclear substance expands and cools down, the emergent quarks and gluons are thermalized (the time $\tau_{eq} \leqslant 1\,\text{fm}/c \approx 3 \times 10^{-24}\,\text{s}$) and may reach local thermodynamic equilibrium during the plasma lifetime $\tau_0 \approx (1\text{–}2)R/c \approx 10\,\text{fm}/c$. In this case, the medium will be set in hydrodynamic motion; recording this may yield experimental information about the properties of hadronic or quark–gluon matter as well as about the limit of their back and forth transition, which should occur at an energy density of $\approx 1\,\text{GeV/fm}^3$ according to QED.

In any case, it is believed [110] that hydrodynamics in RHIC experiments begins to work after a time period of $2 \cdot 10^{-24}\,\text{s}$, which is much shorter than the particle transit time through the nucleus.

The idea of applying hydrodynamic equations to describe relativistic ion collisions belongs to L.D. Landau (1953). It proved to be highly fruitful for the calculation of a broad class of collisional experiments in a wide energy range [126]. Under this approximation the substance motion at high densities is described by the differential equations of mass, momentum, and energy conservation, which are supplemented by the conservation laws for charge numbers (total baryon charge, electric charge, and strangeness). Also employed are semiempirical equations of state of nuclear matter (Figs. 6.37 and 6.38) [48, 49, 49, 52, 55, 61, 63, 75, 87, 96, 102, 118, 118, 126, 127, 139, 141, 142, 150, 216, 220, 238, 246, 256].

It is evident that one of the central issues relating to the validity of hydrodynamic approximation is the question of whether the nuclear matter thermalizes in ultrarelativistic collisions.

Figure 6.39 [97] serves to illustrate the characteristic energy density in nuclear collisions as a function of time. An analysis of the collision and expansion dynamics shows [97] that the transition from a relatively slow one-dimensional expansion to a faster three-dimensional expansion occurs in a characteristic time $\approx 0.3\,\text{fm}/c$.

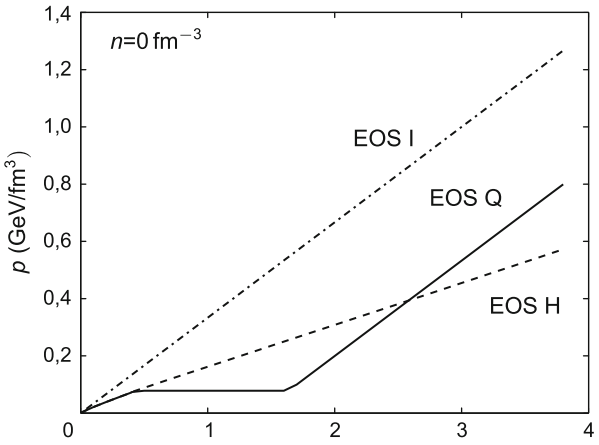

Fig. 6.37 Examples of the equation of state of a resonance hadronic gas (EOS H), ideal gas of massless particles (EOS I), and the equation of state with a phase transition (EOS Q) [126]

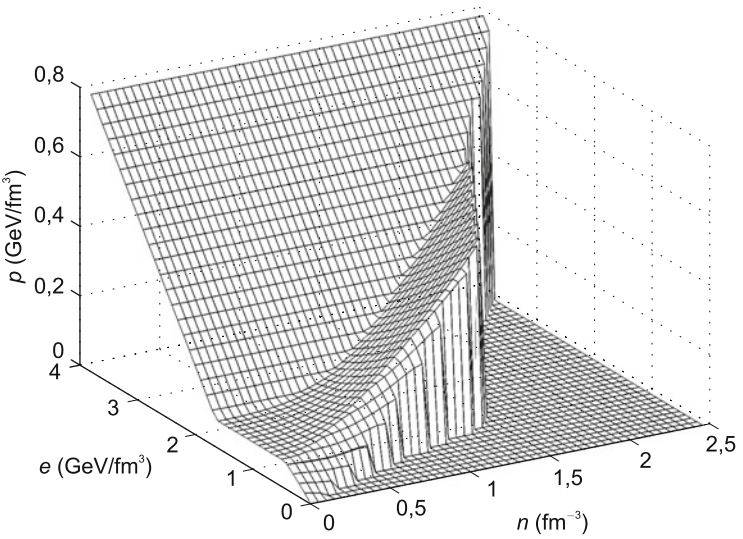

Fig. 6.38 Equation of state (EOS Q) with a quark-hadron phase transition. Plotted in the drawing is the pressure as a function of energy e and partial baryon density n. For each value of n there exists an energy density minimum $e_{\min}(n)$, to which there corresponds a pressure $p_{\min}(e_{\min}, n)$. Below the $e_{\min}$ level the pressure was "manually" set equal to zero

The upper bound of the dark band in Fig. 6.39 corresponds to the assumption that the system is in thermodynamic equilibrium and is an ideal massless gas, while the lower one corresponds to nonequilibrium "frozen" conditions. By the point in time 3 fm/c the plasma is a mixture of quarks, gluons, and hadrons, and for 10 fm/c the quarks and the gluons recombine in hadrons. The lower bound of attainable energy

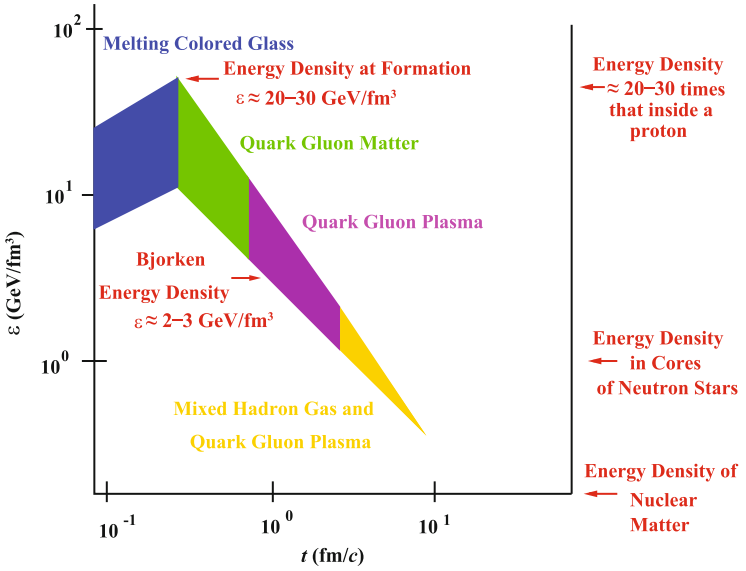

Fig. 6.39 Characteristic energy density in the collision of nuclei as a function of interaction time [97]

density is realized for $t \approx 1\,\text{fm}/c$ and the upper limit (massless gas) for $0.3\,\text{fm}/c$. The general estimate of energy density is of the form [97]

$$(2\text{–}3)\,\text{GeV/fm}^3 \leq E \leq (20\text{–}30)\,\text{GeV/fm}^3.$$

For comparison, the energy density in neutron stars (Sect. 9.3) amounts to $\approx 1\,\text{GeV/fm}^3$.

The emergence of a new form of matter—QGP—should be accompanied by qualitatively new physical phenomena, which should manifest themselves in experiments.

First, the emergence of new degrees of freedom in the plasma must be reflected in the collision and expansion relativistic hydrodynamics, which in turn is described by the equations of motion of a viscous fluid in the conditions of local thermodynamic equilibrium. This formalism is simplified for a nonviscous fluid (the Euler equation), while the experimental manifestation of collective (viscous) effects (see Sect. 6.4) may be indicative of plasma effects.

The emergence of QGP may show up not only in the properties of the equation of state, but also in the behavior of viscosity in the hydrodynamic motion.

The results of such comparisons for the azimuthal components of π, K, p, and Λ flow in Au + Au collisions (200 AGeV) are given in Fig. 6.40 [15, 16, 18, 21, 215]. One can see that simulations and measurements are in good agreement up to energies of about 1 GeV/fm, which fails at higher energies. This disagreement is attributed to the emergence of QGP. The agreement between simulations and experiments is improved by including the lowering of sound velocity in the vicinity

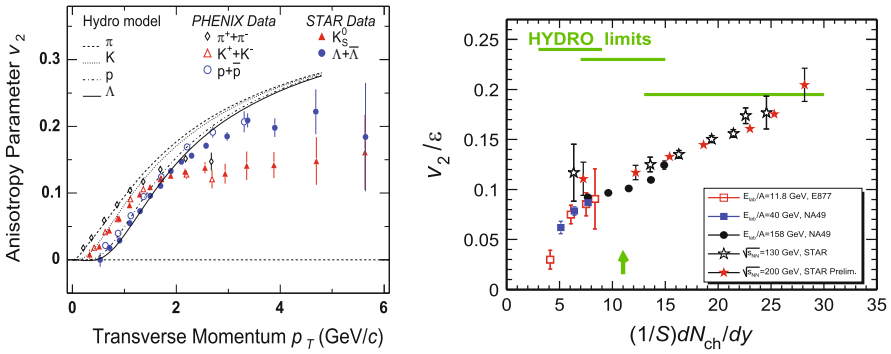

Fig. 6.40 Experimental manifestation of a QGP [97]. *Left*: STAR [15, 16, 215] and PHENIX [18] measurement data. *Right*: Data from [21]

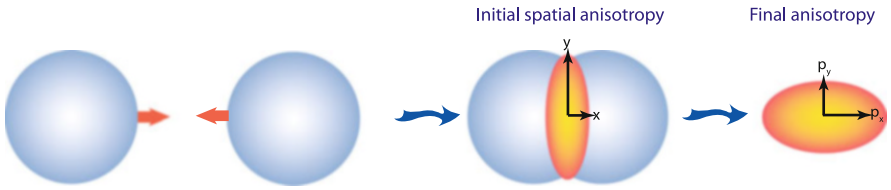

Fig. 6.41 Relativistic nuclear collision, generation of elliptical flows. The high-energy domain is elliptical in shape, so that the spatial anisotropy generates the anisotropy of momenta of the expanding medium [171]

of $T \approx T_c$ and the corresponding "softening" of the equation of state, which are caused by the emergence of this plasma.

Apart from the special features in the equation of state, the emergence of QGP may manifest itself in the behavior of shear viscosity η in hydrodynamic motion:

$$T^{ij}_{diss} = \eta \left(\frac{\partial \upsilon_i}{\partial x^j} + \frac{\partial \upsilon_j}{\partial x^i} - \frac{2}{3} \delta_{ij} \nabla \cdot \upsilon \right) + \zeta \delta_{ij} \nabla \cdot \upsilon.$$

It turns out that QGP behaves not as a gas of noninteracting particles but as a strongly interacting liquid with a vanishingly low viscosity, which, however, has a lower bound, $\frac{\eta}{s} \gtrsim \frac{1}{4\pi} \frac{\hbar}{k}$, which follows from a highly general string theory (see the next Section).

It is precisely these effects that account for the underestimation of elliptical expansion velocities in central (Fig. 6.41) and off-center (Figs. 6.42 and 6.43) collisions, which were measured on the SPS, in comparison with simulations (this underestimation is unavoidable in the framework of three-dimensional (3+1D) hydrodynamics [126]) and a lowering of this departure with increase in impact parameter [97], which is due to a lower efficiency of pressure transfer to the hydrodynamic flow by hadrons in comparison with plasma. In any case, ideally nonviscous flow simulations reliant on Euler equations [35] provide a better

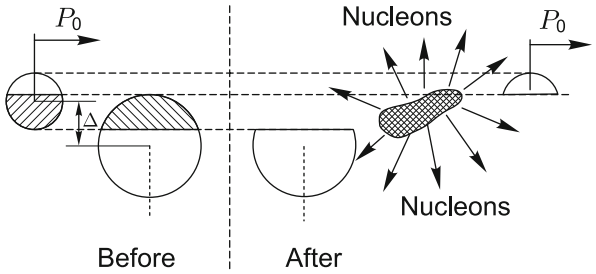

Fig. 6.42 Schematic representation of off-center nuclear collisions [85]

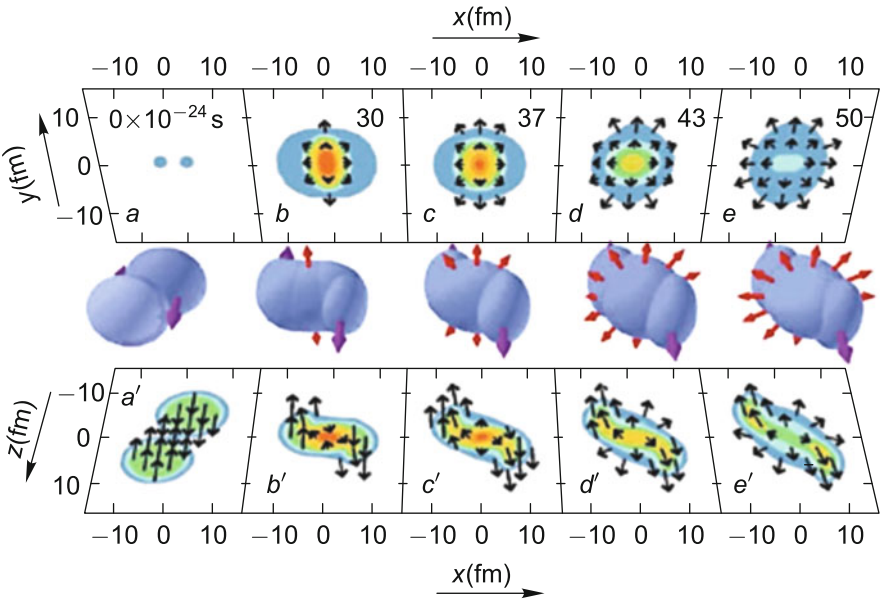

Fig. 6.43 Off-center (b=2 fm) Au+Au collision dynamics for 2 AGeV. The velocity of motion is depicted on the XZ plane and the substance density on the XY plane [85]

agreement with experiments (Fig. 6.44) than the simulations using equations with viscous dissipation.

Interestingly, for moderate energies the RHIC experiments display anomalies in QGP dissipation and yield effective viscosity values that are up to ten times lower than one would expect from the models of weakly nonideal Debye plasma. This is thought to be [97] due to plasma nonideality effects (Figs. 6.59 and 6.60).

It is a striking fact that the hottest and densest matter of that occurring in Nature exceeds all known liquids in degree of noideality, which is characterized by the viscosity of the medium. String theory and QCD calculations yield a ten times lower viscosity value than that of superfluid helium [187]. The issue of viscosity and nonideality is highly general in nature and will be considered in the next section.

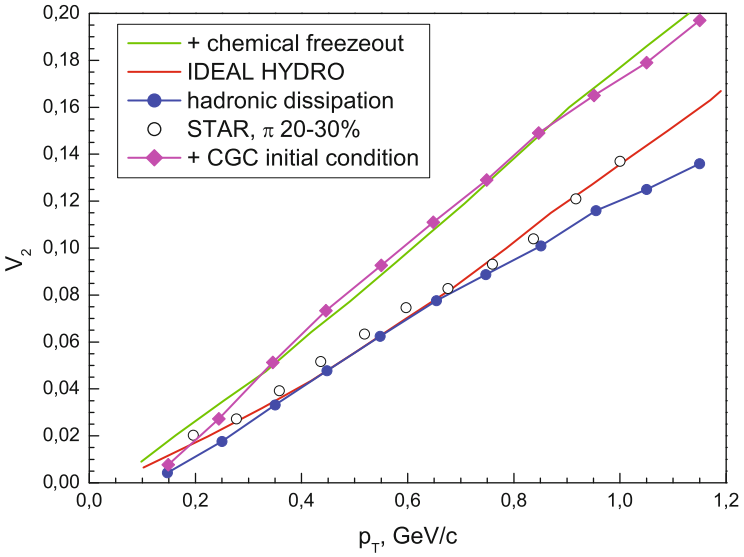

Fig. 6.44 Comparison of measured (*circles*) and calculated expansion velocities in nuclear collisions [35]

An experimental study of the properties of matter in the interaction domain calls for studying the energy loss of different probe partons (quarks, gluons) that traverse it [65]. This is similar to studying the energy loss of electrons that pass through ordinary amorphous media. Recent experimental results obtained on the SPS (Super Proton Synchrotron) and the RHIC (Relativistic Heavy Ion Collider) show clearly that the collective properties of the medium are determinative for heavy ion collisions. The radiative properties of partons, the energy spectra of resultant hadrons, and their correlations change in comparison with those in proton-proton collisions. Induced coherent radiation reflects the collective response of the medium to the partons that penetrate it. In the medium itself there occurs collective motion. The hadrochemical composition of the particles produced is also changed. Productive are both micro- and macroscopic approaches to the theoretical description of the observed effects in the framework of QCD. Mechanical and thermodynamic properties of the medium are studied in the framework of hydrodynamic description. Below we describe both of these approaches and discuss the corresponding experimental data.

Important information about the properties of high-density matter is carried by the measured spectra of charged hadrons produced in collisions. For $p_T \approx 3$ GeV the shape of transverse-momentum charged-hadron spectra changes from an exponential dependence to a power-law one in accordance with the predictions of perturbative QCD. RHIC single-particle distribution data for central Au–Au collisions for an energy of 200 GeV reveal a strong p_T-independent suppression of the hadron fraction with high transverse momenta ($p_T > 4$ GeV). The measurements

cover the interval in p_T up to a value of 20 GeV. The measured large deficit of particles with a high transverse momentum is indicative of partons' energy loss in the medium. It corresponds to the effect of so-called jet suppression (quenching), which manifests itself in a softening of the hadronic spectrum obtained from in-medium partons in comparison with the spectrum in a vacuum. Therefore, the suppression factor is a powerful means for determining the density of the medium.

We see that the effects involving suppression of the jets produced in the relativistic nuclear collisions contain information about the properties of shock-compressed matter [98, 99, 245] and about the emergence of QGP. By the order of magnitude this suppression is determined by the radiation loss of gluons, while the contribution of elastic loss is not large.

The results of such "tomography" for PHENIX experiments are shown in the right part of Fig. 6.45 [97, 242]; they suggest that the reduced initial gluon density must be equal to $dN^g/dy \approx 1000 \pm 200$ to account for the observed jet suppression. These values are in reasonable agreement with another set of independent measurements [97]:

(a) with the values of initial entropy determined from the plasma expansion after the collision,
(b) with the initial plasma parameters that follow from the hydrodynamic simulations of "elliptical" flows,
(c) with density variation rates calculated by the methods of quantum electrodynamics.

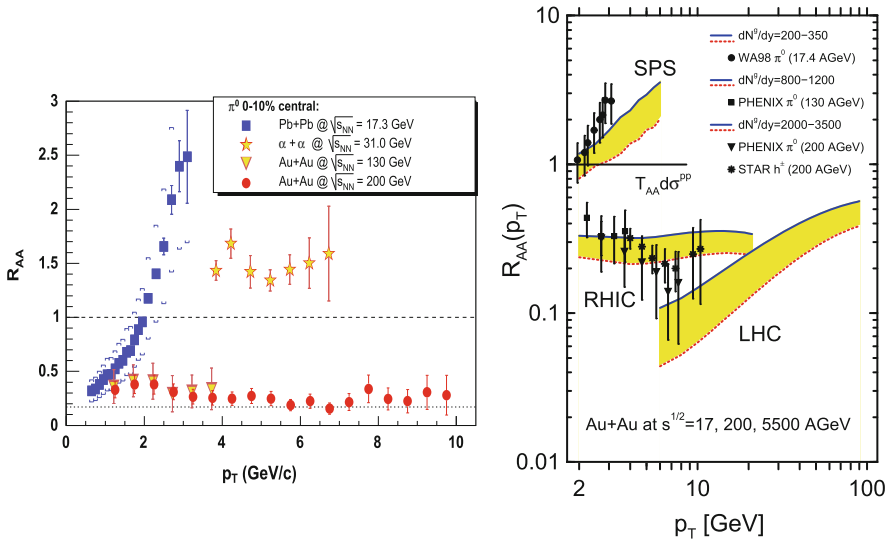

Fig. 6.45 *Left*: π^0 flux quenching data recorded at PHENIX and RHIC in comparison with different ISR and SPS observations (both at CERN). *Right*: Factor $R_{AA} = dN_{AA}/T_{aa}(b)d\sigma_{pp}$ measured at SPS, RHIC, and LHC in comparison with radiative energy loss models [97, 242]

These data sets permit finding the initial energy density in relativistic collisions:

$$E_0 = E(1/\rho_0) \approx \rho_0^2/\pi R^2 \cdot dN^g/dy \approx 20\,\text{GeV/fm}^3 \approx 100E_a,$$

for the characteristic gluon momentum ($P_0 \approx$ 1.0–1.4 GeV), which in turn defines the formation time, $\hbar/P_0 \approx 0.2\,\text{fm}/c$, of the primary nonequilibrium QGP. Under these conditions, local thermodynamic equilibrium, which is necessary for the application of hydrodynamics, sets in for

$$\tau_{eq} \approx (1\text{–}3)B/P_0 < 0.6\,\text{fm}/c.$$

By this point in time the temperature becomes

$$T(\tau_{eq}) \approx (\varepsilon_0/(1\text{–}3)\cdot 12)^{1/4} \approx 2T_c.$$

According to one model [97], for $P_0 \approx$ 2–2.2 GeV the number of minijets must be of the order of 1000.

Studying the correlation between secondary particles by recording correlated binary jets in nuclear collisions yields more comprehensive data about the plasma properties (Fig. 6.46). It was shown [65] that both two- and three-particle correlations exhibit two oppositely directed jet-like peaks (two-jet transitions). Theoretically, to a first approximation the jets are treated as the residual manifestation of the hard scattering of quarks and gluons. The consistency of jet characteristics obtained under different conditions (central and peripheral collisions, protons and gold)are considered [97] as a powerful argument in favor of the applicability of quantum chromodynamic techniques and QGP formation.

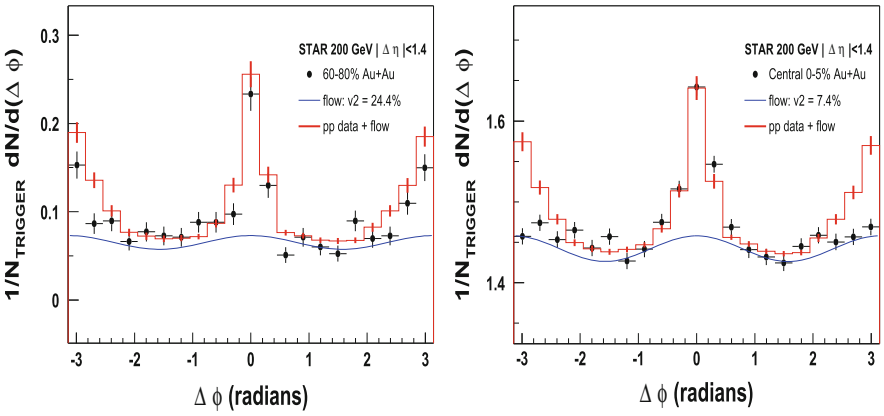

Fig. 6.46 Strongly correlated backward jets in STAR and RHIC experiments [17, 97, 111] in Au+Au collisions (at the *left*) are compared with p+p collisions and with off-center collisions with monojets in head-on Au+Au collisions (at the *right*)

Therefore, the jet quenching effects observed in nuclear collisions allow the energy density of nuclear matter to be determined and conclusions to be drawn about a strong collective interaction (nonideality) of this plasma, proceeding from an analysis of the energy losses of the jets in their motion through the QGP.

Many-particle correlations and totally (calorimetrically) reconstructed jets are the main focus of the effort to study proton-proton and nuclear-nuclear collisions. The first results for totally reconstructed jets in proton-proton, Cu–Cu, and Au–Au collisions show clearly the jet broadening in the quark-gluon medium.

Another manifestation of QGP was the observation of entirely new event topologies in nuclear-nuclear collisions which were termed "the ridge" and "the double-humped event" [65]. In central collision events the trigger jet is located on a pedestal (the ridge), which spans a broad pseudorapidity interval and falls off rapidly in the azimuthal direction. The ridge existence is independent of the presence of the jet peak. The characteristics of this peak coincide with the general characteristic of the particles produced, but the particle spectrum in the ridge is somewhat harder. The emergence of the ridge is unrelated to particles in jet configurations. In peripheral collisions and for high p_T of the trigger particle the ridge vanishes. Both the large pseudorapidity length of the ridge and the presence of large broad clusters revealed by two-particle correlations are indicative of the importance of collective effects.

The azimuthal $\delta\phi = \pi$ peak in the antitrigger (away-side) direction, which is observed in proton-proton collisions, is replaced with a broad antitrigger structure in Au–Au collisions. In the majority of central collision events, clearly discernable are two symmetric maxima (humps) for $\delta\phi = \pi \pm 1.1$. Their position is hardly dependent on the transverse momenta of the trigger and associated particles. The two humps supposedly merge into one broad hump for high p_T of the trigger ($6 < p_T^{\text{trig}} < 10\,\text{GeV}$). This signifies that the antitrigger jet hidden between the two humps becomes visible again—as it must be in the case of a medium of finite size, where a high-p_T parton escapes from the medium and forms a jet. The jets generated by heavy quarks possess similar qualitative properties (though measured with a lower statistics). These features are observed both for two- and three-particle correlations. The existence of these features is undoubtedly associated with collective properties of the medium.

Today, the observational manifestations of QGP (Gyulassy, M.: Quark gluon plasmas: femto cosmology 2008) that are being actively analyzed include

- "Barometric" effects: from the parameters of collective flows (elliptic, longitudinal, radial)
- "Thermodynamic" effects: photons, leptonic pairs, vector mesons
- "Critical" effects: hadronic density fluctuations
- "Tomography": short jets, heavy quark fluxes
- "Exotics": multiquark states, femtometer-dimensional "fullerenes"

Among the interesting hydrodynamic phenomena, special mention should be made of Stöcker's elegant and beautiful idea [221] of the production of conic Mach shock waves (Fig. 6.47), whose properties permit the characteristics of compressed nuclear matter to be judged.

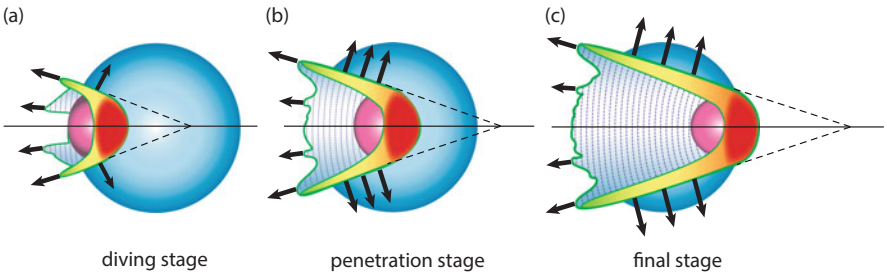

Fig. 6.47 Formation of Mach shock waves in nuclear matter [221] in the collision of a light nucleus (at the *left*) with a "heavy" one

Following [65] in the subsequent discussion, we consider a microscopic approach to the description of QGP. Consistent microscopic description of all processes with participation of several thousand generated particles in the entire phase space in the framework of quantum chromodynamics (QCD) is unrealistic today. This description may be applied to relatively infrequent subprocesses with high p_T, in which the QCD coupling constant is small enough. The description of essentially collective effects is better approached by a macroscopic (including statistical) treatment.

And yet, by applying general QCD principles it is possible to deduce the general features of fields' evolution and reveal typical correlation patterns in heavy-ion collisions. In this context the present-day paradigm, which is discussed below, describes the transition from a color glass condensate (CGC) to a plasma and subsequently to the quark-gluon plasma and the following hadronization [65].

The main source of experimental information about the properties of quark-gluon medium at these stages is the energy loss of partons.

A concept introduced to describe multiple scattering events in hadronic and nuclear collisions in the framework of QCD is the notion of color glass condensate (CGC)—a universal form of matter which controls the high-energy limit of all strong interactions and is the part of the hadron wave function.

Multiparticle production in QCD is due to the partons with short x in nuclear wave functions (CGC). Produced in the collision of two CGC "pancakes" is a matter of extremely high density termed glasma. It precedes quark-gluon plasma (QGP). The glasma consists of color flux tubes localized in the transverse plane and stretching between the valence color degrees of freedom. These tubes generate long-range correlations. The existence of long-range (pseudo)rapidity correlations is related to the early instants of glasma formation in nuclear collisions. The radial flux collimates particles in the direction of the flux and generates azimuthal correlations. In particular, this might explain the hump effect as a combination of long-range correlations in rapidity in the initial state and the radial flux in the final state.

Macroscopic collective properties (CGC, QGP) may manifest themselves in its hydrodynamically described mechanical motion as a whole (for instance, viscosity)

or in its response to external color fluxes (for instance, chromopermittivity) described in the framework of QCD.

As is well known [65], at very high energies gluons become the main components in the wave functions of colliding hadrons. The in-medium gluodynamics equations differ from those in vacuum by the inclusion of chromopermittivity of quark-gluon plasma [65]. Like permittivity in electrodynamics, chromopermittivity describes the linear response of matter to its traversing partons. To the leading order in strong coupling constant the equations are completely similar to electrodynamics equation with substitution of the permittivity for the chromopermittivity. The response of the medium to the action of partons is discussed at length in [65].

Studying the thermodynamic and mechanical characteristics, which vary in the course of the evolution of quark-gluon medium, requires information about the spatio-temporal picture [65]. Lattice simulations and ideas concerning CGC, glasma, and QGP yield certain indications about the transition from the state of confinement to free quarks and gluons. Inelastic collisions may lead to thermalization of the medium. Subsequently this medium expands, and hydrodynamics may be applied for describing this evolution phase. This is described in reviews [61, 75, 104, 126, 207].

The medium is characterized by six independent variables [65]. These are the energy density e, the pressure p, the baryon number n_{B}, and three velocity vector components u_μ. The energy-momentum tensor and the baryon charge current are of the form

$$T^{\mu v}(x) = (e(x) + p(x))u^{\mu}(x)u^{v}(x) - p(x)g^{\mu v},$$
$$j^{\mu}_{\mathrm{B}}(x) = n_{\mathrm{B}}(x)u^{\mu}(x).$$

The evolution of these variables is described by six hydrodynamic equations: five nonlinear partial integro-differential equations obtained from energy, momentum, and baryon-charge local conservation laws:

$$\partial_\mu T^{\mu v} = 0 (v = 0, \ldots, 3), \quad \partial_\mu j^{\mu}_{\mathrm{B}}(x) = 0,$$

and the equation of state relating p, e and n_{B} [20, 23, 37, 38, 42, 48, 49, 52, 55, 61, 63, 87, 96, 102, 118, 120, 127, 139, 141, 142, 150, 159, 168, 216, 220, 238, 246, 256]. The last-named is usually selected in the form closest to QCD lattice data by normalizing to the states that lie below and above the critical temperature (i.e. hadrons and quark-gluon medium). This is a rather arbitrary element of the approach. Furthermore, to solve the (3+1)-dimensional nonlinear equations requires determining the initial conditions. These solutions may be found only numerically with the use of several external parameters [65].

The solutions of hydrodynamic equations yield the spectra of transverse momenta for different sorts of particles, radial and elliptical fluxes, the geometry of interaction region. Their comparison with experimental data permits determining the main thermodynamic, static, and mechanical properties of quark-gluon medium.

A schematic grouping of their values for an energy of 200 GeV is as follows: $T_{eq} \approx 360\,\text{MeV}$, $T_{cr} \approx 170\,\text{MeV}$; $T_{dec} \approx 120\,\text{MeV}$, $\tau_{therm} = \tau_{eq} \approx 0.6 < 1\,\text{fm}$; $\tau_{dec} \approx 7\,\text{fm}$, $e_{th} \approx 25\,\text{GeV/fm}^3$, $e_{cr} \approx 1\,\text{GeV/fm}^3$, $e_{dec} \approx 0.075\,\text{GeV/fm}^3$, $s_{eq} \approx 110\,\text{fm}^3$, $\nu/s \approx 0.1$ ($1/4\pi$ in AdS/CFT), $n_B < 0.5\,\text{fm}^3$. These values testify to a rapid thermalization, a high initial average energy density, and a rather long lifetime of quark-gluon plasma prior to hadronization for a fairly low density and temperature predicted by lattice QCD. Total thermalization in a time shorter than 1 Fermi is required for measuring the magnitude of elliptic flux (Fig. 6.41) and its dependence on centricity, which are highly sensitive to any departures from local thermodynamic equilibrium for low-p_T particles. Collective excitations, resonances, and inelastic interactions maintain the system in the state of thermal equilibrium. A good agreement of the data with ideal fluid dynamics is indicative, as we saw above, of a very low viscosity of QGP. Other transfer (shear, diffusion, thermal conductivity) coefficients do not play a significant role on a macroscopic scale length typical for scattering: this length is much shorter than the macroscopic scale related to the expansion of the medium. Strong nonperturbative interactions must be responsible for the behavior similar to the behavior of an ideal fluid. Hence there comes the term "a strongly interacting quark-gluon plasma" (sQGP). For instance, clusters or colored bound states of massive quasiparticles with heavy quarks may exist in sQGP. Resonance scattering from the constituents of quark-gluon medium may become significant. This all would give rise to collective response on the scale under discussion, to high pressure, large values of chromopermittivity and long-range correlations required, in particular, to account for the increase in production of strange partons due to nonlocal processes. A long "lifetime" counts in favor of the approximate treatment of energy loss in an "infinite" medium.

The hydrodynamics of collisions now is making rapid strides. The main characteristics of low-p_T particles have been described using this approach. At the same time, many factors have to be taken into account like thermodynamics, collective flux models, hadronization, decays of resonances, chemical composition, collision geometry, etc. So far, however, attempts to construct a complete consistent hydrodynamic description have not met with success. Sometimes there appear contradictory statements, for instance, about the energy (from SPS to RHIC) dependence of elliptic flux on rapidity and centrality, its absolute value, the transverse-momentum dependence of different radii, the hadrochemical composition for several particles, etc. It is hoped that these contradictions will soon be resolved using the same set of adjustable parameters. This will allow a deeper understanding of the collective thermodynamic and mechanical properties of the matter and its evolution.

The quest for and study of the physical properties of QGP now is the subject of intensive theoretical and experimental investigations in many laboratories in the world. This research will undoubtedly gain impetus upon commissioning the Large Hadron Collider as a result of implementation of the FAIR and NICA projects (see Sects. 6.7 and 6.8).

There are many distinctions and there is much in common between the quark-gluon plasma and the ordinary plasma, which makes up 98–99 % of the visible Universe and which is terms "electromagnetic" plasma (EMP) [157] (Fig. 6.48 [97]).

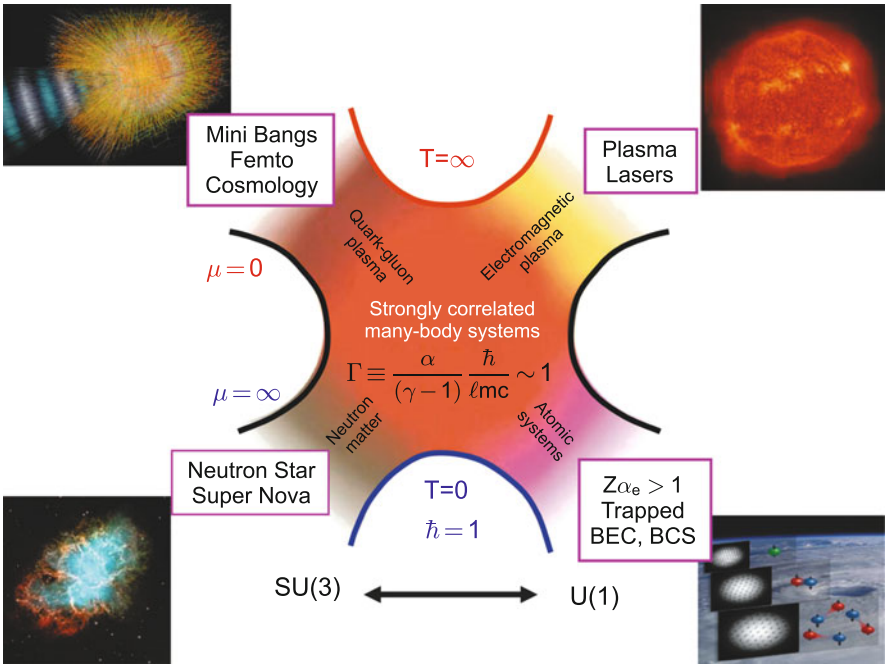

Fig. 6.48 Different lines of research in high energy density physics [97]

The intensity of interparticle interaction in electromagnetic plasmas is described (see Chap. 3) by the nonideality parameter, $\Gamma_{\mathrm{EM}} = \frac{z^2 e^2 n^{1/3}}{kT}$. For quark-gluon plasmas the corresponding parameter is of the form $\Gamma_{\mathrm{CQP}} = \frac{\alpha_s}{1-\gamma}\frac{\hbar}{lmc}$, where α_s is the coupling constant ≈ 0.3–0.5 (Fig. 6.26). The mode of strong nonideality in this case corresponds to moderate temperatures $T \sim (1\text{–}2)T_c$, with a perturbative mode supposedly operating at higher temperatures.

Unlike EMPs, QGP is relativistic or ultrarelativistic. This difference in relativism manifests itself not only in the kinematics of motion but also in that only particles are present in the nonrelativistic case, whose number is conserved, while in the relativistic case also antiparticles are present and conserved is the number of leptons. The particle number density is no longer an adequate characteristic and is replaced by the baryon and strange particle number densities.

An increase in the fraction of various particles in comparison with a very strong suppression of pions was observed in atom-atom collisions for high transverse momenta. Therefore, the hadrochemical composition in atom-atom and proton-proton collisions is different. This is considered as a manifestation of quark-gluon plasma (or, in more general terms, as the effect of a prehadronic state). For high p_T (above 2 GeV) neutral pions and ν mesons are strongly suppressed (approximately five-fold) in central atom-atom collisions in comparison with proton-proton collisions. The change in the hadrochemical composition of high-p_{T} collision products

may reflect a difference in the interactions of different particles in the medium and call for the inclusion of collective (nonlocal) properties of the medium (with possible diffusion prior to hadronization).

Proton production is enhanced for intermediate p_T (in the region $p_T \approx$ 2–5 GeV), so that the proton-to-pion number ratio becomes close to unity.

It is remarkable that the fractions of secondary particles (different for various particles) for very low transverse momenta ($p_T < 0.5$ GeV) are the same for proton-proton, atom-atom, and even e^+e collisions and are independent of the initial energy, as would be expected proceeding from the universality of coherent processes for long-wave gluons.

In EMPs, the large difference in the mass of electrons and ions leads to the difference in their dynamics and kinetics and underlies, in particular, the difference of electron and ion temperatures in relaxation processes. In a QGP, there also are heavy (charmed, top, and bottom) particles, which, however, are fewer in number than the light quarks and gluons, and their lifetime is shorter. That is why the contribution of heavy quarks in QGP dynamics is small. QGPs are described by QCD and EMPs by QED. The latter theory is Abelian, unlike chromodynamics. In QCD, gluons carry color charge, determining the quark–quark and quark–antiquark interaction, and interact with each other. Unlike photons, gluons make a contribution to the color charge density and the color current.

A feature that the QGP and EMP share is the collective nature of interparticle interaction [157]. Despite screening, the radius of effective electromagnetic interaction is normally much longer than the interparticle distance, so that there are many particles in the Debye sphere and their motion is strongly correlated. Quantum electrodynamics gives a solution, which corresponds to the Debye one: $\Phi(r) = (q/r) \times \exp(-m_D^2)$, in which the Debye mass (which plays the part of the inverse Debye radius in the atomic system of units) $m_D^2 = e^2T/3$ is of the order of $(qT)^2$, where q is the constant of QED. Since the number of particles in this density theory $\sim T^3$, the number of particles in the Debye sphere is $\sim 1/q^3$ in the weak-compression limit ($1/q \gg 1$). Interestingly, the pseudopotential of the interparticle interaction of like charges in QGP may become attractive in some cases [157]. The long-range interparticle interaction inherent in EMP and QGP has the consequence that an important role is played by collective effects such as screening, plasma oscillations, and instability.

Unlike experiments with EMPs, where use is made of external electromagnetic or gravitational fields, for QGPs the fields of requisite intensity are inconceivably high, and only self-induced fields are of significance in relativistic collisions.

The description of an EMP is also very different from that of the QGP [157]. For electromagnetic plasmas, under the corresponding time limitations extensive use is made ($m_i \gg m_e$) of a two-fluid (electron–ion) model with different electron and ion temperatures. The local electroneutrality condition hinders appreciable charge separation, which leads to equations of magnetohydrodynamics where the plasma motion takes place under the action of pressure gradients and a magnetic field.

In QGP there is no analog to magnetohydrodynamics, because every quark or gluon may carry charges of different color. On attaining local thermodynamic equilibrium, different color components will therefore possess the same temperature and velocity. Furthermore, a quark–gluon system becomes neutral in color, and in a QGP the hydrodynamics of a neutral fluid without chromodynamic fields is realized. Naturally, in the absence of local thermodynamic equilibrium use is made of more complex kinetic equations with a "collisional" term of one form or another [97].

To close the equations of motion, which express the mass, momentum, and energy conservation laws, necessitates invoking the equations of state. In the simplest case of an ideal ultrarelativistic gas of massless particles it is assumed that $E_{(x)} = 3P(X)$.

Many hydrodynamic and kinetic plasma instabilities typical of EMPs are thought to show up in the QGP [157], although they are extremely hard to observe there. However, the development of these perturbations is associated with the short ($\leqslant$1 fm/c) measured QGP thermalization time and the effect of jet quenching in relativistic nuclear collisions.

The experimentally observed [157] fast matter thermalization, the parameters of elliptical flows, the spectrum of outgoing particles, jet quenching, and low viscosity are attributed [157] to the nonideality of the QGP close to the deconfinement threshold. The nonideality parameter estimate $\Gamma \approx 1.5$–5.0 given above may increase by an order of magnitude when higher-order terms in the interaction potentials are taken into account [157]. This in turn may give rise to a "plasma" phase transition similar to that observed in a strongly nonideal nonrelativistic plasma [73, 78–80].

In [157], the effects of plasma nonideality revealed for compressed EMP are employed in the analysis of the behavior of the viscosity, cross sections, collisions, and stopping power of QGP. In QGP the ratio between the Landau length $\Gamma \approx q^2/E$ and the Debye radius is equal to 1–5; this increases the scattering cross section by a factor of 2–9, which shortens the free path λ and hence the viscosity ($\eta \sim \lambda$) also by an order of magnitude. This is consistent with the measured parameters of elliptical flows and particle spectra in nuclear collisions as well as with the recorded increase of radiation losses.

Interesting analogies [157] are drawn between strongly nonideal QGPs and strongly nonideal "dust" plasmas [78, 79]. In both cases we assume to be dealing with a Newtonian liquid, in which the shear viscosity depends on the velocity of motion. Furthermore, the QGP possesses features of a nanoliquid [157]. In particular, the initial QGP size immediately after a collision is $\approx$10 fm ($\approx$20 interparticle distances), which distinguishes it from a continuous medium. This is also typical for a nonideal "dust" plasma.

In [35], an analysis was made of analogies between a QGP and a strongly nonideal EMP that consists of ions in electrostatic traps cooled by laser and evaporative techniques to ultralow temperatures. In both cases we are dealing with strongly interacting systems with a limited volume and a large number (of order 10^4–10^7) degrees of freedom. Figure 6.49 shows the expansion of a cryogenic ion EMP cloud [167], which exhibits pronounced features of an "elliptical" flow typical

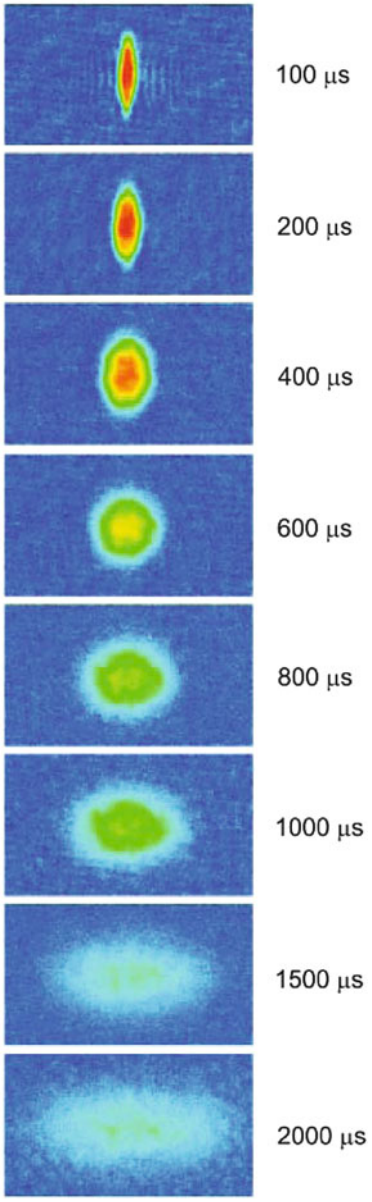

Fig. 6.49 Asymmetric "elliptical" dynamics of nonideal cryogenic ^{6}Li lithium plasma expansion upon deenergizing an electrostatic trap [167]. An analogy with an "elliptical" flow in nuclear collisions

of the expansion of superdense nuclear matter in relativistic collision experiments (Fig. 6.41). Similar energy characteristics of neutral matter and ultracold Fermionic atoms (Fig. 6.50) [88] demonstrate a striking similarity at temperatures that differ by ≈ 20 orders of magnitude.

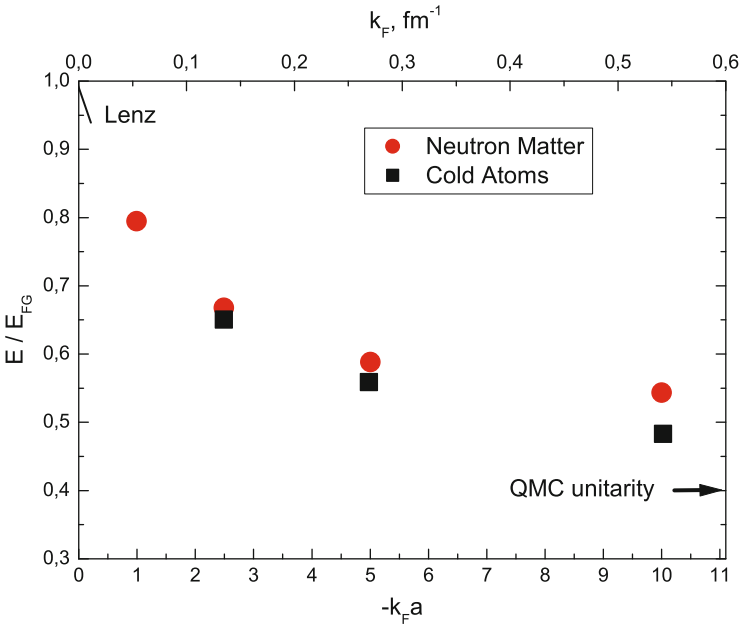

Fig. 6.50 Reduced energy of neutron matter (*circles*) and ultracold atoms (*squares*) [88]. QMC: Quantum Monte Carlo

These analogies may be a helpful aid in the elucidation of several fundamental properties of the QGP, especially those which are hard to derive directly from relativistic ion collision experiments:

– kinetic energy distribution in a compressed medium,
– collective motions and their measures,
– screening,
– collisions and expansion,
– flows, hydrodynamics,
– thermalization,
– correlations,
– interaction with fast particles, stopping power,
– viscosity, dissipation.

Further analogies of this kind can be easily added.

To conclude this section we give a scheme of matter transformation at high energy densities (Fig. 6.51), which in a sense extends the conclusions of Sect. 3.6 (Fig. 3.33) about substance simplification as you move toward extremely high pressures and temperatures.

We see that heavy-ion relativistic collision experiments (SPS, RHIC) have become a source of invaluable information about a new realm of physics—the physics of quark-gluon medium. The experiments suggest that nuclear collisions

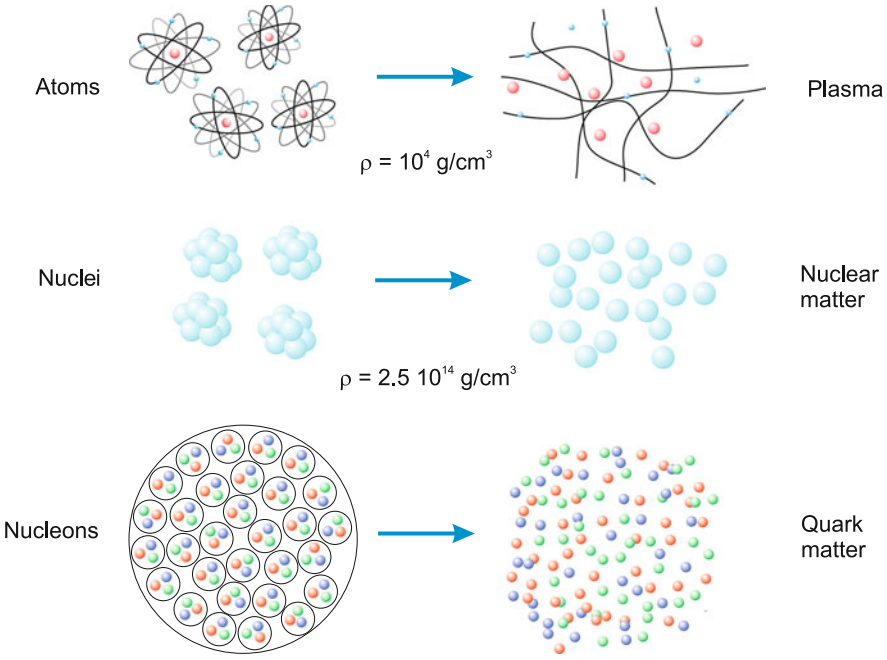

Fig. 6.51 Matter transformation at high energy densities

may not be treated as an additive superposition of proton-proton collisions, so that collective properties of the medium must be taken into account. This is evidenced by the presence of anisotropic fluxes, jet quenching, correlations of special kind like the ridge and double-humped events as well as many other data discussed above.

Theoretical understanding of the evolution of the medium called for invoking QCD to discuss effects like color glass condensate, glasma, thermalization, quark-gluon plasma, hadronization, and so on. We note that the methods of condensed state physics describe the modification of parton energy loss in the substance due to the effects of formation length and collective response of the medium (chromopermittivity)resulting from its polarization. Hydrodynamics was widely used to describe the collective behavior of this medium.

In summary, we mention another approach which relies on the idea of discovering quark-gluon plasma from its own radiation [187], the emission of high-energy photons, which escape absorption and come out of the medium. Physicists endeavor to employ energetic photons to determine the temperature of quark-gluon liquid, much as astronomers measure the temperature of a distant star from its light emission spectrum. But the spectrum measurement is extremely difficult now, because a multitude of other photons are produced in the decay of neutral pions. And though they emerge well after the inverse transformation of the quark-gluon liquid to hadrons, the photons that reach detectors look similar to them.

Many physicists look forward to the attainment of the next energy milestone on the Large Hadron Collider (LHC) in the CERN [187]. Experiments involving the observation of lead nuclei collisions for a total energy above 1 million GeV are expected to commence soon. The instantaneous energy density achieved in the miniexplosions that will take place in the LHC will be several times higher than in collisions on the RHIC and the temperatures will far exceed 10^{13} K. Scientists will be able to simulate and study the conditions which existed during the very first microsecond after the Big Bang.

Of major interest is the question of whether the similarity to a fluid discovered on the RHIC will persist at the higher temperatures and energy densities that will be obtained on the LHC [187]. Some theorists believe that the force acting between quarks will become weak as soon as their average energy exceeds 1 GeV and that quark-gluon plasma will nevertheless behave like a gas. Other researchers do not share this viewpoint. They assert that the QCD force decreases insufficiently fast with increasing energy and that quarks and gluons will therefore remain strongly bound like molecules in a liquid.

6.4 Viscosity and Interparticle Interaction

As we have seen above, one of unexpected and brilliant results obtained on the RHIC accelerator is that a strongly compressed quark-gluon plasma with $P \approx 10^{30}$ bar, $T \approx 10^{12}$ K and $\rho \sim 10\rho_0 \approx 10^{15}$ g/cm^3 behaves not as a gas of quarks and gluons but as a fluid with a vanishingly small viscosity ($\eta/s \sim 0.08$–0.24). This is supposedly a reflection of the general basic properties of an interacting ensemble of particles, which behaves as a nonviscous ideal liquid in the limit of strong interparticle interaction [110, 112, 233].

This feature is inherent in a broad class of physical objects of highly different nature in an extremely broad parameter range (Figs. 6.59, 6.60, and 6.61): 18 orders of magnitude in temperature and 25 orders of magnitude in density [130, 131, 207]. The cases in point are a relativistic supercompressed quark-gluon plasma with $T \approx 10^{12}$ K [110], the substance in the early Universe [247], the viscosity of helium isotopes [14, 122], molecular and atomic liquids, dust plasmas [240], electrons in metals and semiconductors [219, 241], graphene [237], black holes [112], and the Fermi gas of ultracold ($T \approx 10^{-6}$ K) lithium atoms in optical traps [45, 196, 233] (see Figs. 6.59, 6.60, and 6.61).

The strong (collective) interparticle interaction in all of these classical and quantum systems manifests itself as a sharp decrease in shear viscosity, which serves as a means of diagnostics in this case and fulfils the function of a "signal", testifying to the collective behavior of a strongly correlated system. It is significant that such viscosity behavior is in fact model-independent and "nonperturbative".

The notion of ideal liquid corresponds to a macroscopic system which is in local thermodynamic equilibrium and has a vanishingly low shear viscosity, $\eta = \rho v^2 \tau$. Macroscopically, viscosity describes the magnitude of resistance of a medium to its

motion. Microscopically, it is a characteristic of the interaction intensity between different elements of the medium [112]. It is valid to say [110] that viscosity reflects the inability of the medium to transfer momentum to neighboring regions. It reflects local departures from complete equilibrium, which gives rise to friction and flow deceleration.

Shear viscosity describes how perturbations propagate through the medium via interactions. The lower is the viscosity of a fluid, the stronger are the interactions and the higher is the intensity of perturbation transfer. In the other limiting case of an ideal gas of noninteracting particles the shear viscosity has a finite value (Fig. 6.52).

The matter is that viscosity is proportional to the average time between particle collisions (Fig. 6.52) and the system energy density E. The entropy density s is proportional to the particle density N, so that $\frac{\eta}{s} \sim \frac{\tau\varepsilon}{k}$, where ε is the energy per particle. Since the interparticle interaction shortens τ, this leads to a lowering of η. According to the Heisenberg principle, $\eta\varepsilon \gtrsim \hbar$ and $\frac{\eta}{s} \sim \frac{\hbar}{k}$, so that the ideal fluid concentration with $\eta = 0$ contradicts quantum mechanics.

Using the arguments based on the Heisenberg relation, the gauge theory, the string theory, and the holographic principle (see below), which was developed for describing gravitation (Fig. 6.53), in elegant works [130] it has been possible to estimate the lower bound to viscosity, which yielded a very small figure:

$$\left(\frac{\eta}{s}\right)_{\mathrm{g}} = \frac{1}{4\pi}\frac{\hbar}{k} \approx 6.08 \cdot 10^{-13}\,\mathrm{K\,s}.$$

This estimate is underlain by calculations of perturbation propagation by the methods of gauge theory: considered in the framework of this theory is the propagation of a graviton in a multidimensional space from a point at the boundary,

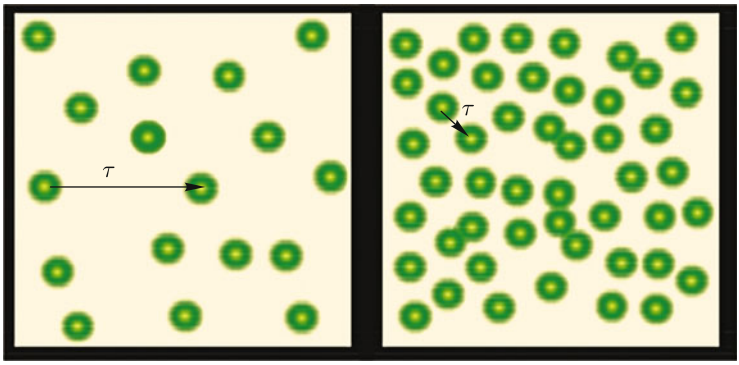

Fig. 6.52 Strongly interacting particles, like those depicted in the *right frame* of the drawing, usually have a short mean free path and a short mean free time τ between the interaction events with other particles of the same type. The system of weakly interacting particles shown in the *left frame* of the drawing lends itself to traditional computational methods with the use of perturbation theory; however, as τ shortens the particles begin to lose their individuality and these methods become inappropriate [112]

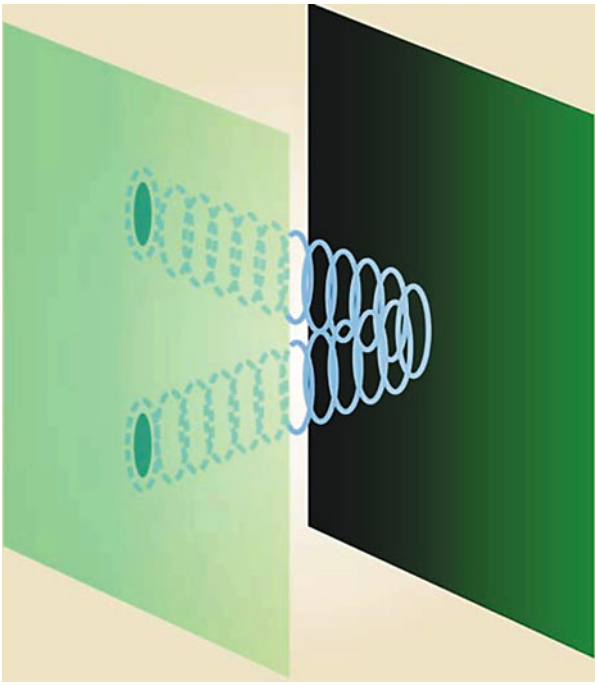

Fig. 6.53 Holographic duality permits transforming hydrodynamic gauge theory calculations to scattering calculations in high-dimensionality space-time theory. The plane at the *left* represents the three-dimensional space, a section of the four-dimensional space–time, for which a dual gauge theory was developed. The motion perpendicular to this plane proceeds in the additional fifth dimension; gravitation operates in the volume of five-dimensional space–time. The plane at the *right* represents the three-dimensional event horizon of a black hole. Intricate calculations of how perturbations propagate in the four-dimensional space–time of the gauge theory are equivalent to a simpler-to-calculate process whereby a graviton (*blue*) is scattered by a black hole in the five-dimensional space–time [112]

its reflection from a black hole in the anti-de Sitter space, and its return back to the boundary (Fig. 6.53) [179]. In this case, the graviton reflection cross section turns out to be close to the area of the black hole horizon and the viscosity proportional to the area of the horizon [179]. In doing this, advantage is taken of an analogy between the physics of a black hole and thermodynamics. A superstring theory of gravity on a ten-dimensional "black" membrane is considered, which has analogies in hydrodynamics. The holographic principle (AdS/CFT) reduces this multidimensional treatment to a lower-dimensionality space. In this case, the entropy of the "black" membrane turns out to be proportional to the area of event horizon, $S = \frac{A}{4G}$, whence there follows the estimate of the lower viscosity bound.

In [131] the methods of the string theory developed for strongly interacting systems were applied to describe "dual" weakly interacting ensembles [112]. It was shown that the ratio η/s must have a nonzero minimum with $\frac{\eta}{s} \gtrsim \frac{1}{4\pi}\frac{\hbar}{k}$.

This relation relates the hydrodynamics and thermodynamics of strongly interacting systems [233]. Specific calculations of the shear viscosity of relativistic gas of hadron resonances [173], perturbative [24] and lattice calculations [153] do not contradict this bound.

With the use of a chiral perturbation theory [54] it was shown that viscosity η/s decreases monotonically with increasing T (with increasing the degree of correlation in the system) and reaches its minimum near the temperature of the QGP phase transition. This behavior of η/s may by itself be an indication of a phase transition in a strongly correlated system. A conclusion about the minimum of η/s in the phase transition to QGP is drawn in [62], where ultrarelativistic molecular dynamics methods were used to show that the expansion and cooling of a fireball is attended with a growth in η/s. This QGP parameter was shown to monotonically grow with increasing T.

For the sake of completeness we mention a paper [43] in which the use of generalized gravitation theory yields other values of the quantum limit.

To analyze viscosity, advantage is taken of the holographic approach—one of the most elegant theoretical approaches to the analysis of strong-interaction dynamics at low and intermediate energies. Its idea consists in that dual theories may be formulated in the space–time of different dimensionality, so that, for instance, the four-dimensional dynamics of some theory with a large interaction constant is equivalent to the five-dimensional dynamics of another theory with a small interaction constant (much as a two-dimensional hologram describes a three-dimensional object). The best known realization of this approach is underlain by the Anti de Sitter/Conformal Field Theory (AdS/CFT) correspondence, which implements the duality between the strong-coupling gauge theory, which enjoys four-dimensional conformal invariance, and multidimensional supergravity with a weak coupling constant. Four-dimensional conformal symmetry includes invariance relative to Poincare group transformations, dilations and inversions.

Experiment shows [112] that ordinary liquids, like water and even liquid helium, possess viscosity which far exceeds this lower bound $\frac{\hbar}{4\pi k}$ (Fig. 6.54), while the viscosity of quark-gluon plasma (Sect. 6.2) and ultracold fermions is only several times higher than boundary values $\left(\frac{\eta}{s}\right)_{\text{bd}}$. This testifies that new forms of matter with record low values of shear viscosity were obtained in this case [110, 112, 233].

We note that the viscosity of a one-component plasma, according to [232], reaches a minimum, $\frac{\eta}{s} = 4.9\,\frac{\hbar}{4\pi k}$, for $\Gamma \approx 12$. The viscosities of a strongly nonideal dust plasma and electromagnetic plasma are shown in Figs. 6.59 and 6.60.

Let us consider these examples in greater detail. We begin with the case of the tenuous Fermi gas of atomic lithium-6 frozen by evaporative cooling to $T \approx 10^{-6}$ K [233]. This system of strongly interacting fermions exhibits the properties of an ideal liquid with the lowest viscosity admitted by quantum mechanics [233].

In the experiment of [233], several hundred thousand lithium-6 atoms were placed in an optical trap; the interactions between them were controlled by external magnetic field. To lower the temperature, use was made of evaporative cooling, which transferred the system of atoms to the quantum mode (Fermi statistics),

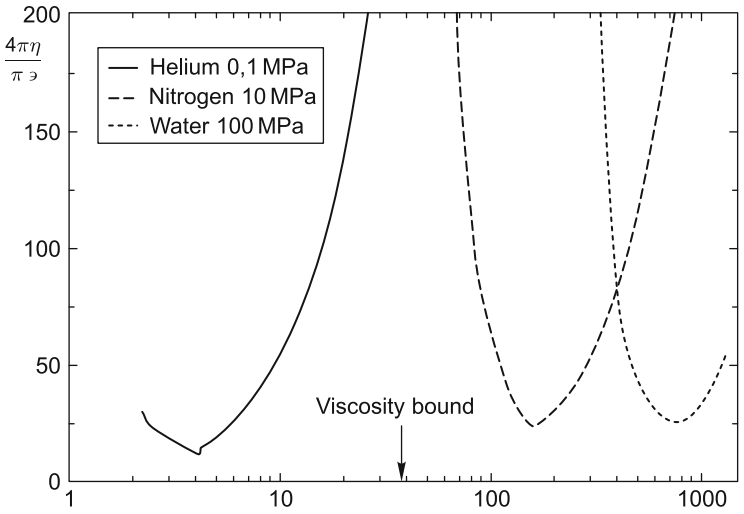

Fig. 6.54 Viscosity of helium, nitrogen, and water [232]

whereby the atomic momentum became so low that the de Broglie thermal wavelength $\lambda \sim \sqrt{\frac{\hbar}{2nmkT}}$ became comparable with the interparticle distance [233].

The interaction between atoms with oppositely directed spins is strongest in the case of Feshbach resonance [123]; its attainment conditions are provided by the imposition of external magnetic field. In this case, the sum of kinetic energy and the energy of magnetic interaction of colliding pairs of particles becomes close to the dimer binding energy. It is significant that the properties of such gas are universal in this regime and depend only slightly on the details of interparticle interaction [233].

Since the optical trap potential is nearly harmonic in shape, in accordance with the virial theorem the total energy E of a particle ensemble is equal to twice the potential energy. The geometrical size of the ensemble was determined from its photograph (Fig. 6.55 [233]). This experimentally recorded ensemble size determines the internal energy of the system. Varying the frequency of trap-forming laser radiation served the purpose of determining the atomic resonance frequency, at which the absorption of laser energy increases and, accordingly, the particle ensemble size becomes larger.

The idea of measuring the entropy S consists in the use of adiabatic variation of magnetic field, which removes the system from the Feshbach resonance and, therefore, transfers it to the mode of weak interparticle interaction. In this case, the entropy S is equal to the easily calculable entropy of the ideal gas, which is equal to the entropy of the strongly interacting ensemble on the strength of adiabaticity of the process.

The thus obtained data are given in Fig. 6.56 [233], where one can see the superfluid-to-normal state transition of a nonideal Fermi system. In [233] it was

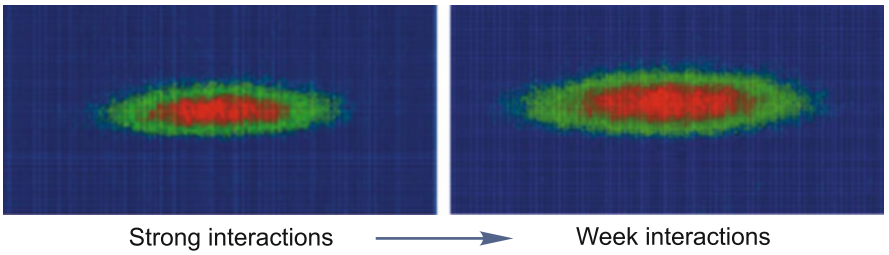

Fig. 6.55 Root-mean-square size of trapped Fermi gas determines it energy and entropy. When particles are strongly interacting ones (at the *left*), measurements of the cloud size permit determining the total energy. By slowly removing the external magnetic field, experimenter can adiabatically transfer the system to a weak interaction mode. In this case (at the *right*) it is possible to calculate entropy from the root-mean-square cloud size. The interaction in the strong mode is attractive; no wonder that the corresponding cloud is two times smaller in size. Both clouds amount to 200 μm horizontally; the highest-density domains are shown in *red* [233]

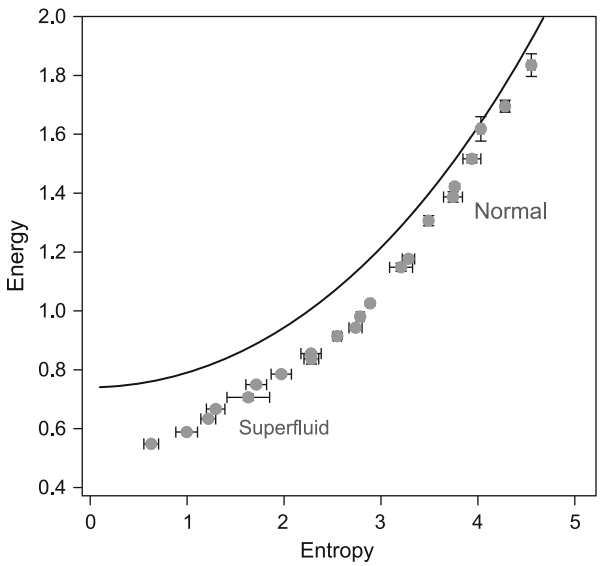

Fig. 6.56 Transition of a strongly interacting Fermi gas of lithium-6 from a superfluid state to the ordinary fluid state, which is "signaled" by a change in energy–entropy scaling. In the plot the energy per particle is normalized to the Fermi energy of an ideal Fermi gas at the trap center, and the entropy per particle is normalized to the Boltzmann constant. The data suggest that the transition occurs when the normalized energy is equal to about 0.8. Plotted for comparison is the energy–entropy dependence for the ideal Fermi gas (*curve*) [233]

shown that this transition occurs for $T \approx 0.2T_{\mathrm{F}}$, where T_{F} is the Fermi temperature and $T = \frac{\partial E}{\partial S}$.

By varying external magnetic fields in experiments [233] it was possible to realize the mode of particle ensemble oscillations—a "heartbeat" mode. The decay

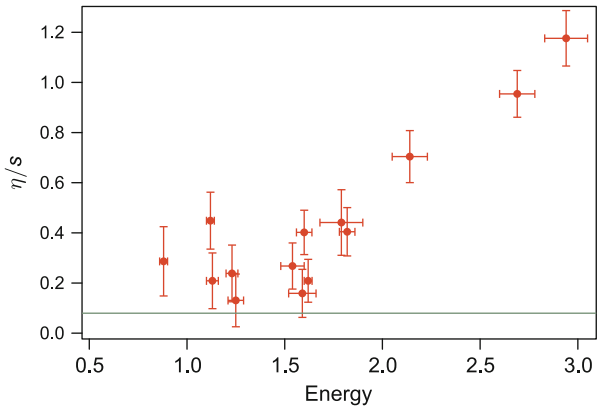

Fig. 6.57 Experimentally determined ratio between the shear viscosity and the entropy density (η/s, *red circles*) for strongly interacting normal lithium-6 compared to the hypothetical lower bound predicted by the string theory (*green line*). The per-particle energy in the calculation is normalized to the Fermi energy; in these units the transition from a superfluid liquid to a normal liquid occurs for a normalized energy value of 0.8. The statistical error bars do not include possible systematic errors arising from the model used to estimate the viscosity [233]

of these heartbeats yields information about the shear viscosity of the system. The resultant data on the shear viscosity of strongly interacting Fermi particles are given in Fig. 6.57 [233] and testify about the realization of a nearly ideal fluid mode. One can see that the measured $\frac{\eta}{s}$ values turn out to be quite close to the lower bound $\frac{1}{4\pi}\frac{\hbar}{k}$ set by the string theory.

Also investigated was the expansion mode of the cigar-shaped bunch upon imparting it an additional energy or terminating the traps current (Fig. 6.49). One can clearly see the ellipticity of the cloud expansion, which is similar to the elliptic fluxes of quark-gluon plasma. In this case the momentum has a dimension $\hbar/\delta$, where δ is the interparticle distance. The shear viscosity is of the form $\nu \sim \alpha\hbar^3/\delta^3 = \alpha\hbar n$. The dimensionless quantity α has the meaning of the ratio between the de Broglie wavelength and the interparticle distance. For the air $\alpha \approx 6000$, for water $\alpha \approx 300$, which testifies to the smallness of quantum effects in this case [233]. However, for liquid helium $\alpha \approx 1$ at the λ point, which corresponds to the quantum mode. Viscosity calculations performed for strongly interacting Fermi systems give $\alpha \approx 0.3$ [44].

The theoretical description of oscillatory processes of plasmas in traps was the concern of paper [45], where a hydrodynamic approximation was substantiated and the characteristics of spectral density for excitations were found.

As we saw in Sect. 6.3, the production of quark-gluon plasma (QGP) in the relativistic collision of heavy nuclear is attended with the emergence of a low-viscosity (ideal) fluid, whose dynamics is described by the hydrodynamics of an ideal liquid consisting of quarks and gluons.

Since detectors record the late expansion stages of quark-gluon plasma, it is possible to judge its characteristics by indirect indications (see Sect. 6.3); the most substantive of them are the data about the "streams" of expanding substance and "hard" processes corresponding to the high values of angular momentum. The hard processes include the production of quarks and the generation of highly collimated hadron jets due to quark collisions in the QGP. On the face of it, this contradicts the principle of asymptotic freedom [110], which predicts a weakening of interactions in the QGP with increase in temperature and density.

Nevertheless, experiments clearly show the formation of "elliptica" streams (Figs. 6.41 and 6.44) in off-center collisions, which are confidently reproduced by hydrodynamic collision simulations. This also is a verification for the description of relativistic collisions by the methods of continuum mechanics under local thermodynamic equilibrium.

In the motion through a dense QGP, the jets experience absorption (suppression), which signifies that the quark-gluon plasma is strongly opaque to them. This effect of jet suppression is illustrated by Fig. 6.58 borrowed from [110], where electrons are indicative of the decay of heavy quarks. Interestingly, since photons are not subject to strong interactions, they are hardly (see Fig. 6.58) absorbed by the QGP. They can therefore carry information about the QGP temperature, which turned out [110] to lie in the 300–600 MeV range and well above the temperature of the phase transition to the QGP, $T_c \approx 170$ MeV.

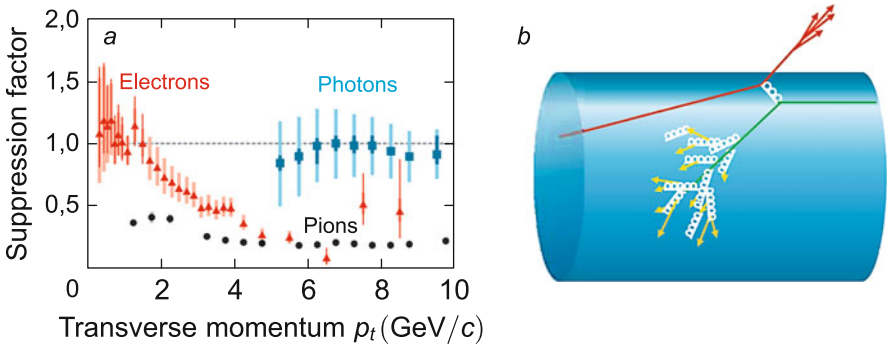

Fig. 6.58 Suppression of jets and heavy-quark hadrons in a quark-gluon plasma (QGP) (**a**); plot of the suppression of pions and yield of electrons with a high transverse momentum p_t in head-on collisions of gold nuclei. The suppression coefficient the ratio between the particle yield and those products which may be expected from a simple superposition of proton-proton collisions allowed in the QGP. Pions with a high value of p_t are indicative of hadron jets, while electrons with a high p_t are indicative of the decay of individual heavy-quark hadrons. By contrast, photons with high p_t values, which are insensitive to nuclear forces, do not experience suppression. The suppression of jets and heavy-quark hadrons in QCD is a characteristic feature of energy loss by way of emission of gluons by high-energy quarks, which generate them (**b**). In QCD a high-energy quark (*red*) scatters and emits gluons (*white ringlets*) prior to showing up and forming a jet [110]

In any case, experimental data [110] suggest that (in view of a strong opacity to quarks and gluons, among other data) QGP is a strongly interacting medium rather than a weakly interacting one, as one might expect from the principle of asymptotic freedom.

Calculations for the lattice model by quantum chromodynamics techniques testify to the existence of peaks of correlation functions for $T \approx (1\text{–}2)T_c$, which is indicative of appreciable quark-gluon correlations.

In any case, the data on jet suppression and elliptical flows may be described assuming a vanishingly low viscosity, which only slightly exceeds its lower bound, $\frac{\eta}{s} \gtrsim \frac{1}{4\pi}\frac{\hbar}{k_B}$.

The data of collision experiments suggest that they are close to the mode of weak asymptotic freedom, in which quantum chromodynamics predicts the screening of color charges at short range. An analogy between the Debye screening of Coulomb charges in electromagnetic plasmas and the color screening in quark-gluon plasmas, which we discuss in Sect. 6.3, may be quite substantive.

We emphasize once again that strongly interacting systems are liable to phase transitions when the interparticle interaction energy, which is responsible for ordering, is far greater than the disordering thermal energy. Among these phase transitions are (see Chaps. 2 and 3):

- dust plasma crystallization,
- ultracold ions and atoms in traps,
- ordering of colloidal systems,
- plasma phase transition in deuterium,
- crystallization of two-dimensional electrons on the surface of liquid helium,
- crystalline beams cooled by laser radiation in accelerators,
- exciton droplets in semiconductors,
- phase layering of metal-ammonia solutions.

Realized in all these case is a strong collective interparticle interaction, which gives rise to new phase states [79].

The quark-gluon plasma under discussion is a representative example of such phase transitions. The corresponding research will be performed in the framework of the international FAIR project (see Sect. 6.7).

Experimental data on the viscosity of strongly nonideal dust (Fig. 6.59) and shock-compressed electron-ion (Fig. 6.60) plasmas show that $\frac{\eta}{s}$ decreases with increase in nonideality (correlation) in the system.

In conclusion we give (Fig. 6.61) the $\frac{\eta}{s}$ data for helium, nitrogen, water, the baryon substance in experiments on the RHIC, quark-gluon plasma, and meson gas in relation to the reduced temperature. One can see that the QGP exhibits the lowest shear viscosity.

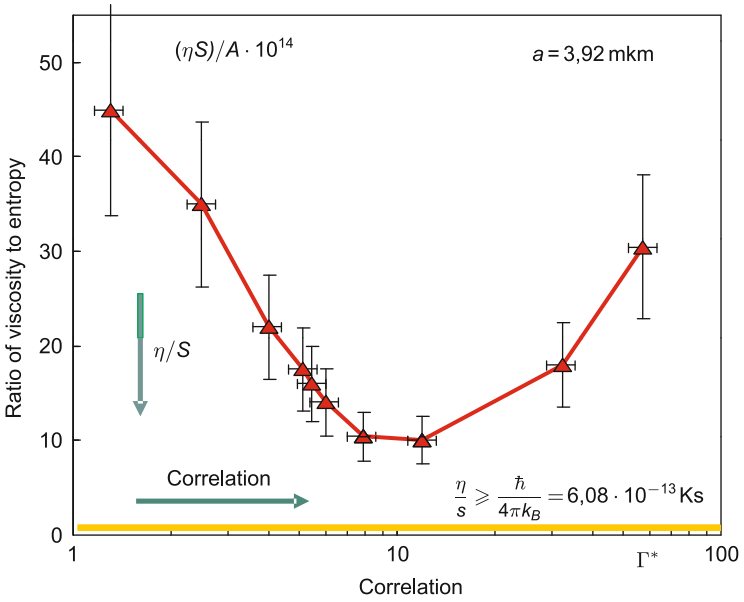

Fig. 6.59 Dust plasma viscosity as a function of nonideality parameter [82]

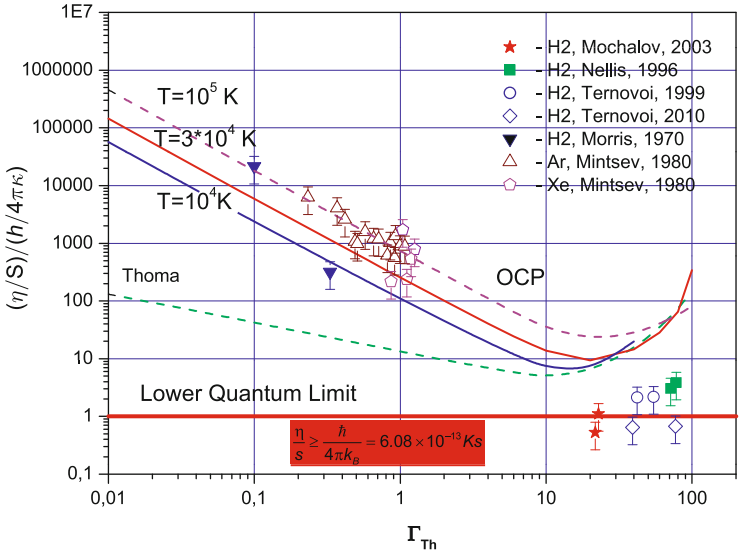

Fig. 6.60 Viscosity of shock-compressed electron-ion plasma [82]

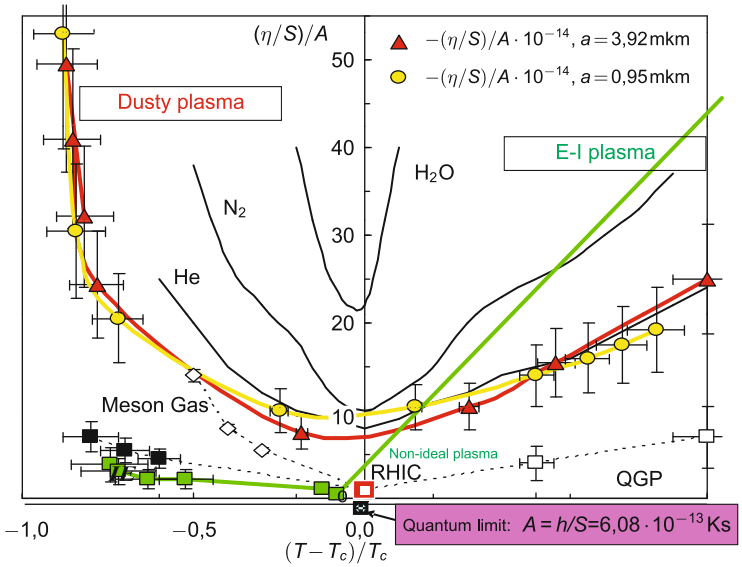

Fig. 6.61 Viscosities of different media in dimensionless parameters [110]

6.5 Extreme Atomic Physics

High-intensity beams of stable and radioactive ions in different charge states with velocities ranging from zero to the velocity of light ($v \approx 0.99c$) as well as ultracold antiprotons are promising tools for obtaining ultrahigh electric and magnetic fields and for investigating their action for ultrashort times. The corresponding investigations will be carried out in the framework of the international FAIR project (see Sect. 6.7). Used in experiments are not only ordinary targets, but also unusual objects such as ultracold electrons, atoms, molecules or clusters, which may also be exposed to the action of intense light fields generated by high-power lasers.

The physics of extremely high electromagnetic fields with stored particle beams is the central subject of the Stored Particle Atomic Physics Research Collaboration (SPARC) at the FAIR project [222]. High-precision experiments will be carried out on the heaviest relativistic ions for the purpose of comprehensive understanding their electron structure and internal dynamics. The results of these experiments will allow a substantive conclusion about the applicability of the basic light–matter interaction theory for an extremely high field on a subattosecond time scale. Experiments of the first type will use relativistic heavy ions for investigating the interaction of highly ionized atoms with electrons and photons under a superhigh electromagnetic field rapidly varying in time and a high value of relativistic Doppler shift [3, 222]. In this case, it becomes possible to exceed by an order of magnitude the critical field intensity value ($\approx 10^{16}$ V/cm) for the spontaneous production of lepton pairs, $((e^+e^-))$, the so-called Schwinger limit [202].

To date, there were only a few experiments on the e^+e^--pair production in the relativistic mode with energies of up to several GeV/nucleon. Since the FAIR project implies operation in the 1–30 GeV/nucleon energy range, these experiments are expected to yield a wealth of new data in this energy range.

In this energy range, new interesting data on atomic physics under the strong effect of electromagnetic interaction are likely to be obtained. Diagnosing these processes calls for invoking modern techniques of photon, electron, and positron spectroscopy [200].

The corresponding elementary processes are diagrammed in Fig. 6.62 [200]. Electron and photon spectroscopies yield information about the excitation mechanisms under high-intensity fields. Producing an e^+e^--pair requires excitation from the negative continuum [200].

Shown in Fig. 6.63 by way of illustration is the angular intensity distribution of the radial electric field of a point source traveling at a relativistic velocity [222]. As is evident from Fig. 6.63, as the velocity of light is approached the electric field in the transverse direction to the trajectory of motion increases, while the longitudinal field component decreases ($\sim \gamma^2$). In this case, the interaction time with a target atom spaced at an impact parameter $b \approx 10^6$ fm is record short—tenths of an attosecond ($\approx 10^{-19}$ s), which is unattainable with other experimental techniques. Therefore, it becomes possible to measure the dependence of the interaction impact parameter separately on the longitudinal and transverse field components for the ionization of inner atomic shells and for their excitation. Implementing these experiments invites the use of high-precision spectroscopic methods to record the emission of photons,

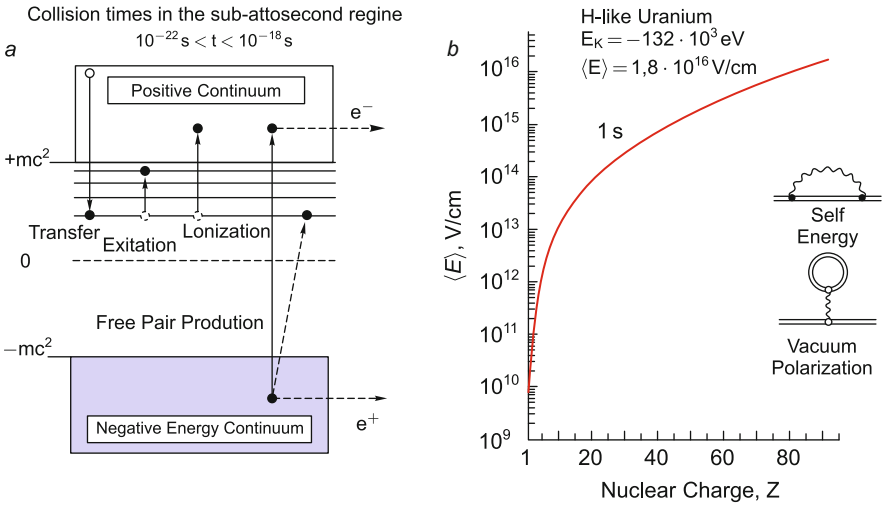

Fig. 6.62 Energy diagram of the single-particle Dirac equation and main atomic processes observed in relativistic ion-atom collisions (**a**). Mathematical expectation of the electric intensity <*E*> for the K-shell electron of a hydrogen-like ion as a function of nuclear charge *Z* (**b**) [200]

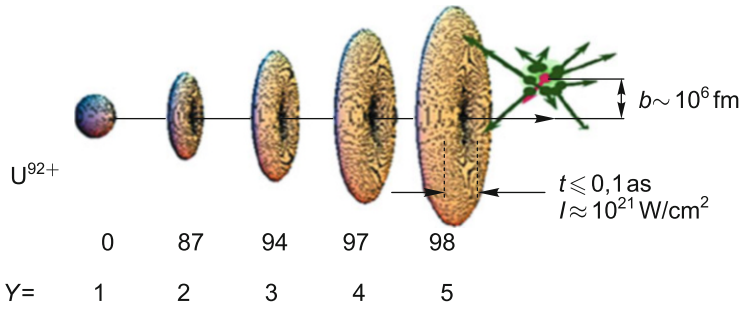

Fig. 6.63 Angular intensity distribution of the radial electric field of a point charge traveling at relativistic velocities (for the Lorentz factor γ of 1–5 in the laboratory frame of reference) [222]

electrons and positrons, which yield the desired information about the mechanisms of excitation in such superhigh fields.

It is noteworthy that the Lorentz factor γ which may be realized on different storage rings of the FAIR facility ranges from 1 to about 30. And so the electric intensity in the interaction with target atoms may exceed the field intensity which retains the 1s electron on the K shell of uranium ions ($E \approx 10^{16}$ V/cm) [222] (Fig. 6.62). In this case, the correction to the ground energy level of uranium ($Z = 92$) is of the order of 500 eV for an accuracy of level energy measurement of 10^{-14} (Fig. 6.62).

Another type of SPARC collaboration experiments is aimed at attaining high ion charge states, up to completely "stripped" uranium nuclei, circulating in a synchrotron ring. The matter is that almost all electrons are stripped off the ions in different accelerator structures (FAIR), and these highly ionized ions may then be decelerated to practically zero velocities and will therefore be accessible to spectroscopic and other measurements. Figure 6.64 gives the characteristic energies and Coulomb field intensities which may be obtained [200] in different GSI facilities. Ions in the NESR storage ring will be cooled from energies of 760 MeV/nucleon to 4 MeV/nucleon, and subsequently to 0.5 MeV/nucleon in the Low-Energy Storage Ring (LSR) facility. This opens up new interesting possibilities for measuring the differential cross sections for photoionization, excitation, polarization, electron-nucleus bremsstrahlung, (e, 2e) processes, etc. This offers unique possibilities for studying highly charged heavy ions at low collision energies, when the Sommerfeld parameter q/r is very large [200]. The objective is a high-precision verification of quantum electrodynamics in extremely high electric fields. In this case it is required to measure the finestructure corrections for one-, two-, and three-electron atoms, particularly 1s 1/2 and 2s 1/2 states. For heavy Li-like ions, direct excitation of 2s–2p transitions becomes possible by directing a laser beam in the opposite direction to the relativistic ion beam due to the Doppler effect (Fig. 6.65) [222].

The emitted photon resulting from laser excitation will exhibit a Doppler shift (proportional to $\sim 2\gamma$), which will permit high-sensitivity measurements with reliable suppression of the scattered primary photons. In particular, the 280 eV

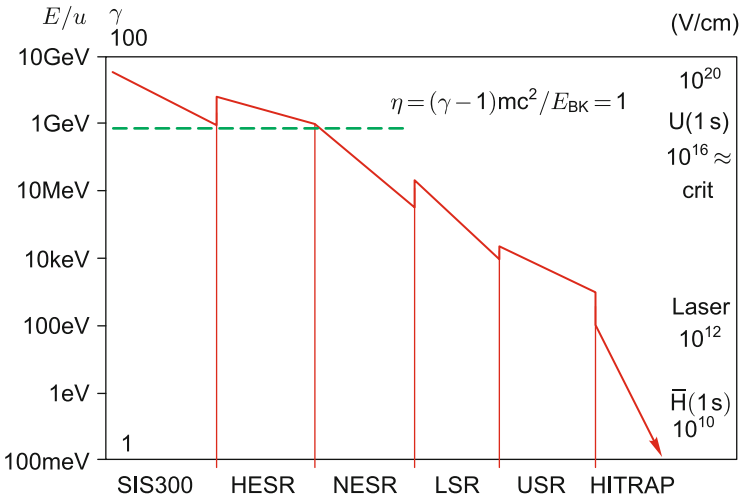

Fig. 6.64 Ion energy and Lorentz factor attainable with different FAIR facilities. Indicated is an adiabaticity value $\eta = 1$ (the characteristic kinetic ion energy corresponding to the velocity for the binding energy of K-shell electrons in uranium). Given on the *right* is the electric field intensity attainable in collisions, bound states, and laser fields. We note that LSR, USR, and HITRAP are storage rings and that the trap facility is located in the FAIR building [222]

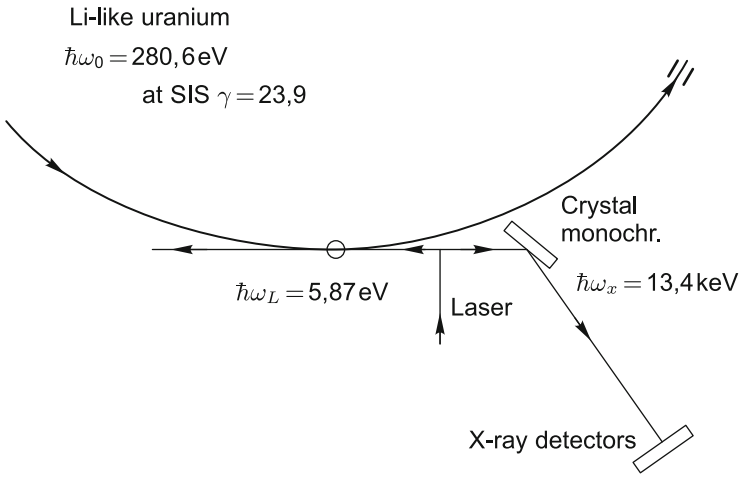

Fig. 6.65 Schematic of the experiment to measure the fine structure of heavy Li-like ions [222]

transition in uranium for a value $\gamma = 23$ may be measured with a record accuracy of ± 0.007 eV. The interaction of a ring-circulating heavy-ion beam with laser radiation will have an important application for beam cooling up to the conditions for the production of highly charged heavy-ion crystalline beams. As we will see in Sect. 7.6, this is a manifestation of a plasma phase transition (crystallization)

caused by the strong Coulomb interaction $\sim \frac{Z^2 e^2}{r_{\text{av}}}$, which exceeds the kinetic energy of cooled ions. This kind of laser cooling improved the beam quality significantly: its length decreased by a factor of two, the diameter by a factor of four, and the momentum scatter by an order of magnitude.

These experiments will be carried out on the New Experimental Storage Ring (NESR) with the use of the PHELIX high-power petawatt laser (Fig. 6.66) [138].

Unlike typical experiments with the use of gaseous targets in this area of physics, a storage ring is able to provide a precision control of the charge-state beam composition as well as the diagnostics of the final states of atoms and electrons at a level of single particles and events. This signifies the possibility of producing unique unperturbed controllable conditions whereby one ion, the field of laser radiation, and one electron participate in the interaction. Therefore, an investigation will be made of fundamental quantum-electrodynamic corrections to the binding energies in atoms, magnetic moments, and magnetic interaction in the ultrahigh field mode. The experiments will employ the SIS 300 synchrotron ring and the NESR ring. Investigations will be carried out using an X-ray crystal spectrometer, a low-temperature calorimeter, a Compton polarimeter, an electron spectrometer, and other high-acceptance diagnostic systems, which make it possible to verify QED models from the spectroscopy of sequential atomic transitions [3, 200].

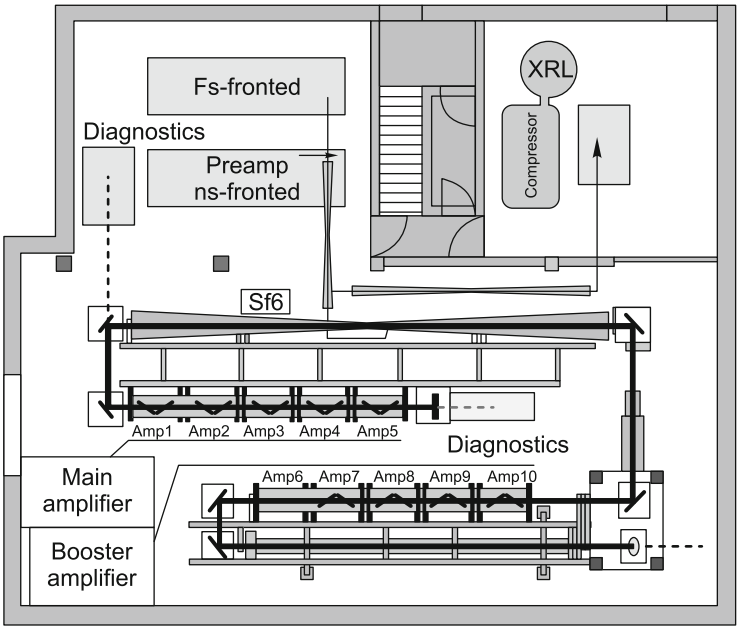

Fig. 6.66 Schematic representation of a petawatt laser [138]

The subjects of planned experimental investigations of the FLAIR collaboration comprise a study of basic symmetries, the effect of gravitation on antimatter, the matter–antimatter interactions, and antimatter atomic physics.

The Facility for Low-Energy Antiproton and Ion Research (FLAIR) [248] under construction is intended for investigating low-energy antiprotons and ions; it comprises new-generation facilities for the production of ultracold antiproton beams required for the highest-resolution spectroscopic investigations of antihydrogen and antihelium atoms captured in traps and cooled with a laser [248]. The antiproton beams generated with an effective efficiency of up to $\approx 10^{12}\,\mathrm{s}^{-1}$ will permit decelerating and capturing antiprotons in numbers 100 times greater than those presently obtained in the CERN [149].

Antiprotons will be produced in the interaction of a high-intensity 29 GeV proton beam with an approximately 8 cm thick generating iridium target [10]. The antiprotons resulting from electron-positron pair production are directed to the CR ring to be cooled for an energy of 3 GeV. The antiproton intensity is next increased in the RESR storage ring, from which they are directed to the NESR ring to be cooled to an energy of 30 MeV. The further deceleration of the antiprotons to energies required for experiments (from 0 to 5 MeV) is achieved in the FLAIR facilities by slowing down the initially fast antiproton beam in two sequential storage rings: the LSR magnetic ring (300 MeV–300 keV) and the USR electrostatic ring (300 keV–20 keV) [239].

The LSR and USR rings make use of beam cooling by electrons to provide a low emittance ($\varepsilon \sim 1\pi$ mm mrad, $\delta p/p \approx 10^{-4}$), and there are internal gas targets for investigating atomic collisions with antiprotons. The Penning trap of the universal HITRAP facility [5] is employed for cooling to cryogenic temperatures and magnetic field deceleration of heavy ions and antiprotons to their complete stop. In these conditions it is possible to measure the electron g-factor in the potential of stable and radioactive U^{238} heavy ions [200]. The study of hyperfine splitting in hydrogen-like ions yields information about the distribution of magnetic moments inside nuclei. Optical pumping of the hyperfine levels of the ground state results in effective polarization of the nuclear spins of radioactive nuclei, thereby providing a unique possibility of verifying the Standard Model.

The availability of this low-energy antiproton beam opens up novel experimental possibilities that have never been realized anywhere in the world. In particular, the superhigh-precision spectroscopy of the hyperfine splitting of the 1.4 GHz line of t he antihydrogen ground state with a relative accuracy of 10^{-4} ($\Delta\nu \approx 100$ kHz) or the 2.5 GHz line arising from the 1s–2s transition with a relative accuracy of about 10^{-10} will permit reaching the sensitivity required for recording *CPT* invariance violations and verifying the results of QED calculations [41, 250].

The trapping and laser cooling of antiprotons opens the way for the experimental investigation into the effect of gravitation on antimatter, unlike the situation when gravitation effects are masked by many orders of magnitude stronger electromagnetic interaction. Planned to this end are the corresponding high-sensitivity experiments on cooled neutral antihydrogen atoms [244].

Collisional experiments on antiprotons and antihelium will permit reconstructing collisional processes for the first time. Owing to the availability of a continuously extracted beam it will be possible to measure the X-ray spectra of antiproton atoms and study nucleus-antinucleus scattering, for instance, on such large antimatter systems like a positively charged antihydrogen atom H^+ (one antiproton and two positrons). Furthermore, combining, in a common facility, unstable nuclei and antiprotons as probe particles opens the door to studies of the structure of exotic nuclei (see Chap. 8).

Therefore, the use of relativistic heavy-ion beams offers unique possibilities for studying atomic and nuclear physics processes under extreme conditions. It is made possible to study the dynamics of relativistic collisions, verify the predictions of quantum electrodynamics in extremely high electromagnetic fields, employ atomic-physics techniques for determining the characteristics of stable and unstable nuclei and, lastly, verifying the Standard Model (see Chap. 10).

6.6 Large Hadron Collider

The study of the basic properties and structure of matter and the evolution of the Universe since its inception have always been among the central problems of contemporary physics. In this connection, the production of extreme states of substance in laboratory conditions, along with observations of astrophysical objects, have been and are giving to researchers new experimental data about the ambient matter and form our basic vision of the world. A special place among research facilities is occupied by relativistic accelerators like the Large Hadron Collider (LHC) (Fig. 6.1) in the CERN, the Relativistic Heavy-Ion Collider (RHIC) (Fig. 6.2) in Brookhaven, USA, as well as the RIKEN cyclotron complex (Japan) and the accelerators TVN-ITEF and Nuclotron (JINR).

In the next three sections we consider briefly the projects of fundamental devices under implementation or implementation-ready, which show promise of a major breakthrough in the near future.

Following [64] we begin our consideration with the Large Hadron Collider (LHC)—a facility with the highest kinetic energy of colliding particles. It gives experimenters a possibility to reach a new—teraelectronvolt—energy level and study the properties of space on progressively smaller scale. We are dealing with verification of the basic predictions of the Standard Model and the quest for effects beyond its framework.

Of greatest interest is the nature of the emergence and diversity of particle masses and fields, the structure of physical vacuum, particle type multiplicity in the Universe, the united description of fundamental forces, including gravitation, the possible existence of supersymmetric partners of all observable particles and additional space–time dimensions, as well as several other basic questions.

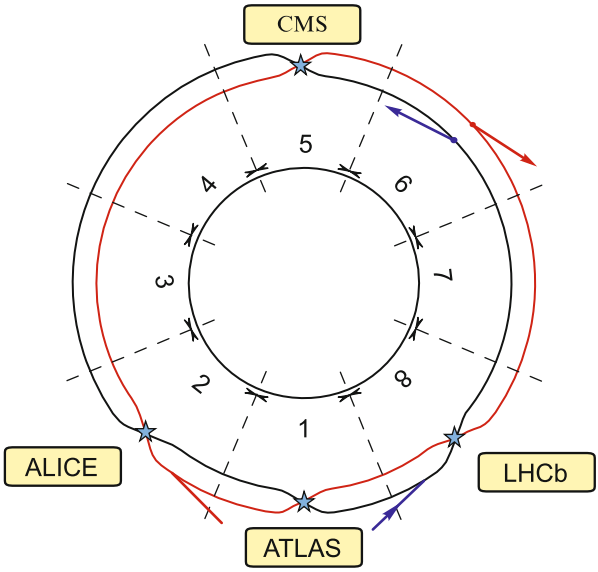

Fig. 6.67 Schematic of the LHC accelerator. The *arrows* indicate the directions of beam propagation. *Asterisks* stand for the four beam collision points, which are the sites of four main detectors [64]

The LHC accelerator is diagrammed in Fig. 6.67. One can clearly see the structure with two counterpropagating beam directions (indicated by arrows). In 2011 the proton energy in each of the beams was equal to 3.5 TeV, so that the total collision energy was equal to 7 TeV. In 2012 the collider operated for a total energy of 8 TeV. The projected total collision energy is 14 TeV [192].

The oppositely directed particle motion in two channels is provided by 1232 superconducting magnets with an induction $B \approx 9\,\mathrm{T}$ each (Fig. 6.68). The magnets operate at a very low temperature (1.9 K) and pressure (10^{-10} Torr). To initially cool the magnets, use is made of up to $1.2 \cdot 10^7\,\mathrm{l}$ of liquid nitrogen and up to $7 \cdot 10^5\,\mathrm{l}$ of liquid helium for their subsequent operation. Engineers have to provide reliable control over 40,000 connections to prevent them from leaking. Apart from the principal magnets, there are over 500 quadrupole superconducting magnets and over 4000 beam-positioning superconducting magnets.

Apart from the high energy of colliding particles, the LHC accelerator should possess a high luminosity of up to $10^{34}\,\mathrm{cm}^{-2}\,\mathrm{s}^{-1}$, which will enable studying rare events with small cross sections. It is precisely these rare events that are of interest for new physics for the sake of which the LHC was constructed. In the investigation of processes with large cross sections it is sufficient to operate in a lower-luminosity mode. This may be attained in different ways, for instance, by beam defocusing, like in the operation with the LHCb (Large Hadron Collider beauty experiment) detector.

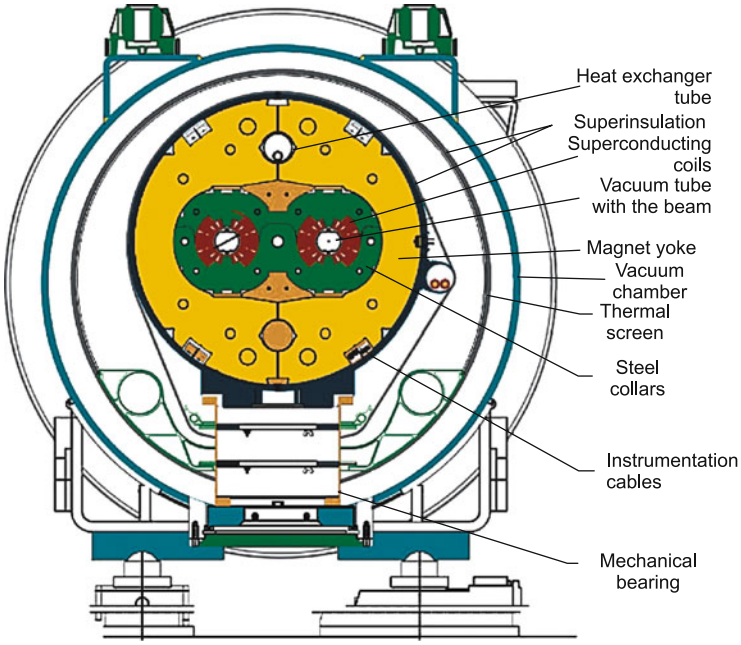

Fig. 6.68 Diagrammatic representation of LHC magnetic system [64]

Four principal detectors, ATLAS (A Toroidal LHC ApparatuS), CMS (Compact Muon Solenoid), ALICE (A Large Ion Collider Experiment), and LHCb, record the products produced at four beam interaction products. To this end, four international collaborations of the same names were developed for operating these detectors (Fig. 6.68). The largest-scale detectors, ATLAS and CMS (Figs. 6.69 and 6.70), are intended for studying proton-proton and ion-ion collision events. The ALICE detector is intended for the investigation of ion-ion collisions, although some data for proton-proton processes will also be obtained on it. The LHCb is intended for recording b-quark production events. In addition the four principal detectors there are subdetectors of smaller size, which operate in concert with the principal detectors: LHCf (LHC forward), Totem, ZDC (Zero Degree Calorimeter), FMS (forward muon spectrometer), CASTOR, and FP420.

The detectors are outstanding engineering structures in themselves. In particular, the ATLAS measures 25 m in height (which is approximately equal to the height of an 8-storey building), 46 m in length, and weighs 7000 t. This size is required to accommodate all trackers and calorimeters so as to maximize the spanned angular range in which the generated particles will be recorded.

The beam structure exhibits special features. The proton flux in the accelerator ring consists of bunches spaced at 25 ns time intervals, or at about 7.5 m. For this repetition rate of the beams, the frequency of their encounters at the interaction points is equal to 30–40 MHz. The majority of beam photons will overfly these

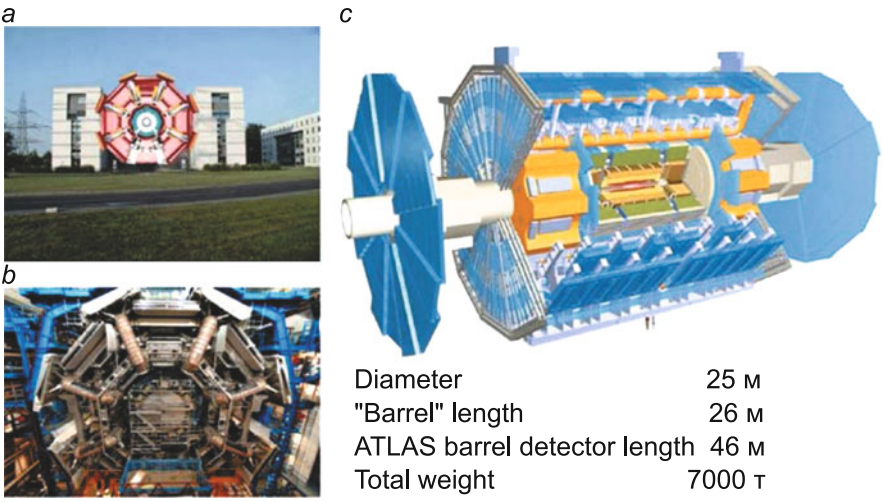

Fig. 6.69 ATLAS detector: (**a**) natural-size detector image superposed upon building 40 in the CERN, which is the site of ATLAS and CMS collaborations; (**b**) general view; (**c**) cross-sectional diagram [64]

points without undergoing interaction and will continue their motion along the accelerator ring. But even in this case, about 20–40 proton–proton interaction events will simultaneously occur at a very short range at every beam encounter. The trigger system must distinguish between the interactions and, furthermore, select those of them which are of physical interest. The triggers must therefore be fast-responding, purpose-oriented, and suited to the corresponding detector objectives [64].

The magnetic fields in detectors are required to bend the trajectories of produced charged particles and amount to 2 T in the ATLAS and to 4 T in the CMS. The trajectory curvature permits measuring the momentum of a particle and determining its mass. This is the main information acquired about the interaction. The particle detection relies on the interaction of charged particles with detector substance. The general "architecture" of the ATLAS, CMS, and ALICE detectors has much in common, while the LHCb is oriented to b quarks, which travel primarily in the forward direction.

Special emphasis is placed on the radiation resistance of the materials in use, because the radiation intensity is very high owing to the short distances from the interaction points. This requirement also holds for the electronic systems that read out the information from detector components and relay it to computer network.

The calorimeters of the detection system absorb and measure electron, photon, and hadron energy fluxes; they also serve as signal triggers, in particular, for the events under study. They are employed to measure the propagation direction and energies of electromagnetic showers. Hadron calorimeters, which are arranged around the electromagnetic calorimeters, also measure the directions and energies of hadronic showers (especially hadronic jets) as well as the missing energy,

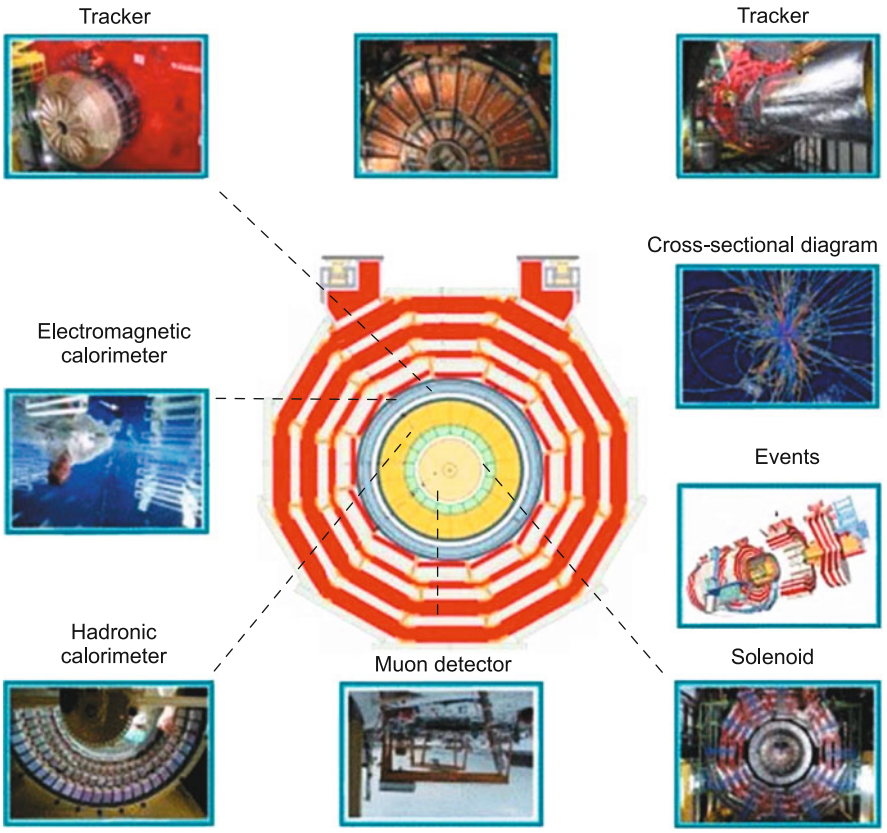

Fig. 6.70 CMS detector: cross-sectional diagram and internal structure with indication of trackers and calorimeters [64]

which may be associated with neutrinos, undetected neutral particles, etc. The peripheral detector parts remotest from the interaction points consist of gas-using devices intended for the identification of muons and measuring their momenta. The operation of these devices is timed to the operation of the rest detectors [64].

The LHC project necessitates the use of huge computational power to store, distribute, and analyze the information arriving from the accelerator. It amounts to several tens of petabytes per year. Developed for this purpose is a special project (Grid), which unites computer centers throughout the world.

Following [64] we briefly discuss the main scientific objectives of the LHC project. This was, in the first place, the program for the quest of the only undiscovered particle of the Standard model—the Higgs boson, which is responsible for the nature of particles' mass and their diversity in the Nature (the top quark mass is 10^{14} times greater than neutrino's mass, and the photon mass is nil at all) [64]. The new particle was indeed discovered in the execution of the program. It is rather

heavy if measured by the yardstick of microworld physics. In this realm of physics the mass is measured in energy units. In these units the electron mass is equal to 0.5 MeV, the proton mass is equal to about 1 GeV, and the mass of the heaviest known elementary particle, t quark, is equal to 173 GeV. And the mass of the new boson is equal to 125–126 GeV (more precisely, 125.3 ± 0.4 (stat.) ± 0.5 (syst.) GeV according to the CMS data [47] and to 126.0 ± 0.4 (stat.) ± 0.4 (syst.) GeV according to the ATLAS data [13], where statistical and systematic uncertainties are given). This new particle (conventionally labeled as H) is void of electric charge. It is unstable and may decay in different ways. It was discovered on the Large Hadron Collider [13, 47] in the study of its decay into two photons, $H \rightarrow \gamma\gamma$, and into two electron–positron and/or muon–antimuon pairs, $H \rightarrow e^+e^-e^+e^-$, $H \rightarrow e^+e^-\mu^+\mu^-$, $H \rightarrow \mu^+\mu^-\mu^+\mu^-$. It is very important to elucidate if there exists only one Higgs boson or there also are other Higgs bosons, and whether this particle has internal structure. Higgs fields are intimately related to astrophysical observations like dark energy (or, in the language of theorists, to the cosmological constant in the gravitation theory) [64].

Another line of research on LHC involves the quest for heavy supersymmetric partners of the known particles; such partners would testify to the supersymmetry of our world. The cross sections for the processes that go beyond the Standard Model are extremely small and are estimated to lie in the range from several femtobarns to several picobarns.

The experimental program of the LHC comprises studying quantum chromodynamic effects like inclusive distributions, production of B mesons or mesons containing both *bottom* and strange quarks, dileptonic spectra, collective effects in ion-ion collisions, etc.[64]. The LHC will also generate different heavy quarks, because the cross sections for $b\bar{b}$ pair production will be around 1 μb and for the top quark production around 1 nb.

The complex structure of physical vacuum with numerous minima, special asymmetries, as well as multidimensional effects possibly underlie many interesting effects. In particular, it is believed that physical vacuum is not empty and is filled with scalar Higgs fields [64].

Supersymmetry may show up in LHC experiments in the detection of light particles like neutrino and gravitino [64]. The supersymmetry implies that the known fermions correspond to their supersymmetric partners—bosons, while such partners are nonexistent in the Standard Model. Their discovery will signify going beyond the framework of the Standard Model, which will probably invite the existence of superparticles. This would give rise to an absolutely new world: we will have at our disposal a natural candidate for the explanation of dark matter and a possibility of unifying all fundamental forces of the nature [64].

Another route beyond the scope of the Standard Model is opened up by the idea of additional dimensions of the space–time. These additional dimensions may be convolved (compactified), so that they have not been heretofore observed but, perhaps, may lend themselves to observation at energies above 1 TeV. In this case, in particular, gravitation may become strong and give rise to black miniholes [64] at LHC energies, which is the subject of anxiety of numerous articles in the press.

The LHC project intends to study the properties of compressed baryon matter at an energy 28 times higher than on the RHIC and 300 times higher than on the SPS. The case in point is the states and properties of quark-gluon plasma in a new energy range, which is extremely important for understanding the behavior of matter under these conditions and, consequently, for understanding the processes that took place in the early Universe, when quarks and gluons were not confined in hadrons and were "free". A change in the nature of collective effects with increasing energy may point to the nature of the transition from hadrons in nuclei to quark-gluon substance during the time interval when the nuclei overlap prior to subsequent hadronization. The behavior of nuclear substance in ion collisions on the LHC may turn out to have little in common with the results of simple extrapolations. Generally speaking it is difficult to predict which route has been taken by the Nature—one of those known to us today or an entirely different one in the new energy domain. To approach an answer to this question we will have to wait for experimental data from the LHC.

Apart from the search for a hot and dense quark-gluon plasma, promise is shown by the quest for a cool and dense condensate of color glass (CGC), which may exhibit new properties of the fields described by quantum chromodynamics [64].

The proton at high energies is a source of partons; the LHC will be a tool for studying a variety of exclusive processes. For instance, it will be possible to distinguish quark-quark, quark-gluon, and gluon-gluon scattering. It will be possible to study their interaction with pomerons and pomeron-pomeron interactions. The strong electromagnetic fields of colliding nuclei may lead to new interesting effects in $\gamma - \gamma$ processes and give rise to unexpected asymmetries [64].

Long-term research in the realm of high-energy physics largely depends on what results will be obtained on the LHC. Further advancement requires raising the proton beam luminosity by an order of magnitude. This project has come to known as Super LHC (SLHC). It will improve the statistics and broaden the mass range wherein the search will be made for supersymmetric particles and additional dimensions [64].

Another long-term project is the International Linear Collider (ILC), where electrons and positrons traveling along rectilinear trajectories in the opposite directions will collide with a total energy of 1 TeV. It will be possible to study the supersymmetric world with a good precision for large masses. The need will supposedly emerge for even higher energies—of several TeV. Then the Compact Linear Collider (CLIC) project will become topical if the need arises to investigate particles of even larger mass[64].

These projects will compete with the projects which plan to double (DLHC) or even triple (TLHC) the LHC energy [64].

The discussion and comparison of different possibilities of choice are underway even now. Concrete solutions may not be approached until the LHC begins operating at full energy of 13–14 TeV and rapidly acquiring data. The future of high-energy physics largely depends on these results.

6.7 FAIR Project

The European Facility for Antiproton and Ion Research (FAIR) is the project of a new research complex based on a multi-purpose accelerator with antiproton and radioactive-nuclei beam parameters that are unrivaled in the world and which offer unique possibilities for carrying out scientific investigations in the most topical areas of modern science and innovative technologies [83].

Being under construction in Darmstadt, Germany, this ultra-modern accelerator complex will provide precisely tuned high-energy beams of antiprotons and different ions of unique quality (brightness, phase density) and intensity. A distinguishing feature of the FAIR project under construction is the availability of high-intensity primary and secondary beams of stable and radioactive nuclei as well as of antiproton beams, which exceed in intensity the presently existing beams in the world by factors of 100–10,000.

Furthermore, experiments on the FAIR will make it possible to substantially advance in the investigation of unknown phase diagram domains of nuclear matter in comparison with the experiments on the RHIC ion collider in the Brookhaven National Laboratory, USA, and the LHC in the CERN [81]. Unlike these laboratories, where emphasis is placed on the investigation of nuclear matter properties at extremely high temperatures but low baryon densities, the FAIR experiments are aimed at the detailed study of matter properties at the highest baryon densities attainable under terrestrial conditions.

The scientific objectives of the program for the FAIR accelerator complex are grouped into the following concrete lines of investigations:

- The study of nuclear structure and nuclear astrophysics with the use of stable ion beams as well as the beams of short-lived (radioactive) nuclei distant from the stability limit;
- Hadronic structure, the theory of strong interactions in the framework of quantum chromodynamics (QCD) primarily using antiproton beams;
- The phase diagram of nuclear matter, quark deconfinement, and quark-gluon plasma;
- The physics of superdense electromagnetic plasma with the use of high-intensity heavy ion beams in unique combination with a petawatt laser;
- Atomic physics, quantum electrodynamics (QED) and ultrahigh electromagnetic fields with the use of highly charged heavy ion beams and antiprotons;
- Applied research and technology developments with ion beams for material science, medicine, and biology.

The experiments which will be carried out on the FAIR call for significant technological innovations:

- new superconducting magnet designs for producing particle beams of highest possible intensity;
- novel techniques for the precision control of beam energy and geometry;

- large detectors capable of tracking the trajectories and parameters of the great number of particles produced in the experiments;
- extremely high data streams arriving from detectors will invite new hardware and software solutions (like the GRID technology) for their processing, accessibility, and storage.

The FAIR is an international project, which is among the basic projects of the European Strategy Forum on Research Infrastructures (ESFRI) [4]. Fifteen countries of the world participate in the project: Austria, Great Britain, Germany, India, Spain, Italy, China, Poland, Russia, Romania, Slovakia, Slovenia, Finland, France, and Sweden. The countries intend to make contributions in the form of deliveries of high-tech equipment and components of experimental facilities as well as in the form of money contributions.

The total project cost, including construction, maintenance, and operation for a period up to 2025 amounts to about 3 billion euros. The cost of construction of the initial phase of the acceleration center and its basic research facilities exceeds 1.5 billion euros.

The construction term of the FAIR facility is set at 8 years. It is planned to complete its construction in 2018. In this case, the commencement of scientific research on several subsystems of the accelerator complex is planned even for 2017.

About 3000 researchers from all over the world will carry out experiments on the FAIR accelerator complex, which are aimed at the study of the basic properties and structure of matter and the evolution of the Universe since its inception. To date, 14 large international collaborations have been set up, which are grouped into four subject lines of research:

- nuclei and nuclear astrophysics—NuSTAR;
- dense baryonic matter—CBM;
- antiproton program—PANDA;
- superdense plasma physics, atomic physics, as well as applied research in material sciences and biology—APPA.

6.7.1 Accelerator Complex

The heavy-ion accelerator complex operating at the Heavy-Ion Research Institute (GSI) in Darmstadt [11] is one of the most successfully operating facilities with a multi-aspect scientific program of international experiments. However, in 2002 a start was made on the development of the concept of a new-generation multipurpose facility with new requirements on the qualitative characteristics and intensity of ion and antiproton beams for executing experimental research in previously unattainable conditions. In 2006, the international scientific community—2500 scientists and engineers from 44 countries—draw a FAIR Basic Technical Report, which specified the engineering diagram and components of the requisite system of accelerators and the types of proposed experiments. The central characteristic of the FAIR is a

complicated and cost-justifiable arrangement of a number of accelerator systems, which is aimed at the production of particle beams in an unprecedentedly broad parameter range. In this case, a critically important feature of the accelerator complex will consist in the capability of simultaneous execution in parallel of up to five different research programs. By and large, the complex will serve different experiments so as if it were intended separately for each of them.

The general view of the FAIR accelerator complex and its main parameters are given in Fig. 6.71 and Table 6.3. The existing UNILAC accelerator and the SIS 18 synchrotron will serve as injectors for the FAIR accelerator complex.

The FAIR complex consists of carefully designed and interconnected systems for the acceleration and storage of high-quality particle beams as well as for obtaining secondary particles produced in the bombardment of targets by the primary beams. High-energy proton and ion beams will be used for producing secondary antiproton beams as well as stable and unstable (radioactive) nuclei. The secondary beams may be employed directly or delivered to a complex system of storage rings, which serve to form the parameters required by experiments.

The basis of the FAIR is provided by two accelerator synchrotron rings with a perimeter of 1100 m (SIS 100 and SIS 300) with respective magnetic rigidities of 100 and 300 T m arranged one above the other in an underground tunnel and intended for ion acceleration—from hydrogen ions (protons) to uranium ions. The presently operating UNILAC and SIS 18 will preaccelerate ions prior to their

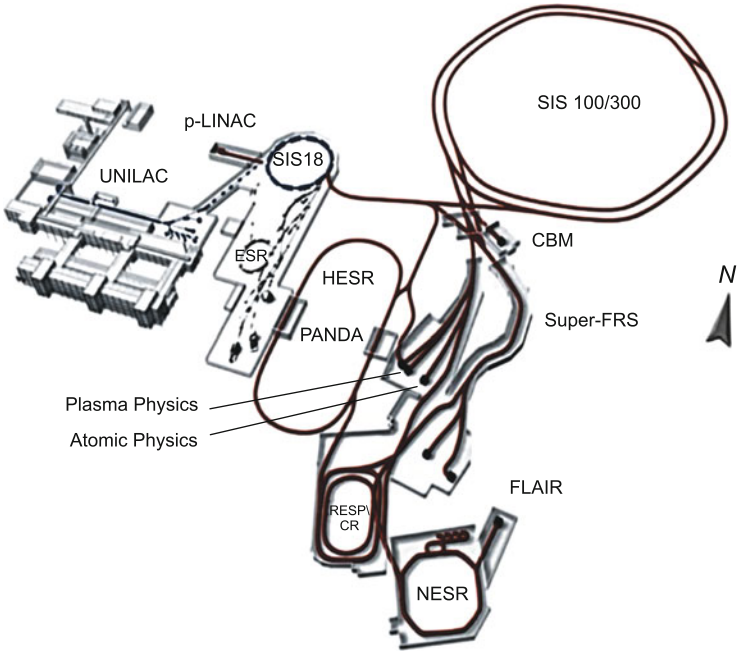

Fig. 6.71 Schematic representation of the FAIR accelerator complex [83]

Table 6.3 Main parameters of synchrocyclotrons and storage rings

Ring	Ring perimeter (m)	Magnetic rigidity (T m)	Beam energy
SIS 100 synchrotron	1084	100	2.7 GeV/nucleon, $^{238}U^{28+}$ 27 GeV, protons
SIS 300 synchrotron	1084	300	34 GeV, $^{238}U^{92+}$
CR (collector ring)	211	13	0.74 GeV/nucleon, $^{238}U^{92+}$ 3 GeV, antiprotons
RESR (recirculation experimental storage ring)	245	13	0.74 GeV/nucleon, $^{238}U^{92+}$ 3 GeV, antiprotons
NESR (new experimental storage ring)	222	13	0.74 GeV/nucleon, $^{238}U^{92+}$ 3 GeV, antiprotons
HESR (high-energy storage ring)	574	50	14 GeV, antiprotons

injection into the new ring SIS 100. The SIS 100 is intended for generating high-intensity pulsed ion beams with the purpose of subsequently converting them to the secondary beams of rare-element nuclei as well as for converting proton beams to antiprotons. The synchrotron ring will consist of superconducting magnetic elements, providing the field of up to 4 T with a frequency of 1 Hz (for a field build-up rate of 4 T/s). The projected intensity in U^{28+} uranium ions will be equal to $5 \cdot 10^{11}$ ions per pulse for an energy of 1 GeV/nucleon and in protons to $4 \cdot 10^{13}$ for an energy of 29 GeV. A new linear proton accelerator meant for an energy of 70 MeV will be constructed for injecting high-intensity proton beams.

Both ion and proton beams will undergo temporal pulse compression for the production, storage, and subsequent cooling of exotic nuclei and antiprotons with respective pulse durations of 60 and 25 ns. Short high-intensity heavy-ion pulses are also required in experiments on plasma physics.

Also possible is a continuous beam mode with an average intensity of $\approx 3 \cdot 10^{11}$ ions per second and an energy of 1 GeV/nucleon on extraction directly from the SIS 100 ring or on beam transfer to and subsequent slow extraction from the SIS 300 ring.

Accelerated uranium nuclei are injected into the SIS 300 ring constructed on the basis of superconducting fast-cycling magnetic elements, which provide a field of up to 6 T and a field build-up rate of 1 T/s. The highest ion energy amounts to 45 GeV/nucleon for Ne^{10+} and to 34 GeV/nucleon for completely ionized uranium U^{92+}. The extraction of the beams with an intensity of up to $\approx 10^{10}$ particles per second with an extraction period of 10–100 ns is provided for use in experiments on heavy ion collisions with the production of superdense nuclear matter.

The SIS 100/300 accelerators are connected by transportation lines with a complicated system of successive rings. The beams injected into these rings are accumulated, "cooled", and prepared for specific experiments. The FAIR will

operate multifunctionally and permit the simultaneous execution of up to five research programs with five different particle beams. This will be achieved by way of coordinated control over the beams in both synchrotrons as well as in the adjacent storage and accelerator rings. Therefore, each experiment will be able to make full use of the highest attainable beam intensities.

Carrying out precision physical experiments requires that the secondary beams possess specific energy and all beam particles move in one direction with the same velocity (minimal longitudinal phase volume). This is achieved using so-called beam "cooling" techniques.

Two types of cooling will be employed in the FAIR:

- beam cooling by electrons (see, for instance, the CERN [11]), whereby the ions are decelerated to a common velocity in the periodic interaction with a parallel beam of electrons possessing a strictly defined velocity;
- stochastic cooling, whereby so-called pickup electrodes determine the geometrical position of the center of the ring-orbiting beam for the generation of the requisite field amplitude of correction devices (kickers) located at the diametrically opposite portion of the CERN storage ring [175, 239].

The beams are cooled and tuned for experiments in the four following rings.

Collector ring (CR), in which the secondary beams of ions and antiprotons undergo stochastic cooling, which decreases the phase volume of the antiproton beam by a factor of $1.6 \cdot 10^4$ (during a 10-s cooling time) and of rare isotope beams by a factor of $1.3 \cdot 10^6$ (during a 1.5-s cooling time). This ring will also be employed for measuring the masses of short-lived nuclei;

Recirculation experimental storage ring (RESR), to which bunches of 10^8 antiprotons with an energy of 3-GeV stochastically cooled in the CR will be delivered once in 10 s. This will permit accumulating up to 10^{11} antiprotons for their subsequent use in the HESR. The RESR will also provide a rapid deceleration (during 1 s) of rare isotopes from an energy of 740 to 100–500 MeV/nucleon.

New experimental storage ring (NESR), which is intended for experiments with exotic ions and antiprotons. It will make use both of cooling by electrons and of stochastic cooling for experiments of different kind, including experiments at very low energies (down to 30 MeV for antiprotons and to 4 MeV/nucleon for radioactive ion beams).

High-energy storage ring (HESR), in which 14.5 GeV antiproton beams are prepared for experiments with the help of cooling by electrons and stochastic cooling.

Antiproton beams for PANDA experiments will be obtained in the following way [156]. Initially the pulsed proton beams with a current of 70 mA, a pulse duration of 40 μs, and a repetition rate of 5 Hz accelerated in a special linear accelerator (p-LINAC) to an energy of 70 MeV will be injected into the SIS 18 synchrotron.

To increase the number of accelerated protons, the SIS 18 synchrotron ring will be filled with eight proton micropulses (bunches) prior to their acceleration

to an energy of 2 GeV required for the subsequent injection into the main FAIR accelerator—the SIS 100 synchrotron.

The protons circulating in the SIS 100 will be accelerated to a final energy of 29 GeV and, prior to their extraction onto an antiproton-producing target, compressed into one bunch about 7.5 m in length, which corresponds to a duration of $\approx$25 ns. Every 10 s the bunch of $2 \cdot 10^{13}$ protons will be directed onto a thick (with an effective thickness of 60–80 mm) iridium or tungsten target, with the resultant production of up to $1 \cdot 10^{8}$ antiprotons (the yield amounts to $5 \cdot 10^{-6}$ per proton) with an average energy of 3 GeV.

The resultant separated short antiproton bunch with a momentum spread $\delta p/p = \pm 3\,\%$ and a transverse emittance $\varepsilon_{x,y} = 200$ mm mrad is then fed to the CR storage ring, where its phase volume is transformed in such a way that the bunch lengthens from $l_b \approx 15$ m to $l_b \approx 45$ m for the corresponding reduction of the momentum spread to $\delta p/p = \pm 1\,\%$. Next, with the use of an adiabatic rebunching the antiproton beam is prepared for its stochastic cooling; on its application the antiproton beam ($\delta p/p = \pm 0.1\,\%$, $\varepsilon_{x,y} = 5\pi$ mm mrad) is bunched once again and delivered to the RESR ring, in which there occurs antiproton accumulation.

In the RESR ring the antiproton beam will undergo stochastic cooling throughout the accumulation time, during which a new antiproton beam is injected into the RESR every 10 s. The rate of antiproton accumulation is comparable to their cooling rate in the CR ring. This signifies that it will be possible to obtain $7 \cdot 10^{10}$ antiprotons per hour. The choice of accumulation time (or the total number of accumulated antiprotons) will be governed by experiment requirements.

The beam of antiprotons with momenta of 3.8 GeV/c stored in the RESR ring is compressed into one bunch prior to its injection into the HESR high-energy storage ring. In the HESR, whose circumference is equal to 574 m, the antiproton beam may be either accelerated or decelerated to the momentum required in a given experiment with a rate of about 0.1 GeV/c per second.

Therefore, the FAIR accelerator complex will provide antiproton beams of unprecedented intensity and quality in the momentum range from 1.5 to 15 GeV/c (or energy range from 0.83 to 14.1 GeV) for annihilation experiments with the use of an internal target and a universal 4π PANDA detector. To compensate the antiproton beam heating, which occurs due to its interaction with the internal target and the intrabeam scattering, the HESR ring will be equipped with a facility for cooling by electrons with an electron energy of up to 4.5 MeV as well as with a stochastic cooling system.

The ultrahigh requirements on the quality and intensity of the beams entail the realization of the extremely complex FAIR accelerating-storage scheme.

Intensity problems. The technical requirements imposed on the fast-cycling magnets [156], in which the magnetic field will rise to 2 T with a rate of 4 T/s in the SIS 100 accelerator and to 6 T with a rate of 1 T/s in the SIS 300 accelerator, compel the developers to go beyond the limitations of modern technologies and proceed to the use of superconductivity with record parameters as regards the field build-up rate.

Induced radioactivity problems. High-intensity particle beams will call for the development of new materials and new radiation-resistant designs of accelerator and detector components capable of withstanding the radiation induced therein.

Accelerator problems. The rapid acceleration of the heavy uranium ions U^{28+} will require complex radiofrequency devices capable of generating extremely high fields with steep leading edges and variable frequency to produce short (50–100 ns) high-intensity particle pulses.

Ultrahigh dynamic vacuum problems. The new materials and technical systems must sustain ultrahigh vacuum conditions (10^{-12} mbar) in the presence of high-intensity ion beams in the vacuum channels of accelerators and storage rings. The inevitable particle loss may give rise to molecular desorption from their wall, which will entail an undesirable increase in residual gas pressure. Specially designed collimators are meant to minimize these effects. The higher, in comparison with the LHC (10^{-10}–10^{-11} mbar), vacuum requirements in accelerator scheme channels arise from the necessity of acceleration ions with a broad spectrum in mass and charge, including those with large cross sections for the capture and/or ionization of orbital electrons.

And now we address the FAIR scientific program.

6.7.2 *Atomic Nuclear Structure, Astrophysics, and Nuclear Reactions with Rare Isotope Beams: NuSTAR (Nuclear STructure, Astrophysics and Reactions)*

The experiments grouped into the NuSTAR direction comprise a broad spectrum of investigations into the physics of atomic nucleus, nuclear astrophysics, fundamental interactions, and symmetries.

Radically new aspects of nuclear structure are found in the investigation of exotic short-lived nuclei, which are carried out using secondary radioactive nuclear beams [92, 158, 161, 164, 193, 225].

Exotic nuclei are characterized by the extreme excess of protons or neutrons and are therefore away from the domain of stability (Fig. 6.72). The structure of such nuclei would be expected to substantially differ from the structure of the nuclei that fill the stability domain [172, 231, 253]. For instance, they have significantly different proton and neutron density distributions distinguished by the existence of a proton/neutron halo. Furthermore, possess new excitation modes, which are nonexistent in stable nuclei. The study of these effects is of major significance for the understanding of the dependence of intranuclear forces as well as the effects of pairing and clusterization on the isotopic spin and density (see, for instance,[158, 185, 194, 234]).

With the use of rare isotopes of the FAIR accelerator complex it will be possible for the first time to determine the properties of many unstable nuclei remote from the stability domain, which exert a significant effect on the astrophysical processes

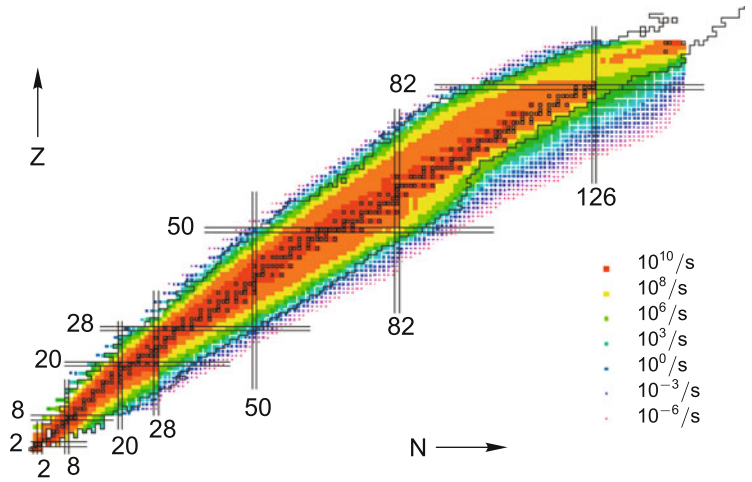

Fig. 6.72 Map of the radioactive beam intensities per second expected in the FAIR (marked in *color* in accordance with the scale column at the *right*). The nuclei of primary beams and the boundaries of known nuclei are shown in *black* [11]

in the Universe that govern the origin of heavy chemical elements, the physics of stellar explosions, stellar nuclear processes, and the properties of compact objects like white dwarfs, neutron and strange stars [161]. New possibilities emerge for the understanding of the physics of thermonuclear explosions on the surfaces of giant stars as well as for the explanation of activity manifestations of new astrophysical phenomena and the evolution of the Universe after the Big Bang.

One of the main FAIR objectives is to obtain the secondary beams of radioactive nuclei for investigating the nuclear structure and the origin of the elements in the Universe. According to modern views [8], there are more than 6000 different nuclei, most of them being unstable, especially those with a substantial difference in proton and neutron numbers. The nuclei of complex and sometimes unusual structure may exhibit unconventional behavior, which sheds light on the operation of forces that keep the nuclei from breaking up.

Despite the fact that some of these rare isotopes exist for only a short time (less than 10^{-6} s), they play a decisive role in the nuclear reactions that give rise to heavy elements in the stars. While light elements are produced throughout the lifetime of the stars in their thermonuclear burn, heavier elements (heavier than iron) are produced, it is believed [74, 136, 176], primarily during the premortal agony of supermassive stars, when they explode as supernovae (see Chap. 9). The elements then propagate through the interstellar space and eventually become the building blocks for next-generation stars and planets. The only way of verifying these ideas is to produce and study the unstable isotopes in a laboratory. The FAIR, like no other laboratory in the world, will produce the yet unknown exotic nuclei and measure their masses, decay modes, and other properties. Shown by way of illustration in Fig. 6.72 is a nuclear map.

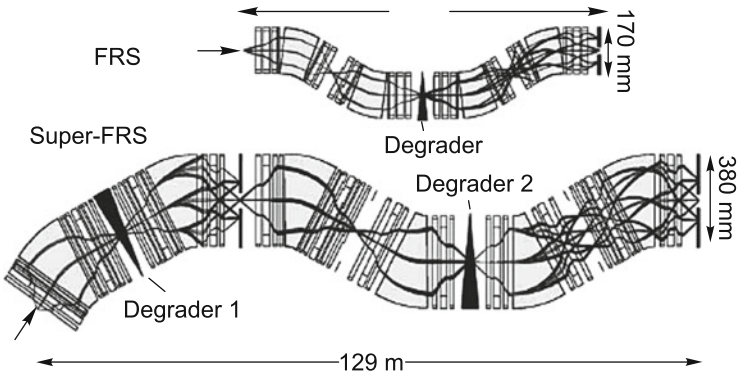

Fig. 6.73 Comparison of the ion-optical schemes of the new Super-FRS separator and the FRS separator presently existing in the GSI. For clarity the longitudinal and transverse scales are taken different but the same for both separators [11]

For this line of research the new accelerator complex will provide the secondary beams of radioactive nuclei throughout the range of charge and mass numbers, from the lightest to the heaviest ones. These secondary rare-isotope beams will be obtained either by way of fragmentation of primary heavy-ion beams or as a result of fission of a ^{238}U beam with an energy of up to 1.5 GeV/nucleon. The beams of nuclei with different charge and mass numbers will be separated using a new, partly superconducting Super-FRS magnetic separator (Fig. 6.73), whose ion-optical scheme is depicted in Fig. 6.73 in comparison with the scheme of the FRS separator presently existing in the GSI.

So, the beams of exotic nuclei are produced in the passage through the target of the primary beam of heavy ions. In doing this the ions split into other nuclei, which are immediately separated in a magnetic separator (Fig. 6.74). This permits obtaining high-purity beams of all kinds of isotopes (including short-lived ones) in a broad energy range and with temporal characteristics matched to specific experiments. For the first time the heaviest radioactive nuclei (up to uranium) will be produced in quantities sufficient for carrying out precision measurements.

The Super-FRS design relies on the operating experience of the fragment separator existing in the GSI, which makes use of the principle of double magnetic analysis with intermediate selection in energy. The high intensity of the primary beams arriving from the SIS 100/300 dictates recourse to a two-stage magnetic separator scheme equipped with wedge-shaped degraders (varied-thickness decelerators), which permit monochromatizing the transmitted secondary beams [198] due to a difference in particle energy loss in the material of different thickness.

The wide-aperture Super-FRS separator will have a large acceptance in momentum ($\pm 2.5\,\%$) and angle (a horizontal divergence of ± 40 mrad and a vertical divergence of ± 20 mrad) as well as an ion-optical resolving power of 1500. The new separator conception with two independent separation stages is intended to cope with a high load and thereby provide efficient background suppression. About

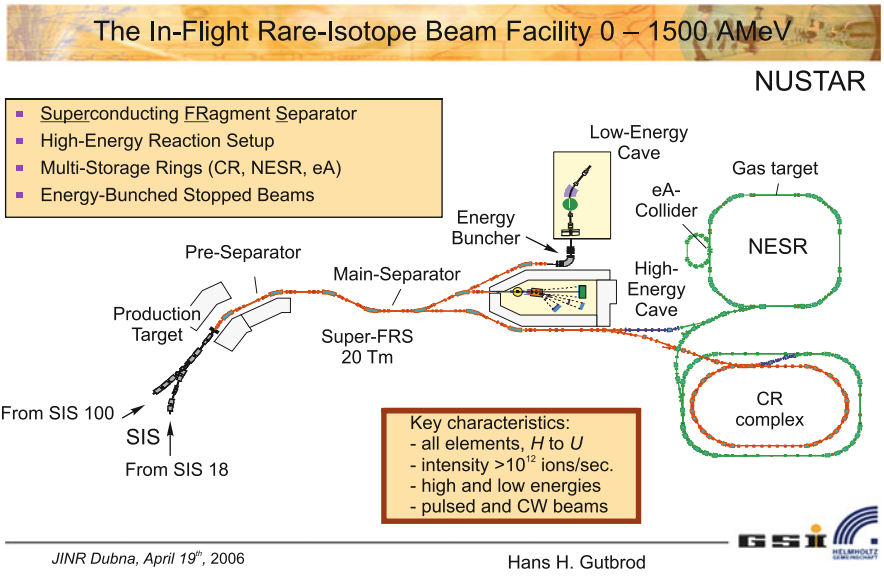

Fig. 6.74 Setup of NuSTAR experiments [11]

30–60 % of the fission fragments will be extracted as spatially separated isotope beams.

Even the shortest-lived isotope beams may be obtained and employed in research on the FAIR accelerators. Secondary beams are obtained at a high purity level in a wide energy range with the capability of providing a different temporal structure (pulsed or quasicontinuous). They can be transported to target stations or injected into storage rings.

At the present time the NuSTAR scientific direction (Fig. 6.74) encompasses eight experiments. This direction embraces more than 800 collaboration participants from 37 countries of the world.

R^{3}B (**R**eactions with **R**elativistic **R**adioactive **B**eams): the structure of atomic nuclei will be investigated in nuclear reactions with high-energy radioactive ion beams. To this end, highly efficient high-resolution universal equipment with a large acceptance will be installed in the focal plane of the high-energy branch of the Super-FRS separator [198].

HISPEC (**Hi**gh Resolution **Spec**troscopy): employing intermediate-energy radioactive beams, investigations will be made of the evolution of the shell structure of highly neutron-excessive medium-heavy nuclei with the use of the reactions of Coulomb excitation, knocking-out, and secondary fragmentation. Furthermore, investigations will be made of the evolution of collective states of the nuclei remote from stability path (see Fig. 6.72) by measuring the lifetimes and gyromagnetic ratios (i.e. the ratio between the magnetic dipole moment of an elementary particle (or a system of elementary particles) and its mechanical moment).

DESPEC (**De**cay **Spec**troscopy): in all DESPEC experiments, use will be made of deep ion implantation into an active substrate (active stopper) prior to ion decay. A multisegment detector will permit correlating in space and time the signal caused by the implantation of a heavy ion and the signal of the subsequent β decay emerging in the detector itself. For exotic nuclei, investigations will be made of unusual decay modes like β-delayed neutron emission and fission, or direct neutron radioactivity. It will be possible to study the properties of the isomeric states of short-lived nuclei.

LaSpec (**La**ser **Spec**troscopy of short-lived nuclei): a multipurpose laser spectroscopy facility will be made for studying stopped, cooled, and spatially bunched radioactive ions [105, 162, 201], which will make it possible to model-independently measure the nuclear spins of isotopes and isomers, magnetic dipole moments, electric quadrupole moments, and route-mean-square radius variations.

MATS (Precision **M**easurements of very short-lived nuclei using an **A**dvanced **T**rapping **S**ystem for highly charged ions): this program is aimed at precision measurements of short-lived nuclear masses. Experimentally, the MATS will be a unique combination of an electron-beam ion trap (EBIT) for obtaining multiply charged ions, ions traps for beam preparation, and a high-precision system based on a Penning electromagnetic trap for measuring masses (with a relative accuracy of about 10^{-9}) and studying decays (conversion electrons and alpha particles)—of radioactive nuclei. A recent review of the works on precision nuclear-physical measurements with the use of ion traps is given in [105].

ILIMA (**I**someric Beams, **Li**fetimes and **Ma**sses): this program is aimed at mass and lifetime measurements of exotic nuclei in the ground and isomeric states at relativistic energies. To this end, exotic nuclear ion beams will be injected into the CR storage ring. The measurements of masses (accurate to ± 50 keV) and lifetimes of very short-lived nuclei (to several microseconds) by way of measurements of the frequency spectra of the ions circulating in the ion storage ring (see, for instance,[182]) will be carried out in the CR operated in an isochronous mode. Longer-lived nuclei (over 1 s), after their preliminary stochastic cooling in the CR, will be directed to the next ring RESR and then injected into the NESR storage ring. Here, they will undergo additional cooling by electrons after which their masses will be measured by the same technique [144]. Transferable particle identification detectors will be installed after one of dipole magnets in the CR and NESR for independent lifetime measurements.

EXL (**Ex**otic nuclei studied in **L**ight-ion induced reactions at the NESR storage ring) plans a study of direct reactions of exotic nuclei with light stable nuclei in inverse kinematics with the help of modern technology of storage accelerators and a universal detector system. Earlier research performed with stable nuclei showed, with confidence, that such direct reactions with light nuclei at intermediate and high energies are a necessary tool in the set of methods for studying the structure of atomic nuclei. The EXL detector system installed on the NESR storage ring will comprise:

- a silicon detector of recoil nuclei of reaction products, which will be arranged around the inner gas-jet target and supplemented with slow-neutron detectors and a highly segmented scintillator assembly for recording γ-ray photons and measuring the total energy of the higher-energy target recoil nuclei;
- detectors of forward outgoing fast neutrons and light charged particles;
- detectors of heavy fragments ejected from the gas-jet target.

ELISe (**El**ectron-**I**on **S**cattering at the NESR) will study the structure of exotic nuclei by way of experiments on elastic, inelastic, and quasi-free scattering of electrons by ions using intersecting ion and electron storage rings (the NESR and ER, respectively) as well as an electron spectrometer operating in combination with a reaction product detector system. The most trustworthy data on the density distribution in atomic nuclei were obtained in precisely the electron scattering experiments. However, until the present time the experiments on the electron scattering by nuclei were limited to stable isotopes. The ELISe program is intended to extent this powerful tool, which has already yielded a wealth of valuable information about the structure of stable nuclei, to the domain of nuclei remote from the stability path. For this purpose the secondary beams of radioactive ions cooled in the NESR storage ring will collide with a high-intensity electron beam circulating in the ER electron storage ring, which has an intersection with the NESR ring.

The secondary beams (see Fig. 6.74) are directed for carrying out experiments along three lines:

- a high-energy branch, where investigations will be made of astrophysically important reactions with high-energy heavy ions for inverse kinematics with the use of highest-efficiency detection and coverage of the total solid angle—the R^3B experiment (in this case, heavy beam particles interact with light target nuclei, while secondary particles are recorded at large angles);
- a low-energy branch, where such nuclear properties as decay modes and energy levels may be studied using monoenergetic low-energy ion beams (from several to 100 MeV/nucleon)—the HISPEC, MATS, LsSpec, and DESPEC experiments;
- a branch directed to the CR-RESR-NESR ring system, where exotic nuclei are accumulated and cooled. Here, experiments will be made to measure the masses and lifetimes of unknown exotic nuclei as well as to study their structure using electron or antiproton beams— the ILIMA, EXL, and ELISe experiments.

In many respects the experiments developed on the FAIR will far outperform the experiments in other research centers that have radioactive nuclear beams. The FAIR will offer significant advantages over similar projects in the USA (in ANL: RIA [254] and in MSU: LEBIT [121]), in Europe (in CERN: REX-ISOL-DE [155], in GANIL: SPIRAL-2 [145], in Louvain-la-Neuve university: CYCLONE [101], in LMU: MAFF [108], in GSI: SHIP [93] and SHIP-TRAP [162]), and Japan (in RIKEN: RIBF [93]) due to the use of new technologies, the high intensities of secondary radioactive beams of highest energy—up to 1.5 GeV/nucleon—(for comparison: 400 MeV/nucleon in RIA and 450 MeV/nucleon in RIKEN) in a wide

mass range, and primarily due to the combination of the Super-FRS wide-aperture fragment separator and the CR-RESR-NESR storage ring system [6].

6.7.3 Compressed Baryonic Matter (CBM) Experiment

The scientific program of the CBM experiment comprises investigations of extreme nuclear matter states and the phase transition to quark-gluon plasma at a high baryon density in nuclear-nuclear collisions, as well as investigations of the structure and equation of state of baryonic matter at densities comparable to those which exist in the cores of neutron and quark-gluon ("strange") stars (see Sect. 9.3) [74]. The program includes the quest for the boundary between baryonic and quark-gluonic matter, the quest for the critical point, the search for indications of the onset of chiral symmetry recovery at a high baryon density (Fig. 6.20) [12], and many other subjects.

The heavy ion beam in the SIS 300 of the FAIR will range up to 35–45 GeV/nucleon in energy for a 1000-fold increase in intensity in comparison with the present-day beam intensity of the SIS 19 accelerator in the GSI and a ten-fold increase in intensity in comparison with the LHC experiments in the CERN (see Sect. 6.6) [203]. The planned activity will make it possible to significantly advance in the investigation of unknown domains of the phase diagram in comparison with experiments on the RHIC ion collider in the Brookhaven National Laboratory in the USA and on the LHC collider in the CERN [64]. In these laboratories the emphasis is placed on the investigations of matter properties at extremely high temperatures but low baryon densities, i.e. at very small values of the baryon chemical potential. By contrast, the CBM experiment at the FAIR is aimed at a detailed study of matter properties at the highest baryon densities attainable under terrestrial conditions (Fig. 6.20).

To investigate how nuclear matter behaves in the domain of high densities typical for supernovae explosions and compact astrophysical objects, experiments will be carried out on the FAIR involving collisions between heavy ions using fixed targets at energies that maximize the compression of the nuclear matter. It is hypothesized that the constituents of atomic nuclei (protons and neutrons) "fuse" into quark-gluon plasma. This phase transition to the new state takes only 10^{-23} s and must be observable in head-on collisions between nuclei at high energies attainable on the SIS 300 FAIR accelerator [85].

Unlike the experiments in the CERN and Brookhaven, where the quest of the critical point is made by recording the spectral characteristics of the fluxes of bulk observables, the high intensity of the primary FAIR beams offers an additional possibility of recording rare events and scanning a vast domain of the phase diagram in particle energy (see Fig. 6.20). In particular, it is planned to directly investigate for the first time the signatures (observable manifestations) of the emergence of a "fireball" from the detection of short-lived vector mesons decaying into electron-positron pairs (Fig. 6.75).

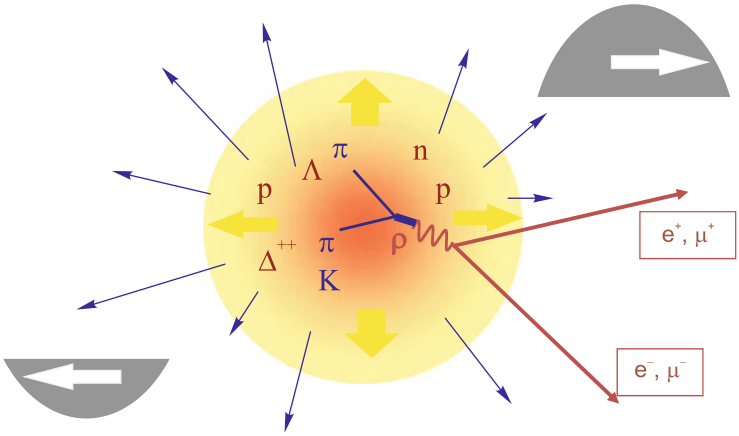

Fig. 6.75 Emergence of a "fireball" in the collision of two nuclei attended with the production of dilepton pairs

The FAIR's 2-to-35 GeV/nucleon energy range for gold ions is well suited for executing experiments in the phase diagram domain with high energy matter densities eight to ten times greater than the normal one.

It is important for an unambiguous data interpretation that it will be possible to make a direct comparison of the data obtained nuclear-nuclear collisions with the data for proton-proton and proton-nuclear collisions, because the FAIR accelerator complex will provide proton beams up to a maximum energy of 90 GeV.

Figure 6.76 [2] is a schematic representation of the detector constructed in the framework of the CBM collaboration. The universal detector system will identify particles produced in the dense reaction zone. The experiment will operate with 10^7 events per second and up to 1000 charged particles in one head-on collision of gold ions [203]. In this case, the particles containing strange and charmed quarks will serve as high-sensitivity diagnostic probes.

A radiation resistant silicon tracker of secondary particles (STS) consists of three plane layers of silicon pixel/strip detectors followed by four microstrip detector layers. The entire detector is accommodated in the gap of a dipole magnet for momentum determination with a resolution of better than 1 %. The purpose of a ring Cherenkov detector (RICH) is to identify electrons and suppress pions in the momentum range of the electrons arising from low-energy vector meson decay. A transition radiation detector (TRD) will record charged particle tracks and identify fast electrons and positrons. The challenge is to develop finely granulated gaseous counters capable of operating at a frequency of 100 kHz/cm^2. At the same time, the pion discrimination factor must amount to several hundreds for an electron detection efficiency of 90 %. Hadrons will be identified using a time-of-flight (TOF) system based on resistive plate chambers (RPCs). The requisite measurement accuracy should not exceed 100 ps for particle fluxes of up to 25 kHz/cm^2. An electromagnetic calorimeter (ECAL) will be employed for identifying electrons and photons as well as for rejecting pions.

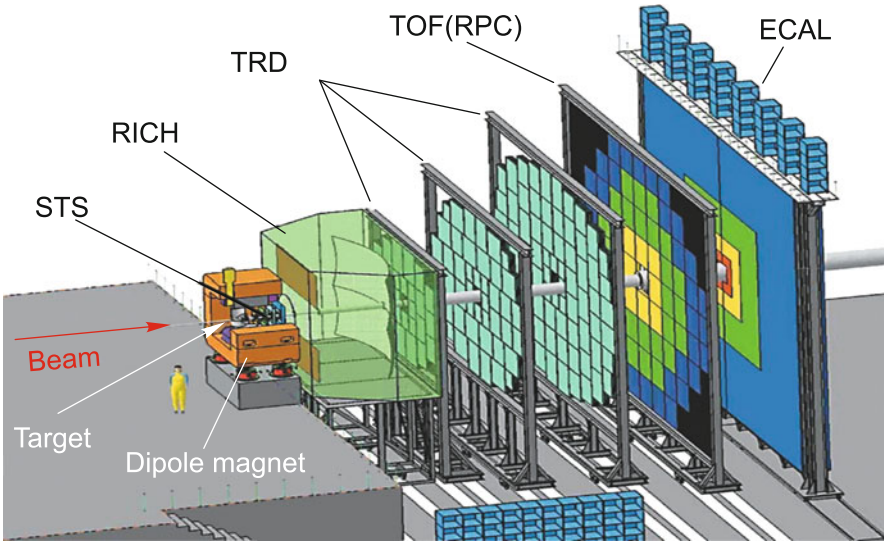

Fig. 6.76 CBM detector

A characteristic feature of the CBM detector will be its record high-rate data collection system for an appropriate conception of the trigger system.

The CBM collaboration numbers more than 350 scientists from 15 countries of the world, which are prepared to begin experiments in 2016 even with ion beams from the SIS 100 accelerator.

6.7.4 Antiproton Program: PANDA Experiment

The physical AntiProton ANnihilation in DArmstadt (PANDA) program covers a wide research field ranging from investigations into the basic problems of hadronic and nuclear physics to verification of fundamental symmetries by way of studying the interaction of accelerated antiprotons with nucleons and atomic nuclei with the help of the universal PANDA detector installed on the axis of the HESR high-energy storage accelerator (see Fig. 6.77).

The program is aimed at the quest of new forms of matter; in this case, an unprecedentedly high accuracy will be reached in the investigation of gluon excitations and in the physics of strange and charmed quarks [11, 72], which is provided by two fundamental virtues of the FAIR accelerator complex:

- a high-intensity antiproton beam with an energy of up to 15 GeV and
- the capability to scan the antiproton energy with an accuracy of ± 10 keV. This all will permit executing the experimental investigations of strong interaction properties at a new level of precision.

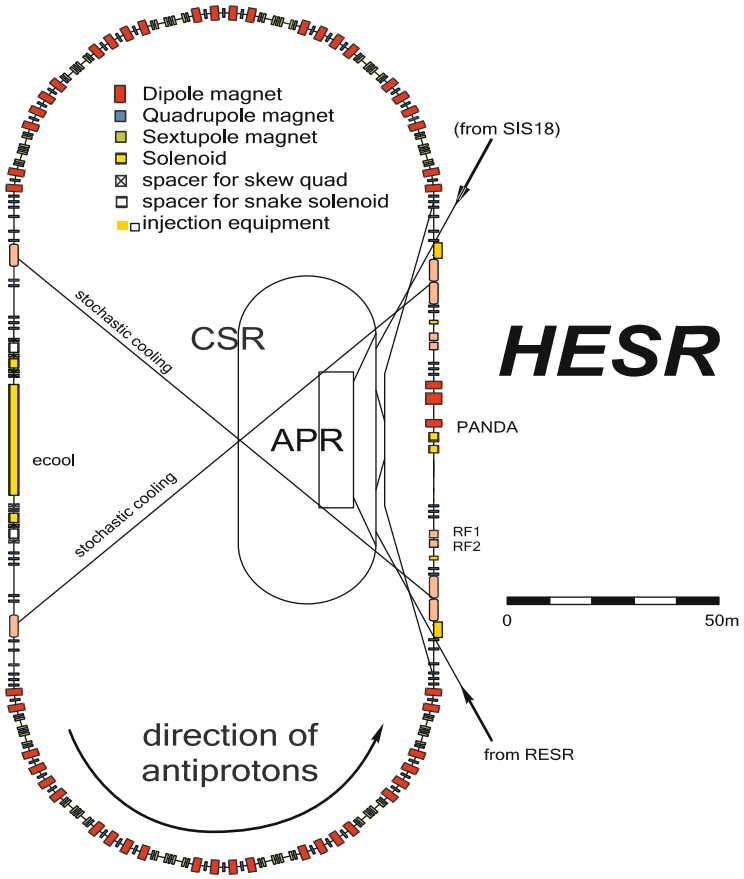

Fig. 6.77 HESR antiproton storage accelerator ring with a PANDA detector [11]

Experimental investigations into the structure of ordinary as well as of exotic hadrons may be carried out using electron, pion, kaon, proton, or antiproton beams. In the course of hadron annihilation, in particular antiproton-nucleon and antiproton-nucleus ones, particles with gluon degrees of freedom, along with particle–antiparticle pairs, are produced in abundance. This permits carrying out spectroscopic investigations with an unprecedented statistics and accuracy. Therefore, the antiproton beams of the FAIR accelerator complex in combination with the PANDA detector will afford the acquisition of qualitatively new data in comparison with the results of experiments performed in the Fermi National Laboratory and in the CERN. The FAIR will provide a 100 times higher intensity of the beam of stored and cooled antiprotons than in the CERN and will also exceed in intensity the beams in the FNAL (USA) and the beams of the J-Park facility being constructed in Japan [11, 25].

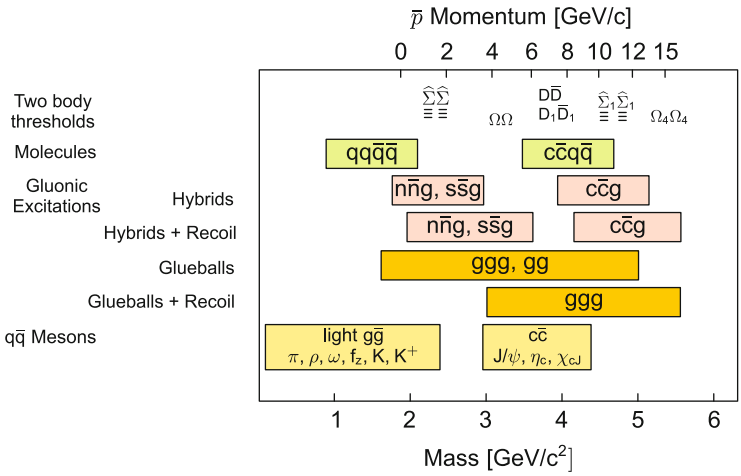

Fig. 6.78 Hadronic mass range which will be available in PANDA experiments. The upper scale shows the corresponding antiproton momenta required for fixed target experiments [11]

For the first time high-precision measurements will become possible not only for electromagnetic, but also for hadronic decay modes in the resonance proton-antiproton annihilation. The quest for gluon excitations (glueballs and hybrids) in the energy range corresponding to charmonium masses (3–5 GeV/c^2, see Fig. 6.78) will also become possible.

The unambiguous determination of gluon modes will be an important milestone in the solution of the problem of quark confinement in hadrons. In particular, a particle consisting of a charmed quark and an antiquark (charmonium) will make it possible to study with a high accuracy the heretofore unexplored aspects of strong interaction, whose main theory now is quantum chromodynamics (QCD). In this case, the PANDA experiment will open up broad possibilities for discoveries, in addition to experiments on the Large Hadronic Collider (LHC) for a relatively high antiproton energy; furthermore, owing to the capability of energy scanning with an accuracy of 10 keV it will enable determining the widths of narrow resonances like, for instance, the states of charmonium.

The scientific PANDA collaboration program comprises:

- the quest for exotic particles like glueballs and hybrids;
- spectroscopy of charmonium states above the threshold of D–anti-D-meson pair production;
- investigations of hypernuclei (including double ones) and charmed nuclei, in which the strange (one or two) or charmed particles take the place of an ordinary nucleon.

Also projected is the use of the PANDA facility for studying rare decays which contain single photons, π^0- and η-mesons in a broad energy range.

Table 6.4 Parameters of PANDA's two experimental modes

Parameter	Operating mode	
	High resolution	High intensity
Momentum range (GeV/c)	1.5–8.9	1.5–15
Number of accumulated antiprotons	$1 \cdot 10^{10}$	$1 \cdot 10^{11}$
Beam luminosity ($\text{cm}^{-2}\,\text{s}^{-1}$)	$2 \cdot 10^{31}$	$2 \cdot 10^{32}$
Momentum resolution $\delta p/p$	$<4 \cdot 10^{-5}$	$1 \cdot 10^{-4}$

It is assumed here that the effective thickness of the inner hydrogen target is $4 \cdot 10^{15}$ atoms/cm^2 and the beam emittance is 0.3 mm mrad

By way of illustration Fig. 6.78 schematically shows the hadronic mass range which will be attainable in PANDA experiments.

It is expected that PANDA experiments will be carried out in two operating modes: a high luminosity mode and a high resolution one. The parameters characterizing these modes are collected in Table 6.4.

The protons accelerated in the SIS 100 to an energy of 29 GeV are employed to generate the beam of antiprotons, which are produced under target bombardment by protons, are subsequently cooled in two rings (CR and RESR) and delivered to the 574-m long High Energy Storage Ring (HESR) schematized in Fig. 6.77. Here, the antiproton beams interact with a proton target (hydrogen) to produce compound particles containing strange and charmed quarks.

In the PANDA experiments use will be made of two types of hydrogen-beam targets:

- a cluster jet target (see, for instance, [69, 186]), in which the clusters are particles consisting of about 10^5 weakly coupled hydrogen atoms, and
- a target represented by a train of frozen hydrogen microspheres falling in a vacuum with characteristic diameters of 20–40 μm [236].

Similar targets of other gases (for instance, neon, nitrogen, argon, xenon) will also be available for PANDA experiments.

The PANDA detector is a 4π detector with an inner fixed target and is installed on the HESR ring. It will have a close to 4π acceptance, high resolutions in tracking, particle identification and calorimetry, will provide efficient data collection and selection of events for a load of $2 \cdot 10^7$ interactions per second in the inner hydrogen target [72].

To provide a high momentum resolution, the detector will consist of two magnetic spectrometers (see Fig. 6.79): the target spectrometer based on a superconducting magnetic solenoid, which is arranged around the antiproton–target interaction point and will be used for measurements at large angles, and the front spectrometer, which has a dipole magnet for measuring the tracks of particles emanating from the target at small angles to the antiproton beam axis.

Both spectrometers will provide tracking, charged-particle identification, electromagnetic calorimetry, and muon identification, which will permit recording the

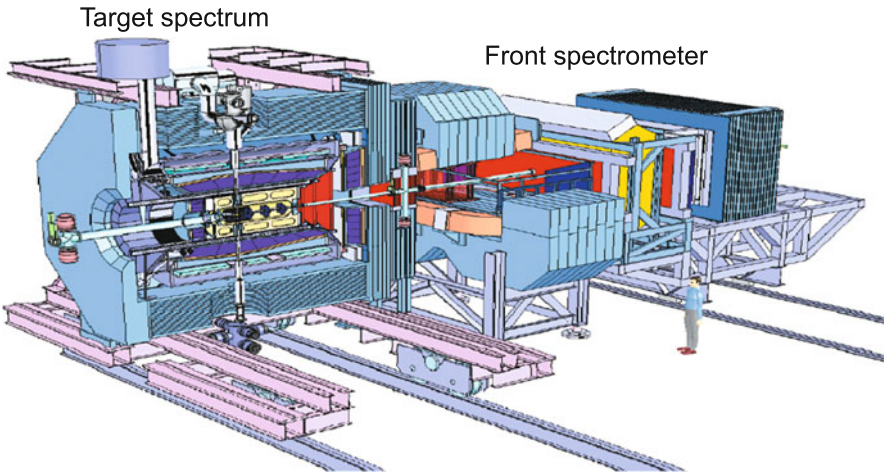

Fig. 6.79 PANDA detector, which consists of two magnetic spectrometers: the target spectrometer (at the *left*) arranged around the antiproton–target interaction point and the front spectrometer (at the *right*) intended for measuring the tracks of particles emanating from the target at low angles to the antiproton beam axis. The overall detector length is equal to 10 m [11]

entire spectrum of the final states that are of significance in attaining the goals of the PANDA research collaboration.

The target spectrometer, which is schematically shown in Fig. 6.80 with indication of its components, will measure the tracks of charged particles in a highly uniform (to within $\pm 2\,\%$) 2-T solenoidal field. The spectrometer configuration (similar to the configuration of detectors in collider experiments) is like the structure of an onion: different types of detectors will be arranged in layers about the axis. Vacuum pipes intended for the introduction and subsequent removal of the target material (i.e. the beam of clusters or pellets) from the antiproton beam will cross the spectrometer vertically downwards, perpendicular to the vacuum pipe with the antiproton beam. In accordance with the angles of particle escape from the target, this spectrometer may be conventionally divided into the following three parts:

- the barrel, which covers the angular range between 22° and 140°;
- the front lid, which broadens the angular range to the lower side, to 5° in the vertical plane and to 10° horizontally;
- the rear lid, which covers the $\approx$145° and 170° angular range.

We briefly describe the main elements of the target spectrometer.

Superconducting solenoid. Providing a 2-T magnetic field in a 4-m long space of diameter 1.9 m and leaving it available for detector installation is a nontrivial problem. The task is additionally complicated by the strict requirements imposed on the uniformity of magnetic field, the presence of magnet-intersecting hot pipes for target beam transport, the need to provide access to detectors, etc. The cryostat of the solenoid will surround all detectors and serve as their support structure. The

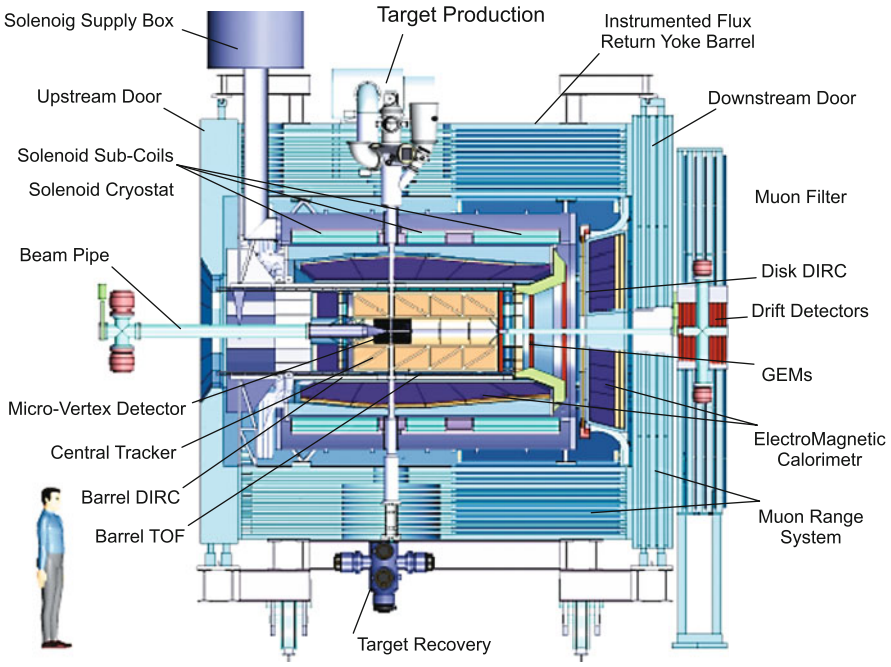

Fig. 6.80 Side view of the target spectrometer of the PANDA detector

magnet yoke will additionally play the role of a muon recording system due to placement of minidrift tubes in it (between 13 iron layers) (the Muon Range System in Fig. 6.80).

A Micro-Vertex Detector (Fig. 6.80—**Micro-Vertex Detector**) is located in the target spectrometer, most closely to the place of interaction of the antiproton beam with the transversal beam of target particles. The Micro-Vertex Detector, whose conception relies on the use of radiation-resistant silicon pixel and strip detectors, is a tracking device for charged particles. This detector is highly important for the precise determination of the vertices of secondary decays of short-lived particles, like charmed or strange hyperons and D mesons.

Central Tracker (Fig. 6.80—**Central Tracker**). Arranged around the micro-vertex detector is the central track detector, which is also barrel-shaped; its operation is based on the ionization of gas in the passage of a charged particle through the gas. The electrons resulting from the ionization drift to the sensor electrode in the field applied, and the charged particle track may be determined from the known drift velocity in the gas and the spatial position of the electrode.

Gas Electron Multipliers (**Gas Electron Multiplier**, Fig. 6.80—**GEM's**). The particles traveling at angles $<22°$ to the axis, i.e. the particles which do not enter the central tracker, will be recorded by three gas electron multiplier stations mounted at distances of 1.17, 1.53, and 1.89 m from the target.

Particle identification. The capability of identifying hadrons and leptons in a broad range of momenta and angles is an important property of the PANDA facility. Particles with momenta greater than 1 GeV/c will be identified by Cherenkov detectors. Slow particles ejected at large angles will be identified by a time-of-flight detector. Since the target spectrometer path length is equal to only 50–100 cm, this detector must have a very good temporal resolution, about 50–100 ps. The time-of-flight detector assembly in the form of a barrel (Barrel TOF in Fig. 6.80—**Barrel TOF**) with inner and outer radii of 42 and 45 cm will cover the angles ranging from 22° to 140°. Faster particles in this angular range will be identified by Detection of Internally Reflected Cherenkov (DIRC) light, like was realized in the BaBar facility [19]. The Cherenkov detector will be a barrel-like assembly (**Disc DIRC** in Fig. 6.80) of 1.7-cm thick quartz plates surrounding the antiproton beam at a distance of 45–54 cm from the axis. A similar Cherenkov detector, though in the form of a disc (Disc DIRC in Fig. 6.81), will be employed for particles ejected forward at angles between 5° and 22°. This disc will be mounted immediately in front of the front lid of the electromagnetic calorimeter.

Electromagnetic calorimeter (Fig. 6.80—**Electromagnetic Calorimeter**). To cope with high loads for a compact design of the target spectrometer, the electromagnetic calorimeter needs a fast scintillation material with a short radiation length X_0. Best suited for this purpose are crystals of lead tungstate ($PbWO_4$)—a high-density inorganic material, which provides a high energy and time resolution in the detection of photons and electrons even in the intermediate energy range [166]. This is precisely the reason why $PbWO_4$ crystals are employed, for instance, in the

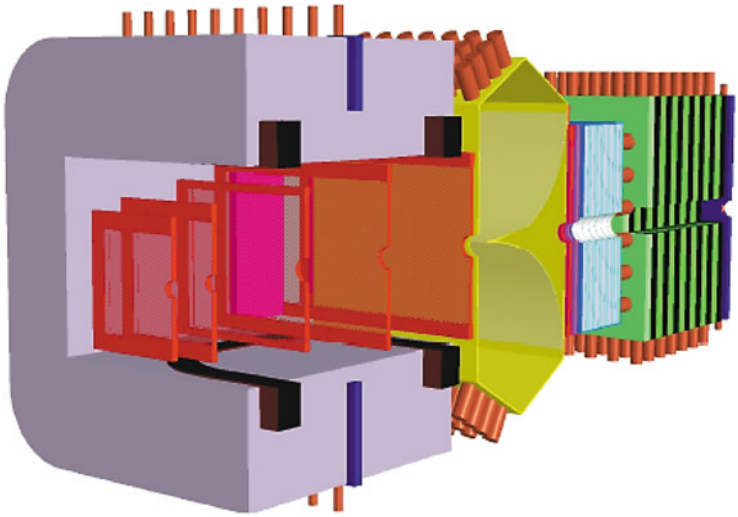

Fig. 6.81 Three-dimensional structural view of the front spectrometer of the PANDA detector. The dipole magnet (at the *left of the figure*) with a 1-m gap and an aperture greater than 2 m possesses a deflecting force of 2 T m

compact muon spectrometer of the CMS collaboration in the CERN [7]. To reach an energy resolution of better than 2 % at an energy of 1 GeV, the crystals in the electromagnetic calorimeter will measure 20 cm in length (i.e. approximately $22X_0$). 11,360 profiled crystals with a front face area of $2.1 \times 2.1\,\text{cm}^2$ will be installed in the calorimeter barrel with an inner radius of 57 cm. The front and rear lids of the barrel will require 3600 and 592 crystals, respectively.

The front spectrometer, whose three-dimensional structure is diagrammed in Fig. 6.81, will record particles emitted in the vertical and horizontal angular ranges of $\pm 5°$ and $\pm 10°$, respectively. To analyze the charged particles with a momentum resolution of ≤ 1 %, use will be made of a dipole magnet with a gap of 1 m and an aperture of 2 m. The deflecting force of the magnet is equal to 2 T m, which makes the antiprotons with the maximum momentum equal to 15 GeV/c deflect by an angle of 2.3° in the field of this dipole magnet. The antiproton beam deflection will then be compensated by two or three beam-positioning magnets installed behind the PANDA facility.

The variations of particle trajectories in the field of the dipole magnet will be measured by a set of multiwire drift chambers. Two chambers will be installed in front of the magnet and another two behind the magnet. This will enable recording the tracks of the highest-momentum particles. Two additional drift chambers will be installed inside the magnet gap for tracking particles with small momenta.

An assembly of plastic scintillator plates with fast photomultipliers at both ends of the plates for signal readout, placed at a distance of 7 m from the target, will serve as stop time-of-flight counters and measure the transit time from the start detector, which is placed near the target, to these stop counters. Similar stop detectors will be additionally installed inside the dipole magnet for recording low-energy particles which cannot escape from this magnet. For an expected time resolution of 50 ps, separation of pions from kaons (π/K) and of kaons from protons (K/p) at a level of three standard errors will be possible for particles with momenta up to 2.8 and 4.7 GeV/c, respectively.

The calorimeter for particles ejected into the front angular domain will consist of two parts. A "Shashlyk"-type calorimeter (see, for instance, [26]) will be employed in the first part intended for detecting photons and electrons with a high resolution and efficiency. An energy resolution $4\,\%/\sqrt{E}$ was obtained for this calorimeter type in [51]. The second calorimeter part will fulfill the function of measuring the energies of neutral hadrons and will also be employed as a fast trigger and an active muon filter. This calorimeter part will be installed immediately behind the "shashlyk"-type calorimeter, in front of the wall of muon identification counters (these counters are similar to the muon counters which surround the superconducting solenoid of the target spectrometer described above). A comprehensive description of the front spectrometer may be found elsewhere [9].

6.7.5 *Electromagnetic Plasma Physics*

Research in the physics of high energy density in matter and extreme states of matter exposed to high-intensity pulsed action is necessary for acquiring new knowledge about the physical processes and material properties under conditions of superhigh pressure, density and temperature. This knowledge forms the scientific basis for challenging energy projects—controlled thermonuclear fusion with inertial confinement of hot plasma, magnetohydrodynamic and magnetocumulative generators, nuclear space facilities, etc. (see Chaps. 3, 4, and 5) [74]. In nuclear powers this knowledge is used for improving nuclear weapons (Chap. 4) and studying the properties of materials of nuclear power facilities experiencing the action of high-power radiation fluxes and for developing new defense and nuclear power technologies.

Unlike quark-gluon plasmas, where the main kinds of interparticle interaction are described by the methods of quantum chromodynamics, in this section we will discuss investigations of electromagnetic plasma, which is dominated by the weaker electromagnetic interaction.

Proceeding from experimental data, highly reliable physicomathematical models are developed, which possess excellent prognostic capacities. Scientists hope that they can underlie computer-aided simulations that will partly replace full-scale tests. The accuracy of predictions of such simulations relies on the basic models employed, the depth of understanding the essence of the physical processes involved, and the reliability of the description of material properties under ultrahigh pressures and temperatures.

Therefore, the practical significance of research in this area stems from the acquisition of reliable experimental data about the substance properties at high energy densities and the construction on this basis of accurate design-theoretical models for developing new equipment for defense and civil applications, inertial thermonuclear fusion, nuclear reactor safety and plasma technologies.

In the execution of full-scale nuclear tests (see Chap. 4) it is possible to obtain experimental data in the 1–1000 g/cm^3 density and 0.1–100,000 eV temperature ranges. In the absence of such tests it is possible to obtain the experimental data on research facilities, which permit covering one or other domain of this range. The largest (see Chap. 5) of them are Omega and NIF (USA), GEKKO-12 (Japan), VULKAN (Great Britain), and Iskra-5 (Russia) high-power lasers, ZX (USA) and Angara-5-1 (Russia) high-power electric discharge systems, SIS 18 (FRG) and TWAC-ITEP (Russia) high-power heavy-ion accelerators, etc. Figure 6.82 shows the capabilities of various facilities in research in different domains of the phase diagram of matter.

On the FAIR complex it will be possible to achieve a pulsed ion-beam intensity of 10^{12} for an energy of up to 1000 MeV/nucleon. By raising the intensity of heavy (up to uranium) ion beams and compressing the beams in time to a pulse duration of 50 ns, the specific energy input of the FAIR facility will be made 600 higher than that of the existing SIS 18 accelerator complex at the Heavy Ion Institute and will exceed

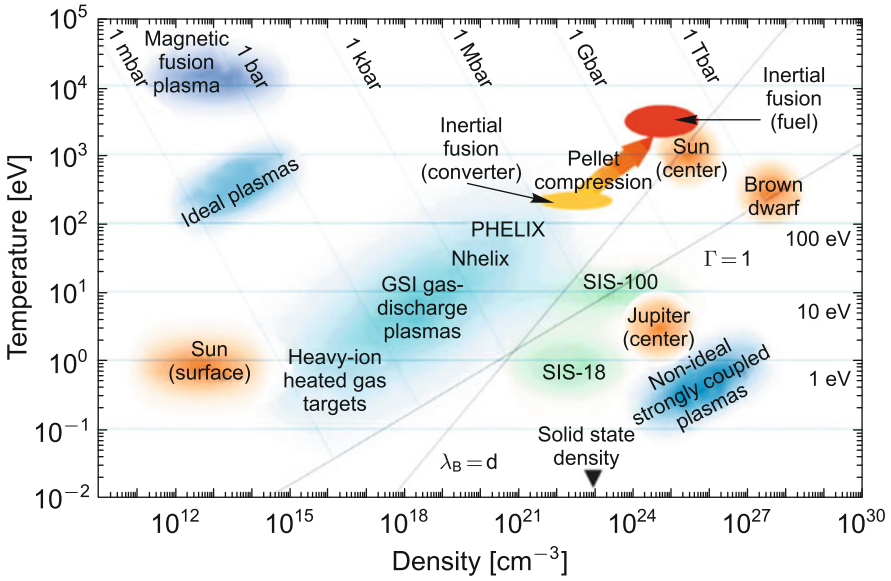

Fig. 6.82 Phase diagram of nuclear matter

ten-fold the parameters of the TWAC-ITEP complex. This will enable studying the properties of superdense nonideal electromagnetic plasmas and of substances under ultrahigh pressure in the pressure and temperature ranges unattainable on other experimental facilities.

On focusing to a spot $\approx$1 mm in diameter, ion beams with the above parameters are able to heat macroscopic volumes of a dense target substance to a temperature of several tens of electronvolts.

The heart of the experimental program on electromagnetic plasmas comprises three basic experiments:

- Heavy Ion Heating and EXpansion ("HIHEX" experiment);
- LAboratory PLAnetary Science ("LAPLAS" experiment);
- Warm Dense Matter ("WDM" experiment).

The most important feature of these three experiments on the physics of high energy density in substance on the FAIR accelerators will consist in the unique possibility of plasma diagnostics using high-energy proton beams (radiography) with the simultaneous use of high-power petawatt laser radiation ($\approx 10^{15}$ W). This laser is capable of producing a target irradiation intensity of 10^{21} W/cm^2. Planned under the program is the construction of a corresponding proton beam transport line from the SIS 18 accelerator to the experimental plasma physics hall as well as the delivery of the high-power laser beam to the target vacuum chambers. The combination of the high-intensity laser pulse, the diagnostic proton beam, and the

high-intensity ion beam opens up new unique experimental possibilities for the FAIR.

HIHEX experiment. High-intensity heavy ion beams with a pulse duration of 50–100 ns make it possible to rapidly (in comparison with the characteristic time of hydrodynamic motion) heat a substance and then observe the expansion of the hot substance in the surrounding medium, i.e. create a high level of energy liberation and successively observe the isentropic expansion. In an experiment of this type [81, 107] the heated material will go through several new interesting states in its expansion. Specifically, as a result of heating, an initial metal of normal density will reach the superheated liquid state with disordered ion component and degenerate electrons. In the course of isentropic expansion the substance goes through the state of a quasi-nonideal Boltzmann plasma and a rarefied gas. On further expansion the degree of degeneracy lowers, which is attended with a redistribution of the energy spectrum of ions and atoms as well as a partial recombination of the dense plasma. Metal–dielectric phase transitions may occur in the disordered electron system, and the plasma in the vicinities of the critical point and the liquid–vapor equilibrium point becomes nonideal. When the isentrope enters the two-phase liquid–vapor domain, there sets in the condensation of the gas phase. At higher levels of energy deposition, the isentropic expansion may be attended by still more exotic effects with a strong variation of plasma ionization degree α and nonideality parameter Γ. In one experiment the thermodynamic parameters of a substance may vary over a broad range: up to six orders of magnitude in pressure and up to four orders of magnitude in density.

In the pressure–entropy diagram (Fig. 6.11 [107]) the states of matter with a high energy density, including the hot compressed ionized substance, the nonideal plasma, the hot expanding liquid and the quasi-ideal plasma, occupy a vast domain.

The presently available information about metal properties obtained by the method of isentropic expansion of shock-compressed material [128] is concentrated primarily along the Hugoniot adiabat and is supplemented with model estimates of the location of critical points in the phase plane (Fig. 6.11). That is why the vast domains of the phase diagram under the shock adiabat, including the domains with the critical points of metals and the nonideal plasma domain ($\Gamma \geq 1$), invite further investigations [32, 33, 214, 255].

The phase diagram domains corresponding to parameters attainable with the SIS 18 and SIS 100 heavy ion accelerator facilities are highlighted (Fig. 6.11). In particular, the SIS 18 operating accelerator produces a heating uranium ion pulse with an intensity of about 10^{10} particles, duration of about 100 ns, and an ion energy of 300 MeV/nucleon. When this pulse is focused onto a target, the energy liberation is at a level of 1 kJ/g. In the future it is planned to increase the beam intensity and raise the energy liberation to a level of 10 kJ/g. The TWAC-ITEP storage accelerator put in service in the ITEP in 2003 is aimed at reaching an energy liberation level of 10–20 kJ/g by concentrating on a target the pulses of copper or cobalt ions with energies of up to 700 MeV/nucleon. The new SIS 100 accelerator in the FAIR project will provide an energy liberation level above 100 kJ/g.

Two large international collaborations (HEDgeHOB and WDM) aim at generating high-entropy states of matter by employing the property of a high-intensity ion beam to liberate its energy in the volume of a substance. The high-power pulsed beams generated by the FAIR accelerators will be capable of producing large volumes of dense plasma with an energy density, which is of interest for the solution of a broad range of basic problems in plasma physics, magnetohydrodynamics, radiative study of materials, planetary geophysics, atomic and molecular physics, etc. The expected parameters of U^{28+} ion beams are collected in Table 6.5.

Figure 6.10 shows the HIHEX experiment scheme, in which a cylindrical target is bulk heated by a high-intensity heavy ion beam. The heated substance (plasma) begins to isentropically expand in the surrounding vacuum. The expansion parameters required for constructing the equations of state of materials are measured using diagnostic systems which involve X-ray backlighting produced by a petawatt laser.

The **"LAPLAS"** experiment implements the regime of strong substance compression by cylindrical implosion on the cylinder axis. The interest in this effect is generated by the feasibility of generating in a laboratory the planetary states of matter existing in the central parts of Jupiter and Saturn giant planets, where the substance has a density of 1–2 g/cm^3 at a pressure of 5–10 Mbar and a temperature of several electronvolts. Furthermore, the experiment bears on the problem of inertial confinement nuclear fusion driven by a heavy ion accelerator [81, 129]. As a rule, the targets are cylindrical layered structures with layers of different initial density (Fig. 6.83).

Table 6.5 Expected beam parameters

Total pulse energy	80 kJ
Pulse duration	50 ns
Total number of particles	$2 \cdot 10^{12}$
Specific power	10 TW/g
Specific energy liberation	>100 kJ/g
Ion energy	≈ 1 GeV/nucleon

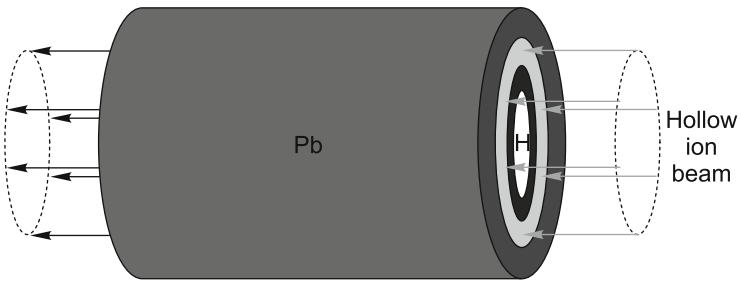

Fig. 6.83 CMS detector: cross-sectional diagram and internal structure with indication of trackers and calorimeters [64]

The central domain is occupied by a substance which should be compressed to the maximum attainable final density, for instance hydrogen or the equimolar mixture of DT. The substance layer (the absorber) which absorbs the ion energy is irradiated by a specially shaped "tubular" beam, which is an annulus in cross section. A solution of the tubular ion beam production problem by way of HF-field-aided beam rotation at the stage of accelerator-to-target transport was proposed in [129, 178]. Several design-theoretical works are dedicated to the search of optimal conditions to provide the uniformity of hydrodynamic response of the absorber substance to the energy liberation induced by this rapidly rotating beam [31, 178].

In this case, special emphasis is placed on the selection of the combination of the parameters of the heating ion beam pulse, the geometrical dimensions of target layers, and their initial densities to provide a close-to-adiabatic mode of fuel compression on the cylinder axis [30], see also [227] and [228]—the so-called quasi-entropic mode.

The objective of the LAPLAS experiment [178, 226] is to study the metallization of hydrogen, which is typical for the state of the inner layers of the giant planets of Jupiter and Saturn. A two-dimensional hydrodynamic code [76] was employed to perform numerical feasibility investigations of a heavy-ion-beam-driven quasi-entropic compression mode with the purpose of realizing the effect of hydrogen metallization, which was predicted by Wigner back in 1935. The numerical experiment dealt with a 3-mm long multilayer cylindrical target with an external radius of 3 mm (see Fig. 6.76). The radius of internal cylinder, which consisted of solid frozen hydrogen, was equal to 0.5 mm. The cylinder face is irradiated by a beam of 10^{12} uranium ions with an energy of 400 AMeV and a pulse duration of 50 ns. An important point is the annular structure of the beam cross section: the beam is focused into a ring with outer and inner radii of 2.0 and 0.5 mm, respectively, and irradiates the cylindrical layer of lead rather than hydrogen. The energy deposition is assumed to be uniform lengthwise of the lead layer, since the range of 400 MeV/nucleon uranium ions in lead amounts to 4.25 mm, with the consequence that the Bragg peak is beyond the target.

A characteristic feature of the experiment consists in the mode of generation of a multitude of sequential reverberating weak shock waves, which compress hydrogen along the isentrope. The BIG-2 two-dimensional hydrodynamic code [76] enables calculating the hydrogen density distribution along the cylinder radius at different points in time. According to the simulation data, as the hydrogen–lead interface executed a relatively slow adiabatic motion towards the cylinder axis there emerges a series of weak reflected shock waves between this interface and the axis, which produce the substance state which corresponds to the metallization of hydrogen. In accordance with the equation of state from the SESAME table, this is a pressure of 3 Mbar, a density of ≈ 1 g/cm^3, and a temperature ≥ 0.1 eV [226]. These parameters remain invariable for 160–200 ns, which is quite sufficient for measuring the conductivity of hydrogen under extreme conditions. Recent experiments in the quasi-adiabatic compression of hydrogen [74, 81] suggest that the pressure-induced metallization sets in even at pressures of about 1 Mbar and a density of ≈ 0.6 g/cm^3.

The **WDM** experiment is targeted at realizing the quasi-isochoric mode of matter heating and attaining the extreme plasma state involving a strong interparticle interaction for large values of the nonideality parameter $\Gamma \geq 1$ [74].

The physical substantiation of the experiment to be performed with the ion beams of the SIS 100 accelerator, which is under development in the framework of the FAIR project, is outlined in [132]. The experiment is aimed at the study of solid hydrogen state for a energy deposition level of 130 kJ/g, which is afforded by a 200 MeV/nucleon uranium ion beam with an intensity of $8 \cdot 10^{10}$ focused to a spot of radius $r_b = 350\,\mu$m. According to the equation of state from the SESAME tables, this corresponds to a temperature of 0.6 eV—the mode of "warm dense matter", in which the entire beam energy is converted to the internal substance energy.

In the case of bulk energy liberation by an ion beam characteristic of ions with energies $E \geq 10$ MeV/nucleon, the specific energy deposition E_s is the governing characteristic, which can be measured with a good accuracy. And if the sample's substance density ρ_0 remains invariable during heating, the thermodynamic substance parameters after irradiation are defined by the quantities ρ_0 and E_s. Therefore, any measurable physical quantities are functions of this, well defined, thermodynamic state.

The choice of the target material is determined by the capabilities of the diagnostic technique, which involves recording of the spectral and angular distribution of the X-ray photons scattered by the substance of the heated sample—the method of Thomson X-ray scattering [94]. This X-ray backlighting with a temporal resolution can be provided by the PHELIX laser, which is under construction in the GSI, Darmstadt. For X-ray photon energies of $\approx$1–3 keV, the choice of target structure materials is nevertheless limited to low-Z elements. To carry out the substance state diagnostics and interpret the data, it is advisable to deal with a uniform density distribution over the sample volume. The simplest target for the execution of a quasi-isochoric experiment is the cylinder of frozen hydrogen of radius $R_h \geq r_b$ (Fig. 6.84). For a rectangular intensity distribution over the beam cross section, the density on the cylinder axis remains constant until the unloading wave reaches the axis. However, for a realistic beam with a Gaussian intensity distribution over its cross section, for which the second derivative of the pressure with respect to radius is nonzero, the density begins to decrease even prior to the arrival of the unloading wave at the axis.

This effect of the hydrodynamic unloading of the heated target domain may be compensated by using an inertia shell (tamper) to confine the frozen hydrogen. To provide the requisite "confinement" of the heated substance by a low-Z material transparent to X-ray photons, the tamper is also heated by the peripheral part of the ion beam. In this case, the heated layer of the tamper produces counterpressure for confining the main substance of the target. For a tamper it is evidently advantageous to use a material with a high sublimation energy to delay the onset of the hydrodynamic expansion of the tamper itself.

Numerical simulations performed using the BIG-2 two-dimensional hydrodynamic code [76] suggest that the tamper density should be lower than that of graphite. That is why a plastic with a density of 1.5 g/cm^3 at normal conditions was

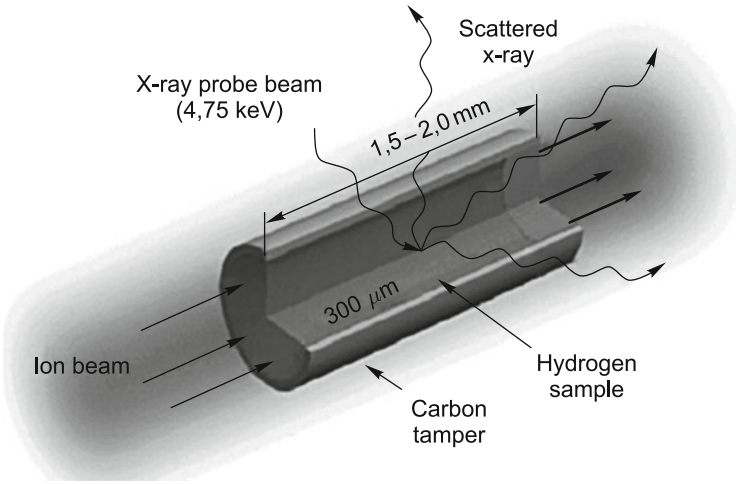

Fig. 6.84 WDM. Scheme of an experiment in the isochoric heating of hydrogen [132]

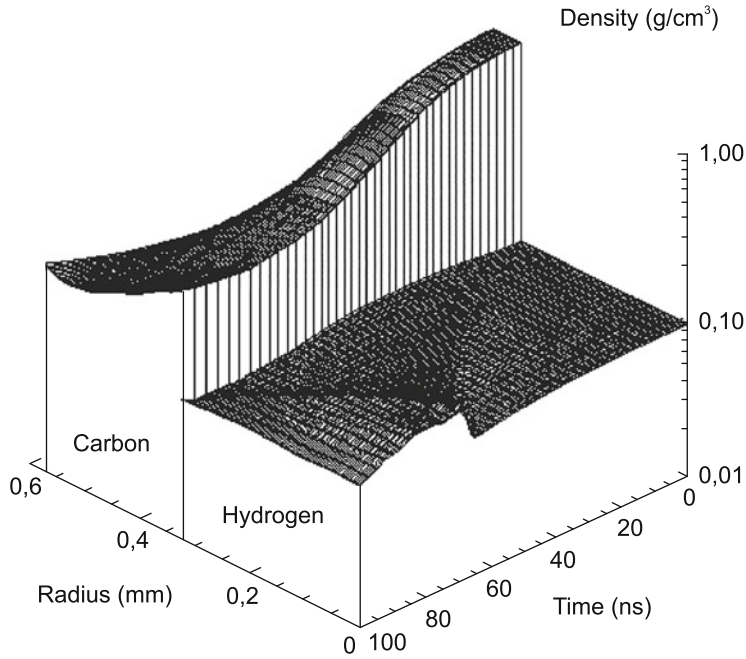

Fig. 6.85 Time dependence of the densities of target layers [144]

chosen as the tamper material. The temporal variation of the target layer densities is shown in Fig. 6.85. Initially the hydrogen density begins to decrease owing to the Gaussian profile of the ion beam. The pressure in the tamper material exceeds

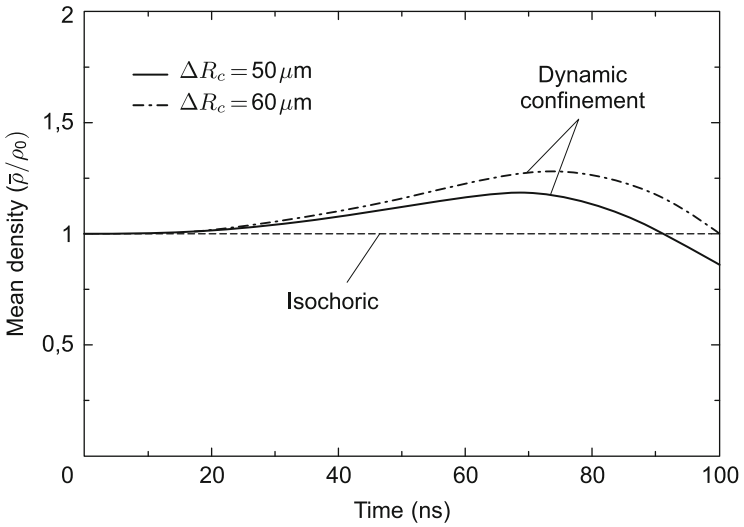

Fig. 6.86 Time evolution of the hydrogen density averaged over the target section [132]

that of hydrogen, and therefore the tamper begins to move inwards and drives a weak shock wave. Later on, when the tamper density becomes lower, the pressure equalizes and the hydrogen–tamper interface stops. Then, the increasing hydrogen pressure returns the interface to its initial position. According to the simulations, by the end of the course of ion irradiation the radial density distribution is nearly uniform.

Figure 6.86 shows the time evolution of the hydrogen density averaged over the target cross section. The tamper thickness may be optimized depending on the result required: minimization of density variations during heating to within 10–15 % ($\Delta R_c = 50\,\mu$m) or attainment, by the end of irradiation, of hydrogen density equal to the initial density 0.1 g/cm^3 ($\Delta R_c = 60\,\mu$m).

Therefore, it was shown that an ion beam is capable to provide, for a prescribed set of initial parameters, a quasi-isochoric heating mode of solid-density hydrogen for a temperature of 5000 °C, i.e. to provide dynamic confinement for 100 ns.

6.7.6 Radiative Study of Materials and Biophysics (BIOMAT)

Heavy ion beams of the FAIR accelerator complex with energies of 10 GeV/nucleon and above are of immediate interest for the study of radiation influence of galactic and solar particles on living biological objects as well as on various materials. The area of practical applications includes the radiative study of materials, the radiation resistance of microelectronic components, nuclear medicine, simulation of the effect of the cosmic radiation of heavy charged particles on living cells and

materials. In this case, of special significance in the formulation and execution of these experiments is the property of fast ions to penetrate to a controllable depth inside the samples.

1. Comprehensive data about the radiological effects of fast heavy charged particles are required for lowering to the minimal necessary level the thickness of expensive radiobiological shielding on the spacecrafts of interplanetary missions [67, 249]. Furthermore, the facility developed for sample irradiation is required for testing and calibrating different instruments and equipment employed in space.

The cosmic radiation of solar and galactic origin poses the greatest hazard in interplanetary space investigations and in the course of manned interplanetary missions, because the personnel and instrumentation are outside of the protective terrestrial magnetic field [60, 67]. Genetic changes and carcinogenic effects may emerge even for low irradiation levels. However, in the case of a solar flare and coronal mass ejection the lethal dose may be accumulated in less than 30 min. While the solar radiation consists primarily of protons and helium nuclei, galactic radiation also comprises heavier particles up to iron (Fig. 6.87).

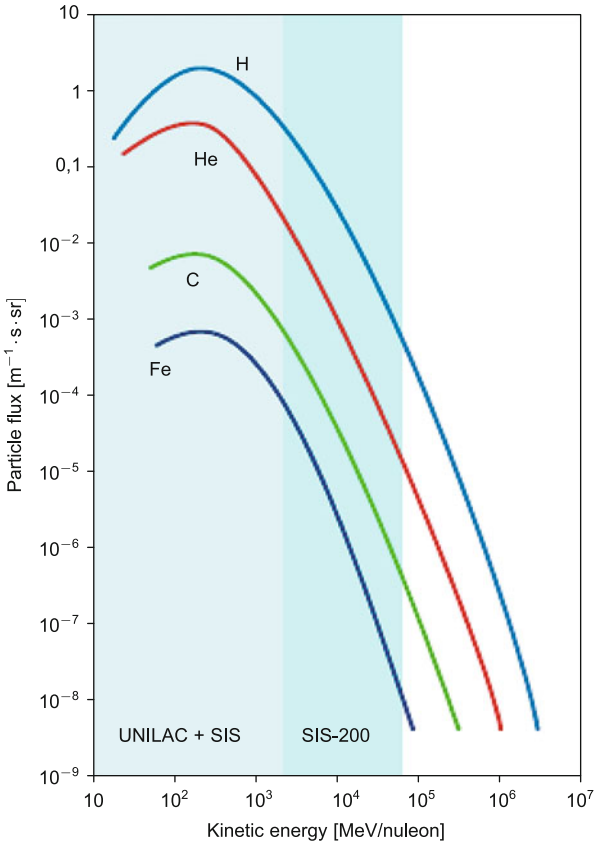

Fig. 6.87 Spectrum of heavy charged particles in galactic cosmic radiation [1]

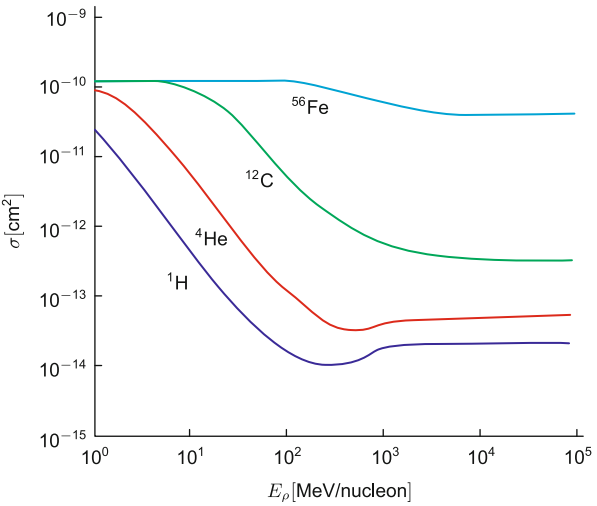

Fig. 6.88 Calculated risk coefficient for the emergence of malignant neoplasms in mammary gland cells under long-term action of heavy charged particles [249]

In this case, since the radiation influence is determined by deceleration energy loss, which is proportional to the squared particle charge in accordance with the Bethe–Bloch formula [39, 81], the risk coefficient (Fig. 6.88 [249]) for relativistic iron ions is three orders of magnitude higher than for protons.

The dose is the governing factor both for living organisms and for electronic devices. Usually the dose is macroscopically defined as the energy absorbed by a unit mass (1 Gy = 1 J/kg). However, of higher significance is the local dose distribution along an individual particle track [59], which amounts to many kilograys at the track center. It is precisely this disproportionately strong response to relatively low macroscopic doses that is observed in many biological systems. This effect of higher radiobiological efficiency (RBE) [133, 134] is attributed to numerous damages caused to both strands of deoxyribonucleic acid (DNA) in the vicinity of a heavy charged particle track. The higher RBE and the effect of fragmentation of a heavy relativistic particle in its deceleration are responsible for enhanced transformation of cells irradiated by iron ions, despite a low intensity in comparison with proton beam intensity.

In the forthcoming experiments on the FAIR, special emphasis will be placed on the effect of relativistic nuclei fragmentation and the resultant shower of secondary low-energy particles with a high RBE for living objects. Since the secondary particles are correlated in space and time, it is planned to investigate the radiobiological effect not only at the genetic molecular level, but also at the cell and living tissue levels [66].

2. Experiments in material science on the FAIR accelerator in the simulation of the influence of the heavy component of galactic cosmic radiation on materials pursue two primary goals:

- calibration of spacecraft's detecting instrumentation employed to record high-energy (>1 GeV/nucleon) cosmic particles with a high resolution in particle mass and charge;

Fig. 6.89 Robotized system for the automatic positioning of biological samples [11]

- study of radiation effects in electronic components employed in the instrumentation of space satellites—from single chips to microprocessors [109]. These effects are responsible for single failures, the occurrence of destructive operational errors, or the disabling of critical functions of spaceborne electronics.

Heavy ions obtained from the SIS 100 will be used in the multipurpose BIOMAT facility equipped with a raster scanning system [100], which will provide an excellent beam quality in the uniform irradiation of a large-surface field in a broad fluence range for particles of different atomic mass. A special robot will be used for positioning the samples (Fig. 6.89).

A broad set of ion beams—from proton to uranium ones—will be required for biophysical and materials research. The highest requisite beam intensities for an energy of 10 GeV/nucleon in the ion mass range from protons ($5 \cdot 10^{10}\,\mathrm{cm}^{-2}$) to iron ($1 \cdot 10^{8}\,\mathrm{cm}^{-2}$) correspond to a dose of 10 Gy uniformly absorbed by a target of $100\,\mathrm{cm}^2$ area in 1 min. Acceptable irradiation times may be achieved for this dose rate, which is highly significant in the irradiation of sensitive biological samples (i.e. cell cultures), which should be in a nutrient medium. The highest intensities of heavier-ion beams—from krypton to uranium ones ($1 \cdot 10^{8}\,1/\mathrm{cm}^2$)—are defined by

the fluxes required for materials research in combination with reasonable exposure times.

The BIOMAT collaboration will use the high-energy ion guide and the experiment site jointly with the SPARC collaboration. Fourteen research groups participate in the collaboration.

3. Experiments in modification of materials by relativistic heavy ion beams. In passing through a solid material, high-energy heavy ions induce ultrahigh electric fields (of the order of 10^{12} V/m) in short ($\approx 10^{-18}$ s) time intervals, which affect atoms and electrons in the vicinity of their path of motion, converting the kinetic energy of the fast particles to the internal energy of the substance. The energy loss excites complicated processes like the generation of fast electrons, which is attended with the Coulomb repulsion of ionized atoms, the emission of X-ray photons and Auger electrons, electron-phonon interaction, etc. [148, 199, 252]. As a result, a fast particle can produce long cylindrical zones several nanometers in radius, in which the material properties are significantly different from the initial ones. By way of example, mention can be made of the crystalline-to-amorphous state transition or the formation of metastable high-pressure high-temperature phases [199, 252].

Studying the transient processes initiated by the passage of a fast particle through a substance is most important for explaining the mechanisms of track formation (Fig. 6.90 [1]).

In particular, electron processes prevail in the track evolution during the time interval from $\approx 10^{-18}$ to $\approx 10^{-13}$ s. Diagnostics of the damage process with a high resolution (at a level of 10^{-14} s) may be achieved by recording convoy and Auger electrons or by X-ray techniques [4, 74]. However, the complete picture of track formation mechanisms involving displacements of atoms due to the excitation by electrons includes slower processes ($\approx 10^{-13}$–10^{-12} s) related to the passage of a shock wave and lattice relaxation [114, 115].

The most important quantitative characteristic used in the description of fast particle deceleration in a solid substance the stopping power dE/dx (the energy loss per unit path length). For nonrelativistic ions ($E_i < 1$ GeV/nucleon) the deceleration

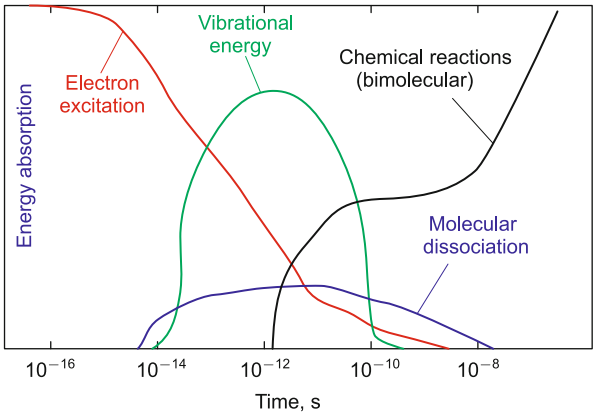

Fig. 6.90 Temporal diagram of energy dissipation in a polymer sample after the passage of a charged particle [1]

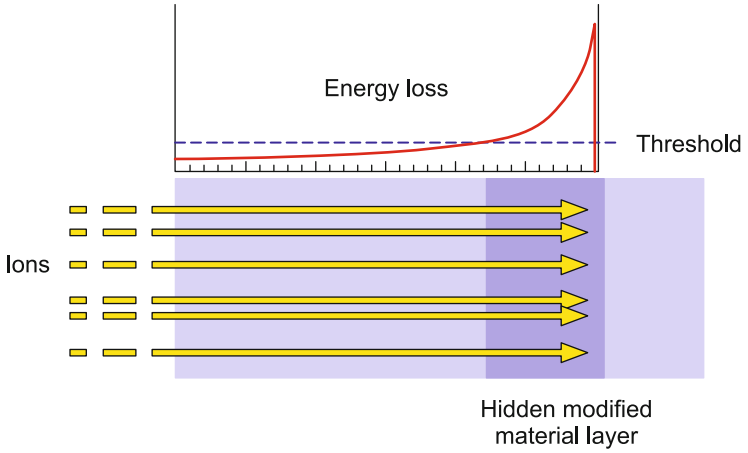

Fig. 6.91 Material modification in the region of Bragg's peak in a precompressed sample [1]

mechanisms have been comprehensively studied theoretically and experimentally [86, 197]. However, for relativistic ions with energies $E_i > 2$ GeV/nucleon the experimental data on the stopping power are quite scarce.

Among the experimental problems in material science to be solved on the FAIR facility is the study of modifications of solids precompressed to a pressure of 25 GPa, in the volume of which a high-intensity heavy ion beam is decelerated. The idea of the experiment is to study the phase transformations of a substance, which is compressed using diamond anvils, in the vicinity of Bragg's peak, where the stopping power is highest [86, 197] (Fig. 6.91 [1]).

Heavy ions release energy in a small volume during a short period of time to provide the threshold structural change of a solid substance, which was in a subthreshold state due to precompression. Furthermore, the ion beam generates acoustic waves in the sample, which also affect the phase transition processes. Therefore, the combination of a high pressure and the local energy liberation by a fast ion-beam will open new possibilities in the generation of those phase transitions which cannot take place on application of the pressure alone. In these investigations it is planned to employ several promising diagnostic techniques, including X-ray and neutron diffraction, optical Raman spectroscopy, and also the resonance measurements of muon spins [218].

In summary it is pertinent to note that these investigations will be carried out on a unique research complex, which has no analogues in the world. A distinctive feature of the FAIR complex is the capability of generating high-intensity primary and secondary beams of stable and radioactive nuclei as well as of antiproton beams, which exceed in intensity the presently available beams by a factor of 100–1000 and offer unique possibilities for performing research in the most topical areas of modern science and technology even in the initial version of the project [224]. A high quality of the beams will be provided due to the capability of their storage,

cooling, and compression. The proposed scheme of the accelerator complex lends itself to optimization of the parallel self-consistent operation of the complex. By and large the complex will be operating for different experiments as if it were intended for each of them separately.

6.8 Heavy-Ion Experiments in the NICA Project

The first accelerator in Russia that allowed beams of high-energy nuclei to be generated was the Synchrophasatron of the Joint Institute for Nuclear Research (JINR) in Dubna [208]. Nowadays this accelerator has been replaced by the Nuclotron, which belongs to a new generation of machines based on the use of superconducting magnets. In the years following the first pioneering Dubna experiments in 1971 on the relativistic acceleration of deuterons, at the Synchrophasatron, and the discovery of the *cumulative effect* in the reactions with nuclei, a new challenging direction in high-energy physics dubbed relativistic nuclear physics [28, 70], a few generations of heavy ion accelerators succeeded each other. Through such technical advances and through the construction of new machines, the laboratory equivalent accessible energy scale grew constantly in time, from a few GeV per nucleon to some tens of TeV per nucleon.

During the entire period of pursuance of heavy ions experiments, there set in a tendency for a steady increase in operating accelerator energy. Progressively more powerful and expensive facilities were made in pursuit of higher energy ion beams. Quite recently an opposite tendency began to show, namely, the trend for lowering the accelerator energy for the purpose of obtaining evidence for the existence of new states of nuclear matter and studying the corresponding phase transitions and critical phenomena. Realized in this case is a deeper thermalization of the substance in relativistic nuclear collisions and the consequential clearer manifestation on new forms of nuclear matter in experiments. Now it is believed that moderate accelerated ion energies are required for this purpose: 8–40 GeV per nucleon in the laboratory frame of reference [212].

According to the existing theoretical notions, nuclear matter may undergo a series of phase transitions of the first kind with increase in temperature and/or baryon charge density. Among them is the phase transition of the first kind involving the recovery of special nuclear interaction symmetry—chiral symmetry, which is severely violated at low temperatures and/or baryon charge density and is recovered at high ones. As a consequence, the existence of a mixed phase corresponding to this transition is predicted [211]—the phase of matter with unbroken and broken symmetry. As we saw above, another predicted phase transition of the first kind is a so-called nuclear matter deconfinement transition to a hypothetical quark-gluon plasma state.

The lowering of energy in heavy ion experiments is, in a sense, a “return to the sources”, because this is a return to the previously mastered energy values. However, its expedience is quite evident: a unique possibility thereby appears to

take advantage of state-of-the-art detectors, modern notions and models, which were nonexistent at the time of execution of the previous experiments at the same energies, so as to refine the existing views, perhaps revise past errors, as well as to supplement the existing experimental data with new ones required from the viewpoint of modern concepts.

The collider project named Nuclotron-based Ion Collider fAcility (NICA) [151, 209, 210], which was initiated in 2007 at JINR, is similarly devoted to exploring heavy ion collisions in the energy range $\sqrt{S_{NN}} = 4$–11 GeV. Such a center-of-mass energy corresponds to about 8–60 GeV per nucleon in the laboratory frame. NICA, with its Multipurpose Particle Detector (MPD), has been defined as the new flagship of the Joint Institute for Nuclear Research in Dubna (JINR). With this instrument, JINR plans to provide a collider facility aimed at the exploration of the high-density region in the QCD phase diagram, thus providing unique opportunities. Specifically NICA will provide collisions of ions over a wide range of atomic masses: nucleon–nucleon, nucleon–nucleus, and nucleus–nucleus collisions are planned. For the time being the maximal foreseen atomic mass is Au^{79+}. Hence, altogether, the actual measurements will range from $Au^{79+} + Au^{79+}$ collisions at a center-of-mass energy up to $\sqrt{S_{NN}} = 11$ GeV with an average luminosity of $L = 10^{27}\,\mathrm{cm}^{-2}\,\mathrm{s}^{-1}$, to proton–proton collisions up to $\sqrt{S_{NN}} = 20$ GeV and an average luminosity of $L \approx 10^{30}\,\mathrm{cm}^{-2}\,\mathrm{s}^{-1}$.

The NICA (Nuclotron-based Ion Collider fAcility) [151, 209, 210] collider project (Figs. 6.92 and 6.93), which is carried out by the JINR (Dubna) since 2007 in close collaboration with the institutes of the RAS, Rosatom, The Ministry

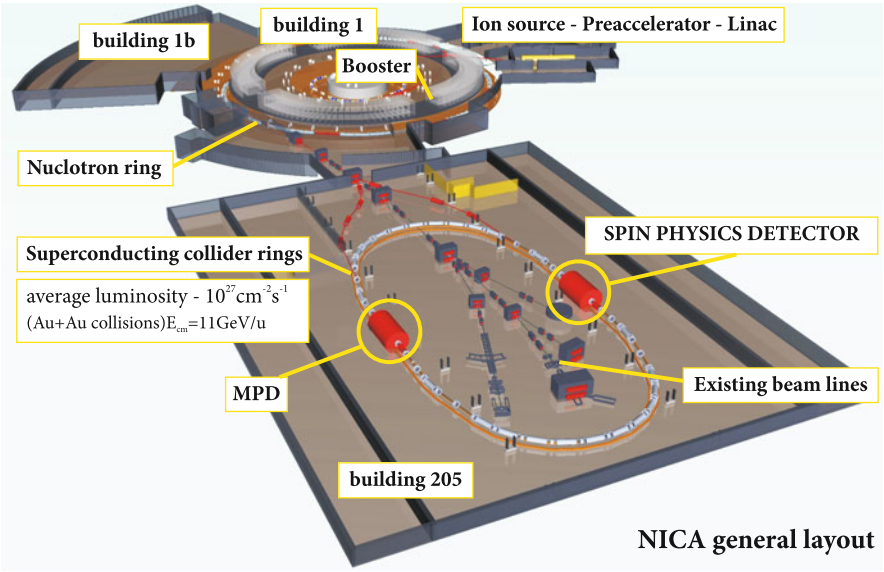

Fig. 6.92 Location of the NICA collider in the JINR accelerator complex area [40, 151]

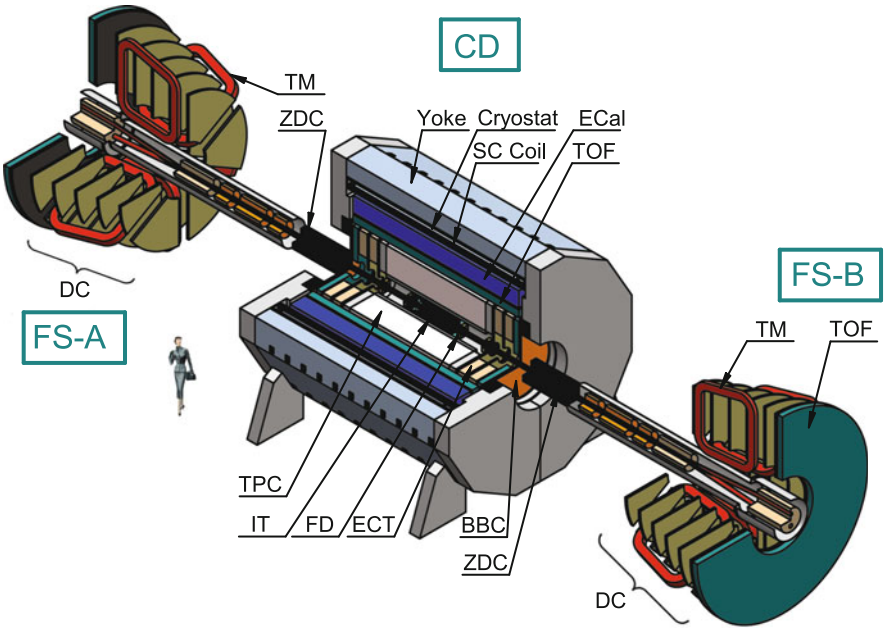

Fig. 6.93 Schematic of the MPD: central detector (CD) and two forward spectrometers (FS-A and FS-B). *BBC* beam–beam counter, *DC* drift chambers, *ECal* electromagnetic calorimeter, *ECT* end-cap tracker, *FD* fast-forward detector, *IT* inner tracker, *SC Coil* superconducting coil, *TM* toroidal magnet, *TOF* time-of-flight system, *TPC* time projection chamber, *ZDC* zero degree calorimeters [213]

of Education and Science of Russia, and several other organizations, is aimed at studying relativistic heavy-ion collisions at energies $\sqrt{s_{NN}} \approx$ 4–11 GeV in the center-of-mass system or of 8–60 AGeV in the laboratory frame. This ambitious project intends to investigate the properties of heated and heavily compressed nuclear matter produced in heavy-ion collisions for the highest baryon charge densities attainable under laboratory conditions, and to search for phase transitions, new nuclear matter states, and new manifestations of the production of a mixed quark-hadron phase. The average luminosity for Au^{79+}+Au^{79+} collisions at an energy $\sqrt{s_{NN}} \approx 10$ GeV is $L \approx 10^{27}\,\mathrm{cm}^{-2}\,\mathrm{s}^{-1}$ and for proton-proton collisions at $\sqrt{s_{NN}} \approx 20$ GeV the figure is $L \approx 10^{30}\,\mathrm{cm}^{-2}\,\mathrm{s}^{-1}$. At present, for world's accelerator centers, namely CERN (SPS), BNL (RHIC), GSI (FAIR), and JINR (NICA), plan experimental programs in this energy range and complement each other, because any experimental results require confirmation.

The scientific goal of the project is to study the properties of heavily compressed baryon substance at the highest density attainable with accelerator technology (see Figs. 6.20 and 6.94) in an effort to discover and investigate new nuclear matter states and new quark-gluon-plasma-type phases.

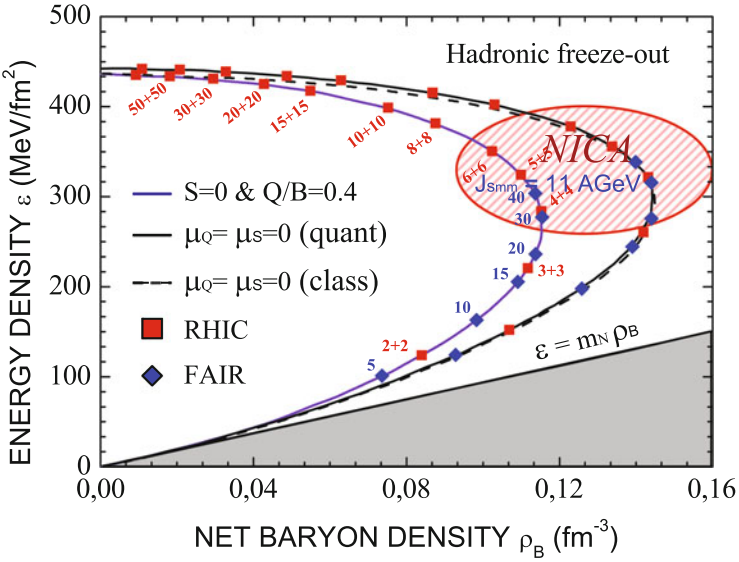

Fig. 6.94 Freeze-out (ceasing of particle interactions in the system) estimated for different colliding energies [183]. The freeze-out baryon density is maximal at the collider energy $\sqrt{S_{NN}} = 4 + 4$ GeV. The *blue numbers* give the energy in the laboratory system, the *red ones* in the center-of-mass system

In the NICA project, an investigation will also be made of electron-nuclear collisions for the purpose of studying the electromagnetic form factor of nuclei and nucleons for high momenta. This line of research comprises studies of spatial charge distribution, magnetization of nucleons and nuclei, as well as parton distribution caused by valence quarks. Measurements of this kind will perhaps yield information about the color transparency of baryon substance, which is important for understanding the properties of QGP and the predictions of quantum chromodynamics at zero temperature.

The project under discussion will provide information about substance behavior in the central domain of the phase diagram in Fig. 6.94, i.e. at a high baryon density and moderate temperature. Also planned is the implementation of other large-scale projects:

- Low-energy RHIC mode in Brookhaven;
- NA61/SHINE at the CERN SPS;
- CBN, FAIR, Darmstadt.

The NICA project is schematized in Figs. 6.20 and 6.94. One of the two MPD (Multi-purpose Particle Detector) detectors (Fig. 6.93) is intended for measuring the characteristics of hot compressed nuclear matter and obtaining data

- on the occurrence of a quark-gluon and/or chiral phase transition;
- on the existence and parameters of critical points;

- on the presence of a mixed quark-gluon phase.

The second SPD (Spin Particle Detector) will study spin physics in heavy ion collisions and in the collision of polarized nucleons and deuterons.

In the NICA project, investigations will be made of the "bulk" properties of hadronic matter like its equation of state, which is critically important for astrophysical applications, including the physics of neutron, quark, and strange stars (see Chap. 9).

The following experiments are planned for the first stage of project implementation:

- the multiplicativity and spectral characteristics of hadrons, including "strange" particles, strange baryons and antibaryons "freeze-out";
- collective fluxes, directional elliptic higher-order fluxes of hadrons and strange particles;
- femptoscopy and correlation for particles.

The second stage will deal with measurements with the aid of electromagnetic fields of photons and dileptons.

Femtoscopy, HBT correlations and event-by-event fluctuations bear important information about the spatio-temporal nature of hot matter in deconfinement conditions as well as about its properties and phase boundaries.

RHIC and SPS experiments suggest that dileptons and photons may be a promising tool for penetrating into the QGP domain. Owing to small electromagnetic interaction cross sections, dileptons and photons escape the interaction domain almost freely and are only slightly distorted on their way to detectors. In this case, the thermal electromagnetic radiation can yield information about the temperature of compressed baryonic matter, provided this radiation is safely separated from the strong background radiation.

Although the NICA energy range is much lower than for RHIC and LHC, this project will permit realizing higher baryonic matter densities precisely where the phase transitions to QGP and chiral structures are expected to occur.

Clearly the NICA project is capable of producing data about the role of nonequilibrium and dimensional effects in relativistic collisions, too.

A study will also be made of the mechanisms of multiparticle production, whereby the hadrons of a nucleus decay into final particles. At high energies (above 15 GeV) this effect is adequately described using quark-and-gluon models. At the same time, these transitions have not been adequately investigated at low energies and will supposedly call for invoking new degrees of freedom.

An important part of the NICA project is the physics of multiplicative effects, which is described by quantum chromodynamic techniques at a high density in the nonperturbative mode [40].

Cumulative processes, which are kinematically forbidden for free nucleons, may yield interesting information about collective properties of the medium and about short-range correlations of quarks and gluons in hot and cold QGPs.

The authors of the NICA project hope that they will manage to obtain new data about the properties of vacuum and hadrons. The matter is that the topological solutions of quantum chromodynamics, which arise from the non-Abelian nature of this theory, may give rise to topological fluctuations in the near-critical domain and, as a consequence, to spatio-temporal domains with broken *P*- or *CP*-invariance.

In heavy-ion collisions this may result in the separation of positive and negative hadrons relative to the reaction plane and give rise to the electric dipole moment in QGP. This charge separation is determined by the ratio between the high magnetic field at the initial instants of collision and the magnitude of topological fluctuations in the heated matter ("the chiral magnetic effect"). This effect was supposedly established in RHIC experiments [243] and is bound to become stronger in QGP. There are grounds to expect that this effect may manifest itself under the NICA experiment conditions.

While on another line of NICA project research related to polarization effects and spin physics, we mention two lines:

- polarization effects in ion collisions;
- spin program with polarized beams.

The former line of research is related to the transformation of the gigantic angular momentum arising in heavy ion collisions to the angular momenta of resultant particles. The study of these processes is related to a deeper insight into the collision dynamics, the chiral properties of the generated medium, and the possible *P*- or *CP*-invariance violation.

The spin program comprises:

- studies of the Drell-Yan effect using longitudinally polarized proton and deuteron beams;
- spin effects in inclusive and noninclusive baryon production;
- light and heavy ions, direct photons;
- studies of spiral amplitudes and double-spin asymmetries in elastic processes.

We therefore see that the NICA project complements the ongoing and planned investigations into the basic properties of compressed baryon matter and will undoubtedly yield many new results in this fascinatingly interesting realm of modern physics.

To complete the section concerned with accelerator projects, we briefly discuss, following [29], an international project whose conceptual stage came under discussion by 1600 scientists from world's 300 laboratories and universities. The case in point is a 30-km long linear electron-positron collider costing 6.7 billion dollars. The facility consists of two linear accelerators of length 11.3 km, one for electrons and the other for positrons (Fig. 6.95).

The projected 30-km long linear collider ILC will be the highest-power facility of this kind. Its linear accelerators (linacs) will accelerate electrons (blue) and positrons (orange) to 250 billion eV (GeV) and then collide them together.

A laser knocks billions of electrons out of a gallium arsenide target in each pulse. Upon acceleration to 5 GeV the electrons are injected into a compressor ring for

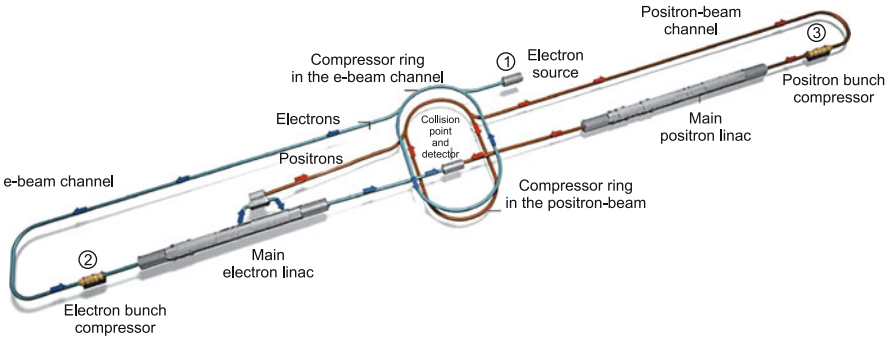

Fig. 6.95 Schematic of the ILC accelerator [29]

increasing the beam density. The electrons are transferred into a compressor where their bunches are further shortened and accelerated to 15 GeV. Then they are injected into the main linear electron accelerator (linac) and their energy is raised to 250 GeV. Halfway in the linac the electron beam is deflected into a special magnet (undulator), where a part of their energy is converted to γ-ray radiation. The gamma-ray photons irradiate a rotating target to produce electron-positron pairs. The positrons are captured, accelerated to 5 GeV, and directed to the second compressor ring.

The positrons travel to the opposite end of the ILC, where their bunches are further compressed and then accelerated to 250 GeV in the second main linac. Magnetic lenses focus the electron and positron beams, which travel towards each other. The particles produced in the electron-positron interaction for 500 GeV at the point of collision are analyzed by detectors.

The key element of this superconducting radio-frequency device is a 1-m long nine-cell niobium resonator, which may be cooled to 2 K. Eight or nine such resonators joined together and submerged into a container with supercooled liquid helium make up a cryomodule. Up to 900 cryomodules will be installed in each ILC linear accelerator, i.e. about 16,000 resonators in the entire collider.

The two superconducting linear accelerators provide electron-positron collisions at an energy of 500 GeV. The ILC will generate, accelerate, and bring into collision almost 3000 electron-positron bunches in a 1-ms long pulse five times per second, which corresponds to a power of 10 MW for each beam.

In the course of compression of electron bunches, the electron energy rises up to 10 GeV; after that they will be injected into one of the two 11.3-km main SCRF linear accelerators, where their energy rises up to 250 GeV. In the midway, at an energy of 150 MeV, the electron bunches will be deflected for producing positron bunches. The positrons will be captured, accelerated to 5 GeV, transferred to another compressor ring and then to the second main linear SCRF at the opposite end of the ILC.

When the energy of the electrons and positrons reaches the final value of 250 GeV and they travel towards the point of collision, several magnetic lenses will focus the bunches into 6-nm thick plane ribbons approximately 600 nm wide.

It is yet unknown where the ILC will be located and whether it will be constructed at all; the decision on this matter depends on the financial support which the governments will be able to provide and on the results obtained on present-day accelerators in the immediate future.

References

1. BIOMAT Collaboration: Letter of Intent for: Materials Research with Relativistic Heavy Ion Beams. http://www.gsi.de/fair/experiments/biomat/BIOMAT_LOI_Mat.pdf
2. Detector CBM: http://www.gsi.de/fair/experiments/CBM/detector.html
3. The SPARC Collab.: Technical report for the design, construction, commissioning and operation of the SPARC Project: Stored Particle Atomic Physics Collaboration at the FAIR Facility. http://www-linux.gsi.de/~sparc/documents/pdf_files/06_01_06_SPARC_TR.pdf
4. ESFRI, the European Strategy Forum on Research Infrastructures: http://ec.europa.eu/research/infrastructures/index_en.cfm?pg=esfri
5. The HITRAP decelerator and trap facility
6. Report of the NSAC Subcommittee on Comparison of the Rare Isotope Accelerator (RIA) and the Gesellschaft für Schwerionenforschung (GSI) Future Facility (2004): http://science.energy.gov/~/media/np/nsac/pdf/docs/ria_gsi_nsac_022604.pdf
7. CMS Technical Proposal, CERN/LHCC 94-38, LHCC/P1 (1994)
8. An international accelerator facility for beams of ions and antiprotons. Conceptual Design Report, p. 12. GSI (2001)
9. PANDA Collaboration, Technical Progress Report for: PANDA (2005)
10. FAIR Baseline Technical Report, vol. 2 (Accelerator and Scientific Infrastructure), p. 471 (2006)
11. FAIR Baseline Technical Report. GSI, Darmstadt (2006)
12. FAIR Baseline Technical Report, vol. 3A (CBM). GSI, Darmstadt (2006)
13. Aad, G., Abajyan, T., Abbott, B., et al.: Observation of a new particle in the search for the Standard Model Higgs boson with the ATLAS detector at the LHC. Phys. Lett. B **716**(1), 1–29 (2012)
14. Abrikosov, A.A., Khalatnikov, I.M.: The theory of a fermi liquid (the properties of liquid 3 he at low temperatures). Rep. Prog. Phys. **22**(1), 329 (1959)
15. Adams, J., Adler, C., Aggarwal, M.M., et al.: Azimuthal anisotropy at the relativistic heavy ion collider: the first and fourth harmonics. Phys. Rev. Lett. **92**(6), 062301 (2004)
16. Adams, J., Adler, C., Aggarwal, M.M., et al.: Particle-type dependence of azimuthal anisotropy and nuclear modification of particle production in $Au + Au$ collisions at $sNN = 200GeV$. Phys. Rev. Lett. **92**(5), 052302 (2004)
17. Adler, C., Ahammed, Z., Allgower, C., et al.: Disappearance of back-to-back high-pT hadron correlations in central Au+Au collisions at sNN=200 GeV. Phys. Rev. Lett. **90**(8), 082302 (2003)
18. Adler, S.S., Afanasiev, S., Aidala, C., et al.: Elliptic flow of identified hadrons in $Au + Au$ collisions at $sNN = 200GeV$. Phys. Rev. Lett. **91**(18), 182301 (2003)
19. Aleksan, R., Amerman, L., Aston, D., et al.: Test of a large scale prototype of the DIRC, a Cherenkov imaging detector based on total internal reflection for BaBar at PEP-II. Nucl. Instrum. Methods Phys. Res. A **397**(2–3), 261–282 (1997)
20. Ali Khan, A., Aoki, S., Burkhalter, R., et al.: Equation of state in finite-temperature qcd with two flavors of improved Wilson quarks. Phys. Rev. D **64**, 074510 (2001)
21. Alt, C., Anticic, T., Baatar, B., et al.: Directed and elliptic flow of charged pions and protons in $Pb + Pb$ collisions at $4A$ and $158AGeV$. Phys. Rev. C **68**(3), 034903 (2003)

22. Anisimov, S.I., Prokhorov, A.M., Fortov, V.E.: Application of high-power lasers to study matter at ultrahigh pressures. Sov. Phys. – Usp. **27**(3), 181–205 (1984)
23. Aoki, Y., Fodor, Z., Katz, S.D., Szab, K.K.: The equation of state in lattice qcd: with physical quark masses towards the continuum limit. J. High Energy Phys. **2006**(01), 089 (2006)
24. Arnold, P., Moore, G.D., Yaffe, L.G.: Transport coefficients in high temperature gauge theories, 2. Beyond leading log. J. High Energy Phys. **2003**(05), 051 (2003)
25. Asner, D.M., Phillips, T.J., Apollinari, G., et al.: P-986 Letter of Intent: Medium-Energy Antiproton Physics at Fermilab (2009)
26. Atoyan, G., Gladyshev, V., Gninenko, S., et al.: Lead-scintillator electromagnetic calorimeter with wavelength shifting fiber readout. Nucl. Instrum. Methods Phys. Res. A **320**(1–2), 144–154 (1992)
27. Atzeni, S., Meyer-ter-Vehn, J.: The Physics of Inertial Fusion. Oxford University Press, Oxford (2004)
28. Baldin, A.M., Malakhov, A.I., Sissakian, A.N.: Some problems of relativistic nuclear physics and multiple particle production (in Russian). Phys. Elem. Part. At. Nucl. **32**(7), 6 (2001)
29. Barish, B., Walker, N., Yamamoto, H.: Building the next generation collider. Sci. Am. **298**(2), 46–51 (2008)
30. Basko, M.M.: Magnetized implosions driven by intense ion beams. Phys. Plasmas **7**(11), 4579–4589 (2000)
31. Basko, M.M., Churazov, M.D., Aksenov, A.G.: Prospects of heavy ion fusion in cylindrical geometry. Laser Part. Beams **20**(03), 411–414 (2002)
32. Batani, D., Koenig, M., Lower, T., et al.: Measuring EOS with lasers. Europhys. News **27**, 210 (1996)
33. Batani, D., Morelli, A., Tomasini, M., et al.: Equation of state data for iron at pressures beyond 10 Mbar. Phys. Rev. Lett. **88**, 235502 (2002)
34. Baumung, K., Bluhm, H.J., Goel, B., et al.: Shock-wave physics experiments with high-power proton beams. Laser Part. Beams **14**(2), 181 (1996)
35. Baym, G.: Nuclear matter under extreme conditions. Nucl. Phys. A **702**(1-4), 3–12 (2002)
36. Baym, G., Chin, S.A.: Can a neutron star be a giant MIT bag? Phys. Lett. B **62**(2), 241–244 (1976)
37. Bernard, C., Blum, T., DeTar, C., et al.: Equation of state for two flavor QCD at $Nt = 6$. Phys. Rev. D **55**(11), 6861–6869 (1997)
38. Bernard, C., Burch, T., DeTar, C., et al.: QCD equation of state with $2 + 1$ flavors of improved staggered quarks. Phys. Rev. D **75**, 094505 (2007)
39. Bethe, H.A.: Handbuch fur Physik, vol. 24/2. Springer, Berlin (1933)
40. Blaschke, D., et al. (eds.): Searching for a QCD mixed phase at the Nuclotron-based Ion Collider fAcility (NICA white paper) (2009)
41. Bluhm, R., Kostelecký, V.A., Russell, N.: CPT and Lorentz tests in Penning traps. Phys. Rev. D **57**, 3932–3943 (1998)
42. Boyd, G., Engels, J., Karsch, F., et al.: Thermodynamics of su(3) lattice gauge theory. Nucl. Phys. B **469**(3), 419–444 (1996)
43. Brustein, R., Medved, A.J.M.: Ratio of shear viscosity to entropy density in generalized theories of gravity. Phys. Rev. D **79**, 021901 (2009)
44. Bruun, G.M., Smith, H.: Frequency and damping of the scissors mode of a fermi gas. Phys. Rev. A **76**, 045602 (2007)
45. Bruun, G.M., Smith, H.: Shear viscosity and damping for a fermi gas in the unitarity limit. Phys. Rev. A **75**, 043612 (2007)
46. Chapline, G., Nauenberg, M.: Asymptotic freedom and the baryon-quark phase transition. Phys. Rev. D **16**(2), 450–456 (1977)
47. Chatrchyan, S., Khachatryan, V., Sirunyan, A., et al.: Observation of a new boson at a mass of 125 GeV with the CMS experiment at the LHC. Phys. Lett. B **716**(1), 30–61 (2012)
48. Cheng, M., Christ, N.H., Datta, S., et al.: QCD equation of state with almost physical quark masses. Phys. Rev. D **77**, 014511 (2008)

49. Cheng, M., Ejiri, S., Hegde, P., et al.: Equation of state for physical quark masses. Phys. Rev. D **81**, 054504 (2010)
50. Chernodub, M.N., Nakamura, A., Zakharov, V.I.: Manifestations of magnetic vortices in the equation of state of a yang-mills plasma. Phys. Rev. D **78**, 074021 (2008)
51. Chiang, I.H., Garber, E., Inagaki, T., et al.: CsI endcap photon detector for a $K^p m \to n^+ vv^-$ experiment at BNL. IEEE Trans. Nucl. Sci. **42**(4), 394–400 (1995)
52. Cho, S., Zahed, I.: Classical strongly coupled quark-gluon plasma. IV. Thermodynamics. Phys. Rev. C **80**, 014906 (2009)
53. Collins, J.C., Perry, M.J.: Superdense matter: neutrons or asymptotically free quarks? Phys. Rev. Lett. **34**(21), 1353–1356 (1975)
54. Cremonini, S.: The shear viscosity to entropy ratio: a status report. Mod. Phys. Lett. **B25**, 1867–1888 (2011)
55. Csernai, L.P., Fai, G., Gale, C., Osnes, E.: Nuclear equation of state with momentum-dependent interactions. Phys. Rev. C **46**, 736–747 (1992)
56. Csikor, F., Egri, G., Fodor, Z., et al.: The QCD equation of state at finite Tμ on the lattice. Prog. Theor. Phys. Supp. **153**, 93–105 (2004)
57. Cuneo, M.E., Adams, R.G., Bailey, J.E., et al.: Generating high-brightness light ion beams for inertial fusion energy. In: Proceedings of IFP/14 (1998)
58. Cuneo, M.E., Vesey, R.A., Bennett, G.R., et al.: Progress in symmetric ICF capsule implosions and wire-array Z-pinch source physics for double-pinch-driven hohlraums. Plasma Phys. Control. Fusion **48**(2), R1–R35 (2006)
59. Curtis, S.B.: Single track effects, biostack and risk assessment. Radiat. Meas. **23**(1), 5–8 (1994)
60. Curtis, S., Vazquez, M., Wilson, J., et al.: Cosmic ray hit frequencies in critical sites in the central nervous system. Adv. Space Res. **22**(2), 197–207 (1998)
61. De, J.N., Agrawal, B.K., Samaddar, S.K.: Equation of state of finite nuclei and liquid-gas phase transition. Phys. Rev. C **59**, R1–R4 (1999)
62. Demir, N., Bass, S.A.: Shear-viscosity to entropy-density ratio of a relativistic hadron gas. Phys. Rev. Lett. **102**, 172302 (2009)
63. DeTar, C., Levkova, L., Gottlieb, S., et al.: QCD thermodynamics with nonzero chemical potential at $N_t = 6$ and effects from heavy quarks. Phys. Rev. D **81**, 114504 (2010)
64. Dremin, I.M.: Physics at the large hadron collider. Phys. Usp. **52**(6), 541–548 (2009)
65. Dremin, I.M., Leonidov, A.V.: The quark - gluon medium. Phys. Usp. **53**(11), 1123–1149 (2010)
66. Durante, M.: Applications of particle microbeams in space radiation research. J. Radiat. Res. **50**(Suppl. A), A55–A58 (2009)
67. Durante, M., Cucinotta, F.A.: Heavy ion carcinogenesis and human space exploration. Nat. Rev. Cancer **8**, 465–472 (2008)
68. Efremov, V.P., Pikuz Jr., S.A., Faenov, A.Y., et al.: Study of the energy release region of a heavy-ion flux in nanomaterials by X-ray spectroscopy of multicharged ions. JETP Lett. **81**(8), 378 (2005)
69. Ekström, C.: Internal targets. CERN Report 92-01, pp. 120–146 (1992)
70. Emel'yanov, V.M., Timoshenko, S.L., Strikhanov, M.N.: Vvedenie v relyativistskuyu yadernuyu fiziku (Introduction to Relativistic Nuclear Physics). Fizmatlit, Moscow (2011)
71. Fodor, Z., Katz, S.D.: Critical point of QCD at finite T and μ, lattice results for physical quark masses. J. High Energy Phys. **2004**(04), 050 (2004)
72. Föhl, K.: The PANDA detector at the future FAIR laboratory. Eur. Phys. J. Spec. Top. **162**, 213–220 (2008). doi:10.1140/epjst/e2008-00796-5
73. Fortov, V.E.: Intense shock waves and extreme states of matter. Phys. Usp. **50**(4), 333 (2007)
74. Fortov, V.E.: Ekstremal'nye sostoyaniya veshchestva (Extreme States of Matter). Fizmatlit, Moscow (2009) [Translated into English: Extreme States of Matter. Series: The Frontiers Collection. Springer, Berlin/Heidelberg (2011)]
75. Fortov, V.E.: Uravneniya sostoyaniya veshchestva (Equations of State of Matter). Fizmatlit, Moscow (2013)

76. Fortov, V., Shutov, A.: Numerical simulations of nonstationary fronts and interfaces by the Godunov method in moving grids. Nucl. Sci. Eng. **123**, 169 (1996)
77. Fortov, V., Rudakov, L., Ni, A.: Application of intense relativistic electron beams in high dynamic pressure thermophysics. Sov. Therm. Phys. Rev. **371**, 589 (1992)
78. Fortov, V.E., Ivlev, A.V., Khrapak, S.A., et al.: Complex (dusty) plasma: current status, open issues, perspectives. Phys. Rep. **421**(1), 1–103 (2005)
79. Fortov, V., Iakubov, I., Khrapak, A.: Physics of Strongly Coupled Plasma. Oxford University Press, Oxford (2006)
80. Fortov, V.E., Ilkaev, R.I., Arinin, V.A., et al.: Phase transition in a strongly nonideal deuterium plasma generated by quasi-isentropical compression at megabar pressures. Phys. Rev. Lett. **99**(18), 185001 (2007)
81. Fortov, V.E., Hoffmann, D.H.H., Sharkov, B.Y.: Intense ion beams for generating extreme states of matter. Phys. Usp. **51**(2), 109 (2008)
82. Fortov, V.E., Petrov, O.F., Vaulina, O.S., Timirkhanov, R.A.: Viscosity of a strongly coupled dust component in a weakly ionized plasma. Phys. Rev. Lett. **109**, 055002 (2012)
83. Fortov, V.E., Sharkov, B.Y., Stöcker, H.: European Facility for Antiproton and Ion Research (FAIR): the new international center for fundamental physics and its research program. Phys. Usp. **55**(6), 582–602 (2012)
84. Freedman, B.A., McLerran, L.D.: Fermions and gauge vector mesons at finite temperature and density. III. The ground-state energy of a relativistic quark gas. Phys. Rev. D **16**(4), 1169–1185 (1977)
85. Friman, B., Höhne, C., Knoll, J., et al. (eds.): The CBM Physics Book. Lecture Notes in Physics, vol. 814, 1st edn. Springer, Berlin (2010)
86. Geissel, H., Scheidenberger, C.: Slowing down of relativistic heavy ions and new applications. Nucl. Instrum. Methods Phys. Res. B **136–138**(0), 114–124 (1998). Ion Beam Analysis
87. Gelman, B.A., Shuryak, E.V., Zahed, I.: Classical strongly coupled quark-gluon plasma. II. Screening and equation of state. Phys. Rev. C **74**, 044909 (2006)
88. Gezerlis, A., Carlson, J.: Strongly paired fermions: cold atoms and neutron matter. Phys. Rev. C **77**(3), 032801 (2008)
89. Ginzburg, V.L.: The Physics of a Lifetime: Reflections on the Problems and Personalities of 20th Century Physics. Springer, Berlin/Heidelberg (2001)
90. Ginzburg, V.L.: On superconductivity and superfluidity (what I have and have not managed to do), as well as on the "physical minimum" at the beginning of the XXI century (December 8, 2003). Phys. Usp. **47**(11), 1155 (2004)
91. Glendenning, N.K.: Compact Stars: Nuclear Physics, Particle Physics, and General Relativity, 2nd edn. Springer, New York (2000)
92. Golovkov, M.S., Grigorenko, L.V., Ter-Akopian, G.M., et al.: The ^{8}He and ^{1}0He spectra studied in the reaction. Phys. Lett. B **672**(1), 22–29 (2009)
93. Goto, A., Yano, Y., Katayama, T.: RIKEN RI-Beam Factory project. J. Phys. G: Nucl. Part. Phys. **24**(8), 1341 (1998)
94. Gregori, G., Glenzer, S.H., Rozmus, W., et al.: Theoretical model of X-ray scattering as a dense matter probe. Phys. Rev. E **67**, 026412 (2003)
95. Gross, D.J., Politzer, H.D., Wilczek, F.: Asymptotic freedom and quantum chromodynamics: the key to the understanding of the strong nuclear forces. Nobel Prize in Physics (2004)
96. Gubser, S.S., Nellore, A.: Mimicking the QCD equation of state with a dual black hole. Phys. Rev. D **78**, 086007 (2008)
97. Gyulassy, M., McLerran, L.: New forms of QCD matter discovered at RHIC. Nucl. Phys. A **750**(1), 30–63 (2005)
98. Gyulassy, M., Plumer, M.: Jet quenching as a probe of dense matter. Nucl. Phys. A **527**, 641–644 (1991)
99. Gyulassy, M., Plumer, M., Thoma, M., Wang, X.N.: High p_t probes of nuclear collisions. Nucl. Phys. A **538**, 37–49 (1992)
100. Haberer, T., Becher, W., Schardt, D., Kraft, G.: Magnetic scanning system for heavy ion therapy. Nucl. Instrum. Methods Phys. Res. A **330**(1–2), 296–305 (1993)

101. Habs, D., Groß, M., Assmann, W., et al.: The Munich accelerator for fission fragments MAFF. Nucl. Instrum. Methods Phys. Res. B **204**, 739–745 (2003)
102. Hamieh, S., Letessier, J., Rafelski, J.: Quark-gluon plasma fireball. Phys. Rev. C **62**, 064901 (2000)
103. Hands, S.: The phase diagram of QCD. Contemp. Phys. **42**(4), 209–225 (2001)
104. Heinz, U.W.: Concepts of heavy-ion physics. In: High Energy Physics - Phenomenology. arXiv:hep-ph/0407360 (2004)
105. Herfurth, F.: Precise nuclear physics measurements with ion traps. Int. J. Mod. Phys. E **18**, 392–404 (2009)
106. Hoffmann, D.H.H., Fortov, V.E., Lomonosov, I.V., et al.: Unique capabilities of an intense heavy ion beam as a tool for equation-of-state studies. Phys. Plasmas **9**(9), 3651–3654 (2002)
107. Hoffmann, D.H.H., Fortov, V.E., Lomonosov, I.V., et al.: Unique capabilities of an intense heavy ion beam as a tool for equation-of-state studies. Phys. Plasmas **9**(9), 3651–3654 (2002)
108. Hofmann, S., Münzenberg, G.: The discovery of the heaviest elements. Rev. Mod. Phys. **72**, 733–767 (2000)
109. Holmes-Siedle, A., Adams, L.: Hand Book of Radiation Effects. Oxford University Press, Oxford (2002)
110. Jacak, B., Steinberg, P.: Creating the perfect liquid in heavy-ion collisions. Phys. Today **63**(5), 39–43 (2010)
111. Jacobs, P., Klay, J.: Jets and high p_t hadrons in dense matter: recent results from star. arXiv:nucl-ex/0308023 (2003)
112. Johnson, C.V., Steinberg, P.: What black holes teach about strongly coupled particles. Phys. Today **63**(5), 29–33 (2010)
113. Kalashnikov, O.K., Klimov, V.V.: Phase transition in the quark-gluon plasma. Phys. Lett. B **88**(3–4), 328–330 (1979)
114. Kambara, T., Kanai, Y., Kojima, T., et al.: Acoustic emission from fast heavy-ion irradiation on solids. Nucl. Instrum. Methods Phys. Res. B **164–165**, 415–419 (2000)
115. Kambara, T., Kageyama, K., Kanai, Y., et al.: Elastic wave from fast heavy ion irradiation on solids. Nucl. Instrum. Methods Phys. Res. B **193**(1–4), 371–375 (2002)
116. Kanel, G.I., Razorenov, S.V., Fortov, V.E.: Shock-Wave Phenomena and Properties of Condensed Matter. Springer, New York (2004)
117. Kapusta, J.I.: Quantum chromodynamics at high temperature. Nucl. Phys. B **88**(3–4), 461–498 (1979)
118. Kapusta, J.I.: Equation of state and phase fluctuations near the chiral critical point. Phys. Rev. C **81**, 055201 (2010)
119. Karsch, F.: Lattice QCD at high temperature and the QGP. arXiv:hep-lat/0601013 (2006)
120. Karsch, F., Laermann, E., Peikert, A.: The pressure in 2, 2+1 and 3 flavour QCD. Phys. Lett. B **478**(4), 447–455 (2000)
121. Kester, O., Sieber, T., Emhofer, S., et al.: Accelerated radioactive beams from REX-ISOLDE. Nucl. Instrum. Methods Phys. Res. B **204**, 20–30 (2003)
122. Khalatnikov, I.M.: An Introduction to the Theory of Superfluidity. Benjamin, New York (1965)
123. Kleppner, D.: Professor Feshbach and His Resonance. Phys. Today **57**(8), 12–13 (2004)
124. Knudson, M.D., Hanson, D.L., Bailey, J.E., et al.: Equation of state measurements in liquid deuterium to 70 GPa. Phys. Rev. Lett. **87**(22), 225501 (2001)
125. Kobayashi, M.: CP violation and flavour mixing. Nobel Lecture, December 8, 2008 (2008). http://www.nobelprize.org/nobel_prizes/physics/laureates/2008/kobayashi_lecture.pdf
126. Kolb, P.F., Sollfrank, J., Heinz, U.: Anisotropic transverse flow and the quark-hadron phase transition. Phys. Rev. C **62**, 054909 (2000)
127. Kolomietz, V.M., Sanzhur, A.I., Shlomo, S., Firin, S.A.: Equation of state and phase transitions in asymmetric nuclear matter. Phys. Rev. C **64**, 024315 (2001)
128. Korobenko, V.N., Rakhel', A.D., Savvatimskii, A.I., Fortov, V.E.: Measurement of the electric conductivity of tungsten in a continuous liquid-to-gas transition. Plasma Phys. Rep. **28**(12), 1008 (2002)

129. Koshkarev, D.G., Churazov, M.D.: Inertsionnyi termoyadernyi sintez na baze tyazheloionnogo uskoritelya-drivera i tsilindricheskoi misheni (Inertial thermonuclear fusion based on a heavy-ion accelerator-driver and cylindrical target). Atom. Energy **91**(1), 47–54 (2001)
130. Kovtun, P., Son, D.T., Starinets, A.O.: Holography and hydrodynamics: diffusion on stretched horizons. J. High Energy Phys. **2003**(10), 064 (2003)
131. Kovtun, P.K., Son, D.T., Starinets, A.O.: Viscosity in strongly interacting quantum field theories from black hole physics. Phys. Rev. Lett. **94**, 111601 (2005)
132. Kozyreva, A., Basko, M., Rosmej, F., et al.: Dynamic Confinement of Targets Heated Quasy-isochorically with heavy ion beams. GSI-2003-2 Annual Report p. 27 (2003)
133. Kraft, G.: Radiobiological effects of very heavy ions: Inactivation, induction of chromosome aberrations and strand break. Nucl. Sci. Appl. **3**, 1 (1987)
134. Kramer, M., Kraft, G.: Calculations of heavy-ion track structure. Radiat. Environ. Biophys. **33**, 91–109 (1994)
135. Krasnikov, N.V., Matveev, V.A.: The search for new physics at the Large Hadron Collider. Phys. Usp. **47**(7), 643 (2004)
136. Kratz, K.L., Pfeiffer, B., Thielemann, F.K., Walters, W.: Nuclear structure studies at ISOLDE and their impact on the astrophysical r-process. Hyperfine Interact. **129**, 185–221 (2000). doi:10.1023/A:1012694723985
137. Kruer, W.L.: The Physics of Laser Plasma Interactions. Addison-Wesley, Reading, MA (1988)
138. Kuehl, T., Bock, R., Borneis, S., et al.: PHELIX status and first experiments. Hyperfine Interact. **162**, 55–62 (2005). doi:10.1007/s10751-005-9203-3
139. Lampert, M.A., Molina-París, C.: Effective equation of state for a spherically expanding pion plasma. Phys. Rev. D **57**, 83–92 (1998)
140. Langanke, L.: A FAIR chance for nuclear astrophysics. In: Kick-Off Event and Symposium on the Physics at FAIR (2007)
141. Letessier, J., Rafelski, J.: Qcd equations of state and the quark-gluon plasma liquid model. Phys. Rev. C **67**, 031902 (2003)
142. Lévai, P., Heinz, U.: Massive gluons and quarks and the equation of state obtained from SU(3) lattice QCD. Phys. Rev. C **57**, 1879–1890 (1998)
143. Lindl, J.D.: Inertial Confinement Fusion. Springer, New York (1998)
144. Litvinov, Y., Geissel, H., Radon, T., et al.: Mass measurement of cooled neutron-deficient bismuth projectile fragments with time-resolved Schottky mass spectrometry at the FRS-ESR facility. Nucl. Phys. A **756**(1–2), 3–38 (2005)
145. Loiselet, M., Berger, G., Breyne, D., et al.: Production and acceleration of Radioactive Beams at Louvain-la-Neuve. In: 14th International Conference on Cyclotrons and Their Application, Cape Town, p. 629 (1995)
146. Gyulassy, M.: Relativistic heavy ions and QGP at FAIR (2007)
147. MacFarlane, J.J., Wang, P., Bailey, J., et al.: Analysis of Kα line emission from aluminum plasmas created by intense proton beams. Phys. Rev. E **47**(4), 2748–2758 (1993)
148. Marletta, G., Bouffard, S., Neumenn, R. (eds.): Proceedings of 5th International Symposium on Swift Heavy Ions in Matter (SHIM 2002), Giardini Naxos, 19–23 May 2002
149. Maury, S.: The Antiproton Decelerator (AD). CERN/PS 99-50 (HP) (1999)
150. Meisinger, P.N., Miller, T.R., Ogilvie, M.C.: Phenomenological equations of state for the quark-gluon plasma. Phys. Rev. D **65**, 034009 (2002)
151. Meshkov, I., Sidorin, A. (eds.): Design and construction of Nuclotron-based Ion Collider fAcility (NICA), conceptual design report (2008)
152. Mesyats, G.A.: Impul'snaya energetika i elektronika (Pulse Power and Electronics). Nauka, Moscow (2004)
153. Meyer, H.B.: Calculation of the shear viscosity in su(3) gluodynamics. Phys. Rev. D **76**, 101701 (2007)
154. Mintsev, V., Gryaznov, V., Kulish, M., et al.: Stopping power of proton beam in a weakly non-ideal xenon plasma. Contrib. Plasma Phys. **39**(1–2), 45–48 (1999)
155. Mittig, W., Villari, A.C.C.: GANIL and the SPIRAL2 project. In: 4th International Conference on Exotic Nuclei and Atomic Masses, ENAM'04, Pine Mountain, GA (2004)

156. Möhl, D.: Stochastic cooling. In: CAS-87. CERN 87-03, vol. 2, pp. 453–533 (1987)
157. Mrowczynski, S., Thoma, M.H.: What do electromagnetic plasmas tell us about the quark-gluon plasma? Annu. Rev. Nucl. Part. Sci. **57**(1), 61–94 (2007)
158. Nakamura, T., Wada, M., Okada, K., et al.: Laser spectroscopy of $^{7,10}Be^{+}$ in an online ion trap. Phys. Rev. A **74**, 052503 (2006)
159. Namekawa, Y., Aoki, S., Burkhalter, R., et al.: Thermodynamics of SU(3) gauge theory on anisotropic lattices. Phys. Rev. D **64**, 074507 (2001)
160. National Research Council: Frontiers in High Energy Density Physics. National Academies Press, Washington, DC (2003)
161. Neidherr, D., Audi, G., Beck, D., et al.: Discovery of ^{229}Rn and the structure of the heaviest Rn and Ra isotopes from penning-trap mass measurements. Phys. Rev. Lett. **102**, 112501 (2009)
162. Neumayr, J.B., Beck, L., Habs, D., et al.: The ion-catcher device for SHIPTRAP. Nucl. Instrum. Methods Phys. Res. B **244**(2), 489–500 (2006)
163. NICA: NICA project site: http://nica.jinr.ru/
164. Nörtershäuser, W., Tiedemann, D., Žáková, M., et al.: Nuclear charge radii of ^{7,9,10}Be and the one-neutron halo nucleus ^{11}Be. Phys. Rev. Lett. **102**, 062503 (2009)
165. Novikov, I.D.: "Big Bang" echo (cosmic microwave background observations). Phys. Usp. **44**(8), 817 (2001)
166. Novotny, R., Beck, R., Doring, W., et al.: Electromagnetic calorimetry with $PbWO_4$ in the energy regime below 1 GeV. IEEE Trans. Nucl. Sci. **47**(4), 1499–1502 (2000)
167. O'Hara, K.M., Hemmer, S.L., Gehm, M.E., et al.: Observation of a strongly interacting degenerate fermi gas of atoms. Science **298**(5601), 2179–2182 (2002)
168. Okamoto, M., Ali Khan, A., Aoki, S., et al.: Equation of state for pure SU(3) gauge theory with renormalization group improved action. Phys. Rev. D **60**, 094510 (1999)
169. Okun', L.B.: Leptony i kvarki, 2nd edn. Nauka, Moscow (1990) [English Transl.: Leptons and Quarks. North-Holland, Amsterdam (1982)]
170. Okun', L.B.: Azy fiziki. Ochen' kratkii putevoditel' (The Basics of Physics. A Very Brief Guide). Fizmatlit, Moscow (2012)
171. Ollitrault, J.Y.: Anisotropy as a signature of transverse collective flow. Phys. Rev. D **46**(1), 229–245 (1992)
172. Orr, N.A., Anantaraman, N., Austin, S.M., et al.: Momentum distributions of ^{9}Li fragments from the breakup of ^{11}Li and the neutron halo. Phys. Rev. C **51**, 3116–3126 (1995)
173. Pal, S.: Shear viscosity to entropy density ratio of a relativistic Hagedorn resonance gas. Phys. Lett. **B684**, 211–215 (2010)
174. Park, B.Y., Lee, H.J., Vento, V.: Skyrmions at finite density and temperature: the chiral phase transition. Phys. Rev. D **80**, 036001 (2009)
175. Parkhomchuk, V.V., Skrinskii, A.N.: Electron cooling: 35 years of development. Phys. Usp. **43**(5), 433–452 (2000)
176. Pfeiffer, B., Kratz, K.L., Thielemann, F.K., Walters, W.: Nuclear structure studies for the astrophysical r-process. Nucl. Phys. A **693**(1–2), 282–324 (2001)
177. Pieranski, P.: Colloidal crystals. Contemp. Phys. **24**(1), 2573 (1983)
178. Piriz, A.R., Tahir, N.A., Hoffmann, D.H.H., Temporal, M.: Generation of a hollow ion beam: calculation of the rotation frequency required to accommodate symmetry constraint. Phys. Rev. E **67**, 017501 (2003)
179. Policastro, G., Son, D.T., Starinets, A.O.: Shear viscosity of strongly coupled $n = 4$ supersymmetric yang-mills plasma. Phys. Rev. Lett. **87**, 081601 (2001)
180. Quigg, C.: The coming revolutions in particle physics. Sci. Am. **298**(2), 46 (2008)
181. Quintenz, J., Sandia's Pulsed Power Team: Pulsed power team. In: Proceedings of 13th International Conference on High Power Particle Beams, Nagaoka (2000)
182. Radon, T., Kerscher, T., Schlitt, B., et al.: Schottky mass measurements of cooled proton-rich nuclei at the GSI experimental storage ring. Phys. Rev. Lett. **78**, 4701–4704 (1997)
183. Randrup, J., Cleymans, J.: Exploring high-density baryonic matter: maximum freeze-out density. In: Searching for a QCD Mixed Phase at the Nuclotron-Based Ion Collider fAcility (NICA White Paper), p. 16. JINR, Dubna (2009)

184. Randrup, J., Ruuskanen, P.V.: Thermodynamic consistency of the equation of state of strongly interacting matter. Phys. Rev. C **69**, 047901 (2004)
185. Regan, P., Garnsworthy, A., Pietri, S., et al.: Isomer spectroscopy using relativistic projectile fragmentation at the N=Z line for A$\sim$ 80 $\rightarrow$ 90. Nucl. Phys. A **787**(1–4), 491–498 (2007). Proceedings of the Ninth International Conference on Nucleus-Nucleus Collisions (NN2006)
186. Reich, H., Bourgeois, W., Franzke, B., et al.: The ESR internal target. Nucl. Phys. A **626**(1–2), 417–425 (1997)
187. Riordan, M., Zajc, W.A.: The first few microseconds. Sci. Am. **294**(5), 34A–41 (2006)
188. Rosmej, O.N., Blazevic, A., Korostiy, S., et al.: Charge state and stopping dynamics of fast heavy ions in dense matter. Phys. Rev. A **72**(5), 052901 (2005)
189. Rubakov, V.A.: Large and infinite extra dimensions. Phys. Usp. **44**(9), 871 (2001)
190. Rubakov, V.A.: Introduction to cosmology. PoS **RTN2005**, 003 (2005)
191. Rubakov, V.A.: Hierarchies of fundamental constants (to items Nos 16, 17, and 27 from Ginzburg's list). Phys. Usp. **50**(4), 390 (2007)
192. Rubakov, V.A.: Large hadron collider's discovery of a new particle with Higgs boson properties. Phys. Usp. **55**(10), 949–957 (2012)
193. Rubio, B., Nilsson, T.: NuSTAR. Nucl. Phys. News **16**(1), 9–14 (2006)
194. Rudolph, D., Hoischen, R., Hellström, M., et al.: Isospin symmetry and proton decay: identification of the 10^+ isomer in ^{54}Ni. Phys. Rev. C **78**, 021301 (2008)
195. Russel, W.B., Saville, D.A., Schowalter, W.R.: Colloidal Dispersions. Cambridge University Press, Cambridge (1989)
196. Schäfer, T.: Ratio of shear viscosity to entropy density for trapped fermions in the unitarity limit. Phys. Rev. A **76**, 063618 (2007)
197. Scheidenberger, C., Geissel, H.: Penetration of relativistic heavy ions through matter. Nucl. Instrum. Methods Phys. Res. B **135**(1–4), 25–34 (1998)
198. Scheidenberger, C., Geissel, H., Maier, M., et al.: Energy and range focusing of in-flight separated exotic nuclei — a study for the energy-buncher stage of the low-energy branch of the Super-FRS. Nucl. Instrum. Methods Phys. Res. B **204**, 119–123 (2003)
199. Schiwietz, G., Grande, P., Skogvall, B., et al.: Influence of nuclear track potentials in insulators on the emission of target Auger electrons. Phys. Rev. Lett. **69**, 628–631 (1992)
200. Schuch, R., Stöhlker, T. (for the SPARC-Collab.): Stored particle atomic physics research collaboration: atomic physics with stored highly-charged heavy ions at the future fair facility. http://www-linux.gsi.de/~sparc/documents/pdf_files/sparc_stori05.pdf
Schuch, R., Stöhlker, T.: Stored Particle Atomic Physics Research Collaboration: Atomic Physics with Stored Highly-Charged Heavy Ions at the Future FAIR Facility
201. Schwarz, S., Bollen, G., Lawton, D., et al.: The low-energy-beam and ion-trap facility at NSCL/MSU. Nucl. Instrum. Methods Phys. Res. B **204**, 507–511 (2003)
202. Schwinger, J.: On gauge invariance and vacuum polarization. Phys. Rev. **82**, 664–679 (1951)
203. Senger, P.: Status of the CBM experiment at FAIR. CBM Progress Report, p. 1 (2009)
204. Sharkov, B.Y. (ed.): Yadernyi sintez s inertsionnym uderzhaniem (Inertial Confinement Nuclear Fusion). Fizmatlit, Moscow (2005)
205. Shuryak, E.V.: Quark-gluon plasma and hadronic production of leptons, photons and psions. Phys. Lett. B **78**(1), 150–153 (1978)
206. Shuryak, E.V.: Quantum chromodynamics and the theory of superdense matter. Phys. Rep. **61**(2), 71–158 (1980)
207. Shuryak, E.: Physics of strongly coupled quark–gluon plasma. Prog. Part. Nucl. Phys. **62**(1), 48–101 (2009)
208. Sissakian, A., Sorin, A.S.: The QCD Phase Diagram NICA, JINR Communication. JINR, Dubna (2009)
209. Sissakian, A.N., Sorin, A.S.: The nuclotron-based ion collider facility (NICA) at JINR: new prospects for heavy ion collisions and spin physics. J. Phys. G: Nucl. Part. Phys. **36**(6), 064069 (2009)
210. Sissakian, A.N., Sorin, A.S., Suleymanov, M.K., et al.: Towards searching for a mixed phase of strongly interacting QCD matter at the JINR nuclotron. arXiv:nucl-ex/0601034 (2006)

211. Sissakian, A.N., Sorin, A.S., Toneev, V.D.: QCDMatter: A Search for aMixed Quark-Hadron Phase. arXiv:nucl-th/0608032 (2006)
212. Sissakian, A.N., Sorin, A.S., Suleymanov, M.K., et al.: Properties of strongly interacting matter and the search for a mixed phase at the JINR nuclotron. Phys. Part. Nucl. Lett. **5**(1), 8–17 (2008)
213. Sissakian, A., et al.: The MultiPurpose Detector – MPD To Study Heavy Ion Collisions at NICA. Conceptual Design Report. JINR, Dubna (2009)
214. Sokolowski-Tinten, K., Bialkowski, J., Cavalleri, A., et al.: Transient states of matter during short pulse laser ablation. Phys. Rev. Lett. **81**, 224–227 (1998)
215. Sorensen, P.R.: Kaon and lambda production at intermediate P_T: insights into the hadronization of the bulk partonic matter created in Au+Au Collisions at RHIC. Ph.D. thesis (2003)
216. Spieles, C., Stöcker, H., Greiner, C.: Phase transition of a finite quark-gluon plasma. Phys. Rev. C **57**, 908–915 (1998)
217. Spielman, R.B., Deeney, C., Chandler, G.A., et al.: Tungsten wire-array Z-pinch experiments at 200 TW and 2 MJ. Phys. Plasmas **5**(5), 2105–2111 (1998)
218. Stammler, T., Gmelin, E., Greubel, K., et al.: Pressure cell and combined cryostat/furnace for high-pressure μsr studies. Hyperfine Interact. **106**, 307–311 (1997). doi:10.1023/A:1012635101482
219. Steinberg, M.S.: Viscosity of the electron gas in metals. Phys. Rev. **109**, 1486–1492 (1958)
220. Steinheimer, J., Dexheimer, V., Bleicher, M., et al.: Hydrodynamics with a chiral hadronic equation of state including quark degrees of freedom. Phys. Rev. C **81**, 044913 (2010)
221. Stocker, H., Hofmann, J., Maruhn, J., Greiner, W.: Shock waves in nuclear matter - proof by circumstantial evidence. Prog. Part. Nucl. Phys. **4**, 133–195 (1980)
222. Stöhlker, T., Backe, H., Beyer, H., et al.: Status and perspectives of atomic physics research at GSI: the new GSI accelerator project. Nucl. Instrum. Methods Phys. Res. B **205**, 156–161 (2003)
223. Strikhanov, M.N.: Problems of the standard model and the status of the accelerator experiment. Herald Russ. Acad. Sci. **83**(3), 194 (2012)
224. Sturm, C., Sharkov, B., Stöcker, H.: 1, 2, 3 ... FAIR ! Nucl. Phys. A **834**(1–4), 682c–687c (2010)
225. Sun, B., Knöbel, R., Litvinov, Y.A., et al.: Large-scale mass measurements of short-lived nuclides with the isochronous mass spectrometry at GSI. Int. J. Mod. Phys. E **18**, 346–351 (2009)
226. Tahir, N.A., Hoffmann, D.H.H., Kozyreva, A., et al.: Metallization of hydrogen using heavy-ion-beam implosion of multilayered cylindrical targets. Phys. Rev. E **63**, 016402 (2000)
227. Tahir, N., Kozyreva, A., Hoffmann, D., et al.: Metallization of hydrogen using heavy ion imploded multi-layered cylindrical targets. Contrib. Plasma Phys. **41**(2–3), 287–290 (2001)
228. Tahir, N., Deutsch, C., Fortov, V., et al.: Intense heavy ion beams as a tool to induce high-energy-density states in matter. Contrib. Plasma Phys. **43**(5–6), 373–376 (2003)
229. Tahir, N.A., Deutsch, C., Fortov, V.E., et al.: Proposal for the study of thermophysical properties of high-energy-density matter using current and future heavy-ion accelerator facilities at GSI Darmstadt. Phys. Rev. Lett. **95**(3), 035001 (2005)
230. Tahir, N.A., Deutsch, C., Fortov, V.E., et al.: Studies of strongly coupled plasmas using intense heavy ion beams at the future FAIR facility: the HEDgeHOB collaboration. Contrib. Plasma Phys. **45**(3–4), 229–235 (2005)
231. Tanihata, I., Hamagaki, H., Hashimoto, O., et al.: Measurements of interaction cross sections and nuclear radii in the light *p*-shell region. Phys. Rev. Lett. **55**, 2676–2679 (1985)
232. Thoma, M.H., Morfill, G.E.: Ratio of viscosity to entropy density in a strongly coupled one-component plasma. Europhys. Lett. **82**(6), 65001 (2008)
233. Thomas, J.E.: The nearly perfect fermi gas. Phys. Today **63**(5), 34–37 (2010)
234. Tomaselli, M., Kuhl, T., Ursescu, D., Fritzsche, S.: Correlation effects on the charge radii of exotic nuclei. Hyperfine Interact. **171**, 243–253 (2006). doi:10.1007/s10751-006-9484-1
235. Troitskii, S.V.: Unsolved problems in particle physics. Phys. Usp. **55**(1), 72–95 (2012)

236. Trostell, B.: Vacuum injection of hydrogen micro-sphere beams. Nucl. Instrum. Methods Phys. Res. A **362**(1), 41–52 (1995)
237. Turlapov, A., Kinast, J., Clancy, B., et al.: Is a gas of strongly interacting atomic fermions a nearly perfect fluid? J. Low Temp. Phys. **150**, 567–576 (2008). doi:10.1007/s10909-007-9589-1
238. Udayanandan, K.M., Sethumadhavan, P., Bannur, V.M.: Equation of state of a quark-gluon plasma using the Cornell potential. Phys. Rev. C **76**, 044908 (2007)
239. Van der Meer, S.: Stochastic damping of betatron oscillations in the ISR. CERN-ISR-PO-72-31. Tech. Rep. (1972)
240. Vaulina, O.S., Petrov, O.F., Fortov, V.E., et al.: Pylevaya Plasma (Eksperiment i Teoriya) (Dust Plasma (Experiment and Theory). Fizmatlit, Moscow (2009)
241. Vignale, G., Ullrich, C.A., Conti, S.: Time-dependent density functional theory beyond the adiabatic local density approximation. Phys. Rev. Lett. **79**, 4878–4881 (1997)
242. Vitev, I., Gyulassy, M.: High - P_T tomography of d+Au and Au+Au at SPS, RHIC, and LHC. Phys. Rev. Lett. **89**(25), 252301 (2002)
243. Voloshin, S.A.: Probe for the strong parity violation effects at RHIC with three particle correlations. Indian J. Phys. **85**(7), 1103–1107 (2011)
244. Walz, J., Hansch, T.W.: A proposal to measure antimatter gravity using ultracold antihydrogen atoms. Gen. Relativ. Gravit. **36**, 561–570 (2004)
245. Wang, X.N., Gyulassy, M.: Gluon shadowing and jet quenching in A+A collisions at $\sqrt{s}$ = 200A GeV. Phys. Rev. Lett. **68**(10), 1480–1483 (1992)
246. Wang, P., Thomas, A.W., Williams, A.G.: Phase transition from hadronic matter to quark matter. Phys. Rev. C **75**, 045202 (2007)
247. Weinberg, S.: Entropy generation and the survival of protogalaxies in an expanding universe. Astrophys. J. **168**, 175 (1971)
248. Welsch, C., Grieser, M., Ullrich, J., Wolf, A.: FLAIR Project at GSI. In: International Workshop on Beam Cooling and Related Topics, COOL05, Galena, IL (2005)
249. Weyrather, W.K., Ritter, S., Scholz, M., Kraft, G.: RBE for carbon track-segment irradiation in cell lines of differing repair capacity. Int. J. Radiat. Biol. **75**(11), 1357–1364 (1999)
250. Widmann, E.: Testing CPT with antiprotonic helium and antihydrogen — the ASACUSA experiment at CERN-AD. Nucl. Phys. A **752**, 87–96 (2005)
251. Wilczek, F.: Qcd made simple. Phys. Today **53**(8), 22–28 (2000)
252. Xiao, G., Schiwietz, G., Grande, P.L., et al.: Indications of nuclear-track-guided electrons induced by fast heavy ions in insulators. Phys. Rev. Lett. **79**, 1821–1824 (1997)
253. Yamazaki, T., Hayano, R., Itahashi, K., et al.: Discovery of deeply bound π^- states in the ^{208}Pb(d,^{3}He) reaction. Z. Phys. A Hadrons Nucl. **355**, 219–221 (1996). doi:10.1007/s002180050101
254. York, R.C.: Rare isotope accelerator (ria) project. Physica C: Supercond. **441**(1–2), 31–37 (2006)
255. Zel'dovich, Y.B., Raizer, Y.P.: Fizika udarnykh voln i vysokotemperaturnykh gidrodinamicheskikh yavlenii, 2nd edn. Nauka, Moscow (1966) [English Transl.: Physics of Shock Waves and High-Temperature Hydrodynamic Phenomena. Dover, Mineola, NY (2002)]
256. Zwanziger, D.: Equation of state of gluon plasma from a fundamental modular region. Phys. Rev. Lett. **94**, 182301 (2005)

Chapter 7
Technical Applications of the Physics of High Energy Densities

7.1 Magnetic Confinement Fusion

Among the numerous technical applications of high energy density physics, controlled thermonuclear fusion is of greatest significance. It relies on the implementation of thermonuclear fusion, which is the source energy for our Sun and other stars and is the basis of life or the cause of death to every living thing.

The discovery of nuclear energy was one of the most outstanding intellectual achievements of mankind. The grandiose scale and significance of thermonuclear fusion reactions in the evolution of the Universe and its role as a stellar energy source was ascertained even in the first third of the twentieth century. In the middle of the twentieth century, people managed to reproduce on the Earth the conditions with record-high energy density required for quasi-controlled fusion by making the most destructive weapon—a thermonuclear bomb. Not only did this outstanding scientific achievement determine the natural-science character of contemporary civilization, but it also determined (as the makers of nuclear weapons had expected) the development of contemporary history and society for decades, making global military conflicts on the Earth impossible. Today, scientists-engineers are mounting unprecedented effort to implement the thermonuclear fusion reactions under controllable conditions, which would provide humanity with an unlimited and ecologically pure energy source and solve forever the energy problem on the Earth.

Taken separately, almost all parameters required for the ITER have been achieved on the existing facilities (Table 7.1).

The history of controlled fusion is impressive and dramatic; it is full of hopes and disappointment, bright breakthroughs and failures. In his concluding speech to the 1961 Conference in Salzburg concerned with achievements in plasma theory, M.N. Rosenbluth said: "Let me close by saying that while it is unfortunately true that theorists have not told the experimentalists how to build a thermonuclear machine, it is also true that we have been looking hard for very many years for a fundamental reason why a plasma fusion reactor should be impossible and we have not found any

© Springer International Publishing Switzerland 2016

V.E. Fortov, *Extreme States of Matter*, Springer Series in Materials Science 216,
DOI 10.1007/978-3-319-18953-6_7

Table 7.1 Parameters attained in tokamaks and the ITER project

Parameters	Current level	Requirements on ITER
Temperature (keV)	50 (TFTR)	15
Density (10^{20} m^{-2})	15 (Alcator-C mode)	1
Lifetime (s)	1 (JET)*	3
Minor radius (m)	1.1 (JET)*	2
Major radius (m)	3 (JET)*	6
Discharge duration (s)	360 (Tore Supra)	400
Heating power (MW)	50 (TFTR)	70
Fusion power (MW)	16 (JET)*	500
Burn duration (s)	10 (JET)*	400

The asterisk indicates those parameters in which lag will be eliminated after the construction of ITER tokamak

such reason." Next he added: "... I believe the chances are very good that in twenty years or so mankind will have solved the problem of controlled fusion if only he has not lost in the meantime the far more difficult struggle against uncontrolled fusion".

Now, 60 years after the commencement of controlled nuclear fusion research we may conclude that the complexity of the problem was strongly underestimated in the initial stage of the work, especially so when it is considered that the final objective, namely the demonstration of electric power production by a thermonuclear power plant, is still several decades away [21].

In Sect. 3.1 we discussed the types of exothermal nuclear reactions and their required physical conditions with extremely high energy densities. Applied for their practical realization are two thermal insulation methods for hot plasma confinement—magnetic and inductive. In the former, which has been given priority, the plasma with thermonuclear parameters—a temperature of $\approx 10^8$ K and a density of 10^{19}–10^{20} m^{-3}—is confined by magnetic fields of induction 4–8 T in a continuous or quasicontinuous mode. This line has received the name magnetic confinement. Its leader is a toroidal tokamak facility, which was developed in the I.V. Kurchatov Institute of Atomic Energy in the 1950s–1960s of the past century and which underlies the International Thermonuclear Experimental Reactor (ITER) constructed jointly by seven countries in France [4]. The project was formulated with the inclusion of a vast base of experimental data (Fig. 7.1) and simulation results obtained with model codes that took into account the main processes in a tokamak.

The reader may familiarize himself with the works on plasma heating and its magnetic confinement from review [21]. Here, we mention only several results. The most impressive events consisted in the release of substantial thermonuclear power in deuterium-tritium plasma experiments on the TFTR (11 MW, 1994) and JET (16 MW, 1997) tokamaks (Fig. 7.2) [21]. The highest value of $Q = P_{\text{fus}}/P_{\text{aux}}$ attained on the JET facility was ≈ 0.65. These results were recorded in the regimes with hot ions, $T_{\text{i}} \gg T_{\text{e}}$, which are not typical for the reactor. In the reactor-like

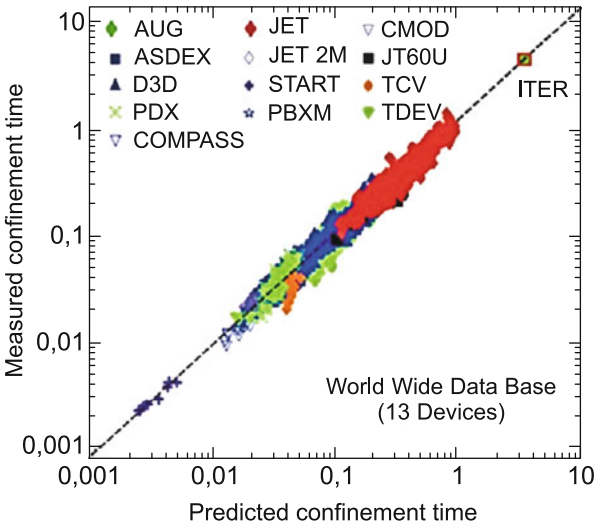

Fig. 7.1 Comparison of experimental confinement times and ITER scaling (H98(y,2))

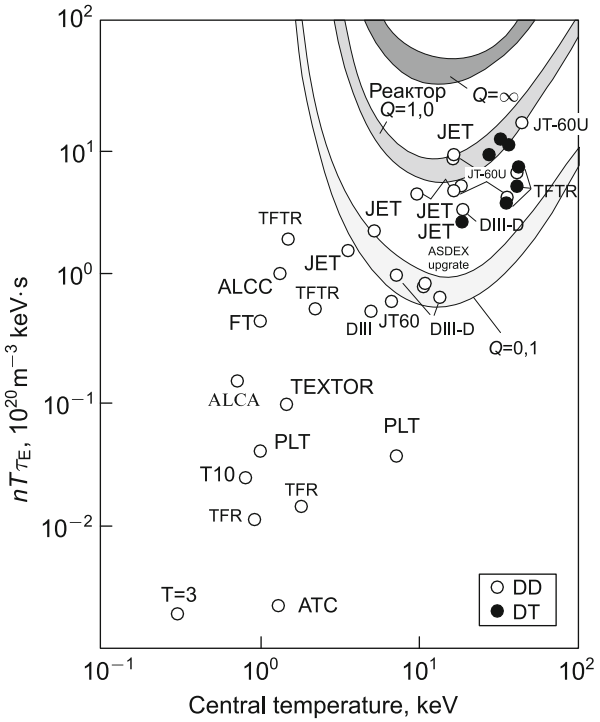

Fig. 7.2 Experimental $nT\tau_E$ value as a function of central ion temperature. Marked off are the zones with the values of $Q \equiv P_{fus}/P_{aux} = 0.1$, 1.0, and ∞ [21]

H-mode at the JET facility with $T_i \approx T_e$, a thermonuclear power $P_{fus} = 3$–5 MW was obtained in a long ($\approx$5 s) pulse. Similar results were achieved on the JT-60U facility in deuterium discharges: the equivalent value of Q_{eqv} calculated for a DT

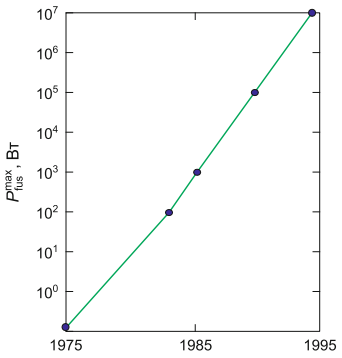

Fig. 7.3 Growth dynamics of fusion power generated in different experimental facilities over a period of 20 years (1975–1995)

plasma amounted to ≅1.25 in a short pulse for $T_i \gg T_e$, and to ≅0.5 in the quasistationary mode [21].

Figure 7.2 depicts the values of a factor $M = n_i(0)T_i(0)\tau_E$ as a function of $T_i(0)$, which were obtained in experiments on several tokamaks [21]. The shaded domains of M values in Fig. 7.2 correspond to the calculated values $Q = 0.1$, 1.0, and ∞ for a DT plasma. When the JET and TFTR data with $T_i \gg T_e$ are excluded in accordance with the aforesaid, and it is considered that the DT reaction ignition mode at $T_i(0) \approx 30$ keV calls for a value of $M \approx 100$, one can see from this figure that the distance (in units of ΔM) from the modes with the best quasistationary discharges at the JET and JT-60U facilities to the mode with DT reaction ignition amounts to 20–30 [21].

Figure 7.3 exhibits the maximal thermonuclear power measured in DT discharges, or the equivalent power calculated from the DD plasma parameters in different tokamaks, P_{fus}^{max}, as a function of calendar date between 1975 and 1995 [21]. One can see that P_{fus}^{max} rose by a factor of 10^8 over the 20-year period. This was achieved by constructing new, larger facilities and equipping them with higher-power additional heating. On obtaining the record-high power pulses at the JET and JT-60U facilities, no further increase occurred in P_{fus}^{max}. The new superconducting facilities constructed during the last decade, which are smaller in size than JET and JT-60U, are intended for the realization and investigation of stationary discharges rather than the attainment of high P_{fus}^{max} values. The further increase in P_{fus}^{max} (by a factor of 30–50 in comparison with the values attained in JET and TFTR) should occur when ITER reaches its design objectives, i.e. about 2027.

The plasma configuration and the general setup are schematized in Figs. 7.4 and 7.5.

To compensate for the effect of charge separation owing to the differently directed toroidal drifts of electrons and ions, which leads to a radial ejection of a plasma column onto the wall, a toroidal current is excited in the plasma. As a result, the combined magnetic lines of force of the external magnetic field and the field of the in-plasma current spiral about the toroid axis, and a free charge flow along the lines of force removes the charge separation. Therefore, the tokamak plasma may exist only in the presence of current in it. In the simplest case, the excitation

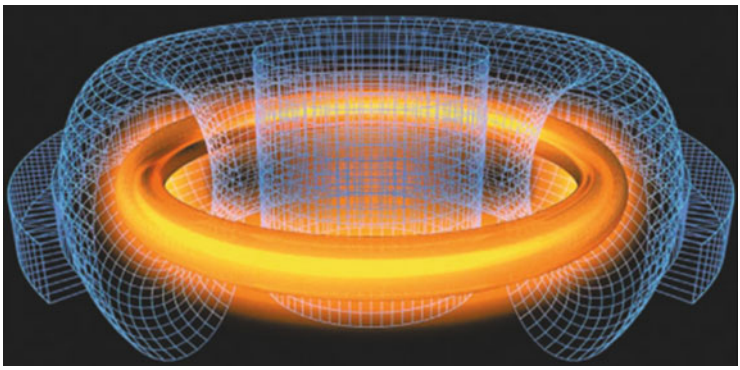

Fig. 7.4 Plasma position in a tokamak [69]

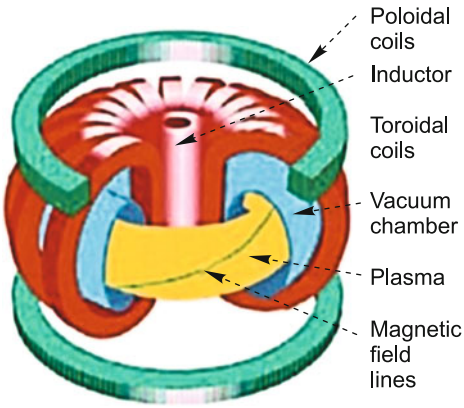

Fig. 7.5 Conceptual sketch of a tokamak [69]

of current is effected by the induction electric field of the central solenoid. That is why early in its development the tokamak was considered as a pulsed system, whose lifetime was determined by the buildup time of the magnetic flux of the central solenoid. Subsequently, however, the possibility of noninductive in-plasma current generation was found. There are two reasons. One of them is related to the entrainment of electrons in the excitation of high-frequency waves in the plasma and in the injection of a beam of neutrals; the other is related to the special feature of electron paths in the presence of pressure gradient in the plasma, which produce the so-called bootstrap current. According to modern views and several experimental observations, it is possible to sustain a stationary current in a tokamak, which permits counting on future reactor tokamaks. The poloidal magnetic field of external coils interacts with the current of the plasma column and prevents it from being ejected along the major torus radius. The magnetic field lines spiral about the toroid axis and make up a system of embedded magnetic surfaces (Fig. 7.6).

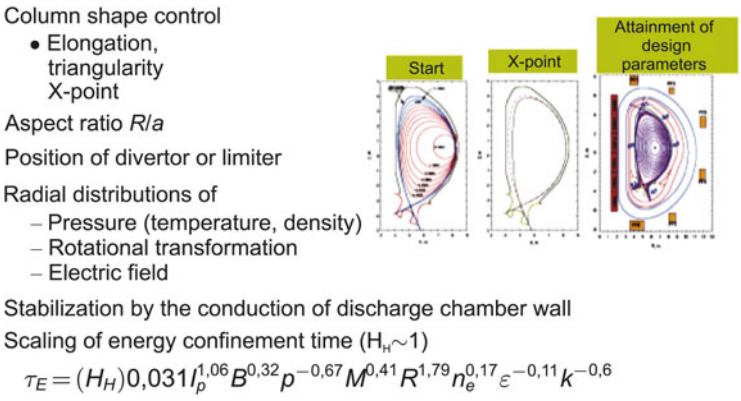

Fig. 7.6 Main physical parameters of a tokamak

Among them, the surfaces on which a line closes to itself after several revolutions possess special properties. Such surfaces are termed rational. The plasma behavior in the vicinity of rational surfaces exhibits several special features. There is a boundary surface termed separatrix beyond which there are no magnetic surfaces. The magnetic lines of force outside of the separatrix go beyond the torus and close on the chamber walls. By selecting the magnitude of poloidal coil currents the open magnetic lines of force near the separatrix may be brought to one domain termed a divertor. The divertor is intended for removing the reaction products and impurities that find their way into the plasma. The plasma flowing out along these lines, which contains impurities and the fusion reaction products—alpha particles—is neutralized at the divertor plates, while the gas is evacuated from the volume. The tokamak plasma is vulnerable to numerous magnetohydrodynamic and kinetic instabilities. The development of some of MHD instabilities leads to magnetic field line reconnection inside of the plasma (the so-called internal disruptions) and the formation of islands with intrinsic closed magnetic surfaces, which increases the particle and energy loss from the tokamak. In the most dangerous case, a disruption instability develops, which leads to the ejection of a plasma column to the chamber wall and discharge termination. In the case of disruption the first reactor wall experiences a high load of electrodynamic nature and thermal damage by plasma fluxes and electron beams, which accompany the disruption development. Disruptions must be ruled out in reactor modes; at least, admissible in the conceptual designs of industrial thermonuclear stations is no more than one disruption per year. That is why methods for the prediction and prevention of disruptions are developed, as are the methods for the mitigation of their consequences by injecting large masses of strongly radiating substance into the plasma. The task of controlling the plasma maintenance mode involves selection of the radial distributions of the current and pressure in the plasma column, whereby a stable configuration is realized. The discharge mode of a tokamak is controlled by external actions on the plasma exerted by additional heating and current drive sources.

Modern techniques of additional plasma heating and current generation in tokamaks of reactor size are based on the simultaneous action of neutral atomic beams and high-frequency wave excitation. Injectors of the beams of neutral particles with an energy of the order of 1 MeV have a beam power of tens of MW. On entering the plasma, the neutrals are ionized and captured to heat the plasma and excite a current. The making of such stationary operating injectors is a intricate engineering-physical problem. Another approach to heating and current generation relies on plasma wave generation by external antennas. In magnetized plasma there are many wave types and several characteristic resonance frequencies: the harmonics of electron and ion cyclotron frequencies, resonances on the upper and lower hybrid frequencies. The frequencies lie in a range from tens of megahertz to hundreds of gigahertz. The power level required for a reactor amounts to tens of megawatts, like for neutral beam injectors. However, for HF techniques of additional heating the task of making generators of such power is simpler to solve, because there exist high-power generator lamps developed for accelerators and radio communication. An exception is provided only by generators with frequencies above 100 GHz for plasma heating at the electron cyclotron resonance. Gyrotrons with a power of about a megawatt and a pulse duration longer than 1000 s have recently been made and described (ITER project). The plasma–wave interaction physics is rich in diverse linear and nonlinear effects of oscillation transformation types, refraction and collisionless absorption effects. Today it cannot be considered as being fully investigated. However, the future reactors will not be able to do without beam and high-frequency power sources for tokamak heating and, in some cases, stabilizing instabilities.

The most important problem of the future reactor tokamak is to ensure efficient thermal plasma insulation, which is characterized by the energy confinement time determined loss–heating power balance. A contribution to the tokamak energy loss is made by diffusion processes and the nonlocal transfer related to MHD-mode development. At present, so complex and multicomponent a system as a tokamak is impossible to simulate from first principles. And so, proceeding from many thousands of experiments, scalings were obtained to predict the confinement time, which contain the dependence of the confinement time on the numerous tokamak parameters. The scaling employed in the ITER project is shown in Fig. 7.1. One can see that the confinement time of the first experimental reactor tokamak should exceed the presently achieved level by a factor of three.

The tokamak plasma energy loss is primarily determined by electron and ion plasma transport. The radiative loss makes an insignificant contribution to the energy balance of a tokamak, because the effective ion charge is not higher than 2 for a small amount of heavy impurities coming from the chamber wall to the plasma. For the deuterium–tritium fuel cycle the radiation of electrons at the cyclotron frequencies may be neglected. The particle energy loss is determined by turbulent mechanisms and the characteristics of particle trajectories in the toroidal magnetic field in the neoclassical approximation. Observed in tokamaks was the formation of transport barriers, in which the heat transfer coefficients exhibit a sharp decrease and attain classical values. A possible cause of barriers formation is the velocity gradient

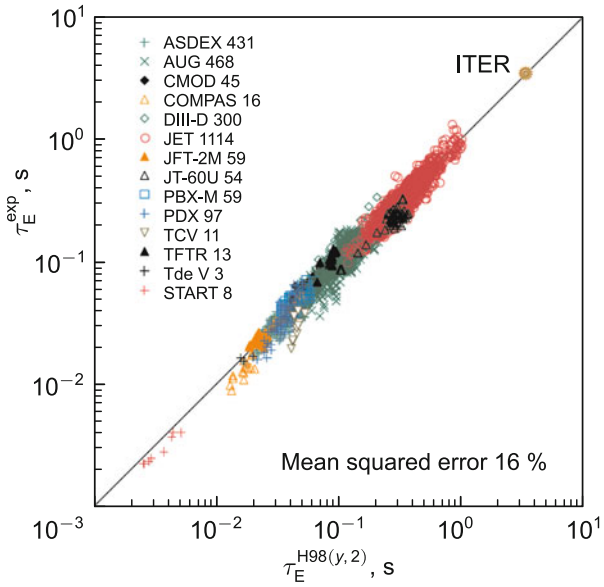

Fig. 7.7 Comparison of the thermal plasma energy confinement time τ_E^{exp} in the H-mode for 14 tokamaks indicated in the drawing with empirical scaling $\tau_E^{H98(y,2)}$ [21]

of azimuthal plasma rotation about the torus axis, which suppresses the development of local instabilities. Of special importance for the reactor mode is the transport barrier which emerges at the plasma boundary. The mode with a transport barrier at the plasma boundary is referred to as the H-mode. It is characterized by a strong temperature gradient at the plasma boundary and an improved energy confinement. The scaling depicted in Fig. 7.7 corresponds to the H-mode. A transition to the H-mode occurs when the power of additional heating exceeds some threshold value, for which scalings have also been obtained. Also known are modes with internal-barrier formation. Internal barriers are expected to significantly increase the fusion reaction intensity and the reactor power. The attractiveness of the H-mode is clouded by the development of localized mode instabilities at the plasma boundary. The periodically emerging plasma ejections to the surface of the first wall of the tokamak chamber result in a pulsed damage and the inflow of impurities to the discharge plasma. As a result, damages of the first wall and receiving divertor plates will limit the reactor service life.

At the stage of development of the methods for combatting localized mode instability, in the course of ITER construction the main line of the quest is an increase in plasma ejection frequency and the consequential lowering of the energy of a pulsed ejection. Considered among the ways of controlling the instability development is the chaotization of magnetic lines of force near the boundary by high-frequency fields, the periodic injection of tiny solid granules, and other measures. Even at the construction stage of the first experimental reactor it became evident that the future of reactor tokamaks depends on the solution of the problem

of the first wall of reactor chamber. The first wall is within a few centimeters from the plasma surface. That is why the ejection of wall material has a strong effect on the plasma composition, although in some modes the transport of impurities to the plasma center, which leads to its radiative cooling, is limited. For a wall material it is therefore reasonable to select low-Z materials like carbon or beryllium. Their drawback is a low resistance to pulsed plasma energy ejections. An alternative is a tungsten wall, but the issue of tungsten ion penetration to the plasma center has not been adequately studied. It has been suggested to cover the walls with a layer of liquid lithium. The results obtained on small tokamaks give grounds for optimism, but the engineering and physical aspects of the applicability of a lithium wall coating of a reactor tokamak have not been studied. A serious disadvantage of lithium coatings is that the admissible wall temperature is limited to the lithium vaporization temperature (1350 °C), which lowers the thermodynamic reactor efficiency.

Another operating-capacity problem of an energy reactor tokamak is the formation of dust from the products of wall erosion. Although the dust density in the surface plasma layer is not high, of the order of $10^{-5}\,\mathrm{cm}^{-3}$, and it has no direct effect on the plasma dynamics, the hazard of dust formations consists in the capture of tritium and its emission when the chamber is opened. According to estimates, in the reactor operation the amount of deposited tritium promptly reaches its limiting value. So far the techniques of deposited tritium removal are still in the development stage.

The problems of making a thermonuclear reactor tokamak mentioned above are only a part of the major problem of changing over to thermonuclear power engineering. A start-up of the experimental ITER reactor will be a decisive step. The ITER project (Table 7.2) is designed to produce a DT plasma with $P_{\mathrm{fus}} = 400$–$500\,\mathrm{MW}$ and $Q \geq 10$ in the induction mode with a pulse duration of about 500 s. The feasibility of achieving the "controllable DT-plasma burn", i.e. the modes with $Q > 30$, should also be investigated. It is supposed that the ITER will be the last physical facility, at which it will be possible to demonstrate the tokamak plasma confinement modes for an intense fusion reaction (thermonuclear plasma burn). It is expected that the emergence of a significant alpha-particle population in the tokamak plasma will give rise to the build-up of new instabilities, so-called Alfven modes, because of the nonequilibrium character of the ion distribution function. It will be necessary to study the effect of these instabilities, in particular, on the plasma and alpha-particle confinement. An enhanced loss of the alpha-particles, which heat the plasma, will not permit lowering the power of additional heating sources in the stationary mode of reactor operation. The existing theories do not predict a catastrophic effect of the Alfven modes on the plasma stability and alpha-particle loss. However, an experimental confirmation will be required. Therefore, the main physical task of the ITER is to study the physics of thermonuclear plasma burning in a reactor tokamak.

Another ITER mission is to demonstrate the operating capacity of the crucial technologies of a tokamak thermonuclear reactor: control over the mode of operation and over additional heating and instability suppression, tritium handling, superconducting magnetic system operation.

Table 7.2 Comparison of ITER design parameters and one of DEMO versions (Stationary mode ($\geq 10^6$ s)) [21]

Parameter	ITER		DEMO
	Inductive mode	Stationary mode	
Plasma current I (MA)	15	9	15
Magnetic field on plasma axis B_t (T)	5.3	5.18	6.8
Maximum field on superconductor B_{max} (T)	11.8	11.8	14.6
Minor plasma radius a (m) Major plasma radius R (m) Ion temperature on plasma axis $T_{i(0)}$ (keV)	2 6.2 2.3	1.85 6.35 25	2.1 6.5 45
MHD stability margin q_{95} at radius $r = 0.95a$ Ratio of $\langle n_e \rangle$ to Greenwald limit, $\langle n_e \rangle / n_G$	3.0 0.85	5.3 0.75	5.3 1.0
Confinement improvement factor $H_{H98(y,2)}$	1.0	1.4	1.3
$\beta_N = \beta(100aB/I)$	1.8	3.0	3.9
Bootstrap current fraction f_{BS}	0.15	0.5	0.79
Noninductive current fraction f_{NI}	0.21	1	1
Fusion power P_{fus} (MW)	400	350	3000
Plasma heating power $P_{heat} = P_\alpha + P_{aux}$ (MW)	120	140	654
Thermal plasma energy W_{th} (MJ)	320	290	1215
Fraction of radiative energy loss $f_{rad} = P_{rad}/P_{heat}$	0.5	0.57	0.86
$Q = P_{fus}/P_{aux}$	10	5	54
Disruption rate $f_{disruption}$	$\approx$0.1 (per pulse)	$\approx$0.1 (per pulse)	$\leq$1 (per year)

For a 400-s long pulse and an inductive plasma current drive the thermonuclear power is expected to be ten times higher than the power consumed by the tokamak. In the stationary mode of duration 3000 s, an attempt will be made to teach the gain $Q = 5$. Works on ITER construction are jointly performed by seven countries: Europe, India, China, Korea, Russia, USA, and Japan. Attaining modes with $Q = 10$ is planned for the late 1920s. Plans to change over to experimental-industrial reactor tokamaks are discussed in the project member countries. Today, the projects of demonstration reactors under discussion exceed or match the ITER in size. The electric power of an industrial reactor should be higher than 1 GW.

Apart from tokamaks, other facilities with magnetic confinement are also investigated in the world's laboratories. Most significant is a stellarator (Figs. 7.8 and 7.9), which offers several advantages over tokamaks. The main virtue of the stellarator is that the rotational transformation of magnetic lines of force is achieved by selecting magnetic field coils with a complex three-dimensional geometry. That is why there is no need to excite the current for confining the stellarator plasma and, hence, there are no MHD instabilities arising from the current flow. The stellarator is free from the most hazardous tokamak instability—the disruption instability. The physics and technology of stellarators has been less elaborated in comparison with

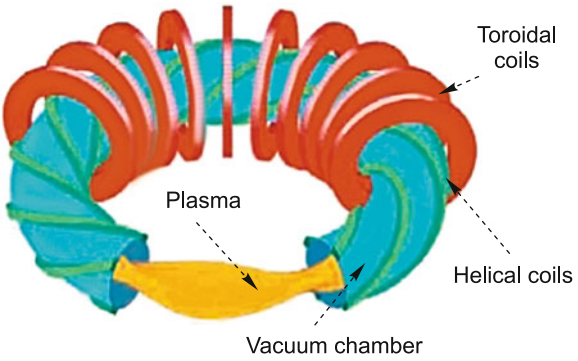

Fig. 7.8 Conceptual sketch of a stellarator [69]

Fig. 7.9 Wendelstein 7-X stellarator assembly in the Max Planck Institute of Plasma Physics, Germany [69]

tokamaks, while the structure of its magnetic system is highly complicated and is poorly suited for the accommodation of a blanket intended for absorbing the neutron flux. The stellarator divertor intended for removing alpha particles and impurities from the plasma is radically different from a tokamak divertor and is technically more sophisticated. The accommodation of the thermal insulator intended to protect the cryogenic superconducting magnetic system from the neutron flux is also a major problem. As a consequence, in conceptual projects of a reactor stellarator the major chamber radius is long, of the order of 15 m, and the output electric power amounts to several gigawatts, which is too high for an industrial power plant.

The parameters of a version of a demonstration thermonuclear power plant (DEMO) for $P_{\text{fus}} = 3\,\text{GW}$ are collected in Table 7.2, where they are compared with the ITER parameters in inductive and stationary modes. Another important task of the ITER is to carry out nuclear-technological tests required for designing the DEMO and producing tritium.

7.2 Laser Inertial Confinement Fusion

7.2.1 Direct-Drive Laser Fusion

Two lines of thermonuclear research are presently under development: controlled thermonuclear fusion with magnetic (Fig. 7.10) and inertial confinement. In the case of magnetic confinement the thermonuclear plasma heated to $T \approx 10\,\text{keV}$ is confined by magnetic fields under quasistationary conditions. The current status and prospects of this line are shown in Fig. 7.2.

Controlled thermonuclear fusion with inertial confinement relies on the feasibility of obtaining positive thermonuclear energy release in the form of microexplosions initiated by laser, X-ray, or heavy-ion radiation with an energy of several megajoules and duration of about 1 ns. This line of research is the most significant pragmatic motivation for research in high-energy-density physics [19, 43, 129, 153, 164, 189, 213]. To this end, the world's largest NIF laser facility (Livermore, USA) [162] was put in operation; its pulse energy amounted to 1.8 MJ in March 2012. Another megajoule laser facility, MJL (Bordeaux, France) [39] (Fig. 7.11) is being constructed. Different new schemes of high-current Z pinches [53, 222] are under investigation. Planned for the future, in the framework of the FAIR project [1], is the commissioning of a new-generation relativistic heavy-ion accelerator. These facilities will be used (along with the thermonuclear program) for simulating the physical processes in thermonuclear weapons and studying nuclear physics.

The temperature dependence of the thermonuclear reaction rates (Fig. 4.8) makes deuterium–tritium fusion the reaction of choice; a temperature of ≈2–10 keV

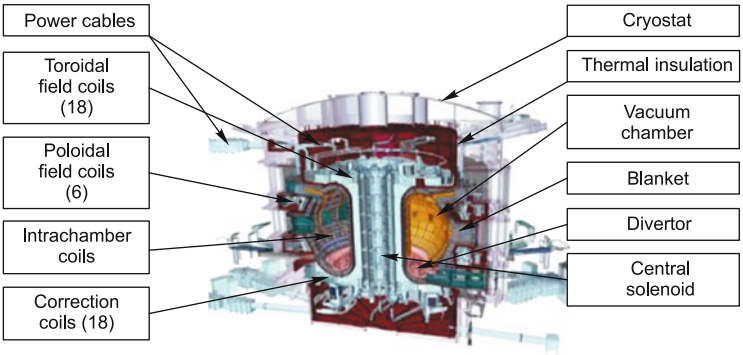

Fig. 7.10 Experimental thermonuclear ITER reactor

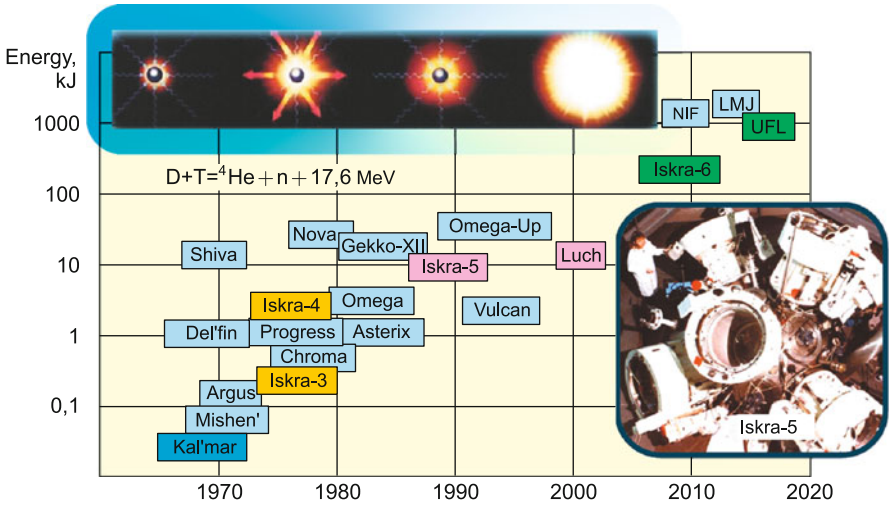

Fig. 7.11 Laser facilities for inertial confinement fusion

is required to make this reaction highly efficient. For a thermonuclear plasma expansion velocity of 10^8 cm/s, this leads to a characteristic time of $\approx 10^{-9}$ s in the case of a spherical target $\approx 10^{-1}$ cm in diameter. The energy balance condition for this thermonuclear reaction (the Lawson criterion [19, 129, 153, 164]) is of the form

$$n\tau \approx \rho r/4c_s m_i \approx 2 \times 10^{14}\ \text{s/cm}^3,$$

which corresponds to $\rho r \approx 0.1$–$3\ \text{g/cm}^2$ and requires the thermonuclear fuel to be compressed to densities of hundreds of grams per cubic centimeter. At a temperature of 10 keV this corresponds to tremendous pressures of 100–200 Gbar. In particular, to release a thermonuclear energy equivalent to 0.1 tons of trinitrotoluene or 500 MJ requires 3 mg of the deuterium–tritium fuel, which corresponds to a microtarget $\approx$ 300 μm in diameter. As a result of laser irradiation, the fuel density at the target center amounts to $90\ \text{g/cm}^3$ for a compression energy of 30 kJ and a pressure of 13.5 Gbar, which may be achieved for an implosion rate of 1.4×10^7 cm/s. These parameters may vary significantly, depending on the specific target design and the "driver" selected.

The attainment of so high a compression is hindered by the high plasma temperature, which is lowered by way of "soft" quasi-adiabatic compression. To achieve this requires a special profiling of the laser radiation, which has to build up in time by the end of compression [19, 29, 41, 104, 153, 164].

By and large, despite the relative simplicity of the initial idea and its practical realization in nuclear weapons 60 years ago, the technical problems encountered in the implementation of pulsed controlled thermonuclear fusion have turned out to be

extremely complicated. The main problem consists in the efficient delivery of long-wavelength laser radiation energy to the dense thermonuclear plasma. In particular, the 1-μm long-wavelength laser radiation is efficiently absorbed by the plasma with a critical density of $\approx 10^{21}$ cm^{-3}, which is more than one order of magnitude lower than the density of liquid hydrogen phase. This circumstance seriously hinders the direct laser heating of thermonuclear plasmas, making preferable the use of short-wavelength (X-ray) radiation. In addition, the thermonuclear reaction rate, which is proportional to n^2, will be low at low densities, requiring additional means for confinement.

Therefore, all schemes of pulsed thermonuclear fusion proposed to date involve compression of microtargets by irradiation of their external surface with intense directional energy fluxes (Figs. 7.12 and 7.13), which leads to the heating and expansion of the outer part of a target and gives rise to ablation pressure responsible for the compression of the target towards its center (Fig. 7.14). This approach is favored by the circumstance that the requisite irradiation energy decreases ($\sim 1/n^2$) with increasing compression. At the same time, the coefficient of energy transfer to the target is small in the ablation scheme and does not exceed 10 %, and the dynamic compression itself is hindered by the development of Rayleigh–Taylor instability, which disturbs the symmetry of compression and is responsible for the mixing of target layers. Furthermore, increasing the thermonuclear plasma density shortens the range of alpha particles, which "get stuck" in the dense target to form the thermonuclear burn wave traveling from the center of the microsphere to its periphery (Fig. 7.12).

At the instant of peak compression, at the target center there occurs a thermonuclear burn, which propagates from the target center to the periphery in the form

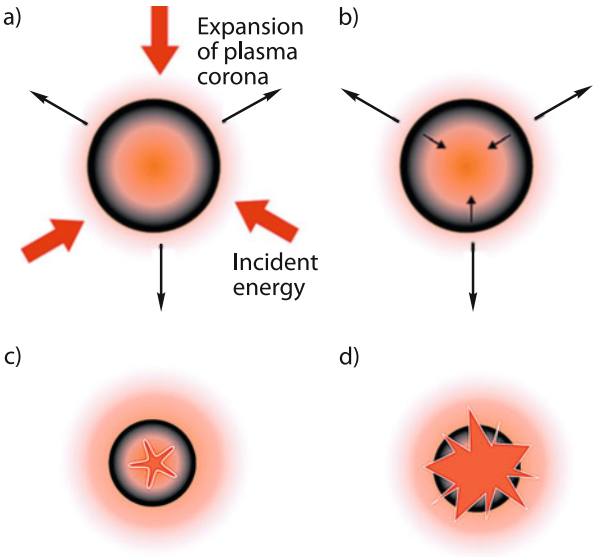

Fig. 7.12 Thermonuclear target operating scheme [129]. (**a**) Absorption. (**b**) Acceleration. (**c**) Compression. (**d**) Thermonuclear burn

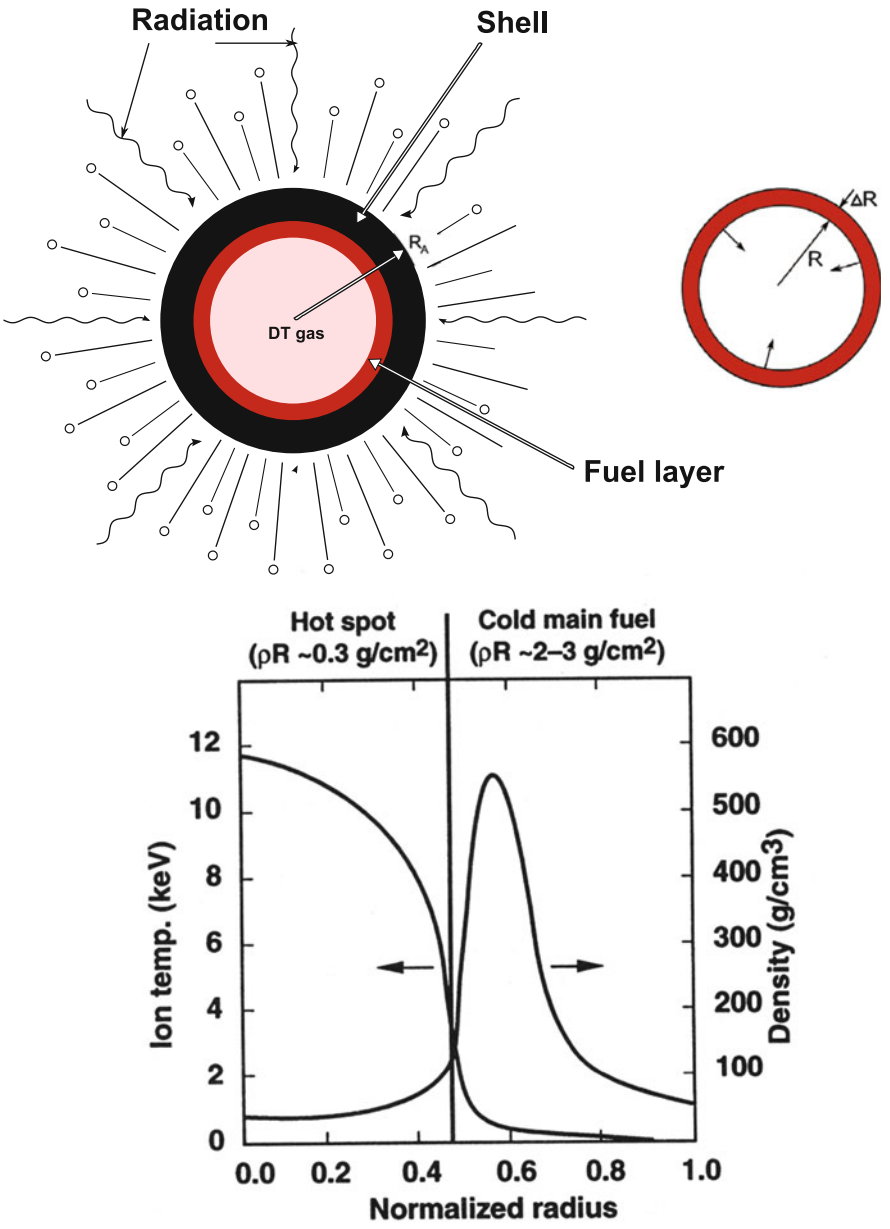

Fig. 7.13 Variation of parameters in a thermonuclear target [129]

of a wave (Fig. 7.12). The parameter distribution in such a target is depicted in Fig. 7.13. This scheme of controlled thermonuclear fusion with inertial confinement

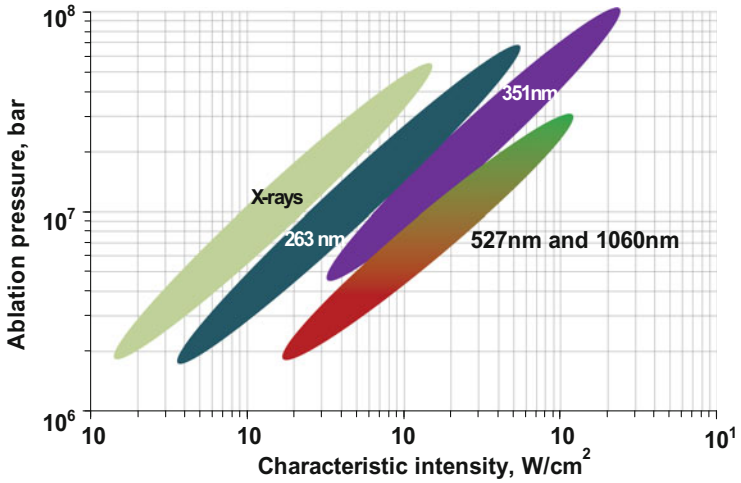

Fig. 7.14 Dependence of the ablation pressure on the intensity and wavelength of the electromagnetic radiation of a driver [129]

is referred to as direct-drive laser fusion, because the target is compressed and heated under ablation plasma pressure ($P \approx 100$ Mbar, $T \approx 10^6$ K) (Fig. 7.14) produced at its outer surface by focused laser radiation. A large number of direct-drive thermonuclear target designs have been put forward (Figs. 7.12 and 7.15), where the energy density is as high as 10^{16}–10^{17} J/cm^3, which is comparable with astrophysical conditions. The dependence of the ablation pressure on the intensity of electromagnetic radiation of different wavelengths is depicted in Fig. 7.14. One can see that the short-wavelength radiation is the radiation of choice in the production of high energy densities in controlled nuclear fusion (CNF) plasmas [19, 153, 164].

Several specific thermonuclear targets with their corresponding temporal irradiation intensity profiles are given in Fig. 7.15.

An important problem in the practical implementation of pulsed controlled thermonuclear fusion is, apart from the development of a high-power driver, the attainment of a high irradiation symmetry and accordingly the symmetry of dynamic plasma compression. To reduce the distortion effect of the Rayleigh–Taylor instability in the course of laser-driven compression, the so-called indirect-drive scheme [19, 43, 129, 153, 164] has been developed (Fig. 7.16), whereby the compression of the spherical target (Fig. 7.16b) is effected by the thermal soft X-rays from the side walls of a cylindrical capsule (Fig. 7.16) heated by laser radiation.

In the scheme (Fig. 7.16) and photograph (Figs. 7.17 and 7.18) of the thermonuclear NIF target, the spherical deuterium–tritium (DT) target (Fig. 7.16b) is accommodated in a gold cylinder irradiated from two sides by 192 laser beams. Upon incidence on the inner cylinder surface (Fig. 7.16a) (intensity of order 10^{15} W/cm^2) they vaporize it to produce high-intensity soft X-rays in the cylindrical cavity. These X-rays in turn cause highly symmetric spherical compression of the

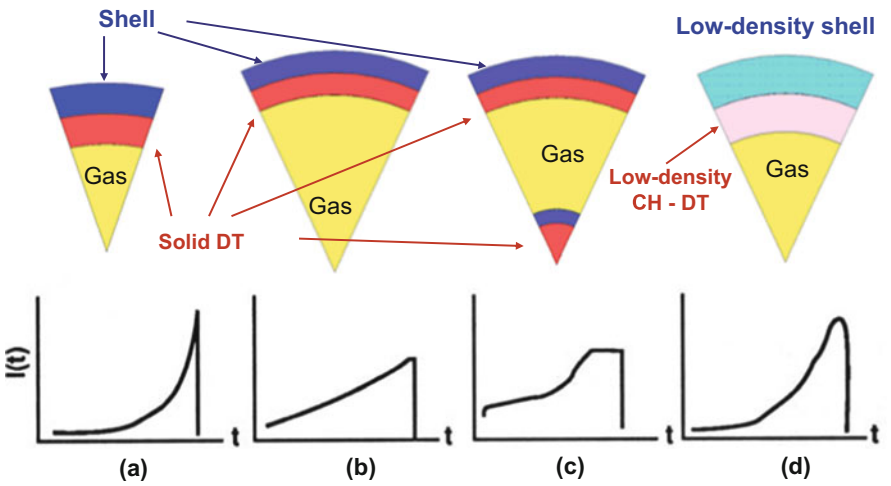

Fig. 7.15 Structures of the thermonuclear targets for the CNF with inertial plasma confinement and the corresponding temporal profiles of laser irradiation [129]

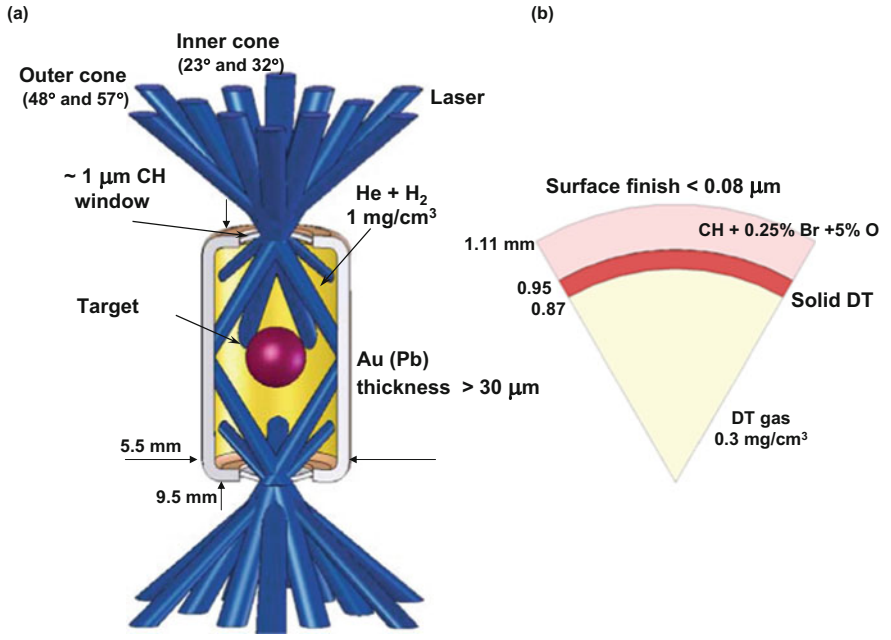

Fig. 7.16 Scheme of an indirect-drive thermonuclear target (**a**) for the NIF laser system and cross section (**b**) of the thermonuclear sphere inside the target irradiated by X-rays

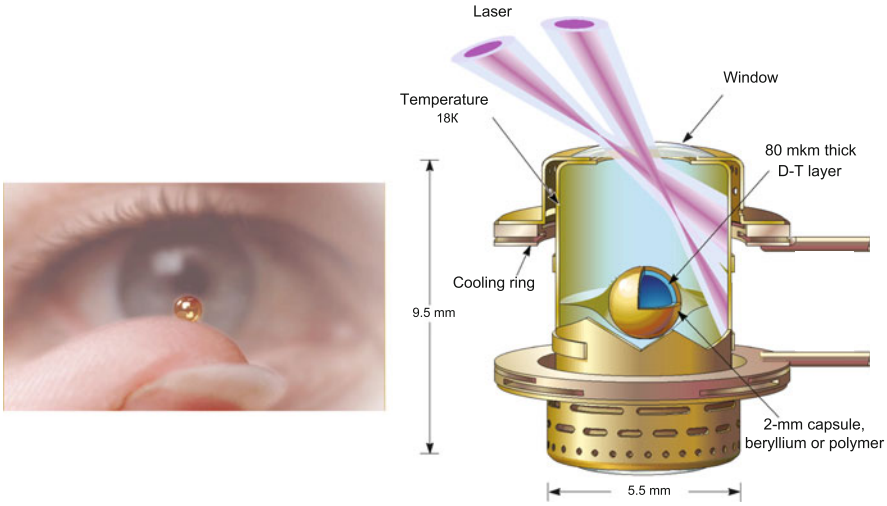

Fig. 7.17 Photograph of an indirect-drive target and scheme of its irradiation by 192 laser beams of the NIF facility [189]

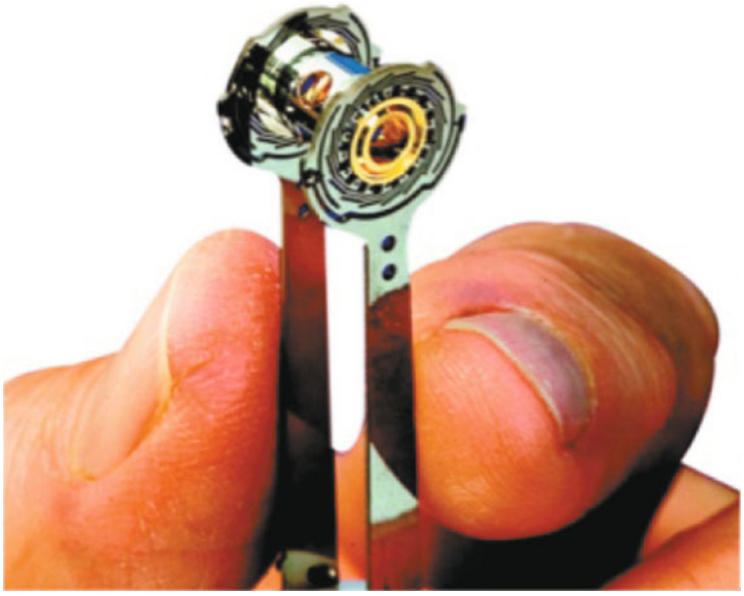

Fig. 7.18 Photo of the thermonuclear target [185]

thermonuclear target (Fig. 7.16b). To obviate the distortion effect of the edge of the plasma on the compression symmetry, the cylinder interior is filled with a low-density ($n \approx 10^{21}\,\mathrm{cm}^{-3}$) plasma produced by the ionization of aerogels. Similar schemes for the thermonuclear targets for heavy ions are described in [82, 213].

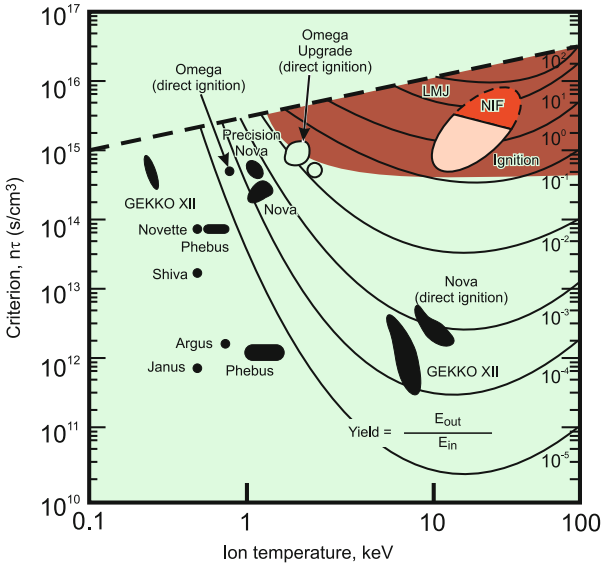

Fig. 7.19 Capabilities of lasers for controlled thermonuclear fusion with inertial plasma confinement [129]

The operation of these thermonuclear targets is attended with complex nonlinear processes—beam filamentation and focusing, incoherent scattering, the generation of plasma waves (stimulated Raman and Brillouin scattering), nonthermal electrons and ions, two-plasmon decay, and many other phenomena, some of which have been adequately studied on smaller facilities and with the use of sophisticated computer codes.

The capabilities of the existing laser systems for inertial thermonuclear fusion and of those under construction are illustrated by Table 3.3 and Fig. 7.19, which show that the commissioning of the NIF and LMJ megajoule-level lasers will afford thermonuclear ignition conditions and energy-positive CNF conditions.

At the same time, the vigorous progress of laser technology permanently engenders new technical solutions and physical ideas, which strongly affect the development of the laser fusion program. In particular, the realization of crystal and glass laser pumping by semiconductor laser diodes raises the total system efficiency to 30–35 %.

The results of experiments on the NIF laser are depicted in Fig. 7.20 [100]. One can see that a record-high soft X-ray radiation temperature ($\approx$300 eV) was achieved and a highly symmetric DT-target compression was realized with a neutron yield of $\approx 2 \cdot 10^{14}$. Experiments on the NIF laser are considered in more detail in the next section.

As discussed in Chap. 5, the invention of the chirping technique has enabled relativistic plasmas to be generated, when the electrons in the electric field of the light wave are accelerated to velocities that approach the velocity of light. This

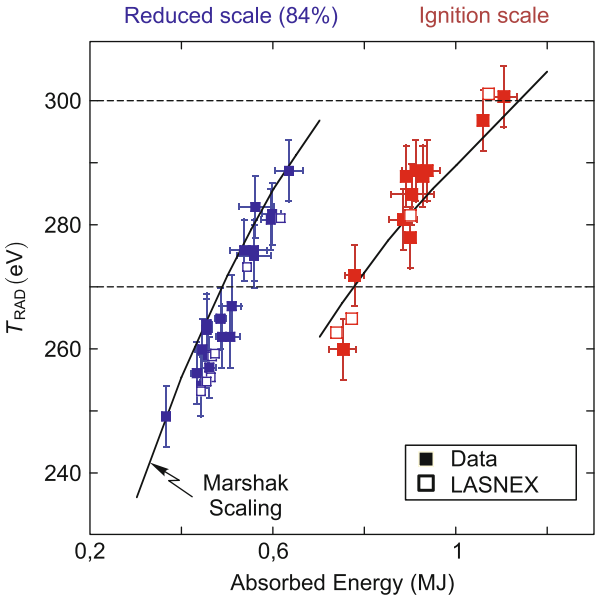

Fig. 7.20 Experimental and theoretical temperatures of the radiation in thermodynamic equilibrium with the capsule walls plotted versus absorbed laser energy. The measured values were obtained using a broadband X-ray DANTE spectrometer; the simulations were made in the framework of a radiative-hydrodynamics model using LASNEX codes with a detailed configuration inclusion. Marshak scaling establishes correspondence between the absorbed laser energy converted to X-rays with a 90 % efficiency and the radiative loss. The data suggest that the ignition temperature in the capsule $T_{RAD} \approx 300$ eV for an absorbed laser energy of ≥ 1.1 MJ [100]

lowers the critical frequency of plasma oscillations due to the relativistic increase in electron mass and therefore shifts the plasma transparency bound towards higher densities to improve the conditions for thermonuclear ignition.

Nonlinear effects in the plasma, which are induced by the high intensities of laser radiation, are responsible for its conversion to high-order harmonics, which is also advantageous from the viewpoint of energy transport efficiency in dense plasmas. In any case, the transition to short-duration and high-intensity laser radiation is obviously expedient from the standpoint of laser fusion efficiency. Yet another idea for harnessing these short-pulse lasers in thermonuclear fusion is related to the notion of "fast ignition" [228], which will be considered in Sect. 7.2.3.

7.2.2 Towards Thermonuclear Ignition: NIF Experiments

The author of this book hopes that this section will be of merely historical significance by the instant of publication of this book, because the laser-driven ignition of a thermonuclear reaction with a positive energy yield will have been

accomplished by that time—the endeavors to implement the physical demonstration of laser fusion concept will meet with success. So far, NIF experts make impressive efforts to ignite the thermonuclear fusion reaction, overcome severe difficulties encountered on this path, demonstrate incredible resourcefulness, and harness unique experiment instrumentation, which is at the forefront of modern high energy density physics.

In March 2009, the NIF reached an energy level of ≈1.1 MJ, thereby exceeding the level of previous lasers by a factor of 30. Now it operates at full power (≈411 TW) and energy (≈1.875 MJ at target) in 192 beams, which should produce extremely high energy densities: a plasma temperature of ≈100 million K, a density of ≈1000 g/cm^3, and a pressure of ≈140 Gbar.

A fusion target for the NIF laser is schematized in Figs. 7.16 and 7.17; a detailed description of its structure and the physics of its operation are given in [115]. The precision of layer assembly is at a level of 0.1–1 μm and its surface roughness is at a level of ≈1 nm. A DT-ice layering should proceed 1.5 K below the triple point and the curvature of this inner layer should be accurate to within 1 μm. A photograph of the fusion target with the cryogenic system is shown in Fig. 7.21.

The NIF is equipped with 35 diagnostic complexes: measurement of X-ray and neutron radiation parameters as well as of the energy and spectral parameters of the radiating emanating from the external capsule, interferometric measurements of shock wave parameters, X- and gamma-ray spectral measurements of thermonuclear radiation (for more details, see [165]). The scientific areas of fusion research at the NIF are outlined in Fig. 7.22 [49, 97, 185]. They deal with investigations of the adiabaticity and symmetry of target compression, target layer velocities, the UV-laser-to-soft-X-ray radiation conversion efficiency (81–91 %) [100, 147], and the instability characteristics of all that is required for successful target ignition. Investigated at the first stage are the characteristics of laser-generated soft X-ray radiation. The next (tuning) phase is concerned with the study of spherical target compression: the study of target layer dynamics, shock waves and other hydrodynamic characteristics required for the ignition of thermonuclear reaction

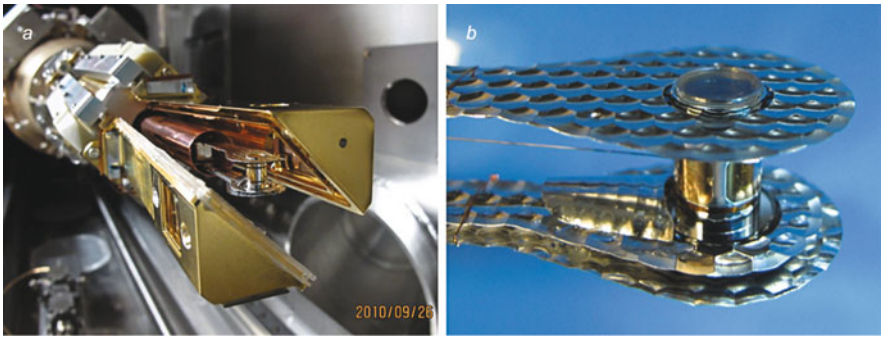

Fig. 7.21 Photo of the thermonuclear target for the NIF laser [102]

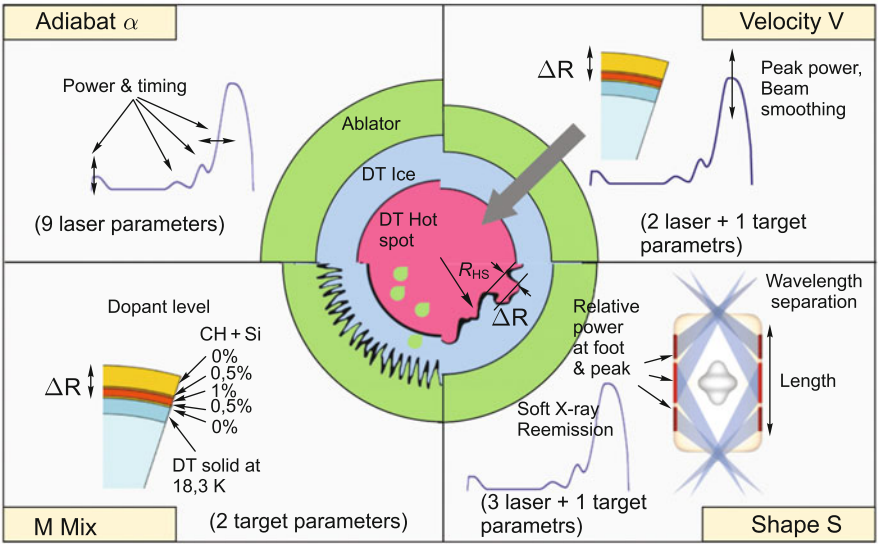

Fig. 7.22 Scientific lines of research on thermonuclear fusion at the NIF [49, 97, 185]

at the target center. The third phase involves the laser-driven compression of a 74/24/2 % mixture of tritium, hydrogen, and deuterium for the purpose of obtaining moderate neutron yields and testing the diagnostic tools. The objective of the fourth phase is the implementation of ignition of the fusion reaction with an energy yield of 10–20.

In experiments with an energy of 1.6 MJ, the temperature of radiation in the capsule was measured at >300 eV, the plasma pressure was estimated at >100 Gbar; the control of compression pulse and a DT-reaction neutron yield of $\approx 8 \cdot 10^{14}$ were demonstrated. The data on the radiation temperature for energies of up to 655 kJ are given in Fig. 7.23 [147].

The record high energy densities presented in Fig. 7.24 [97] were obtained using neutron and X-ray diagnostics [97]. Figure 7.25 shows the corresponding experiment setup, where the record values of the density and pressure were recorded.

As shown in [36], changing the hohlraum shell material from gold to uranium resulted in an increase in implosion velocity of $18 \pm 5\,\mu$m/ns. The instability of mixing processes was spectroscopically studied in [98, 117, 198, 237]. Measurements of the hard (>100 keV) bremsstrahlung emanating from the fusion target made it possible to estimate the change in adiabatic exponent caused by plasma degeneracy. An in-depth comparison of simulations and laser experiments was made in a detailed study [47]. Numerical simulations showed the emergence of jets and strong mixing of the shells of laser targets. The data of experiments are given in Figs. 7.26 [117] and 7.27. The fine tuning of laser radiation parameters and fusion target characteristics in an effort to achieve ignition is the concern of [156].

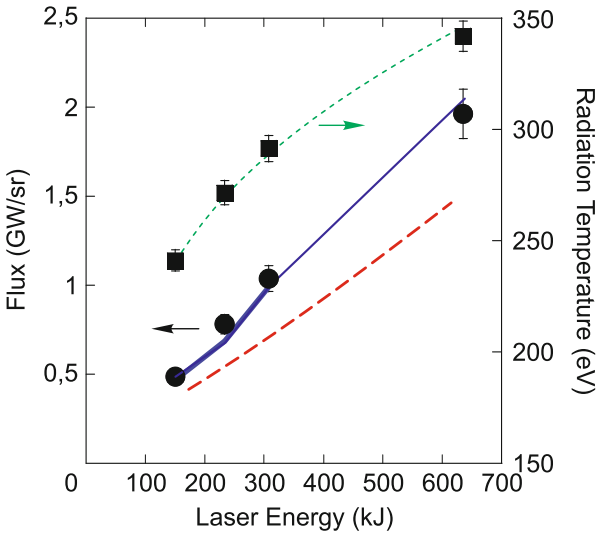

Fig. 7.23 Measured X-ray flux and temperature versus laser energy. The *curves* stand for simulations. The conversion coefficient is ≈88 % [147]

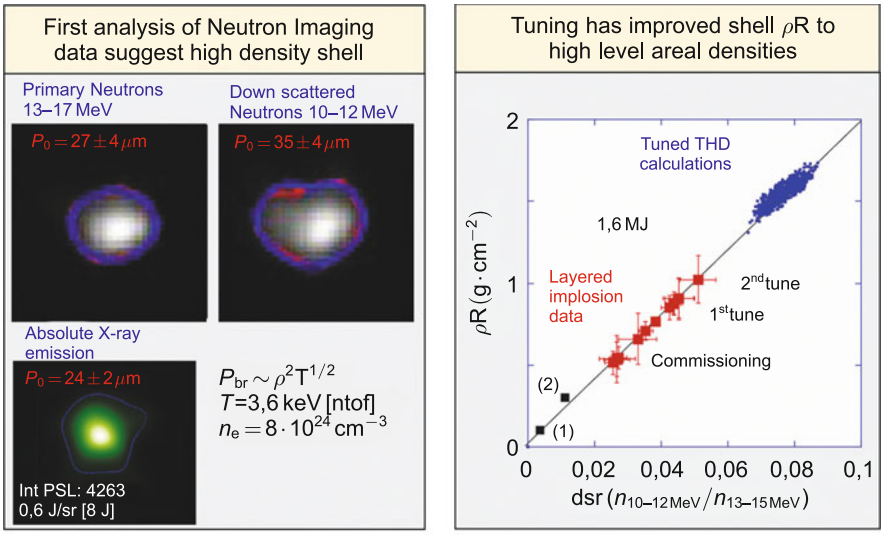

Fig. 7.24 Thermonuclear plasma parameters measured from X-ray and neutron radiations [97]

The experiments made to date have yielded the highest Lawson-criterion values for all controlled fusion facilities: $P\tau \approx 10$ atm s (see Chap. 3 and Fig. 7.28). The reached plasma parameters ($\rho R \approx 1$ g/cm^2, $T_i \approx 3$ keV) are quite close to ignition

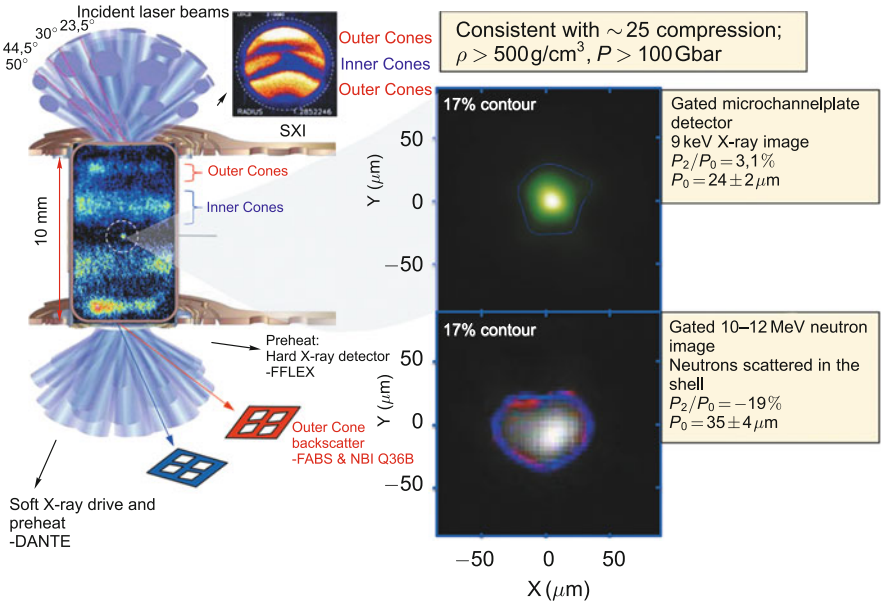

Fig. 7.25 Schematic representation of the experiment on laser-driven compression of fusion targets [97]

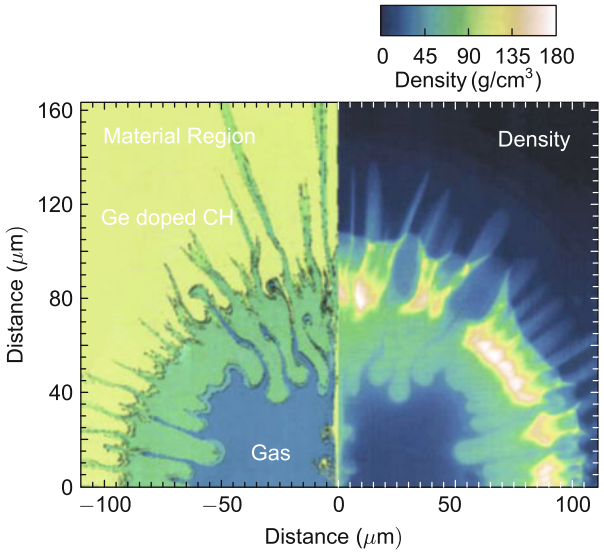

Fig. 7.26 Data on instability development in the laser-driven compression of fusion targets [117]

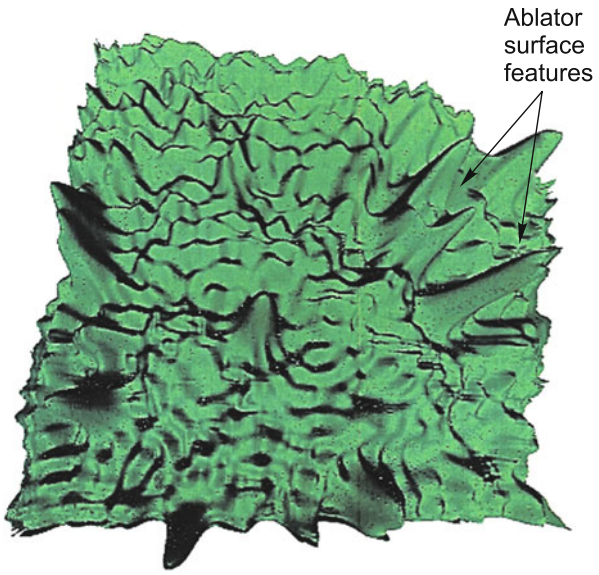

Fig. 7.27 Numerical simulation of the fuel–ablator interface [47]

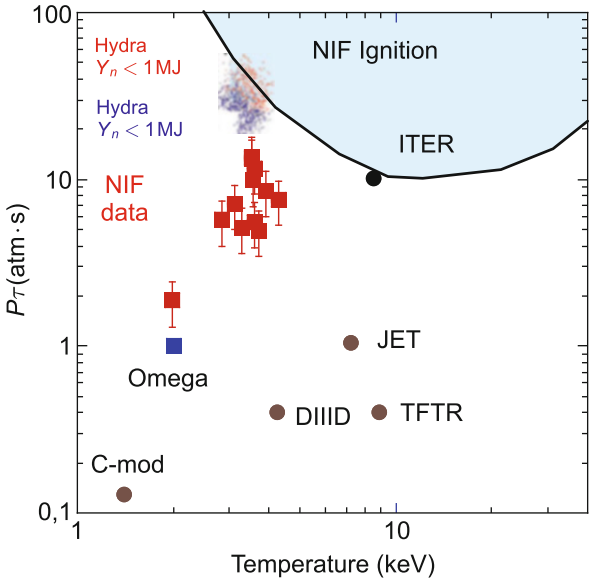

Fig. 7.28 Ignition criterion for the NIF [29]

conditions, which is confirmed by the data of HYDRA code simulations [29] with an energy liberation above and below 1 MJ.

Experiments performed on the NIF are described in greater detail in [49, 61, 85, 96–99, 101, 102, 125, 138, 147, 155, 165, 168, 178, 183, 185, 199, 201, 219, 219].

7.2.3 *Fast Ignition*

The advent of ultrahigh-power short-pulse lasers opens up new fascinating possibilities for laser fusion, making it possible to separate the processes of adiabatic compression and heating of the thermonuclear plasma [19, 145]. In this scheme, the thermonuclear target is compressed to high densities, but is heated to a temperature well below thermonuclear temperatures by a laser pulse of nanosecond duration. Then, the inner part of the compressed fuel is additionally heated by intense fluxes of megaelectronvolt electrons or ions arising from femtosecond laser irradiation to initiate the thermonuclear burn of the entire target [19, 130, 164, 190, 196, 227, 228] (Figs. 7.29 and 7.30). Furthermore, at extremely high intensities of laser irradiation one would expect effects promoting a deeper penetration of the light energy into the supercritical-density plasma. Owing to the action of the ponderomotive forces of the light wave on electrons, electrons and ions will be forced out of the laser beam region, resulting (owing to this self-focusing) in the formation of a low-density plasma channel. Via this channel the light energy will be delivered beyond the critical surface into the interior of the precompressed target and initiate its thermonuclear ignition (Fig. 7.30). This scheme, which is referred to as "fast ignition" [228], exhibits a higher thermonuclear yield and, what is highly important, a higher immunity to instabilities and mixing, because the stages of compression and heating are separated in time in this case. The requirement of optimal target operation leads to the conclusion that the duration of the laser pulse that compresses the thermonuclear fuel to 200–300 g/cm^3 should be equal to ≈10–20 ns.

The main problems of this scheme are associated with the efficient generation and transfer of ultrahigh-intensity energy fluxes into the interior of the compressed dense plasma. Estimates show [189] that it is necessary to heat a plasma volume of the order of the electron or α-particle range ($\rho r \approx 0.5$ g/cm^2) to 10 keV. For a plasma density of ≈300 g/cm^3 this amounts to ≈10 μm in a time ≈ 10–20 ps [19,

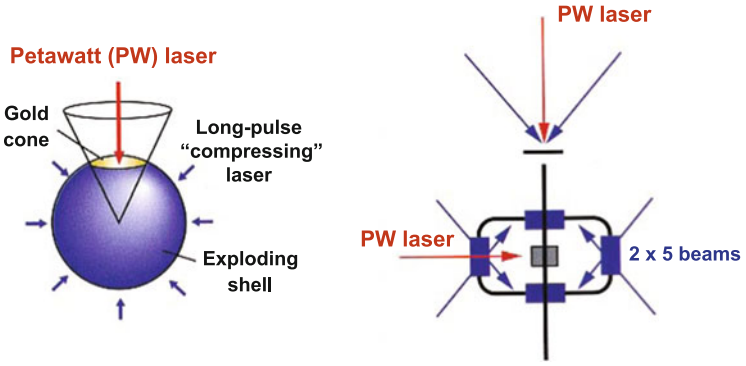

Fig. 7.29 Fast ignition scheme. *Red arrows* indicate the petawatt laser radiation to heat the compressed target and the *blue ones* stand for the nanosecond laser radiation for target compression

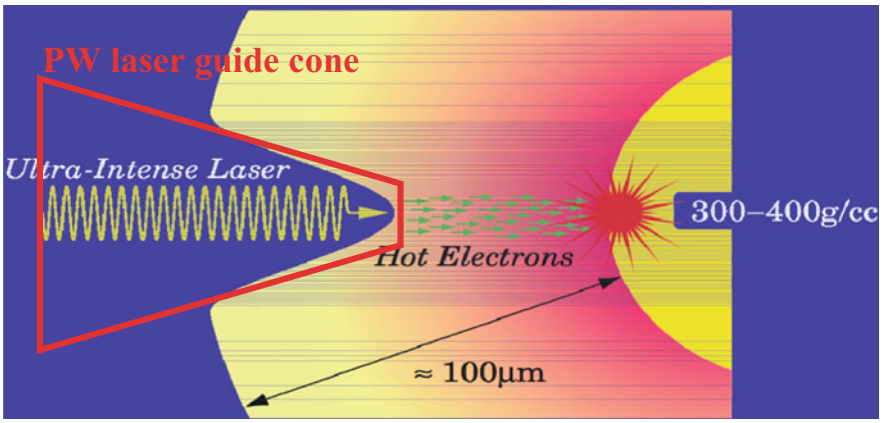

Fig. 7.30 Scheme of "fast" thermonuclear target ignition. Electron current > 500 MA

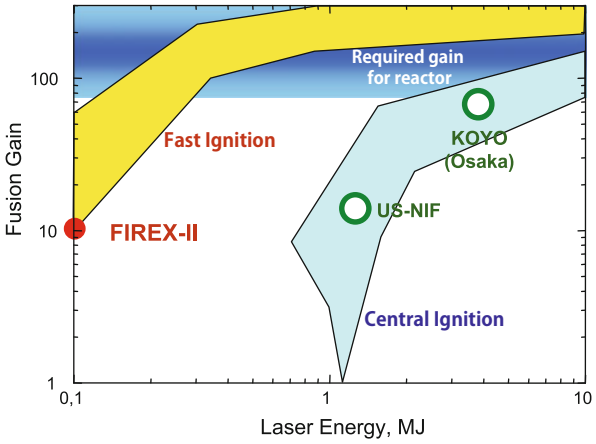

Fig. 7.31 Thermonuclear gain coefficient versus laser energy [181]

150, 164]. The corresponding energy is equal to ≈3 kJ for a power of 4×10^{14} W and an intensity of $\approx 10^{20}$ W/cm^2. In a different version of this scheme, use can be made of electrons or protons with an energy of 1–5 MeV, which are comparable to α-particles in range.

Modern short-pulse lasers furnish the requisite intensities of $\approx 10^{15}$–10^{20} W/cm^2 and generate a wide spectrum of effects useful for fast ignition in 10^{21}–10^{26} cm^{-3} density plasmas—relativistic self-focusing and filamentation, quantum and sausage-type instabilities, as well as formation of vacuum channels and a set of new diverse particle acceleration mechanisms. Also possible is the generation of magnetic fields of superhigh intensity ($\approx 10^9$ G) and multimegaelectronvolt-energy ions [180, 197].

An important role in the study of these effects is played by computer simulations [92, 196], which predict, in particular, a highly efficient (up to 30 %) energy transfer from laser radiation to megavolt-range electrons (Fig. 7.31). In this

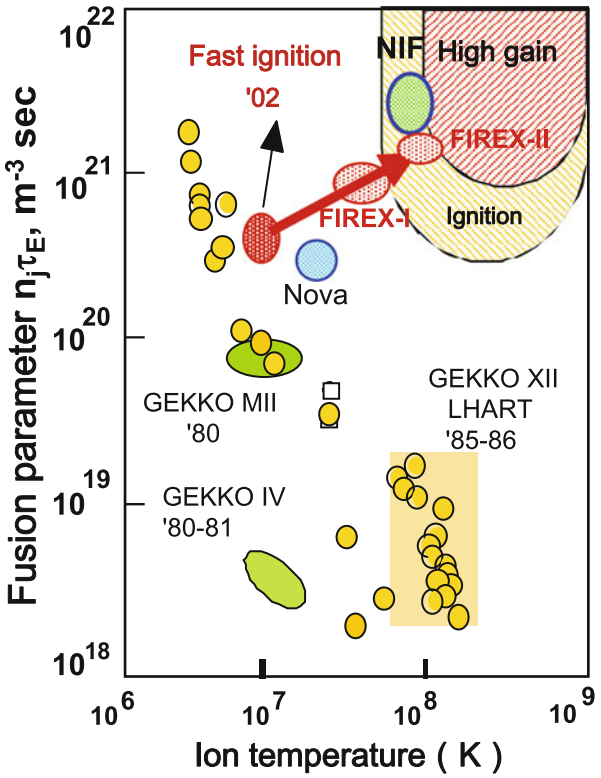

Fig. 7.32 Comparison of "direct-drive" and "fast-ignition" thermonuclear schemes [181]

case there emerge several new acceleration mechanisms—heating by oscillating ponderomotive forces, transverse-to-longitudinal electric field transformation in superdense plasma layers, acceleration of electrons in the betatron resonance in relativistic laser channels [186, 196]. The rich variety of these effects is currently the subject of careful studies. In particular, about 20 % of the energy of a short-pulse laser was transferred to the compressed thermonuclear target in experiments conducted at Osaka University [149].

The authors of [34, 130, 190, 203] came up with the idea of igniting the compressed fuel by the fast ions of laser plasma rather than electrons.

Kodama et al. [34, 203] came up with the idea of igniting compressed fuel not by electrons, but by the fast ions of the laser plasma. A comparison of "direct-drive" and "fast-ignition" thermonuclear schemes is shown in Fig. 7.32.

The action of high-power laser radiation on clusters has come under vigorous scrutiny [44, 48, 57–60, 70, 88, 89, 92, 121, 141, 144, 154, 157, 166, 186, 187, 191, 200, 212, 217, 251, 252, 256, 257], because it permits the production of extremely high plasma temperatures, the investigation of strongly nonequilibrium effects, and the generation of neutron fluxes. The fact is that direct photoionization

takes the place of thermal collisional ionization beginning with intensities of 10^{21}–10^{22} W/cm^2. In this case, the photoelectrons escape from a cluster to violate the fundamental condition of plasma electroneutrality [79], resulting in the generation of intense electric fields. A "Coulomb explosion" occurs, with the effect that the ions are accelerated to high ($\approx$1 MeV) energies [70, 157, 191] and fusion neutrons are generated [59]. This opens up interesting new possibilities for the development of compact laser-driven neutron generators for numerous technical and medical applications [146].

Another manifestation of "Coulomb explosion" was recorded in the experiments of Okihara et al. [194], which involved the laser irradiation of a plastic (C_5H_{10}) foam with a density of $\approx$10 mg/cm^3 at $q \approx 10^{18}$ W/cm^2. Ions with an energy of 200 keV were obtained, their parameters corresponding to the "Coulomb explosion" model.

7.3 Heavy-Ion Beam Fusion

The initiation of controlled thermonuclear reactions by heavy-ion ($A > 80$) beams [213] offers several potential advantages, for example the high efficiency and reliability of accelerators and that the ion accelerators developed for experiments in high-energy physics are ready for operation. Considered for this purpose is the multigigaelectronvolt level of ion energies for a total beam energy ranging into the megajoules; these beams should be squeezed to 10 ns and focused onto millimeter-sized targets. To meet these conditions requires going beyond the limits defined by the space charge, which calls for the suppression of diverse instabilities and the study of collective effects in high-current beams as well as of several other complex processes. In particular, the rise in beam emittance (the rise of beam temperature) may be caused by collective processes (up to beam "crystallization" [205, 208]), the imperfection of magnetic field systems for the "reflection" from conducting surfaces, and inter-ion forces.

The beam propagation in the reactor chamber also invites careful analysis [189] of background plasma dynamics and reverse currents (stream and filamentation instabilities), "peeling" of the beam by the background plasma, its photoionization, etc. [189].

Research into ion beam generation and high-energy-density physics involving ion beams is being vigorously pursued in several research centers: GSI, Germany (Fig. 6.9); Berkeley, USA; ITEF, Russia; IPKhF, ITES OIVT RAN, Russia [80, 82, 127, 213], where a wealth of interesting new data was obtained concerning the absorption of heavy ions by plasmas, shock-wave dynamics, isochoric target heating, plasma spectra, etc. [30, 68, 82, 128, 172, 182, 202, 204, 229, 230].

Of special interest is the project [229] to use the GSI heavy-ion accelerator (SIS 100) in combination with the petawatt PHELIX laser (Fig. 6.10).

Work on the use of heavy ions in high-energy-density physics is described in greater detail in reviews [82, 127].

7.4 Laser-Plasma Acceleration of Charged Particles

Currently, many laboratories in the world have high-power short-pulse lasers (with a pulse duration τ_L shorter than a picosecond, $\tau_L < 10^{-12}$ s) (see Table 3.3), which are employed in studies of different processes and the development of numerous applications. One of these applications involves the elaboration of compact laser-plasma high-energy electron and ion accelerators on the basis of new-generation femtosecond lasers.

The dimensions of modern electron accelerators are determined by the intensity of the accelerating field, which is equal to 10^7–$10^8\,\mathrm{V\,m^{-1}}$ and is limited by the breakdown in the acceleration system. That is why the problem of particle acceleration in plasmas rather than in vacuum has long been under discussion. On the one hand, in this case there is no breakdown-defined limitation and on the other the electric intensity in a relativistic charge-density wave (whose phase velocity is close to the velocity of light) may achieve huge magnitudes. Indeed, a simple estimate made with the aid of the Poisson equation permits this intensity to be related to the electron plasma density n_e:

$$E \cong \alpha (n_e\,[\mathrm{cm^{-3}}])^{1/2}\,[\mathrm{V\,cm^{-1}}],$$

where $\alpha = \delta n/n_e$ is the dimensionless amplitude of the plasma wave (δn is the amplitude of electron density oscillations). For an electron density $n_e = 10^{17}\,\mathrm{cm^{-3}}$ and $\alpha = 0.3$, the accelerating field intensity in the plasma wave amounts to $10^8\,\mathrm{V\,cm^{-1}}$, which is two or three orders of magnitude higher than the acceleration rate in traditional radio-frequency accelerators. Figures 7.33 and 7.34 depict schematically one stage of a laser-plasma wakefield accelerator [6].

We consider several aspects of laser-driven acceleration following Belyaev et al. [26]. As shown in Chap. 5, the advent of new-generation solid-state lasers has

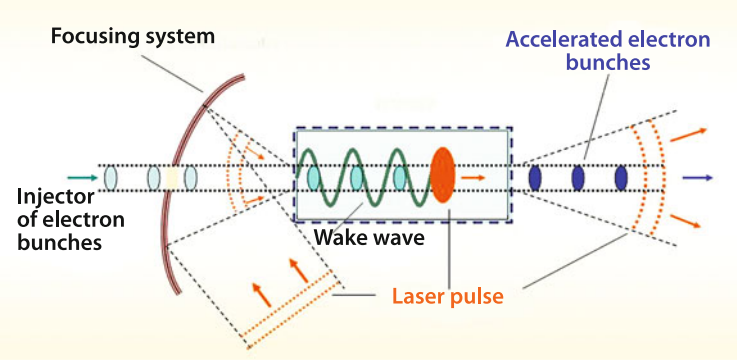

Fig. 7.33 Schematic of one stage of a laser-plasma wakefield accelerator [6]

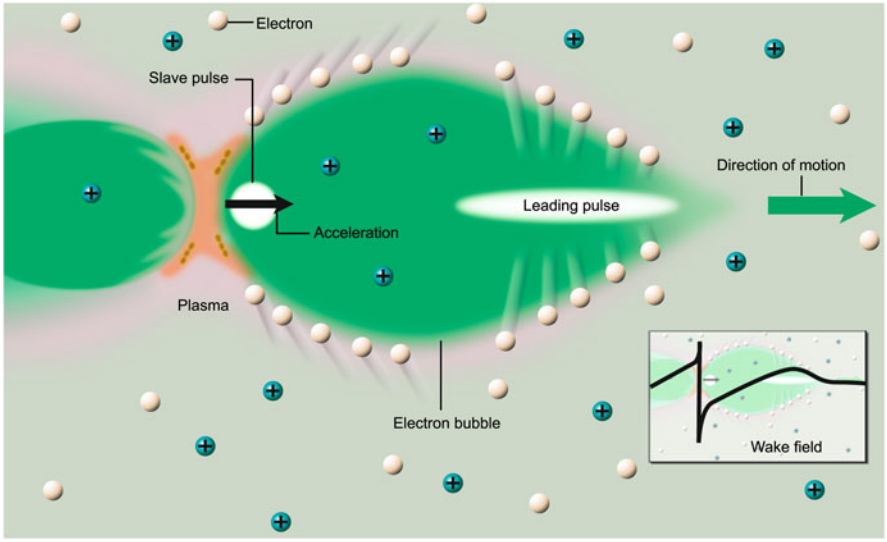

Fig. 7.34 A wakefield acceleration scheme [139]. The leading laser pulse expels electrons (shown in *white*) to produce a positively charged domain (*green*). The accelerating electric field propagates along the axis (*bottom right*)

led to unique conditions of laser target irradiation by 20–1000 fs long light pulses with radiation intensities in the 10^{17}–10^{21} W/cm^2 range.

At these intensities previously unattainable superhigh electric fields are produced in a laser pulse, which far exceed the atomic electric field $E_{at} \approx 5.14 \times 10^9$ V/cm. These conditions give rise to fascinating dynamics of laser radiation interaction with the plasma produced when the leading pulse edge or the prepulse interacts with a solid-state target. Laser radiation is rather efficiently transformed [26] to streams of fast charged particles—electrons and atomic ions. Their interaction with the surrounding target material leads to hard X-ray generation in the ionization of inner atomic shells and to different nuclear and photonuclear reactions.

The relativistic nature of laser radiation intensity I is realized when $\alpha > 1$, where α is the dimensionless momentum of an electron oscillating in the electric field of linearly polarized laser radiation expressed by the formula [26]

$$\alpha = \frac{eE}{mc\omega} = 0.85\lambda \left(\frac{I}{10^{18}}\right)^{1/2}$$

$$E = 27.7\, I^{1/2}$$

Here, e and m are the electron charge and mass, E is the electric amplitude of laser radiation field (V/cm), λ is the radiation wavelength (μm) ω is the frequency of laser radiation, c is the speed of light (cm/s), and I is the radiation intensity (W/cm^2).

Terawatt-power laser systems of modest size enable intensities with $\alpha > 1$ to be attained, which corresponds to electric intensities above 10^{10} V/cm. Under these fields there occurs above-barrier ionization of atoms in atomic times on the order of 10^{-17} s, while the resultant electrons are accelerated to relativistic energies in the MeV range in the course of the laser pulse.

The authors of [56] proposed the use of electrons accelerated in a laser plasma (10^{18}–10^{19} W/cm^2) for generating terahertz electromagnetic radiation. To this end, use was made of the geometry of a "virtual cathode" (vircator), in the field of which the high-frequency oscillations of the electron beam take place (see Sect. 5.2).

The acceleration of atomic ions in femto- and picosecond laser plasmas is a secondary process: it is caused by the emergence of high quasi-static electric fields arising from spatial charge separation (Fig. 7.35), which in turn is due to the motion of a fast electron bunch. At laser radiation intensities exceeding $I \geq 10^{18}$ W/cm^2 it is possible to obtain directional beams of high-energy ions with an energy $E_\mathrm{i} > 1$ MeV.

In [119, 243], a petawatt laser [90] was employed for generating protons of energy ≈ 67 MeV in a plane geometry. Using a different coherent acceleration scheme, by irradiating (1–2 J, 45 fs) a thin diamond target by a laser pulse of intensity 10^{19}–10^{20} W/cm^2 it was possible to obtain protons with an energy of 113 MeV and carbon ions with an energy of 71 MeV [226]. A 40-J 700-fs long laser pulse [123] produced 35-MeV protons and 185-MeV carbon ions. With more modest laser pulses (40 fs, 0.5 TW), protons with an energy $E \approx 5.5$–7.5 MeV were obtained using ice nanotargets [255].

At present, the generation of high-energy proton and ion beams in a laser plasma under ultrashort-pulse irradiation is a rapidly advancing area of research. This is due, in particular, to their practically important applications in the areas such as proton acceleration, structural material studies, proton radiography, short-lived radioiso-

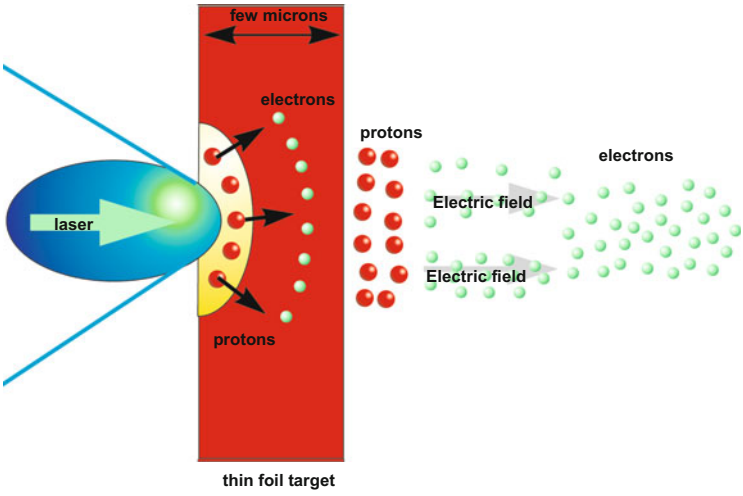

Fig. 7.35 Scheme of electron and ion generation in a laser-produced plasma [142]

tope production for medical applications, and controlled laser thermonuclear fusion. Laser radiation with intensities $I \geq 10^{18}\,\mathrm{W/cm^2}$ also makes possible the initiation of a number of nuclear reactions that were previously realizable only with the use of elementary particle accelerators.

Several mechanisms [26] of fast electron generation are presently under discussion that involve the action of a laser pulse on a plasma with a density much higher than the critical one. When a laser pulse does not have a prepulse (a high contrast ratio), the laser radiation interacts with a solid-state-density plasma with a sharp boundary. In this case the mechanism of "vacuum heating" is realized, as well as the so-called $v \times B$ mechanism (B is the amplitude of the magnetic induction of the laser wave) caused by the longitudinal (along the direction of laser pulse propagation) ponderomotive force. The $v \times B$ mechanism becomes significant at relativistic intensities, when the electron oscillation energy is comparable to or higher than the electron rest energy $mc^2 = 511\,\mathrm{keV}$.

There also is a mechanism of fast electron generation at the plasma resonance on the critical plasma surface when the electric vector of laser radiation has a projection on the density gradient (normally at oblique incidence of laser radiation on a target), and the laser frequency coincides with the plasma frequency.

Unlike the ponderomotive $v \times B$ mechanism, the "vacuum heating" and the resonance absorption mechanism emerge for nonrelativistic (substantially lower, $\alpha < 1$) intensities as well.

Another mechanism of fast electron generation in the subcritical plasma region in front of the target is considered [26], which operates due to betatron resonance in the emerging magnetic field. In this regime, electrons are accelerated by the transverse ultrarelativistic electric field of the laser wave in the direction of wave polarization, while the azimuthal magnetic field induced by fast electron current produces the magnetic part of the Lorentz force. This force turns the electrons in such a way that they gradually reverse their direction of motion. For an exact betatron resonance, their reflection takes place at the moment the transverse electric field changes its direction, so that the electrons are permanently in the acceleration regime.

There also exist other electron acceleration mechanisms, which require specific experimental conditions; among them is acceleration in the wake wave, which we consider in greater detail below. In the case of resonance absorption, the field near the critical plasma surface is substantially higher than the field of incident laser radiation.

We do not set ourselves the task of describing numerous laser acceleration mechanisms at length (see the review [26]) but list the different mechanisms of electron heating in Table 7.3.

The feasibility of harnessing lasers to excite relativistic charge-density waves in tenuous plasmas was first discussed by Tajima and Dawson [233], who, however, placed emphasis on the resonance method of excitation using two-frequency laser irradiation of moderate intensity. The possibility of employing high-intensity short pulses generated by modern lasers for the excitation of charge-density waves (so-called wake plasma waves) attracted considerable attention and provoked lively

Table 7.3 Comparison of different mechanisms of electron heating in dense media [26]

Heating mechanism	When it applies
Stimulated inverse bremsstrahlung in the scattering of electrons from ions	Intensities below 10^{15} W/cm^2
Longitudinal ponderomotive electron acceleration in the skin layer	Relativistic intensities above 10^{19} W/cm^2
Vacuum heating	High contrast ratio, moderate intensities, short pulses
Resonance absorption of laser radiation	Low contrast ratio, long pulses
Electron acceleration by a laser wake wave	Gas targets, substantial subcritical plasma region, ultrashort pulses
Cyclotron mechanism	The presence of external constant magnetic field
Betatron mechanism	Vortical electric field produced by a varying magnetic flux penetrating the orbit of electrons

discussion after the publication of [111, 223] (see also [27, 31], the reviews [6, 71, 112], and references therein).

The charge separation field, which occurs when the ponderomotive force expels electrons from the region occupied by the laser pulse, gives rise to a charge-density wave behind the laser pulse, the phase velocity of the wave being equal to the group velocity of the laser pulse. In a tenuous plasma, the latter is quite close to the velocity of light, and therefore the phase velocity of the wake plasma wave is also close to the velocity of light, just right to efficiently accelerate relativistic electrons (Figs. 7.36 and 7.37). Even the first experiments [6] showed that such a wake wave is indeed excited by a short (subpicosecond) laser pulse quite efficiently and may accelerate electron bunches to high energies ranging into the tens and hundreds of MeV.

Recent successful experiments performed practically simultaneously in different laboratories in Europe and the USA had the effect that even skeptics turned their attention to the possibility of harnessing laser-plasma acceleration techniques in high-energy physics (Fig. 7.38). In particular, the year 2004 saw the demonstration of the possibility of producing quasi-monoenergetic electron bunches (Fig. 7.39) accelerated to an energy of about 100 MeV over a length of several millimeters and possessing a small emittance [76, 93], which is of significance for the use of such bunches in hard radiation sources and for multistage acceleration for high-energy physics.

A new confirmation of the theoretical predictions about the significance of channeled propagation of a laser pulse for producing electron bunches of the

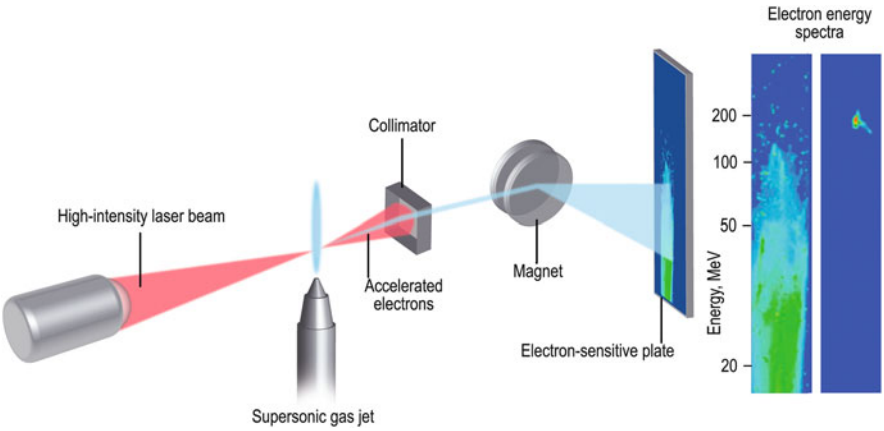

Fig. 7.36 Laser wakefield accelerator scheme [139]

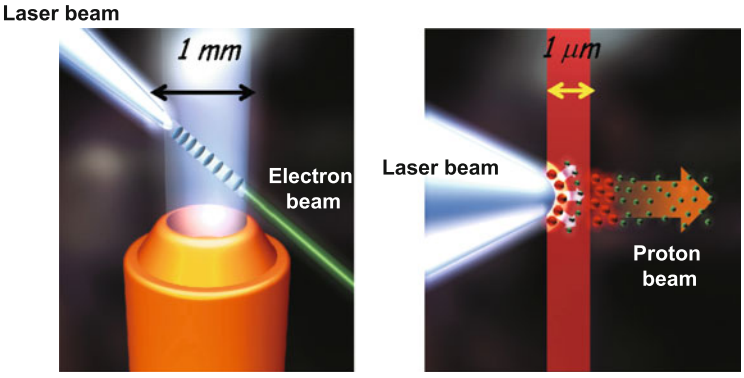

Fig. 7.37 Direct (at the *left*) and wakefield laser acceleration

gigaelectronvolt (10^9 eV) energy range was obtained in the National Berkeley Laboratory [161] (Fig. 7.40).

An experiment on the two-stage laser acceleration of electrons [195] is schematized in Fig. 7.41. This scheme makes use of two-stage acceleration technique, whereby the first stage produces an electron flux of energy ≈ 100 MeV with a relatively high spread in energy. This flux is delivered to the second acceleration stage, which produces a ≈ 0.5 GeV beam with a small energy spread (less than 5 % FWHM). The parameters of the thus accelerated electrons are shown in Fig. 7.42.

The wake plasma wave is most efficiently generated by a laser pulse under resonance conditions when the pulse duration τ_e is close to a half-period of the wave, i.e., provided

$$c\tau_e \approx \lambda_p/2 \cong \pi\, c/\omega_p = \pi/k_p,$$

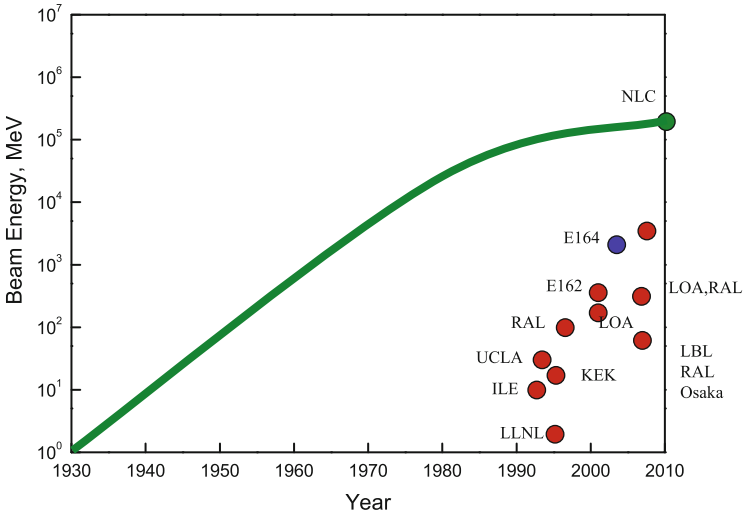

Fig. 7.38 Progress in laser-driven electron acceleration

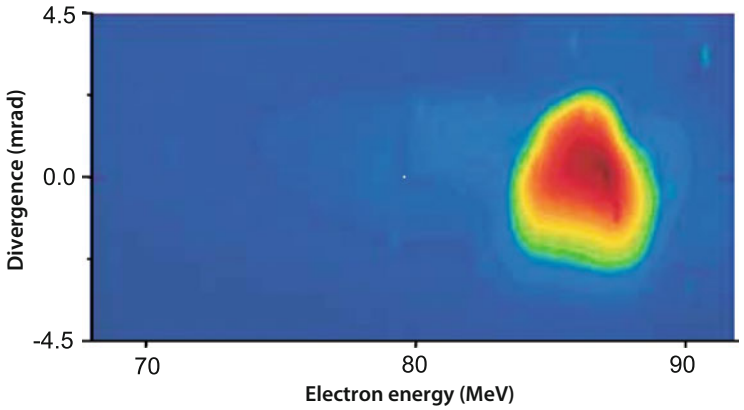

Fig. 7.39 Energy spectrum and angular divergence of an accelerated bunch containing 2×10^9 electrons [93]

where $\omega_p = (4\pi e^2 n_e/m)^{1/2}$ is the electron plasma frequency, k_p is the wave vector of the plasma wave, and c is the velocity of light. These expressions show that the accelerating field intensity increases with plasma density and, accordingly, with shortening of the laser pulse that excites the wake wave. In this case, however, it is well to bear in mind that increasing the plasma density lowers the group velocity of the pulse and, accordingly, the phase velocity of the wake plasma wave, which shortens the possible acceleration length (and decreases the maximum energy gain) of a relativistic electron due to its earlier escape from the accelerating phase of the wave. For instance, for laser radiation with a wavelength $\lambda_e \approx 1\,\mu$m and a

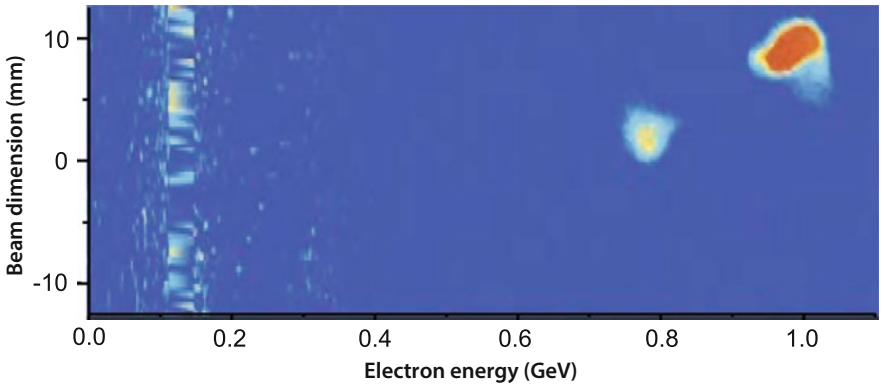

Fig. 7.40 Energy spectrum and dimension of the accelerated electron bunch in the channeled propagation of a laser pulse through a capillary [161]

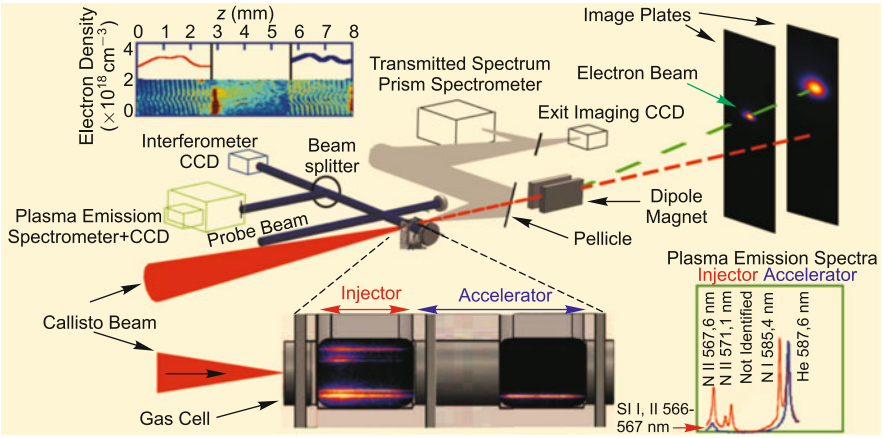

Fig. 7.41 Schematic of experiments in two-stage laser acceleration [195]

plasma density $n_e \approx 10^{17}\,\mathrm{cm}^{-3}$, the maximum acceleration length is 1 m. For an acceleration rate $E \approx 10\,\mathrm{GV/m}$ (for $\alpha \approx 0.3$) this corresponds to the maximum gain $\Delta\varepsilon_{\max} \approx 6\,\mathrm{GeV}$ in accelerated-electron energy. In this case, the duration of the laser pulse intended for the resonance excitation of the wake wave should be of the order of 100 fs.

The main difficulty encountered in attaining these parameters is the requirement that the high intensity of the laser pulse, which should be of the order of $10^{18}\,\mathrm{W/cm}^2$ in the example given above, be maintained throughout the entire propagation length ($\approx$1 m). In the absence of any optical channeling mechanisms for the laser radiation, the propagation length for the high-intensity laser pulse (and, accordingly, the efficient acceleration length) is limited by the diffraction length. For realistic parameters of the lasers of the terawatt power range (bearing in mind the necessity

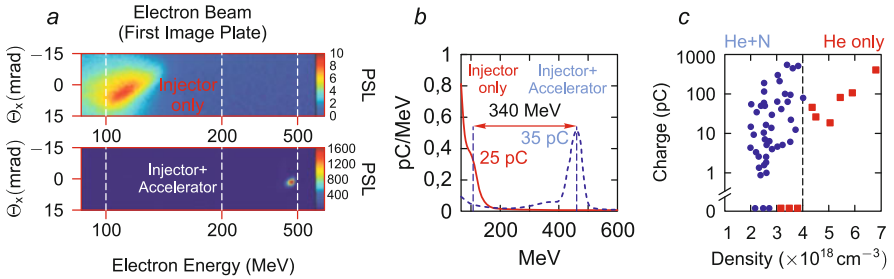

Fig. 7.42 Electron beam parameters after a two-stage acceleration [195]

of attaining the high radiation intensity), the diffraction length turns out to be much shorter than the maximum acceleration length. This is why attaining ≈1–10 GeV electron energies without channeling of the laser pulse requires its focal spot to be increased in order to increase its diffraction length, which calls for petawatt (10^{15} W) laser power level to maintain the high intensity [113, 114, 163]. When advantage is taken of channeled laser pulse propagation, the required power level may be lowered by more than an order of magnitude [161].

The optical channeling of a laser pulse as a way to overcome its diffraction spreading is possible owing to its self-focusing or when a plasma channel with an on-axis density minimum is produced to afford waveguided radiation propagation [45, 65]. A highly promising technique for propagating high-intensity laser pulses for tens and hundreds of Rayleigh lengths is the use of dielectric gas-filled capillaries, in which the plasma is produced either by a discharge [131, 221, 254], or by the optical ionization of the gas by the wake-wave-generating laser pulse itself [51, 52]. That is why much attention is presently being paid to studies of different ways of producing plasma channels and the propagation of short laser pulses through them [28, 50, 134, 144, 188], as well as to investigations into the generation mechanisms and structure of wake waves in gas-filled capillaries [10, 12–14, 81, 218].

The simple laws indicated above, which define the resonance excitation of the wake wave, are valid under the conditions of weak nonlinear dynamics of a laser pulse (under the conditions of weak relativity, when the oscillation energy of the electron in the laser field does not exceed its rest energy). The inclusion of the nonlinearity of laser pulse propagation has led to the discovery of new regimes of generation of high-intensity plasma fields when the linear resonance condition $c\tau_e \approx \lambda_p/2$ is not fulfilled. In particular, when the laser pulse length is far greater than the plasma wavelength, the mechanism of high-intensity wake-wave generation is due to the self-modulation of the laser pulse, with the result that the pulse intensity turns out to be longitudinally modulated with a scale length close to the plasma wavelength [7–9, 11, 16, 17, 54, 112, 122, 151, 184, 224]. The self-modulation stems from the development of a laser-pulse instability. Depending on the plasma and laser radiation parameters, this self-modulation may be related to either the self-focusing of the laser pulse or its forward stimulated Raman scattering, and is accompanied by

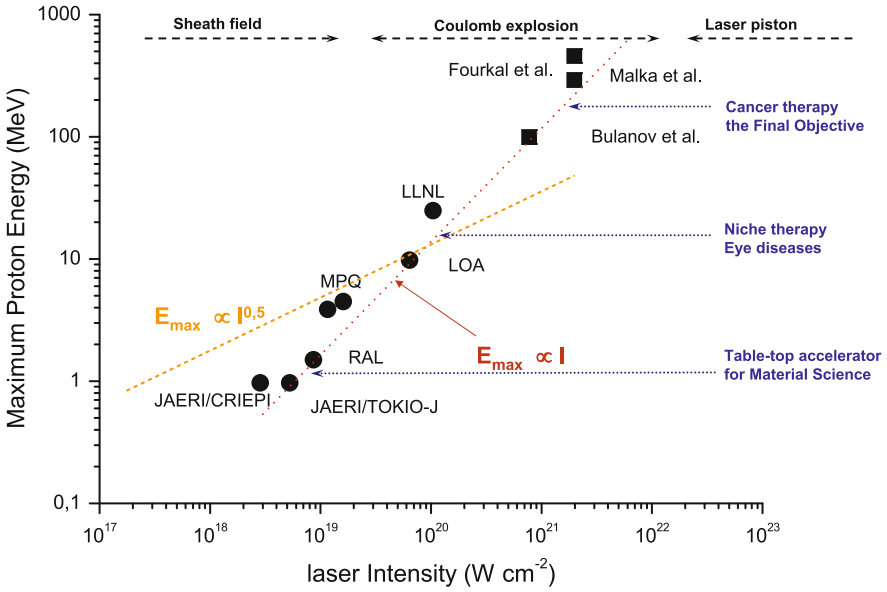

Fig. 7.43 Parameters of laser ion accelerators

the stimulated generation of a wake wave. As a consequence, the amplitude of the plasma wave may far exceed the magnitude generated by a short laser pulse under linear resonance conditions.

A strongly nonlinear regime of generation of the accelerating charge-separation field was recently discovered in the opposite limiting case of an ultrashort laser pulse ($c\tau_e < \lambda_p/2$) of ultrarelativistic intensity. Under these conditions, all plasma electrons immediately behind the laser pulse are expelled by the ponderomotive force (the so-called bubble regime, Fig. 5.10) [46, 169, 196], and the wake wave in the wave-breaking regime entrains the small fraction of background electrons and accelerates them with record acceleration rates [15, 72, 116, 132, 153, 171, 175, 192].

When a relativistically intense laser pulse irradiates a thin foil, the laser energy may be efficiently converted to a well-collimated beam of accelerated ions [20, 24, 25, 32, 33, 67, 74, 75, 78, 84, 91, 95, 124, 133, 158, 170, 193, 244, 246, 250].

Among the applications of the laser-plasma ion acceleration that are being actively developed, mention should be made of the "fast ignition" in inertial thermonuclear fusion (Sect. 7.2.3) and the proton therapy of malignant tumors [20, 25, 83, 84, 149, 232] (Fig. 7.43). The employment of protons in radiation therapy and oncology offers several significant advantages over other kinds of radiation. This is primarily due to the fact that the deceleration of prescribed-energy protons in a substance takes place in a localized region in the vicinity of the Bragg peak (for carbon, see Fig. 7.44 [25, 82, 127, 167, 213]), where the bulk of beam energy is deposited, thereby reducing the irradiation of healthy body tissue (Fig. 7.45).

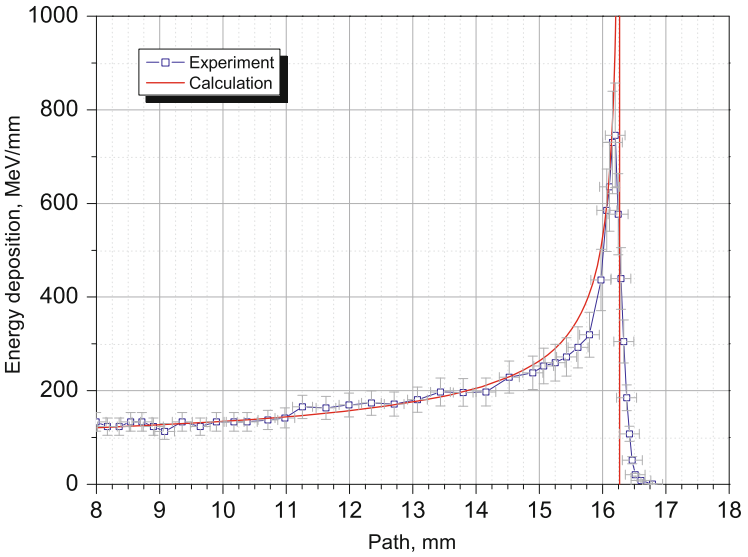

Fig. 7.44 Energy deposition profile for a beam of 250 MeV/nucleon C^{6+} nuclei in a copper target [22, 82]

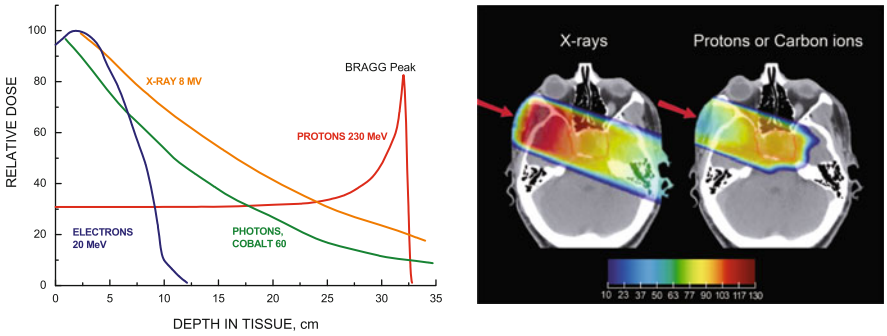

Fig. 7.45 Proton and hadron therapy [142]

We emphasize that the necessary condition for the successful use of accelerated ions for the above purposes is their high energy monochromaticity. In particular, the energy-spread in the proton beam intended for hadron therapy may not exceed 2 %. Esirkepov et al. [73] proposed two-layer targets for the production of quasi-monoenergetic beams of accelerated protons and analyzed them in a realistic three-dimensional geometry to demonstrate the feasibility of generating well-localized high-energy proton bunches with an energy-spread $\Delta E/E \approx 3\,\%$ (see Fig. 7.46).

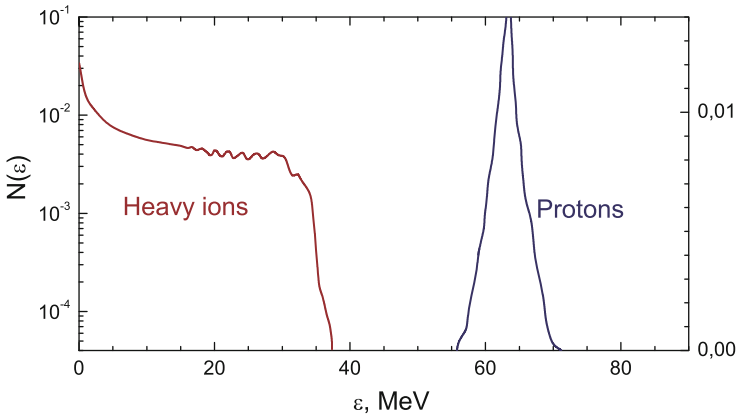

Fig. 7.46 Spectra of accelerated protons and heavy ions [73]

7.5 Synchrotron Sources, Free-Electron Lasers and High-Intensity Sources of Terahertz Radiation Pulses

At present, free-electron lasers [2, 3, 38, 40, 42, 63, 64, 66, 77, 94, 120, 126, 135–137, 143, 152, 173, 174, 179, 207, 210, 235, 236, 238, 248] permit extremely intense radiation fluxes of femtosecond duration to be obtained in a broad (from the far-ultraviolet to soft X-ray) wavelength range (Table 7.4, Fig. 7.47).

These circumstances make free-electron lasers a promising tool for studying ultrafast chemical and biochemical processes with atomic-scale spatial resolution, for analyzing biological structures, for studying in real time the kinetics of physicochemical transformations, for investigating strongly nonideal and astrophysical plasmas, and for many other applications requiring atomic-scale spatial resolution and high temporal resolution. Figure 7.48 is a diagrammatic sketch of the FLASH free-electron laser at DESY, Germany [2, 3].

Today this facility is the champion in radiation brightness, and the brightness of this device will exceed that of the majority of facilities of this kind by 6–9 orders of magnitude. In this case, the pulse duration will shorten from 50 to 10 fs for a total pulse energy of 10–50 mJ and a wavelength of 6.5–60 nm. Recall that in 10 fs the light traverses a distance of only $\approx 3\,\mu$m. The 260 m long FLASH facility with a power of 5 GW consists of a superconducting linear electron accelerator with a current of 1–2 kA, which imparts to the electrons a kinetic energy of 440–700 MeV and an energy-spread of ≈ 0.1 %. This electron flux is applied to a 27 m long undulator section, in which there forms X-ray electromagnetic radiation in the form of sequences of 800 pulses with an energy up to 50 μJ each, with a repetition rate of ≈5–10 Hz, an average radiation power of 100 mW, and a peak brightness of 10^{29}–10^{30} photons/(s mrad mm^2 0.1 %BW) [2].

Table 7.4 Synchrotron radiation sources

Facility name	Location	Country	Energy (GeV)	Perimeter (m)	Year of start-up	Notes
Advanced Photon Source (APS)	Argonne National Laboratory	USA	7.0	1104	1995	0.31 mA per pulse and $\Delta\tau = 11.37$ ns, interpulse time
Canadian Light Source	University of Saskatchewan	Canada	2.9	174	2004	250 mA
Australian Synchrotron	Melbourne	Australia	3	216	2007	
ANKA	Karlsruhe Institute of Technology	Germany	2.5	110.4	2000	
LNLS	Campinas	Brazil	1.37	93.2	1997	
SESAME	Allaan	Jordan	2.5	125	Under design	
Advanced Light Source	Lawrence Berkeley Laboratory	USA	1.9	196.8	1993	
National Synchrotron Light Source	Brookhaven National Laboratory	USA	2.8	170	1982	
Stanford Synchrotron Radiation Light Source	SLAC National Accelerator Laboratory	USA	4.5	2199	1973	Current = 1.5 A, 3400 160-fs long bunches, interbunch time 2.1 ns, 890-pole wiggler $E = 8.2$ keV, flux 10^{33} photon/(s mm^2 mrad^2) (0.1 % $\Delta E/E$)
Soleil	Paris	France	3	354	2006	
Shanghai Synchrotron Radiation Facility	Shanghai	China	3.5	432	2007	Current = 200–300 mA, emittance = 3.9 nm rad
Swiss Light Source	Paul Scherrer Institute	Switzerland	2.8	288	2001	
BESSY II	Helmholtz-Zentrum Berlin in Berlin	Germany	1.7	240	1998	

European Synchrotron Radiation Facility (ESRF)	Grenoble	France	6	884	1992	
ELETTRA	Triesta	Italy	2" 2.4	260	1993	
Diamond Light Source	Oxfordshire	UK	3	561.6	2006	
FLASH, DESY	Hamburg	Germany	4.5	289	2007	$\lambda = 6.8$–$47\,\text{nm}$, $t = 10$–$70\,\text{fs}$, $P_{\text{max}} = 1$–5 GW, $I = 10^{29}$–10^{30} photons/(s mm^2 mrad^2)
PETRA III	DESY	Germany	6.5	2304	2009	
SPring" 8	RIKEN	Japan	8	1436	1997	
National Synchrotron Radiation Research Center	Hsinchu Science Park	Taiwan	3.3	518.4	2008	
Synchrotron Light Research Institute (SLRI)	Nakhon Ratchasima	Thailand	1.2	81.4	2004	
Indus 2	Raja Ramanna Centre for Advanced Technology, Indore	India	2.5	36	2005	
PLS, PAL	Pohang	South Korea	2.5	280.56	1994	

(continued)

Table 7.4 (continued)

Facility name	Location	Country	Energy (GeV)	Perimeter (m)	Year of start-up	Notes
Kurchatov Synchrotron Radiation Source (SIBIR" 2)	Kurchatov Institute, Moscow	Russia	2.5	124	1999	Current = 150 mA (75 60-ps bunches), 19-pole wiggler, $B = 7.5$ T, photons energy up to 200 keV, $I =$ 10^{12}–10^{14} photons/ (s mm^2 mrad^2)
Siberian Synchrotron Radiation Centre (SSRC)	Budker Institute of Nuclear Physics, Novosibirsk	Russia	6	366		Current =80 mA (4 100-ps bunches), 7-pole wiggler, $B = 1.2$ T, photons energy up to 100 keV, $I = 10^{13}$ photons/ (s mm^2 mrad^2)

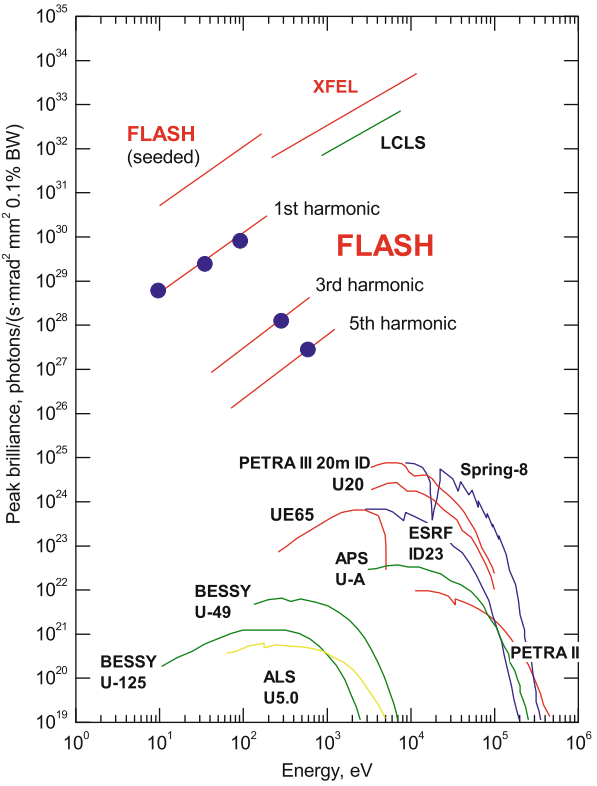

Fig. 7.47 Peak brilliance (BW: bandwidth) of the experimental facilities FLASH and XFEL (Germany), LCLS, APS (USA), SPring-8 (Japan), ESRF (France), and SLS (Switzerland). The DESY facilities are indicated in *red*. *Blue circles* stand for the measured values. PETRA III began working in 2009 and the European XFEL will be commissioned in 2013 [2, 3, 55]

With their unique radiation parameters, free-electron lasers permit a broad spectrum of investigations in different areas of science and technology that are quite frequently inaccessible by other means of generation and diagnostics.

Owing to its short wavelength (comparable to atomic dimensions), this radiation is suitable for studying the structure of individual atoms and molecules, while its short duration makes it possible to follow the kinetics and mechanism of chemical and biological reactions by effecting the selective excitation of the selected degrees of freedom (Fig. 7.49) [42, 64, 66, 77, 126, 137, 152, 173, 174, 179, 210, 236, 238, 248]. This will enable, in particular, studies of three-dimensional biological structures as well as determination of the location and role of its specific constituent structural elements, which is of great importance in developing new-generation medicines and polymers, as well as in constructing complex spatial molecular structures.

In the more distant future, the application of this technique is expected to enable researchers to trace the variation of the electronic spectrum, magnetic properties, reactivity, and other physicochemical properties of clusters under continuous number variation of their constituent atoms from several atoms to solid-state values, $\approx 10^{23}$ atoms.

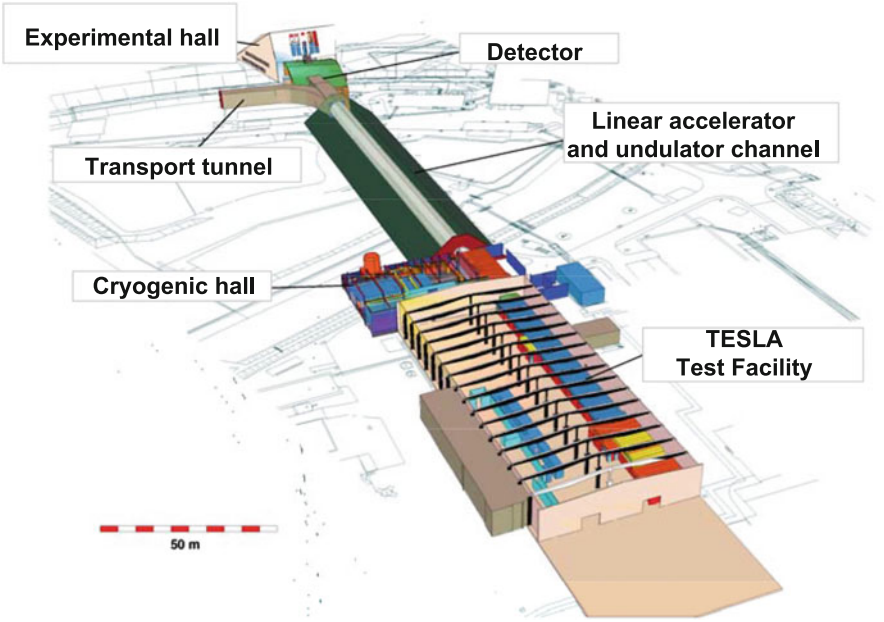

Fig. 7.48 Diagrammatic sketch of the FLASH free-electron laser facility [2, 3]

The physics of shortwave electromagnetic radiation–plasma interactions exhibits significant special features and shows great promise from the standpoint of studies in high energy densities in laser plasma [2, 64, 77, 179, 236, 248]. As we saw in Chap. 5 and Fig. 7.14, the passage to short-wavelength radiation is highly advantageous for this purpose, shifting the critical density, where $\omega_e \approx \omega_p$, to the higher-density domain—from $n_{ec} \approx 10^{21}\,\mathrm{cm}^{-3}$ for infrared to $n_{ec} \approx 10^{24}\,\mathrm{cm}^{-3}$ for ultraviolet radiation. This substantially improves the efficiency of laser energy delivery to the plasma and simplifies the laser interaction physics by shifting the instability thresholds, reducing the importance of nonthermal electrons, surface effects, etc. Owing to the short duration of the laser pulse it heats only the electron component, leaving the ions cool and thereby avoiding hydrodynamic motion at the initial stage of the process and effecting a uniform spatial energy deposition in the substance.

Estimates show [2] that the use of free-electron lasers will enable (by way of bulk heating and the generation of shock and radiation waves) extremely high energy densities to be obtained and investigations of the equation of state, ionic composition, transient dynamics, and optical properties of the plasma under astrophysical conditions to be carried out.

Owing to the high photon energy of the X-ray laser radiation, it is especially well suited for studying multiphoton ionization and producing highly charged ions in laser plasmas. Furthermore, highly ionized states (such as Fe^{+23}) may by produced by means of electron ionization of ions in traps [2]. The electric fields in the vicinity of the nuclei of these ions are tremendous in magnitude, enabling

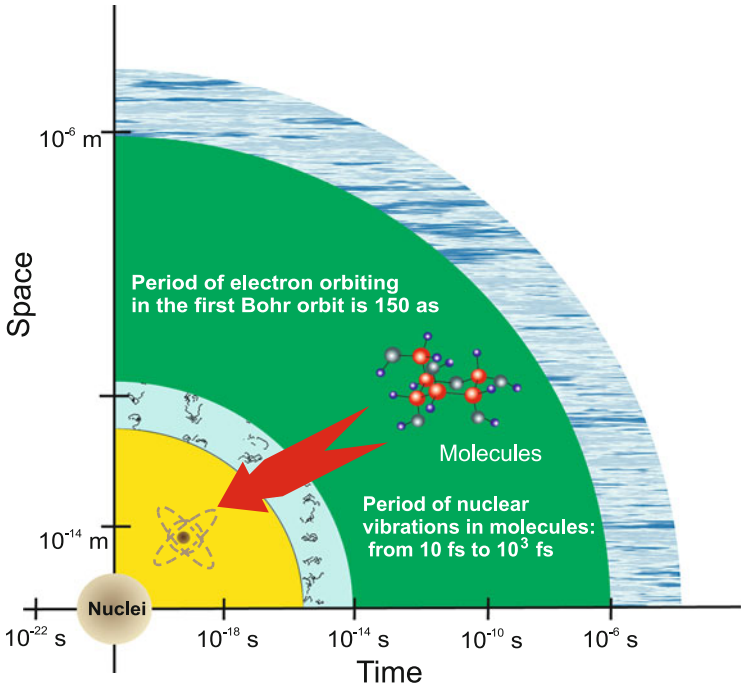

Fig. 7.49 Spatiotemporal characteristics of atomic and nuclear objects [142]

the use of the corresponding spectra (including those occurring in the interaction of the ions with the high-intensity laser field) for a high-precision verification of quantum electrodynamics, which describes electromagnetic forces and is a part of the Standard Model of elementary particles.

The free-electron laser at the Jefferson Laboratory, USA, was used to advantage for the simultaneous generation of high-power femtosecond X-ray radiation (by the interaction of Thomson scattering and the infrared radiation of the electron beam in the wiggler), infrared free-electron laser radiation, and terahertz radiation in the linear accelerator [37, 38, 63, 71].

Several schemes for producing high-intensity electromagnetic radiation with the use of lasers are presently under development. Considered in this connection are the above laser accelerators of femtosecond-long electron beams for the generation of electromagnetic radiation from the gigahertz range to X-rays. This radiation may emerge, for instance, as diffraction or transition radiation of a short particle beam. X-ray radiation may result from the interaction of a relativistic electron beam with a fraction of its parent laser radiation.

A particular lasing scheme is considered as applied to free-electron lasers. According to this scheme, the propagation of a high-intensity electron beam through a plasma with a low (in comparison with the beam density) density leads to the formation of a positively charged plasma cylinder owing to the ejection of

plasma electrons in the radial direction by the leading edge of the laser beam. The relativistic electrons of the beam execute radial betatron oscillations in this ion channel to radiate electromagnetic energy in the X-ray range. This X-ray generation mechanism was proposed and realized in [242]. Similar betatron oscillations are also executed by the electrons captured by the wakefield of a short laser pulse (see Sect. 7.4) [5, 87, 140, 148, 206, 211, 234, 253]. Hard X-ray radiation is also observed in this case.

Of considerable interest is electromagnetic radiation in the terahertz range, which may be employed to carry out diagnostics and spectroscopy of materials in which the transition energy between quantum states is quite low, about 0.01 eV, corresponding to photons with a frequency of the order of a teraherz and a radiation wavelength of 100 μm. These materials include, in particular, practically all organic materials, including biological and medical objects, many semiconductors, and high-temperature superconductors. Not only will the development of high-power terahertz radiation sources open up new vistas for medical diagnostics, but they may also become a reliable tool in the sphere of security (detection of drugs, explosives, etc.).

The terahertz-frequency range extends from far infrared radiation to microwave submillimeter radiation. The methods presently employed for the generation of both optical and microwave radiation are ineffective for the generation of this radiation. The output power of available semiconductor sources, which operate at low temperatures, is at a level of 0.1–0.01 W. With the aid of a free-electron laser it is possible to attain an output power of about 20 W. This power is insufficient for broad application of the terahertz radiation. This is precisely why attention is being paid to a different, new laser-plasma terahertz radiation source, which may exceed a megawatt in power.

The recording of low-frequency electromagnetic radiation of the terahertz range in the irradiation of gaseous and solid-state targets by high-intensity short laser pulses of femtosecond duration was first reported by Hamster et al. [118]. The authors attributed the observed effect to the conversion of terahertz-frequency plasma oscillations, which are excited in the plasma by a laser pulse, to electromagnetic radiation.

The work reported in [118] attracted the attention of researchers primarily from the standpoint of the physical mechanisms underlying the transformation of plasma oscillation energy to electromagnetic radiation and their efficiency, as well as from the standpoint of the properties and power of the electromagnetic radiation that may be obtained in the interaction of high-power short laser pulses with the plasma. The transformation of longitudinal plasma waves to transverse electromagnetic waves is possible, for instance, in the presence of plasma density nonuniformity or under imposition of an external magnetic field.

The generation of low-frequency (terahertz) electromagnetic radiation in the propagation of a short laser through a periodically nonuniform (stratified) plasma was studied in [105] (see also [18, 106, 225]). The effect is related to the transformation of wake plasma fields of the laser pulse to transverse electromagnetic waves by plasma density modulations. This problem, as applied to a plasma with

random nonuniformities, when the laser pulse propagates through the plasma with density fluctuations, was considered in [106].

In a plasma with a regular nonuniformity, the low-frequency terahertz radiation of the laser pulse was investigated both numerically [214] and analytically [215, 216]. The excitation of terahertz radiation by the laser pulse in the plasma is also possible in the presence of an external magnetic field. In this case, the generation of terahertz wave fields is related to the Vavilov–Cherenkov effect, because the velocity of the laser pulse exceeds the phase velocity of the slow extraordinary wave excited by the pulse. This problem was investigated in the cases of transverse propagation of laser pulse relative to the external magnetic field [23, 62, 220, 247, 249] and longitudinal (along the magnetic field) propagation of the laser pulse [109].

The generation of terahertz-frequency electromagnetic waves at the intersection of a plasma boundary by an electric bunch accelerated and formed in the wake wave of the laser pulse was investigated in [159, 160, 209, 240, 241] and is due to the transition Ginzburg–Frank radiation. The low-frequency transition radiation of the laser pulse at its intersection with a tenuous plasma boundary is discussed in [108, 110]. The excitation of terahertz waves traveling from the boundary into vacuum and into the plasma interior is related in this case to the ponderomotive action of the laser pulse and the emergence of an eddy current at the plasma boundary. Along with the generation of bulk electromagnetic waves there also occurs the transition radiation of terahertz surface waves, which travel along the plasma boundary [86].

Terahertz radiation may be generated in a tenuous plasma in the interaction of two counterpropagating short laser pulses [107]. In this case a small-scale standing plasma wave is excited in the interaction region, which produces radiation at double the plasma frequency. The process under discussion is based on the elementary process of two-plasmon coalescence with the production of a photon. The generation of terahertz radiation also occurs in the optical breakdown of a gas when the laser pulse is focused with an axicon. When an external permanent electric field [103] or a microwave field [35] is applied, the ionization wave excites a plasma wave traveling at a supraluminal speed, which is radiated due to the Vavilov–Cherenkov effect.

The phenomenon of terahertz and subterahertz radiation generation in the propagation of a low-intensity laser pulse through the atmosphere has been observed in many experiments (see, for instance, [239]). The authors of [18, 225] attribute the occurrence of this radiation to density modulations in the plasma filament produced in the ionization of the air.

It is pertinent to note that other laser-assisted methods of terahertz radiation production are also discussed in the literature, which rely on nonlinear (four-wave) wave interactions [245].

7.6 Plasma in Accelerators

Charged-particle beams in modern high-energy accelerators are yet another typical example of high-energy density physics [189]. Although the density of these accelerated bunches is not high, their acceleration and the collective interaction between themselves and the accelerating fields corresponds to substantial energy densities. Moreover, slight variation of relative particle velocities after laser or electron cooling results in high values of the nonideality parameter of such beam-produced plasma.

A demonstration example is "crystalline" beams [205, 208], which emerge under the laser cooling of ions accelerated in a synchrotron. When the relative ion velocity corresponds to a temperature on the order of millikelvins, the Coulomb interaction effects become significant and give rise to the "crystallization" of this plasma (Fig. 7.50).

Other mechanisms of plasma generation in accelerators are also possible [189]. The plasma may emerge under the action of the cyclotron radiation of accelerated particles, in the ionization of the residual gas, or when the beam finds itself at the wall. In the last-mentioned case, for the GSI and CERN LHC accelerators the energy releases involved stretch into the megajoule range [82, 231]. In this case, the emergent electrons with a density of 10^5–$10^7\ \mathrm{cm}^{-3}$ arrive at the center of the acceleration channel to give rise to a two-stream "beam–plasma" instability, cause a loss of the particles under acceleration, and impair the beam emittance. In many

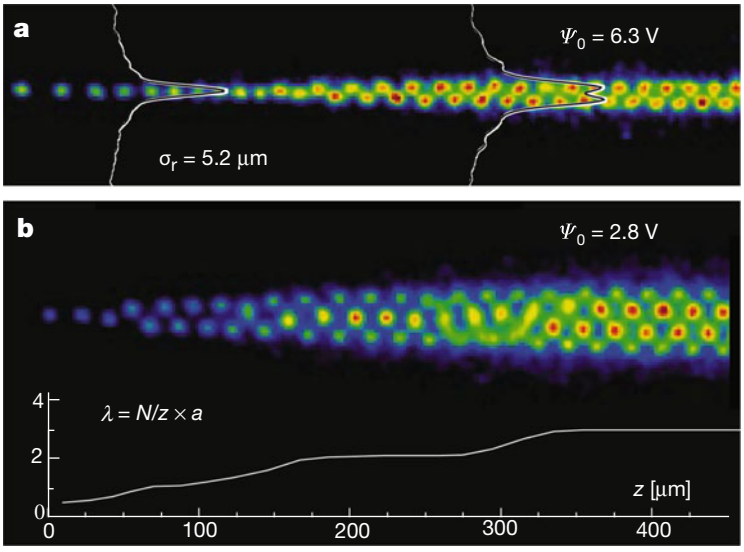

Fig. 7.50 Crystalline beams in accelerators [205, 208]

respects these processes are similar to the effects occurring in laser plasmas and may be analyzed by the methods of high-energy-density physics.

A broad spectrum of plasma states with high energy densities emerges in the operation of pulsed high-current accelerators and high-power microwave generators [176, 177]. The application of a high (megaelectronvolt) pulsed voltage to the vacuum gap in these devices results in the electric microexplosion of cathodic micropoints and the explosive emission of high-current electron beams. The energy densities attainable in this case amount to $\approx$1–10 MJ/cm^3 for pressures ranging into megabars. The accelerators and microwave generators designed on this principle find wide industrial application and are a demonstration of the practical use of basic research in high-energy-density physics.

The next generation of high-power lasers will make it possible to achieve power densities $> 10^{23}$ W/cm^2, whereby the longitudinal electric field will be >1 TV/cm. Particles in these fields may be accelerated to relativistic energies over short distances, which lengthens their lifetime.

Calculations [196] show that the irradiation of a metallic target at an intensity of 10^{23} W/cm^2 may produce 5 GeV protons, which in turn may give rise to pions with a lifetime of $\approx$20 ns, the laser irradiation lasting for $\approx$10 fs. By employing the laser acceleration mechanism it is possible to rapidly (in several picoseconds) raise the energy and lifetime of the pions by a factor of 100 to 15 GeV and 2 μs. This lengthened lifetime basically makes it possible to take advantage of conventional acceleration techniques to accelerate pions to the gigaelectronvolt range, where pions will decay into muon and neutrino beams.

A pion source would be of interest for the development of accelerators of pions as particles without quark structure and producing a weaker synchrotron radiation. Devices for studying gamma–gamma collisions might become another elegant direction of combined use of accelerators [189] and lasers.

References

1. Fair project web site
2. New flash brochure, http://hasylab.desy.de/news_events/announcements/new_flash_brochure/
3. The European X-Ray Laser Project XFEL http://xfel.desy.de/
4. ITER Physics Basic, vol. 39 (1999)
5. Albert, F., Phuoc, K.T., Shah, R., et al.: Full characterization of a laser-produced keV X-ray betatron source. Plasma Phys. Control. Fusion **50**(12), 124008 (2008)
6. Andreev, N.E., Gorbunov, L.M.: Laser-plasma acceleration of electrons. Phys. Usp. **42**(1), 49 (1999)
7. Andreev, N.E., Gorbunov, L.M., Kirsanov, V.I., et al.: The theory of laser self-resonant wake field excitation. Phys. Scr. **49**(1), 101–109 (1994)
8. Andreev, N.E., Kirsanov, V.I., Gorbunov, L.M.: Stimulated processes and self-modulation of a short intense laser pulse in the laser wake-field accelerator. Phys. Plasmas **2**(6), 2573–2582 (1995)

9. Andreev, N.E., Kirsanov, V.I., Sakharov, A.S., et al.: On the phase velocity of plasma waves in a self-modulated laser wake-field accelerator. Phys. Plasmas **3**(8), 3121–3128 (1996)
10. Andreev, N.E., Gorbunov, L.M., Kirsanov, V.I., et al.: Structure of the wake field in plasma channels. Phys. Plasmas **4**(4), 1145–1153 (1997)
11. Andreev, N.E., Gorbunov, L.M., Kirsanov, V.I., Sakharov, A.S.: Self-modulation of high-intensity laser pulses in underlense plasmas and plasma channels. AIP Conf. Proc. **396**(1), 61–74 (1997)
12. Andreev, N.E., Chizhonkov, E.V., Frolov, A.A., Gorbunov, L.M.: On laser wakefield acceleration in plasma channels. Nucl. Instrum. Methods Phys. Res. A **410**(3), 469–476 (2002)
13. Andreev, N.E., Cros, B., Gorbunov, L.M., et al.: Laser wakefield structure in a plasma column created in capillary tubes. Phys. Plasmas **9**(9), 3999–4009 (2002)
14. Andreev, N.E., Nishida, Y., Yugami, N.: Propagation of short intense laser pulses in gas-filled capillaries. Phys. Rev. E **65**(5), 056407 (2002)
15. Andreev, N.E., Kuznetsov, S.V., Cros, B., et al.: Laser wakefield acceleration of supershort electron bunches in guiding structures. Plasma Phys. Control. Fusion **53**(1), 014001 (2011)
16. Antonsen Jr., T.M., Mora, P.: Self-focusing and Raman scattering of laser pulses in tenuous plasmas. Phys. Rev. Lett. **69**(15), 2204–2207 (1992)
17. Antonsen Jr., T.M., Mora, P.: Self-focusing and Raman scattering of laser pulses in tenuous plasmas. Phys. Fluids B **5**(5), 1440–1452 (1993)
18. Antonsen Jr., T.M., Palastro, J., Milchberg, H.M.: Excitation of terahertz radiation by laser pulses in nonuniform plasma channels. Phys. Plasmas **14**(3), 033107 (2007)
19. Atzeni, S., Meyer-ter-Vehn, J.: The Physics of Inertial Fusion. Oxford University Press, Oxford (2004)
20. Atzeni, S., Temporal, M., Honrubia, J.J.: A first analysis of fast ignition of precompressed ICF fuel by laser-accelerated protons. Nucl. Fusion **42**(3), L1–L4 (2002)
21. Azizov, E.A.: Tokamaks: from A D Sakharov to the present (the 60-year history of tokamaks). Phys. Usp. **55**(2), 190–203 (2012)
22. Bakhmetjev, I.E., Fertman, A.D., Golubev, A.A., et al.: Research into the advanced experimental methods for precision ion stopping range measurements in matter. Laser Part. Beams **21**(1), 1–6 (2003)
23. Bakunov, M.I., Bodrov, S.B., Maslov, A.V., Sergeev, A.M.: Two-dimensional theory of Cherenkov radiation from short laser pulses in a magnetized plasma. Phys. Rev. E **70**(1), 016401 (2004)
24. Bamber, C., Boege, S.J., Koffas, T., et al.: Studies of nonlinear QED in collisions of 46.6 GeV electrons with intense laser pulses. Phys. Rev. D **60**(9), 092004 (1999)
25. Batani, D., Jafer, R., Redaelli, R., et al.: Effects of laser prepulse on proton generation. Nucl. Instrum. Methods Phys. Res. A **620**(1), 76–82 (2010)
26. Belyaev, V.S., Krainov, V.P., Lisitsa, V.S., Matafonov, A.P.: Generation of fast charged particles and superstrong magnetic fields in the interaction of ultrashort high-intensity laser pulses with solid targets. Phys. Usp. **51**(8), 793 (2008)
27. Berezhiani, V.I., Murusidze, I.G.: e^+e^- – Pair production by a focused laser pulse in vacuum. Phys. Lett. A **148**(6–7), 338–340 (1990)
28. Berg, L., Skupin, S., Nuter, R., et al.: Ultrashort filaments of light in weakly ionized, optically transparent media. Rep. Prog. Phys. **70**(10), 1633 (2007)
29. Betti, R., Chang, P.Y., Spears, B.K., et al.: Thermonuclear ignition in inertial confinement fusion and comparison with magnetic confinement. Phys. Plasmas **17**(5), 058102 (2010)
30. Bieniosek, F., Barnard, J., Leitner, M., et al.: Diagnostics for near-term warm dense matter experiments. Nucl. Instrum. Methods Phys. Res. A **577**(1–2), 284–288 (2007)
31. Bulanov, S.V., Kirsanov, V.I., Sakharov, A.S.: Excitation of ultrarelativistic plasma waves by pulse of electromagnetic radiation. JETP Lett. **50**(4), 198 (1991)
32. Bulanov, S.S., Bychenkov, V.Y., Chvykov, V., et al.: Generation of GeV protons from 1 PW laser interaction with near critical density targets. Phys. Plasmas **17**(4), 043105 (2010)
33. Bulanov, S.V., Echkina, E.Y., Esirkepov, T.Z., et al.: Unlimited ion acceleration by radiation pressure. Phys. Rev. Lett. **104**, 135003 (2010)

34. Bychenkov, V.Y., Rozmus, W., Maksimchuk, A., et al.: Fast ignitor concept with light ions. Plasma Phys. Rep. **27**(12), 1017–1020 (2001)
35. Bystrov, A.M., Vvedenskii, N.V., Gildenburg, V.B.: Generation of terahertz radiation upon the optical breakdown of a gas. JETP Lett. **82**(12), 753–757 (2005)
36. Callahan, D.A., Meezan, N.B., Glenzer, S.H., et al.: The velocity campaign for ignition on NIF. Phys. Plasmas **19**(5), 056305 (2012)
37. Carr, G.L., Martin, M.C., McKinney, W.R., et al.: High-power terahertz radiation from relativistic electrons. Nature **420**(6912), 153–156 (2002)
38. Carr, G.L., Martin, M.C., McKinney, W.R., et al.: Very high power THz radiation at Jefferson Lab. Phys. Med. Biol. **47**(21), 3761–3764 (2002)
39. Cavailler, C.: Inertial fusion with the LMJ. Plasma Phys. Control. Fusion **47**(12B), B389–B403 (2005)
40. Chalupský, J., Juha, L., Hájková, V., et al.: Non-thermal desorption/ablation of molecular solids induced by ultra-short soft X-ray pulses. Opt. Express **17**(1), 208–217 (2009)
41. Chang, P., Betti, R., Spears, B.K., et al.: Generalized measurable ignition criterion for inertial confinement fusion. Phys. Rev. Lett. **104**, 135002 (2010)
42. Chapman, H.N., Fromme, P., Barty, A., et al.: Femtosecond X-ray protein nanocrystallography. Nature **470**(2), 73–77 (2011)
43. Chen, F.F.: Introduction to Plasma Physics and Controlled Fusion, vol. 1, 2nd edn. Springer, New York (1984)
44. Chen, L.M., Liu, F., Wang, W.M., et al.: Intense high-contrast femtosecond *K*-shell X-ray source from laser-driven Ar clusters. Phys. Rev. Lett. **104**, 215004 (2010)
45. Clark, T.R., Milchberg, H.M.: Optical mode structure of the plasma waveguide. Phys. Rev. E **61**(2), 1954–1965 (2000)
46. Clark, E.L., Krushelnick, K., Davies, J.R., et al.: Measurements of energetic proton transport through magnetized plasma from intense laser interactions with solids. Phys. Rev. Lett. **84**(4), 670–673 (2000)
47. Clark, D.S., Haan, S.W., Cook, A.W., et al.: Short-wavelength and three-dimensional instability evolution in national ignition facility ignition capsule designs. Phys. Plasmas **18**(8), 082701 (2011)
48. Colgan, J., Abdallah Jr., J., Faenov, A.Y., et al.: Observation and modeling of high resolution spectral features of the inner-shell X-ray emission produced by 10^{-10} contrast femtosecond-pulse laser irradiation of argon clusters. High Energy Density Phys. **7**(2), 77–83 (2011)
49. Collins, S.H., et al.: In: The 17th APS Shock Compression of Condensed Matter, Chicago (2011)
50. Couairon, A., Mysyrowicz, A.: Femtosecond filamentation in transparent media. Phys. Rep. **441**(2–4), 47–189 (2007)
51. Courtois, C., Couairon, A., Cros, B., et al.: Propagation of intense ultrashort laser pulses in a plasma filled capillary tube: simulations and experiments. Phys. Plasmas **8**(7), 3445–3456 (2001)
52. Cros, B., Courtois, C., Malka, G., et al.: Excitation of accelerating wakefields in inhomogeneous plasmas. IEEE Trans. Plasma Sci. **28**(4), 1071–1077 (2000)
53. Cuneo, M.E., Vesey, R.A., Bennett, G.R., et al.: Progress in symmetric ICF capsule implosions and wire-array Z-pinch source physics for double-pinch-driven hohlraums. Plasma Phys. Control. Fusion **48**(2), R1–R35 (2006)
54. Decker, C.D., Mori, W.B., Tzeng, K.C., Katsouleas, T.C.: Modeling single-frequency laser-plasma acceleration using particle-in-cell simulations: the physics of beam breakup. IEEE Trans. Plasma Sci. **24**(2), 379–392 (1996)
55. DESY: PETRA III: http://petraiii.desy.de/
56. Didenko, A., Rashchikov, V., Fortov, V.: On possibility of high-power terahertz emission from target under the action of powerful laser pulses. Tech. Phys. Lett. **37**, 256–258 (2011). doi:10.1134/S1063785011030205
57. Ditmire, T., Tisch, J.W.G., Springate, E., et al.: High-energy ions produced in explosions of superheated atomic clusters. Nature **386**(6620), 54–56 (1997)

58. Ditmire, T., Springate, E., Tisch, J.W., et al.: Explosion of atomic clusters heated by high-intensity femtosecond laser pulses. Phys. Rev. A **57**(1), 369–382 (1998)
59. Ditmire, T., Zweiback, J., Yanovsky, V.P., et al.: Nuclear fusion from explosions of femtosecond laser-heated deuterium clusters. Nature **398**(6727), 489–492 (1999)
60. Ditmire, T., Zweiback, J., Yanovsky, V.P., et al.: Nuclear fusion in gases of deuterium clusters heated with a femtosecond laser. Phys. Plasmas **7**(5), 1993–1998 (2000)
61. Döppner, T., Thomas, C.A., Divol, L., et al.: Direct measurement of energetic electrons coupling to an imploding low-adiabat inertial confinement fusion capsule. Phys. Rev. Lett. **108**, 135006 (2012)
62. Dorranian, D., Starodubtsev, M., Kawakami, H., et al.: Radiation from high-intensity ultrashort-laser-pulse and gas-jet magnetized plasma interaction. Phys. Rev. E **68**(2), 026409 (2003)
63. Douglas, D.R., Jordan, K.C., Merminga, L., et al.: Experimental investigation of multibunch, multipass beam breakup in the Jefferson Laboratory free electron laser upgrade driver. Phys. Rev. ST Accel. Beams **9**(6), 064403 (2006)
64. Doumy, G., Roedig, C., Son, S.K., et al.: Nonlinear atomic response to intense ultrashort X rays. Phys. Rev. Lett. **106**, 083002 (2011)
65. Durfee III, C.G., Milchberg, H.M.: Light pipe for high intensity laser pulses. Phys. Rev. Lett. **71**(15), 2409–2412 (1993)
66. Dzelzainis, T., Chalupsky, J., Fajardo, M., et al.: Plasma emission spectroscopy of solids irradiated by intense XUV pulses from a free electron laser. High Energy Density Phys. **6**(1), 109–112 (2010)
67. Echkina, E., Inovenkov, I., Esirkepov, T., et al.: Dependence of the ion energy on the parameters of the laser pulse and target in the radiation-pressure-dominated regime of acceleration. Plasma Phys. Rep. **36**, 15–29 (2010). doi:10.1134/S1063780X10010022
68. Efremov, V.P., Pikuz Jr., S.A., Faenov, A.Y., et al.: Study of the energy release region of a heavy-ion flux in nanomaterials by X-ray spectroscopy of multicharged ions. JETP Lett. **81**(8), 378 (2005)
69. Egorov, I.: Zvezdy na Zemle: Termoyad (Stars on the Earth: thermonuclear fusion). Popul-yarnaya Mekhanika (5), 86 (2012)
70. Eloy, M., Azambuja, R., Mendonca, J.T., Bingham, R.: Interaction of ultrashort high-intensity laser pulses with atomic clusters. Phys. Plasmas **8**(3), 1084–1086 (2001)
71. Esarey, E., Sprangle, P., Krall, J., Ting, A.: Overview of plasma-based accelerator concepts. IEEE Trans. Plasma Sci. **24**(2), 252–288 (1996)
72. Esarey, E., Schroeder, C.B., Leemans, W.P.: Physics of laser-driven plasma-based electron accelerators. Rev. Mod. Phys. **81**, 1229–1285 (2009)
73. Esirkepov, T.Z., Bulanov, S.V., Nishihara, K., et al.: Proposed double-layer target for the generation of high-quality laser-accelerated ion beams. Phys. Rev. Lett. **89**(17), 175003 (2002)
74. Esirkepov, T., Borghesi, M., Bulanov, S.V., et al.: Highly efficient relativistic-ion generation in the laser-piston regime. Phys. Rev. Lett. **92**(17), 175003 (2004)
75. Esirkepov, T., Yamagiwa, M., Tajima, T.: Laser ion-acceleration scaling laws seen in multiparametric particle-in-cell simulations. Phys. Rev. Lett. **96**(10), 105001 (2006)
76. Faure, J., Glinec, Y., Pukhov, A., et al.: A laserplasma accelerator producing monoenergetic electron beams. Nature **431**(7008), 541–544 (2004)
77. Fäustlin, R.R., Bornath, T., Döppner, T., et al.: Observation of ultrafast nonequilibrium collective dynamics in warm dense hydrogen. Phys. Rev. Lett. **104**, 125002 (2010)
78. Flacco, A., Ceccotti, T., George, H., et al.: Comparative study of laser ion acceleration with different contrast enhancement techniques. Nucl. Instrum. Methods Phys. Res. A **620**(1), 18–22 (2010)
79. Fortov, V.E. (ed.): Entsiklopediya nizkotemperaturnoi plazmy (Encyclopedia of Low-Temperature Plasma). Nauka, Moscow (2000)
80. Fortov, V.E.: Intense Shock Waves and Extreme States of Matter. Bukos, Moscow (2005)

81. Fortov, V.E., Ivlev, A.V., Khrapak, S.A., et al.: Complex (dusty) plasma: current status, open issues, perspectives. Phys. Rep. **421**(1), 1–103 (2005)
82. Fortov, V.E., Hoffmann, D.H.H., Sharkov, B.Y.: Intense ion beams for generating extreme states of matter. Phys. Usp. **51**(2), 109 (2008)
83. Fourkal, E., Shahine, B., Ding, M., et al.: Particle in cell simulation of laser-accelerated proton beams for radiation therapy. Med. Phys. **29**(12), 2788–2798 (2002)
84. Fourkal, E., Li, J.S., Xiong, W., et al.: Intensity modulated radiation therapy using laser-accelerated protons: a Monte Carlo dosimetric study. Phys. Med. Biol. **48**(24), 3977–4000 (2003)
85. Frenje, J.A., Casey, D.T., Li, C.K., et al.: Probing high areal-density cryogenic deuterium-tritium implosions using downscattered neutron spectra measured by the magnetic recoil spectrometer. Phys. Plasmas **17**(5), 056311 (2010)
86. Frolov, A.A.: Excitation of surface waves at a plasma boundary by a short laser pulse. Plasma Phys. Rep. **33**(3), 179–188 (2007)
87. Fuchs, M., Weingartner, R., Popp, A., Major, Z., Becker, S., Osterhoff, J., Cortrie, I., Zeitler, B., Horlein, R., Tsakiris, G.D., Schramm, U., Rowlands-Rees, T.P., Hooker, S.M., Habs, D., Krausz, F., Karsch, S., Grüner, F.: Laser-driven soft-X-ray undulator source. Nat. Phys. **5**(09), 826–829 (2009)
88. Fukuda, Y., Faenov, A.Y., Pikuz, T., et al.: Soft X-ray source for nanostructure imaging using femtosecond-laser-irradiated clusters. Appl. Phys. Lett. **92**(12), 121110 (2008)
89. Fukuda, Y., Faenov, A.Y., Tampo, M., et al.: Energy increase in multi-MeV ion acceleration in the interaction of a short pulse laser with a cluster-gas target. Phys. Rev. Lett. **103**, 165002 (2009)
90. Gaillard, S.A., et al.: Abstract no. g06.003. In: Proceedings of the APS 51st Annual Meeting of the Division of Plasma Physics. APS, New York (2009)
91. Gaillard, S.A., Flippo, K.A., Lowenstern, M.E., et al.: Proton acceleration from ultrahigh-intensity short-pulse laser-matter interactions with cu micro-cone targets at an intrinsic $\sim 10^8$ contrast. J. Phys.: Conf. Ser. **244**(2), 022034 (2010)
92. Gavrilenko, V.P., Faenov, A.Y., Magunov, A.I., et al.: Observation of modulations in Lyman-α line profiles of multicharged ions in clusters irradiated by femtosecond laser pulses: effect of a dynamic electric field. Phys. Rev. A **73**, 013203 (2006)
93. Geddes, C.G.R., Tóth, C., van Tilborg, J., et al.: High-quality electron beams from a laser wakefield accelerator using plasma-channel guiding. Nature **431**(7008), 538–541 (2004)
94. Giannessi, L., Bacci, A., Bellaveglia, M., et al.: Self-amplified spontaneous emission free-electron laser with an energy-chirped electron beam and undulator tapering. Phys. Rev. Lett. **106**, 144801 (2011)
95. Gizzi, L., Betti, S., Frster, E., et al.: Laser-accelerated ions from layered targets. Nucl. Instrum. Methods Phys. Res. A **620**(1), 83–87 (2010)
96. Glebov, V.Y., Forrest, C., Knauer, J.P., et al.: Testing a new NIF neutron time-of-flight detector with a bibenzyl scintillator on OMEGA. Rev. Sci. Instrum. **83**(10), 10D309 (2012)
97. Glenzer, S.H.: Update on the national ignition campaign (2012)
98. Glenzer, S.H., MacGowan, B.J., Michel, P., et al.: Symmetric inertial confinement fusion implosions at ultra-high laser energies. Science **327**(5970), 1228–1231 (2010)
99. Glenzer, S.H., MacGowan, B.J., Meezan, N.B., et al.: Publisher's note: demonstration of ignition radiation temperatures in indirect-drive inertial confinement fusion hohlraums [Phys. Rev. Lett. 106, 085004 (2011)]. Phys. Rev. Lett. **106**, 109903 (2011)
100. Glenzer, S.H., MacGowan, B.J., Meezan, N.B., et al.: Demonstration of ignition radiation temperatures in indirect-drive inertial confinement fusion hohlraums. Phys. Rev. Lett. **106**, 085004 (2011)
101. Glenzer, S.H., Callahan, D.A., MacKinnon, A.J., et al.: Cryogenic thermonuclear fuel implosions on the national ignition facility. Phys. Plasmas **19**(5), 056318 (2012)
102. Glenzer, S.H., Spears, B.K., Edwards, M.J., et al.: First implosion experiments with cryogenic thermonuclear fuel on the national ignition facility. Plasma Phys. Control. Fusion **54**(4), 045013 (2012)

103. Golubev, S.V., Suvorov, E.V., Shalashov, A.G.: On the possibility of terahertz wave generation upon dense gas optical breakdown. JETP Lett. **79**(8), 361–364 (2004)
104. Goncharov, V.N., Sangster, T.C., Boehly, T.R., et al.: Demonstration of the highest deuterium-tritium areal density using multiple-picket cryogenic designs on OMEGA. Phys. Rev. Lett. **104**, 165001 (2010)
105. Gorbunov, L.M., Frolov, A.A.: Emission of low-frequency electromagnetic waves by a short laser pulse in stratified rarefied plasma. J. Exp. Theor. Phys. **83**(5), 967–973 (1996)
106. Gorbunov, L.M., Frolov, A.A.: Emission of low-frequency electromagnetic waves by a short laser pulse propagating in a plasma with density fluctuations. Plasma Phys. Rep. **26**(8), 646–656 (2000)
107. Gorbunov, L.M., Frolov, A.A.: Electromagnetic radiation at twice the plasma frequency emitted from the region of interaction of two short laser pulses in a rarefied plasma. J. Exp. Theor. Phys. **98**(3), 527–537 (2004)
108. Gorbunov, L.M., Frolov, A.A.: Low-frequency transition radiation from a short laser pulse at the plasma boundary. J. Exp. Theor. Phys. **102**(6), 894–901 (2006)
109. Gorbunov, L.M., Frolov, A.A.: On the theory of Cherenkov emission from a short laser pulse in a magnetized plasma. Plasma Phys. Rep. **32**(6), 500–513 (2006)
110. Gorbunov, L.M., Frolov, A.A.: Transition radiation generated by a short laser pulse at a plasma–vacuum interface. Plasma Phys. Rep. **32**(10), 850–865 (2006)
111. Gorbunov, L.M., Kirsanov, V.I.: The excitation of plasma waves by an electromagnetic wave packet. J. Exp. Theor. Phys. **93**, 509 (1987) (in Russian)
112. Gorbunov, L., Kirsanov, V., et al.: In: Trudy FIAN, vol. 219, p. 3. Nauka, Moscow (1992)
113. Gorbunov, L.M., Kalmykov, S.Y., Mora, P.: Laser wakefield acceleration by petawatt ultrashort laser pulses. Phys. Plasmas **12**(3), 033101 (2005)
114. Gordienko, S., Pukhov, A.: Scalings for ultrarelativistic laser plasmas and quasimonoenergetic electrons. Phys. Plasmas **12**(4), 043109 (2005)
115. Haan, S.W., Lindl, J.D., Callahan, D.A., et al.: Point design targets, specifications, and requirements for the 2010 ignition campaign on the national ignition facility. Phys. Plasmas **18**(5), 051001 (2011)
116. Hafz, N.A.M., Jeong, T.M., Choi, I.W., et al.: Stable generation of GeV-class electron beams from self-guided laser-plasma channels. Nat. Photonics **2**, 571–577 (2008)
117. Hammel, B.A., Scott, H.A., Regan, S.P., et al.: Diagnosing and controlling mix in National Ignition Facility implosion experiments. Phys. Plasmas **18**(5), 056310 (2011)
118. Hamster, H., Sullivan, A., Gordon, S., et al.: Subpicosecond, electromagnetic pulses from intense laser-plasma interaction. Phys. Rev. Lett. **71**(17), 2725–2728 (1993)
119. Hatchett, S.P., Brown, C.G., Cowan, T.E., et al.: Electron, photon, and ion beams from the relativistic interaction of petawatt laser pulses with solid targets. Phys. Plasmas **7**(5), 2076–2082 (2000)
120. Hau-Riege, S.P., London, R.A., Bionta, R.M., et al.: Wavelength dependence of the damage threshold of inorganic materials under extreme-ultraviolet free-electron-laser irradiation. Appl. Phys. Lett. **95**(11), 111104 (2009)
121. Hayashi, Y., Pirozhkov, A.S., Kando, M., et al.: Efficient generation of Xe K-shell X-rays by high-contrast interaction with submicrometer clusters. Opt. Lett. **36**(9), 1614–1616 (2011)
122. Hegelich, B.M., Albright, B.J., Cobble, J., et al.: Laser acceleration of quasi-monoenergetic MeV ion beams. Nature **439**, 441–444 (2006)
123. Henig, A., Kiefer, D., Markey, K., et al.: Enhanced laser-driven ion acceleration in the relativistic transparency regime. Phys. Rev. Lett. **103**, 045002 (2009)
124. Henig, A., Steinke, S., Schnürer, M., et al.: Radiation-pressure acceleration of ion beams driven by circularly polarized laser pulses. Phys. Rev. Lett. **103**, 245003 (2009)
125. Hicks, D.G., Spears, B.K., Braun, D.G., et al.: Convergent ablator performance measurements. Phys. Plasmas **17**(10), 102703 (2010)
126. Hoener, M., Fang, L., Kornilov, O., et al.: Ultraintense X-ray induced ionization, dissociation, and frustrated absorption in molecular nitrogen. Phys. Rev. Lett. **104**, 253002 (2010)

127. Hoffmann, D.H.H., Fortov, V.E., Lomonosov, I.V., et al.: Unique capabilities of an intense heavy ion beam as a tool for equation-of-state studies. Phys. Plasmas **9**(9), 3651–3654 (2002)
128. Hoffmann, D., Tahir, N., Udrea, S., et al.: High energy density physics with heavy ion beams and related interaction phenomena. Contrib. Plasma Phys. **50**(1), 7–15 (2010)
129. Hogan, W.J. (ed.): Energy from Inertial Fusion. IAEA, Vienna (1995)
130. Honrubia, J.J., Fernández, J.C., Temporal, M., et al.: Fast ignition of inertial fusion targets by laser-driven carbon beams. Phys. Plasmas **16**(10), 102701 (2009)
131. Hooker, S.M., Spence, D.J., Smith, R.A.: Guiding of high-intensity picosecond laser pulses in a discharge-ablated capillary waveguide. J. Opt. Soc. Am. B **17**(1), 90–98 (2000)
132. Hosokai, T., Zhidkov, A., Yamazaki, A., et al.: Electron energy boosting in laser-wake-field acceleration with external magnetic field $B \sim 1$ T and laser prepulses. Appl. Phys. Lett. **96**(12), 121501 (2010)
133. Huang, L.G., Lei, A.L., Bin, J.H., et al.: Improving proton acceleration with circularly polarized intense laser pulse by radial confinement with heavy ions. Phys. Plasmas **17**(1), 013106 (2010)
134. Huntington, C.M., Thomas, A.G.R., McGuffey, C., et al.: Current filamentation instability in laser wakefield accelerators. Phys. Rev. Lett. **106**, 105001 (2011)
135. Inogamov, N.A., Anisimov, S.I., Zhakhovsky, V.V., et al.: Ablation by short optical and X-ray laser pulses. In: Proc. SPIE 7996, Fundamentals of Laser-Assisted Micro- and Nanotechnologies 2010, p. 79960T (2010)
136. Inogamov, N.A., Faenov, A.Y., Zhakhovsky, V.V., et al.: Two-temperature warm dense matter produced by ultrashort extreme vacuum ultraviolet-free electron laser (EUV-FEL) pulse. Contrib. Plasma Phys. **51**(5), 419–426 (2011)
137. Jiang, Y.H., Rudenko, A., Pérez-Torres, J.F., et al.: Investigating two-photon double ionization of D_2 by XUV-pump–XUV-probe experiments. Phys. Rev. A **81**, 051402 (2010)
138. Johnson, M.G., Frenje, J.A., Casey, D.T., et al.: Neutron spectrometry—an essential tool for diagnosing implosions at the national ignition facility (invited). Rev. Sci. Instrum. **83**(10), 10D308 (2012)
139. Joshi, C.: Plasma accelerators. Sci. Am. **294**(2), 40–47 (2006)
140. Kando, M., Pirozhkov, A.S., Kawase, K., et al.: Enhancement of photon number reflected by the relativistic flying mirror. Phys. Rev. Lett. **103**, 235003 (2009)
141. Kaplan, A.E., Dubetsky, B.Y., Shkolnikov, P.L.: Shock shells in Coulomb explosions of nanoclusters. Phys. Rev. Lett. **91**(14), 143401 (2003)
142. Khazanov, E.A., Sergeev, A.M.: Petawatt laser based on optical parametric amplifiers: their state and prospects. Phys. Usp. **51**(9), 969 (2008)
143. Khorsand, A.R., Sobierajski, R., Louis, E., et al.: Single shot damage mechanism of Mo/Si multilayer optics under intense pulsed XUV-exposure. Opt. Express **18**(2), 700–712 (2010)
144. Kim, K.Y., Milchberg, H.M., Faenov, A.Y., et al.: X-ray spectroscopy of 1 cm plasma channels produced by self-guided pulse propagation in elongated cluster jets. Phys. Rev. E **73**, 066403 (2006)
145. Kirzhnits, D.A.: Extremal states of matter (ultrahigh pressures and temperatures). Sov. Phys. – Usp. **14**(4), 512–523 (1972)
146. Kishimoto, Y., Masaki, T., Tajima, T.: High energy ions and nuclear fusion in laser-cluster interaction. Phys. Plasmas **9**(2), 589–601 (2002)
147. Kline, J.L., Glenzer, S.H., Olson, R.E., et al.: Observation of high soft X-ray drive in large-scale hohlraums at the National Ignition Facility. Phys. Rev. Lett. **106**, 085003 (2011)
148. Kneip, S., McGuffey, C., Martins, J.L., et al.: Bright spatially coherent synchrotron X-rays from a table-top source. Nat. Phys. **6**(10), 980–983 (2010)
149. Kodama, R., Norreys, P.A., Mima, K., et al.: Fast heating of ultrahigh-density plasma as a step towards laser fusion ignition. Nature **412**(6849), 798–802 (2001)
150. Konyukhov, A.V., Likhachev, A.P., Oparin, A.M., et al.: Numerical modeling of shock-wave instability in thermodynamically nonideal media. J. Exp. Theor. Phys. **98**(4), 811–819 (2004)
151. Krall, J., Ting, A., Esarey, E., Sprangle, P.: Enhanced acceleration in a self-modulated-laser wake-field accelerator. Phys. Rev. E **48**(3), 2157–2161 (1993)

152. Krikunova, M., Maltezopoulos, T., Azima, A., et al.: Time-resolved ion spectrometry on xenon with the jitter-compensated soft X-ray pulses of a free-electron laser. New J. Phys. **11**(12), 123019 (2009)
153. Kruer, W.L.: The Physics of Laser Plasma Interactions. Addison-Wesley, Reading, MA (1988)
154. Kugland, N.L., Neumayer, P., Döppner, T., et al.: High contrast Kr gas jet K alpha X-ray source for high energy density physics experiments. Rev. Sci. Instrum. **79**(10), 10E917 (2008)
155. Kyrala, G.A., Seifter, A., Kline, J.L., et al.: Tuning indirect-drive implosions using cone power balance. Phys. Plasmas **18**(7), 072703 (2011)
156. Landen, O.L., Edwards, J., Haan, S.W., et al.: Capsule implosion optimization during the indirect-drive National Ignition Campaign. Phys. Plasmas **18**(5), 051002 (2011)
157. Last, I., Schek, I., Jortner, J.: Energetics and dynamics of Coulomb explosion of highly charged clusters. J. Chem. Phys. **107**(17), 6685–6692 (1997)
158. Lee, K., Lee, J.Y., Park, S.H., et al.: Dominant front-side acceleration of energetic proton beams from plastic targets irradiated by an ultraintense laser pulse. Phys. Plasmas **18**(1), 013101 (2011)
159. Leemans, W.P., Geddes, C.G.R., Faure, J., et al.: Observation of terahertz emission from a laser-plasma accelerated electron bunch crossing a plasma-vacuum boundary. Phys. Rev. Lett. **91**(7), 074802 (2003)
160. Leemans, W.P., van Tilborg, J., Faure, J., et al.: Terahertz radiation from laser accelerated electron bunches. Phys. Plasmas **11**(5), 2899–2906 (2004)
161. Leemans, W.P., Nagler, B., Gonsalves, A.J., et al.: GeV electron beams from a centimetre-scale accelerator. Nat. Phys. **2**(10), 696–699 (2006)
162. Li, C.K., Sguin, F.H., Frenje, J.A., et al.: Charged-particle probing of X-ray driven inertial-fusion implosions. Science **327**(5970), 1231–1235 (2010)
163. Lifschitz, A.F., Faure, J., Malka, V., Mora, P.: GeV wakefield acceleration of low energy electron bunches using petawatt lasers. Phys. Plasmas **12**(9), 093104 (2005)
164. Lindl, J.D.: Inertial Confinement Fusion. Springer, New York (1998)
165. Lindli, J.D.: Nif ignition target design, requirements, margins, and uncertainties. In: Proceedings of 6th International Conference IFSA, San Francisco (2009)
166. Lu, H.Y., Liu, J.S., Wang, C., et al.: Efficient fusion neutron generation from heteronuclear clusters in intense femtosecond laser fields. Phys. Rev. A **80**, 051201 (2009)
167. Lykov, V.A., Baidin, G.V.: Computer simulation of laser proton acceleration for hadron therapy. J. Phys.: Conf. Ser. **244**(2), 022046 (2010)
168. Mackinnon, A.J., Kline, J.L., Dixit, S.N., et al.: Assembly of high-areal-density deuterium-tritium fuel from indirectly driven cryogenic implosions. Phys. Rev. Lett. **108**, 215005 (2012)
169. Maksimchuk, A., Gu, S., Flippo, K., et al.: Forward ion acceleration in thin films driven by a high-intensity laser. Phys. Rev. Lett. **84**(18), 4108–4111 (2000)
170. Maksimchuk, A., Flippo, K., Krause, H., et al.: Plasma phase transition in dense hydrogen and electron–hole plasmas. Plasma Phys. Rep. **30**(6), 473–495 (2004)
171. Malka, V., Faure, J., Gauduel, Y.A., et al.: Principles and applications of compact laserplasma accelerators. Nat. Phys. **4**(06), 447–453 (2008)
172. Mancic, A., Robiche, J., Antici, P., et al.: Isochoric heating of solids by laser-accelerated protons: experimental characterization and self-consistent hydrodynamic modeling. High Energy Density Phys. **6**(1), 21–28 (2010)
173. Mancuso, A.P., Gorniak, T., Staier, F., et al.: Coherent imaging of biological samples with femtosecond pulses at the free-electron laser FLASH. New J. Phys. **12**(3), 035003 (2010)
174. Martins, M., Wellhöfer, M., Sorokin, A.A., et al.: Resonant multiphoton processes in the soft-X-ray regime. Phys. Rev. A **80**, 023411 (2009)
175. McGuffey, C., Thomas, A.G.R., Schumaker, W., et al.: Ionization induced trapping in a laser wakefield accelerator. Phys. Rev. Lett. **104**, 025004 (2010)
176. Mesyats, G.A.: Impul'snaya energetika i elektronika (Pulse Power and Electronics). Nauka, Moscow (2004)
177. Mesyats, G.A., Yalandin, M.I.: High-power picosecond electronics. Phys. Usp. **48**(3), 211 (2005)

178. Michel, P., Divol, L., Williams, E.A., et al.: Tuning the implosion symmetry of ICF targets via controlled crossed-beam energy transfer. Phys. Rev. Lett. **102**, 025004 (2009)
179. Michel, D.T., Depierreux, S., Stenz, C., et al.: Exploring the saturation levels of stimulated raman scattering in the absolute regime. Phys. Rev. Lett. **104**, 255001 (2010)
180. Mima, K.: Present status and prospects of firex project for fast ignition laser fusion (2008)
181. Mima, K., Fast Ignition Research Group: Present status and future prospects of laser fusion and related high energy density plasma research. AIP Conf. Proc. **740**(1), 387–397 (2004)
182. Mintsev, V., Gryaznov, V., Kulish, M., et al.: Stopping power of proton beam in a weakly non-ideal xenon plasma. Contrib. Plasma Phys. **39**(1–2), 45–48 (1999)
183. Moody, J.D., Michel, P., Divol, L., et al.: Multistep redirection by cross-beam power transfer of ultrahigh-power lasers in a plasma. Nat. Phys. **8**(4), 344–349 (2012)
184. Mori, W.B., Decker, C.D., Hinkel, D.E., Katsouleas, T.: Raman forward scattering of short-pulse high-intensity lasers. Phys. Rev. Lett. **72**(10), 1482–1485 (1994)
185. Moses, E.I.: The National Ignition Facility and the National Ignition Campaign. IEEE Trans. Plasma Sci. **38**(4, Part 2, SI), 684–689 (2010). 36th IEEE International Conference on Plasma Science, San Diego, CA, May 31–Jun 05, 2009
186. Mourou, G.A., Tajima, T., Bulanov, S.V.: Optics in the relativistic regime. Rev. Mod. Phys. **78**(2), 1804–1816 (2006)
187. Nakamura, T., Fukuda, Y., Yogo, A., et al.: High energy negative ion generation by Coulomb implosion mechanism. Phys. Plasmas **16**(11), 113106 (2009)
188. Nakatsutsumi, M., Marques, J.R., Antici, P., et al.: High-power laser delocalization in plasmas leading to long-range beam merging. Nat. Phys. **6**(10), 1010–1016 (2010)
189. National Research Council: Frontiers in High Energy Density Physics. National Academies Press, Washington, DC (2003)
190. Naumova, N., Schlegel, T., Tikhonchuk, V.T., et al.: Hole boring in a DT pellet and fast-ion ignition with ultraintense laser pulses. Phys. Rev. Lett. **102**, 025002 (2009)
191. Nishihara, K., Amitani, H., Murakami, M., et al.: High energy ions generated by laser driven Coulomb explosion of cluster. Nucl. Instrum. Methods Phys. Res. A **464**(1–3), 98–102 (2001)
192. Norreys, P.A.: Laser-driven particle acceleration. Nat. Photonics **3**(8), 423–425 (2009)
193. Ogura, K., Shizuma, T., Hayakawa, T., et al.: Proton-induced nuclear reactions using compact high-contrast high-intensity laser. Appl. Phys. Express **2**(6), 066001 (2009)
194. Okihara, S., Esirkepov, T.Z., Nagai, K., et al.: Ion generation in a low-density plastic foam by interaction with intense femtosecond laser pulses. Phys. Rev. E **69**(2), 026401 (2004)
195. Pollock, B.B., Clayton, C.E., Ralph, J.E., et al.: Demonstration of a narrow energy spread, ~ 0.5 gev electron beam from a two-stage laser wakefield accelerator. Phys. Rev. Lett. **107**, 045001 (2011)
196. Pukhov, A.: Strong field interaction of laser radiation. Rep. Prog. Phys. **66**(1), 47–101 (2003)
197. Pukhov, A., Meyer-ter-Vehn, J.: Laser wake field acceleration: the highly non-linear broken-wave regime. Appl. Phys. B **74**(4–5), 355–361 (2002)
198. Regan, S.P., Epstein, R., Hammel, B.A., et al.: Hot-spot mix in ignition-scale implosions on the NIF. Phys. Plasmas **19**(5), 056307 (2012)
199. Regan, S.P., Falk, K., Gregori, G., et al.: Inelastic X-ray scattering from shocked liquid deuterium. Phys. Rev. Lett. **109**, 265003 (2012)
200. Robbie, S.O., Doyle, H., Symes, D., Smith, R.: A study of ambient upstream material properties using perpendicular laser driven radiative blast waves in atomic cluster gases. High Energy Density Phys. **8**(1), 55–59 (2012)
201. Robey, H.F., Celliers, P.M., Kline, J.L., et al.: Precision shock tuning on the national ignition facility. Phys. Rev. Lett. **108**, 215004 (2012)
202. Rosmej, O.N., Blazevic, A., Korostiy, S., et al.: Charge state and stopping dynamics of fast heavy ions in dense matter. Phys. Rev. A **72**(5), 052901 (2005)
203. Roth, M., Cowan, T.E., Key, M.H., et al.: Fast ignition by intense laser-accelerated proton beams. Phys. Rev. Lett. **86**(3), 436–439 (2001)
204. Roth, M., Alber, I., Bagnoud, V., et al.: Proton acceleration experiments and warm dense matter research using high power lasers. Plasma Phys. Control. Fusion **51**(12), 124039 (2009)

205. Schatz, T., Schramm, U., Habs, D.: Crystalline ion beams. Nature **412**(6848), 717–720 (2001)
206. Schlenvoigt, H.P., Haupt, K., Debus, A., et al.: A compact synchrotron radiation source driven by a laser-plasma wakefield accelerator. Nat. Phys. **4**(2), 130–133 (2008)
207. Schneider, J.R.: FLASH from accelerator test facility to the first single-pass soft X-ray free-electron laser. J. Phys. B: At. Mol. Opt. Phys. **43**(19), 194001 (2010)
208. Schramm, U., Schatz, T., Bussmann, M., Habs, D.: Cooling and heating of crystalline ion beams. J. Phys. B **36**(3), 561–571 (2003)
209. Schroeder, C.B., Esarey, E., van Tilborg, J., Leemans, W.P.: Theory of coherent transition radiation generated at a plasma-vacuum interface. Phys. Rev. E **69**(1), 016501 (2004)
210. Seibert, M.M., Ekeberg, T., Maia, F.R.N.C., et al.: Single mimivirus particles intercepted and imaged with an X-ray laser. Nature **470**(2), 78–81 (2011)
211. Seres, J., Seres, E., Verhoef, A.J., et al.: Laser technology: source of coherent kiloelectronvolt X-rays. Nature **433**(02), 596 (2005)
212. Shao, Y.L., Ditmire, T., Tisch, J.W.G., et al.: Multi-keV electron generation in the interaction of intense laser pulses with Xe clusters. Phys. Rev. Lett. **77**(16), 3343–3346 (1996)
213. Sharkov, B.Y. (ed.): Yadernyi sintez s inertsionnym uderzhaniem (Inertial Confinement Nuclear Fusion). Fizmatlit, Moscow (2005)
214. Sheng, Z.M., Wu, H.C., Li, K., Zhang, J.: Terahertz radiation from the vacuum-plasma interface driven by ultrashort intense laser pulses. Phys. Rev. E **69**(2), 025401 (2004)
215. Sheng, Z.M., Mima, K., Zhang, J.: Powerful terahertz emission from laser wake fields excited in inhomogeneous plasmas. Phys. Plasmas **12**(12), 123103 (2005)
216. Sheng, Z.M., Mima, K., Zhang, J., Sanuki, H.: Emission of electromagnetic pulses from laser wakefields through linear mode conversion. Phys. Rev. Lett. **94**(9), 095003 (2005)
217. Sherrill, M.E., Abdallah, J., Csanak, G., et al.: Spectroscopic characterization of an ultrashort-pulse-laser-driven ar cluster target incorporating both Boltzmann and particle-in-cell models. Phys. Rev. E **73**, 066404 (2006)
218. Shvets, G., Wurtele, J.S., Chiou, T.C., Katsouleas, T.C.: Excitation of accelerating wakefields in inhomogeneous plasmas. IEEE Trans. Plasma Sci. **24**(2), 351–362 (1996)
219. Spears, B.K., Glenzer, S., Edwards, M.J., et al.: Performance metrics for inertial confinement fusion implosions: aspects of the technical framework for measuring progress in the national ignition campaign. Phys. Plasmas **19**(5), 056316 (2012)
220. Spence, N., Katsouleas, T., Muggli, P., et al.: Simulations of Cerenkov wake radiation sources. Phys. Plasmas **8**(11), 4995–5005 (2001)
221. Spence, D.J., Butler, A., Hooker, S.M.: Gas-filled capillary discharge waveguides. J. Opt. Soc. Am. B **20**(1), 138–151 (2003)
222. Spielman, R.B., Deeney, C., Chandler, G.A., et al.: Tungsten wire-array Z-pinch experiments at 200 TW and 2 MJ. Phys. Plasmas **5**(5), 2105–2111 (1998)
223. Sprangle, P., Esarey, E., Ting, A., Joyce, G.: Laser wakefield acceleration and relativistic optical guiding. Appl. Phys. Lett. **53**(22), 2146–2148 (1988)
224. Sprangle, P., Esarey, E., Krall, J., Joyce, G.: Propagation and guiding of intense laser pulses in plasmas. Phys. Rev. Lett. **69**(15), 2200–2203 (1992)
225. Sprangle, P., Penano, J.R., Hafizi, B., Kapetanakos, C.A.: Ultrashort laser pulses and electromagnetic pulse generation in air and on dielectric surfaces. Phys. Rev. E **69**(6), 066415 (2004)
226. Steinke, S., Henig, A., Schnurer, M., et al.: Efficient ion acceleration by collective laser-driven electron dynamics with ultra-thin foil targets. Laser Part. Beams **28**(01), 215–221 (2010)
227. Stephens, R.B., Akli, K.U., Bartal, T., et al.: Energy injection for fast ignition. Plasma Fusion Res.: Rev. Articles **4**, 016 (2009)
228. Tabak, M., Hammer, J., Glinsky, M.E., et al.: Ignition and high gain with ultrapowerful lasers. Phys. Plasmas **1**(5), 1626–1634 (1994)
229. Tahir, N.A., Deutsch, C., Fortov, V.E., et al.: Proposal for the study of thermophysical properties of high-energy-density matter using current and future heavy-ion accelerator facilities at GSI Darmstadt. Phys. Rev. Lett. **95**(3), 035001 (2005)

230. Tahir, N.A., Deutsch, C., Fortov, V.E., et al.: Studies of strongly coupled plasmas using intense heavy ion beams at the future FAIR facility: the HEDgeHOB collaboration. Contrib. Plasma Phys. **45**(3–4), 229–235 (2005)
231. Tahir, N.A., Kain, V., Schmidt, R., et al.: The CERN Large Hadron Collider as a tool to study high-energy density matter. Phys. Rev. Lett. **94**(13), 135004 (2005)
232. Tajima, T.: Summary of Working Group 7 on "Exotic acceleration schemes". AIP Conf. Proc. **569**(1), 77–81 (2001)
233. Tajima, T., Dawson, J.M.: Laser electron accelerator. Phys. Rev. Lett. **43**(4), 267–270 (1979)
234. Thomas, A.G.R., Krushelnick, K.: Betatron X-ray generation from electrons accelerated in a plasma cavity in the presence of laser fields. Phys. Plasmas **16**(10), 103103 (2009)
235. Togashi, T., Takahashi, E.J., Midorikawa, K., et al.: Extreme ultraviolet free electron laser seeded with high-order harmonic of ti:sapphire laser. Opt. Express **19**(1), 317–324 (2011)
236. Toleikis, S., Fustlin, R., Cao, L., et al.: Soft X-ray scattering using FEL radiation for probing near-solid density plasmas at few electron volt temperatures. High Energy Density Phys. **6**(1), 15–20 (2010)
237. Town, R.P.J., Rosen, M.D., Michel, P.A., et al.: Analysis of the National Ignition Facility ignition hohlraum energetics experiments. Phys. Plasmas **18**(5), 056302 (2011)
238. Treusch, R., Feldhaus, J.: FLASH: new opportunities for (time-resolved) coherent imaging of nanostructures. New J. Phys. **12**(3), 035015 (2010)
239. Tzortzakis, S., Mechain, G., Patalano, G., et al.: Coherent subterahertz radiation from femtosecond infrared filaments in air. Opt. Lett. **27**(21), 1944–1946 (2002)
240. van Tilborg, J., Schroeder, C.B., Esarey, E., Leemans, W.P.: Pulse shape and spectrum of coherent diffraction-limited transition radiation from electron beams. Laser Part. Beams **22**, 415–422 (2004)
241. van Tilborg, J., Schroeder, C.B., Filip, C.V., et al.: Temporal characterization of femtosecond laser-plasma-accelerated electron bunches using terahertz radiation. Phys. Rev. Lett. **96**(1), 014801 (2006)
242. Wang, S., Clayton, C.E., Blue, B.E., et al.: X-ray emission from betatron motion in a plasma wiggler. Phys. Rev. Lett. **88**(13), 135004 (2002)
243. Wilks, S.C., Langdon, A.B., Cowan, T.E., et al.: Energetic proton generation in ultra-intense laser-solid interactions. Phys. Plasmas **8**(2), 542–549 (2001)
244. Willingale, L., Petrov, G.M., Maksimchuk, A., et al.: Front versus rear side light-ion acceleration from high-intensity laser–solid interactions. Plasma Phys. Control. Fusion **53**(1), 014011 (2011)
245. Yampolsky, N.A., Fraiman, G.M.: Conversion of laser radiation to terahertz frequency waves in plasma. Phys. Plasmas **13**(11), 113108 (2006)
246. Yan, X.Q., Wu, H.C., Sheng, Z.M., et al.: Self-organizing GeV, nanocoulomb, collimated proton beam from laser foil interaction at 7×10^{21} $\mathbf{W}/\mathrm{cm}^2$. Phys. Rev. Lett. **103**, 135001 (2009)
247. Yoshii, J., Lai, C.H., Katsouleas, T., et al.: Radiation from Cerenkov wakes in a magnetized plasma. Phys. Rev. Lett. **79**(21), 4194–4197 (1997)
248. Young, L., Kanter, E.P., Krassig, B., et al.: Femtosecond electronic response of atoms to ultra-intense X-rays. Nature **466**(07), 56–61 (2010)
249. Yugami, N., Higashiguchi, T., Gao, H., et al.: Experimental observation of radiation from Cherenkov wakes in a magnetized plasma. Phys. Rev. Lett. **89**(6), 065003 (2002)
250. Zhang, Z.M., He, X.T., Sheng, Z.M., Yu, M.Y.: High-density highly collimated monoenergetic GeV ions from interaction of ultraintense short laser pulse with foil in plasma. Phys. Plasmas **17**(4), 043110 (2010)
251. Zhang, L., Chen, L.M., Yuan, D.W., et al.: Enhanced Kα output of Ar and Kr using size optimized cluster target irradiated by high-contrast laser pulses. Opt. Express **19**(25), 25812–25822 (2011)
252. Zhang, L., Chen, L.M., Wang, W.M., et al.: Electron acceleration via high contrast laser interacting with submicron clusters. Appl. Phys. Lett. **100**(1), 014104 (2012)

253. Zhidkov, A., Esirkepov, T., Fujii, T., et al.: Characteristics of light reflected from a dense ionization wave with a tunable velocity. Phys. Rev. Lett. **103**, 215003 (2009)
254. Zigler, A., Ehrlich, Y., Cohen, C., et al.: Optical guiding of high-intensity laser pulses in a long plasma channel formed by a slow capillary discharge. J. Opt. Soc. Am. B **13**(1), 68–71 (1996)
255. Zigler, A., Palchan, T., Bruner, N., et al.: 5.5–7.5 MeV proton generation by a moderate-intensity ultrashort-pulse laser interaction with H_2O nanowire targets. Phys. Rev. Lett. **106**, 134801 (2011)
256. Zweiback, J., Ditmire, T.: Femtosecond laser energy deposition in strongly absorbing cluster gases diagnosed by blast wave trajectory analysis. Phys. Plasmas **8**(10), 4545–4550 (2001)
257. Zweiback, J., Cowan, T.E., Smith, R.A., et al.: Characterization of fusion burn time in exploding deuterium cluster plasmas. Phys. Rev. Lett. **85**(17), 3640–3643 (2000)

Chapter 8
Nuclear Transformations Under Strong Compression

Figure 7.49 shows the characteristic dimensions and times of the motion of molecular, atomic and nuclear objects [45], and Fig. 8.1 shows the characteristic dimensions of different structural substance states. Because atomic and nuclear dimensions differ by 5–6 orders of magnitude away from nuclear densities $\rho \ll \rho_0 \approx 2.8 \cdot 10^{14}\,\mathrm{g/cm^3}$, these processes may be treated independently. Despite the fact that they are, of course, rigidly bound for any ρ, since the nuclear structure and charge directly define the electron structure of an atom or ion as well as its chemical properties and the aggregate substance state.

Proceeding from this fact, in the preceding chapters we focused out attention on the electron and ion substance components and the description of their thermodynamic properties in different parts of the phase diagram. In this case, the processes in nuclei were not considered owing to the insufficiently high ($\rho \lesssim 10^{10}\,\mathrm{g/cm^3}$) plasma density, so that the nuclear properties were assumed to be the same as under normal laboratory conditions.

Ascending the pressure and temperature scales and approaching the nuclear range of interparticle distances (the neutrino size is $\approx$0.16 fm [2]) and densities $\rho \sim \rho_0$, we ought to account for nuclear transformations, which correspond to the emergence of new forms of nuclear matter under ultraextreme conditions [26, 28, 34] (Fig. 8.2 [28]). The possibilities that appear in this case are shown on the phase diagram of nuclear matter (Fig. 6.20), where the experimental capabilities of modern accelerators: RHIC, LHC (high temperatures and moderate densities of nuclear matter), as well as FAIR SIS 300 (a high baryon density). Also given in the diagram are the parameters of neutron stars [34, 79] emerging in the gravitational collapse of massive ($M > M_\odot$, $M_\odot$ is the solar mass) [26, 34] stars at the final stages of their evolution.

© Springer International Publishing Switzerland 2016

V.E. Fortov, *Extreme States of Matter*, Springer Series in Materials Science 216,
DOI 10.1007/978-3-319-18953-6_8

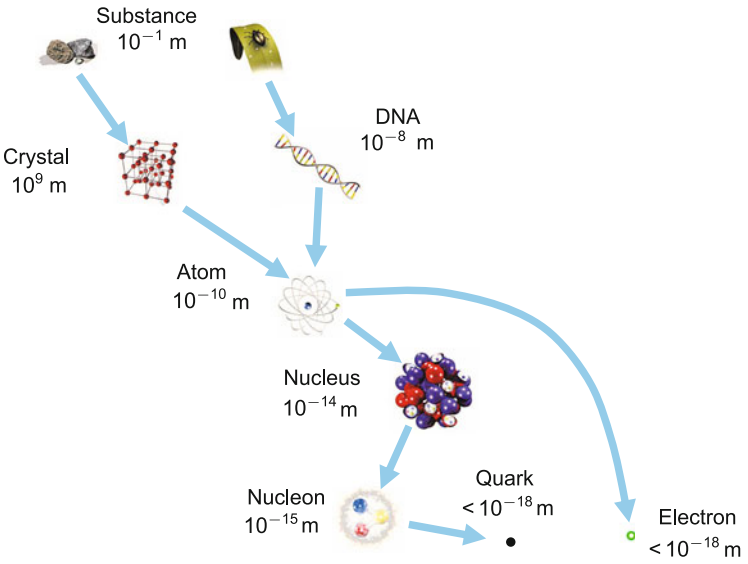

Fig. 8.1 Typical dimensions of the structural elements of substances

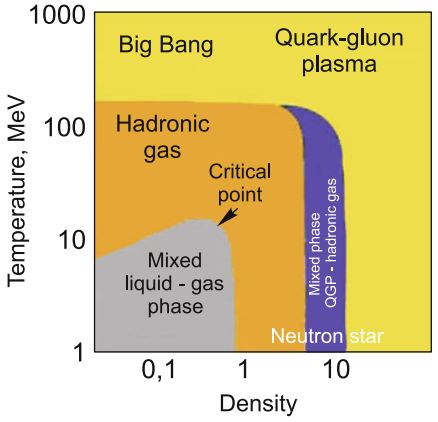

Fig. 8.2 Schematic diagram of heavily compressed substance. The temperature is in MeV, the density in fractions of the nuclear density ρ_0 With increasing pressure and density there emerges quark-gluon plasma with a phase transition of the Ist kind. The drawing borrowed from [28]

8.1 Extreme States of Neutron Stars

Depending on the initial mass of a star of solar chemical composition, three types of compact remnants may emerge upon completion of the thermonuclear evolution in the stellar interior: white dwarfs, neutron stars, as well as black holes [47, 105] and heretofore undiscovered quark stars [34, 79].

A neutron star is a possible final product of the evolution of a main-sequence star (a "normal" star) [79]. They come into being in IInd-type supernovae explosions. This explosion occurs when the predecessor star of a supernova exhausts its nuclear "fuel": from hydrogen to oxygen and magnesium. The final product of subsequent nuclear fusion transformations are the isotopes of iron group elements, which accumulate at the stellar center (see Chap. 4). The pressure of degenerate electron Fermi gas prevents this iron-nickel stellar core from collapsing under the force of gravity. But even within several days after oxygen burning the iron core mass exceeds the Chandrasekar limit $1.44\,M_\odot$—the greatest mass whose gravitational contraction can be withstood by the pressure of degenerate electrons. Then there sets in a gravitational collapse—the catastrophic contraction of the stellar core with the liberation of huge gravitational energy ($>10^{53}$ erg) and the emergence of a shock wave, which throws off the outer shells of the giant star with a velocity which ranges up to 10 % of the velocity of light. The stellar interior continues to contract with a velocity of the same order of magnitude. As this takes place, atomic nuclei merge in essence into one gigantic nucleus. If its mass exceeds the maximum mass ($\approx$2–3 $M_\odot$) which the pressure of degenerate neutrons is able to keep from gravitational contraction, nothing can stop this contraction and eventually there forms a black hole.

It is believed that the collapse with the formation of a black hole may result in a hypernova outburst, which is hundreds of times brighter than a supernova one, which may be a source of mysterious cosmic gamma-ray bursts seen from distant galaxies (see Sect. 10.3). For smaller masses there forms a neutron star kept from gravitational contraction by the pressure of nuclear matter. In this case, about 1 % of liberated energy converts to the kinetic energy of expanding shells, which subsequently form a nebula—a supernova remnant—and only about 0.01 % ($\approx 10^{49}$ erg) transforms to electromagnetic radiation, which is nevertheless capable of outshining the emission of a whole galaxy and is observed as a supernova.

Not every star can terminate its evolution as a supernova (all the more as a hypernova): this is the destiny of only sufficiently massive stars with $M > 8\,M_\odot$. On going through the stage of a giant, a less massive star at the end of its lifetime gradually sheds its outer shells, while the remaining central part contracts to become a white dwarf.

A neutron star is born with a temperature of over 10^{10}–10^{11} K and then cools—initially rapidly but later on slower and slower—liberating energy by way of neutrino radiation from its interior and electromagnetic radiation from its surface.

Neutron stars are perhaps the most exotic astronomical objects, in which there is a wide spectrum of superextreme states of matter [33, 34, 79, 104] practically inaccessible to laboratory investigation. That is why neutron stars in a sense play the role of a "cosmic laboratory", when their observable manifestations permit judging about the behavior of substance under superextreme conditions—at supernuclear densities, superhigh magnetic fields, the superfluidity of the baryon component and high-intensity nuclear transformations of ultracompressed substance.

Naturally, the observable manifestations of these processes are also highly diversified: radio and X-ray pulsars, flaring X-ray sources, γ-ray sources, X-ray transients and magnetars, etc. [91, 104, 105].

Neutron stars are not the only objects in whose interior the substance is compressed to densities unattainable in a laboratory [79]. Other representatives of the class of compact stars are white dwarfs and hypothetical quark stars [79]. While the size of a neutron star is defined primarily by the balance of gravitational forces and the pressure of degenerate neutrons, in white dwarfs the gravitational contraction is opposed by the pressure of degenerate electrons and in quark or strange stars by the pressure of quark-gluon plasma.

Neutron stars are much smaller than white dwarfs. For a mass $M \sim M_\odot$ the white dwarfs have a radius $R \approx 10^4$ km comparable to the terrestrial radius and approximately a thousand times greater than the radius of a neutron star [34, 79]. That is why the substance density in their interior does not range up to even one thousandth fraction of the nuclear density ρ_0. According to theoretical models, the quark stars with $M \sim M_\odot$ may be even more compact than the neutron ones. Quark stars have not been observed so far, and the very possibility of their existence has not been amply borne out.

Neutron stars are the smallest observable stars in the Galaxy [34, 41, 79]. Their radii are of the order of 10 km, which is 10^5 times smaller than the dimensions of ordinary stars. However, the neutron star masses M are of the order of the solar mass $M_\odot$ and group about a value $1.4\,M_\odot$. The average substance density $\overline{\rho} = 3M/4\pi R^3 = 7 \cdot 10^{14}$ g/cm^3 of neutron stars is several times higher than the ordinary nuclear density $\rho_0 = 2.8 \cdot 10^{14}$ g/cm^3. Therefore a neutron star may be conventionally represented as a huge atomic nucleus of size $\approx$10 km. At the center of the star the density may range up to 10–20 time the nuclear density. Possible at these densities at the neutron star center is the condensation of pions, hyperons, and kaons. In this case we are dealing with strange or quark stars [42, 79]. The possibility of the formation of strange quarks is also under discussion.

For neutron stars [79], unlike the ordinary ones, a prominent role is played by the effects of general relativity. On the other hand, neutron star observations may yield valuable information about the manifestation of the effects of this theory.

A neutron star consists of a crust—inner and outer—in which there occurs substance neutronization, and a core—also inner and outer. The number of protons and electrons in the inner crust and outer core amounts to several percent of the number of neutrons. The gravitational energy of a neutron star is equal to an appreciable fraction ($0.2Mc^2$) of its rest energy.

The existence of neutron stars was predicted by Baade and Zwicky [3] in 1934, 2 years after the discovery of neutrons. Despite their small size, neutron stars are among the most active stars: they emit energy in the entire range of electromagnetic waves—from radiowaves to superhigh-energy photons above 1 TeV. Rapidly revolving neutron stars experience high energy losses. In particular, the pulsar in Crab Nebula radiates an energy of 10^{38} erg/s, which is many orders of magnitude greater than the energy of solar radiation. The energy emanated in the radio frequency band accounts for only small fraction, 10^{-5}–10^{-6} of the energy

loss. The highest-power radio pulsars also radiate in other ranges: optical, X-ray, and γ-ray ranges.

Neutron stars, which are associated with short-period radiation sources—pulsars, which were discovered in 1967–1969—are the final stage of evolution of the ordinary stars with $M > 8\,M_{\odot}$, when gravitational forces compress substance to nuclear densities to give rise to neutron substance [47, 48, 105], which was predicted by L.D. Landau back in 1932. Neutron stars exist owing to the mutual repulsion—between neutrons and protons rather than electrons—which emerges due to the Pauli principle.

Apart from being radio pulsars, neutron stars are also sources [41, 79] of high-power X-ray radiation (X-ray pulsars), γ- and X-ray flares (magnetars), and permanent X-ray radiation emanating from the centers of supernova remnants, very weak optical stars. The radiation of neutron stars permits solving several basic physical problems. First and foremost, the case in point is the investigation of the equation of state of superdense substance, $\rho > \rho_0$.

The thermonuclear burn of silicon ^{32}Si with the production of the ^{56}Fe, ^{58}Fe, ^{60}Fe, ^{62}Ni, etc. isotopes closes the chain of thermonuclear reactions in the nondegenerate core of a massive star, because the subsequent thermonuclear fusion is possible only with energy absorption (see Chap. 4). The density at the stellar center amounts to $\approx 3 \cdot 10^9$ g/cm^3, $T \approx 8 \cdot 10^9$ K for a core mass 1.5–2 $M_{\odot}$ [105]. An important process which stimulates gravitational collapse is the photodissociation of iron nuclei into 13 alpha particles: $\gamma + {}^{56}_{23}\mathrm{Fe} \rightarrow 13\,{}^{2}_{4}\mathrm{He} + 4n$, and substance neutronization.

Following [48], according to L.D. Landau's predictions, the particles which make up nuclei (protons and neutrons) are capable of forming, apart from atomic nucleus, one more stable system—neutron substance [47, 48]. It consists primarily of neutrons, with a small admixture of protons and electrons. On the strength of the Pauli principle, the neutron substance is immune to neutron decay by the scheme $n \rightarrow p + e^- + \bar{\nu}$, because the energy level of the electron that might be emitted in the decay is already occupied by other electrons which enter into the substance composition.

Neutron substance is produced under the superheavy compression of ordinary substance consisting of electrons and nuclei, which emerges in the gravitational collapse of a star that goes through the stage of supernova explosion. Under this compression, when the substance density ranges up to about 10^{11} g/cm^3, it and, hence, the electron energy become high enough to initiate the inverse β decay: $p + e^- \rightarrow \mathrm{n} + \bar{\nu}$—the electron energy suffices to overcome the neutron-proton mass difference. As a result, with increasing pressure there occurs an accelerating process of electron capture by nuclei with the transformation of protons to neutrons. The neutron levels inside a nucleus turn out to be occupied and the next neutrons pass into the continuum to form a neutron Fermi liquid. And so, for a density which is not much lower than the nuclear one there emerges the neutron substance state, which fills the inner part of neutron stars.

A characteristic property of neutron stars is their superhigh (nuclear) density, $\rho \approx 2.8 \cdot 10^{14}$ g/cm^3 or 0.17 baryon/fm^3. However, unlike atomic nuclei in which nucleons are confined by the strong interaction, in a neutron star the nucleons are

confined by gravitational forces and the neutron β decay is suppressed by the strong electron degeneracy of compressed substance.

In the neutronization the elastic modulus of the degenerate substance becomes lower [105], because the electron density decreases with retention of the baryon density and the substance becomes "softer". The growth of pressure with density moderates and the effective adiabatic exponent of the substance, $\gamma = d \log P / d \log \rho$, decreases from 5/3 to 4/3 and leads, in accordance with the virial theorem, to a violation of mechanical stability of the object [105]. That is why the substance neutronization is one of the main physical processes which results in the collapse of massive stars at the late stages of their evolution.

The substance neutronization is extremely difficult to model in laboratories even with the use of superheavy compression in laser thermonuclear targets or in relativistic nuclear collisions; however, perhaps it will be possible to employ its equivalent process of the absorption of electron antineutrinos from, for instance, high-power sources with reactor strontium [39].

An additional cause for the loss of hydrostatic stellar stability is due to the effects of general relativity, when the substance pressure makes a contribution to attractive force and thereby increases the force which tends to compress the substance [47, 48]. In this case, the collapse of the core of a massive star is accompanied with a type II or Ib/c supernova outburst (see Chap. 9).

In the substance neutronization a star rapidly loses stability: the loss of elasticity results in compression and heating, but the negative heat capacity of ordinary stars no longer works in this case, because the degenerate gas pressure, which opposes compression, depends only slightly on the temperature. Furthermore, the bulk of energy released in the gravitational compression is carried away by neutrinos produced in the neutronization. And even if the temperature growth in the collapse removes degeneracy and increases the electron gas pressure, the energy removal persists due to antineutrinos in the course of beta decays of neutron-excess nuclei.

The main mechanism of neutrino energy loss in the outer core of a neutron star involves so-called modified URCA processes [79], which consist of the sequence of reactions $n + N \rightarrow p + N + e + \overline{\nu}_e$ and $p + N + e \rightarrow n + N + \nu_e$, where $N = n$ or $N = p$ is an intermediary nucleon. The participation of an intermediary nucleon distinguishes the modified URCA processes from the ordinary beta decay and beta capture processes, which are referred to as direct URCA processes.

The term "URCA process" was introduced by G.A. Gamow and M. Schoenberg [79]. Gamow reminisced: "We termed it an Urca process, partly to mention the casino in which we first met and partly because this process is as efficient in sucking energy out of the star as the Casino de Urca is in sucking money out of the pockets of the gamblers. When submitting our paper on the URCA process to the Physical Review for publication I feared that the publishers may ask why we termed this process "urca". On giving some thought to this question I decided to say that this was an abbreviation of "unrecordable cooling agent", but they never asked the question".

The collapse of a star terminates at densities of the order of atomic nuclear density, whereby neutron degeneracy effects become significant and the substance

compressibility becomes capable of opposing the action of gravitational forces. The freely falling outer stellar layers strike against the solid surface of the compressed core and bounce off, which is believed to be the cause of shell shedding and the observable effect of a supernova outburst. But numerical simulations suggest that this mechanism is insufficient for the explosion of a supernova shell. Today it is commonly assumed that the cause of explosion is some non-one-dimensional effects: magnetic field, supersonic convection, stellar core rotation, etc. [24, 38, 40, 46].

The transformation of stars from dense white dwarfs to superdense neutron and quark stars shows (Fig. 8.3) that in the process there emerges an instability stage. Eventually there forms a compact star with $M \approx M_{\odot}$, a size of only about 10 km (Fig. 8.4), an initial temperature of the order of 10^{11} K, and a core density of ≈ 1.5–$15\rho_0$, which possesses intense magnetic ($B \approx 10^{11}$–10^{16} Gs) and gravitational (acceleration of gravity of $\approx (2\text{–}3) \cdot 10^{14}\,\mathrm{cm/s^2}$) fields, which calls for invoking general relativity for its description. Neutron stars (radio pulsars), which rotate with a period of 0.0016–1 s, are the only astrophysical objects in which the revolution slowing-down (and hence the evolution) is determined by electrodynamic forces. The neutron stars that are parts of binary systems manifest themselves as compact X-ray sources [105].

Despite the small size, the spectrum of substance states (Fig. 8.5) and the physical processes (Figs. 8.5 and 8.6) in a neutron star are extremely diversified. The atmosphere of a neutron star has a thickness ranging from tens of centimeters to

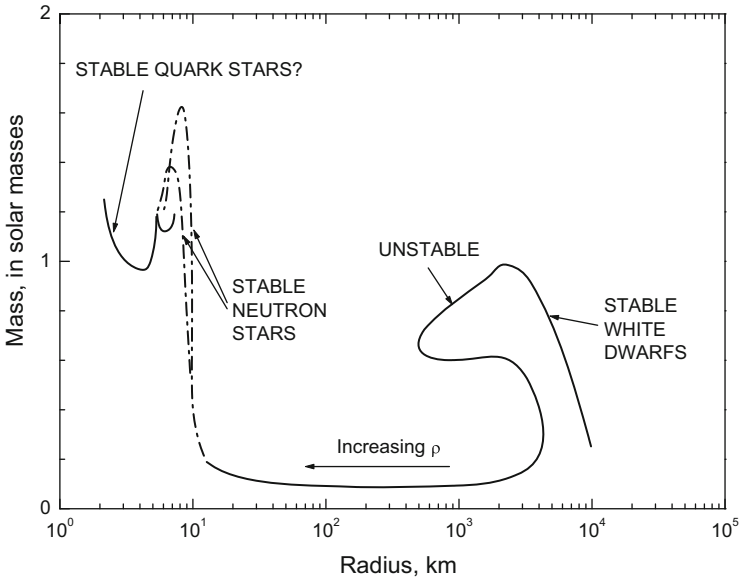

Fig. 8.3 Transition to neutron and quark stars [60]

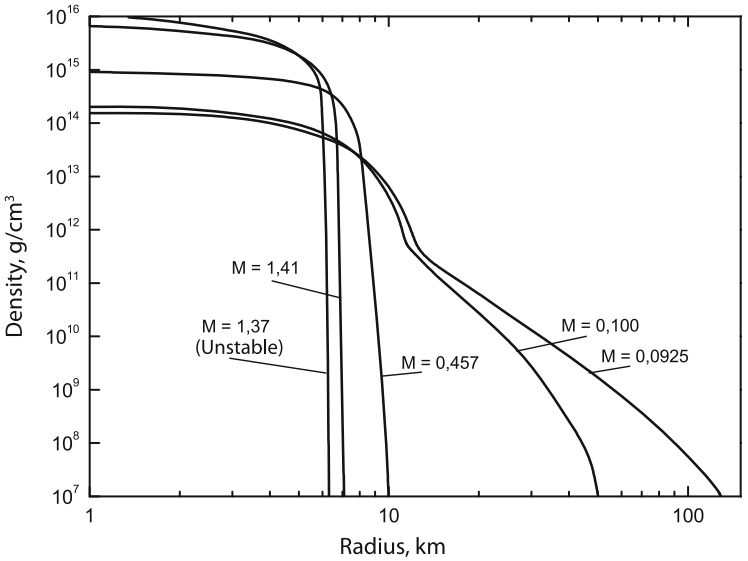

Fig. 8.4 Density distribution in neutron stars of different mass M (in units of solar mass $M_\odot$) [9]

several millimeters and a density of 0.1–100 g/cm^3; it consists of a nonideal plasma with $T \leq 10^6$ K and possesses a huge magnetic field.

The atmosphere of a neutron star may consist of the elements of the iron group formed at the stage of star production or of light elements like hydrogen and helium due to their accretion. Owing to a strong gravity, the atmosphere of a neutron star is quite thin (0.1–10 cm) and dense (0.1–100 g/cm^3), so that its substance is strongly nonideal from the standpoint of interparticle interaction. When the stellar temperature is not too high, the crust may see the formation of light atoms, molecules, metals droplets and clusters. In the case of a high magnetic field the crust may be condensed, with a small amount of gas above it. Superhigh magnetic fields may result in quantum electrodynamic effects (like vacuum polarization) significant for radiative processes. All these problems are a strong hindrance to the calculation of the composition and optical properties of the atmosphere and, consequently, of the radiative properties of the star itself and are therefore of major interest for theoretical astrophysics, nonideal plasma physics, and nuclear physics [91, 104].

The outer crust several hundred meters in thickness [104] consists of a dense plasma, in which the electron state undergoes a Boltzmann-to-degenerate state transition with depth and then (for $\rho \gg 10^6$ g/cm^3) a transition to the degenerate relativistic gas. For $\rho \geq 10^4$ g/cm^3 there occurs a pressure-induced complete plasma ionization. On further compression there occurs β capture and substance neutronization.

At the boundary of the core of a neutron star ($2\rho_0 < \rho < 20\rho_0$) atomic nuclei vanish, and neutrons in the inner core may be superfluidic, has an effect on the

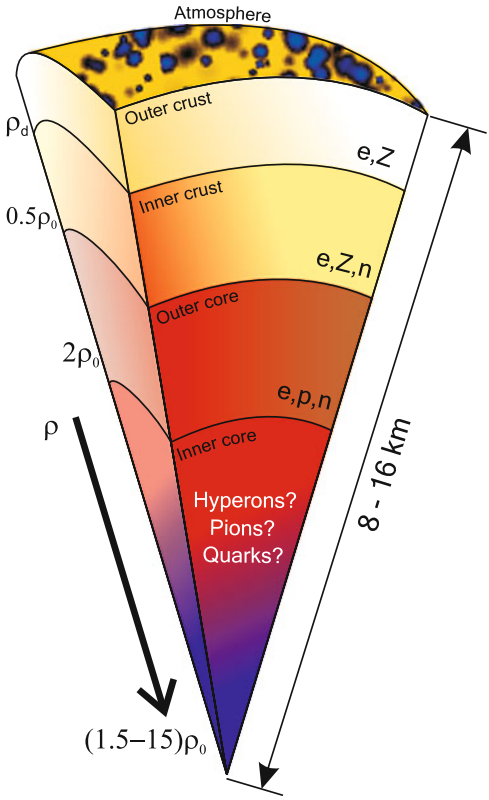

Fig. 8.5 Schematic sectional view of a neutron star of mass $1.4\,M_{\odot}$. The parameters of the star depend heavily on the equation of state of its layers [104, 105]; $\rho_0 = 2.8 \cdot 10^{14}$ g/cm^3

cooling dynamics and neutrino luminosity of the object. The superfluidity of neutron substance may be observed in the sudden rotation failure of some pulsars in the course of slowing down, which is caused by the interaction of normal and superfluid substance components in the inner core. In some cases the failure dynamics is attributable to the superfluid vortex separation from the stellar crust. The evolution of magnetic field "frozen" into the star permits drawing conclusions about the superconductivity of the stellar core. Since the inner stellar temperature depends heavily on the critical temperature of nucleons' transition to the superfluid state, it has been suggested [72] to employ a neutron star as a "thermometer" for measuring the critical temperatures of nucleons in asymmetric nuclear matter, which would yield indirect information about the equation of state of nuclear substance.

Superfluidity also affects oscillation damping. The existence of a gap in the dispersion relation of superfluid particles may sharply decrease the volume viscosity and moderate the damping of oscillations [103]. On the other hand, mutual friction is equivalent to a high effective viscosity. The appearance of superfluidity in a cooling neutron star depends on the cooling mode and the values of T_c. Perhaps, superfluidity has no time to emerge in a young neutron star and has no effect on the

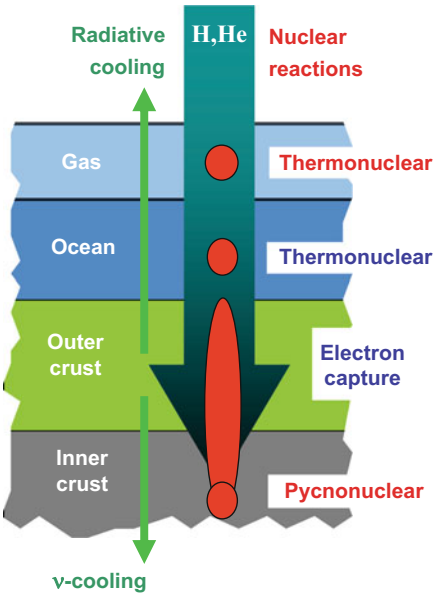

Fig. 8.6 Physical processes in a neutron star

oscillation modes. However, it may strongly damp the oscillations of older neutron stars [103].

The lowering of surface temperature with time in a cooling neutron star is controlled, in particular, by the neutrino luminosity and heat capacity of the star. The existence of a gap in the dispersion relation of superfluid particles changes the heat capacity and lowers the rate of neutrino reactions with participation of these particles, which may also be employed for determining $T_c \approx 3 \cdot 10^8$ K.

The cooling of neutron stars may be highly sensitive to the superfluidity of neutrons and protons in their cores. The temperatures of the emergence of nucleonic superfluidity are in turn sensitive to the equation of state of superdense substance. This furnishes the possibility in principle to investigate the nucleonic superfluidity and after that the equation of state of neutron stellar cores.

The composition of the inner core of a neutron star is inexactly known, because the physics of strong interactions in superdense substance is insufficiently known [47, 105]. The core perhaps consists of nucleon-hyperon matter, pion condensate, quark-gluon plasma, or some other exotic states. According to [104], if the properties of the crust ($\rho < 0.5\rho_0$) of a neutron star are described by nonideal plasma models, the description of the properties of supernuclear density matter (for $\rho \geq \rho_0$) is extremely difficult because of the incompleteness of laboratory data and the absence of a closed theory of supernuclear density matter [69].

Many neutron stars that are parts of binary systems manifest themselves as X-ray pulsars in the flow of substance to the star with a high ($>10^{10}$ Gs) magnetic field. For a lower magnetic field the substance accumulates on the stellar surface and there occurs a thermonuclear explosion on the attainment of some critical value,

which shows up as regular X-ray bursts. Unlike explosions on the surface of a white dwarf, the powerful gravitational field of a neutron star does not permit the explosion products to separate from the star and returns them back.

According to [54], the mechanism of generating extreme magnetic fields boils down to the following. All stars possess a weak magnetic field, and it may strengthen as a result of star compression. During the collapse of the core of a massive star, which ends with the production of a neutron star, its dimensions decrease by a factor of 10^5, and the magnetic field must therefore rise by a factor of 10^{10}. The neutron stars possessing a powerful magnetic field are termed magnetars [54].

Also considered is a different convective mechanism of magnetic fields [54]. The gas in a star may circulate due to convection. The hotter portions of the ionized gas come to the surface and the cooler ones sink. Since the ionized gas is a good conductor of electric current, the magnetic field lines that run through the gas are entrained by the flow of substance (the effect of "freezing-in" of magnetic field lines). The field may therefore build up.

This effect, which has come to be known as the dynamo mechanism [54], may be responsible for the emergence of stellar and planetary magnetic fields. The dynamo mechanism may operate at any stage of life of a massive star if its turbulent nucleus rotates fast enough. Furthermore, convection is especially strong during precisely the short period after the core transformation to a neutron star [54].

In the course of evolution the magnetic field changes its shape and generates electric currents flowing along the magnetic field lines outside of the star, which in turn generate X-ray radiation. The magnetic field simultaneously travels through the hard crust to generate flexural and tensile stress in it. This heats the inner stellar layers and sometimes leads to crust breaking, which it accompanied with powerful star shaking. The electromagnetic energy released in this case produces dense clouds of electrons and positrons as well as sudden soft gamma-ray flares (Fig. 9.53).

The substance structure under high magnetic fields ($B > 10^{12}$ Gs) inherent in neutron stars is quite unusual [41] (Fig. 8.7). Under such fields the cyclotron radius of atomic electrons is shorter than the Bohr radius, an atom is strongly compressed in the direction perpendicular to the magnetic field and is needle-shaped. The properties of the substance formed by suchlike atoms may be judged by the interaction of the surface of a neutron star, at which the substance density amounts to 10^5 g/cm^3, and its magnetosphere.

As discussed in Chap. 6, quark-gluon plasma is an exotic superdense matter state. This plasma was recently discovered in a laboratory; it consists of quarks, antiquarks, and gluons [30, 36, 66, 84]. Quark-gluon plasmas possess maximum densities and may emerge at the center of a neutron star or in the collapse of an ordinary star (Fig. 9.54). In this case, we are dealing with quark stars and hybrid stars, which consist of the quark-gluon matter at the center and a hadronic shell [89]. In this case, quark stars must be smaller in size than neutron stars because of a higher compressibility of the quark-gluon plasma (Fig. 9.55). Considered as a candidate for a quark-gluon or hybrid star is, for instance, the RXL1856 star with a radius of more than 16 km, which was detected in the X-ray range by the Newton and Chandra space telescopes.

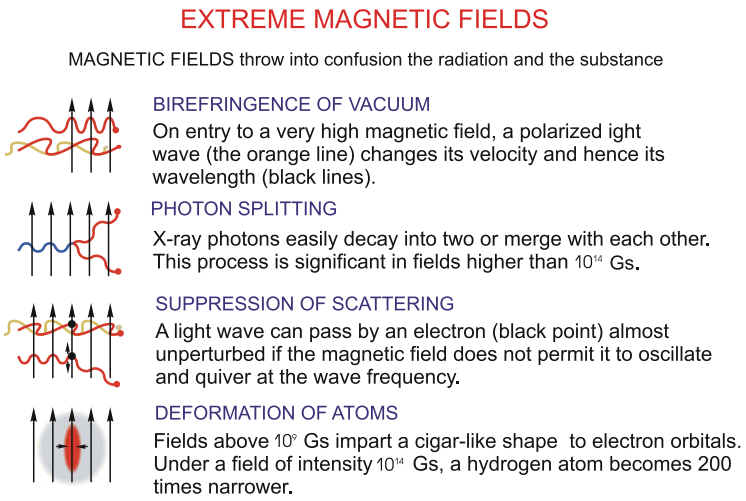

Fig. 8.7 Effect of magnetic field on the radiation and the substance [54]

8.2 Compression: Nuclear Structures

As we move to the right along the nuclear density scale in Fig. 7.49, for $\rho \gtrsim 10^{10}\,\mathrm{g/cm^3}$ [34, 49] nuclei become unstable relative to β decay with a maximum neutron excess $\delta \sim \frac{N-Z}{A} \sim 0.3$, where N, Z, and A—are the respective numbers of neutrons, protons, and nucleons. With increasing compression the neutron excess δincreases and for $\delta > 3$ the neutron energy levels cease to be bound. The nuclei turn out to be immersed in the medium of free neutrons and cannot exist under these conditions, decaying with the emission of neutrons in a time of $\approx 10^{-20}$ s.

Our knowledge about this matter for $10^{11}\,\mathrm{g/cm^3} \lesssim \rho \lesssim 10^{14}\,\mathrm{g/cm^3}$ and $0.3 \lesssim \delta \lesssim 0.8$ relies only on theoretical constructions partly confirmed by astronomical observations of neutron stars—exotic and, as we saw in the foregoing, the most extreme astronomical objects emerging in the gravitational collapse of a variety of stars at the final stages of their evolution. However, the capabilities of the theory of multiparticle nuclear systems are quite limited in this area, like are the capabilities of experiments, especially in the $\rho > \rho_0 = 2.5 \cdot 10^{14}\,\mathrm{g/cm^3}$ density domain characteristic of symmetric nuclear matter. These substance neutronization processes are the basis for the calculation of the structure and dynamics of neutron stars [34]; to describe their thermodynamics, highly sophisticated models have been developed, which are generalized in monograph [34]. In the subsequent discussion we follow this work.

In the density range under consideration the characteristic distance between the nuclei is comparable to their size, which corresponds to “nuclear” plasma densities of $\approx 10^{14}\,\mathrm{g/cm^3}$. To describe these supercompressed situations, use is made of three models [34]. These are Hartree-Fock calculations with an effective nucleon

interaction potential [14], calculations by means of the Thomas–Fermi method at finite temperatures [59, 67], calculations by liquid drop model [56], etc.

The thermodynamic of nuclear matter under the conditions close to the onset on neutronization is described in [10]. This permitted calculating the properties of neutron-excess nuclei at different temperatures. In particular, the highest density whereby the ^{84}Se nucleus (with $\frac{Z}{A} \approx 0.405$) exists was estimated at $\approx 8.2 \cdot 10^9$ g/cm^3. Many neutron-excess nuclei and several new nuclear structures stable at a heavy compression have been discovered to date [34].

Using the theoretical methods developed to date it has been possible to calculate the composition and energy of several nuclear structures; those of which that are equilibrium are referred to as "cold catalytic matter".

Calculations show [34] that the minimal value of E equal to 930.4 MeV is realized for a bcc lattice of ^{56}Fe. This corresponds to $\rho \approx 7.86$ g/cm^3 and $n_b = 4.73 \cdot 10^{24}$ cm^{-3}. We note that ^{56}Fe is not the weakest-bound free nucleus. The highest binding energy per nucleon

$$b = [(A - Z)m_n c^2 + Zm_p c^2 - M(A, Z)c^2]/A$$

is reached for ^{62}Ni: $b(^{62}\text{Ni}) = 8.7945$ MeV, for ^{56}Fe this quantity $b(^{56}\text{Fe}) = 8.7902$ MeV, and $b(^{58}\text{Fe}) = 8.7921$ MeV. The energy of the bcc lattice of ^{56}Fe remains the main state of the cold substance up to 10^{30} dyne/cm^2 and $\rho \approx 10^6$ g/cm^3 [86]. Under these conditions the substance is a plasma, to which a one-component plasma model may be applied.

For $\rho \gg 10^9$ g/cm^3 the electrons become ultrarelativistic and $\mu_e \sim P^{1/4}$. As P increases, replacement of $((A, Z))$ by $((A', Z'))$ with a higher nuclear energy W_N but lower $\frac{A'}{Z'}$ becomes energy-advantageous, because the increase in $\frac{W_N}{A}$ is greater than the decrease in $\frac{Z\mu_e}{A}$. This accounts for the effect of substance neutronization under its heavy compression [34, 49].

The density jump in the neutronization [49] obeys the relation [34]

$$\frac{\Delta\rho}{\rho} \approx \frac{\Delta n_b}{n_b} \approx \frac{Z}{A}\frac{A'}{Z'} - 1.$$

The equilibrium parameters of nuclei in cold dense matter are collected in Table 8.1 borrowed from [32], which shows the highest densities at which these nuclei still persist; μ_e is the chemical potential at this density.

The transformation of a nucleus to the next nucleus brings about the phase transition of the Ist kind with a density jump $\frac{\Delta\rho}{\rho}$ given in the last column in Table 8.1 [32].

The line above the horizontal bar in Table 8.1 corresponds to the highest density whereby the ground state of the matter contains nuclei with laboratory-measured masses. The last line in Table 8.1 corresponds to the density at the boundary of neutron stability (neutron drip), which is estimated [34] at $\rho_{\text{ND}} \approx 2.2 \cdot 10^{11}$ g/cm^3.

As already noted, to describe the neutron matter for $\rho \lesssim 10^{14}$ g/cm^3 use is made of the methods for calculating the properties of atomic nuclei under ordinary

Table 8.1 Nuclei in the ground state in cold dense matter [32]

Element	Z	N	Z/A	$\rho_{\max}$ (g/cm^3)	μ_e (MeV)	$\Delta\rho/\rho$ (%)
^{56}Fe	26	30	0.4643	$7.96 \cdot 10^6$	0.95	2.9
^{62}Ni	28	34	0.4516	$2.71 \cdot 10^8$	2.61	3.1
^{64}Ni	28	36	0.4375	$1.30 \cdot 10^9$	4.31	3.1
^{66}Ni	28	38	0.4242	$1.48 \cdot 10^9$	4.45	2.0
^{86}Kr	36	50	0.4186	$3.12 \cdot 10^9$	5.66	3.3
^{84}Se	34	50	0.4048	$1.10 \cdot 10^{10}$	8.49	3.6
^{82}Ge	32	50	0.3902	$2.80 \cdot 10^{10}$	11.4	3.9
^{80}Zn	30	50	0.3750	$5.44 \cdot 10^{10}$	14.1	4.3
^{78}Ni	28	50	0.3590	$9.64 \cdot 10^{10}$	16.8	4.0
^{126}Ru	44	82	0.3492	$1.29 \cdot 10^{11}$	18.3	3.0
^{124}Mo	42	82	0.3387	$1.88 \cdot 10^{11}$	20.6	3.2
^{122}Zr	40	82	0.3279	$2.67 \cdot 10^{11}$	22.9	3.4
^{120}Sr	38	82	0.3167	$3.79 \cdot 10^{11}$	25.4	3.6
^{118}Kr	36	82	0.3051	$(4.32 \cdot 10^{11})$	(26.2)	

The upper part was obtained with experimentally measured nuclear masses and the lower part was obtained from the mass Moeller formula. The last line corresponds to neutron stability boundary. The table was borrowed from [34]

(laboratory) conditions. These are the Hartree–Fock method for a given neutron–neutron interaction potential, the quasiclassical Thomas–Fermi approximation, and the compressible liquid drop model.

According to these calculations, the number of neutrons outside of the atomic nucleus increases and the number of protons inside of it decreases with increasing compression.

The results of these calculations were generalized [34, 65] in the form of analytical formulas convenient for calculating the equation of state of the inner crust of neutron holes.

8.3 Thomas–Fermi Model

According to [34], in the vicinity of neutron stability boundary the number of nucleons in an elementary cell increases rapidly with compression and may range up to $A_{\text{cell}} \approx 1000$ for $\rho \approx 10^{13}$ g/cm^3 [65]. This seriously complicates the application of the Hartree-Fock method by increasing sharply the amount of requisite calculations (see the problem of Kon's "exponential" barrier [50]. On the other hand, the increase in the number of nucleons in an elementary cell justifies the application of a simpler quasiclassical approximation (see Sect. 3.6).

Numerous calculations by this model (for more details, see [34]) yielded a neutron evaporation (neutron drip) density $\rho_{\text{ND}} \approx 4 \cdot 10^{11}$ g/cm^3. According to [15],

Z remains practically invariable ($Z \approx 30$) for $10^{11}\,\mathrm{g/cm^3} \le \rho \le 5 \cdot 10^{13}\,\mathrm{g/cm^3}$ and then drops to $Z \approx 20$ for $\rho \approx 10^{17}\,\mathrm{g/cm^3}$.

The liquid-drop model [34] proceeds from separating out the bulk $E_{\mathrm{n,bulk}}$ and surface $E_{\mathrm{n,surf}}$ parts of the total energy:

$$E_{\mathrm{cell}} = E_{\mathrm{n,bulk}} + E_{\mathrm{n,surf}} + E_{\mathrm{coul}} + E_e,$$

where the first three terms depend on the size and shape of a nucleus. The nucleons are then divided into three subsystems: the neutron bulk liquid "i", the lower-density liquid "o", and the surface liquid at the "i–o" interface denoted by "s". The entire system is in mechanical and "chemical" equilibrium. Inside the nucleus in phase ff the nucleon densities $n_{p,i}$, $n_{n,i}$ are constant, while $n_{n,0}$ and $n_{p,0} = 0$ in phase "o". The nucleus size itself can be defined in terms of the proton radius r_p so that $(4\pi r_p^3 n_p)/3 = Z$.

The equilibrium parameter values are found by minimizing $\varepsilon = \frac{E_{\mathrm{cell}}}{V_c}$ for a given n_b. In doing this, account is taken of the conditions for chemical and mechanical equilibrium (for more details, see [34]), which yield five additional minimization conditions.

Calculations by one of the most modern versions of the liquid-drop model [22] as applied to the conditions of the lower crust of a pulsar suggest that the number of nucleons in a nucleus A increases with density and ranges up to ≈300 for $\rho \approx 10^{14}\,\mathrm{g/cm^3}$ and $A_{\mathrm{cell}} \approx 1000$. In this case, the number of protons varies quite slowly, $Z \approx 40$. For $\rho \approx 10^{14}\,\mathrm{g/cm^3}$ the nuclei turn out to be quite heavy and neutron-excessive, which brings up the question about their stability with respect to deformations and fission.

According to the calculations of [34], for $\rho < 10^{13.5}\,\mathrm{g/cm^3}$ the ground state of nuclear matter consists of spherical nuclei, which are stable with respect to decay into differently shaped structures, fragments, or *npe*-gas. The nuclear shape sphericity in this domain follows, for instance, from the liquid-drop model, which minimizes the spherical shape owing to the contribution $E_{\mathrm{n,surf}} + E_{\mathrm{coul}}$ for $r_p \ll r_c$. It is likely that the situation changes for $\rho > 10^{13.5}\,\mathrm{g/cm^3}$, where $r_p > r_c \gtrsim 0.5$.

Exotic nuclear shapes emerge [34] when the nuclear volume comes to exceed ≈50 % of the total volume of the system, and the nuclear matter with a spherical neutron "bubble" becomes energy-prominent.

To determine non-spherical structures requires minimizing the ε functional with the inclusion of surface effects [34].

The historically first works of this kind were performed in the calculation of the gravitational collapses of massive stars. As shown in [34], for $T \gtrsim 10^{10}\,\mathrm{K}$ and an entropy of (1–2) k_{B} per nucleon, prior to transition to the homogeneous plasma state there occurs a series of phase transitions involving changes in nuclear shapes. Spherical nuclei in a nucleon gas ($3N$) as well as spherical "bubbles" ($3B$) in dense nuclear matter were considered. In the two-dimensional case a study was made of nuclear cylinders ($2N$) and hollow cylinders ($2B$) in a nuclear gas. In one case, parallel layers of nuclear matter separated by the nuclear gas $1N$ were analyzed. It

was determined that with increasing density there occurs a $3N \rightarrow 2N \rightarrow 1N \rightarrow 2B \rightarrow 3B$ transformation with the subsequent transition to homogeneous matter. These transitions go in the direction of increasing fraction of the higher density (nuclear) phase.

In the analysis of the situation for $\rho \gtrsim 10^{14}\,\mathrm{g/cm^3}$, in [58] it was shown that the very position and existence of exotic nuclear structures depends on the form of the N–N interaction potential. The $3N \rightarrow 2N \rightarrow 1N \rightarrow 2B \rightarrow 3B$ transitions begin for $n_{cc} \approx 0.064\,\mathrm{fm^{-3}} \approx \frac{1}{3}\,n_0(1.1 \cdot 10^{14}\,\mathrm{g/cm^3})$ and terminate with the transition of $3B$ to a homogeneous *npe*-substance for $n_{cc} \approx 0.096\,\mathrm{fm^{-3}}$; $\rho_{cc} \approx 1.6 \cdot 10^{14}\,\mathrm{g/cm^3}$. The energy between the exotic phases is quite low, $\lesssim \mathrm{keV\,fm^{-3}}$.

As shown in [71], in the relativistic Thomas–Fermi (RTF) model the existence domain of exotic phases is quite narrow: $(1.0\text{–}1.5) \cdot 10^{14}\,\mathrm{g/cm^3}$. In [95], an even more narrow range, $0.050\text{–}0.058\,\mathrm{fm^{-3}}$, was obtained for the structural transitions.

Outside of the domain of experimentally studied nuclei, the equation of state of the nuclear substance has been poorly studied. For $\rho > \rho_{\mathrm{ND}}$ the nuclear properties depend progressively heavier on the ambient neutron gas, whose pressure increases with increasing total pressure. The equation of state of nuclear matter consists of nucleon Hamiltonian, which describes the nucleon interaction for $\rho \leq 2\rho_0$. Non-nucleon degrees of freedom will be significant at higher densities. An effective nuclear Hamiltonian is introduced is introduced for the description in the $10^{11} < \rho \leq \rho_0\,\mathrm{g/cm^3}$ domain. In this case, the effective interactions are defined in such a way as to describe the properties of the ordinary (laboratory) nuclei, because the main contribution to the pressure for $\rho \geq 10^{13}\,\mathrm{g/cm^3}$ is made by neutrons and the effective nuclear forces provide an adequate description of the neutron gas of subnuclear density. Although we have no direct experimental information about the neutron substance, there are reasonably reliable numerical data about its properties for $n_n \lesssim n_0$[75, 76].

A comparison of two equations of state of the neutron substance is shown in Fig. 8.8 [34]. One can see that the transition to the *npe*-liquid appreciably increases the slope of the curves: there occurs an increase in substance "rigidity".

The slope of the curve is described by the adiabatic exponent

$$\gamma \sim \left(\frac{\rho}{p}\right)\left(\frac{\delta p}{\delta \rho}\right)$$

(see Fig. 8.9).

For $\rho < \rho_{\mathrm{ND}}$ the adiabatic exponent $\gamma \sim \frac{\rho}{p}\left(\frac{\partial p}{\partial \rho}\right)$ is close to $4/3$[34], because in this domain the ultrarelativistic gas P_e and lattice P_i pressures are proportional to $\rho^{4/3}$. The pressure above the density jump is defined by the "soft" equation of state of the liquid-drop model, which lowers γ. After the domain of "stability curve" the equation of state becomes much more rigid, with an appreciable increase in γ in the ρ_{cc} domain. The subsequent growth of γ is associated with the disappearance of nuclei and the emergence of the liquid of neutrons, protons, and electrons.

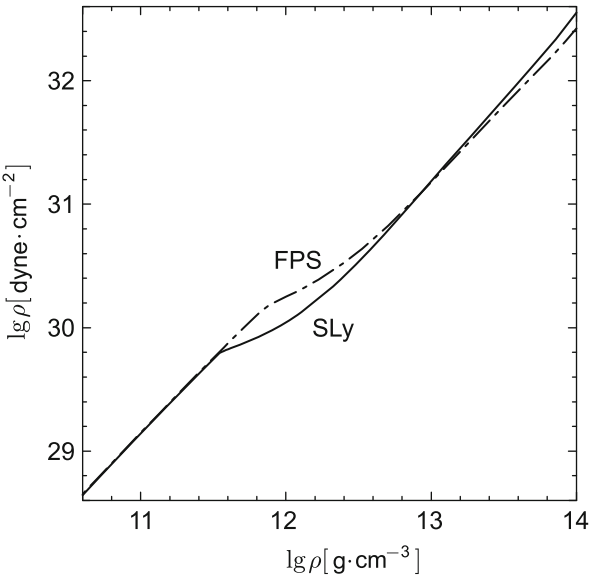

Fig. 8.8 Comparison of SLy and FPS equations of state [34]

Here we shall not describe the strength properties of a nuclear crystal for $\rho < \rho_{cc}$, which were analyzed for the relativistic case in [17] and for the nonrelativistic case in [34]. These properties are significant in the description of the crust of a neutron star for $\rho \lesssim 10^{14}$ g/cm^3. Considered in this case are bcc lattices and polycrystalline structures. Data on the shear moduli of the Coulomb one-component bcc lattice plasma with neglect of screening by degenerate electrons are given in [68]. The following expression was obtained for the shear modulus:

$$\mu = \frac{1}{5}(2b_{11} + 3c_{44}) = 0.1194\,\frac{n_N(Ze)^2}{r_c}.$$

In an isotropic medium this expression is of the form:

$$\mu = 0.0159(Z/26)^{2/3}P_e,$$

where P_e is the pressure of ultrarelativistic electron gas. Therefore,

$$\mu/K = 0.016(Z/26)^{2/3}(P_e/\gamma P) \ll 1.$$

For this crystal the Poisson coefficient is $\sigma \simeq 1/2$ and the Young modulus is $E \simeq 3\mu$.

The plasma in magnetic field has been the object of numerous investigations in connection with research on controlled thermonuclear fusion [26, 27] and magnetohydrodynamic generators, as well as in connection with astrophysical applications [34].

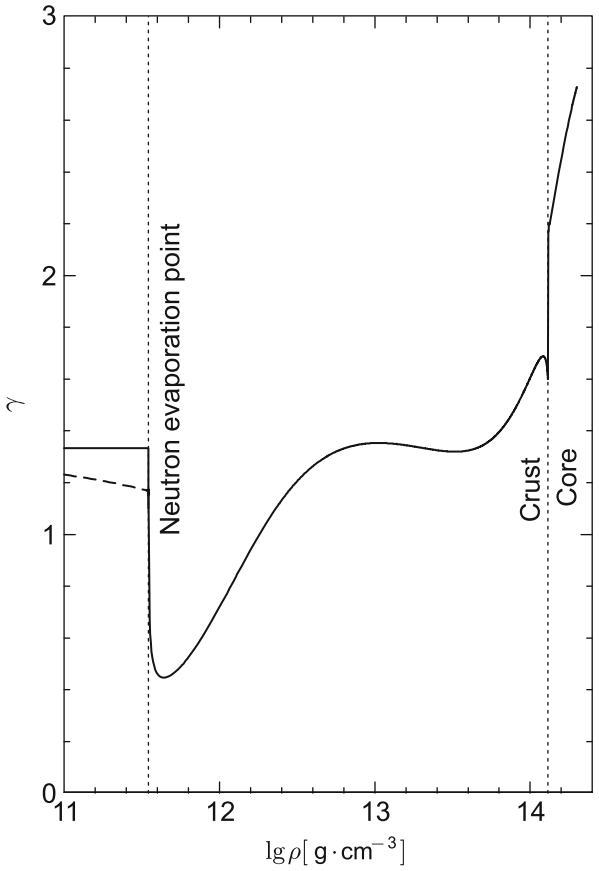

Fig. 8.9 Adiabatic exponent γ for the ground state of the substance of a neutron star for the HP model up to the neutron evaporation point and for the CLDM model [22, 23] for higher ρ[34]

In the latter case, as we saw above, emphasis is placed on neutron stars, where typical fields range up to $\approx 10^{12}$ Gs or $\approx 10^{15}$ Gs for magnetars [26, 27]. Under such fields the electron and ion motion transverse to the magnetic field is quantized into Landau orbitals of length $a_m \sim \left(\frac{\hbar c}{eB}\right)^{1/2}$. The ratio between the Bohr radius a_0 and this length is the field intensity parameter $\gamma = \left(\frac{a_0}{a_m}\right)$. For large γ the Lorentzian force acting on the valence atomic electrons exceeds the Coulomb nuclear forces. Relativistic effects affect the Landau electron energy levels when the magnitude of the field (in relativistic units)

$$b = \hbar\omega_c/(m_e c^2) = B/B_r \gtrsim 1.$$

Here, $\omega_c = \frac{eB}{(m_e c^2)}$ is the electron cyclotron frequency and $B_r = m_e^2 c^3/(e\hbar) \approx 4.4 \cdot 10^{13}$ Gs is the relativistic magnetic field.

In this notation the magnetic field is called strong for $\gamma \gg 1$ (radio pulsars) and superstrong for $b \gg 1$ (magnetars).

The thermodynamic functions of ideal electron gas in magnetic field are given in [34].

The effect of magnetic fields on the thermodynamics and structure of substance (see Fig. 8.7) is set forth at length in [34], which presents an exhaustive literature list and convenient approximation formulas.

When the density becomes higher than $\rho > \rho_0 \approx 2.8 \cdot 10^{14}\,\mathrm{g/cm^3}$, the nuclear substance transforms to new forms, which are different from the well-known nuclear structures at normal conditions ρ_0 and are therefore referred to as "exotic" [34]. The existence of these states is caused by the properties of strong (hadronic) interaction (pion and kaon condensations) as well as by the quark structure of baryons.

8.4 Meson, Pion, and Kaon Condensations

In the exposition of this section we shall follow monograph [34].

Pions are the lightest mesons; they may be present in a system as free particles and replace electrons in a condensate for $\rho > \rho_0$[4]. The idea of pion condensate formation due to πN attraction was developed in [61, 62, 87, 88], where a change in symmetry was noted and an important role of nuclear correlations for the existence of such a condensate was emphasized. The formation of a pion condensate, according to [34], "softens" the equation of state of nuclear substance.

Kaons are the lightest strange mesons and, according to [44], must form a condensate for$\rho > 3\rho_0$ on the strength of $K^- N$ attraction. Kaon condensation, according to [34], sharply "softens" the equation of state as well.

Since quarks are the main building elements of hadrons, for sufficiently high densities they may "dissociate" to form quark substance, or quark-gluon plasma (see Sect. 6.3). The equation of state of quark-gluon plasma was calculated in the framework of the lattice model [20] developed for quantum chromodynamics. The properties and models of the quark-gluon plasma were considered in Chap. 6.

Like in a gas, the strong NN interaction may be represented as the sum of a short-range repulsion and a long-range attraction, and therefore crystallization is possible in the system. In this case, possible in the neutron matter is the formation of complex structures like alternating layers of liquid crystals, quasione-dimensional filaments, etc. As this takes place, each of the coexisting phases may be electrically charged. It is evident that the formation of crystalline structures may lead to strength effects.

A large uncertainty in the equation of state of nuclear matter permitted advancing [102] a heuristic hypothesis that the exotic structures emerging under heavy compression which are in β equilibrium will also be stable under normal conditions, forming hypothetical "self-bounded" states [57] or Q matter [5]. Suchlike hypotheses underlie the construction of modern models of "strange" stars [26, 27, 34].

Exchange of virtual pions is responsible for the long-range component of N–N interaction. The energy ω_n and momentum K of a pion do not satisfy the ordinary

formulas $\omega_n^2 = m_\pi^2 c^2 + k^2 c^2$. The virtuality of pions consists in that they live for a time $\sim \frac{\hbar}{m_\pi c^2} \approx 5 \cdot 10^{-24}$ s and travel a characteristic length $\sim \frac{\hbar}{m_\pi c} \approx 1.4$ fm.

Owing to a strong pion–nucleon interaction, the ground state of dense nuclear matter must comprise the Bose–Einstein condensate of pions [61, 62, 87, 88]. This condensation may be described on the basis of the theory of a nuclear Fermi liquid [64] or in terms of a Lagrangian [87, 88].

The former approach involves a stability analysis of the spatially homogeneous state of $npe\mu$ substance in β equilibrium. It turns out [34, 61, 62] that the system for $\rho > \rho_0$ loses stability with respect to periodic structures—density waves. In the consideration of stability for $\rho > \rho_0$ it was possible to determine different perturbation branches and their stability.

Pion condensation plays an important role in the calculation of neutrino emission, because it opens the URCA process with momentum conservation in the normal $npe\mu$ substance.

Calculations of the equation of state of the $npe\mu$ substance under the conditions of β equilibrium between hadrons and leptons proceed [34] from minimization of the total energy density:

$$\varepsilon(n_b, n_q^{(h)}, n_e, n_\mu) = \varepsilon(n_b, n_q^{(h)}) + \varepsilon_e(n_e) + \varepsilon_\mu(n_\mu),$$

for a fixed baryon density and under the electroneutrality condition:

$$n_n + n_p = n_b, \quad n_p + n_{\pi_s^+} = n_{\pi^-} + n_e + n_\mu.$$

The possibilities that open up in this case are depicted in Fig. 8.10 [34]. One can see a strong "softening" of the equation of state due to pion condensation, which has the effect that $\upsilon_s^2 < 0$ (in the *CB* portion in Fig. 8.10).

Figure 8.10c deserves special mention, for it predicts [62, 63] the formation of anomalous nuclei of significantly higher density than the ordinary ones.

In astrophysics this leads to the possibility of existence of anomalous stars of size of about a golf ball [34, 37].

In the case of finite temperatures the peak of pion condensation remains invariable. This is a strong $\pi^- n$ attraction, which is opposed by an increase in kinetic energy due to the ordering of condensate state. An increase in T shifts the condensation towards higher densities [55]. At the same time, for $k_B T \gtrsim 30$ MeV the thermal pion gas also makes a contribution to the thermodynamics of the system.

The critical temperature T_{crit}^{π} of pion condensation [52, 55] is equal to $k_B T_{\text{crit}}^{\pi} \gtrsim 60$ MeV.

Kaon condensation was long considered as a process of little significance due to the large kaon mass $m_K c^2 = 493.6$ MeV. The stability condition for kaons K^- in the medium:

$$\mu_{K^-} = m_K c^2 = \mu_e.$$

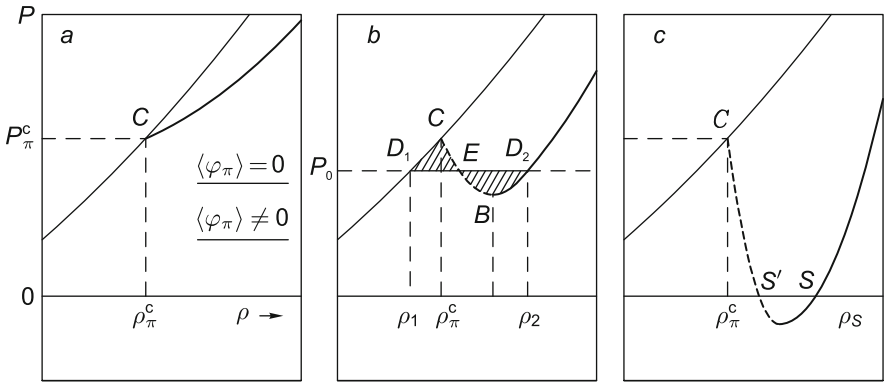

Fig. 8.10 Three qualitatively different equations of state of pion-condensed media. *Bold solid lines* show pion-condensed phases, while *thin solid lines* refer to the normal phase: (**a**) phase transition of the second kind with a moderate softening; (**b**) a strong softening, which implies a phase transition of the first kind for $P = P_0$; (**c**) a very strong softening, which leads to stably "anomalous" superdense self-bounded states for $P = 0$ and $c = c_s$[34]

A kaon may occupy the lower energy state only at high densities

$$n_b > \frac{1}{3\pi^2}\left(\frac{m_K c}{\hbar}\right)^3 \approx 33 n_0 \cdot \frac{x_e}{0.1},$$

where $x_e = n_e/n_b$.

Due to a strong kaon–baryon interaction, kaons form a condensate at densities several times higher than the nuclear one ρ_0[34, 81].

In the $npe\mu$ substance K^- may be produced by way of the reactions

$$e + N \to K^- + N + \nu_e, \quad n + N \to p + K^- + N,$$

whereby its energy $\omega_K < \mu_e$. Nuclear experiments under normal conditions testify to a strong attraction of K^- with an energy ranging from -80 to -120 MeV, and the potential depth is known for $n_b \sim (2\text{–}3)n_0$. Like in the pion case, kaon condensation strongly increases the emission of neutrinos, resulting in enhanced stellar cooling.

Calculations of the effect of kaon condensate on the equation of state of nuclear substance are performed in the framework of an average field model [34]. To construct the corresponding potentials and parameters of the average field model, advantage is taken of the experimental data on kaon-nucleon collisions as well as of the data of the quark model of hadrons and equilibrium nuclear properties [81]. Depending on the intensity of kaon-nucleon attraction, kaon condensation may be a phase transition of the first (for $U_{K^-} \lesssim -90$ MeV) or second ($U_{K^-} \gtrsim 80$ MeV) kind.

Estimates of the bounds of kaon condensation yield a value $n \gtrsim (3\text{–}5)n_0$ [53, 73] and predict a twofold density jump in the transition and a strong "softening" of the equation of state.

The effect of temperature on kaon condensation was investigated in [77, 78], where it was shown that the effect is small for $T \lesssim 60\,\text{MeV}$ and consists in the shift of the condensation bound $\rho_c^k(T) > \rho_c^k(0)$. The data on the parameters of the corresponding critical points are supposedly absent [34].

For a collision energy $E_{e_{ab}} \sim 100\,\text{MeV/nucleon}$ of heavy nuclei the temperatures are not high enough for appreciable hadronization. Possible in this case is the effect of pressure decrease below the normal nuclear density, which is called the "liquid–gas" transition in the nuclear substance [92].

The critical point of this nuclear phase transition corresponds to $T \sim 18\,\text{MeV}$, $\rho \sim 0.4\rho_e$. The occurrence of this transition may manifest itself in the features of fragment distributions in relativistic nuclear collisions. The details of this effect are described in [21].

8.5 Nucleons and Hyperons Under Supercompression

As we saw above, nuclei cannot exist at a density $\rho > (1.5\text{–}2) \cdot 10^{14}\,\text{g/cm}^3$, and the system passes into a quasi-homogeneous plasma of neutrons, protons, and electrons. This state of matter is rather reliably described by the methods of many-body theory, which is validly employed for describing the nuclear structure. In this state, baryons are in β equilibrium with electrons (and with muons if the electron Fermi energy is higher than $m_\mu c^2 \approx 105.7\,\text{MeV}$). Such states of neutron stars are referred to as "$npe\mu$ matter"; it is found in the outer core of neutron stars [34].

Under higher densities the substance passes into a so-called hyperon state [34].

Since we are dealing with densities higher than the ordinary nuclear density, our knowledge about such states are quite scarce, which opens the way to various qualitative assumptions. For instance, here the substance may lose homogeneity with the formation of pion and kaon condensates; the deconfinement of quarks with the production of quark-gluon plasma may also take place (see Sect. 6.3).

The Bose condensation of pions (the lightest of mesons) in nuclear matter is ordinarily hindered by strong pion-nucleon repulsion. However, in superdense matter there may occur collective excitations—quasiparticles with the properties of pions, which may condense with the loss of translation invariance [79]. Further research revealed the possibility of formation of different pion condensate phases. It became clear [79] that short-range correlations and the formation of ordered structures in dense matter impede pion condensation.

Kaons (K mesons)—the lightest strange mesons—are produced in compressed nuclear substance due to the reactions $e + N \to K^- + N + \nu_e$ and $n + N \to p + K^- + N$, where N is a nucleon, whose participation provides momentum conservation along with energy conservation. The possibility of Bose condensation of kaons for $\rho \gtrsim 3\rho_0$ has been studied by many authors [81]. Similarly to the case of

pion condensation, in a neutron star we have to do with K^--like quasiparticles. They have a smaller mass than an isolated K meson, which makes their Bose condensation possible. The formation of kaon condensate depends on the presence of hyperons and has a strong effect on the properties of the nucleon constituent of the substance. Like in the case of pion condensate, in the condensation of pions the translation invariance is lost. The condensate may be formed by way of a phase transition of the first or second kind, depending on the force of attraction between kaons and nucleons [31]. Both pion and kaon condensations make the equation of state significantly softer.

The calculation of the equation of state for $\rho \gtrsim 10^{14}$–$10^{15}\,\mathrm{g/cm^3}$ involves determination of the ground state of the system of hadrons and leptons and is made by minimizing the free energy for given electric and baryon charges.

This is an extremely intricate physical problem solved for an almost complete absence of experimental information—there are observational data only on neutron stars [34], supernova explosions [26, 27], and relativistic nuclear collisions.

Before setting out to discuss the equation of state of nuclear matter, we emphasize once again that the case in point is the description of a homogeneous isotropic nuclear medium characteristic of astrophysical objects. In experiments on nuclear collisions (see Chap. 6) we are dealing with a finite system of nucleons, for which the conditions of homogeneity and thermodynamic equilibrium should be separately verified (see [26, 27]). Also at issue in this case is local thermodynamic equilibrium—an approximation which underlies transient gas dynamics.

In the subsequent discussion we adhere to [34].

For $\rho \sim \rho_0$, nuclei contain no more than 10 % of protons and electrons, and so they may be neglected and the system may be treated as consisting purely of neutrons. A large number of calculations of the equation of state have been made for this matter (see [34, 100] and references therein), which suffer from large uncertainty for $\rho \sim 3\rho_0$, because about half of the nucleon energy is determined by the poorly known potentials of nucleon interactions.

The next step—calculation of the equation of state for the $npe\mu$ substance in β equilibrium—is made proceeding from the data on asymmetric nuclear matter [34]—a homogeneous mixture of nucleons [1]—as well as the methods of Brueckner–Bethe–Goldstone (BBG) expansions [8].

To describe the contribution made by nucleons and hyperons to the equation of state of matter requires knowledge of the corresponding interaction potentials [96] with the subsequent calculation of their thermodynamic potentials using, for instance, the Hartree–Fock technique. In the calculations [96] account was taken of nucleons, Σ, Λ, Ξ hyperons and Δ resonances, which turned out to be present in the system for $\rho \gtrsim 1.2 \cdot 10^{15}\,\mathrm{g/cm^3}$. The results were found to depend heavily on the form of interparticle interaction.

Calculations of the equation of state by the Green function [98, 99] and BBG techniques demonstrated a "softening" of the equation of state of substance on including the hyperon subsystem.

The models of nuclear matter are developed for calculating the equation of state of homogeneous and infinite nuclear substance as well as for describing heavy

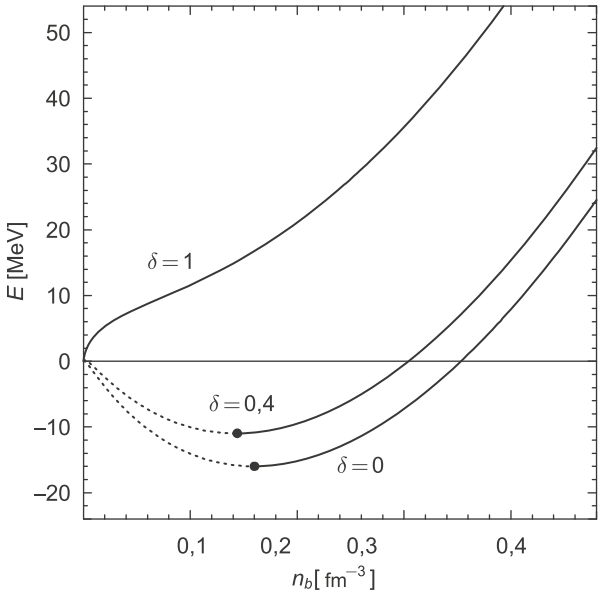

Fig. 8.11 Energy per nucleon as a function of baryon number density for symmetric nuclear matter ($\delta = 0$), for asymmetric nuclear matter with $\delta = 0.4$ (this asymmetry corresponds to the neutron evaporation point in crust of a neutron star and in the central core of a newly born protoneutron star), and purely neutron matter ($\delta = 1$). The minima of the E($E(n_b)$) curves are marked with points. The *dashed segments* correspond to negative pressure. These calculations were performed for the SLy4 model of the effective nuclear Hamiltonian, which was employed for calculating the SLy equation of state [23]. This gives $n_0 = 0.16\,\text{fm}^{-3}$ and $E_0 = -16.0\,\text{MeV}$ [34]

multinucleon nuclei. In the former case the Coulomb energy for an infinite system may be eliminated. In the equation of state for the fluid nuclear model discussed above (Chap. 4) this is effected by the passage $E_{\text{coul}} = 0$ and $A \to \infty$. In this limit the energy per nucleon E depends only on the neutron and proton densities. The properties of this system are conveniently expressed in terms of the nucleon number density n_b and the asymmetry parameter $\delta = (n_n - n_p)/n_b$. The case $\delta = 0$ corresponds to symmetric nuclear matter and $\delta = 1$ to the neutron matter. The former case is most simple: owing to the charge symmetry it is possible to consider only one type of particles—nucleons. The symmetric matter and the neutron matter are good approximations for describing the bulk properties of heavy nuclei and neutron stars, respectively. In the former case, for ordinary nuclei under terrestrial conditions $\delta^2 \lesssim 0.04$.

Calculations of nuclear matter properties serve as a material for comparison with multiparticle nuclear models (see [8]). E and n_e at the minima of the curves (Fig. 8.11) are denoted by E_0 and n_0, so that $B_0 = -E_0$ is the greatest binding energy per nucleon in nuclear matter. A comparison of short-range repulsion and long-range attraction determines the "saturation" in the nucleon-nucleon interaction. $B_0 = -E_0$ is the binding energy at saturation and n_0 is the saturation density.

Let us consider the case of small δ typical for nuclei at normal conditions:

$$E(n_b, \delta) \simeq E_0 + S_0\delta^2 + \frac{K_0}{9}\left(\frac{n_b - n_0}{n_0}\right)^2,$$

where S_0 and K_0 are the symmetry and compressibility energies:

$$S_0 = \frac{1}{2}\left(\frac{\partial^2 E}{\partial \delta^2}\right)_{n_b=n_0,\delta=0}, \quad K_0 = 9\left(n_b^2\frac{\partial^2 E}{\partial n_b^2}\right)_{n_b=n_0,\delta=0}.$$

S_0 defines the increase in energy due to a small asymmetry; K_0 defines the $E(n_b)$ curve at a point $n_b = n_0$ and describes the increase in energy with increasing pressure.

The numerical values of the quantities in equilibrium are determined from experimental data on the nuclear properties at normal conditions and are as follows (with different degrees of accuracy): $n_0 = 0.16 \pm 0.01\,\text{fm}^{-3}$, $B_0 = 16.0 \pm 1.0\,\text{MeV}$, $S_0 = 32 \pm 6\,\text{MeV}$, $K_0 = 231 \pm 5\,\text{MeV}$ [34].

The Hamiltonian of the system must comprise the contributions from particles or interactions. These contributions or usually determined by the methods of quantum chromodynamics (QCD). In this case, the Coulomb term in the Hamiltonian is negligible and the weak interaction is implicitly present in channels for the attainment of equilibrium.

Unfortunately, the practical realization of this formalism runs into serious difficulties, and therefore use is made of simplified models in which quarks are treated as being bound in hadrons (baryons and mesons) rather than treated separately. Next introduced into the Hamiltonian is a phenomenological model of strong (hadronic) interaction reliant on mesoscopic theories, where the strong hadronic interaction is described by a meson exchange model and the corresponding pseudopotentials are introduced. The parameters of these pseudopotentials are found on the basis of numerous experiments on nucleon scattering and experimental data on the properties of deuterium ^{2}H. Experimental data on NH and HH interactions are confined to low-mass Λ and Σ hyperons. For other hyperons, experimental information is even more scarce.

Apart from pair interactions, for $\rho \geq 10^{15}\,\text{g/cm}^3$ a significant contribution is made three- and multiparticle interactions, the data on them being quite scarce.

At first we consider a simplified minimalistic model [34] based on extension of the $npe\mu$ model to the domain $\rho \geq 2\rho_0$.

Historically, the main task of nuclear physics was to find the forces binding nucleons into a nucleus. Modern phenomenological potentials are constructed on the basis of a huge number of experiments on nucleon-nucleon scattering at energies of up to 350 MeV, above which there set in inelastic pion production processes.

The effective nucleon-nucleon interaction potential is a complex and quite frequently cumbersome tensor function of spatial, spin, and isospin variables:

$$\hat{\upsilon}_{ij} = \sum_{u=1}^{18} \upsilon_u(r_{ij})\hat{O}_{ij}^u,$$

where the first 14 operators are charge-independent, i.e. are invariant with respect to time in the isotopic space:

$$\hat{O}_{ij}^{u=1,\ldots,14} = 1,\ \tau_i \cdot \tau_j,\ \sigma_i \cdot \sigma_j,\ (\sigma_i \cdot \sigma_j)(\tau_i \cdot \tau_j),\ \hat{S}_{ij},\ \hat{S}_{ij}(\tau_i \cdot \tau_j),\ \hat{L} \cdot \hat{S},\ \hat{L} \cdot \hat{S}(\tau_i \cdot \tau_j),$$
$$\hat{L}^2,\ \hat{L}^2(\tau_i \cdot \tau_j),\ \hat{L}^2(\sigma_i \cdot \sigma_j),\ \hat{L}^2(\sigma_i \cdot \sigma_j)(\tau_i \cdot \tau_j),\ (\hat{L} \cdot \hat{S})^2,\ (\hat{L} \cdot \hat{S})^2(\tau_i \cdot \tau_j).$$

Even this complex representation has a limitation: it is local and depends on $\mathbf{r}_{ij}$, and does not describe nonlocal terms—for instance, meson exchange.

Three-particle interactions begin to play a part with increasing ρ and are required for describing the binding energy between ^{3}H and ^{4}He. One way to take them into account [80, 90] consists in modifying the medium-range potential and the single-pion exchange.

The relativistic corrections caused by the passage from the co-moving frame of reference to the laboratory one decrease the repulsive part of the potential and make a contribution to the equation of state at high densities [1].

At the hadronic level, strong nucleon-nucleon interaction is the result of meson exchange between the nucleons. In field terms this is a result of the interaction between nucleon and meson fields.

The complete modern theory of strong interaction is the theory of quantum chromodynamics (QCD), where the main fields are those of quarks and gluons. Quarks and gluons do not arise directly in the meson exchange model for the strong interaction under consideration, and the substance consists of mesons, nucleons, and their resonances. The meson exchange model successfully describes nucleon-nucleon interactions at energies $\lesssim$350 MeV, the properties of ^{2}H and diluted nuclear systems, and operates on nuclear and meson fields ψ and φ. In this case, mesons have a mass $\lesssim$1 GeV/c^2, which does not permit describing short-range interactions for $\lesssim$0.2 fm.

Meson-nucleon interaction is described by the corresponding term in the Lagrangian, which depends on the properties of meson field symmetry under rotation and reflection.

As regards symmetry, considered are the following types of mesons: pseudoscalar (the field φ^{ps}, the mass m_{ps}), scalar (the field $\varphi^{(s)}$, the mass m_s) and vectorial (the field $\varphi_\mu^{(v)}$, $\mu = 0, \ldots 3$, the mass m_v).

Experiment gives [34]: $m_\pi c^2 = 138$ MeV, $m_\eta c^2 = 548$ MeV, $m_\rho c^2 = 769$ MeV, $m_\omega c^2 = 783$ MeV, and $m_\delta c^2 = 983$ MeV. The terms in the corresponding Hamiltonian describe the prescribed types of interactions and field symmetries, and contain pure adjustable parameters for describing experimental data [34].

The contribution from single-particle exchange by π- and ω–mesons reflects two important properties of nucleon-nucleon interaction. The π exchange results in long-range ($\frac{\hbar}{(m_\pi c)} \approx 1.4$ fm) forces, while the ω exchange is responsible for the short-range ($\frac{\hbar}{(m_\omega c)} \approx 0.25$ fm) repulsion and for the reasonable magnitude of the spin-orbit term.

The two-pion exchange is responsible for the medium-range ($\frac{\hbar}{(2m_\pi c)} \approx 0.7$ fm) attraction, in which excited resonance states also make their contribution. Summing the corresponding Feynman diagrams gives the scattering matrices, the calculations which may be compared with ^{2}HH collision experiment data.

To perform multiparticle calculations requires interaction pseudopotentials, which are constructed proceeding from the field-theory meson-exchange methods described above. This is usually done in the framework of a single-boson exchange (SBE) model, when the multipion exchange is described by the scalar σ meson ($m_\sigma c^2 \approx 550$ MeV) exchange with the corresponding σ-nucleonic coupling constant.

The interaction term depends not only on the distance between the particles, but also on their neighbors and their wave functions.

The single-component exchange model permits describing with a good accuracy $\approx$4300 results of *pp*- and *np* collisional experiments at energies $\lesssim$350 MeV.

Detailed data on the potentials may be found in [93, 101].

Data on nucleon-hyperon and hyperon-hyperon interactions are quite scarce. There are only a few points on nucleon-hyperon interactions and no points on hyperon-hyperon interactions. Available are data on hypernuclei with $A = 3$ and $A = 4$. Under these conditions, considerations about the types of interaction symmetries are invoked for constructing the corresponding potentials (for more details, see [34]).

The energy of nuclear matter is calculated in the following formulation [34]: a system of A_b nucleons (N neutrons and Z protons) is considered in the limit $V \to \infty$, $Z/A_b = const$. In homogeneous nuclear matter $n_n = \frac{N}{V}$, $n_p = \frac{Z}{V}$, and $n_b = \frac{A_b}{V} = n_n + n_p$. The Coulomb energy and proton–neutron mass difference are neglected.

To calculate the equation of state of nuclear matter, use is made of the method of Green function, which is basically a version of the perturbation method, or variational methods, which involve minimizing the Hamiltonian in the space of multiparticle wave functions $\{\psi_{\text{var}}\}$[1].

It is well known that the main properties of atomic nuclei may be described by two, on the face of it, different models: the shell model and the liquid-drop model. In the former model the multiparticle problem reduces to the problem of the motion of a single particle in some average field of other particles. In the liquid-drop model the nucleons interact with each other so strongly that their motion is completely collective, so that the nucleus resembles a droplet of strongly coupled nucleons. An analysis of the features of these models from the standpoint of field theory is given in [43], where the interaction of nucleons is effected by scalar and vector mesons. In this case, the scalar meson determines long- and medium-range attraction, which explains the formation of nuclei out of nucleons and the magnitude of potential minimum, while the vector meson defines repulsion and thereby the nuclear binding energy. Analogous models [25, 43] were developed by introducing similar meson fields and including relativistic effects.

An average field model with the introduction of electroneutral field of σ- and ω mesons, where $m_\sigma c^2 \approx 600$ MeV, was proposed in [43]. The contribution of

ω mesons to the interparticle potential is negative in character and increases with density. As a result, the potential has a minimum, which determines the nuclear binding energy.

The relativistic generalization of the model of [43] was set forth in [25], where the average field of the system is calculated in the Hartree approximation. The relativistic average field model has many attractive features. It is simple from the computational viewpoint even for multicomponent baryon matter consisting of nucleons and hyperons. Its Lorentzian invariance ensures that the perturbation propagation velocities are always lower than the velocity of light.

However, this model also has disadvantages. The meson approach implies that the average internucleon distance r_{NN} is much shorter than the virtual meson path $r_\phi = \frac{\hbar}{m_\phi c}$, which is fulfilled for $n_b \gg 100 n_0$. There where the model corresponds to experiment, $r_{\mathrm{NN}} \gg r_\phi$. There are other drawbacks as well (see [34]).

According to density functional method (DFM) [51], the energy of a multiparticle system is a functional of the single-particle density. The ground state energy is determined by minimizing this functional of the single-particle density. The model of the density functional method is significantly simplified in the case of a homogeneous spin-nonpolarized nuclear matter, where everything depends on n_p and n_n. The parametric form of the dependence $\varepsilon_n(n_n, n_p)$ is selected so as to satisfy experimental data or is inferred from more exact models [18, 19]. Several functionals for the equation of state may be found in [34, 83].

With increasing density, hyperons begin to replace high-energy neutrons [34]. Introduced in lieu of the nucleon energy density $\varepsilon_N(n_n, n_p)$ is a more general baryon functional $\varepsilon_B(n_B)$, where n_B is the set of densities of baryon particles B:

$$\sum n_B = n_b.$$

For $n_b \lesssim 10 n_0$ it would suffice to consider six light baryons: the nuclear charge doublet N, the charge singlet Λ, the charge triplet Σ, and the charge doublet Ξ. The parameters of these baryons are collected in Table 8.2. The baryon field possesses well-defined properties in an isospin space, nucleons and hyperon Ξ are represented by an isospin field, Λ by an isoscalar field, and Σ by an isovector field.

To calculate the equation of state [34] we consider a scheme consisting of nucleons, electrons, and muons. The nucleons are a strongly interacting Fermi liquid; the electrons and muons are a quasi-ideal Fermi gas:

$$\varepsilon(n_n, n_p, n_e, n_\mu) = \varepsilon_N(n_n, n_p) + \varepsilon_e(n_e) + \varepsilon_\mu(n_\mu).$$

The equilibrium conditions

$$\mu_n = \mu_p + \mu_e, \quad \mu_\mu = \mu_e$$

Table 8.2 Masses, electric charges, strangenesses, and average measured lifetime of a baryon octet

Baryon	mc^2 (MeV)	$Q(e)$	S	$\tau(s)$
p	938.27	1	0	$>10^{32}$
n	939.56	0	0	886
Λ^0	1115.7	0	−1	$2.6 \cdot 10^{-10}$
Σ^+	1189.4	1	1	$0.80 \cdot 10^{-10}$
Σ^0	1192.6	0	−1	$7.4 \cdot 10^{-20}$
Σ^-	1197.4	−1	−1	$1.5 \cdot 10^{-10}$
Ξ^0	1314.8	0	−2	$2.9 \cdot 10^{-10}$
Ξ^-	1321.3	−1	−2	$1.6 \cdot 10^{-10}$

The baryon number, spin, and parameter ratio of all these baryons are 1, 1/2 and +1 respectively

are reflective of the weak interaction processes

$$n \to p + e + \overline{\nu}_e, \quad p + e \to n + \nu_e,$$
$$n \to p + \mu + \overline{\nu}_\mu, \quad p + \mu \to n + \nu_\mu.$$

The substance is usually transparent to neutrinos, and they make no contribution to the thermodynamics.

For ultrarelativistic electrons

$$\mu_e = \hbar c p_{Fe} \approx 122.1 \left(\frac{n_e}{0.05 n_0}\right)^{1/3} \text{MeV}.$$

For medium-relativistic muons

$$\mu_\mu = m_\mu c^2 \sqrt{1 + \left(\frac{\hbar p_{F\mu}}{m_\mu c}\right)^2}.$$

Muons are present when $\mu_e > m_\mu c^2 = 105.65\,\text{MeV}$.

The pressure

$$P = n_b^2 \left(\frac{d(\varepsilon/n_b)}{dn_e}\right).$$

Figure 8.12 shows the equations of state of the nuclear matter [34] calculated using five models. The BBB1 and BBB2 models are the Brueckner–Bethe–Goldstone models calculated with different nucleon-nucleon potentials and triple interaction models. The APR and APR* models are based on the variational method with the same nucleon-nucleon interaction potentials but with a new triple interaction potential improved using experimental data. The UIX* repulsive part of triple nucleon interactions is stronger than in UIX forces of the APR equation of state. However, this has a weak effect on the equation of state. Finally, the SLy

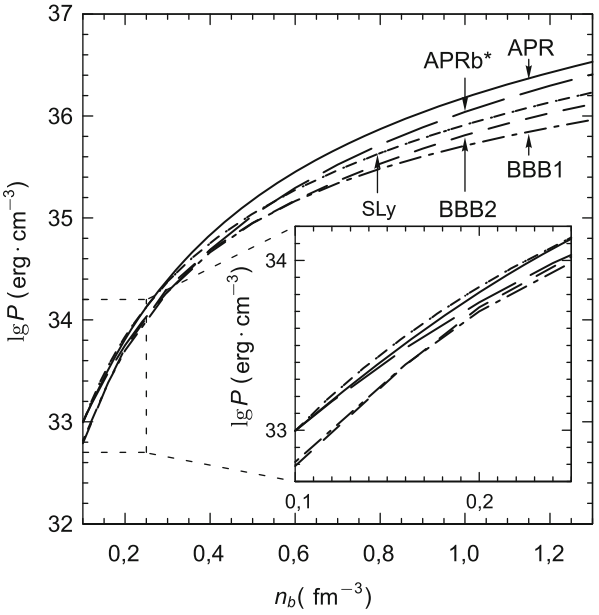

Fig. 8.12 Pressure in relation to the baryon number density for several equations of state (Table 8.3) of $npe\mu$ matter in β equilibrium [34]

equation of state is based on the density functional method and is close to the APR model. As we have already seen, the fraction of protons has a strong (cubic) dependence on the symmetry energy.

An assumption that the substance has the same composition for $\rho \gtrsim 2\rho_0$ as under lower compressions form the basis for the so-called "minimal" model [34], which underlies several models (Table 8.3 [34]). The results of calculations by the APR and APRb* equations of state are compared in Fig. 8.12 [34]. One can see that the inclusion of relativistic calculations and improvement of the triple nucleon interaction potential has only a weak effect on the equation of state even for $n_b \simeq 1.2\,\mathrm{fm}^{-3}$. The APR and APR* models are "softer" than the models with older versions of the potential.

Figure 8.13 gives the density dependence of the adiabatic exponent

$$\gamma = \frac{n_b}{P}\frac{dP}{dn_b} = \frac{P+\varepsilon}{P}\frac{dP}{d\varepsilon}.$$

The oscillations of $\gamma(n_b)$ are reflective of the physical processes in compressed $npe\mu$ substance described above.

With increasing compression, for $\rho \gtrsim 2\rho_0$, as noted above, in the system there sets in the production of hyperons. Their condensation is calculated by conventional thermodynamic methods [34] and is depicted in Figs. 8.14 and 8.15. The appearance

Table 8.3 Selected equations of state (EOS) of the cores of neutron stars [34]

EOS	Model	Reference
BPAL12	$npe\mu$ energy density functional	[13]
BGN1H1	$np\Lambda\Xi e\mu$ energy density functional	[6]
FPS	$npe\mu$ energy density functional	[74]
BGN2H1	$np\Lambda\Xi e\mu$ energy density functional	[6]
BGN1	$npe\mu$ energy density functional	[6]
BBB2	$npe\mu$ Brueckner theory, NN Paris potential + UVII NNN Urbana potential	[7]
BBB1	$npe\mu$ Brueckner theory, A14 NN Argonne potential + UVII NNN Urbana potential	[7]
SLy	$npe\mu$ energy density functional	[23]
APR	$npe\mu$ variational theory, A18 NN Argonne potential + UVII NNN Urbana potential	[1]
APRb*	$npe\mu$ variational theory, A18 NN Argonne potential with stress correction + UVII NNN Urbana potential	[1]
BGN2	$npe\mu$ effective nucleon energy functional	[6]

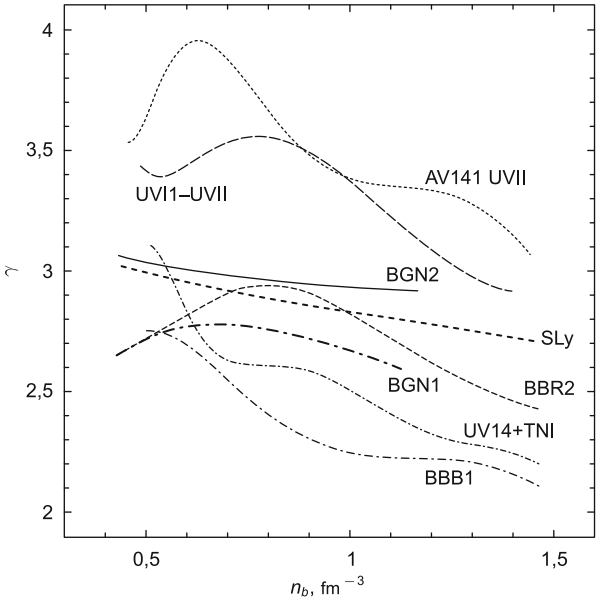

Fig. 8.13 Adiabatic exponent of $npe\mu$ matter in the inner core of a neutron star in relation to the baryon density for several equations of state. All the equations, excepting three equations of state, were borrowed from Table 8.3 and the remaining ones from [100]

of hyperons in the system is easily seen in the composition curves (Figs. 8.14 and 8.15). For instance, $n_\Lambda \simeq n_n$ for $n_b = 8n_0$. According to calculations [34], with increase in compression there initially emerge Σ^- hyperons. The hyperonization of

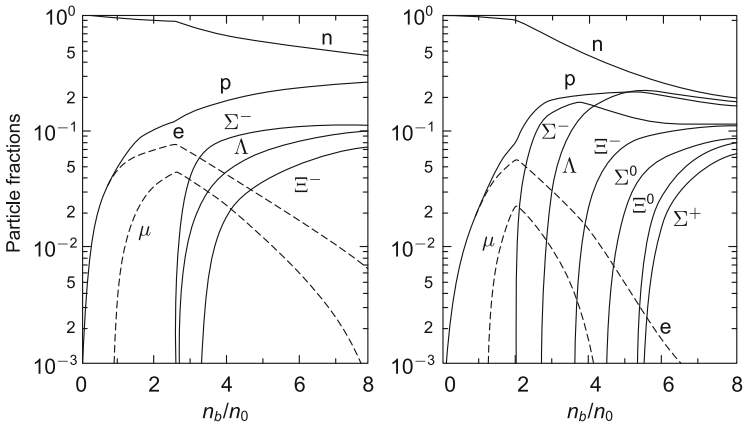

Fig. 8.14 Particle fractions $x_j = n_j/n_b$ as functions of the baryon number density n_b (in units of $n_0 = 0.16\,\mathrm{fm}^{-3}$) are calculated by a formula from [35] for two relativistic baryon interaction models. At the *left*: effective chiral model [35]. At the *right*: relativistic average field model TM1 [94]

substance results in its deleptonization: the negatively charged particles e and μ are replaced by Σ^- and other negative hyperons, and eventually there persist only Σ^+ hyperons. The so-called "baryon soup" emerges for $n_b \simeq 1\,\mathrm{fm}^{-3}$.

The emergence of baryons "softens" the equation of state, because high-energy neutrons are replaced by massive low-energy baryons (which produce a lower pressure). Figure 8.16 serves to illustrate this "softening" of the equation of state. The change of adiabatic exponent γ is shown in Fig. 8.17.

We note that the equation of state depends heavily on the model for $n_b \geq 5n_0$. In particular, little is known about three-particle interactions including hyperons.

General constraints on the equation of state are required in the domain $\rho > \rho_0$, where our knowledge about the behavior of nuclear substance are especially limited. The main requirements of general nature on the equation of state are causality and Lorentz invariance. They may be formulated in different ways. For instance, by introducing the requirements of ultrabaricity $p > \varepsilon$ and causality $\frac{dp}{d\varepsilon} > 1$.

The circumstances of the violation $v_s > c$ for several equations of state are marked by points in Fig. 8.18.

The problem of interrelation between the constraint $v_s < c$, Lorentzian invariance, and causality was analyzed in [11, 12, 16, 70, 85]. Two questions are raised:

(a) does Lorentzian invariance impose constraints on the equations of state?
(b) is the condition $\frac{dp}{d\varepsilon} > 1$ sufficient for the fulfillment of causality condition?

How is the equation of state under discussion related to the principle of causality? The condition $v_s > c$ may be indicative of the violation of causality, because a signal propagates faster than light in this case. However, $v_s > c$ may result from the interference of several special components of sound waves, when high-frequency components are amplified and low-frequency ones attenuate.

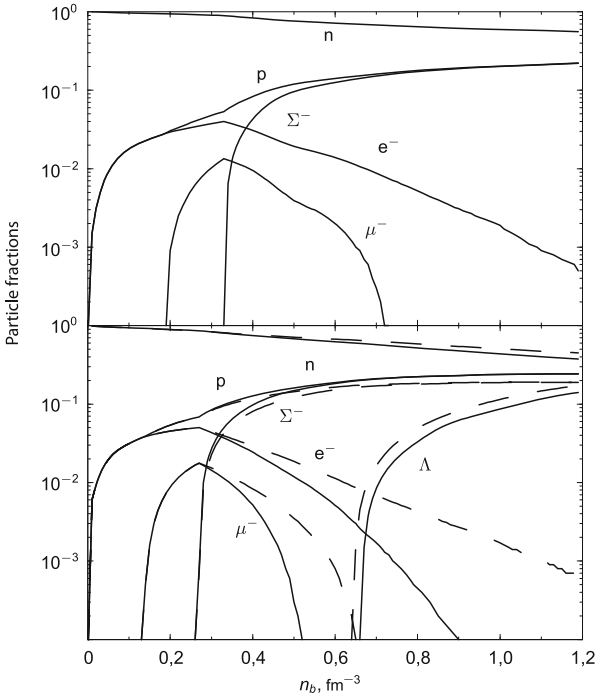

Fig. 8.15 Particle fractions $x_j = n_j/n_b$ as functions of n_b calculated by a formula from [97] in the BHF approximation for two baryon interaction models. The *upper panel*: Nijmegen model *E*[82], only Σ^- hyperon is present in the cores of neutron stars. The *lower panel*: the APR model for the nucleon sector (Table 8.3 [1]) and Nijmegen model *E* [82] for the NH and HH interactions. Unlike the *upper panel*, Λ is present in the dense matter. *Solid lines* in *both panels*: all baryon-baryon (NN, NH, HH) interactions are included. *Dashed lines* in the *lower panel*: HH interactions are (artificially) disengaged [34]

To summarize, it is valid to say that Lorentzian invariance and causality do not rule out the possibility that $v_s > c$. However, the corresponding disconfirmative example pertains to ultrahigh densities, which are higher than the characteristic quark deconfinement densities.

In summary of this section, we emphasize the following. As discussed above, our experimental data about the properties of nuclear matter are quite scarce when we are dealing with temperatures and densities exceeding the ground state with $\rho_0 \simeq 0.15\,\mathrm{fm}^{-3}$ [92]. In this domain the hadronic matter may exhibit a great variety of properties and structures, quite often of a highly exotic nature. Possible for $T < 20\,\mathrm{MeV}$ and $\rho < \rho_0$ is nuclear evaporation [92] and for high densities $\rho > 3\rho_0$ the emergence of hadronic nuclear substance (pion condensate and isomers).

The pionization of nuclear matter is predicted to take place for $T > 50\,\mathrm{MeV}$. The phase transition caused by the deconfinement of quarks and transition of nuclear matter to the state of quark-gluon plasma takes place for $\rho > 5$–$10\rho_0$

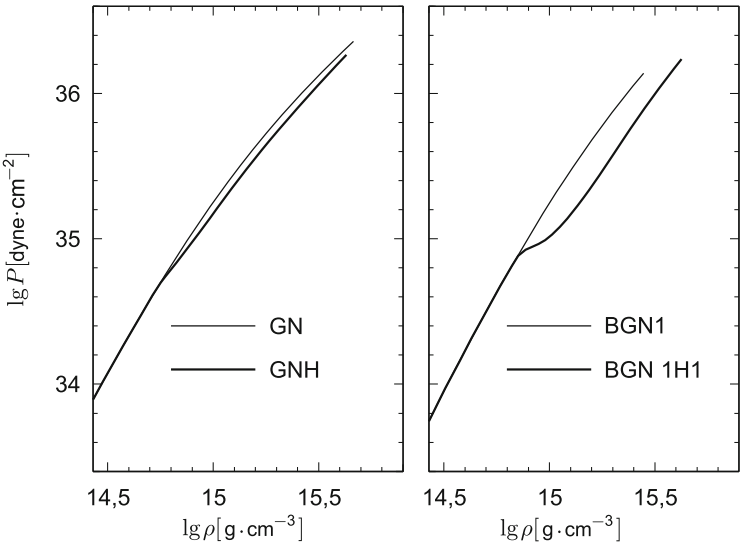

Fig. 8.16 "Softening" of the equation of state by the presence of hyperons. Each panel shows the equation of state with (*bold line*) and without hyperons (*thin line*). At the *left*: equation-of-state model of [29]. At the *right*: BGN1 and BGN1H1 equations of state from [6] (see Table 8.3) [34]

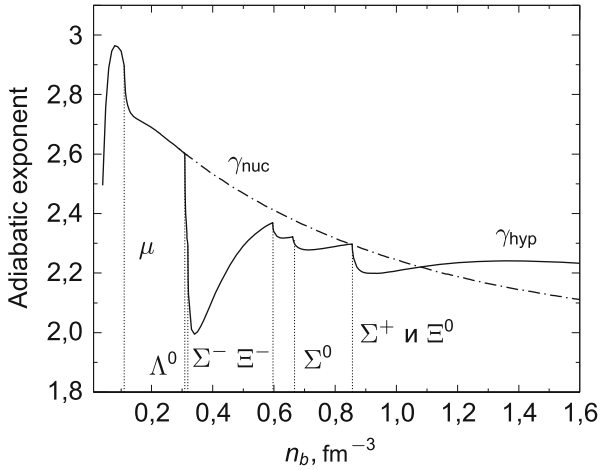

Fig. 8.17 Adiabatic exponent γ as a function of n_b in the core of a neutron star. The calculations were performed for a model equation of state [29]. *Solid line* (γ_{hyp}): hyperonic substance (*vertical dotted lines* indicate the thresholds of the emergence of muons and hyperons); the *dash-dotted line* (γ_{nuc}) corresponds to the case when the appearance of hyperons is artificially forbidden

and $T \approx$ 150–250 MeV. These exotic states of matter supposedly emerged in the first milliseconds after the Big Bang (see Sect. 10.4) and emerge in the course of

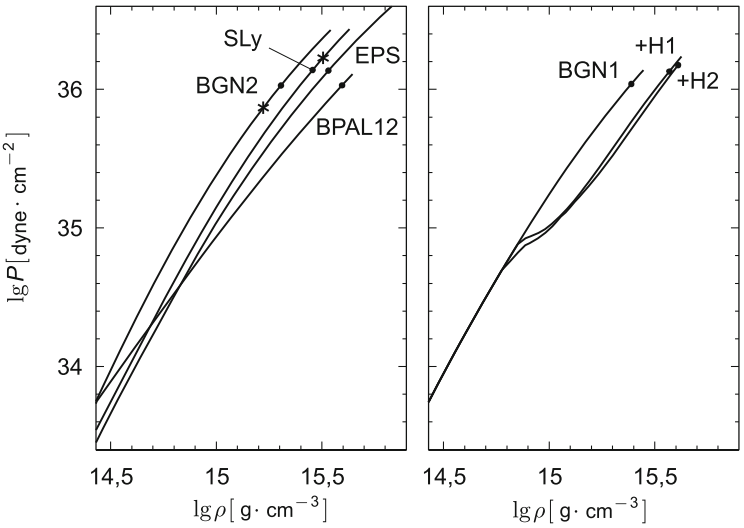

Fig. 8.18 Model equations of state of the core of a neutron star (see Table 8.3). *Black points* correspond to the highest densities in stable neutron stars, while *asterisks* indicate the densities above which the equations of state are superluminal ($v_s > c$)

supernova explosions [26, 27] and neutron star production [34] as well as in the relativistic collisions of heavy nuclei [92].

Of special interest are the works on the prediction of heavy compressions in nuclear collisions performed by the "Frankfurt" school of physics headed by W. Greiner and H. Stöcker [92]. Not only was a beautiful hydrodynamic theory of heavy nuclear collisions constructed in these elegant works, but they also were concerned with the development of a method for obtaining equations of state proceeding from observable collisional data (fragments, pions, etc.).

References

1. Akmal, A., Pandharipande, V.R., Ravenhall, D.G.: Equation of state of nucleon matter and neutron star structure. Phys. Rev. C **58**, 1804–1828 (1987)
2. Alex Brown, B.: Neutron radii in nuclei and the neutron equation of state. Phys. Rev. Lett. **85**, 5296–5299 (2000)
3. Baade, W., Zwicky, F.: Cosmic rays from super-novae. Proc. Natl. Acad. Sci. USA **20**(5), 259–263 (1934)
4. Bahcall, J.N., Wolf, R.A.: Neutron stars. II. Neutrino-cooling and observability. Phys. Rev **140**, B1452–B1466 (1965)
5. Bahcall, S., Lynn, B.W., Selipsky, S.B.: New models for neutron stars. Astrophys. J. **362**, 251–255 (1990)
6. Balberg, S., Gal, A.: An effective equation of state for dense matter with strangeness. Nucl. Phys. A **625**, 435–472 (1997)

7. Baldo, M., Bombaci, I., Burgio, G.F.: Microscopic nuclear equation of state with three-body forces and neutron-star structure. Astron. Astrophys. **328**, 274–282 (1997)
8. Baldo, M., Fiasconaro, A., Song, H.Q., et al.: High density symmetric nuclear matter in Bethe-Brueckner-Goldstone approach. Phys. Rev. C **65**, 017303 (2001)
9. Baym, G., Pethick, C., Sutherland, P.: The ground state of matter at high densities: equation of state and stellar models. Astrophys. J. **170**, 299 (1971)
10. Baym, G., Pethick, C., Sutherland, P.: Statistical mechanics of simple coulomb systems. Astrophys. J. **170**, 299–317 (1971)
11. Bludman, S.A., Ruderman, M.A.: Possibility of the speed of sound exceeding the speed of light in ultradense matter. Phys. Rev. **170**, 1176–1184 (1968)
12. Bludman, S.A., Ruderman, M.A.: Noncausality and instability in ultradense matter. Phys. Rev. D **1**, 3243–3246 (1970)
13. Bombaci, I.: An equation of state for asymmetric nuclear matter and the structure of neutron stars. In: Bombaci, I., Bonaccorso, A., Fabrocini, A., et al. (eds.) Perspectives on Theoretical Nuclear Physics, pp. 223–237. Edizioni ETS, Pisa (1995)
14. Bonche, P., Vautherin, D.: A mean field calculation of the equation of state of supernova matter. Nucl. Phys. A **372**, 496–526 (1981)
15. Buchler, J.R., Barkat, Z.: Properties of low-density neutron-star matter. Phys. Rev. Lett. **27**, 48–51 (1971)
16. Caporaso, G., Brecher, K.: Must ultrabaric matter be superluminal? Phys. Rev. D **20**, 1823–1831 (1979)
17. Carter, B., Quintana, H.: Foundations of general relativistic high-pressure elasticity theory. Proc. Roy. Soc. Lond. Ser. A **331**, 57–83 (1972)
18. Chabanat, E., Bonche, P., Haensel, P., et al.: A skyrme parameterization from subnuclear to neutron star densities. Nucl. Phys. A **627**, 710–746 (1997)
19. Chabanat, E., Bonche, P., Haensel, P., et al.: A skyrme parameterization from subnuclear to neutron star densities. Part II. Nuclei far from stabilities. Nucl. Phys. A **635**, 231–256 (1997)
20. Chodos, A., Jaffe, R.L., Johnson, K., et al.: New extended model of hadrons. Phys. Rev. D **9**, 3471–3495 (1974)
21. Csernai, L.P., Kapusta, J.I.: Entropy and cluster production in nuclear collisions. Phys. Rep. **131**(4), 223–318 (1986)
22. Douchin, F., Haensel, P.: Inner edge of neutron-star crust with sly effective nucleonnucleon interactions. Phys. Lett. B **485**, 107–114 (2000)
23. Douchin, F., Haensel, P.: A unified equation of state of dense matter and neutron star structure. Astron. Astrophys. **380**, 151–167 (2001)
24. Drake, R.P.: High-Energy-Density Physics. Springer, Berlin, Heidelberg (2006)
25. Duerr, H.P.: Relativistic effects in nuclear forces. Phys. Rev. **103**, 469–480 (1956)
26. Fortov, V.E.: Ekstremal'nye sostoyaniya veshchestva (Extreme States of Matter). Fizmatlit, Moscow (2009). [Translated into English: Extreme States of Matter. Series: The Frontiers Collection. Springer, Berlin, Heidelberg (2011)]
27. Fortov, V.E.: Extreme states of matter on earth and in space. Phys. Usp. **52**(6), 615–647 (2009)
28. Friman, B., Höhne, C., Knoll, J., et al. (eds.): The CBM Physics Book. Lecture Notes in Physics, vol. 814, 1st edn. Springer, Berlin (2010)
29. Glendenning, N.K.: Neutron stars are giant hypernuclei? Astrophys. J. **293**, 470–493 (1985)
30. Glendenning, N.K.: Compact Stars: Nuclear Physics, Particle Physics, and General Relativity, 2nd edn. Springer, New York (2000)
31. Glendenning, N.K., Schaffner-Bielich, J.: Kaon condensation and dynamical nucleons in neutron stars. Phys. Rev. Lett. **81**, 4564–4567 (1998)
32. Haensel, P., Pichon, B.: Experimental nuclear masses and the ground state of cold dense matter. Astron. Astrophys. **283**, 313–318 (1994)
33. Haensel, P., Potekhin, A., Yakovlev, D.: Neutron Stars 1: Equation of State and Structure. Springer, New York (2007)

34. Haensel, P., Potekhin, A.Y., Yakovlev, D.G.: Neutron stars 1: Equation of state and structure. Astrophysics and Space Science Library, vol. 326. Springer, New York (2007)
35. Hanauske, M., Zschiesche, D., Pal, S., et al.: Neutron star properties in a chiral SU(3) model. Astrophys. J. **537**, 958–963 (2000)
36. Hands, S.: The phase diagram of QCD. Contemp. Phys. **42**(4), 209–225 (2001)
37. Hartle, J.B., Sawyer, R.F., Scalapino, D.J.: Pion condensed matter at high densities: equation of state and stellar models. Astrophys. J. **199**, 471–481 (1975)
38. Imshennik, V., Nadyozhin, D.: Supernova-1987A, and the emergence of the blast wave at the surface of the compact presupernova. Sov. Astron. Lett. **14**(6), 449–452 (1988)
39. Imshennik, V.S.: Experimental possibilities for studying the neutronization of matter in stars. Phys. At. Nucl. **58**(5), 823–831 (1995)
40. Imshennik, V.S.: Explosion mechanism in supernovae collapse. Space Sci. Rev. **74**(3-4), 325–334 (1995)
41. Istomin, Y.N.: Electron–positron plasma generation in the magnetospheres of neutron stars. Phys. Usp. **51**(8), 844 (2008)
42. Ivanov, Y.B., Khvorostukhin, A.S., Kolomeitsev, E.E., et al.: Lattice QCD constraints on hybrid and quark stars. Phys. Rev. C **72**, 025804 (2005)
43. Johnson, M.H., Teller, E.: Classical field theory of nuclear forces. Phys. Rev. **98**, 783–787 (1955)
44. Kaplan, D.B., Nelson, A.E.: Strange goings in dense nucleonic matter. Phys. Lett. B **175**, 57–63 (1986)
45. Khazanov, E.A., Sergeev, A.M.: Petawatt laser based on optical parametric amplifiers: their state and prospects. Phys. Usp. **51**(9), 969 (2008)
46. Kifonidis, K., Plewa, T., Janka, H.T., Müller, E.: Nucleosynthesis and clump formation in a core-collapse supernova. Astrophys. J. Lett. **531**, L123–L126 (2000)
47. Kirzhnits, D.A.: Extremal states of matter (ultrahigh pressures and temperatures). Sov. Phys. Usp. **14**(4), 512–523 (1972)
48. Kirzhnits, D.A.: Lektsii po fizike (Lectures on Physics). Nauka, Moscow (2006)
49. Kirzhnits, D.: Field-Theoretical Methods in Many-Body Systems. Pergamon Press, Oxford (1967)
50. Kohn, W.: Electronic structure of matter - wave functions and density functionals. Nobel Lecture, January 28, 1999 (a year later) (1999)
51. Kohn, W., Sham, L.J.: Self-consistent equations including exchange and correlation effects. Phys. Rev. **140**, A1133–A1138 (1965)
52. Kolehmainen, K., Baym, G.: Pion condensation at finite temperature (ii). Simple models including thermal excitations of the pion field. Nucl. Phys. A **382**, 528–541 (1982)
53. Kolomeitsev, E.E., Voskresensky, D.N.: Negative kaons in dense Baryonic matter. Phys. Rev. C **68**(1), 015803 (2003)
54. Kouveliotou, C., Duncan, R., Thompson, C.: Magnetars. Sci. Am. **288**(2), 35–41 (2003)
55. Kunihiro, T., Takatsuka, T., Tamagaki, R.: Neutral pion condensation in hot and dense nuclear matter. Prog. Theor. Phys. Suppl. **112**, 197–219 (1993)
56. Lattimer, J.M., Pethick, C.J., Ravenhall, D.G., Lamb, D.Q.: Physical properties of hot, dense matter: the general case. Nucl. Phys. A **432**, 646–742 (1985)
57. Lee, T.D., Wick, G.C.: Vacuum stability and vacuum excitation in a spin-0 field theory. Phys. Rev. D **9**, 2291–2316 (1974)
58. Lorenz, C.P., Ravenhall, D.G., Pethick, C.J.: Neutron star crusts. Phys. Rev. Lett. **70**, 379–382 (1993)
59. Marcos, S., Barranco, M., Buchler, J.R.: Low entropy adiabats for stellar collapse. Nucl. Phys. A **381**, 507–518 (1982)
60. Gyulassy, M.: Quark gluon plasmas: femto cosmology (2008)
61. Migdal, A.B.: Stability of vacuum and limiting fields. Zh. Eksp. Teor. Fiz. **61**, 2209–2224 (1971)
62. Migdal, A.B.: Phase transitions in nuclear matter and non-pair nuclear forces. Zh. Eksp. Teor. Fiz. **63**, 1993–1999 (1972). [Engl. transl.: Sov. Phys. JETP **36**, 1052–1055]

63. Migdal, A.B.: Meson condensation and anomalous nuclei. Phys. Lett. B **52**, 172–174 (1974)
64. Migdal, A.B., Saperstein, E.E., Troitsky, M.A., Voskresensky, D.N.: Pion degrees of freedom in nuclear matter. Phys. Rep. **192**, 179–437 (1990)
65. Negele, J.W., Vautherin, D.: Neutron star matter at subnuclear densities. Nucl. Phys. A **207**, 298–320 (1973)
66. Novikov, I.D.: "Big Bang" echo (cosmic microwave background observations). Phys. Usp. **44**(8), 817 (2001)
67. Ogasawara, R., Sato, K.: Nuclei in the neutrino-degenerate dense matter. II. Prog. Theor. Phys. **70**, 1569–1582 (1983)
68. Ogata, S., Ichimaru, S.: First-principles calculations of shear moduli for monte carlo simulated coulomb solids. Phys. Rev. A **42**, 4867–4870 (1990)
69. Okun', L.B.: Leptony i kvarki, 2nd edn. Nauka, Moscow (1990). [English Transl.: Leptons and Quarks. North-Holland, Amsterdam (1982)]
70. Olson, T.S.: Maximally incompressible neutron star matter. Phys. Rev. C **63**, 015802 (2000)
71. Oyamatsu, K.: Nuclear shapes in the inner crust of a neutron star. Nucl. Phys. A **561**, 431–452 (1993)
72. Page, D., Applegate, J.H.: The cooling of neutron stars by the direct Urca process. Astrophys. J. **394**, L17–L20 (1992)
73. Pandharipande, V.R., Pethick, C.J., Thorsson, V.: Kaon energies in dense matter. Phys. Rev. Lett. **75**(25), 4567–4570 (1995)
74. Pandharipande, V.R., Ravenhall, D.G.: Hot nuclear matter. In: Soyeur, M., Flocard, H., Tamain, B., Porneuf, M. (eds.) Nuclear Matter and Heavy Ion Collisions, pp. 103–132. Reidel, Dordrecht (1989)
75. Pethick, C.J., Ravenhall, D.G.: Matter at large neutron excess and the physics of neutronstar crusts. Annu. Rev. Nucl. Sci. **45**, 429–484 (1995)
76. Pethick, C.J., Ravenhall, D.G., Lorenz, C.: The inner boundary of a neutron-star crust. Nucl. Phys. A **584**, 675–703 (1995)
77. Pons, J.A., Miralles, J.A., Prakash, M., Lattimer, J.M.: Evolution of proto-neutron stars with kaon condensates. Astrophys. J. **553**, 382–393 (2001)
78. Pons, J.A., Reddy, S., Ellis, P.J., et al.: Kaon condensation in proto-neutron star matter. Phys. Rev. C **62**(3), 035803 (2000)
79. Potekhin, A.Y.: The physics of neutron stars. Phys. Usp. **53**(12), 1235–1256 (2010)
80. Pudliner, B.S., Pandharipande, V.R., Carlson, J., Wiringa, R.B.: Quantum monte carlo calculations of $a \leq 6$ nuclei. Phys. Rev. Lett. **74**, 4396–4399 (1995)
81. Ramos, A., Schaffner-Bielich, J., Wambach, J.: Kaon condensation in neutron stars. In: Blaschke, D., Glendenning, N.K., Sedrakian, A. (eds.) Physics of Neutron Star Interiors. Lecture Notes in Phys, vol. 578, pp. 175–202 (2001). [nucl-th/0011003]
82. Rijken, T.A., Stoks, V.G.J., Yamamoto, Y.: Soft-core hyperon-nucleon potentials. Phys. Rev. C **59**, 21–40 (1999)
83. Rikovska Stone, J., Miller, J.C., Koncewicz, R., et al.: Nuclear matter and neutron-star properties calculated with the skyrme interaction. Phys. Rev. C **68**(3), 034324 (2003)
84. Rubakov, V.A.: Introduction to cosmology. PoS **RTN2005**, 003 (2005)
85. Ruderman, M.A.: Causes of sound faster than light in classical models of ultradense matter. Phys. Rev. **172**, 1286–1290 (1968)
86. Salpeter, E.E.: Energy and pressure of a zero-temperature plasma. Astrophys. J. **134**, 669–682 (1961)
87. Sawyer, R.F.: Condensed π^- phase in neutron-star matter. Phys. Rev. Lett. **29**, 382–385 (1972)
88. Scalapino, D.J.: π^- condensate in dense nuclear matter. Phys. Rev. Lett. **29**, 386–388 (1972)
89. Schertlera, K., Greinera, C., Schaffner-Bielichc, J., Thoma, M.: Quark phases in neutron stars and a third family of compact stars as signature for phase transitions. Nucl. Phys. A **677**(1-4), 463–490 (2001)
90. Schiavilla, R., Pandharipande, V.R., Wiringa, R.B.: Momentum distributions in $a = 3$ and 4 nuclei. Nucl. Phys. A **449**, 219–242 (1986)

91. Shapiro, S.L., Teukolsky, S.A.: Black Holes, White Dwarfs, and Neutron Stars. Wiley, New York (1983)
92. Stöcker, H., Greiner, W.: High energy heavy ion collisions–probing the equation of state of highly excited hardronic matter. Phys. Rep. **137**(5-6), 277–392 (1986)
93. Stoks, V.G.J., Klomp, R.A.M., Terheggen, C.P.F., de Swart, J.J.: Construction of high-quality nn potential models. Phys. Rev. C **49**, 2950–2962 (1994)
94. Sugahara, Y., Toki, H.: Relativistic mean-field theory for unstable nuclei with non-linear σ and ω terms. Nucl. Phys. A **579**, 557–572 (1994)
95. Sumiyoshi, K., Yamada, S., Suzuki, H., Hillebrandt, W.: The fate of a neutron star just below the minimum mass: does it explode? Astron. Astrophys. **334**, 159–168 (1998)
96. Tsuruta, S., Cameron, A.G.W.: Some effects of nuclear forces on neutron-star models. Can. J. Phys. **44**, 1895–1922 (1966)
97. Vidaña, I., Polls, A., Ramos, A., et al.: Hyperon-hyperon interactions and properties of neutron star matter. Phys. Rev. C **62**, 035801 (2000)
98. Weber, F., Weigel, M.K.: Baryon composition and macroscopic properties of neutron stars. Nucl. Phys. A **505**, 779–822 (1989)
99. Weber, F., Weigel, M.K.: Neutron star properties and the relativistic nuclear equation of state of many baryon matter. Nucl. Phys. A **493**, 549–582 (1989)
100. Wiringa, R.B., Fiks, V., Fabrocini, A.: Equation of state for dense nucleon matter. Phys. Rev. C **38**, 1010–1037 (1988)
101. Wiringa, R.B., Stoks, V.G.J., Schiavilla, R.: Accurate nucleon-nucleon potential with charge-independence breaking. Phys. Rev. C **51**, 38–51 (1995)
102. Witten, E.: Cosmic separation of phases. Phys. Rev. D **30**, 272–285 (1984)
103. Yakovlev, D.G.: Superfluidity in neutron stars. Phys. Usp. **44**(8), 823–826 (2001)
104. Yakovlev, D.G., Levenfish, K.P., Shibanov, Y.A.: Cooling of neutron stars and superfluidity in their cores. Phys. Usp. **42**(8), 737 (1999)
105. Zasov, A.V., Postnov, K.A.: Obshchaya astrofizika (General Astrophysics). Vek 2, Fryazino (2006)

Chapter 9
High Energy Densities in Planets and Stars

High-energy-density physics underlies the contemporary understanding of the structure of astrophysical objects and their evolution, which takes place under the action of gravitational forces and thermonuclear energy release [54].

It is hard to imagine a domain of intellectual activity that underwent greater changes over the past century than cosmology. Scientists have radically revised their viewpoint on the structure of surrounding world.

The scale and diversity of these phenomena are astounding, and comprehending them calls for the latest ideas and data from the cutting edge of modern physics. In this case, the observations of astrophysical objects are carried out over a broad range of the electromagnetic spectrum, from hard γ-rays to waves with meter-long wavelength (Figs. 9.1 and 9.2), providing unique information about the physical processes at ultrahigh energies unattainable by modern accelerators. According to Academician Ya.B. Zel'dovich's figurative statement, the universe is "an accelerator for the poor", which does not demand from them multibillion expenses for the construction of experimental facilities.

The Universe consists of the ordinary substance, photons, relict radiation, hidden mass, and "vacuum-like" matter which manifests itself as a nonzero cosmological constant [17, 39]. By an ordinary substance are meant primarily protons, electrons, and neutrons. Hydrogen is the dominant element. There also are helium and a small amount of lithium. Heavy atoms are present in a very small amount in the Universe. The number of protons in our Universe of size 10^{28} cm is of the order of the Eddington–Dirac number $N = 10^{80}$. The substance density in the Universe $\rho_{\text{sub}} = 10^{-31}$ g/cm^3. This substance exists in the form of stars, comets, interstellar gas, meteorites, and cosmic rays.

According to modern views [104], about 74 % of the energy-mass is due to the antigravitating "dark energy". The gravitating mass ("dark", or hidden mass) accounts for about a quarter of the average density of the Universe, about 22 % is due to the "dark" matter; the ordinary baryon substance presented in the periodic Mendeleev table accounts for only about 4 %. These 4 % of the matter are contained

© Springer International Publishing Switzerland 2016

V.E. Fortov, *Extreme States of Matter*, Springer Series in Materials Science 216,
DOI 10.1007/978-3-319-18953-6_9

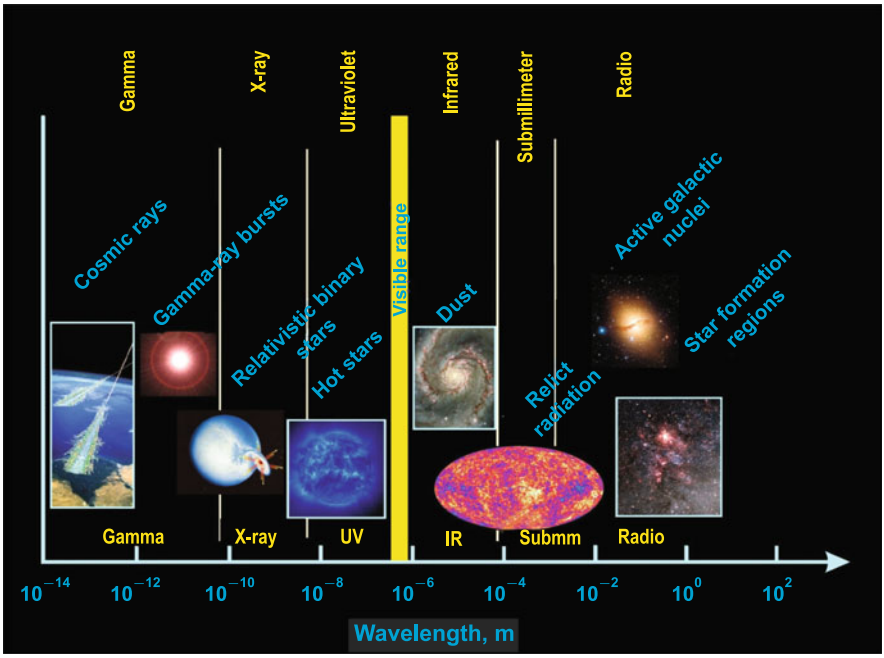

Fig. 9.1 Spectral regions of observations of astrophysical objects (L.M. Zelenyi, 2007, Private communication)

in stars, planets, and the interstellar medium. The interstellar medium accounts for 4/5 of the mass of baryon matter, and only 0.5 % of the average density of the Universe is concentrated in the stars. They occupy only 10^{-25} of the volume of the Universe. Despite these modest "average" figures, the stars truly play an outstanding role in our Universe, because their bright radiation reaches us through great distances and is the main source of information about diverse transformations of mass and energy in the Universe. It is precisely in the stars that there take place irreversible thermonuclear transformations, production of heavy elements, and the generation of exotic forms of matter inaccessible to us—neutron substance, quark-gluon plasma, etc. And while the information about the first hundreds of thousands of years of the evolution of the Universe is provided by relict radiation, we judge the history of the next billions of years by stellar observations.

The range of matter parameter variations in the universe is extremely broad [36, 107]: from empty space[1] and the tenuous intergalactic gas with a density of 10^{-30} g/cm^3 to extremely high neutron star densities of 10^{14}–10^{17} g/cm^3

[1]This figure follows from the measurements of gravitational effects in empty space and is consistent with the notion of the upper bound, which follows from the lower limit of the curvature of space [15].

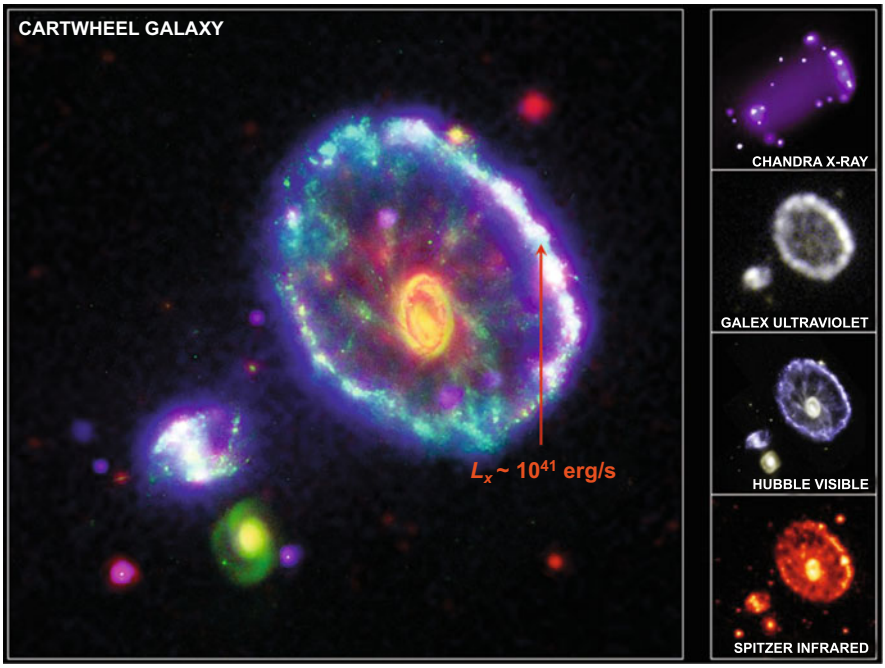

Fig. 9.2 Cartwheel Galaxy images in different spectral regions (L.M. Zelenyi, 2007, Private communication)

(Table 9.1). The temperature of the intergalactic gas with a density $n \approx 10^{-4}$–$10^{-3}\,\mathrm{cm}^{-3}$ amounts to 10^7–10^8 K, but may range up to a billion degrees when heated by shock waves (arising from the shedding of stellar shells, stellar collisions and explosions, the collisions of gas clouds, etc.). Inside neutron stars (see Chap. 8) it is equal to 10^8–10^{11} K [54]. 99 % of visible matter is heated to temperatures exceeding 10^5 K.

While the magnetic field amounts to $\approx 10^{-9}$ Gs in intergalactic space and 10^{-6} Gs near the galactic plane, at the surface of neutron stars it is 22 orders of magnitude higher. The record is held by the recently discovered magnetars—neutron stars produced in supernovae bursts. The magnetars exhibit a tremendous magnetic field—up to 10^{15} Gs, which corresponds to densities of $\approx 10^8\,\mathrm{g/cm}^3$, approaching the density of nuclear matter [64].

Gigantic black holes entirely absorb stellar systems and hot galactic nuclei. It is not unlikely that the magnetic tunnels ("wormholes") [51], which have recently come under discussion, connect our and other universes. The gravitational accretion of matter gives rise to highly collimated jets, beams of charged particles accelerated to ultrahigh energies. Supernovae explosions generate shock waves, plasma ejections, turbulent plasma, and dust clouds, producing the material for the formation of stars [36, 71, 107, 115]. Neutron stars measuring several kilometers

Table 9.1 Characteristic parameters of matter in nature and in the laboratory

Object	T (K)	ρ (g/cm^3)	P (bar)
Intergalactic gas	10^7–10^8	10^{-30}–10^{-3}	10^{-17}–10^{-7}
Earth, center	5×10^3	10–20	3.6×10^6
Jupiter, center	$(1.5–3) \times 10^4$	5–30	$(3–6) \times 10^7$
Exoplanets	10^3–10^5	1–30	10^7–10^8
Diamond anvils	4×10^3	5–20	5×10^6
Shock waves	10^7	13–50	5×10^9
Controlled thermonuclear fusion, magnetic confinement	10^8	3×10^{-9}	50
Controlled thermonuclear fusion, inertial confinement	10^8	150–200	2×10^{11}
Sun	1.5×10^7	150	10^{11}
Red giant	$(2–3) \times 10^7$	10^3–10^4	5×10^{12}
White dwarf	10^7	10^6–10^9	10^{16}–10^{22}
Relativistic collision of gold nuclei, 100 GeV/nucleon, Brookhaven	2×10^7–7×10^{13}	10^{15}	10^{30}
Neutron star, black hole, gamma bursts	10^8–10^{11}	10^{14}–5×10^{15}	10^{25}–10^{27}
Early universe (Planck conditions)	10^{32}	10^{94}	10^{106}

rotate at kilohertz frequencies and act on the plasma with their gigantic magnetic fields to generate high-intensity X-ray radiation.

Detailed astronomical observations testify to the predominance of new forms of matter such as dark matter and dark energy. As this proceeds, we recognize that the structure of even the closest planets of the Solar System is as yet imperfectly understood.

There constantly emerge new efficient methods for the investigation of stars [104]. Optical interferometry permits measuring the size and even the shape of the stars. High-precision cosmic photometers have offered outstanding possibilities in astroseismology: acoustic waves which come from the stellar interior to the surface provide information about the structure of the photosphere and thereby make it possible to obtain data about the stellar interior with the use of optical telescopes.

It is desired to reproduce to some extent these exotic states and the transformations of matter in laboratory conditions by way of relativistic nuclear collisions, at the focus of ultrahigh-power lasers, in imploding plasma pinches, or in supercomputer simulations [71]. In this case, the difference in laboratory and astrophysical scales amounts to many (up to 25) orders of magnitude, calling for the selection of adequate dimensionless variables and a careful analysis of similarity criteria [19, 89]. The existing and fundamentally possible technical capabilities along with the prospects of high energy density cumulation were described in the previous chapters and constitute the technical basis for laboratory astrophysics [19, 89, 105], a rapidly

developing area of high-energy-density physics. Laboratory astrophysics has to do with the experimental study of the equation of state, intense shock, radiative, and magnetohydrodynamic waves, the hydrodynamics of mixing, supersonic and relativistic jets, radiating streams, the optical properties of photoionized plasmas, the transport and kinetic properties of strongly compressed hot matter, and relativistic plasmas. These processes are intimately related to a wide class of astrophysical objects and phenomena, such as supernovae (Figs. 9.3 and 9.4), neutron stars, astrophysical jets (Fig. 9.5) accelerated by radiation, molecular and dust clouds, black holes, "wormholes", γ-ray bursts, planets, and exoplanets.

The central element for constructing the structure and evolution of astrophysical objects is the physical properties of strongly compressed and heated matter [54]. These are the equations of state, the composition of plasma, its optical properties, and its transfer coefficients—viscosity, thermal conductivity, diffusion, electrical conductivity, stopping power for particles, etc. These data are required in a wide range of the parameters of state, with only narrow bands of these parameters attainable by laboratory measurements today. At the same time, theoretical models developed for hot plasmas or cold dense matter operate in rather broad ranges [28, 32, 54, 71].

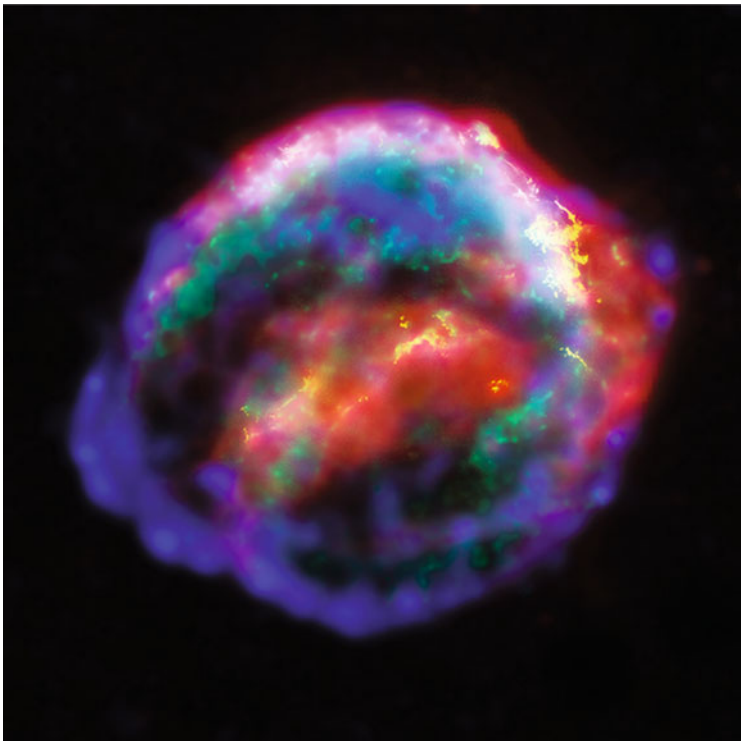

Fig. 9.3 Kepler supernova remnant (in X-ray and infrared radiation) [70]

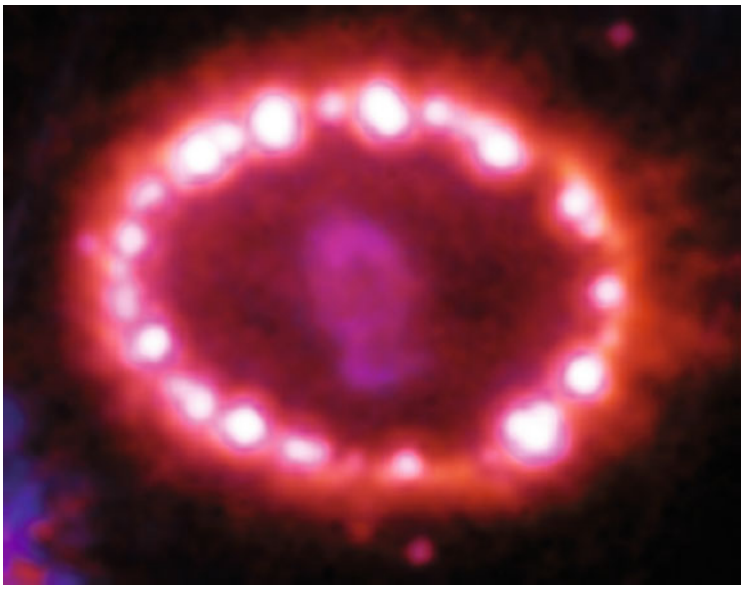

Fig. 9.4 Gas ring heated by an intense shock wave around the supernova 1987A (SN1987A) [70]

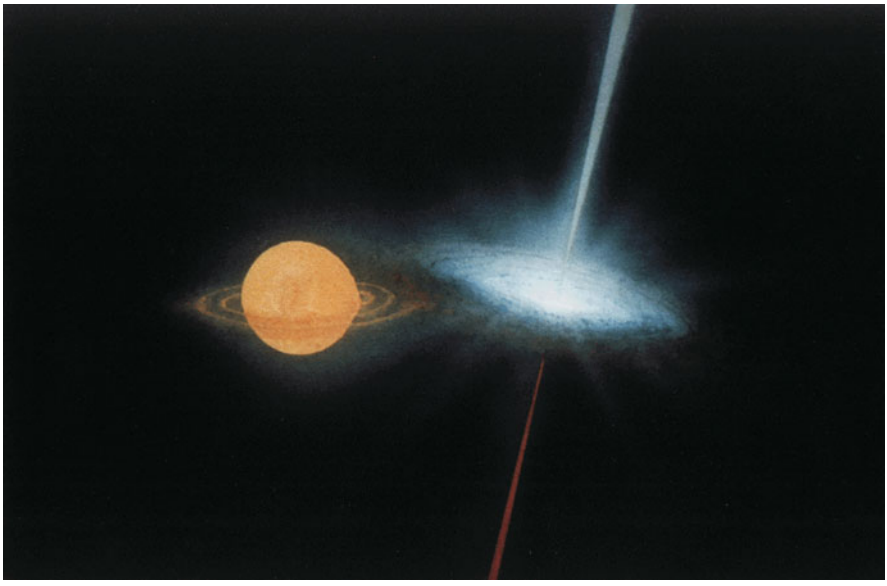

Fig. 9.5 Sketch of the binary object SS433 [107]. At the *left* is a massive star, whose matter flows to a compact object at the *right* (a neutron star or a black hole), which give rise to two relativistic jets with velocities of $\approx 1/4$ the speed of light

Let us briefly consider examples of astrophysical objects; in doing this we shall primarily follow [71] and view them only from the standpoint of high-energy-density physics.

9.1 Planets and Exoplanets

The comprehensive information about the giant planets of the Solar System obtained by unmanned stations as well as the discovery of hundreds of planets outside of the Solar System (exoplanets) has lent strong impetus to planetary research [10, 82]. The evolutional and structural models elaborated in this area rely on qualitative information about the physical properties of compressed hot matter in the megabar and ultramegabar pressure ranges (Figs. 2.2 and 3.36, Table 9.1).

9.1.1 Planets of the Solar System

Figure 9.6 [84] shows the dimensions and the average distance to the Sun for the planets of the solar system, and Figs. 9.7 and 9.8 their masses and composition. The data points in Fig. 9.7 are located near the average density of $\approx 3\,\mathrm{g/cm^3}$, although they fall within the range between $0.5\,\mathrm{g/cm^3}$ for cometary nuclei and $7.7\,\mathrm{g/cm^3}$ for metal asteroids and meteorites. The biggest planet—Jupiter—is ten times smaller in size than the Sun, but it has a density close to the solar one (1.33 and $1.41\,\mathrm{g/cm^3}$, respectively). Saturn is close to Jupiter in size, but its density is about half—$0.70\,\mathrm{g/cm^3}$. The densities of Uranus and Neptune are 1.27 and $1.64\,\mathrm{g/cm^3}$; together with Jupiter and Saturn they make up the group of giant planets of the Solar System. The Earth ($5.52\,\mathrm{g/cm^3}$), Venus ($5.24\,\mathrm{g/cm^3}$), Mars ($3.94\,\mathrm{g/cm^3}$), and Mercury ($5.43\,\mathrm{g/cm^3}$) constitute the terrestrial group of planets with a high average matter density. This circumsolar matter in its turn accounts for 0.134 % of the mass of the Solar System, the overwhelming amount of which (99.866 %) is accounted for by the Sun—a star, a yellow dwarf.

The solar mass is about $2 \cdot 10^{30}\,\mathrm{kg}$, the Sun is 333,000 more massive than the Earth and 1000 times more massive than Jupiter.

The most massive stars of the known ones are approximately 100 times more massive than the Sun. These massive stars are only 1500 times "heavier" than the lowest-mass stars. In this case, the stars vary trillion-fold in luminosity [104].

The stars vary not so greatly in size, but also significantly—by nearly a billion times (not counting neutron stars). In this case, the largest stars are not necessarily the most massive ones. There are stars which exceed our Sun approximately 1500-fold in diameter, and some of them are not much different from the Sun in mass and their average density is millions of times lower than the solar one. This is despite the fact that the average solar density amounts to $1.4\,\mathrm{g/cm^3}$, which only slightly higher than the water density [104].

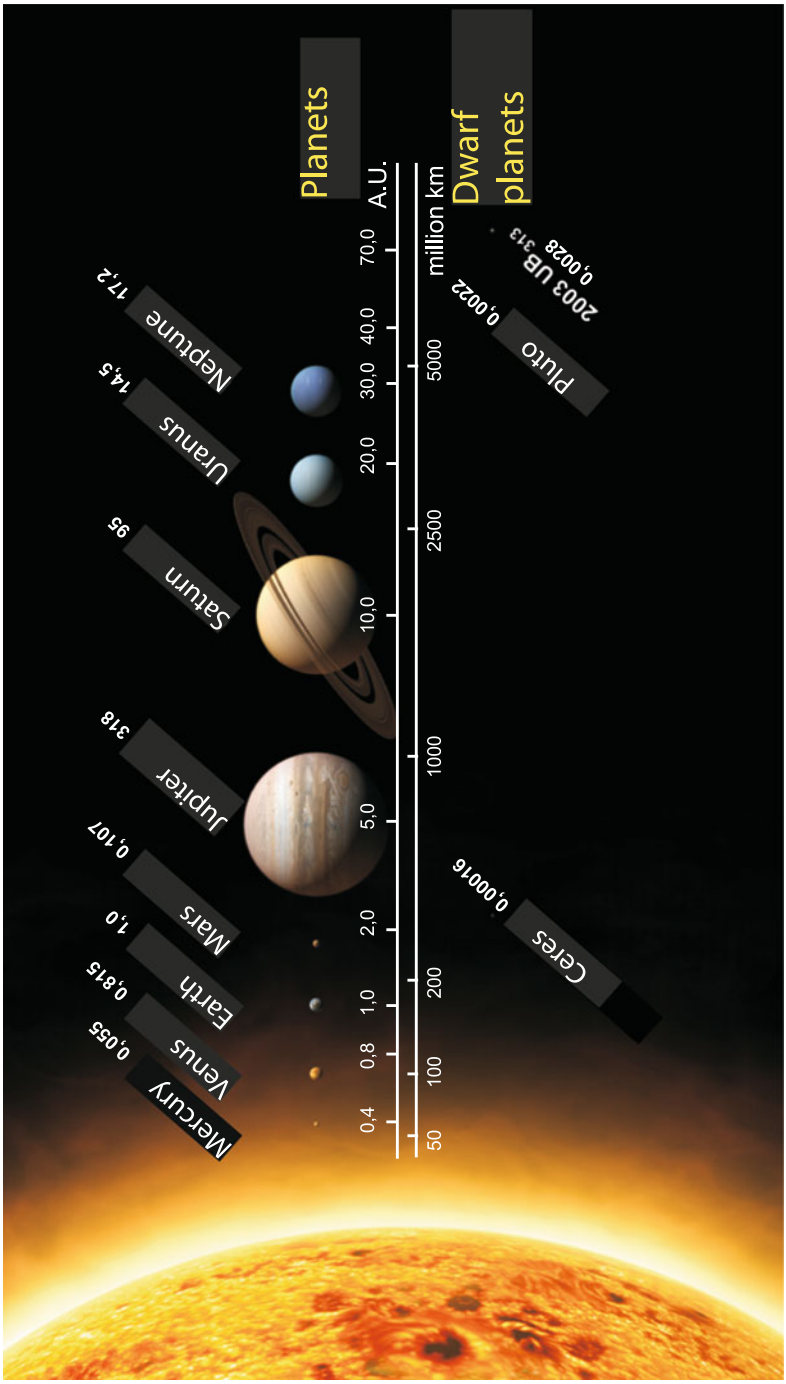

Fig. 9.6 Masses of planets (in units of terrestrial mass) and their average distances to the Sun [84]

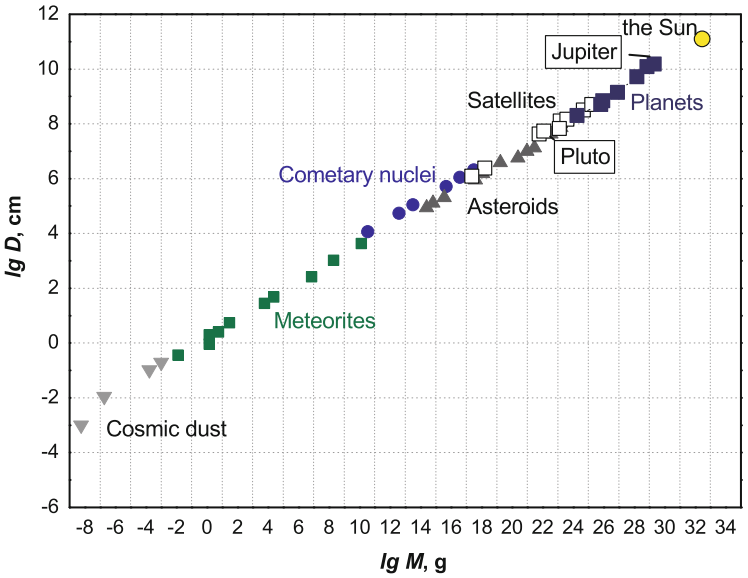

Fig. 9.7 Masses and dimensions of the objects of the Solar System. All of them are located almost in one line, corresponding to an average density of about 3 g/cm^3 [99]

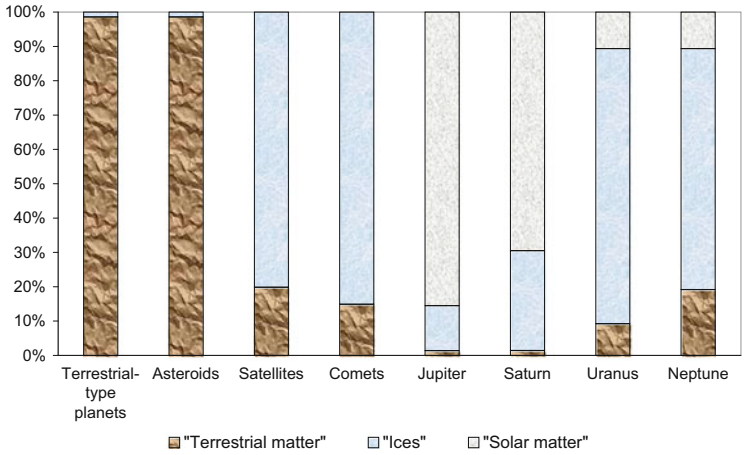

Fig. 9.8 Relative content of different types of matter in the objects of the Solar System [99]

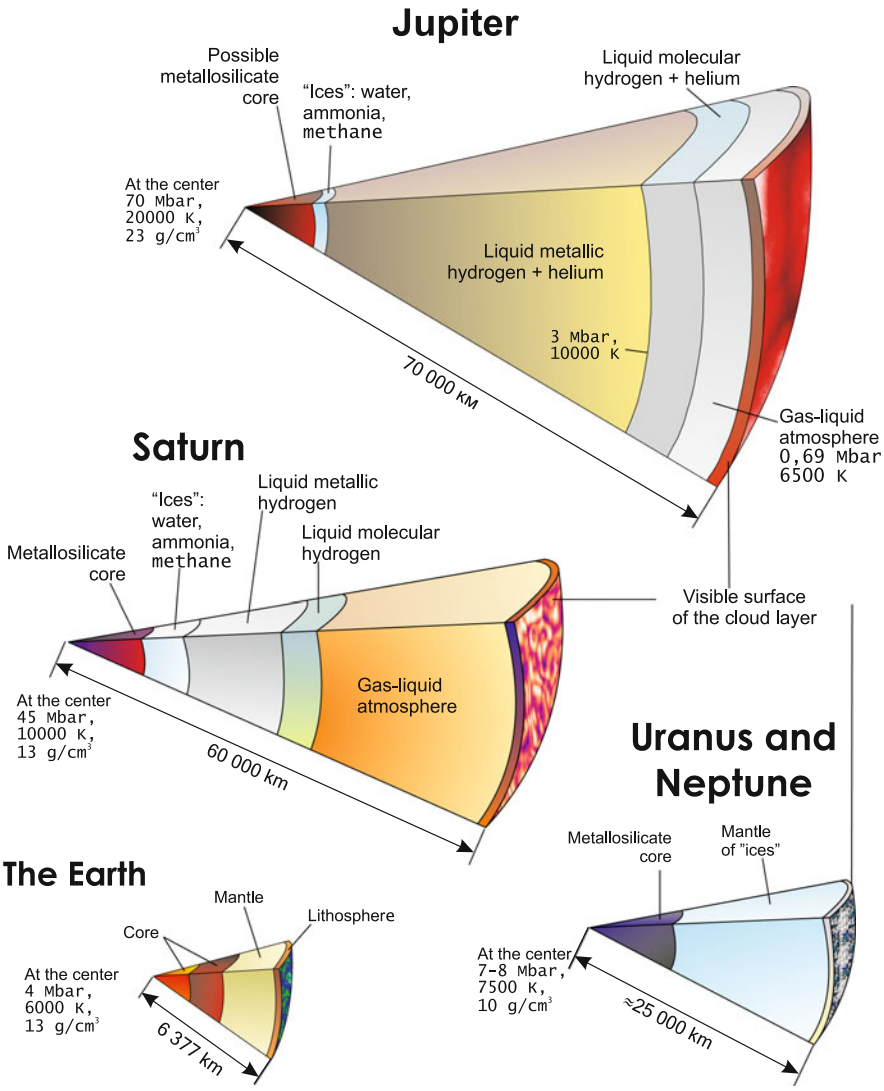

Fig. 9.9 Diagram of the internal structure of the giant planets as compared with terrestrial structure [84]

Figures 9.9 and 9.10 show the structure and characteristic parameters of several giant planets of the Solar System, which account for 99.5 % of the mass of circumsolar matter. One can see that complex structures and diverse physical processes are involved, which researchers should learn to reproduce in laboratories and describe by theoretical models of dense plasmas at megabar pressures.

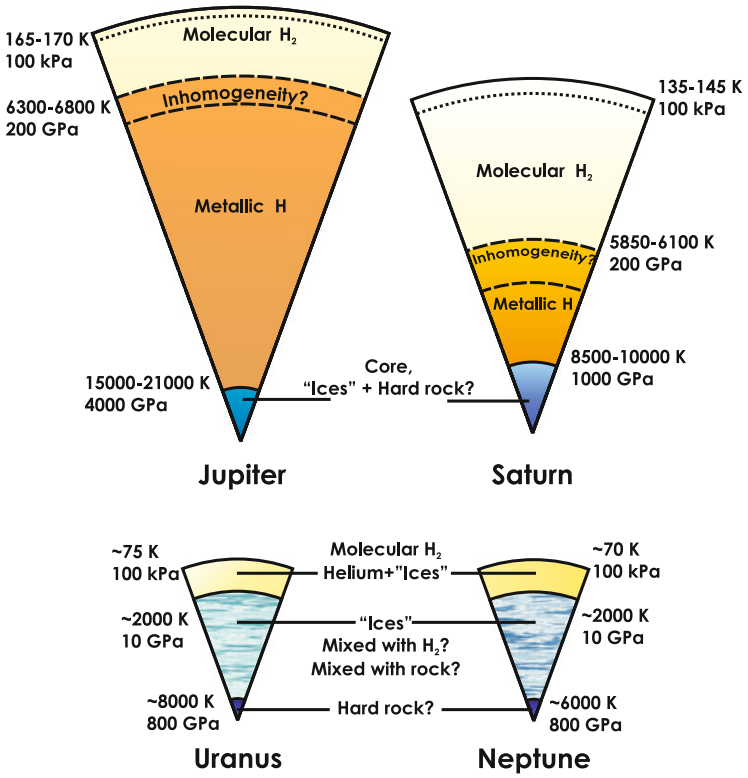

Fig. 9.10 Structure and physical conditions of the giant planets of the Solar System [35]

Figure 9.11 shows the location of planetary matter on the phase diagram and the conditions accessible to dynamic experiments. Figure 9.12 presents the phase diagram of iron, where the terrestrial states and Fe Hugoniot curves are shown. The internal structure of the Earth is shown in Fig. 9.13.

9.1.2 Exoplanets

Much less observational information has been gained about the planets that are outside of the Solar System. To date, several hundreds of such objects have been discovered since 1992. Astronomers detect these objects from the lowering of stellar brightness at the instant the planet crosses in front of the stellar disc, between the star and the terrestrial observer ("shadowing" method, Fig. 9.14 [91]). Figure 9.15 shows a rare picture of the exoplanet-satellite of the star Gliese 229 made by the Hubble space telescope. The bright halo at the right is the optical exposure of the photodetector. The mass of this exoplanet is 20–60 times the mass of Jupiter.

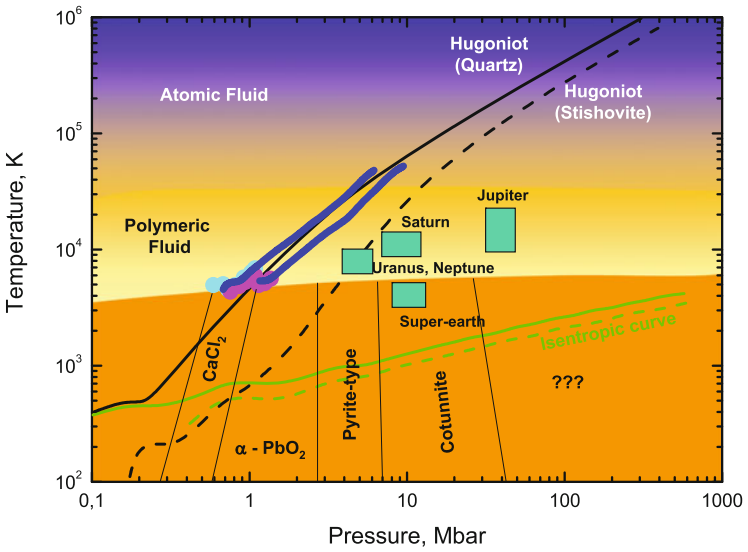

Fig. 9.11 Location of substances in the phase diagram

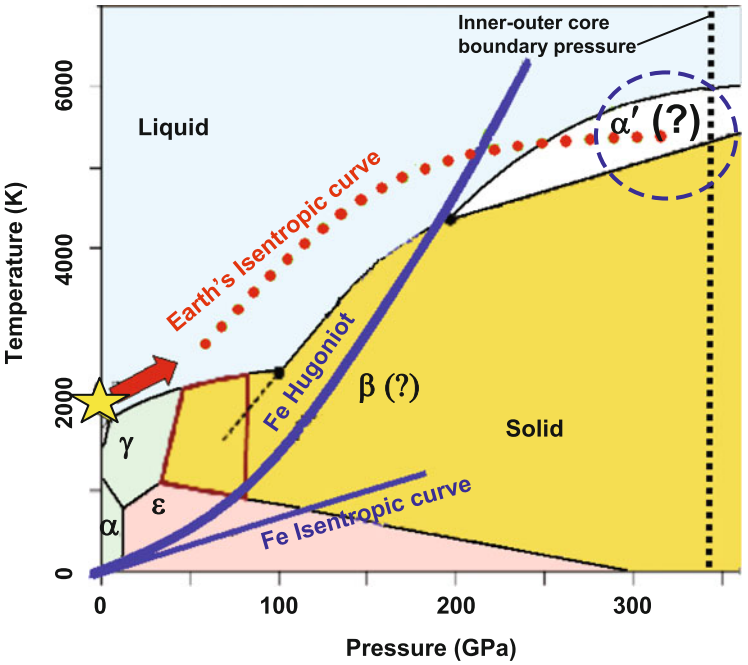

Fig. 9.12 Phase diagram of iron with indication of terrestrial states and the Hugoniot adiabatic curve

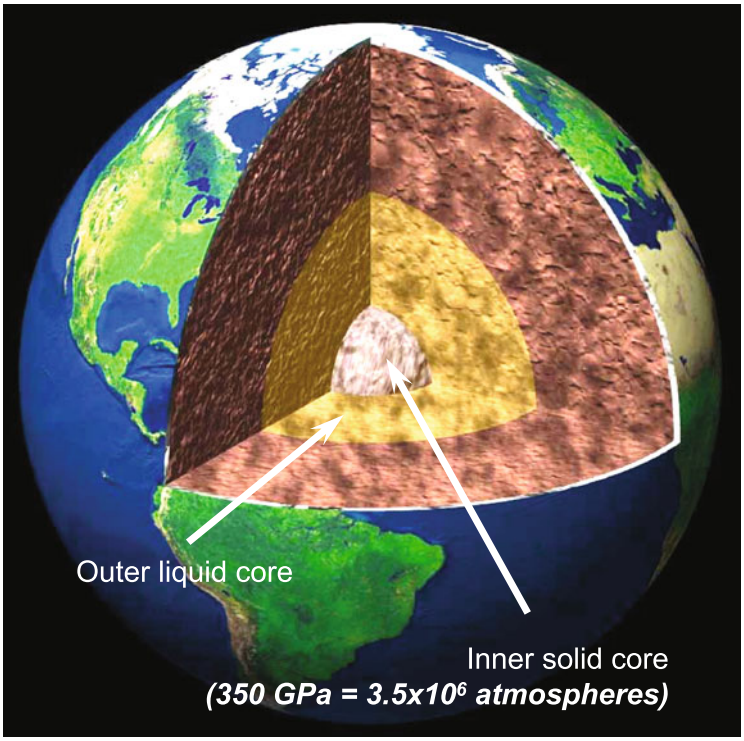

Fig. 9.13 Internal structure of the Earth

Only one of the planets discovered—Gliese 581, which is at a distance of 20.5 light years from the Earth—only vaguely resembles our planet (temperature of 15–55 °C). The NASA's Kepler space mission, launched in March 2009, is engaged in the search for Earth-like exoplanets. The exoplanets discovered to date are primarily classed as quite massive objects (see Fig. 9.16 [10, 35, 82]) with a broad spectrum of orbit dimensions, which is responsible for the wide diversity of the physical conditions of their matter.

In particular, the exoplanet DH2094586, which was discovered in 1998, resembles Jupiter in structure and by parameters (somewhat exceeding it in temperature), with a domain of a plasma phase transition and the phase layering of hydrogen and helium plasmas. Researchers predict [35], in the majority of instances, the occurrence of a massive core containing heavy elements (with a mass up to 100 terrestrial masses). Figures 9.16 and 9.17 show the dimensions and masses of a number of giant planets and exoplanets as well as their chemical composition in comparison with several planets of the Solar System.

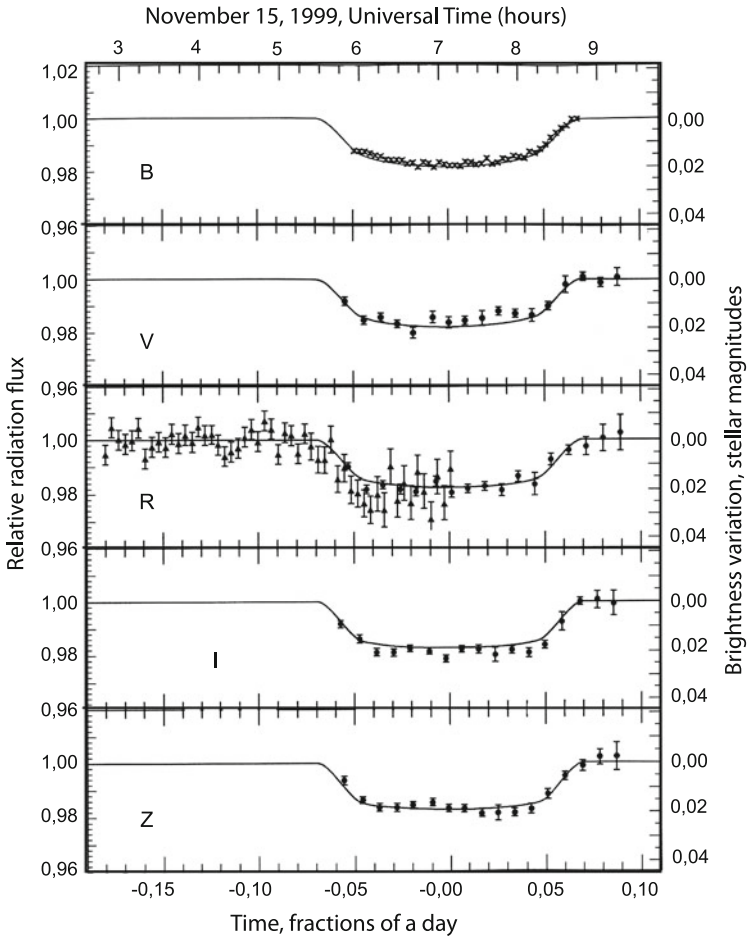

Fig. 9.14 V376 Pegasi was the first variable star in our galaxy that was found to vary in brightness owing to a transit of a planet across its disk [91]. The star is dimmed in the transit of the planet by several percent in all spectral ranges (B, V, R, I, Z)

Figure 9.18 shows the element abundance according to [10]; the circles indicate the compounds significant for giant planets and exoplanets.

A continuation of active investigations of giant planets and exoplanets with spacecraft is planned for the near future. The Cassini space probe will measure the gravitational field of Saturn with high precision; the CoRoT probe and Kepler (launched in December 2006 and March 2009, respectively) should discover tens of new exoplanets; the Juno spacecraft (launched in 2011) will measure the gravitational and magnetic fields of Jupiter with high precision; and Kronos (launch after 2015) is intended to measure the parameters of Saturn.

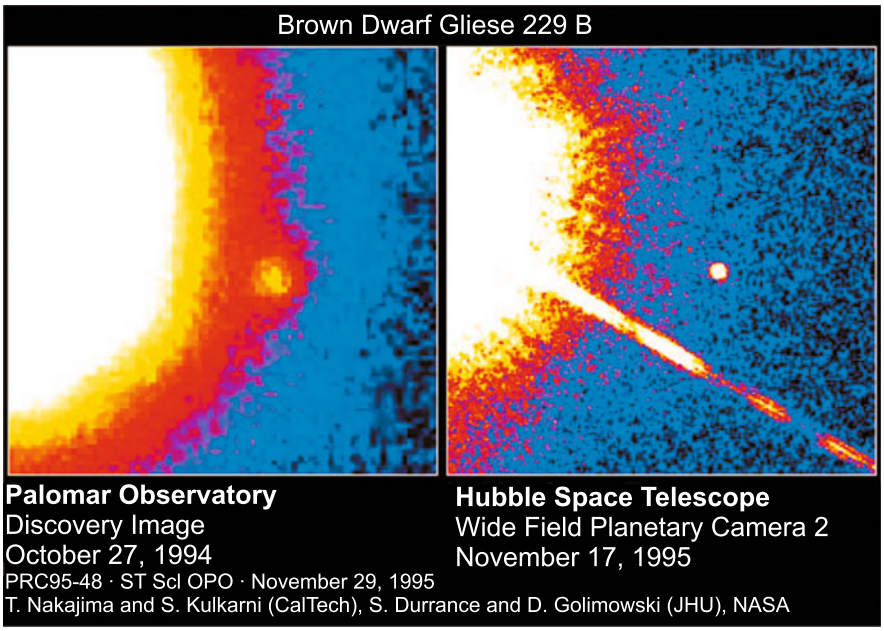

Fig. 9.15 Photograph of a satellite of the star Gliese 229. The image was obtained by the Hubble Space Telescope [98]

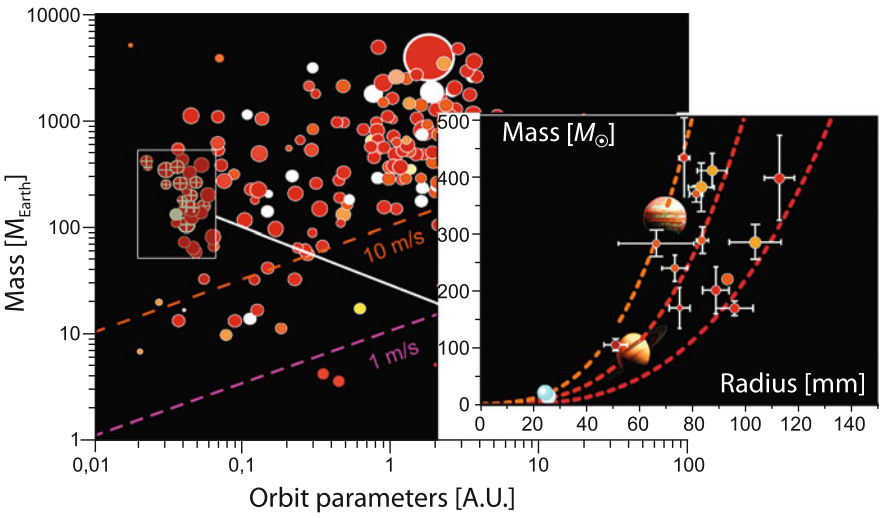

Fig. 9.16 Characteristics of exoplanets [35]

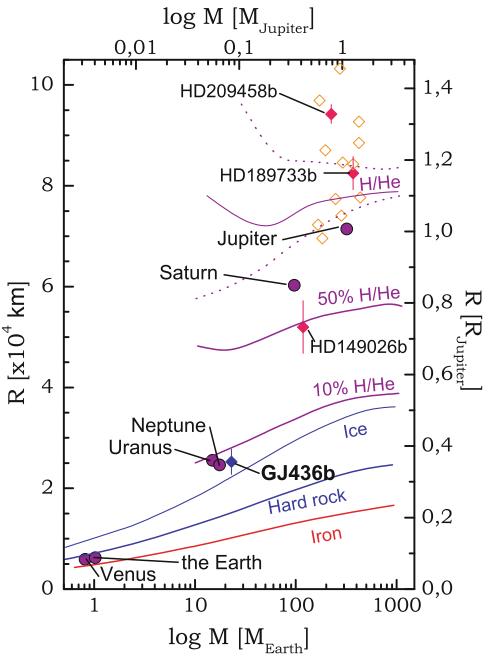

Fig. 9.17 Characteristics and chemical composition of exoplanets compared with several planets of the Solar System [35]

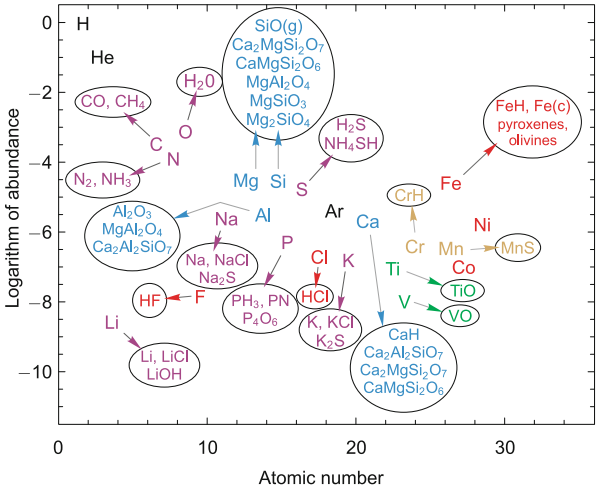

Fig. 9.18 Abundance of chemical elements according to [10]

To interpret the data of terrestrial and space measurements as well as to construct, on their basis, models of evolution, structure, and energetics of these objects requires reliable data about the physical properties of nonideal plasmas in the megabar pressure range (Figs. 9.9 and 9.10). At issue is a dense multicomponent plasma with a strong collective interparticle interaction, where pressure-induced ionization—so-called "cold" ionization—is of paramount importance along with thermal ionization effects. The pressures at the center of Jupiter (Figs. 9.9, 9.17, and 9.22) amount to $\approx$40–60 Mbar for a temperature of (15–20) $\times 10^3$ K, while the pressure at the center of the brown dwarf GL 229 is equal to $\approx 10^5$ Mbar [115].

Experiments on the multiple (quasi-adiabatic) shock compression of hydrogen, helium, and their mixtures performed with pneumatic guns [73] and explosive loading devices (Fig. 9.19) [30, 32, 33] yield the required information about pressure-induced ionization (Fig. 9.20) [26, 30, 32] and about the phase transition (Fig. 9.21) [33] in this plasma. The measurements suggest that the plasma phase transition takes place on the deuterium isentropic curve at $P \approx 1.2$ Mbar and the pressure-induced ionization occurs in a similar pressure range for a plasma density of $\approx$0.5–1.0 g/cm^3. This permitted the radius in Jupiter at which metallization occurs to be measured, shifting it towards greater radii (Fig. 9.22) [28, 72].

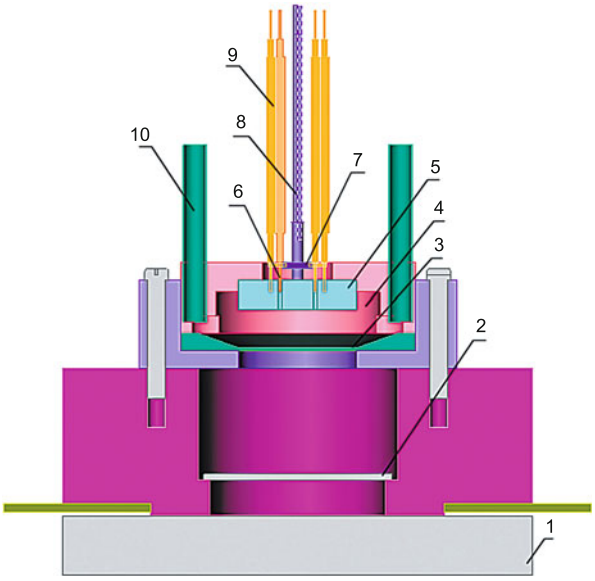

Fig. 9.19 Explosion generator for the shock-wave compression of plasmas [30]. 1: explosive charge, 2: steel plate, 3: bottom of experimental plate, 4: substance under investigation, 5: leuco-sapphire window, 6: indium electrodes, 7: shunt resistance, quartz-quartz optical fiber, 9: coaxial electric cables, 10: gas supply lines

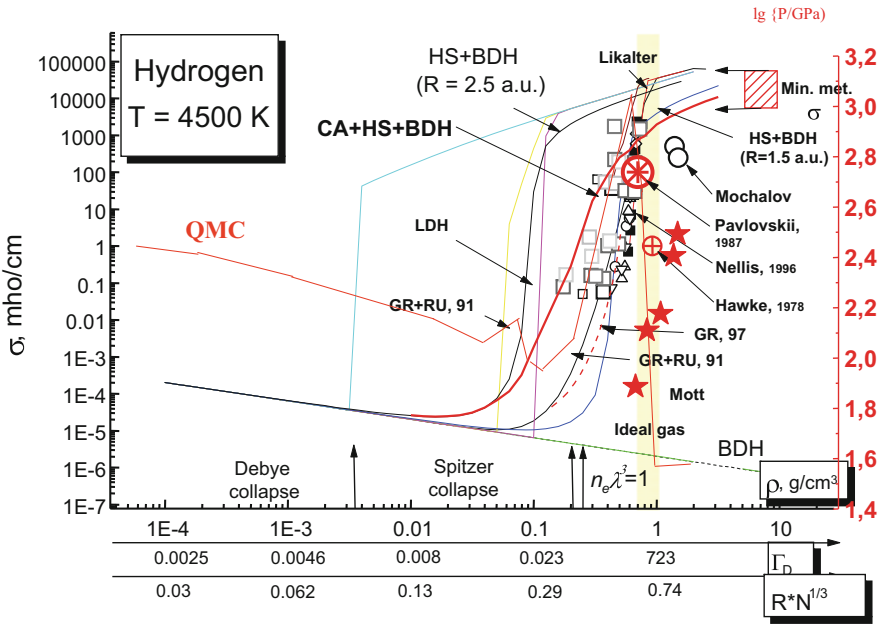

Fig. 9.20 Pressure-induced ionization of nonideal hydrogen plasmas [30, 42, 73, 78]. The area of a thermodynamic phase transition [33] is marked in *yellow*; *asterisks* indicate the data of density measurements by pulsed X-ray radiography [33]. *QMC* Calculations by a quantum Monte Carlo technique [8, 23, 24]

The magnitude of "cold"-ionization pressure is of consequence in estimating the convective effects and the generation of Jupiter's high (10–15 Gs) magnetic field. The occurrence of a plasma phase transition is of interest in estimating the energy (including gravitational energy) liberation in the phase separation of helium and heavy elements (Fig. 9.23), as well as in estimating thermal fluxes. Therefore, the phase diagrams of hydrogen, helium, and hydrogen–helium mixture plasmas, plasma phase transitions, metallization boundaries, the mutual solubility of chemical elements and nonideal plasmas of different composition, as well as the possibility of "helium rain" occurring at high P and T invite further investigation [71].

9.1.3 Low-Mass Stars and Substars

Close to planetary objects in dimensions are brown dwarfs, low-mass stars, and substars, in the interior of which nuclear reactions have died out [6] owing to the insufficiency of mass (commonly this is 0.07–0.09 of the solar mass and a size comparable to that of Jupiter). These "unsuccessful stars" range from Jupiter to

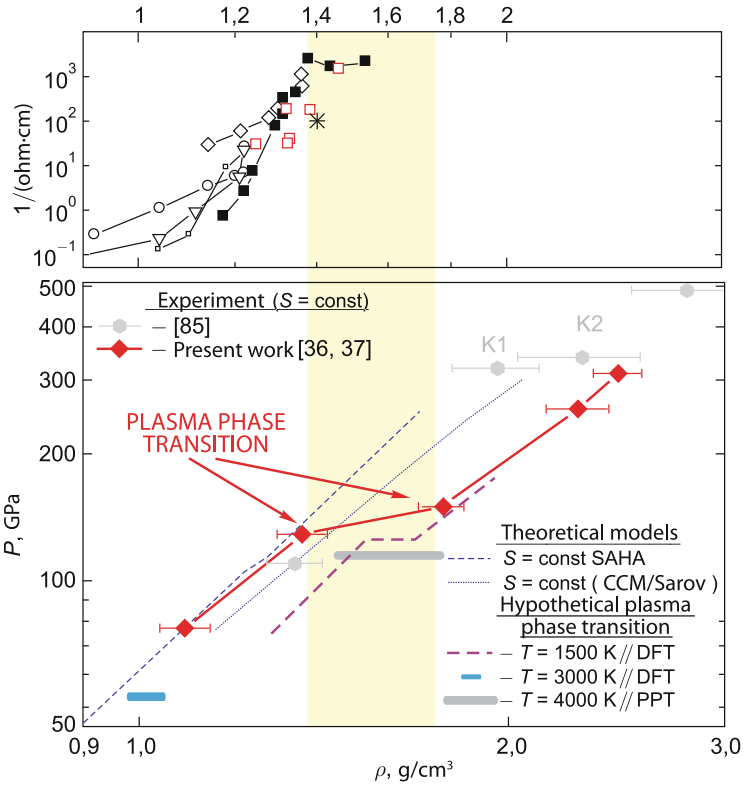

Fig. 9.21 Recording of the adiabatic compressibility of a deuterium plasma [33]. The domain of the plasma phase transition is marked in *yellow*. *Top*: D_2-density-scaled electric conductivity data (Fig. 9.20)

the Sun in mass and consist of a hydrogen–helium degenerate or partly degenerate nonideal plasma with a pressure of about 10^5 atmospheres at the center, while the plasma in white dwarfs is completely degenerate [2, 11, 57, 82].

As in the case of planets, studying and constructing atmospheric models of brown dwarfs and other substellar objects is an extremely intricate task, which calls for comprehensive thermodynamic and spectral calculations of molecular multicomponent plasmas (millions of spectral lines and bands). Account should also be taken of the occurrence of a condensate, the shift and broadening of spectral lines, as well as the presence of metals and their compounds. All of this is required, in particular, for calculating the luminosity of these scarcely observable objects and determining their contribution to the hidden galactic mass.

By and large, the optical properties of stellar plasmas are one of the central areas of application of high-energy-density physics to astrophysics [83], because radiation determines the energy transfer inside the stars, their evolution, and observable luminosity, yielding the bulk of observational information about these objects.

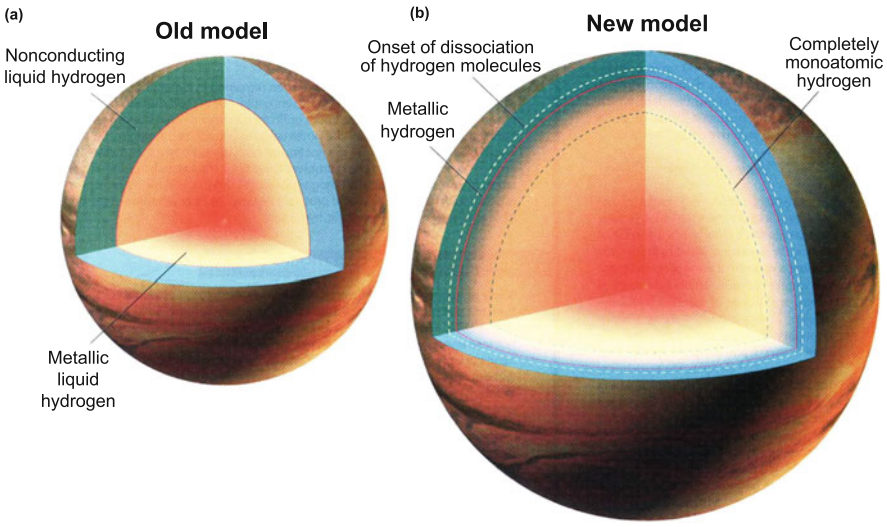

Fig. 9.22 Schematic of Jupiter's structure before (**a**) and after (**b**) measurements of electric conductivity in shock-compressed hydrogen [72]. The zone of the metallic core has shifted from 0.75 to ≈0.9 of Jupiter's radius (**b**)

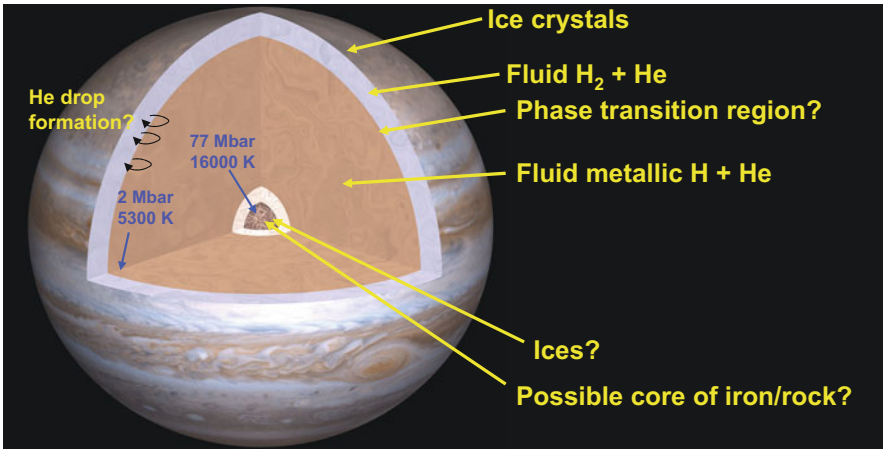

Fig. 9.23 Detailed structure of Jupiter

Sophisticated computer programs, spectroscopic databases, and high-level radiation-transfer programs combined with hydrodynamic motion codes have been developed for this purpose. In particular, [66] contains a list of 6 million lines of H_2O and [77] 300 million lines. But even they do not provide a complete description of water vapor bands for late-type stars and brown dwarfs. An adequate inclusion of nonideality effects in compressed plasmas and condensate formation in the form of clusters and dust constitute a special problem in this case [2].

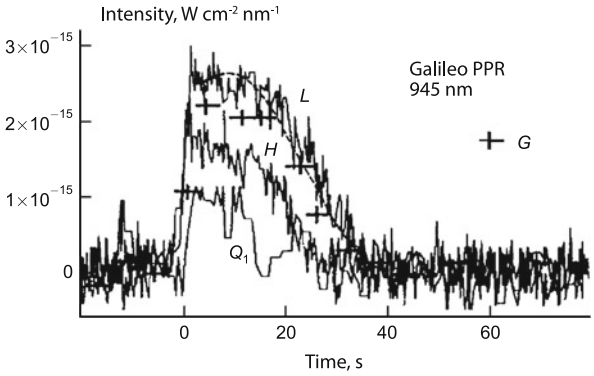

Fig. 9.24 Brightness curves recorded by the Galileo spacecraft for the impacts of comet Shoemaker–Levy 9. The observations were carried out at a wavelength $\lambda = 945$ nm. The *dashed curve* is an analytical solution [29, 55]

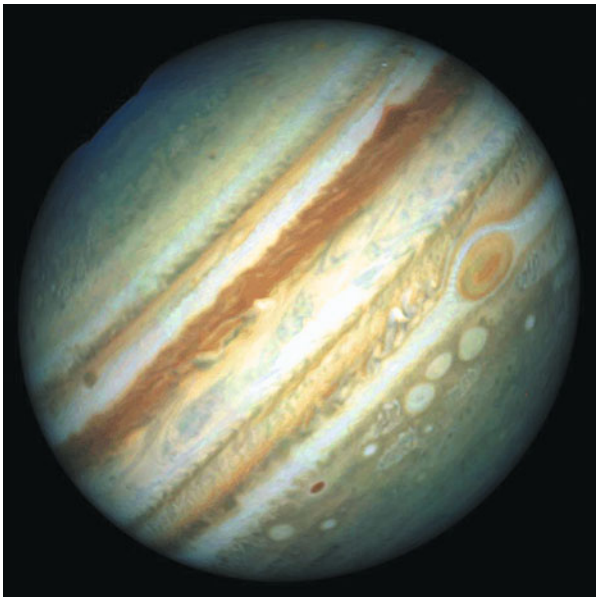

Fig. 9.25 Result of the impacts of fragments of comet Shoemaker–Levy 9 on Jupiter. Below the *red spot* in the lower part one can see *white vortices*, the impact marks [29, 55]

As an example of calculations of this kind, we give an analysis of optical phenomena on the impact of the comet Shoemaker–Levy 9 on Jupiter [29, 55], which enabled the composition and structure of Jupiter's atmosphere to be determined more precisely, revealing the effect of shock acceleration in an exponential atmosphere, and explaining the optical signals (Fig. 9.24) recorded on the Earth and by space probes (Figs. 9.25 and 9.26).

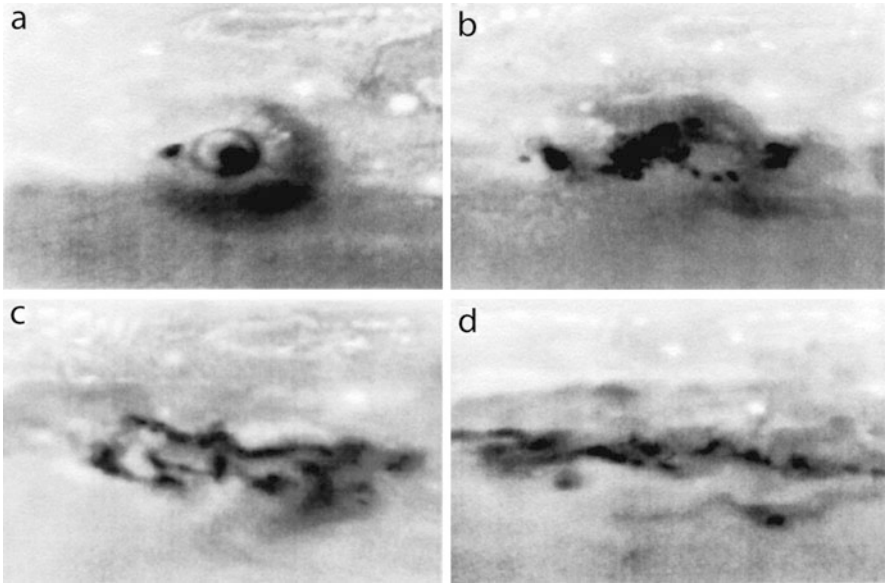

Fig. 9.26 Photographs showing the evolution of vortices at the point of impact of the fragments of comet Shoemaker–Levy 9 on Jupiter: (**a**) July 18, 1994 (approximately 1 h after the impact); (**b**) July 23, 1994; (**c**) July 30, 1994; (**d**) August 24, 1994

Not only do the optical plasma properties determine the brightness, spectra, and structure of stellar objects, but they may also lead to large-scale pulsations [115] with a loss of stellar stability, like the long-period (11 month) oscillations of the star Mira (Omicron Ceti) discovered in 1596 (Fig. 9.27). In such stars (Cepheids) there develop oscillations of the radius and radiation temperature due to an increase in optical opacity coefficient $\kappa(T, \rho, Z)$ of the plasma, which is a complex function of the plasma composition, temperature, and density [25]. An increase in $\kappa(T, \rho, Z)$ blocks the thermal flux from the center to the outer layers of the star to give rise to a pressure growth, which in turn generates a compression wave, leading to the expansion of the shell, its cooling, and a decrease in density. If $\kappa(T, \rho, Z)$ decreases on expansion, this increases the energy flux, which gives rise to radial stellar oscillations and pulsations of the observable temperature. Clearly the dynamics of this process is determined by the plasma composition and the ionization of helium and hydrogen for 4×10^3 K and 1.5×10^4 K.

Radiative processes are of great importance in the description of the origin, evolution, and structure of interstellar objects. Figure 9.28 shows the positions of stars in a luminosity–spectral class diagram.

These pulsations manifest themselves in observations as Cepheid variability. The radial pulsations are such that the substance moves only along the stellar radius and the stellar shape remains invariable and approximately spherical. Only atmospheres pulsate: pulsations do not penetrate deep into the stellar interior. The

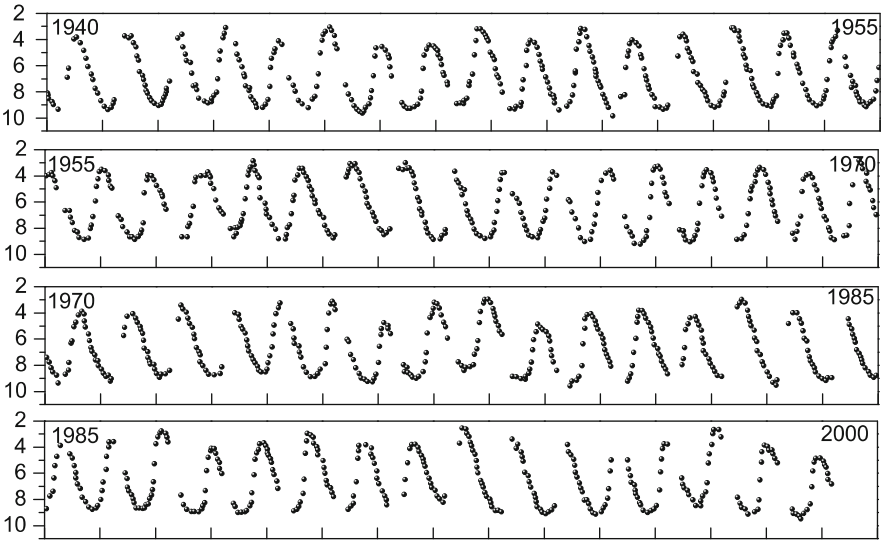

Fig. 9.27 Mira (Omicron Ceti) brightness variations over 60 years, according to the information of the American Association of Variable Star Observers. Indicated is the visual stellar magnitude averaged over 10 days [91]

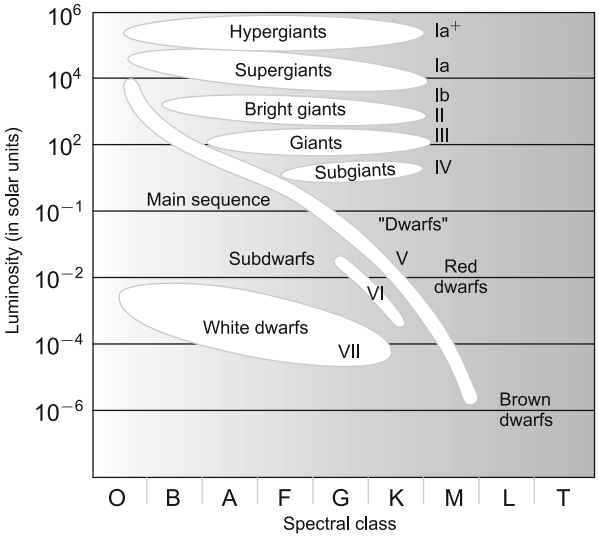

Fig. 9.28 Schematic form of Hertzsprung–Russell diagram in its modern form. The domains occupied by main stellar sequences (groups) are indicated. Shown on the *right* of a sequence name is its luminosity class, which is usually given along with the spectral class of a star [104]

stellar atmosphere heats up under compression and cools under expansion. The Cepheid luminosity peaks when the surface temperature is close to its maximum and the star begins to expand upon contraction to the smallest diameter.

Radiative processes are of great importance in the description of the origin, evolution, and structure of interstellar objects. Figure 9.28 shows the positions of stars in a luminosity–spectral class diagram.

9.2 Production and Evolution of Single Stars

At first let us consider the dynamics of stellar production and heating [104], which proceeds by way of gravitational collapse of the substance of interstellar gas clouds.

9.2.1 Origin of Stars

Qualitatively, the density perturbation growth mechanism is as follows [38]. A domain of enhanced matter density produces gravitational field around itself. It attracts the ambient matter, which finds its way into this domain to produce an even stronger density gradient. When the substance contracts to the center, its pressure increases to give rise to sound waves, which travel to the periphery. When their velocity is lower than the velocity of the falling gas, the cloud continues to collapse. The process continues until the density difference $\delta\rho/\rho$ becomes of the order of unity. After that the dynamics enters a nonlinear stage—the enhanced-density domain collapses to give rise to a compact gravitationally coupled object.

An analysis of gravitational instability growth by the example of Newtonian gravitational theory and classical hydrodynamics in the framework of plane space–time leads [38] to perturbation instability in a gravitating liquid: the perturbations with a small initial amplitude of wavelength $\lambda > \lambda_{\text{J}}$, where

$$\lambda_{\text{J}} \equiv \frac{2\pi}{q_{\text{J}}} = \sqrt{\frac{u_s^2 \pi}{G\rho}},$$

grow exponentially, the density contrast ratio becomes large with time, $\delta\rho \sim \rho$, and a nonlinear mode sets in. The characteristic time of the process is

$$t_{\text{J}} = \frac{1}{\Omega_{\text{J}}} = \frac{1}{\sqrt{4\pi G\rho}}.$$

After the onset of the nonlinear mode there occurs a rapid collapse and a compact object is formed. The critical wavelength λ_{J} has come to be known as the Jeans wavelength and the instability itself as the Jeans instability [38]. Worthy of mention

is the universal character of the Jeans instability: the critical wavelength λ_J exists for every medium and is defined only by the density ρ of the medium and the sound velocity u_s in it. We also mention that the Jeans time coincides, by the order of magnitude, with the free-fall time for a uniform ball of density ρ.

The mass of a ball equal in diameter to the Jeans wavelength is referred to as the Jeans mass; by the order of magnitude, this is the minimal mass of an object resulting from the Jeans instability. Taking into account the dark matter, it is equal to $\sim 1000\, M_\odot$.

The time of the emergence of the first stars from the clouds of baryon and dark matter of mass 10^5–$10^6\, M_\odot$ amounts to 30–100 million years after the Big Bang. The first stars were intense sources of hard ultraviolet radiation, which impeded the production of other stars [63]. Their radiation constantly heated the ambient space. That is why the cosmic gas gradually heated up to temperatures at which the role of atomic hydrogen increased in importance and the process of star formation quickened, because atomic hydrogen at temperatures above 10,000 K radiates more energy than molecular hydrogen [63].

The masses of first-generation stars were in the range 30–$100\, M_\odot$.

Not only have the suitable clouds of such gas been discovered using infrared and radio telescopes [104], but it has also been determined how these clouds lose stability and contract under the force of gravity, commencing their conversion to stars.

The structure observed by astronomers is typical [63] for the development of gravitational instability in nonrelativistic collisionless matter. In the initial quasi-isotropic expansion of the medium there develops anisotropy. In enhanced-density domains the expansion of gravitating substance moderates, terminates, and is replaced with a collapse. Initially of the collapse takes place in one of the three dimensions, leading to self-intersections (caustics) and the formation of oppositely directed one-dimensional flows. Subsequently the domains of gravitationally self-trapped matter relax and next spherize to form numerous multiflux gravitationally coupled systems—dark matter haloes. These well-understood and much-studied processes are borne out by numerical experiments with participation of billions collisionless gravitating particles and are consistent with observations for the greater part [63].

It has been possible to analyze these processes using sophisticated codes for supercomputers. Such an analysis is exemplified in Fig. 9.29 [1], which depicts a computer-simulated picture of the origin of two protostars 200 million years after the Big Bang.

Figure 9.30 [1] shows how the light emitted by a bright massive star (at the center) ejects the circumstellar substance to distances of thousands of light years.

It was determined that immediately prior to the onset of compression the gas temperature at the depth of such clouds amounts to only 10–30 K and sometimes even to 3–5 K. They consist primarily of hydrogen molecules and helium atoms. The rest chemical elements are scarce and are mostly concentrated in dust particles of size about 0.1 μm. Although these clouds are regarded as being quite dense according to "interstellar standards", they are extremely tenuous according to

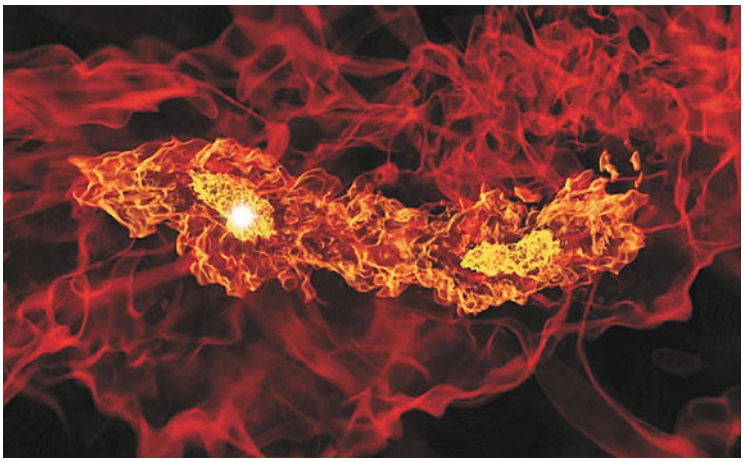

Fig. 9.29 Computer simulation of the origin of two protostars. The *color brightness* corresponds to the magnitude of the density. The drawing was borrowed from [1]

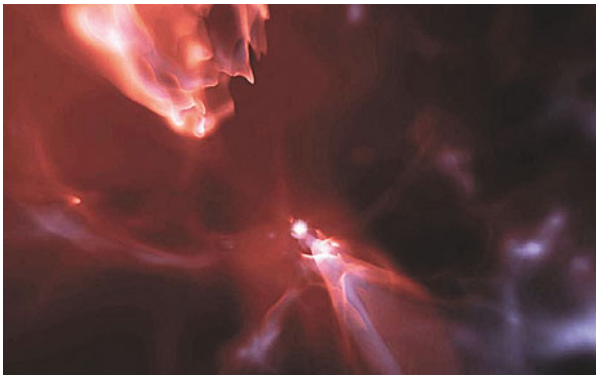

Fig. 9.30 Mathematical simulation [1] of the expulsion of interstellar medium by the radiation of a bright massive star

terrestrial ones: the average distance between the particles is about several meters, with about 2 billion molecules present in 1 m^3 of the gas, which is 10^{16} times lower than in the air at normal conditions. The gas-and-dust nebula which made up our Sun 5 billion years ago was therefore approximately 10 million times larger in size than our present-day Sun.

Although the regions of interstellar gas concentration are referred to as "clouds" from force of our earthly habit, they differ from atmospheric clouds by the significance of the role of gravity. Small interstellar clouds are capable to withstand the force of gravity. However, they collide accidentally with one another and merge to increase their mass and with it the role of gravity.

Once a cloud begins to contract under intrinsic gravity, it cannot stop. The matter is that with decreasing cloud size (R) the force of gravity (GM/R^2) increases much faster than the counteracting force of gas pressure (P). This takes place due to the high efficiency of substance cooling: all the heat released during compression escapes from the cloud in the form of infrared radiation of the dust. The cloud temperature remains almost invariable at a very low level of only several degrees, until the cloud density becomes so high that infrared photons can hardly escape from the cloud. That is why the pressure gradient (the expulsive force) grows rather slowly ($P/R \sim \rho T/R \sim \rho^{4/3}$) and the weight of a cloud volume element rises significantly faster ($\rho M/R^2 \sim \rho^{5/3}$).

As the cloud contracts and its density increases, the force of gravity predominates over the force of gas pressure to a progressively greater degree. This is the reason why the rate of cloud compression progressively increases, and the cloud size decreases 1000-fold in about half a million years. As this takes place, the cloud volume becomes one billion times smaller and the average gas density by the same degree.

The density grows fastest in the central regions, so that the substance becomes opaque to infrared radiation at precisely the cloud center. This effect sharply decreases the efficiency of cooling. The central regions begin to heat up rapidly, the gas pressure in these regions begins to grow faster and moderates contraction. Before long the pressure becomes so high that the contraction terminates and a hydrostatically equilibrium core forms inside the cloud. Outside of the core the gas is transparent to infrared radiation as before and continues to fall towards the center almost freely.

The shell gas falling at a velocity of several kilometers per second runs into the immobile substance of the core, and slows down abruptly to stop completely. In this case, its kinetic energy converts to heat, about 50 % of it going to heat the gas and the being radiated outside. Initially this radiation consists of infrared photons, but then there appears a progressively increasing number of visible-light photons in the emission spectrum. However, the thick outer shell is opaque to visible light, which is absorbed by dust particles and reradiated in the infrared region. That is why a protostar appears to an external observer as a bright but rather cold source of infrared radiation; the dust cocoon hides the stellar germ from optical telescopes.

After the shell precipitates on the core almost completely and becomes transparent, the core as if hatches out of the cocoon—a protostar transforms to a young star.

For definiteness we consider [102] the mass of an interstellar cloud of one solar mass ($1\ M_\odot$) that transforms into a star owing to gravitational instability. For a temperature of 5–10 K and a density $n \approx 10^5\,\mathrm{cm}^{-3}$ its radius is $R \approx 3 \times 10^6$ AU $\approx 10^9 R_{\mathrm{sun}}$. Initially on the collapse of the cloud the gravitational force increases the kinetic energy of the particles moving towards the center, while the temperature remains constant, because collisions play only a minor role and the thermal energy is removed by infrared radiation, for which the cloud is still transparent. During this isothermal compression, the gravity is $\sim R^{-2}$ and the matter-expelling Archimedean force is $\sim R^{-1}$. So, while early in the collapse these

forces are of the same order of magnitude, the role of the latter drops sharply with decreasing radius. The isothermal compression, which corresponds to free fall, lasts for $\approx 10^5$ years, following which the protostar loses transmittance in the IR range, its radiative cooling is hindered, and the compression passes into the adiabatic regime accompanied by a rise in temperature. The increase of temperature and pressure in this regime slows down the compression of the cloud, in which there occur dissociation and ionization reactions at temperatures of $\approx 10^3$ K and 10^4 K to additionally moderate the increase of matter temperature. However, on completion of the dissociation and ionization, the process becomes adiabatic once again. The protostar goes over to a quasi-equilibrium state, whereby the force of gravity is balanced by the plasma pressure and the radiative losses are compensated by a slow compression, which leads to the release of gravitational energy. In a characteristic time of $\approx 5 \times 10^7$ years, the gravitational compression heats the core of the protostar to thermonuclear temperatures, so that the star becomes a main-sequence star (Figs. 9.28 and 9.31).

The stages of temporal solar evolution are shown in Table 9.2 borrowed from [104].

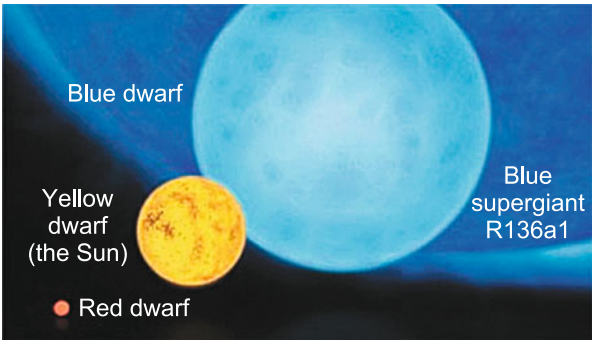

Fig. 9.31 Relative dimensions of stellar objects [60]

Table 9.2 Stages of solar evolution [104]

Evolution stage	Time (years)[a]	T_{eff} (K)	$L/L_\odot$	$R/R_\odot$	T_c (K)	ρ_c (g/cm^3)
1. Onset of protostar contraction	0	10	10^{-4}	$2 \cdot 10^6$	10	10^{-19}
2. Emergence of stellar core	$3 \cdot 10^5$	10	10^{-4}	$2 \cdot 10^6$	$2 \cdot 10^4$	$2 \cdot 10^{-2}$
3. The core contains half-mass	$7 \cdot 10^4$	300	26	$2 \cdot 10^3$	$8 \cdot 10^5$	0.25
4. Beginning of slow contraction	$8 \cdot 10^5$	4400	1.6	2.1	$4 \cdot 10^6$	1.5
5. Minimal L at convection stage	$8 \cdot 10^6$	4400	0.5	1.6	$6 \cdot 10^6$	11
6. Minimal L before the main sequence	$1.6 \cdot 10^7$	5900	1.1	1.0	$1.3 \cdot 10^7$	83
7. Zero-age main sequence	$1.0 \cdot 10^7$	5700	0.7	0.87	$1.4 \cdot 10^7$	90
8. Present-day sun	$4.6 \cdot 10^9$	5800	1.0	1.0	$1.5 \cdot 10^7$	156

[a]Indicated is the time elapsed after the previous stage

Nowadays, this qualitative model has been replaced by sophisticated two- and three-dimensional models of the evolution of protostars with the inclusion of rotation, convection, thermal and density-induced ionization, and a comprehensive description of the optical properties of multicomponent plasmas [85].

In the transformation of a gravitationally unstable cloud into a star there occur titanic changes in the physical conditions of the matter: the density rises by 20 and the temperature by 6 orders of magnitude. The matter undergoes a series of transformations from molecular and solid states to superdense relativistic plasma states.

Under stationary conditions a star is in the state of hydrostatic equilibrium—the plasma pressure increases with depth, the weight of every spherical layer being precisely compensated by the difference of the pressure forces at its inner and outer boundaries [104]. When the pressure at some point becomes higher (or lower) than the weight of the overlying layers, the star will slightly expand or, respectively, contract and the equilibrium will be restored. Since the information about gas pressure changes is transferred by acoustic waves, the star restores mechanical equilibrium in a time taken for the sound waves to travel a distance equal to the stellar diameter. This time is rather short: about one hour for the Sun. As a rule, the characteristic times of the thermal processes occurring in a star (the core-to-surface energy transfer time or the thermonuclear fuel burn time, etc.) are much longer—hundreds of thousands, millions, or even billions of years. That is why in the restructuring of the star in the course of its evolution the gas pressure always manages to change in such a way that the star remains in the state of equilibrium.

The principal energy source in the subsequent stellar evolution is thermonuclear burn (see Chap. 4), which is responsible for the production of heavy elements and takes place in strongly compressed matter at extremely high temperatures (Fig. 9.32 [50]). As we saw in Chap. 4, to realize thermonuclear fusion reactions the nuclei must be brought to an internuclear distance $r \leq 10^{-15}$ cm (the range of nuclear forces) by overcoming the Coulomb electromagnetic repulsion energy. The energy released in the hydrogen-helium fusion reaction is 10^3 times higher than the energy spent to overcome the Coulomb repulsion.

High plasma temperatures—tens or hundreds of keV—are required to implement thermonuclear reactions. The fuel for thermonuclear reactions is the chemical elements lighter than iron; their abundance in the interstellar medium and outer stellar layers is shown in Fig. 9.33 [104]. In the central stellar layers the fraction of the elements heavier than hydrogen (especially He, C, N, and O) is significantly higher.

In the course of this burning (Table 9.3 [87]), hydrogen transforms into helium (10 million K), which passes into carbon and oxygen (100–200 million K). Carbon at ≈800 million K yields neon, sodium, and magnesium, and oxygen at 2 billion K gives silicon and sulfur. A temperature of ≈ 4 billion K is required to transform silicon into iron and the neighboring elements. Here the thermonuclear burn terminates, because expenditures of energy are required to produce heavier elements (see Fig. 4.3, the peak of binding energy for ^{56}Fe and ^{60}Ni).

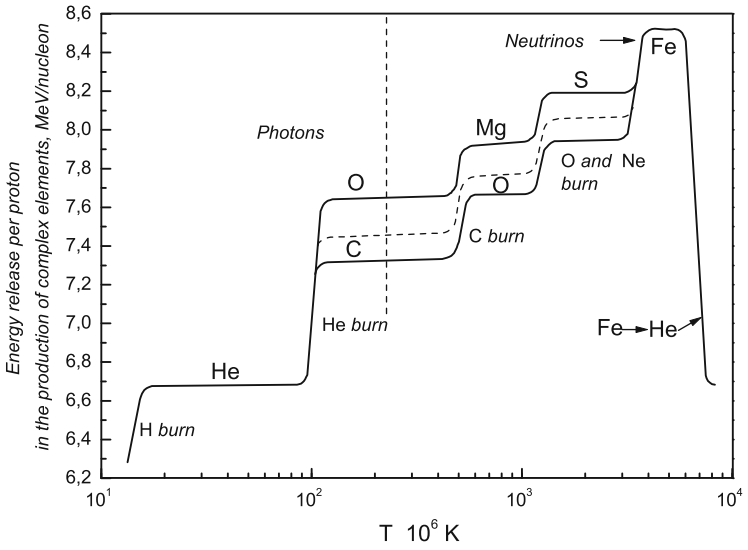

Fig. 9.32 Energy liberation in the sequential burning of hydrogen, helium, carbon, oxygen, and neon. The *upper curve* represents the transformation of oxygen and the *lower curve* the transformation of carbon. The same takes place at other stages. It is not unlikely that the energy variation in real stars corresponds to the *dashed curve* [50]

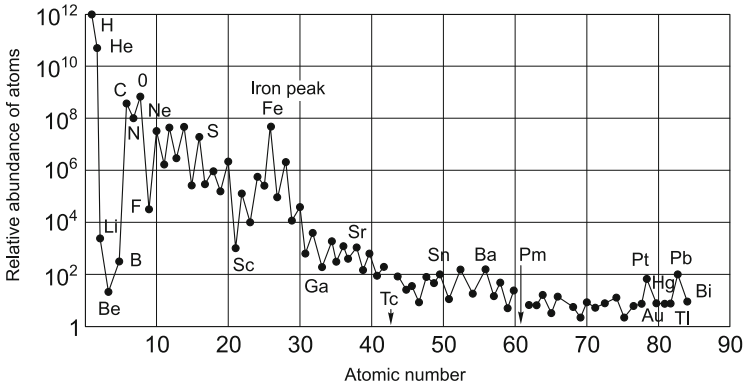

Fig. 9.33 Relative abundance of chemical elements in the interstellar medium and outer stellar layers [104]

One can see from Fig. 4.3 that the fusion of atomic nuclei is attended with binding-energy liberation only up to the production of $^{56}_{26}$Fe iron nuclei and that the fusion of heavier elements, on the contrary, required expenditures of heavier elements. That is why nuclear reactions can supply stars with thermal energy until all nuclei of light elements transform to iron nuclei. Elements heavier than iron are synthesized in stellar interior only during explosive processes [104], for instance in

Table 9.3 Main stages of thermonuclear stellar burn [87]

Main component of a nuclear reaction	Central stellar temperature (K)	Central density (kg/m^3)	Stage duration
Hydrogen	4×10^7	5×10^3	7×10^6 years
Helium	2×10^8	7×10^5	5×10^5 years
Carbon	6×10^8	2×10^8	600 years
Neon	1.2×10^9	4×10^9	1 year
Oxygen	1.5×10^9	10^{10}	6 months
Silicon	2.7×10^9	3×10^{10}	1 day
Core collapse			0.2 s
Core explosion			

supernova explosions, when a fast stellar contraction is attended with the liberation of a huge amount of energy. Among heavy nuclei, only nuclei with the number of protons $Z < 83$, i.e. up to bismuth inclusive, man be perfectly stable. And though some nuclei with $Z > 83$ may persist for a rather long time (for instance, the lifetime of $^{238}_{92}$U uranium nuclei is about 5 billion years), they all are subject to decay into two or several nuclei of lower charge.

These elements (Cu, Sn, Ag, Pb, Th, U) are synthesized by neutron capture in the explosions of type II supernovae and red giants.

In the strongly compressed plasma of astrophysical objects the static and dynamic charge screening lowers the repulsive potential barrier between ions (see Sect. 4.1), which increases the rate of thermonuclear plasma burn [45, 90, 111]. In the solar plasma this reaction acceleration amounts to several percent, while for a supernova the reaction rate may increase by a factor of several million.

This is the reason why the study of thermonuclear burn in stationary and transient modes under physical conditions close to the astrophysical ones might become one of the most important research lines in the area of laboratory astrophysical plasma (see Fig. 2.1). Because in nearly 99 % of the stars observed in the sky, hydrogen and/or helium is burning for parameters attainable for OMEGA, NIF, and MJL laser systems as well as petawatt lasers (Chap. 5).

9.2.2 Evolution of Single Stars

Following [115], we now outline a brief picture of the evolution of single stars (Fig. 9.34).

The mass of low-mass stars $M < 0.08\,M_\odot$ is too small for the onset of thermonuclear burning of hydrogen. Of significance at the center of such stars are the effects of electron degeneracy and Coulomb nonideality, and the object is an

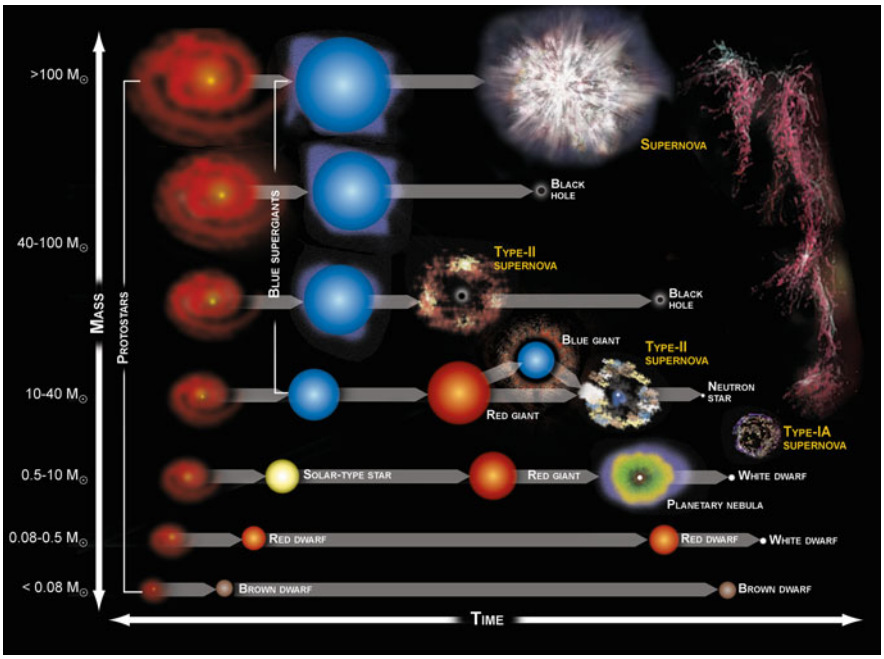

Fig. 9.34 Diagram of stellar evolution [59]

intermediate case between planets and stars. They are referred to as unsuccessful or "fusion-free" stars.

Stars of mass $0.08\,M_\odot < M < 0.5\,M_\odot$ are entirely convective, which averts the subsequent ignition of the layer part upon hydrogen burnout in the core. Such stars do not become red giants, which heat up with time. In the dynamics of these objects [104] the high elasticity of degenerate gas terminates the compression of the stellar core, and the intensity of thermonuclear reactions does not become high enough to maintain the luminosity of the star. Nor can the layer source provide heat for a long time: as it recedes from the stellar center the shell progressively expands, and finally its outer part escapes from the star. Nuclear reactions gradually decay, and of the star there remains a hot helium core surrounded by a light but rather lengthy shell of nondegenerate hot gas. As the gas becomes cooler, it settles on the surface of the helium core, which is comparable to the Earth in size but is thousands of times more massive.

Therefore, the final products of the evolution of stars with $M < 0.5\,M_\odot$ are very dense ($\approx 1\,\mathrm{t/cm^3}$) compact objects—helium white dwarfs. The degenerate gas pressure is hardly dependent on the temperature, and therefore white dwarfs, unlike ordinary stars, are hardly compressible despite the permanent loss of heat, and their evolution consists in slow cooling. However, since the hydrogen burn time for single stars of mass smaller than $0.9\,M_\odot$ exceeds the age of the Universe, the helium white dwarfs have no time to form from the single stars. Having no time to evolve during

the cosmological time, small-mass stars once produced in the Galaxy serve as a material for reconstructing the history of star formation. However, if a small-mass star is a component of a binary system, a part of its mass may flow to the accretion center and the exposed helium core of about a half the solar mass may turn into a white dwarf during cooling.

For stars of mass $0.5\,M_\odot < M < 2.5\,M_\odot$, after hydrogen burning there forms a degenerate helium core of mass about $0.5\,M_\odot$. For stars with $M > 0.5\ M_\odot$, the degeneracy of electron gas does not set in by the point in time when the temperature rises to 150 million K, and the helium-to-carbon transformation begins. The stellar interior ceases to contract, because a nuclear energy source turns on there; a similar situation took place when the young star was becoming a main sequence star. The star now has two nuclear energy sources: the central source, in which helium burns, and a layerwise one, in which helium is produced from hydrogen. The stellar shell adjusts itself to the changes of conditions, decreases in size, and slightly warms up. The effective stellar temperature increases. During this period a part of the shell substance weakly coupled to the main stellar mass escapes to the ambient.

Then the star enters a rather long period of its life, during which carbon is accumulated in its interior. When its density increases, a fraction of carbon transforms to oxygen in the course of the reaction $\mathrm{He} + \mathrm{C} \rightarrow \mathrm{O}$.

At this stage of stellar evolution there emerge radial pulsations, which arise from the combination of gravitational forces, pressure, and the characteristics of the optical properties of hot plasma [104].

At the stage of a red-giant there occurs thermonuclear burn of the hydrogen layer source. The onset of helium burn and its transformation to carbon proceeds under conditions of plasma degeneracy and is attended with a short-duration energy liberation (a helium flare). The stellar shell expands and gradually disperses in space. The final product of evolution is a carbon-oxygen white dwarf of mass of about $0.5\,M_\odot$, which cools down.

Since our Sun is in precisely this stellar mass range, directly related to it are the hydrogen (Fig. 4.6) and carbon-nitrogen (Fig. 4.7) energy cycles considered at length in Sect. 4.1.

In accordance with Einstein's formula, in the radiation of energy E the solar mass decreases each second by a value $\frac{E}{c^2} \approx 4$ million t [104]. This is several times greater than the mass which the solar wind carries away from the Sun.

In accordance with the proton-proton scheme (Fig. 4.6), helium is produced in the fusion of four protons, each of which will have a mass defect of $\approx 1\,\%$ on becoming a part of helium. If all hydrogen burns out by this scheme, the solar mass will become lower by $0.01\,M_\odot$ and the energy liberation will be $E \approx 0.01\,M_\odot$. For a luminosity $L_0 = const$ this gives a solar lifetime of ≈ 100 billion years; considering that only the central part ($\approx 10\,\%$ of the solar mass) is burning in reality, this lifetime will amount to ≈ 10 billion years [104].

The temporal evolution of the Sun is represented in Fig. 9.35 [7], which provides the answer to the question of how long the Sun will shine: for about 5 billion more years. Following [7], we assume a crude estimate for the average lifetime is

$$t = 10 \text{ billion years} \left(\frac{M}{M_\odot} \right)^{-3},$$

which shows how rapidly the stellar lifetime decreases with the stellar mass. Since the brightness of the most massive stars $L \sim M$, with an increase in stellar mass the stellar lifetime ceases to shorten and tends to the value ≈3.5 million years, which is extremely short on the space scale. If a massive star were born only 10 million years ago, today it is no longer in the main sequence, yet low-mass stars born even at the dawn of the evolution of the universe (which is approximately 14 billion years old) will live for a long time.

At the main-sequence stage there occurs a gradual, very slow increase of the stellar temperature, radius, and brightness. In the case of the Sun (Fig. 9.36), for instance, during the nearly 5 billion years of its life the surface temperature has

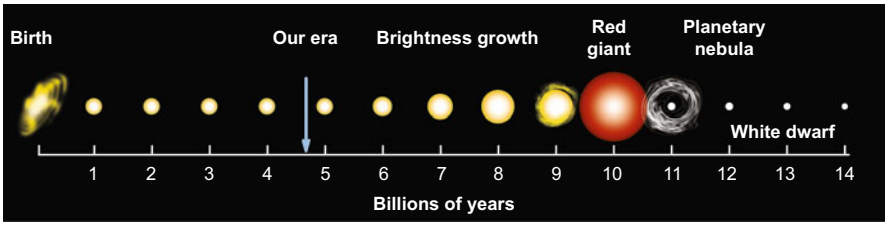

Fig. 9.35 Solar evolution. Dimensions are not shown to scale [7]

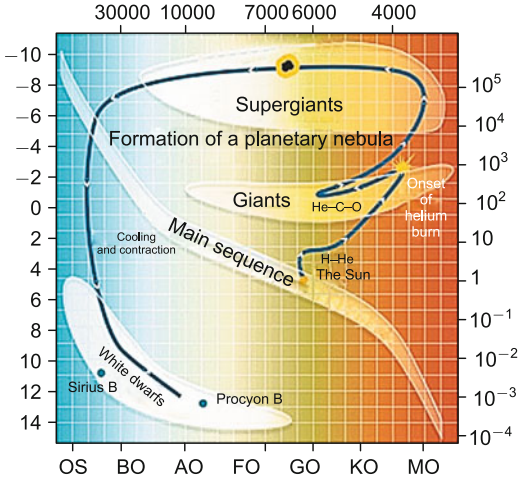

Fig. 9.36 Relative dimensions of stellar objects [61]

increased by only 2 %, the radius by 10 %, and the brightness by about 30 %. During the next 4 billion years its temperature will hardly change, the radius will increase by a factor of 1.5, and the brightness will rise twofold. Stars pass through all other evolution stages—both the periods of stellar formation and those of decline—relatively quickly.

Estimates given in [104] suggest that the burn of hydrogen proceeds quite slowly in stars. By dividing the solar luminosity ($4 \cdot 10^{26}$ W) by the mass ($0.1\,M_\odot = 2 \cdot 10^{29}$ kg) of its central region involved in nuclear reactions, we obtain the average power of heat release per unit mass of the "burning" solar substance: $q = 0.002$ W/kg. This low energy release has no analogues among household electric appliances. For instance, for an ordinary lamp this parameter is equal to 3000 W/kg and for an electric iron to 1000 W/kg; a notebook with an internal energy source dissipates a power of about 10 W/kg and far exceeds the Sun in specific energy liberation. Even a human in a tranquil state liberates heat in the amount of about 10 W/kg, like a giant star, and does not shine only because his mass is far below the stellar mass.

The Sun produces the amount of heat per unit of its active mass equal to the heat released in the rotting of fallen wet leaves, while the specific solar power amounts to tenths of the specific power of a human heart. So that the nuclear solar fuel "glows" or even "rots" rather than "burns". The nuclear burn of hydrogen in low-mass stars is still slower: for instance, a red dwarf of mass $0.1\,M_\odot$ exhibits a luminosity tens of thousands of times lower than the solar one, and therefore its q figure is thousands of times still lower than that of the Sun.

Despite the small changes in appearance, a star radically changes its internal structure during its lifetime: while initially it is a uniform sphere of hydrogen with an admixture of helium, by the end of its life the star has a core of practically pure helium surrounded by a shell of the initial hydrogen–helium mixture. In this case, a solar-type star burns about 10 % of its initial mass during its lifetime.

Upon complete hydrogen burn-up in the core, if the conditions are insufficient for the ignition of helium (10^8 K, 10^5 g/cm^3), nuclear reactions subside and the central stellar part begins to shrink dramatically and thereby heat up. When the temperature at the surface of the core in contact with hydrogen becomes as high as 10^7 K, hydrogen begins to burn in the source layer around the core. As this takes place, more energy is released than in the burning of the hydrogen core before, and the star becomes brighter. The stellar radius increases, the temperature decreases, and the surface reddens. In this case, the star abandons the main sequence and finds itself in the branch of subgiants and then red giants. The source of energy at this stage is the burning of hydrogen in the constantly increasing source layer, which gives more and more energy to the star. The stellar radius and brightness continue to increase and the temperature remains almost invariable. for a solar-type star this process will take about 100 million years.

In the branch of giants, the helium core, which increases in mass, continues to contract. The layer heat source—the domain of hydrogen burning around the core—becomes progressively thicker and more powerful, while the stellar shell expands and becomes cooler. The zone of the shell entrained in convection becomes more

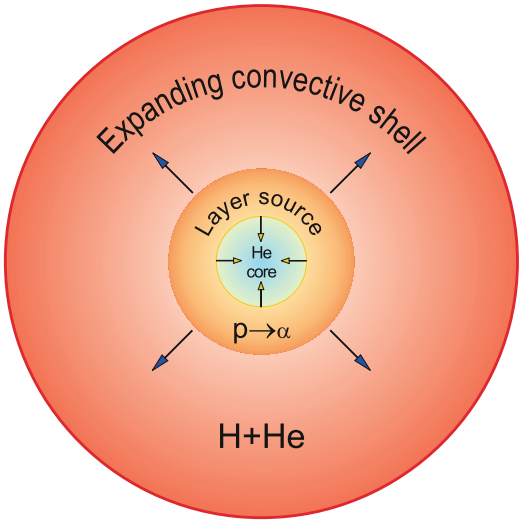

Fig. 9.37 Structure of a red giant [7]. At the center is a degenerate, gradually contracting core of helium produced in the course of hydrogen burn; it is void of nuclear reactions. Around the core is a progressively expanding layer energy source, where hydrogen burns. The extensive convective hydrogen-helium stellar shell expands

and more lengthy. Finally the lower boundary of the convective zone descends to the hydrogen burn layer. The burn products (primarily carbon and nitrogen) are carried out to the surface and change the composition of the stellar atmosphere. The star continues to increase in radius and brightness, the temperature remaining moderate.

At the red giant stage, a star is unstable: its isothermal helium core continues to contract, the hydrogen-burn layer broadens, and its convective shell becomes progressively larger (Fig. 9.37). The radius of a red giant with a solar mass amounts to $200\,R_\odot$ at the phase of greatest extent. At this point in time, the solar surface will touch the orbit of the Earth. And though the solar surface temperature will decrease to 3100 K during this period, the luminosity of this giant red ball will rise to 2400 times the present-day luminosity of the Sun. The evolution of life on Earth will terminate. However, in the vicinity of Pluto's orbit the conditions for life will become favorable. An analysis shows that life on the Earth may exist provided the solar mass is in the 1.6×10^{30}–2.4×10^{30} kg range. Outside of this range the terrestrial climate would be colder than the Martian or hotter than the Venusian one. Measurements of the solar mass yielded a value of 2×10^{30} kg. The red giant stage is relatively short, and therefore only a relatively small fraction of the stars are observed at this stage—several percent of the total number.

For more massive $(2.5M_\odot < M < 8M_\odot)$ *objects*, the helium core is nondegenerate upon hydrogen burn, and after the red giant stage there occurs the nondegenerate burning of helium with the production of carbon and oxygen. The inner stellar region ceases to contract, because a nuclear energy source is turned on there. The star has two nuclear energy sources: the central one, where helium burns, and the layerwise source, in which helium is produced from hydrogen. The stellar shell adjusts itself to the changes of conditions, decreases in size, and slightly warms

up. During this period a part of the shell substance weakly coupled to the main stellar mass escapes to the ambient [104].

After that the star enters a rather long period of its life during which carbon is accumulated in its interior. When its density increases, a fraction of carbon transforms to oxygen in the course of the reaction He + C $\rightarrow$ O. As a result, inside the red giant there forms a degenerate (C–O) core of mass $1.2\,M_\odot$. Due to development of thermal instabilities the shell is shed off with the formation of a planetary nebula, which shines due to the ultraviolet radiation of the hot ($T \approx 10^5$ K) core; the core gradually cools down and turns into a relatively cool (C–O) white dwarf.

When helium in the central region runs out, the stellar core devoid of energy sources begins to contract, and it is not long before the temperature and density at its outer boundary rise to the extent that helium begins to burn there [104]. Since then the core is surrounded by two layerwise sources: hydrogen burns in the outer source and helium burns in the inner one. As this takes place, the density in the core itself becomes so high that the electron gas becomes degenerate and its pressure terminates the contraction of the central region. The emergence of two layerwise sources is attended with an increase in stellar size and a lowering in effective stellar temperature: in the diagram the star shifts upwards and to the right, into the domain of red supergiants ranging from 100 to $1000R_\odot$ in radius. The star becomes structurally nonuniform: the degenerate supergiant's core is only two–three times greater than the Earth in size, while the radius of the entire star exceeds the radius of the terrestrial orbit!

Calculations suggest that the nuclear fuel of the layerwise sources burns not steadily but in a pulse-like manner, in the form of short (several years long) high-intensity flares spaced at intervals thousands of years long. Each flare generates a shock wave, which propagates outside and expels a part of the shell to the ambient to significantly decrease the solar mass. Owing to its huge size, the shell of a red supergiant is relatively weakly coupled to the core, and therefore such stars also lose mass intensely in the intervals between the flares: their outer layers contract and expand with a characteristic time of about a hundred days, which also generates shock waves and the matter outflow to the ambient with a velocity of about 10 km/s.

These stars pulsate for the same reason as cepheids. As a rule, the pulsations of red giants are not strictly periodic, but in return their amplitude is very high: during one cycle, the stellar radius changes by a factor of several tens and the luminosity changes by thousands of times!

The model of a one-component plasma of C and O ions against the neutralizing degenerate electron background applies to these objects quite well. The characteristic parameters of white dwarfs are $\rho \approx 10^6\,\mathrm{g/cm^3}$ and $T \approx 10^6 - 10^8$ K, which leads to a strong plasma nonideality $\Gamma \approx 5$–500. This plasma is liable to Coulomb crystallization. According to astroseismological observations, about 90 % (5×10^{32} g) of the star BMP 37093 is in the crystalline state ("diamond" core; Fig. 9.38).

In the narrow mass range ($8M_\odot < M < 10$–$12M_\odot$) the thermonuclear burn proceeds to give a mixture of oxygen, neon, and magnesium. Further reactions are

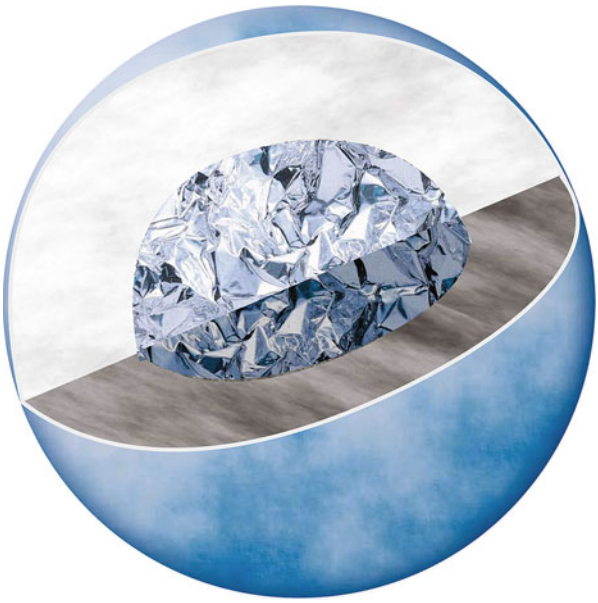

Fig. 9.38 White dwarf BMP 37093 with a plasma crystal core

Fig. 9.39 New star explosion dynamics [59, 70]

not realized because the stellar shell disperses in the form of a planetary nebula. The result of evolution after the shell shedding is an (O–Ne–Mg) white dwarf with a mass close to the Chandrasekhar limit ($\sim 1.2\,M_{\odot}$).

Figure 9.39 shows the explosion dynamics of a new star [59, 70], when the Chandrasekhar limit is not reached by way of accretion, resulting in a weaker explosion than in the case of a supernova.

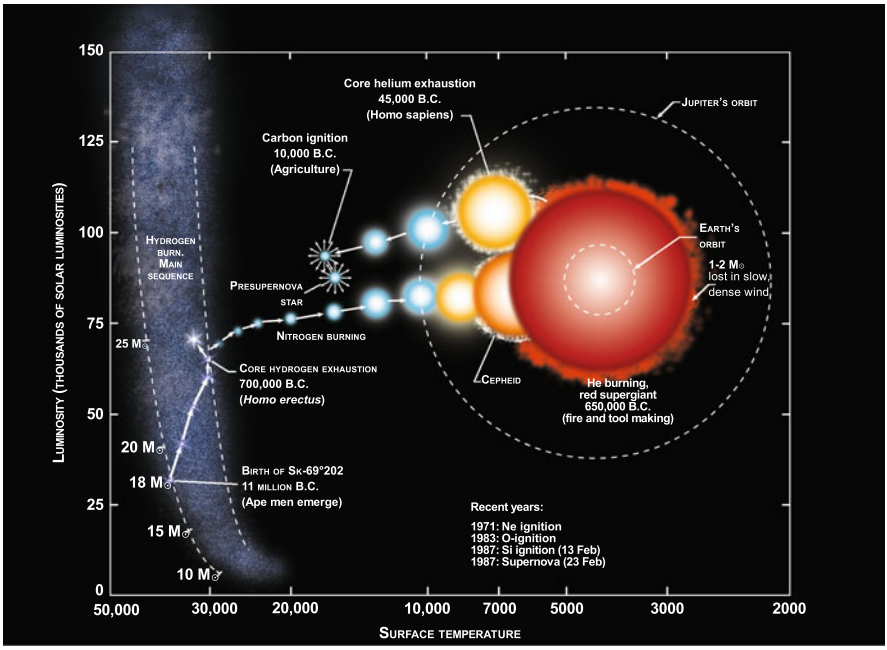

Fig. 9.40 Evolution of the supernova SN 1987A in comparison with human evolution

The thermonuclear evolution in the core of a massive star ($10–12 M_\odot < M < 30–40 M_\odot$) proceeds under nondegenerate conditions to produce the elements Fe, Co, and Ni (Figs. 9.40 and 9.41).

Massive supergiants ($M > 8 M_\odot$) that are at the latest stages of their evolution have a complex structure. In the stellar core new elements are synthesized, their complexity increasing with depth, up to iron. Such a supergiant has an inert iron core surrounded by burning shells of silicon, neon, oxygen, helium, and hydrogen.

According to [104], the heat transfer in the shells of red supergiants is effected by convection, which embraces the domain from layerwise sources of helium and hydrogen burn to the photosphere. As a result, the products of thermonuclear reactions find their way to the lower part of the shell. As the outer shell layers, which consist primarily of hydrogen and helium, escape to the ambient, the stellar atmosphere is progressively enriched in nuclear fusion products arriving from the interior. This is precisely the way there emerge single carbon stars—supergiants, whose spectra exhibit strong lines of CN, C_2, SiC_2 and some other molecules; this testifies to a high content of carbon in the outer stellar layers. The gas flowing out of the atmospheres of these stars gradually cools down. When its temperature becomes lower than 1500 K, carbon atoms begin to condense into dust particles.

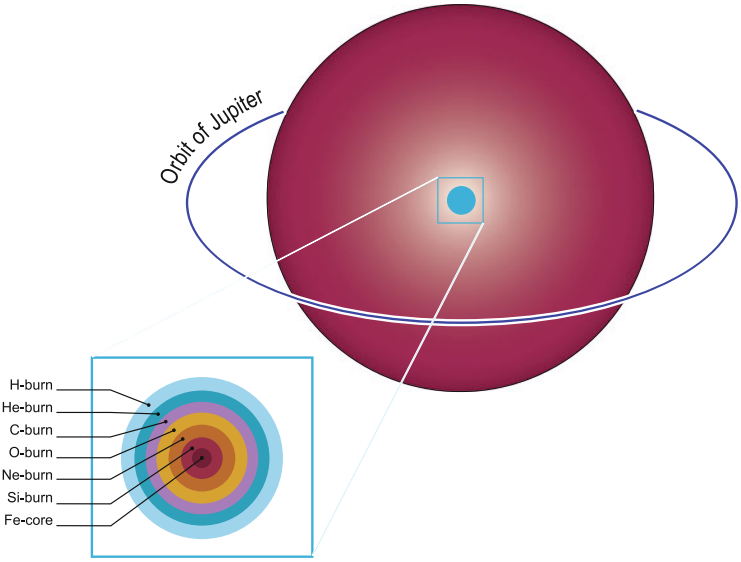

Fig. 9.41 Structure of a red supergiant [7]

By the end of the supergiant stage, which lasts for several hundred thousand years, almost all of the stellar shell is shed to expose the hot degenerate carbon-oxygen core. As it turns out, the greater the mass of a star, the greater part of its mass it loses in the course of its evolution. The mass of a white dwarf cannot exceed the Chandrasekhar limit, which is approximately equal to $1.4\,M_\odot$ (otherwise the dwarf will collapse). It is precisely these two circumstances which determine the upper bound of the mass range considered in this section (8–$10\,M_\odot$): this is the initial mass of those stars for which the degenerate carbon-oxygen core does not exceed the Chandrasekhar limit by the end of evolution.

All compact stars whose equilibrium is maintained by degenerate electron gas are usually termed white dwarfs [104], although their color may vary greatly: from white-blue to red. Furthermore, approximately 10 billion years after birth these stars cool down to the extent that they cease to radiate in the optical range.

The reason why the lower bound of the stars that leave behind a white dwarf is precisely defined ($0.5\,M_\odot$) and the upper bound is approximately determined (8–$10\,M_\odot$) is quite simple. Low-mass stars are conservative: they hardly lose substance in the course of evolution, and therefore their models are highly reliable. But the evolution of a massive star depends on many factors difficult to account for: rotation, magnetic field, convection characteristics, stellar wind intensity, etc. Therefore the upper bound of the initial mass of the ancestors of white dwarfs so far has not been determined precisely. In any case, experts believe that it certainly lies in the range between 8 and $10\,M_\odot$.

In the stars of mass above $10\,M_\odot$ the electron gas degeneracy does not inhibit the heating of inner layers to a temperature of $\approx 10^9$ K, at which carbon and oxygen can participate in diverse nuclear reactions with the production of heavier elements. Examples of such nuclear reactions:

$$^{12}_{6}\mathrm{C}+^{12}_{6}\mathrm{C} \rightarrow ^{24}_{12}\mathrm{Mg},\ ^{12}_{6}\mathrm{C}+^{12}_{6}\mathrm{C} \rightarrow ^{20}_{10}\mathrm{Ne}+^{4}_{2}\mathrm{He},\ ^{12}_{6}\mathrm{C}+^{4}_{2}\mathrm{He} \rightarrow ^{16}_{8}\mathrm{O},\ ^{16}_{8}\mathrm{C}+^{16}_{8}\mathrm{O} \rightarrow ^{32}_{16}\mathrm{S},\ \ldots$$

The subsequent stellar evolution comes to the burnup of successively heavier elements [104], the core compression, and the formation of new layerwise sources at the outer core boundary.

After the onset of nuclear reactions with participation of carbon and oxygen the main part of liberated energy is carried away by neutrinos and antineutrinos: at a temperature of 10^9 K, there take place a lot of processes that result in the production of these particles, which are free to escape from the star [104]. In particular, the nucleus of silicon $^{28}_{14}\mathrm{Si}$ may capture a free electron, emit a neutrino, and transform to a nucleus of aluminum $^{28}_{13}\mathrm{Al}$, which is unstable and before long turns into the initial nucleus $^{28}_{14}\mathrm{Si}$ and in doing this generates an electron and an antineutrino. As a result, neither a silicon nucleus nor an electron vanish but a neutrino and an antineutrino make their appearance, with a part of the kinetic energy of the free electron, i.e. of the thermal gas energy, spent to produce them.

At the late stages of evolution, neutrinos carry away the stellar thermal energy quite efficiently, making the stellar nuclear reactor work at full power so as not to let the substance cool down. A change over to a new kind of nuclear fuel requires an increase in gas temperature, which in turn results in an increase in neutrino radiation intensity. This is the reason why each new kind of nuclear fuel burns up faster and faster: carbon and oxygen take several hundred years to transform to elements of the silicon group, while their subsequent transformation to iron takes several tens of years.

The hotter is the gas, the higher is the average energy of photons generated in it [104]. When the temperature rises to a billion Kelvin and silicon begins to burn, there emerge γ-ray photons in appreciable amount, their energy being so high that in the collisions with nuclei they split them into several nuclear fragments, thereby causing photodissociation. The fragments enter in fusion reactions, so that the "burning" of silicon is in reality a large set of reactions.

Most often, γ-ray photons detach α particles from nuclei; α particles actively enter in fusion reactions, and therefore the main result of silicon "burning" is the chain of transformations: $^{28}_{14}\mathrm{Si} \rightarrow ^{32}_{16}\mathrm{S} \rightarrow ^{36}_{18}\mathrm{Ar} \rightarrow ^{40}_{20}\mathrm{Ca} \rightarrow ^{44}_{22}\mathrm{Ti} \rightarrow ^{48}_{24}\mathrm{Cr} \rightarrow ^{52}_{26}\mathrm{Fe} \rightarrow ^{56}_{28}\mathrm{Ni} \rightarrow$ etc. The nickel nucleus is unstable and lives for about 6 days, after which it absorbs an electron to turn into a cobalt isotope: $^{56}_{28}\mathrm{Ni} + \mathrm{e}^- \rightarrow ^{56}_{27}\mathrm{Co} + \nu$. This nucleus is also unstable and turns, with a decay period of about 77 days, into a stable iron nucleus: $^{56}_{27}\mathrm{Co} + \mathrm{e}^- \rightarrow ^{56}_{26}\mathrm{Fe} + \nu$.

For a while the liberated energy exceeds the energy spent to split nuclei, but only until an iron-nickel stellar core is formed. The synthesis of elements heavier than $^{56}_{26}\mathrm{Fe}$ is attended, as we saw (Fig. 4.3), with energy absorption rather than liberation. In this case, spent on photodissociation is the thermal energy released

in the contraction of inner stellar regions. Because of this, the gas temperature and pressure grow too slowly to counterbalance the force of gravity, which increases during contraction. As a result, the hydrostatic equilibrium is disturbed and the stellar core begins to collapse rapidly. The gas heats up to 10^{10}–10^{11} K, which leads to a high-intensity burst of neutrino radiation.

The further development of events and the destiny of a star depend on many factors. The most important of them is the stellar mass at the instant its iron-nickel core begins to collapse. At the final stage of evolution it may be two to three times smaller than the mass with which the star once entered the main sequence (Fig. 9.28). This is because massive stars permanently lose their substance. The gas flows off their surface with a velocity ranging from several hundred to several thousand kilometers per second [104]. For stars with $M > 10\,M_\odot$, at all evolution stages the luminosity is so high that the radiation pressure in the outer layers exceeds the force of gravity and makes the shell substance escape from the star. The stars lose up to $3 \cdot 10^{-6}\,M_\odot$ of substance annually; late in the evolution the mass loss rate rises by a factor of 10–30. The higher is the stellar mass, the higher is its luminosity and, hence, the stronger is the stellar wind emanating from the star. As a result, more massive stars lose the greater part of their initial mass by the instant an iron core forms at their center and begins to collapse.

The core of a Fe–Co–Ni star of mass 1.5–$2\,M_\odot$ is subject to several instabilities and collapses with the formation of a neutron star (see Sect. 8.1).

Let us revert to the final stages of the evolution of massive stars. We paused at a point that, at some instant, an iron stellar core is formed, which loses stability and begins to contract rapidly. For stars of mass below $\approx 40\,M_\odot$ while in the main sequence, the collapsing nucleus turns into a neutron star—an object of mass 1.5–$3.0\,M_\odot$, about 10 km in radius, and with an average density of hundreds of millions of tons per cubic centimeter. Under these conditions the substance consists primarily of neutrons, whose degenerate gas pressure counterbalances the tremendous force of gravity compressing these compact bodies [104]. The physics of neutron stars will be considered at length in the next section; now we shall discuss the destiny of the outer part of a massive star.

As a result of iron core collapse in about 0.1 s in the central stellar region there forms [104] a space approximately 1000 km in size with a neutron star at its center. The substance which had not managed to turn into iron prior to the onset of the collapse rushes to this cavity. According to one hypothesis, on accelerating to 100,000 km/s and striking against the surface of the neutron, star this substance of the outer layers heats up and generates an intense shock wave, which rushes outwards and not only stops the downfall of gas but also makes it expand. When traveling through the nuclear fuel-rich substance, the shock wave "ignites" it, so that nuclear energy feeds this detonation wave and maintains its high velocity. It is precisely this process which is responsible for the expansion of the bulk of stellar mass to the ambient with a velocity of thousands of kilometers per second, thereby explaining the phenomenon of supernova explosion at the instant of the death of a massive star. Of fundamental importance in this scenario supposedly

is the asymmetry of collapse, which in turn may be associated with rotation and magnetic field [104].

This final stage of the life of a massive star is associated with a strong burst of neutrino radiation, and the shock wave that recedes from the neutron core explodes the star from within. The process is attended with a supernova explosion of type II (when an extended hydrogen shell has survived) or Ib/c. In this case, the brightness of such a supernova is extremely high and may exceed the total brightness of all the remaining stars of the Galaxy. Subsequently, for several tens of thousands of years the shed shell remnants exist in the form of a luminous nebula—a supernova remnant.

Nowadays it is generally agreed [104] that a supernova outburst signifies the last catastrophic stage of stellar evolution. Having used up all thermonuclear energy sources, a massive star cannot resist the force of gravity and collapses swiftly. White dwarfs may not have a mass exceeding the solar mass by more than one-and-a-half times. A more massive collapsing star does not stop at the stage of a white dwarf and contracts to a neutron star or a black hole. Released in this case is gravitational energy—there occurs a supernova outburst. The neutron star or black hole remaining at the site of explosion is surrounded by a gradually dispersing nebula—the gaseous supernova remnant. As we see, supernovae like new stars are also very old. The phenomenon of a supernova signifies stellar death, and therefore, unlike new stars, supernovae cannot burst again.

9.2.3 Supernova Stars

These objects (Fig. 9.42 [21]) are among the most interesting and striking astronomical phenomena (the scheme of production is shown in Fig. 9.43). The brightest of supernovae was recorded on May 1, 1006; Chinese chronicles also note less bright outbursts in 185, 386, and 393 AD. Having existed for several years, SN 1006 exceeded Venus and competed with the Moon in brightness, because it was not far from the Solar System, approximately 7000 light years away. The Crab Nebula is the well-known and thoroughly studied remnant of the supernova discovered on July 4, 1054, according to observation chronicles in Japan, China, and Korea. According to modern views, supernova explosions occur with a frequency of about once in a 100 years.

Significant progress in the observation of supernovae was achieved [104] due to the use of automated telescopes. For instance [104], the modest Katzman Automatic Imaging Telescope (KAIT) only 0.76 m in diameter, which is located at Lick Observatory (California), now discovers about 80 supernovae annually; this is much more than was only recently discovered by all observatories of the world. Each bright night KAIT automatically photographs selected portions of the sky to obtain about 7000 galactic images every week. A fresh portrait of each galaxy is automatically compared with its previous images to reveal candidates for supernovae.

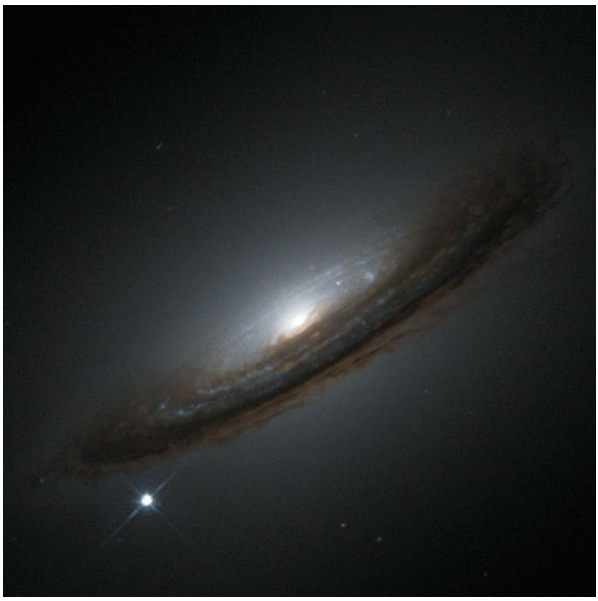

Fig. 9.42 The supernova that flared up in the Galaxy NGC 4526 in 1994. The image was obtained by the Hubble Space Telescope [21]

The apparent brightness–time curves (the so-called light curves) for type-Ia supernovae are quite similar. During the first 10–20 days the stellar brightness rises several-fold to attain its peak and then decreases at the same rate during the same period of time. Later on, the brightness decreases exponentially and the star vanishes in 1–3 years. Type-Ia supernovae exhibit a small spread in absolute peak brightness, which permits their use as "cosmic or standard candles"—sources of light for measuring distances in space. Type-II supernova brightness curves differ from those of type-Ia supernovae in that they exhibit a several-fold lower peak intensity, a longer decay time, and a different spectral composition of the radiation.

Anomalous optical effects observed in remote supernova bursts underpin a radical revision of the existing notions of the physical properties of empty space and of the structure and evolution of the universe [16, 71]. Owing to their extremely high brightness, supernovae are observed at great, truly cosmological distances, making it possible to estimate the apparent brightness of these sources as a function of their distance from the Earth. The brightness was shown to decrease faster than would be expected from cosmological models. This corresponds to the situation whereby the cosmological expansion proceeds with acceleration rather than with moderation, as was considered before, which leads to models of "dark" energy (see Sect. 10.1.5). This discovery radically changes our understanding of the modern stage of the cosmological evolution of the universe and calls for a search for other manifestations of this effect, perhaps in the area of high-energy-density experimental physics.

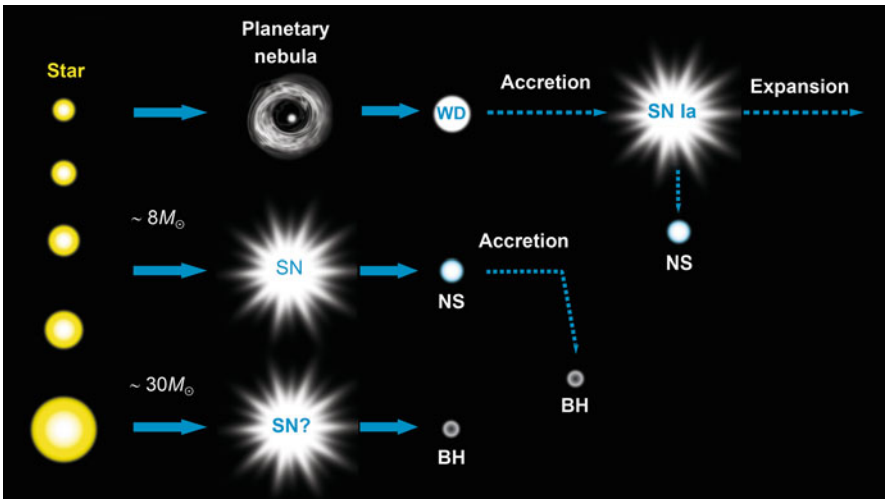

Fig. 9.43 Scheme of stellar evolution that gives rise to supernovae. Low-mass stars transform to white dwarfs (WDs). A planetary nebula may emerge in this case. When a white dwarf is part of a close binary system, it may gain enough mass to explode as a type-Ia supernova (SN). The matter could disperse completely, but a neutron star may be formed (NS). Higher-mass stars transform to neutron stars upon supernova explosion. This compact object may also increase its mass in a close binary system and collapse (most likely without an explosion) into a black hole (BH). Most massive stars form black holes. It is still unknown whether this process is accompanied by a supernova explosion

Supernovae are subdivided into two types according to the nature of their spectra. Those with bright hydrogen lines are labeled type-II supernovae and those with a deficit of hydrogen, type I. As a rule, type-I supernovae are brighter. They are in turn subdivided into subtypes Ia and Ib: the spectra of the former exhibit clear absorption lines of silicon, while the spectra of the latter exhibit those of helium. Most likely, type-Ia supernovae emerge in the catastrophic thermonuclear explosion of a carbon-oxygen white dwarf. Other supernova types are associated with the gravitational collapse of the cores of supermassive stars.

In cosmological investigations, advantage is taken of type-Ia supernovae, because they are thought to be suited to cosmological observations better than other supernovae. First, type-Ia supernovae are very bright (their stellar brightness is -19) and rank below only the biggest galaxies (-22) and quasars (-25) in this respect. Second, their own luminosity at maximum light may be reconstructed from the slope of its observed light curve (i.e. the temporal dependence of stellar brightness). Third, there are grounds to believe that the bursts occurring at different cosmological times should not be much different (i.e. the cosmological evolution of the population of these objects should not be highly significant). Lastly, supernovae of this type have been theoretically studied rather well. This all permits observers to employ type-Ia supernovae as bright radiation standards in deep space.

In supernovae, owing to their high temperature $T \approx 30\,\text{MeV}$, there exists an ultrarelativistic ($kT \gg mc^2$) plasma of massless particles. For $T \approx 10\,\text{MeV}$, the energy density of this plasma is $\approx 4 \times 10^{23}\,\text{J/cm}^3$; photons account for one third of this energy density; the plasma frequency $\omega_{\text{pl}} \approx 1.5 \times 10^{21}\,\text{Hz}$ and the Debye radius $\lambda_D \approx 10^{-11}\,\text{cm}$.

9.2.4 Collapse of Supermassive Stars ($M > 30$–$40\,M_\odot$)

It is not unlikely that supermassive stars ($M > 30$–$40 M_\odot$) collapse to form black holes with a mass of about $10 M_\odot$. So far, reliable models of this process have not been introduced, although the data of astronomical observations about the existence of black holes of stellar masses appear to be rather convincing.

Ejected into the ambient after supernova explosions is the substance which underwent transformations in the thermonuclear reactors of stellar interior [104] and was efficiently enriched in elements heavier than helium. The substance ejected by supernovae can participate in the formation of next-generation stars or go to form planets. It is hard to imagine life without carbon and oxygen. It may be suggested that life would not have appeared in the Universe if there were no supernovae [104].

As we shall see below, neutron stars may not have a mass greater than 2–$3\,M_\odot$. An analysis suggests [104] that in stars whose mass at origin exceeds $40\,M_\odot$ there forms an iron core of mass greater than $3\,M_\odot$. The collapse of such cores should give rise to black holes rather than neutron stars. It is believed [104] that intense gamma-ray bursts lasting more than 2 s (the so-called long bursts), which are observed by orbital observatories approximately once a day, emerge in the collapse of the cores of rapidly rotating massive stars with their transformation to black holes. In this case, around the newborn star a part of the substance of collapsing core forms a massive accretion disk, which is absorbed by the hole within several seconds. The further disk substance accretion onto the hole is attended with the ejection of two gas jets with relativistic velocities in the directions perpendicular to the disk plane (see Sect. 10.1). This all takes place under the stellar shell which has not managed to respond to core rearrangement. The powerful jets break through the stellar shell and generate bursts of gamma-ray radiation directed along the disk axis. Simultaneously generated in the disk plane is a shock wave, which travels outwards and sheds the stellar shell. We take this for a supernova outburst, which is sometimes referred to as a hypenova, because in this case the energy radiated in the explosion is greater by an order of magnitude than for "ordinary" supernovae. According to [104], the burst GRB080319B corresponded to the total radiation of 10 millions of galaxies like our own. According to experts' estimates, by this firework the Nature marked the death of a star of mass of about $50\,M_\odot$.

Depending on the stellar mass (dimension), in stars there operate different mechanisms of energy transfer (Fig. 9.44) from the thermonuclear burn domain in the compressed plasma of the central region to the stellar periphery with subsequent energy radiation into open space [7].

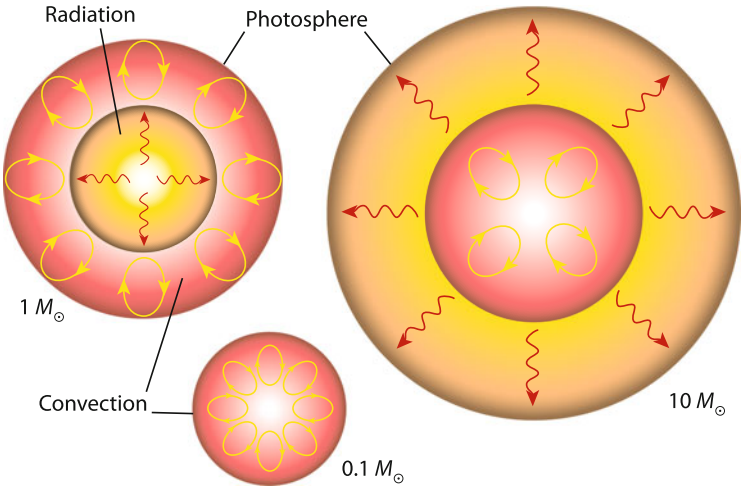

Fig. 9.44 Mechanisms of energy transfer in main-sequence stars [7]

In stars sufficiently large in size the energy released in thermonuclear reactions is transferred by radiation. In the solar core the energy is transferred by radiation and in a rather opaque shell the energy is transferred by convection. However, when many plasma particles capable of absorbing a photon occur in its path, the photon will be absorbed on traversing some distance, thereby transferring energy from one part of the star to another. This process termed radiative heat transfer is one of the main mechanisms of transferring heat from central stellar regions to the outer layers.

The substance inside stars is, as a rule, quite opaque. The photon mean free path in the solar interior is equal to 1 mm. In the solar core a photon traverses on average only about 0.1 mm from the instant of its production to its end. The absorbed photon is almost immediately superseded with a new one, and this continues until the distant descendants of the first photon produced in a nuclear reaction reach the stellar edge. Only there, in the stellar atmosphere, where the density is low and the gas is almost transparent, the photons escape from the star and carry away the energy produced in nuclear reactions.

The distribution of plasma parameters in the Sun is given in Fig. 9.45.

Substantially lower-mass stars (red dwarfs, $0.1\,M_\odot$) are entirely convective. In stars much more massive than the Sun, in the hot and rather transparent shell the energy is transferred by radiation, but in the core the radiation does not cope with this task and convection develops there.

To conclude this discussion, we give Table 9.4, from [7], which summarizes the schemes of single-star evolution.

There is much in common between the processes in the stars and thermonuclear weapon (see Chap. 4): a similar type of fuel, similar thermonuclear fusion reactions, the decisive role of radiative heat transfer, etc. But there also is a tremendous difference: a thermonuclear explosion lasts for tens of nanoseconds, while the stars

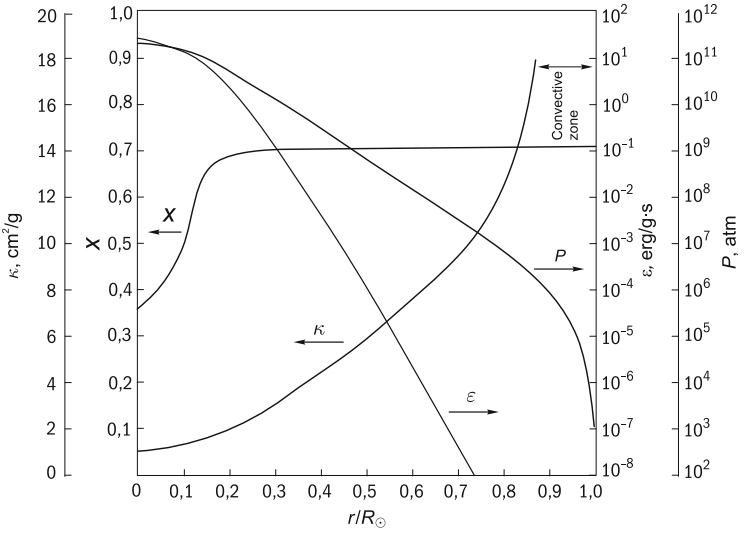

Fig. 9.45 Distribution of solar plasma parameters [104]: X—hydrogen mass fraction; P—pressure; κ—opacity coefficient; ε—specific (per unit mass) energy production rate

shine for billions of years. The reason lies with the stability of the processes due to the enormous difference in scale and the role of gravitation.

Following [104] we assume that the central temperature becomes slightly higher than the equilibrium one due to random fluctuations. And so the rate of nuclear reactions will increase with the consequential rise in heat liberation intensity. As a result, the gas will heat up even higher, the rate of nuclear reactions has to rise, and so on. An avalanche-like burn of hydrogen must therefore occur with the liberation of a huge amount energy, which might result in stellar explosion, as is the case in the explosion of a hydrogen bomb, but not inside of the star, and here is why.

An increase in temperature of the stellar interior rises the gas temperature, which disrupts the hydrostatic stellar equilibrium. The gas expands and in doing so does work against the force of gravity. The internal energy of the gas is expended for this, and therefore its temperature becomes lower. What matters is the process kinetics, what occurs faster: the increase in nuclear reaction rates which leads to an explosion, or the star manages to cool down by way of expansion and reach a new stable state. Therefore, a star, if it is able to promptly react to variations in thermonuclear reaction rates, will be a self-regulated thermonuclear reactor.

The response time of a star is determined by the characteristic time of its hydrodynamic expansion and compression. If mechanical equilibrium is maintained in the star, this time coincides with the characteristic time of stellar compression under the force of gravity (the free-fall time). This time depends only on the average stellar density and is equal to about an hour for solar type stars.

Table 9.4 Evolution of a single star [7]

	Intermediate mass ($0.5–8M_\odot$)		High mass ($8–100M_\odot$)	
Low mass ($0.08–0.5M_\odot$)	$0.5–3M_\odot$	$3–8M_\odot$	$8–10M_\odot$	$> 10M_\odot$
Burning of hydrogen in the core				
Helium white dwarf	Burning of hydrogen in the core			
	Degenerate helium core	*Nondegenerate helium core*		
	Helium flare			
	Quiet burning of helium in the core			
	Burning of hydrogen and helium in layer sources			
	Planetary nebula		*Degenerate carbon-oxygen core*	*Nondegenerate carbon-oxygen core*
	Carbon-oxygen white dwarf		Carbon detonation	
			Burning of carbon and subsequent elements (O, Ne, Si, Fe, Ni . . .) in the core.	
			Burning of carbon and subsequent elements (O, Ne, Si, Fe, Ni . . .) in layer sources	
			Planetary nebula	*Type-II supernova explosion*
			O, Ne, Mg. . . *white dwarf or neutron star*	*Black hole*

Now we will estimate the characteristic time of nuclear reactions. Let us have a glance at the main pp-chain reactions (Fig. 4.6):

$$\mathrm{p} + \mathrm{p} \rightarrow {}^{2}\mathrm{H} + \mathrm{e}^{+} + \nu \text{ tens of billions of years},$$

$${}^{2}\mathrm{H} + \mathrm{p} \rightarrow {}^{3}\mathrm{He} + \gamma \text{ several seconds},$$

$${}^{3}\mathrm{He} + {}^{3}\mathrm{He} \rightarrow {}^{4}\mathrm{He} + 2\mathrm{p} \text{ several million years}.$$

Give here are the characteristic time intervals during which hydrogen, deuterium, and helium nuclei search for a reaction partner under the conditions typical for the solar core. The first reaction in this chain goes much slower than the remaining ones, because it requires a proton-to-neutron transformation controlled by the weak interaction. This goes 10^{18} times slower than the fusion of deuterium with the next proton, which is controlled by the strong interaction. However, since the transmission capacity of any line is determined by its bottleneck, it is precisely the tens-of-billions-of-years that are the characteristic time of nuclear fusion rearrangement in the solar interior. As we see, this is overwhelmingly longer than the time of mechanical stellar response [104].

The self-control of a star is possible, because its expansion and cooling occurs in a time much shorter than the characteristic time of temperature growth in the course of hydrogen burn. In the explosion of a hydrogen bomb the self-control of this kind in nonexistent: its fuel burns up much faster than the increased pressure manages to scatter it. To achieve this, the bomb designers had to employ special, "fast-burning" hydrogen isotopes—deuterium and tritium, whose thermonuclear reactions go without participation of the slow-operating weak interaction [104].

So, for the burn of stellar nuclear fuel to be stable, an increase in temperature must lead to an increase in gas pressure. But the degenerate gas pressure is hardly dependent on the temperature, and so the way of self-adjustment described above does not work when thermonuclear reactions go in a strongly degenerate gas, and a thermonuclear explosion must occur at the stellar center. However, in stars of mass below $0.5\,M_{\odot}$ the degeneracy is so strong that compression terminates before the temperature rises significantly, and therefore helium does not ignite at all. In stars of mass greater than $2.3\,M_{\odot}$ the ignition of helium occurs in a nondegenerate gas. But in stars of mass ranging from 0.5 to $2.3\,M_{\odot}$ the burning of helium commences precisely at a strong degeneracy of electron gas. As a result, in the twinkling of an eye the core luminosity rises to a value $\sim 10^{10} L_{\odot}$, which is close to the total luminosity of all stars of our Galaxy—this effect is termed a helium flare. So monstrous an energy release lasts for only a few seconds: when the temperature rises by about 30 % the gas becomes nondegenerate and the self-control mechanism immediately springs into operation to transfer the nuclear reactions to the mode of stationary "burning".

During the flare, only about 1 % of helium manages to burn, the stellar luminosity remaining almost invariable in this case: virtually all thermal energy of the thermonuclear explosion is expended to do work against the force of gravity in the

core expansion. This episode in the stellar life may be called an internal explosion. It passes almost unnoticeably for observers, but this is an important stage of stellar evolution.

What is the greatest mass of stellar objects? From the observations of components of binary systems it has been possible to determine the existence of stars in the mass range from 0.05–0.1 $M_\odot$ to 80–90 $M_\odot$ [102]. With increase in stellar mass the stellar temperature rises steeply, as does the radiation pressure on the outer layers. This results in the excitation of radial oscillations, loss of stability, and shedding of the stellar shell. This mechanism imposed a mass limit (the Ledoux-Schwarzschild-Harm limit) at a level of 60 $M_\odot$. For a more detailed consideration of the scattering of oscillation energy in shock waves and several other dissipative effects the stellar mass limit rose to 100 $M_\odot$. The majority of stars satisfy this criterion, although there are likely to exist objects of greater mass: the hot supergiant η Car in the nebula NGC 3372 with a luminosity of $5 \cdot 10^6$ solar luminosities must have a mass of about 200 $M_\odot$, while the intense supernova SN 1961v in the galaxy NGC 1058 supposedly has a mass of the order of 2000 $M_\odot$ [102].

The R136a1 superstar is only 160,000 light years away from the Earth and has a mass of 260 $M_\odot$ (320 $M_\odot$ at birth). It ejects substance intensively and has reduces its mass by 17 % over a million year period.

After [104], the cause of death of stars with an initial mass of around 100 $M_\odot$ is the transformation of the highest-energy photons to electrons and positrons ($\gamma \rightarrow e^+ + e^-$) rather than the photodissociation of iron nuclei. A γ-ray photon may decay only in the vicinity of an atomic nucleus, to which is transferred a fraction of the momentum and kinetic energy of the photon. This process plays a significant part when the temperature $T > 10^9$ K, but the efficiency of electron-positron pair production lowers at high densities, with the onset of electron gas degeneracy. To produce a pair in a nondegenerate gas it would suffice to have a photon energy only slightly higher than $2m_e c^2$, but this is insufficient in a degenerate gas: all lower energy levels are already occupied, and the new born electron must therefore have a sufficiently high kinetic energy. Here the considerations are the same as in matter neutronization.

When the temperature in the central regions of the most massive stars is as high as 10^9 K, the electron gas is not yet degenerate, and therefore the electron-positron pair production plays an important role in precisely suchlike stars. Thermal energy is expended on pair production, and so, like in the case of iron photodissociation, the gas elasticity becomes lower and the gas pressure ceases to compensate the force of gravity. The central stellar regions begin to contract rapidly and their temperature rises steeply. By the instant of stability loss, hydrogen in the central stellar regions has been converted to helium and helium in its turn initially to carbon and then to oxygen. The sharp increase in temperature "ignites" oxygen and there occurs a thermonuclear explosion, which destroys the star completely and scatters its substance in the ambient without survival of its dense core.

However, the picture of supermassive star destruction may turn out to be more complicated. Considered in recently published papers is the possibility that at first the thermonuclear explosion at the stellar center does not completely destroy the star

but merely sheds a small part of its shell—about 10 % of the total stellar mass. After this the hydrostatic stellar equilibrium is regained, but in about a thousand years it is disrupted once again, there occurs a new explosion, and this may be repeated several times until the star is completely destroyed.

The reason why the number of massive star observations is small may lie with the fact that such stars are infrequently born and their lifetime is short. There simply are no such stars in the Galaxy in our time. However, it is not improbable that stars with $M > 150\,M_\odot$ are not formed at all: as the mass of a protostar increases, its luminosity rises so high that the radiation pressure terminates the accretion of shell's substance onto the stellar nucleus after it reaches some maximal mass value [104]. The accretion may be suppressed not only by light pressure, but also by the wind coming from the surface of accretion disk; according to observations, its intensity increases progressively with the protostar's mass.

9.2.5 Brown and White Dwarfs

The lower stellar-mass bounds are quite diffuse, because small stars are hard to observe owing to their weak glow: a red dwarf of mass $0.06\,M_\odot$ has a temperature of only 2000 K. Examples of light stellar objects are provided by the binary system Ross 614 with components of mass 0.059 and 0.051 $M_\odot$, and the system LHS 1047 with the lowest-mass component with a weight of only $0.055\,M_\odot$ [102]. Calculations suggest that in stars with a mass below 0.07–0.1 $M_\odot$ the temperature is low and insufficient for thermonuclear burning, and gravitational compression is their energy source. The term "star" is scarcely applicable to low-mass objects without a thermonuclear energy source. Adjacent to this limit are objects of mass 0.02–0.04 $M_\odot$, referred to as "brown" dwarfs, which is indicative of their infrared radiation. By indirect techniques, astronomers have succeeded in detecting even lower-mass objects such as satellites of mass $0.009\,M_\odot$ in the system BD 68°946, which are transition objects intermediate in mass between stars and planets [102].

Inside of themselves brown dwarfs are a completely ionized hydrogen-helium plasma [11]. The degeneracy parameter $\psi = kT/kT_\mathrm{F}$, where T_F is the Fermi temperature, ranges from 2 to 0.05 for very-low-mass stars and brown dwarfs, and therefore the thermodynamic properties of the partially degenerate electron gas are to be taken into account when describing the internal state. Figure 9.46 serves to illustrate the central characteristics of low-mass stars and substellar objects in the mass range from Jupiter to the Sun [11]. Below $\sim 0.35\,M_\odot$, the stellar interior becomes completely convective and, since the gas still remains in the classic mode ($\psi \geq 1$), the mass increases in proportion to the stellar radius R and the central density ρ_c decreases with increasing mass as M^{-2}. Below the limit of hydrogen burn, electron degeneracy begins to dominate, and therefore $M \sim R^{-3}$ and the density increases with mass again. The mass dependence of the radius $R \sim M^{-1/3}$, like for white dwarfs, takes place under complete degeneracy; however, for a partial degeneracy the dependence is more gently sloping—the radius of a brown dwarf

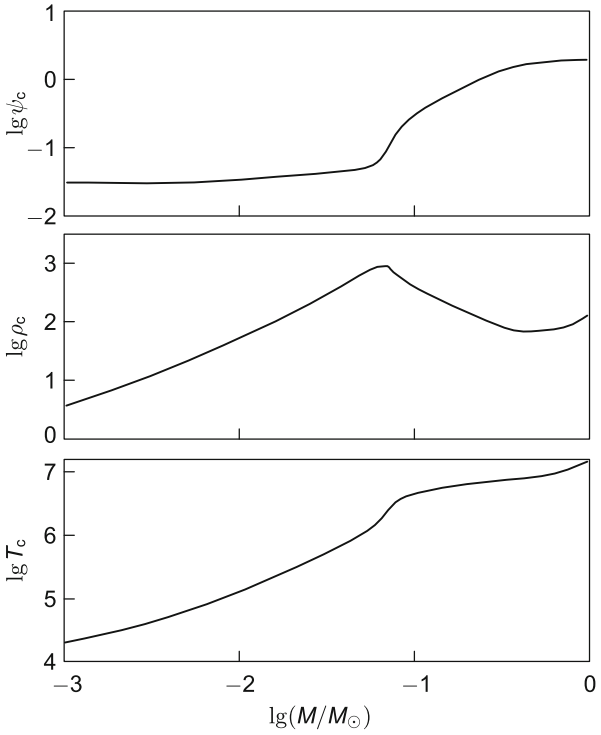

Fig. 9.46 Degeneracy parameter ψ, central density ρ_c and the central temperature T_c for low-mass stars and brown dwarfs with the solar content of heavy elements and a 5 billion year age [6]

depends only slightly on the mass. For a solar age and metallicity the radius of a brown dwarf is like that of Jupiter ($0.1R_\odot$).

The temporal variation of the temperature at the center of a low-mass object is depicted in Fig. 9.47.

Constructing the model of a brown dwarf atmosphere is an intricate task, because it is required to calculate molecular absorption (millions of spectral lines), take into account the presence of condensates, etc. Also, an important point is that the luminosity of brown dwarfs is only 10^{-2}–10^{-5} of the solar luminosity. This seriously complicates the quest of these low-luminous objects [6].

Therefore, in nature there exist and constantly come into being stellar objects in the $\sim$(100–0.05) $M_\odot$ mass range admissible by contemporary physical models, although a small number of objects lying outside of this range are also observed.

We have ascertained that the lifetime of a star is determined by its mass [87]. The greater the mass, the higher the temperature, density, and pressure inside and the higher the efficiency of the nuclear burn of the main fuel—hydrogen. So, large stars live for a shorter time, but shine brighter (Table 9.5).

One can see that small stars, which use energy economically, live much longer. Were our Sun only 1.5 times more massive, it would have ceased to exist long ago and the human mind would not have had time to come into existence.

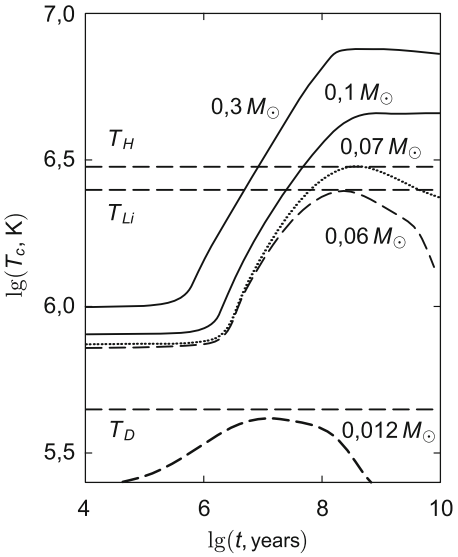

Fig. 9.47 Central temperature T_c as a function of age for different masses. T_{H}, T_{Li} and T_{D} denote the hydrogen, lithium and deuterium burn temperatures [11]

Table 9.5 Dependence of the stellar lifetime on the stellar mass [87]

Stellar mass ($M_\odot$)	Lifetime (years)
50	3–5 million
10	30 million
1.5	3 billion
1.0	10 billion
0.1	1 trillion

The chemical composition of stars and the interstellar medium is of paramount importance to the physics of these objects. In particular, the oxygen-group elements (C, N, O) are catalysts of nuclear reactions and the iron-group elements determine the optical thickness and luminosity of stars. The commonly accepted atomic composition of the interstellar medium and the Sun is as follows: for every 1000 hydrogen atoms there are 100 helium atoms and two or three atoms of heavier elements. In this case, half of the atoms of the interstellar medium are combined in molecules and many atoms of heavy elements are in dust particles or molecules. Of course, these are only approximate values of the composition. In a number of stars, the content of heavy components may be 3–4 orders of magnitude below the value specified above [102].

White dwarfs [57], whose accretion may lead to type-Ia supernovae, are quite interesting astrophysical objects from the standpoint of realization of extreme states. In the evolution of stars of mass 8–10 $M_\odot$, thermonuclear burning terminates at the stage of a helium or carbon-oxygen degenerate core. This thermonuclear burning in the degenerate core is inherently explosive, and the increased temperature may partly remove the degeneracy and moderate energy liberation. That is why the outer shell of a red giant may come off: a thermal instability may develop at the interface

between the layer source and the degenerate core, with the subsequent formation of a planetary nebula. Interestingly, positive ions here form a crystal lattice [115]—a kind of a phase transition in a nonideal plasma [8, 20, 23, 24, 26, 31, 33, 68, 79, 88, 92, 94, 96].

A different kind of stellar activity will emerge [115] when a white dwarf is part of a binary system, in which matter flows from the neighboring star to the white dwarf under the action of gravitational forces, thereby increasing its mass. As the Chandrasekhar limit [115] is approached, thermonuclear burning that is explosive in character (type-Ia supernova model) develops at the center of the white dwarf. A highly important problem arises in the development of models of this explosion: a deflagration burn wave mode is realized early in the explosion. Eventually it passes to the detonation mode of C-O burning with a transition to the iron-group elements with prevalence of the famous ^{56}Ni nucleus, which furnishes, in its radioactive decay to ^{56}Co and then to ^{56}Fe, the entire energetics of the light curve of a type-Ia supernova [47]. However, as in the case of O–Ne–Mg white dwarfs, this does not necessarily occur, because the neutronization of matter may commence prior to the thermonuclear burning, and a collapse to a neutron star may then occur.

The presence of white dwarfs in binary stellar systems manifests itself in a broad class of variable stars, which are referred to as explosive variables [115]. Their main distinguishing feature consists in the occurrence of periodic or irregular flares of different amplitude, and the typical dimension of such a systems falls within the range between a fraction of the solar radius to several solar radii.

Stars in which the explosions are relatively small and take place in near-surface layers are termed nova-like stars. Also known are stars with higher-power flares, when explosions involve deeper layers of the stellar interior (several percent of the radius) as well. These stars are referred to as novae. Lastly, when the explosion encompasses a substantial part of a star, we are dealing with a so-called supernova.

The energy parameters of explosions also vary greatly. For the "weakest" astronomical explosions—solar flares—the time scale is about 10^3 s and about 10^{32} erg is released in this case. For novae, $t \approx 10^8$ s and the corresponding energy $E \approx 10^{45}$ erg. For supernovae, $t \approx 10^{10}$ s and $E \approx 10^{50}$ erg. In galactic nuclei, it is likely that $t \approx 10^{15}$ s and $E \approx 10^{65}$ erg, etc.

The physical reasons for the flares in different kinds of explosive variables are different. Single high-power flares, which are typical for nova stars, are caused by the thermonuclear explosion of the matter accumulated on the surface of a white dwarf in the accretion from the neighboring main-sequence star or from a subgiant of approximately solar mass that had undergone a minor evolution. Calculations suggest that single flares are possible only in a specific range of masses of white dwarfs and of rates of matter accretion on their surface. For very low flow rates, the matter gradually degenerates and joins the white dwarf. For very high rates, the matter remains nondegenerate and the burning may proceed in a slack quasi-stationary mode. For the new star to be stable, degeneracy should take place in the matter incident on the surface and the temperature growth should not be accompanied by a pressure increase and a shell expansion, resulting in a thermonuclear explosion. Since the gravitational energy of the matter under these

conditions is almost a hundred times lower than the caloricity of thermonuclear energy liberation, under an explosive thermonuclear burn the particles acquire a far greater velocity than the "escape velocity" on the surface of the white dwarf, and the exploded shell disperses in the interstellar medium.

The kinetics of white-dwarf evolution involves comprehensive data about the equation of state of the plasma, about its optical and transport properties, and is employed for the temporal analysis of the corresponding galactic domains. Unfortunately, only the outer regions of these objects are presently accessible to our experimental observations.

At the same time, modern computer codes make it possible to carry out conceptual numerical modeling of supernova explosions [19]. Figure 9.48 [19, 53] shows the data of the two-dimensional simulation of a type-II supernova explosion, which clearly shows the development of hydrodynamic instabilities in the course of plasma expansion.

In several scenarios of stellar evolution (a supernova, a nova), thermonuclear burning emerges in the inner degenerate plasma domains and is then transferred to the outer regions by way of convection. In this case, there develop convective instabilities, resulting in the explosion of the object [65]. Similar convective processes, though without local thermonuclear energy liberation, are thought to take place in the outer regions of white dwarfs as well.

Unfortunately, convective effects in degenerate plasmas have not been adequately studied [71], which invites appropriate laboratory experiments.

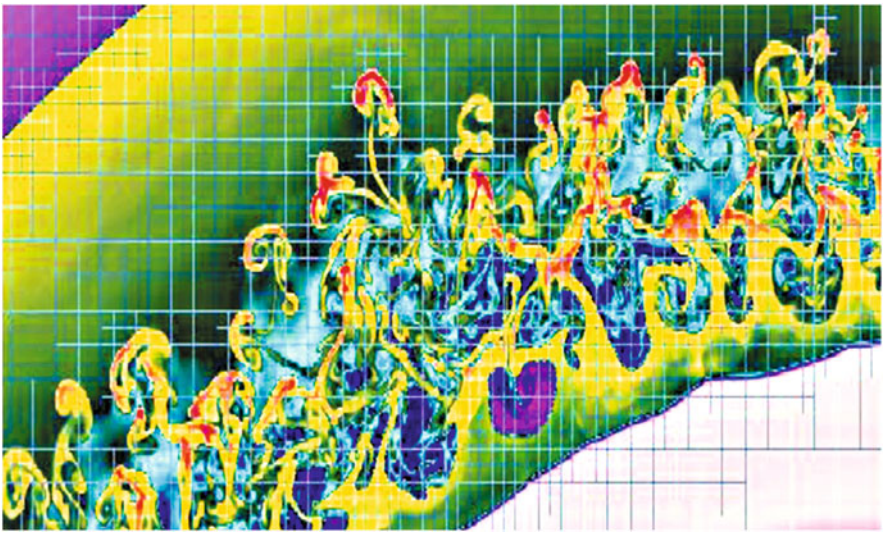

Fig. 9.48 Two-dimensional numerical simulation of the SN1987A supernova explosion [19, 53]

The available high-pressure techniques—diamond anvils, intense shock waves driven by light-gas guns, electrodynamic facilities, chemical and nuclear explosives, lasers, and high-current pinches—enable (see Chap. 3) studies of the equations of state and the optical and transport properties of strongly compressed plasmas up to a record high pressure of 4 Gbar [4, 5, 106, 110], as well as pressures up to 10 Gbar to be attained inside laser microtargets, so far without quantitative measurements of the plasma properties. In several cases [30, 33, 56, 73] it is possible to effect quasi-adiabatic compression and strongly suppress the effects of material heating.

It is hoped that the future NIF and LMJ facilities will radically broaden the attainable parameter range and enable conditions to be reached that are typical for terrestrial group planets, exoplanets, giant planets, brown dwarfs, and intermediate-mass stars, as well as for the outer layers of white dwarfs.

9.3 Superextreme States in the Cosmos

Depending on the initial mass of a star of solar chemical composition, three types of compact remnants may emerge in the stellar interior upon completion of thermonuclear evolution: white dwarfs, neutron stars, and black holes [54, 115].

As we saw above, massive stars end their life with a tremendous explosion; after this, of a giant which was many times greater than the Sun there remains a neutron star—a small (the size of a small asteroid), extremely dense (denser than an atomic nucleus) rapidly rotating ball with a high magnetic field. The enormous force of gravity at the surface of the neutron star prevents its destruction even when it rotates like some radio pulsars, at a frequency of about 1000 rotations per second (in this case, the surface velocity amounts to about 20 % of the velocity of light) [104].

9.3.1 Neutron and Quark Stars

Physicists consider a neutron star as one of the most interesting astronomical objects in view of the set of its amazing properties. Despite its high temperature, its substance is superfluid and superconductive: the conditions required for these "supereffects" arise because of the enormous density in the interior of the neutron star. Of keen interest from the standpoint of plasma physics is the atmosphere of such a star, where charged particles interact with a superhigh magnetic field (up to 10^{14} Gs and even higher), which will never be obtained in terrestrial laboratories.

Furthermore, neutron stars are the most important objects for verifying the Einstein gravitation theory—the general theory of relativity. Its difference from the Newtonian theory manifests itself clearly under strong gravitational fields, which are inherent in precisely the neutron stars. Moreover, those of them that manifest themselves as radio pulsars may serve as magnificent clocks, which permit revealing

subtle relativistic effects in stellar motion and in the course of time. We will revert to this later on.

More than 2000 neutron stars have been discovered in our Galaxy and several tens of them outside its confines. Most of them are radio pulsars, while the remaining ones are X-ray or gamma-ray sources. Astronomers believe that there are at least 100 million of old neutron stars, which are hard to discover, because their surface has cooled down and the rotation has slowed down. The falling gas is accelerated to nearly 100,000 km/s by the attraction of a neutron star and, striking against the surface, heats up to millions of degrees. Astronomers record the X-ray radiation emerging in this case with the use of cosmic observatories.

In Sect. 8.1, the structure, dynamics, and other characteristics of neutron stars were minutely considered from the standpoint of realization therein of the states of matter with a high energy density. Here we continue this consideration.

Neutron stars are perhaps the most exotic astronomical objects, in which a broad spectrum of superextreme states of matter occur [40, 114] that are virtually unattainable for laboratory research. That is why neutron stars in a sense fulfill the function of a "cosmic laboratory", as their observable manifestations permit one to judge the behavior of matter under superextreme conditions: at supernuclear densities, in superstrong magnetic fields, with regard to the superfluidity of the baryonic component and intensive nuclear transformations of ultracompressed matter. It is reasonable that the observable manifestations of these processes are also highly diversified: these are radio and X-ray pulsars, X-ray flare sources, γ-sources, X-ray transients, etc. [95, 114, 115].

Neutron stars are the smallest observable stars in the galaxy [46]. Their radii R are of the order of 10 km, which is 10^{-5} times the size of an ordinary star. However, the neutron star masses M are of the order of the solar mass $M_\odot$ and group about the value $1.4M_\odot$. The average matter density $\overline{\rho} = 3M/4nR^3 = 7 \times 10^{14}\,\mathrm{g/cm^3}$ of neutron stars is several times higher than the conventional nuclear density $\rho_0 = 2.8 \times 10^{14}\,\mathrm{g/cm^3}$. For convenience a neutron star may therefore be seen as a huge atomic nucleus 10 km in size. At the center of the star, the density may exceed the nuclear density by a factor of 10–20. At these densities, the condensation of pions, hyperons, and kaons is possible at the center of a neutron star. The possibility that strange quarks are produced is also under discussion.

The superfluidity of the baryon constituent of the matter of neutron stars is one of their most interesting features. According to modern models, the superfluidity is caused by the Cooper pairing of baryons with opposite momenta under the action of the attractive component of strong interaction of the particles. The superfluidity appears when T is below the critical temperature T_c and gives rise to a gap Δ in the baryon dispersion relation near the Fermi level.

Predicted [113] for the inner crust of a neutron star was the superfluidity of free neutrons as well as of nucleons in atomic nuclei. Neutrons, protons, and other particles may be superfluidic in the core of neutron star. The superfluidity of charged particles, for instance protons, signifies superconductivity.

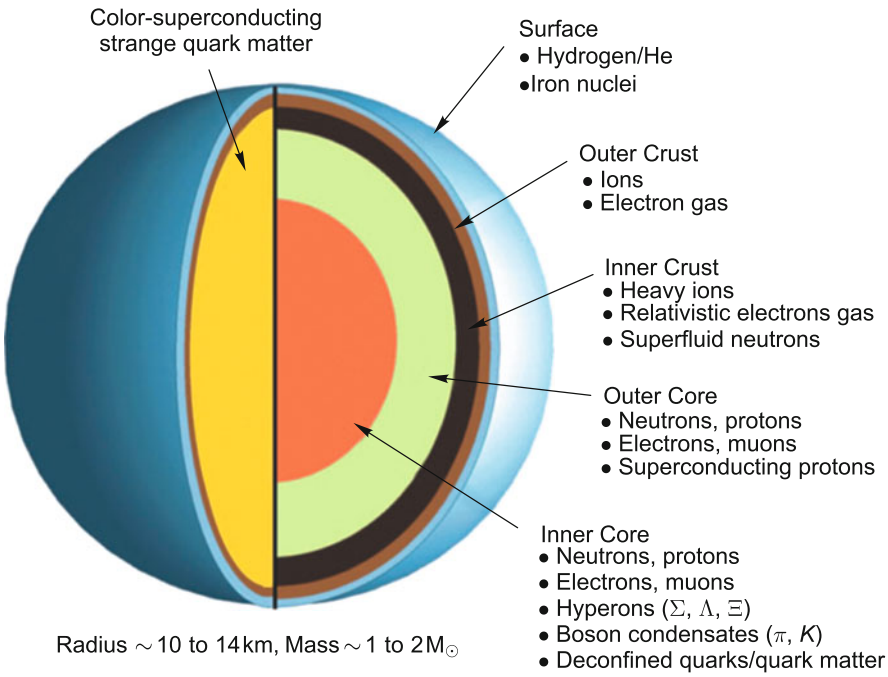

Fig. 9.49 Structure of a hybrid or strange star based on the theory of nuclear matter. Borrowed from [34]

Possible in hyperonic matter is the pairing of hyperons and in quark matter the pairing of quarks.

In these cases, calculations yield critical temperatures $T_c \lesssim 10^{10}$ K and lower. A new type of quark superfluidity was predicted, which consists in the pairing of different quarks (ud, us, ds). In this case, for a characteristic quark Fermi energy of $\approx$500 MeV one might expect a critical temperature $T_c \approx 50\,\text{MeV} \approx 5 \cdot 10^{11}$ K.

The further compression of neutron stars may result in quark deconfinement (see Sect. 6.5) and quark-gluon plasma production. The structure of such a hypothetical quark star is depicted in Fig. 9.49 [34].

9.3.2 Radio Pulsars

A very important achievement which follows from observations of neutron stars that manifest themselves as radio pulsars is the verification of the general theory of relativity, i.e. the measurement of post-Newtonian corrections to the dynamics of

motion of two neutron stars that make up a close binary. In particular, the shortening of the orbital period arising from the lowering of the binding energy of the stars due to their emission of gravitational waves was measured for the pulsar B1913+16. The parameters of interstellar medium—electron density, magnetic field, parameter nonuniformity—are determined from the delay of the arrival of the radio signal and its polarization. The timing of radio pulsars permits the cosmic background of gravitational waves to be studied.

Finally, studying active neutron stars makes it possible to investigate the electrodynamic processes occurring in superhigh magnetic fields, $B > 10^{12}$ Gs, inherent in neutron stars.

When the magnetic field of a neutron star in a close binary system is extremely high (10^{12}–10^{14} Gs), a special kind of accretion on the neutron star may occur, whereby the matter of the normal star together with the magnetic field frozen in it are incident along the induction lines in the regions of the magnetic poles. In this case, the excess angular momentum is transferred to the star by magnetic field rather than hydrodynamic motion. The velocities of falling on the surface of the neutron star can reach up to several hundred thousand kilometers per second, and small (hundreds of square meters) polar regions of the surface experience tremendous fluxes of matter and energy, which generate a plasma temperature of $\approx 10^9$–10^{10} K. The released energy is radiated in the form of hard photons emanating from two hot "X-ray" spots (Fig. 9.50). The strong magnetic field makes the radiation of these spots anisotropic.

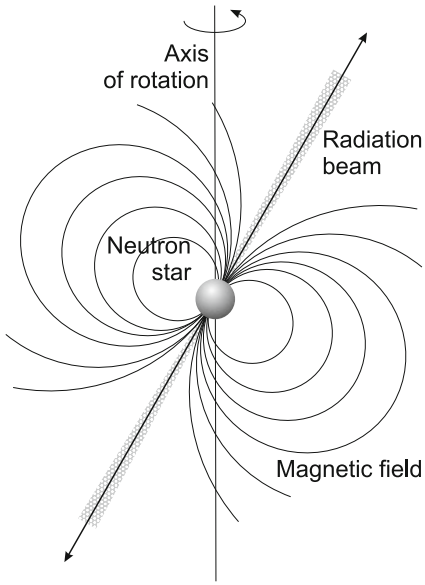

Fig. 9.50 Neutron star with a magnetosphere. Shown are the magnetic lines of force of the neutron star, with the magnetic dipole axis inclined to the axis of stellar rotation. The pulsar radiation in one of the models emanates from two cones (the conic beams in the drawing) coaxial with the magnetic dipole [80]

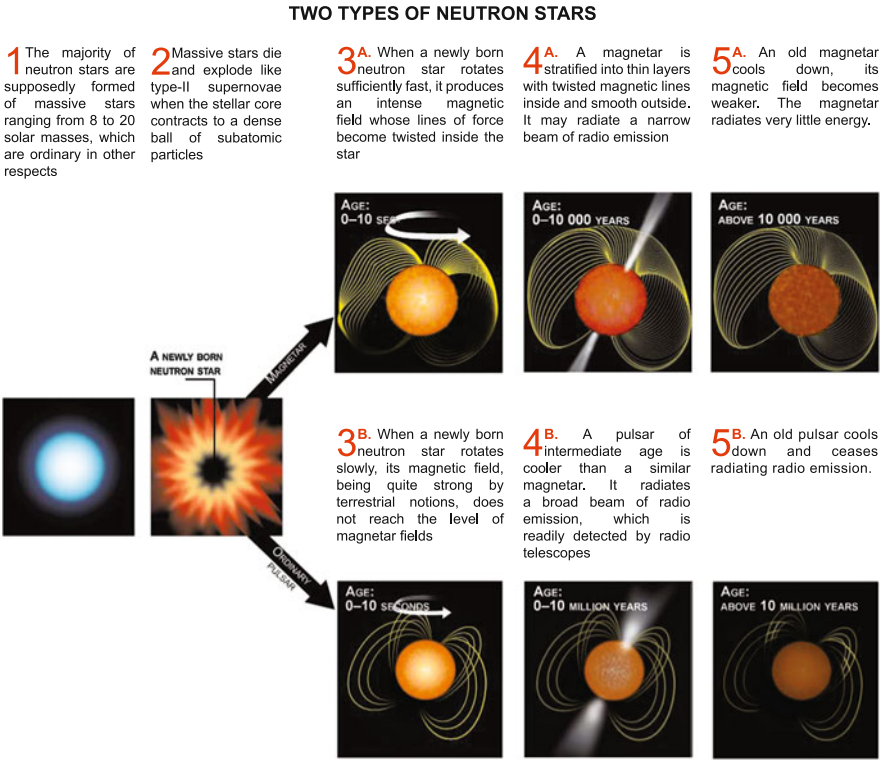

Fig. 9.51 Two types of neutron stars [58]

Since the magnetic axis in the general case does not coincide with the axis of mechanical rotation, an observer will record one or two X-ray radiation pulses during one revolution of the neutron star about its axis. Such sources are referred to as X-ray pulsars [115] (Fig. 9.50). In the case of gamma radiation we talk about γ-ray bursts. When the magnetic field is captured in the course of evolution, the neutron star shows up as a magnetar [58], a star possessing a superhigh magnetic field (Fig. 9.51 [58]).

A magnetic intensity on the order of 10^{18} Gs, where the energy of the magnetic field is comparable to the gravitational energy E_s, is believed to be the limiting magnitude of the magnetic field of a neutron star [46].

Observations suggest [46] that the energy lost by a gyrating neutron star (radio pulsar) goes primarily to form a relativistic particle stream, which is referred to as the pulsar wind. This particle flux amounts to 10^{40} particles per second.

9.3.3 Magnetars

As mentioned above, there are neutron stars which make up a non-numerous (10 % of all neutron stars) class of highly active stars; they produce bright gamma- and X-ray flares, and the magnetic field of some of them is much higher than that of pulsars.

Such stars—magnetars (Fig. 9.52)—rotate relatively slowly with a period $P \approx 5$–10 s, but decelerate much faster than pulsars, $dP/dt \approx 10^{-10}$–10^{-12} s/s. The X-ray radiation flux generated by such a star, $W_x \approx 10^{35}$–10^{36} erg/s, is far greater than the rotation energy lost by the star. The energy stored in its magnetic field is also higher than the stellar rotation energy. This is indication that the source of stellar activity is the magnetic field rather than the stellar rotation, as with radio pulsars. Such stars are therefore referred to as magnetars.

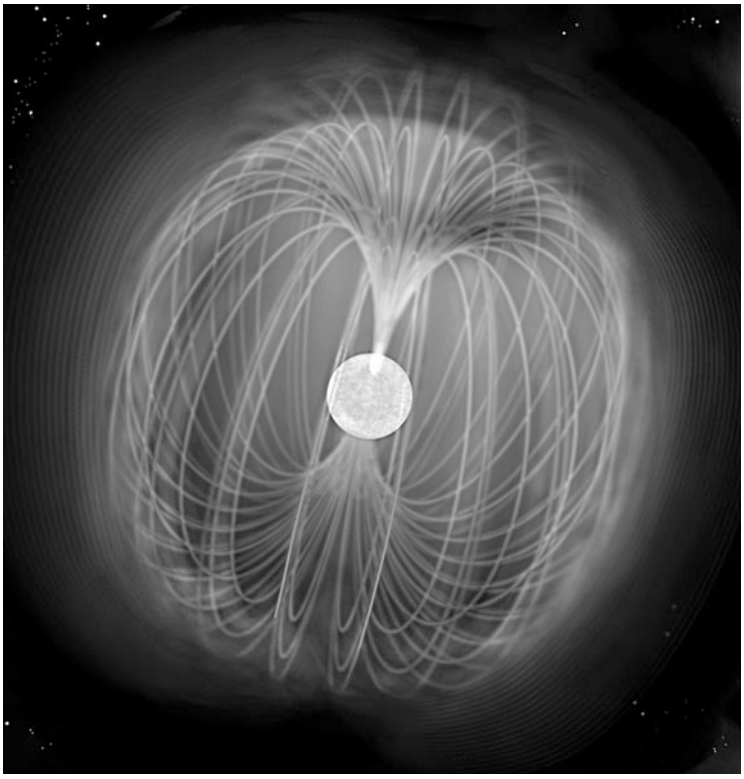

Fig. 9.52 Magnetar is a neutron star whose activity is associated with the liberation of energy stored in its magnetic field. The known candidates for magnetars possess a magnetic field of up to 10^{15} Gs, its energy density corresponding to a substance with a density of tens of tons per cubic centimeter. This field may give rise to new interesting physical effects, which are impossible to investigate in a laboratory [104]

The high magnetic field in the magnetosphere of a neutron star furnishes conditions for plasma production and the formation of wind—the flux of relativistic electrons and positrons emitted by active stars.

Effective particle production begins when the magnetic induction $B_c = m^2c^3/e\hbar = 4.4 \cdot 10^{13}$ Gs, whereby the spacing of the neighboring Landau levels is equal to the electron rest energy, $\hbar\omega_c = mc^2$. Under this field the vacuum becomes unstable relative to the production of electron-positron pairs, which make a significant contribution to the radiation dynamics of these exotic objects.

An important feature inherent in relativistic astrophysical objects is the existence of gigantic magnetic fields, which determine to a large measure the dynamics of their motion and radiative characteristics.

The recorded radiation of a neutron star is primarily soft X-rays; this radiation becomes accessible 10^5–10^6 years after the stellar birth. Recently recorded was a new class of neutron stars—magnetars [64, 75]—which possess an ultraintense magnetic field up to 10^{15} Gs; this field affects their gamma-ray radiation formed together with the thermal radiation of the surface [64, 115].

An example of such an object is provided by the brightest gamma-ray burst recorded in our galaxy to date; its source is the neutron star SGR-1806-20, which belongs to the class of magnetars and is at a distance of ≈50,000 light years from the Earth. The burst lasted for only ≈0.1 s, and the amount of energy released within several seconds after the burst was greater than the energy radiated by our Sun in 250,000 years.

For the SGR 1806-20 magnetar—the highest-power magnet in the universe—the measured magnetic field turned out to be the record breaking $\approx 10^{15}$ Gs, which corresponds to a density of $\approx 10^{13}$ g/cm^3, approaching the density of nuclear matter. For comparison, the induction of the solar magnetic field varies from 1 to 5 Gs, while the terrestrial magnetic field amounts to only 0.31–0.62 Gs. If SGR 1806-20 were in the place of the Moon, its magnetic field would change the arrangement of molecules in all living organisms. However, fortunately there are no such extreme stellar objects in the solar neighborhood (the nearest magnetar is ≈13,000 light years distant). The magnetic field of SGR 1806-20 is several hundred times that of ordinary radio pulsars. In this case, the stellar surface temperature is as high as $\approx 10^6$ K. Due to this superintense magnetic field alone, a piece of iron at the surface of SGR 1806-20 would experience a force 150 million times stronger than terrestrial gravity.

The extremely short duration of the burst testifies [64] to the fact that the source of its energy is the dissipation of magnetic field stored in the magnetosphere and not in the core of the neutron star. The resultant expansion of the "magnetic cloud" with a small fraction of the baryon component (with $M < E/c^2$) is determined by the magnetic field. It is strongly relativistic and anisotropic, and retains these properties for several weeks after the burst.

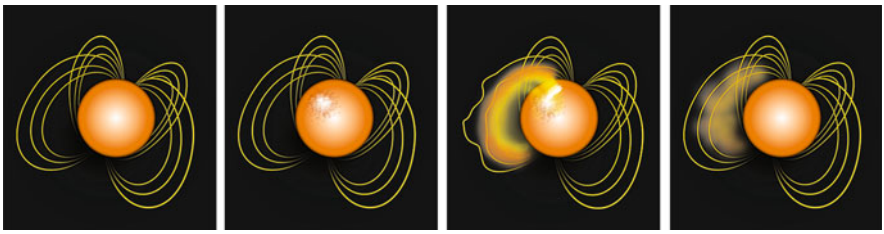

Fig. 9.53 Magnetar burst formation [58]

In magnetars there occur extremely strong magnetic bursts. In this case, the stellar surface cracks under the action of the Lorentz force and protons escape from these cracks, which interact with the magnetic field and radiate energy. The stellar magnetic field is determined from the amount of this energy [64, 75]. Zasov and Surdin [116] came up with the following model of magnetic magnetar bursts.

A magnetar is calm most of the time, but the stress induced by the magnetic field in its solid crust gradually increases (phase 1 in Fig. 9.53). At some point in time, the stress in the crust exceeds its ultimate strength, and the crust breaks into a multitude of small fragments (phase 2). This "starquake" gives rise to a pulsating electric current, which rapidly decays to leave an incandescent plasma ball (phase 3). The plasma ball radiates X-rays from its surface, cools down, and vaporizes within a few seconds (phase 4).

Only 14 magnetars have been discovered to date, although it is assumed that our galaxy should contain at least several million of them.

It is pertinent to note that the existence of magnetars is sometimes associated [44] with the hypothetic possibility of traveling in time and space with a transition to a different domain of the universe via a "wormhole", provided the development of instabilities does not make this process unfeasible.

In the analysis of observational data it is very important to have ideas about the physical properties of the partially ionized dense plasma of the outer layers of a neutron star in the presence of intense ($B \approx 10^{11}$–10^{16} Gs) magnetic fields [40, 95].

It is common knowledge that strong magnetic fields radically change the properties of matter. In particular, for $H \approx 150$ MOe the equation of state becomes four times more rigid. For $B \approx 10^{12}$ Gs, the pressure of the magnetic field at the surface of a neutron star amounts to about 40 Pbar (petabars). For

$$B \gg B_0 = m_e^2 e^3 c/\varepsilon^2 \hbar^3 \approx 2.35 \times 10^9 \text{ Gs}$$

(ε is the permittivity), the cyclotron electron energy,

$$\hbar\omega_e = \hbar\,(eB/m_e c) = 11.58B/10^{12}\,\text{keV},$$

is much higher than the electron–nucleus Coulomb interaction energy. Under the conditions of a neutron star, the Coulomb force is a weak perturbation with respect to the magnetic one, and for typical stellar temperatures the electrons are in the Landau level [36, 40]. Since the motion is limited in the direction perpendicular to the magnetic field, atoms and ions assume a cylindrical shape and have high binding energies [52, 81]. Such ovoid atoms make up thread-like molecular chains with covalent bonds, which in turn may form a three-dimensional condensate. Furthermore, when an atom moves in a constant magnetic field, in its frame of reference, due to the Lorentz transformation, there emerges an electric field, which may ionize the system [52, 81]. Much is still unclear about the structure as well as the electronic and mechanical properties of such an exotic state of strongly magnetized matter [40, 71].

The central element in the understanding of the structure and evolution of stellar objects (especially of the structure of neutron stars), the collapse of stars, supernova explosions, etc. is the equation of state as well as the composition and optical properties of the nonideal plasmas of stellar matter [25, 32, 40, 54]. Their equation of state includes the important condition for nuclear statistical equilibrium, but it is applicable only for extremely high temperatures ($\approx 5 \times 10^{10}$ K). The corresponding equations of state are formulated for an arbitrary collection of atomic nuclei (including unstable ones) with the inclusion of the strong Coulomb nonideality effects of the matter, which is sometimes referred to as a Coulomb liquid [69]. Apart from the great complexities of describing strongly nonideal plasmas, there are additional complications arising from the inclusion of a magnetic field, which hinders the correct description of the relation between the nuclear center-of-mass motion and the electronic structure. Only the first steps have been made along this path. A phase transition of a nondegenerate gas to the state of a macroscopic condensate is predicted to occur at relatively moderate fields and temperatures [26, 32, 33]. With increasing field and falling temperature, the saturation vapor density of this condensate will become lower, lengthening the optical free paths and thereby making it easier for the thermal radiation to escape from the stellar center occupied by the condensate of metallic liquid [71].

Describing the radiation transfer in ionized plasmas with $T > 10^6$ K and magnetic fields $B > 10^{14}$ Gs involves certain difficulties. One of them is related to the ion cyclotron resonance at a proton energy $0.63\,(Z/A)\,B/10^{14}$ keV.

Another problem is related to the polarization of the vacuum and virtual electron–positron pair production at ultrahigh magnetic fields,

$$B > B_{\mathrm{cr}} = m_{\mathrm{e}}^2 c^3 / e\hbar = 4.4 \times 10^{13}\ \mathrm{Gs},$$

which change the dielectric properties of the medium, polarize the proton motion, and thereby change the radiative plasma properties. In these fields, the orbitals of bound electrons are strongly perturbed by the magnetic field: $h\omega_c/E_{\mathrm{c}} > 1$, where $\hbar\omega_{\mathrm{c}}$ is the electron energy at the cyclotron frequency and E_{c} is the Coulomb energy [49].

Poorly studied is the effect of "vacuum resonance", whereby the influence of plasma and vacuum on the linear polarization becomes weaker, giving rise to resonance effects in absorption and scattering [71]. This effect manifests itself at proton energies

$$E_{\mathrm{v}}(\rho) \approx 1.0\,(Y_{\mathrm{e}}\rho)^{1/2}\left(B/10^{14}\right)^{-1} f\,(B)\ \mathrm{keV},$$

where ρ is the density in g/cm^3, $Y_{\mathrm{e}} = Z/A$, and $f(B)$ is a weakly varying function of the field induction B.

Already today, new-generation superhigh-power short-pulse lasers generate fields of $\approx 10^9$ Gs in laser-produced plasmas (see [18, 67] and Chap. 5). The advancement of this line of research may provide new information about the radiation capacity and spectra of astrophysical plasmas in intense magnetic fields.

An ingenious way of studying physical effects in superhigh magnetic fields is discussed in [48]. For an electron–hole plasma (liquid) in semiconductors, the fields lowered by a factor $(\varepsilon m_0/m)^2 \approx 10^4$–$10^3$ (where m_0 is the proton mass and m is the hole mass) compared to an electron-proton plasma will still be "superhigh". The electron–hole plasma is therefore a unique condensed object accessible for laboratory research in superhigh magnetic fields.

9.3.4 Strange Stars

As we saw in Sect. 6.3, the quark–gluon plasma (QGP) is an exotic superdense state of matter. Such a plasma has been recently produced in the laboratory: it consists of quarks, antiquarks, and gluons [37, 41, 74, 86]. The QGP possesses the highest density and may emerge at the center of a neutron star or in the collapse of an ordinary star (Fig. 9.54). In this instance they are referred to as quark stars or hybrid stars and consist of quark–gluon matter at the center and a hadronic shell [93]. In this case, quark stars should be smaller than neutron ones owing to the higher compressibility of the QGP (Fig. 9.55). A candidate for a quark-gluon star or a hybrid star is the star RXJ1856 with a radius of more than 16 km, which was detected by the Newton and Chandra Space Telescopes in the X-ray range.

In this connection we mention the hypothesis [112] that the plasma of almost-free quarks is an absolutely stable state of matter not only at high pressures, but also at zero pressure. If so, possible in lieu of a neutron star are so-called strange stars, which consist almost entirely of quark matter of density $\gtrsim \rho_0$.

The superdense states of matter and, in particular, quark-gluon plasmas may also manifest themselves in *black holes*—the objects predicted by the general relativity, in which the gravitational field is so high that the escape velocity is equal to the velocity of light [12, 107]. However, the idea of "black holes" was first

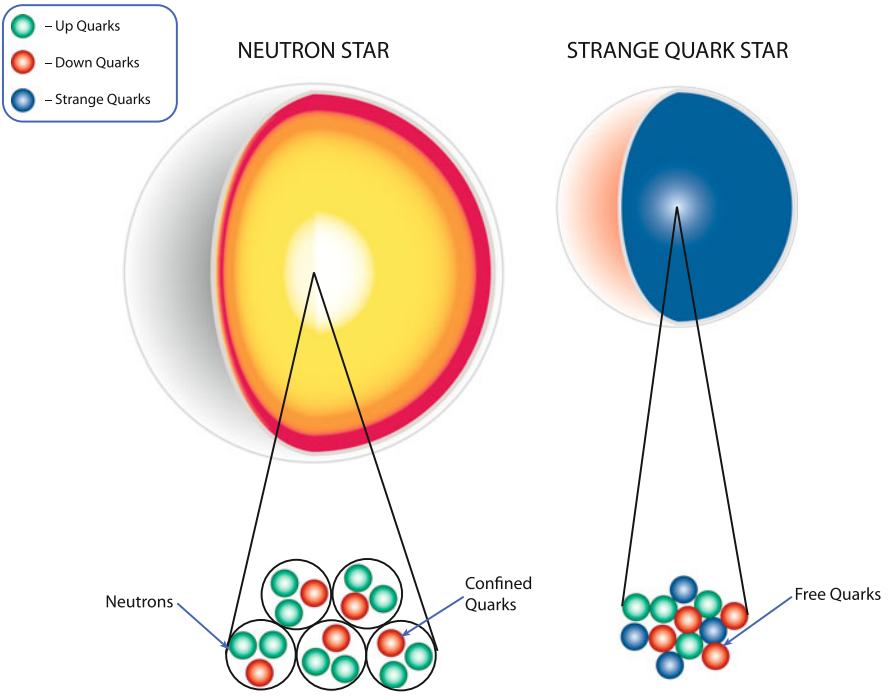

Fig. 9.54 Neutron and quark stars

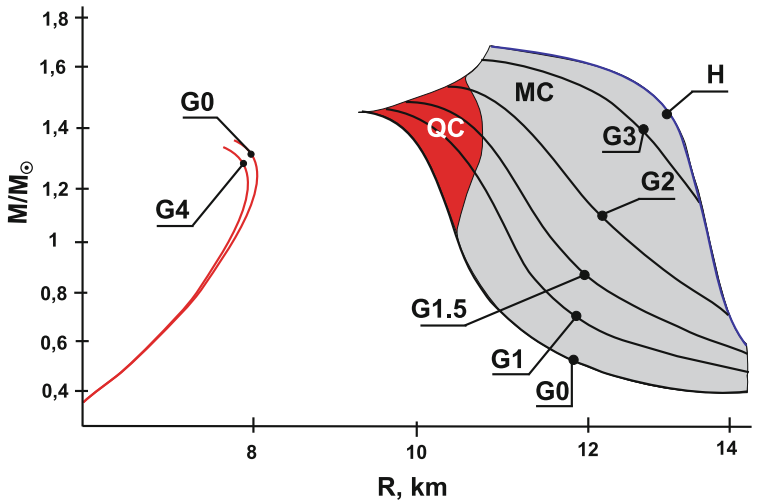

Fig. 9.55 Dimensions of quark and hybrid stars [93]

proposed by the Cambridge lecturer J. Michell supposedly in 1783 and somewhat later by Laplace proceeding from the corpuscular theory of light [44]. A black hole is a domain of space–time surrounded by an event horizon—a surface of size $r_{\rm bh} = 2GM/c^2 \sim 3M/M_\odot$ km—from which no information can escape to become accessible to an external observer. The surface of a black hole acts as a valve of a kind, which transmits matter only in one direction—inside the object—and even light cannot escape from it. This unique property of black holes leads to an interesting fact: to an external observer it appears as a hot body, which is a source of thermal radiation. According to Schwarzschild, any sufficiently heavy nonrotating star, upon exhausting its nuclear fuel, inevitably collapses and turns into a black hole. The critical mass is defined by the condition that the stellar mass exceeds, at the stage of termination of all nuclear reactions in it, three solar masses. A star of mass greater than the critical one begins to contract due to gravitational forces, and no physical interaction can stop this process. This phenomenon is called the gravitational stellar collapse. The condition for the emergence of a black hole necessitates a superdense compression of substance: for the Sun $r_{\rm bh} \approx 3$ km, for the Earth $r_{\rm bh} \approx 1$ cm, for the Moon $r_{\rm bh} \approx 0.12$ mm.

9.3.5 Black Holes

Realized in black holes are the most "extreme" states of matter comparable, perhaps, with the most initial stages of the Big Bang.

The conditions for the emergence of black holes correspond to the compression of matter to some critical density $\rho_{\rm c} = 2 \cdot 10^{16} (M_\odot/M)^2$ g/cm^3, which is inversely proportional to the object mass. For a typical black hole of stellar mass ($M = 10\,M_\odot$), the gravitational radius is equal to 30 km, and the critical density is equal to $2 \cdot 10^{14}$ g/cm^3, which is equal to the density of atomic nucleus.

For a black hole in the galactic nucleus ($M = 10^{10}\,M_\odot$), the gravitational radius is equal to 3×10^{15} cm = 200 AU, which is five times the Sun–Pluto distance. The critical density in this case is 0.2×10^{-3} g/cm^3, which is several times lower than the density of the air (1.3×10^{-3}g/cm^3).

For the Earth ($M = 3 \times 10^{-6} M_\odot$), the critical density is extremely high and equal to 2×10^{27} g/cm^3, which is higher than the density of an atomic nucleus by 13 orders of magnitude.

Black holes are divided into three types:

– A black hole of stellar mass $M = (3\text{–}50)M_\odot$. At the end of stellar evolution there forms a white dwarf (if the mass of the stellar core $M_c \leq 1.2\,M_\odot$), a neutron star (if $M_c \leq 3\,M_\odot$), or a black hole (if $M_c \geq 3\,M_\odot$).
– Supermassive black holes in galactic nuclei ($M = 10^6$–$10^{10} M_\odot$).

– Primary black holes formed at the early stages of evolution of the Universe, the so-called "eternal" black holes. Observationally, so far little is known about them. In total, 10 million black holes are believed to exist in the Galaxy.

According to the presently existing notions [39], our Galaxy (which we observe as a Milky Way) may contain at its center a black hole with a mass of about $3 \cdot 10^6 M_\odot$ measuring about 0.05 astronomical units. The Galaxy ≈80,000 light years in diameter and ≈6000 light years in thickness has a spherical halo of radius of the order of 10^5 light years. The Sun and the Earth are 26,000 light years away from the Galaxy center and rotate about the Galactic center with a period of 230 million years, having described only 22 rotations over the 5 billion years of its existence.

It is possible to indirectly infer the presence of these objects from their gravitational action (Fig. 9.56) on neighboring objects: in our galaxy there are about 20 candidates for black holes of stellar mass, while supermassive black holes (millions of times more massive than the Sun) are probably present in 300 galaxies [103]. However, there are even more of these objects. During their long history, many stars should collapse on using up their fuel, so that the number of black holes may be comparable to the number of visible stars and, according to Hawking [44], their mass may explain the high rates of galactic rotation (see Figs. 10.33 and 10.34).

Einstein's general theory of relativity endows black holes with surprising properties. According to Cherepashchuk [13], on the event horizon the course of time terminates in the view of an external observer. A spacecraft sent to a black hole would never intercept the event horizon from the standpoint of a distant observer but would continuously slow down as the horizon is approached. An astronaut in his spacecraft is in principle capable of penetrating beyond the event horizon, but

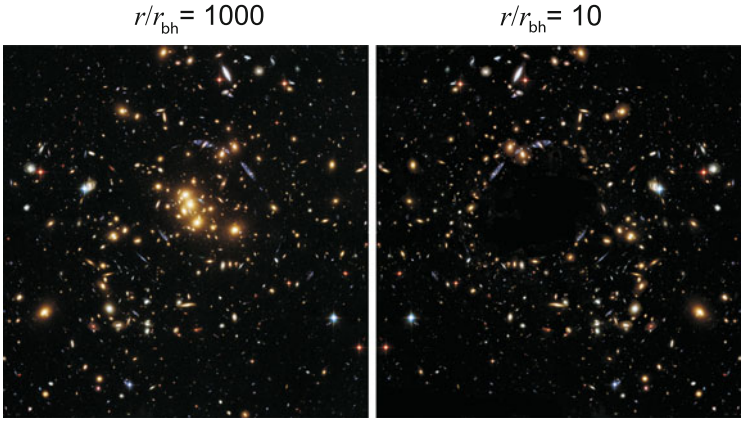

Fig. 9.56 Black hole against the stellar sky background. At a distance of 1000 r_{bh} its presence is hard to discern (the *left drawing*); at a distance of 10 r_{bh} (the *right drawing*) it distorts the appearance of the stellar sky [80]

he will be unable to transmit any information to the external observer. In this case, the astronaut falling freely below the event horizon would probably see a different universe and even his own future. This is due to the fact that the spatial and time coordinates change places inside the black hole and travel in space is replaced here by travel in time [13].

The properties of rotating black holes are even more extraordinary. Their event horizon is smaller in radius and is embedded in an ergosphere—a space-time domain in which bodies are bound to move continuously, being entrained by the vertical gravitational field of the rotating black hole [13].

It is very difficult to detect black holes, and all the more, to measure their parameters. Anyway, a Nobel Prize has not yet been awarded for their discovery.

Astronomically, to discover a black hole one has to measure the object's mass, demonstrate that its radius does not exceed r_{bh}, as well as to obtain observational evidence that the object does "practically" have an event horizon. The masses of black holes are safely measured from the motion of the nearby gas and stars. In this case, since $r \gg r_{bh}$, in the majority of cases it would suffice to use the Newtonian law of gravitation.

The radii of black holes are extremely hard to measure. So far use is made of coarse ($r < 10r_{bh}$) indirect estimates: studies of high-power X-ray emission in the accretion of substance onto a black hole, an analysis of fast variability, studies of spectral line profiles, etc.

Among the special features of the dynamics of black holes is the mode whereby under the radiation pressure from the central regions of accretion disk there occurs a high-power quasispherical substance flow at velocities of thousands of kilometers per second. A new and unexpected feature of this disk substance accretion onto a relativistic object is the formation of well-collimated (the divergence angle is below 1°) relativistic (with a velocity of $\sim$0.26 c) substance ejections. It is pertinent to note that collimated relativistic jets with a plasma velocity of $\sim$0.9 c have been discovered.

Black holes of stellar mass may be produced either in the accretion-induced collapse of neutron stars in binary systems or in the collapse of the nuclei of massive single stars [115]. The necessary conditions for the production of black holes emerge at the final stage of evolution of stars with masses greater than approximately $3M_{\odot}$ (Fig. 9.57 [14]). The uncontrollable compression of such a star—its collapse—eventually leads to the fulfillment of the condition $R < r_{bh}$ and the production of a black hole of mass between 3 and 100 $M_{\odot}$.

Recent years have seen the discovery of gigantic black holes with masses as great as millions of solar masses. A part of them existed even 13 billion years ago. The formation mechanism of these giants is still not perfectly understood. They either arose from the coalescence of black holes of smaller size or resulted from gravitational accretion.

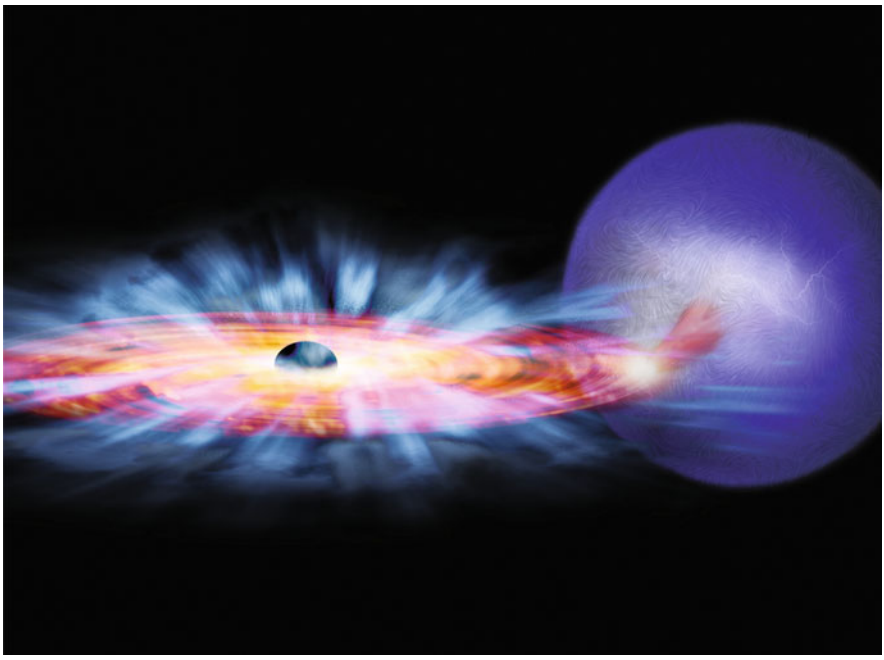

Fig. 9.57 The binary system GRO J1655-40 in the Scorpio constellation consists of a normal star of mass $2M_{\odot}$ (at the *right*) and a black hole of mass $7M_{\odot}$. The drawing was made using the data of the Chandra X-ray Observatory (by M. Weiss; the image is taken from the site http://chandra.harvard.edu). The matter of the normal star flows to the black hole. "Wind" blows from the accretion disk of the black hole under the action of magnetic forces, while magnetic forces in the inner region force the matter to approach the black hole [14]

9.3.6 Quasars

Heavier, massive and supermassive, black holes with masses up to $10^9 M_{\odot}$ emerge due to the collapse of huge masses of gas at the centers of globular star clusters, in galactic nuclei, and in quasars. Light black holes with masses below $3M_{\odot}$ might be formed due to the growth of density fluctuations of the supercompressed matter of the early universe (primary black holes). Predicted for these primary, or "eternal", black holes, which existed from the Universe's inception and did not result from stellar collapse, is the existence of a "bridge" at their center—the passage to another Universe with a different space.

Astrophysicists relate black holes to compact X-ray sources in our galaxy and the nearest one. Most of them are X-ray binary systems, in which the optical star—the donor—delivers matter to the neighboring relativistic object: a neutron star or a black hole (Fig. 9.58 [14]).

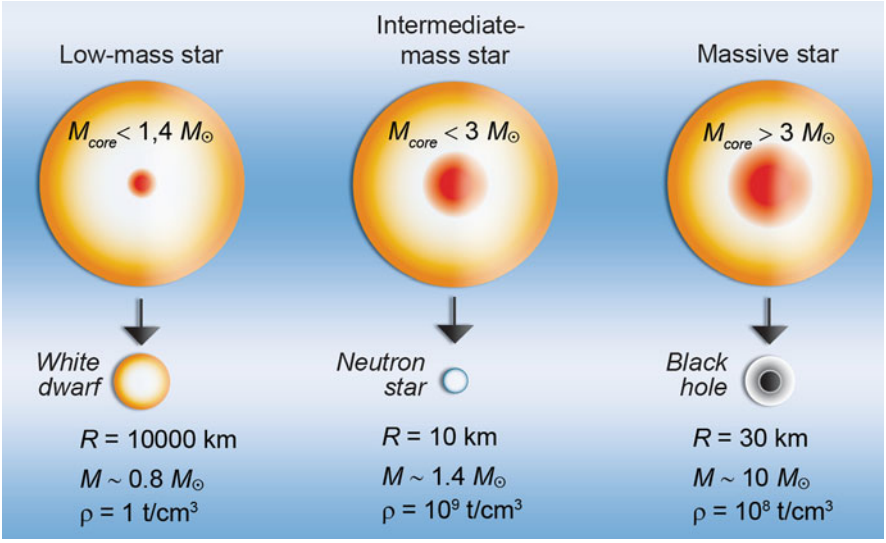

Fig. 9.58 Schematic of the occurrence of a black hole compared to the evolution of stars of different mass [14]

The accretion of this matter is accompanied by tremendous energy liberation in the X-ray range with a luminosity of $\approx 10^{36}$–10^{39} erg/s, which is millions of times higher than the bolometric luminosity of the Sun. This means that the optical star plays the role of a probing body in the gravitational field of a relativistic object. In this case, the black hole candidates differ from neutron stars not only in their greater mass (by more than a factor of three) and the absence of a magnetic field, but also in observable manifestations—these high-power X-ray radiators are neither X-ray pulsars nor type I X-ray bursters [12, 36, 37]. The radiation intensity of these objects ranges up to gigantic values of 10^{27} W/cm^2, which exceeds the record intensities for focused laser radiation by six orders of magnitude (Sect. 3.2, Tables 3.2 and 3.3). For a typical black hole with a mass $M = 10\,M_\odot$ and a supernuclear density $\rho \approx 10^{16}$ g/cm^3, available models suggest that the pressure is at a level of 2–3×10^{24} Mbar.

Quantum mechanics introduces some corrections to the models of black holes: with retention of the event horizon, a black hole ceases to be "black" but becomes a radiation source [44]. The nature of this radiation is the same as for electron–positron pairs produced by a strong electric field, which increases the energy of virtual (short-lived) pairs in vacuum, making them real. The pairs in the strong gravitational field of a black hole are produced in a similar way. These pairs emerge in the "empty" space domain located in front of the event horizon. One of the components of this pair becomes a real particle outside of the event horizon and, having a positive energy, may escape to infinity; the other particle emerges inside the horizon and falls, with a negative energy, into the black hole. Eventually the

black hole becomes a source of a continuous stream of particles going to infinity. No particle intersects the event horizon in the formation of this radiation. In the analysis of this picture, Hawking discovered [44] that the properties of this radiation are the same as for the radiation of a hot black body of radius $r_{\rm bh}$ heated to a temperature (in kelvin)

$$T \sim \frac{\hbar c^3}{8\pi kGM} \sim 0.5 \times 10^{-7} M_\odot / M.$$

In this case it was shown [44] that the smaller the black hole, the higher its brightness temperature, and the easier the black hole is to notice. Like all hot bodies, for the description of which the second law of thermodynamics was formulated, black holes possess a large amount of entropy and may emit particles (vaporize). A single black hole with a mass equal to about one million solar masses (like the one that is thought to be located at the center of our galaxy) possesses an entropy that exceeds 100-fold the entropy of all the particles in the observable universe.

In the course of radiation, the mass of the black hole decreases and its temperature rises, which enhances the emission and thereby speeds up the mass loss. That is why the black hole "flares up" with time, its temperature rising rapidly, and the black hole ceases to exist within a finite time on exhausting its mass.

One scenario of the universe's evolution (see Sect. 10.4) implies that it will eternally expand. Distant galaxies will vanish from our view. Those which remain close to us will transform into black holes, which will vaporize into the surrounding medium. It is not unlikely that billions of years later the universe would be empty. Then and only then would it possess the maximum possible entropy. The universe would come to a state of equilibrium, and from then on nothing would ever happen in it.

It is significant that the last moments prior to the disappearance of a black hole will occur in the regime of a high-power explosion with an energy liberation of 10^{30} erg in a time of about 0.1 s. Such explosions might be observable at a long distance from the Earth. This does not apply to stellar objects and even more so to massive and supermassive black holes: even for a mass equal to the solar one, the temperature is equal to an insignificant fraction of a degree and the lifetime is much longer than the life of the universe. Only primary black holes with a mass of about 10^{15} g are therefore capable of exploding in our epoch. Unfortunately, such explosions have never been observed.

An interesting radiation-induced change of accretion dynamics is related to the so-called Eddington luminosity limit [115], above which the light pressure exceeds the gravitational attraction. A classical example of a binary system in which a supercritical accretion to a compact object is realized is SS433 (Fig. 9.5 [27]), a massive binary star, which emanates directed matter jets traveling at a velocity of $\approx 0.26\,c$, where c is the velocity of light. Binary systems with relativistic jets have come to be known as galactic microquasars. In most of them, the compact objects are greater than $3M_\odot$ in mass and are reliable black hole candidates. It is likely that the near-critical accretion to a black hole is always accompanied by the production

of relativistic jets; however, the mechanism of their formation is as yet imperfectly understood.

It is likely [115] that supermassive (with $M > 10^5$–$10^{10} M_\odot$) black holes are the central elements of a number of galaxies. The matter falling freely on a black hole is accelerated to velocities close to the speed of light, and near the black hole this stream spins into a dense and extremely hot accretion disk due to the existence of the initial angular momentum. The energy of this "spinning top" is the principal energy reservoir of the active galactic nucleus. It is there and not in the black hole itself that high-power short-wavelength radiation fluxes are generated, and due to its magnetic field there occurs acceleration of protons and electrons to very high energies; these protons and electrons are ejected in the form of well-collimated jets perpendicular to the accretion disk plane. In some cases, the jets emanating from galactic centers measure hundreds of kiloparsecs in length and end in huge clouds [103].

By and large, this picture resembles that which is realized in the matter accretion to a black hole or a neutron star, but the scale of energy in this case is many orders of magnitude greater. The bulk of the energy of the active nucleus is the energy of matter released in its fall into a deep gravitational well produced by a supermassive black hole. As in the case of accretion onto compact stellar remnants, in the accretion disk around this object the energy of the falling gas is partly converted into thermal energy and partly into disk rotation energy. Integrally, the released energy turns out to be tens of times higher than the nuclear energy contained in the nuclei of the falling matter due to its acceleration to velocities close to the speed of light in the gravitational field of the black hole.

It is not unlikely that at the centers of quasars there are black holes with masses of $\sim 10^8 M_\odot$, which accounts for the high-power radiation emanating from the polar regions of these objects [44].

The gravitational accretion of matter is the principal source of mass and energy for many astrophysical objects, for example binary stars, binary X-ray sources, quasars, active galactic nuclei, and jet ejections [115]. Although accretion theory has long been known, it gained a new impetus with the discovery of the first X-ray sources. As noted above, the accretion of matter onto stars (including neutron stars) may take place on their inner surface or on the outer surface of the magnetosphere of a strongly magnetized star. In this case, the gravitational energy of the falling matter is converted to heat and is reradiated into open space.

A different situation arises in the accretion to black holes (Fig. 9.59), which are possibly present in the binary X-ray sources of our galaxy or in active galactic nuclei. In this case, as discussed earlier, the matter transits the "event horizon" of a black hole, while the corresponding radiation cannot come out. Unlike the accretion onto stars, the radiation capacity of accretion to black holes is a priori unknown and depends on several factors, such as the angular momentum of the falling matter and the matter-entrained magnetic field. For the spherical accretion of nonmagnetized gas, the efficiency of energy conversion to radiation may amount to 10^{-8}, while the presence of a magnetic field increases its magnitude to 10 % [71, 74, 86, 95].

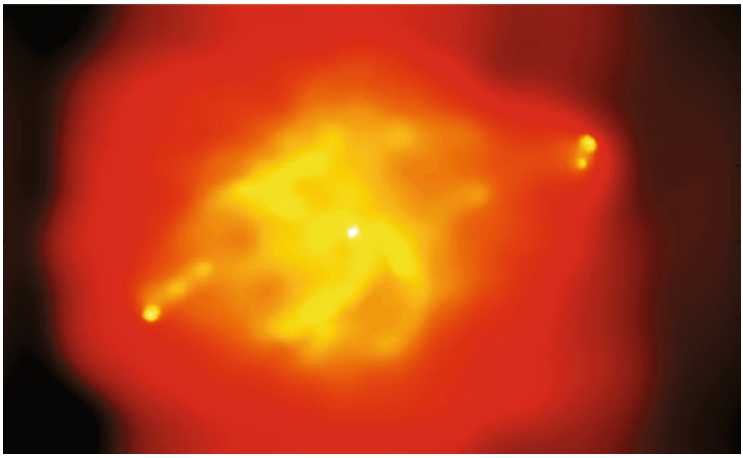

Fig. 9.59 Accretion of matter onto a black hole [19] in the galaxy Cygnus A. One can see cosmic jets responsible for high-power X-ray and radio radiation. Under deceleration due to the ambient medium, they produce "hot spots" and gigantic cavities. The radio emission power of the object Cygnus A is $\approx 10^{45}$ erg/s, which is approximately 10 million times the emission power of the Andromeda Galaxy

The small value of this quantity is of significance in explaining the extremely low luminosity of the neighborhood of black holes at the center of our galaxy. Both jets and emanating plasma streams make a contribution of their own to the low luminosity (Fig. 9.60).

Viscosity is a special problem in the theory of matter accretion [71]. Normally viscosity lowers the effect of the angular momentum to enhance the accretion. For a laminar viscous flow, molecular viscosity is low and a stationary accretion disk should be massive and thick, and the accretion rate should be low in this case. This does not correspond to the observations of high accretion rates for binary X-ray sources.

The discrepancy may be explained [71, 117] by assuming that the real viscosity coefficient far exceeds the "molecular-kinetic" value, for instance, by assuming the accretion disk to be turbulent and introducing the corresponding turbulent viscosity.

Explaining the accretion disk turbulence [101, 108, 109] calls for special consideration [71]. In the linear approximation, a Keplerian disk is stable (after Rayleigh [22]) against axially symmetric perturbations, which conserve the angular momentum. For a very high Reynolds number, $Re = \rho V \ell / \eta \approx 10^{10}$, the amplitude of nonlinear perturbations will be small, so that the development of turbulence from nonlinear perturbations is possible even when linear perturbations are stable.

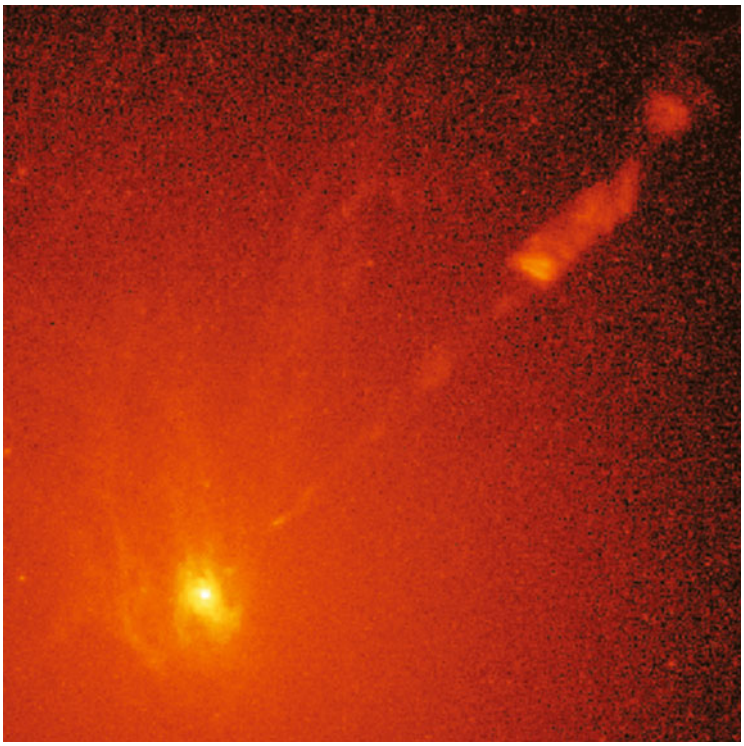

Fig. 9.60 Jet formation in the accretion of matter onto a massive object [19] at the center of the galaxy M87. The jet consists of high-velocity particles and exhibits a structure of inhomogeneities (clusters) measuring ≈10 light years

At the present time, magnetohydrodynamic instabilities as the cause of accretion disk turbulization are being studied intensively. The linear (magnetorotational) instability of differentially rotating disks (the Alfvén velocity is below the velocity of sound) may develop into a turbulent regime, which it has been possible to model employing sophisticated three-dimensional magnetohydrodynamic (MHD) codes.

Laboratory experiments in this area involve rotating liquid metals, though for lower-than-required values of the magnetic Reynolds number Re_{m} owing to the substantial magnetic diffusion in metals [101]. Another type of laboratory experiment might involve laser-produced plasma, in which it is possible to generate ≈100 kT fields and high accelerations.

Apart from the magnetorotational instability [108, 109], Rossby wave instability [22, 71] may be significant in accretion problems involving an unmagnetized flow with a nonmonotonic profile of the density, pressure, or entropy [22]. Two-dimensional simulations of such situations revealed the emergence of three to five long-lived vortices, appreciably changing the accretion dynamics, which is of importance in studying the formation of planets around young stars.

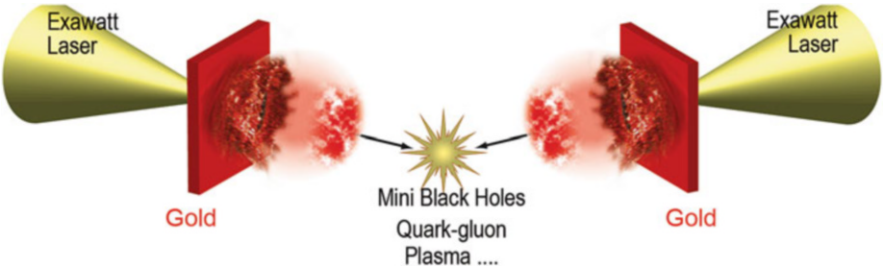

Fig. 9.61 Laser-assisted production of a QGP and a mini black hole [3, 9]

At present, as we see, considerable attention is being given to binary systems in which one of the objects is a collapsing object such as a neutron star, a black hole, or a white dwarf. Active galactic nuclei and quasars are at the other extreme. Their anomalous luminosity results from falling-matter energy conversion to a massive black hole located at the galactic center. The corresponding high-intensity X-ray radiation from these objects ionizes the matter in the falling accretion disk and transforms it to the plasma state, making significant the effects of magnetic field, radiation, and Coulomb interaction on the dynamics of motion. To study the physics of these processes, advantage is taken of the high-energy X-ray cosmic observatories Chandra and XMM. In this case, many questions [71] concerning plasma photoionization in equilibrium and kinetic modes remain to be answered.

High-current Z-pinches, lasers, and relativistic heavy-ion accelerators (see Chaps. 3 and 5) can to a certain extent sufficiently reproduce the photoionization effects in plasmas, providing a clearer insight into the dynamics of matter accretion to black holes.

Arkani-Hamed et al. [3] and Bleicher [9] came up with the interesting idea of producing mini black holes in terrestrial conditions (Fig. 9.61). In this formulation, two exawatt lasers generate colliding ion streams with energies $\gtrsim 1$ TeV by irradiating gold targets, which should give rise to a black hole with a radius of $\approx 10^{-4}$ fm.

9.3.7 "Wormholes"

More recently, one more mechanism of the origination of black holes related to the collapse of so-called "magnetic tunnels" or "wormholes" [62, 100] has come under discussion [51].

A "wormhole" [97] is a hypothetical object described by the nonsingular solution of Einstein's equation with two large (or infinite) space-time domains connected by a throat. The two large space-time domains may lie in the same Universe or even belong to different universes in a Multiuniverse model. In the latter case, "traversable" tunnels furnish a unique possibility to investigate other universes.

These highly exotic objects supposedly emerged at early stages after the Big Bang and have persisted for various reasons until the present time. According to the

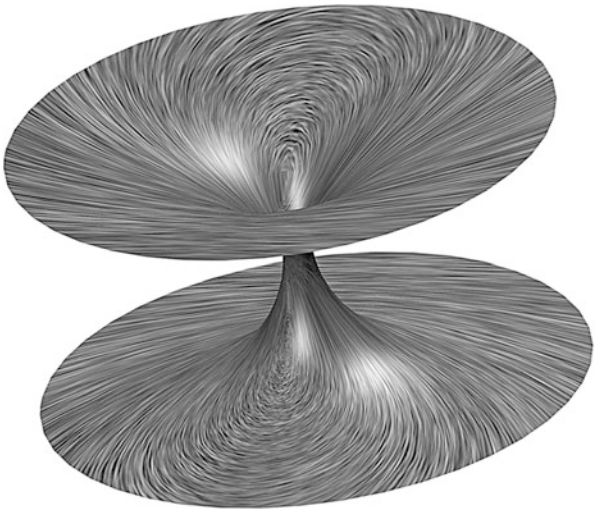

Fig. 9.62 Wormhole connecting two spaces (two universes) [87]

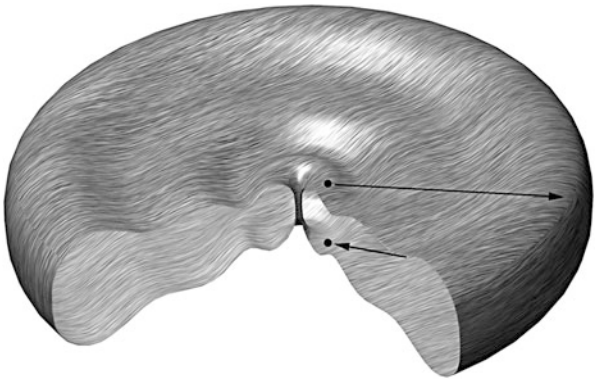

Fig. 9.63 Wormhole connecting two local regions of the same space. The path between them in ordinary space may be far longer than the path through the wormhole. For obviousness, our space is curved [87]

chaotic inflation model, which underlies modern cosmology [51], apart from our universe there may exist an infinite number of other universes, which originate in a scalar field in different spatial domains and at different points in time to make up a "spatio-temporal foam" [62, 100]. Some parts of our and other universes may be connected by traversable spatio-temporal tunnels—"wormholes" (Figs. 9.62 and 9.63 [87])—which existed in the initial scalar field and persisted after inflation. There emerges an intriguing possibility of studying the multielement universe and searching for specific manifestations of extraordinary-type astrophysical objects—entrances to the tunnels.

Kardashev et al. [51] considered different models of a "wormhole" sustained by the electromagnetic field penetrating through these holes and by the combination of magnetic field and "phantom" energy, magnetic field and "phantom" matter, which was introduced to account for the accelerated universe expansion discovered recently [74, 86]. In this case, the "phantom" energy and "phantom" matter should possess extraordinary equations of state close to the vacuum one, $P/E < -1$, and be isotropic or anisotropic. Shatskii et al. [97] investigated the dynamics of a spherical model of a wormhole filled with matter consisting of magnetic field and dust with a negative mass density.

The entrance to such a magnetic tunnel, which is a magnetic monopole of macroscopic dimensions, turns out to be amenable to observation, and the accretion of the ordinary matter onto it may give rise to a black hole with a radial magnetic field. Kardashev et al. [51] discuss the likelihood that some active galactic nuclei and other objects of the galaxy are or were entrances to these magnetic holes, which range in mass from 2 kg to 2 billion solar masses. The long cosmological lifetime of these objects is attributable to the circumstance that the Hawking evaporation effect [43] is not operable for them, because they lack the event visibility horizon. This is the difference between wormholes and primary black holes, which have a lower mass bound of 10^{15} g. A wormhole may manifest itself as a binary system formed by the entrance to a spatial throat, which produces multiply connected topology, emitting nonthermal radiation and gamma-ray bursts.

Table 9.6, taken from [51], shows the throat parameters (ν_G is the oscillation frequency of a probe particle and ν_H is the gyrofrequency) of a magnetic "wormhole" estimated for a quasar nucleus, objects with the critical field for electron–positron pair production, objects of terrestrial and solar mass, objects with the critical magnetic field for monopole–antimonopole pair production, and an object of Planck's mass.

One can see that "wormhole" parameters correspond to ultrahigh energy densities, which may be comparable to those in the immediate vicinity of the Big Bang. Attention is drawn to the extremely high magnetic fields of these objects. For fields $B = m_e^2 c^3/e\hbar \approx 4.4 \times 10^{13}$ Gs a level's Landau excitation energy exceeds the rest energy of the electron. Positronium atoms acquire stability at fields above 10^{24} Gs; they are spontaneously produced in the vacuum to fill the entire medium. The breakdown of the vacuum and monopole pair production take place at fields of $\approx 2.6 \times 10^{49}$ Gs, which leads to a "wormhole" mass of only 1.8 kg, which is supposedly the lower bound for these objects.

Also discussed is the feasibility of observing—against the background of cosmic objects—entrances to magnetic tunnels or black holes produced by way of accretion from relict black holes [51]. The difference in structure and rate of spatial decay of these objects from the structure of ordinary black holes may serve as an indication. Furthermore, the rotation of a monopole excites a dipole electric field, resulting in relativistic particle acceleration. In this case, electrons are accelerated toward one pole and protons toward the other. Such unidirectional jets are observed to emanate from some sources, for instance, the 3C273 quasar [51]. A black hole may be distinguished from the entrance to a "wormhole" by the absence of an

Table 9.6 Parameters of wormholes of different mass [51]

$M_\infty = 2M_0$	r_0 (cm)	B_0 (Gs)	$\rho\,(r_0)$ (g/cm^3)	ν_G (Hz)	ν_H (Hz)
6×10^{42} g $= 3 \times 10^9\, M_\odot$	4.5×10^{14}	7.8×10^9	2.7×10^{-3}	7.6×10^{-6} (1.5 days)	2.2×10^{16}
10^{39} g $= 5 \times 10^5\, M_\odot$ (pair production $e^\pm$)	7.4×10^{10}	4.4×10^{13}	9.7×10^4	0.045 (22 c)	1.3×10^{20}
2×10^{33} g $= M_\odot$ (the Sun)	1.5×10^5	2.3×10^{19}	2.4×10^{16}	2.4×10^4	6.6×10^{25}
6×10^{27} g $= M_\oplus$ (the Earth)	0.45	7.8×10^{24}	2.7×10^{27}	7.6×10^9	2.2×10^{31}
5×10^{10} g (positronium)	3.5×10^{-18}	10^{42}	4.4×10^{61}	9.7×10^{26}	2.7×10^{48}
1.8×10^3 g (pair production $\mu^\pm$)	1.3×10^{-25}	2.6×10^{49}	3×10^{76}	2.6×10^{34}	7.3×10^{55}
2×10^{-5} g (Planck's mass)	1.5×10^{-33}	2.3×10^{57}	2.4×10^{92}	2.3×10^{42}	6.6×10^{63}

event horizon in the latter: a luminous object incident on the "wormhole" would be continuously observed with an alternating red or blue shift. Observations of the gravitationally lensed quasar Q09577+561 supposedly lend credence to this model [51]. A distinctive feature of the "wormhole" as a strongly relativistic object without an event horizon is the possibility of occurrence of periodic oscillations of the stellar mass relative to the throat (see Table 9.6) accompanied by the corresponding variation of the recorded red shift. In the motion of radiating sources along circular orbits around the entrance to the tunnel, a compact source will also change its flux and red shift. Lastly, an external observer may discover radiation at the gyrofrequencies and observe effects related to $e^{\pm}$ and $\mu^{\pm}$ pair production [51].

Binary systems involving entrances to magnetic tunnels as well as the approach of two entrances to the same magnetic tunnel may also be accompanied by observable radiative effects. In particular, the second of these processes ends with the transformation to a black hole without magnetic field and with the radiation of an external magnetic field. The electromagnetic pulse accelerates electron–positron pairs, which may explain the observed gamma-ray bursts.

Kardashev et al. [51] also considered other possibilities for the observable manifestations of new types of primary cosmological objects—entrances to "wormholes" and specific black holes resulting from them. In any case, the discovery of "wormholes" opens up intriguing possibilities for investigating the multielement universe and even paves the way to semifantastic ideas of traveling via "wormholes" into the past by a "time machine" in violation of the causality principle and to other universes before these tunnels collapse to black holes [62, 100].

Figure 9.64 [76] depicts the Hillas diagram with the characteristic magnitudes of magnetic fields and dimensions of astrophysical objects. It also demonstrates their capabilities as particle accelerators. Solid lines represent estimates of dimensions

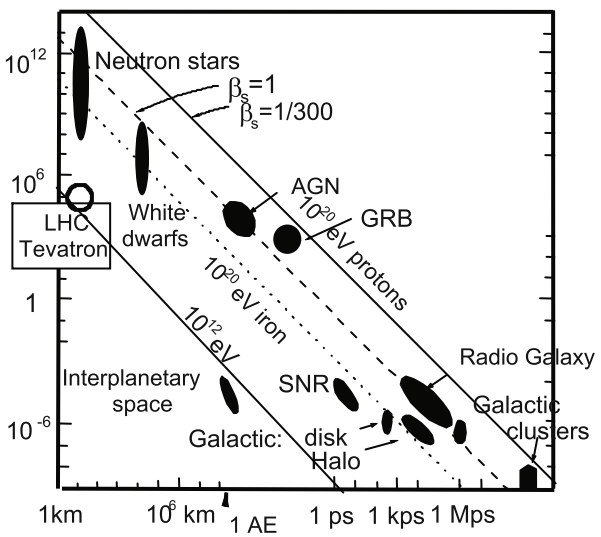

Fig. 9.64 Hillas diagram showing the characteristic magnitudes of magnetic fields and dimensions of astrophysical objects [76]

(in parsecs) and magnitudes of magnetic field (in gauss) of the objects capable of accelerating protons to energies of 10^{20} and 10^{21} eV for a shock wave velocity 1/300 the speed of light. The dotted line represents the same for iron nuclei. Dark spots indicate the observed dimensions and magnetic fields of different astrophysical objects. It seems that in the universe known to us there are no, under the assumptions made about the particle acceleration mechanism (Fermi) itself, obvious candidates for the role of a zevatron accelerator—an accelerator of observable-energy cosmic particles. Also shown for comparison here are the characteristics of the Tevatron accelerator and the LHC operating on the Earth.

References

1. Abel, T.: The first stars, as seen by supercomputers. Phys. Today **64**(4), 51–56 (2011)
2. Allard, F., Hauschildt, P.H., Alexander, D.R., Starrfield, S.: Model atmospheres of very low mass stars and brown dwarfs. Annu. Rev. Astron. Astrophys. **35**, 137–177 (1997)
3. Arkani-Hamed, N., Dimopoulos, S., Dvali, G.: Phenomenology, astrophysics, and cosmology of theories with submillimeter dimensions and TeV scale quantum gravity. Phys. Rev. D **59**(8), 086004 (1999)
4. Avrorin, E.N., Vodolaga, B.K., Simonenko, V.A., Fortov, V.E.: Intense shock waves and extreme states of matter. Phys. Usp. **36**(5), 337–364 (1993)
5. Avrorin, E.N., Simonenko, V.A., Shibarshov, L.I.: Physics research during nuclear explosions. Phys. Usp. **49**(4), 432 (2006)
6. Balega, Y.Y.: Brown dwarfs: substars without nuclear reactions. Phys. Usp. **45**(8), 883–886 (2002)
7. Baturin, V.A., Mironova, I.V., Surdin, V.G.: Fizika i jevoljucija zvezd (Physics and evolution of stars). In: Surdin, V.G. (ed.) Astronomiya: Vek XXI (Astronomy: XXIst Century), p. 120. Vek 2, Fryazino (2007)
8. Bezkrovniy, V., Filinov, V.S., Kremp, D., et al.: Monte Carlo results for the hydrogen Hugoniot. Phys. Rev. E **70**(5), 057401 (2004)
9. Bleicher, M.: How to create black holes on Earth. Eur. J. Phys. **28**(3), 509–516 (2007)
10. Burrows, A., Hubbard, W.B., Lunine, J.I., Liebert, J.: The theory of brown dwarfs and extrasolar giant planets. Rev. Mod. Phys. **73**(3), 719–765 (2001)
11. Chabrier, G., Baraffe, I.: Theory of low mass stars and substellar objects. Annu. Rev. Astron. Astrophys. **38**, 337–377 (2000)
12. Cherepashchuk, A.M.: Masses of black holes in binary stellar systems. Phys. Usp. **39**(8), 759 (1996)
13. Cherepashchuk, A.M.: Chernye dyry v dvojnyh zvezdnyh sistemah (Black holes in double star systems). In: Soifer, V.N. (ed.) Sovremennoe estestvoznanie. Entsiklopediya (Modern Natural Science. Encyclopedia), vol. 4, p. 228. Magistr-Press, Moscow (2000)
14. Cherepashchuk, A.M.: Chernye dyry vo Vselennoj (Black holes in the Universe). In: Surdin, V.G. (ed.) Astronomiya: Vek XXI (Astronomy: XXIst Century), p. 219. Vek 2, Fryazino (2007)
15. Cherepashchuk, A.M., Chernin, A.D.: Vselennaja, zhizn', chernye dyry (The Universe, Life, Black Holes). Vek 2, Fryazino (2004)
16. Chernin, A.D.: Cosmic vacuum. Phys. Usp. **44**(11), 1099 (2001)
17. Chernin, A.D.: Dark energy and universal antigravitation. Phys. Usp. **51**(3), 253 (2008)
18. Disdier, L., Garconnet, J.P., Malka, G., Miquel, J.L.: Fast neutron emission from a high-energy ion beam produced by a high-intensity subpicosecond laser pulse. Phys. Rev. Lett. **82**(7), 1454–1457 (1999)
19. Drake, R.P.: High-Energy-Density Physics. Springer, Berlin, Heidelberg (2006)

20. Dubin, D.H.E., O'Nail, T.M.: Trapped nonneutral plasmas, liquids and crystals (the thermal equilibrium states). Rev. Mod. Phys. **71**, 87 (1999)
21. Efremov, Y.N.: Zvezdnye ostrova (Star Islands). Vek 2, Fryazino (2005)
22. Faber, T.E.: Fluid Dynamics for Physicists. Cambridge University Press, Cambridge (1977)
23. Filinov, V.S., Bonitz, M., Levashov, P., et al.: Plasma phase transition in dense hydrogen and electron–hole plasmas. J. Phys. A **36**(22), 6069–6076 (2003)
24. Filinov, V.S., Levashov, P.R., Bonitz, M., Fortov, V.E.: Calculation of the shock Hugoniot of deuterium at pressures above 1 Mbar by the path-integral Monte Carlo method. Plasma Phys. Rep. **31**(8), 700–704 (2005)
25. Fortov, V.E. (ed.): Entsiklopediya nizkotemperaturnoi plazmy (Encyclopedia of Low-Temperature Plasma). Nauka, Moscow (2000)
26. Fortov, V.E.: Intense Shock Waves and Extreme States of Matter. Bukos, Moscow (2005)
27. Fortov, V.E. (ed.): Explosive-Driven Generators of Powerful Electrical Current Pulses. Cambridge International Science, Cambridge (2007)
28. Fortov, V.E.: Intense shock waves and extreme states of matter. Phys. Usp. **50**(4), 333 (2007)
29. Fortov, V.E., Gnedin, Y.N., Ivanov, M.F., et al.: Collision of comet Shoemaker–Levy 9 with Jupiter: what did we see. Phys. Usp. **39**(4), 363 (1996)
30. Fortov, V.E., Ternovoi, V.Y., Zhernokletov, M.V., et al.: Pressure-produced ionization of nonideal plasma in a megabar range of dynamic pressures. J. Exp. Theor. Phys. **97**(2), 259–278 (2003)
31. Fortov, V.E., Ivlev, A.V., Khrapak, S.A., et al.: Complex (dusty) plasma: current status, open issues, perspectives. Phys. Rep. **421**(1), 1–103 (2005)
32. Fortov, V., Iakubov, I., Khrapak, A.: Physics of Strongly Coupled Plasma. Oxford University Press, Oxford (2006)
33. Fortov, V.E., Ilkaev, R.I., Arinin, V.A., et al.: Phase transition in a strongly nonideal deuterium plasma generated by quasi-isentropical compression at megabar pressures. Phys. Rev. Lett. **99**(18), 185001 (2007)
34. Friman, B., Höhne, C., Knoll, J., et al. (eds.): The CBM Physics Book. Lecture Notes in Physics, vol. 814, 1st edn. Springer, Berlin (2010)
35. Gelliot, T.: Understanding the evolution of giant planets: importance of equation of state. Presented at the International Workshop on Warm Dense Matter, University of Rostock, Germany (2007)
36. Ginzburg, V.L.: The Physics of a Lifetime: Reflections on the Problems and Personalities of 20th Century Physics. Springer, Berlin, Heidelberg (2001)
37. Glendenning, N.K.: Compact Stars: Nuclear Physics, Particle Physics, and General Relativity, 2nd edn. Springer, New York (2000)
38. Gorbunov, D.S., Rubakov, V.A.: Vvedenie v teoriyu rannei Vselennoi. Kosmologicheskie vozmushcheniya. Inflyatsionnaya teoriya, vol. 2. Krasand, Moscow (2010)
39. Grib, A.A.: Osnovnye predstavleniya sovremennoi kosmologii (The Basic Representations of Modern Cosmology). FizMatLit, Moscow (2008)
40. Haensel, P., Potekhin, A., Yakovlev, D.: Neutron Stars 1: Equation of State and Structure. Springer, New York (2007)
41. Hands, S.: The phase diagram of QCD. Contemp. Phys. **42**(4), 209–225 (2001)
42. Hawke, P.S., Burgess, T.J., Duerre, D.E., et al.: Observation of electrical conductivity of isentropically compressed hydrogen at megabar pressures. Phys. Rev. Lett. **41**(14), 994–997 (1978)
43. Hawking, S.W.: Particle creation by black holes. Commun. Math. Phys. **43**(3), 199–220 (1975)
44. Hawking, S.W.: A Brief History of Time: From the Big Bang to Black Holes. Bantam Books, Toronto (1988)
45. Ichimaru, S.: Nuclear fusion in dense plasmas. Rev. Mod. Phys. **65**(2), 255–299 (1993)
46. Istomin, Y.N.: Electron–positron plasma generation in the magnetospheres of neutron stars. Phys. Usp. **51**(8), 844 (2008)

47. Ivanova, L.N., Imshennik, V.S., Chechotkin, V.M.: Pulsation regime of the thermonuclear explosion of a star's dense carbon core. Astrophys. Space Sci. **31**(2), 497–514 (1974)
48. Jeffries, C.D., Keldysh, L.V. (eds.): Electron–Hole Droplets in Semiconductors. North-Holland, Amsterdam (1983)
49. Kadomtsev, B.B.: Selected Works [in Russian], vol. 1. Nauka, Moscow (2003)
50. Kaplan, S.A.: The Physics of Stars. Wiley, Chichester (1982). [Original in Russian: Fizika Zvezd, 2nd edn. Nauka, Moscow (1970)]
51. Kardashev, N.S., Novikov, I.D., Shatskii, A.A.: Magnetic tunnels (wormholes) in astrophysics. Astron. Rep. **50**(8), 601–611 (2006)
52. Karnakov, B.M., Mur, V.D., Popov, V.S.: Contribution to the theory of Lorentzian ionization. JETP Lett. **65**(5), 405–411 (1997)
53. Kifonidis, K., Plewa, T., Janka, H.T., Müller, E.: Nucleosynthesis and clump formation in a core-collapse supernova. Astrophys. J. Lett. **531**, L123–L126 (2000)
54. Kirzhnits, D.A.: Extremal states of matter (ultrahigh pressures and temperatures). Sov. Phys. Usp. **14**(4), 512–523 (1972)
55. Klumov, B.A., Kondaurov, V.I., Konyukhov, A.V., et al.: Collision of comet Shoemaker–Levi 9 with Jupiter: what shall we see? Phys. Usp. **37**(6), 577 (1994)
56. Knudson, M.D., Hanson, D.L., Bailey, J.E., et al.: Equation of state measurements in liquid deuterium to 70 GPa. Phys. Rev. Lett. **87**(22), 225501 (2001)
57. Koester, D.: White dwarfs: Recent developments. Astron. Astrophys. Rev. **11**(1), 33–66 (2007)
58. Kouveliotou, C., Duncan, R.C., Thompson, C.: Intensely magnetic neutron stars alter the quantum physics of their surroundings. Sci. Am. **288**(2), 35 (2003)
59. Levin, A.: Kosmicheskie bomby (Space bombs). Populyarnaya mehanika (Pop. Mech.) **8**(58), 38 (2007)
60. Levin, A.: Oni byli pervymi: samye starye zvezdy (They were the first: the oldest stars). Populyarnaya Mekhanika **103**(5), 42–46 (2011)
61. Levin, A.: Vozrast mirozdaniya: slushaem pul's vselennoi (The age of the universe: listening to the pulse of the universe). Populyarnaya Mekhanika **115**(5), 54–60 (2012)
62. Lobo, F.S.N.: Phantom energy traversable wormholes. Phys. Rev. D **71**(8), 084011 (2005)
63. Lukash, V.N., Mikheeva, E.V., Malinovsky, A.M.: Formation of the large-scale structure of the universe. Phys. Usp. **54**(10), 983–1005 (2011)
64. Lyutikov, M.: Magnetar giant flares and afterglows as relativistic magnetized explosions. Mon. Not. R. Astron. Soc. **367**(4), 1594–1602 (2006)
65. Mezzacappa, A.: Ascertaining the core collapse supernova mechanism: the state of the art and the road ahead. Annu. Rev. Nucl. Part. Sci. **55**(1), 467–515 (2005)
66. Miller, S., Tennyson, J., Jones, H.R.A., Longmore, A.J.: Computation of frequencies and linestrengths for triatomic molecules of astronomical interest. In: Jorgensen, U.G. (ed.) Molecules in the Stellar Environment. Lecture Notes in Physics, vol. 428, pp. 296–309. Springer, Berlin, Heidelberg (1994)
67. Mima, K., Ohsuga, T., Takabe, H., et al.: Wakeless triple-soliton accelerator. Phys. Rev. Lett. **57**(12), 1421–1424 (1986)
68. Murray, C.A., Wenk, R.A.: Observation of order–disorder transitions and particle trajectories in a model one-component plasma: time resolved microscopy of colloidal spheres. In: Van Horn, H.M., Ichimaru, S. (eds.) Strongly Coupled Plasma Physics, p. 367. University of Rochester Press, Rochester (1993)
69. Nadyozhin, D.K., Yudin, A.V.: The influence of Coulomb interaction on the equation of state under nuclear statistical equilibrium conditions. Astron. Lett. **31**(4), 271–279 (2005)
70. NASA, Hubblesite: http://hubblesite.org/
71. National Research Council: Frontiers in High Energy Density Physics. National Academies Press, Washington (2003)

72. Nellis, W.J.: Shock compression of hydrogen and other small molecules. In: Chiarotti, G.L., Hemley, R.J., Bernasconi, M., Ulivi, L. (eds.) High Pressure Phenomena, Proceedings of the International School of Physics "Enrico Fermi" Course CXLVII, p. 607. IOS Press, Amsterdam (2002)
73. Nellis, W.J.: Dynamic compression of materials: metallization of fluid hydrogen at high pressures. Rep. Prog. Phys. **69**(5), 1479–1580 (2006)
74. Novikov, I.D.: "Big Bang" echo (cosmic microwave background observations). Phys. Usp. **44**(8), 817 (2001)
75. Palmer, D.M., Barthelmy, S., Gehrels, N., et al.: A giant gamma-ray flare from the magnetar SGR 1806-20. Nature **434**(7037), 1107–1109 (2005)
76. Panasyuk, M.I.: Stranniki vselennoj ili jeho Bol'shogo Vzryva (Wanderers of the Universe or a Big Bang Echo). Vek 2, Fryazino (2005)
77. Partridge, H., Schwenke, D.W.: The determination of an accurate isotope dependent potential energy surface for water from extensive ab initio calculations and experimental data. J. Chem. Phys. **106**(11), 4618–4639 (1997)
78. Pavlovski, A., Boriskov, G., et al: Isentropic solid hydrogen compression by ultrahigh magnetic field pressure in megabar range. In: Fowler, C., Caird, R., Erickson, D. (eds.) Megagauss Technology and Pulsed Power Applications, p. 255. Plenum Press, London (1987)
79. Pieranski, P.: Colloidal crystals. Contemp. Phys. **24**(1), 25–73 (1983)
80. Popov, S.B., Prohomov, M.E.: Zvezdy: zhizn' posle smerti (Stars: a life after death). In: Surdin, V.G. (ed.) Astronomiya: Vek XXI (Astronomy: XXIst Century), p. 183. Vek 2, Fryazino (2007)
81. Popov, V.S., Karnakov, B.M., Mur, V.D.: Quasiclassical theory of atomic ionization in electric and magnetic fields. Phys. Lett. A **229**(5), 306–312 (1997)
82. Rebolo, R., Martin, E.L., Zapatero Osorio, M.R. (eds.): Brown dwarfs and extrasolar planets. In: Astronomical Society of the Pacific Conference Series, vol. 134. ASP, San Francisco (1998)
83. Richer, J., Michaud, G., Rogers, F., et al.: Radiative accelerations for evolutionary model calculations. Astrophys. J. **492**(2, Part 1), 833–842 (1998)
84. Rodionova, Z.F., Surdin, V.G.: Planety solnechnoj sistemy (Planets of the Solar System). In: Surdin, V.G. (ed.) Astronomiya: Vek XXI (Astronomy: XXIst Century), p. 34. Vek 2, Fryazino (2007)
85. Rubakov, V.A.: Large and infinite extra dimensions. Phys. Usp. **44**(9), 871 (2001)
86. Rubakov, V.A.: Introduction to cosmology. PoS **RTN2005**, 003 (2005)
87. Rubin, S.G.: Ustroistvo nashei vselennoi (The Constitution of Our Universe). Vek 2, Fryazino (2006)
88. Russel, W.B., Saville, D.A., Schowalter, W.R.: Colloidal Dispersions. Cambridge University Press, Cambridge (1989)
89. Ryutov, D.D., Remington, B.A., Robey, H.F., Drake, R.P.: Magnetodynamic scaling: from astrophysics to the laboratory. Phys. Plasmas **8**(5), 1804–1816 (2001)
90. Salpeter, E.E.: Nuclear reactions in the stars. I. Proton–proton chain. Phys. Rev. **88**(3), 547–553 (1952)
91. Samus', N.N.: Peremennye zvezdy (Variable stars). In: Surdin, V.G. (ed.) Astronomiya: Vek XXI (Astronomy: XXIst Century), p. 162. Vek 2, Fryazino (2007)
92. Schatz, T., Schramm, U., Habs, D.: Crystalline ion beams. Nature **412**(6848), 717–720 (2001)
93. Schertlera, K., Greinera, C., Schaffner-Bielichc, J., Thoma, M.: Quark phases in neutron stars and a third family of compact stars as signature for phase transitions. Nucl. Phys. A **677**(1–4), 463–490 (2001)
94. Schramm, U., Schatz, T., Bussmann, M., Habs, D.: Cooling and heating of crystalline ion beams. J. Phys. B **36**(3), 561–571 (2003)
95. Shapiro, S.L., Teukolsky, S.A.: Black Holes, White Dwarfs, and Neutron Stars. Wiley, New York (1983)
96. Shashkin, A.A.: Metal–insulator transitions and the effects of electron–electron interactions in two-dimensional electron systems. Phys. Usp. **48**(2), 129 (2005)

97. Shatskii, A.A., Novikov, I.D., Kardashev, N.S.: A dynamic model of the wormhole and the Multiverse model. Phys. Usp. **51**(5), 457 (2008)
98. Shevchenko, V.V.: Solnechnaja sistema (The Solar System). In: Soifer, V.N. (ed.) Sovremennoe estestvoznanie. Entsiklopediya (Modern Natural Science. Encyclopedia), vol. 4, p. 125. Magistr Press, Moscow (2000)
99. Shevchenko, V.V.: Priroda planet (The nature of planets). In: Surdin, V.G. (ed.) Astronomiya: Vek XXI (Astronomy: XXIst Century), p. 93. Vek 2, Fryazino (2007)
100. Shinkai, H., Hayward, S.A.: Fate of the first traversable wormhole: black-hole collapse or inflationary expansion. Phys. Rev. D **66**(4), 044005 (2002)
101. Stefani, F., Gundrum, T., Gerbeth, G., et al.: Experimental evidence for magnetorotational instability in a Taylor–Couette flow under the influence of a helical magnetic field. Phys. Rev. Lett. **97**(18), 184502 (2006)
102. Surdin, V.G.: Rozhdenie zvezd (Star Production). Editorial URSS, Moscow (1999)
103. Surdin, V.G.: Fundamental'nye vzaimodejstvija (Fundamental Interactions). In: Surdin, V.G. (ed.) Astronomiya: Vek XXI (Astronomy: XXIst Century), p. 8. Vek 2, Fryazino (2007)
104. Surdin, V.G. (ed.): Zvezdy (The Stars), 2nd edn. Astronomiya i astrofizika (Astronomy and Astrophysics). Fizmatlit, Moscow (2009)
105. Takabe, H.: Hydrodynamic instability, integrated code, laboratory astrophysics and astrophysics. In: Hora, H., Miley, G.H. (eds.) Edward Teller Lectures: Lasers and Inertial Fusion Energy, p. 313. Imperial College Press, London (2005)
106. Trunin, R.F.: Shock compressibility of condensed materials in strong shock waves generated by underground nuclear explosions. Phys. Usp. **37**(11), 1123 (1994)
107. Vacca, J.R. (ed.): The World's 20 Greatest Unsolved Problems. Prentice Hall PTR, Englewood Cliffs (2004)
108. Velikhov, E.P.: Stability of a plane Poiseuille flow of an ideally conducting fluid in a longitudinal magnetic field. Zh. Eksp. Teor. Fiz. **36**(4), 1192–1202 (1959)
109. Velikhov, E.P.: Stability of an ideally conducting liquid flowing between rotating cylinders in a magnetic field. Zh. Eksp. Teor. Fiz. **36**(5), 1398–1404 (1959)
110. Vladimirov, A.S., Voloshin, N.P., Nogin, V.N., et al.: Shock compressibility of aluminum at $p > 1$ Gbar. JETP Lett. **39**(2), 82 (1984)
111. Waxman, E.: Gamma-ray bursts and collisionless shocks. Plasma Phys. Controlled Fusion **48**(12B), B137–B151 (2006)
112. Witten, E.: Cosmic separation of phases. Phys. Rev. D **30**, 272–285 (1984)
113. Yakovlev, D.G.: Superfluidity in neutron stars. Phys. Usp. **44**(8), 823–826 (2001)
114. Yakovlev, D.G., Levenfish, K.P., Shibanov, Y.A.: Cooling of neutron stars and superfluidity in their cores. Phys. Usp. **42**(8), 737 (1999)
115. Zasov, A.V., Postnov, K.A.: Obshchaya astrofizika (General Astrophysics). Vek 2, Fryazino (2006)
116. Zasov, A.V., Surdin, V.G.: Raznoobrazie galaktik (A variety of galaxies). In: Surdin, V.G. (ed.) Astronomiya: Vek XXI (Astronomy: XXIst Century), p. 329. Vek 2, Fryazino (2007)
117. Zubko, V., Dwek, E., Arendt, R.G.: Interstellar dust models consistent with extinction, emission, and abundance constraints. Astrophys. J. Suppl. Ser. **152**(2), 211–249 (2004)

Chapter 10
High Energy Densities Outside of Compact Astrophysical Objects

In the previous chapter we considered the processes and effects inside of the cosmic objects compressed by gravitational forces to a compact size: planets, stars, etc. We now turn our attention to the discussion of high-energy objects in the remaining part of the Universe.

10.1 Cosmic Jets, Radiative Shock Waves and Molecular Clouds

At a certain stage of the evolution of a protostar, the excess parent gas flows off the protostar (Fig. 10.1 [150]). Massive protostars are typically characterized by a spherically symmetric outflow, because any unidirectional structures are destroyed here by radiation and the stellar wind. Typical for low-mass protostars and young stars are unidirectional gas flows, which are evidently due to the conversion of rotational energy to the kinetic energy of a jet [149]. The reason for the collimation of these jets and flows as well as one of their energy sources probably is circumstellar disks, which are about 1 pc in diameter and up to hundreds of $M_\odot$ in mass.

Axially symmetric flows [177] have long been discussed in connection with numerous astrophysical problems [109, 163, 177, 181]. Among the flows of this class are the accretion to ordinary stars and black holes [22, 143, 181], axially symmetric stellar (solar) wind [20, 101, 116, 154], jet ejections from young stellar objects [82], and the ejection of particles from the magnetospheres of rotating neutron stars [19, 100]. Magnetohydrodynamic (MHD) models are actively being developed also in connection with the theory of the structure of the magnetospheres of supermassive black holes, which are believed to be the "central engine" of active galactic nuclei and quasars [16, 120].

The interrelation [163] of different cosmic objects is illustrated in Fig. 10.2.

© Springer International Publishing Switzerland 2016

V.E. Fortov, *Extreme States of Matter*, Springer Series in Materials Science 216,
DOI 10.1007/978-3-319-18953-6_10

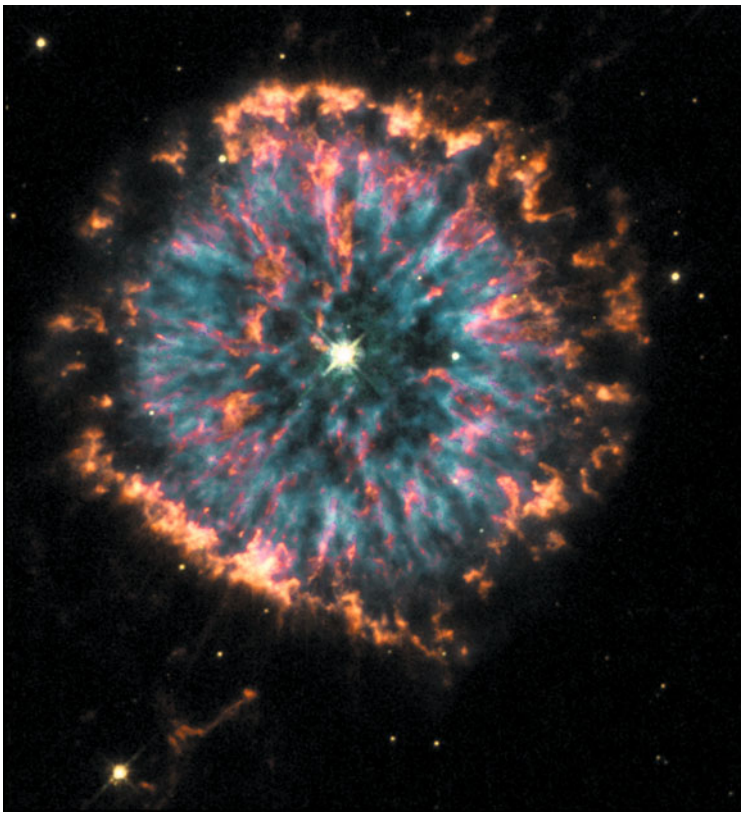

Fig. 10.1 Planetary nebula NGC 6751 in the Aquila constellation. One can see the streams of gas escaping from the central star. Photo from the Hubble Space Telescope [150]

10.1.1 Cosmic Jets

High-power ($\approx 10^{39}$ W), long (0.01–2 pc long), and well-collimated (with divergence angles of 5–20° and even less than 1°) differently directed molecular and plasma relativistic jets (with velocities up to $0.9c$) are observed in many active galaxies, quasars, and old compact stars [46, 109, 163, 177] (Figs. 9.5, 9.60, 10.3, and 10.4). In the case of the most active quasars, these jets are often accompanied by electromagnetic radiation with a wide spectrum—from radio-frequency emission $\approx 10^8$ Hz to superhard gamma-ray radiation with a frequency of 10^{27} Hz. Well-collimated jets with velocities of 100–300 km/s are also observed for many young stars.

Observations and theoretical analysis suggest that the acceleration and focusing of these plasma jets is effected by the magnetic fields rotating together with accretion disks, the fields taking the energy from the accretion masses or from the rotating black holes.

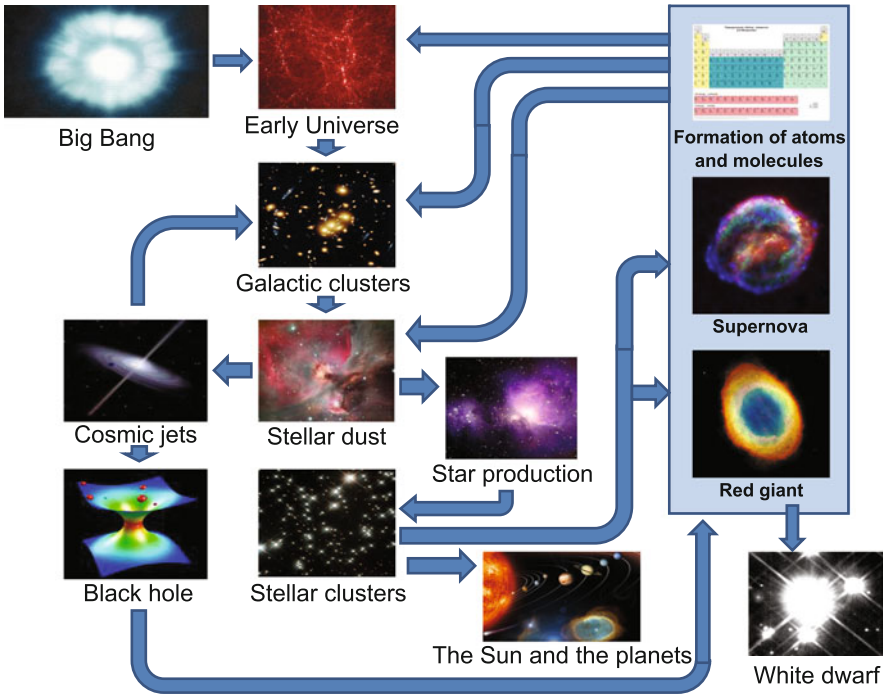

Fig. 10.2 Schematic of the interrelation between different cosmic objects [163]

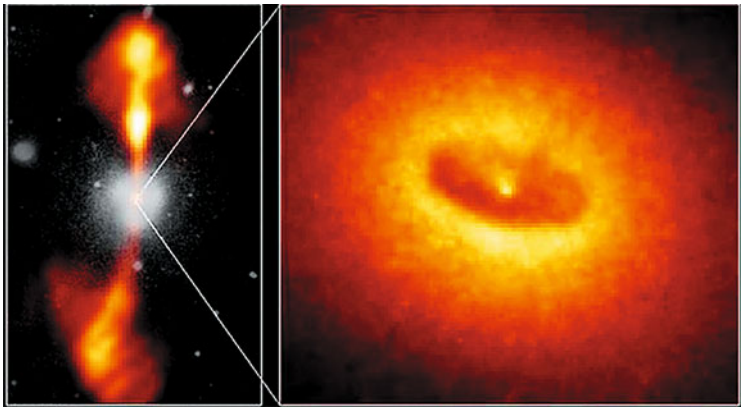

Fig. 10.3 Active elliptical galaxy NGC 4261 in the Virgo constellation is the high-power radio source 3C 270. *Left panel*: General view (at the frame center) with the image of elongated radio emission regions superimposed on it. Each of the radio emission streams has moved away from the galactic center by 20 kpc. *Right panel*: Photo of the central galactic region obtained from the Hubble Space Telescope. The galactic nucleus is surrounded by a massive gas-dust disk about 300 kpc in diameter [178]

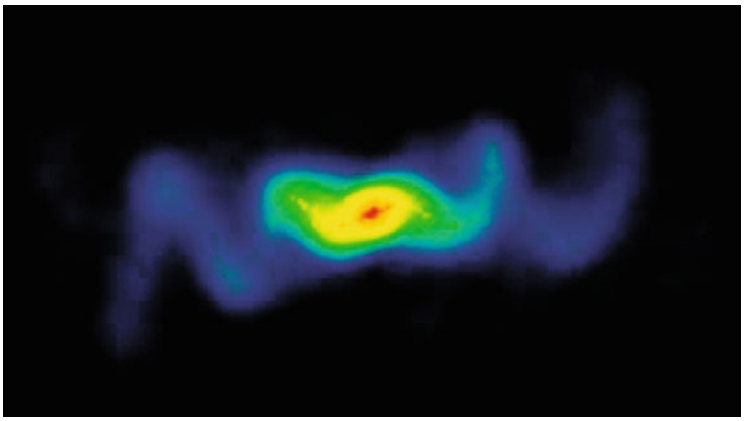

Fig. 10.4 Radio image of the jets from the black-hole candidate SS4333, which is part of a binary system with an ordinary star $M \sim 10M_{\odot}$, which emanates a strong stellar wind [163]

For many stellar objects the hydrodynamic [18, 44, 46] jet dynamics mode is realized, where the jet energy and angular momentum are generated by the electromagnetic field and kinetic energy of the ambient matter [109].

The hydrodynamic approach is underlain by the unipolar inductor model, i.e. the model of a constant current source [18]. All compact objects are really assumed to have a rapidly rotating central body (a black hole, a neutron or young star) and a regular magnetic field, which gives rise to strong induction electric fields. The electric fields in turn give rise to longitudinal electric currents and efficient particle acceleration. The collimation mechanism in this model is associated with the well-known property of attraction of parallel currents.

Following [18] we outline the basic propositions of the dynamic model of jet ejections. The center of a parent galaxy is assumed to accommodate a supermassive black hole (its mass ranges up to 10^6–$10^9\,M_{\odot}$), onto which there occurs accretion of the surrounding substance. In this case, the energy source of activity of galactic nuclei may be the energy of black hole rotation

$$E_{\text{tot}} = \frac{J_r \Omega^2}{2} \approx 10^{62} \left(\frac{M}{10^9 M_{\odot}} \right) \left(\frac{\Omega r_g}{c} \right) \text{ erg},$$

as well as the energy of accretion matter. Here, $r_g = 2GM/c^2$ is the black hole radius, J_r is the moment of inertia, Ω is the angular velocity of the black hole, M is its mass, and c is the velocity of light. The case for a supermassive object is favored by the fact that the Eddington luminosity

$$L_{\text{Edd}} \approx 10^{47} \left(\frac{M}{10^9\, M_{\odot}} \right) \text{ erg } \text{ cm}^{-1}$$

(i.e. the luminosity at which the force of radiation pressure is equal to the gravitational force acting on the accretion matter) is close to the typical luminosity

of active galactic nuclei [181]. Furthermore, the active phase duration $t_d = E_{\text{tot}}/L_{\text{Edd}}$ estimated by the previous formulas is of the order of 10^7 years, which also is in good agreement with observations.

Next, it is commonly assumed that the substance accretion is inherently disk-like. In this connection, there appears a preferred direction in space—the axis of rotation—along which jet elections are formed. Since a black hole itself cannot have an intrinsic magnetic field, the large-scale magnetic field in the neighborhood of a black hole is believed to be generated in the accretion disk.

According to modern views, massive central objects are present in the majority of galaxies and remain active until substance in sufficient amount is falling onto them. This limits the duration of their active life.

It will be recalled that the diffuse regions of radio emission near active galaxies, which are tens or sometimes hundreds of kiloparsecs away from their nuclei, were associated—almost immediately after their discovery in the early 1960s—with jet plasma ejections (jets) streaming from their nuclei. It is precisely the jets that deliver matter and energy to these domains, which the jets derive from the active nucleus (Fig. 10.5). Observations show that jets can be accelerated and collimated quite close to the galactic nucleus like, for instance, in the case of the nearest active galaxy (Fig. 10.6).

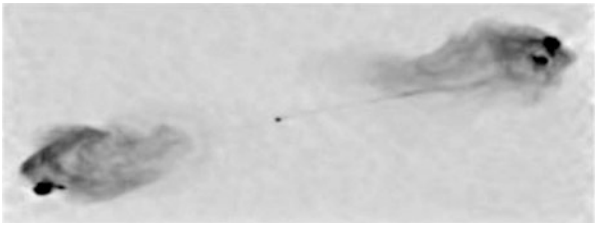

Fig. 10.5 Radio image (5 GHz) of the active regions and jets flowing from the nucleus of the galaxy Cygnus [18]. The distance between the bright regions is approximately equal to 80 kpc, which is 9–10 orders of magnitude longer than the size of the central black hole

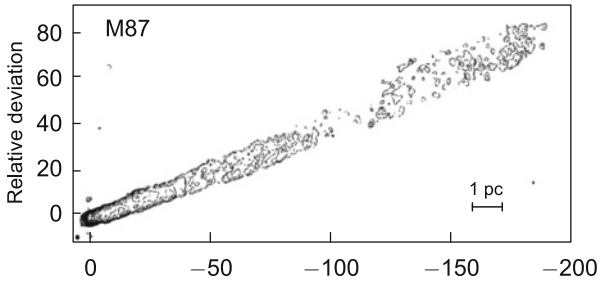

Fig. 10.6 Radio image of the jet ejection from the galaxy M87 near the central black hole. The transverse jet dimension is about 1 pc [18]

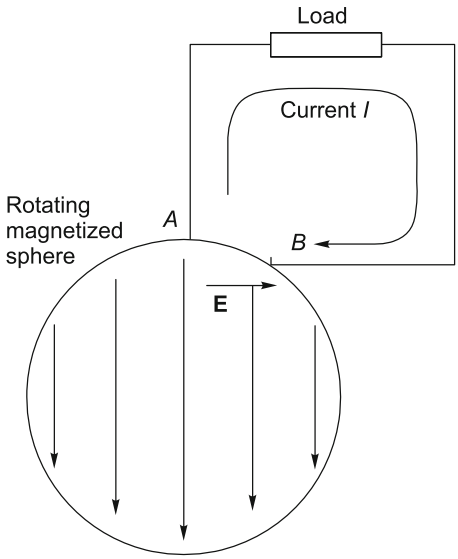

Fig. 10.7 Unipolar inductor—a direct current source. In a magnetized sphere the electric current flows in opposition to the electric field [18]

The matter of jets emanating from active galactic nuclei is of high energy: the Lorentz factor of a jet as a whole amounts to at least several units. In the galaxy M97, for instance, this motion is directly observed, the Lorentz factor of the emanating matter being $\gamma \approx 6$. In many cases, the matter retains its relativistic velocities up to huge distances from the nucleus before it appreciably slows down in the interaction with intergalactic matter. Another amazing property of the jets is their high degree of collimation: the divergence angle amounts to only several degrees.

The main MHD theory of compact objects is schematized in Fig. 10.7. In this unipolar induction model [18], as shown in Fig. 10.7, a rotating magnetized sphere can play the part of a battery which defines the energy release of the central engine. Under the assumption of a high conductivity of the sphere, the condition for magnetic field line freezing-in

$$E_{\text{in}} + \frac{\Omega x r}{c} x B_{\text{in}} = 0$$

leads to the emergence of a potential difference δU between points A and B. By the order of magnitude, this potential difference may be estimated as

$$\delta U \sim E R_0 \sim \frac{\Omega R_0^2}{c} B,$$

where R_0 is the transverse dimension of the work region. As a result the total energy release W_{tot} on the external resistor is

$$W_{\text{tot}} = I \delta U.$$

It is noteworthy [18] that the energy source in a unipolar inductor is the kinetic energy of rotation. As is clear from Fig. 10.7, the charges inside the sphere move in the opposite direction to the electric field. This becomes possible due to the force with which the lattice acts on the charges transferred along the conductor and therefore breaking the freezing-in condition inside the sphere. And, conversely, the Ampere force exerted by the surface electric current on the substance of the sphere results in its deceleration. So, the operation of the unipolar inductor (or, as it is sometimes called, the unipolar Faraday generator) is based not on the Faraday effect as such (when the EMF induced in a frame is due to the variation of magnetic flux), because the magnetic flux in the circuit remains invariable. The reverse situation is also possible: when a potential difference is applied to a magnetized sphere, the sphere begins to rotate.

The operation of the central engine necessitates:

- a rotating body,
- a regular magnetic field,
- a good conductor.

In this case, the current and hence the energy loss will be defined by the magnitude of the external resistance.

Transference of this model to real astrophysical objects is outlined in [18] and calls for a highly sophisticated analysis.

For extragalactic, microquasar, and gamma-burst jets, a different (Poynting) mechanism is thought to operate, in which the electromagnetic field is the main source. In any case, the jet velocities exceed the "escape velocity" sufficiently for the jets to leave the accretion disk.

The occurrence of bipolar streams in the evolution of a protostar appears to somewhat paradoxical: there occur simultaneously both accretion and jet efflux of matter. However, this is considered to be the principal mechanism by which the protostar can rid itself of the excess angular momentum and magnetic flux during collapse.

Of significant interest are recently discovered structures in the radio continuum and 21 cm line, which tower above the accretion disk, are referred to as "worms", and measure 100–300 pc. It is likely that they owe their origin to hot plasma streams emanating from star formation regions [149].

Laboratory experiments on plasma jets in collisional and collisionless regimes may be carried out in high-current Z-pinch facilities (Sect. 3.8). The energy exchange and the generation of radiation and shock waves may be studied in the collisional regime. By lowering the density of targets it is possible to model the penetration of the jets into the targets, their dynamics, and thermalization.

A comparison of radiative hydrodynamic processes in the laboratory and in astrophysics was made by Falize et al. [47], who found similarity criteria for the reproducibility conditions of radiative hydrodynamic phenomena.

In any case, the use of Z-pinches and lasers [38] has made it possible to obtain hydrodynamic plasma jets with Mach number $M \approx 5$–10, where $M = v/c_s$ and c_s is the velocity of sound, and strongly radiating jets with $M \approx 50$–60 [109, 172] in laboratory conditions. A new class of high-energy, electroneutral, and well-collimated proton jets with an energy up to 100 MeV was produced employing picosecond terawatt lasers [34, 74, 78, 89, 90, 105, 125].

The Poynting acceleration mechanism is close in geometry to the geometry of a magnetically shielded diode system with a potential $m_e c^2/e$ applied to it, which leads to the generation of intense charged-particle streams. The same pulsed high-current accelerators with an operating voltage of $\approx 10^6$ V [97, 162] are employed for the simulation of plasma jets from the accretion regions.

10.1.2 Radiative Shock Waves

Gigantic pulsed energy releases in astrophysical objects are inseparably linked with the generation of intense shock waves, solitons, and contact surfaces in cosmic plasmas [38, 109, 163, 177] (Fig. 10.8), which may be caused by a supernova explosion, stellar wind, a galactic spiral wave, or the mutual collision of clouds and stars, among others.

Fig. 10.8 Cat's Eye Nebula (NGC 6543) [107] located 1 kpc away from the Sun. Seen at the *center* is the remnant of the star that shed its plasma shells. Photo from the Hubble Space Telescope

When an explosion wave leaves a dense medium, its radiative cooling time becomes shorter than its hydrodynamic time. Such radiative explosion waves may emerge at the final stages of supernovae evolution, at the stage of the afterglow of gamma-ray bursts and supernovae.

In dense molecular clouds [109, 163, 177], the temperatures of shock-compressed plasmas range up to tens of millions of degrees. These waves are subject to radial oscillations if the cooling time increases slowly with temperature. Furthermore, dense cooled domains are sometimes longitudinally unstable. Extensive computer calculations have shown that the propagation rate of such radiative waves in the interstellar medium is $n = (d \ln R/d \ln t) \approx 1/3$, where R is the radius of the radiation waves ($R(t) \sim t^n$), t, is time and n the propagation rate, which is below the Sedov–Taylor rate of 2/5, but is higher than the simple self-similar limit of 2/7 [44]. That is why the study of radiative explosion waves in astrophysics is of significance, connecting complex hydrodynamic and radiative processes in plasmas (Fig. 10.9) [99, 165].

The study of radiative explosion waves (Fig. 10.10) in a laboratory requires the production of a strongly radiating, but optically thin domain of shock-compressed gas [38, 110]. Experiments at Lawrence Livermore National Laboratory with the Falcon short-pulse laser irradiating a xenon jet made it possible to produce and investigate radiative waves and to analyze their attenuation rate [173].

Nicolai et al. [110] investigated the structure, dynamics, and main parameters of laser-produced jets. By varying the gas parameters and its chemical composition they studied regimes ranging from the adiabatic to strongly radiating. It was possible to reproduce the basic features of astrophysical jets, such as the formation of detached shock waves, the region of shock-compressed plasma, a contact surface, and the Mach disk.

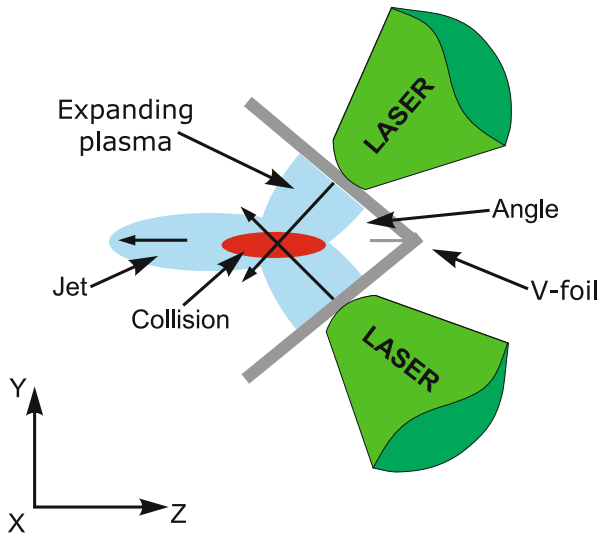

Fig. 10.9 Schematic of experiment [165] on laser generation of plasma jets. Two lasers irradiate thin foils of thickness 3–5 μm each, with the effect that the intersection of two backside jets produces a longitudinal jet

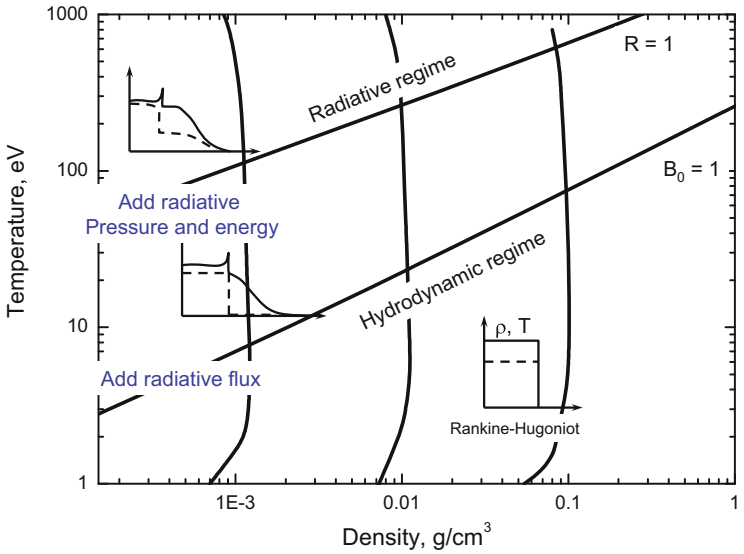

Fig. 10.10 Radiative shock waves in xenon. $R = E_{\text{th}}/E_{\text{rad}} = \frac{\frac{3}{2}\rho_0 T/m}{\frac{4\sigma}{3c}T^4}$. Here $B_0 = \frac{\rho_0 C_v T V_s}{\sigma T^4}$

Interstellar space is not empty or uniform (Figs. 10.11 and 10.12). It is filled with low-density matter, radiation, and a magnetic field with the corresponding characteristic energy density of $\approx$1 eV/cm^3. On average, 1 cm^3 of interstellar space contains no more than one hydrogen atom and far fewer other chemical elements. In 1 km^3 of this space there are no more than ten dust particles, measuring 1 μm each. The matter temperature varies over a wide range—from $\approx$10 K to 10^6 K. Dense gas and dust domains have come to be known as clouds (or nebulae), Figs. 10.13 and 10.14, of size 100–300 pc, up to $10^7 M_\odot$ in mass, and are classed as diffuse ($T \approx 10^2$–10^3 K, $n \approx 1$–10^2 cm^{-3}), dark (10–10^2 K, 10^2–10^4 cm^{-3}), molecular (5–50 K, 4×10^2–10^6 cm^{-3}), or globular (10–30 K, 10^3–10^6 cm^{-3}). It is likely that some of them came into being in the regions of active star formation, and the emergence of molecules in turn is an indication that the medium has cooled down, become denser, and is ready for star formation [149]. A wide spectrum of molecules has been discovered, up to structures containing 13 atoms (cyano-decapeptide), which are produced in gas-phase ion reactions and on the surface of dust particles possessing catalytic properties. Surdin [149] showed that the simplest molecules are formed in 10^4–10^5 years, while it takes tens of millions of years to form a 10–13 atom molecule.

Fig. 10.11 Milky Way in the direction of the Norma constellation in the infrared range. The *central strip*: a 9″-long and 2″-wide part of the Milky Way. *Top* and *bottom rows*: Enlarged fragments of the central image that show typical objects and structures of the Milky Way—star formation regions, dense and diffuse interstellar clouds, and planetary nebulae. The photos were made by the NASA Spitzer Space Telescope in the 3.6–8.0 μm infrared range in 2005 [108]

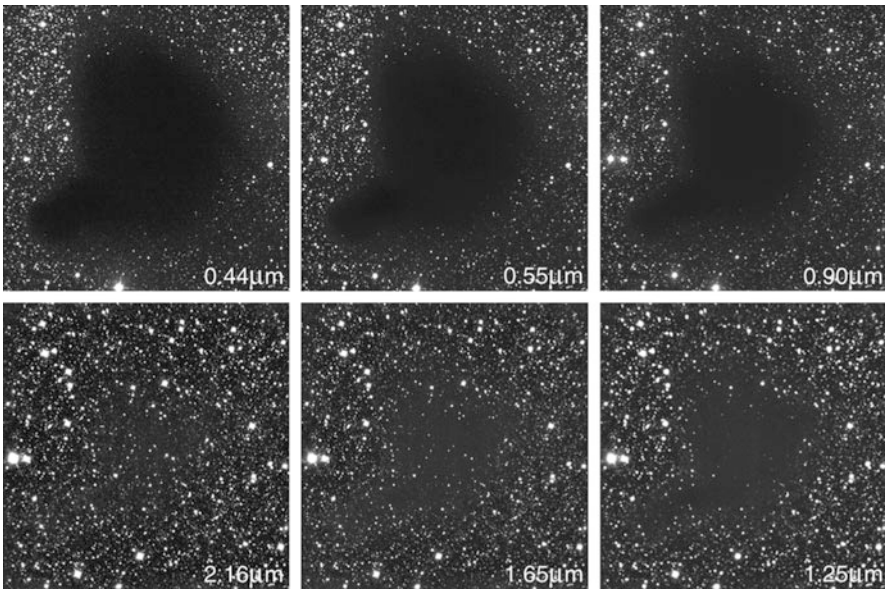

Fig. 10.12 Gas-dust cloud B 68 measuring 0.2 pc in the Ophiuchus constellation located 150 pc away from the Earth. No stars are seen behind it in the visible range (the *first photo*). However, infrared rays experience weaker absorption by the interstellar dust, and the cloud becomes progressively more transparent with increasing wavelength (indicated in micrometers). Photo from the ESO VLT Telescope [43, 150]

Dust particles ranging from 0.01 μm to 0.2–0.3 μm in size are present in the interstellar medium and participate in the catalytic synthesis of molecules, entrap stellar radiation and transfer its momentum to the interstellar gas, thereby participating in the radiation balance, and are, of course, an important factor in star and planet formation. Although the dust mass is only 0.03 % of the total mass of the galaxy, its luminosity amounts to 30 % of stellar luminosity and completely determines the IR radiation of the galaxy (see Fig. 9.1). The radiation-induced expulsion of dust from the atmospheres of red giants as well as nova and supernova explosions are the main dust generators in space [(3–4) $\times 10^{-3} M_{\odot}$ per year].

According to estimates, in our Galaxy the number of planetary nebulae located within tens of parsecs away from us lies in a range from 8000 to 40,000 [151].

10.1.3 Molecular Clouds

The equilibrium in giant molecular clouds is maintained by gravitational forces and the dynamic pressure of large-scale matter streams, such as collimated jets up to 10^{37} erg/s in power, shock waves, collisions with other clouds, and star

Fig. 10.13 Cone Nebula (NGC 2264) [107]

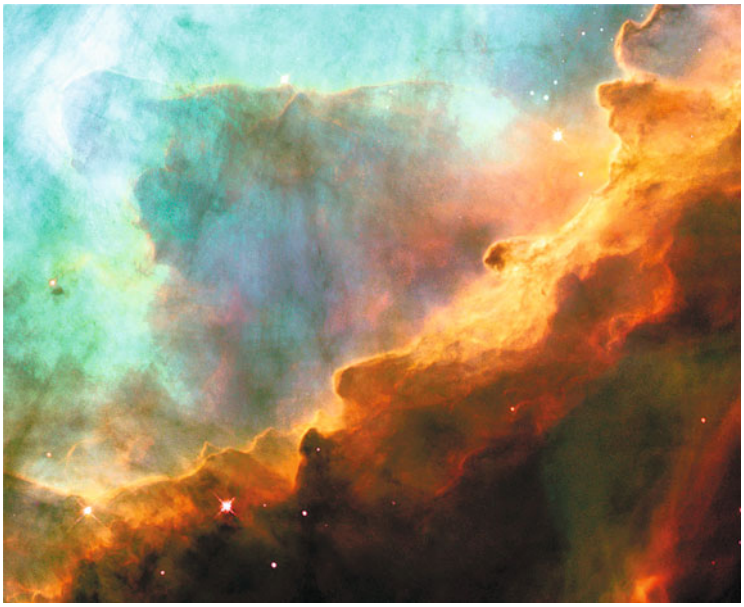

Fig. 10.14 Omega/Swan Nebula (M17) [107]

formation [149]. The last-named process eventually ruins the molecular clouds, which last up to 10^7–10^8 years on the average. On the other hand, massive interstellar clouds themselves may exert a destructive effect on stellar clusters (for more details, see [149]).

The precursors of planetary nebulae are classed with intermediate-mass stars: from 0.8 to $8\,M_\odot$ [151]. The stars of initial mass $> 8\,M_\odot$ in the main sequence do not go through the stage of a planetary nebula but experience a core collapse, flare up in this case as supernovae and shed their massive shell, and their core turns into a neutron star or a black hole. The stars of mass smaller than $0.8\,M_\odot$ cannot produce a planetary nebula: they turn into carbon-oxygen white dwarfs.

Several models are discussed in the analysis of interstellar cloud formation: agglomeration in accidental collisions, the Parker (or magnetic Rayleigh–Taylor) instability, the gravitational (Jeans) instability, and gas densification by the expanding gas shells around star formation domains.

The amount of interstellar gas in galaxies depends on many factors [177]—star formation, gas shedding by post-evolution stars (Figs. 10.8 and 10.15), accretion onto a galaxy, etc. Atomic and molecular gas accounts for the bulk of gas mass in disk galaxies (Fig. 10.16 [168]). About 97 % of the mass is accounted for

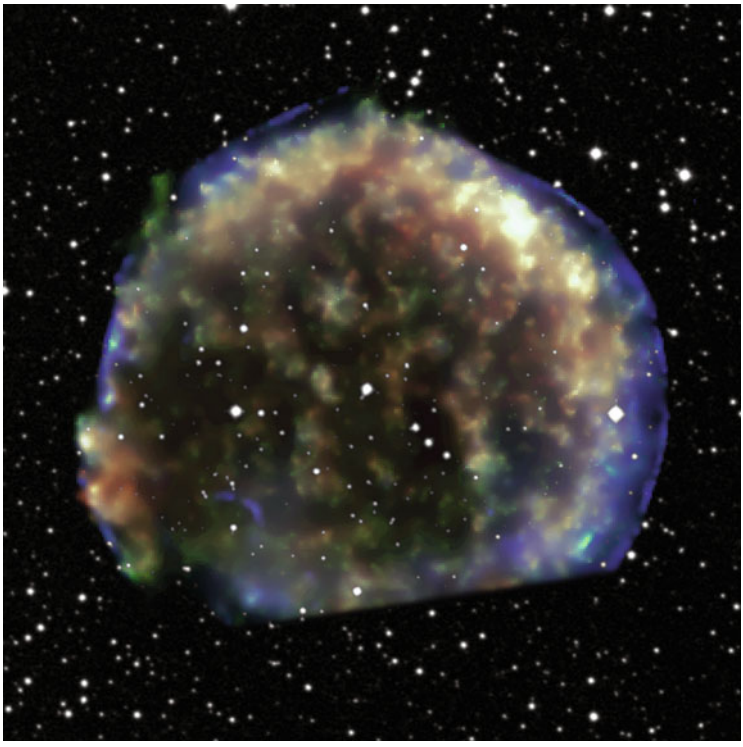

Fig. 10.15 Image of the result of the Tycho (SN 1572) supernova explosion [38]

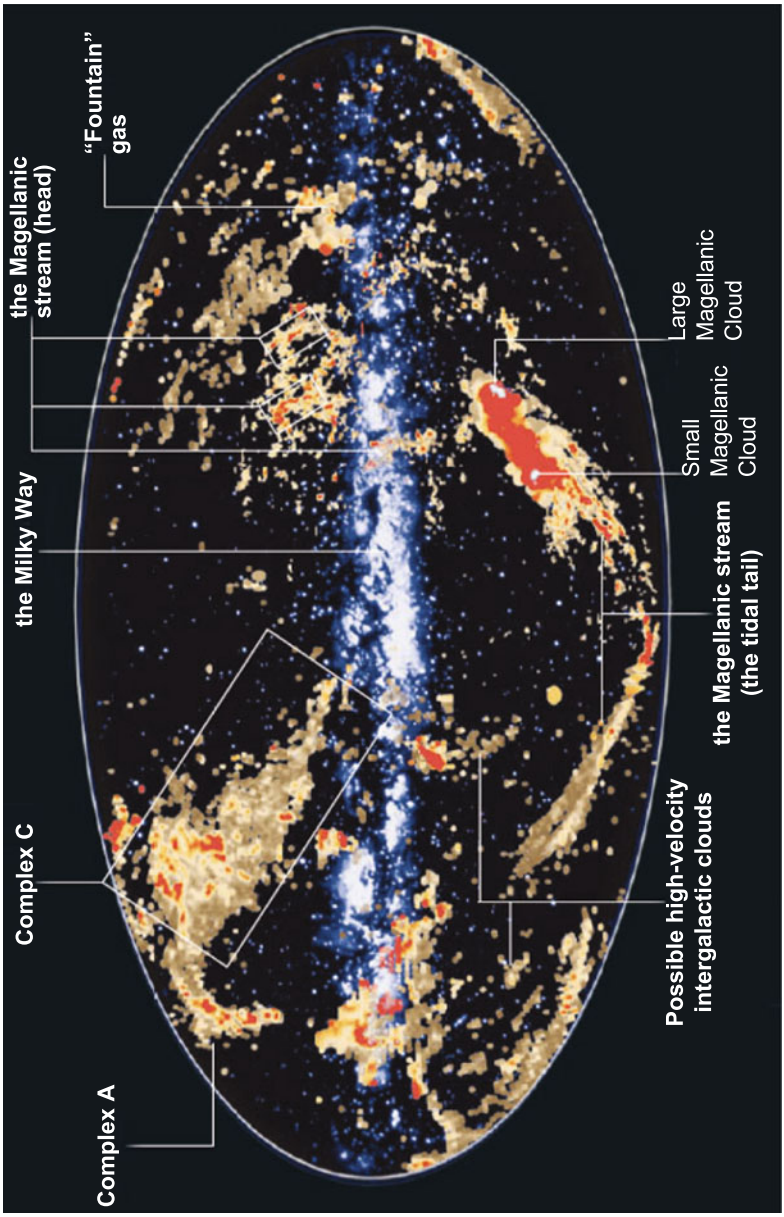

Fig. 10.16 Galactic gas distribution constructed from the data on neutral hydrogen distribution (*colored spots*) and superimposed on the image of the galaxy in visible light (*white color*). The galactic disk is viewed from the side; the galactic nucleus is at the *center*. High-velocity hydrogen clouds (in particular, the complexes A and C) can be seen above and below the disk [168]

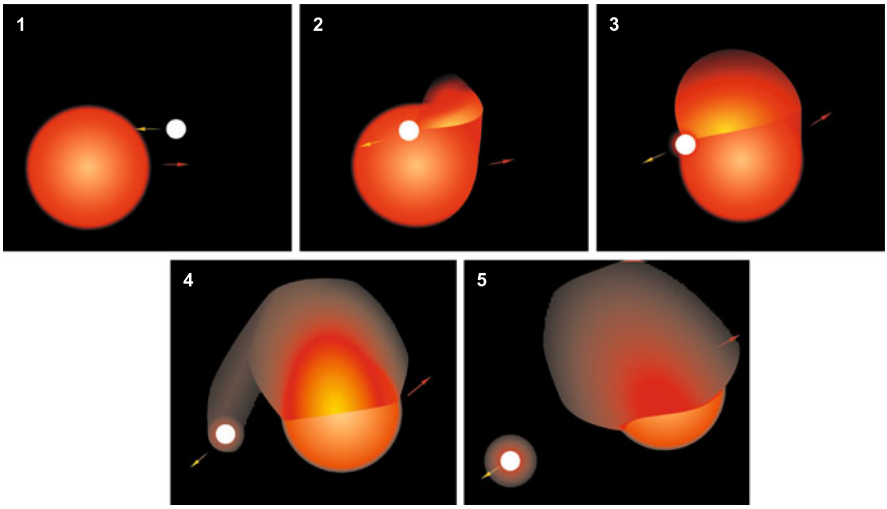

Fig. 10.17 Collision of a white dwarf with an inflated red giant [144]. The dwarf remains intact on collision and entrains a part of the gas of the giant. The giant itself disintegrates, although its nucleus remains intact, and transforms into another white dwarf

by hydrogen (70–75 %) and helium (20–25 %). The interstellar gas medium is nonuniform (Fig. 10.16 [168]) on many scales due to density waves, shock waves, solitons, and hot or, conversely, cold giant clouds. The hot, or coronal, gas has a temperature of $\approx 10^5$–10^6 K and dimensions of hundreds of parsecs. It owes its origin to the activity of young stars: stellar wind, star formation, supernova bursts, etc. The hot gas in giant galaxies results from the ejection of the gas shell by red giants in the course of their evolution or collision (for instance, with a white dwarf, Fig. 10.17 [144]). Since a substantial energy fraction of a supernova explosion is transferred to the ambient medium, there emerge expanding regions of hot gas (Fig. 10.18 [178]) and shock waves propagating through the interstellar gas. They foster star formation by compressing dense gas regions, speeding up their cooling and further compression, thereby giving impetus to star formation (Fig. 10.19). The same role is played by the shock waves generated by strong tidal interactions in compact galactic systems. That is why cool and dense molecular clouds illuminated by bright and young nearby massive stars fulfill the role of a "stellar incubator" in the universe (Figs. 10.13, 10.14, 10.20, 10.21, and 10.22).

The high-intensity stellar radiation incident on the clouds produces ablation pressure, which is supplemented by the pressure of the stellar wind (Fig. 10.23 [1]). As a result, the cloud is compressed by shock waves and set in motion away from the radiating object. The Cone (Fig. 10.13), Omega (Fig. 10.14), Rosette, and NGC 3603 nebulae are good cases in point. The interest in dense molecular clouds located near bright stars arises from the hypothesis that they are the birthplace of new stars [177]. Great interest is aroused by the shape of extraordinary columns in nebulae (Fig. 10.13), which might have resulted from Rayleigh–Taylor type [44]

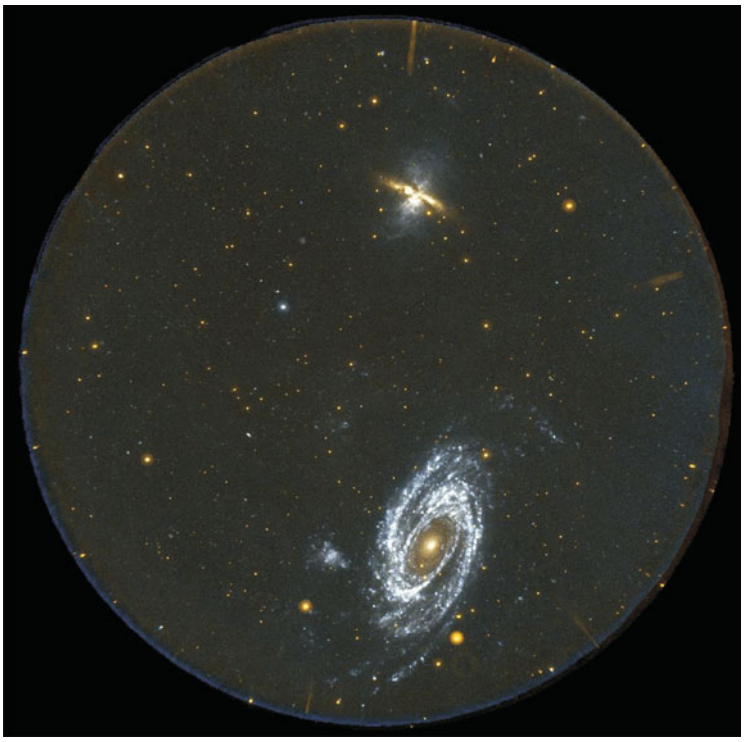

Fig. 10.18 Galaxies M81 (*bottom*) and M82 (*top*) viewed in the ultraviolet spectral range. The explosive nature of star formation in M82 is demonstrated by the ejection of gas heated by the stars of the central part of the galaxy [178]

instabilities of the ablation front. An alternative explanation relies on the "cometary" model, whereby the matter under irradiation is carried out from the dense regions to the clouds, as is the case in cometary tails.

Observations made with the Hubble Space Telescope [107] and the ground-based BIMA millimeter interferometer yielded valuable information about the velocity distribution and the matter dynamics inside the clouds, making it possible to verify many hypotheses for the radiative matter dynamics, the role of the cloud matter in the formation of stars, etc. (Figs. 10.24 and 10.25).

Molecular gas is observed not only in the CO line but also in OH, H_2, NH_3, HCN, and HCO^+ lines. This is indication that molecules persist for a long time after nebula ionization. Dust protects them from the hard radiation of the core and, in doing this, heats up to become a source of IR radiation.

In many astrophysical objects, along with the charged component, there is a significant admixture of neutral atoms and molecules [28]. In the galactic disk, apart from hot, rarefied, and completely ionized caverns with a temperature $T \approx 10^6\,\mathrm{K}$ and a density $n \approx 2 \cdot 10^{-3}$ ions/cm^3, there is a "warm" phase ($T \approx 10^4\,\mathrm{K}$,

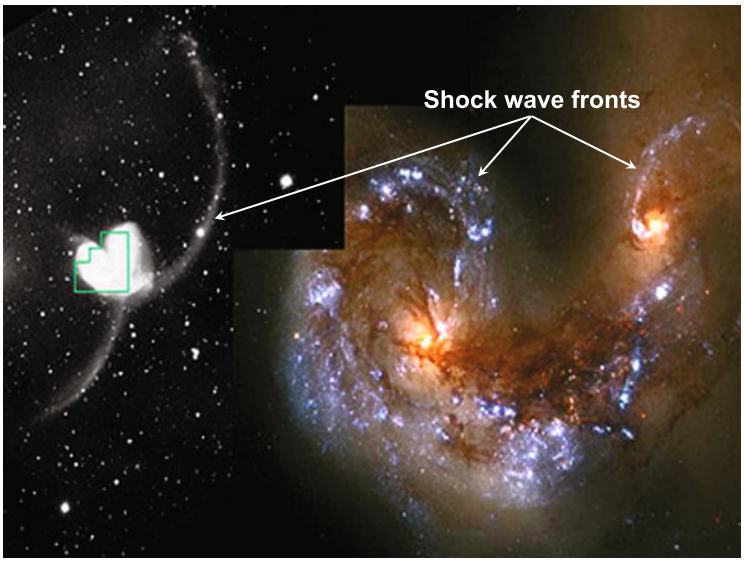

Fig. 10.19 The interacting Antennae Galaxies (NGC4038/9). At the *right*: A photo from the Hubble Space Telescope shows active star formation in the central regions of the merging galaxies [178], including shock wave fronts

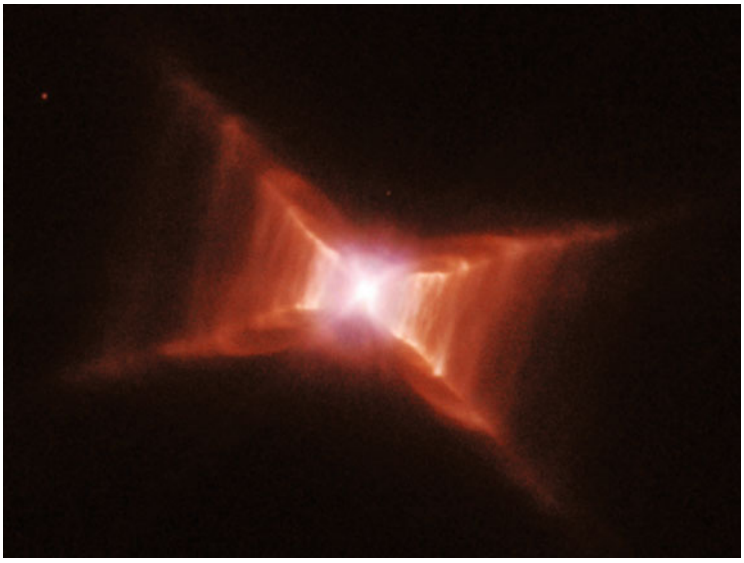

Fig. 10.20 The Red Rectangle Nebula, which surrounds the star HD 44179. One can see the ejected gas jets [14]

Fig. 10.21 Newborn stellar cluster (region N90) surrounded by the residual gas of which it was formed [150]

$n \approx 0.2\,\text{particles/cm}^3$), in which the degree of ionization is about 0.1 and which occupies tens of percent of the volume. In cool neutral clouds, which are the main sources of star formation and frequently contain rapidly evolving young active stars, the matter density is 2–3 orders of magnitude higher but the temperature and the degree of ionization lower. Also quite low is the degree of matter ionization in the photospheres of the Sun and many stars. In the solar photosphere it is only about 10^{-3}. In all of the mentioned and many other objects, apart from the partly ionized background plasma, there also are suprathermal particles, relativistic (cosmic rays) and nonrelativistic, whose sources may be located in the object under consideration as well as far beyond it. It goes without saying that similar conditions are also possible in the objects of terrestrial origin (the ionosphere) [28].

10.1.4 Planetary Nebulae

A planetary nebula is, to a first approximation, an ionized gas shell surrounding a hot star (core) at its center. Outer shell regions may contain neutral gas [151].

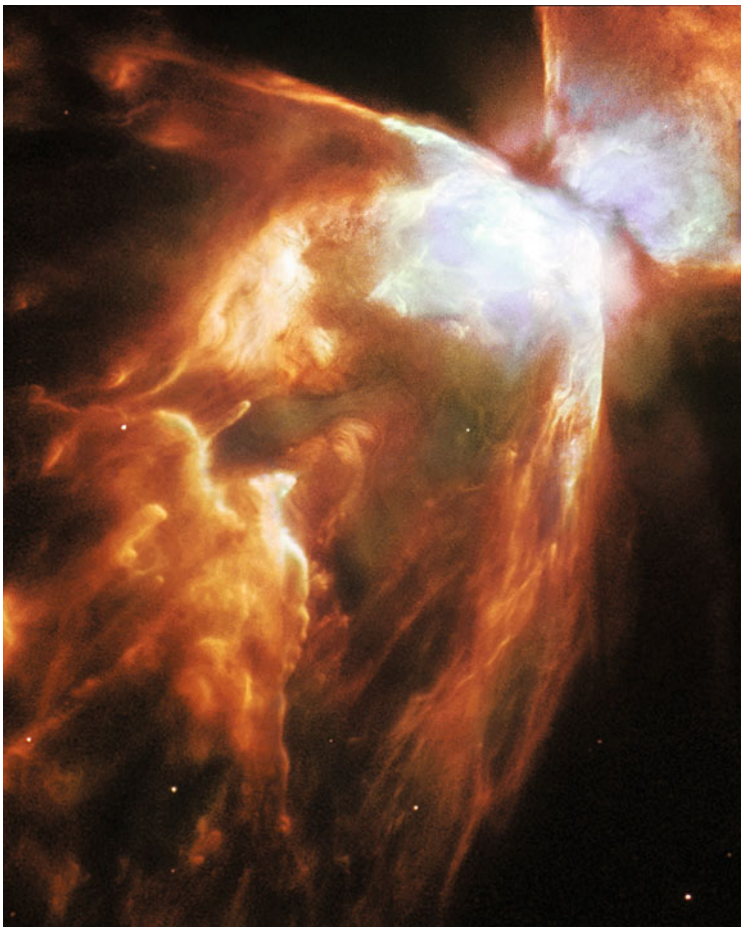

Fig. 10.22 At the *top right* of the photo is the central star of the planetary nebula NGC 6302—one of the hottest—surrounded by a dense, dusty, and carbon-saturated torus [14]

Not only are dust particles present in the interstellar medium and molecular clouds, but they can also form dust clouds of their own, which are detected by excess infrared radiation. Today more than 100 young planets are known with gas-dust disks that contain the matter of a planetary system under formation [149]. An analysis of the IR spectra of the dust disks suggests that the particle dimensions are rather large—from 0.5 μm to several centimeters.

The jet dynamics of dust clouds and dust disks is affected by the fact that the dust particles may be charged (owing to photoionization) and form a so-called dust plasma [51], which possesses unusual properties in many respects and, as evidenced by experiments, increased viscosity (for more details, see [50, 51]).

Planetary nebulae play an important role in the evolution of the interstellar galactic medium. They deliver matter to this medium for the formation of next-

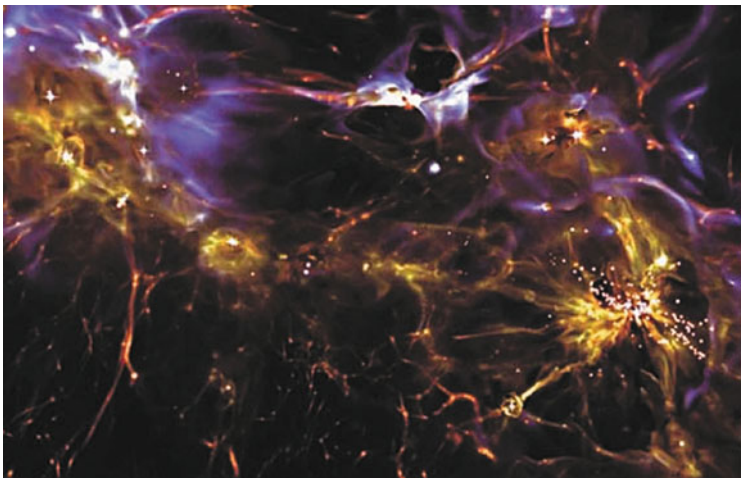

Fig. 10.23 Mathematical simulation [1] of the origination of galaxies

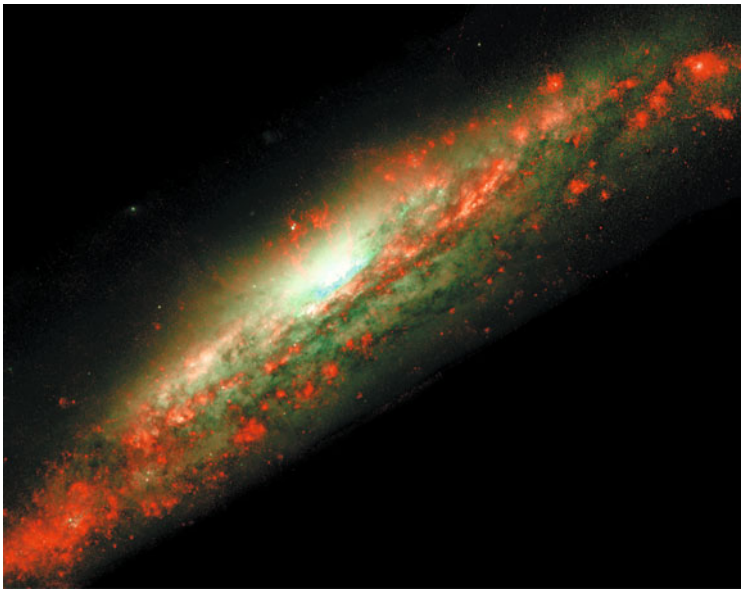

Fig. 10.24 Photo of the galaxy NGC 3079 obtained from the Hubble Space Telescope, which demonstrates the high activity of the nucleus. Hot gas ejections into intergalactic space provide the material for the production of young stars [163]

generation stars; as this takes place, the medium is enriched in the products of nucleosynthesis from the interior of the star that generated this nebula [151].

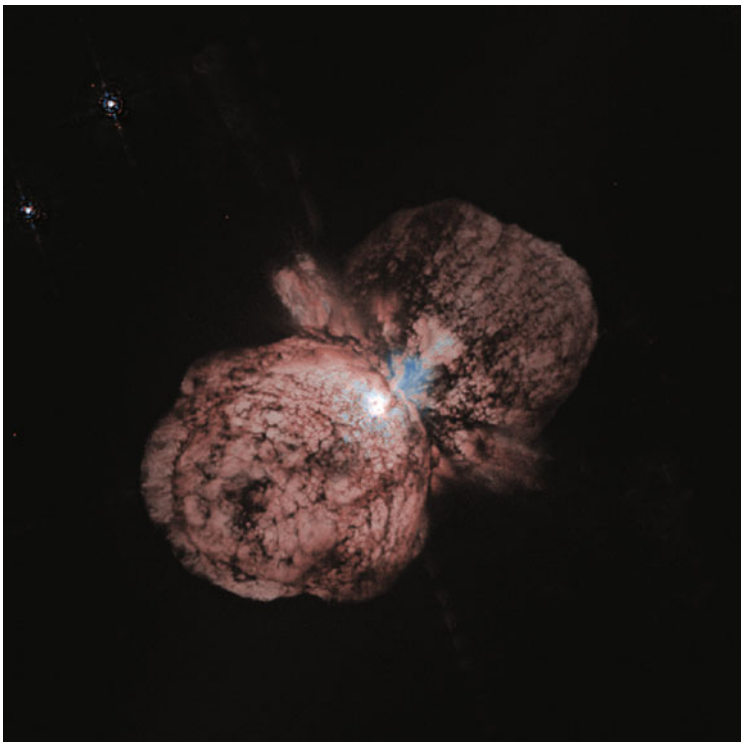

Fig. 10.25 Huge gas and dust clouds from the supermassive star Eta Carinae are the material for new stellar objects [107, 163]

In our Galaxy a new planetary nebula is formed approximately once a year. The mass which the stars return to the interstellar medium in the form of a solar wind and a dispersing planetary nebula amounts to $3.3\,M_{\odot}$ per year.

Approximately 95 % of all stars in the Galaxy end their evolution in the form of a white dwarf. Approximately 60 % of them go through this stage rather quickly to ionize their shells and form planetary nebulae. Data about these nebulae yield estimates of stellar dying in the Galaxy in the modern era and permit judging about the history of star formation in it [151].

Although planetary nebulae are visually bright objects due to their emission lines, they do not make a significant contribution to the optical brightness of galaxies, because they are small in number due to their short lifetime. However, since low-mass stars in the post-asymptotic stage evolve too slowly to ionize their shed nebulae, the stars may be a source of significant ultraviolet galactic luminosity.

To describe the initial phase of spontaneous star formation, different models [1, 149] are taken advantage of: the gravitational (Jeans) model generalized to the case of general relativity theory by Lifshits [85], the magnetohydrodynamic model, thermal instability, as well as the model of shock-wave compression of interstellar

matter. Along with spontaneous star formation, also considered is induced formation stimulated by the explosion in the birth of a neighboring star, which gives rise to compression waves and a "chain" reaction of star formation [85]. In support of this stimulated mechanism we mention the domain around the emission nebula Omega (M17). On one side of this nebula there is a gas-free space with a group of young stars (in the emission nebula itself there are even younger stars), and on the other side there is a molecular cloud with indications of star formation.

Imshennik and coworkers [73] also provide other examples of stimulated star formation waves traveling along one molecular cloud on a $\approx$100 pc scale. Conceivably, in this case an analogy with the propagation of combustion and detonation waves through chemically active media is appropriate. The more so as Öpik [114] came up with the idea that the shock wave from a supernova explosion triggers star formation. The mechanisms of interstellar cloud compression by external radiation pressure and the idea of the instability of the gas shells compressed by the stellar wind stream were considered as the mechanism for the triggering of the self-propagating or epidemic wave of star formation. At the same time, the birth of a star and a stellar system in the parent cloud frequently leads to its disintegration and may lend impetus to the formation of new interstellar clouds.

The exchange of matter between stars and the interstellar medium is schematized in Fig. 10.26 [149]. The interstellar medium is constantly replenished with the material of stars in their explosion, while the stars themselves are produced from the interstellar medium (Fig. 10.27 [136], Fig. 10.28 [69]). In this case, from this turnover there steadily drop out the indestructible remnants of evolution: white dwarfs, neutron stars, black holes, and planets. By and large the stars of mass 1 $M_\odot$ return 40 % of their matter to the interstellar medium and a star of mass $9M_\odot$ more than 90 % [149]. The total stellar mass flux into the interstellar medium is $\sim 1 M_\odot$ per year, while the gas inside the interstellar medium passes from the diffuse medium to molecular clouds and back with a rate of $10^2 M_\odot$ per year, the expenditure of material for star formation amounting to only $\approx$1–3 % of the latter figure.

However, by no means all of this baryon matter is as easily observable as the matter that finds its way into bright stars, nebulae, and other visible objects [54]. The matter is that, should we collect all the matter visible in telescopes, the result will account for only tenths of the total amount of matter which resulted from the Big Bang. This deficit of substance is not related to "dark" energy and "dark" matter (96 % of observable Universe) and relates to the remaining 4 % of baryon matter [54].

The initial amount of baryon density after the Big Bang is estimated [54] from the relict microwave radiation and is done independently in the content of helium, lithium, and deuterium. This gives 4 % of the total mass of the Universe. Entering in the composition of galaxies [54], baryons are omnipresent: in stars, stellar remnants, neutral gases (atomic as well as molecular), ionized gases, dust, planets, and finally in human beings.

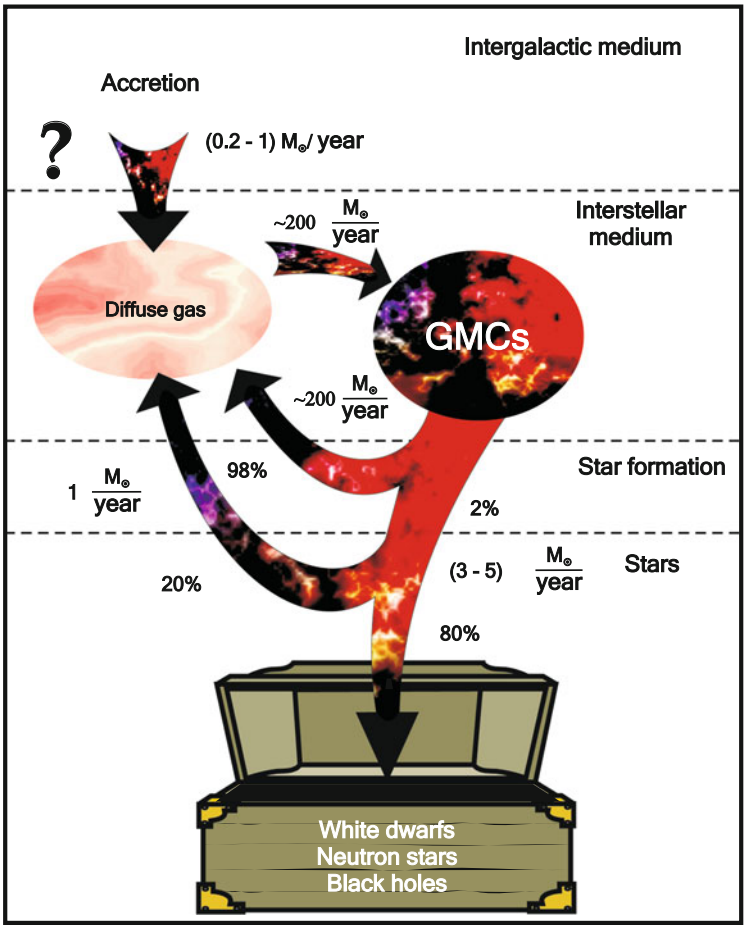

Fig. 10.26 Matter exchange between the stars and the intergalactic medium [149]

With the use of electromagnetic spectra, the amount of observable baryons is estimated at only 10 % of the initial amount of baryons which were present in the early Universe. The missing baryons are perhaps in the elusive state of warm-hot intergalactic medium (WHIM) [54]. If attempts to confirm the existence of this matter and precisely determine its localization meet with success, then may be, it will suffice to account for the fate of the missing baryons [54].

The existence of WHIM may explain the low efficiency of galaxy production. The evolution of a large-scale structure has the effect that the intergalactic gas becomes too tenuous and hot (ions are heated by their acceleration in gravitational fields) to assemble in dense cool clouds required for the formation of galaxies. However, a part of the baryons did form galaxies—otherwise neither stars, nor planets, nor you and I would have come into existence [54].

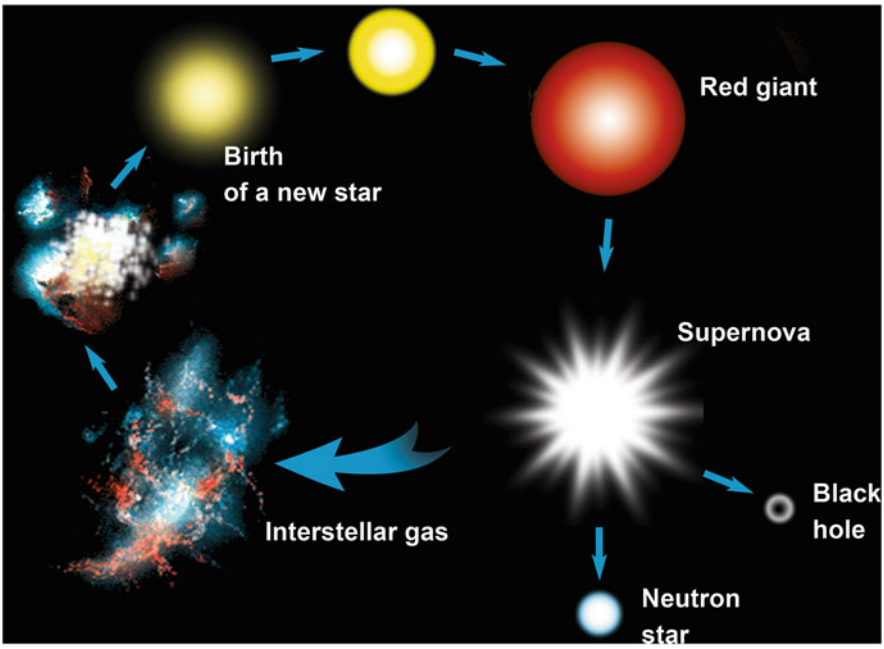

Fig. 10.27 Matter turnover in galaxies. A typical young star comes into being in a gas cloud, is in a quasi-stationary state for a long time, as our Sun is now, and passes into the stage of a red giant upon exhaustion of hydrogen. A red giant explodes to deliver heavy elements into ambient space and replenish the gas clouds with the nuclei of heavy chemical elements [136]

In earlier eras, the galaxy formation was more efficient. About 8 billion years ago the average rate of star formation was 10–20 times higher than today. The majority of galaxies which we now observe were formed at precisely that period.

The baryon exchange between galaxies and their surrounding space is of importance not only for the investigation of galactic evolution, but also for the verification of the WHIM [54]. Due to the continuous processes of cooling and heating, baryons circulate between the intergalactic space, stars, and galactic gas. Constantly fought is the "battle" for baryons: galaxies grow by winning them from the ambient space. Estimates suggest that about half of the baryons that now are present in one or other galaxy observed by astronomers have visited the intergalactic space at least once. Most likely, this cycle took place many times. The baryons which your body consists of would have participated in this cycle with a periodicity of about once in 14 billion years.

This baryon conception [54] shows that the evolution of galaxies is merely a small part of the large-scale evolution of the intergalactic medium. Galaxies are no more than one of the many cyclic baryon transformation processes most of which

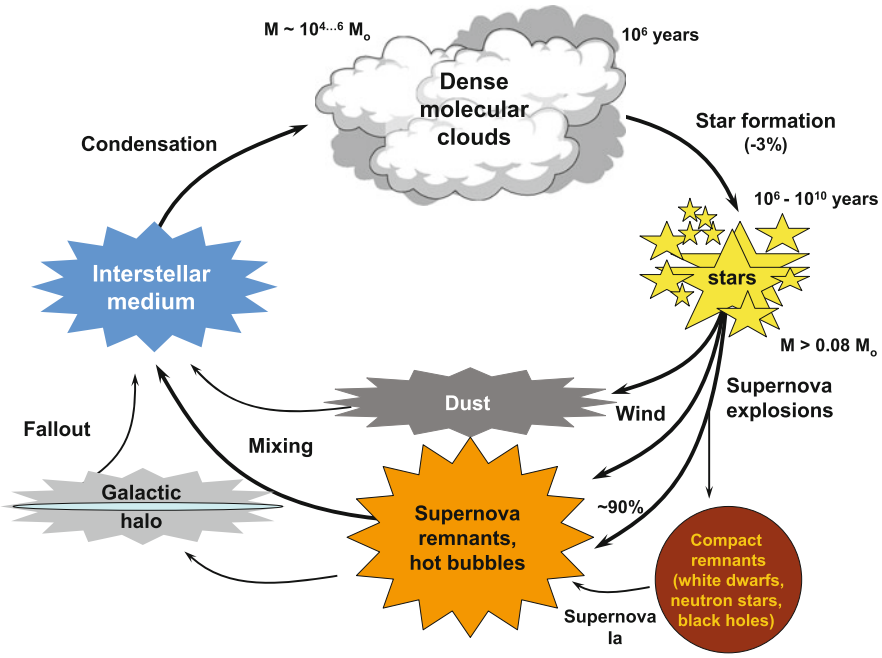

Fig. 10.28 Dynamics of the formation of cosmic structures [69]

occur outside of the galaxies. According to the anthropic principle (see Sect. 10.4.6), we fortunately appeared at the place and time where baryons were in a stable state. In other places of our Universe or in other epochs this is not nearly so. On dying 5 in billion years (see Sect. 9.2.2), the Sun would incinerate the inner planets of our system, the outer ones will be vaporized, and heavy elements will find their way into the interstellar space, but certainly without us.

10.1.5 "Dark" Matter and "Dark" Energy

While on the subject of matter transformation in the universe, we cannot help mentioning the problem of "dark" matter and "dark" energy, which has intrigued researchers since 1998–1999. According to contemporary notions [134], about 70–75 % of the mass–energy in the universe is accounted for by the so-called "dark" energy, Fig. 10.29 and Table 10.1, which manifests itself only via gravitational effects and is not directly related to known particles. It might be represented by Einstein's cosmological constant [33].

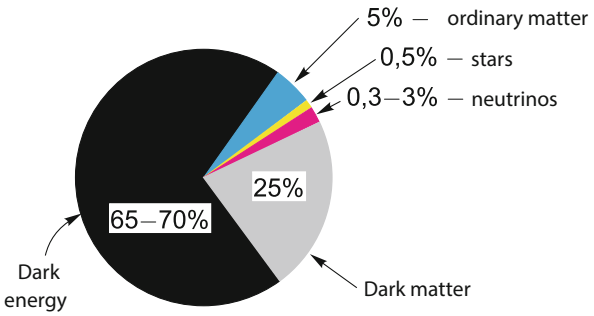

Fig. 10.29 Energy balance in the modern universe [134]

While on the subject of matter transformation in the Universe, there is no escape from mentioning the problem of "dark" matter and "dark" energy, which has fascinated researchers since 1998–1999. According to modern views [61, 134], the so-called "dark" energy (Fig. 10.29, Table 10.1) comprises approximately 70–75 % of the mass-energy of the Universe, manifests itself only via gravitational effects, and is not related directly to the known particles. It may be represented by Einstein's cosmological constant [33].

The advent [88] of the notion that in nature there exists dark energy—a weakly interacting physical substance which runs through the entire space of the visible Universe—was the number one sensation in the physics of the end of the twentieth century and came as a surprise to the majority of researchers, especially to those working at the junction of cosmology and elementary particle physics. The matter is that the known energy scales typical for fundamental interactions are of the order of 1 GeV (strong interactions), 100 GeV (electroweak interactions), and 10^{19} GeV (gravitational interactions), and there were no grounds to believe that in nature there exist one more, much lower energy scale. However, it turned out that dark energy is characterized by a scale $E_v \approx 10^{-3}$ eV determined by the fact that the dark energy density $\rho_v = E_v$.

Furthermore, in the modern Universe there holds, to within one order of magnitude, an approximate equality

$$\rho_v \approx \rho_D \approx \rho_B,$$

where ρ_D and ρ_B are the dark matter and baryon mass densities. For this equality there are no and have never been any evident a priori grounds of any value [88]. We emphasize that the approximate equality $\rho_D \approx \rho_B$ is true at any instant of cosmological evolution after the formation of baryon asymmetry and the generation of dark matter, because ρ_D and ρ_B decrease in a similar way—and rather rapidly—in the expansion of the Universe. On the other hand, ρ_v depends only slightly or not at all on time, so that the equality $\rho_v \approx \rho_D$ is true in precisely the modern epoch, after the emergence of the structure of the Universe and the appearance of stars.

Table 10.1 Composition of the universe [144]

Substance	Typical particles	Typical particle mass (energy) [eV]	Number of particles in the visually graspable universe	Probable contribution to the total mass of the universe [%]	Evidence for its existence
Ordinary ("baryonic") matter	Protons, electrons	$10^6 \ldots 10^9$	10^{78}	5	Direct observations, estimate of element abundance
Radiation	Photons of the microwave cosmic background	10^{-4}	10^{87}	0.005	Observations with radio telescopes
Hot dark matter	Neutrinos	≤ 1	10^{87}	0.3	Neutrino measurements, models of galaxy formation
Cold dark matter	Supersymmetric particles	10^{11}	10^{77}	25	Estimate from galaxy dynamics
Dark matter	"Scalar" particles	10^{-30} (assuming that dark energy comprises particles)	10^{118}	70	Acceleration of universe expansion from the data of supernova observations

One of independent arguments is as follows. An analysis of the data of galactic catalogues on spatial matter distribution and the use of several different methods for determining the mass of clusterized ("aggregated") matter in combination with measurements of relict radiation anisotropy and the Hubble parameter have led to recognition [88] that the total mass density of nonrelativistic matter, which makes up the nonuniform structure of our Universe—galaxies and their formations (groups, clusters, chains, walls, superclusters, voids)—does not exceed 30 % of the critical density ρ_c:

$$\Omega_{\mathrm{M}} \equiv \frac{\rho_{\mathrm{M}}}{\rho_c} \lesssim 0.3,$$

where

$$\rho_{\mathrm{M}} = \rho_{\mathrm{D}} + \rho_{\mathrm{B}}, \quad \rho_c = \frac{3H_0^2}{8\pi G} \simeq 10^{-29}\,\mathrm{g/cm^3},$$

and $H_0 \simeq 70\,\mathrm{km/(s\,Mpc)}$ is the Hubble constant. This is one of the most important results in modern cosmology. Its interpretation, which prevailed for a rather long time, was that the Universe possessed a nonzero spatial curvature.

However, this interpretation encountered difficulties. First, from the theoretical viewpoint an appreciable spatial curvature is extremely hard to reconcile with the idea of the inflating Universe: without special fitting of parameters, inflation models lead to extremely low values of the spatial curvature R_{c}^{-2}. Second, the present-day age of the open Universe void of dark energy amounts to about 11 billion years, while estimates of the age of the oldest objects in the Universe (for instance, globular star clusters) yielded and now yield higher figures of 12–14 billion years. There also were several other arguments against the open Universe model with a strong spatial curvature.

If the spatial curvature is nonexistent, the density data $\Omega_{\mathrm{M}} \lesssim 0.3$ suggest that at least 70 % of the energy density in the present-day Universe are due to the existence of a matter such that may not be perturbed by the fields of structures and remains "nonaggregated" (nonclusterized) in the course of cosmological evolution. The latter requirement signifies that the effective pressure of this matter is negative and sufficiently high in magnitude, i.e. $p \approx -\rho$. This is the dark energy.

The main indication of the existence of this kind of energy is the acceleration of the universe's expansion, which follows from observations showing that distant supernovae turn out to be systematically weaker than would be expected from the linear Hubble law (Fig. 10.30). Consequently, in the past it expanded more slowly than today.

The first group of observers [119, 130], who reported their results in 1998, possessed data on only several supernovae of the necessary type. However, even that was sufficient [32] to notice the cosmological effect in the law describing the decrease of apparent brightness with distance. It turned out that the brightness decreased, on average, appreciably faster than would be expected from the

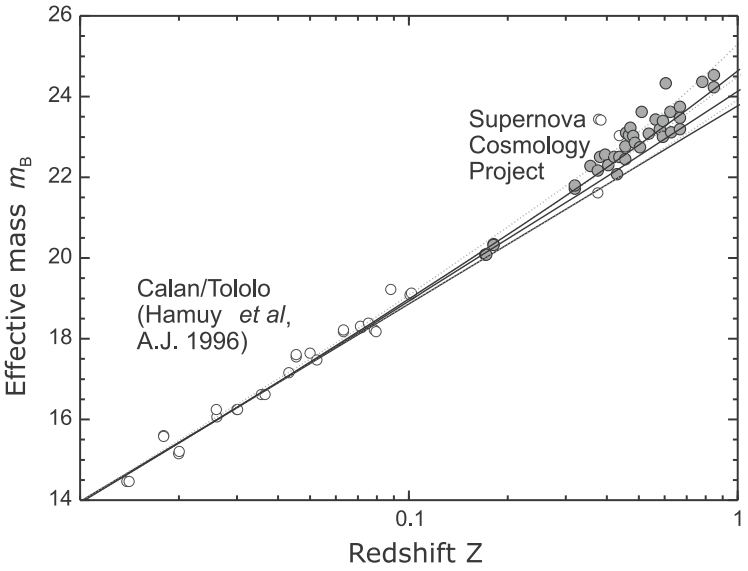

Fig. 10.30 Stellar magnitude at the peak of brightness for type-Ia supernovae as a function of redshift Z (data from [118]). The upward deviation, towards lower brightness of the farther supernovae, from the *straight line* (the linear Hubble law) is indicative of an accelerated expansion of the universe

cosmological theory, which at that time was considered standard. This additional blinding signifies that to a given red shift there corresponds some effective addition in distance. But this is possible when the cosmological expansion accelerates, i.e. when the velocity with which a source recedes from us increases with time and not decreases.

The hidden mass, or dark matter, as it is termed in recent years, is only slightly below vacuum in density:

$$\Omega_{\mathrm{D}} = \frac{\rho_{\mathrm{D}}}{\rho_c} = 0.3 \pm 0.1.$$

Dark matter radiates neither light nor other electromagnetic waves and practically does not interact with electromagnetic radiation whatsoever [32]. In our Galaxy, the amount of dark matter is approximately ten times greater than that of the luminous stellar substance. It makes up a vast invisible corona, or halo, around the stellar disk of the Milky Way and, supposedly, all sufficiently massive isolated galaxies and the largest cosmic systems—galactic clusters and superclusters. Like in our Galaxy, dark matter amounts to 90 %, and sometimes more, of the total mass of these systems. It manifests itself only due to the gravitation it produces; it was precisely due to its gravitational effect that it was first discovered in the 1930s by F. Zwicky, who studied the kinematics and dynamics of a rich galactic cluster in the constellation Coma Berenices. In this constellation, galaxies move at velocities

of about a thousand kilometers per second, and for these velocities it is possible to retain them in the observed constellation volume only provided the total mass of the constellation is approximately ten times greater than the mass of its constituent galaxies. The physical nature of dark matter carriers is still unknown. A very broad range of possibilities is under discussion: from elementary particles with a low mass (below the electron mass) to dwarf stars, massive (greater than the solar mass) black holes, etc.

Next to the dark matter is [32] the luminous substance of stars and galaxies. Its cosmic density is an order of magnitude lower than the density of dark matter:

$$\Omega_{\mathrm{B}} = \frac{\rho_{\mathrm{B}}}{\rho_c} = 0.02 \pm 0.01.$$

Finally, the fourth component of the cosmological medium is radiation, or an ultrarelativistic medium, of density [32]

$$\Omega_{\mathrm{R}} = \frac{\rho_{\mathrm{R}}}{\rho_c} = 0.8 \cdot 10^{-5}\alpha,$$

where the constant factor $1 < \alpha < 10$–30 takes into account the contribution of neutrinos, gravitons, and other possible ultrarelativistic particles and fields of cosmologic origin, which is additional to the very well-measured contribution of relict radiation.

This effect is associated [33] with antigravity—a new physical effect discovered at distances of 5–8 billion light years, at the edge of the expanding universe. Antigravity shows up as the cosmic repulsion of distant galaxies, which exceeds gravitational attraction. This antigravity is produced not by galaxies or other bodies but by the previously unknown form of energy–mass referred to as "dark" energy, which accounts for 70–80 % of the entire energy–mass of the observable universe. This "dark" energy manifests itself only due to its property of producing antigravity. Otherwise it is invisible and imperceptible: it does not emit, absorb, or scatter light. It possesses negative pressure and its density is constant; its pressure–density ratio $w = P/\epsilon_\Lambda = -0.97 \pm 0.09$. The problem is that the dark energy density value ϵ_Λ is very small:

$$\epsilon_\Lambda \approx 0.75\rho_{\mathrm{c}} \approx 4 \cdot 10^{-6}\ \mathrm{GeV\,cm^{-3}}.$$

The value of the "dark" energy density is many orders of magnitude smaller than the magnitudes arising from dimensionality considerations for the fundamental interactions, i.e., strong, electroweak, and gravitational [135]:

$$\epsilon_\Lambda \sim 10^{-46}\epsilon_{\mathrm{QCD}} \sim 10^{-54}\epsilon_{\mathrm{EW}} \sim 10^{-123}\epsilon_{\mathrm{grav}},$$

while the energy scale itself ($M_\Lambda = \epsilon_\Lambda^{1/4} \approx 10^{-3}\,\mathrm{eV}$) is much smaller than the energy scales of the known interactions $\Lambda_{\mathrm{QCD}} \approx 200\,\mathrm{MeV}$, $M_{\mathrm{W}} \approx 80\,\mathrm{GeV}$, and $M_{\mathrm{Pl}} \approx 10^{19}\,\mathrm{GeV}$ (Pl stands for Planck).

In the mid-1960s, a "material" interpretation [60] of the cosmological constant was proposed, which supposes the existence in the Universe of a perfectly uniform macroscopic medium of density

$$\rho_{\mathrm{v}} = \frac{\Lambda}{8\pi G},$$

where G is the Newtonian gravitational constant; hereinafter the velocity of light is assumed to be equal to unity, $c = 1$. This density is invariable in time and space and remains the same in all frames of reference.

The medium of density ρ_{v} possesses negative pressure p_{v} and its equation of state (i.e. the pressure–density relationship) is as follows:

$$p_{\mathrm{v}} = -\rho_{\mathrm{v}}.$$

The medium with so unusual an equation of state is unlike any "normal" liquids or gases. Following [33] we enumerate its most important special properties.

1. This medium cannot serve as a frame of reference [33]. When there are two frames of reference moving relative to each other at some nonzero velocity, the medium with the proposed equation of state will be comoving with both of them. Herein lies the main mechanical property of the vacuum. So that the medium described by this equation of state is the vacuum
2. The medium with such equation of state is invariable and "eternal". Its energy is the absolute and temporally constant minimum of energy contained in the world space. This is another indispensable property of the vacuum.
3. The medium with the pressure defined by the given equation produced anti-gravitation rather than gravitation. The matter is that, according to the general relativity, gravitation is defined not only by the density of a medium (as is assumed by the Newtonian theory), but also by its pressure. In this case, the "effective gravitating density" in the general case is expressed as the sum of two terms [33]:

$$\rho_{\mathrm{eff}} = \rho + 3p.$$

Note that the factor 1 by the density and the factor 3 by the pressure in the right side of this formula emerge because time is one-dimensional and space is three-dimensional.

When we are dealing with the equation of state of the vacuum, the sum in the right side of the equation for ρ_{eff} turns out to be negative:

$$\rho_{\mathrm{eff}} = \rho_{\mathrm{v}} + 3p_{\mathrm{v}} = -2\rho_{\mathrm{v}} < 0.$$

A negative effective density signifies "negative" gravitation. Unlike the universal gravitation, the universal antigravitation tends not to draw bodies together but, on the contrary, move them away from each other. When two probe particles are placed in the vacuum, which are initially immobile relative to each other, the vacuum will next make them mutually recede.

4. In terms of Newtonian physics, the vacuum produces a force but does not experience (as a macroscopic medium) the action of either the external gravitational forces or of its own antigravitation [33]. As is well known, three masses are recognized in physics: active gravitational mass, i.e. the mass which produces gravitation; passive gravitational mass, i.e. the mass which experiences gravitation, "senses" it; and the inert mass, which enters the left side of the Newtonian equation of motion. These three kinds of mass are inherent in all objects of the nature, all bodies and energies, including the vacuum. The effective gravitating density, which has just been mentioned, is the density of active gravitational mass. For any uniform medium the density of passive gravitational mass is given by the relation $\rho_{\text{pass}} = \rho + p$. For the vacuum, this quantity vanishes: $\rho_{\text{pass}} = \rho_{\text{v}} + p_{\text{v}} = 0$. This is the reason why the vacuum experiences neither the external nor its own gravitation. In accordance with the equivalence principle, which the general relativity relies on, the inert mass (its density is given by the formula $\rho_{\text{in}} = \rho + p$) of the vacuum is also equal to zero.
5. Since the dark energy density is a constant value, the vacuum may be thought of as a medium which evenly fills the space on all scales—from cosmological to arbitrarily small [33]. To be more precise, in the small scale domain we may legitimately speak only about fractions of a millimeter but not smaller, because the gravitational theory itself with its inverse square law has been experimentally verified only to submillimeter distances. With a good safety margin, the vacuum may be assumed to exist and be strictly uniform, at least down to a small scale of about a centimeter. The bodies embedded in dark energy (at least, the bodies of macroscopic size) do not force it out of the volumes they occupy—the dark energy density is the same inside and outside of the bodies.

Unlike Newtonian gravity, the force of antigravity increases linearly with distance [33], which has serious implications for the dynamics of the universe's motion after the Big Bang [33]. It turns out that zero acceleration occurred when the universe was 7–8 billion years old. Since that time the universe has begun to expand by an exponential law. The value of the cosmological constant is close to the critical density at that time and is equal to $\approx 10^{-56}\,\text{cm}^{-2}$. Since the age of the modern universe is about 14 billion years, it turns out that the history of the universe is divided into two nearly equal parts: during its first part there prevailed the gravitation of dark matter, baryons, and radiation, while the second part was dominated by the antigravity of dark energy.

Another manifestation of dark energy is afforded by the WMAP (Wilkinson Microwave Anisotropy Probe) spacecraft, which observed nonuniformities of the temperature distribution of the relic radiation background—"imprints" of the primary pregalactic structure of the universe, whose development later led to the

emergence of galaxies. The evolution of these variations and their observable quantitative characteristics depend on the physical parameters of the universe as a whole and, in particular, on its geometry.

The most significant (and supposedly the most reliable) finding of WMAP is that the total world's energy density ρ_0 is close to the critical density $\rho_c = (3/8\pi G)H_0^2 = (1 \pm 0.1) \times 10^{-29}\,\mathrm{g/cm^3}$, where $H_0 = 72 \pm 0.4\,\mathrm{km/(s\,Mpc)}$ is the Hubble constant. In this case, the strict equality of these densities is not ruled out. These data are indicative of the high density of the universe, which exceeds the density of ordinary and dark matter.

According to the WMAP data, the matter density in the universe is equal to the critical value with a high degree of accuracy. This signifies that dark energy should account for 70–80 % of the total density. The point is that the contribution of other energies (baryons, dark matter, and radiation) is severely bounded above to about 30–20 % of the critical density, which is known in advance from a set of other independent cosmological requirements. Today it is agreed that 26 % of matter is due to hidden mass and only 4 % due to visible matter.

Such overestimation of the mass of the universe follows from nonuniformity of the distribution of galaxies and the analysis of mass evolution in accumulations of galaxies.

We now give [33] the WMAP data about the energy composition and age of the Universe. The dark energy (the corresponding index is V), dark matter (index D), baryon (index B), and radiation (index R) densities are given in terms of the critical density:

$$\Omega_\mathrm{V} = \frac{\rho_\mathrm{V}}{\rho_c} = 0.75 \pm 0.05,$$

$$\Omega_\mathrm{D} = \frac{\rho_\mathrm{D}}{\rho_c} = 0.23 \pm 0.07,$$

$$\Omega_\mathrm{B} h^2 = \frac{\rho_\mathrm{B}}{\rho_c} = 0.022 \pm 0.001,$$

$$\Omega_\mathrm{R} h^2 = \frac{\rho_\mathrm{R}}{\rho_c} = 7 \cdot 10^{-5}.$$

Here, h is the Hubble constant measured in units of 100 km/(s Mpc): $h = H/100 = 0.72 \pm 0.04$.

These data relate to the modern state of the Universe, which, according to the WMAP data, is

$$t_0 = 13.7 \pm 3\,\text{billion years}.$$

The dark energy density was estimated even in the first experiments and turned out to be quite low: $\approx 0.7 \times 10^{-29}\,\mathrm{g/cm^3}$ [33]. In a cubic meter of space, this dark energy mass is equal to the mass of three hydrogen atoms. For a medium with such

a density, the force of antigravity is also vanishingly small: it is balanced by the gravitational attraction of two hydrogen atoms spaced 50 cm apart [33].

Also associated with dark matter are the hypothetical Weakly Interacting Massive Particles (WIMPs), which emerged at the early stages of formation of the universe (Fig. 10.31). This class comprises neutrinos, neutralinos, photinos, gravitinos, axions, etc. It is significant that the fraction of the average density of the baryon matter component relative to the average density of the nonbaryon one (WIMPs) amounts to only ≈0.07. At the same time, the fraction of the average density of visible matter relative to the total average density of the universe amounts to only ≈0.003–0.007.

Galaxies and galactic clusters are supposedly [157] surrounded by giant halos of dark matter. To be consistent with the data of direct astronomical observations, such huge masses must consist of particles which interact only slightly with ordinary matter or contact primarily with each other. They manifest themselves only in that they use gravitational interaction with luminous matter.

As astronomers believe [157], formed first in the galactic production history was the dark matter halo, which next drew the ordinary matter into the resultant potential well. The ordinary matter, being flexible with respect to various changes, gradually developed and generated the rich family of presently observable galaxies, while the inert dark mass persisted in its initial form and configuration. As for the dark energy, its only role known from observations is the motive force of the accelerated expansion of the modern Universe. Available observations testify to the fact that the dark energy has hardly changed throughout the life of the Universe.

The predicted hypothetical particles responsible for dark matter received the name weakly interacting massive particles (WIMPs). They derive their name from

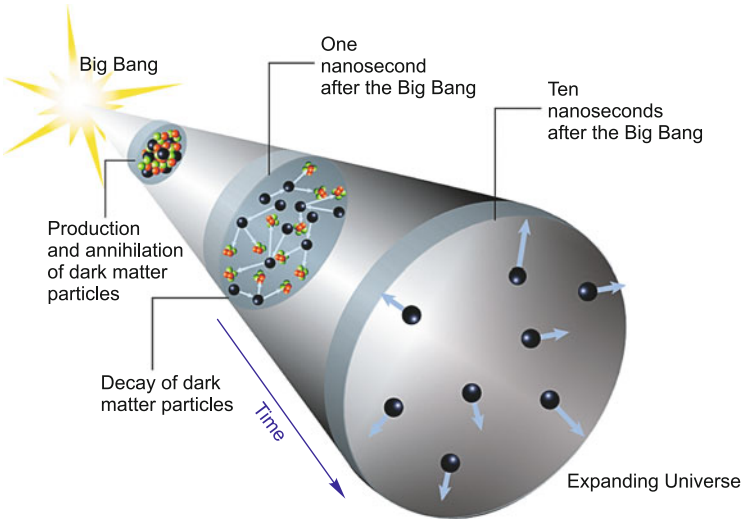

Fig. 10.31 WIMP production after the Big Bang [157]

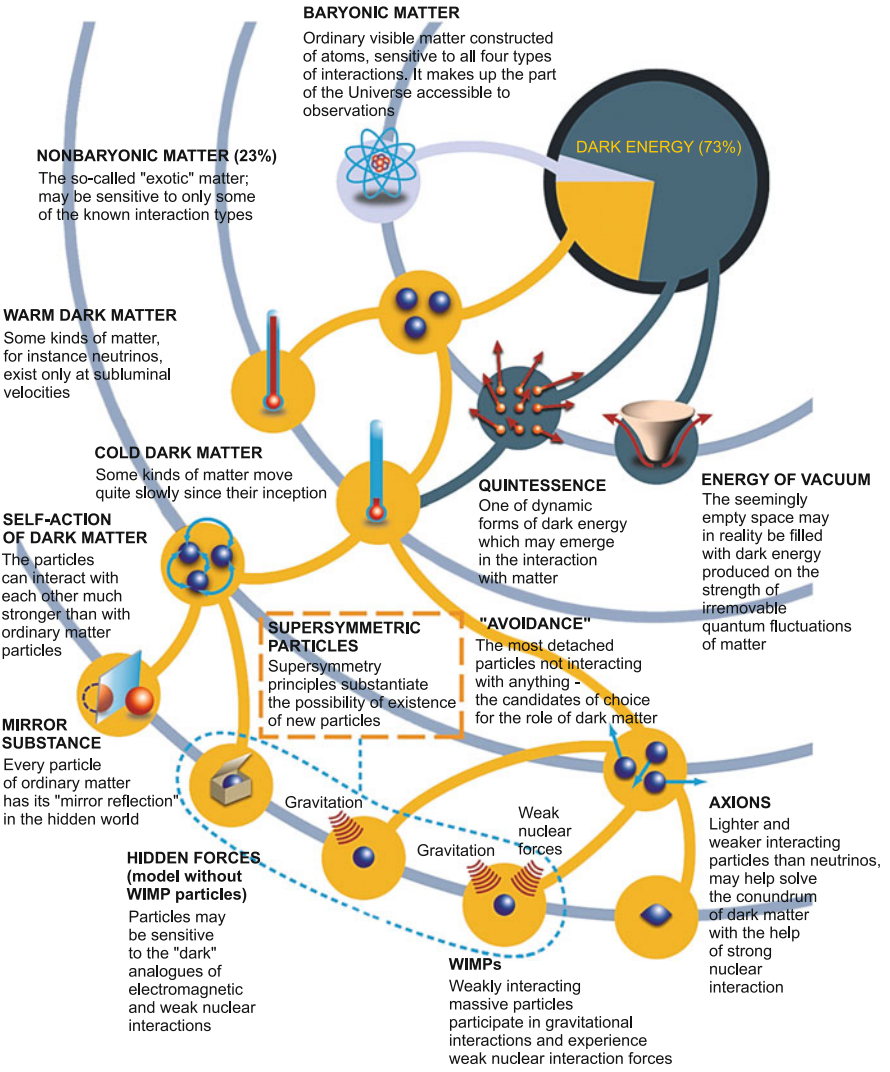

Fig. 10.32 Dark energy and matter [157]

the fact that they interact, apart from gravitation, only via weak nuclear interactions. Being insensitive to electromagnetic interactions, which prevail in our everyday life, WIMPs are completely invisible, and any their direct action on the ordinary particles is weak. Therefore, these hypothetical particles are good candidates for the role of cosmological dark matter. The capacity of WIMPs to account for the nature of dark matter depends on the amount of such particles. Therefore, the solution of the cosmological problem comes to depend on elementary particle physics. Like other particles, WIMPs might have been produced in the Big Bang (Fig. 10.32).

In the hot, dense early Universe, the production and annihilation of dark matter particles—WIMPs—were in the state of dynamic equilibrium. As the Universe expanded, its temperature became lower, and so there was no longer enough energy for producing new dark-energy particles. Therefore, the decay of these particles came to be the dominant process. The theory yields adequate predictions of the amount of WIMPs, which are comparable with observations.

Among this list of candidates for "dark" mass carriers are more or less preferable objects; however, the final answer to the question as to what hidden mass consists of has to be provided by observations, probably the LHC-based ones.

An additional point in favor of the existence of "dark" energy is the solution of the so-called Hubble–Sandage paradox [33]. This consists in the following: for a strong nonuniformity and obvious randomness of matter distribution at a distance of up to 20 Mpc, there exists a regular matter expansion flow with direct proportionality between velocity and distance, which is valid for a uniform distribution. Indeed [33], in the range from several to several tens of megaparsecs cosmic matter is distributed quite nonuniformly. It conglomerated in separate bunches—galaxies, galactic groups and clusters, which are randomly strewn over space. Under these conditions the Friedman model is inapplicable: the assumption of matter distribution uniformity is not fulfilled.

However, detailed observations showed [140] that a regular expansion flow obeying the Hubble law $v = H_s R$ is traced with confidence in a broad spatial range from 4 to 200 Mpc. It turns out that the regular galactic kinematics is in no way impeded by the strong nonuniformity of their distribution inside a uniformity cell. In this case, the Hubble constant H_s measured inside the uniformity cell is close to the value of the global quantity H_0 furnished by the WMAP observations.

It seems that the existence of dark energy resolves this paradox. The dark energy has a perfectly uniform density and dominates everywhere beyond heavy crowdings of matter, making almost the whole universe nearly uniform. The contradiction between the regularity of galactic motion and the irregularity of their spatial distribution inside a uniformity cell is thereby removed: in the presence of the dominant dark energy background, the total mass/energy distribution also turns out to be nearly regular [33].

Lukash and Rubakov [88] consider the measurement of peculiar galactic velocities in clusters and superclusters, gravitational cluster lensing, the measurement of galactic rotation curves, the determination of luminosity–mass relationships, the temperature measurement of X-ray clusters, etc. as arguments for existence of "dark" energy.

The theoretical models of "dark" energy effects are analyzed by Rubakov and Tinyakov [135]: the cause of accelerated expansion might be associated with new low-energy physics (the quintessence model [32]).

The equation of state of such energy is of the form $p = \omega\rho$, where ρ is the dark energy density [87]. A value $\omega < -1/3$ corresponds to cosmic expansion, $\omega = -1$ to the cosmological constant, and $\omega < -1$ to phantom energy. In the latter case, the system possesses negative entropy and temperature, and the energy is not conserved in such a system [87].

Another model of gravity modification at long range proceeds from the brane-world theory and the idea of high and infinite additional dimensions [133]. In such theories, ordinary matter is localized on a three-dimensional hypersurface (brane) embedded in a higher-dimensional space. Rubakov's idea [133] is that gravitons may propagate over "our" brane for a finite (though long) time to subsequently go to additional dimensions.

Light transits through this invisible matter like through the vacuum. The amount of this invisible substance increases in the "voids" between galaxies. In our Galaxy, the amount of "hidden mass" (dark energy) is by an order of magnitude equal to the amount of ordinary mass, while in the "voids" it is ten times greater. In the solar system itself there is no "hidden matter". It is confined in the neighborhood of the Galaxy—its halo.

The discovery of dark energy explained much in observational cosmology. For the first time in the development of science, there appeared a Standard cosmological model which satisfied the entire set of observational data and which has no serious competitors today. The Standard model describes nicely both the evolution of the Universe as a whole and the formation of its structure. Despite the influence of dark energy, the structure generation is still going on in the modern Universe and will continue for about 10 billion years [88].

One of the problems of multidimensional theories is the quest for a mechanism for hiding the additional dimensions, so that the space-time appears effectively as the usual four-dimensional one when studying ordinary physical effects. The proposed modes [133] introduce and analyze the "compactness" of additional dimensions, which provides the effective four-dimensionality of the space-time over distances exceeding the scale of compactification (the size of additional dimensions). In this case, the extra dimensions must be of microscopic size. According to the prevailing opinion, the compactification scale must be of the order of the Planckian length. It seems to be hopeless to directly discover the additional dimensions on the Planckian scale (a distance $l_{\mathrm{Pl}} \approx 10^{-33}$ cm, the corresponding energy $M_{\mathrm{Pl}} \approx 10^{19}$ GeV).

The remaining 30 % of the mass–energy of the universe exists in the form of matter—particles possessing mass. The most common of them are protons, neutrons, and electrons, which account for one sixth of matter, i.e., for 4–5 % of the entire universe. The major part of this mass is due to the energy of motion of quarks and gluons, which are parts of protons and neutrons. A smaller amount (0.3–1.0 %) of the universe's mass is accounted for by three neutrino families. Yet another part—the fourth, cosmic energy, component—is "radiation", which is taken to mean relic photons (as well as perhaps gravitons); radiation accounts for no more than several hundredths of one percent of the total density. The remaining 20–25 % of the universe's mass–energy is constituted by "dark" matter invisible to us, whose existence is evidenced by its gravitational effect on observed cosmic objects. It is thought to consist of massive particles of mass 10 GeV–1 TeV, which are not among the particles of the Standard model, for it makes up galaxy-sized clusters. Their lifetime should be comparable to the age of the modern universe of $\approx$14 billion years.

The particles of "dark" matter possess ordinary properties relative to gravitational interactions: they are capable of assembling in clusters, forming gravitational fields, etc., which is of consequence for the formation of structures in the universe—galaxies and their clusters. Studying these structures and the polarization of microwave relic radiation suggests that the "dark" matter particles were nonrelativistic even at the very early stages of the evolution of the universe. At the same time, the "dark" matter particles are void of electric charge and interact only weakly with matter, which hinders their detection.

The particles of "dark" matter possess ordinary properties relative to gravitational interactions: they are capable of gathering in clusters, forming gravitational fields etc., which is of significance in the formation of structures in the Universe—galaxies and their clusters. Studying these structures and the polarization of microwave relict radiation suggests that the particles of "dark" matter were nonrelativistic even at the early stages of the evolution of the Universe. At the same time, the particles of "dark" matter have no electric charge and interact extremely weakly with substance, which hiders their detection.

Back in 1933, the Swiss astrophysicist Fritz Zwicky [26] was operating a small telescope in the USA and realized that the galactic cluster Coma Berenices cannot be gravitationally coupled without the presence of an additional mass, which was later called the hidden mass. In the last decades, it became clear that the abundance of dark matter in the Universe is much higher than the abundance of visible matter and baryon matter. A new avenue of investigation made its appearance—MD cosmology, whose task is to elucidate what particles the dark matter consists of. Formally, this component of the Universe may even be baryonic in nature. Estimates [26] suggest that more than a half of the dark substance may be baryonic in nature. Furthermore, in the Universe there may exist the nonradiating remnants of black holes of Planckian mass (10^{-5} g) and perhaps preon stars with $M \sim 10^2 M_\oplus$ (the Earth's mass $M_\oplus \approx 6 \cdot 10^{27}$ g).

To describe the remaining part of dark matter, weakly interacting heavy particles—a neutralino and an axion of mass 10^{-5}–10^{-6} eV [26]—are introduced. Also considered [26] are other versions of dark-matter particles. These are sterile (supersymmetric) neutrinos, gravitinos, axinos, light scalar particles, light Higgses, Kaluza–Klein dark matter, superheavy dark matter, nontopological solitons, charged massive particles (CHAMPs), superweakly interacting massive particles (SWIMPs), the dark matter of the membrane world, fourth-generation heavy neutrinos, mirror particles, etc.

One of the early observable manifestations of "dark" matter is presented in Fig. 10.33.

According to Newtonian mechanics, the rotational velocity of gravitationally bound masses should be inversely proportional to the square root of the distance to the center of rotation. Data measurements presented in Fig. 10.33 [137, 138] show, however, that the remote galactic parts rotate with the same velocity as the parts nearest to the center and in doing so do not fly away due to the centrifugal force. This is an indication that the galactic mass increases linearly with radius, so that the

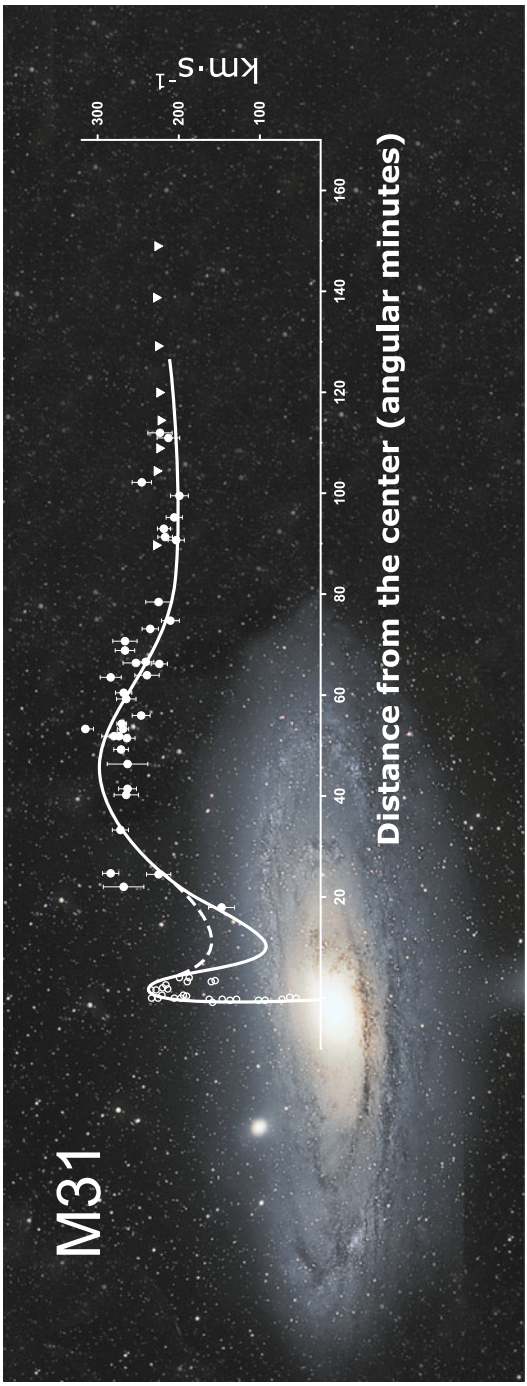

Fig. 10.33 Photo of the Andromeda galaxy (M31) with radial velocity distribution superimposed on it. The data were obtained by light (*circles*) and radio measurements [137, 138]. The velocity of rotation remains invariable beyond the visible image, which is an indication that the mass of M31 increases linearly with radius

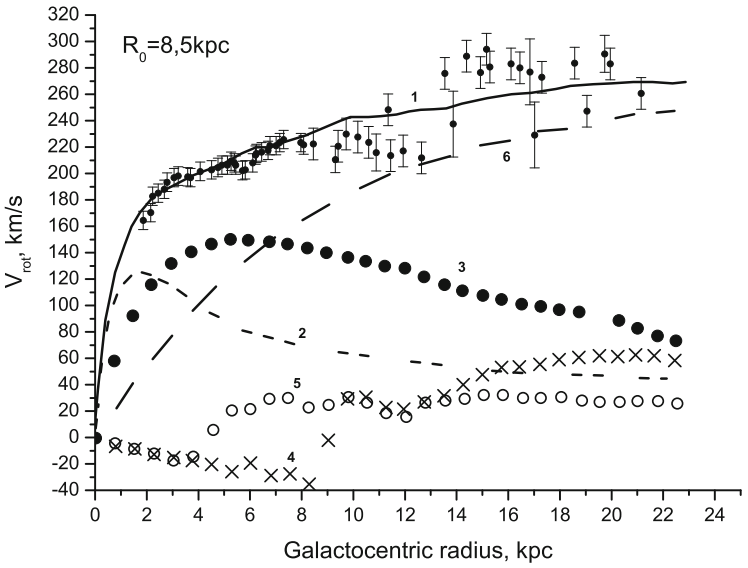

Fig. 10.34 Summary curve of galaxy rotation (1) and its constituent rotation curves for individual galaxy constituents: the badge (2), the stellar disk (3), the neutron hydrogen layer (4), the molecular hydrogen layer (5), and the halo of unobservable dark matter (6), whose contribution determines the rotation curve at long distances from the *center*. From [113]

greater part of the gravitating though invisible mass is located far beyond the limits of the visible galactic image [45].

A similar example of anomalous rotation of our Galaxy, which comprises 10^{11} stars, is given in Fig. 10.34 [41], which shows the rotational velocity as a function of the distance from the Galaxy center. In the innermost regions, the rotation is close to the solid-state one in character; then the velocity decreases slightly, but still farther, up to the most distant objects with measurable velocities, the rotational velocity remains constant or slowly increases. By the 1970s, this was borne out by neutral hydrogen observations in our Galaxy and in the majority of other ones. The almost generally accepted explanation of this fact is that the Galaxy is surrounded by a vast cloud of gravitating, though not observable baryon matter located at distances from 10^{-5} to several parsecs from the Galaxy center [175, 176].

In this case, the intense γ-ray radiation and neutrino fluxes observed from galactic centers and halos are caused by the annihilation of dark matter [175, 176].

To date, a considerable amount of other observational data of various nature has also been obtained, which testify to the existence of "dark" mass in the Universe [156]. Apart from cosmological data, the data of infrared astronomical observations [175, 176] and gravitational field measurements in galaxies and their clusters also point to the existence of large quantities of "dark" matter.

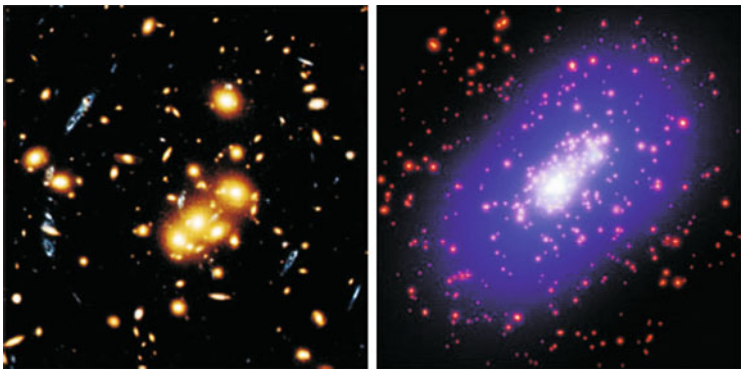

Fig. 10.35 Gravitational lensing of a remote galaxy. Photographs in the direction of the galactic cluster 0024+1654 obtained with the Hubble Space Telescope [107]

Figure 10.35 shows the gravitational "probing" data, when the gravitational field of a cluster curves the light rays emanating from the galaxy located behind the cluster. The gravitational field therefore acts as an optical lens. Several images of this remote galaxy are sometimes observed in this case. In the left half of Fig. 10.35 they are in blue. The curvature of light rays depends on the mass distribution in the cluster. When the lensing effect is taken into account, there results the image of the radiating galaxy shown in blue in the right half of Fig. 10.35. One can see that it is very different from the luminous ("visible") matter. The masses of galactic clusters determined in this way suggest that the "dark" mass accounts for about 25 % of the total energy density in the universe. This corresponds to the estimates that follow from a comparison between observations and the theories of the formation of galaxies and clusters of galaxies.

These are estimates of the virial or dynamic masses of galactic clusters, which are several times greater than the visible cluster masses obtained by direct summation of observable galactic masses that are estimated from the mass–brightness dependence. Galaxies in the clusters move much faster ($V \gg 1000\,\text{km/s}$) than follows from the estimate of the visible matter mass.

Figure 10.36 [136] shows a photo of the UGC 10214 galaxy: a stream of matter flows from this galaxy towards an invisible gravitating center, which supposedly consists of dark matter.

The presence of hidden mass is also attested by the discovery of hot ($T = (3\text{–}10) \times 10^7\,\text{K}$, $n_e > 0.001\,\text{cm}^{-3}$) gas in galactic clusters and other observational data. To solve several theoretical problems (the problem of the formation of large-scale structure in the universe, cosmological problems involving the explanation of the recently discovered spatial fluctuations of the relic microwave background, etc.) it is also necessary to invoke the hidden mass.

According to [26], the present-day value of dark energy density

$$\rho_{\text{DE}} = \rho_\Lambda \sim 10^{-47}\,\text{GeV}^4 \approx 0.7 \cdot 10^{-29}\,\text{g/cm}^3,$$

Fig. 10.36 Tadpole galaxy (UGC 10214). According to one hypothesis, the matter "tail" was formed due to the attraction of an invisible "dark" galaxy [136]

is exceeded by 123 orders of magnitude by the density in the Planckian era

$$\rho_\Lambda \sim 2 \cdot 10^{76}\,\mathrm{GeV}^4 (\approx 0.5 \cdot 10^{94}\,\mathrm{g/cm}^3) \quad \text{for} \quad M_{\mathrm{Pl}} = 1.2 \cdot 10^{19}\,\mathrm{GeV}.$$

A large number of papers (see reviews [23, 25, 26, 53, 117, 171]) are concerned with the explanation of this huge difference of 123 orders of magnitude. Over the first 10^{-5} s after the Big Bang, the Universe lost 78 orders of magnitude due to a series of phase transitions [26], the last being a quark-chromodynamic one. During the subsequent period of expansion, the rate of vacuum energy variation was 10^{57} times lower than its variation rate in the quantum period of evolution.

As it turns out [26], with an energy decrease from 10^{19} GeV to 150 MeV over the period of early evolution of the Universe, the condensates of quantum fields compensated 78 orders of magnitude of vacuum energy density in only 10^{-5} s. Next, in 14 billion years ($\approx 4 \cdot 10^{17}$ s) the vacuum component lost 45 orders of magnitude more due to production of new quantum states in the expansion of the Universe.

That is, 123 orders of magnitude of the vacuum energy are lost in ordinary physical processes.

The study of molecular and dust clouds in laboratory conditions may be carried out with the use of high-power lasers and high-current devices, which model the ablation dynamics of clouds, the stability of interfaces, and the effect of radiation on the structure and development of radiative hydrodynamic instabilities. Furthermore, the generation of shock waves in such media may give rise to substantial nonuniformities and turbulent processes. Research into the generation of laser-driven shock waves and of compression waves with Z-pinches is now in progress [36, 38, 62, 127, 145] and may yield much new information for the understanding of molecular clouds in space. The imposition of a magnetic field on the experimental volume makes the clouds "stiffer" and substantially alters their dynamics and structure.

The interstellar medium exhibits one more activity of a specific kind by generating maser radiation at the lines of the water hydroxyl molecule (OH), silicon dioxide, and methanol (CH_3OH). The maser effect consists in the fact that the linewidths correspond to a temperature of only 10^2 K for a brightness temperature of 10^{16} K [149]. This laser radiation is highly variable: its polarization, intensity, lineshapes, etc. sometimes change radically over a day or even several minutes, which corresponds to the masing regions of size of order 1 AU. These sources range in luminosity from 1 to 10^3 solar luminosities. They are located in the domains of active star formation, which are rich in gas and massive stars, as well as in galaxies with active nuclei. Chemical reactions, IR radiation, or supersonic gas expansion into vacuum may be the sources of population inversion of the cosmic masers, which is thought to be realized in the atmospheres of protostars and old supergiants.

Magnetic fields exist throughout cosmic space, including the interior of the Earth and the interstellar and intergalactic media. The origin and structure of these fields are only partly understood, and this applies specifically to the fields of neutron stars and giant planets [109]. Most thoroughly elaborated is the model of terrestrial field generation (the "dynamo" model), which relies on detailed measurements and extensive magnetohydrodynamic calculations [13, 146].

Transient magnetodynamic phenomena, which determine stellar activity, present a special problem. For the Sun they are well known as the cycles of its magnetoactivity, coronal plasma ejections, sunspots, and other long-observed phenomena (Figs. 10.37 and 10.38), which result from the complex nonlinear interaction of magnetic fields and the solar plasma.

Magnetohydrodynamic phenomena on the Sun have been studied, of course, most thoroughly [7]. Continuous observations are made of magnetic instabilities and the interconnection topology of magnetic field lines on the solar surface. The dynamics of motion and compression of magnetic flux tubes is quite often transient, explosive in character, and the magnetic field strength amounts to 3000–4000 Gs in sunspots for an average magnetic induction of $\approx$1 Gs. The temperatures in solar flares amount to 10^8–10^9 K, while the plasma parameters in the solar interior are $T \approx 1.5 \times 10^7$ K, $\rho \approx 150$ g/cm^3, and $P \approx 0.2$ Tbar; the time of photon diffusion from the core to the solar surface is $\approx 10^5$ years.

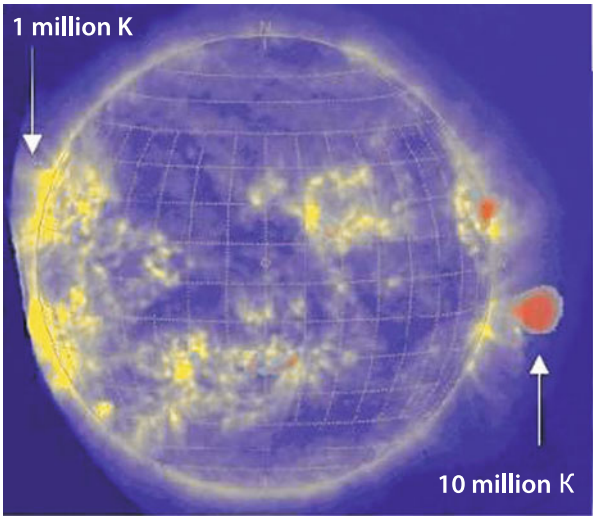

Fig. 10.37 Solar flare; the flare temperature reaches 10 million K

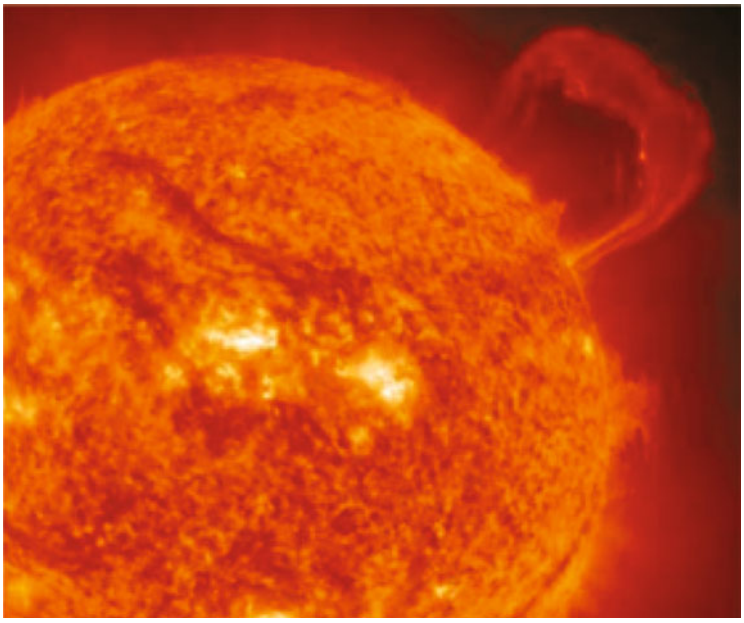

Fig. 10.38 Plasma ejection on the Sun [7]. The plasma follows the magnetic flux lines

Laboratory experiments supplemented with three-dimensional mathematical simulations [111, 184] provide a basis for the explanation of complex field self-organization effects in the magnetoactive plasma.

It is significant that such effects of local energy cumulation give rise to global solar oscillations, which are recorded with a very high degree of accuracy. The characteristics of these oscillations depend on the composition and thermodynamic properties of the solar plasma, which yields a unique high-precision experimental material for verifying multicomponent plasma models and defining more precisely the elemental composition of the solar plasma [12]. The results of such a comparison are presented in Fig. 10.39, where the adiabatic exponent of the solar plasma obtained by helioseismology techniques is compared with the adiabatic exponents of several theoretical models. As in the case of neutron stars, the Sun fulfils the function of a "cosmic laboratory" for experiments in the area of high energy densities.

More often than not, magnetic Reynolds numbers for astrophysical plasmas prove to be quite high, making the magnetic energy dissipation insignificant in the majority in cases [109]. But, as in aerodynamics, several important cases make an exception. These are the solar corona heating and the injection of the solar wind [111, 184], the circulation of planetary magnetospheres, and the emission from accretion disks. The rearrangement of magnetic lines of force is a special problem [111, 184]. These effects are most likely to manifest themselves in magnetospheres, double layers, and plasma jets, which are intimately related to occurrence of instabilities. In this case, kinetic processes and scale factors are as yet imperfectly understood.

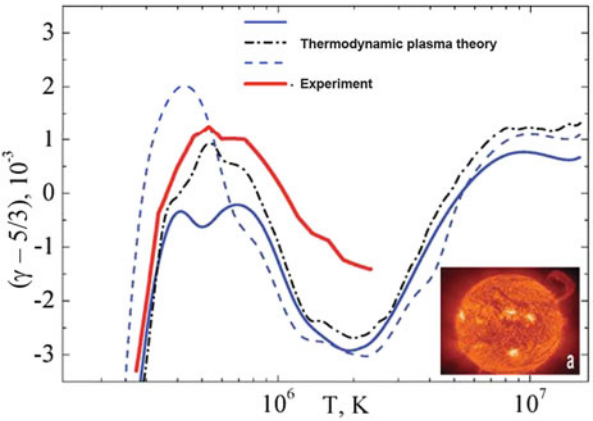

Fig. 10.39 Solar "seismology". Comparison of experimental data on the adiabatic compressibility coefficient of the solar plasma with several theoretical plasma models [12, 49, 52]. The *inset* (*a*) is a photograph of the Sun with solar prominences and bright regions of local energy release, which generate global oscillations and acoustic waves in the solar plasma

The structure of magnetohydrodynamic turbulence of interplanetary and interstellar plasmas is studied from the origin of radio waves [109, 142, 177]. Measurements testify to its anisotropy. Theoretical models suggest that in the incompressible fluid limit, when passing (via a cascade) from large vortices to small ones, there occurs strengthening of the gradient of the field directed perpendicular to the background magnetic field. In this case, it is not clear if an inertial range of vortex scales forms and if the inverse passage of cascades towards large scales occurs, or if Alfv'en waves are generated, which escape from the turbulence region [109].

Laboratory and computer-assisted numerical experiments in this area would be highly interesting and informative.

10.2 Cosmic Rays

As far back as the beginning of the last century, it was reliably determined [106] that a stream of charged particle is incident on the Earth from space, the particle energies spanning a wide range from kiloelectronvolts to 10^{20} eV (Figs. 10.40 and 10.41).

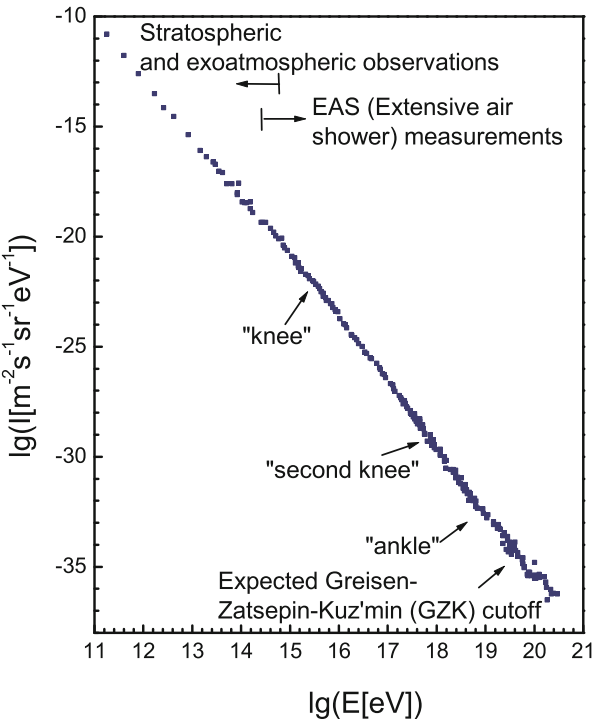

Fig. 10.40 Observed energy spectrum of cosmic rays [106, 177]

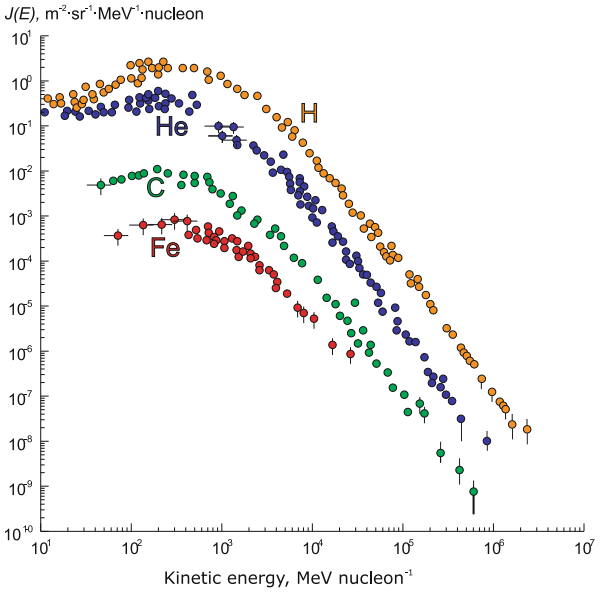

Fig. 10.41 Differential spectra of galactic cosmic rays (CRs): protons H, helium He, carbon C, and iron Fe nuclei [147]

Cosmic rays with a huge energy of $\approx 3 \times 10^{20}$ eV (which corresponds to the energy of a tennis ball, 50 J) were first recorded in 1991. Since then, tens of events with an energy of $\approx 10^{20}$ eV were detected at different facilities [106]. The events were detected by recording the fluorescence of atmospheric cascades in the atmosphere or in specifically constructed detector arrays at the Earth's surface. The spatial distribution of the incident particles was observed to be surprisingly isotropic. When protons are involved, the effect of a magnetic field on them is small, and most likely they are of extragalactic origin.

Cosmic rays are inherently a strongly rarefied relativistic gas, whose molecules only slightly interact with each other, with a power-law energy spectrum (Fig. 10.40) rather than the Maxwellian one. At the same time, cosmic rays experience collisions with the particles of the interstellar medium and interact with the interstellar magnetic field. Although the cosmic ray flux near the Earth is low, ≈ 1 particle/(cm^2 s), its energy density, ≈ 1 eV/cm^3, is comparable to the density of electromagnetic radiation from all galactic stars or to the energy density of the thermal motion of the interstellar gas and the kinetic energy of the turbulent motion, as well as to the energy density of the galactic magnetic field [63]. The flux of superhigh-energy particles is extremely low, about 1 particle/km^2 in 100 years, but it is the origin and propagation of precisely these particles that arouses the greatest interest.

The model developed in [58] is based on the following assumptions [124]: the bulk of cosmic rays are of galactic origin, and they diffuse in interstellar magnetic fields. The sources of cosmic rays are supernova explosions. The highest-energy particles (above 10^{18}–10^{19} eV) are of extragalactic origin.

The energy limit [63, 179] arising from the ionization proton energy losses due to the scattering from relic radiation photons at an energy of $\approx 5 \times 10^{19}$ eV was revealed for protons that had traversed a distance of more than 50 Mpc. The superhigh-energy particles beyond this limit [7, 12, 63, 70, 103, 106, 111, 152, 153, 164, 179, 184] are being most actively studied in the search for their sources and mechanisms of acceleration [112].

According to the "proton–neutrino–proton" model [170], it is neutrinos that propagate through large distances in space and not protons, which should have ultrahigh energies at the place of production so as to eliminate attenuation arising from the scattering by relic radiation photons. This model admits the existence of superhigh-energy particle sources located at cosmological distances outside of our galaxy, which is most likely.

Unfortunately, available data do not permit an unambiguous determination of the sources of superhigh energy cosmic rays, but it is clear that the physical conditions in these sources should be extreme. By their energy characteristics, supernovae and their remnants are best suited for the sources of cosmic rays in the Galaxy [58]. It takes to convert approximately 10–20 % of the kinetic energy of supernova ejection to the energy of relativistic particles to provide the observed cosmic ray energy density of $\approx 1.5\,\text{eV/cm}^3$. Direct evidence for the presence of relativistic particles in supernova remnants follows from the observations of nonthermal radiation in radio-, X-, and gamma-ray regions.

Data on synchrotron radio-frequency radiation point to the presence of 50 MeV–30 GeV energy electrons in supernova remnants [124]. In the case of Cas A, this synchrotron radiation was recorded in the infrared range, which testifies to the presence of electrons with energies up to about 200 GeV. The discovery of nonthermal X-ray radiation with a characteristic power law spectrum and energies of up to several tens of keV in approximately ten young galactic supernova remnants is explained by the synchrotron radiation of the electrons of very high energy, up to 10–100 TeV. The inverse Compton scattering of background photons by the electrons with so high an energy and the generation of gamma-ray radiation in the interaction of protons and nuclei of energy up to ≈ 100 TeV with the nuclei of gas explain the TeV-gamma rays detected from several young supernova remnants. The spatial distribution of nonthermal radiation in all ranges testifies that the particle acceleration in the shell remnants of supernovae occurs directly at the shock waves generated by supernova explosions.

A natural condition which the sources must satisfy is geometrical: a particle should not leave the accelerator before it gains the requisite energy. It is commonly assumed that the particle is accelerated by the electric field and confined by the magnetic one; then, the geometrical criterion is that the Larmor particle radius should not exceed the linear size of the accelerator [123].

The criteria which ultrahigh-energy particle accelerators must satisfy are outlined in [123]:

- the particle under acceleration must remain inside the accelerator in the course of acceleration (the geometrical criterion);
- every source must have a sufficient store of energy for transferring to particles (individual power);
- the radiative loss must not exceed the energy gain;
- the losses by interactions must not exceed the energy gain;
- the total number and overall power of the sources must be high enough to provide the observed cosmic ray flux;
- the accompanying photon, neutrino, and lower-energy cosmic ray radiation must not exceed the observational limitations for an individual source as well as for a diffuse flux.

According to these criteria, only some of the galaxies are suited for the acceleration of particles of observed energies, while the majority are not.

It is obvious that cosmic rays should be accelerated by some nonthermal mechanism, because the temperature at the center of the most massive stars does not exceed several tens of keV. And so to study these particles both the classical Fermi mechanism [48] (Fig. 10.42 [115]) and stochastic mechanisms [2, 3] are invoked, whereby the particles are accelerated in their stochastic interaction with magnetic domains or collisionless shock waves generated by supernova explosions or matter ejections from active galactic nuclei, whose turbulent zone is the site of development of diverse instabilities. However, at high energies there occur significant radiation energy losses here, even at energies below the Zatsepin–Kuz'min limit [63, 179].

Data on the composition of cosmic rays also suggest [124] that particle acceleration occurs at the shock wave propagating through the interstellar medium or in the wind of a presupernova star. According to [159], account should also be taken of the plasma-pinch acceleration mechanism. It turns out, in particular, that after taking account of such atomic properties as the first atomic potential or volatility, the chemical composition of cosmic ray sources is found to be close to the normal composition of local interstellar medium and solar photosphere. Perhaps, ions and dust particles are accelerated in the partially ionized interstellar gas and/or in the hot interstellar gas "bubbles" with a high supernova outburst frequency.

The mechanism of cosmic ray acceleration in supernova remnants is a version of the Fermi acceleration mechanism of the Ist kind [124]. The fast particle acceleration takes place in a gas flow compressed by a shock wave due to multiple crossing of the shock front by diffusing fast particles. The diffusion of the particles is due to their scattering by magnetic field nonuniformities.

The mechanism of acceleration in the field of a wake wave (see Sect. 7.4) driven by magnetohydrodynamic shock waves of a gamma-ray burst was proposed in [30]. Consideration yields high (of the order of 10^{19} V/cm), close to Schwingerian, wake fields in a relativistic moving plasma, which are also invoked to describe the gamma spectra of these relativistic sources.

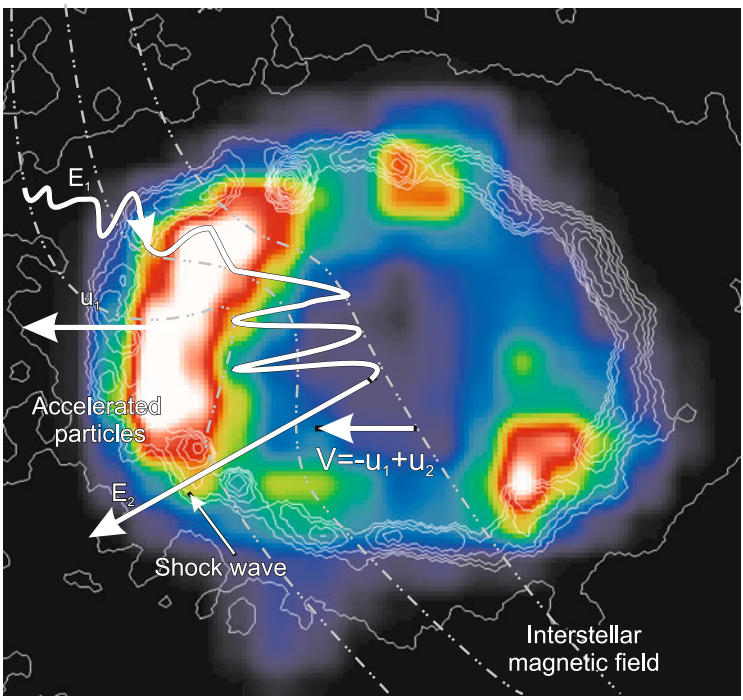

Fig. 10.42 SN 1987 supernova explosion remnants. The picture shows the qualitative illustration of the Fermi particle acceleration mechanism of the first kind at the shock wave. The photo is from the X-ray telescope of the Chandra satellite [115]

The wake acceleration mechanism may be realized in the acceleration of electrons in the jets of massive black holes [59, 143], which emit high-power X-ray radiation. It is produced by the bremsstrahlung and synchrotron mechanisms in relativistic jets from the streams of well-collimated electrons (or positrons) with an energy of $\approx$1 GeV. The role of Alfv'en waves in wake wave generation and their capabilities for particle acceleration are discussed in [30, 105].

Supernova remnants are the main [124], but certainly not the only, sources of relativistic particles in the interstellar medium. In particular, pulsars, which generate high-energy electron-positron pairs, may be responsible for the presence of positrons in the observed cosmic rays. The measured flux of positrons with energies above 10 GeV turned out to be higher than the expected flux of secondary positrons produced in the interaction of cosmic rays with the atoms of the interstellar gas, and the contribution of pulsars explains, in principle, this disagreement. The final elucidation of the nature of the high positron flux in cosmic rays is of critical importance, because the alternative explanation implies that these positrons are the products of dark matter decay.

The central problem of cosmic ray astrophysics is the question of the origin of the highest-energy particles, $E > 10^{19}$ eV. A sharp decrease in particle flux observed at energies higher than approximately $5 \cdot 10^{19}$ eV testifies that these particles have experienced interactions with the photons of the background radiation of the Universe for more than $3 \cdot 10^9$ years and are of extragalactic origin. In this case, ultrahigh-energy protons lose energy for the production of electron-positron pairs and pions (the Greisen-Zatsepin-Kuz'min effect), and nuclei additionally undergo photodisintegration. The cosmic rays with energies below 10^{17} eV are of Galactic origin and are accelerated in supernova remnants.

The electromagnetic acceleration mechanism is associated with the generation of transient electric fields, for instance in the magnetospheres of pulsars, neutron stars, and magnetars, where magnetic fields at the surface range up to 10^{12} Gs and for magnetars up to 10^{14} Gs on a scale of several kilometers. For a rotation frequency of only $10^{-3}\,\mathrm{s}^{-1}$, this would suffice for accelerating particles up to 10^{19} eV. We note that the direct (though not generally accepted) method of measuring induction B in neutron stars is based on cyclotron lines. However, the observed radiation by ultrahigh-energy particles is isotropic and clearly does not correlate with the position of the radiating object.

Particle acceleration may occur both in the central regions of active galaxies (in the immediate vicinity of a black hole and accretion disk) and in lengthy structures (jets, radio "ears", hot spots, and knots) [123].

According to simple estimates [124], from the standpoint of energy characteristics the jets of galaxies with active nuclei may be the sources of observed ultrahigh-energy cosmic rays. To maintain in the intergalactic medium the cosmic-ray intensity observed at energies above 10^{19} eV requires a sources power of the order of $3 \cdot 10^{36}\,\mathrm{erg/(s\,Mpc^3)}$. At the same time, the jets of galaxies with active nuclei liberate kinetic energy at a level of $10^{40}\,\mathrm{erg/(s\,Mpc^3)}$.

It is pertinent to note that the term "active galactic nuclei" is usually employed for describing a domain which occupies a considerably larger size than a black hole with accretion disk and which often comprises inner jets (and sometimes more massive structures).

The results of specific measurements of magnetic fields in the central regions of galactic nuclei are shown in Fig. 10.43 [123].

As we saw in Sect. 10.1, the nuclei of active galaxies feed large-scale (from subparsec to megaparsec), more or less rectilinear jets (see Sects. 10.1.1)—relativistic (in high-power radio galaxies, blazers and quasars) or nonrelativistic (in Seyfert galaxies). It is assumed that all jets are fed from the central black hole. On scales shorter than 1 pc, the main contribution to the energy flux is determined by magnetic field, but on scales of the order of 1 pc the energy of relativistic particles begins to prevail. Internal shock waves (knots) and terminal shock waves (hot spots), lengthy jet-fed regions of intergalactic space, may be observed in relativistic jets. Magnetic fields in such objects of size 10^{-2}–10^2 kpc are estimated at 10^{-6}–10^{-3} Gs.

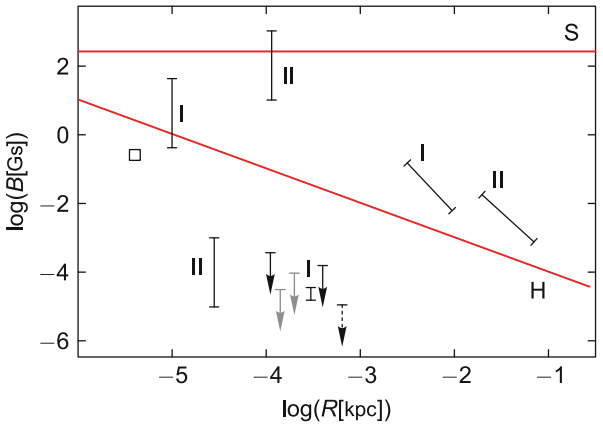

Fig. 10.43 Diagram in size R–magnetic field B coordinates for the central regions of active galaxies: Seyfert galaxies (*square* and *arrows*), FRI radio galaxies (error bars marked "I"), FRII radio galaxies and quasars (error bars marked "II"). *Arrows* stand for the upper bounds determined from Zeeman splitting in megamasers (*dashed* [167], *grey* [104], *black* [95]). The *black* (I) *vertical* error bar—Faraday splitting [180]. The *square* [94], *grey* (I) *vertical* [6], *black* (II) *vertical* [161] and *inclined* (I, II) [31] error bars relate to estimates reliant on the method of synchrotron self-absorption. The parameter domain admissible for proton acceleration up to 10^{20} eV is located between lines H and S (*line* H represents Hillas's limit, *Line* S is the limit due to synchrotron losses for inductive acceleration) [123]

According to [123], cosmic gamma-ray bursts produce magnetic fields of 10^{-2}–10^{8} Gs on a scale of 10^{-13}–10^{-3} kpc. A comparison of observations in radio and X-ray regions confidently testifies that the radiation of several jets is associated with accelerated particles and that the acceleration of these particles takes place not only in a finite number of shock waves, but also with the help of some distributed mechanism. Proved in some cases was the existence of ordered fields in jets, which leaves room for inductive acceleration [123].

High energy density plasmas play a significant role in the understanding of such phenomena, and cosmic showers may be studied in plasma and accelerator laboratories. Here, the leading part is played by shock waves driven by numerous galactic sources like active galactic nuclei and jets, gamma-ray bursts, collisions, galactic clusters, etc. The magnetic reconnection mechanism, which is alternative to the shock-wave one, has been elaborated in less detail to date.

The highest-energy particles may be produced due to magnetohydrodynamic "wind", which is induced about a rapidly rotating magnetized neutron star [109, 143, 174]. These powerful magnets accelerate heavy nuclei in galaxies or their clusters of size 3 million light years. The unipolar inductors of this kind may exist in the accretion disks of massive black holes. Presently underway are intensive numerical investigations of such accelerator effects and their partial physical modeling.

It remains a problem to explain the propagation of accelerated particles through the huge galactic-sized distances in the Universe. In this case, the magnitude and structure of the intergalactic fields themselves has not been adequately studied.

To summarize this section, we give the *R–B* (domain size–magnetic field) Hillas diagram (Figs 10.44 and 10.45 [123]) with the indication of the corresponding astrophysical objects and the limits of different acceleration mechanisms.

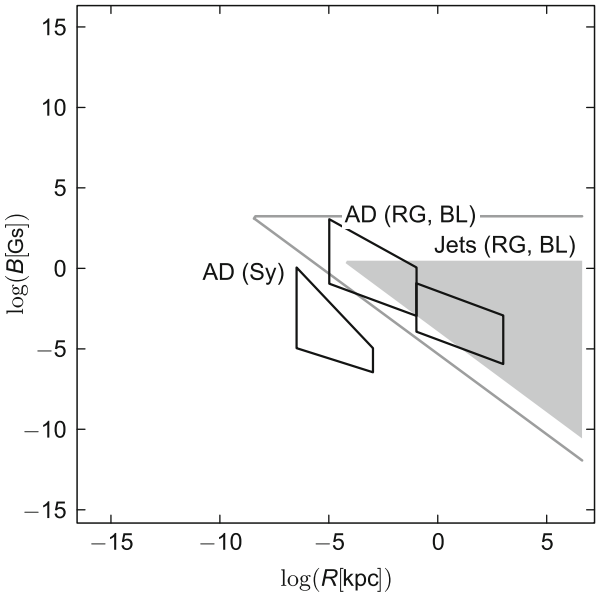

Fig. 10.44 *R–B* diagram with limitations following from geometry and radiative loss for inductive acceleration in the mode whereby the main loss is due to synchrotron radiation. Indicated are the parameter domains corresponding to the objects in which this mechanism may be realized: the central parsecs (AD) of active galaxies—from low-power Seyfert (Sy) ones to high-power radio galaxies (RG) and blazers (BL)—and the relativistic jets (Jets) of powerful active galaxies. The *shaded domain* corresponds to the parameter domain in which protons may be accelerated to energies of 10^{20} eV. *Grey lines* bound the allowed parameter domain for the acceleration of iron nuclei to an energy of 10^{20} eV. The lower boundaries of the allowed domains are defined by the Hillas limit and the upper (horizontal) ones indicate the limitations arising from the radiative loss. All quantities are given in rest frame of the accelerator; in going to the laboratory frame, for a relativistic jet the highest energy must be multiplied by the Lorentz factor of the jet (the characteristic values range from $\approx$10 for leptonic jets to $\approx$100 for hadronic ones) [123]

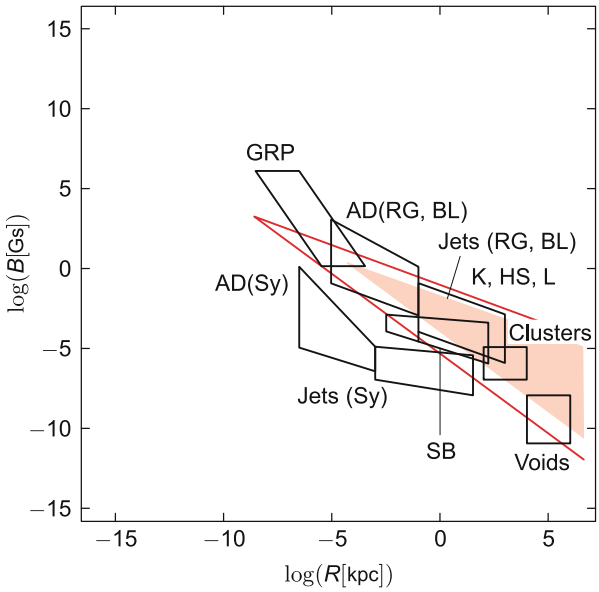

Fig. 10.45 *R–B* diagram with limitations following from geometry and radiative loss for diffusive acceleration (the main loss is due to synchrotron radiation). Indicated are the parameter domains corresponding to the objects in which this mechanism may be realized: the central parsecs (AD) of active galaxies from low-power Seyfert (Sy) ones to high-power radio galaxies (RG) and blazers (BL); relativistic jets (Jets), knots (K), hot spots (HS), and the radio ears (L) of powerful active galaxies (RG and BL); the nonrelativistic ejections of low-power active galaxies (Sy); SB galaxies; gamma-ray bursts (GRB); galactic clusters (Clusters) and large-scale voids (Voids). The *shaded domain* corresponds to the parameter domain in which protons may be accelerated to energies of 10^{20} eV. *Grey lines* bound the allowed parameter domain for the acceleration of iron nuclei to an energy of 10^{20} eV. The lower boundaries of the allowed domains are defined by the Hillas limit and the upper ones indicate the limitations arising from the radiative loss. All quantities are given in rest frame of the accelerator; in going to the laboratory frame, for a relativistic jet and a GRB shell the highest energy must be multiplied by the Lorentz factor of the jet (the characteristic values range from $\approx$10 for leptonic jets to $\approx$100 for hadronic ones and GRBs) [123]

10.3 Gamma-Ray Bursts

In modern astrophysics, gamma-ray bursts are the most mysterious objects [56, 109, 177] with record energy release—excluding the Big Bang. They were accidentally discovered by the American satellites Vela 5A and B intended for monitoring nuclear explosions in the atmosphere. The bursts are detected with a frequency of more than one per day in randomly regions of the sky (Figs. 10.46, 10.47, 10.48, and 10.49), and their duration ranges from milliseconds to seconds in the 0.1–100 MeV energy range. Some of them, being compact objects, are billions of light years distant and radiate an energy of 10^{51}–10^{53} erg per burst. The recorded spectra suggest that these radiators are optically thin with respect to the outgoing radiation.

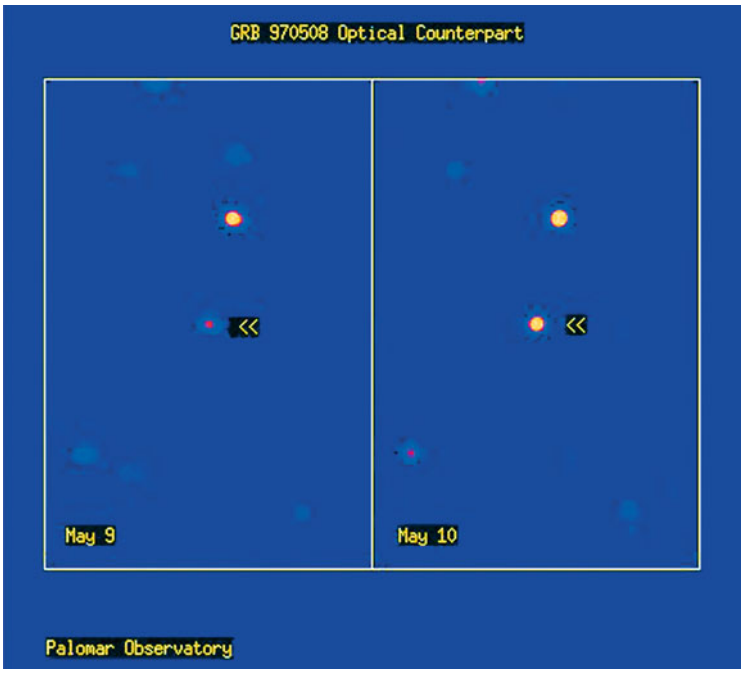

Fig. 10.46 Gamma-ray burst GRB970508 [163]. The photograph shows the variation of the optical radiation of the GRB970508 burst when its brightness increased

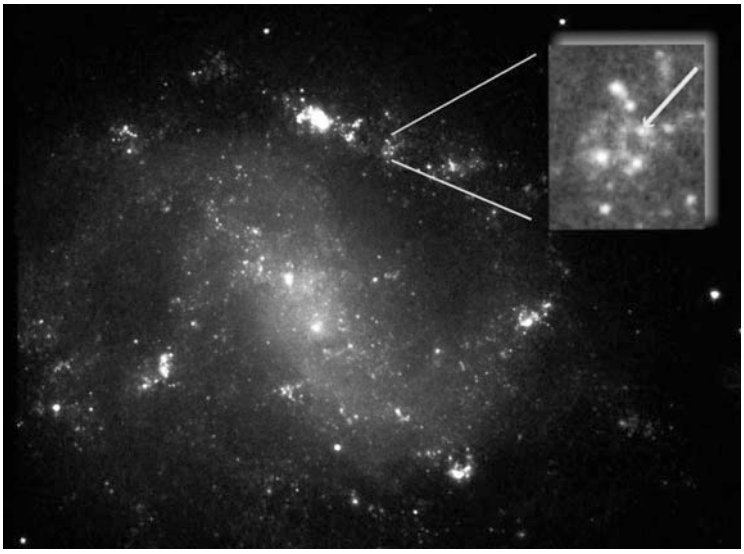

Fig. 10.47 Explosions of stars in the galaxy ESO 184-G82. The *inset* shows the star formation region of size ≈300 light years with a gamma-ray burst [163]

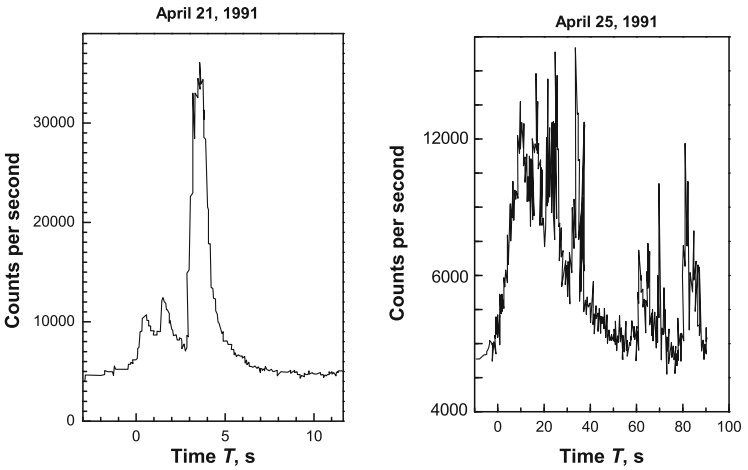

Fig. 10.48 Temporal variation of gamma-ray burst intensity (taken from [163])

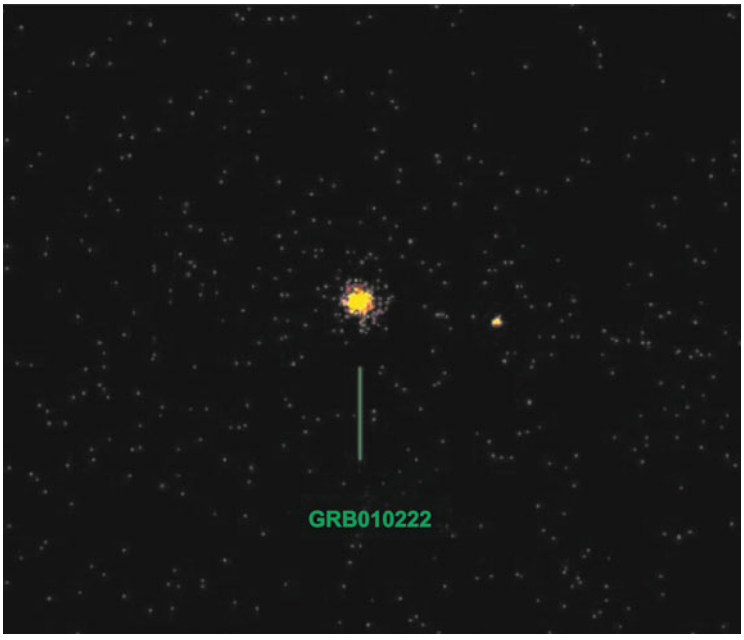

Fig. 10.49 Gamma-ray burst GRB010222. It was observed in the gamma-ray range for only several seconds, but the explosion aftereffects in the X-ray, visible, infrared, and radio ranges were observed for several days as the expansion of a "fireball" [163]

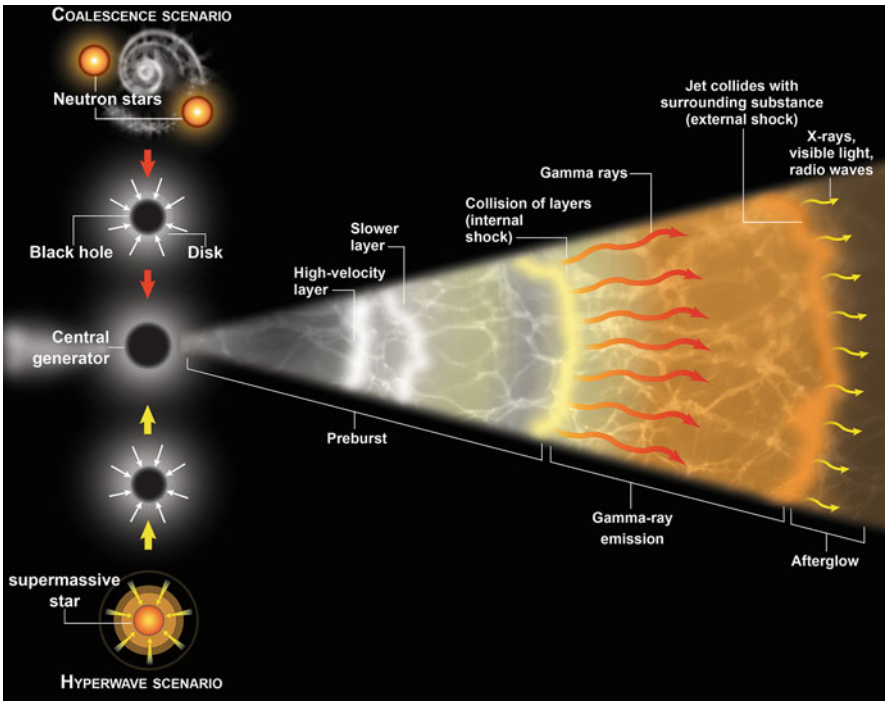

Fig. 10.50 Gamma-ray bursts may arise from either the coalescence of two neutron stars or the collapse of a supermassive star, in either case giving rise to a black hole and a disk of matter surrounding it. This system next ejects a matter jet with shocks inside of it [55]

The relativistic "fireball" model proposed for gamma-ray bursts in [98, 122] reduces to the following: as a result of the collision (coalescence) of two neutron stars [21] or the gravitational collapse of a supermassive star (Fig. 10.50) there occurs a $\approx 10^{52}$ erg energy release in a small domain filled with relativistic photons and leptons with a small admixture of baryons. This "fireball" with an initial temperature of 1–10 MeV expands with relativistic velocities and generates, by way of the synchrotron or inverse Compton mechanism, gamma-ray radiation by electrons accelerated by the Fermi mechanism in optically thin shock waves. A small number of baryons are also accelerated to relativistic energies and transport part of the energy away from the "fireball", generating outside of it outward and backward shock waves, whose X-ray radiation is recorded as a gamma-ray burst (Figs. 10.49 and 10.51). A substantially longer X-ray afterglow results from diverging shock waves. The ordinary duration of this radiation is ≥ 2 s.

It is generally agreed [5, 57, 98, 122, 177] that the predecessors of such objects are massive collapsing stars [122]. The shock waves generating gamma-ray radiation [40] emerge after the detachment of a "fireball" from the surface of a star, and the rotation of the star may transform the "fireball" into a powerful jet.

Fig. 10.51 Gamma-ray burst GRB030329 in the spiral galaxy NGC 3184 is related to a supernova explosion [163]

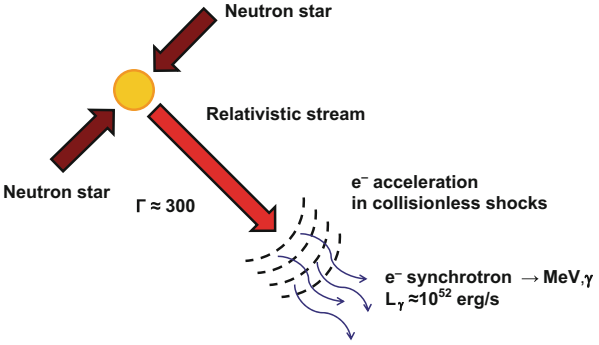

Fig. 10.52 Gamma-ray burst scenario with "fireball" formation [169]

The second class of short-duration bursts with a duration $t \approx 2$ s is related to the mutual absorption of binary neutron stars (Figs. 10.52 and 10.53) or a neutron star and a black hole. Also probable in this case is the emergence of one or two jets along the axis of rotation [40]. This mutual absorption may be a source of gravitational waves; research into the detection of gravitational waves has been pursued in recent decades [66, 67].

The typical density of matter in accretion disks and jets is $\rho \geq 10^{14}\,\mathrm{g/cm^3}$, which corresponds to the density of nuclear matter or neutron stars. As the "fireball" expands, inelastic nuclear collisions increase in importance and the relative velocity of neutrons and protons becomes comparable to the velocity of light. Inelastic *n*- and *p*-collisions produce charged pions, gigaelectronvolt muons, and electronic

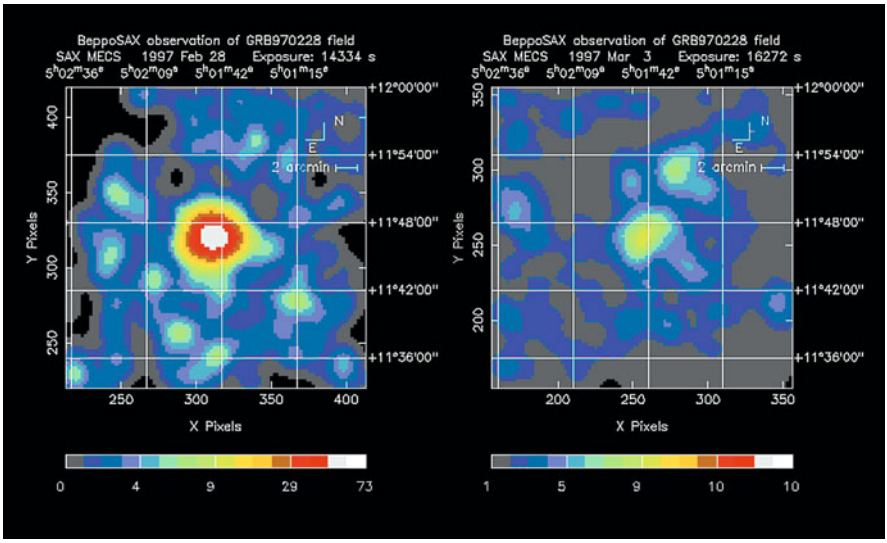

Fig. 10.53 Development of the gamma-ray burst GRB 970228. *Left*: Photo made on 28.02.1997. *Right*: Photo made 4 days later [163]

neutrinos, which should be detected by spacecraft [109]. Powerful relativistic jets from gamma-ray bursts correspond to Lorentz factors $\gamma \geq 100$ and extremely high energy fluxes (10^{50}–10^{52} erg/s or 10^{43}–10^{45} W). The energy density in the jet core, of the order of 10^{30} erg/cm^3, is sufficient for the spontaneous production of electron–positron pairs or nuclear reactions [56, 76, 109].

Further, at distances of $\geq 10^{11}$ cm, the electron mean (collision-)free path exceeds the characteristic jet dimension, and collisionless internal and external shocks accelerate electrons by the Fermi mechanism [48] with a relativistic distribution spectrum. Their interaction with the turbulent magnetic field generates nonthermal gamma-ray radiation, X-ray and optical radiation, which is recorded by recording instruments.

Furthermore, superimposed on the power-law continuum is the characteristic X-ray radiation arising from the interaction of the heated plasma regions with the disintegrating jets emanating from stellar surfaces.

The nonthermal spectrum in the shock-wave model of a "fireball" described above stems from the assumption that the Fermi acceleration model obeys the power law $N(j_e) \sim \gamma_e^{-p}$, with $p \approx 2$–2.5. This is quite consistent with observations [109]. To attain reasonable efficiency, the ratio between the accelerated electron energy and the accelerating energy should not be too small, $E_e \approx 1$, while the ratio between the magnetic energy and the total energy $E_e \leq 1$ depends on whether the synchrotron or inverse Compton spectral peak corresponds to the observed knee in the spectrum in the megaelectronvolt energy range.

In addition to that, the plasma wake acceleration mechanism [105] may also be of significance in gamma-ray bursts, because in the collision of neutron stars or the collapse of a star there emerge strong Alfvén shock or soliton waves as well as relativistic plasma ejections. In this case, to explain the gamma-ray signal shape requires taking into account the conditions of its transmission through the plasma atmosphere. Interestingly, the Alfvén (MHD) shock waves may carry an appreciable ($\approx 10^{-2}$) fraction of the "fireball" energy, i.e., up to $\approx 10^{50}$ erg. When propagating from the center, they may have a narrow front with a giant magnetic field of $\approx 10^{10}$ Gs behind it, which may compete with the Fermi particle acceleration mechanism [17].

The same mechanisms that are responsible for electron acceleration may also be applied to the acceleration of protons up to 10^{20} MeV.

Terawatt to petawatt short-pulse lasers (see Chap. 5, Sect. 3.5), which produce intensities of $\approx 10^{20}$ W/cm^2, are best suited to the laboratory modeling (at least, partial) of these processes. Impressive results have already been obtained in this area: well-collimated MeV-proton beams [34, 42, 89–92], electron and positron beams with energies of 100 MeV [15, 24, 27, 126], thermally relativistic plasma with $T_e > m_e c^2$, which corresponds to "fireball" conditions, as well as superhigh (>100 MT) magnetic fields [37, 93, 102, 105, 125, 155]. These ultraextreme plasma conditions are already approaching the parameters of gamma-ray bursts.

As noted in Chap. 7, the advent of petawatt lasers opens up new avenues for the production of relativistic and electron–positron plasma in the laboratory. At intensities above $\approx 2 \times 10^{18}$ W/cm^2 these lasers generate electrons with an energy $kT > m_e c^2$ in laser plasmas [9, 79, 81, 86, 105, 126, 182]. Electron–positron pairs [15, 27, 35, 84] emerge in the interaction of these electron streams with heavy targets by the Bethe–Heitler mechanism.

Experiments performed with a high-power laser have shown [68, 96, 128, 129] that the yield of the pairs even exceeded the theoretical estimates. In this case, two-sided irradiation simulations suggest that the expansion of the pairs proceeds faster than the expansion of gold ions. Here, the collision of two "fireballs" may be realized for the purpose of simulating the shock-wave gamma-ray burst model and studying the "fireball" energy conversion to the internal energy and gamma-ray radiation.

The laser-produced electron–positron plasma may also be employed for modeling episodical annihilation effects in the neighborhood of black holes. In the two-sided irradiation of a gold target, 2 MJ 0.1 PW lasers with a pulse duration of ≈ 10 ns are capable [109] of producing a pair density that is several hundred times the electron background density. This would allow the theoretical limitations, $kT \approx 20mc^2$, given by Sunyaev, Zel'dovich, and Levich [148, 183] to be verified.

Observations of the SN1987 supernova explosion in the Large Magellanic Cloud yielded [72] a wealth of new and unexpected information and gave strong impetus to laboratory astrophysics [38, 96, 128, 129, 139]. In particular, calculations and experiments exposed the important role [4, 39, 96, 129, 163] of hydrodynamic instabilities and mixing in the hydrodynamics of stellar explosions, much as this is critical for laser thermonuclear fusion. At the present time, the

corresponding experiments aimed at studying the Rayleigh–Taylor and Richtmyer–Meshkov instabilities in laser targets are being actively conducted in many plasma laboratories [38, 96, 105, 129, 139] and are yielding a wealth of data helpful for understanding transient astrophysical phenomena.

A significant part in the description of supernova explosions is assigned to one-, two-, and three-dimensional numerical simulations [4, 38, 39]. These calculations are based on the following assumption: as a result of gravitational stratification, the initial supernova structure (prior to the explosion) consists of an outer layer of hydrogen, next a helium layer, and so on up to the iron inner core. The gravitational collapse of this inner core gives rise to a radially diverging intense shock wave, which has high parameters at the helium–hydrogen interface, $\rho \approx 2.3\,\mathrm{g/cm^3}$, $T \approx 6\,\mathrm{keV}$, $P \approx 75\,\mathrm{Gbar}$, and leads to the development of the Richtmyer–Meshkov instability [4, 39, 44, 96, 129].

Remington et al. [128] employed the Nova laser to model a supernova explosion in the laser-to-soft-X-ray radiation conversion scheme. X-ray radiographic measurements enabled them to trace the nonlinear development stages of instabilities and to compare them with the data of numerical simulations.

It is likely that ultrarelativistic ultrahigh-energy-density plasma conditions are most amply reproduced in relativistic heavy-ion collisions. Figure 10.54 serves to illustrate the analogy between the expansion of the universe after the Big Bang and a "mini explosion" occurring in a laboratory in relativistic ion collisions in the RHIC accelerator in the domain of space $\approx$0.01–1 fm and time $\approx 10^{-23}$ s.

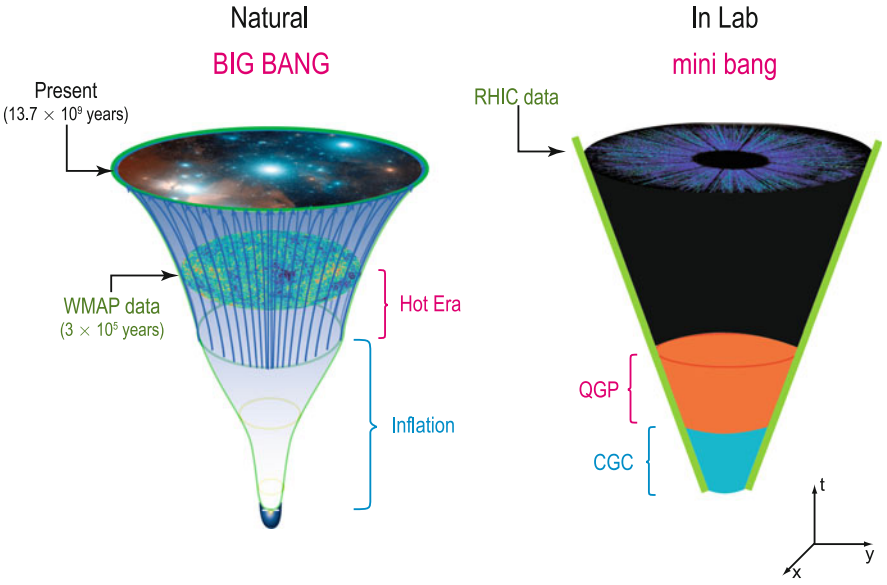

Fig. 10.54 Analogy between the Big Bang and a "mini explosion" in relativistic nuclear collisions

However, the experimental implications of ultrarelativistic effects may supposedly be recorded under presently attainable laboratory conditions, for instance, in studies of spontaneous proton decay. The point is that one of the three constituent quarks may, owing to quantum fluctuations, gain sufficiently high energy to result in proton decay. Despite the negligible probability of this process ($\approx 10^{33}$ years), for a large number of neutrons this process might be detectable in massive specimens. In a salt mine of Ohio State, eight thousand tons of water were used for this purpose. The absence of experimental detection of spontaneous proton decay yielded a lower bound for the proton lifetime, which is of consequence in constructing Grand Unification models [69].

10.4 Matter Transformation After the Big Bang

Figures 10.55 and 2.2 give a comparison of the capabilities of modern accelerators that reproduce in terrestrial laboratories the most "extreme" conditions occurring in nature—those of the "Big Bang". We see that elementary particle cosmology makes it possible to advance a long way in the measurement of the interaction of high-energy particles, which were of primary importance at the first instants of the life of the universe and defined its evolution for billions of years to come. Studying the evolution of the early universe furnishes a unique opportunity to investigate high-energy phenomena that it is impossible to reproduce in a laboratory.

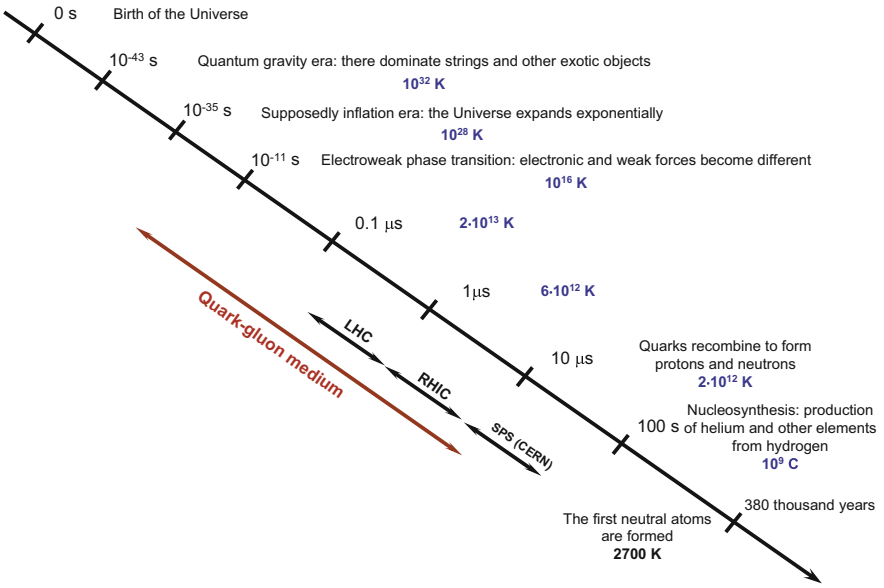

Fig. 10.55 Cosmic time scale. Universe expansion after the Big Bang [131]

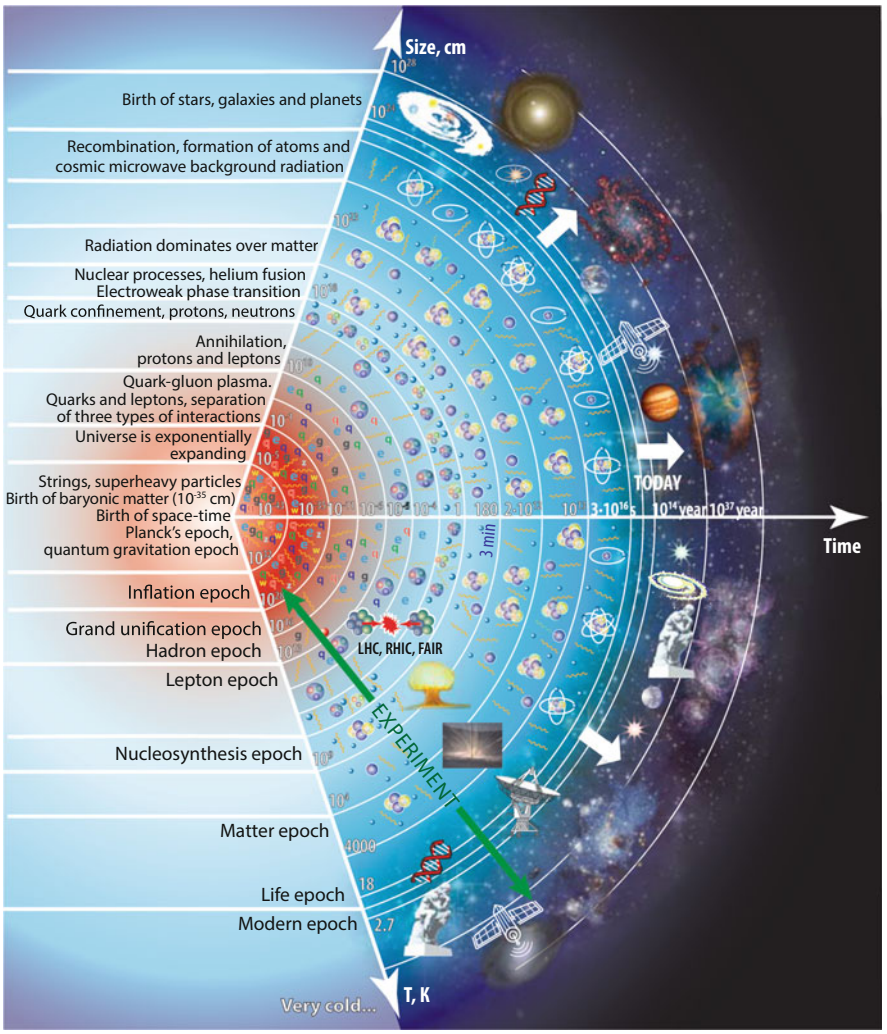

Fig. 10.56 Time scale after the Big Bang

According to modern notions [136, 141], the temporal evolution of the universe proceeded highly nonuniformly—whereas it is relatively slow nowadays, at the early stages it was strikingly fast, so that major qualitative changes of the state of the universe occurred in a split second. The universe we now observe emerged about 13.7–15 billion years ago from some initial singular state with infinitely high temperature and density, and since then it has uninterruptedly expanded and cooled down to present-day dimensions, of the order of 10^{28} cm, and average temperatures of the order of 2.7 K. According to the Big Bang theory (see Fig. 10.56, which gives the orders of magnitude of the quantities corresponding to the events occurring),

the subsequent evolution will depend on the present-day expansion velocity of the universe and the average matter density in the modern universe. If ρ is lower than some critical value ρ_{cr}, which is known from the theory and is expends on the expansion velocity, the universe will eternally expand; if $\rho > \rho_{cr}$, some day the expansion will be terminated by gravitational forces and the reverse compression phase will commence, the universe reverting to its initial singular state.

The lifetime of our Galaxy is determined in different ways. One of them involves monitoring of the glow of white dwarfs [83]. The compact and initially very hot celestial bodies are the final life stage of virtually all stars, with the exception of the most massive ones. To turn into a white dwarf, a star has to completely burn its thermonuclear fuel and experience several cataclysms—for instance, to become a red giant for some time.

A typical white dwarf consists almost entirely of carbon and oxygen ions embedded in degenerate electron gas and has a thin atmosphere made up primarily of hydrogen or helium. Its surface temperature lies in the range between 8000 and 40,000 K, while its central zone is heated to millions or even tens of millions of degrees. Suchlike stars are quite numerous, but they burn hydrogen extremely slowly and therefore live for many tens and hundreds of millions of years. They have simply had not enough time to exhaust their hydrogen fuel so far.

Now that a white dwarf cannot maintain thermonuclear fusion reactions, it shines at the expense of the stored energy and therefore cools down slowly. It is possible to calculate the rate of this cooling and determine on this basis the time taken for the surface temperature to decrease from the initial temperature to the observed one. Since we are dealing with the age of the Galaxy, it is required to search for the longest-living, and therefore coolest, white dwarfs. Modern telescopes permit discovering intragalactic dwarfs with a surface temperature below 4000 K, whose luminosity is 30,000 time lower than the solar one. So far they have not been found: they are either nonexistent at all or they are very few. Hence it follows that our Galaxy cannot be older than 15 billion years; otherwise they would be present in appreciable numbers [83].

The coolest of the presently known white dwarfs were detected by Hubble Space Telescope in 2002 and 2007 [83]. Calculations showed that they age amounts to 11.5–12 billion years. To this must be added the age of predecessor stars (from half a billion to billion years). Hence it follows that the Milky Way is by no means younger than 13 billion years. So that the final estimate of its age derived from white dwarf observations is approximately 13–15 billion years.

Estimates based on the analysis of relict radiation spectrum (the study of acoustic modes) yield a figure of 13.5–14 billion years for the age of the Universe. Estimates made by other methods yield close figures for the age of our Universe.

From the measurement data it follows that our universe expands by 5–10 % every billion years. However, the uncertainty in universe density estimates is substantially higher. The total mass of all visible stars in galaxies is less than one hundredth of ρ_{cr}. The inclusion of the mass of dark matter yields an average density of $\sim 0.1\rho_{cr}$. It is therefore most likely that our universe will eternally expand, unless some new mass sources are discovered. However, if the compression stage does set in, in any

case this will happen no earlier than in ≈10 billion years, when the Sun has gone out and terrestrial life has terminated.

But even if sapient life survives epidemics, mutations, and wars, manages to make provision for energy, and conserves or makes acceptable a human environment, before the eyes of our distant descendants there will appear, according to the model in [80], the unattractive view of the surrounding universe—the view of a dark abyss with scarce inclusions of rare stars amidst invariable emptiness. According to Krauss and Scherrer [80], this will result from the increasingly fast expansion, which with the lapse of time will make our galaxies recede from us with a seemingly supraluminal velocity and make them completely vanish from an observer's view. This process rules out the existence of reference objects for measuring the degree of expansion and also "washes out" all characteristic features remaining after the Big Bang. In other words, all observable manifestations of the Big Bang that have ever existed, and which are so plentiful in the universe surrounding us today, will be smoothed out.

In the model in [80], the accelerated expansion of the universe may lead to the formation of a fixed "event horizon"—an imaginary sphere from outside of which neither matter nor radiation will ever reach the observer inside. In such a model the universe becomes something like an "external black hole", when matter and radiation turn out to locked outside of the event horizon and not inside it. In this case, our "local group" of galaxies (including our galaxy, the Andromeda Nebula, and several dwarf companion galaxies) will merge into a single stellar supercluster. All other galaxies will vanish from an observer's view. This process will take about 100 billion years.

The relic radiation will virtually vanish as well; its maximum will shift to a wavelength in the meter range, while its intensity will decrease by many orders of magnitude. Furthermore, the electron component of the interstellar matter will not let this radiation into our galaxy.

The amounts of hydrogen and helium, which were produced during the first three minutes after the Big Bang, will considerably decrease due to thermonuclear reactions in stars, which, according to [80], will wipe out one more important consequence of the Big Bang. It is anticipated that the observable universe will collapse into a black hole in the distant future, which will happen before that to our galaxy as well.

Figure 10.57 shows the prospects for the course of events in the future as distant as 100 trillion years. The night sky of the Earth will radically change when our galaxy, the Milky Way, merges with its closest neighbors and distant galaxies vanish from our sight. In 5 billion years the Andromeda Nebula will fill the sky almost completely. The Sun will transform to a red giant and subsequently burn out. In 100 billion years, the Milky Way, the Andromeda Nebula, and other small galaxies will make up a giant ball-shaped galaxy. In 100 trillion years, the last star goes out and black holes shine dimly, along with artificial sources (if any) contrived by supercivilizations. The supergalaxy contracts to a black hole.

Fig. 10.57 Evolution of the observable part of the universe [80]

Table 10.2 Main epochs of the evolution of the early universe [141]

Name of epoch corresponding to its physical processes	Time elapsed after the Big Bang (s)	Temperature (K)
Emergence of classical space-time	10^{-43}	10^{32}
Inflation stage	$\approx 10^{-42}$–10^{-36}	Varies over very wide limits
Production of matter	10^{-36}	$\approx 10^{29}$
Production of a baryon excess	10^{-35}	$\approx 10^{29}$
Electroweak phase transition	10^{-10}	$\approx 10^{16}$–10^{17}
Quark confinement	10^{-4}	$\approx 10^{12}$–10^{13}
Primary nucleosynthesis	1–200	$\approx 10^{9}$–10^{10}

The main stages of the temporal evolution of the early Universe are represented in Table 10.2 [141] and in Fig. 10.58. Over the period of its existence, the Universe expanded from the Planckian length of 10^{-33} cm to the modern scale of $\approx 10^{28}$ cm. In the physics of elementary particles we have experimentally advanced to only

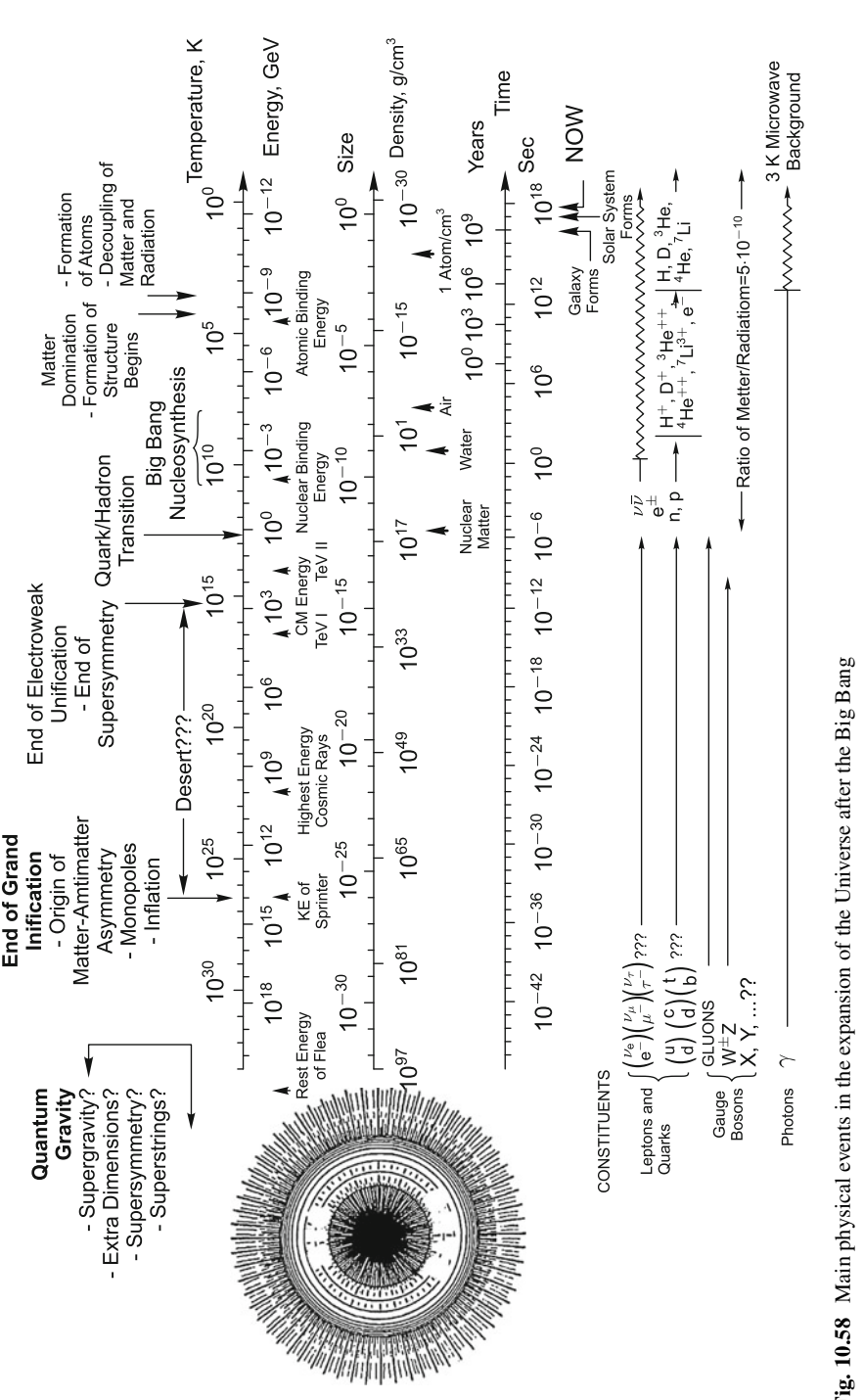

Fig. 10.58 Main physical events in the expansion of the Universe after the Big Bang

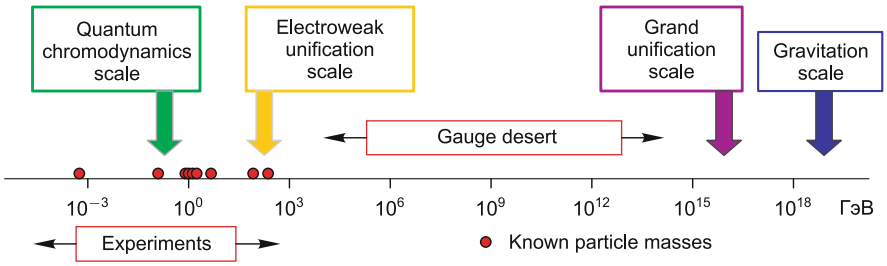

Fig. 10.59 Hierarchy of interaction energy scales [158]

10^{-15} cm. The new LHC accelerator-collider will permit us to advance an order of magnitude further.

The interaction energy scales are given in Fig. 10.59 [158].

Following [136, 141] in the subsequent discussion, let us consider these evolution stages.

10.4.1 Inception of the Universe

The very early time ranging from 10^{-43} s to 2–3 min is the most interesting and hard-to-describe period of the history of the universe, which saw the formation of its most essential properties. These properties now manifest themselves as the Hubble expansion, the large-scale structure of the universe, and the physical laws operating in the part of the universe observable to us.

The fundamental difficulties are aggravated in attempts to approach the "origin of the universe", more closely, i.e., to peer into the first hundredth of a second. To do this requires a profound knowledge of elementary particle physics in the superhigh-energy domain, which we do not have now, for the reason that these energies are unattainable with terrestrial accelerators. In the further advancement towards the origin of the universe there emerges the even more difficult problem of "quantization of gravity", which has no solution so far, not even a basically satisfactory one. That is why all attempts to investigate the earliest moments of the existence of our universe are in essence purely theoretical constructs.

The instant of universe's origin is the epoch of the birth of classical space-time. Generally accepted at the present time is the theory of the Big Bang, i.e., the origination of the universe from a singularity (from spatio-temporal foam, as is sometimes said) [141]. At the instant of the birth of the universe, the matter density ρ and temperature T amounted to Planck's values: $\rho_{\text{Pl}} \approx 10^{93}$ g/cm^3, $T_{\text{Pl}} \approx 1.3 \times 10^{32}$ K; under these conditions, the gravitational interaction is comparable with the others (strong, weak, electromagnetic) in strength and should be considered with the inclusion of quantization.

The enormous energies afforded by present-day accelerators are clearly insufficient for reproducing in laboratory experiments the conditions corresponding to the "Grand Unification" parameter domain $\approx 10^{15}$ GeV. To do this would require a Solar-System-sized accelerator.

Since the instant of the Big Bang, the universe has been continuously expanding, the matter temperature has been lowering, and the volume increasing. In the description of the birth of the universe, advantage is taken of the most general ideas of the quantum evolution of the universe as a whole. One of them asserts that the total mass of the closed universe is equal to zero. This signifies that the entire universe may come into being without energy expenses and with the initial geometrical dimension of the order of the Planck one.

As the universe expands, it borrows energy from the gravitational field to produce more matter. The positive energy of the matter is exactly balanced by the negative gravitational energy, so that the total energy balance is equal to zero.

10.4.2 Inflation

10^{-43}–10^{-42} s after the origin of the classical space-time, an inflation stage in the universe sets in [136, 141] (Fig. 10.60 [71]), which lasts until the stage of Grand Unification at $\approx 10^{-35}$ s, when the relic radiation emerges. Analyzing the inflation stage calls for the extrapolation of the known physical laws by 30 orders of magnitude on the spatial scale. Beyond that stage is thought to lie the limit of human philosophizing [65] and, as noted even by Tertullian—the great Christian philosopher of antiquity—this limit is precisely the boundary with the realm of theology.

To a high degree of accuracy the observable Universe is uniform and isotropic. In the framework of the Big Bang theory, these evident, on the face of it, properties have no satisfactory explanation, which is a serious problem or, to be more exact, a set interrelated problems. A successful solution of these problems is proposed by the inflation theory [61]. Furthermore, the inflation theory provides an elegant mechanism for generating primary nonuniformities in the Universe, which also is a problem for the theory of a hot Big Bang. This is precisely why the inflation theory is quite convincing.

According to the inflation theory, the stage of a hot Big Bang was preceded by the stage of a fast (close to exponential) expansion of the Universe—the inflation stage. At this stage, the equation of state of matter was close to the vacuum one, $p \approx -\rho c^2$, the energy density varied slowly with time, the Universe expanded rapidly to become uniform on a large scale and spatially planar with to a high accuracy. Upon cessation of inflation, a more or less long stage of post-inflation heating set in, with the result that vacuum-like energy eventually converted to heat. Only then did the stage of the hot Big Bang come. This all supposedly went on for an extremely short time.

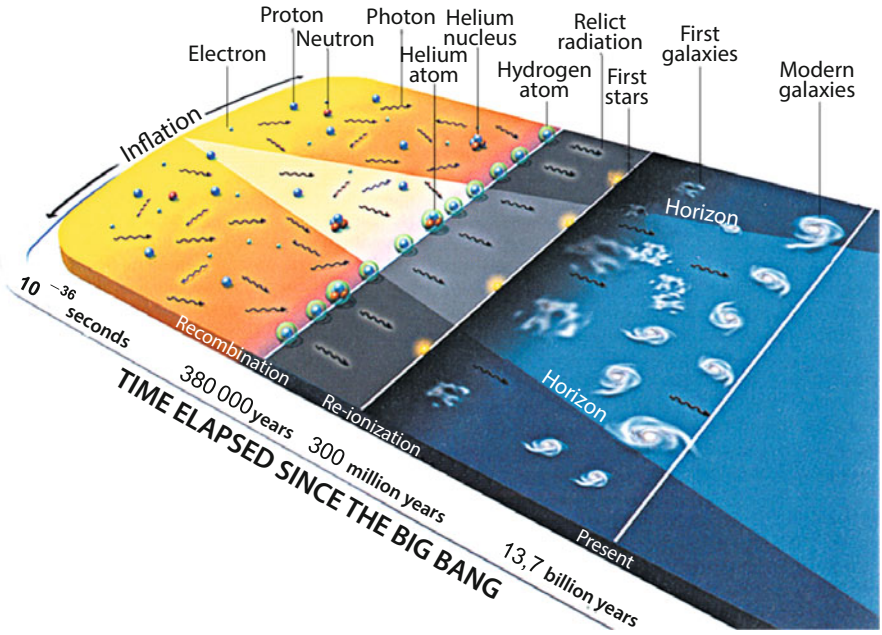

Fig. 10.60 Temporal scale of the universe. During inflation the universe expanded rapidly and the plasma, which consisted of photons and charged particles, propagated far beyond the horizon limiting the domain within the sight of a hypothetical observer. The onset of recombination occurred 380 thousand years later: the first atoms and the relic radiation emerged. 300 million years later, the light of the first stars ionized the major part of the hydrogen and helium [71]

Although the inflation theory has not been amply borne out by observations, several of its versions lead to predictions which may be verified in a relatively near future. It is remarkable that studying the properties of the Universe on the present-day cosmological scale is able to elucidate the properties of the Universe and its filling matter at the very first instants of evolution. This is one of the most glowing manifestations of the close interrelation between micro- and macrophysics existing in nature.

The first inflation model elaborated by Starobinskii (for more details, see [61]) is based on the gravitation theory with a Lagrangian containing both the first and higher powers of the curvature scalar. In this theory the Friedman equation is modified for high values of the Hubble parameter, resulting in the cosmological solution with a scale factor which grows exponentially during the long period of evolution. This model also contains the mechanism of post-inflation heating, which has the effect that the evolution of the Universe enters the hot stage. The Starobinskii model is quite successful from this viewpoint.

Recent times have seen the introduction of models [61] in which gravitation is described by the general relativity and the inflation mode emerges due to the presence of specific matter in the Universe. In actual truth, the Starobinskii model also falls into this category.

In order for the accelerated expansion to take place, the matter filling the Universe must have negative pressure:

$$p < -\frac{1}{3}\rho c^2.$$

The inflation stage is characterized by an ultimately high negative pressure $p \sim -\rho c^2$, whereby the very laws of ordinary gravitational physics are different. The matter in this state is the source of repulsion rather than attraction. It is not unlikely that the very early universe was filled not only with particles, but also with a temporal form of dark energy (with the inflaton field) with a very high density. This energy brought about the expansion of the universe with a very high acceleration, following which it decayed to form high-temperature plasma, which later divided into the usual matter and radiation. There only remained a weak trace of dark matter, which became significant only in the modern epoch. During the inflation stage, the volume of the universe increased by many orders of magnitude (by a factor of 10^{1000} in some models), so that the entire universe found itself in one causally connected domain, the kinetic expansion energy of the universe and its potential energy were equalized. During that stage there emerged the physical conditions which later led to the universe's expansion by the Hubble law.

Since the interparticle distance variation rate is proportional to the distance itself and the rate of expansion $R \sim e^{bt}$, this stage is termed inflatory: in the case of inflation, the growth of monetary aggregate obeys the same law of exponential growth.

Unlike the explosion of chemical explosives, where the expansion of the detonation products is related to the pressure gradient, the expansion in the case of the Big Bang springs from the negative pressure in a homogeneous medium—antigravity—which existed early in the existence of the universe.

During the inflation, gravitational repulsive forces accelerate particles, so that subsequently they move under their own inertia and form the Hubble expansion law.

Estimates show [61] that the minimal inflation duration is $\Delta t_{\text{infl}}^{\min} \approx 10^{-42}$–$10^{-9}$ s for $T = M_{\text{Pl}}$—1 TeV. During this short time the Universe manages to expand to a degree that the domains of initially Planckian size become cosmologically large. In this case, it is assumed that [61] the instant of the onset of inflation is the Planckian moment t_{Pl}, although some point in time $t_i \gg t_{\text{Pl}}$ may act as the instant of the onset of inflation.

In the proposed models, a high temperature sets in the Universe upon completion of inflation and post-inflation heating, which automatically signifies that the requisite entropy is present at the hot stage. At the same time, the mechanisms responsible for the inflation do not require that a large entropy should be in the

Universe early in the inflation stage; far from it. Entropy is generated during the post-inflation heating, when the energy of vacuum-like matter, which does not carry a high entropy, is converted to heat. To state it in different terms, the post-inflation heating process is strongly nonequilibrium from the standpoint of thermodynamics; it results in the production of entropy in the Universe.

At the inflation stage there occurred yet another important process [136, 141]: the production of small density perturbations from vacuum quantum fluctuations of a scalar field and of gravitational waves from quantum metric fluctuations. The vacuum quantum fluctuations, which normally manifest themselves only on a microscopic scale, rapidly increased in the exponentially expanding universe to become cosmologically significant. Therefore, the clustering of galaxies, which emerged at a later time, and the galaxies themselves are macroscopic manifestations of quantum fluctuations in the infancy of the universe.

From the observations of relic radiation anisotropy (10^{-5}–10^{-6}) (Fig. 10.61) it is therefore possible to reconstruct the spectrum of primary perturbations. From the primary perturbation spectrum and the gravitational wave spectrum it is possible to reconstruct the physical laws of the inflation stage, i.e., in the 10^{16} GeV energy domain. This is the aim of the experiments RELICT, COBE (Cosmic Background Explorer), and of the ground-based experiments Tenerife, Saskatoon, and CAT (Cosmic Anisotropy Telescope).

The difference in temperature between the domains of the early universe were sufficiently large that the extra gravity in higher-density domains terminated their infinite expansion and caused their contraction under self-gravity, with the resultant production of stars and galaxies, so that the map of Fig. 10.61 basically contains the prehistory of all structures of the universe.

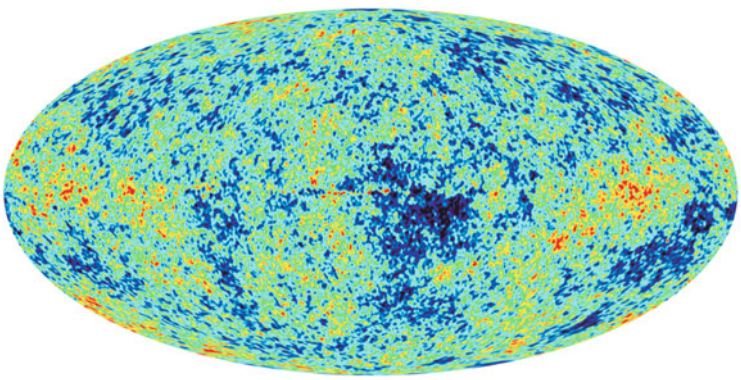

Fig. 10.61 Structure and angular distribution of the relic radiation reflect the state of the early universe. The primary nonuniformities of matter are equal to 10^{-5}–10^{-6} (L.M. Zelenyi, 2007, Private communication)

Monograph [61] contains an analysis of how modern galaxies and stars, which exceed the average density by a factor of 10^5–10^6, are formed from the initially small perturbations $\frac{\delta T}{T} \approx 10^{-4}$–$10^{-5}$. It analyzes in detail how the uniformities of substance density and metric develop in the expanding Universe. From the standpoint of observations, several interrelated aspects are here of special interest. The first is the density perturbation growth, which is eventually responsible for the formation of structures (galaxies, galactic clusters, etc.). The second is related to the observed relict radiation anisotropy and polarization; these are caused, one way or another, by density nonuniformities and, independent of them, perturbations of another type—gravitational waves (to be more precise, tensor perturbations). A comparison of theory and observations permits receiving answers to the two cosmologically critical questions:

- what was the spectrum of cosmological perturbations that existed at the early stage of hot Big Bang;
- what are the main properties of the Universe's medium—the ordinary substance, dark matter, and dark energy.

The primary perturbation spectrum defines the initial data for their evolution; had there been no primary perturbations at all, the Universe would have remained strictly uniform and isotropic and its structures would have never made their appearance.

It was shown [61] that relatively small-scale perturbations grow to the values $\frac{\delta\rho}{\rho} \approx 1$, while large-scale perturbations remain small (linear) up to the modern epoch.

The question of what was the mechanism for the emergence of the primary density and metric perturbations themselves is not solved in the framework of the hot Big Bang theory, which is a problem of this theory. Inflation theory provides an elegant answer to this question.

Following [61], we give the characteristic values of the astrophysical objects resulting from instability development. A compact object formed due to a collapse is of mass

$$M(R) \simeq \frac{4\pi}{3} R^3 \rho_{\mathrm{M},0},$$

where $\rho_{\mathrm{M},0}$ is the modern average mass density of dark matter and baryons. For a critical density $\rho_c = 1.5 \cdot 10^{11} M_\odot/\mathrm{Mpc}^3$, $\Omega_\mathrm{M} = 0.24$ ($\delta\rho \sim \exp(\Omega t)$), to a galaxy size $R = 1\,\mathrm{Mpc}$ there corresponds an object of mass $M \simeq 1.5 \cdot 10^{11} M_\odot$. This mass scale is typical for ordinary (non-dwarf) galaxies. We emphasize that we are dealing with the total mass, including the dark matter halo mass. So, the scales corresponding to galaxies:

$$R \approx (1\text{–}3)\,\mathrm{Mpc} \Leftrightarrow (10^{11}\text{–}4 \cdot 10^{12}) M_\odot.$$

Our Galaxy is large: its mass amounts to about $10^{12}M_{\odot}$. The specified size is the modern size of domains from which matter accumulates in galaxies. The dimensions of galaxies themselves are considerably smaller, they amount to 10–100 kpc, so that the matter density in central galactic regions exceeds the average density by factors of 10^5–10^6.

Galactic clusters are characterized by appreciably higher values of R and M:

$$R \approx (10\text{–}30)\,\text{Mpc} \;\Leftrightarrow\; (10^{14}\text{–}4 \cdot 10^{15})M_{\odot}.$$

These are the largest gravitationally coupled objects in the Universe. Their dimensions amount to 1–10 Mpc and the matter density in their central regions is 100–1000 times higher than the average one.

Perhaps, the smallest stellar formations embedded in dark matter halos are dwarf galaxies. For them, the corresponding estimates are of the form:

$$R \approx (40\text{–}400)\,\text{kpc} \;\Leftrightarrow\; (10^{7}\text{–}10^{10})M_{\odot}.$$

Baryons are "blown out" from halos of smaller mass by the radiation of the first stars and by substance fluxes resulting from the explosions of these stars. The mass scale $M \sim 10^5 M_{\odot}$ is nevertheless of interest: the first stars are produced in the halos of such mass. For these halos

$$R \approx 10\,\text{kpc} \;\Leftrightarrow\; 10^5 M_{\odot}.$$

From the standpoint of structure formation, of greatest significance are dark matter perturbations. They generate gravitational potentials in which ordinary substance finds its way upon recombinations.

As we saw above [61], for the inflation to be realized. the equation of state of the vacuum must have negative pressure:

$$p = -\rho c^2.$$

With this equation of state the scale factor changes by the law

$$a(t) = const \cdot e^{H_{\text{vac}}t},$$

where H_{vac} is independent on time and equal to

$$H_{\text{vac}} = \sqrt{\frac{8\pi}{3}\frac{\rho_{\text{vac}}}{M_{\text{Pl}}^2}}.$$

When the ordinary substance is also present in the Universe with a nonzero vacuum energy, the expansion with time will nevertheless be described by the exponential law, because the vacuum energy density remains constant in the expansion

of the Universe and the substance energy density becomes lower. Therefore, the assumption that the vacuum possesses positive energy leads naturally to inflationary expansion. However, also needed is a mechanism which terminates inflation and has the effect that the Universe heats up and passes into the hot stage. This mechanism may be the decay of scalar field [61].

Following [61], we describe in detail the solution of entropy problem proposed by the inflation. During the inflation, the matter in the Universe has no entropy but in return possesses substantial energy density, which slowly decreases with expansion. At the end of the inflation this energy converts to the thermal energy in a very large volume formed in the course of inflationary expansion, which results in a tremendous increase in entropy.

Therefore, the outlined scenario of chaotic inflation yields the following cosmological picture. The Universe is initially filled with the substance of Planckian density and, generally speaking, is poorly described by the laws of classical physics, so that even the ordinary notions about the classical space–time are inapplicable in this case. Some clusters of this quantum Universe, which were initially of nearly Planckian size, "inflated" due to inflation. The presently observable domain of the Universe occupies a part of one of these "inflated" clusters.

In this case, a microscopic (of Planckian size) region of the Universe extends during the inflation time to a domain of size $R \approx 10^{10^{13}}$ and $10^{10^{7}}$.

The theory of inflation and post-inflation heating successfully solves [61]—no difference whether on a Planckian or gigantic size—the problems relating to the initial data of the hot Big Bang era. Nevertheless, quite legitimate is the formulation of the question of whether the hot stage might have been preceded by some other, not inflationary, stage of the evolution of the Universe. One of logical possibilities is that the expansion of the Universe was preceded by its collapse, with a "rebound" upon the attainment of a rather high energy density, when contraction gave way to expansion.

In the framework of the classical general relativity, the change from contraction to expansion necessitates the existence of matter with highly unusual properties.

In the era when contraction gives way to expansion the Hubble parameter increases from negative values to positive ones, so that $H > 0$. This is possible only when $p < -\rho c^2$, with $\rho > 0$ on the strength of the Friedman equation.

The forms of matter known to us, including scalar and vector fields with standard Lagrangians, do not satisfy this equation of state. The hypothetic matter with this property is termed phantom (also used is the term phantom energy). Constructing self-consistent field-theoretic models with phantom properties is a highly nontrivial task.

Another possibility is that the rebound is caused by purely quantum processes not amenable to description in the framework of the classical general relativity. This possibility is discussed, for instance, in the framework of the pre-Bang scenario. Here, the difficulty is that the quantum theory of gravitation or a substitute theory (for instance, the superstring theory) are not elaborated to the extent to answer the

question of whether the rebound is possible in the quantum mode, and if yes, what is the state of the Universe upon reaching the mode of classical expansion.

Still more attractive is the concept of pulsating (cyclic) Universe. This scenario implies that the Universe or its part repeatedly passes through the periods of expansion replaced with contraction, subsequent rebound, and re-expansion. According to this picture, we are in one of these cycles. The uniformity and spatial planeness of the observable Universe may then be with dark energy dominance late in the cycles—the beginning of such a stage is taking place now.

The state of matter with a negative pressure is unstable; the substance must transit to a state with positive pressure. That is why the inflationary phase of Universe's development terminates rather quickly to give way to the stage of ordinary matter production (Fig. 10.62, Table 10.3) [136].

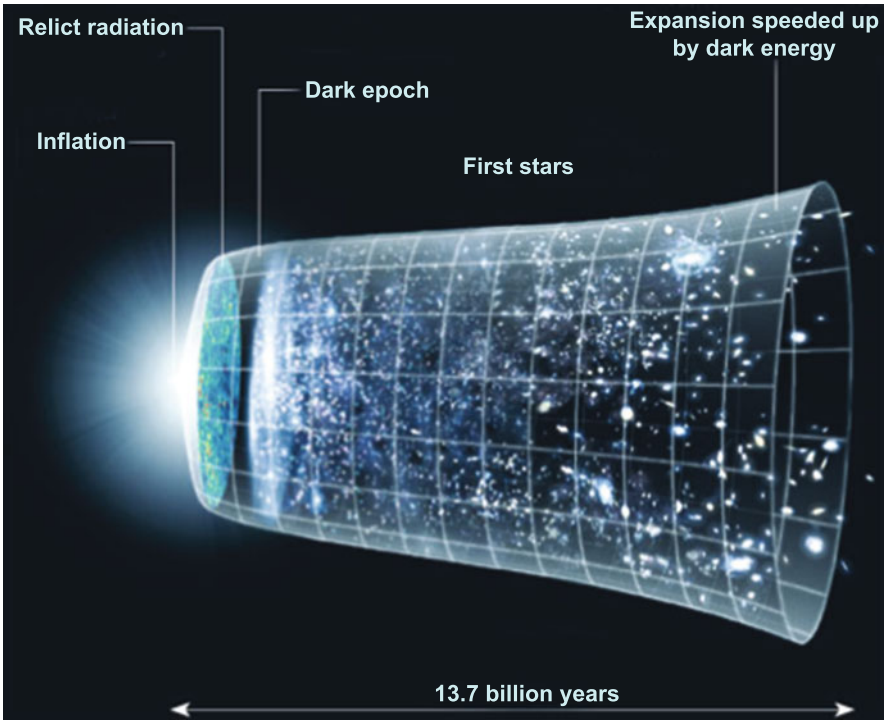

Fig. 10.62 Expansion of the universe with the distinguished initial stage (L.M. Zelenyi, 2007, Private communication)

Table 10.3 History of the universe: main stages [136]

Time	Radiation temperature (K)	Comments
10^{-43}–10^{-37} s	Above 10^{26}	Inflation.
10^{-6} s	Above 10^{12}	Plasma of quarks, gluons, electrons, and their antiparticles.
3×10^{-5} s	10^{12}–10^{9}	Quarks and gluons form protons and neutrons.
10^{-4} s–3 min	10^{12}–10^{9}	Production of deuterium, helium, and lithium nuclei.
15 thousand years	10^{4}	Equality of matter and radiation energy densities.
300 thousand years	4000	Formation of atoms from light nuclei and electrons. The universe becomes transparent for photons.
15 million years	300	Nothing particularly notable, except that the temperature of space was equal to room temperature and comfortable to human beings.
1–3 billion years	20	Formation of the first stars and galaxies.
3 billion years	10	Production of heavy nuclei in the explosion of the first stars; emergence of next-generation stars.
3–15 billion years	3	Emergence of planets and sapient life.
10^{14} years	Subsequently very cold	New stars have ceased to emerge.
10^{37} years		All low-luminosity objects have exhausted their energy. Black holes and elementary particles have persisted.
10^{100} years		All black holes have evaporated. Tenuous gas of stable elementary particles—electrons, three kinds of neutrinos, and possibly protons.

10.4.3 Post-Inflationary period

According to Kirzhnits [77], from this point on, $\approx10^{-37}$ s after the Big Bang, the universe underwent, after Friedman, a relatively slow expansion, and its temperature and density lowered with time. The starting temperature was about 10^{29} K, i.e., $\approx10^{16}$ GeV, which exceeds the X- and Y-boson masses. The condensate of Higgs particles, which is responsible for the emergence of this mass, is absent under these conditions; the X- and Y-bosons are massless, and the state of matter is realized that corresponds to complete symmetry between the strong, weak, and electromagnetic interactions. The matter itself is a hot dense plasma made up of massless particles (quarks, leptons, photons, gluons, W-, Z-, X-, and Y-particles) and massive Higgs particles. In this case, quarks and gluons transform freely into each other, and their relative densities are defined only by the temperature.

At the point in time, $\approx 10^{-33}$ s, when the temperature had lowered to 10^{14} GeV = 10^{27} K (the X- and Y-boson mass), there occurred a phase transition with the emergence of a condensate of the corresponding Higgs particles. Production of pairs of X-mesons with a mass of the order of 10^{15} GeV occurred, which decayed into quarks and leptons. According to A.D. Sakharov's idea, the baryon charge was not conserved at that time and particle–antiparticle CP symmetry violation occurred. This is how today's matter was produced with the number of protons $\approx 10^{80}$, which is close to the current value (the Eddington–Dirac number). That epoch is termed the epoch of Grand Unification of electromagnetic, weak, and strong interactions.

From that point on, the symmetry between the strong and electroweak interactions broke down, the mutual transformations of quarks and leptons strongly moderated, and a start was made on the formation of baryon matter asymmetry in the universe with the extraordinary predominance of matter over antimatter. Modern theories are able to explain (see, for instance, [136]) how this asymmetry emerges naturally in the course of evolution of the primary state in which the particle and antiparticle densities were equal.

An interesting implication of the possible formation of high-amplitude field fluctuations at the stage of post-inflationary heating is the generation of gravitational waves [61]. At this stage the field fluctuations may be long in wavelength; in essence, the only model-independent limitation is that these lengths may not exceed the current Hubble size. The parameters of these waves are estimated in [61]: $W_0 \approx 20$ Hz, $\lambda \approx 10^5$ km.

At the point in time $\approx 10^{-12}$ s, when the temperature had lowered to 10^2 GeV–10^{15} K (the W- and Z-boson mass), there occurred the second (electroweak) phase transition, with the emergence of the second condensate of those Higgs particles that are responsible for W- and Z-boson masses. From that point on their masses became nonzero, the symmetry between the electromagnetic and weak interactions broke down, and the matter itself was a plasma made up of massive leptons, quarks, gluons, and massless photons.

The next phase transition is thought to have taken place at $\approx 10^{-5}$ s, when the temperature had lowered to a value of ≈ 100 MeV, 10^{11}–10^{12} K (the characteristic scale of quark–gluon interaction when quark confinement occurs). As a result of this transition, the quark–gluon plasma transformed into a system of hadrons by way of quarks and antiquarks merging with the production of baryons and mesons of the corresponding resonances. At a temperature of 10^{11}–10^{12} K there occurs quark confinement ("no escape"). Quarks may exist in the free state only in a very hot plasma with a temperature $T > 10^{11}$ K. In the early universe, when the temperature far exceeded this value, there were no protons and neutrons and there existed a "quark soup". Due to the expansion of the universe the temperature lowered, quarks begin to combine to form protons and neutrons, and are no longer encountered in nature as separate particles (there is "no escape").

The technology of modern acceleration experiments enables the states in the temporal neighborhood only tenths–hundredths of a second after the Big Bang to be reproduced (Fig. 10.55); it is expected that commissioning of the LHC, RHIC,

FAIR, etc. accelerators will permit advances into the milli- to microsecond range. The subsequent epochs are characterized by the absence of quarks and gluons in the free state, and leptons, hadrons, and photons are the structural constituents of the matter. In this case, with decreasing temperature there occurs decay of unstable particles and the annihilation of pairs of baryons and heavy leptons.

Cosmological limitations correspond to a possible neutrino mass of $\leq$0.3 eV. The neutrino decoupling from baryon-electron-photon plasma occurs at temperatures of the order of 2–3 MeV. Neutrinos make an appreciable contribution to the total energy density at all stages of the hot Big Bang era. That is why they have a significant effect on the evolution of cosmological perturbations.

Prior to the annihilation of e^+e^- pairs, the neutrino temperature T_ν coincides with the photon temperature but becomes lower after it; under the approximation of instantaneous neutrino decoupling, it related to the photon temperature by the expression [61]

$$T_\nu(t) = \left(\frac{4}{11}\right)^{1/3} T(t).$$

In this case, the homogeneous part of the neutrino distribution function coincides nicely with the Fermi–Dirac distribution. The neutrino number density decreases as α^{-3} and in the modern era is $n_{\nu,0} = 112\,\mathrm{cm}^{-3}$ for each of the three active neutrino types.

After the epoch of proton and neutron production, the subsequent evolution of the universe led to the epoch of nucleosynthesis $\approx$1–100 s (a temperature of $\approx$0.1–1 MeV$\approx 10^9$–10^{11} K—the characteristic nuclear scale), during which primary nucleosynthesis occurred and the lightest matter constituents with atomic weight $A < 5$ were formed. The time interval between $t \approx 1$ and $t \approx 200$ s is of considerable importance in the life of the universe. The primary light nuclei were formed during this period: ^{4}He (25 %), deuterium ^{2}H (3×10^{-5} %), ^{3}He (2×10^{-5} %), ^{7}Li (10^{-9} %), i.e., a start wa made on the origination of the matter we are accustomed to. The rest of the isotopes, although they were produced during this epoch, were finally formed as matter components much later.

Approximately 1 s after the Big Bang, the primary plasma temperature lowered to 10^{10} K, which corresponds to an energy of $\approx$1 MeV.

With a decrease in temperature to $T = 0.7$ MeV, these weak-interaction reactions practically terminated and the neutron-to-proton number ratio became constant and equal to the number ratio at the close of the process. At that stage of the universe, protons and neutrons existed in the free form, not combined into nuclei. Later, when the temperature lowered to 100 keV, the majority of neutrons (with the exception of those which had managed to decay) were bound in the production of deuterium in the course of the reaction $p + n \rightarrow {}^2\mathrm{H} + \gamma$.

Deuterium, in its turn, efficiently captured primary plasma baryons to produce ^{3}He and tritium (^{3}H). On capturing one more proton or neutron there emerged ^{4}He, in which practically all undecayed neutrons ended up. The absence of suitable nuclei

with a mass number $A = 5$ impeded subsequent reactions, making the production of heavier elements (^{3}He + ^{4}He $\rightarrow ^7$Be, 3^4He $\rightarrow ^{12}$C, etc.) a highly improbable event.

On further temperature lowering, the substance consisted of H and He nuclei, electrons, photons (their density n_γ is 10^9 times higher than the nuclear density), and neutrinos, which hardly interact with the rest of the substance. This era is spoken of as "radiation-dominated" epoch due to the prevalence of the contribution of electromagnetic radiation to the substance energy.

In this era (the "fireball" era), relict radiation was the main form of matter. The closer are we to the inception of the Universe, the higher is the frequency of this radiation.

With expansion of the Universe, the plasma and radiation temperatures would become lower. The radiation frequency also had to decrease, with the effect that the initially visible light became invisible and shifted to the radio-frequency band. Today it is recorded as the radio-frequency radiation with a temperature $T \approx 2.4\,\mathrm{K}$ and is called the relict radiation. Unlike the ordinary light, the relict radiation has no source: the entire Universe as if shines or "floats" in the ocean of light [64].

The relict radiation density $\rho_{\mathrm{rad}} = 10^{-34}\,\mathrm{g/cm^3}$, and today it is lower than the ordinary substance density. But this has not always been so. The point is that the substance density is inversely proportional to the volume, which signifies $\rho_{\mathrm{sub}} \sim R^{-3}$ in terms of the length scale. The expansion of the Universe changes the spacing of electromagnetic radiation wave crests to increase the wavelength. That is why the relict radiation photon energy is inversely proportional to R and the relict radiation density $\rho_{\mathrm{rad}} \sim R^{-4}$. When we move into the past with $R \rightarrow 0$, the density ρ_{rad} rises faster than ρ_{sub}.

We note, however, that the ratio between the photon number (not energy) density and the proton number density remains invariable: $n_\gamma / n_b = 10^9$. This quantity is called specific entropy.

The time determined from the condition for the onset of hydrogen transparency, which for some coincidence is the time when $\rho_{\mathrm{sub}} = \rho_{\mathrm{rad}}$, is called the recombination time. Before this point in time $\rho_{\mathrm{sub}} < \rho_{\mathrm{rad}}$, and the corresponding epoch is called the "fireball era" [64]. The temperature of relict radiation depends on the scale factor, $T \sim R^{-1}$. The recombination era is characterized by temperatures of the order of several thousand degrees. At higher temperatures, atoms cannot exist, because electrons would be immediately torn away from their shells. The relict radiation was seen in the visible region; in this epoch the sky was not dark, it was glittering, gradually becoming red and then invisible with expansion!

A significant property of the relict radiation is its isotropy: its properties are the same in all directions, which is an important confirmation of Friedman's isotropic model of the Universe.

For a high frequency there occurred particle–antiparticle production by photons. That is why the relic radiation in the very early universe [65] is more often used in reference to the plasma of particles and antiparticles rather than a photon gas. Such a plasma is termed an ambiplasma. For $kT = m_e c^2$, we are dealing with the leptonic era; for a higher temperature $kT \sim m_p c^2$, we are dealing with the hadronic era.

In the fireball epoch, protons, neutrons, and electrons, as well as the light elements deuterium, tritium, helium, and lithium, which were produced during the first three minutes of the universe, played only an insignificant role. The light pressure was so high that massive particles were uniformly scattered about the universe and could not form any structures such as galaxies, stars, and planets by gravitational attraction. However, dark matter, which did not interact with relic electromagnetic radiation, was something else again. Due to gravitational interaction, that dark energy was able to curl long before similar processes involved visible matter.

During the epochs under discussion, the primary plasma obeyed the radiation-dominated equation of state $p = \rho c^2/3$. In this epoch there occurred annihilation of electron–positron pairs with their transformation to photons. Experiments involving underground nuclear explosions [10, 11, 160, 166] yielded a plasma and photon temperature of $\approx 10^7$ K and an energy density of 10^9 J/cm^3, corresponding to the states several minutes distant from the Big Bang, which are close to the lower bound of the radiation-dominated regime. This predominance is no longer manifested during the epoch 10^8–10^{10} s (other estimates suggest a figure of $\approx 10^{12}$ s) (the temperature $\approx 10^4$–10^5 K corresponds to $\approx$1–10 eV, the characteristic atomic energy scale), when the energies of electrons and nuclei are insufficient to overcome their electromagnetic attraction and electrons recombine with nuclei to give rise to neutral atomic matter transparent to photons.

Until that time, in the "fireball" era the universe expanded by the law $R \sim \sqrt{t}$; later, when matter came to play a leading part, the expansion law approximately assumed the form $R \sim t^{2/3}$.

10.4.4 Recombination Era

In the recombination epoch the light pressure lowered to the extent that particles were attracted to one another. Since all that took place gradually and the relic radiation did not cease at once to interact with visible matter by passing to the radio frequency band, there existed some period when the universe heard the "first sound" [65]! This sound is also referred to as the "Sakharov acoustic oscillations" after A.D. Sakharov, who hypothesized that they existed in the early universe. The situation is that, as noted above, between the particles of visible matter there were counteracting forces of gravitational attraction and repulsion due to electromagnetic pressure. That is why the particles alternately approached each other and moved away, and as the pressure lowered there emerged decaying oscillations of particle density similar to sound oscillations. That sound was a "whisper"—an infrasound with a wavelength of the order of the horizon in the recombination era. However, where it was heard, there emerged density perturbations, which subsequently turned into galaxies.

The curling of particles and hence higher-density domains emerged where there already existed nonuniformities caused by dark matter. Without dark matter galaxies would not have been formed by the present time. The visible matter nonuniformities caused nonuniformities in the temperature distribution of the relic radiation (Fig. 10.61), which are the reflection of the first sound and the nuclei of future galaxies.

The recombination epoch coincided with the universe "transparentization" epoch: the plasma disappeared and the matter became transparent. The temperature of this epoch is quite well known from laboratory physics: $T \approx 4500$–$3000\,\mathrm{K}$.

After recombination, photons reach the observer virtually without interacting with matter and make up the relic radiation. Nowadays its energy spectrum corresponds to the spectrum of a blackbody heated to a temperature of 2.75 K. The difference between the temperatures ≈3000 and ≈3 K arises from the fact that the universe has expanded by about a factor of 1000 since the transparentization epoch.

The medium of the modern Universe consists of several components: baryons, photons, neutrinos, and dark matter. At relatively late stages of cosmological evolution, individual components experienced no interaction between each other. Prior to recombination these components were the baryon-electron-photon plasma, dark matter, and neutrinos; after recombination, photons also decouple.

After recombination, which went on in the early Universe at a temperature $T \simeq 0.25\,\mathrm{eV}$, the Universe became transparent or, to be more exact, almost transparent to the primary plasma photons. These photons have persisted in the Universe until the present time and are observed in the form of relict radiation. Measurements of relict radiation characteristics permits obtaining extremely valuable information about the Universe in the era of recombination and estimating the age of the Universe. Furthermore, the post-recombination propagation of relict photons was affected by the expansion of the Universe and the processes related to structure formation. That is why the relict radiation carries valuable information also about more recent stages of Universe development.

The energy spectrum shape of relict radiation coincides with a high degree of accuracy with the shape of the Planckian spectrum. This statement results from the data analysis of numerous relict radiation observations at different frequencies. Small variations of radiation intensity in relation to the arrival direction are variations of the temperature—the only characteristic of the Planckian spectrum. The average temperature of relict photons (they number approximately 400 in $1\,\mathrm{cm}^3$) is $T_0 = 2.725 \pm 0.001\,\mathrm{K}$.

A small angular temperature variation $\delta T/T \approx 10^{-3}$ exhibits a clearly defined dipole nature and is attributable to terrestrial motion. A smaller variation structure has an amplitude $\delta T/T \approx 10^{-5}$, and it is precisely this structure that is underlain by a highly nontrivial physics. Apart from the angular dependence of the temperature of relict radiation, of major interest is its polarization, which also depends on the arrival direction of relict photons.

It is significant that the prerequisites for the production of future galaxies are found even in the "fireball" era, in which weak nonuniformities (density fluctuations) were produced, which disturb the general uniformity and isotropy of the uniform and isotropic plasma. These are the "nuclei" of future galaxies. After the recombination era, when the temperature of the universe became lower and the radiation ceased to strongly interact with matter particles and to "scatter" them in space, these "nuclei" attracted particles due to gravitation. In 1993, the first experimental data were obtained from the COBE satellite. The temperature of some regions ("spots") of the sky is slightly (10^{-5}–10^{-6}, Fig. 10.61) different from that of other areas.

After the recombination era, the "dark ages" [65] set in: the relic radiation had decoupled from matter, and the stars in galaxies had not started shining. In that era there emerged protogalaxies as gas clouds. They collided with each other to form black holes. These black holes admitted visible matter, which shone, and there emerged quasars. The relic radiation manifested itself only weakly, the dominant role being played by dark and visible matter.

Approximately 5 billion years ago there occurred yet another important event in the history of the expansion of the universe. The cosmological constant came into play [65]. Earlier it had counted for very little: being a constant small quantity, it was below the matter density of the relic radiation. The universe started expanding exponentially. Due to relative acceleration, galaxies experienced stronger repulsion from each other, which hindered their mutual collisions; this circumstance turned out to be of consequence for the possibility of the emergence of the Sun, the Solar System, the Earth, and life on it.

One more major milestone is located between the recombination epoch and our time—the formation of the large-scale structure of the universe, or the formation of galaxies. This epoch falls in the time when the temperature of relic plasma photons was $T \leq 30\,\mathrm{K}$. In the intervening period there lies the epoch of nonlinear evolution of extragalactic objects, i.e., the epoch of ordinary galaxies, quasars, and clusters and superclusters of galaxies.

At that time, the universe as a whole continued to expand and cool down. In domains with a somewhat higher density than the average, however, the matter expansion moderated due to the additional gravitational attraction and entered the phase of gravitational compression with a slow rotation. The increase of the angular velocity of this rotation in the compression of the matter has the effect that the centrifugal force comes to be of the order of the gravitational one. Here is how rotating galaxies came into being [69].

Hydrogen and helium in these galaxies were compressed by gravitational forces and heated up, fostering thermonuclear fusion reactions. The corresponding temperature growth stopped the gravitational compression, resulting in solar-type stars. Because of stronger gravity, more massive stars heated up to higher temperatures and burned up their hydrogen in a shorter time (in several hundred million years);

thermonuclear transformation of helium to heavier elements such as carbon and oxygen began. After that, the central regions compressed to a superdense state like a black hole or a neutron star, while the outer regions, which contained heavy elements, were carried into interstellar space as a result of a supernova explosion to provide the material for the next generation of planets and stars. In particular, our Sun is a second- or third-generation star. The evolution of stellar objects is considered in greater detail in Sect. 9.2.

We emphasize once again that the atoms of our body were produced inside the stars, and atomic nuclei were produced even during the first three minutes of the life of the universe. Figuratively speaking, when we peer into huge distances, it is as if we are looking into the distant past because of the finiteness of the speed of light: very far away is the "place" where the atomic nuclei of our body were born and, still earlier, the elementary particles themselves [65]. In this sense the universe appears like an enormous "house", in which, according to the anthropic principle (see below), everything was prepared for the advent of human beings and which retains "photographs" from their first steps to our days.

We give the formula [177] that describes the temperature variation during the early expansion stage, down to $T \approx 10^{12}$ K:

$$T = \frac{1.3}{\xi^{1/4}\sqrt{t}} \text{ MeV}.$$

By inverting this formula we obtain the point in time after the onset of expansion at which the temperature of relativistic particles was equal to T:

$$t = \frac{1.7}{(T\ [\text{MeV}])^2\, \xi^{1/2}} \text{ s}.$$

10.4.5 Nucleosynthesis

Beginning from the atomic epoch, the photon gas has cooled independently of the rest of matter, nowadays manifesting itself as the relic radiation.

The nucleosynthesis stage is the final stage relating to the early universe. It terminated three minutes after the Big Bang.

The nucleosynthesis epoch is followed by the hidden-mass domination stage, which set in at about a temperature of $T \approx 10^6$ K, depending on the type of hidden matter carrier. Beginning with this epoch, small perturbations of matter density developed, which built up to the extent that there emerged galaxies (5–10 billion years after Big Bang), stars, and planets (10–11.5 billion years).

At this point, the cosmological stage, i.e., that relating to the universe as a whole, of matter formation of our surrounding universe may be thought of as being complete. The subsequent stages are inherently local and involve the formation of the structure of the universe—the large-scale structure (clusters and superclusters), galaxies, stars, and planets. The prevalent form of visible matter at these stages is the plasma state (cosmic plasmas: circumplanetary, interplanetary, intraplanetary plasmas, the plasma of stars and stellar atmospheres, the plasma of quasars and galactic nuclei, interstellar and intergalactic plasmas, quark–gluon plasma).

Of special significance from the standpoint of matter composition formation is the hot stellar plasma, in which there occurs the synthesis of the nuclei of light elements up to carbon (the stars of the main sequence and red giants). Heavier elements are produced in the explosion of supernovae—the catastrophic late stages of stellar evolution—by way of neutron capture with subsequent β-decay. This picture of element production allowed Carl Sagan to consider that we are all made of stellar matter.

Also produced in supernova explosions are cosmic rays—a strongly nonequilibrium component of matter. At the last stages of their evolution, stars move to the state of either a white dwarf, whose matter is an ideal, "simple" metal (a crystal lattice of nuclei surrounded by a nearly free electron gas), or a black hole, or a neutron star. The latter, as discussed above, contains a liquid (superfluid) core, made up of neutrons with a small admixture of protons and electrons (neutron matter); the inner crust, consisting of a crystal lattice of neutron-excessive nuclei, an electron gas, and a neutron liquid; and the outer crust, which is structurally similar to the matter of a white dwarf.

Following [151], we outline a more detailed picture of the production of chemical elements in the Universe. We start from that evolution stage wherein the Universe consisted of a mixture of quarks, gluons, leptons, neutrinos, and photons at the first instants after the Big Bang. As our Universe expanded, the substance density and temperature became lower, which permitted quarks to combine to form neutrons and protons (nucleons). Nucleon-nucleon collisions would produce the first simplest atomic nuclei; however, because of collisions with photons and other particles of tremendous energy, these nuclei immediately decayed to separate nucleons. With expansion of the Universe, the substance density and temperature decreased, which raised the survival probability of the nuclei. The thermonuclear reactions (Sect. 4.1)

$$\mathrm{n} + \mathrm{p} \to {}^{2}\mathrm{D},$$

$${}^{2}\mathrm{D} + {}^{2}\mathrm{D} \to {}^{3}\mathrm{He} + \mathrm{n},$$

$${}^{2}\mathrm{D} + {}^{2}\mathrm{D} \to {}^{3}\mathrm{T} + \mathrm{p},$$

$${}^{3}\mathrm{T} + {}^{2}\mathrm{D} \to {}^{4}\mathrm{He} + \mathrm{n}$$

gave rise to deuterium ^{2}D and tritium ^{3}T nuclei and the helium isotopes ^{3}He and ^{4}He. But, since there are no stable nuclei of atomic mass 5, it was impossible to synthesize the nuclei heavier than ^{4}He by sequential attachment of protons or

neutrons to helium isotopes. Furthermore, by the instant there formed an appreciable amount of helium, the substance temperature lowered to the extent that the reactions

$$^3\mathrm{He} + {}^4\mathrm{He} \rightarrow {}^7\mathrm{Be},$$

$$^4\mathrm{He} + {}^4\mathrm{He} \rightarrow {}^8\mathrm{Be},$$

$$^8\mathrm{Be} + {}^4\mathrm{He} \rightarrow {}^{12}\mathrm{C}$$

were inefficient owing to a stronger Coulomb repulsion in comparison with protons. That is why in about 3 min after the inception of the Universe the primary synthesis of the elements terminated. Calculations and observations suggest that by this moment the substance of the Universe consisted of hydrogen by 75 % and of the ^{4}He isotope by 25 %. There were also small amounts of deuterium ($\approx$0.003 %) and the light helium isotope ^{3}He ($\approx$0.002 %); the heavier-than-helium elements had been synthesized in negligible amounts. As for free neutrons and tritium, which were present in appreciable amounts during nucleosynthesis, they soon vanished, being unstable particles:

$$\mathrm{n} \rightarrow \mathrm{p} + \mathrm{e}^- + \tilde{\nu},$$

$$^3\mathrm{T} \rightarrow {}^2\mathrm{D} + \mathrm{e}^- + \tilde{\nu}.$$

In the modern era, i.e. approximately 13.5–14.5 billion years after the inception of the Universe, the abundance of hydrogen and helium remains almost the same as at the instant of completion of the primary nucleosynthesis. However, the abundance of heavier elements became considerably higher. The mass fraction of these elements in the interstellar gas of our Galaxy amounts to 2–3 %. Most abundant in the interstellar medium are oxygen atoms, the number of carbon atoms is two times smaller, and further, in the order of decreasing number of atoms, are nitrogen, neon, iron, silicon, etc.

All elements heavier than helium were synthesized in stars [151]. Although thermonuclear reactions take place deep in the interior of a star, the products of these reactions may well find their way into its ambient space. The first possibility consists in the convective transfer of nuclear transformation products to the outer stellar layers and from there into the interstellar medium together with the stellar wind. Such processes are most efficient at the late stages of stellar evolution.

As we saw, the second possibility of enriching the interstellar medium in heavy elements is supernova explosions, when a shock wave ejects the stellar substance in all directions to turn it to the interstellar gas. Not only does the shock wave entrain the gas when propagating from the stellar center to the surface, but it also heats the gas to an enormous temperature. As a result, thermonuclear reactions commence behind the shock front. In the course of these reactions, the substance transforms from hydrogen to nickel almost instantly; the heat released in this case feeds the shock wave and forms a thermonuclear detonation wave, not letting it die down. And though the synthesis of heavier-than-iron elements (Fig. 4.3) goes

with energy absorption rather than energy liberation, the amount of energy released in a supernova explosion is so enormous that there appears a possibility to spend a certain part of it for the synthesis of even very heavy elements like uranium. Generally speaking, the heavier is the element, the lower is the probability of its synthesis, although there are exceptions to this rule caused by the special features of different atomic nuclei and the occurrence probabilities of one or other fusion reaction. As for nickel, like in the "quite" burning in the central regions of massive stars, produced in largest amount is its unstable isotope $^{56}_{28}$Ni, which beta decays to cobalt, which in its turn decays to the stable iron isotope $^{56}_{26}$Fe.

As discussed above, the greater is the mass of a star at inception, the greater is the part of its mass it sheds to the interstellar medium by the instant of its death, and the most massive stars (100–150 $M_\odot$) are completely destroyed. Furthermore, the lifetime of a star shortens with increase in its mass. These two circumstances make massive stars into the main suppliers of heavy elements. The first stars in the Universe consisted only of hydrogen and helium. Several million years later, the most massive of them perished and ejected the first portions of heavy elements into the interstellar medium. The gas enriched in this substance mixed with the hydrogen-helium gas of the interstellar medium. Some time later, this mixture gave rise to a new generation of stars; the most massive of them died soon to further increase the density of heavier-than-helium elements. During the lifetime of the Universe, thousands of massive star generations managed to come into being and perish, each time raising the fraction of heavy elements in the interstellar medium. Also born, of course, were low-mass stars, which have persisted to our days and retained in their outer layers the chemical composition corresponding to the interstellar medium they were formed of. In globular star clusters older than 10 billion years, astronomers discovered stars which contained heavy elements in amounts 100 times smaller than in the surface solar layers. Recently, it has been possible to discover stars in whose substance the amount of heavy elements is tens of thousands of times lower than in the Sun. These are presumably the oldest stars of our Galaxy.

The outlined scenario is of major consequence for our life [151]. It exists thanks to organic molecules, which are hydrogen compounds with virtually all elements of the periodic table and, above all, with carbon. This signifies that all living things consist of matter which formerly, and more than once, was in the stellar interior and went through thermonuclear stellar reactors.

Therefore, we see that our universe has gone through an extremely stormy youth full of extraordinarily bright events. The "Planck temperature" $T = 10^{32}$ K was reached in 10^{-43} s after the beginning of the universe, $T = 10^{13}$ K was reached in 10^{-6} s, $T = 10^{11}$ K in 0.01 s, $T = 10^{10}$ K in 1 s, $T = 10^{9}$ K in 1 min, $T = 10^{4}$ K (change of epochs) in 100,000 years, and $T = 10^{3}$ K in 1 million years. Therefore, primary nucleosynthesis was completed within several minutes of the "birth of the universe" and the formation of atoms within 1 million years. After this rather stormy period, the initial evolution stage was completed and the routine senile expansion phase is reached, which we now observe approximately 15 billion years after the "birth of the universe".

The evolution stages of the Earth and the Sun in the close-to-modern times are reasonably well known [83]. Modern helioseismology permits determining the solar age directly, which is equal to 4.56–4.58 billion years, according to the latest data. Since the duration of gravitational condensation of the protosolar cloud continued for only billions of years, it is valid to say that no more than 4.6 billion years have passed since the onset of this process to our days. This being so, the solar substance contains a lot of heavier-than-helium elements, which were produced due to nuclear reactions in the interior of previous-generation massive stars burned and exploded in the form of supernovae. This signifies that the life span of the Universe is far greater than the age of the solar system.

According to radiometric dating, the oldest rock on the Earth is the grey gneiss of northwestern Canada—its age is estimated at 4.03 billion years [83]. Crystallized even earlier (4.4 billion years) were the tiny grains of the mineral zircon, natural zirconium silicate, found in the gneiss in Western Australia. Since the terrestrial crust already existed at that time, our planet must be somewhat older. As for meteorites, the most precise information is provided by the dating of calcium-aluminum inclusions in the substance of carbonaceous chondrite meteorites, which has hardly changes after its formation from the gas-dust cloud which surrounded the newborn Sun [83]. The radiometric age of suchlike structures in the Efremovka meteorite found in the Pavlodar region of Kazakhstan is equal to 4 billion 567 million years.

As we saw above, the human life on the Earth will decease in about 5 billion years owing to the burnout of solar thermonuclear fuel. Of course, in the event that the Lord in His kindness would continue to bear the mankind on the Earth until that time.

10.4.6 Our Time

Figure 10.63 shows the scenario of the universe's evolution discussed in [29]. According to Carroll [29], the universe sprang into existence as a highly uniform plasma and will go out of existence on turning into almost empty space, i.e., the universe evolves from a low-entropy state to a high-entropy state—the final state being termed "heat death".

The vigorous epochs of biological progress, of the origination of life and civilization that we witness nowadays fall precisely in this routine development process of the universe (Fig. 10.64). In particular, the planet Earth was formed about 5 billion years ago, elementary organic life about 4 billion years ago, and DNA and the genetic code about 3.5 billion years ago. Plants and animals emerged about 1.2 billion years ago. Early human ancestors came into existence about one million years ago and the *Homo sapiens* species about 200,000 years ago. This species began to speak only ≈50,000 years B.C. and write 6000–8000 years ago. Modern civilization is believed to have appeared at the end of the last glacial period—about 10 thousand years B.C., when the Earth's temperature approached the modern level of ≈15 °C. The last mammoth vanished from Taimyr and the Wrangel island only

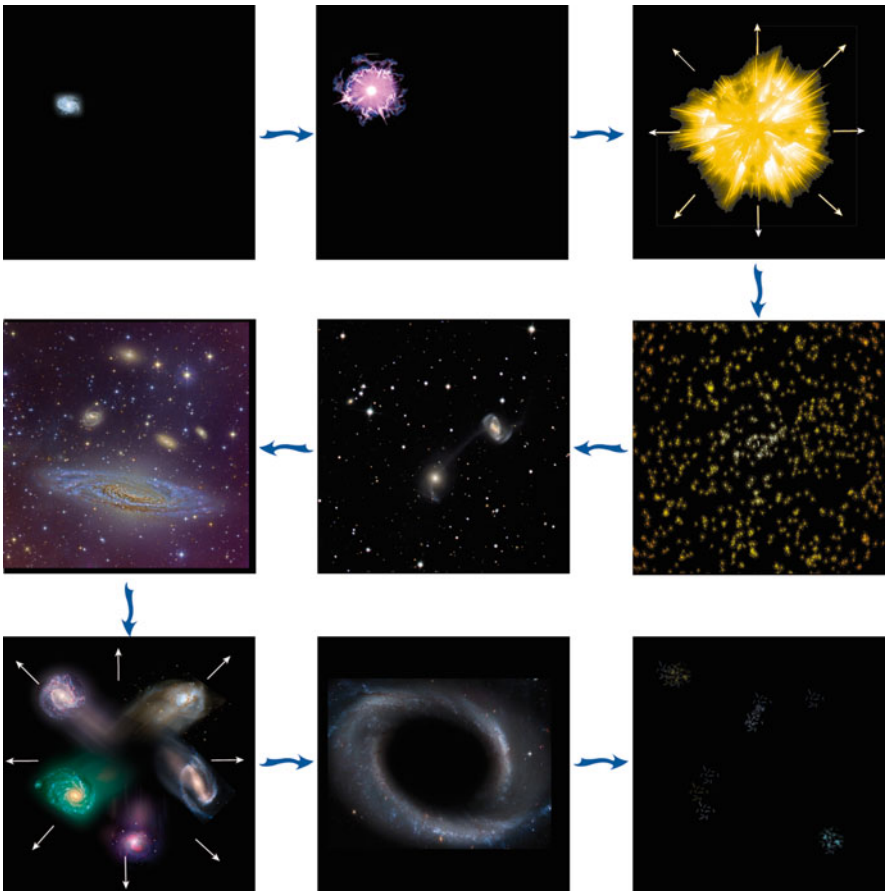

Fig. 10.63 Evolution of the universe [29]. Initially space is almost empty; quantum fields fluctuate in some domains. Next the space expands exponentially (inflation) and fills everywhere with the nearly uniform primary plasma. Aggregates of matter give rise to stars and galaxies, which fly apart due to accelerated expansion. Giant black holes contained at the centers of some galaxies take up everything around them and in turn slowly evaporate. The space becomes empty once again...

≈4 thousand years ago. The first towns emerged 6000–7000 years ago, the Christian civilization 2000 years ago, and the technical one only 200 years ago.

Since then, humans have so developed that they have become capable of posing questions about the physics of extreme states of matter. By the order of magnitude, the time of the rise of civilization corresponds to an estimate (about 5 thousand years ago) given by St. Augustine (Fig. 10.65) in his writing The City of God [69]. Answering the question as to what God was occupied with before creating the universe, he said that God was preparing hell for those who put such questions [69]. The possibility of the emergence of living and sapient subjects who

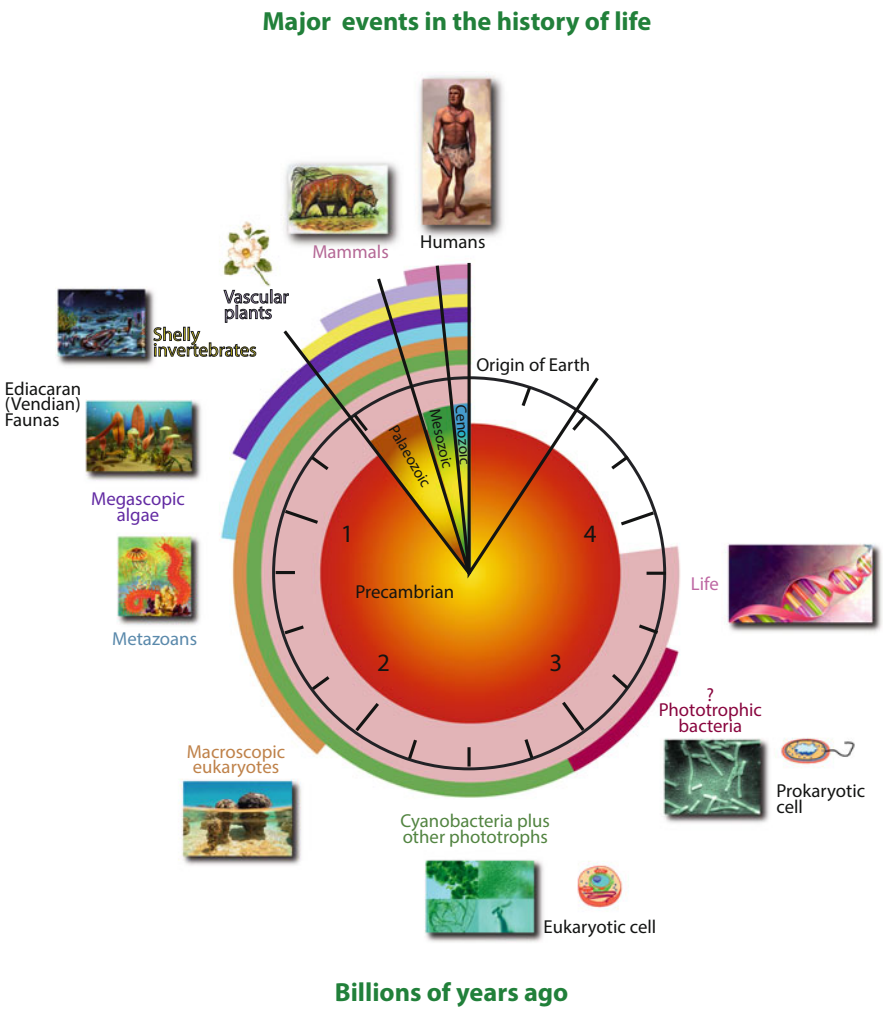

Fig. 10.64 Main milestones in the history of life (in billions of years)

ask such questions and dare cognize the universe is one of the most challenging and interesting questions of the natural sciences.

The question of the origin of life is the most interesting and most difficult among the fundamental problems of the universe [132].

The discovery of numerous remnants of fossil bacteria in the most ancient terrestrial sedimentary rock of age up to 3.5 billion years was one of the most amazing discoveries made by geologists and paleontologists at the end of the past century [8, 132].

Fig. 10.65 Earliest portrait of St. Augustine (sixth century)

Bacteria are the most ancient and plural form of life on our planet. They have most fully mastered the Earth's space for habitation and have far surpassed more complex organisms in this aspect. In modern conditions, bacterial life exists virtually everywhere: on land, in water, which they can inhabit at temperatures from -10 to $+120\,^{\circ}\mathrm{C}$, deep under the ice in Antarctica and in high atmospheric layers. At temperatures below -10 and above $+120\,^{\circ}\mathrm{C}$ bacteria can pass into a dormant state, in which they retain a higher tolerance to unfavorable temperature conditions, dehydration, and increased irradiation doses. Dormant cells may be in a viable state for a long time (up to 2 million years and over); in particular, when extracted from permafrost, they germinate under suitable conditions.

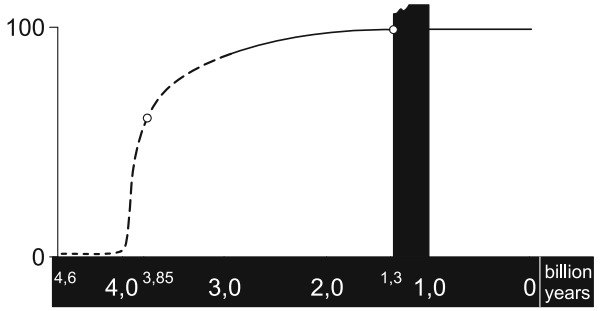

Fig. 10.66 Increase in water amount at the early stages of Earth's existence, 1.3–1.0 billion years is the period of possible stabilization of the salt composition and water volume on terrestrial surface [132]

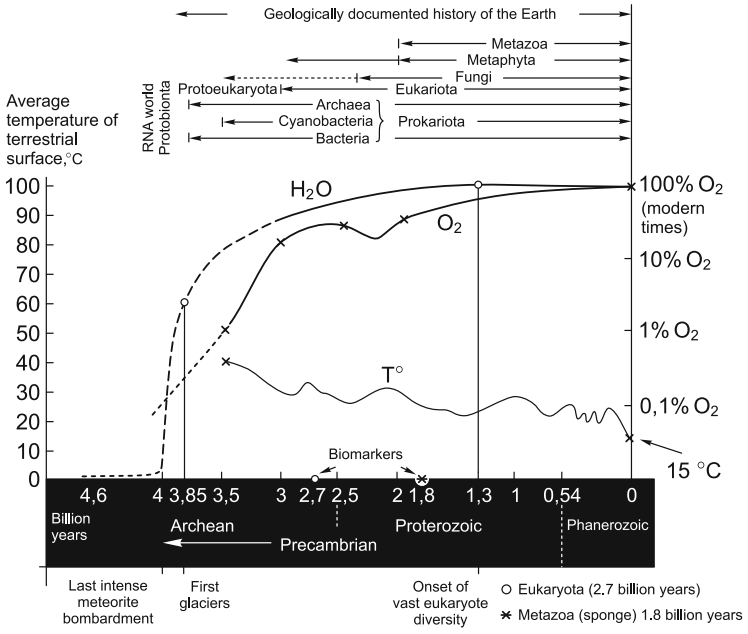

Fig. 10.67 Schematic of geological events in Precambrian Era [132]

The advent of life is related to the presence of water on the Earth (Fig. 10.66), which had not existed on the Earth earlier and which began to accumulate on it after the cessation of the period of intense meteorite bombardment (Fig. 10.67). About 4 billion years ago, sediments began to form in shallow water basins and life blossomed out on our planet. Apart from bacteria, including cyanobacteriae (see their photographs in Fig. 10.68), it is not improbable that the Earth was inhabited by green algae and, perhaps, even fungi. The surface of land was inhabited by microorganisms even in the Archean time [132].

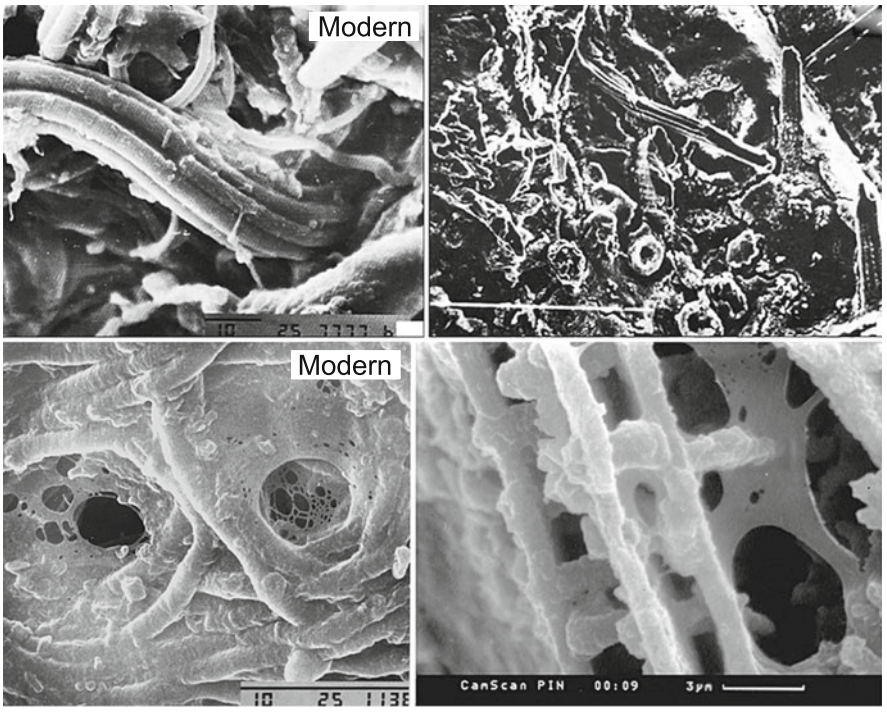

Fig. 10.68 Modern and fossil (Cambrian and Ordovician) cyanobacteriae ≈2.8 billion years of age. Of special interest is the excellent integrity of the fibers and films 10–20 μm in thickness [132]

The volume of water comparable to the present one was formed about 1.3 billion years ago, and since then we see a vast expansion of various organisms. The RNA world as a separate state, if at all, existed until 4.0 billion years ago and may be prior to Earth's formation. The likelihood of the origin of life on precisely the Earth is extremely low. Conceivably life appeared on a planet of "terrestrial type" long before Earth's formation and was brought to the Earth by meteorites [132].

Life on Earth came into existence at least 3.5–4 billion years ago, but during the first billions of years it was rather primitive, without significant diversity. The late Precambrian, approximately 650 million years ago, saw the advent of metazoans, which evolved into organisms with a hard skeleton; its existence enables geologists to rather safely determine the changes in fauna in the distant past. The sharp broadening of species diversity in the Cambrian—the first geological period of the eon of visible life, which began ≈545 million year back—is referred to as the Cambrian explosion. Since that time, the general evolution trend has led towards progressively greater biological diversity.

Against this background, however, catastrophic events of planetary scale occurred more than once, which led to drastic life reductions and received the name of mass extinctions. One of such mass extinctions is well known owing to

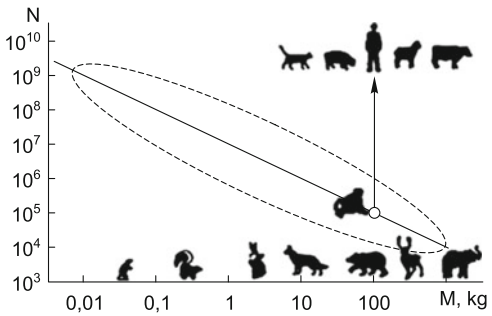

Fig. 10.69 Animal numbers of different species of the Earth in relation to their mass [75]

the disappearance of dinosaurs on the verge of the Cretaceous and Palaeogene (≈65 million years ago). Since the 1980s of the past century, the dominant hypothesis to explain this event is the fall of a large meteorite, whose crater 180 km in diameter is located on the Yucatan peninsula in Latin America. Attempts to apply the meteorite hypothesis to other events of mass extinction have not met with success. For them, the dominant hypothesis is quantitatively anomalous volcanism and its attendant discharge of toxic gases into the atmosphere. Furthermore, the volcanic hypothesis may also be invoked for explaining the Cretaceous-Palaeogene mass extinctions.

Of special significance for our surrounding world is, of course, the advent of a human endowed with mind, language, and culture. This is precisely the difference between us and animals, and this is the reason why we are a hundred thousand times (a huge number) greater in number than creatures comparable to us—bears, wolves, big monkeys (Fig. 10.69) [75]. Recent research of molecular biologists suggests that the crucial event supposedly was the mutation of one or two genes HAR1 F, which determine the organization of brain during the 5th–9th weeks of embryo development. This research is outlined by the supervisor of an international project Katherine Pollard in her article "What makes us human?" [121]. According to this model, at present there are grounds to believe that such a sudden point-like change in the genome of our distant ancestors, which occurred 5–4 million years ago, could lead to a qualitative leap in brain organization. This became the reason for the development of social consciousness and culture, which led to an extraordinary growth in human population. As a consequence of this mutation, after a long epoch of anthropogenesis there appeared speech and language, and humans mastered fire and stone tools. Since then, the biological nature of humans has little changed despite our rapid social progress. Understanding this is of significance today, when it became clear that the nonlinear dynamics of human population growth, which is based on the informational collective growth mechanism and obeys its intrinsic forces, determines not only our explosive development, but also its limit [75].

A characteristic feature of this anomalously rapid growth is that it is described not by the exponential law

$$N \sim N_0 e^{-T/T_E},$$

but by a stronger dependence—hyperbolic [75]:

$$N = \frac{210^{11}}{2025 - T} = \frac{C}{T_1 - T}.$$

The main property of hyperbolic (explosive) development is that the growth rate is proportional not to the first power of the population, as in an exponential growth reflecting the human capacity for reproduction, but to the second power—the squared world's population. This points to an important law, which may be interpreted as a cooperative growth described by quadratic interaction, which is proportional to N^2 [75].

This growth rate underlies all developed notions about collective interactions and the ensuing conclusions [75]. According to the aforesaid, the human population growth results from the cooperative population growth mechanism; as shown in [75], the collective mechanism makes this model an effective tool in the description of the growth on the scale of mankind.

Therefore, according to the model of [75], the growth proportional to the squared human population is determined not by the development of independent units but depends on the collective interaction of the entire mankind.

Curiously enough, but one of the early interpretations of this explosive human population growth observed on the Earth sometimes boils down to the statement that the marital interaction of man and woman (the number of pairs $\sim$N) is less efficient than extramarital interaction ($\sim N^2$). Supposedly, this was intuitively understood as far back as by W. Shakespeare (1564–1816), who wrote ("King Lear"):

Why bastard? wherefore base?
When my dimensions are as well compact,
My mind as generous, and my shape as true,
As honest madam's issue? Why brand they us
With base? with baseness? bastardy? base, base?
Who, in the lusty stealth of nature, take
More composition and fierce quality
Than doth, within a dull, stale, tired bed,
Go to the creating a whole tribe of fops,
Got 'tween asleep and wake?

In any case, as the year of 2050 is approached, growth deceleration mechanisms will emerge, and by that time the Earth's population will reach a permanent limit of 9–11 billion people [75].

With the use of these models, the total number of persons who have ever lived on Earth is estimated at $\approx$98 billion people [75].

In the description of the history of mankind, the nonlinear dynamics of world's population growth leads us to conclude that the development itself transforms the rate of time flow [75]. This is clear, first of all, from the exponential shortening

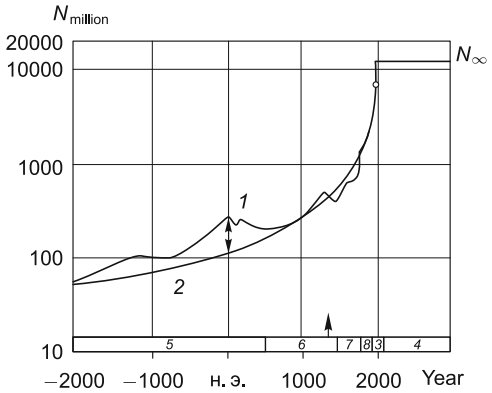

Fig. 10.70 World population from 2000 B.C. to 3000 [75]

of historical periods; this shortening is a manifestation of the relativity of time in history, which is significant for understanding the growth (Fig. 10.70). To be specific, the Ancient World lasted for about three thousand years, the Middle Ages for one thousand years, Modern Times for three hundred years, and the Modern History for slightly more than one hundred years.

According to [75], the growth acceleration has the effect that, after every cycle, the remaining development takes the time equal to about a half of the preceding stage. For instance, after the Lower Paleolithic, which lasted for one million years, there remains half a million years to our time, and 500 years have passed after the millennium of the Middle Ages. By this moment the historical process has been accelerated a thousand times. This transformation of the duration of historical process also manifests itself in that the history of Ancient Egypt and China lasted for thousands of years and is numbered in dynasties, while the tread of European history was determined by separate reigns. The Roman Empire was breaking up for a millennium and a half—from the fall of Rome in 500 to the fall of Constantinople in 1500. Modern empires, for instance the British Empire, broke up in a decade, and the Soviet one even faster. Therefore, in a nonequilibrium self-similar growth the development experiences compression, when the rate of a historical process rises as a demographic transition is approached, which inevitably leads to a growth crisis.

Supposedly, this was well understood by anthropologists: when representing the entire range of time in the lithic age, from the million years of Lower Palaeolithic to ten thousand years of the Neolithic, they traditionally address themselves to the logarithmic (and not linear) time scale. According to [75], the history of mankind is depicted on a logarithmic scale in Table 10.4.

Therefore, an analysis [75] leads to the conclusion that the cause of global demographic transition is related to the attainment of the limit of world population growth rate and not to the Malthusian population principle, whereby resources are the limiting factor [75]. However, in the epoch of fast changes, when their time becomes comparable with a human lifetime, the question arises about the stability of growth and development.

Table 10.4 History of mankind on a logarithmic time scale [75]

Epoch	Period	Date, years	Population	Cultural cycle	ΔT, years	History, culture, technology
C	T_1	2150	$10 \cdot 10^9$	Stabilization of Earth population		Passage to the limit $11 \cdot 10^9$
						Change of age distribution - aging
		2050	$9 \cdot 10^9$			Globalization
		2000	$6 \cdot 10^9$	World demographic transition	45	Urbanization
B	11	1955	$3 \cdot 10^9$		45	Computers. Internet Nuclear energy
	10	1840	$1 \cdot 10^9$	Modern history	125	World Wars Electrification and radio communication
	9	1500		Modern Times	340	Industrial revolution Typography
	8	500 A.D.		Middle Ages	1000	Geographic discoveries Fall of Rome, Muhammad
	7	2000 B.C.	10^8	Ancient World	2500	Christ, "Axial Age" Greek civilization India, China, Buddha and Confucius
	6	9000		Neolithic	7000	Mesopotamia, Egypt Written language, towns, bronze Domestication of livestock, agriculture
	5	29000	10^7	Mesolithic	20000	Ceramics, microlites
	4	80000		Mousterian	51000	Settlement in America Languages, shamanism
	3	0,22 million	10^6	Acheulian	140000	Homo sapiens Speach, mastering of fire
	2	0.60 million		Chellean/ Abbevillian	380000	Settlement in Europe and Asia, hand axes
	1	1.6 million	10^5	Oldowan	1000000	Pebble Culture, chopper Homo habilis
A	T_0	4-5 million 5-7 million	(1)	Anthropo-genesis Emergence of HAR1 F gene	2800000	Onset of socialization Development of hominids with great abilities of brain and mind

The World Wars of the twentieth century were the most terrible global catastrophes in the history of mankind, when the population became smaller by 8–10 % in the lifetime of two generations. Then, on the eve of the war in 1913, the economies of Russia and Germany were growing by 10 % per year and the population of Russia was annually increasing by 2 %, and the loss of political and economical stability of Europe may be attributed to these high growth rates.

We see that in the course of evolution our universe undergoes several changes as it transforms to increasingly complex and diverse structures [65]. After the origin of classical space-time there emerge the first elementary particles, the first nuclei (3 min), atoms (recombination era) of light elements, galaxies and stars; carbon and heavy elements are synthesized inside stars and ejected into space in explosions; planets are formed and, finally, there emerges organic life and the most complex object in the universe: the human brain, consisting of 10^{11} neurons (of the order of the number of stars in the galaxy), each of which is much more complex than a star. This took an extremely long time (about 15 billion years), during which the universe came a long way, increasing by a factor of 10^{61}. Were the atoms of our body capable of telling their story from their birth from vacuum onwards, they would have spoken about all the eras that we analyzed in the foregoing....

How is the existence of human beings related to the basic properties of the universe? Over what range may these properties vary for our life to take place? It turns out that this range is extremely narrow.

We shall adduce several examples. As noted by Stephen Hawking [69], had the expansion velocity of the first-second universe differed by 1 millionth from the critical value, human beings would not have come into being in it. In one case the universe would have turned out to be too hot and would have rapidly contracted, and in the other case it would have been too cold for us, and the galaxies would not have been formed. Only some "middle" path leads to humans.

A hydrogen atom is an absolutely stable element. The reaction

$$\mathrm{p} + \mathrm{e}^- \to \mathrm{n} + \nu,$$

where p, e^-, n, ν are the proton, electron, neutron, and neutrino, respectively, is strictly forbidden at low energies (temperatures), because

$$m_\mathrm{e} \sim 0.511\,\mathrm{MeV} < \Delta m_\mathrm{N} = m_\mathrm{n} - m_\mathrm{p} \approx 1.3\,\mathrm{MeV}.$$

However, should the mass m_e be (ideally) increased, this reaction would be possible, which would lead to catastrophic consequences: the impossibility of galaxies and, hence, stars being formed, because the existence of neutral hydrogen is required for the formation of galaxies.

Another example is the "resonance" in the nuclear reaction involving the production of carbon from helium and beryllium accompanied by the emission of γ-ray photons:

$$2\mathrm{He}^4 \to \mathrm{Be}^8, \quad \mathrm{He}^4 + \mathrm{Be}^8 \to \mathrm{C}^{12} + 2\gamma.$$

The probability of this nuclear reaction rises when the energy of ^{4}He and ^{8}Be is equal to 7.65 MeV, which may occur in stars at high temperatures. Were it not for this resonance, carbon would not have been produced in quantities sufficient for the origin of life [65]. Furthermore, the resultant carbon might immediately transform to oxygen by the reaction $^4\mathrm{He} + {}^{12}\mathrm{C} \rightarrow {}^{16}\mathrm{O}$, and carbon-based organic life would not have been able to emerge. In this case, however, by sheer luck the figures diverged slightly and the resonance in the reaction involving the production of oxygen and the disappearance of carbon turned out to be forbidden. Indeed, the energy of $^4\mathrm{He} + {}^{12}\mathrm{C}$ is 7.166 MeV, while the energy of ^{16}O is 7.118 MeV, and this reaction is impossible in the rest frame of ^{16}O. So, an energy difference of 0.05 MeV inside a star resolved the problem of the future advent of human beings.

The biproton ^{2}He is an unstable particle. This instability arises from the Coulomb repulsion of protons (its potential energy is $\approx$2 MeV). However, estimates show that were the potential energy of nuclear attraction only 50 keV higher, the nucleus ^{2}He would be stable, which would lead to the reaction $\mathrm{p} + \mathrm{p} \rightarrow {}^2\mathrm{He} + \gamma$ with the consequence that all protons would have burned up in the course of primary (cosmological) nucleosynthesis.

The list of such examples can be easily extended. Peculiar coincidences are encountered when comparing the magnitudes of the fundamental constants [65]:

- electromagnetic interaction constant (fine structure constant) $\alpha \approx 10^{-2}$;
- gravitational constant (dimensionless) $\alpha_\mathrm{G} \approx 10^{-38} - 10^{-40}$;
- Fermi constant of weak interaction $\alpha_\mathrm{W} \approx 10^{-5}$;
- strong interaction constant $\alpha_\mathrm{S} \approx 10$;
- number of protons in the universe $N_p \approx 10^{80} \approx \alpha_\mathrm{G}^{-2}$;
- mass of the universe $M \approx \alpha_\mathrm{G}^{-2} m_p$, where m_p is the proton mass;
- galactic mass $M \approx \alpha^4 \alpha_\mathrm{G}^{-2} m_p$;
- stellar mass $M_\mathrm{star} \approx \alpha_\mathrm{G}^{-3/2} m_p$;
- planetary mass $M_\mathrm{pl} \approx \alpha_\mathrm{G}^{3/2} M_\mathrm{star}$ (Jupiter's mass);
- mass of a human $M_\mathrm{homo} = \sqrt{M_\mathrm{pl} m_p}$.

Are these coincidences accidental? What is most amazing, small variations of the fundamental constants lead to the conclusion that man (like every living thing on the basis of carbon), for one reason or another, could not come into being. And the galaxies themselves would be entirely different, e.g., without hydrogen. That is why one of the formulations of the anthropic principle reduces to the statement that the metagalaxy is unstable relative to variations of the value of the fundamental constants. Of course, the coincidence of figures mentioned above tell not so much about human beings as about a creature of carbon, and a human being is not much different from animals in this case.

The so-called convective stars, in which heat is transferred by way of convection (as in the Sun) and which have planets, exist because [65] $\alpha_\mathrm{G} = \alpha^{20}$. Supernovae explode because $\alpha_\mathrm{G} = (\alpha_\mathrm{W})^8$. Atoms exist as systems of nuclei, which are confined by the strong interaction, and electrons, which are confined in orbits due to electromagnetic interactions, because $\alpha = (\alpha_\mathrm{S})^{-3}$.

Lastly, the universe's expansion in the contemporary epoch is determined by the cosmological constants, which has the significance that our era commenced at about the instant the Sun came into existence. Owing to the accelerated repulsion of other galaxies from us, our galaxy is protected against collisions with them, which underlies the stability of the emerging Solar planetary system and biological evolution on the Earth.

However, an insignificant change of these constants radically changes the entire universe! The universe is like a finely tuned musical instrument! All these coincidences and tunings are reflected in the so-called anthropic principle in cosmology, which is also referred to as the reasonability principle. Here, we are dealing with an investigation of the metagalaxy structure stability relative to variations of the numerical values of the fundamental constants α of the four interactions, the masses m_{p} and m_{e}, and the dimensionality of space.

In its weak form it holds that the observable properties of the universe depend on man as the observer [65]. The point is that we as observers may exist at the time when we observe all visible objects and when all the relations we have established are fulfilled; at a different time there is "no one" to observe all this. Some coincidences are due to the properties of our observation in space and time.

The strong anthropic principle holds that the universe is so constructed that man was bound to come into being in it, which is close to the biblical anthropocentric idea regarding man as the goal of creation. The universe evolves in such a way that there emerges a creature, man, capable of unraveling the mathematical laws of evolution and seeing their hidden significance.

Of course, the coincidences of the figures given above simply concern a creature made of carbon, rather than specifically a human being—who is little different from animals in this case. However, there exists a formulation of the strong anthropic principle that implies the creation of an observer. If the universe is quantal, according to one of the versions of interpretation of quantum mechanics, the human observer defines its wave function, so that the Big Bang itself and the evolution of the universe proceed in such a way that the observer is bound to emerge. It is assumed that there exist, in addition to our universe, infinitely many—10^{10}—other universes in which the fundamental constants do not obey the relations inherent in our world. The fundamental constants assume other values there. However, the point is that there are no humans in those worlds! We therefore see these relations not because we are the pinnacle of creation but because we cannot exist in other worlds!

In the further discussion of these difficult world-view problems we descend into the realms of philosophy or even theology, which is clearly beyond the scope of this book.

In the general form, this principle holds that the physical laws in the metagalaxy are not only sufficient for the main stable states (atomic nuclei, atoms, stars, galaxies), but are necessary as well.

References

1. Abel, T.: The first stars, as seen by supercomputers. Phys. Today **64**(4), 51–56 (2011)
2. Achterberg, A.: Particle acceleration by an ensemble of shocks. Astron. Astrophys. **231**(1), 251–258 (1990)
3. Achterberg, A., Gallant, Y.A., Kirk, J.G., Guthmann, A.W.: Particle acceleration by ultrarelativistic shocks: theory and simulations. Mon. Not. R. Astron. Soc. **328**(2), 393–408 (2001)
4. Arnett, D.: Oxygen-burning hydrodynamics. 1: Steady shell burning. Astrophys. J. **427**(2), 932–946 (1994)
5. Arnett, D.: Supernovae and Nucleosynthesis. Princeton University Press, Princeton (1996)
6. Artyukh, V.S., Chernikov, P.A.: Physical conditions in the nucleus of the radio galaxy 3C 274. Astron. Rep. **51**, 808–812 (2007)
7. Aschwanden, M.J.: Physics of the Solar Corona: An Introduction with Problems and Solutions, 2nd edn. Springer, Berlin (2006)
8. Astaf'eva, M., Gerasimenko, L., Geptner, A., et al.: Iskopaemye bakterii i drugie mikroorganizmy v zemnykh porodakh i astromaterialakh (Fossil Bacteria and other Microorganisms in Terrestrial Rock and Astromaterials). Paleontological Institute of the Russian Academy of Sciences, Moscow (2011)
9. Atzeni, S., Meyer-ter-Vehn, J.: The Physics of Inertial Fusion. Oxford University Press, Oxford (2004)
10. Avrorin, E.N., Vodolaga, B.K., Simonenko, V.A., Fortov, V.E.: Intense shock waves and extreme states of matter. Phys. Usp. **36**(5), 337–364 (1993)
11. Avrorin, E.N., Simonenko, V.A., Shibarshov, L.I.: Physics research during nuclear explosions. Phys. Usp. **49**(4), 432 (2006)
12. Ayukov, S.V., Baturin, A., Gryaznov, V.K., et al.: Analysis of the presence of small admixtures of heavy elements in the solar plasma by using the SAHA-S equation of state. JETP Lett. **80**(3), 141–144 (2004)
13. Balbus, S.A., Hawley, J.F.: A powerful local shear instability in weakly magnetized disks. I - Linear analysis. II - Nonlinear evolution. Astrophys. J. **376**(1), 214–233 (1991)
14. Balick, B., Frank, A.: The extraordinary deaths of ordinary stars. Sci. Am. **291**(1), 50 (2004)
15. Bamber, C., Boege, S.J., Koffas, T., et al.: Studies of nonlinear QED in collisions of 46.6 GeV electrons with intense laser pulses. Phys. Rev. D **60**(9), 092004 (1999)
16. Begelman, M.C., Blandford, R.D., Rees, M.J.: Theory of extragalactic radio sources. Rev. Mod. Phys. **56**(2), 255–351 (1984)
17. Bell, A.R.: The acceleration of cosmic rays in shock fronts. I. Mon. Not. R. Astron. Soc. **147–156**, 022105 (1978)
18. Beskin, V.S.: Magnetohydrodynamic models of astrophysical jets. Phys. Usp. **53**(12), 1199–1233 (2010)
19. Beskin, V.S., Gurevich, A.V., Istomin, Y.N.: Physics of the Pulsar Magnetosphere. Cambridge University Press, Cambridge (1993)
20. Bisnovatyi-Kogan, G.S.: Stellar Physics: 1: Fundamental Concepts and Stellar Equilibrium. Springer, Berlin, Heidelberg (2001)
21. Blinnikov, S.I., Novikov, I.D., Perevodchikova, T.V., Polnarev, A.G.: Exploding neutron stars in close binaries. Sov. Astron. Lett. **10**(3), 177 (1984)
22. Bondi, H., Hoyle, F.: On the mechanism of accretion by stars. Mon. Not. R. Astron. Soc. **104**, 273 (1944)
23. Bousso, R.: The cosmological constant. Gen. Relativ. Gravit. **40**, 607–637 (2008)
24. Bula, C., McDonald, K.T., Prebys, E.J., et al.: Observation of nonlinear effects in Compton scattering. Phys. Rev. Lett. **76**(17), 3116–3119 (1996)
25. Burdyuzha, V.V.: The cosmological constant (a modern view). Astron. Rep. **53**(5), 381 (2009)
26. Burdyuzha, V.V.: Dark components of the universe. Phys. Usp. **53**(4), 419–424 (2010)
27. Burke, D.L., Field, R.C., Horton-Smith, G., et al.: Positron production in multiphoton light-by-light scattering. Phys. Rev. Lett. **79**(9), 1626–1629 (1997)

28. Bykov, A.M., Toptygin, I.N.: Instabilities of a multicomponent plasma with accelerated particles and magnetic field generation in astrophysical objects. Phys. Usp. **50**(2), 141–174 (2007)
29. Carroll, S.M.: The cosmic origins of time's arrow. Sci. Am. **298**(6), 48 (2008)
30. Chen, P., Tajima, T., Takahashi, Y.: Plasma wakefield acceleration for ultrahigh-energy cosmic rays. Phys. Rev. Lett. **89**(16), 161101 (2002)
31. Chernikov, P.A., Artyukh, V.S., Tyul'Bashev, S.A., Lapaev, K.A.: Study of the physical conditions in active galactic nuclei. Physical conditions in the cores of two nearby radio galaxies. Astron. Rep. **50**, 202–209 (2006)
32. Chernin, A.D.: Cosmic vacuum. Phys. Usp. **44**(11), 1099 (2001)
33. Chernin, A.D.: Dark energy and universal antigravitation. Phys. Usp. **51**(3), 253 (2008)
34. Clark, E.L., Krushelnick, K., Davies, J.R., et al.: Measurements of energetic proton transport through magnetized plasma from intense laser interactions with solids. Phys. Rev. Lett. **84**(4), 670–673 (2000)
35. Cowan, T.E., Hunt, A.W., Phillips, T.W., et al.: Photonuclear fission from high energy electrons from ultraintense laser-solid interactions. Phys. Rev. Lett. **84**(5), 903–906 (2000)
36. Cuneo, M.E., Vesey, R.A., Bennett, G.R., et al.: Progress in symmetric ICF capsule implosions and wire-array Z-pinch source physics for double-pinch-driven hohlraums. Plasma Phys. Controlled Fusion **48**(2), R1–R35 (2006)
37. Disdier, L., Garconnet, J.P., Malka, G., Miquel, J.L.: Fast neutron emission from a high-energy ion beam produced by a high-intensity subpicosecond laser pulse. Phys. Rev. Lett. **82**(7), 1454–1457 (1999)
38. Drake, R.P.: High-Energy-Density Physics. Springer, Berlin, Heidelberg (2006)
39. Drake, R.P., Leibrandt, D.R., Harding, E.C., et al.: Nonlinear mixing behavior of the three-dimensional Rayleigh–Taylor instability at a decelerating interface. Phys. Plasmas **11**(5), 2829–2837 (2004)
40. Edens, A.D., Ditmire, T., Hansen, J.F., et al.: Studies of laser-driven radiative blast waves. Astrophys. Space Sci. **298**(1–2), 39–47 (2005)
41. Efremov, Y.N.: Spiral'naja struktura nashej galaktiki (Spiral structure of our galaxy). In: Surdin, V.G. (ed.) Astronomiya: Vek XXI (Astronomy: XXIst Century), p. 313. Vek 2, Fryazino (2007)
42. Esirkepov, T., Yamagiwa, M., Tajima, T.: Laser ion-acceleration scaling laws seen in multiparametric particle-in-cell simulations. Phys. Rev. Lett. **96**(10), 105001 (2006)
43. European Southern Observatory: http://www.eso.org/
44. Faber, T.E.: Fluid Dynamics for Physicists. Cambridge University Press, Cambridge (1977)
45. Faber, S.M., Gallagher, J.S.: Exploding neutron stars in close binaries. Annu. Rev. Astron. Astrophys. **17**, 135–187 (1979)
46. Fabrika, S.: The jets and supercritical accretion disk in SS433. Astrophys. Space Phys. Rev. **12**, 1 (2004)
47. Falize, E., Bouquet, S., Michaut, C.: Radiation hydrodynamics scaling laws in high energy density physics and laboratory astrophysics. J. Phys. Conf. Ser. **112**(4), 042016 (4pp) (2008)
48. Fermi, E.: On the origin of the cosmic radiation. Phys. Rev. **75**(8), 1169–1174 (1949)
49. Fortov, V.E. (ed.): Entsiklopediya nizkotemperaturnoi plazmy (Encyclopedia of Low-Temperature Plasma). Nauka, Moscow (2000)
50. Fortov, V.E., Khrapak, A.G., Khrapak, S.A., et al.: Dusty plasmas. Phys. Usp. **47**(5), 447 (2004)
51. Fortov, V.E., Ivlev, A.V., Khrapak, S.A., et al.: Complex (dusty) plasma: current status, open issues, perspectives. Phys. Rep. **421**(1), 1–103 (2005)
52. Fortov, V., Iakubov, I., Khrapak, A.: Physics of Strongly Coupled Plasma. Oxford University Press, Oxford (2006)
53. Frieman, J.A., Turner, M.S., Huterer, D.: Dark energy and the accelerating universe. Ann. Rev. Astron. Astrophys. **46**(1), 385–432 (2008)
54. Geach, J.E.: The lost galaxies. Sci. Am. **304**(5), 46–53 (2011)

55. Gehrels, N., Piro, L., Leonard, P.J.T.: The brightest in the universe – gamma-ray bursts Herald the birth of a black hole. Sci. Am. **287**(6), 84–91 (2002)
56. Ginzburg, V.L.: The Physics of a Lifetime: Reflections on the Problems and Personalities of 20th Century Physics. Springer, Berlin, Heidelberg (2001)
57. Ginzburg, V.L.: On superconductivity and superfluidity (what I have and have not managed to do), as well as on the "physical minimum" at the beginning of the XXI century (December 8, 2003). Phys. Usp. **47**(11), 1155 (2004)
58. Ginzburg, V.L., Syrovatskii, S.I.: The Origin of Cosmic Rays. Pergamon Press, Oxford (1964)
59. Glendenning, N.K.: Compact Stars: Nuclear Physics, Particle Physics, and General Relativity, 2nd edn. Springer, New York (2000)
60. Gliner, E.: Algebraic properties of the energy-momentum tensor and vacuum-like states of matter . J. Exp. Theor. Phys. **22**(2), 378 (1966)
61. Gorbunov, D.S., Rubakov, V.A.: Vvedenie v teoriyu rannei Vselennoi. Kosmologicheskie vozmushcheniya. Inflyatsionnaya teoriya, vol. 2. Krasand, Moscow (2010)
62. Grabovskii, E.V., Vorob'ev, O.Y., Dyabilin, K.S., et al.: Excitation of intense shock waves by soft x radiation from a Z-pinch plasma. JETP Lett. **60**(1), 1 (1994)
63. Greisen, K.: End to the cosmic-ray spectrum? Phys. Rev. Lett. **16**(17), 748–750 (1966)
64. Grib, A.A.: Osnovnye predstavleniya sovremennoi kosmologii (Basic Notions of Modern Cosmology). Fizmatlit, Moscow (2008)
65. Grib, A.A.: Osnovnye predstavleniya sovremennoi kosmologii (The Basic Representations of Modern Cosmology). FizMatLit, Moscow (2008)
66. Grishchuk, L.P.: Relic gravitational waves and their detection. In: Lämmerzahl, C., Everitt, C.W.F., Hehl, F.W. (eds.) Gyros, Clocks, Interferometers. . . : Testing Relativistic Gravity in Space. Lecture Notes in Physics, vol. 562, p. 167. Springer, Berlin, Heidelberg (2001)
67. Grishchuk, L.P.: Relic gravitational waves and cosmology. Phys. Usp. **48**(12), 1235 (2005)
68. Hansen, J.F., Edwards, M.J., Froula, D.H., et al.: Laboratory observation of secondary shock formation ahead of a strongly radiative blast wave. Phys. Plasmas **13**(2), 022105 (2006)
69. Hawking, S.W.: A Brief History of Time: From the Big Bang to Black Holes. Bantam Books, Toronto (1988)
70. Hayashida, N., Honda, K., Honda, M., et al.: Observation of a very energetic cosmic ray well beyond the predicted 2.7 K cutoff in the primary energy spectrum. Phys. Rev. Lett. **73**(26), 3491–3494 (1994)
71. Hu, W., White, M.: The cosmic symphony. Sci. Am. **290**(2), 44–53 (2004)
72. Imshennik, V., Nadyozhin, D.: Supernova-1987A, and the emergence of the blast wave at the surface of the compact presupernova. Sov. Astron. Lett. **14**(6), 449–452 (1988)
73. Ivanova, L.N., Imshennik, V.S., Chechotkin, V.M.: Pulsation regime of the thermonuclear explosion of a star's dense carbon core. Astrophys. Space Sci. **31**(2), 497–514 (1974)
74. Kando, M., Nakajima, K., Arinaga, M., et al.: Interaction of terawatt laser with plasma. J. Nucl. Mater. **248**(1), 405–407 (1997)
75. Kapitsa, S.P.: Paradoksy rosta. Zakony razvitiya chelovechestva (Paradoxes of Growth. Laws of Mankind Development). Alpina Non-Fiction, Moscow (2012)
76. Kirzhnits, D.A.: Extremal states of matter (ultrahigh pressures and temperatures). Sov. Phys. Usp. **14**(4), 512–523 (1972)
77. Kirzhnits, D.A.: Lektsii po fizike (Lectures on Physics). Nauka, Moscow (2006)
78. Kodama, R., Tanaka, K.A., Sentoku, Y., et al.: Observation of ultrahigh gradient electron acceleration by a self-modulated intense short laser pulse. Phys. Rev. Lett. **84**(4), 674–677 (2000)
79. Kodama, R., Norreys, P.A., Mima, K., et al.: Fast heating of ultrahigh-density plasma as a step towards laser fusion ignition. Nature **412**(6849), 798–802 (2001)
80. Krauss, L.M., Scherrer, R.J.: The end of cosmology? Sci. Am. **298**(3), 46–53 (2008)
81. Kruer, W.L.: The Physics of Laser Plasma Interactions. Addison-Wesley, Reading (1988)
82. Lada, C.J.: Cold outflows, energetic winds, and enigmatic jets around young stellar objects. Annu. Rev. Astron. Astrophys. **23**, 267–317 (1985)

83. Levin, A.: Vozrast mirozdaniya: slushaem pul's vselennoi (The age of the universe: listening to the pulse of the universe). Populyarnaya Mekhanika **115**(5), 54–60 (2012)
84. Liang, E.P., Wilks, S.C., Tabak, M.: Pair production by ultraintense lasers. Phys. Rev. Lett. **81**(22), 4887–4890 (1998)
85. Lifshits, E.M.: Gravitational stabilities of the expanding world. J. Exp. Theor. Phys. **16**, 587 (1946)
86. Lindl, J.D.: Inertial Confinement Fusion. Springer, New York (1998)
87. Lobo, F.S.N.: Phantom energy traversable wormholes. Phys. Rev. D **71**, 084011 (2005)
88. Lukash, V.N., Rubakov, V.A.: Dark energy: myths and reality. Phys. Usp. **51**(3), 283 (2008)
89. Mackinnon, A.J., Borghesi, M., Hatchett, S., et al.: Effect of plasma scale length on multi-MeV proton production by intense laser pulses. Phys. Rev. Lett. **86**(9), 1769–1772 (2001)
90. Maksimchuk, A., Gu, S., Flippo, K., et al.: Forward ion acceleration in thin films driven by a high-intensity laser. Phys. Rev. Lett. **84**(18), 4108–4111 (2000)
91. Maksimchuk, A., Flippo, K., Krause, H., et al.: Plasma phase transition in dense hydrogen and electron–hole plasmas. Plasma Phys. Rep. **30**(6), 473–495 (2004)
92. Mangles, S.P.D., Murphy, C.D., Najmudin, Z., et al.: Monoenergetic beams of relativistic electrons from intense laser–plasma interactions. Nature **431**(7008), 535–538 (2004)
93. Mason, R.J., Tabak, M.: Magnetic field generation in high-intensity-laser–matter interactions. Phys. Rev. Lett. **80**(3), 524–527 (1998)
94. Matveenko, L.I., Kellermann, K.I., Pauliny-Toth, I.I.K., et al.: The structure of the nucleus of the Seyfert galaxy NGC1275. Sov. Astron. Lett. **6**, 42 (1980)
95. McCallum, J.N., Ellingsen, S.P., Lovell, J.E.J.: Magnetic field limits and spectral variability in the circinus galaxy h2o megamasers. Mon. Not. R. Astron. Soc. **376**(2), 549–556 (2007)
96. McCray, R.: Supernova 1987A revisited. Annu. Rev. Astron. Astrophys. **31**, 175–216 (1993)
97. Mesyats, G.A.: Impul'snaya energetika i elektronika (Pulse Power and Electronics). Nauka, Moscow (2004)
98. Meszaros, P., Rees, M.J.: Relativistic fireballs and their impact on external matter – models for cosmological gamma-ray bursts. Astrophys. J. **405**, 278–284 (1991)
99. Michaut, C., Falize, E., Cavet, C., et al.: Link between laboratory and astrophysical radiative shocks. J. Phys.: Conf. Ser. **112**(4), 042013 (4pp) (2008)
100. Michel, F.C.: Theory of Neutron Star Magnetospheres. University of Chicago Press, Chicago (1991)
101. Mihalas, D.: Stellar Atmospheres, 2nd edn. W.H. Freeman, San Francisco (1978)
102. Mima, K., Ohsuga, T., Takabe, H., et al.: Wakeless triple-soliton accelerator. Phys. Rev. Lett. **57**(12), 1421–1424 (1986)
103. MinZayyang, T., et al.: In: Van Horn, H., Ichimaru, S. (eds.) Proc. 26^{th} Int. Cosmic Ray Conf. (ICRC), vol. 3, p. 125. Utah University, Salt Lake City (1999)
104. Modjaz, M., Moran, J.M., Kondratko, P.T., Greenhill, L.J.: Probing the magnetic field at subparsec radii in the accretion disk of NGC 4258. Astrophys. J. **626**(1), 104 (2005)
105. Mourou, G.A., Tajima, T., Bulanov, S.V.: Optics in the relativistic regime. Rev. Mod. Phys. **78**(2), 1804–1816 (2006)
106. Nagano, M., Watson, A.A.: Observations and implications of the ultrahigh-energy cosmic rays. Rev. Mod. Phys. **72**(3), 689–732 (2000)
107. NASA, Hubblesite: http://hubblesite.org/
108. NASA, Jet Propulsion Laboratory: http://www.jpl.nasa.gov/
109. National Research Council: Frontiers in High Energy Density Physics. National Academies Press, Washington (2003)
110. Nicolaï, P., Stenz, C., Kasperczuk, A., et al.: Studies of supersonic, radiative plasma jet interaction with gases at the Prague Asterix Laser System facility. Phys. Plasmas **15**(8), 082701 (2008)
111. Nishida, A.: The Earth's dynamic magnetotail. Space Sci. Rev. **91**(3–4), 507–577 (2000)
112. Olinto, A.V.: Ultra high energy cosmic rays: the theoretical challenge. Phys. Rep. **333–334**, 329–348 (2000)

113. Olling, R.P., Merrifield, M.R.: Two measures of the shape of the dark halo of the Milky Way. Mon. Not. R. Astron. Soc. **311**(2), 361–369 (2000)
114. Öpik, E.J.: Stellar associations and supernovae. Irish Astron. J. **2**(8), 219–233 (1953)
115. Panasyuk, M.I.: Stranniki vselennoj ili jeho Bol'shogo Vzryva (Wanderers of the Universe or a Big Bang Echo). Vek 2, Fryazino (2005)
116. Parker, E.N.: Dynamics of the interplanetary gas and magnetic fields. Astrophys. J. **128**, 664 (1958)
117. Peebles, P.J.E., Ratra, B.: The cosmological constant and dark energy. Rev. Mod. Phys. **75**, 559–606 (2003)
118. Perlmutter, S., Aldering, G., Della Valle, M., et al.: Discovery of a supernova explosion at half the age of the Universe. Nature **391**(6662), 51–54 (1998)
119. Perlmutter, S., Aldering, G., Goldhaber, G., et al.: Measurements of Ω and Λ from 42 high-redshift supernovae. Astron. J. **517**(2), 565 (1999)
120. Phinney, E.S.: Black hole-driven hydromagnetic flows flywheels vs. fuel. In: Ferrari, A., Pacholczyk, A.G. (eds.) Astrophysical Jets. Reidel, Dordrecht (1983)
121. Pollard, K.: What makes us human? Sci. Am. **300**(5), 32-37 (2009)
122. Price, P.A., Berger, E., Reichart, D.E., et al.: GRB 011121: a massive star progenitor (2002). arXiv:astro-ph/0203467v1
123. Ptitsyna, K.V., Troitsky, S.V.: Physical conditions in potential accelerators of ultrahigh energy cosmic rays: updated Hillas plot and radiation-loss constraints. Phys. Usp. **53**(7), 691–701 (2010)
124. Ptuskin, V.S.: The origin of cosmic rays. Phys. Usp. **53**(9), 958–961 (2010)
125. Pukhov, A.: Strong field interaction of laser radiation. Rep. Prog. Phys. **66**(1), 47–101 (2003)
126. Pukhov, A., Meyer-ter-Vehn, J.: Laser wake field acceleration: the highly non-linear broken-wave regime. Appl. Phys. B **74**(4–5), 355–361 (2002)
127. Quintenz, J., Sandia's Pulsed Power Team: Pulsed power team. In: Proc. 13th Int. Conf. on High Power Particle Beams. Nagaoka, Japan (2000)
128. Remington, B.A., Kane, J., Drake, R.P., et al.: Supernova hydrodynamics experiments on the Nova laser. Phys. Plasmas **4**(5), 1994–2003 (1997)
129. Remington, B.A., Arnett, D., R. Paul, D., Takabe, H.: Modeling astrophysical phenomena in the laboratory with intense lasers. Science **284**(5419), 1488–1493 (1999)
130. Riess, A.G., Filippenko, A.V., Challis, P., et al.: Observational evidence from supernovae for an accelerating universe and a cosmological constant. Astron. J. **116**(3), 1009 (1998)
131. Riordan, M., Zajc, W.A.: The first few microseconds. Sci. Am. **294**(5), 34A–41 (2006)
132. Rozanov, A.Y.: Kogda poyavilas' zhizn' na Zemle? (When did life appear on the earth?). Her. Russ. Acad. Sci. **80**(3), 305 (2010)
133. Rubakov, V.A.: Large and infinite extra dimensions. Phys. Usp. **44**(9), 871 (2001)
134. Rubakov, V.A.: Hierarchies of fundamental constants (to items Nos 16, 17, and 27 from Ginzburg's list). Phys. Usp. **50**(4), 390 (2007)
135. Rubakov, V.A., Tinyakov, P.G.: Infrared-modified gravities and massive gravitons. Phys. Usp. **51**(8), 759 (2008)
136. Rubin, S.G.: Ustroistvo nashei vselennoi (The Constitution of Our Universe). Vek 2, Fryazino (2006)
137. Rubin, V.: Seeing dark matter in the Andromeda Galaxy. Phys. Today **59**(12), 8–9 (2006)
138. Rubin, V.C., Ford, W.K. Jr., Krishna Kumar, C.: Stellar motions near the nucleus of M31. Astrophys. J. **181**, 61–78 (1973)
139. Ryutov, D.D., Remington, B.A., Robey, H.F., Drake, R.P.: Magnetodynamic scaling: from astrophysics to the laboratory. Phys. Plasmas **8**(5), 1804–1816 (2001)
140. Sandage, A., Tammann, G.A., Saha, A., et al.: The Hubble constant: a summary of the Hubble Space Telescope program for the luminosity calibration of type Ia supernovae by means of Cepheids. Astrophys. J. **653**(2), 843–860 (2006)
141. Sazhin, M.V.: Kosmologija rannej vselennoj (Cosmology of the Early Universe). In: Soifer, V.N. (ed.) Sovremennoe estestvoznanie. Entsiklopediya (Modern Natural Science. Encyclopedia), vol. 4, p. 253. Magistr-Press, Moscow (2000)

142. Schekochihin, A.A., Cowley, S.C., Dorland, W.: Interplanetary and interstellar plasma turbulence. Plasma Phys. Controlled Fusion **49**(5A), A195–A209 (2007)
143. Shapiro, S.L., Teukolsky, S.A.: Black Holes, White Dwarfs, and Neutron Stars. Wiley, New York (1983)
144. Shara, M.: When stars collide. Sci. Am. **287**(5), 44–51 (2002)
145. Spielman, R.B., Deeney, C., Chandler, G.A., et al.: Tungsten wire-array Z-pinch experiments at 200 TW and 2 MJ. Phys. Plasmas **5**(5), 2105–2111 (1998)
146. Stefani, F., Gundrum, T., Gerbeth, G., et al.: Experimental evidence for magnetorotational instability in a Taylor–Couette flow under the influence of a helical magnetic field. Phys. Rev. Lett. **97**(18), 184502 (2006)
147. Stozhkov, Y.I.: Kosmicheskie luchi (Cosmic rays). In: Soifer, V.N. (ed.) Sovremennoe estestvoznanie. Entsiklopediya (Modern Natural Science. Encyclopedia), vol. 4, p. 191. Magistr-Press, Moscow (2000)
148. Sunyaev, R.A., Zeldovich, Y.B.: Distortions of the background radiation spectrum. Nature **223**(5207), 721–722 (1969)
149. Surdin, V.G.: Rozhdenie zvezd (Star Production). Editorial URSS, Moscow (1999)
150. Surdin, V.G.: Mlechnyj put' (The Milky Way). In: Surdin, V.G. (ed.) Astronomiya: Vek XXI (Astronomy: XXIst Century), p. 267. Vek 2, Fryazino (2007)
151. Surdin, V.G. (ed.): Zvezdy (The Stars), 2nd edn. Astronomiya i astrofizika (Astronomy and Astrophysics). Fizmatlit, Moscow (2009)
152. Takahashi, Y., Hillman, L.W., Tajima, T.: Relativistic lasers and high-energy astrophysics: Gamma ray bursts and highest energy acceleration. In: Tajima, T., Mima, K., Baldis, H. (eds.) High-Field Science, p. 171. Kluwer/Plenum, New York (2000)
153. Takeda, M., Hayashida, N., Honda, K., et al.: Extension of the cosmic-ray energy spectrum beyond the predicted Greisen–Zatsepin–Kuz'min cutoff. Phys. Rev. Lett. **81**(6), 1163–1166 (1998)
154. Tassoul, J.L.: Theory of Rotating Stars. Princeton University Press, Princeton, NJ (1978)
155. Tatarakis, M., Watts, I., Beg, F.N., et al.: Laser technology: Measuring huge magnetic fields. Nature **415**(6869), 280 (2002)
156. The European X-Ray Laser Project XFEL http://xfel.desy.de/
157. Trodden, M., Feng, J.: Dark worlds: A shadow cosmos, woven silently into our own, may have its own rich inner life. Sci. Am. **303**(5), 38–45 (2010)
158. Troitskii, S.V.: Unsolved problems in particle physics. Phys. Usp. **55**(1), 72–95 (2012)
159. Trubnikov, B.A.: Shock-wave and plasma-pinch mechanisms of galactic cosmic-ray production. J. Exp. Theor. Phys. **101**(1), 160 (2005)
160. Trunin, R.F.: Shock compressibility of condensed materials in strong shock waves generated by underground nuclear explosions. Phys. Usp. **37**(11), 1123 (1994)
161. Tyul'Bashev, S.A.: The physical parameters of several extragalactic radio sources displaying rapid variability. Astron. Rep. **49**, 967–972 (2005)
162. Tzortzakis, S., Mechain, G., Patalano, G., et al.: Coherent subterahertz radiation from femtosecond infrared filaments in air. Opt. Lett. **27**(21), 1944–1946 (2002)
163. Vacca, J.R. (ed.): The World's 20 Greatest Unsolved Problems. Prentice Hall PTR, Englewood Cliffs (2004)
164. Vainshtein, S.I., Zeldovich, Y.B., Ruzmaikin, A.A.: The Turbulent Dynamo in Astrophysics. Nauka, Moscow (1980)
165. Vinci, T., Loupias, B., Koenig, M., et al.: Laboratory astrophysics using high energy lasers: need for 2D simulation. J. Phys. Conf. Ser. **112**(4), 042012 (4pp) (2008)
166. Vladimirov, A.S., Voloshin, N.P., Nogin, V.N., et al.: Shock compressibility of aluminum at $p > 1$ Gbar. JETP Lett. **39**(2), 82 (1984)
167. Vlemmings, W.H.T., Bignall, H.E., Diamond, P.J.: Green bank telescope observations of the water masers of NGC 3079: accretion disk magnetic field and maser scintillation. Astrophys. J. **656**(1), 198 (2007)
168. Wakker, B.P., Richter, P.: Our growing, breathing galaxy. Sci. Am. **290**(1), 38–47 (2004)

169. Waxman, E.: Gamma-ray bursts and collisionless shocks. Plasma Phys. Controlled Fusion **48**(12B), B137–B151 (2006)
170. Weiler, T.J.: Cosmic-ray neutrino annihilation on relic neutrinos revisited: a mechanism for generating air showers above the Greisen–Zatsepin–Kuzmin cutoff. Astropart. Phys. **11**(3), 303–316 (1999)
171. Weinberg, S.: The cosmological constant problem. Rev. Mod. Phys. **61**, 1–23 (1989)
172. Willingale, L., Mangles, S.P., Nilson, P.M., et al.: Collimated multi-MeV ion beams from high-intensity laser interactions with underdense plasma. Phys. Rev. Lett. **96**(24), 245002 (2006)
173. Woolsey, N.C., Ash, A.D., Cortois, C., et al.: Collisionless plasma astrophysics simulation experiments using lasers. AIP Conf. Proc. **827**, 365–375 (2006)
174. Yakovlev, D.G., Levenfish, K.P., Shibanov, Y.A.: Cooling of neutron stars and superfluidity in their cores. Phys. Usp. **42**(8), 737 (1999)
175. Zakharov, A.F., Nucita, A.A., De Paolis, F., Ingrosso, G.: Apoastron shift constraints on dark matter distribution at the galactic center. Phys. Rev. D **76**, 062001 (2007)
176. Zakharov, A., Capozziello, S., De Paolis, F., et al.: The role of dark matter and dark energy in cosmological models: theoretical overview. Space Sci. Rev. **148**, 301–313 (2009)
177. Zasov, A.V., Postnov, K.A.: Obshchaya astrofizika (General Astrophysics). Vek 2, Fryazino (2006)
178. Zasov, A.V., Surdin, V.G.: Raznoobrazie galaktik (A variety of galaxies). In: Surdin, V.G. (ed.) Astronomiya: Vek XXI (Astronomy: XXIst Century), p. 329. Vek 2, Fryazino (2007)
179. Zatsepin, G.T., Kusmin, V.A.: Top boundary of cosmic ray spectrum. JETP Lett. **4**(3), 78 (1966)
180. Zavala, R.T., Taylor, G.B.: Faraday rotation measures in the parsec-scale jets of the radio galaxies m87, 3c 111, and 3c 120. Astrophys. J. Lett. **566**(1), L9 (2002)
181. Zel'dovich, Y.B., Novikov, I.D.: Relativistic Astrophysics (in Russian). Nauka, Moscow (1967). [English Transl.: Relativistic Astrophysics. University of Chicago Press, Chicago (1971)]
182. Zel'dovich, Y.B., Raizer, Y.P.: Fizika udarnykh voln i vysokotemperaturnykh gidrodinamicheskikh yavlenii, 2nd edn. Nauka, Moscow (1966). [English Transl.: Physics of Shock Waves and High-Temperature Hydrodynamic Phenomena. Dover, Mineola (2002)]
183. Zel'dovich, Y.B., Levich, E.V., Syunyaev, R.A.: Stimulated Compton interaction between Maxwellian electrons and spectrally narrow radiation (in Russian). Zh. Eksp. Teor. Fiz. **62**(4), 1392–1408 (1972)
184. Zelenyi, L.M., Verigin, M.I., Zakharov, A.V., et al.: The heliosphere and the interaction of the terrestrial planets with the solar wind. Phys. Usp. **48**(6), 615 (2005)

Chapter 11
Conclusion

The science of the structure of matter at high energy densities and cosmic physics are closely related and interwoven [1]. On the one hand, the solution of almost any cosmophysical problem is impossible without invoking information about the structure of matter of the corresponding celestial object. On the other hand, cosmic physics furnishes nuclear and subnuclear physical information, which will substantially supplement the data obtainable in terrestrial laboratories. This applies, for instance, to the characteristics of nuclear forces (pulsar data) and to the number of neutrino species (cosmological data).

The role of cosmos (especially, of the Universe as a whole) as a source of fundamental data would be expected to rise in importance in the future as well. This is so because the limits of the potential of accelerator physics are already in sight. At the same time, the permanently emerging new opportunities in experimental high-energy-density physics give hope that the ultraextreme states of matter that are so typical of the Universe around us can be reproduced under laboratory conditions.

And though the limiting pressures in laboratory plasmas so far differ from the highest astrophysical values by 20–30 orders of magnitude, this gap is rapidly shrinking. The physical processes in a laboratory and in space quite frequently exhibit an amazing diversity and, at the same time, striking similarities, thereby testifying, at the least, to the uniformity of the physical principles of the behavior of matter over an extremely broad range of pressures (42 order of magnitude) and temperatures (up to 10^{13} K).

This all defies the most vivid imagination, and, as pointed out by Voltaire, "... in nature this phenomenon is perfectly natural and commonplace. The domains of some rulers in Germany and Italy, which can be circled in about a half hour, when compared with the empires of Turkey, Moscow, or China, give only a faint idea of the remarkable contrasts that are hidden in all of nature" (Voltaire, Le Micromegas, Paris 1752).

© Springer International Publishing Switzerland 2016

V.E. Fortov, *Extreme States of Matter*, Springer Series in Materials Science 216,
DOI 10.1007/978-3-319-18953-6_11

Reference

1. Kirzhnits, D.A.: Lektsii po fizike (Lectures on Physics). Nauka, Moscow (2006)